Copyright © 2003 Swets & Zeitlinger B.V., Lisse, The Netherlands

PROCEEDINGS OF THE INTERNATIONAL SYMPOSIUM ON GROUNDWATER PROBLEMS RELATED TO GEO-ENVIRONMENT, OKAYAMA, JAPAN, 28–30 MAY 2003

Groundwater Engineering – Recent Advances

Edited by
Iichiro Kono
Makato Nishigaki
Mitsuru Komatsu
Okayama University, Okayama, Japan



A.A. BALKEMA PUBLISHERS LISSE / ABINGDON / EXTON (PA) / TOKYO

Copyright © 2003 Swets & Zeitlinger B.V., Lisse, The Netherlands

Copyright © 2003 Swets & Zeitlinger B.V., Lisse, The Netherlands

All rights reserved. No part of this publication or the information contained herein may be reproduced, stored in a retrieval system, or transmitted in any form or by any means, electronic, mechanical, by photocopying, recording or otherwise, without written prior permission from the publisher.

Although all care is taken to ensure the integrity and quality of this publication and the information herein, no responsibility is assumed by the publishers nor the author for any damage to property or persons as a result of operation or use of this publication and/or the information contained herein.

Published by: A.A. Balkema, a member of Swets & Zeitlinger Publishers
www.balkema.nl and www.szp.swets.nl

ISBN 90 5809 385 9

Printed in the Netherlands

Copyright © 2003 Swets & Zeitlinger B.V., Lisse, The Netherlands

Table of Contents

Preface XI

Organization XIII

Acknowledgements XV

Invited lectures

Multiple manifestations of hydrogeologic scaling and their joint theoretical interpretation 3
S.P. Neuman & V. Di Federico

Observational method for tunnel construction considering environmental impact to groundwater 17
Y. Ohnishi, H. Ohtsu, T. Nishioka, Y. Naka, T. Yasuda & K. Takahashi

Evaluation of benefits of partial source zone treatment using intermediate-scale physical model testing and numerical analysis 25
S. Saenton & T.H. Illangasekare

The contribution of natural attenuation processes for the remediation of contaminated sites 37
P. Werner

Dynamics of solute exchange between a fracture and the surrounding matrix 41
R. Wallach

Groundwater mechanics in flood risk management 53
F.B.J. Barends

Keynote lectures

Mitigation of the effects induced by the rise of the water table around underground structures 69
A. Cividini & G. Gioda

Evaluating risk after remediation for NAPL contaminated sites 75
K. Soga, I.H. Kulasooriya, A.C. Mesquita, J.W.E. Page & W.A.P. Waduge

Groundwater and geoenvironmental quality issues in the Langat Basin, Malaysia 89
M.R. Taha

Saline water intrusion into fresh groundwater aquifer at eastern area, Cheju Island, Korea 99
G.C. Jeong, S.A. Booh, Y.S. Ko & B.D. Ro

Operational systems for water management under extreme climatic conditions 111
P.-W. Graeber

Characterization and modeling of hydraulic property of fractured rock mass 119
A. Kobayashi

Dewatering at excavation sites

Construction management to secure the water sealing function of underground LPG storage cavern tanks 135
H. Megumi, K. Shibata, K. Baba & T. Tobase

Copyright © 2003 Swets & Zeitlinger B.V., Lisse, The Netherlands

Blow-out of soil particles during construction of a caisson type pile 139
T. Tanaka, S. Minami & R. Matsuura

Three-dimensional numerical investigation of piping for excavations in cohesionless soils 145
F. Cai & K. Ugai

An example of groundwater control measures in large-scale open-cut works 151
A. Ogata & N. Ikoma

Simplified design method of deepwells placed in excavation area 161
N. Kohsaka & A. Ishikawa

Effects of subsurface water on stability of slopes

Changes in strength characteristics of rock-powder under the action of carbonic acid 171
N.P. Bhandary, K. Hirota, R. Yatabe & K. Yokota

Failure of cut slopes in the Izumi group and associated action of groundwater 177
J. Uchida, R. Yatabe, K. Yokota & N. Yagi

The change in suction and water content in natural Masado slopes due to rainfall 181
Thi Ha, T. Moriwaki, Y. Sasaki, S. Kano & A.K. Dissanayake

Preservation of natural groundwater flow

Influence of spatial distribution of caves on salt-water intrusion in Ryukyu limestone aquifer in Komesu underground dam basin, Okinawa Island 191
M. Imaizumi, S. Ishida, T. Tsuchhara & M.A. Fazal

Soil structure and change of free groundwater in the Kanto Loam formation 199
H. Narioka & M. Komamura

Instability of foundations undergoing rise in groundwater level 205
K. Yasuhara, S. Murakami & S. Mitsuyama

Simulations on the effects of tillage on pressure head, subsurface drainage, and groundwater recharge 211
T. Moroizumi

Basic concept on preservation of natural groundwater flows from intercepting by underground structure 217
M. Tambara, M. Nishigaki, T. Hashimoto, Y. Shinshi & K. Daito

Investigation procedure for preserving groundwater flows 223
T. Hashimoto, Y. Ando, K. Noda, J. Miyagawa

Design on groundwater flow preservation measures 229
I. Komatsu, T. Sugimura, K. Namikawa, N. Imai, T. Ogata, Y. Sakayama, N. Kohsaka & Y. Matsuda

Construction of preservation facilities on natural groundwater flows 237
S. Kusumoto, H. Omae, T. Sato, M. Watanabe, N. Kobayashi & K. Nishida

Methods on observing groundwater flow and maintaining facilities for preserving natural groundwater flows 243
S. Hamate, Y. Hanaoka, T. Kozato & T. Sugimoto

Groundwater flow preservation measures for linear underground structures in urbanized areas 247
S. Noda, M. Nishigaki, M. Terashima, T. Yamashita & T. Kisanuki

Preservation countermeasures for groundwater flow against the linear open cut tunnel in low alluvial plain with dissected valley 255
Y. Arai, M. Ohnishi, G. Imai, T. Kisanuki & M. Hirayama

Copyright © 2003 Swets & Zeitlinger B.V., Lisse, The Netherlands

A monitoring technique of remediation of groundwater using resistivity cones 265
M. Fukue, K. Kita, T. Minato, K. Makito & T. Chida

Groundwater studies and mitigation programs for arsenic contamination in Bangladesh 271
M.A. Fazal, M. Imaizumi, S. Ishida, T. Tsuchihara & T. Kawachi

Nitrate pollution in groundwater in the lower reach of the Yellow River, case study in Shandong Province, China 279
J. Chen, C. Tang, Y. Sakura & Y. Shen

Some considerations on the restorative effectiveness and efficiency of the groundwater pumping in impervious wall 285
K. Aoki, K. Hioki, K. Harada & M. Yamamoto

Numerical simulation of impact by precipitation on bioremediation process of hydrocarbon-contaminated groundwater 291
D.J. Song & A. Katayama

Copper adsorption by decomposed granite soil and its effect on the breakthrough curve 299
S. Sasaki & R. Lynch

Centrifuge modeling of LNAPL infiltration in sand deposits with an impervious sheet 305
Y. Hayashi & H.G.B. Allersma

In-situ electrokinetic and hydraulic remediation of saturated aquifer contaminated by heavy metal 311
S. Shiba, K. Yamaberi, Y. Hirata & T. Seno

A designing method for in-situ bioremediation of TCE contaminated groundwater with cometabolic degradation 317
T. Kawai, J. Kawabata, M. Goto & S. Otuka

Subsurface environmental change after HRC injection 323
M. Nakashima, X. Wu & M. Nishigaki

Remediation of hydrocarbon contamination in groundwater using in-situ biosparging 329
K.R. Reddy & J.A. Adams

Nitrogen contamination from fertilizer in tea plantation, Kiku River basin, Japan 335
H. Ii, K. Yamano, T. Hirata, T. Tanaka & M. Nishikawa

Electro-chemical remediation of VOCs contaminated groundwater 343
T. Miura & H. Kubo

Evaluation of remedial actions for a contaminated site using risk assessment approaches 351
M. Kamon, T. Inui, T. Katsumi, A. Doi & D. Miyagi

DNAPL contaminant mass outflux rate and its relation to remediation cleanup level 359
J.W.E. Page, K. Soga & N.S. Gowers

Contaminant migration from a line source: a mathematical model 367
A.P.S. Selvadurai

Influence of the kinematic viscosity of oil contaminants in the compaction and hydraulic conductivity in certain type of soils 373
J.C. Rojas, L.M. Salinas & I.D. Garnica

Large-scale model test of ethanol-bentonite slurry cutoff wall 379
M. Asada, A. Ishikawa & S. Horiuchi

Field investigation of groundwater contamination due to nitric acid in Matsumoto Basin, Nagano, Japan 387
S. Nakaya, A. Ikeuchi, I. Ohmiya, H. Komiya, H. Masuda & M. Kusakabe

On predicting the effects of hexavalent chromium leached from cement treated soil 393
N. Tsuneoka, H. Mori & T. Obata

Copyright © 2003 Swets & Zeitlinger B.V., Lisse, The Netherlands

Field survey and determination of hydraulic properties

A study on evaluating hydraulic conductivity of soil with numerical analysis of groundwater flow and resistivity investigation 403
Y. Sun & M. Inoue

A study on clogging characteristics of recharge well depended on hydraulic gradient 409
T. Shimizu & M. Aoki

Studies on natural and artificial recharge mechanisms in diluvial upland using ^{222}Rn concentration in groundwater as tracer 417
S. Ishida, M. Imaizumi, T. Tsuchihara & M.A. Fazal

Estimation method of permeability distributions of rock mass with fracture frequency 423
A. Kobayashi, S. Aoyama, K. Inoue & I. Fukushima

Application of directional core drilling system to geological evaluation of liquefied petroleum gas underground storage base at Kurashiki site 431
K. Kojima, T. Otake, T. Tani & Y. Moriguchi

Strong evidence for permeability scale effect in fractured rock 437
W.A. Illman, S.P. Neuman, V.V. Vesselinov & A.G. Guzman

Subsurface structure and groundwater of the Takamatsu crater (cauldron) by CSAMT method and boring data 443
S. Hasegawa, S. Kanayama, T. Kozato & H. Ishii

Discrimination of shallow and deep permeable zones by time-series electric prospecting in a rock mass slope 451
E. Tamura, S. Hasegawa, S. Tsuruta & S. Kanayama

Investigations and tests for evaluating the permeability of pyroxene andesite 459
T. Kakue & H. Kishi

Laboratory column test for measuring long-term partial saturation in sand 467
A. Ishikawa, N. Kohsaka, N. Miyake & M. Amari

Comparison of analysis methods of slug test data sets: usage of Hvorslev and Cooper et al. methods 471
Y. Shinshi, H. Kano, S. Takeuchi & K. Nakano

Determination of unsaturated hydraulic conductivity taking account of in-situ test 475
T. Sugii & T. Okumura

Application of highly viscous fluid tests to jointed rock masses and evaluation of test results 483
H. Kishi, T. Kakue & M. Nishigaki

Modeling and analysis of groundwater flow

A new three-dimensional analysis system for seepage problem applying a meshless method 493
H. Sakurai & M. Kawahara

A groundwater flow analysis at coastal area considering regression and transgression 501
M. Tanaka, J. Kawabata, M. Toida, T. Hishiya, E. Sugimoto, M. Nishigaki & T. Hasegawa

Numerical analysis for seepage of rainwater and evaporation of pore water in unsaturated soil 509
K. Sako, R. Kitamura & Y. Miyamoto

Groundwater modelling of the Triassic Sandstone aquifer in the Selby area, North Yorkshire, UK 517
K. Yoshida, L.J. West & S.H. Bottrell

VRML modeling of subsurface and groundwater movement 523
K. Yamada

Copyright © 2003 Swets & Zeitlinger B.V., Lisse, The Netherlands

An integrated stream and groundwater model for simulating groundwater-stream exchange in an alluvial plain, Kofu basin 531
X.-W. Zhang, X.-H. Zhang, K. Takeuchi & H. Ishidaira

Experimental study of permeability of a minute gap 539
T. Yoden, T. Deguchi & N. Matsui

The effect of underground liquefied petroleum gas storage base construction to the surface oil-refinery complex facilities at Kurashiki 545
J. Oriyama, T. Otake, K. Taniuchi & T. Yamaishi

Geochemical approaches to understanding a deep groundwater flow system in the Tono area, Gifu-ken, Japan 555
R. Metcalfe, K. Hama, K. Amano, T. Iwatsuki & H. Saegusa

Hydrogeological modeling and groundwater flow simulation for effective hydrogeological characterization in the Tono area, Gifu, Japan 563
H. Saegusa, K. Inaba, K. Maeda, K. Nakano, G. McCrank & A. Sawada

Fundamental characteristics of transport phenomenon in unsaturated zone 571
K. Inoue, A. Kobayashi, N. Teramura & S. Aoyama

Prediction error of groundwater behavior by inverse modeling with bootstrap re-sampling method 579
K. Masumoto

Analysis of groundwater flow around a fault zone in fractured rock mass – use of fractured rock aquifer as a reliable groundwater sources for Tangalle area, Sri Lanka 585
D.G.K.M. Kumari, K. Watanabe & Y. Morita

Use of DEM to model the contact force between soil particles in moist condition 593
H. Fujimura & H. Kiyama

Advection and dispersion analysis in Gaussian and non-Gaussian random field of permeability 597
S. Nishimura, A. Murakami, T. Nishiyama & H. Fujii

Case studies on designs of multi-well system with matrix scheme 605
Y. Shinshi, H. Kano & T. Wada

Numerical modeling of the groundwater flow changes due to the construction of the Äspö Hard Rock Laboratory 611
T. Hasegawa & Y. Tanaka

3D lattice Boltzmann simulation of fluid flow in fractured rock 619
T. Miyoshi, T. Matsuoka, S. Murata & Y. Ashida

Copyright © 2003 Swets & Zeitlinger B.V., Lisse, The Netherlands

Preface

Since time immemorial, man has depended much on surface water supplies. However, increased human population and industrialization in the last century has led to increased exploitation of groundwater resources in order to meet the demand for freshwater supplies. The demand for groundwater resources has further increased as a result of climate change and variable rainfall patterns that are now common in most parts of the world and which may be the cause of the drying up of rivers. In addition to exploiting the groundwater, the soil is exploited in agriculture, engineering and construction. Urbanization has also led to the exploitation of the deeper layers of the soil, during the construction of underground structures. Resulting from this has been the interruption of natural flow of groundwater. Contamination and pollution from industries and modern way of living by man are also having telling effects on the geo-environment. The effects of all these are varied and it is important to understand them and the soil and groundwater. So that, in the end, we could manage the geo-environment on a sustainable basis.

This book contains peer reviewed papers presented at the *International Symposium on Groundwater Problems Related to Geo-environment* held in Okayama, Japan, in May 2003. The symposium was organized to promote the exchange of ideas, and the latest developments in research and practice in the fields of geo-environment and groundwater from all over the world. The papers in the book have been grouped into six major themes. These are dewatering at excavation sites, effects of subsurface water on stability of slopes, preservation of natural groundwater flow, contamination of soil and groundwater: investigation, prediction and remediation, field survey and determination of hydraulic properties and modeling and analysis of groundwater flow.

The symposium was organized by the Japanese Geotechnical Society, in collaboration with the Japan Society of Civil Engineers, the Japan Society of Irrigation, Drainage and Reclamation Engineering and the Japanese Association of Groundwater Hydrology. We would like to express our gratefulness to Professors H. Fujii and T. Hanamura of Okayama University for undertaking the roles of vice-chairmen of the symposium. We also wish to thank the members of the organizing, the advisory and executive committees for their kind co-operation in the preparation and organization of the symposium. Our sincere gratitude also goes to all the keynote and invited lecturers of the symposium for their expert contributions. Last, but not the least, we are very grateful to all and sundry for making the symposium a success.

I. Kono
M. Nishigaki
M. Komatsu

Copyright © 2003 Swets & Zeitlinger B.V., Lisse, The Netherlands

Organization

ORGANIZING COMMITTEE
I. Kono, *Chairman*
M. Nishigaki, *Vice-Chairman/Secretary General*
T. Hanamura, *Vice-Chairman*

Advisory Members:

K. Ito	A. Omata	S. Kamewada
S. Kusati	Y. Kotani	N. Kobayashi
H. Komada	I. Seko	T. Hashimoto
M. Hirayama	H. Fujii	M. Furuichi
T. Maekawa	N. Miyake	K. Mori
H. Yamaji	M. Yamashita	

International Advisory Members:

T.H. Illangasekare	Y. Ohnishi	M. Kamon
G. Gioda	P.W. Graeber	A. Kobayashi
G.C. Jeong	K. Soga	M.R. Taha
C. Tang	S.P. Neuman	F.B.J. Barends
H. Yokota	P. Werner	R. Wallach

Scientific Members:

K. Aoki	M. Asada	H. Ii
T. Ishida	K. Ugai	M. Enoki
T. Katsumi	J. Kawabata	R. Kitamura
Y. Sakura	Y. Sasaki	S. Sasaki
K. Sato	K. Jinno	T. Sugii
K. Daito	T. Tanaka	N. Tsuneoka
K. Nakagawa	M. Nakashima	S. Nakaya
S. Hasegawa	T. Hishiya	M. Fukue
K. Fukumura	H. Fujimura	K. Masumoto
T. Moriwaki	K. Yasuhara	R. Yatabe
Y. Yamaguchi	R. Yoshioka	K. Watanabe

EXECUTIVE COMMITTEE

Members:

S. Imamura	A. Irie	T. Ohnishi
K. Okuyama	T. Katuhara	M. Kawasaki
K. Kankam-Yeboah	N. Kosaka	M. Komatsu
M. Shimomura	Y. Shinshi	K. Takimoto
Y. Takeshita	N. Tanaka	Y. Tsuchiya
T. Adrin	H. Narioka	S. Nishimura
T. Nishiyama	Y. Maeda	S. Mikake
A. Murakamii	J. Morita	T. Moroizumi
S. Yoshida		

Copyright © 2003 Swets & Zeitlinger B.V., Lisse, The Netherlands

Acknowledgements

The editors would like to express their sincere gratitude to the following persons, who helped to review the manuscripts and to improve the technical standard of the papers in this proceeding.

K. Ando
H. Ito
H. Komine
T. Shiraishi
S. Tanaka
H. Nakajima
S. Hosoya
T. Yoden
T. Ishii
T. Ogawa
T. Shimizu
M. Takahashi
M. Tanaka
T. Hasegawa
K. Miyakawa
Y. Ijiri
K. Kamiya
M. Shimo
A. Takeuchi
M. Chijimatsu
S. Hamate
K. Momii

Copyright © 2003 Swets & Zeitlinger B.V., Lisse, The Netherlands

Invited lectures

Copyright © 2003 Swets & Zeitlinger B.V., Lisse, The Netherlands

Multiple manifestations of hydrogeologic scaling and their joint theoretical interpretation

S.P. Neuman
Department of Hydrology and Water Resources, University of Arizona, Tucson, Arizona, USA

V. Di Federico
DISTART, Università di Bologna, Bologna, Italy

ABSTRACT: There is mounting evidence that hydrogeologic variables exhibit isotropic or directional dependencies on scales of measurement (data support), observation (extent of phenomena such as a dispersing plume), sampling window (domain of investigation), spatial correlation (structural coherence) and spatial resolution (descriptive detail). It appears possible to interpret these multiple scale-dependencies within a unified theoretical framework.

1 MULTIPLE MANIFESTATIONS OF SCALE DEPENDENCE

There is growing evidence that hydrogeologic variables tend to vary with scale. This scale dependence manifests itself in a multiplicity of ways, reviewed briefly in the following paragraphs.

1.1 *Dependence on support volume*

One manifestation of hydrogeologic scaling is the observed dependence of permeabilities on their scale of measurement (support volume, Figure 1).

Figure 2 depicts two superimposed profiles of hydraulic conductivity as determined by packer tests in a single borehole penetrating fractured granitic rocks near Finnsjön Lake in Sweden (Andersson et al., 1998). One profile represents permeabilities obtained from measurements of steady state pressure and flow rate during continuous injection of water into borehole intervals of 20 m, the other into intervals of 2 m. The packer test results clearly depend on the nominal scale of the test.

Figure 3 shows superimposed profiles of air permeability as determined by packer tests in four bore-holes penetrating unsaturated fractured tuff at the University of Arizona Apache Leap Research Site (ALRS) near Superior, Arizona (Chen et al., 2000). The permeabilities were obtained by Guzman et al. (1996) from measurements of steady state pressure and flow rate during continuous injection of air into borehole intervals of 0.5, 1, 2 and 3 m. Taking the distance between packers to represent a nominal support scale one finds that, in general, the amplitude and frequency of spatial variations in permeability decrease as the support scale increases.

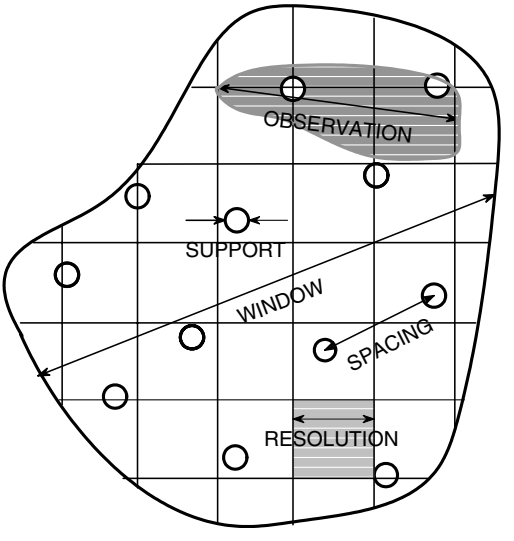


Figure 1. Some of the scales affecting hydrogeologic variables.

Figure 4 summarizes laboratory and field permeability data from crystalline rocks at a variety of sites and suggests that these data vary with the scale of

Copyright © 2003 Swets & Zeitlinger B.V., Lisse, The Netherlands

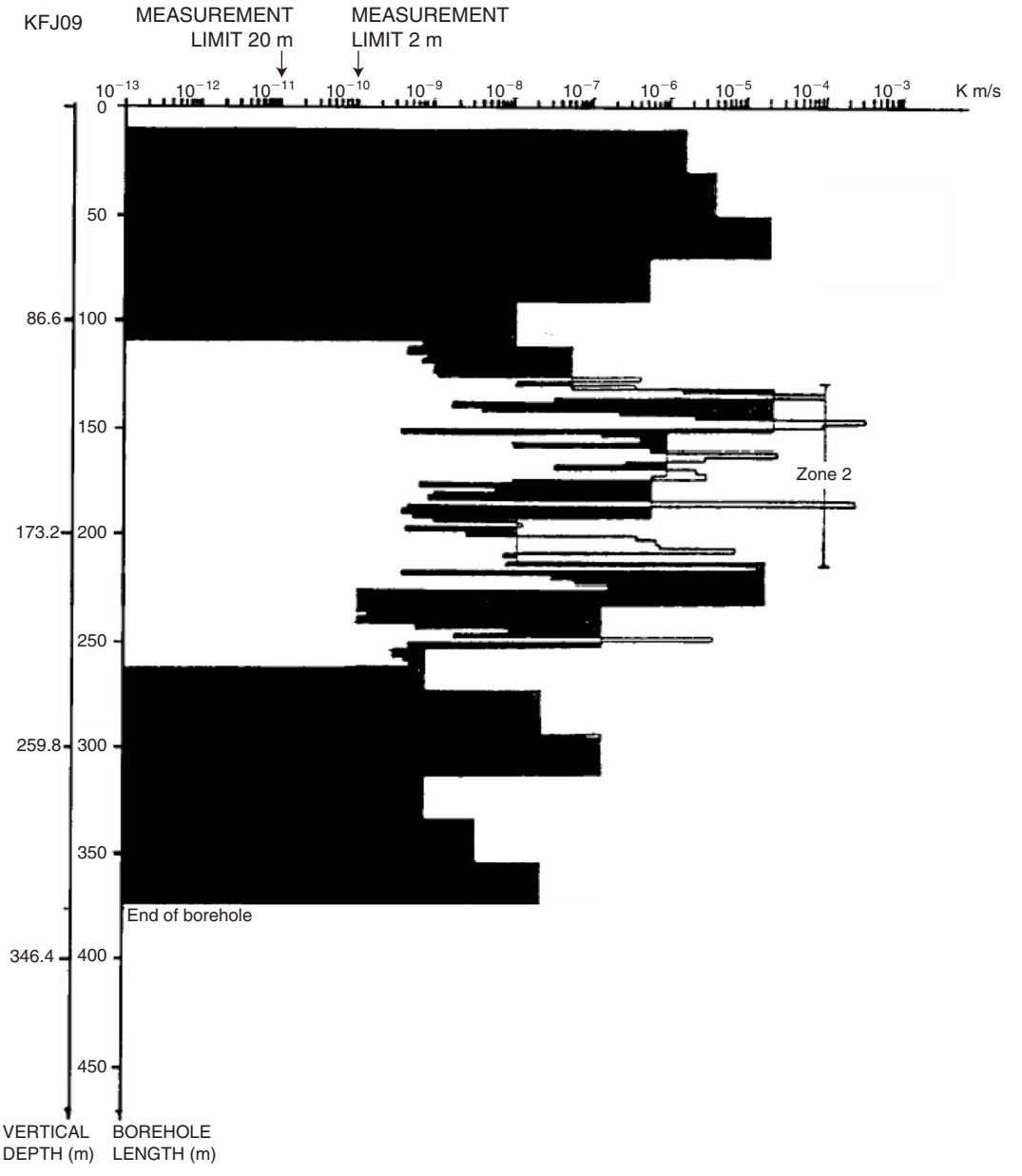


Figure 2. Hydraulic conductivity of fractured granitic rocks near Finnsjön, Sweden, as determined in 2-m and 20-m sections of a borehole (from Andersson et al., 1998).

measurement (Clauser, 1992, adapted by Neuman, 1994).

Variations of permeability or transmissivity with scale have also been reported by Bradbury and Muldoon (1990), Rovey and Cherkauer (1995), Tidwell and Wilson (1997), Sánchez-Villa et al. (1996), Schulze-Makuch and Cherkauer (1998) and Schulze-Makuch et al. (1999). Martnez-Landa et al. (2000) have observed a notable scale effect when comparing the results of pulse, Horner, cross-hole and inflow tests in a saturated block of fractured granite at the Grimsel underground laboratory in Switzerland.

Copyright © 2003 Swets & Zeitlinger B.V., Lisse, The Netherlands

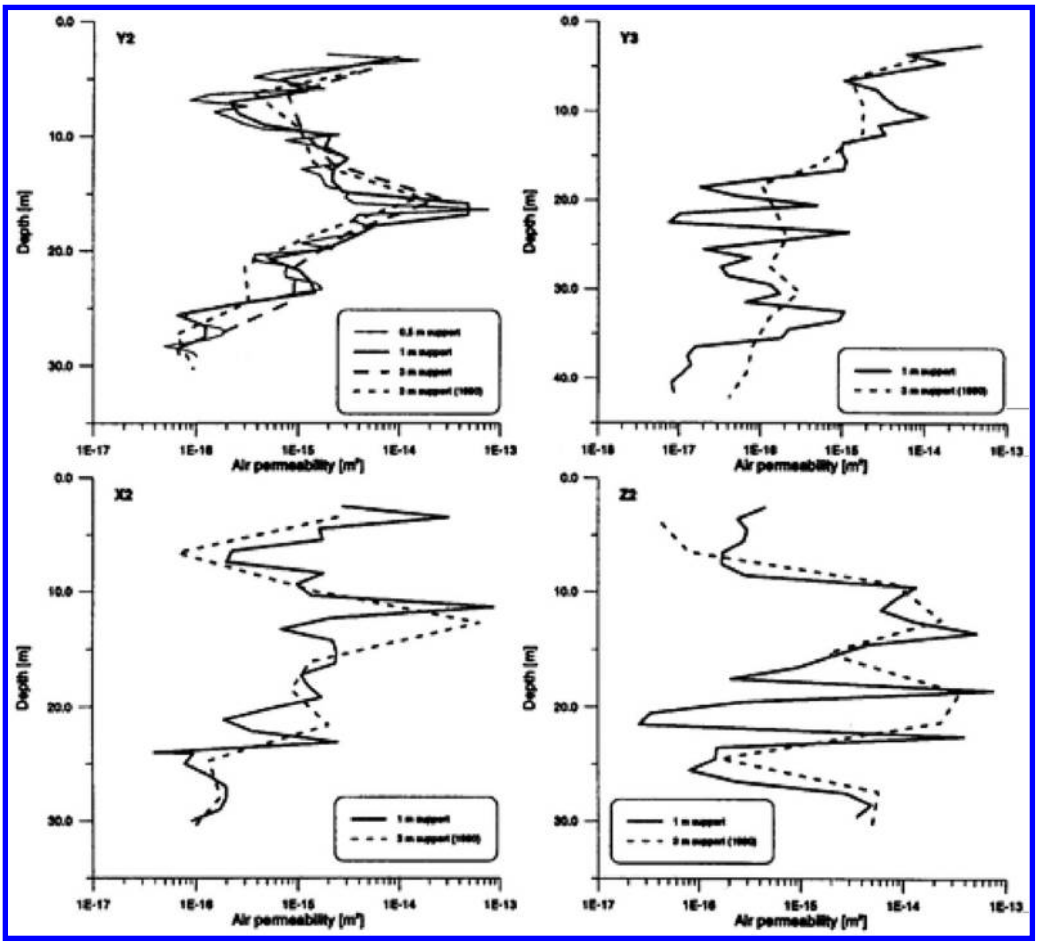


Figure 3. Variation of air permeability with depth and support scale at the ALRS (Chen et al., 2000).

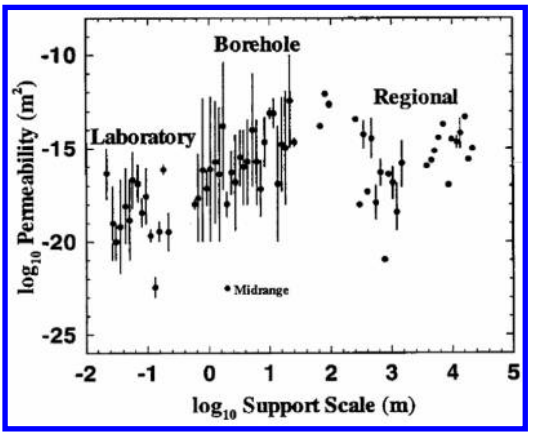


Figure 4. Permeability of crystalline rocks as a function of experimental scale (Clauser, 1992, adapted by Neuman, 1994).

Figure 5 compares permeabilities obtained for various hydrogeologic units at Yucca Mountain, Nevada, using single-hole and cross-hole pneumatic and hydraulic tests (Zyvoloski et al., 2002). As single-hole tests tend to sample smaller rock volumes than cross-hole tests, they generally yield lower values of permeability. Permeabilities obtained by model calibration are included for comparison.

1.2 *Dependence on observation scale*

Another manifestation of scaling is revealed when one considers apparent longitudinal dispersivities, from a variety of laboratory and field tracer studies world-wide, versus the scale of observation (Figure 6; Neuman, 1995). The latter is the scale at which a phenomenon, such as the propagation and spreading of a plume, is manifested (Figure 1). The dispersivity is termed apparent because it is determined on the basis

Copyright © 2003 Swets & Zeitlinger B.V., Lisse, The Netherlands

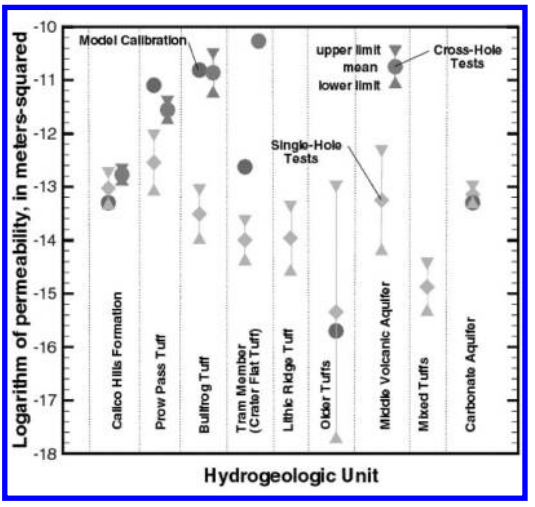


Figure 5. Permeabilities obtained for various hydrogeologic units at Yucca Mountain, Nevada, using single-hole and cross-hole pneumatic and hydraulic tests (Zyvoloski et al., 2002).

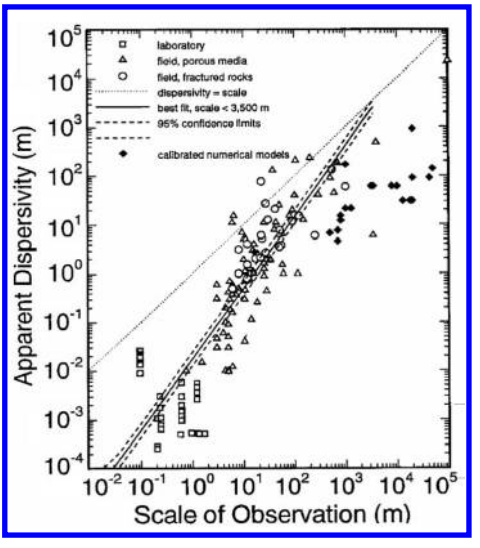


Figure 6. Apparent longitudinal dispersivities versus scale of observation (from Neuman, 1995).

of traditional advection-dispersion models which treat it as a constant. As Figure 6 clearly shows, the dispersivity is not constant but tends to increase with the scale of observation.

1.3 *Dependence on window scale*

Yet another manifestation of scaling is seen in Figure 7. Here λ represents the apparent integral scale of log hydraulic conductivities or transmissivities, which is

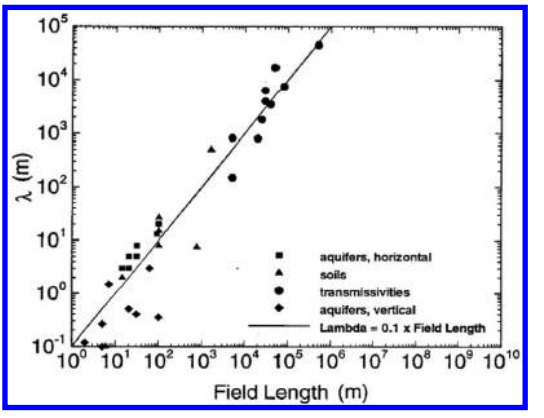


Figure 7. Apparent integral scale (λ) of natural-log hydraulic conductivities and transmissivities at various sites versus window scale (field length) (from Neuman, 1994; data from Gelhar, 1993).

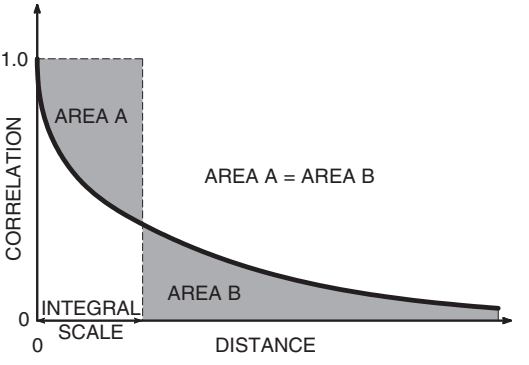


Figure 8. Definition of integral scale.

a measure of the distance within which these quantities are spatially auto-correlated and beyond which they are uncorrelated or weakly correlated (Figure 8). The integral scale is termed apparent because it is derived from variogram or spatial covariance models that consider it to be a constant. As Figure 7 clearly indicates, λ is not a constant but tends to increase with the size of the domain, or sampling window, containing the measured log conductivities or transmissivities (Figure 1).

1.4 *Dependence on resolution (and support) scale*

Another scale impacting hydrogeologic variables is their spatial resolution (Figure 1). Apparent dispersivities represented by open symbols in Figure 6 were derived from models that consider medium properties (permeability, transmissivity, porosity) to be spatially uniform. As such, these models provide zero resolution of the way in which these properties vary in

Copyright © 2003 Swets & Zeitlinger B.V., Lisse, The Netherlands

space; the scale of resolution is as large as the domain being modeled. Apparent dispersivities represented by full diamonds were derived from calibrated numerical models that consider medium properties to exhibit some degree of spatial variability. This increased level (reduced scale) of spatial resolution is seen to bring about a reduction in the rate at which apparent longitudinal dispersivities increase with the scale of observation. In other words, apparent dispersivity depends on the scale at which medium heterogeneity is being resolved.

To illustrate the dependence of permeability and porosity on both support and resolution scales we consider once again air injection tests conducted in partially saturated fractured tuff at the ALRS. Single-hole tests yielded values of air permeability at various locations throughout the tested rock volume on nominal scales of 0.5, 1.0, 2.0, and 3.0 m as illustrated in Figure 3. Cross-hole tests were conducted at the site by Illman et al. (1998) and analyzed in two ways: (a) by considering pressure records from individual borehole monitoring intervals one at a time, while treating the rock as being spatially uniform, and (b) by considering pressure records from multiple tests and borehole monitoring intervals simultaneously, while treating the rock as being randomly heterogeneous. The first approach included type-curve (Illman and Neuman, 2001) and numerical inverse analyses (Vesselinov et al., 2001a–b) of pressure data yielding a series of equivalent air permeabilities and air-filled porosities for a uniform medium at zero spatial resolution. The second approach (ibid) yielded a high-resolution geostatistical inverse estimate of how air permeability (Figure 9) and air-filled porosity (Figure 10), defined on grid blocks having a length-scale of one-meter, vary spatially throughout the tested rock volume. It amounted to three-dimensional pneumatic "tomography" or stochastic imaging of the rock at a spatial resolution scale of 1 m.

The results of these analyses have revealed a steep increase in the mean values of log permeability and log porosity estimates with the scale of estimation. The smallest scale, on the order of 1 m, corresponds to single-hole test results and to tomographic estimates based on the cross-hole tests. The largest scale, on the order of a few tens of meters, corresponds to type-curve and numerical inverse estimates obtained from cross-hole tests upon treating the rock as being spatially uniform. Mean values obtained by different methods of analysis at any given scale of estimation were generally comparable. Yet mean values obtained under the uniform rock assumption were consistently larger than those obtained by allowing pneumatic properties to vary spatially over distances of 1 m. For example, the mean of base 10 log permeability estimates obtained by numerical inversion of pressure data from five cross-hole tests (labeled PP4, 5, 6, 7, 8) when

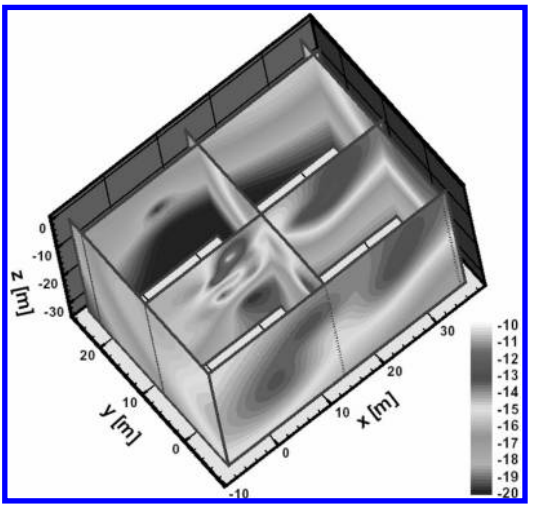


Figure 9. Three-dimensional tomographic image of base 10 log air permeability estimated by simultaneous inversion of cross-hole tests PP4, PP5 and PP6 at ALRS (Vesselinov et al., 2001b).

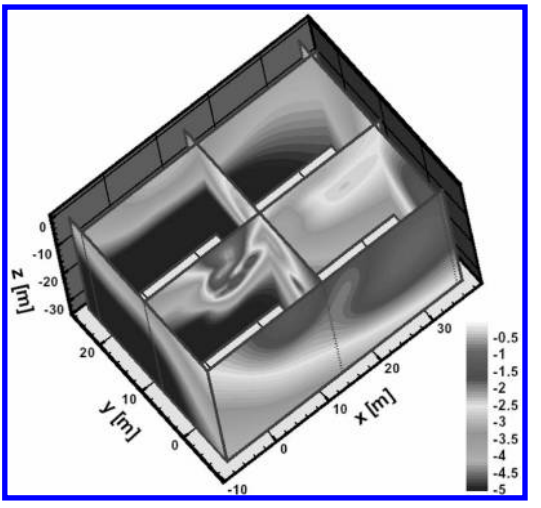


Figure 10. Three-dimensional tomographic image of base 10 log air-filled porosity estimated by simultaneous inversion of cross-hole tests PP4, PP5 and PP6 at ALRS (Vesselinov et al., 2001b).

treating the rock as being uniform exceeded the mean of tomographic inverse estimates from three of these tests (PP4, 5, 6) by 2.00 (Vesselinov et al., 2001b). This represents a 100-fold increase in the associated values of permeability. Corresponding estimates of porosity show an increase by a factor of about 22. The mean of log permeability estimates obtained by numerical inversion of pressure data from cross-hole tests PP4, 5, 6, 7, 8 when treating the rock as being uniform

Copyright © 2003 Swets & Zeitlinger B.V., Lisse, The Netherlands

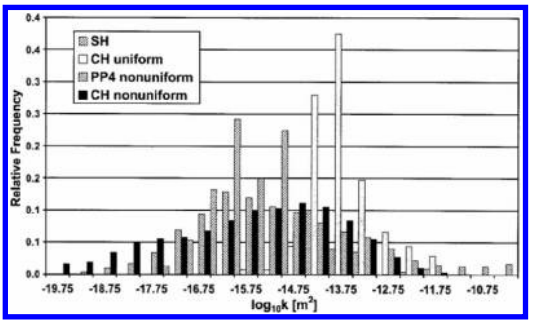


Figure 11. Histograms of log air permeability estimated at the ALRS by various approaches; SH = Single hole tests, CH = Cross-hole tests (Vesselinov et al., 2001b).

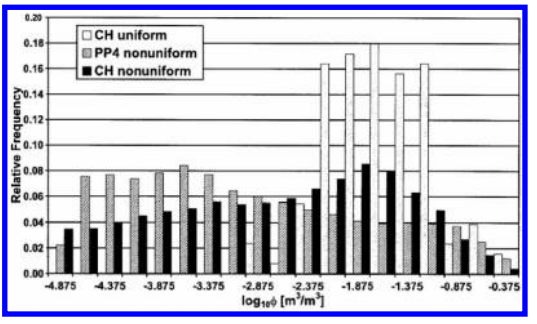


Figure 12. Histograms of log air-filled porosity estimated at the ALRS by various approaches; CH = Cross-hole tests (Vesselinov et al., 2001b).

exceeds the average of mean tomographic inverse estimates from three of these tests (PP4, 5, 6) by 1.38. This represents an increase in the associated values of permeability by a factor of about 24. Corresponding estimates of porosity show an increase by a factor of about 11.

The scale effect at the ALRS is reflected in histograms of estimates presented in Figures 11 and 12 (Vesselinov et al., 2001b). Histograms representing estimates of equivalent uniform pneumatic properties over relatively large rock volumes are offset to the right relative to those that represent estimates of spatially varying properties over smaller rock volumes. We see that treating the rock as being uniform on the scale of cross-hole tests yields higher mean estimates of permeability and porosity than are obtained upon resolving smaller-scale spatial variations in these fractured rock properties.

A similar finding was reported by Martinez-Landa et al. (2000) in the context of cross-hole tests in saturated fractured granites at the Grimsel site in Switzerland, interpreted by means of a numerical inverse model. Both findings are in line with an earlier conclusion by Neuman (1990, 1994) that the scale effect diminishes as one improves the degree to which spatial variability is explicitly resolved by the model that one uses to estimate these parameters.

1.5 *Directional dependence*

Hydrogeologic variables may exhibit different scaling behaviors in different directions. The most common manifestation of such anisotropy is the tendency of integral scales to be much larger parallel than normal to geologic stratification (Hufschmied, 1985; Sudicky, 1986). Hewett (1992), Molz and Boman (1993), Perez and Kalkar (1993), and Molz et al. (1998) have dealt with cases in which variables appeared to scale as fractional Brownian motion (fBm) parallel to stratification and fractional Gaussian noise (fGn) perpendicular to it. The theory presented later in this paper focuses on the first type of statistical anisotropy.

1.6 *Is the permeability scale effect real?*

Some authors have dismissed the observed increase in permeability with support scale as the artifact of a skin effect due to inadequate development of borehole test intervals (Butler and Healey, 1998a–b). It has been shown by Illman and Neuman (2000) that this argument does not apply to the ALRS. Rovey and Niemann (2001) have likewise demonstrated that skin effect was at most of minor importance in their analysis of hydraulic test data from outwash sand.

The observed permeability scale effect at the ALRS is clearly unrelated to the method of testing: there is consistency between single-hole and cross-hole test results. The scale effect is likewise unrelated to the method of test interpretation: there is consistency between results obtained by means of steady-state analytical formulae from single-hole test data (which in turn compare well with transient type-curve (Illman and Neuman, 2000) and inverse (Vesselinov and Neuman, 2001) analyses of the same data), and type-curve as well as numerical inverse interpretations of cross-hole test data.

Rovey (1998) has shown numerically that a scale effect may arise from the dual nature of a porous fractured rock. It has been pointed out by Chen et al. (2000) that this does not apply to the ALRS where airflow was restricted largely to fractures, the matrix having remained almost completely saturated with water.

Sánchez-Villa et al. (1996) have demonstrated numerically that randomly varying transmissivities could exhibit a scale effect due to deviations from log normal distribution. At the ALRS, spatial increments of 1-m scale log permeability data corresponding to lags of 1–3 m are indeed represented more accurately by a Lévy stable than by a Gaussian distribution (Hyun, 2002). However, increments corresponding to larger lags are virtually Gaussian.

Copyright © 2003 Swets & Zeitlinger B.V., Lisse, The Netherlands

The permeability scale effect at the ALRS appears to be real, and the same is probably true at many other sites.

2 UNIFIED THEORETICAL FRAMEWORK FOR INTERPRETATION OF HYDROGEOLOGIC SCALE DEPENDENCIES

We saw how (a) permeability varies with its support scale; (b) dispersivity varies with the scale of plume observation; (c) spatial correlation varies with the scale of the sampling window; and (d) permeability, porosity and dispersivity vary with the scales of their spatial resolution. A unified scaling theory that captures all of these phenomena, including statistical anisotropy, has recently been advanced by Di Federico and Neuman (1997, 1998a–b) and Di Federico et al. (1999); see also Neuman and Di Federico (1998). It rests on the observation that log permeability, $y = \ln k$, and other parameters such as porosity often appear to represent statistically nonhomogeneous (nonstationary) random fields with homogeneous spatial increments. When such a field is statistically isotropic and unbounded, it is associated with a power variogram $\gamma(s) = as^{2H}$, where a is a constant, s is separation distance (lag), and H is a Hurst coefficient. Since the variogram scales as $\gamma(rs) = r^{2H}\gamma(s)$, the field is self-affine and within the range $0 < H < 1$ constitutes a random fractal with dimension $D = E + 1 - H$, where E is Euclidean dimension. If the field is additionally Gaussian, it constitutes fractional Brownian motion (fBm).

2.1 *Truncated power variograms*

It has been demonstrated by Neuman (1990), Di Federico and Neuman (1997) and Di Federico et al. (1999) that the power variogram of a statistically isotropic or anisotropic fractal field can be constructed as the superposition of an infinity of exponential or Gaussian variograms of overlapping, homogeneous random fields (modes) having mutually uncorrelated increments and variance σ^2 proportional to a power $2H$ of the integral scale. The exponential variograms of several such modes are illustrated in Figure 13. Low- and high-frequency cutoffs may be introduced to filter out the effects of finite sampling window and nonzero data support, respectively. Intermediate cutoffs may be introduced to account for lacunarity due to gaps in the multiscale hierarchy, created by a hiatus of modes associated with discrete ranges of scales.

Following Di Federico et al. (1999), consider a statistically homogeneous and anisotropic random field $y(\boldsymbol{x})$ characterized by an elliptical variogram function. This means that there exist a system of principal

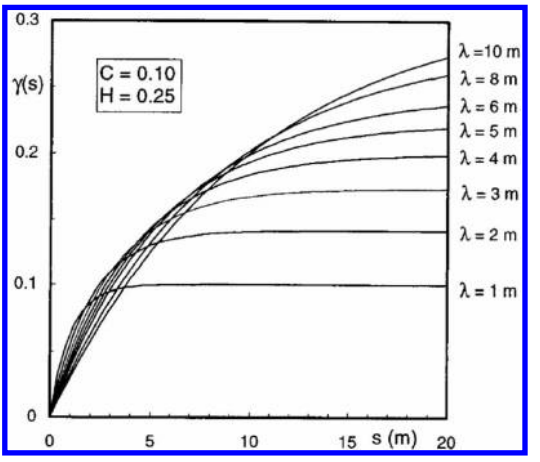


Figure 13. Superposition of exponential variograms with integral scales λ and variances $\sigma^2 = C/n^{2H}$ where C is the same as A in this paper, $n = 1/\lambda$ is mode number and $H = 0.25$ (after Di Federico and Neuman, 1997).

Cartesian coordinates $\boldsymbol{x}$, and corresponding principal spatial autocorrelation or integral scales λ, λ_2 and λ_3, such that the variogram becomes isotropic when $\boldsymbol{x}$ is transformed according to

$$\tilde{\boldsymbol{x}} = \mathbf{e}^{-1}\boldsymbol{x} \tag{1}$$

where

$$\mathbf{e} = \begin{pmatrix} 1 & 0 & 0 \\ 0 & e_2 & 0 \\ 0 & 0 & e_3 \end{pmatrix} \quad e_2 = \lambda_2/\lambda \quad e_3 = \lambda_3/\lambda \tag{2}$$

Then the variogram of $y(\mathbf{x})$ is given by

$$\gamma(\tilde{s}; n_l, n_u) = \gamma(\tilde{s}; n_l) - \gamma(\tilde{s}; n_u) \tag{3}$$

where for exponential modes $(0 < H < \frac{1}{2})$

$$\gamma(\tilde{s}; n_m) = \frac{A}{2Hn_m^{2H}}\left[1 - \exp(-n_m\tilde{s}) + (n_m\tilde{s})^{2H}\Gamma(1-2H, n_m\tilde{s})\right] \tag{4}$$

and for Gaussian modes $(0 < H < 1)$

$$\gamma(\tilde{s}; n_m) = \frac{A}{2Hn_m^{2H}}\left[1 - \exp\left(-\frac{\pi}{4}n_m^2\tilde{s}^2\right) + \left(\frac{\pi}{4}n_m^2\tilde{s}^2\right)^H \Gamma\left(1-H, \frac{\pi}{4}n_m^2\tilde{s}^2\right)\right] \tag{5}$$

Here

$$\tilde{s} = |\tilde{\boldsymbol{s}}| = s(\boldsymbol{u}^T\boldsymbol{e}^{-2}\boldsymbol{u})^{1/2} \tag{6}$$

Copyright © 2003 Swets & Zeitlinger B.V., Lisse, The Netherlands

is a separation distance in the transformed isotropic coordinates, $s = |\boldsymbol{s}|$ being the magnitude of a separation vector $\boldsymbol{s}$ in the original anisotropic coordinates and $\boldsymbol{u}$ a unit vector parallel to a given direction in these same coordinates; $n_l = 1/\lambda_l$ and $n_u = 1/\lambda_u$ are lower and upper cutoff modes associated with integral scales λ_l and λ_u, respectively; $m = l, u$; A is a constant having dimensions $[L^{-2H}]$ where L represents length; and $\Gamma(a, x)$ is the incomplete gamma function. The cutoff integral scales are related to the transformed length scales of the sampling window, $\tilde{L}_l$, and data support, $\tilde{L}_u$, via $\lambda_l = \mu\tilde{L}_l$ and $\lambda_u = \mu\tilde{L}_u$ where μ is an empirical constant. In the transformed isotropic domain of $\tilde{\boldsymbol{x}}$, $\tilde{L}_l$ and $\tilde{L}_u$ delineate cubic window and support volumes, which attain brick shapes upon back transformation into the original anisotropic coordinates.

Di Federico and Neuman (1997) have established empirically on the basis of Figure 7, and Hyun (2002) has confirmed numerically, that $\mu = 1/3$.

In the limit as $n_l \to 0$ ($\lambda_l \to \infty$ corresponding to an unbounded window) and $n_u \to \infty$ ($\lambda_u \to 0$ corresponding to zero support), (3) reduces to the power variogram

$$\gamma(s) = A_0 s^{2H} \tag{7}$$

where

$$A_0 = A\Gamma(1 - 2H)/2H \tag{8}$$

for exponential modes and

$$A_0 = A(\pi/4)^H \Gamma(1 - H)/2H \tag{9}$$

for Gaussian modes, Γ being the gamma function. Otherwise, (3) is a truncated power variogram with all modes having principal integral scales λ larger than λ_l and smaller than λ_u filtered out (excluded).

For $n_l \neq 0$ ($\lambda_l < \infty$, corresponding to a finite window), the truncated power variogram (3) defines a statistically homogeneous random field with finite variance

$$\sigma^2(n_l, n_u) = \sigma^2(n_l) - \sigma^2(n_u) \tag{10}$$

autocovariance

$C(\tilde{s}; n_l, n_u) = \sigma^2(n_l, n_u) - \gamma(\tilde{s}; n_l, n_u)$ given by

$$C(\tilde{s}; n_l, n_u) = C(\tilde{s}; n_l) - C(\tilde{s}; n_u) \tag{11}$$

and finite integral scale in the direction of $\boldsymbol{u}$ expressed as

$$I(n_l, n_u, \boldsymbol{u}) = \frac{2H}{1 + 2H} \frac{n_u^{1+2H} - n_l^{1+2H}}{n_u n_l (n_u^{2H} - n_l^{2H})} (\boldsymbol{u}^T \boldsymbol{e}^{-2} \boldsymbol{u})^{1/2} \tag{12}$$

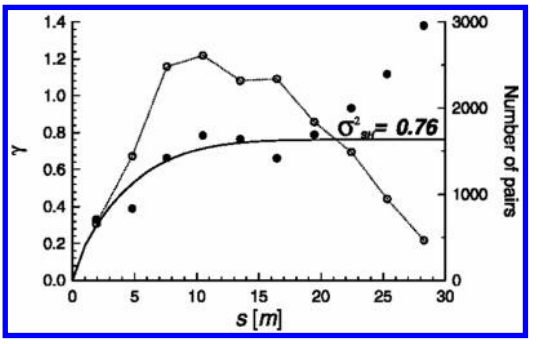


Figure 14. Truncated Gaussian variogram model (solid curve) with $A_0 = 0.19$, $2H = 0.75$, $\sigma^2 = 0.76$, and $\lambda_l = 9.02$ m fitted to 1-m scale single-hole base 10 log permeability data (solid circles) at the ALRS. Open circles represent number of data pairs (Hyun et al., 2002).

where

$$\sigma^2(n_m) = \frac{A}{2Hn_m^{2H}}. \tag{13}$$

In the absence of a high-frequency cutoff where $n_u \to \infty$ (zero support), (12) simplifies to

$$I(n_l, \boldsymbol{u}) = \frac{2H}{1 + 2H} \frac{1}{n_l} (\boldsymbol{u}^T \boldsymbol{e}^{-2} \boldsymbol{u})^{1/2} \tag{14}$$

In the isotropic case where $e_2 = e_3 = 1$ and $\tilde{s} \equiv s$, $(\mathbf{u}^T \mathbf{e}^{-2} \mathbf{u}) \equiv 1$.

Equations (1–11) establish an unambiguous relationship between the variance (σ^2), integral scale (I), and transformed length scales of data support ($\tilde{L}_l$) and sampling window ($\tilde{L}_u$) under either isotropic or anisotropic conditions. Suppose that one has fitted a truncated variogram model to a set of data which, in the transformed isotropic domain, have support scale $\tilde{L}_u$ and lie within a sampling window of scale $\tilde{L}_l$. The fit has yielded optimum estimates of the variogram parameters A and H, as is illustrated for air permeability data at the ALRS in Figure 14. The model could then be used to predict the way in which σ^2 and I would vary if the window was enlarged (upscaled) or reduced (downscaled); this was done in the context of the ALRS by Hyun et al. (2002).

2.2 *Consistency with data*

By analyzing jointly dispersivity (Figure 6) and permeability (Figure 7) data from many sites, Neuman (1990, 1994) found that they support a generalized power model with $H \simeq 0.25$. Figure 7 suggests that integral scales tend to increase linearly with domain size at a generalized rate of about 1/10. This is seen to be consistent with (14), expressed in equivalent

Copyright © 2003 Swets & Zeitlinger B.V., Lisse, The Netherlands

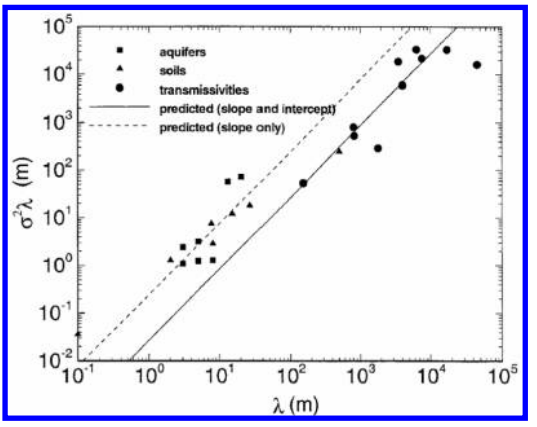


Figure 15. Product of variance σ^2 and apparent horizontal correlation scale λ of natural log hydraulic conductivities and transmissivities at various sites versus λ (after Neuman (1994); data from Gelhar (1993, Table 6.1). Predictions correspond to $\gamma(s) \propto s^{2H} \simeq s^{1/2}$.

isotropic coordinates, if one adopts $H \simeq 0.25$ and writes $1/n_l = \lambda_l = \mu \tilde{L}_l \simeq \tilde{L}_l/3$.

Equation (13) coupled with $\lambda_l = \mu \tilde{L}_l$ implies that when $\tilde{L}_l \gg \tilde{L}_u$, the variance increases as a power of domain size according to $\sigma^2 \propto \tilde{L}_l^{2H}$ and so $\sigma^2 \lambda_l \propto \tilde{L}_l^{1+2H}$. For juxtaposed natural log hydraulic conductivities and transmissivities from many sites we expect $H \simeq 0.25$ and so $\sigma^2 \lambda_l \propto \tilde{L}_l^{1.5}$. Indeed, Figure 15 (after Neuman, 1994) shows that when the hydraulic conductivity data (squares and triangles) from Gelhar's (1993) Table 6.1 are juxtaposed on a log-log plot of $\sigma^2 \lambda$ versus apparent integral scale λ (or, equivalently, $\tilde{L}_l$), they are scattered closely about a (dashed) line having the predicted slope of 1.5; the corresponding transmissivity data (circles) are scattered closely about another (solid) line having the same slope. The offset between the two lines was attributed by Neuman (1994) to a reduction in variance obtained when hydraulic conductivities are averaged over the vertical to yield transmissivities. This explanation is in turn qualitatively consistent with (10) which, coupled with $\lambda_u = \mu \tilde{L}_u$, predicts a reduction in variance with support scale according to

$$\sigma^2 \propto \left(\tilde{L}_l^{2H} - \tilde{L}_u^{2H} \right) \tag{15}$$

2.3 *Up- and down-scaling permeability*

To predict how permeability would vary with support scale, Di Federico et al. (1999) have considered three-dimensional steady state flow through a box embedded in a multivariate Gaussian, statistically homogeneous and anisotropic log permeability field. The block is larger than the support scale of the field but is smaller

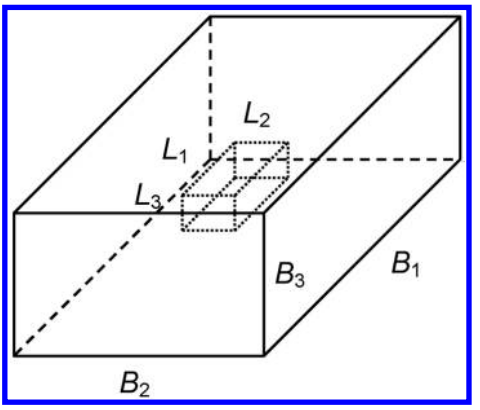


Figure 16. Box-shaped domain embedded in larger domain (Di Federico et al., 1999).

than a surrounding sampling window (Figure 16). It is oriented parallel to the principal coordinates of statistical anisotropy.

The field is characterized by a truncated power variogram with $n_u = \infty$ ($\lambda_u = 0$), corresponding to zero support scale. Flow takes place under a uniform mean (across the ensemble of all y realizations) hydraulic gradient of magnitude J acting parallel to L_1 between two constant head boundaries (the other four boundaries being no-flow in the mean). In the transformed isotropic domain, the box becomes a cube with sides spaced a distance $\tilde{L}$ apart.

Let $q(\boldsymbol{x})$ be the corresponding mean flux at any point $\boldsymbol{x}$ within the cube and define the effective permeability, $k_{eff}(\boldsymbol{x})$, of the box at $\boldsymbol{x}$ via

$$q(\boldsymbol{x}) = a k_{eff}(\boldsymbol{x}) J \tag{16}$$

where α is the ratio between the unit weight and dynamic viscosity of the fluid. Upon invoking a conjecture due to Landau and Lifschitz (1960), Di Federico et al. (1999) found that

$$\frac{k_{eff}(\boldsymbol{x}; H, \lambda_l)}{k_g} = \exp\left\{ \sigma^2(H, \lambda_l) \left[\frac{1}{2} - D_{st}(\boldsymbol{x}, H) \right] \right\} \tag{17}$$

where k_g is the geometric mean of k within the window ($\ln k_g$ being the mean of y); σ^2 is given by (13); and the function D_{st}, given by (50) of Di Federico et al., depends on whether the truncated variogram is composed of modes having exponential (equation 4) or Gaussian (equations 5) variograms. Figure 17 shows how D_{st} varies with H in the first case. Figure 18 shows how k_{eff}/k_g at the center of the box varies with L_1 and the Hurst coefficient H.

Figure 19 shows how the normalized equivalent air permeability of unsaturated fractured tuff at the ALRS

Copyright © 2003 Swets & Zeitlinger B.V., Lisse, The Netherlands

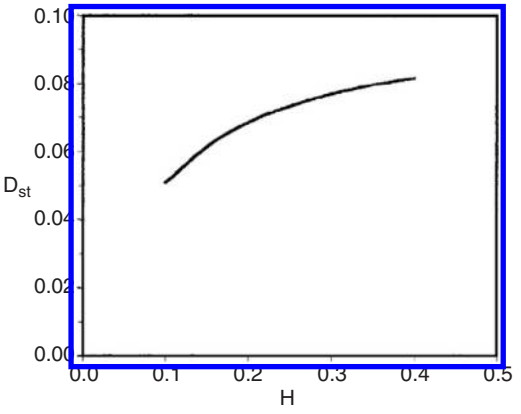


Figure 17. D_{st} normalized by e_2e_3 versus H (Di Federico et al., 1999).

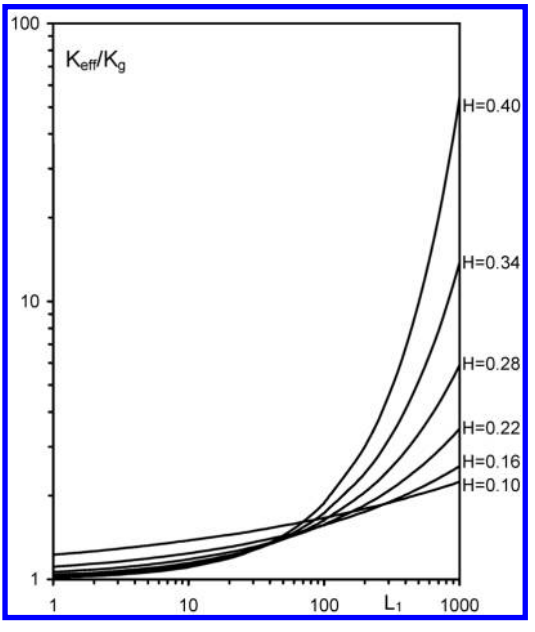


Figure 18. k_{eff}/k_g at center of box versus L_1 for various H (Di Federico et al., 1999).

varies with support scale for three sets of cross-hole inverse estimates. The results can be used to up-scale and down-scale air permeability at the site.

Hyun et al. (2002) have shown that despite considerable uncertainty about the magnitude of the observed scale effect at the ALRS (as reflected by the range of the curves in Figure 19), the scaling frame-work described in this section provides a viable (if not complete) explanation of how log permeability varies with support and resolution scales at the site.

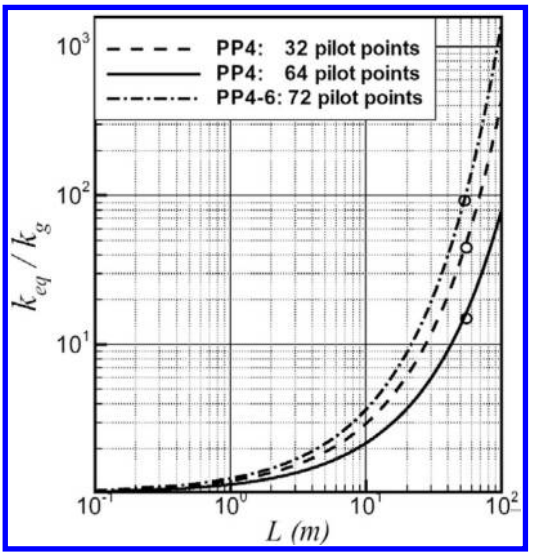


Figure 19. Normalized equivalent air permeability of unsaturated fractured tuff at ALRS versus box scale L for three sets of cross-hole inverse results. Circles correspond to cross-hole estimates (Hyun et al., 2002).

As the underlying log permeability field is fractal, k_{eq} is a random variable whose variance and spatial autocorrelation function, conditioned on a known mean value of support-scale conductivity across the window, are given explicitly by Di Federico et al. (1999). It is convenient (though not necessary) to think of the sampling window as a flow region and of the block as an element of a computational grid superimposed on this region. Then the equivalent hydraulic conductivity of the block can be thought of as an upscaled value based (and conditioned) on smaller-scale measurements, which however is uncertain and so associated with some known variance and spatial covariance. The theory allows one to distinguish between spatial fluctuations in conductivity on scales larger than a grid block, which can be resolved by the computational grid, and smaller-scale subgrid fluctuations which cannot be so resolved.

2.4 *Scaling of apparent longitudinal dispersivity*

The scaling framework described in this section allows the application of standard methods of stochastic analysis to problems of flow and transport in random media with continuously evolving scales of heterogeneity between two limits: a lower limit proportional to measurement or support scale and an upper limit proportional to sampling domain or window size. Di Federico and Neuman (1998b) used a standard method of perturbation to solve the stochastic problem of advective solute transport under mean uniform

Copyright © 2003 Swets & Zeitlinger B.V., Lisse, The Netherlands

steady state groundwater flow in an infinite, two- or three-dimensional multiscale hierarchy of random log permeability fields y. They developed leading-order expressions for the displacement covariance and dispersion coefficient of an ensemble of solute "particles" advected through such flow fields and elucidated their explicit dependence on the Hurst coefficient, cutoff scales, and mean particle displacement s.

One of the authors' findings indicated that when a finite low-frequency cutoff $\lambda_l < \infty$ is present, an asymptotic quasi-Fickian regime develops as the mean travel distance s becomes large relative to λ_l and the plume has sampled all heterogeneities relevant to the domain scale. During this regime the longitudinal dispersion coefficient takes on a constant (Fickian) asymptotic value proportional to λ_l^{1+2H}.

During the early preasymptotic regime where $s \ll \lambda_l$, the dispersivity grows linearly with s when the latter is large compared to the support scale of y ($\lambda_u \ll s$). This linear growth rate is slower than the supralinear rate (proportional to s^{1+2H}) indicated by open symbols in Figure 6. The corresponding apparent dispersivities were derived from Fickian models which do not apply unless s is at least of order λ_l. If the tracer data, in fact, represented preasymptotic regimes ($s \ll \lambda_l$) but were interpreted on the basis of a Fickian assumption ($s \sim \lambda_l$), then theory would yield an apparent growth rate proportional to s^{1+2H}. Setting $H \simeq 0.25$ yields a growth rate proportional to $s^{1.5}$ consistent with the open symbols in Figure 6. Similar behavior was predicted by Neuman (1995) on the basis of a conditional preasymptotic theory without a formal low-frequency cutoff.

Virtually all open symbols in Figure 6 represent ergodic, rather than nonergodic, apparent dispersivities. This is so because they were obtained not from measurements of plume spread about its actual center of mass but from forced fits between deterministic Fickian models of dispersion, which do not account directly for medium heterogeneity, and measured tracer breakthrough (concentration versus time) data at one (or at most a few) sampling location in space. The velocity in such Fickian models represents, at best, unconditional mean velocity. Therefore the model plume trajectory defines not the actual but the mean position of the plume center of mass. The model dispersivity represents, at best, the mean rate at which the plume spreads about its center of mass, and is therefore ergodic rather than non-ergodic. As the dispersivities represented by open symbols in Figure 6 were derived from the same model, they represent apparent ergodic values regardless of whether or not (we suspect not) ergodic conditions actually prevailed during the corresponding tracer studies. It is for this reason that the same dispersivities can be validly compared with the theoretical expressions of Di Federico and Neuman (1998b).

The solid symbols in Figure 6 derive from models which account explicitly for medium heterogeneity and are therefore not directly comparable to these expressions.

2.5 *Hydrogeologic rationale*

Neuman (2002) has demonstrated mathematically that the above scaling model of overlapping modes is consistent with a representation of multimodal spatial variability in which space is filled by a discrete number of juxtaposed (mutually exclusive) materials or categories (such as geologic facies or soil types), each having its own architecture (spatial arrangement) and attributes (such as permeability or porosity). In this representation, the spatial distribution of categories is characterized by indicator random variables $I_i(\boldsymbol{x})$ and their attributes by random fields $y_i(\boldsymbol{x})$, $i = 1, \ldots, M$. A given attribute $y(\boldsymbol{x})$ is expressed as

$$y(\boldsymbol{x}) = \sum_{i=1}^{M} I_i(\boldsymbol{x}) y_i(\boldsymbol{x}) \tag{18}$$

where

$$I_i(\boldsymbol{x}) = \begin{cases} 1 & \text{if category } i \text{ occurs at } \boldsymbol{x} \\ 0 & \text{otherwise} \end{cases} \tag{19}$$

$$\sum_{i=1}^{M} I_i(\boldsymbol{x}) = 1 \tag{20}$$

The probability of attribute i is

$$p_i(\boldsymbol{x}) = \Pr\{I_i(\boldsymbol{x}) = 1\} = E\{I_i, (\boldsymbol{x})\} \tag{21}$$

$$\sum_{i=1}^{M} p_i(\boldsymbol{x}) = 1 \tag{22}$$

and the joint probability of attributes i and j is

$$\begin{aligned} p_{ij}(\boldsymbol{x}, \boldsymbol{\chi}) &= \Pr\{I_i(\boldsymbol{x}) = 1, I_j(\boldsymbol{\chi}) = 1\} \\ &= E\{I_i(\boldsymbol{x}) I_j(\boldsymbol{\chi})\} \end{aligned} \tag{23}$$

Figure 20 illustrates how a Markov version of such an indicator model can be used to generate random realizations of hydrofacies architecture by conditional Monte Carlo simulation.

In general, the indicator variables and their attributes are auto- and cross-correlated within and between categories. Neuman (2002) has demonstrate mathematically that when (a) $I_i(\boldsymbol{x})$ and $y_i(\boldsymbol{x})$ are statistically homogeneous and anisotropic with identical directions and ratios of principal integral scales, and (b) the categories overlap in a way which preserves their local architecture, $p_i(\boldsymbol{x}) = p_i$ becomes a

Copyright © 2003 Swets & Zeitlinger B.V., Lisse, The Netherlands

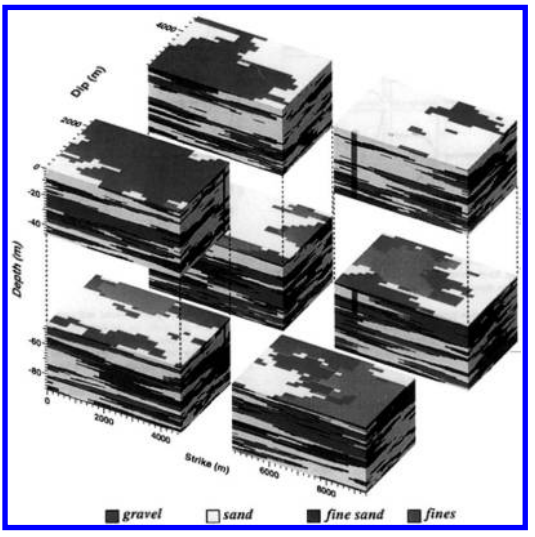


Figure 20. Conditional simulation of hydrofacies architecture in a portion of the Kings River alluvial fan. Conditioning data consist of core and geophysical logs from seven boreholes (after Carle et al., 1998).

constant representing the volumetric proportion of the ith category in space and

$$\gamma_y(\tilde{s}) = \sum_{i=1}^{M} p_i \gamma_{yii}(\tilde{s}). \quad (24)$$

This states that the variogram $\gamma_y(\tilde{s})$ of an attribute, sampled jointly over overlapping statistically homogeneous and anisotropic categories, is the sum of the variograms $\gamma_{yii}(\tilde{s})$ of statistically homogeneous and anisotropic components of this attribute sampled over individual categories, weighted by their volumetric proportions. Hence the spatial increments of attributes associated with overlapping categories are mutually uncorrelated. The latter is a key premise underlying the multiscale theory in this paper, which is thus seen to be consistent with the multimodal spatial variability representation in (18).

The concept of overlapping categories applies in practice when attributes correspond to a representative mixture of the categories, such as the permeability and porosity of a rock mass containing a hierarchy of superimposed fracture sets, or the dispersivity of a plume that covers an evolving range of heterogeneity scales.

3 CONCLUSIONS

a. Hydrogeologic variables exhibit dependencies on scales of measurement (data support), observation (extent of phenomena such as a dispersing plume), sampling window (domain of investigation), spatial correlation (structural coherence) and spatial resolution (descriptive detail). They may also exhibit directional dependence.
b. All these dependencies are captured by the scaling theory described in this paper.
c. This scaling theory is consistent with available data and with an indicator representation of hydrogeologic variability.

ACKNOWLEDGMENTS

This work was supported by the U.S. Nuclear Regulatory Commission under contract NRC-04-97-056, NSF/ITR Grant EAR-0110289, and MURST 60%: Modellazione degli acquiferi ad elevata eterogeneità.

REFERENCES

Andersson, J.-E., Ekman, L., Gustafsson, E., Nordqvist, R., and Tiren, S. 1988. *Hydraulic Interference Tests and Tracer Tests Within the Brändan Area, Finnsjön Study Site, The Fracture Zone Project – Phase 3*. Tech. Rep. 89–12, Swedish Nuclear Fuel and Waste Management Co. SKB, Stockholm.

Bradbury, K.R., & Muldoon, M.A. 1990. Hydraulic conductivity determinations in unlithified glacial and fluvial materials. In Nielson D.M. and Johnson, A.I. (eds.), *Ground Water and Vadose Zone monitoring, ASTM STP*, 1053: 138–151.

Butler, J.J., Jr. & Healey, J.M. 1998a. Relationship between pumping-test and slug-test parameters: Scale effect or artifact? *Ground Water* 36: 305–313.

Butler, J.J., Jr. & Healey, J.M. 1998b. Discussion of papers: Authors' reply. *Ground Water* 36: 867–868.

Carle, S.F., Labolle, E.M., Weissmann, G.S., van Brocklin, D. & Fogg, G.E. 1998. Conditional simulation of hydrofacies aarchitecture: A transition probability/Markov approach. 147–170 in *Hydrogeologic Models of Sedimentary Aquifers*, Fraser, G.S. & Davis, J.M. (eds.). Concepts in Hydrogeology and Environmental Geology No. 1, SEPM (Soc. Sedim. Geol.) Special Publication.

Chen, G., Illman, W.A., Thompson, D.L., Vesselinov, V.V. & Neuman, S.P. 2000. Geostatistical, type curve and inverse analyses of pneumatic injection tests in unsaturated fractured tuffs at the Apache Leap Research Site near Superior, Arizona, 73–98, in *Dynamics of Fluids in Fractured Rocks*, Faybishenko B. et al. (eds.), Geophysical Monograph 122, AGU, Washington, DC.

Clauser, C. 1992. Permeability of crystalline rocks. *Eos Transactions*, American Geophysical Union 73(21): 233.

Di Federico, V. & Neuman, S.P. 1997. Scaling of random fields by means of truncated power variograms and associated spectra. *Water Resour. Res.* 33(5): 1075–1085.

Di Federico, V. & Neuman, S.P. 1998a. Flow in multiscale log conductivity fields with truncated power variograms. *Water Resour. Res.* 34(5): 975–987.

Di Federico, V. & Neuman, S.P. 1998b. Transport in multiscale log conductivity fields with truncated power variograms. *Water Resour. Res.* 34(5): 963–973.

Copyright © 2003 Swets & Zeitlinger B.V., Lisse, The Netherlands

Di Federico, V., Neuman, S.P., & Tartakovsky, D.M. 1999. Anisotropy, lacunarity, upscaled conductivity and its covariance in multiscale fields with truncated power variograms. *Water Resour. Res.* 35(10): 2891–2908.

Gelhar, L.W. 1993. *Stochastic Subsurface Hydrology*. Prentice Hall, N.Y.

Guzman, A.G., Geddis, A.M., Henrich, M.J., Lohrstorfer, C.F., & Neuman, S.P. 1996. Summary of Air Permeability Data From Single-Hole Injection Tests in Unsaturated Fractured Tuffs at the Apache Leap Research Site: Results of Steady-State Test Interpretation. NUREG/CR-6360, U.S. Nuclear Regulatory Commission, Washington, D.C.

Hewett, T.A. 1992. Modelling reservoir heterogeneity with fractals. In Geostatistics Troia, Soares, A. (ed.), Kluwer Acad., Norwell, Mass.

Hufschmied, P. 1985. Estimation of three-dimensional statistically anisotropic hydraulic conductivity field by means of single well pumping tests combined with flowmeter measurements. 110–116 in *Proceedings of the International Symposium on the Stochastic Approach to Subsurface Flow*. Int. Assoc. for Hydraul. Res., Montvillargenne, France.

Hyun, Y., Neuman, S.P., Vesselinov, V.V., Illman, W.A., Tartakovsky, D.M., & Di Federico, V. 2002. Theoretical interpretation of a pronounced permeability scale effect in unsaturated fractured tuff. *Water Resour. Res.* 38(6): 10.1029.

Hyun, Y. 2002. Multiscale analyses of permeability in porous and fractured media. Ph.D. dissertation, University of Arizona, Tucson.

Illman, W.A. & Neuman, S.P. 2000. Type-curve interpretation of multi-rate single-hole pneumatic injection tests in unsaturated fractured rock. *Ground Water* 38: 899–911.

Illman, W.A. & Neuman, S.P. 2001. Type-curve interpretation of a cross-hole pneumatic injection test in unsaturated fractured tuff, *Water Resour. Res.* 37: 583–603.

Illman, W.A., Thompson, D.L., Vesselinov, V.V. & Neuman, S.P. 1998. Single-Hole and Cross-Hole Pneumatic Tests in Unsaturated Fractured Tuffs at the Apache Leap Research Site: Phenomenology. Spatial Variability, Connectivity and Scale, *Rep. NUREG/CR-5559*, prepared for U.S. Nuclear Regulatory Commission, Washington, D.C.

Landau, L.D. & Lifshitz, E.M. 1960. *Electrodynamics of Continuous Media*. Pergamon, New York.

Martínez-Landa, L., Carrera, J. Guimerà, J., Vazquez-Suñé, E., Vives, L. & Meier, P. 2000. Methodology for the hydraulic characterization of a granitic block. 340-345, in *Calibration and Reliability in Groundwater Modelling; Coping with Uncertainty*. ModelCARE 99, Stauffer, F., Kinzelbach, W., Kovar K. & Hoehn, E. (eds.), IAHS Publication 265, IAHS Press, Wallingford, Oxfordshire, UK.

Molz, F.J. & Boman, G.K. 1993. A stochastic interpolation scheme in subsurface hydrology. *Water Resour. Res.* 29(11): 3769–3774.

Molz, F.J., Hewett, T.A. & Boman, G.K. 1998. A pseudo-fractal model for hydraulic properties in porous medium. 341–372 in *Fractals in Soil Sciences*, Baveye, P., Parlange, J.-Y., & Stewart, B.A.. (eds.). CRC Press, Boca Raton, Fla.

Neuman, S.P. 1990. Universal Scaling of Hydraulic Conductivities and Dispersivities in Geologic Media. *Water Resour. Res.* 26: 1749–1758.

Neuman, S.P. 1994. Generalized Scaling of Permeabilities: Validation and Effect of Support Scale. *Geophys. Res. Let.* 21: 349–352.

Neuman, S.P. 1995. On advective dispersion in fractal velocity and permeability fields. *Water Resour. Res.* 31(6): 1455–1460.

Neuman, S.P. 2002. Relationship between juxtaposed, overlapping and fractal representations of multimodal spatial variability. *Water Resour. Res.*, under review.

Neuman, S.P. & Di Federico, V. 1998. Correlation, flow and transport in multiscale permeability fields. *In Scale Dependence and Scale Invariance in Hydrology*. Sposito, G. (ed.), Cambridge University Press, New York, New York: 354–397.

Perez, G. & Kalkar, M. 1993. Assessing distributions of reservoir properties using horizontal well data. 399-436 in *Reservoir Characterization III*, Linville, B., Burchfiled, T.E. & Wesson, T.C. (eds.). Pennwell, Tulsa, Okla.

Rovey II, C.W. 1998. Digital simulation of the scale effect in hydraulic conductivity. *Journal of Hydrology* 6: 216–225.

Rovey II, C.W. & Cherkauer, D.S. 1995. Scale dependency of hydraulic conductivity measurements. *Ground Water* 33: 769–780.

Rovey II, C.W. & Niemann, W.L. 2001. Wellskins and slug tests: Where's the bias? *Journal of Hydrology* 243: 120–132.

Sanchez-Vila, X., Carrera, J. & Girardi, J.P. 1996. Scale effects in transmissivity. *Journal of Hydrology* 183: 1–22.

Schulze-Makuch, D. & Cherkauer, D.S. 1998. Variations in hydraulic conductivity with scale of measurements during aquifer tests in heterogenous, porous carbonate rock. *Hydrogeology Journal* 6: 204–215.

Schulze-Makuch, D., Carlson, D.A., Cherkauer, D.S. & Malik, P. 1999. Scale dependency of hydraulic conductivity in heterogeneous media. *Ground Water* 37: 904–919.

Sudicky, E. A. 1986. A natural gradient experiment on solute transport in a sand aquifer: spatial variability of hydraulic conductivity and its role in the dispersion process. *Water Resour. Res.* 22(13): 2069–2082.

Vesselinov, V.V. & Neuman, S.P. 2001. Numerical inverse interpretation of single-hole pneumatic tests in unsaturated fractured tuff. *Ground Water* 39: 685–695.

Vesselinov, V.V., Neuman, S.P. & Illman, W.A. 2001a. Three-dimensional numerical inversion of pneumatic cross-hole tests in unsaturated fractured tuff: 1. Methodology and borehole effects. *Water Resour. Res.* 37: 3001–3017.

Vesselinov, V.V., Neuman, S.P. & Illman, W. A. 2001b. Three-dimensional numerical inversion of pneumatic cross-hole tests in unsaturated fractured tuff: 2. Equivalent parameters, high-resolution stochastic imaging and scale effects. *Water Resour. Res.* 37: 3019–3041.

Zyvoloski, G., Kwicklis,E., Eddebbarh, A.A., Arnold, B., Faunt, C. & Robinson, B.A. 2002 (in press). The Site-Scale Saturated-Zone Flow Model for Yucca Mountain: Calibration of Different Conceptual Models and Their Impact on Transport. *Jour. Contam. Hydrol.*

Copyright © 2003 Swets & Zeitlinger B.V., Lisse, The Netherlands

Observational method for tunnel construction considering environmental impact to groundwater

Y. Ohnishi & H. Ohtsu
Kyoto University, Kyoto, Japan

T. Nishioka & Y. Naka
Hanshin Expressway Public Corp., Kyoto, Japan

T. Yasuda & K. Takahashi
Pacific Consultants Co. Ltd., Osaka, Japan

ABSTRACT: This paper reports on the details of an observational method for groundwater work and the numerical analysis and evaluation techniques involved, which was developed for the construction of the Inariyama Tunnel that aimed to enhance the economical and rational aspects of the tunneling work with due consideration for the groundwater issues to be produced by the tunnel construction. The Inariyama Tunnel is a mountain tunnel excavated in the alternation of sandstone and slate between the Paleozoic and Mesozoic Eras. The tunnel was planned to go straight below a surface water system and near precious lakes, which required environmental and groundwater considerations. The authors managed to develop a groundwater impact evaluation system that incorporated the actual excavation process while conserving the surrounding water environment by performing a preliminary 3-D FEM seepage analysis[1] and immediately feedbacking the actual excavation data.

1 INTRODUCTION

Groundwater issues in tunnel construction work give rise to the need for safety measures such as the prevention of cutting face failure caused by a large amount of leakage water.[2] In terms of the surrounding environment, groundwater issues include the groundwater drainage impacts on the surrounding groundwater environment and the reduction in existing water resources groundwater levels.[3,4] This paper reports on the details of an observational method for groundwater work and the numerical analysis and evaluation techniques involved, which was developed for the construction of the Inariyama Tunnel that aimed to enhance the economical and rational aspects of the tunneling work with due consideration for the groundwater issues to be produced by the tunnel construction. The observational method for groundwater work described in this study is an evaluation system designed to keep track of the excavation process by repeatedly performing immediate validation and predictive analysis based on preceding excavation data. It consists of the following stages:

(i) 3-D model development: Based on the topographic form and geology, develop a large-scaled 3-D ground model that represents the hydraulic and geological conditions,[5] aquifer structure and surface waters.

(ii) Validation analysis based on the immediately proceeding excavation data: In the advanced prediction of the complex groundwater behavior during excavation work using the 3-D FEM seepage analysis, and then feedback the actual excavation data to validate the model.

(iii) Predictive analysis: Make a prediction of the groundwater behavior in an area to be excavated, while keeping on improving the accuracy of the ground model. By repeating each process, selecting the best execution method for a condition that is nearest to the actual one, determining allowable impacts, proposing a groundwater environment conservation measure, and performing the final impact evaluation.

The use of the above observational method for groundwater in the construction of the Inariyama Tunnel controlled the impacts on the surface water system and nearby precious lakes, thereby allowing for the relevant conservation measures. This paper reports on the predictive evaluation of complex groundwater behavior and its validation results, determination

Copyright © 2003 Swets & Zeitlinger B.V., Lisse, The Netherlands

of allowable impacts, proposal of the best execution method, and the validation of the final impact evaluation.

2 SURROUNDING ENVIRONMENT

2.1 *Geological overview*

The topographic form around the tunnel is composed of gently inclined, highly weathered and eroded mountainous slopes, with hilly areas and alluvial fans at their base. The surrounding geology consists of the Tamba layer group (clayslate, shale, sandstone and chert) between the Carboniferous Period of the Paleozoic Era and the Jurassic Period of the Mesozoic Era. Of these, the clayslate and sandstone form an alternation. The strike of the strata runs from northwest to southeast; its dip is generally south facing; and there are several fault-crushing belts running from northeast to southwest in the alternation of sand and mud. As shown in Figure 1, the tunnel excavation route was planned to run from the mountainous area to the plain areas at the base.

2.2 *Hydraulic and geological properties*

According to the Lugeon testing on boring locations No. 1 and 3 shown in Figure 1, the permeability coefficient of rock grounds with few cracks were $k = 3.0 \times 10^{-5}$ to 1.0×10^{-4}cm/sec, while that of the fault-crushing belts running across the tunnel showed a large value of $k = 1.0 \times 10^{-3}$cm/sec. The fault-crushing belts were found in every 2 to 5 m in well cores, which meant that the ground as a whole was forming a huge fault-crushing belt. A boring survey showed that the groundwater level generally followed the topographic form except at the boring location No. 3, where there were pore pressure differences in the vertical direction.

2.3 *Tunnel construction conditions*

The short-bench cut method was adopted for the Inariyama Tunnel, which had double cutting faces for the Eastern Tunnel and Western Tunnel whose excavation cross-section was 80 m^2 each. The 1.3-km section shown in the tunnel profile of Figure 1 is covered in this study. Halfway across the section, there is a valley with an overburden of 70 m formed by the catchment of the small river. There are also precious lakes (Lake A and Lake B) at the left foot of the mountain 300 m away from the tunnel route. Both the New Austrian Tunneling Method (NATM) and shield tunneling method were adopted here, whose joint (i.e. the shield machine's turning point) was planed to be near the STA 80 in Figure 1.

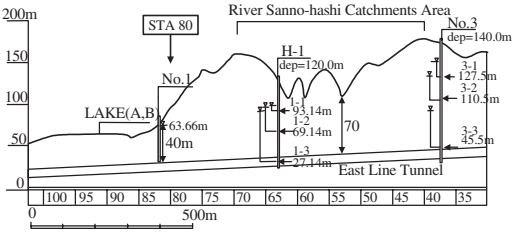


Figure 1. Location of the crossings of the tunnel measurement points No. 1, No. 3, H-1: Vertical boring.

3 OBSERVATIONAL METHOD FOR GROUNDWATER

3.1 *Development of large-scaled 3-D model*

The 3-D seepage analysis is best suited as the basic numerical model here, because it better allows for the presence of highly permeable fault-crushing belts, complex topographic form that includes a mountain river, as well as the inclusion of construction conditions such as the excavation process. The fact that the fault-crushing belts in the alternation of sand and

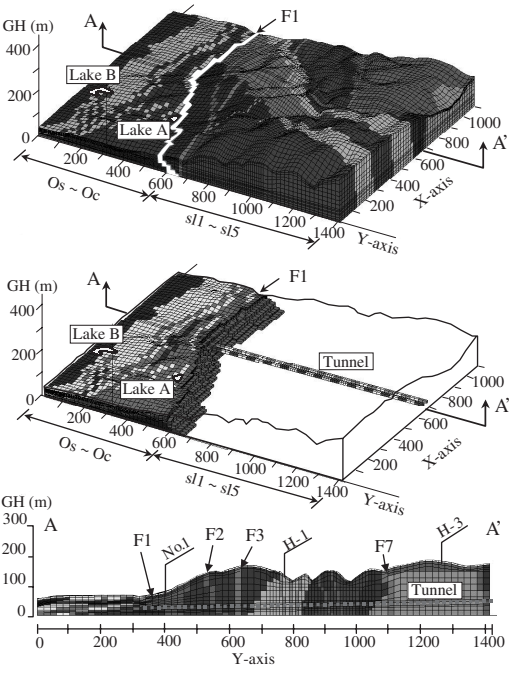


Figure 2. Distribution of fault zone in the 3-D geological profile.

Copyright © 2003 Swets & Zeitlinger B.V., Lisse, The Netherlands

Table 1. Hydraulic properties of 3-D model.

Code	Geology	Permeability X, Y, Z direction (cm/s)	Volume water content (%)	Specific storage (cm^{-1})
sl1–sl5	Tamba group alternation	1.0×10^{-5}	5	0.0001
F2–F7	Fault zone	1.0×10^{-3}	7	0.00001
F1	Fault zone	1.0×10^{-3}	7	0.00001
Os–Oc	Osaka group	1.0×10^{-4}	10	0.0001

Table 2. Detail of observational method for groundwater according to each construction stage.

Construction stage	Work description	Purpose
Step 0	Nearing the mountain river 3-D seepage analysis	– Preliminary predictive evaluation – Exploring drill (L = 30 m) – Perform a surface water countermeasure
Step 1	Excavation work right below the mountain river	– Exploring drill (L = 30 m) – Water supply for the surface water
Step 2	Excavation work right below the mountain river completed	– Exploring drill (L = 30 m) – Water supply for the surface water
Step 3	Numerical analysis on the preliminary prediction of the F1 Fault zone 3-D seepage analysis	– Prediction of excavation impacts – Control of impacts on the neighboring lake
Step 4	Horizontal boring between the F1 Fault zone and the shield machine's turning point	– Confirmation of rock conditions and permeability – Leakage water from horizontal boring holes
Step 5	Numerical analysis based on the data taken in 3-D seepage analysis Step 4	– Evaluation of impacts during the main pit excavation – Determination of the right or wrong of the measure for the lake
Step 6	Working on the shield machine's turning point	– Exploring drill (L = 30 m)
Step 7	Excavation completed	– Confirmation of leakage water during excavation
Step 8	Numerical analysis taking into account the result of Step 6 3-D seepage analysis	– Prediction of post-excavation and beyond

mud were giving considerable impacts on groundwater behavior, a fault-crushing belt model was considered to be best suited as the 3-D ground model here. Figure 2 shows the 3-D ground model used in this study. The finite element mesh is composed of 107,502 elements and 116,200 nodal points. For the fault zones, the high permeability value of 10^{-3} cm/sec obtained in the Lugeon testing was selected as permeability. The permeability values of other geological zones are shown in Table 1.

3.2 *Procedure for the observational method for groundwater*

Table 2 shows the detailed procedure for the observational method for groundwater. Steps 0, 1 and 2 cover the prediction of impacts on the surface water caused by the tunnel route running right below the mountain river. These steps set out the procedure for evaluating the measures for conserving the surface water. Steps 3, 4, 5, 6, 7 and 8 cover the prediction of impacts on nearby Lake A. These steps set out an evaluation procedure based on the data on the preceding horizontal boring and excavation work.

3.3 *Determination of allowable impact and proposal for the best groundwater measure*

When constructing a mountain tunnel, the need for reasonable and economical measures become greater where there is a greater need for determining the current condition based on the immediate preceding excavation data and thus taking a large scale measure. In the case of the Inariyama Tunnel, during tunnel excavation the surface water above the tunnel route was to be supplemented with publicly supplied water. Thus, it is essential to perform a precise impact evaluation to determine a restoration location and the optimum volume of water to be restored. In addition, it was expected that a considerably large-scale measure would be needed for the lake nearby, no matter whether it was to be taken inside the tunnel

Copyright © 2003 Swets & Zeitlinger B.V., Lisse, The Netherlands

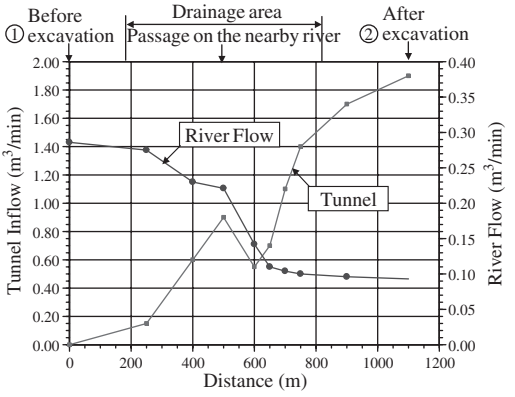


Figure 3. Results of comparison between calculated river flow and tunnel inflow.

or on the ground surface. For the surface water, the allowable user water level was defined as allowable impacts during the excavation work. On the other hand, considering the importance of the lake, an execution method that would give minimum impacts should be adopted in principle.

3.4 *Evaluation of impacts on mountain river's surface water*

According to the results of the 3-D seepage analysis for predicting the impacts on surface water in Step 0, the tunnel leakage inflow was expected to be 1.0 to 1.4 m^3/min when excavating through the valley area. This is shown in Figure 3. As the cutting face is being driven right below the valley, the impact on surface water becomes evident, as shown by a decrease in the river flow. The reduction of surface water is about 0.20 m^3/min when the cutting face is driven beneath. Considering the fact that the base flow of the surface water was found to be 0.15 to 0.20 m^3/min in an on-site survey, the surface water was expected to almost dry up after excavation has been through. Note that the volume of surface water was calculated as the sum of seepage volume at the ground model's seepage nodal points between upper and lower reaches.

Based on the prediction results for the impacts during excavation right below the valley, the need for a surface water measure was proposed in practice. Restoration of reduced water with publicly supplied water was proposed here. Furthermore, detailed measures were designated based on the prediction results, such as the restoration location and the volume of water to be restored that would match the length of the reduced flow section and the reduction level. As a result, impacts on surface water were predicted with a high level of accuracy, detailed measures were taken according to the procedure from Step 0 to Step 2, and

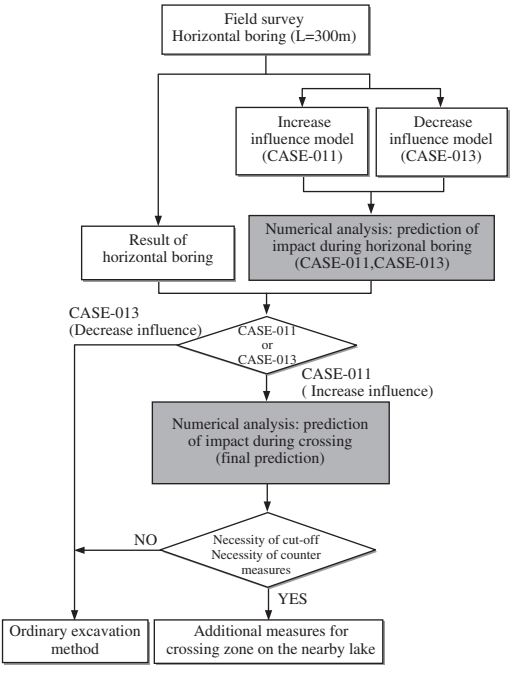


Figure 4. Flowchart of observational method.

thus, the volume of surface water was successfully conserved.

3.5 *Evaluation of impacts on neighboring lake*

The main pit excavation impacts on the lake were evaluated according to the procedure shown in Figure 4. When evaluating the impacts on a lake, it is essential to evaluate the hydrological balance of the lake including the lake's storage performance, unlike the evaluation of groundwater level and surface water. Therefore, it was necessary to perform an analysis of the hydrological balance of the lake based on the lake size and the results of 3-D seepage analysis including the reduction in groundwater discharge and inflow river water:

The basic equation for the hydrological balance is as follows

$$P - E + Qsin - Qout = \Delta S - Gin$$

P − E: Effective precipitation on the lake surface
Qsin: Volume of water flowing in from upper reaches
Qout: Volume of water flowing out of the lake outlet
ΔS: Lake storage (Water level change: Δh)
−Gin: Volume of groundwater flow out of the lake.

Analysis of lake's hydrological balance showed that the groundwater discharge at the lakebed would be about 80 l/min. Combined with inflow water from the upper reaches, this groundwater discharge would flow down

Copyright © 2003 Swets & Zeitlinger B.V., Lisse, The Netherlands

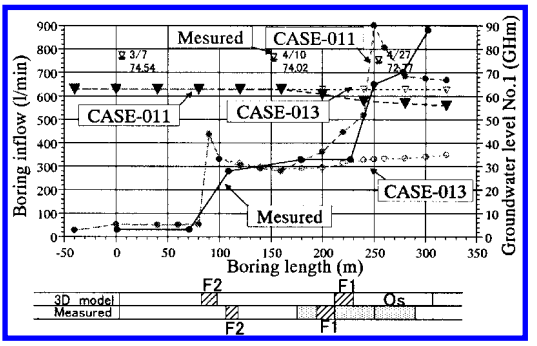


Figure 5. Results of comparison between calculated and measured of the boring inflow and ground water level.

into Lake B on the lower reach, in the form of lake's storage volume and outflow discharge to the lower reach.

3.6 *3-D seepage analysis between shield's turning point and F1 fault zone (The Mt. Inari fault)*

As seen from the evaluation flow in Figure 4, the procedure for evaluating the impacts on lakes consists of the preliminary analysis prior to horizontal boring (Step 3), collection of horizontal boring data (Step 4), and predictive analysis during the main pit excavation based on the data obtained in Steps 3 and 4. Examining and evaluating how the F1 and F2 fault zones would be distributed with what permeability coefficient were of particular importance, which was carried out based on the horizontal boring data taken in Step 4.

3.6.1 *Preliminary evaluation of horizontal boring (Step 3)*

(i) Conditions of the maximum impacts on Lake A

The model here represents a case where there is a high level of permeability both in the F1 fault zone and the alternation of sand and mud that comes before it, the tunnel leakage water reaches a considerable level, and the groundwater reduction area expands alongside the F1 fault zone during the drainage boring and main pit excavation. As shown in Figure 5, the amount of drainage in this model increases to 300 l/min in the F2 fault zone before the F1, and then to around 650 l/min in the alternation of sand and mud and through the F1 fault zone. The water level of No-1 borehole hardly changes with this drainage level until the cutting face reaches the F2 fault zone, but starts to show a gradual decrease once the flow rote has exceeded 300 l/min. The eventual decrease in the water level is expected to be 7 m to 8 m.

(ii) Conditions of the minimum impacts on Lake A

The model here represents a case where the permeability of the F1 fault zone is as small as that of the alternation of sand and mud that comes before it, the amount of drainage water is small, and the groundwater reduction area does not expand that much. As in the CASE-011, the amount of drainage increases to 300 l/min in the F2 fault zone before the F1, but afterwards, the leakage water shows no increase; most of the leakage water gushed from the F2 fault zone. Therefore, the water level of the No-1 borehole hardly changes when the cutting face is driven through the F1 and F2 fault zones.

Table 3. Cases covered in the preliminary analysis of horizontal boring.

Numerical case	Ground model description	Permeability, k (cm/sec)
CASE-011	Maximum impact: F1 Fault zone + The alternation of sand and mud in front of the F1 Fault zone	10^{-3}
CASE-013	Minimum impact: F1 Fault zone + The alternation of sand and mud in front of the F1 Fault zone	10^{-5}

Table 4. Cases covered in the impact evaluation during main pit excavation.

Numerical case	Numerical condition description
CASE-011-05	Drive through the F1 Fault zone in NATM
CASE-011-06	Stop drilling at No. 81 +00 before reaching the F1 Fault zone

3.6.2 *Predictive analysis of impacts on the lake during main pit excavation (Step 5)*

The CASE-011 shown in Table 3, where the F1 fault zone and the alternation of sand and mud had a high permeability of $k = 10^{-3}$cm/sec, was found to be better here according to the results of the preliminary analysis of horizontal boring in Step 3 and the actual data of horizontal boring taken in Step 4. Therefore, the CASE-011 model was used in the predictive analysis during the main pit excavation. This represents the evaluation procedure for Step 5.

(i) CASE-011-05: Drive through the F1 fault zone (Mt. Inari fault zone) in NATM.

As shown in Figure 6, there was almost no leakage water in the F2 fault zone before F1 due to the horizontal boring's drainage effect. However, a large amount of leakage water of about 650 to 850 l/min was expected in the alternation of sand and mud near the F1 fault zone as well as inside the zone. It was expected that

Copyright © 2003 Swets & Zeitlinger B.V., Lisse, The Netherlands

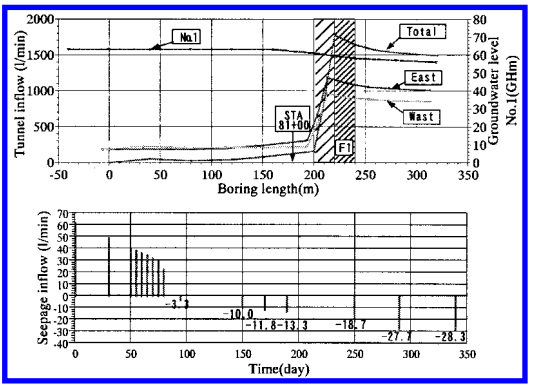


Figure 6. Seepage inflow and tunnel inflow (CASE011-05: Increase influence).

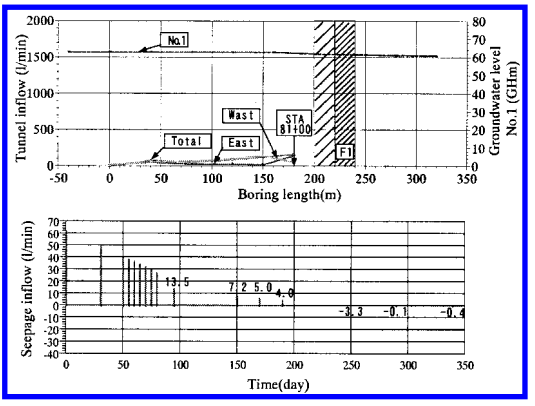


Figure 7. Seepage inflow and tunnel inflow (CASE011-06: Decrease influence).

the water level of No-1 borehole would be affected by the accelerated reduction of groundwater level during the main pit excavation. The final water level reduction was expected to be 10 to 12 m. Furthermore, as shown in Figure 6, the discharge from the lakebed decreased in accordance with the reduction in groundwater level. The discharge was expected to be 64 l/min at the start and then transformed to seepage. It was expected that the seepage would reach 28 l/min as the main pit excavation proceeds. The reduction was expected to be 92 l/min. Therefore, it was predicted that the tunnelward seepage from the lakebed would increase during the main pit excavation.

(ii) CASE-011-06: Stop drilling at No. 81 +00 before reaching the F1 fault zone

As shown in Figure 7, the amount of tunnel leakage water increases from 100 to 120 l/min during excavation before reaching the F1 fault zone. The groundwater level hardly reduces during the main

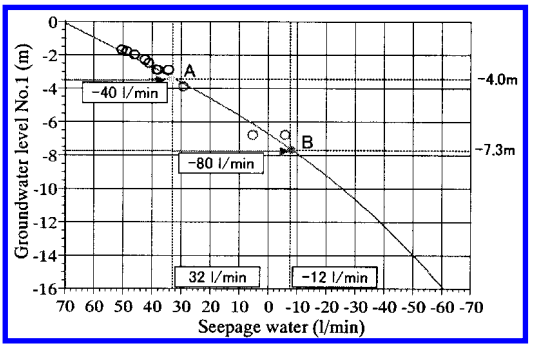


Figure 8. Comparison between calculated and measured the ground water level and the seepage water (Lake A).

pit excavation. The final reduction level is 8.0 m, which is solely caused by the horizontal boring. It was expected that the lakebed would start experiencing seepage during the horizontal boring and increase to 3.3 l/min during that process. The final seepage would be 0.4 l/min during the main pit excavation, with the reduction level being about 60 l/min. Therefore, if the main pit was excavated through the F1 fault zone, the tunnel leakage water would increase to a value somewhere between 650 and 850 l/min. As for the impact on the lake, it was predicted that the discharge would develop into storage seepage, and the water level would be reduced by about 90 l/min in the end. On the other hand, if the excavation work was stopped before reaching the F1 fault zone, it was predicted that there would be no post-excavation increase in leakage water, keeping the final water level reduction to about 60 l/min. In the actual construction work, the main pit excavation was stopped before reaching the F1 fault zone (near the location No. 81).

Figure 8 shows correlation between the groundwater level at the No-1 borehole and the amount of groundwater discharge from the bed of Lake A, which was obtained from the results of 3-D seepage analysis of the two cases and those of the analysis of lake's hydrological balance. As shown in the figure, it was assumed that the groundwater discharge would stop when the water level was reduced by 7 m at the No-1 borehole, and afterwards, the lake's storage would be drawn to the tunnel. Figure 9 shows changes in groundwater level in both cross-sectional and longitudinal directions during the main pit excavation. Thus, the Inariyama Tunnel construction work managed to conserve the surrounding environment and took various measures not detrimental to the excavation work. It was made possible through the development of groundwater flow models and relevant impact assessment in the preliminary predictive analysis based on past construction records and geological surveys. Prediction accuracy was also improved through feedback of preceding boring and monitoring data.

Copyright © 2003 Swets & Zeitlinger B.V., Lisse, The Netherlands

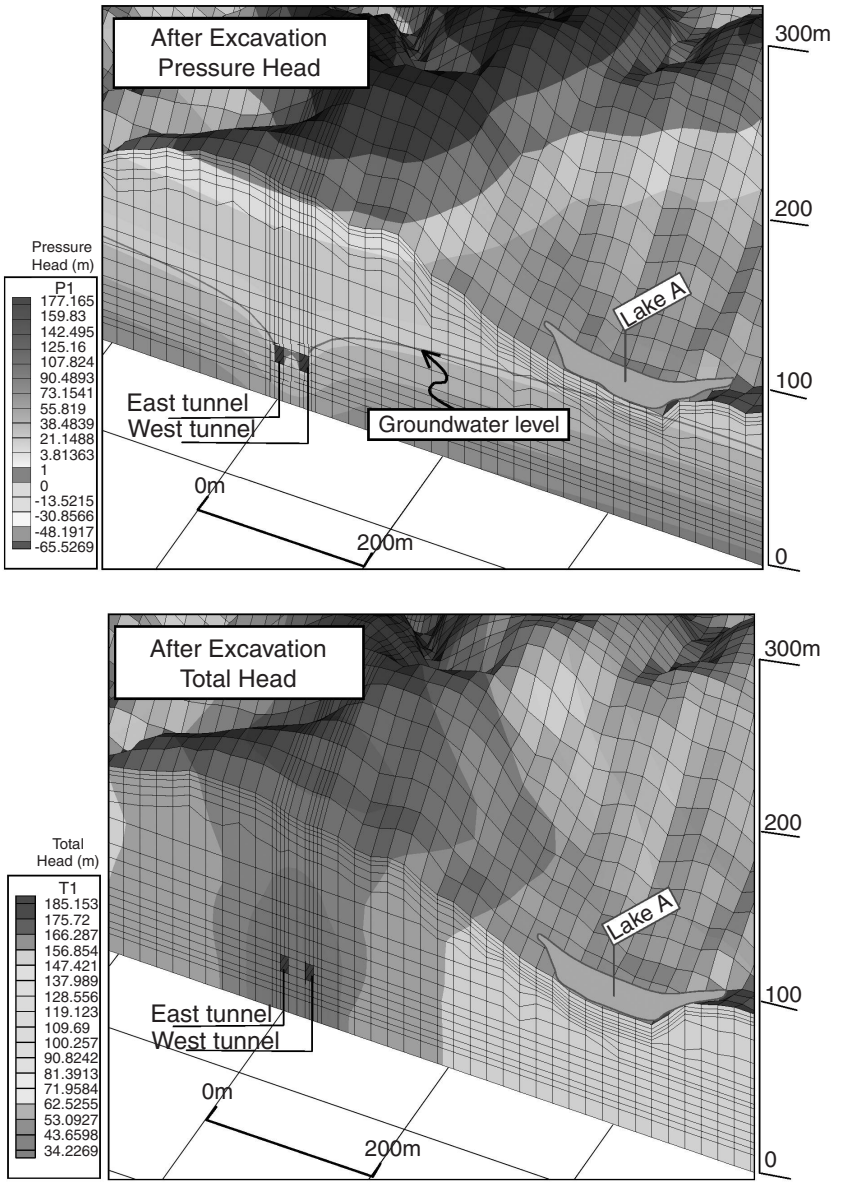


Figure 9. Results of ground water level change around the lake (Lake A) (Step 8: CASE-011-06).

4 CONCLUSIONS

When constructing an underground structure such as a tunnel, it is often difficult to assess the ground stability and permeability prior to the commencement of work. Therefore, the use of an observational method plays a vital role in construction management, which observes and measures the behavior of leakage water, groundwater and surface water during excavation work, then analyzes the results and reflects them in succeeding operations. When excavating through a sensitive area such as in the case of the Inariyama Tunnel that was planned through an environmental conservation area, it is particularly crucial to carry out the appropriate and speedy groundwater work and conservation measures. In such a case, the reliability and rationality of tunneling work can be enhanced through timely evaluation of impacts on the surrounding environment and the

Copyright © 2003 Swets & Zeitlinger B.V., Lisse, The Netherlands

feedback of such information to the actual work. The observational method for groundwater work described here brought about the following benefits: execution of successful measures for conserving the surface water level according to work progress; and control of impacts on lakes nearby. It was also fruitful to have managed to determine the allowable impacts due to the excavation of sections near sensitive areas, propose the best execution method, and validate the actual excavation data and final impacts. Conventionally, numerical analysis of groundwater is often used as a preliminary evaluation, which is performed prior to the commencement of work. In the construction of Inariyama Tunnel, numerical analysis was incorporated in actual excavation process; it was this aspect that made it possible to carry out effective and economical excavation work, while giving due consideration for the environmental issues regarding the surrounding area. By using real-time data for predictive analysis and feedbacking the result in the succeeding work, it was made possible to develop a control system that manages highly accurate evaluation, achieving both work efficiency and environmental conservation. The authors believe this system can be applied to other tunnel construction projects.

REFERENCES

1. Ohnishi, Y., Shibata, H. & Nishigaki, M. 1985. *Finite Element Analysis of Seepage Flow in Regularly Jointed Rock Mass. 5th Int. Cont. on Numerical Methods in Geomechanics. Nagoya.* 673–680.
2. Ohnishi, Y. & Tanaka, M. 1996. *Evaluation of the Effect of Tunnel Excavation for Surrounding Groudwater. Proc. IGCS. Japan.* 31: 2137–2138. (In Japanese)
3. Ohnishi, Y., Tanaka, M. & Yasuda, T. & Takahashi, K. 1997. *Evaluation of the Effect of Tunnnel Excavation for Surrounding Groudwater*. *Proc. IGCS. Japan*. 32: 1997–1998. (In Japanese)
4. Ohnishi, Y., Ohtu, H., Yasuda, T. & Takahashi, K. 1998. *Assessment of Influence in Ground Water Surroundings at Urban Tunnels. Proc. ITA. World Tunnel Congress '98*: 489–494.
5. Ohnishi, Y., Ohtu, H., Yasuda, T. & Takahashi, K. 1999. *Analysis of groundwater behavior around the crossing of adjacent tunnels. Proc. ITA. World Tunnel Congress '99*: 147–154.

Copyright © 2003 Swets & Zeitlinger B.V., Lisse, The Netherlands

Evaluation of benefits of partial source zone treatment using intermediate-scale physical model testing and numerical analysis

S. Saenton & T.H. Illangasekare
Division of Environmental Science and Engineering, Colorado School of Mines, Golden, USA

ABSTRACT: A debate has started recently in the scientific and remediation community on benefits of partial source zone treatment of NAPL contaminated sites (not fully removing the entrapped free phase NAPL sources), with respect to achieving clean up goals as measured by the reduction in the concentrations of the dissolved constituents in the downstream plume. The uncertainty associated with the removal of NAPLs from source zones could be attributed to a number of factors that include lack of data or information on the extent and timing of the spill, complex entrapment configurations created by the unstable behavior (fingering), geologic heterogeneity, and unavailability of accurate techniques for characterization of these heterogeneities and location of the sources. Data for the resolution of issues related benefits of partial source zone treatment is not expected to come from field sites. Laboratory studies in intermediate-scale test tanks provide accurate data sets to investigate this issue, as it is possible to conduct controlled experiments under known conditions of aquifer heterogeneity. The source depletion and the downstream concentrations in the dissolved plume can be monitored during remediation. The data generated in controlled experiments are used to validate numerical models to conduct theoretical analysis. This paper discusses this approach and presents results from such a study where benefits of partial source zone treatment using surfactants were evaluated using intermediate-scale testing and numerical modeling.

1 INTRODUCTION

Nonaqueous phase liquids (NAPLs) such as gasoline and chlorinated solvents are common organic pollutants found in contaminated soils and aquifers (Mercer & Cohen, 1990). These organic liquids in the entrapment zone below the spill site slowly dissolve into the flowing groundwater generating the downstream contaminant plume in which concentrations are usually found to exceed regulatory standards. Although several technologies have been proposed recently for NAPL clean-up, their ability to completely remediate these contaminated sites is still in doubt. Such uncertainty however is not only caused by the ineffectiveness of the remediation technique, but it could be attributed to the unavailability of the methods for characterization of aquifer heterogeneities and the inability to accurately characterize the saturation distribution of NAPL in the source zone. These factors result in errors in both volume estimation and locating the NAPL in the source zone. Consequently, complete removal of NAPL mass from source zone becomes impossible or impractical using any available clean-up technology.

Geologic heterogeneity heterogeneity is one of the primary factors that controls the migration and distribution of NAPL in the subsurface (Illangasekare et al., 1995; Illangasekare, 1998). It also complicates the characterization of the source zone and the effectiveness of NAPL remediation. Through an experimental and a numerical modeling study, Saenton et al. (2002) demonstrated that uncharacterized aquifer heterogeneity can cause significant uncertainty in the removal of NAPL from source zones. In that study, the effectiveness of surfactant-enhanced aquifer remediation (SEAR) for the removal of *p*-xylene contaminated soils in heterogeneous formations was investigated. A numerical model validated using data generated in intermediate scale test tanks was used to simulate the mass removal during surfactant injection. The analysis of the numerical model results showed that the required clean-up time varies with different NAPL entrapment and distributions (referred to as entrapment architecture) depending on the aquifer heterogeneity. In some cases, some of the entrapped NAPL was not removed even after long treatment periods because the treating reagents (e.g. surfactants) completely by-passed the low permeability zones.

In a recent study, Sale and McWhorter (2001) pointed out the limited near-term benefits of partial source zone treatment in achieving cleanup goals with expected reduction of dissolved contaminant concentrations downstream of source zone. They concluded that mass removal form source zone is ineffective

Copyright © 2003 Swets & Zeitlinger B.V., Lisse, The Netherlands

unless a large fraction of the entrapped NAPL free phase is removed. In other words, the reduction of dissolved contaminant concentration of the downstream plume may not be achieved unless significant fraction of NAPL in the source zone is removed. It should be noted that Sale and McWhorter (2001) study was conducted under very simplistic conditions. These simplifications include, uniform flow fields, simple entrapment architecture that consisted of a number of NAPL pools and a dissolution model that did not allow for changes in the NAPL saturation. Hence, it is premature to generalize the applicability of their findings to field sites that produce complex NAPL entrapment configurations and non-uniform flow fields under conditions of heterogeneity. This paper further investigates this issue by considering the application of SEAR technology that partially removes free phase NAPL from a heterogeneous source zone. Analysis is conducted in heterogeneous systems under complex entrapment architecture and non-uniform flow fields. The downstream concentrations in the dissolved plume, which is a function of mass depletion rate or the amount of NAPL mass left in the source zone, will be monitored and the consequences of incomplete source zone treatment will be evaluated. The feasibility of using multiple tracers (conservative and partitioning) to characterize NAPL source zones prior to and post remediation will be evaluated.

The data generated from controlled natural and enhanced dissolution experiments were used to validate existing numerical models (Saba, 1999; Saenton et al., 2002). These models were used to conduct a set of numerical experiments. Numerical simulation of natural and enhanced dissolution of NAPL (in this case, tetrachloroethene or PCE) were conducted to represent conditions in a 9.75-m long and 1.2-m high two-dimensional, vertical intermediate-scale test tank containing a PCE source zone. The multiphase flow code, UTCHEM (Delshad et al., 1996) was used to simulate the PCE entrapment architecture after a spill, thus creating the source zone in heterogeneous formations for this simulation study.

2 BACKGROUND

2.1 *DNAPL migration and entrapment*

Once a DNAPL (denser that water NAPL) is spilled on the ground surface or leaked into the underground, the free phase starts to move through soil pores and fractures under the influence of capillary and gravitational forces. During its migration, a fraction of these organic liquids is left behind or trapped and adsorbed onto soil particles. It has been demonstrated that aquifer heterogeneity controls the migration and the distribution of DNAPLs in the subsurface (Illangasekare et al., 1995; Illangasekare, 1998). The migration and distribution of NAPL are controlled by pore characteristics of the soils as well as properties of the fluids in the multiphase system. Therefore, in highly heterogeneous subsurface formations, the distribution and the saturation of NAPLs in the source zone can vary greatly from residuals to fully saturated lenses (pools).

Entrapment of NAPLs in the porous medium occurs when capillary forces are sufficiently high to overcome viscous and gravitational forces. The amount of NAPL entrapped in the porous medium is usually expressed by the saturation value, which is the ratio of entrapped NAPL volume to the volume of pore space. NAPL entrapment can occur in both pore- and macro-scales where the latter mechanism causes the existence of high-saturation zone. Macro-scale entrapment is a result of macro-scale variations in soil conditions such as layers and lenses that produces soil texture changes across interfaces. For example, when a NAPL encounters a coarse/fine sand interface, the capillary barrier effect created by the high entry pressure of finer soil will halt the migration of the NAPL to the finer soils resulting in the entrapment of NAPL in the coarser soil.

The development of many multiphase flow models has been reported (e.g. Kaluarachchi & Parker, 1990; Sleep & Sykes, 1993; Delshad et al., 1996; Dekker & Abriola, 2000). These models in general are designed to solve a coupled set of partial differential equations:

$$\frac{\partial}{\partial t}(\phi S_i \rho_i) = \vec{\nabla} \cdot \left[\frac{\rho_i k_{r,i}}{\mu_i} \mathbf{k}(\nabla p_i - \rho_i g \nabla z) \right] + \rho_i q_i, \tag{1}$$

where i denotes phase (oil or water), ϕ is porosity, S is saturation, ρ is phase density, $\mathbf{k}$ is permeability tensor, k_r is relative permeability, μ is dynamic viscosity, p is pressure of the fluid, and q represents source/sink. In this study, the multiphase flow simulator UTCHEM was used to simulate a PCE spill to generate the source zone entrapment architecture. UTCHEM is a three-dimensional, multicomponent, multiphase compositional finite-difference simulator for multiphase flow and contaminant transport in porous media. A detailed description of UTCHEM can be found in (Delshad et al., 1996).

2.2 *Dissolution of nonaqueous phase liquids*

2.2.1 *Normal dissolution*

A process that is fundamental to this study is the dissolution of entrapped NAPL to the flowing aqueous phase, both under natural groundwater flow and enhanced conditions created through the use of surfactants. Based on methods developed in chemical engineering a liner-driving model for mass transfer from entrapped NAPLs in soils has been proposed (e.g. Miller et al., 1990):

$$J = -\hat{k}(c - c_s), \tag{2}$$

Copyright © 2003 Swets & Zeitlinger B.V., Lisse, The Netherlands

where J is the NAPL-water mass transfer rate per unit volume of porous medium, $\hat{k}$ is the lumped mass transfer coefficient, c_s and c are apparent aqueous solubility and the solute concentration in the bulk aqueous phase, respectively. The value of $\hat{k}$ is usually calculated based on correlations containing a modified form of Sherwood (Sh) number: $\mathrm{Sh} = \hat{k}d_{50}^2/D_m$, where D_m is molecular diffusion coefficient, and d_{50} is the median particle diameter (Bird et al., 1960). For simple flow systems, it is possible to derive relationships between Sherwood Number and other dimensionless groups such as Reynolds (Re), Schmidt (Sc), and Peclet (Pe) numbers. These functional relationships are referred to as Gilland-Sherwood models. Similar system specific empirical relationships have been proposed for NAPL dissolution (e.g. Miller et al., 1990; Powers et al., 1992; Imhoff et al., 1994). It should be noted that lumped mass transfer coefficients that are estimated using the modified Sherwood number quantifies the mass transfer that occurs at the representative elemental volume (REV) scale that is larger than the pore-scale where mass transfer occurs at the NAPL/water interfaces. Saba and Illangasekare (2000) suggested a Gilland-Sherwood model for natural dissolution as that considers the scale at which the mass transfer coefficient is defined and incorporated the effect of bypassing of water due to reduction in relative permeability due to NAPL entrapment. This relationship is given as,

$$Sh = \alpha(\mathrm{Re})^{\beta}(\mathrm{Sc})^{\gamma}\left(\frac{\theta_n d_{50}}{\tau L^*}\right)^{\eta}, \qquad (3)$$

where the parameter τ is the tortuosity factor of the porous medium, and L^* is the dissolution length. L^* accounts for the path length of the NAPL entrapment zone in which dissolution occurs. This characteristic length parameter allows for the correction of the scale dependent mass transfer coefficient. The Schmidt (Sc) and Reynolds (Re) numbers are the properties of flowing fluids where $\mathrm{Sc} = \nu D_m^{-1}$ and $\mathrm{Re} = d_{50}U''\nu^{-1}$. U'' and ν are the average linear pore velocity and the kinematic viscosity of the flowing fluid, respectively. θ_n is the volumetric NAPL content. The constants $\alpha, \beta, \gamma, \eta$, and ξ are system specific empirical parameters. These parameters are usually obtained by fitting a model such as the one given by eqn. 3 to data generated from dissolution experiments conducted in a controlled 1-D column. Although one-dimensional column experiment provide a fundamental understanding of the processes or parameters that governs mass transfer, it is necessary to have a dissolution model that can account for the effect of flow-bypassing (Saba and Illangasekare, 2000) as well as the scale-dependency on the mass transfer (Nambi & Powers, 2000). Saba and Illangasekare (2000) demonstrated that neglecting the dimensionality of the flow field can result in orders of magnitude errors in estimates of mass transfer coefficients using these empirical relationships. In this study, dissolution experiment conducted in a bench-scale, 2-D test tank was used to generate data necessary to determine the empirical coefficients in Eq. (3).

2.2.2 *Enhanced dissolution using surfactants*

Conventional pump-and-treat remediation methods have been found to be ineffective in the removal of any significant NAPL mass due to low rates of natural dissolution that occurs under rate limited conditions (dissolution rates much smaller than the equilibrium solubility limits). Remediation engineers have now focused on a more aggressive NAPL removal technologies such as bioremediation, in situ chemical oxidation, co-solvent flushing and surfactant-enhanced dissolution (SEAR). In a number of laboratory studies, it has been demonstrated that surfactants can effectively remove entrapped DNAPLs from contaminated soils (Fountain et al., 1991; Pennell et al., 1993). Surfactant-enhanced NAPL recovery has also been implemented at field sites, which in some cases have produced promising results (Abdul et al., 1992; Martel et al., 1998).

Surfactants remove NAPLs from contaminated soils through two primary mechanisms: enhanced solubilization and mobilization. In the first, the apparent aqueous solubility of organic components in the NAPL phase is dramatically increased 10–100 folds by the partitioning of NAPL into the pseudo-organic phase formed by surfactant molecules called micelles. Surfactant can also mobilize the entrapped non-aqueous phase liquids because the NAPL-water interfacial tension is lowered in the presence of surfactants. With reduced surface tension, capillary force that holds nonaqueous phase liquids in-place becomes smaller. Consequently, NAPL can mobilize and move to other locations. This mobilization is however riskier and sometimes undesirable especially for DNAPL remediation because these mobilized organic liquids may migrate to undetectable locations in the aquifer making it impossible to clean-up.

In many surfactant-flushing studies, it has shown that the efficiency of remediation is largely affected by the rate-limited dissolution of organic constituents in the NAPL phase (Pennell et al., 1993, 1994; Mason & Kueper, 1996). The dissolution (or solubilization rate) can be quantified using similar laboratory and modeling procedures that were used in the development of correlations for natural dissolution Such a relationship was developed by and Saba et al. (2001) for surfactant enhanced dissolution. This relationship is given as:

$$Sh = \alpha(\mathrm{Re})^{\beta}(\mathrm{Sc})^{\gamma}\left(\frac{\theta_n}{1-\theta_n}\right)^{\eta}\left(\frac{d_{50}}{\tau L^*}\right)^{\xi}, \qquad (4)$$

Copyright © 2003 Swets & Zeitlinger B.V., Lisse, The Netherlands

where the empirical parameters will be determined from inverse modeling using experimental data on enhanced dissolution of PCE in the presence of Tween-80 surfactant solution.

2.2.3 *Numerical model for NAPL dissolution*

The numerical model used to simulate the natural and enhanced dissolution of PCE (a DNAPL used in this study) is the same model that was used in previous studies conducted in our research group. The model consists of a finite-difference groundwater flow code (MODFLOW) and finite-difference contaminant transport simulation code with a dissolution package incorporated into a transport simulator (MT3D). The rate-limited mass transfer is modeled using equations (3) and (4) for normal and enhanced dissolution, respectively. The detailed model description and its implementation can be found in previous studies (Saba, 1999; Saba and Illangasekare, 2000; Saenton et al., 2002).

2.2.4 *Multiple tracers test*

Multiple tracers tests originally developed in the petroleum industry for the characterization of oil reservoirs have been proposed to characterize NAPL contaminated sites (Jin et al., 1995). This method uses suite of chemical tracers to detect the presence of NAPL free phase and provide an estimate of its *effective* or average NAPL saturation ($\bar{S}_N$). Based on the estimated average NAPL saturation, the amount of NAPL, usually measured by volume (V_N), within the tracer-swept region can be estimated. The theory behind this method and its experimental and/or field implementations have been described elsewhere (Jin et al., 1995; Annable et al., 1998). The theory is based on the tracer partitioning relationship between the aqueous and NAPL phases which is usually assumed to be a linear relationship:

$$K_p = \frac{c_n}{c_w}, \tag{5}$$

where c_n is the concentration of partitioning tracer in nonaqueous phase, and c_w is the partitioning tracer concentration in the aqueous phase. K_p is NAPL-water partition coefficient. The average saturation over the tracer-swept volume can be determined based on a retardation factor defined by the following relationship:

$$R = 1 + \frac{K_p \bar{S}_N}{(1 - \bar{S}_N)} = \frac{\bar{t}_p}{\bar{t}_n}, \tag{6}$$

where R is the retardation factor for partitioning tracer compared to conservative tracer, which is the ratio of the average travel times for partitioning and conservative tracers. The average travel times are calculated using the temporal moments based on the following expression

$$\bar{t}_i = \frac{\int t \cdot c_i(t) \cdot dt}{\int c_i(t) \cdot dt}. \tag{7}$$

Although partitioning tracer technique has been widely used to determine the amount of nonaqueous phase liquid present in subsurface environments, this method is generally limited to the characterization of NAPL source zone at *low* saturations (Wilson & Mackay, 1995; Hunkeler et al., 1997). The characterization of high saturation entrapped NAPL is still doubtful in terms of the accuracy in estimating the total NAPL volume in the tracer-swept zone. Based on the numerical simulation study by Jin et al. (1997), NAPL volume at high saturation (in this case, a TCE pool) is always underestimated and the associated error is found to be as high as 60%. From their study, the partitioning tracers test cannot detect all the NAPL mass in the pool. This implies that the only a fraction of DNAPL in the entrapment zone can be detected. Dai et al. (2001) demonstrated the limitation of the technique under non-homogenous entrapment configurations.

In this research we intend to evaluate the feasibility of using multiple tracers test to evaluate the remediation performance by considering the *change* that occurs in the source zone after surfactant flushing. The retardation factors as well as the breakthrough curve patterns of the partitioning tracers prior to and after remediation will be compared and analyzed.

3 DISSOLUTION EXPERIMENTS AND RESULTS

3.1 *Two-dimension horizontal dissolution cell*

A bench-scale, two-dimension test tank was designed and constructed for tracer and DNAPL dissolution studies (natural and enhanced). The tank composed of clear plexiglas walls for top and bottom plates, and aluminum metal pieces for sides. Internal void volume of the tank is nominally $65.0 \times 24.0 \times 5.0\,\text{cm}^3$. The tank is filled with well-characterized sand #70, and the source zone placed at the center is filled by #16 sand (Unimin Corporation). The source zone is 16.5-cm long and 5.0-cm wide (Figure 1). Source zone was filled to approximately one-third of its total thickness of 5.0-cm with red-dyed (Sudan IV, Sigma Chemicals) tetrachloroethene or PCE (Aldrich Chemicals). The total volume of PCE injected into the source zone using a glass syringe is $31.0\,\text{cm}^3$. The tank was then flipped over for two days to allow the injected PCE to "wet" the sands in the source zone. After one day, the tank was flipped back allowing the PCE to drain by gravity for 24 hours. The resultant theoretical PCE saturation

Copyright © 2003 Swets & Zeitlinger B.V., Lisse, The Netherlands

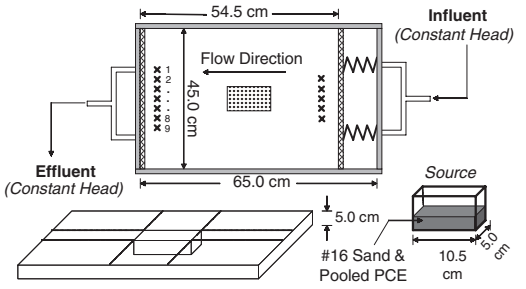


Figure 1. 2-D horizontal dissolution cell setup.

distribution as a function of depth $S_{nw} = S_{nw}(z)$ was determined using the method suggested by Moreno-Barbero et al. (2002). This theoretical saturation profile is also verified using a dual-gamma system that measures the in situ NAPL saturation using photon attenuation (Gago et al., 2002). This saturation profile was used in the subsequent numerical simulations. Two constant-head reservoirs were installed upstream and downstream of the tank to maintain continuous and steady flow of deionized water (ROPure®, Barnstead/Thermolyne Corporation) through the packed sand. Three injection ports located upstream of the source zone were used for tracer solution injection. A Multichannel Syringe Pump (Soil Measurement Systems) was used to provide a constant flow rate of the injected tracer solution. Nine sampling ports located downstream were used to extract samples of aqueous solution. The outlet was also used as an additional sampling location to monitor total flow rate as well as to check total mass balance.

3.1.1 *Natural dissolution*

As soon as the hydraulic gradient was applied to the tank (after the source zone preparation was done) that produces the flow rate of 8.08 $cm^3\,min^{-1}$ (or seepage velocity $\bar{v} = 3.59 \times 10^{-2}$ cm min^{-1}: for experiment 1 referred to as EXP01), the transient break through concentration was monitored. The collected aqueous samples were analyzed using HP6890 Gas Chromatography with Flame Ionization Detector (Hewlett Packard). Figure 2 shows experimental data as well as the model fit (equation 3). The optimized parameters for natural dissolution are listed in Table 1.

3.1.2 *Enhanced dissolution*

In the surfactant-enhanced dissolution experiments, the non-ionic surfactant Polyoxyethylene Sorbitan Mono-oleate or Tween-80 was used. Tween-80 is a non-toxic biologically degradable, food-grade surfactant. The surfactant solution was prepared from concentrated Tween-80 at a concentration of 50.0 g L^{-1}. The surfactant solution was stirred overnight to allow complete dissolution. This solution was then injected

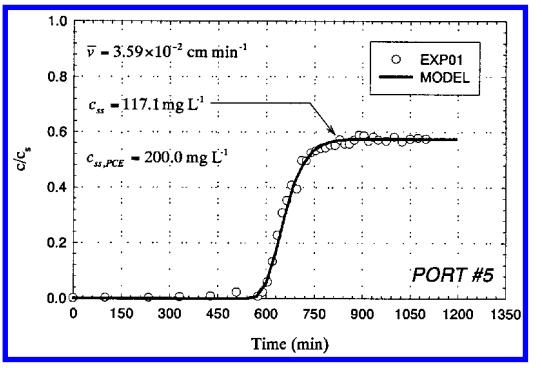


Figure 2. Transient concentration of PCE at port #5 and model fit.

Table 1. Values of optimized empirical parameters for normal and enhanced dissolution obtained from inverse modeling.

Parameters	Natural	Enhanced
α	9.17	0.561
β	0.216	0.207
γ	0.5	0.5
η	1.071	1.98
ξ	–	0.273

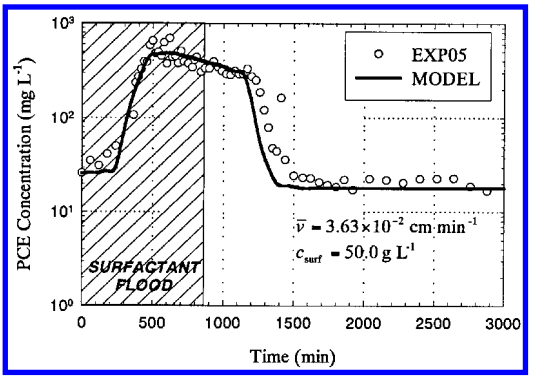


Figure 3. Surfactant enhanced dissolution: experimental and numerical model results.

through three injection ports at a rate of 2.774 $cm^3\,min^{-1}$ into the dissolution cell where the groundwater was flowing at a steady rate of 8.17 $cm^3\,min^{-1}$. The reservoir was flooded for 865 min (14.4 hr) and the concentration of PCE was monitored downstream.

Figure 3 shows PCE concentration in the effluent as a function of time. It can be seen that Tween-80 effectively enhanced the dissolution of PCE and removed the PCE free phase from zones where high mass transfer occurred. This is confirmed by comparing the

Copyright © 2003 Swets & Zeitlinger B.V., Lisse, The Netherlands

resulting steady-state effluent concentrations before and after surfactant flood, which decreased from 27.0 to 17.1 mg L^{-1}.

The model fit to experimental data is illustrated in Figure 3 and the inverse modeling results (optimized empirical parameters) are listed in Table 1. These calibrated surfactant-enhanced and natural dissolution models will be used in numerical simulations. Specifically we will use these validated numerical tools to investigate the consequences of partial source zone treatment where a fraction of the free-phase NAPL is recovered from the entrapment zone.

After the post-surfactant tracers test (EXP07), the surfactant solution was injected to the system three more times (14–15 hr flush duration) in order to investigate the effect of partial source zone treatment. As can be seen in Figure 4, the downstream concentration of the PCE (in the effluent) decreases when more PCE mass is removed (based on mass balance calculations). Although, approximately 80% PCE mass is removed from the source zone (primarily from the transition zone of low to intermediate saturations), downstream PCE concentration is still found to be high.

3.1.3 *Multiple tracers test*

The multiple tracer solution containing 350 mg L^{-1} bromide (as NaBr) and 325 mg L^{-1} 2,2-dimethyl-3-pentanol (DMP) was injected through three injection ports for 1 to 3 hours depending on the total flow rate used in each experiment. Aqueous sample were collected at the outlet at 10 to 60 min intervals. These samples were analyzed using HP7840 Gas Chromatography with Flame Ionization Detector (Hewlett Packard) for DMP and Ion Chromatography with Conductivity Meter (Dionex) for bromide. The total steady-state flow rate used in all experiments ranged from 3.0 to 9.0 cm^3 min^{-3}.

In order to compare results from pre- and post-surfactant flushing tracer tests, the experimental conditions must be the same with respect to average seepage velocity. In this case, we will compare the two data sets which are identified as EXP03 (pre) and EXP07 (post). The seepage velocity for EXP03 and EXR07 are 1.58×10^{-2} and 1.61×10^{-2} cm min^{-1}, respectively. Figures 5 and 6 show the experimental results for both pre- and post-remediation as well as the corresponding retardation factors. The value of PCE-water partition coefficient of DMP was determined previously as $K_p = 25.71$ (Moreno-Barbero et al., 2002).

The results of the moment analysis conducted on the tracer breakthrough data are listed in Table 2. As

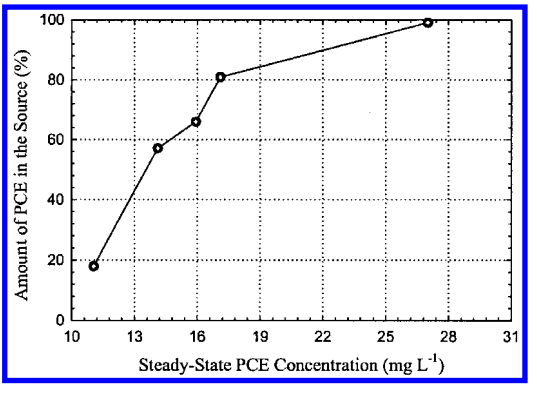


Figure 4. Steady-state PCE concentration as a function of PCE mass left in the source zone after each surfactant floods.

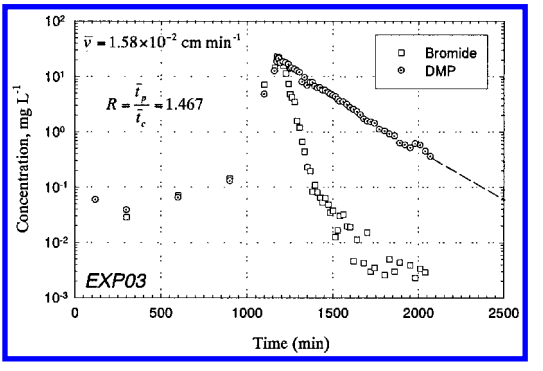


Figure 5. Multiple tracers test experimental results for EXP03 (pre-remediation).

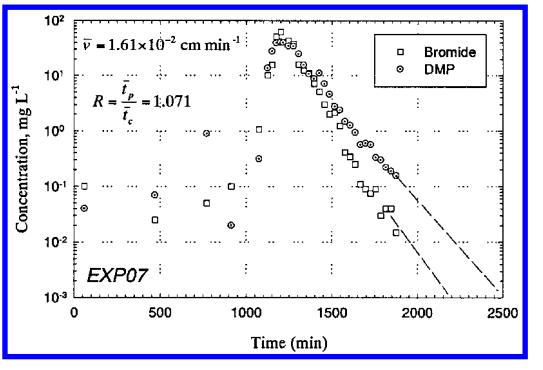


Figure 6. Multiple tracers test experimental results for EXP07 (post-remediation).

Table 2. Results from temporal moment analysis for pre- and post-remediation multiple tracers test.

Experiment	R	$\bar{S}_N$	V_N (cm^3)
Pre-Remediation (EXP03)	1.465	0.0178	6.13
Post-Remediation (EXP07)	1.071	0.00275	0.93

Copyright © 2003 Swets & Zeitlinger B.V., Lisse, The Netherlands

expected, the average saturation as well as the volume of NAPL that the partitioning tracers test can detect for pre-remediation is larger than the volume obtained from post-remediation tracers test. However, both detectable volumes are significantly smaller than the original volume of PCE in the source zone (31.0 cm^3). From the above results, it can be seen that the 14.4-hour duration surfactant flood removed 84.8% of detectable PCE mass. Interestingly, despite the near 85% removal of NAPL free phase, the steady-state PCE concentration for pre- and post-remediation drops only by 36.7% (from 29.0 to 17.1 mg L^{-1}).

4 NUMERICAL SIMULATION STUDY OF PARTIAL SOURCE ZONE TREATMENT

4.1 *Intermediate-scale test tank*

A set of numerical simulations was conducted to represent conditions in a two-dimensional, intermediate-scale, heterogeneous-packed test tank with the dimension of 9.75-m long 1.2-m high and 0.06 m thick. The tank consists of homogeneous and heterogeneous zones (see Figure 7). Two constant-head supplies are used to maintain a steady hydraulic gradient throughout the experiment. The homogeneous part of the tank consists of #8 sand within which an injection well is placed to deliver a treating agent for NAPL mass removal by enhanced dissolution. The heterogeneous zone is packed using five sand of different sieve sizes (#16, #30, #50, #70, and #110). The properties of these sands are listed in Table 3.

The heterogeneity was designed as a spatially correlated random field with statistical parameters similar to heterogeneous field sites. This heterogeneous packing assumes a log-normal distribution of hydraulic conductivity with a mean value $\mu_{\ln K}$ of 4.18 (cm hr^{-1}) and a variance $\sigma^2_{\ln K}$ of 1.22. The correlation lengths in lateral (λ_h) and vertical (λ_v) directions are 50.8 and 5.08 cm, respectively. The heterogeneous zone consists of 1280 cells of 25.4 cm in length and 2.54 cm in depth which corresponds to 32 columns and 40 layers resulting in 16 lateral and 20 vertical correlation lengths. A more detailed discussion of tank setup and packing can be found in Barth (1999) and Barth et al. (2001a&b).

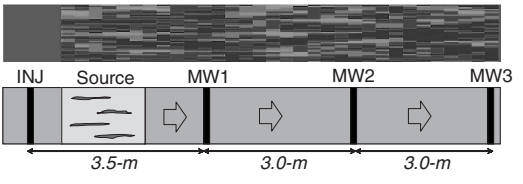


Figure 7. Heterogeneous distribution of five different sands in the test tank used in this study (top). The bottom diagram shows the locations of the injection well, the source zone, and the general flow direction.

Table 3. Sand properties used in the experiments.

Sand Type	#16	#30	#50	#70	#110
K (cm hr^{-1})	1550.0	540.0	133.0	48.6	15.1
d_{50} (mm)	1.08	0.5	0.32	0.2	0.12
$S_{r,w}$	0.07	0.26	0.29	0.30	0.26

4.2 *PCE spill simulation*

The NAPL source zone (1.54-m × 1.02-m) is created from a spill simulation using version 9.3 of UTCHEM. The location of the source zone is shown in Figure 6. The source zone is discretized into 40 layers and 24 columns. The capillary pressure-saturation relationship assumes Brooks-Corey drainage model. Total PCE spill volume is 2.03 L (the average saturation is $\bar{S}_{nw} = 0.085$) and the spill rate is 2.0 L d^{-1}. The spill location is at the center of the top layer. The spill simulation was conducted for a long time for the spill (migration of PCE) to reach a static state. The resulting simulated PCE distribution is shown in Figure 8. As can be seen from the distribution pattern, most of the PCE is entrapped in high permeability zones. Some PCE is pooled on top of the low permeability lenses while PCE residuals are found in several locations throughout the source zone. This saturation distribution will be used in the subsequent normal and enhanced dissolution simulation studies.

The results of the particle tracking simulations shown in Figure 9 (using MODPATH), show the flow paths of particles introduced at the injection wells at the source zone prior to and after the PCE spill. As can be seen from Figure 9, the flow bypasses the entrapped PCE zone (see dash ellipses). Therefore, it should be expected that the injected surfactant solution will bypass the entrapment zone, thus reducing the effectiveness of the remediation.

4.3 *Normal dissolution simulation*

The source zone created from the UTCHEM simulation is embedded in the test tank. A hydraulic gradient of 10^{-3} was used to represent natural groundwater flow conditions. The calibrated model developed previously (in Section 3.1.1) was used to simulate normal dissolution of PCE based on Gilland-Sherwood relationship in Eq. (3) and the empirical parameters in Table 1. Figure 10 shows the reduction of mass of PCE in the source zone due to the natural dissolution. The depletion rate was found to be 2.105 mg d^{-1}.

The downstream plume concentration in three monitoring wells calculated based on the discharge weighted average are plotted in Figure 11. The

Copyright © 2003 Swets & Zeitlinger B.V., Lisse, The Netherlands

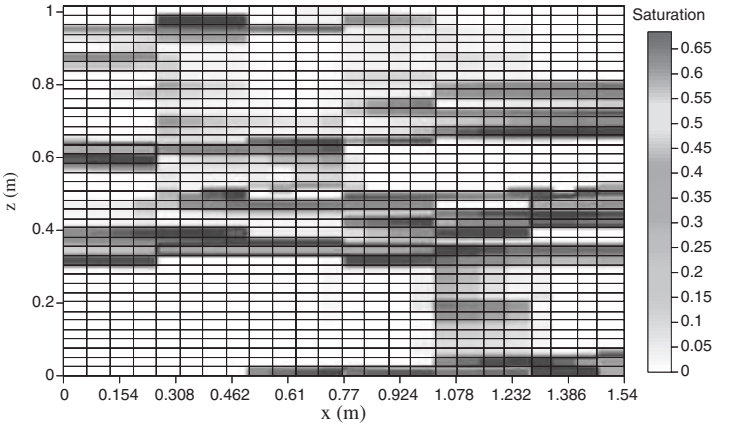


Figure 8. Steady-state PCE spill distribution in the source zone.

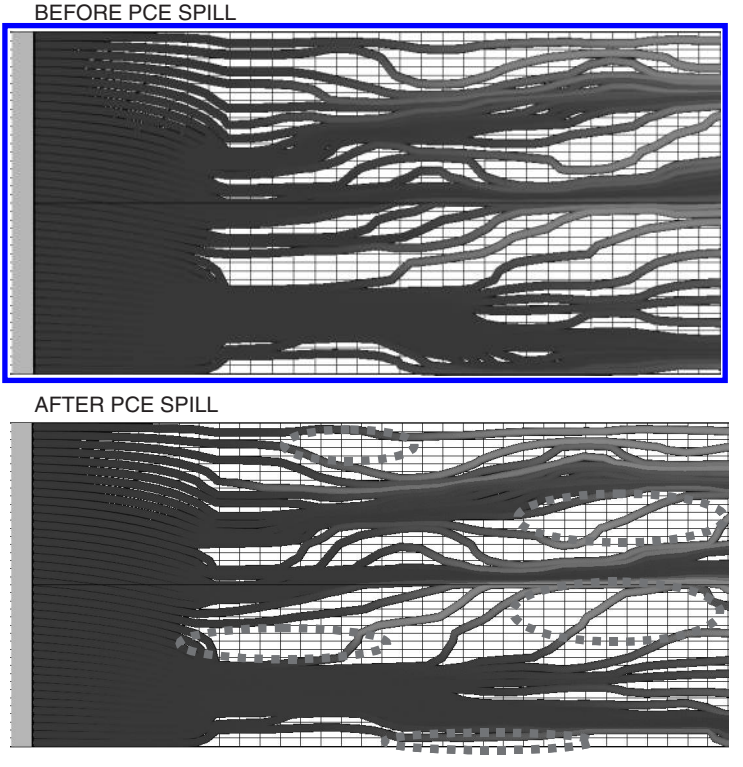


Figure 9. Particle-tracking simulation results for the flow paths of particles introduced at the injection well.

concentrations of PCE at three monitoring wells reached steady-state at 75 to 150 days. The steady-state concentration is approximately $120\,\mu g\,L^{-1}$ where as the regulated maximum contaminant level or MCL for tetrachloroethene (PCE) is $5\,\mu g\,L^{-1}$. Obviously, the source zone needs further remediation in order to reduce the downstream concentration.

4.4 *Surfactant enhanced remediation simulation*

In surfactant-enhanced remediation simulation a fully penetrated extraction well was placed at the right end of the source zone. A surfactant solution containing Tween-80 at a concentration $50.0\,\mu g\,L^{-1}$ is injected upstream of the source zone through an injection well

Copyright © 2003 Swets & Zeitlinger B.V., Lisse, The Netherlands

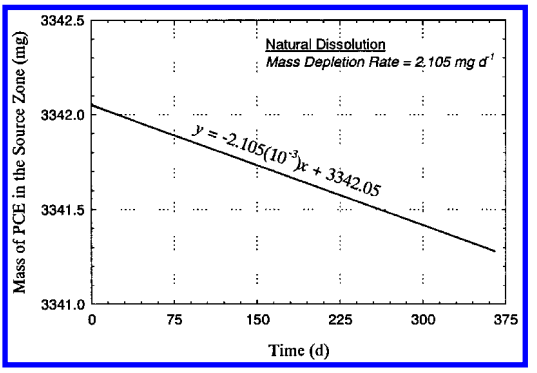


Figure 10. Mass depletion rate of PCE for natural dissolution.

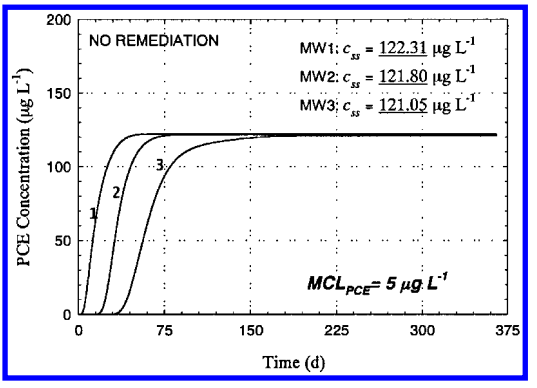


Figure 11. Downstream PCE concentration in three monitoring wells.

at the flow rate of 75.0 $cm^3\,min^{-1}$ which is approximately equal to the total steady-state groundwater flow rate of the tank under the hydraulic gradient of 10^{-3}. Mass of the PCE zone remaining in the source zone as a function of treatment time is shown in Figure 12.

The PCE concentration downstream at the monitoring well as a function of mass removal in the source zone was determined. The surfactant flood is simulated for time Δt. As a result, this will extract PCE mass of Δm_1 from the source zone. The natural dissolution model then takes over to simulate the steady-state PCE concentration $c_{ss}^{\Delta m_1}$ for the particular distribution of PCE that has a mass of $m_0 - \Delta m_1$ in the source zone where m_0 is the original mass of PCE. Figure 13 shows the steady-state PCE concentration at monitoring well MW1 as a function of percentage mass removal. From this plot, it can be seen that for this particular case, it is necessary to remove at least 80% of the total PCE mass from the source zone to observe any significant concentration drop in the downstream plume. If the MCL is of concern, more than 99% of the total mass has to

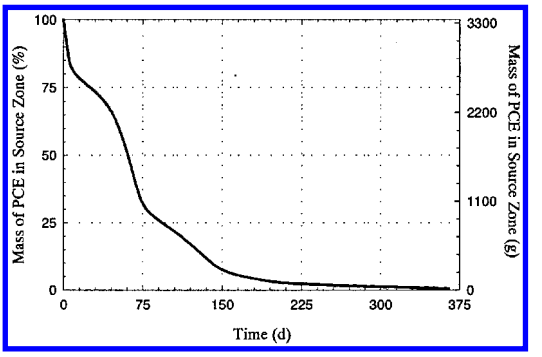


Figure 12. Mass of PCE in the source zone as a function of clean-up time.

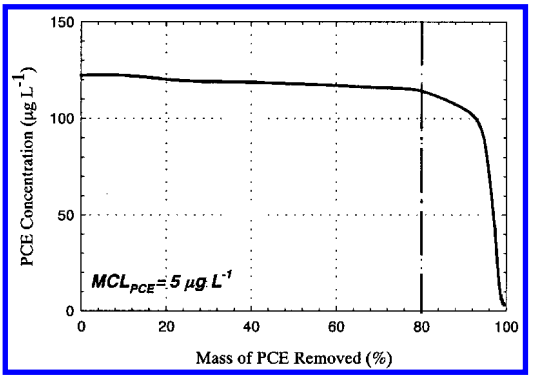


Figure 13. PCE concentration in MW1 as a function of mass of PCE removed from the source zone.

be removed in order to lower the plume concentration below 5.0 $\mu g\,L^{-1}$.

Although this numerical result is based on only one realization of the spatially correlated hydraulic conductivity field, it agrees relatively well with the preliminary experimental results (single-source PCE) shown in Figure 4. An ongoing research is now investigating the numerical experiments based on more realizations of random fields in order to draw a valid conclusion regarding the effect of partial source zone treatment.

5 CONCLUSIONS

This study evaluated the effects of partial removal of NAPLs from source zones. A previous investigation by Sale and McWhorter (2001) pointed out the limited near-term benefits of partial source zone treatment in achieving cleanup goals. The conclusions of this study cannot be generalized because of simplifying assumptions that were made with respect to the source architecture and flow field. This study

Copyright © 2003 Swets & Zeitlinger B.V., Lisse, The Netherlands

presented a methodology that used experimentally validated numerical models that simulate natural and enhanced dissolution in heterogeneous aquifers where NAPLs are entrapped in complex architecture. Preliminary results based on a limited number of simulations suggest that a very high fraction of NAPL mass has to be removed from the source zone to make any significant impact on the plume concentrations downstream of the source zone. However, to make any general conclusions applicable to field sites and for other remediation technologies, further studies are needed. Such a study is currently in progress where the benefits of other source zone technologies in reducing plume concentrations are evaluated. These technologies include biotreatment, chemical oxidation and thermal recovery. This study also demonstrated the limitations of using multiple tracer techniques to characterize the source zones both prior to and post treatment.

ACKNOWLEDGEMENTS

The authors gratefully acknowledge the following funding sources: (1) National Science Foundation Major Research Instrumentation Award BES-997708, (2) National Science Foundation Award EAR-0107095 (3) Department of Defense SERDP Grant CU-1294 and (4) Royal Thai Government. The assistance provided by Dr. Donping Dai to conduct the chemical analysis is thankfully acknowledged.

REFERENCES

Annable, M.D., Rao, P.S.C., Hatfield, K., Graham, W.D., Wood, A.L., & Enfield, C.G. 1998. Partitioning tracers for measuring residual NAPL: Field-scale test results. J. Environ. Eng. 124(4): 498–503.

Abdul, A.S., Gibson, T.L., Ang, C.C., & Smith, J.C. 1992. In situ surfactant washing of polychlorinated biphenyls and oils from contaminated soils. Ground Water 30: 219–231.

Barth, G.R. 1999. Intermediate-scale tracers test in heterogeneous porous media: Investigation of density, predictability, and characterization of NAPL entrapment. Ph.D. Thesis, University of Colorado.

Barth, G.R., Illangasekare, T.H., Hill, M.C., & Rajaram, H. 2001a. A new tracer-density criterion for heterogeneous porous media. Water Resour. Res. 37(1): 21–31.

Barth, G.R., Hill, M.C., Illangasekare, T.H., & Rajaram, H. 2001b. Predictive modeling of flow and transport in a two-dimensional intermediate-scale, heterogeneous porous medium. Water Resour. Res. 37(10): 2503–2512.

Bird, R.B., Stewart, E.W., & Lightfoot, E.N. 1960. Transport phenomena. John Wiley, New York.

Dai, D., Barranco, F., & Illangasekare, T.H. 2001. Partitioning and Interfacial Tracers for Differentiating NAPL Entrapment Configuration: "Column-Scale Laboratory Results". *Environmental Science and Technology* 35(24): 4894–4899.

Dekker, T.J., & Abriola, L.M. 2000. The influence of field-scale heterogeneity on the infiltration and entrapment of dense nonaqueous phase liquids in saturated formations. J. Contam. Hydrol. 42: 187–218.

Delshad, M., Pope, G.A., & Sepehrnoori, K. 1996. A compositional simulator for modeling surfactant enhanced aquifer remediation. J. Contam. Hydrol. 23(1-2): 303–327.

Fountain, J.C., Klimek, A., Beikirch, M.G., & Middleton, T.M. 1991. Use of surfactants for in situ extraction of organic pollutants from a contaminated aquifer. J. Hazard. Mat. 38(3): 295–311.

Gago, J.L., Middleton, G., Hill, E.H., & Illangasekare, T.H. 2002. Real time monitoming of NAPL sources using photon attenuation techniques on chlorinated solvents. Poster presentation at 2002 Denver Annual Meeteng (Oct. 27–70, 2002), Geological Society of America.

Hunkeler, D., Hoehn, E., Höhener, P., & Zeyer, J. 1997. ^{222}Rn as a partitioning tracer to detect diesel fuel contamination in aquifers: Laboratory study and field observations. Environ. Sci. and Technol. 31(11): 3180–3187.

Illangasekare, T.H., Ramsey, J.L., Jensen, K.H., & Butts, M. 1995. Experimental study of movement and distribution of dense organic contaminants in heterogeneous aquifers: An experimental study. J. Contam. Hydrol. 20(1): 1–25.

Illangasekare, T.H. 1998. Flow and entrapment of nonaqueous phase liquids in heterogeneous soil formations. In, H.M. Selim & L. Ma (eds). Physical nonequilibrium in soil. Ann Arbor Press. p. 417–423.

Imhoff, P.T., Jaffe, P.R., & Pinder, G.F. 1994. An experimental study of complete dissolution of a nonaqueous phase liquid in saturated porous media. Water Resour. Res. 30(2): 307–320.

Jin, M., Delshad, M., Dwarakanath, V., McKinney, D.C., Pope, G.A., Sepehrnoori, K., & Tilburg, C.E. 1995. Partitioning tracer test for detection, estimation, and remediation performance assessment of subsurface nonaqueous phase liquids. Water Resour. Res. 31(5): 1201–4231.

Jin, M., Butler, G.W., Jackson, R.E., Mariner, P.E., Pickens, J.F., Pope, G.A., Brown, C.L., & McKinbey, D.C. 1997. Sensitivity models and design protocol for partitioning tracer test in alluvial aquifers. Ground Water 31(6): 964–972.

Kaluarachchi, J.J., & Parker, J.C. 1990. Mudeling multicomponent organic chemical transport in three-phase porous media. J. Contam. Transp. 5, 349.

Martel, R., Galinas, P.J., & Saumure, L. 1998. Aquifer washing by micellar solutions: 3. Field test at the Thouin sand pit. J. Contam. Hydrol. 30: 33–48.

Mason, A.R., & Kueper, B.H. 1996. Numerical simulation of surfactant enhanced solubiization of pooled DNAPL. Environ. Sci. Technol. 30(11): 3205–3215.

Mercer, J.W., & Cohen, R.M. 1990. A review of immiscible fluids in the subsurface: Properties, models, characterization and remediation. J. Contam. Hydrol. 6: 107–163.

Miller, C.T., Poirier-McNeil, M.M., & Mayer, A.S. 1990. Dissolution of trapped nonaqueous phase liquids: Mass transfer characteristics. Water Resour. Res. 23(11): 2783–2793.

Moreno-Barbero, E. 2000. Evaluation of surrogates DNAPLs for partition and dissolution intermediate-scale tests. Appendix III for NSF Progres Report.

Moreno-Barbero, E., Dai, D., & Illangasekare, T.H. Evaluation of the partition interwell tracer technique for possible

Copyright © 2003 Swets & Zeitlinger B.V., Lisse, The Netherlands

characterization of DNAPL pools. American Geophysical Union, 2002 Fall Meeting Abstracts, vol. 83 (47).
Nambi, I.M., & Powers, S.E. 2000. NAPL dissolution in heterogeneous systems: An experimental investigation in a simple heterogeneous system. J. Contam. Hydrol. 44: 161–184.
Pennell, K.D., Abriola, L.M., & Weber, Jr., W.J. 1993. Surfactant enhanced solubilization of residual dodecane in soil columns: 1. Experimental investigation. Environ. Sci. Technol. 16(1): 35–53.
Pennell, K.D., Abriola, L.M., & Pope, G.A. 1994. Surfactant enhanced remediation of soil columns contaminated by residual tetrachloroethylene. J. Contam. Hydrol. 16: 35–53.
Powers, S.E., Abiola, L.M., & Weber, Jr., W.J. 1992. An experimental investigation of nonaqueous phase liquid dissolution in saturated subsurface systems: Steady-state mass transfer rates. Water Resour. Res. 28(10): 2691–2705.
Saba, T.A. 1999. Upscaling of mass transfer from entrapped NAPLs under natural and enhanced conditions. Ph.D. Thesis. University of Colorado.
Saba, T.A., & Illangasekare, T.H. 2000. Effect of groundwater flow dimensionality on mass transfer from entrapped nonaqueous phase liquid contaminants. Water Resour. Res. 36(4): 971–979.
Saba, T.A., Illangasekare, T.H., & Ewing, J. 2001. Surfactant enhanced dissolution of entrapped NAPLs in multidimensional flow fields. J. Contam. Hydrol. 51(1-2): 63–82.
Saenton, S., Illangasekare, T.H., Soga, K., & Saba, T.A. 2002. Effect of source zone heterogeneity on surfactant enhanced NAPL dissolution and resulting remediation endpoints. J. Contam. Hydrol. 59(1-2): 63–82.
Sale, T., & McWhorter, D.B. 2001. Steady-state mass transfer from single-component dense non-aqueous phase liquids in uniform flow fields. Water Resour. Res. 37(2): 393–404.
Sleep, B.E., & Sykes, J.F. 1993. Compositional simulation of groundwatercontamination by organic compounds. Water Resour. Res. 29(6): 1697–1708.
Wilson, R.D., & D.M. Mackay. 1995. Direct detection of residual nonaqueous phase liquid in the saturated zone using SF_6 as a partitioning tracer. Environ. Sci. Technol. 29(5): 1255–1258.

Copyright © 2003 Swets & Zeitlinger B.V., Lisse, The Netherlands

The contribution of natural attenuation processes for the remediation of contaminated sites

P. Werner
Dresden University of Technology, Dresden, Germany

ABSTRACT: Contaminated sites are common in all industrial countries. Regarding Germany there are about 300 000 (!) such sites known. It will be impossible from technical and financial point of view to remediate all sites by classical means. Therefore there is a need of a realistic risk assessment of the hazardous compounds concerning their impact on the receptors atmosphere, soil, groundwater and surface water. Natural attenuation offers large benefits to owners and managers of contaminated sites and could even be applied as part of the remediation strategy.

1 INTRODUCTION

Under certain circumstances natural attenuation processes can be successful measures for reducing risk to human beings and the environment from organic and inorganic contaminants in soil and groundwater.

Natural attenuation relies upon natural processes, rather than engineered approaches, for its effectiveness. These natural processes, according to the U. S. Environmental Protection Agency, include biodegradation, dispersion, dilution, sorption, volatilisation, radioactive decay; and chemical or biological stabilisation, transformation, or destruction of contaminants. The German approach comprises the same processes excluding dilution.

The preferred processes are biodegradation for organic and stabilisation for heavy metals because they reduce potential exposure, effecting more permanent protection. Natural attenuation is frequently relied upon as a safeguard from contaminants remaining after engineered remediation of a site, such as source removal. In order to confirm that natural attenuation is protective, a good conceptual model of a site that details the effective natural attenuation processes is required, and long-term monitoring to insure that the relevant processes are occurring and that undesirable contaminant movement or transformation is not occurring. This is termed monitored natural attenuation.

2 FATE OF THE COMPOUNDS IN SOIL AND GROUNDWATER

In order to explain the principles in the application of natural attenuation the situation existing in tar contamination is described. Tar contaminations can be found essentially at coalgasification plants, kokeries, wood preserving industries, chemical industries based on polyaromatic-compounds and so-called “tar lakes”, which are common not only in Eastern Germany but also in Eastern countries like Poland or Czech Republic.

Common to all sites mentioned are polyaromatic hydrocarbons (PAH). But according to the technologies applied and industrial branches more soluble hazardous compounds in even high quantities can be found in the subsurface, too. Those compounds are: phenols, monoaromatic compounds and aliphatic hydrocarbons, which might have a higher impact on the groundwater than the PAHs it self, due to their higher solubility and mobility.

Each contaminated site has its own history and therefore requires an individual risk assessment. All organic compounds existing in those sites are biodegradable in principle. But the fate is controlled by the physico-chemical and microbial environmental conditions.

The natural biodegradation of PAH, mineraloils, monoaromatic compounds and phenols is a well known process since along time and encouraged people to apply this process for active remediation technologies at contaminated sites (Cerniglia 1984, Smith 1990).

To which extend the natural attenuation processes can be active at the site depends on the environment. There is still a lack of knowledge on the complexity of the different interactions in the subsurface.

Some decisive factors governing the processes are:

- speciation and concentrations of the hazardous compounds

Copyright © 2003 Swets & Zeitlinger B.V., Lisse, The Netherlands

- composition of the contaminant cocktail
- availability of different electron acceptors required for the mineralisation
- redox potential
- pH value
- temperature
- geology
- hydrology
- daughter products

(Shiaris 1989, Loveley et al. 1994, Christensen 1995).

If there are more than one electron acceptor existing in the subsurface, they are used by the microorganisms one by one according the redoxpotential. Electron acceptors can be: oxygen, nitrate, sulphate, oxides of iron and manganese, carbonate.

According experiences from practice the most limiting factor is the deficiency of oxygen in the system.

Based on many investigations in lab scale a lot of reliable data on the aerobic biodegradation of aromatic hydrocarbons are existing (Cerniglia and Heitkamp 1989, Kästner et al. 1993). All monoaromatic compounds and all 2, 3 and 4 ring PAHs are well biodegradable in the presence of oxygen.

Many out of those compounds are also biodegradable under anoxic conditions like denitrification, sulphate reduction, iron and manganese reduction and even under methanogenic conditions. But the knowledge on the efficiency of those processes for the natural attenuation at the site and in the plume is still weak.

3 MICROBIAL DEGRADATION OF SOME DIFFERENT HAZARDOUS COMPOUNDS

3.1 *Mineral oils*

Mineral oils are a mixture of different compounds and their properties vary with respect to solubility, toxicity, adsorbability and biodegradability. The properties depend on the length of the C-chains and their spherical position in the molecules. The longer the chain the less biodegradable to compound is. The biodegradability of mineral oils decrease according the following ranking:

Alkanes – Iso-Alkanes – Alkenes – Alkines – Cycloalkanes

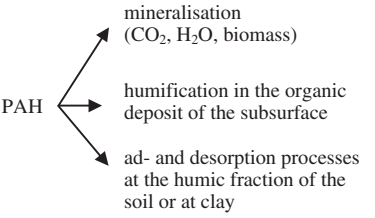
Many investigations confirm this behaviour and in some site samples undergoing natural attenuation processes the alkane fraction disappeared completely while the other compounds are still existing or show at least a weaker biodegradability (Anonymus 1991).

In general mineral oils are readily biodegradable under aerobic conditions and oxygen is the limiting factor. But biodegradation could be proved under anoxic conditions with electron acceptors others than oxygen, too (Bregnard et al. 1997, Ackersberg et al. 1991, Rueter et al. 1994).

3.2 *Polyaromatic hydrocarbons*

The fate of the PAHs can roughly be compared with the fate of the mineral oils. The higher the molecular weight is the less soluble in water and the less biodegradable the compounds are.

Moreover PAHs are well absorbable and even can be integrated in natural humic fractions, too (Kästner et al. 1993). The following schematic demonstrates the possible natural fate of PAHs:



Adsorption processes decrease the biodegradation capacity of PAHs but do not prevent them completely.

All PAHs are biodegradable under aerobic conditions. Most of the publications addressing the anoxic degradation of PAH are related to denitrification. Mihelcic and Luthy described the degradation of naphthalene under denitrifying conditions in 1988. This process could be proved by Al-Bashir et al. 1990, Mihelcic and Luthy 1991, Bregnard et al. 1996, Rockne et al. 1997, too.

PAH-biotransformation up to 4 – ring compounds under anoxic conditions could be found by Leduc et al. 1992 and Mills et al. 1997. Most of the investigations concerning naphthalene and phenanthrene address sulphate reducing conditions (Langenhoff et al. 1996, Coates et al. 1996, Coates et al. 1997, Zhang and Young 1997). Partially the investigations were extended to benzo(a)pyrene (Leduc et al. 1992, Flyvbjerg et al. 1993, Sharak Genther et al. 1997). The data existing so far prove the mineralisation of 2 and 3 ring PAHs under sulphate reducing conditions. The knowledge on the fate of 4 ring PAHs is still weak, but their biodegradation seems possible.

There are also indications on the metabolisation of PAHs under iron and manganese reducing conditions (Lyngkilde and Christensen 1992, Coates et al. 1996, Langenhoff et al. 1996). Even under methanogenic conditions at least a partial degradation of some PAHs seems possible (Parker and Montheit 1995).

3.3 *Monoaromatic compounds*

This group of contaminants comprises benzene, toluene, ethylbenzene and xylenes. They are moderately soluble in water, readily biodegradable and weakly absorbable. Benzene is highly toxic and

Copyright © 2003 Swets & Zeitlinger B.V., Lisse, The Netherlands

carcinogenic, but as a rule best biodegradable among this group.

Under aerobic environmental conditions the kinetic of biodegradation of all those compounds is very high. Moreover they are biodegradable under anoxic and even under methanogenic conditions, too (Vogel and Grbic'-Galic' 1987). Some research groups could prove the mineralisation of BTEX-compounds under sulphate reducing conditions (Edwards et al. 1991, Beller 1992, Weiner et al. 1998). Edwards et al. 1991 describe a ranking in the biodegradation as follows: toluene, p-xylene and o-xylene. No transformation in the presence of sulphate could be observed for benzene and ethylbenzene on the other hand. Loveley et al. (1995 and 1996) could prove the degradation of benzene during sulphate reducing conditions. Even under iron-reducing conditions BTEX compounds can be oxidised. It is remarkable that the rate of minerlization under the conditions is almost as high as under aerobic conditions (Loveley et al. 1994).

The microorganism can use the iron oxides existing in the subsurface for the oxidation of the monoaromatic compounds in the frame of a natural attenuation process. According Baedecker et al. 1993, Bennet et al. 1993 and Eganhouse et al. 1993 this process in predominant for the oxidation of benzene, toluene, ethylbenzene and xylenes during a case study at a refinery site. Iron reduction is present in environments where nitrate and sulphate is depleted.

Wilson (1986) as well as Vogel and Grbic'-Galic' (1987) observed a slow mineralization of benzene, toluene and o-xylene even under methanogenic conditions.

3.4 *Phenolic compounds*

Large quantities of phenolic compounds can be found at tar contaminated sites, too, essentially when the gasification process is based on lignite. Phenols are readily biodegradable in concentrations lower than 200 mg/l. Higher concentrations cause inhibition or even mortality of the microorganism (Anonymus 1991).

The predominant degradation pathway is aerobic and similar to that of the monoaromatic compounds. Anoxic degradation using electronacceptors others than oxygen is common, too. An increasing substitution of methyl groups in the molecule (cresole) causes a dramatic decrease in the biodegradability.

Phenols also can polymerise due to microbial activity and can be integrated in the humic fraction located in the subsurface.

4 APPLICABILITY OF NATURAL ATTENUATION

Natural attenuation only can serve as a remedy technology when the cause and link effect between contaminant loss and the underlying controlling mechanism is well documented. This requires footprints of the destruction or the immobilization process. Therefore natural attenuation is a knowledge based remediation which requires reliable monitoring tools. Only monitored natural attenuation (MNA) will be acknowledged by the regulators. The monitoring tools are not yet developed for all processes occurring in the subsurface and research in this field is still required.

The MNA strategy is applied already in large scale in the USA since several years and will be successful also in other parts of the world. It will be a challenge to enhance natural attenuation processes as a low cost and effective technology.

5 CONCLUSION

Natural attenuation processes have the potential to destroy or to immobilize many contaminants existing in the subsurface but so far it is well established only for a few types of contaminants namely BTEX-compounds. Although almost all hazardous organic compounds present in contaminated sites undergo natural attenuation processes which are controlled by following factors (selection):

- Availability, acceptance and amount of electronacceptors in the subsurface (oxygen, nitrate, etc.)
- Toxicity of the target compounds
- Composition of the contaminant cocktail
- Competitive biodegradation of the target compounds
- Environmental conditions (namely redox, pH, temperature, humidity, hydrology, geology)

The level of effort to evaluate a site depends on site complexity and the contaminant type. Reliable protocols of the sites are required for decision making.

Aerobic and anoxic degradation of the compounds are predominant for natural attenuation processes, while methanogenic processes only play a minor role in the elimination of the contaminants.

The interactions between the different compounds under the different environmental conditions are highly complex and not enough elucidated so far. The knowledge on the processes occurring in the subsurface in still very weak and a reliable predicting modelling requires still a lot of research activity.

REFERENCES

Aeckersberg F., Bak F., Widdel F.: Anaerobic oxidation of saturated hydrocarbons to CO_2 by a new type of sulfate-reducing bacterium. Arch Microbiol., 156: 5–14, 1991.

Al-Bashir B., Cseh T., Leduc R., Samson R.: Effect of soil/contaminant interactions on the biodegradation of naphthalene in flooded soil under denitrifying conditions. Appl. Microbiol. Biotechnol., 34: 414–419, 1990.

Anonym: Handbuch der mikrobiologischen Bodensanierung. Band 7 der Materialien zur Altlastenbearbeitung.

Copyright © 2003 Swets & Zeitlinger B.V., Lisse, The Netherlands

Landesamt für Umweltschutz Baden Württemberg, 1991.
Baedecker, M. J., Cozzarelli, I. M., Eganhouse R. P., Siegel D. I., Bennett, P.C. Crude oil in a shallow sand and gravel aquifer – III. Biogeochemical reactions and mass balance modeling in anoxic groundwater. Applied Geochemistry, 8: 569–586, 1993.
Beller H. R., Grbic'-Galic' D., Reinhard M.: Microbial degradation of toluene under sulfate-reducing conditions and the influence of iron on the process. Appl. Environ. Microbiol., 58: 786–793, 1992.
Bennet P. C., Siegel D. E., Baedecker M. J., Hult M.-F.: Crude oil in a shallow sand and gravel aquifer – II. Organic geochemistry. Applied Geochemistry, 8: 529–549, 1993.
Bregnard T. P.-A., Häner A., Höhener P., Zeyer J.: Anaerobic Degradation of Pristane in Nitrate-Reducing Microcosms and Enrichment Cultures. Appl. Environ. Microbiol., Vol. 63, No. 5, p. 2077–2081, 1997.
Bregnard T. P.-A., Hohener P., Haner A., Zeyer J.: Degradation of weathered diesel fuel by microorganisms from a contaminated aquifer in aerobic and anaerobic microcosms. Environ. Toxicol. Chem., 15: 299–307, 1996.
Cerniglia C. E., Heitkamp M. A.: Microbial degradation of PAH in the aquatic environment. In: Varanasi U. (ed.). Metabolism of polycyclic aromatic hydrocarbons in the aquatic environment, CRC Press Inc., Boca Raton: 41, 68, 1989.
Cerniglia C. E.: Microbial transformation of aromatic hydrocarbons. In: Atlas R. M. (ed.), Petroleum microbiology, Macmillan Publishing Company, New York: 99–128, 1984.
Christensen T. H., Bjerg P. L., Heron G.: Redox buffering in shallow aquifers contaminated by leachate and implications for the development of reduced plumes and in situ remediation. Procedings of Contaminated Soil '95, W. J. van den Brink, R. Bosman and F. Arendt (eds.), Kluwer Academic Publishers, 911–919, 1995.
Coates J. D., Anderson R. T., Lovley D. R.: Oxidation of polycyclic aromatic hydrocarbons under sulfate-reducing conditions. Appl. Environ. Microbiol., 62: 1099–1101, 1996.
Coates J. D., Anderson R. T., Woodward J. C., Phillips E. J. P., Lovley D. R.: Anaerobic hydrocarbon degradation in Petroleum-Contaminated harbor sediments unter sulfate-reducing and artificially imposed iron-reducing conditions. Environ. Sci. Technol., 30: 2784–2789, 1996.
Coates J. D., Woodward J., Allen J., Philip P., Lovley D. R.: Anaerobic degradation of polycyclic aromatic hydrocarbons and alkanes in petroleum-contaminated marine harbor sediments. Appl. Environ. Microbiol., 63/9: 3589–3593, 1997.
Davis J., Klier N., Carpenter C.: Natural biological attenuation of benzene in ground water beneath a manufacturing facility. Ground water, 32: 2, 215–226, 1994.
Edwards E. A., Wills L. E., Reinhard J., Grbic'-Galic' D.: Anaerobic degradation of toluene and xylene by aquifer microorganisms under sulphate-reducing conditions. Appl. Environ. Microbiol., 58: 794–800, 1991.
Flyvbjerg J., Arvin E., Jensen B. K., Olsen S. K.: Microbial degradation of phenols and aromatic hydrocarbons in creosote-contaminated groundwater under NO_3^- reducing conditions. J. Contamin. Hydrol., 12: 133–150, 1993.
Heitkamp M. A., Freeman J. P., Cerniglia C. E.: Napthalene biodegradation in environmental microcosms: Estimates of degradation rates and characterization of metabolites. Appl. Environ. Microbiol., 53: 129–1360, 1987.
Kästner M., Mahro B., Wienberg R.: Biologischer Schadstoffabbau in kontaminierten Böden. Hamburger Berichte 5, Economica Verlag GmbH, Bonn, 1993.
Langenhoff A. A. M., Zehnder A. J. B., Schraag G.: Behaviour of toluene, benzene and napthalene under anaerobic conditions in sediment columns. Biodegradation, 7: 267–274, 1997.
Leduc R., Samson B., Al-Bashir B., Al-Hawari J., Cseh T.: Biotic and abiotic disapearence of four PAH compounds from flooded soil under various redox conditions. Wat. Sci. Tech., 26: 51–60, 1992.
Loveley D. R., Woodward, J. C., Chapelle F. H.: Stimulated anoxic biodegradation of aromatic hydrocarbons using Fe(III)ligands. Nature, 370: 128–131, 1994.
Loveley D. R., Coates J. D., Woodward J. C., Phillips E. J. P.: Benzene oxidation coupled to sulfate reduction. Appl. Environ. Microbiol., 61(3): 953–958, 1995.
Loveley D., Woodward, J. C., Chapelle, F. H.: Rapid anaerobic Benzene Oxidation with a variety of chelated Fe (III) forms. Appl. and Env. Microbiology, 62, 288–291, 1996.
Lyngkilde J., Christensen T. H.: Fate of organic contaminants in the redox zone of a landfill leachate pollution plume (Vejen, Denmark). J. Contam. Hydrol., 10: 291–307, 1992.
Mihelcic J. R., Luthy R. G.: Microbial degradation of acenapthene and naphthalene under denitrification conditions in soil-water systems. Appl. Environ. Microbiol., 54: 1188–1198, 1988.
Mihelcic J. R., Luthy R. G.: Sorption and microbial degradation of naphthalene in soil-water suspensions under denitrification conditions. Environ. Sci. Technol., 25: 169–177, 1991.
Mills M. A., Bonner J. S., McDonald T. J., Autenrieth R. L.: Bioremediation of an experimental oil spill in a wetland. In: In situ and On-site Bioremediation, Pap., 1997.
Parker W. J., Montheith H. D.: Fate of polynuclear aromatic hydrocarbons during anaerobic digestion of municipal wastewater sludges. Water Environ. Res., 67/7: 1052–1059, 1995.
Rueter P., Rabus R., Wilkes H., Aeckersberg F., Rainey F.A., Jannasch W., Widdel F.: Anaerobic oxidation of hydrocarbons in crude oil by new types of sulphate-reducing bacteria. Nature, Vol. 372, 1994.
Shiaris M. P.: Seasonal biotransformation of naphthalene, phenanthrene and benzo[a]pyrene in surficial estuarine sediments. Appl. Environ. Microbiol., 55: 1391–1399, 1989.
Smith M. R.: The biodegradation of aromatic hydrocarbons by bacteria. Biodegradation, 1: 191–206, 1990.
Vogel, T. M., Grbic'-Galic' D.: Transformation of Toluene and Benzene by Mixed Methanogenic Cultures. Appl. Environ. Microbiol., 53: 254–260, 1987.
Weiner J.M., Lauck T.S., Lovely D.R.: Enhanced Anaerobic Benzene Degradation with the Addition of Sulfate. Bioremediation Journal, 2 (3 + 4): 159–173, 1998.
Wilson B. H., Smith G. B., Rees J. F.: Biotransformation of selected alkylbenzenes and halogenated aliphatic hydrocarbons in methanogenic aquifer material. A microcosm study. Environ Sci. Technol., 20: 997–1002, 1986.
Zhang X., Young L.: Carboxylation as an initial reaction in the anaerobic metabolism of naphthalene and phenanthrene by sulfidogenic consortia. Appl. Environ. Microbiol., 36, Nr. 63/12: 4759–4764, 1997.

Copyright © 2003 Swets & Zeitlinger B.V., Lisse, The Netherlands

Dynamics of solute exchange between a fracture and the surrounding matrix

R. Wallach
Department of Soil and Water Sciences, Hebrew University of Jerusalem, Israel

ABSTRACT: The exchange of dissolved chemicals between fractures and the surrounding matrix has a major effect on the concentration at the flow path outlet and, on a larger scale, on contaminant transport in fractured rock systems and structured soils. A model for dissolved chemical transport in a discrete fracture accompanied by simultaneous exchange with the surrounding porous matrix is presented. The fracture transport is modeled by a kinematic wave equation which ignores longitudinal dispersion, and the lateral solute transport in the matrix, where fluid is stagnant, is modeled by a diffusion equation. The exchange of dissolved chemicals between the fracture and matrix is assumed to take place through a boundary layer along the fracture–matrix interface. The "matrix" is assumed a composite medium composed from a thin transition layer at the interface between the matrix and the fracture and the "real" elsewhere. The transition layer has diffusion properties different from those of the rest of the matrix. The boundary condition at the transition layer–matrix interface assumes no contact resistance at the surface of separation and continuity of solute flux and concentration. The boundary-layer model with a uniform matrix was successfully verified by fitting its output to breakthrough curves measured for highly fractured clay-till soils. The transient concentration variation inside a chalk matrix due to NaI diffusion from a fracture and its back-diffusion from the contaminated matrix into the fracture was measured by a medical-based X-ray CT scanner. The variations of the relative concentration (c/c_0) within the matrix could be divided into two distinct patterns: a sharp concentration decrease ("transition layer") that takes place within a thin layer adjacent to the matrix–fracture interface, followed by a diffusion-type concentration decrease along the rest of the chalk matrix. These measurements verify the concept of transition layer at the matrix–fracture interface and enabled to study its effect on fractured rock contamination and remediation dynamics. A simplified mathematical model that assumes a linear concentration variation within the transition layer, similar to the model for the boundary layer showed good agreement with the relative concentrations measured during both the diffusion and the back-diffusion phases. Application of the model to a field site in the Negev desert, Israel, suggested that the rock matrix that had been subjected to 20 yr of contaminant diffusion would require more than 200 yr before it would stop releasing contaminants into the intersecting fractures. According to these calculations, remediation efforts based on clean water injection into the fractures seems to be an unfeasible option.

1 INTRODUCTION

Subsurface solute diffusion from fractures into the rock matrix has long been recognized as one of the major controls on contaminant attenuation and remediation in fractured rocks. Over the past two decades, a large number of expensive attempts to remediate contaminated waste-disposal sites located over fractured aquitards have been reported (after Wood, 1996). These remediation efforts failed where solute fluxes between the fractures and the matrix have been ignored or erroneously estimated. In low-permeability rocks, diffusion becomes the dominant transport mechanism as fractures and joints may form pathways for rapid water flow and solute migration, enabling the contamination of large volumes of rock matrix. As such, laboratory and field diffusion testing has become a necessary component in the overall design and evaluation processes associated with waste-disposal practice in fractured terrain.

Concentration changes inside a rock due to matrix diffusion from fractures have been typically estimated by solving the diffusion equation, following the measurement of breakthrough curves at the fracture outlet (e.g. Foster, 1975; Neretnieks, 1980; Grisak & Pickens, 1980, 1981; Tang et al., 1981; Fujikawa et al., 1993; Parker et al., 1994, Wallach & Parlange, 2000, among others). Maloszewski & Zuber (1993)

Copyright © 2003 Swets & Zeitlinger B.V., Lisse, The Netherlands

had examined various transport models in fractured formations and found that those ignoring the diffusion component are significantly less accurate than those including it. In only a few experiments has the concentration distribution inside a rock matrix been measured directly. Mazurek et al. (1996) measured the distribution of radioactive tracers in a clay pit by analyzing crushed samples. This experiment provided the concentration distribution at the time of the analysis but not the temporal concentration changes. Wan et al. (1996) were able (with some limitations) to track the diffusion process from a fracture to the matrix using glass micro-model methods. Tidwell et al. (2000) acquired tracer concentration images by directing an X-ray beam at the face of a rock while recording the transmitted intensity field on film.

Transport through media with both mobile and stationary fluid-where diffusion takes place-usually occurs through cracks, fissures, fractures, and macropores or interaggregate pores. The models used to predict this transport are usually based on the idea of dual porosity first proposed by Barenblatt et al. (1960). With this approach, low-permeability matrix blocks are separated by a high permeability fracture network. Thus the main fluid convection takes place in the fractures, while the matrix blocks act as fluid sources or sinks for the fractures. In problems involving contaminant transport, the matrix blocks also act as sinks for the contaminant: that is, contaminant-bearing fluid is convected through the fracture while it diffuses into the matrix.

Basic models for such systems assume that the dissolved chemicals move along the preferential flow paths (mobile fluid) mainly by convection and are simultaneously transferred to the surrounding matrix (immobile fluid). Two main approaches have been used to model the fracture–matrix exchange. The widely used assumption used in the diffusion models is that concentration over crack width is constant and equal to the matrix concentration at the interface between the two domains. This mass transfer model was combined with different transport equations for a single crack in a porous matrix [Tang et al., 1981; Neretnieks et al., 1982; Neretnieks, 1983; Moreno & Rasmuson, 1986; Fujikawa & Fukui, 1990; Maloszewski & Zuber, 1990; and others]. In the following we focus on the interface between the fracture and the matrix and assume that the diffusion related properties do not abruptly change. We postulate that there is a boundary layer at the flowing and stagnant fluids (fracture and matrix) and that the matrix porosity is not uniform in the lateral direction (perpendicular to the fracture axis). The sharp porosity decrease at the vicinity of the fracture–matrix interface is denoted herein as "transition layer". In the following we demonstrate the effect of the boundary and transition layers at the matrix–fracture interface on the solute exchange dynamics between the fracture and by mathematical models and measured data.

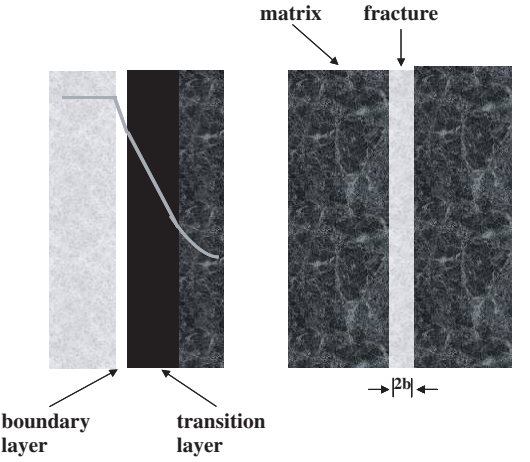


Figure 1. The fracture–matrix system together with the boundary and transition layers and an illustration of the lateral concentration variation.

2 THE BOUNDARY AND TRANSITION LAYERS AT THE FRACTURE–MATRIX INTERFACE

The matrix–fracture system is shown on the right hand side of Figure 1. A close look at the fracture–matrix interface on the left hand side of Figure 1 reveals the concentration variation along the fracture, boundary and transition layers, and matrix continuum. The flowing mathematical model describes the convection in the fracture and lateral diffusion through the boundary and transition layers into the matrix.

Fluid flow through the crack is steady, one-dimensional and isothermal. The concentration in the fracture is assumed to be laterally uniform beyond the boundary layer. Following the model presented by Wallach & Parlange (2000), the dissolved chemical transport in the crack is modeled by the kinematic wave approach and the chemical exchange between the fracture and the matrix through the stagnant boundary layer is rate-limited. The kinematic wave is a good approximation for the convection–dispersion equation for such system and enables an evaluation of an analytic solution.

$$\frac{\partial c_f}{\partial t} + v\frac{\partial c_f}{\partial z} = -k[c_f - c_1(-1,t)] \qquad (1)$$

The "matrix" is a composite medium. It is composed from a thin transition layer at the interface between the matrix and the fracture and the "real" elsewhere. The transition layer has diffusion properties different from those of the rest of the matrix.

For simplicity it is assumed that the matrix is semi-infinite, $-l < x < \infty$, where x is the distance into the matrix perpendicular to the flow direction

Copyright © 2003 Swets & Zeitlinger B.V., Lisse, The Netherlands

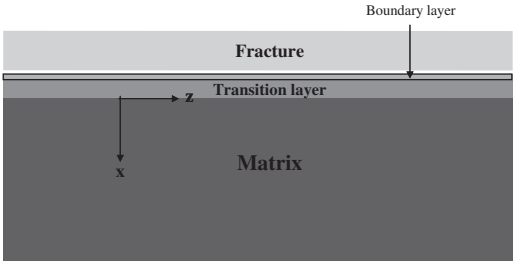


Figure 2. The coordinates in fracture–matrix system.

(Figure 2). The diffusion coefficient in the transition layer, $-l < x < 0$ is D_1 and the concentration is defined as c_1 there, while the corresponding quantities in $x > 0$ are D_2 and c_2.

The differential equation for the transition layer and matrix are

$$\frac{\partial c_1}{\partial t} = D\frac{\partial^2 c_1}{\partial x^2} \qquad -l < x < 0, \quad t > 0 \tag{2}$$

$$\frac{\partial c_2}{\partial t} = D\frac{\partial^2 c_2}{\partial x^2} \qquad x > 0, \quad t > 0 \tag{3}$$

The boundary conditions for (2) at the interface with the fracture boundary is

$$-\frac{\theta D_1}{b}\frac{\partial c_1(-1,t)}{\partial x} = k[c_f - c_1(-1,t)]; \tag{4}$$

The boundary conditions for (2) at the interface between the fracture and the transition layer ($x = -1$) is

$$-\frac{\theta D_1}{b}\frac{\partial c_1(-1,t)}{\partial x} = k[c_f - c_1(-1,t)]; \tag{4}$$

where 2b is the crack width and θ is the transition layer porosity. The boundary layer introduces an additional characteristic time scale to the equilibrium model that postulates an equal concentration over crack width and the matrix interface, namely, rate-limited mass transfer between the crack and the matrix. Under certain circumstances, this additional time scale plays a major role in determining the concentration distribution along the crack and at its outlet.

The mass transfer coefficient that describes the chemical transfer driven by a concentration gradient across the hydrodynamic boundary layer is generally described in a simplistic way by the film theory. The concentration is assumed to vary linearly within the boundary layer from its value at the matrix interface and the laterally uniform concentration in the flowing fluid (Figure 1). The concentration gradient throughout the boundary layer is not known because the thickness of the concentration boundary layer cannot be measured. The mass transfer coefficient depends upon relative velocity near the interface and the thickness of the film. If bulk flow in the crack is reasonably steady, then the thickness of the film is essentially constant. The mass transfer coefficient can be indirectly determined by way of experimental conditions, commonly done by fitting transport models to measured breakthrough curves (BTCs). Alternatively, a relationship can be obtained directly between the rate of mass transfer and hydrodynamic conditions at the boundary. For example,

$$b\frac{kL}{D} = 0.626\left(\frac{Lv\rho}{\mu}\right)^{1/2}\left(\frac{\mu}{\rho D}\right)^{1/3} \tag{5}$$

where ρ is the fluid density and μ is its dynamic viscosity, L is the fracture length. Equation (4) is written in this form to emphasize its relation to the dimensionless numbers $Sh = kL/D$ (Sherwood number), $Re = Lv\rho/\mu$ (Reynold number) and $Sc = \mu/\rho D$ (Schmidt number). Different mass transfer correlations for different fluids, geometries and values of Reynold number are given in Weber & DiGiano (1996). Equation (4) can be used in cases where the fracture shape is regular and well defined with a priori known b, and L.

The boundary condition at the interface between the transition layer and matrix assumes that there is no contact resistance at the surface of separation, $x = 0$.

$$c_1 = c_2 \qquad x = 0 \tag{6}$$

$$D_1\frac{\partial c_1}{\partial x} = D_2\frac{\partial c_2}{\partial x} \qquad x = 0 \tag{7}$$

The solution to the problem of matrix to layers (eqs 2–3) and boundary conditions (eqs 6–7) for zero intial concentration and the surface $x = -l$ maintained at constant concentration c_0 is given by Carslaw & Jaeger (1959), and is

$$c_1 = c_0\sum_{n=0}^{\infty}\alpha^n\left\{\operatorname{erfc}\frac{(2n+1)l + x}{2\sqrt{D_1 t}} - \alpha\operatorname{erfc}\frac{(2n+1) - x}{2\sqrt{D_1 t}}\right\} \tag{8}$$

$$c_2 = \frac{2\beta c_0}{\beta + 1}\sum_{n=0}^{\infty}\alpha^n\operatorname{erfc}\frac{(2n+1)l + \beta x}{2\sqrt{D_1 t}} \tag{9}$$

where $\beta = (D_1/D_2)^{1/2}$, $\alpha = (1-\beta)/(1+\beta)$.

An analytic solution of the entire system of differential equations (including the fracture) and associated boundary conditions is complicated. Before an effort to find a solution is allocated it is essential to find out whether the boundary and transition layers exist and what is their effect on the transport dynamics. In the following, intermediate stages of the entire effort are presented. The research group continues

Copyright © 2003 Swets & Zeitlinger B.V., Lisse, The Netherlands

its experimental and mathematical efforts to reach a complete understanding of the transport processes at fracture matrix interface and their effect on the entire solute transport in the fracture and matrix during contamination and remediation.

2.1 *The boundary layer effect on the breakthrough curve at the fracture outlet*

Wallach & Parlange (2000) presented an analytical solution for the case where the matrix is uniform matrix. The system consists of a fracture a uniform matrix and a boundary layer at their interface (Figs. 1 and 2). The solution was developed by using the Laplace transform. The model was verified by comparing its simulated output to measured BTCs of two experimental studies [Kluitenberg and Horton, 1990; Sidle et al., 1998].

In their study, Kluitenberg and Horton used undisturbed cores of glacial-till-derived soil to displace $CaSO_4$ with by $CaCl_2$ during saturated, steady fluid flow. The column length was 33 cm and the diameter 18 cm. Other physical properties of the soil are given in Table 1 in Kluitenberg and Horton (1990). Following the displacement study, a dye solution was applied at the column inlet and the column was sectioned horizontally in 5-cm increments to allow visual characterization of the stained and unstained soil voids. The dye was transmitted through the lower half of the column in one continuous 2-mm diameter channel (column B, Table 2 in Kluitenberg and Horton, 1990). Since the fracture configuration in column B fit the model assumption of a single-fracture displacement with simultaneous matrix exchange better than the other columns, its BTC was used for the model validation. The predicted BTC fit the measured BTC well: both are shown in Figure 3. By using the kinematic wave equation for fracture transport (1), the predicted BTC increases more sharply than the curved, measured BTC increase soon after initial breakthrough. Note that the dispersion in the predicted BTC is formed solely by the solute exchange between the fracture and matrix.

The average pore water velocity, $1.1\,\mathrm{cm\,min^{-1}}$, determined by Kluitenberg and Horton by the solute flux through the entire soil porosity, is much smaller than the velocity in the preferential flow path determined by the measured first breakthrough time. The flow velocity in the continuous fracture along the entire column length as estimated directly from the measured BTC is $v = 23\,\mathrm{cm\,min^{-1}}$. This velocity was determined by neglecting hydrodynamic dispersion in the column and assuming a larger first breakthrough time than was actually measured. The model-estimated parameters obtained by best fit between the simulated and measured BTCs were $k = 4.5\,\mathrm{min^{-1}}$, and $b^2/D\theta^2 = 1.4\,\mathrm{min^{-1}}$. Note that the equivalent fracture aperture, b, depends on the matrix diffusion coefficient

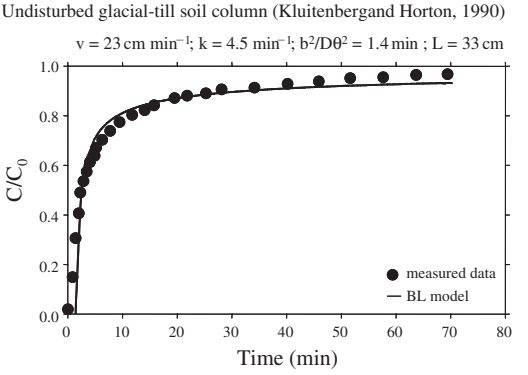


Figure 3. Comparison between predicted and measured (Kluitenberg & Horton, 1990) BTCs.

and vice versa (both unknown). This model was also verified by its successful comparison to natural gradient tracer test of Sidle et al. (1998) which simulated one-dimensional flow in a large ($4\,\mathrm{m} \times 4.8\,\mathrm{m}$ surface area) isolated block of fractured till in Denmark (Wallach & Parlange, 2000).

Recognizing the existence of a boundary layer (BL) at the fracture–matrix interface, rather than assuming an equilibration of concentrations (LE), affects the shapes of BTCs at the fracture outlet. A qualitative analysis of this effect was presented by Wallach & Parlange (1998). The analysis divided the role of the boundary layer resistance on fracture–matrix solute exchange into two stages. The first is soon after displacement initiation, when the lateral chemical flux into the matrix is mostly controlled by boundary layer resistance. Subsequently, the rate of matrix diffusion predominantly controls this flux and the BL model can be replaced by the LE model which involves easy mathematical manipulations and no induction of major errors. The extension of the first stage, during which the boundary layer resistance controls solute exchange, depends on the value of the dimensionless parameter $\varepsilon = kb^2/\theta^2 D$.

The outcome of this quantitative analysis is shown in Figure 3 where simulated breakthrough curves (BTCs) at the fracture's outlet were calculated by the BL and LE models for similar parameters.

The two simulated BTCs deviate initially and come closer as time progresses, as was qualitatively discussed in Wallach & Parlange (1998). Since chemical transport in the crack by both BL and LE models is expressed by the kinematic wave equation, the first chemical appearance at a certain point along the fracture occurs at the same instant. The BL model predicts lower solute influx into the matrix than does the LE model, owing to the lower predicted concentration at the fracture–matrix interface. The varying concentration differences between the interface and fracture lead

Copyright © 2003 Swets & Zeitlinger B.V., Lisse, The Netherlands

to higher predicted concentrations at the fracture outlet by the BL model. The difference between the concentrations at the fracture–matrix predicted by the two models is initially high and decreases with time as more solute enters the matrix. As time progresses, the differences between the fracture–matrix interface and fracture concentrations converge to a finite value that provides a solute flux equal to the flux predicted by the LE model, the latter being solely controlled by the matrix concentration gradient at the interface.

The parameter ε has a significant effect on the deviation between BTCs predicted by the BL and LE models and its extent during the first stage. This parameter is similar to the Biot number, Bi, used by Crittenden et al. (1986) and others to estimate the role of different rate-limited processes on the adsorption of chemical onto soil aggregates. Larger ε and Bi values denote a higher effect of the mass transfer coefficient (fast time scale) than matrix diffusion on solute flux to the matrix, and that concentration through the boundary layer becomes rapidly uniform. This can be obtained by relatively large k or small D values. In contrast, high diffusion coefficients in the matrix (smaller ε values) cause rapid removal of solutes from the fracture–matrix interface into the bulk matrix and extend the time during which the mass transfer coefficient controls the flux. Although not rate-limited parameters, crack width, b, and matrix porosity, θ, have a significant effect on ε since both are raised to the second power.

2.2 *The transition layer and its effect on the concentration distribution in the matrix*

2.2.1 *Matrix diffusion and back-diffusion CT measurement*

The verification of models in which diffusion was assumed to control the solute transport in the matrix was widely based on its effect on the breakthrough curves shape at the fracture outlet. A direct evidence of the concentration distribution within the matrix should include concentration measurement at high spatial resolution within the matrix. This can be efficiently and accurately done by non-invasive methods, such as CT, MRI, and others.

Polak et al. (in press) monitored the concentration changes inside a chalk matrix due to NaI diffusion from a fracture and the back-diffusion process from the contaminated matrix into the fracture using a medical-based X-ray CT scanner (Figure 4). The sample used in the experiment was a 20-cm long, 5-cm diameter chalk core retrieved from a corehole at a depth of ~18.3 m. The study area is located in the northern Negev desert of Israel and is underlain by fractured Eocene chalk formations with a thickness of 285 m.

The characteristics of the mass transfer between the fracture and the surrounding matrix were obtained by

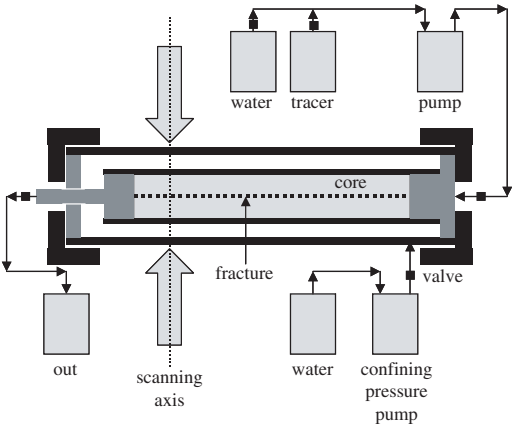


Figure 4. Schematic diagram of the experimental setup.

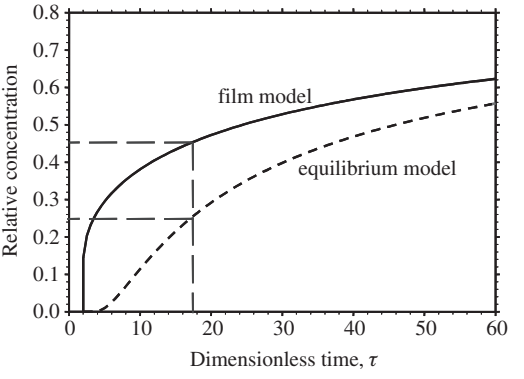


Figure 5. Comparison between BTCs calculated by the boundary-layer (——) and local-equilibrium (----) models for similar parameter values.

the concentration distribution within the matrix. The time-dependence of the diffusion and back-diffusion processes was monitored by consecutive scans. The diffusion and back-diffusion experiments were conducted on an artificially fractured chalk core. The confined core was placed in the scanner and the concentration distribution within the core was monitored.

Following core saturation, the tracer solution (5% by weight of NaI) was injected into the fracture using a peristaltic pump at a constant concentration and rate of 2.5 $cm^3 min^{-1}$ (Figure 5). The volume of the fracture void was about 10 cm^3, hence it was replaced every 4 min. This injection process lasted for 6 days, during which the core was scanned eight times (hereafter denoted as sequences 1 through 8). The scanner produces two-dimensional slices through the sample with a thickness of 4 mm and an in-plane pixel resolution of about 0.25 mm. The X-ray energy level used in the

Copyright © 2003 Swets & Zeitlinger B.V., Lisse, The Netherlands

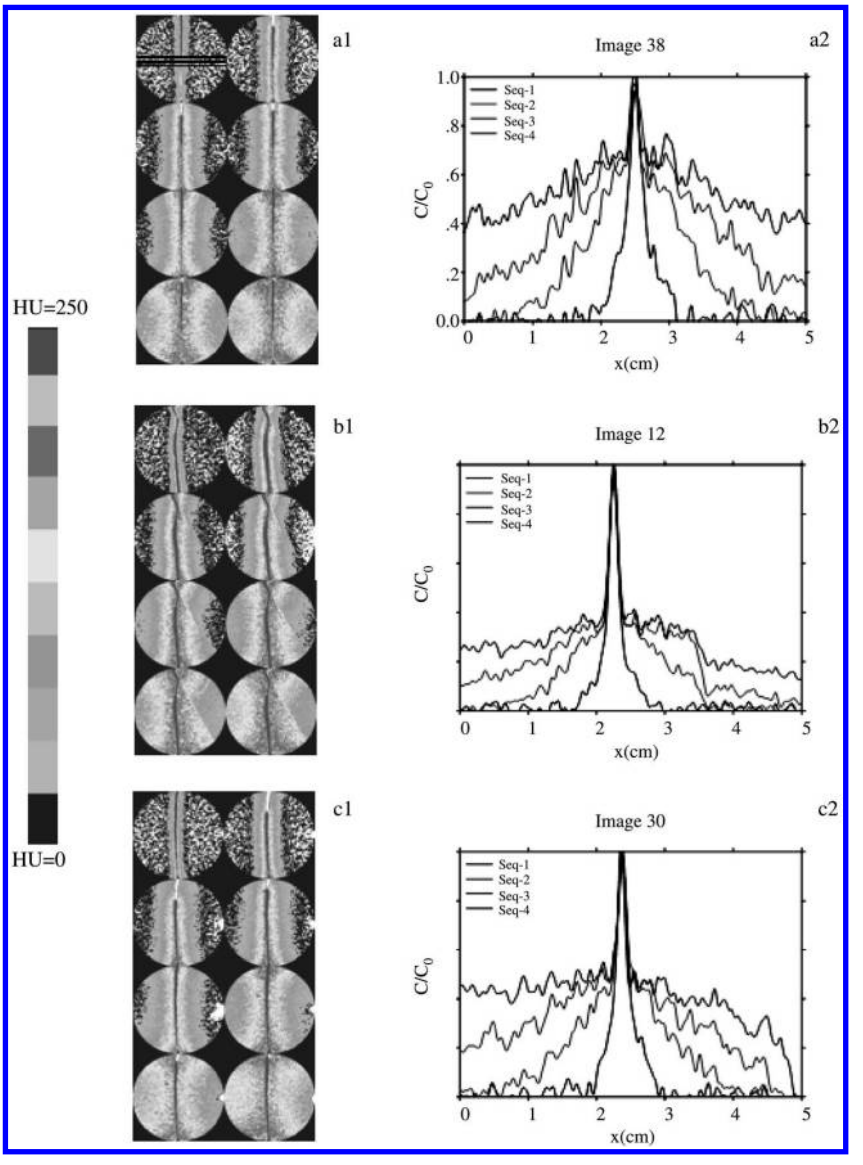


Figure 6. Tracer distribution during the diffusion phase in the scanned core, presented as both concentrations (in CT numbers) and relative concentrations during scan sequences 1, 3, 6, and 8 in images 38, 12 and 30 (a1,2; b1,2; and c1,2, respectively). The CT numbers refer to the attenuation coefficient, converted to an internationally standardized scale, known as Hounsfield units (HU). The scale is linear, and HU units for air and water are defined as −1000 and 0, respectively. High HU numbers correspond to high-density materials.

experiment was 130 kV at 105 mA and the acquisition time for each scan was 4s. The X-ray energy level used in the experiment was 130 kV at 105 mA and the acquisition time for each scan was 4s.

After 6 days of tracer-solution injection, distilled water was injected using the same peristaltic pump at the same flow rate. The water injection generated a reverse concentration gradient of the tracer from the matrix to the fracture. The flow rate ensured complete removal of the tracer from the fracture without accumulation. This water injection lasted for 11 days, during which the core was scanned 10 times to track tracer migration from the matrix to the fracture.

The tracer's lateral distribution in the matrix for the three selected images during the eight scan sequences is shown in Figure 6 (a1, b1, c1) in CT numbers and

Copyright © 2003 Swets & Zeitlinger B.V., Lisse, The Netherlands

in Figure 6 (a2, b2, c2) in terms of relative concentration, C/C_0. Figure 6a refers to image 38, where both sides of the fracture resembled each other. This resulted in a similar temporal diffusion pattern as evidenced by the identical colored bands in the eight scanning sequences (a1) as well as by the four relative concentration graphs (a2). The effect of the sealed boundaries at the core's top and bottom began dominating tracer diffusion from the third day (fifth scan) through tracer migration from the core edges down and up toward the matrix center. The distribution of C/C_0 across the chalk matrix (a2) formed two distinct zones. The first zone was characterized by a sharp concentration decrease over a thin distance adjacent to the fracture–matrix interface, hereafter denoted transition zone. In the second zone, adjacent to the first one and further into the matrix, the concentration decrease followed a diffusion-type pattern.

Image 12 (Figure 6b1) contained a natural fracture, first observed after the core's fracturing, that ran across the upper right face of the artificial fracture. The natural fracture appeared impermeable to water and the saturation of the right face of the natural fracture lagged behind its counterpart on the left. Saturation was finally accomplished by water advecting from the top of the artificial fracture. A similar pattern was observed during tracer injection (b1, second scan on) and was reflected in the sharp relative concentration decrease in the naturally fractured zone (b2, at 3.7 cm along the x-axis). The white circle located at the right edge of image 30 (Figure 6c1) demonstrates the effect of a broken core on the diffusion process. The lack of color indicates lack of tracer accumulation, as also evidenced by the zero relative concentration (c2) in this zone. In fact, this hole at the core edge acts like a sink.

The results of the back-diffusion phase measured by Polak et al. (in press) are exemplified through the same three images used to examine the diffusion phase. Figure 7 presents the tracer concentration decrease (in CT numbers) in the matrix of these three images during six of the 10 scan sequences (a1, b1 and c1), as well as the calculated relative concentration (C/C_0) during 4 of these scans (a2, b2 and c2). Note that the first picture and graph for each image represent the last sequence of the diffusion experiment.

Tracer displacement by the water injected into the fracture was documented in image 38 (where both sides of the fracture were almost identical) as a white line in the center of the image (Figure 7a1). The relative concentration in the fracture dropped to almost zero as soon as back-diffusion started (Figure 7a2, scan sequence 1). However, tracer concentrations away from the fracture did not change much with respect to their distribution during the end of the diffusion phase. Note that while tracer movement from the matrix into the fracture was occurring near the fracture as a result of the reversed concentration gradient, tracer further away from the fracture continued diffusing towards the core edge (scan sequence 3, Figure 7a2). By the end of the back-diffusion experiment, tracer concentration inside the core matrix had dropped to almost zero (blue color in scan sequence 10, Figure 7a1 and 7a2, respectively), although the relative concentration at the core's edges was still higher than that near the fracture. Similar to observations during the diffusion experiment, concentration patterns during back-diffusion in this image were alike on both faces of the fracture. The bottom part of the fracture appears closed (Figure 7a1), probably as a result of the confining pressure applied to the core.

The natural impermeable fracture intercepted by image 12 slowed the tracer's back-diffusion (Figure 7b). Whereas the left face of the core exhibited a decreasing concentration pattern similar to those observed for image 38, tracer relative concentration simultaneously increased in the right face (Figure 7b1, 7b2). The reduction in back-diffusion rate was also visible at the end of the experiment (scan sequence 10) where the left side of the artificial fracture was almost tracer-free, while in the right side the relative concentration was much higher (0.02 vs. 0.1, respectively). By the end of the experiment, the tracer had not been completely displaced from the artificial fracture void (Figure 7b1 and scan sequence 10 in Figure 7b2).

In image 30, the hole in the core's edge that acted like a sink during the tracer diffusion phase turned out to be a tracer source, as evidenced by the red spot on the right side of the core (Figure 7c1) and the increasing relative concentration (scan sequence 10, Figure 7c2).

2.2.2 *Modeling the Diffusion and back-diffusion – the transition layer concept*

Attempts to fit the models of Grisak & Pickens (1980, 1981) and Sudicky & Frind (1982) to the measured concentration distributions failed as they could not simultaneously predict the sharp concentration decrease near the fracture–matrix interface and the concentration decrease further into the matrix (Figure 8). These commonly used models for chemical transport along a fracture surrounded by porous matrix assume a continuous concentration variation at the fracture–matrix interface. The simulated curve (using the Sudicky and Frind's model) shown in Figure 8 was calculated with a diffusion coefficient of 4×10^{-6} cm^2s^{-1} and provides the best fit between the measured and predicted data. This value of the diffusion coefficient used for this simulation is within the range of independently measured values in this chalk (Polak et al., 2002).

The failure of the aforementioned models to simulate the sharp concentration decrease near the fracture–matrix interface possibly indicates that the assumption of equal fracture and matrix concentrations at their interface should be replaced by a different approach

Copyright © 2003 Swets & Zeitlinger B.V., Lisse, The Netherlands

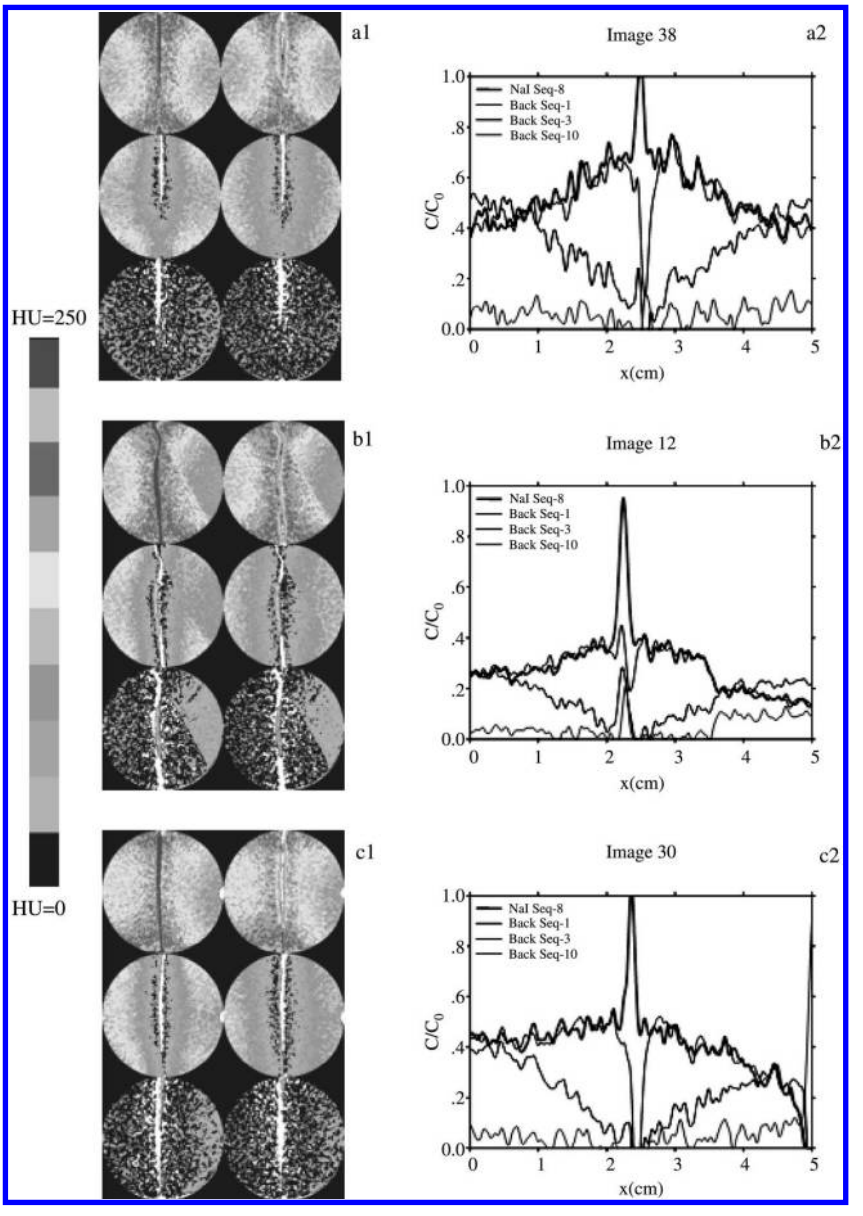


Figure 7. Tracer distribution during the back-diffusion phase in the scanned core, presented as both concentrations (in CT numbers) and relative concentrations during scan sequences 8 (last for the diffusion phase) and 1, 3 and 10 in images 38, 12 and 30 (a1,2; b1,2; and c1,2, respectively).

in that zone. The sharp concentration decrease near the matrix–fracture interface indicates the presence of a transition layer, the diffusion coefficient of which is significantly higher than that of the bulk matrix, but lower than that in the fracture. This transition layer consists of mini-fissures and small fractures that developed when the fracture was formed (Labuz et al., 1987; Huang & Kim, 1993). These mini-fissures and small fractures have a higher porosity, which leads to a higher diffusion coefficient.

As a first approximation, it is assumed that the transition-layer concept (eqs 6–7) for this experiment will be simplified and conceptually treated as a boundary-layer (eq. 4), in which the concentration

Copyright © 2003 Swets & Zeitlinger B.V., Lisse, The Netherlands

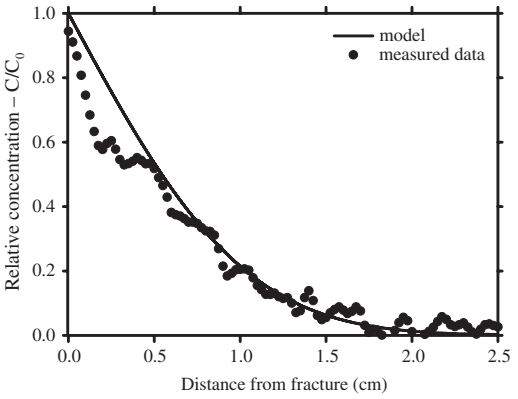


Figure 8. Measured (scanned) NaI concentrations along the right side of image 38 and its predicted concentrations using the model of Sudicky and Frind (1982).

varies linearly between its value at the fracture and its value at the interface between the transition layer and the bulk matrix. This approximation is related to the fact that the fracture concentration in this experiment was kept artificially constant. The concept of a thin layer having no storage but with a fixed resistance to diffusion is identical to the concept of well-bore skin in groundwater hydrology and petroleum engineering.

The simplified approach for the transition layer to predict the measured concentration distribution within the matrix (Figs 6 and 7) was used in Polak et al. (in press). This approach postulates that the transition layer is thin and that the concentration varies linearly within this layer (similar to the assumption used previously by Wallach and Parlange for the boundary layer. The concentration distribution within the the matrix $c_2(x,t)$ for the finite core matrix dimension was obtained by applying the numerical inversion to eq. (12) in Wallach & Parlange (2000) and eq. (19) in Polak et al. (in press). The Stehfest algorithm (Stehfest, 1970) inverse Laplace transform was used for this purpose.

The analysis of the measured data and the model predictions presented from hereon are relevant to either side of the fracture (left or right) of each image. The origin of the x-axis in the following figures is at the interface between the transition-layer and the bulk matrix. The transition-layer width was determined from the measured lateral concentration distribution within the matrix in the region where the concentration sharply decreased. As it turns our, this layer contained two to three CT pixels (0.5 to 0.75 mm). Figure 9a presents the measured concentrations and fitted curves for image 38 at three of the eight scan times run during the diffusion phase. The fitted values for the three time steps were $D = 4 \times 10^{-6}\ cm^2 s^{-1}$ and $\varepsilon = 0.18$. Note that each curve in Figure 9a represents the average of five cross section in the middle

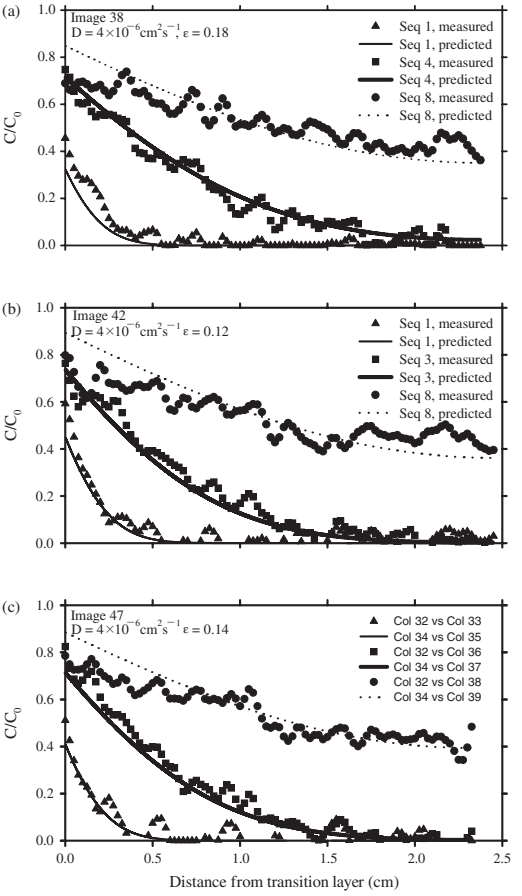


Figure 9. Measured (scanned) and modeled NaI concentrations in the diffusion experiment along image 38(a), 42(b) and 47(c) in three different scan sequences.

of the sample. The fitted diffusion coefficient, D, was kept constant for the entire core whereas the value of ε was changed for the different images in order to obtain the best fit to the measured data. Because D is constant ($4 \times 10^{-6}\ cm^2 s^{-1}$), b = 0.05 cm (half the fracture width as estimated in prior experiments), and L and θ are calculated from the CT measurements, the fitted ε values actually provide the fitted values of the mass-transfer coefficient, k, eq. (8). The measured and fitted values for images 38, 42 and 47 are presented in Table 1, where it can be seen that the variations among the fitted k values are small.

The initial tracer concentration inside the rock matrix at the beginning of the back-diffusion phase in Polak et al. (in press) was identical to that at the end of the diffusion phase. Because the results were calculated in the Laplace domain and the inversion back to the time domain was performed numerically,

Copyright © 2003 Swets & Zeitlinger B.V., Lisse, The Netherlands

Table 1. Fitting parameters used for the model: D, the diffusion coefficient; b, half the average fracture width as estimated by a method presented by Grader et al. (2000); L, the length from the transition-layer–matrix interface to the core edge calculated from the CT measurements; θ, calculated porosity; ε, the fitting parameter, and k, the calculated mass-transfer coefficient.

Parameter	Image 38	Image 42	Image 47
$D \times 10^{-6}$ (cm^2s^{-1})	4	4	4
b (cm)	0.05	0.05	0.05
L (cm)	2.375	2.45	2.325
θ(cm^3cm^{-3})	0.3	0.3	0.31
ε	0.18	0.12	0.14
$k \times 10^{-5}$ (s^{-1})	5.6	8.1	7.6

the superposition principle was applied to replace the initial condition into a boundary conditions. The diffusion model was run for each image from the beginning of the diffusion phase, using fitting parameters identical to those used during the diffusion phase for each image. The model was then run again from the beginning of the back-diffusion phase without changing the parameters' values. The concentration distribution for the back-diffusion phase was obtained by subtracting the latter from the former. Consequently, the initial condition of the back-diffusion phase was modified into two new boundary conditions (the concentration values at different times).

Figure 10 (a–c) presents the measured (CT scanned) and predicted relative tracer concentrations for images 38, 42, and 47 at the beginning of the back-diffusion phase (scan sequence 1) and during two more of the 10 scans performed. The model successfully predicted the concentration decrease near the transition layer–matrix boundary from $c/c_0 = 0.6$ in scan sequence 1 down to 0.1 in scan sequences 3 and 5. It also successfully simulated the aforediscussed relative concentration increase at the core's edge (sealed boundary) for sequence 3.

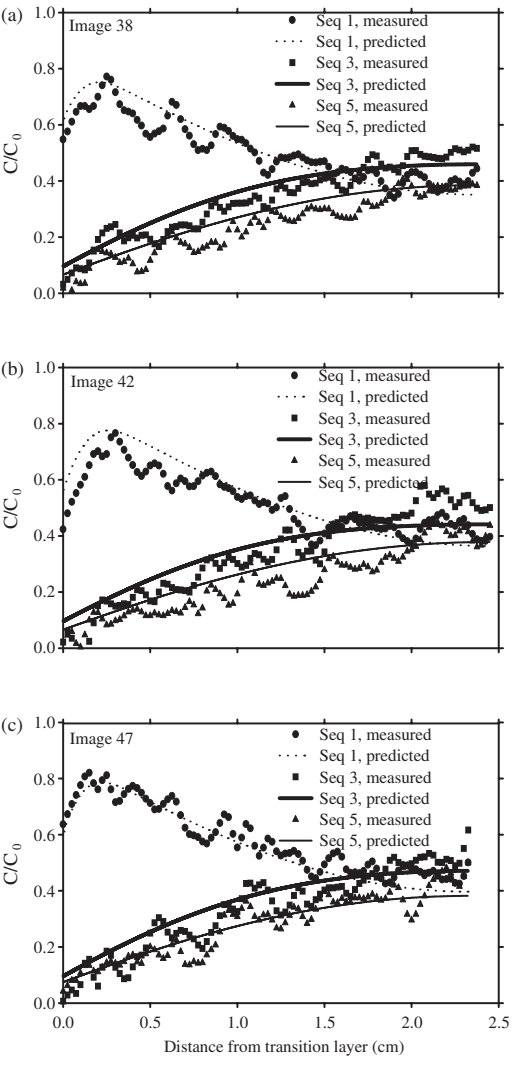


Figure 10. Measured and modeled NaI concentrations in the back-diffusion experiment along image 38(a), 42(b) and 47(c) in three different scan sequences.

3 DISCUSSION

The conceptual postulation that the dynamic of chemical exchange between a fracture and the surrounding matrix depends on the properties of the interface between the two was described both mathematically and experimentally. The interface properties that were related herein are the boundary layer due to the flow in the fracture and the transition layer that counts for the gradual variation of the porosity from 1 in the fracture to the actual porosity within the fracture. Each one of these two properties has its individual effect on the concentration breakthrough curve at the fracture outlet and the transient concentration distribution within the matrix perpendicular to the fracture axis. Before developing a solution to the set of differential equations that describe the entire problem, the effect of the boundary and transition layers independently analyzed.

Using a matrix of uniform porosity, the comparison between the boundary layer model (BL) and the widely used model that assumes a concentration boundary condition at the fracture–matrix interface (LE) provides an insight into the role of the different rate-limited processes on transient dissolved chemical variation with time at different locations along the fracture. The solute displacement can be divided into two

Copyright © 2003 Swets & Zeitlinger B.V., Lisse, The Netherlands

stages regarding the boundary layer effect on predicted BTCs. During the first stage, soon after displacement initiation, the boundary layer is the limiting factor for solute flux from the fracture to the matrix, and this induces deviations between the BL and LE models. Use of the LE model during the first stage provides an underestimation of the displaced chemical mass at the fracture outlet. During the following stage, the solute flux into the matrix is controlled mainly by matrix diffusion, especially by the concentration gradients near the interface. At this stage both models predict similar concentrations at the fracture outlet.

The dimensionless parameter ε that combines the fracture and matrix properties, has a significant effect on the deviation between BTCs predicted by the BL and LE models and its extent during the first stage. This parameter is similar to the Biot number, Bi, used by Crittenden et al. (1986) and others to estimate the role of different rate-limited processes on the adsorption of chemical onto soil aggregates. Larger ε and Bi values denote a higher effect of the mass transfer coefficient (fast time scale) than matrix diffusion on solute flux to the matrix, and that concentration through the boundary layer becomes rapidly uniform. This can be obtained by relatively large mass transfer coefficient, k, or small D values. In contrast, high diffusion coefficients in the matrix (smaller ε values) cause rapid removal of solutes from the fracture–matrix interface into the bulk matrix and extend the time during which the mass transfer coefficient controls the flux. Although not rate-limited parameters, crack width, b, and matrix porosity, θ, have a significant effect on ε since both are raised to the second power.

The transient concentration variation inside a chalk matrix due to NaI diffusion from a fracture and its back diffusion from the contaminated matrix into the fracture, as was measured by a medical-based X-ray CT scanner, verified the concept of a non uniform matrix porosity at its interface with the fracture. The matrix was conceptually divided into two distinct patterns: a sharp concentration decrease ("transition layer") that takes place within a thin layer adjacent to the matrix–fracture interface, followed by a diffusion-type concentration decrease along the rest of the chalk matrix.

Following the successful prediction of the measured data, the mathematical model was used in Polak et al. (in press) to estimate the probable duration of remediation efforts on a field scale. The study area used for this purpose is an industrial complex in the northern Negev desert, Israel. It hosts chemical plants as well as many solid- and liquid-waste-disposal sites that have been continuous contamination sources for the 27 years of its operation. This complex was constructed on fractured chalk formations with fracture spacing of $\sim$5 m. These fractures are considered the main conduits for contaminant transport to the subsurface

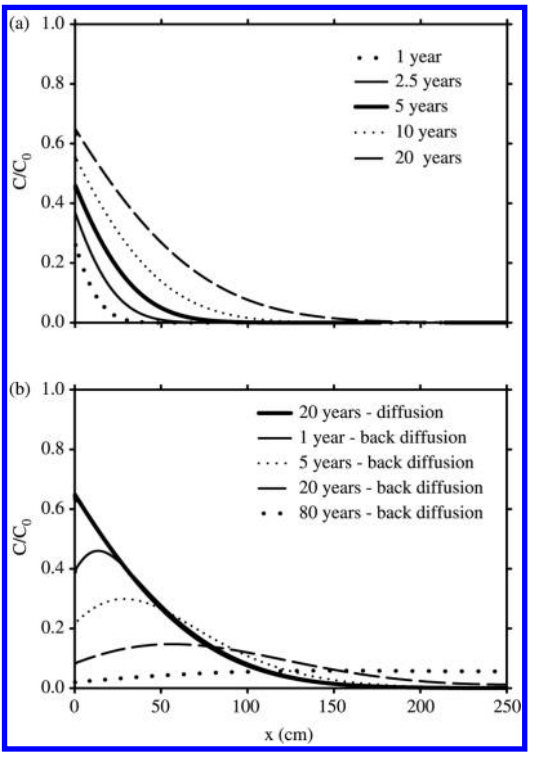


Figure 11. Model prediction of tracer distribution in the 250-cm wide rock matrix following its diffusion during five different time periods (a), and its redistribution following back-diffusion during different time periods (b).

(Nativ et al., 1999). The core used for the diffusion and back-diffusion experiments was taken from a corehole located on site.

Figure 11a displays the modeled tracer relative concentrations in the rock matrix following 1, 2.5, 5, 10 and 20 yr of its diffusion from the fracture. The model was applied to a lateral distance of 250 cm (half the typical fracture spacing on site) of unfractured chalk block (with a sealed boundary at its end) and with $\varepsilon = 0.15$ and $D = 4 \times 10^{-6}$ cm^{2}s^{-1} as the fitting parameters. The modeling results followed a typical diffusion pattern in the chalk matrix and 20 yr of tracer diffusion resulted in a calculated lateral penetration of $\sim$150 cm into the matrix.

Figure 11b displays the modeled distribution of the relative tracer concentrations (in logarithmic scale) inside the rock matrix for the back-diffusion phase, thereby simulating the impact of flushing clean water into the fractures (e.g. pump-and-treat practice). The model parameters (ε and D) were kept identical to those used in the diffusion phase. Whereas the bold line represents the distribution of the relative tracer concentration following 20 yr of diffusion (initial condition),

Copyright © 2003 Swets & Zeitlinger B.V., Lisse, The Netherlands

the other lines display the calculated distributions following 1, 5, 20, and 80 yr of back-diffusion. These simulations clearly show that while the relative tracer concentration near the fracture drops to almost zero after a long flushing, it continues to progress deeper into the rock matrix further away from the fracture. In fact, according to the model, the tracer is expected to reach the sealed boundary at 250 cm 20 yr after flushing of the fracture is initiated, thereby transforming the rock matrix into a long-term contaminant source for the fracture. Obviously, according to these calculations, remediation through clean-water injection into the fractures would take hundreds of years, rendering it practically impossible.

REFERENCES

Barenblatt, G.I., Zheltov, I.P. & Kochina, I.N. 1960. Basic concepts in the theory of seepage of homogeneous liquids in fissured rocks. J. Appl. Math. Mech. 24: 1286–1303.

Carslaw, H.S. & Jaeger, J.C. 1959. *Conduction of Heat in Solids*. Oxford University Press.

Crittenden, J.C., Hutzler, N.J. & Geyer, D.G. 1986. Transport of organic compounds with saturated groundwater flow: Model development and parameter sensitivity. Water Resour. Res. 22(3): 271–284, 6.

Foster, S.S.D. 1975. The chalk groundwater tritium anomaly – a possible explanation. J. Hydrol. 25: 159–165.

Fujikawa, Y. & Fukui, M. 1990. Adsorptive solute transport in fractured rock: Analytical solutions for delta-type source conditions. J. Contam. Hydrol. 6: 85–102.

Fujikawa, Y. Fukui, M. Drew, D.J. & Vandergraaf, T.T. 1993. Analysis of the migration of instantaneously injected cesium in artificial fractures of Lac du Bonnet granite, Manitoba, Canada. J. Contam. Hydrol. 14: 207–232.

Grader, A.S., Balzarini, M. Radaelli, F. Capasso, G. & Pellegrino, A. 2000. Fracture-matrix flow: quantification and visualization using X-ray computer tomography. AGU Geophysical Monograph 122.

Kluitenberg, G.J. & Horton, R. 1990. Effect of soluble application method on preferential transport of solutes in soil. Geoderma 46: 283–297.

Huang, J.I. & Kim, K. 1993. Fracture process zone development during hydraulic fracturing. Int. J. Rock Mech. Min. Sci. 30: 1295–1298.

Labuz, J.F., Shah, S.P. & Dowding, C.H. 1987. Fracture process zone in granite: evidence and effect. Int. J. Rock Mech. Min. Sci. 24: 235–246.

Maloszewski, P. & Zuber, A. 1990. Mathematical modeling of tracer behavior in short-term experiments in fissured rocks. Water Resour. Res. 26(7): 1517–1528.

Maloszewski, P. & Zuber, A. 1993. Tracer experiments in fractured rocks: matrix diffusion and the validity of models. Water Resour. Res. 29: 2723–2735.

Mazurek, M., Alexander, W.R. & MacKenzie, A.B. 1996. Contaminant retardation in fractured shales: matrix diffusion and redox front entrapment. J. Contam. Hydrol. 21: 71–84.

Moreno, L. & Rasmuson, A. 1986. Contaminant transport trough a fractured porous rock: Impact of the inlet boundary condition on the concentration profile in the rock matrix. Water Resour. Res. 22(12): 1728–1730.

Nativ, R., Adar, E. & Becker, A. 1999. A monitoring network for groundwater in fractured media. Ground Water 37: 38–47.

Neretnieks, I. 1980. Diffusion in the rock matrix: an important factor in radionuclide retardation? J. Geophys. Res. 85(B8): 4379–4397.

Neretnieks, I. 1993. A note on fracture flow dispersion mechanisms in the ground. Water Resour. Res. 19(2): 364–370.

Neretnieks, I., Eriksen, T. & Tahtinen, P. 1982. Tracer movement in a single fissure in granitic rock: Some experimental results and their interpretation. Water Resour. Res. 18(4): 849–858.

Parker, B.L., Gillham, R.W. & Cherry, J.A. 1994. Diffusive disappearance of immiscible-phase organic liquids in fractured geologic media. Ground Water 32: 805–820.

Polak, A., Nativ, R. & Wallach, R. 2002. Matrix diffusion in northern Negev chalk formations and its correlation to porosity. J. Hydrol. 268: 203–213.

Polak, A., Grader, A.S., Wallach, R. & Nativ, R. Chemical Diffusion between a Fracture and the Surrounding Matrix: Measurement by Computed Tomography and Modeling. Water Resour. Res. (in press).

Sidle, R.C., Nilsson, B., Hansen, M. & Fredericia, J. 1998. Spatially varying hydraulic and solute transport characteristics of a fractured till determined by field tracer tests, Funen, Denmark. Water Resour. Res. 34(10): 2515–2527.

Stehfest, H. 1970. Numerical inversion of Laplace transforms. J. Assoc. Comput. Mach. 13: 47–49.

Sudicky, E.A. & Frind, E.O. 1982. Contaminant transport in fractured porous media: analytical solutions for a system of parallel fractures. Water Resour. Res. 18: 1634–1642.

Tang, D.H., Frind, E.O. & Sudiki, E.A. 1981. Contaminant transport in fractured porous media: Analytical solution for a single fracture. Water Resour. Res. 17(3): 555–564.

Tidwell, V.C., Meigs, L.C., Christian-Frear, T. & Boney, C.M. 2000. Effects of spatially heterogeneous porosity on matrix diffusion as investigated by X-ray absorption imaging. J. Contam. Hydrol. 42: 285–302.

Wallach, R. & Parlange, J.-Y. 1998. Modeling transport in a single crack by the dual-porosity concept with a boundary layer at the interface, J. Contamin. Hydrol. 34: 121–138.

Wallach, R. & Parlange, J.Y. 2000. Applying the boundary layer concept to model transport of dissolved chemicals in preferential flow paths. Water Resour. Res. 36: 2845–2851.

Weber, W.J. Jr. & DiGiano, F.A. 1996. *Process Dynamics in Environmental Systems*, John Wiley & Sons, Inc., New York, NY.

Wan, J. Tokunaga, T.K. Tsang, C.F. & Bodvarsson, G.S. 1996. Improved glass micromodel methods for studies of flow and transport in fractured porous media. Water Resour. Res. 32: 1955–1964.

Wood, W.W. 1996. Diffusion: the source of confusion? Ground Water 34: 193.

Copyright © 2003 Swets & Zeitlinger B.V., Lisse, The Netherlands

Groundwater mechanics in flood risk management

Frans B.J. Barends
GeoDelft & TUDelft, Delft, Netherlands

ABSTRACT: Floods have an increasingly important effect on the environment, both to human life and nature. Flood risks seem to rise everywhere, more and more. How to approach? The probabilistic method that includes natural uncertainty in loading and human response is outlined. In this article, a particular dike failure mechanism is considered: dike uplift. Uplift is related to the local groundwater flow. The state of the art is addressed. A dedicated countermeasure, applying inside dike reinforcement techniques, is described: dike doweling. Validations by sophisticated methods and centrifuge-model tests are presented. As such, dike doweling limits the environmental impact; it remains unseen, effective and sustainable.

1 THE IMPACT OF FLOOD HAZARDS

When natural hazards, such as floods occur, it is front page news. Television, newspapers and magazines will report the impact on society by these events. Depending on the magnitude of the disaster the impact on society can vary from no loss of lives to hundreds and the damage can be many millions of Euros. In such cases the society becomes seriously aware of the risk of natural disasters and it demands minimising the risk. The costs for achieving this can be a hot political issue.

1.1 *World-wide data collection on flood hazards*

CRED, Centre for Research on Epidemiology and Disasters, supported by the University of Leuven (Belgium), collects all types of epidemics. The database (www.cred.be) reveals that flood hazards rank after wind storms but before earthquakes. It is believed that in near future floods will occur at higher frequency.

The NASA-supported Dartmouth Flood Observatory supports the Global Archive of Large Flood Events (www.dartmouth.edu), which contains major flood disaster data since 1925. The information presented in this archive is derived from a wide variety of news, governmental, instrumental, and remote sensing sources. It is presented in order to facilitate research into the causes of extreme flood events, provide international warning of such floods, and improve

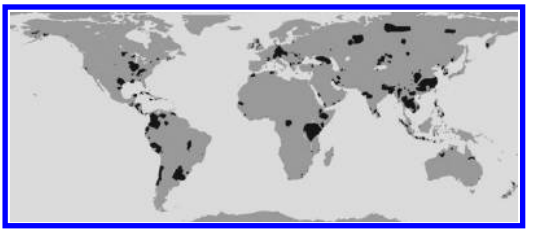


Figure 1. Flood disasters in 2002 (Dartmouth Flood Archive).

widespread access to satellite-based measurements and mapping. The archive is *active* because current year events are added immediately. Figure 1 shows the large floods in 2002.

Some examples of gathered experiences.

Table 1. Flood in north-western Europe, 1993 Dec. 12–31.

	Several days of torrential rain and snowmelt			
Country	Germany	France	Belgium	Netherlands
Drowned	4	4	1	1
Land (km^2)	250	80	20	130
Damage (M€)	580	510	12	52
Germany	"worst since 1926"			
France	"worst in the century"			
Belgium	"worst flood for more than 60 years"			
Netherlands	"highest river level since 1926 by 12 cm"			

Copyright © 2003 Swets & Zeitlinger B.V., Lisse, The Netherlands

Table 2. Comparison of two flood impacts in the Netherlands.

Year	1953	1995
Land inundated (km^2)	2000	130
Drowned persons	1835	2
Cattle/poultry	187000 (drowned)	500000 (evacuated)
Evacuated persons	72000	210000
Lost houses/industry	3300	3500
Damage (M€)	800	220

Table 3. Water defence infrastructure in the Netherlands.

Netherlands	Length (km)	Value (M€)
Major defence structure	2000	30000
Sea dike	1300	13000
River dike	1900	15000
Bosom dike	4000	20000
Inland embankment	20000	50000
Total		153000

The total impact of floods in Europe since 1925 numbers 9387 deaths, 303675 homeless, 6.8 million persons affected, and 104.7 billion Euros damage.

The massive water-defence infrastructure in a vulnerable country like Netherlands is being built over centuries. The actual economic value of this infrastructure is in the order of 150 billion Euros (Table 3), and yearly about 1% is spent on maintenance and management. If maintenance is neglected, the cost of proper repair will become astronomical.

A magnitude to distinguish flood impacts is suggested: duration $\times$ severity $\times$ affected $\times 10^{-4}$. Here, flood severity is defined, according to:

1. large events: significant damage to structures or agriculture; fatalities; and a decade-long reported interval since the last similar event.
2. very large events: greater than 20 years but less than 100 years recurrence interval, and/or a local recurrence interval of at 10–20 yr and affecting a large geographic region (>5000 km^2).
3. extreme events: with an estimated recurrence interval greater than 100 years.

More than 50 years ago, floods were more common in the Netherlands, and those who lived near the river or sea were accustomed. Houses and farms could stand high waters for a while. The calamity plan consisted of four steps:

– take batteries and a radio for the latest news,
– move valuable belongings and raise furniture,
– block the toilet pipe, avoiding sewerage inflow,
– take food, go upstairs and wait.



Figure 2. Impact of floods afflicts many in various ways.

Today, water defences are improved, such that the public forgot about floods and became used to full protection. Building and infrastructures, living and working in vulnerable areas increased significantly. Now, many more values are in jeopardy.

This *feeling* is not realistic. Floods will happen, and a proper calamity plan, more comprehensive as before, is required. It is important to include specific public and private actors. There is a role for

– governments on lawfulness and strictness,
– authorities on carefulness and accountability,
– science on accuracy and exactness, and
– public on awareness and understanding

in determining, accepting and applying relevant mitigating measures to minimise the impact of flood hazards. In this process communication is inevitable.

1.2 *The role of geotechnical engineering*

Geotechnical engineering plays an important role in associating the risk, i.e. occurrence of a flood and its impact, to the likelihood of loss of functioning of water-defence structures, i.e. failure mechanisms. In the last decades major contributions are made to:

– understand the principal failure mechanisms;
– determine parameters which describe the soil;
– model and predict the behaviour of dikes;
– design alternative constructions;
– plan and apply mitigation measures;
– install warning systems.

The focus in geotechnical engineering is mainly on the first 4 bullets. In near future, the last three will become more relevant.

In many countries governments retreat as problem solver and act as problem owner. Specialised institutes in the market (consultancy companies, universities, contractors, geotechnical institutes, etc.) will be held responsible for gathering and applying relevant knowledge. Hence, communication will move from a scientific (geotechnical) language towards a socio-economic one, i.e. what are the benefits. The role of the engineer is changing. He has to convince and create

Copyright © 2003 Swets & Zeitlinger B.V., Lisse, The Netherlands

public awareness. A problem is that in the absence of hazards politics and societies become complacent, awareness dims over time, and maintenance of water-defence structures is neglected.

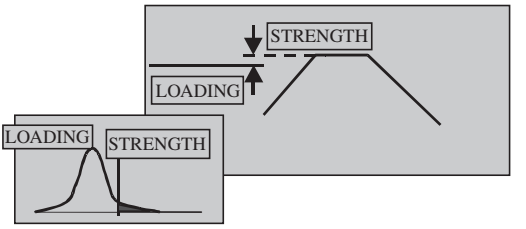
2 A PHILOSOPHY BEHIND FLOOD RISK MANAGEMENT

The unique form of self-government – the water schap – which may be regarded as having fostered the independent spirit of the western Netherlands, began to emerge in the first half of the twelfth century. Best translated today as Water Board, the waterschap is authorised to manage water levels in the western lowlands by building and maintaining embankments, dikes and sluices. The Water Boards have continued to function in much the same form to this day, when water has become a crucial factor in many aspects of life such as industry and recreation and their attendant problems, like water quality control. The Water Boards exercise authority over 1300 kilometres of sea dikes and 1900 kilometres of main river dikes. It is difficult to estimate exactly the length of all the bosom dikes and inland water embankments under Water Board control, it runs into the thousands of kilometres.

A Water Board's regulations mostly include detailed provisions for the recruiting and the functioning of the dike army. When danger threatens, the troops must be on alert, patrolling the dike and standing by with sandbags and equipment to stop occurring breaks. Members of the 'army' must be instilled with the need to defend their families, community and country and have an intimate knowledge of the lie of the land. By law, all male residents aged between 18 and 60 have, if necessary, to report for duty. An administrative and a technical department carry on the Board's everyday work. The administrative department prepares policy and gives legal and financial direction to all the work of water management to be carried out by the technical department. The technical department cares for the design, execution and management of dikes, pumping stations, purification plant, roads and buildings.

2.1 *Dike technology*

There are, roughly speaking, four types of dikes in the Netherlands: river, coastal, estuarine dikes and the embankments around bosom waters, i.e. the canals and lakes used as storage basins to regulate polder water levels. These four types differ in design and construction. When, in the past, the authorities had to decide how high to build a dike, they took the highest known level as their standard. The many *wielen*, deep pits scoured out by water swirling through breaches, now to be seen as pools along the lines of the dikes, bear silent witness to our forefathers' failure to get their calculations right.



black tail represents the likelihood of failure

$$\textit{Probability of failure: } P_{L>S} = \int_{x=S}^{\infty} f_L \, dx$$

Figure 3. Water exceeding crest determined inundation risk.

After the catastrophic 1953 floods the authorities decided that the height to which the dikes ought to be raised, should conform, as far as possible, to scientifically calculated criteria. Their basic principle was not that flood water levels should never exceed the height of the dike, since this would be impossible to finance, but rather that the likelihood of floodwater overflowing the dike would be acceptably small. This principle is in the Dutch laws, since 1953.

In vulnerable areas, for example, an inundation risk of once in ten thousand years: $P_{L>S} = 10^{-4}$, is considered acceptable, otherwise about $P_{L>S} = 2 \cdot 10^{-3}$. The heights derived from these base levels are known as draft levels (Figure 3). Besides the draft level, the effect of surf rolling up the seaward slope must be taken into account when calculating the height of the dike crest. This seaward slope will, if properly designed, break the surf so it does not surge as high. Dikes in very exposed places are designed with a 'sill' built into the slope at storm tide level.

The body of the dike must be protected against the force of the waves and the effect of tidal currents. Dikes in the Netherlands are mostly faced with turf as a basic covering. Depending on the angle of the slope and the force of the waves' attack, basalt, concrete blocks and/or asphalt are used as revetment. Fortunately, high tide levels never last long. A normal tide cycle lasts twelve hours, consequently the water hardly ever gets a chance to percolate deep into the dike so the angle of the inland slope can be allowed to be fairly steep.

Water levels on the non-estuarine upper reaches of the rivers are determined by weather conditions upstream, such as rainfall and thaw. These days, the necessity of dike improvement is based on exceedence of a certain river discharge occurring about once in two thousand years, a figure derived from statistics. High water on the upper river reaches lasts considerably longer than in a storm tide area, and waves do not generally play as great a role. These two factors are reflected in the design of the most desirable river dike cross-section. The riverside slope may, consequently, be angled more steeply and the revetment need not

Copyright © 2003 Swets & Zeitlinger B.V., Lisse, The Netherlands

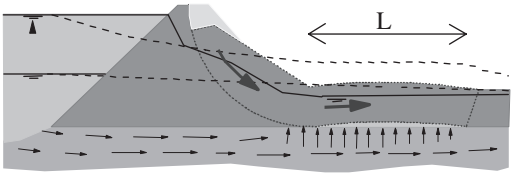


Figure 4. The uplift phenomenon.



Figure 5. Piping, sand ejecting wells at a dike's lee-side.

be of heavy quality as on the coast. The angle of the slope may not, however, be too steep for turf to grow properly grass cover or for a stone revetment to be satisfactorily placed. The longer periods of high water give the ground water table within the body of the dike opportunity to rise.

In order to prevent seepage, the inland side of the dike is often given a gentler slope. A peculiar phenomenon is uplift (Figure 4), occurring when ground water pressures are high enough to lift the covering ground layer at the lee-side slope. In some cases local erosion arises in the form of sand boils, which undermine the dike (Figure 5). Another criterion is overtopping, when water gulps over the dike crest with subsequent erosion of the lee-side slope.

The bosom embankments are the smallest of all the four types of dike. They are mostly constructed of clay and peat. The core below the crest often consists of a great variety of materials as, in the course of time, local authorities have used sand, rubble, and clay as available to add to the dike's height. The strain which bosom embankments have to withstand differs from other types of dike. They are, for example, subjected to a practically constant high water level. Their ground water table is, consequently, fairly high. The subsequent saturation forms a hazard, especially during periods of high rainfall, as earth-slides occurring along the inland slope might inflict inundation.

2.2 *Dike design*

The most ancient dam is found at Jawa in Jordan, six millennia ago, built of earth with a protective coat of masonry. The dam of Kafara, on Wadi Garawi, south of Cairo, dates back 4.5 millennia. It is 12 meter high and 84 meter wide at the base, thus with a slope of 1:3.5, on either side, and its construction showed two distinct functions: stability by the two parallel outer embankments of rock and mortar, and imperviousness by the central filling of materials of the bed of the valley. In ancient Netherlands a consistent dike design was developed by monks; it also consisted of the two separate functions: an impermeable part by dense sea weed, and a stabile part by an earth body of clay, reinforced by coupled rows of short wooden piles and a carefully placed stone toe against wave attack. Until 1850 dikes were made symmetric, like the dam of Kafara, with slopes of about 1:2.5.

At present, a Dutch dike is faced with an impermeable layer. This is mostly clay but sometimes supplemented by asphalt. Apart from being impermeable, the layer must also resist scouring. A grass cover with a healthy layer of turf is usually sufficient for dikes on non-tidal river reaches. Dikes subjected to heavier attack are equipped with a revetment of stone or concrete blocks. The core of a dike provides support for the clay layer and gives the whole sufficient volume and weight to resist the pressure of the water piled against it. It is usually not seen or felt, but a dike displaces horizontally for about a decimetre or two when subjected to high water!

Other than the clay facing, the core must be permeable. Any water that does manage to percolate through must be allowed to flow away safely so the body of the dike does not become saturated and weaker, as higher saturation significantly decreases soil shear resistance. On the inland side the sand core is again faced with clay to prevent it being washed away, either by rain or by water overtopping the crest. Provision is made along the foot of the inland slope to allow water, which has penetrated the core to drain away safely. Such drainage is vital for the stability.

These general features may vary from place to place. Much depends on local factors which can differ widely such as the type of ground below the dike, the materials available in the past, the pressure the dike must withstand, and the traditions and customs of the area. The evaluation of the relative importance of the various criteria of dike construction or dike improvement and subsequently the assessment of an economically optimal design is achieved by the application of the probabilistic approach, which involves a close inspection of water levels and corresponding failure mechanisms, their probability and their coherence (Figure 6). This approach has gained national support in the last twenty years and has become the accepted design philosophy of modern dike design and maintenance in the Netherlands.

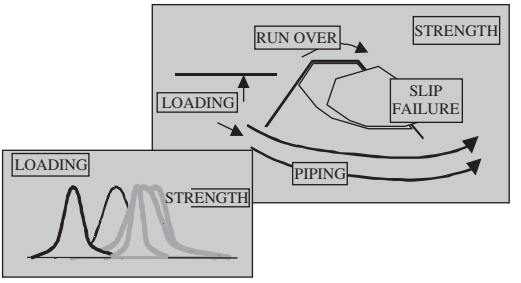
2.3 *Dike ring approach*

The strength of the chain of defences is never greater than their weakest link. This anticipates a safety norm of an area protected by a sequence of dikes, referred

Copyright © 2003 Swets & Zeitlinger B.V., Lisse, The Netherlands

Table 4. Structural elements and failure mechanisms.

element	link	principle limit states
height		overtopping
		wave overtopping
outer slope		erosion outer slope
		instability outer slope
core		leakage
		settlement
inner slope		erosion inner slope
		instability inner slope
subsoil		uplift
		piping



The likelihood of failure is the integration of probabilities of various mechanisms under their relevant loading conditions

$$P_{failure} = \int_0^\infty f_S \left(\int_{x=S}^\infty f_L \, dx \right) dy$$

Figure 6. Considering all components in a stability analysis.

to as a dike-ring. For each area surrounded by a dike-ring the safety norm is related to the economic, social and environmental values assigned to the protected area. The required safety of individual dike sections is related to the safety of the entire dike-ring area and to the specific role the considered dike plays (see Figure 8). Dike technology is therefore based on three major elements:

- the safety philosophy: the dike-ring approach, application of probabilistic methods, and research on new economically and ecologically sound ways to retain the water.
- functional analysis: the design and the control of functions of water-defence systems; control-guidelines, technical elaboration of various failure mechanisms, and re-search on new ways of realisation of structural elements.
- rational maintenance: methods for preventive maintenance, methods for error detection and monitoring, and efficient techniques of maintenance.

2.3.1 *Safety philosophy*

Disasters due to technical failure seem always to be less acceptable than natural catastrophes. An important question is whether disasters due to technical failure can be avoided and whether damage due to natural catastrophes can be minimised. An observation is that in a society full with sophisticated technical systems disasters are unavoidable. Accidents are the logic consequence of a society that lives on technology. The discussion about safety mainly deals with probability theory and social acceptance. There exists an apparent subjective safety during a period of absence of accidents, i.e. complacency. Safety assessment, therefore, comprises the evaluation of risk sensation involving objective personal and social acceptance and the analysis of probability of failure involving various realistic events. The new Water Retainment Act provides the possibility to base the safety philosophy on likelihood of inundation. Three risk components determine the relation between safety level and a probability of failure or malfunctioning: personally acceptable risk, optimised economic risk, and socially acceptable risk.

2.3.2 *Functional analysis*

The basic function of a dike is to retain the water. Various elements can be distinguished each playing a characteristic role in the functioning of the dike. These principal elements are:

- a crest height above the design water level;
- outer slope: a watertight cover in order to keep the inner groundwater table and leakage low and resistant against rapid drawdown, ice and earthquake;
- the core of the dike conveys the horizontal load due to the water to the subsoil;
- inner slope: a permeable cover to keep groundwater table and leakage low and stable under overtopping and earthquake;
- the subsoil provides suitable stability and has a water retaining function.

In urban areas existing buildings in and on the dike can jeopardise its function. The watertight cover is locally interrupted, differential settlements can cause cracks and maintenance becomes more complicated. Using functional analysis two principal solutions can be defined for the situation of buildings on a dike: fully integrated, when the buildings and their foundations are also the water retaining structure or building and dike are functionally separated. This can be achieved by various measures. In these solutions the effects on the elements of the dike must be considered precisely and in detail (leakage, stability, erosion, etc.). For trees on the dike the same holds. Trees are admitted when they do not interfere with the principal dike function.

The problems related to buildings and trees can be solved in a technical way; the question of control and maintenance remains. When the water retaining function and building are fully integrated, frequent inspection is necessary. Uncontrolled changes in the buildings by their owners may be a danger to the dike function and a threat to the safety. It is recommended

Copyright © 2003 Swets & Zeitlinger B.V., Lisse, The Netherlands

to plan the design for a period of 100 years. If buildings are outside the technical dike profile the inspection is more complicated, particularly when the fundamental elements (watertight screen) are not directly visible. The quality can be checked by adequate measurements during high waters. For buildings in the lee-side area a regular inspection of the cellars and the maintenance of the lee-side slope is required. The present-day development of houses in the river forelands, although officially prohibited, became lucrative and popular, but it raises a serious new political issue, as safety is at stake during high river discharges (viz. flood hazard in 1993).

2.3.3 *Rational maintenance*

The technical component of management is maintenance, which consist of inspection, taking measures and allocation of personnel, materials and equipment. The condition of a water-defence system will degenerate in the course of time. Moreover, the loading conditions may change, and new insight in the evaluation of strength of elements in the system may arise. Two fundamental activities, periodical control and taking measures in time, form the backbone of a proper maintenance policy. Periodic control implies a comparison between actual condition and the minimum condition requested. The important question is how the system will behave until the next moment of inspection. The following steps are distinguished:

- determination of functional demands;
- evaluation of the condition;
- comparison with the norms;
- choice of measures;
- optimisation.

Important aspects in this procedure are the concept of fixed and variable data, the degeneration model and the system of diagnosis. How to determine the actual strength of an existing dike? Pilot studies have been performed to clarify the approach for practical purposes. Preliminary results are compiled in a practical control-guideline, at present in use.

2.4 *Failure mechanisms or malfunctioning*

For a typical dike cross-section various failure mechanisms (limit states) can be distinguished. Traditionally, much attention is given to the mechanism of overtopping and wave overtopping. By the selection of a proper crest height with respect to the exceedence of design water levels and wave heights a safe dike profile can be accomplished. Breaches in the past have proved that overtopping was not always the cause of inundation. Piping, micro-instability and slope-slides have induced flood disasters. Also situations which did not happen so far could be added, such as collision during high water by a large ship. A similar consideration applies to structures in the dike (sluices, floodgates, locks, pumping stations), when they participate in the water-retaining function of the dike. Excess loading may also exceed the bearing capacity of the foundation causing large unacceptable displacements. History shows that structures in dikes present a major threat.

An aspect of special concern is the human factor, i.e. the manual operation of sluices, locks and floodgates during high waters. In the analysis the probability of the human error should be considered. For a dike-ring the probability of failure of any dike section and of any structure may lead to inundation of the area, as the total strength is not greater than its weakest link. Therefore, the probability of inundation increases with the length of dikes in a dike-ring.

Usually, a dike, which is well designed and performs the functions required, also satisfies the safety conditions of the various failure mechanisms. The function water-retaining demands a suitable crest height, a suitable water tightness of the dike body and subsoil, a suitable stability to transfer the water level induced shear force, and a suitable resistance of the dike to all forces which are related to its existence (stream forces, wave loading, tourist damage). If the principal elements are well designed, i.e. the crest height, the outer slope, the core, the inner slope, and the subsoil, then the principle limit states or failure mechanisms are dealt with automatically.

2.5 *Dealing with uncertainties and risk perception*

The safety of a certain mechanism is controlled by investigation of the critical situation, the limit state, where loading and mobilised strength are in equilibrium, and any increase of loading causes collapse. A distinction is made between ultimate limit state and service limit state. The former is the extreme situation when breaching occurs, the latter when any designed function is being jeopardised. Sometimes a limit state can not be assessed by calculations. Physical tests and pilot tests or engineering experience is used. The probability method, in fact, elucidates and quantifies the relative importance of uncertainties. It is here, that conventional deterministic calculation methods apply as a cornerstone in an integral approach.

Uncertainties are classified as intrinsic (related to nature: time, stochastic water levels, and space, soil heterogeneity) and epistemic (related to models: statistics, incomplete data, inaccuracy, scale). This is practically possible by the definition of dike-rings. For each ring a safety norm is determined and the safety norm of all other elements in the dike-ring system are related to this norm. The inundation approach comprises the following aspects:

- loading (tides, waves, earthquakes);
- mechanisms (failure mechanisms per type of structure and element);

Copyright © 2003 Swets & Zeitlinger B.V., Lisse, The Netherlands

– calculation methods (probabilistic models, partial safety factors);
– inundation scenarios, damage evaluation;
– decision models accounting for values and loss.

This approach requires the evaluation of economic, social, and cultural damage by inundation (Figure 7).

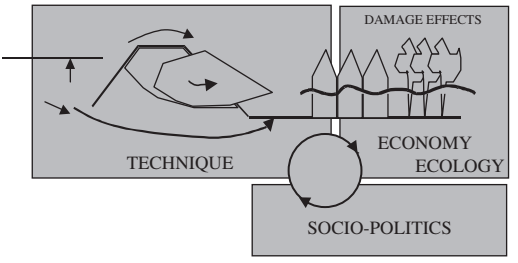


Figure 7. Modern decision process for inundation risk management, a multi-disciplinary and socio-economic approach.

It requires awareness for natural and environmental values and a social acceptance of a change of the role that existing water-defence systems may play. The amount of damage is, in fact, a directive for the effort one should implement to keep the probability of this failure low. The calculation methods and decision models define how the information obtained can be used to make a rational decision.

In a recent study (RWS-DWW, 2000) the flood probability per dike-ring (Figure 8) and the estimated flood damage (Figure 9) has been determined. For the dike-ring South-Holland (the largest) the corresponding flood risk becomes

$$\text{Risk} = \text{Probability} \times \text{Damage} = 10^{-4}\, 300000 = 30\,\text{M€}$$

This result reflects the economic value of water-defence structures. In this approach other consequences (victims, emotions, stress, damage to nature, landscape and cultural history) are not included.



Figure 8. Dike-rings in the Netherlands. The grey colour refers to probability of failure in a ring: dark 10^{-4} to light 10^{-3}.

Copyright © 2003 Swets & Zeitlinger B.V., Lisse, The Netherlands

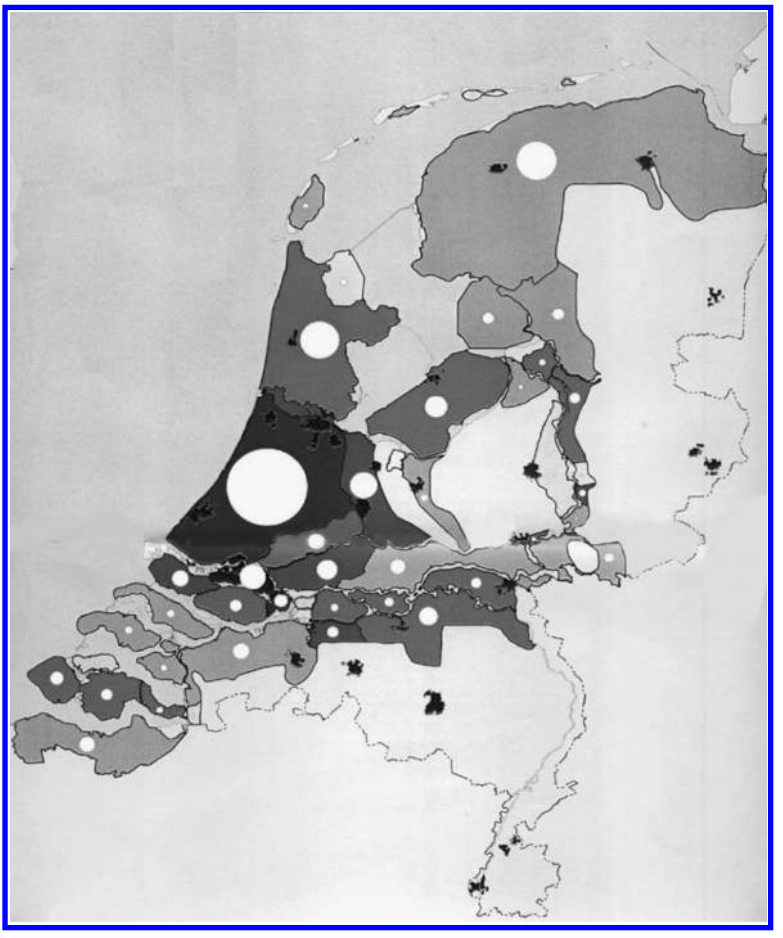


Figure 9. Economic flood damage per dike ring; the white circle scale: largest = 300 billion Euros (South-Holland).

Mere intuition and experience have in the past, addressed these risks. Today, it is possible to objectively quantify and qualify uncertainties for well-described scenarios. Societies do call for this approach being confronted with an increasing pressure on space allocation for work and living for a growing population with altering needs. In the coming decade the Dutch will face the issue how to handle flood risks and what level of security is appropriate.

3 THE UPLIFT PHENOMENON

Uplift pressures in pervious strata underlying dikes and their effect to slope stability, recognised in the late seventies in the UK (Marsland & Randolph, 1978; Padfield & Schofield, 1983), was also experienced in the Netherlands. In the UK-studies, using geocentrifuge tests, the phenomenon of non-emergent slip surfaces was observed, but results then showed that uplift pressures may modify the nature of the most critical failure mechanism, but do not appear to affect significantly the current factor of safety against collapse. In the Netherlands, however, the Wolferense dike, supposedly with a Bishop slope stability factor above 1.7, suddenly and surprisingly collapsed in 1981. Moreover, the unforeseen collapse of the dike at Streefkerk in 1984 (Figure 10) was of a similar nature, and it gave impetus to study the uplift phenomenon thoroughly. Uplift is an important failure mechanism in the lower reaches of rivers in the Netherlands.

3.1 *Uplift length*

Pore pressures induced by high river levels, rising as high as the weight of the overlaying relatively impervious top layer, create a thin water zone of length L (Figure 4), with a constant pore pressure, equal to the overburden weight. Since shear resistance in this zone vanishes completely, the dike stability is influenced.

Copyright © 2003 Swets & Zeitlinger B.V., Lisse, The Netherlands



Figure 10. Uplift induced dike slope failure at Streefkerk.

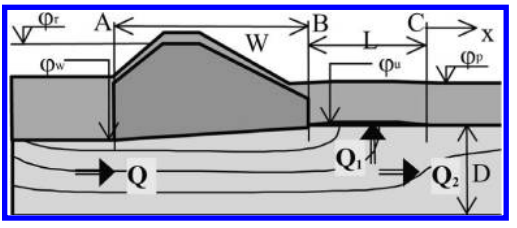


Figure 11. Scheme of groundwater flow; uplift condition.

The length of the uplift zone can be established analytically, considering three zones: (I) foreland, (II) dike and uplift area, (III) hinterland. The corresponding steady groundwater flow, incorporating leakage through the covering layer, except under the dike, and a constant potential in the uplift zone (Figure 11), is described, as follows:

I. $x < -W - L$:

$$\varphi = (\varphi_w - \varphi_r) \times \exp((x + W + L)/\lambda'') + \varphi_r$$

III. $x > 0$:

$$\varphi = (\varphi_u - \varphi_p) \times \exp(-x/\lambda') + \varphi_p$$

Resulting discharges of zone II become:

$$\text{I} \rightarrow \text{II} \qquad Q = KD(\varphi_r - \varphi_w)/\lambda'' \tag{1}$$

$$\text{II} \rightarrow \text{III} \qquad Q_2 = KD(\varphi_u - \varphi_p)/\lambda' \tag{2}$$

The flow through zone II: $-W - L < x < 0$, is characterized by inflow Q (at A) and outflow Q_1 into the uplift zone (BC), and outflow Q_2 (at C). The length of L is yet undetermined. The flow field in zone II is established using conformal mapping, which gives for the complex potential (see Annex 1).

$$\Omega = -(2iQ/\pi)\text{arcsin}[\sin(iz\pi/2D)/\cos(iL\pi/2D)] \tag{3}$$

In A, under the dike toe, the potential is φ_w, and

$$\Omega = \Phi + i\Psi = -K(\varphi_w - \varphi_u);$$
$$z = x + iy = -W - L$$

Elaboration yields

$$Q = \pi K(\varphi_w - \varphi_u)/2\text{arcsinh} \times [\sin((W + L)\pi/2D)/\cos(L\pi/2D)]$$

Next, eliminating φ_w with equation (1), gives

$$Q = \pi K(\varphi_r - \varphi_u)/2(\text{arcsinh} \times [\sin((W + L)\pi/2D)/\cos(L\pi/2D)] + \pi\lambda''/2D)$$

From the complex solution (3) the ratio of discharges can be found (see Annex 1).

$$Q_2/Q = (2/\pi)\arcsin(1/\cos(L\pi/2D))$$

Substitution into equations (1) and (2) yields an implicit expression for the uplift length L.

$$(2/\pi)\arcsin(1/\cos(L\pi/2D)) = (2D(\varphi_u - \varphi_p)/(\lambda'(\varphi_r - \varphi_u))\{\pi\lambda''/2D + \text{arcsinh}[\sin((W + L)\pi/2D)/\cos(L\pi/2D)]\}$$

For $L > D > W$ this simplifies to

$$L = (2D/\pi)\ \ln[(1 + \cos(\alpha))/\sin(\alpha)] \tag{4}$$

with

$$\alpha = \pi(W + \lambda'')(\varphi_u - \varphi_p)/(2\lambda'(\varphi_r - \varphi_u))\ \text{[rad]}$$

If the foreland has no covering layer, it is advised to use $\lambda'' = 0.44D$. This approach is extended for time dependent flow, including consolidation in the clay layer (Barends, 1982 & 1988), using the method of the transient leakage factor. The uplift zone develops after some delay. A typical situation is elaborated and presented in Figure 12. Here φ_c determines the characteristic delay between moment of river level rise and start of uplift. The uplift zone grows initially rapidly, then slower to a stationary value. The discharge inflow in the uplift zone, leaking away through the upper layer, causes a relatively thin water film of only 2.5 cm after 3 days. It is important to consider this phenomenon when evaluating the lee-side slope stability with standard methods (Bishop).

At present, a well-validated design method for the uplift slope stability is available (Van, 2001). Recently, a real scale field test on a river dike of 5 meter height at Bergambacht, the Netherlands, was performed with success (Koelewijn, 2002), elucidating the true danger of the uplift phenomenon. In 2002 several studies were undertaken to develop a new and practical enforcement method with limited environmental effects.

Copyright © 2003 Swets & Zeitlinger B.V., Lisse, The Netherlands

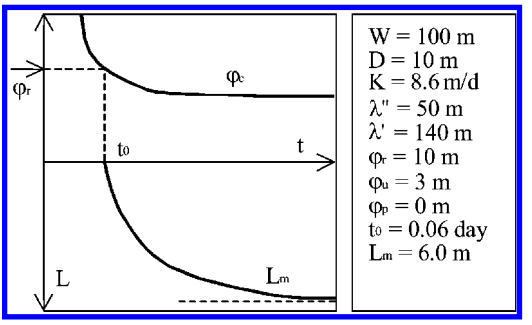


Figure 12. Transient uplift development for a specific case.

4 DIKE DOWELING

The focus is on underground soil stabilisation by doweling using ground mixing or short sheetpiling. For such reinforcement there is not a proper design method available. In fact, existing methods for sheetpiling design do not apply, as safety requirements against dike failure may allow for local relatively large deformations. The presented study deals with a practical design method for such underground stabilisation in the uplift zone, based on the theory of stationary viscoplasticity. Results are validated by sophisticated FEM modelling and centrifuge tests.

4.1 *Viscoplasticity*

Viscoplastic deformation occurs when soil is incapable of supporting deviatoric stresses without motion (Zienkiewics et al., 1978). The total strains are then so large that it is generally accepted to disregard elastic strains and consider creep strains given by a constitutive law defining the strain rate as function of stresses, treating it as a viscous fluid of a non-Newtonian kind. Though there are numerical methods to solve complicated cases, here, the focus is on using simple analytical elementary slip line solutions to indicate the effect of doweling by short sheetpiling to the likelihood of uplift failure of a dike, as shown in Figure 13. Few analytical slip line solutions with compatible creep and stress states exist and are useful, such as the viscoplastic wedge, the Rankine wedge (Annex 2) and plane extrusion.

4.2 *Slope stability*

To determine the effect of a dowel in dike stability a critical slip line method is examined using an elementary viscoplastic solution: wedge or extrusion. The slip line method, used here, is simplified by disregarding local stress variation and considering average shear. The approach of viscoplastic elements is easily built in existing advanced slip line methods including

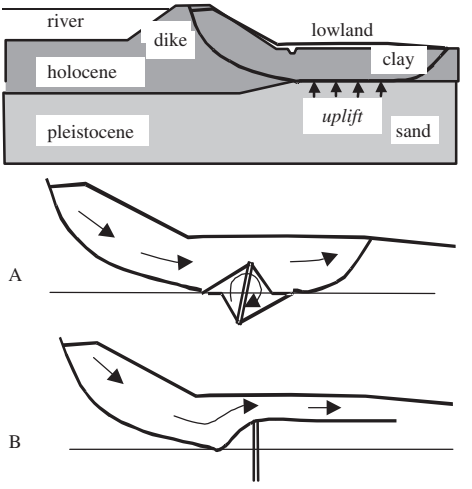


Figure 13. Slip failure, and the effect of uplift and doweling. A: effect of a dowel; plastic wedges. B: plane extrusion.

local stress variation. A kinematic system is chosen (Figure 13A or 13B) and the work rate during motion is considered, with and without the dowel. The difference in terms of the stability factor Γ shows the actual effect of the dowel. The stability factor is defined, according to

$$\Gamma = \frac{\text{(resistance)}}{\text{(loading)}} = \frac{\text{(work rate by shear resistance)}}{\text{(work rate by loading)}}$$

The slip line stability without a dowel is considered as a reference (Figure 14). Total weight per meter width of the considered slipping body is G. The shear stress k along the slip line s is considered constant. The net work rate becomes

$$W_{,t} = Gr\beta_{,t} - \int_{AB} R\beta_{,t} k ds = \beta_{,t}(Gr - s_{AB}Rk)$$

The situation becomes critical when $W_{,t} \downarrow 0$, corresponding to $\Gamma = 1$, or

$$k = Gr/(Rs_{AB})$$

A specific situation, for $\beta = 20°$ and a circle segment with an apex of $\alpha = 120°$, is worked out, see Figure 14. $G = \gamma V \approx 1/2(\alpha - \sin[\alpha])\gamma R^2 = 0.614\gamma \times R^2$; $\theta = 10° = 0.175$ rad; $r \approx (1 - 2/3(1 - \cos[\alpha/2])) \times \theta R = 0.117R$; $s_{AB} = \alpha R = 2.09R$. Thus, slip occurs for the given geometry, if $k \leq 0.034\gamma R$.

When the segment moves slightly (rotation $\beta_{,t}$) the stability increases, as r reduces. The dynamic shear resistance is usually smaller than the static resistance: $k_{\text{dyn}} = \mu k$, with $\mu < 1$. The equilibrium is restored if $r = k_{\text{dyn}} R s_{AB}/G \approx (1 - 2/3(1 - \cos[\alpha/2]))(\theta - \beta_{,t})R$.

Copyright © 2003 Swets & Zeitlinger B.V., Lisse, The Netherlands

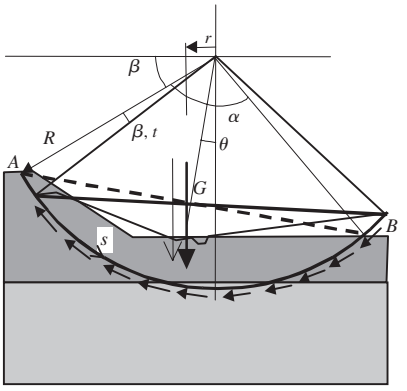


Figure 14. The reference stability approach.

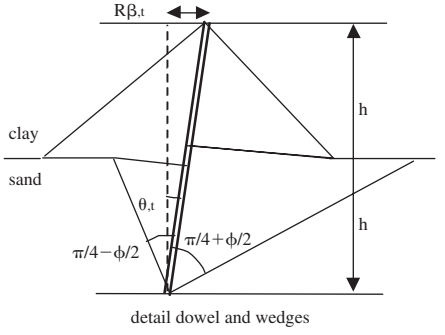


Figure 15. System of Rankine wedges for a rotating dowel.

This yields $\mu = 1 - \beta_{,t}/\theta$. For $\mu = 0.7$, it follows that $\beta_{,t} = 0.3\theta = 0.525$ rad (=3°). It implies that the slip will stop after a displacement of $R\beta_{,t}\cos[\beta]$. If $R \approx 25$ m, it corresponds to a vertical displacement at the crest of 1.20 m. Such a displacement was observed at Streefkerk (Figure 10).

4.2.1 *Short sheetpiling as rotating dowel; viscoplastic and Rankine wedges*

The stability can be improved by a short dowel (sheetpiling) placed in the underground across the sand–clay interface in the uplift zone (Figure 13A). When failure occurs, according to the assumed slip line, the dowel will rotate and induce four wedges: two plastic wedges in the clay and two Rankine wedges in the sand (Figure 15). The additional viscoplastic work induced by these wedges represents the stability improvement, in comparison to the situation without doweling.

The total body will shift $R\beta_{,t}$ along failure slip line s. At the interface it will cause the dowel to rotate: $\theta_{,t} = R\beta_{,t}/2h$. The total work rate by the resistance becomes (Annex 2), assuming shear resistance (k, k') in the clay and (k_s, k_s') in the sand (k' reflects soil-dowel shear).

$$
\begin{aligned}
&W_{,t} + \Delta W_{,t} \\
&\quad = \int_{AB} R\beta_{,t} k ds + 2(k + (1/2)k')|\theta_{,t}|h^2 \\
&\qquad + (k_s/|\sin[\pi/2 + \varphi]| + (1/2)k_s'/ \\
&\qquad\quad |\tan[\pi/4\varphi/2]|)|\theta_{,t}|h^2 + (k_s/|\sin[\pi/2 - \varphi]| \\
&\qquad + (1/2)k_s'/|\tan[\pi/4 - \varphi/2]|)|\theta_{,t}|h^2 \\
&\quad = R\beta_{,t}\{k(s_{AB} - h) + h(k + (1/2)k') \\
&\qquad + h(k_s + (1/2)k_s')/\cos\varphi\} \\
&\quad = R\beta_{,t} k s_{AB}\{1 + \xi h/s_{AB}\}
\end{aligned}
$$

with

$$\xi k = (1/2)k' + (k_x + (1/2)k_s')/\cos\varphi$$

Since $R\beta_{,t} k s_{AB}$ represents the work rate without doweling, comparison with the stability factor yields $\Gamma_{\text{dowel}}/\Gamma = 1 + \xi h/s_{AB}$, and therefore, $\xi h/s_{AB}$ represents the additional relative stability by the dowel. Notice, that a dowel in clay (lower part also clay, fully plastic: $\varphi = 0$) with clay-dowel friction $k' = (1/3)k$ results in $\xi = 1.3$ (stability Γ about 6% higher). Yet, as k_s is usually larger than k, the doweling effect will mainly originate from the sand. In this regard it should be noticed that due to uplift conditions the strength of the sand is limited.

As an example, the specific situation considered before, with $\beta = 20°$ and a circle segment with an apex of $\alpha = 120°$, is worked out. If $R = 24$ m, $s_{AB} = 50.26$ m, $h = 2$ m, $\varphi = 30°$, $k_s = 2k$, $k_s' = 2k' = (2/3)k$, then $\xi = 3.41$ and the additional stability becomes $\xi h/s_{AB} = 0.136$. Hence, the stability factor Γ improves with about 13%. Thus, the dowel is effective. When under higher loading the enforced dike collapses the dowel will rotate much more than the overall sliding rotation; in the present case 6 times: $\theta_{,t} = R\beta_{,t}/2h = 6\beta_{,t}$. The reuse of an existing dowel after a sliding event must be considered with doubt.

It could be well so that a new circular sliding plane arises just above the dowel. For the considered situation, elaboration yields a stability factor 14% higher; it is of similar order. Hence, both mechanisms may occur simultaneously.

4.2.2 *Rigid vertical dowel; viscoplastic extrusion and wedges*

The stability can be improved by a massive rigid dowel (i.e. soil–cement mixing) placed in the underground across the sand–clay interface in the uplift zone, such that rotation is avoided (Figure 13B). When failure occurs, according to the assumed slip system, the dowel may locally force the clay to flow over, according to a well-known extrusion problem

Copyright © 2003 Swets & Zeitlinger B.V., Lisse, The Netherlands

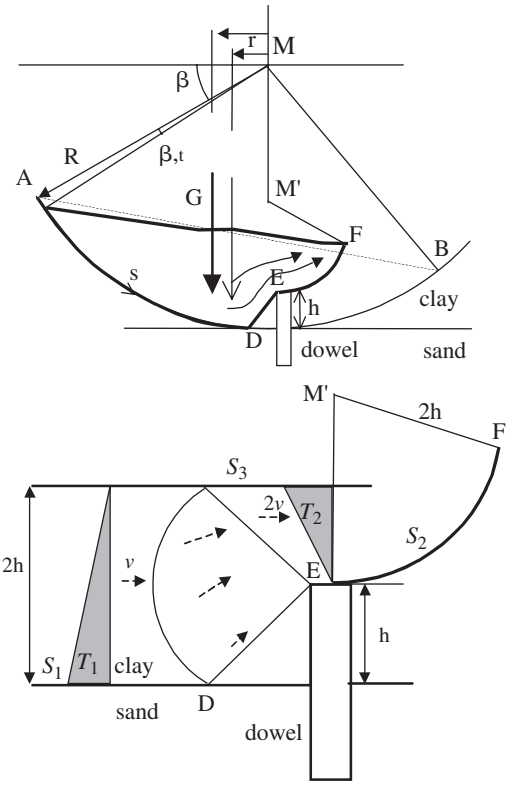


Figure 16. Failure state with extrusion (overflow).

(Figure 16). This system is more complicated; for an approximate solution rigorous assumptions are to be adopted. Two viscoplastic wedges are introduced to make the kinematics compatible. The additional viscoplastic work induced by this doweling represents the stability improvement, in comparison to the situation without doweling.

The total body will shift with velocity $R\beta_{,t}$ along failure slip line S_{AD}. The rigid dowel will force the soil to flow over. To adjust the rotating soil before D to uniform velocity v the viscoplastic wedge T_1 is introduced. Its clockwise angular velocity is $b/2h = \beta_{,t}(R-2h)/2h$. Next, viscoplastic extrusion is applied. Soil flows with velocity v between s_1 and s_3 to between s_2 and s_3, ending with velocity $2v$. To change the uniform flow there into rotating soil, compatible with the soil above (rotating with $\beta_{,t}$) the viscoplastic wedge T_2 is introduced. Its counter-clockwise angular rotation is v/h. The vertical deformation related to these wedges is supposed to take place without significant resistance. The soil in sector EF can now rotate around M' and slip occurs only along EF with velocity $2v = 2\beta_{,t}(R-2h)$. The slip along DE is accounted for in the work rate formula for the extrusion. Local slip near E along s_3 is disregarded, and so is the local vertical differential displacement above E.

The total work rate by the resistance becomes, for the specific situation considered before, with $\beta = 20°$ and a circle segment with an apex of $\alpha = 120°$.

$$
\begin{aligned}
W_{,t} &= \text{slip}(AD+EF) + \text{extrusion} + \text{wedge}(T_1+T_2)\\
&= \int_{AD} R\beta_{,t}k ds + \int_{EF} 2\beta_{,t}(R-2h)k ds + (\pi+2)khv\\
&\quad + k(2h)^2\beta_{,t}(R-2h)/2h + kh^2\beta_{,t}(R-2h)/h\\
&= R\beta_{,t}k\{0.57s_{AB} + 0.35s_{AB}(R-2h)/\\
&\quad R + (\pi+5)h(R-2h)/R\}\\
&= R\beta_{,t}ks_{AB}(1-0.08-0.7h/R+\eta h/s_{AB})
\end{aligned}
$$

with

$$\eta = (\pi+5)(R-2h)/R$$

The term $-0.08 - 0.7h/R + \eta h/s_{AB}$ represents the additional relative resistance by the rigid dowel. In comparison to the situation without a dowel, the moving soil weight G decreased (by strip DEFB) with about 25%, but the arm r increased 2.7 times. The work rate $Gr\beta_{,t}$ by the weight increases therefore to: $G(1-0.25)r(1+1.7)\beta_{,t} = 2.02Gr\beta_{,t}$. Hence, $(-0.08-0.7h/R+\eta h/s_{AB})/2.02$ represents the additional relative stability due to rigid doweling. For a specific case (see previous example): $R = 24$ m, $S_{AB} = 50$ m, $h = 2$ m, this additional stability becomes 13.2%. For this situation the rigid dowel increases the stability factor with 13%.

It could be well so that a new circular sliding plane arises just above the dowel. For the considered situation, elaboration yields for this mechanism a stability factor 14% higher. It is of the same order. Hence, both mechanisms may occur simultaneously.

4.3 *Validation by finite element calculation*

Standard dike stability improvement by bank widening is not always possible due to existing buildings and infrastructure. For a particular situation in the Netherlands the application of inside fortification using short sheetpiling is considered. It could save more than 1 M€/km, in comparison to a standard dike improvement (an additional embankment). Figure 17 shows a finite element simulation (PLAXIS). The critical state is reached with the so-called φ, c-reduction. The uplift zone, behind the short sheet-piling, appears, connected to the ditch in the hinterland. The pattern of plastic zones is quite complicated. One may recognise, on the left, two slip circles resulting in a massive plastic zone before the sheetpiling, diverting above and behind into three distinct slip surfaces. At the down rear side of the sheetpiling a Rankine type of plastic wedge occurs in the sand layer. The calculation showed a stability factor improvement of 7.5%.

Copyright © 2003 Swets & Zeitlinger B.V., Lisse, The Netherlands

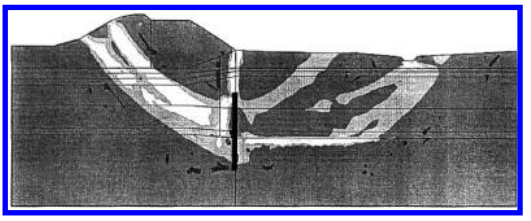


Figure 17. Finite element simulation (van Loon, 2002).

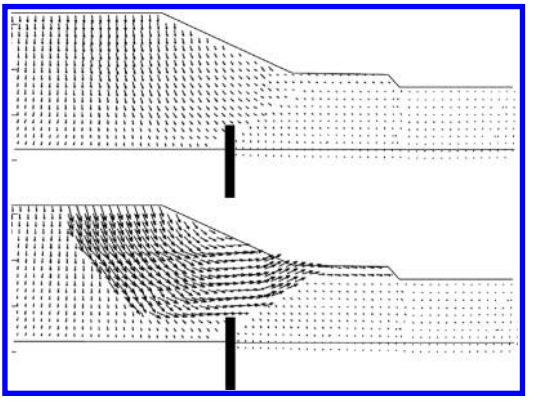


Figure 18. Deformation patterns centrifuge tests; upper one after 48 hr 37 min, lower one after 48 hr 38 min at 82 g (Van Eekelen, 2002).

4.4 *Centrifuge testing*

Geodelft performed centrifuge tests with deep unanchored short dowels, to quantify its efficiency, observe failure patterns, evaluate numerical predictions, and check the sustainability. The model was composed of organic clay, the dike body of Spesswhite clay. After a consolidation period at 45 g, repeated tests were performed with 80% loading (pore pressures in the deep sand layer) at 45 g to 60 g. Next, 100% loading was applied under 60 g, and subsequently the weight was raised by gradually increasing g. A similar reference test, without doweling, failed at about 68 g. The dowel model failed at 82 g (Figure 18): an improvement of about 11%. The deformations before failure were notably less in comparison to the reference test, repeated loading at 80% revealed sustainability, and unexpected failure modes did not appear.

5 FINAL REMARK

The approach by viscoplastic zones yields in principle an upper limit, since the occurrence of other lower energy failure patterns cannot be excluded. Therefore, the results are compared with consistent numerical stress–strain elastoplastic analysis, which in principle yields a lower limit, as the method approximates the initiation of a possible failure, while satisfying equilibrium conditions, but kinematics are not fully developed. The physical tests in the large centrifuge at GeoDelft completes the approach.

The method of viscoplastic zones, in fact, represents a simple and direct way to estimate the effect of a dowel. Particularly, viscoplastic and Rankine wedges can be easily incorporated in common slip circle methods, like Bishop's and Van's method.

The analysis shows that the application of doweling may improve the stability significantly, in the range of 10–15%. Moreover, the anchorage of dowels in the sand is important with respect to the sustainability of their functioning. The method of inside dike doweling is now mature for practical application. It is an efficient countermeasure for the uplift failure of river dikes.

REFERENCES

Barends, F.B.J. (1982) Transient flow in leaky aquifer systems. Int. Conf. on *Modern Approach in Groundwater Resources Management*, Capri.

Barends, F.B.J. (1988) *Uplift of the hinterland at high waters*. (Dutch). GeoDelft, Rp-290831/2.

Koelewijn, A.R. (2002) The practical value of slope stability models. *Learned and Applied Soil Mechanics out of Delft (Barends & Steijger, eds)*. Balkema, Lisse, p:107–114.

Marsland, A. & Randolph, M.F. (1978) A study of the variation and effect of water pressures in the pervious strata underlying Carayford Marshes. *Géotechnique* 28(4):435–464.

Padfield, C.J. & Schofield, A.N. (1983) The development of centrifugal models to study the influence of uplift pressures on the stability of a flood bank. *Géotechnique* 33(1):57–66.

RWS-DWW (2000) *Damage by floods*. (Dutch). W-DWW-2000-060.

Van, M.A. (2001) New approach for uplift-induced slope failure. *XVth ICSMGE Proceedings*, Istanbul, Balkema, Lisse, p:2285–2288.

Van Eekelen, S.J.M. (2002) *Short sheetpiling*. (Dutch). GeoDelft, Rp-400920/41.

Van Loon, L. (2002) *Optimization of sheetpiling in uplift situations; feasibility study*. GeoDelft, Rp-400920/15.

Zienkiewicz, O.C., Jain, P.C. & Onate, E. (1978) Flow of solids during forming and extrusion: some aspects of numerical solutions. *Jl. Solid Structures*, 14:15–38.

ANNEX 1 *Conformal mapping*

Figure A1 shows the conformal mapping for equation (3).

Here, $\zeta = -iz\pi/2D$, $W = \sin(\zeta)$, $a = \cos(iL\pi/2D)$, $\Xi = \arcsin(W/a)$, and $\Omega = 2Q/\pi i\Xi$.

Copyright © 2003 Swets & Zeitlinger B.V., Lisse, The Netherlands

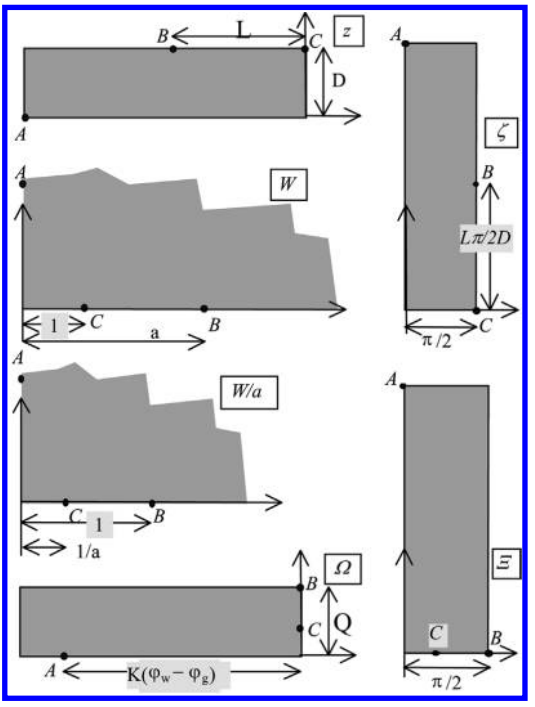


Figure A1. Conformal mapping, after Verruijt.

ANNEX 2 *Rankine wedge*

An element of a viscoplastic stationary motion with an analytical solution is a Rankine wedge (Figure A2). The wedge OAB will after a small

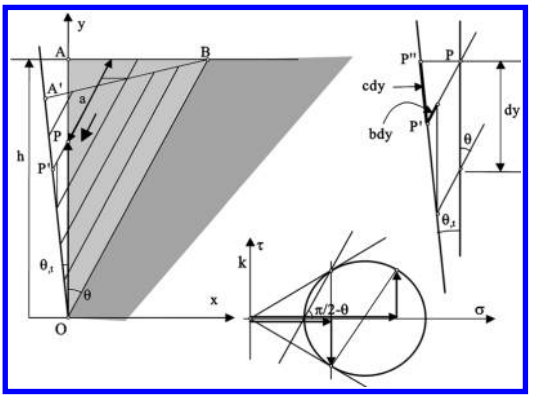


Figure A2. Principle of the Rankine wedge.

rotation $\theta_{,t}\,dt$ undergo a plastic deformation by single-directional frictional sliding and move into shape OA′B, while the outside remains rigid. Assuming a constant maximum shear stress k along the θ-inclined sliplines within OAB, the work rate is determined by $W_{,t} = k\int a|b|dy = k\int 2(h-y)|\theta_{,t}|/\sin[2\theta]dy = k|\theta_{,t}|h^2/\sin[2\theta]$. The additional work rate along the border line OA is added, taking into account an interface shear stress k': $\Delta W_{,t} = k'\int_{OA}|c|dy = k'\int y|\theta_{,t}/\tan\theta|dy = k'|\theta_{,t}/\tan\theta|\int y\,dy = k'|\theta_{,t}/\ 2\tan\theta|h^2$. Hence, the total work rate becomes: $W_{,t} + \Delta W_{,t} = (k/\sin[2\theta] + (1/2)k'/\tan\theta)|\theta_{,t}|h^2$. For the active state: $\theta = \pi/4 - \phi/2$ and for the passive state $\theta = \pi/4 + \phi/2$, with ϕ the soil friction angle. For $\theta = \pi/4$ the total work rate becomes similar to the work rate for the full-plastic wedge. The effect of gravity is disregarded.

Copyright © 2003 Swets & Zeitlinger B.V., Lisse, The Netherlands

Keynote lectures

Copyright © 2003 Swets & Zeitlinger B.V., Lisse, The Netherlands

Mitigation of the effects induced by the rise of the water table around underground structures

A. Cividini & G. Gioda
Politecnico (Technical University) di Milano, Milan, Italy

ABSTRACT: A finite element approach is discussed for the analysis of low-pressure injections of diluted chemical solutions in granular deposits. This technique represents, in fact, a possible provision to reduce the "natural" permeability of pervious soils and to limit the seepage flow towards underground openings that were not properly waterproofed. The grouting process is modelled as the advective-dispersive flow of a liquid containing a solute. First, an empirical law is presented for the variation of permeability with time and with the concentration of the grouting mixture. Then, the equations governing the process and their finite element formulation are discussed. Finally, the results of a series of two- and three-dimensional analyses are illustrated and some conclusions are drawn on the effectiveness of the treatment.

1 INTRODUCTION

Since about 1975 a series of industrial and agricultural changes led to an appreciable increase of the water table level in the city of Milan. The phreatic surface is gradually reaching an elevation higher than that of various underground facilities, which have been completed between 1960 and 1980, and that were not properly waterproofed since at that time the water table was at a much lower level. As a consequence, some extensive leakage of water took place at various locations within these structures and, in particular, within subway tunnels.

One of the geotechnical provisions envisaged to limit these negative effects is based on the low pressure grouting of the granular soil surrounding the structures to decrease its permeability and to reduce the seepage flow towards them.

An experimental and numerical study concerning the mentioned provision is summarized in the following that was carried out in the framework of a research project supported by the Milan Subway Company "*Metropolitana Milanese*".

First, on the basis of a series of laboratory tests, an empirical law is derived that governs the variation with time of the permeability of granular soils subjected to low pressure injections of sodium silicate solutions (Cividini, 2000). The equations governing the problem at hand, and their finite element formulation, are subsequently discussed. Finally, the empirical law is adopted in some numerical examples to get an insight into the effectiveness of the treatment.

2 LABORATORY INVESTIGATION

The laboratory investigation was carried out on samples of granular soil that were compacted in layers of small thickness within a "permeameter". This consists of a Plexiglas pipe (10 cm in diameter and 45 cm in height), within which the fluid flow takes place in the vertical direction. The hydraulic gradient is generated by means of a container filled with water, or with the silicate solution, placed at a proper elevation above the sample base.

During the grouting stage of the tests, performed by inducing a seepage flow of sodium silicate solutions within the samples, the volume of fluid leaving the samples and the pore pressure at different elevations within them were recorded during time. Depending upon the characteristics of the grouting solution, the total duration of the tests ranged between 20 and 30 days.

Since the chemical properties of the mixture play a major role in the effectiveness of the grouting treatment (e.g. Karol, 1968; Nonveiller, 1989), three different solutions have been used during the laboratory tests. They consist of solution of SiO_2 and of Na_2O with different ratios between the two components. Phosphoric acid was added to them, since the time required for the formation of the silica gel is influenced by the solution pH.

Some typical experimental results, in terms of the variation of the average hydraulic conductivity of the entire sample during time, are reported in Figure 1. They show that for the tested granular soil the grouting

Copyright © 2003 Swets & Zeitlinger B.V., Lisse, The Netherlands

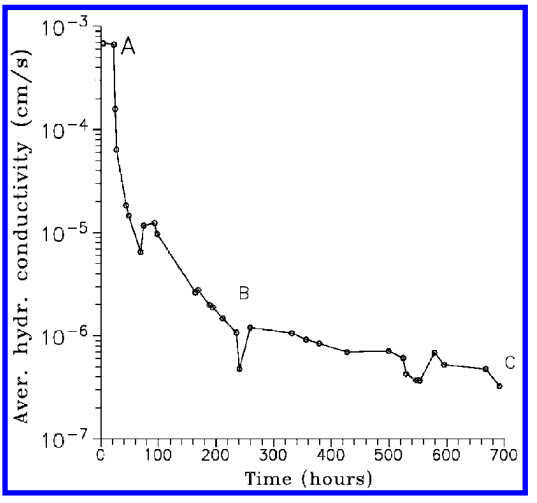


Figure 1. Variation with time of the average hydraulic conductivity of the sample. Points A, B denote the beginning and the end of grouting and point C denotes the end of the test.

through diluted solutions of sodium silicate may lead to a reduction of the hydraulic conductivity of two to three orders of magnitude.

A main scope of this experimental investigation was to derive an empirical law, applicable to numerical analyses, expressing the variation of the hydraulic conductivity with time. For this purpose, the linear laws depicted in Figure 2 were adopted as an engineering approximation of the results of tests. Here k_i and k_g denote, respectively, the initial (natural) hydraulic conductivity and that of the grouted soil, t_g represents the time necessary for the complete formation of the silica gel and $k_{\min}(t)$ is the hydraulic conductivity corresponding to the maximum concentration of the solution $c_{\max}$.

On these bases, the variation of the hydraulic conductivity k with time t and concentration c can be expressed as follows

$$k(t,c) = k_i - c \cdot [k_i - k_{\min}(t)] / c_{\max}, \tag{1a}$$

$$k_{\min}(t) = k_i \cdot \left(k_g / k_i\right)^{t/t_g}, \quad \text{if } 0 \le t \le t_g, \tag{1b}$$

$$k_{\min}(t) = k_g, \quad \text{if } t \ge t_g. \tag{1c}$$

The assessment of validity of this empirical law was based on the numerical simulation of the experimental results in Figure 1, as discussed in Section 4.

3 FINITE ELEMENT FORMULATION

The continuity equation for the advective-dispersive flow (see e.g. Bear & Verruijt, 1987; Rowe & Booker, 1997) is obtained by imposing that the accumulation

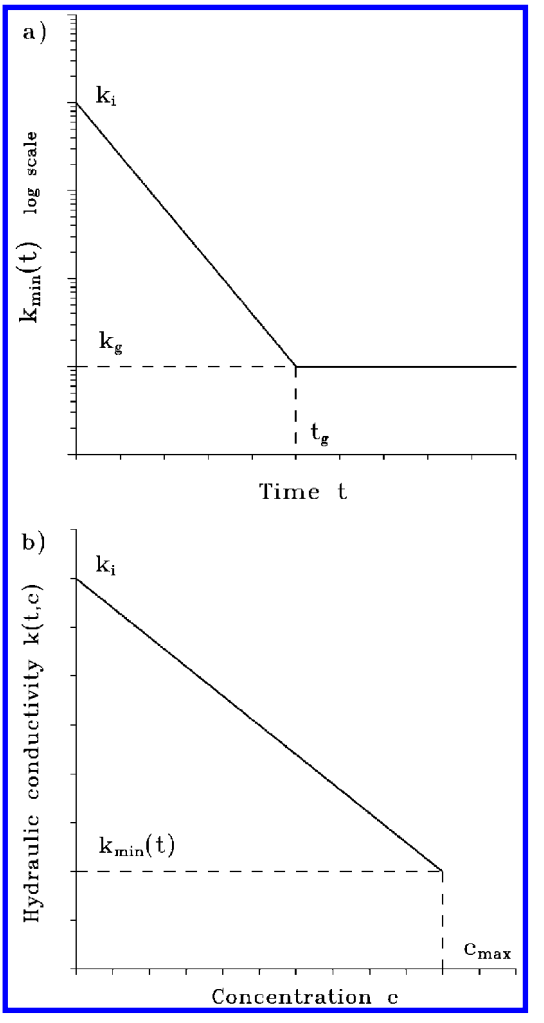


Figure 2. Adopted variation of the hydraulic conductivity of the soil with time a) and concentration b).

rate of the solute, produced by seepage and by the dispersive flux, compensates the variation of the mass of substance contained within a soil element. This, in turn, is due to the variation of concentration, c, and porosity, n, during time and to the contribution of possible internal sources having a known flux q_c.

The finite element formulation of the problem governed by the above continuity equation can be based on a procedure quite similar to that adopted for seepage or diffusion analyses. The procedure, the details of which have been presented by Cividini (2000) and are omitted here for briefness, leads to the following matrix form of the solving equations,

$$\underline{A} \cdot \underline{c} + \underline{H} \cdot \underline{c} + \underline{M} \cdot \dot{\underline{c}} = \underline{a}, \tag{2}$$

Copyright © 2003 Swets & Zeitlinger B.V., Lisse, The Netherlands

where

$$\underline{A} = \int_V \underline{B}^T \underline{K} \cdot \underline{B} \cdot \underline{h} \cdot \underline{f}^T dV, \tag{3a}$$

$$\underline{H} = n \cdot \int_V \underline{B}^T \underline{D} \cdot \underline{B}\, dV, \tag{3b}$$

$$\underline{M} = n \cdot \int_V \underline{f} \cdot \underline{f}^T dV \tag{3c}$$

and

$$\underline{a} = -n \cdot \int_V \underline{f} \cdot q_c\, dV. \tag{3d}$$

In Equations 2–3, $\underline{c}$ and $\underline{h}$ are the nodal concentration and hydraulic head vectors, $\underline{K}$ and $\underline{D}$ are the matrices of permeability and of dispersive coefficients, $\underline{M}$ is the mass matrix and $\underline{B}$ is the matrix of the derivatives of the shape functions $\underline{f}$.

It is worthwhile observing that the finite element evaluation of the nodal hydraulic heads is governed by the following equation,

$$\underline{P} \cdot \underline{h} = \underline{b}, \tag{4}$$

where

$$\underline{P} = \int_V \underline{B}^T \underline{K} \cdot \underline{B}\, dV \tag{5a}$$

and

$$\underline{b} = \int_V \underline{f} \cdot q_w\, dV. \tag{5b}$$

The compressibility of the soil skeleton is neglected in Equations 4–5 (i.e. the porosity n does not vary with time) and q_w represents the imposed flux due to possible internal sources.

Among the various numerical schemes, proposed in the literature for the time integration of advective-dispersive flow problems (see e.g. Wendland & Schmid, 2000), here a two-step time integration is adopted. The first step consists in determining the hydraulic head vector $\underline{h}$ by means of Equation 4. If the hydraulic conductivities are constant, and if the boundary conditions do not vary with time, the assumptions of incompressibility of the soil skeleton and of the liquid phase lead to a time independent distribution of the hydraulic head. Hence, under the above assumptions, only the time dependent change of the concentration vector $\underline{c}$ has to be evaluated during the second step of the analysis through an iterative procedure.

This step is subdivided into a series of time increments Δt during which a linear variation of vector $\underline{c}$ is assumed. Since $\underline{A}$ is in general non-symmetric, its contribution can be moved to the right hand side of Equation 2 to preserve the symmetric nature of the system matrix. This leads to the following recursive solution equation for $\underline{c}_{t+\Delta t}$,

$$\begin{aligned} &\left[\vartheta \Delta t \cdot \underline{H} + \underline{M}\right] \cdot (\underline{c}_{t+\Delta t})_i \\ &\quad = \Delta t \cdot \underline{a} - \left[(1-\vartheta)\Delta t \cdot \underline{H} - \underline{M}\right] \cdot \underline{c}_t \\ &\qquad -\Delta t \cdot \underline{A} \cdot \left[\vartheta (\underline{c}_{t+\Delta t})_{i-1} + (1-\vartheta)\underline{c}_t\right], \\ &\quad 0 \le \vartheta \le 1, \end{aligned} \tag{6}$$

where i denotes the iteration number.

Note that the evaluation of the nodal pore pressures is "uncoupled" from that of the concentrations, with a consequent saving in size of the relevant arrays of the finite element code. Possible spurious oscillations of the computed nodal concentrations can be drastically reduced if values of the integration parameter ϑ greater than 0.5 are adopted in the calculations.

The extension of this integration technique to the case of non-constant permeability (caused by the time dependent increase of the viscosity of the water-solute mixture) is straightforward. Since the variation with time of the hydraulic conductivity leads to a time dependent distribution of the hydraulic head, an iterative procedure should be employed to evaluate both vectors $\underline{h}$ and $\underline{c}$ at the end of each time increment Δt.

For the first iteration the nodal concentrations at time $t + \Delta t$ are set equal to those at time t and the permeability of the soil elements reached by the grouting mixture is determined through the adopted empirical law. Then, a first approximation of the nodal hydraulic heads and concentrations at time $t + \Delta t$ is determined following the described two-step scheme. The time increment is repeated, updating the values of the hydraulic conductivity on the basis of the computed values of the concentration at time $t + \Delta t$. The iterations are repeated until further changes of the final nodal variables become negligible.

When convergence has been reached, the iterative procedure is applied to the solution for the subsequent time increment. As to the time required for calculation, a rapid convergence was observed for all examined cases, leading to a computational effort comparable to that necessary to solve non-linear or unconfined seepage problems (see e.g. Cividini & Gioda, 2000).

4 APPLICATIONS

First, the numerical simulation of the laboratory tests was carried out for validating the empirical law expressed by Equation 1. Figure 3 reports the pore pressure distributions recorded along the sample height at the beginning of the test and during the

Copyright © 2003 Swets & Zeitlinger B.V., Lisse, The Netherlands

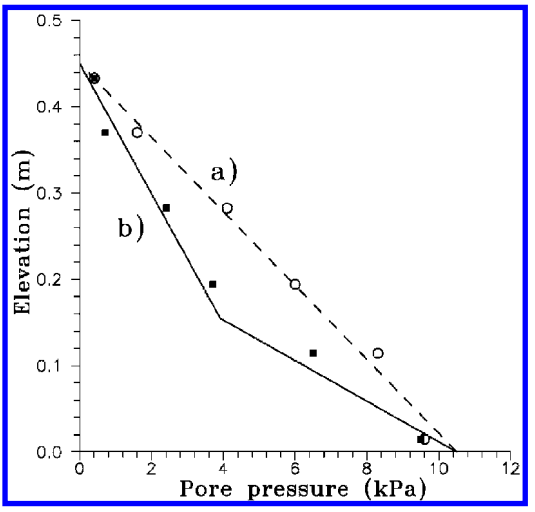


Figure 3. Pore pressure recorded along the sample height (dots) and numerical interpretation of the experimental results (dashed and solid lines): a) before grouting, b) during the test, before the complete formation of the silica gel.

grouting process, before the formation of the silica gel has been completed.

The comparison between experimental and numerical results shows that the adopted relationship between hydraulic conductivity, time and concentration leads to an acceptable approximation of the experimental data.

The described finite element approach was subsequently adopted in the numerical simulation of a grouting treatment in which the solution is injected from the tip of a single pipe. The analyses were carried out in axisymmetric regime, adopting the mentioned empirical law for expressing the time dependent variation of the permeability of the grouted soil.

A soil portion of 10 m × 10 m was discretised into 4 node, isoparametric finite elements. At the beginning of calculation this zone is subjected to a constant hydraulic head distribution of 10 m, whilst the hydraulic head at the pipe tip is kept equal to 15 m. The left vertical side of the mesh (where the pipe is located and that represents the axis of symmetry) and its bottom side are impervious, while the hydraulic head is imposed on the remaining sides. The problem was solved by considering a reduction of two orders of magnitude of the hydraulic conductivity at the end of grouting, with respect to the initial permeability of the natural soil.

The results of calculations are summarised in Figure 4 showing the contour lines of the hydraulic head and of the concentration for different time values. The results indicate that the formation of the silica gel, and the parallel reduction of the hydraulic conductivity, tends to limit the increase during time of the size of the treated zone.

On this basis it could be concluded that the silica gel formation should be delayed, to increase the spreading of the solution and, hence, to improve the effectiveness of the treatment. This result should not be neglected in choosing the chemical characteristics of the grouting solution.

Finally, the finite element approach was applied to the analysis of the three-dimensional problem depicted in Figure 5. This refers to a sequence of vertical pipes, with spacing d between each other. Three injection points are situated, at a distance d, along each pipe. The central injection point is 5 m below the water table. The dashed zone in Figure 5 represents the part of the porous medium discretised into finite elements.

It should be considered that in actual field applications the grouting treatment takes place simultaneously from several injection points. Consequently, the numerical simulations were carried by applying the grouting pressure, for 25 hours, first at points A_2, B_1 and B_3 and, subsequently, at points B_2, A_1 and A_3. In these simulations the ratio between injection h_{inj} and in situ h_{situ} hydraulic heads ranges between 2 and 5, while the distance d among the pipes, and among the injection points, is between 0.5 m and 1.5 m.

At the end of each grouting analysis the portion of the finite element grid bounded by the two horizontal planes through points A_1 and B_1, and through points A_3 and B_3, was subjected to a unit hydraulic gradient in the z direction. This permits evaluating the "equivalent" hydraulic conductivity k_{eq} in the horizontal direction at the end of treatment. The results of analyses are summarized in Figure 6, which shows the variation of the ratio between "equivalent" and "natural" hydraulic conductivities k_{eq}/k_i with the ratio h_{inj}/h_{situ} for various values of the distance d.

5 CONCLUDING REMARKS

The joint use of experimental and numerical techniques could contribute to the solution of complex geotechnical problems and could represent a useful tool for engineers during the design stage of projects.

To this end, an application has been discussed of laboratory and numerical (finite element) procedures to the analysis of the low pressure grouting of granular soils.

It was observed that the numerical analysis is able to provide a reasonable evaluation of the grouting process and of the subsequent behaviour of the treated soil. This requires the calibration of the relevant material parameters and the "validation" of the numerical

Copyright © 2003 Swets & Zeitlinger B.V., Lisse, The Netherlands

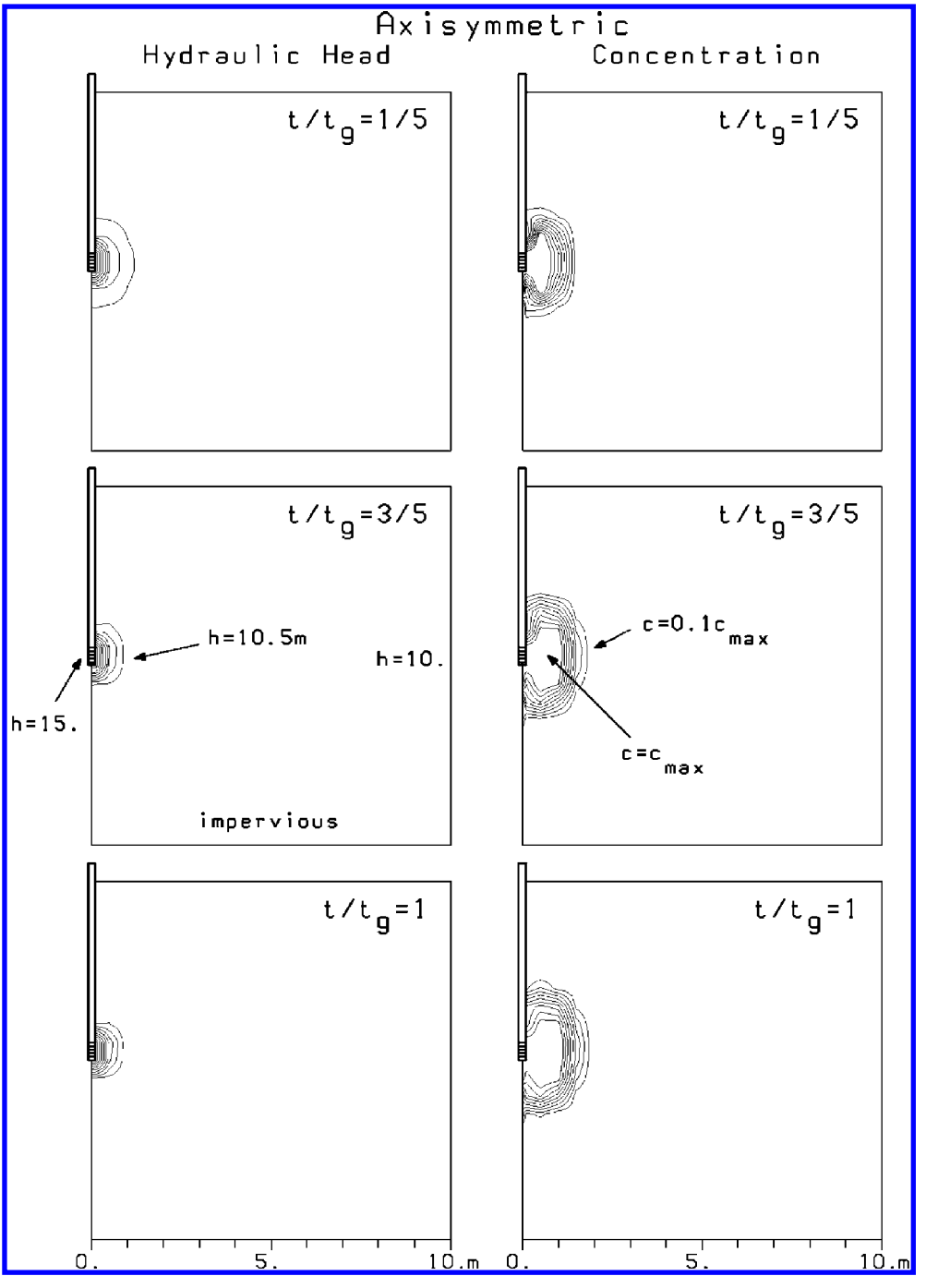


Figure 4. Contour lines of the hydraulic head and of the concentration for different time values. (Contour line intervals: hydraulic head 0.5 m, concentration 0.1.)

Copyright © 2003 Swets & Zeitlinger B.V., Lisse, The Netherlands

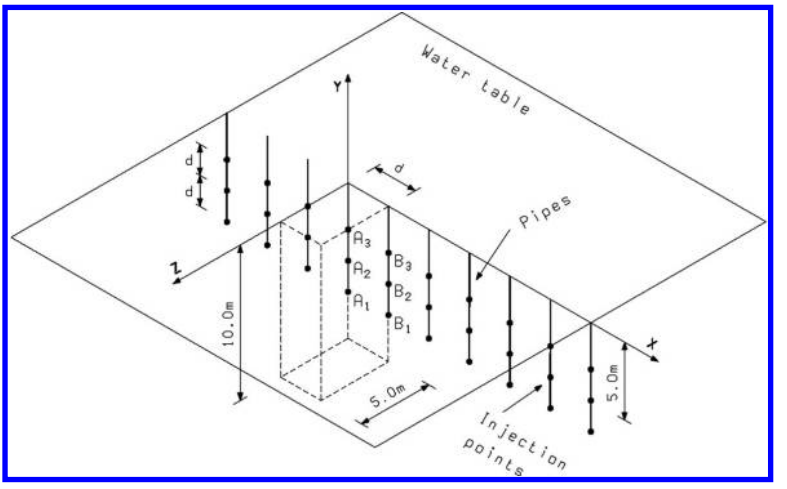


Figure 5. Scheme of the three-dimensional analysis of the grouting treatment.

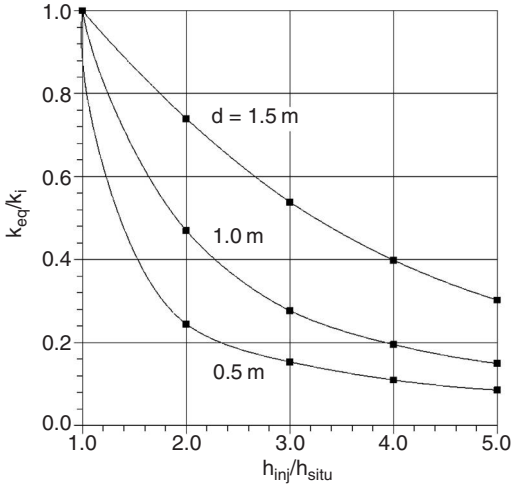


Figure 6. Ratio between equivalent k_{eq} and natural k_i hydraulic conductivities vs. the ratio between injection h_{inj} and in situ h_{situ} hydraulic heads, for different values of the pipe distance d.

procedure. These two steps were based here on the interpretation of a series of laboratory tests. The application of the numerical technique to the analysis of an in situ treatment leads to diagrams that relate the pipe spacing and the injection pressure to the reduction of permeability of the treated soil.

ACKNOWLEDGEMENTS

The financial support of the Ministry of University and Research of the Italian Government is gratefully acknowledged.

REFERENCES

Bear, J. & Verruijt, A., 1987. *Modeling groundwater flow and pollution*. Dordrecht (Holland): D. Reidel Publishing Company.

Cividini, A., 2000. A study of the low pressure grouting of granular soils. In *"Developments in Theoretical Geomechanics", (D.W. Smith & J.P. Carter Eds.); Proceedings of The John Booker Memorial Symposium, Sydney*, 525–546; Rotterdam (the Netherlands): Balkema.

Cividini, A. & Gioda, G., 2000. Finite element analysis of free surface seepage flows. *Chapter 20 in "Modeling in Geomechanics", (M. Zaman, G. Gioda & J.R. Booker Eds.),* 505–524; Chichester (UK): John Wiley & Sons Ltd.

Karol, R.H. 1968. Chemical grouting technology. *Journal of the Soil Mechanics and Foundations Division*, ASCE, 94: 175–204.

Nonveiller, E., 1989. *Grouting theory and practice*. New York (USA): Elsevier.

Rowe, R.K. & Booker, J.R., 1997. Recent advances in modeling of contaminant impact due to clogging. *Proc. 9th Int. Conference of International Association for Computer Methods and Advances in Geomechanics; Wuhan, People Republic of China*, 43–56; Rotterdam (the Netherlands): Balkema.

Wendland, E. & Schmid, G., 2000. A symmetrical streamline stabilization scheme for high advective transport. *International Journal for Numerical and Analytical Methods in Geomechanics*, 24: 29–45.

Copyright © 2003 Swets & Zeitlinger B.V., Lisse, The Netherlands

Evaluating risk after remediation for NAPL contaminated sites

K. Soga, I.H. Kulasooriya, A.C. Mesquita, J.W.E. Page & W.A.P. Waduge
University of Cambridge, Engineering Department, Cambridge, UK

ABSTRACT: Although recent development of source-zone treatment technologies shows that in-situ removal of nonaquoues phase contaminants from soils is possible, the efficiencies in the field condition are still limited due to significant uncertainties about the value of source zone remediation. This paper addresses the need of quantifying the mass flux coming out from the "remediated" or "treated" source zone for accurate risk calculation and long-term performance assessment. Accurate assessment of risk and appropriate corrective action requires site-specific identification of applicable risk factors. Some experimental data and numerical simulation results are used to show that the uncertainties comes from site heterogeneity and accompanying complex NAPL entrapment condition as well as from the physical and chemical changes during remediation operations.

1 INTRODUCTION

In many industrial countries, a large number of brownfield sites are under pressure for infrastructure redevelopment to meet everlasting industrial and societal demands. For instance, as part of their sustainable development initiative, the UK government has set a target that 60% of new homes are to be built on brownfield lands. Since these sites are often contaminated by chemicals used in previous industrial operations, some form of site remediation may become necessary. Historical practices in site remediation relied on establishing cleanup goals set to back-ground conditions. However, in the authors' opinion, cleanup progress has been limited despite major efforts during the past two decades, and effective technologies for treating many areas of soil contamination to background levels are still yet to be developed.

Because of technological and fiscal limitations associated with cleaning up hazardous sites to background conditions, many governments have now adopted risk-based methods for cleanup management and environmental remediation. For example, the UK government has developed a legal frame-work "for improving the quality of all historically contaminated land so that it is fit for its current use and no longer causes significant risk to people or the environment" (Part IIA of the Environment Protection Act 1990; Environment Act 1995: emphasis by the authors). The legislation under this framework was brought in force in 2000 (The Contaminated Land Regulations 2000) and the practicing guidance and associated risk assessment model called the Contaminated Land Exposure Assessment (CLEA) model were published in 2002 (see the Environment Agency: www.environment-agency.gov.uk). Similar legislative practice is conducted in North American countries as well as European countries.

When infrastructure is to be developed at brownfield sites, risk assessment process is applied to identify remedies that will primarily reduce health risk and that will be cost effective. Through this process, risk assessment is used to evaluate cleanup end-points (i.e. cleanup goals) for soil and groundwater so that the most appropriate corrective action(s) can be determined. As every brownfield site is unique in its own, there is no particular solution or remediation technology that can be used to clean up all brownfield sites in the short term. Hence, any environmental solution for contaminated lands requires a long-term view and the selection of remediation techniques should be made as part of the life cycle assessment of the new infrastructure that will be developed. The considerations for assessment include not only potential future use of the site but also maintenance and demolishing needs of the infrastructure during its life time as shown in Fig. 1. A question then arises; which remediation methods are appropriate so that the long-term risk after remediation can be predictable as well as controllable?

With the above background and question in mind, the aim of this paper is to address the need for assessing the long-term performance of remediation technology under the current framework of contaminated land risk assessment. The content of the paper is limited to in-situ remediation of nonaqueous phase liquids (NAPLs) contaminated sites due to the authors'

Copyright © 2003 Swets & Zeitlinger B.V., Lisse, The Netherlands

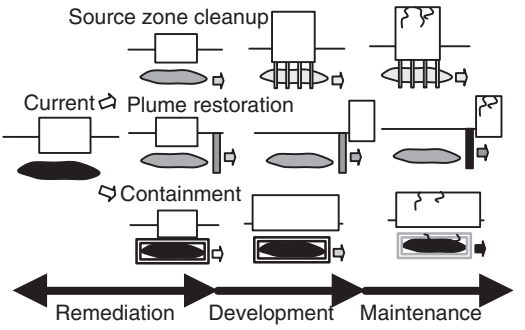


Figure 1. Infrastructure development and life cycle assessment.

technical knowledge in this area. In the next Section, the limited efficiencies of the current NAPL remediation methods are reviewed and discussed in relation to risk assessment procedures. In Section 3, some preliminary experimental and numerical data that can be used to assess the long-term performance of remediation technologies are presented. Finally, concluding remarks are given in Section 4.

2 EFFICIENCIES OF CURRENT REMEDIATION TECHNOLOGIES

2.1 *Complexity of NAPL contamination*

In many industrial countries, accidental surface release and improper disposal of petroleum products (e.g. jet fuel, refinery wastes, diesel etc.) and volatile organic solvents are recognised as two of the most widespread causes of groundwater contamination by chemical compounds. In the subsurface, these contaminants often persist as a separate phase from the aqueous (water) phase due to their generally low solubility and are termed *n*on-*a*queous *p*hase *l*iquids (NAPLs). NAPLs that are less dense than water, including many petroleum products, are termed light non-aqueous phase liquids (LNAPLs) and these commonly collect and pool at, or above, the water table. The other type of NAPL is denser than water (DNAPL) and continues on a downward migration through the water table under the influence of gravity into the saturated zone below. Chlorinated solvents are a common form of this contaminant.

When NAPL contaminants are spilled into the subsurface, its heterogeneity has been shown to increase the complexity of NAPL movement and subsequent entrapment. The complex spatial distribution is controlled by unstable fingering, preferential channelling and both micro- (pore) and macro-scale (layering and soil texture contrast) heterogeneity of subsurface formations (e.g. Schwille, 1989; Keuper and Frind, 1991; Illangasekare et al., 1995).

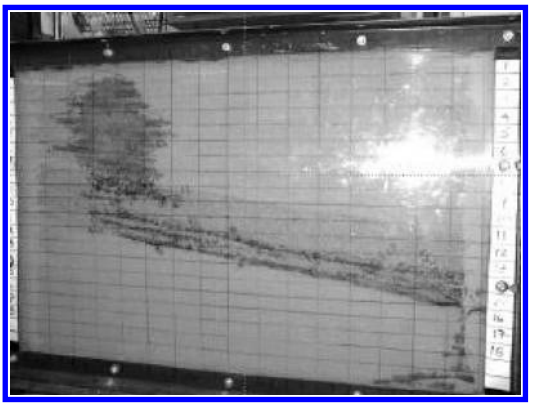


Figure 2. DNAPL movement along inclined layer.

In the presence of layers, NAPL will sink (if the underlying layer is coarser) or spread at the interface (if the underlying layer is finer). Even a relatively thin, low permeability layer will inhibit downward percolation and force the contaminant to spread laterally (Dominico and Schwartz, 1990). Since the flow is driven by gravity, if the layered system is inclined, the resulting migration pattern is combination of sinking and spreading; the NAPL spreads downwards along an interface with a finer layer following the topography of the boundary. An example of this is shown from a laboratory model test in Fig. 2 (Coumoulos et al., 2000). The experiment was conducted in a tank that was about 70 cm deep and it is showing a DNAPL migration pattern at shallow depths when capillary barriers are in place. The experiment demonstrated that, at shallow depths, it is possible that the DNAPL will travel downwards along an interface in order to increase its pressure before entering the underlying finer layer.

Complex DNAPL entrapment in a heterogeneous soil condition is shown in Fig. 3 (Soga et al., 2002a). A 2.25 m long soil tank was filled with five different sands under water and the filling arrangement was obtained based on a numerical simulation using a spatially correlated random field generator. A model DNAPL migrated from lens to lens depending on the permeability of sand lenses, mobilising through relatively high permeability sands. The observed lateral spreading was primarily due to the lower degree of lateral heterogeneity compared to vertical heterogeneity.

As surface water infiltrates and groundwater flows through the zone where NAPLs are entrapped (the NAPL source zone), a small amount of the NAPL contaminants slowly dissolves into the aqueous phase and these contaminants have the potential to be transported great distances from the source zone as a plume (Fig. 4). Although NAPL dissolution into local ground water is very limited, the generated aqueous

Copyright © 2003 Swets & Zeitlinger B.V., Lisse, The Netherlands

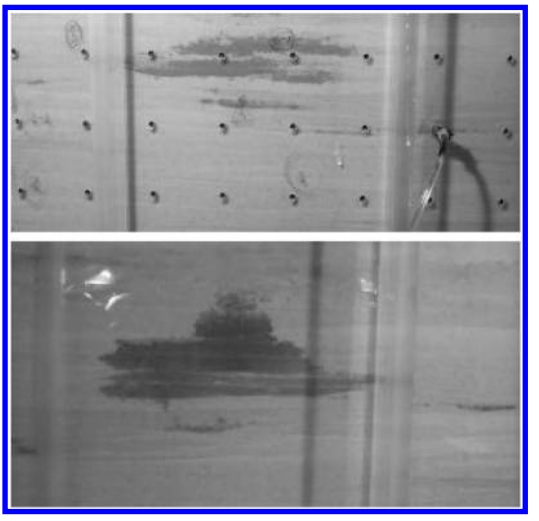


Figure 3. DNAPL movement in heterogeneous soil model.

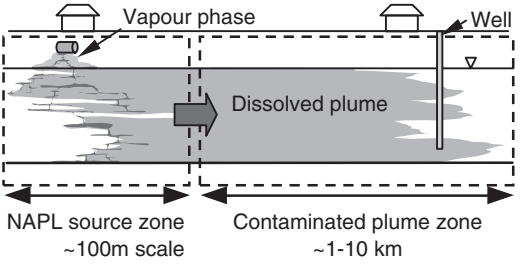


Figure 4. Source and plume zones of NAPL sites.

concentrations are typically a number of orders of magnitude greater than the maximum levels permitted for human health safety.

2.2 *Remediation technologies and their efficiencies*

The different scales of heterogeneity affect the condition of the NAPL source zone, which in turn influences the degree of groundwater contamination and success of any remediation approach. Much research is concerned with the development of remediation strategies to either (a) "remove" the pure phase NAPL contaminants from the ground (source zone remediation), or (b) 'control" or "treat" the plume to reduce the chemical concentrations in the groundwater to "safe" levels (plume remediation).

Although plume control technologies have reached a mature stage in the authors' opinion, it is now widely recognised that such technologies for NAPL contaminated sites have to be employed for decades or even longer to substantially reduce contamination levels.

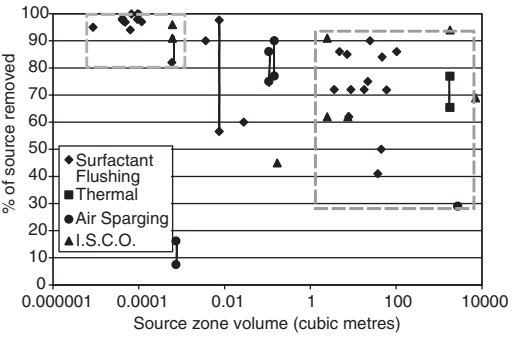


Figure 5. Removal efficiencies of selected source zone remediation technologies (Soga et al., 2003).

This is due to the low aqueous solubility of NAPLs and large NAPL/water interfacial tensions at the source zone (Johnson and Pankow, 1992). Hence, the environmental community has been developing a number of innovative source zone remediation techniques to remove NAPLs from the subsurface. However, previous source zone remediation attempts have shown that it is very difficult to achieve complete field-scale contaminant removal. A study by the US National Research Council (1999) concluded that "although a range of technologies is emerging to help clean up DNAPL-contaminated sites, the number of carefully controlled field tests is insufficient to establish the ultimate cleanup level attainable for each technology."

Soga et al. (2002b; 2003) reviewed source zone remediation studies available in literature and summarized the efficiencies of several insitu remediation technologies (air sparging, steam injection, surfactant injection, and chemical oxidation). In Fig. 5, the percentage of maximum free NAPL phase removal is plotted against the source volume of tested area. The data has been selected from studies conducted at different experimental scales, ranging from 1-D column experiments to full-scale 3-D field tests. The efficiency problem associated with upscaling of the source zone volume is very clearly displayed. For the reported column experiments, the degree of source zone removal is limited to a small range of very high values. However, a wider range of efficiencies exists for field-scale remediation efforts. For typical field scale source saturations, on average only 60% of the DNAPL mass/volume is removed. As well as a decrease in the maximum possible remediation level moving from the 1-D column to the 3-D field situation, the range of achievable source removal efficiencies increases substantially. There exists a significant uncertainty associated with upscaling from laboratory to actual field conditions. This highlights the limited and highly variable efficiencies of current source zone remediation techniques applied in the field scale.

Copyright © 2003 Swets & Zeitlinger B.V., Lisse, The Netherlands

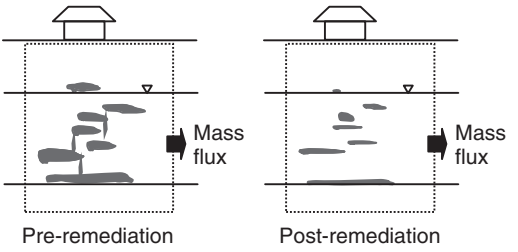


Figure 6. Mass flux before and after remediation.

2.3 *Risk assessment of NAPL source zone and mass flux approach*

The irregular distribution of entrapped and pooled NAPL in source zone areas, coupled with natural variations in hydraulic conductivity and capillary properties, makes complete mass removal virtually infeasible for most source zone treatment technologies. Having previously observed that a significant fraction of the contamination will still remain after treatment, what level of remediation is acceptable, and how "safe" is a "safe site"?

It is perhaps more appropriate to assess the success of any remediation attempts in terms of the reduction of down-gradient risk that can be achieved. For instance, a clean-up technology might remove 70% of the contaminant mass, but the process of remediation could change the characteristics or morphology of the remaining 30% and result in elevated downstream risk. Alternatively, a 20% reduction in NAPL mass could be sufficient to change its subsurface distribution into a condition of significantly reduced mass transfer (such as a greatly reduced NAPL surface area) with a corresponding reduction in receptor risk.

Considering the risk assessment procedure currently adopted in practice, attention for source zone remediation should focus on understanding and ideally quantifying the mass transfer from entrapped NAPL in the source zone into ground water flowing through the source zone before and after remediation as shown in Fig. 6. The fundamental physical process for determining both pre- and post-remediation status of the solute plume is the mass transfer (both temporal and spatial) from the entrapped NAPL source. Therefore, for a given ground water flow condition, the mass flux (i.e. the release rate of contaminant mass due to transfer from NAPL to the aqueous phase) leaving the source after remediation will determine whether the source is still a threat to ground water.

In order to measure the impacts of source treatment, or to understand the real risks posed by a residual source, it is essential to have accurate estimates of mass release from a source zone before and after treatment. The mass release rate can change as a function of time and a key practical question is to understand how much reduction in time or monitoring of the system can be achieved by a source removal activity. Furthermore, there is also a need to predict the future mass flux released from the source zone, which will allow site-specific remediation targets to be set.

In recent years, monitored natural attenuation (MNA) has become widely used for NAPL contaminated sites. There is little doubt that MNA will be used for many sites after aggressive source zone treatment. However, there are questions regarding the conditions under which MNA can be used with confidence. Combining temporal mass flux evaluation with estimates of natural attenuation capacity can allow us to develop meaningful risk-based source-plume management strategies. Hence, integrated modeling and measurement of both the mass flux from the post-remediation source and natural attenuation capacity of the subsurface environment will be essential.

For this purpose, factors that control the mass flux emanating from the source zone undergoing remediation need to be examined. As the NAPL source is removed, due to the relative inaccessibility to the flowing groundwater, it is possible that mass flux from the source zone will substantially decrease, even though considerable contaminant mass remains. On the other hand, various treatment technologies have the capacity to increase mass flux by spreading the contaminated zone (through NAPL mobilization) or by increasing the NAPL/aqueous interfacial area (through solubilization). At present, however, significant uncertainty exists about the source zone behaviour following the termination of any source zone remediation technology. It is difficult to determine the "success" of source removal efforts, or to set reasonable performance goals for such efforts.

3 RISK EVALUATION UNDER POST REMEDIATION CONDITION

3.1 *Potential questions*

As described in the previous section, little is known of the influence of source zone treatment on contaminant mass fluxes, composition, and source zone architecture. There is also a need to understand the influence of source remediation technologies on natural attenuation processes, particularly since some of the technologies involve drastic changes in the subsurface environmental conditions. Such information is essential for evaluating potential risk reduction and the cost/benefits of applying a particular remediation technology. Some specific questions that need to be answered to achieve this are

– What does a treatment system leave behind? What are the potential impacts on water quality parameters down gradient of a treated area?

Copyright © 2003 Swets & Zeitlinger B.V., Lisse, The Netherlands

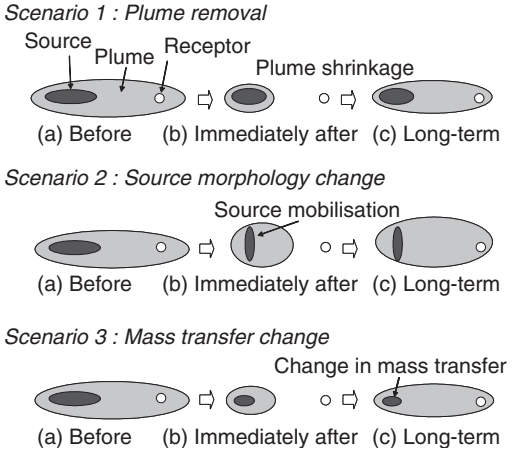


Figure 7. Plume behaviour after source zone remediation.

– How does treatment impact the flow field? Does treatment increase the effective permeability as a result of mass removal or mass destruction? Does the treatment block the formation as a result of precipitation or plugging?
– How do residual materials continue to react both biologically and chemically? What is the biological diversity before remediation and how does it change as a result of remediation?
– What hazards are associated with any byproducts produced as a result of treatment (e.g., metabolites from bioremediation or oxidation)?
– How long does the system take to return to a point at which there is no environmental concern?

Possible scenarios after source zone remediation are shown schematically in Fig. 7. In Scenario 1, the remediation method temporarily reduces the solute plume volume. However, the remaining free phase source continues to generate dissolved contaminant mass and eventually its aqueous concentration starts to increase again. Although receptor concentrations after remediation are reduced, remediation will eventually fail due to large mass release rate from the remaining source zone. In Scenario 2, source zone volume is reduced but source zone distribution is spread. The increase in the NAPL surface area available for mass transfer would potentially cause a gradual increase in post-remediation mass flux. Scenario 3 illustrates chemical, physical and biological changes of the NAPL properties followed by remedial actions, which may increase or decrease the mass transfer rate from any NAPL source.

These scenarios highlight the importance of understanding source zone dissolution behaviour and the effects of aquifer heterogeneity on the rate of contaminant mass removal. Furthermore, it would be extremely beneficial if the long-term source zone dissolution activity could be predicted, especially for the in-situ conditions following the completion of any remediation activities. Using experimental data and numerical simulation results, the discussion in the subsequent sections focuses on the dissolution behaviour of NAPL source before and after selected source zone remediation technologies are applied.

3.2 *Laboratory investigation of dissolution behaviour after remediation*

3.2.1 *Enhanced flushing remediation*

Enhanced flushing technologies, based on flushing NAPL source zone with chemical agents such as cosolvents, surfactants and complexing agents, have shown promise as an alternative to the basic pump and treat method (e.g. Annable et al., 2000). Addition of chemical agents to the flushing solution can remove NAPL by increasing the apparent solubility of the NAPLs as well as by mobilising the free phase by decreasing the interfacial tension (Fountain et al., 1991).

A series of column experiments were performed to investigate the mass transfer behaviour before and after surfactant remediation. In the experiments, medium sized sands (British Standard Fraction C; 300–600 μm) were filled in a 30 cm long column with 5 cm internal diameter. NAPL (either PCE or HFE (Methoxynonafluorobutane)) was then injected from the bottom and residual NAPL was formed by injecting water from the top at a rate of 0.2 m/day and pushing free NAPL out of the bottom of the column.

In order to remove the residual NAPL, surfactants were flushed vertically downwards in the column. Two different surfactants, Aerosol 80I and Tween 80, were used. Aerosol 80I removes DNAPL mainly by mobilization, whereas Tween 80 removes DNAPL mainly by enhanced dissolution. In the present column experiments, the final removal efficiencies ranged between 78 to 94%.

Before and after surfactant flushing, 3–4 pore volumes of water were injected at 0.4 m/day to obtain a steady state aqueous concentration. In some cases, surfactant flushing was interrupted at a stage before the effluent concentration decreased so that the mass transfer process under an incompletely removed condition could be examined. In such a case, the steady state aqueous concentration was measured at 0.4 m/day after removing the surfactant remained in the column.

Figure 8 shows the normalised DNAPL aqueous concentrations (measured steady state concentrations divided by the maximum solubility) versus the average DNAPL saturation from the initial residual conditions down to removed conditions. The results show that the steady state concentrations at residual conditions (S_{NAPL} = 15–20%) are about 30–50% of the maximum solubility concentration. It is also observed that

Copyright © 2003 Swets & Zeitlinger B.V., Lisse, The Netherlands

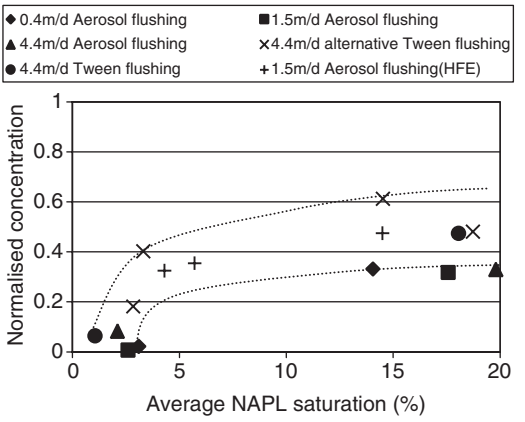


Figure 8. Steady state concentration before and after surfactant remediation.

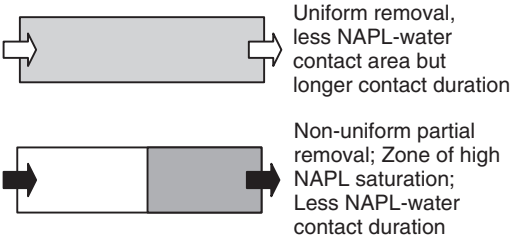


Figure 9. Possible removal conditions within a soil column.

the removal of DNAPL down to $S_{\mathrm{NAPL}} = 5\%$ did not reduce the steady state aqueous concentration. It is only when the average NAPL saturation became less than 5% that a noticeable decrease in steady state aqueous phase concentration was observed. The results also show that this trend is similar for different surfactants and flushing rate.

In summary, when DNAPL entrapped in the residual condition is to be removed, at least 60% removal is necessary to see any decrease in the aqueous phase concentration. However, it should be noted that the removal may not be uniform throughout the column as shown in Fig. 9. This may result in mass flux depending on column length and the NAPL saturation distribution. The limited decrease observed in the present experiments requires further careful data examination, which is a subject of the current study.

One of the potential complications in using surfactant is that, for certain surfactants such as Aerosol 80I, the interfacial tension between NAPL and the aqueous phase dramatically decreases and NAPL can remobilise and move in the direction of gravity during the flushing stage (Pennell et al., 1994). Soga et al. (2002a) compared the mass flux from a PCE source

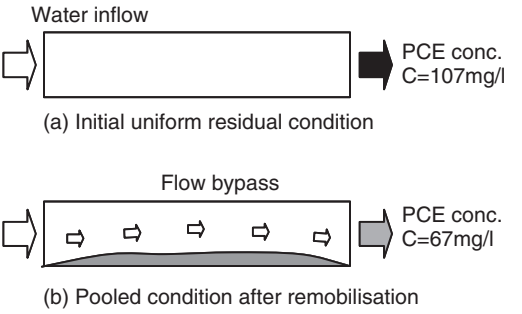


Figure 10. Steady state PCE concentrations of residual and pooled conditions.

in a residual condition to that from a pooled condition created in the same column by injecting surfactant and mobilising the PCE. An anionic surfactant, Aerosol, was used to remove PCE.

PCE was initially uniformly distributed at residual saturation condition as shown in Fig. 10(a). Under the steady state water flow condition, the PCE aqueous phase concentration was 107 mg/l. The column was then placed in the horizontal direction. As surfactant was introduced to achieve lateral flow conditions, the PCE mobilised downwards and then pooled on the bottom of the column as shown schematically in Fig. 10(b); the actual spatial distributions of PCE NAPL in the columns are reported in Kulasooriya et al. (2002). The mass flux from the PCE in the pooled condition reduced to 67 mg/l due to bypass of water around the pooled source. This change in morphology from residual to pooled conditions decreased the mass flux despite no significant change in PCE volume in the column. The result indicated the positive effect of mass flux reduction by PCE mobilization during surfactant remediation.

In the column experiments described above, the DNAPL pooled on the bottom boundary of the horizontally placed column. In the field, this boundary could represent an impermeable clay layer. However, if there is no such low permeability layer available, DNAPL can migrate downwards. This unwanted mobilization of DNAPL during surfactant remediation was shown by the tank experiment reported in Soga et al. (2002a). Figure 11 shows the remobilisation of DNAPL during surfactant remediation in a heterogeneous soil model. Before remediation, the spilled sources generated dissolved phase contaminants for a given ground water flow condition. The dissolved concentration was high at the top (24.2 to 37.3 mg/l at Point 1 in Fig. 11(b)) but very small concentrations were measured at the bottom half of the tank (0.1 to 0.3 mg/l at Points 3 and 4). After remediation, the concentrations at the top half decreased (17.6 to 18.5 mg/l at Point 1) but the concentrations at the bottom increased

Copyright © 2003 Swets & Zeitlinger B.V., Lisse, The Netherlands

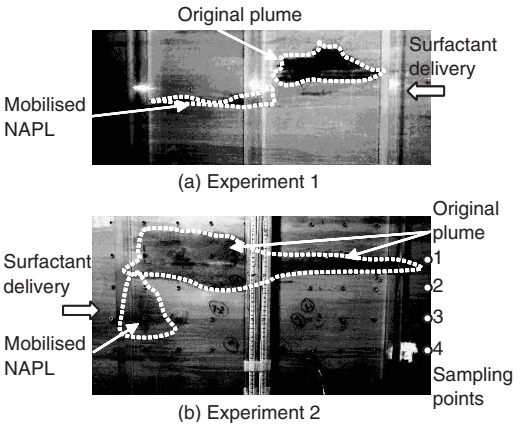


Figure 11. NAPL spreading during surfactant remediation.

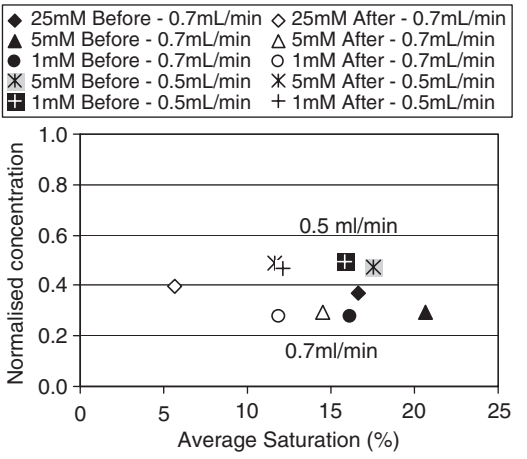


Figure 12. Steady state PCE concentration before and after chemical oxidation remediation.

dramatically (17.0 to 17.8 mg/l at Points 3 and 4) due to gradual dissolution of the mobilised DNAPL as shown in the figure. In this tank experiment, introduction of surfactant created a different end-point entrapment morphology (e.g. low saturation zones with increased relative water permeability), resulting in a greater NAPL-water contact area. This in turn generated concentrations that increase with time in previously uncontaminated area.

3.2.2 *Chemical oxidation*

In-situ chemical oxidation is based on the delivery of chemical oxidants to contaminated media, usually to convert the contaminants to innocuous products (Yan and Schwartz, 2000; Huang et al., 2001 and 2002; Nelson et al., 2001). For instance, injection of potassium permanganate ($KMnO_4$) into PCE contaminated subsurface facilitates the oxidation of PCE to chloride and carbon dioxide. The balanced oxidation-reduction reaction can be written as follow:

$$KMnO_4 + 3C_2Cl_4 + 4H_2O \rightarrow 6CO_2 + MnO_2^- + 4K^+ + 12Cl^- + 8H^+$$

Most environmental studies with permanganate have focused on the chemical oxidation of contaminated soil and groundwater without free-phase DNAPL present. Recently, the use of chemical oxidation on the degradation of contaminants when present as free phase NAPL in porous media has gained some attention.

In order to investigate the mass transfer behaviour after employing chemical oxidation remediation, a series of column experiments were conducted in a 30 cm long borosilicate glass column of 5 cm internal diameter packed with well-characterized sand (British Standard Fraction C). PCE was injected in the column from the bottom similar to the surfactant flushing column experiments described in the previous section. A typical residual PCE saturation achieved by this procedure was $S_{NAPL} = 17$–20%. The chemical oxidation experiments were then conducted by injecting 1, 5 or 25 mM $KMnO_4$ in 200 mM Na_2HPO_4 solutions at a flow rate of 2 ml/min. The buffer solution ($Na_2HPO_4 - pH9$) was necessary to reduce the effect of gas formation, which can be a detrimental process to porous media. The final removal efficiencies ranged between 25 and 65% after flushing 51 to 74 pore volumes of $KMnO_4$ solutions.

Steady state aqueous phase PCE concentrations were measured before and after chemical oxidation remediation. Figure 12 shows the normalised DNAPL aqueous concentrations (measured steady state concentrations at two different water flow rates (0.5 and 0.7 ml/min) divided by the maximum solubility) versus the average DNAPL saturation from the initial residual conditions down to removed conditions. A slower water flow rate gives higher PCE concentrations due to the rate-limited behaviour. The figure clearly shows that no significant reduction in the aqueous phase concentration was achieved after the chemical oxidation operation. Similar observations were made in the surfactant experiments shown in the previous section.

It is known that addition of chemical oxidants can cause the production of gases or precipitates that may reduce permeability or limit the delivery and mixing of the reagents (Schroth et al., 2001; Schnarr et al., 1998). A close examination of Fig. 12 indicates that a better removal efficiency was obtained when a higher $KMnO_4$ concentration was used. However, it was also found that more MnO_2 precipitated. Figure 13 shows the change in colour of the tested sand before and after

Copyright © 2003 Swets & Zeitlinger B.V., Lisse, The Netherlands

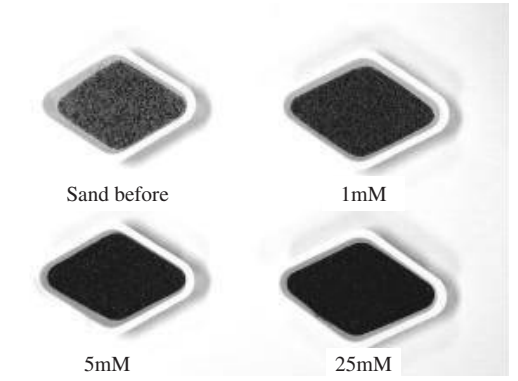


Figure 13. MnO_2 precipitations after chemical oxidation.

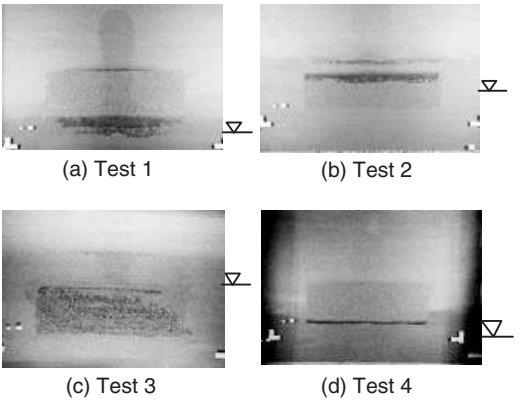


Figure 14. Different toluene entrapment conditions.

chemical oxidation. In fact, in one of the experiments that injected 25 mM $KMnO_4$ solution, the pores totally clogged and it became impossible to inject the oxidants into the column. For other columns, the decrease in porosity was estimated to be 10 and 18% for 1 and 5 mM $KMnO_4$, respectively, using a tracer technique.

In summary, the chemical oxidation experiments showed that the degree of NAPL removal achieved was not able to decrease the mass release rate after remediation. However, extensive pore clogging was obtained by the precipitation of MnO_2. MacKinnon and Thomson (2002) found from their soil tank experiment that the formation and deposition of MnO_2 precipitates decreased the mass transfer of PCE into the aqueous phase. This is because MnO_2 deposits within the model aquifer decreased the velocity of water directly above the PCE pool and hence the overall mass transfer from the remaining PCE pool. The implications of these findings are two-fold; MnO_2 precipitation may limit the process of pool oxidation, but also, from a positive perspective, it may inhibit the subsequent formation of a PCE plume.

3.2.3 *Air sparging*

Air sparging is perhaps one of the most popular techniques used for cleaning up subsurface contaminated with volatile organic compounds (VOCs) and chlorinated solvents. In air sparging operations, air is injected into or below contaminated aquifer. The injected air rises through saturated zone towards the unsaturated zone due to a buoyancy effect. As the air passes through either non-aqueous phase liquids (NAPLs) or contaminated ground water, VOCs are stripped into air channels where they are carried into the unsaturated zone. Once the contaminated air comes to the unsaturated zone, it is extracted using soil vapour extraction systems.

The nature and extent of the air pathways determines the region of influence of remedial processes. The efficiency depends on microscopic effects such as the mode of air flow (channels or bubbles) and air channel density as well as macroscopic effects such as the spatial distribution of air paths. Site geology or subsurface heterogeneity is considered to have significant influence on the efficiency of air sparging remediation. In the field, injected air is likely to travel in channels with irregular or asymmetric shapes because of the heterogeneous nature of the subsurface (Ji et al., 1993; Johnson et al., 1993; Hinchee et al., 1994; Ahlfeld et al., 1994).

Laboratory tank experiments were performed to evaluate NAPL removal performance under well-defined heterogeneous soil conditions (Waduge et al., 2003). The soil models had a coarser sand lens inside a finer sand matrix and four different toluene entrapment conditions were created by varying the location of the water table in the models as shown in Fig. 14. Air sparging was then performed to remove the entrapped toluene and the gas concentration at an extraction well was measured continuously to evaluate the efficiency of the system.

The air sparging operation in the experiments included several shut down periods of a fixed duration to observe the increase in vapour concentration when the operation restarted. The rebound in gas concentration at the extraction well before and after the shutdown period is plotted against the amount of toluene left inside the soil models as shown in Fig. 15. It was found that the amount of concentration rebound after 14 hours of shutdown period was proportional to the amount of toluene left in the system. For a given toluene volume, Test 3 gave the smallest rebound since most of the NAPL was entrapped below the water table, whereas Test 1 had the largest rebound because the majority of the NAPL was left in the unsaturated zone. Extrapolation of the trend lines shows that the rebound will be negligible when NAPL of about 100 g is left in the sand lens. On the other hand, in Test 1, a much larger removal of NAPL was necessary to achieve the

Copyright © 2003 Swets & Zeitlinger B.V., Lisse, The Netherlands

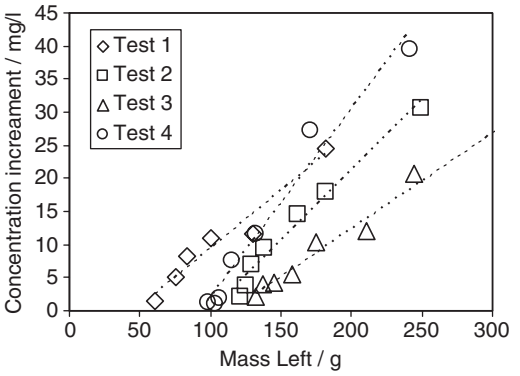


Figure 15. Increase in gas concentration after shutting periods versus toluene mass left in the tanks.

same condition. The results indicate the importance of NAPL entrapment condition on the mass transfer behaviour during and after remediation.

3.3 *Numerical investigation of mass transfer from source zone*

Meaningful risk assessment and cost/benefit analyses are not possible without an understanding of uncertainty. Evaluating the uncertainty in model predictions is particularly essential in the risk assessment associated in post-treatment source zone mass flux reduction. Thus, there is a need for developing tools and methodologies that can quantify and reduce the uncertainty associated with parameter estimation and model predictions.

NAPL dissolution is primarily controlled by the source zone contaminant distribution or entrapment morphology, which in turn is directly related to the aquifer heterogeneity (Sale and McWhorter, 2001; Brusseau et al., 2002). The macro-scale distribution of NAPL defines the overall geometry of the source zone and is an important determinant of the total mass/volume of NAPL that is present. The local distribution of NAPL is equally important because NAPL present in subregions of fine-grained material is less accessible to remediation agents than that present in subregions of coarse material. Consequently, any potential down gradient risks should be correlated with source zone heterogeneity.

To investigate the above issue, a series of numerical simulations were performed to model typical DNAPL spill and dissolution behaviours for aquifers of variable heterogeneity. An 2D aquifer domain of 50 m long and 10 m deep was specified and a permeability field that can be described as a normal probability density function was applied (Soga et al., 2002; Page and Soga, 2003). Multiple spatially correlated random fields were generated using representative values of the

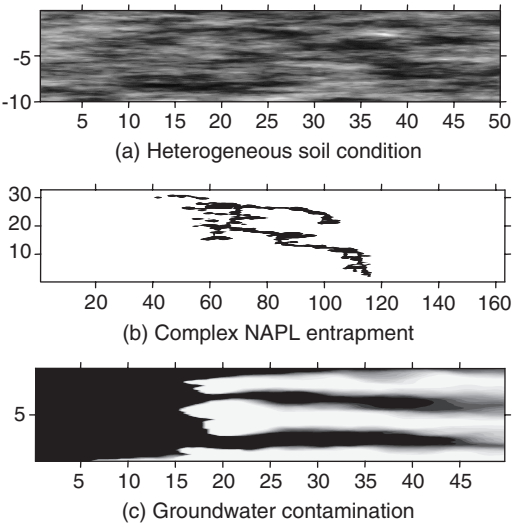


Figure 16. Example of numerical simulation results.

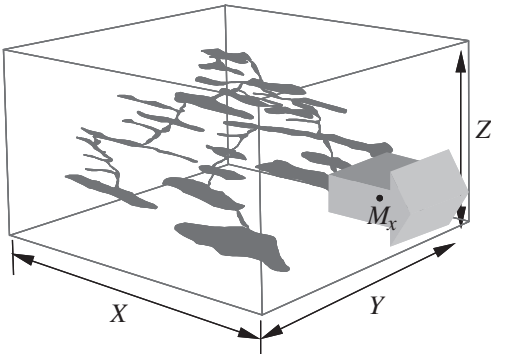


Figure 17. Mass outflux from a NAPL source zone.

mean and variance of the permeability field, as a well as a measure of the soil bed continuity in both horizontal and vertical directions.

For each realization, 500 litres of PCE was spilled over 100 days, followed by a 900 day period for redistribution. Dissolution of the DNAPL from each entrapment morphology was modelled over 3000 days at two different groundwater flow velocities. The dissolution was modeled as a rate-limited. The permeability fields, PCE entrapment morphologies and aqueous phase DNAPL concentrations after 2000 days of dissolution for one of the aquifer realizations are presented in Fig. 16. The temporal total PCE mass leaving each source zone at the down gradient boundary (a product of the local aqueous concentration, cross-sectional area of flow and local Darcy velocity) was then recorded (see Fig. 17).

Copyright © 2003 Swets & Zeitlinger B.V., Lisse, The Netherlands

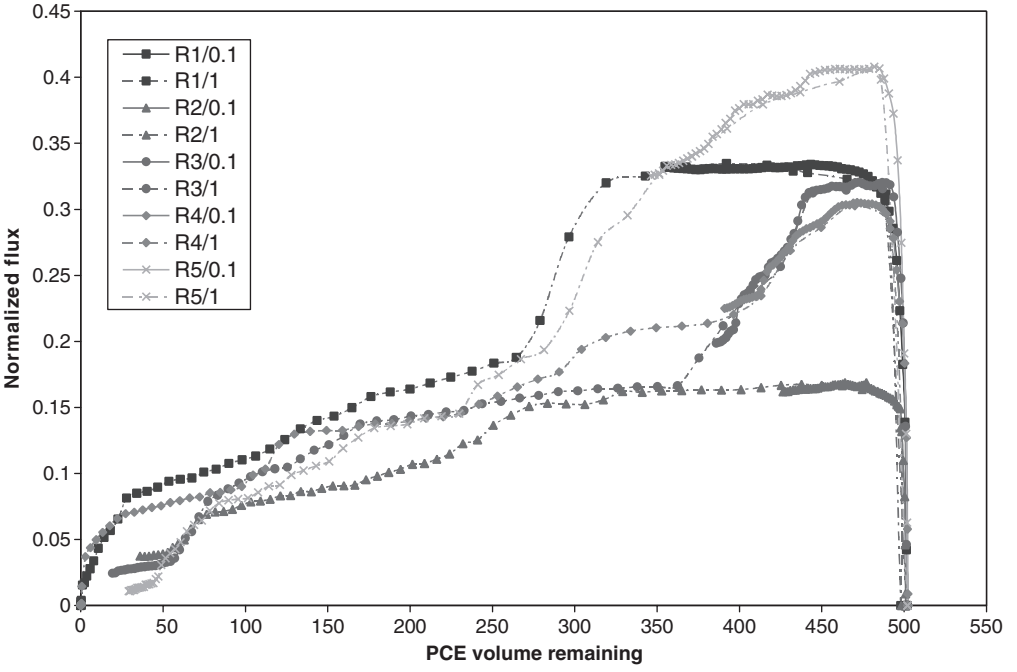


Figure 18. Normalised mass flux released from five different realizations.

The computed variations in PCE mass flux exiting each source zone are shown in Fig. 18. In the figure, the flux (normalized by the groundwater flow rate and aqueous PCE solubility limit) is plotted as a function of the volume of PCE remaining in the source zone aquifer domain. For each aquifer realization, the normalized dissolution profiles are independent of the groundwater flow velocity under which the mass transfer processes originally took place. Hence, for a given value of the mass transfer coefficient, the rate-limited behaviour at the numerical element level did not affect the mass release rate in the domain level.

The results in Fig. 18 show that the dissolution profiles are very different for each realization. Despite all realizations being characterized by the same stochastic parameters, considerable variation exists between each profile. This is particularly true for the early stages of dissolution. Consequently, it is clear that the aquifer heterogeneity is very important factors for influencing and/or controlling the rates of DNAPL mass transfer and subsequent removal of PCE from each source zone.

A closer examination of Fig. 18 indicates that the temporal mass flux variations for each aquifer domain all display a step-like pattern consisting of an initially high and relatively constant rate of dissolution, followed by one or more periods of rapid flux decrease for a very small reduction in PCE volume. The first of these rapid drops in the normalized mass flux represents the stage during dissolution when most, if not all of the residual, low saturation DNAPL has been removed. With only higher saturation and pooled contaminant remaining, subsequent dissolution is limited with mass transfer only serving to decrease the length of higher saturation morphologies. Pools will therefore be removed at different rates and times, and this is responsible for the "multiple" step-like dissolution profiles of some aquifer domains.

In terms of defining a remediation target, if source zone remediation was to be implemented in aquifer realization two and 50% PCE volume reduction was achieved, the resulting mass flux would not be significantly different to the pre-remediation value. For realization five, on the other hand, the same remediation efficiency could result in at least a 50% reduction in mass out flux.

The considerable spread between data from each realisation and its non-linear trend is not of great value for field application. Attention is then focused on a more detailed investigation of the causes of this variation. A number of studies investigating DNAPL dissolution have shown that it is the leading edge of the contaminant where most of the mass transfer occurs (Sale and McWhorter, 2001). This is very important for pooled NAPL because during the early stages of dissolution, the rate of mass transfer will decrease

Copyright © 2003 Swets & Zeitlinger B.V., Lisse, The Netherlands

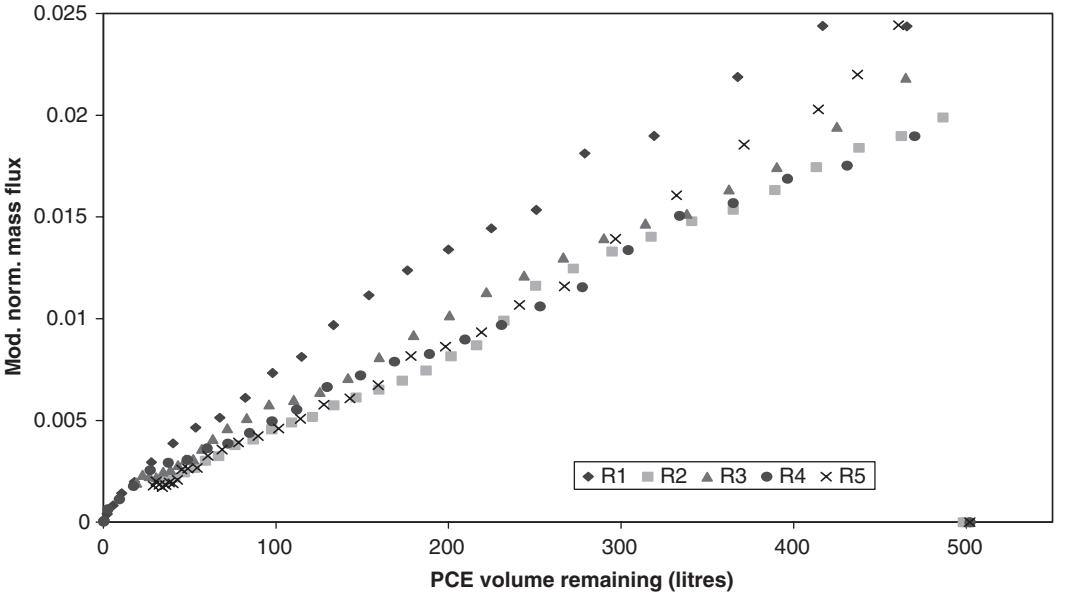


Figure 19. Modified, normalised mass flux as a function of DNAPL volume remaining in the source zone.

along the length of the pool due to flow bypass, but at later stages with reduced length and low NAPL saturation, the relative transfer rate becomes high. Hence, the distribution of the DNAPL with respect to the groundwater flow direction appears to be very important.

In this study, the X and Z dimensions of the entrapped DNAPL computed in each simulation shown in Fig. 17 were used to calculate the total volume of the contaminated aquifer region and to estimate "effective DNAPL saturation" perpendicular to the groundwater flow direction (Page and Soga, 2003). The normalised mass flux values are then divided by the "effective saturation" value and these modified values are plotted in Fig. 19. It is evident from this figure that, by considering the spatial variations in the PCE distribution, the modified normalized source zone dissolution behaviours fall within a band of data that displays a linear trend for all realizations. In effect, a large amount of uncertainty that arises during field-scale studies can be eliminated if the spatial distribution of NAPL source is evaluated. A relationship such as DNAPL volume versus modified normalized mass flux in Fig. 19 can then be used to assess remediation success and evaluate natural attenuation efficiency, even when the fine and detailed aquifer permeability variations and soil distributions are unknown. It is possible that subsurface condition with different stochastic parameters gives a different linear trend, which is currently under investigation.

4 CONCLUDING REMARKS

Under the pressure of infrastructure development at brownfield sites, there is increasing regulatory and public pressure to remediate source zones of NAPL contaminated sites. Although recent development of source-zone treatment technologies shows that source removal is possible, the efficiencies in the field condition are still limited due to significant uncertainties about the value of source zone remediation. That is, we do not know how well they will work and how they can be optimised. There is a need to define appropriate methods that can measure or define the "success" of such efforts (i.e. performance assessment).

This paper addresses the need for quantifying the mass flux coming out from the "remediated" or "treated" source zone for accurate risk calculation and long-term performance assessment. Accurate assessment of risk and appropriate corrective action requires site-specific identification of applicable risk factors. Some experimental data and numerical simulation results have been used to show that the uncertainties comes from site heterogeneity and its accompanying complex NAPL entrapment condition as well as from the physical and chemical changes during remediation operations.

The design and assessment of source zone removal technologies should focus on the ability of a specific technology to reduce NAPL saturation to a condition suitable for the mass flux observed down-stream of

Copyright © 2003 Swets & Zeitlinger B.V., Lisse, The Netherlands

the entrapment zone to meet an acceptable value. It is important to note that this value does not refer to a specific value of NAPL saturation, but a site-specific effective saturation defined by the state of the NAPL (controlled by the in-situ conditions), and the entrapment morphology (determined by the site heterogeneity and spill condition).

ACKNOWLEDGEMENT

The authors thank Professor T.H. Illanagasekare of the Colorado School of Mines for his useful comments made in relation to the discussion described in this paper.

REFERENCES

Ahlfeld, D., Dahmani, A. & Ji, W. 1994. A conceptual model of field behavior of air spargin and its implications for application, *Ground Water Monit. Rem.*, Fall, 132–139.

Annable, M.D., Hirasaki, G.J., Jackson, R.E., Jawitz, J.W., Jin, M., Lawson, J.B., Londergan, J., Meinardus, H., Miller, C.A., Pope, G.A., Rao, P.S.C., Rhue, R.D., Simpkin, T.J., Szafranski, R. & Tanzil, D. 2000. *NAPL removal: surfactants, foams and microemulsions.* Boca Raton: Lewis.

Brusseau, M.L., Zhang, Z., Nelson, N.T., Cain, R.B., Tick, G.R. & Oostrom, M. 2002. Dissolution of nonuniformly distributed immiscible liquid: intermediate-scale experiments and mathematical modelling. *Environ. Sci. Technol.*, 36, 1033–1041.

Coumoulos, H., Soga, K. & Illangasekare, T.H. 2000. 1g and centrifuge tests on DNAPL migration in saturated porous media with inclined layers – modelling techniques, *Proc. Of International Symposium on Physical Modelling and Testing in Environmental Geotechnics*, La Baule, 301–308.

Domenico, P.A. & Schwartz, F.W. 1990. *Physical and Chemical Hydrology*, John Wiley and Sons.

Fountain, J.C., Klimek, A., Beikirch, M.G. & Middleton, T.M. 1991. The Use of Surfactants for Insitu Extraction of Organic Pollutants from a Contaminated Aquifer, *Journal of Hazadeous Material*, 28, 295–311.

Hinchee, R.E. 1994. Air sparging state of the art, *Air sparging for site remediation*, (Hinchee, R.E. (ed.), Lewis, 1–12.

Huang, K.C., Hoag, G.E., Chheda, P., Woody, B.A. & Dobbs, G.M. 2001. Oxidation of chlorinated ethenes by potassium permanganate: a kinetics study, *Journal of Hazardous Materials*, B87, 155–169.

Huang, K.C., Hoag, G.E., Chheda, P., Woody, B.A. & Dobbs, G.M. 2002. Kinetics and mechanism of oxidation of tetrachloroethylene with permanganate. *Chemosphere*, 46, 815–825.

Illangasekare, T.H., Yates, D.N. & Armbruster, E.J. 1995. Effect of heterogeneity on transport and entrapment of nonaqueous phase waste products in aquifers: an experimental study, *ASCE Journal of Environmental Engineering*, 121(8), 571–579.

Ji, W., Ahlfeld, A., Lin, D.P. & Hill, E. 1993. Laboratory study of air sparging: air flow visualization, *Ground Water Monit. Rem.*, 13(4), 115–127.

Johnson R.L. & Pankow, J.F. 1992. Dissolution of dense chlorinated solvents into groundwater. 2. Source functions for pools of solvents. *Environ. Sci. Technol.*, 26(5), 896–901.

Johnson, R., Johnson, P., McWhorter, D., Hinchee, R. & Goodman, I. 1993. An overview of in situ air sparging, *Ground Water Monit. Rem.*, 13(4), 127–134.

Keuper, B.H. & Frind, E.O. 1991. Two-phase flow and heterogeneous porous media, 1. model development, *Water Resources Research*, 27, 1049–1057.

Kulasooriya, I.H., Soga, K., Dai, D. & Illangasekare, T.H. 2002. Effect of flow direction on surfactant enhanced remediation of DNAPL, *Proceedings of 4th International Congress on Environmental Geotechnics*, de Mello and Almeida (Eds.), 2, 829–834.

MacKinnon, L.K. & Thomson, N.R. 2002. Laboratory-scale in situ chemical oxidation of a perchloroethylene pool using permanganate, *Journal of Contaminant Hydrology*, 56, 49–74.

National Research Council 1999. *Research needs in subsurface*, National Academy Press.

Nelson, M.D., Parker, B.L., Al, T.A., Cherry, J.A. & Loomer, D. 2001. Geochemical reactions resulting from in situ oxidation of PCE-DNAPL by KMnO4 in sandy aquifer. *Environmental Science and Technology*, 35, 1266–1275.

Noureldin, N.A., Zhao, D. & Lee, D.G. 1997. Heterogeneous permanganate oxidations. 7. The oxidation of aliphatic side chains, *Journal of Organic Chemistry*, 62, 8767–8772.

Page, J.W.E. & Soga, K. 2003. The effect of heterogeneity DNAPL contaminant mass flux rate and its relation to remediation clean-up level, *Proceedings of IS*-Okayama.

Pennell, K.D., Jin, M., Abriola, L.M. & Pope, G.A. 1994. Surfactant-enhanced remediation of soil columns contaminated by residual tetrachloroethylene, *Journal of Contaminated Hydrology*, 16, 35–53.

Sale, T.C. & McWhorter, D.B. 2001. Steady state mass transfer from single-component dense nonaqueous phase liquids in uniform flow fields, *Water Resources Research*, 37(2), 393–404.

Schroth, M.H., Oostrom, M., Wietsma, T.W. & Istok, J.D. 2001. In-situ oxidation of trichloroethene by permanganate: effects on porous medium hydraulic properties. *Journal of Contaminant Hydrology*, 50, 79–98.

Schwille, F. 1998. *Dense chlorinated solvents in porous and fractured media: model experiments*, Translated from German by J.J. Pankow, Lewis Publishers.

Shnarr, M., Truax, C., Farquhar, G., Hood, E., Gonullu, T. & Stickney, B. 1998. Laboratory and controlled field experiments using potassium permanganate to remediate trichloroethylene and perchloroethylene DNAPL in porous media. *Journal of Contaminant Hydrology*, 29, 205–224.

Soga, K., Kulasooriya, I.H., Waduge, W.A.P., Illangasekare, T.H. & Dai, D. 2002a. Surfactant remediation of DNAPL – column and tank experiments, *Environmental Geomechanics*, Vulleit, L., Laloui, L. and Schrefler, B. (eds.), EPFL Press, Monte Verita, 361–366.

Soga, K., Page, J. & Gowers, N. 2002b. NAPL source zone remediation-mass flux approach, *Proceedings of the 4th*

Copyright © 2003 Swets & Zeitlinger B.V., Lisse, The Netherlands

International Congress on Environmental Geotechnics, de Mello and Almeida (Eds.), 2, 1069–1081.
Soga, K., Page, J.W.E. & Illangasekare, T.H. 2003. A review of source zone remediation efficiency and the mass flux approach, submitted to the *Journal of Hazardous Materials*.
Yan, Y.E. & Schwartz, F.W. 2000. Kinetics and mechanisms for TCE oxidation by permanganate. *Environmental Science and Technology*, 34, 2535–2541.
Waduge, W.A.P., Soga, K. & Kawabata, J. 2003. Effect of LNAPL entrapment on air sparging efficiency, submitted to the *Journal of Hazardous Materials*.

Copyright © 2003 Swets & Zeitlinger B.V., Lisse, The Netherlands

Groundwater and geoenvironmental quality issues in the Langat Basin, Malaysia

M.R. Taha
Universiti Kebangsaan, Malaysia

ABSTRACT: The Langat basin is one of the most important areas in Malaysia. Just south of Kuala Lumpur, the capital city of Malaysia, the basin is a major source of water supply for the city. In addition, it hosts major national institutions of utmost importance. These include Putrajaya (the national administrative centre), the Kuala Lumpur International Airport (KLIA), Cyberjaya (the national multimedia centre) and a number of universities. These set-ups and the continuing overflow of development from Kuala Lumpur may potentially result in the emergence of environmental and social problems. A problem that warrants attention and solution is the gradual increase in water deficiency in the basin. In order to cope with the water deficit in the basin, the government is considering using groundwater as an alternative water source. In this regard, good groundwater management is needed to assure the sustainable utilization of this groundwater resource and minimal disturbance and modification of the hydrology of the basin ecosystem. Thus, monitoring of groundwater quality is important to ensure its supply is not contaminated and corrective measures can be taken if alarming levels of pollutants are detected. In this study it was found that the groundwater quality is generally good. However pollution threats are many as the basin continue to thrive in development. Main potential threats include the ever increasing generation of waste, "unengineered" landfill, and extensive industrial and agricultural activities. Thus in order for the basin to maintain groundwater and geoenvironmental quality for its sustainable development various precautionary measures are essential and proposed in this paper.

1 INTRODUCTION

In Malaysia, although groundwater has been used for domestic, municipal, industrial, and agricultural purposes, its use is still marginal compared to its availability. Numbers vary but most estimation led to only 5% total usage. Thus, its storage capacity of about 63 billion cubic metres (Abdul-Rahman 2001) remains largely untapped. This in addition to high quality (generally) raw water and its ease of availability have made groundwater a prime target to meet demands during "hard times". For example, during the water crisis in the Klang Valley (areas covering the capital city and its nearby urban areas) in 1998, groundwater was extracted in many places for domestic water supply. However, indiscriminate pumping of groundwater have caused a number of adverse effects such as settlement of ground, usage of contaminated groundwater, enhanced migration of contaminant plumes and salt water intrusion.

The Langat Basin, with its explosion in development could potentially have to rely on groundwater to meet it ever increasing demand. It must also be emphasized that the basin provided majority of water for the Klang Valley especially through the Langat and Semenyih Dam schemes. The Mid-term review of the Seventh Malaysia Plan 1996–2000 describes the necessity of sustainable development of groundwater as an alternative source in case of emergency. Therefore ensuring groundwater quality and quantity can be considered important priorities for maintaining sustainability in the basin. The work described in this paper deals with some groundwater (and geoenvironmental) quality issues in the Langat basin, Malaysia. The basin is important as it represents the backbone of the country's development of recent times. It hosts many important national set-ups such as Putrajaya (the national administrative centre), the Kuala Lumpur International Airport (KLIA) in Sepang, Cyberjaya (the national multimedia centre) and a number of universities. Thus keeping the basin healthy for sustainable development presents a challenge that affects the whole of Malaysia. The study described in this paper is part of an on-going research project entitled Ecosystem Health of the Langat Basin: An Intergrated Approach for Environmental Management (Hasan 2000, and Mokhtar 2001).

Copyright © 2003 Swets & Zeitlinger B.V., Lisse, The Netherlands

2 THE LANGAT BASIN PROFILE

2.1 *General*

The Langat Basin is located in the West of Peninsular Malaysia in the state of Selangor (Figure 1). It lies adjacent and to the south of the Klang Valley, the most highly developed urban conurbation in Malaysia, where Kuala Lumpur, the nation's capital is located. The districts that made up the basin include Hulu Langat, Sepang, Kuala Langat and Seremban). The heart of the basin was the Langat river system (and the Semenyih River, its main tributary), which flows from the middle of mountain range to the coast of the state of Selangor. The total land area of the basin is estimated about 2937 km^2 with an annual rainfall of approximately between 1,500 and 2,700 mm. The highest point is Gunung (mount) Nuang at 1495 m above sea level located near the northeast tip of the basin bordering the state of Pahang.

Government policies and plans, since the Third Malaysia Plan (RMK3) which started in 1975 had promoted rapid development of infrastructure in the Basin (Ahmad Fariz Mohamed and Jamaluddin Jahi 2000). Extensive infrastructures that have been and will be developed are providing catalyst for economic development in the Basin. These have accelerated economic development in the Basin. Equipped with Government policies and strategies, economic activities in the basin have grown at a rapid pace. These developments spur an influx of commerce and industry into the basin that will in turn induce changes in its demography, landscape and ecology.

2.2 *Geology and geotechnics*

The simplified geology of the basin is shown in Figure 2. From the mountain area in the east-northeast region (about a third of the area), the bedrocks consisted of schist and phyllite, and granitic rock formation of Permian age dominates. The bedrocks near the middle of the basin, buried in the rolling hills are called the Kenny Hill and Kajang Hill Formation (both metasedimentary deposits) consisted of mainly shale and quartzite. In the low flatlands close to the coast, Quartenary layers are deposited on the bedrocks. These consist of a top peat layer (0.5–5.5 m thick), clayey deposits (40–50 m thick) and sand and gravel layers of several to 40 m thick (JICA and MGDM 2002). The aquifer in the sand and gravel layers (also known as the Simpang Formation) has been known and considered to have a great potential for groundwater development.

With regard to geotechnical and geoenvironmental applications, the granite residual soil of the basin

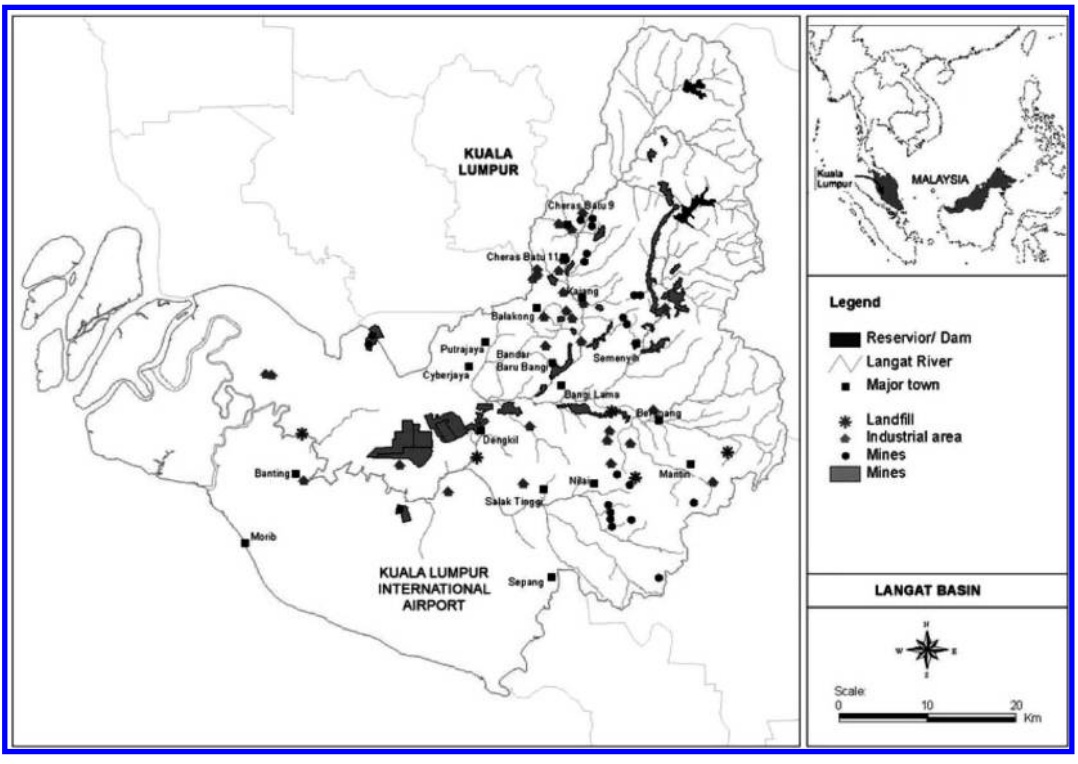


Figure 1. The Langat basin, state of Selangor, Malaysia.

Copyright © 2003 Swets & Zeitlinger B.V., Lisse, The Netherlands

have been much studied by the author and his co-workers. This is a result of many slope failures that have occurred in this formation throughout peninsular Malaysia. The most recent being the Hillview landslide of November 2002 in which 8 people were killed in the incident. This event gained extensive coverage in the local media because almost 10 years ago a landslide occurred nearby collapsing a massive condominium killing 48 people. In addition, the recent event totally demolishes the house of a former military chief of Malaysia killing his wife, a son, son and daughter-in-law, two grandchildren and two maids. Specifically, the soil (0.5 m from the surface) has 42% clay, 23% silt, and 35% sand. Its strength parameters reduced significantly to about 10% of its cohesion intercept and 50% its angle of internal friction when soaked (Taha et al. 1998). This was attributable to the lack of suction, less lubrication preventing slipping, and movement of soil particles. However, for clay liners, the granite residual soil is an excellent material complying with most recommended geotechnical characteristics (Taha et al. 2002), and good adsorption characteristics (Taha et al. 2003).

3 WATER DEMAND, SUPPLY AND QUALITY

Rapid development and high rates of population increase in Langat basin has resulted in the emergence of social problems, increase of water and air pollution and loss of natural habitat (Hasan 2000). Water pollution has become one of the main environmental problems in the basin and increased water deficiency can worsen the situation. Should urbanization and industrialization in the basin proceed in an uncontrolled manner, there will be an increasing pressure on the availability of raw water with adequate quality for extraction and processing.

In 1995 the estimated total demand for water in the Basin was 373 million litres per day (MLD) based on demands from the districts of Hulu Langat, Kuala Langat and Sepang. Demand was projected to increase to 583 MLD in the year 2000. The Basin currently produces approximately 1052 MLD however about 65% of water is transferred to supply the Klang Valley. Water transferred for use outside the Basin does not return to the basin's waterways. This affects river volume and flow rates as well as the hydrology of the basin. Such changes are also expected to affect the ecology of the basin.

River is the main source of raw water for water treatment plants in Malaysia. In late 1997 and early 1998, a water crisis occurred in many parts of Selangor including the Klang Valley due to severe drought. In addition, in October 1997, four water treatment plants were shutdown due to ammonia pollution and accidental spillage of diesel into the Langat River. These incidents polluted the water supply and the treatment

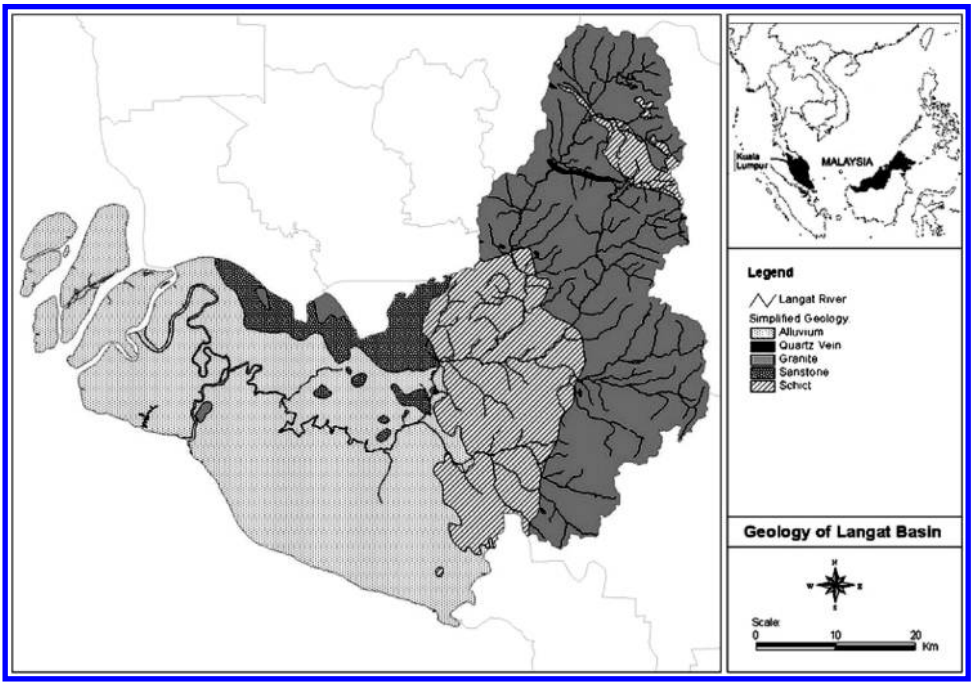


Figure 2. The general geology of the Langat basin.

Copyright © 2003 Swets & Zeitlinger B.V., Lisse, The Netherlands

plants were not capable of treating the polluted water immediately.

4 GROUNDWATER SUPPLY, DEMAND AND QUALITY

The importance of groundwater can be argued based of the following facts (Hasan 1997):

- streams and other surface water bodies are being polluted more and more;
- groundwater globally consists of about 91% of the liquid freshwater on earth;
- in many parts of the world, groundwater is often the only water available;
- it is stored in aquifers and is less susceptible to variation in supply, quality or to pollution;
- groundwater can be drawn on during dry periods when the surface waters are inadequate;
- groundwater development scheme is not so capital intensive as that of a large reservoir project; and
- groundwater scheme can be introduced gradually to keep pace with demand and a degree of flexibility is possible.

It was mentioned that in order to cope with the water deficit in the state of Selangor, groundwater is now being considered as a possible alternative water source. This alternative is highly justified by the facts mention at the beginning of this section and also due to opposition to the construction of new reservoir (and dams) as the water demand increases. Indeed, particularly in the Langat basin, some factories have already started shifting their industrial water source from surface water to groundwater. Uncontrolled use of groundwater however can induce serious environmental problems, e.g. land subsidence, saltwater intrusion to the aquifer, and desiccation of freshwater and peat swamps due to declining groundwater levels. In addition, in the state of Selangor, groundwater pollution caused by discharge from mining, factories and solid waste disposal sites has been reported in some areas (Nasiman and Mohd Nazan 1997).

A total of 121 wells were reviewed focusing on their usage and distribution (Figure 3). The total rate of water extracted in the Langat basin in 1999 from the ground was estimated at 25.07 million m^3/year. Industrial activity utilized 12.13 million m^3/year of groundwater followed by domestic activity. Although the rates between industry and domestic usage did not show much difference, the number of factories which used groundwater were smaller (15 wells) than domestic (56 wells). Table 1 shows usage of groundwater for each activity within each district in Langat basin.

Data reviewed show that the highest rate of water extracted from ground was in Kuala Langat district (close to the coastal region) with an estimated amount of 2,506.19 m^3/hour (60,148.56 m^3/day).This is followed by Hulu Langat and Sepang districts (Figure 4). The figure for Kuala Langat District was boosted by the occurrence of an excellent groundwater aquifer near Olak Lempit. The aquifer (in the aforementioned Simpang Formation) is located in the coastal lowlands and in the inland valley floor of major rivers. It has a proven potential as a groundwater resource in the basin. Currently the aquifer is being heavily tapped (for free) for industrial use by a factory in the district. Since the government does not restrict the development and usage of groundwater, private companies

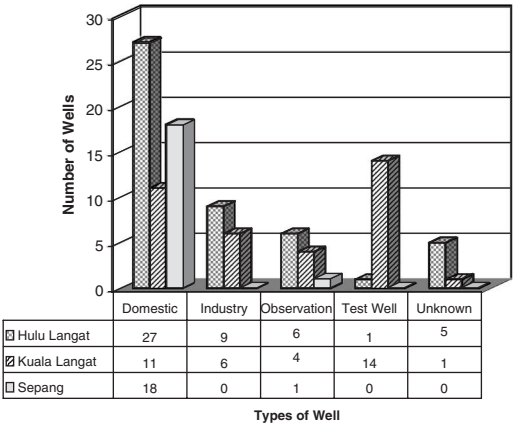


Figure 3. Type of well in Langat basin. (Source: JICA and MGDM 2002.)

Table 1. Usage of groundwater in Langat basin. (Source: JICA and MGDM 2002.)

	Usage (million m^3/year)					
District	Domestic	Industry	Observation	Test well	Unknown	Total
Hulu Langat	0.96	1.09	0	0	0.16	**2.21**
Kuala Langat	9.88	11.04	0.95	0.08	0	**21.95**
Sepang	0.91	0	0	0	0	**0.91**
Seremban	N.A	N.A	N.A	N.A	N.A	**N.A**
Total	**11.75**	**12.13**	**0.95**	**0.08**	**0.16**	**25.07**

Copyright © 2003 Swets & Zeitlinger B.V., Lisse, The Netherlands

continue to operate in an economic manner. As long as the cost of groundwater development is lower than using regular means of water supply, this practice will continue until the state formulate its comprehensive groundwater legislation.

5 IN SITU MEASUREMENTS OF SELECTED WATER QUALITY PARAMETERS OF OPEN WELLS

The water quality of a number of wells were measured for two different days in one in July and the other in August 2000. A few days of rain occurred subsequent to the week of the second round of sampling, and hence noticeable increase in depth of water column were observed in a majority of wells. In all, twelve open wells and 11 tube wells were studied in which some fundamentals groundwater quality parameters were measured in situ. The water quality parameters that were measured include temperature (°C), dissolved oxygen (mg/l), water depth (m from surface), conductivity (mS/cm), pH, redox potential (mV), oxygen saturation (%), and salinity (‰). Readings were recorded using the Hydrolab Surveyor 3 portable multisensor probe at three depth levels for deep water columns and only two or one for shallower ones.

When the average values of parameters over all depth levels at all the wells on both dates were compared, it was observed that (i) the temperature is almost similar on both dates, i.e. within the 25.10 to 29.32°C range; (ii) on the whole the DO values were apparently higher on 7/8/00 than 16/7/00 at most wells, probably due to fresher input of rain water within the week prior to the second date of measurement; (iii) the conductivity values is about the same at all wells for the two dates of measurement, i.e. within the 0.189 to 0.414 mS/cm range, and the maximum reading was observed at Kampung Salak Tinggi; (iv) average values of pH were also about the same for both dates at all wells, ranging from 6.81 to 9.94, (v) redox values were also very similar on both dates at almost all the wells, ranging from 222 to 494 mV, indicating oxidized waters; (vi) oxygen saturation values were higher on 7/8/00 than 16/7/00 at most wells, and the profiles for oxygen saturation and DO were similar; (vii) salinity values were very similar on both dates at all wells, all values within the narrow range of 0.1 to 0.30 ‰, indicating presence of fresh water only without salt contamination.

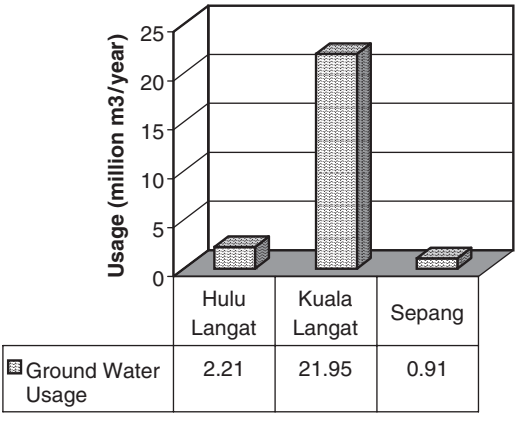


Figure 4. Rate of groundwater usage in each district within the Langat basin. (Source: JICA and MGDM 2002.)

6 IN SITU MEASUREMENTS OF SELECTED WATER QUALITY PARAMETERS OF MGDM TUBE WELLS IN LANGAT BASIN

The same in situ water quality parameter measurements as the ones in open wells were carried out on samples of the Mineral and Geosciences Department of Malaysia (MGDM) tube wells in the Langat basin. It consisted of tubes which were buried into the ground with a diameter which are smaller than the diameter of the Hydrolab Multiprobe. Thus water samples were pumped up into a bucket for water quality measurements. The rate of pumping into the bucket was about 110 liters per minute. At all wells, the first ten minutes of water pumped was discarded, and the water collected over minutes 10, 15 and 20 (up to 25 for some) were tested using the Hydrolab Surveyor.

Two sets of measurements were carried out on these tube wells, the first on 9/8/00, and the second on 15/8/00. On 9/8/00 the water temperature ranged from 27.39°C to 29.48°C. The shallowest well was 1.3 m deep and the deepest was 50.5 m. Dissolved oxygen was a minimum 0.28 mg/l and maximum at 8.91 mg/l. Oxygen saturation was a minimum 3.2% and maximum at 63.3%, this seems to be in line with observations of the DO values. Conductivity ranged from 0.273 mS/cm to 15.0 mS/cm, with ten of the wells having conductivity values of less than 4.0 mS/cm. Salinity values were between 0.1‰ to 8.7‰. It is evident as expected that values for salinity and conductivity are very much related. Values for pH ranged from 5.61 to 9.76. Redox potentials for the well waters ranged from −65 mV to 306 mV.

Generally the values of all the parameters for the tube wells were about similar to values of the open wells, with exceptions as explained above. The tube wells are definitely deeper and narrower than the open wells. The range of values for the different types of wells do overlap with one another, hence the conclusions that the water characteristics of well waters in Langat basin, be it open or tube, are indicative of fairly good quality water based on these specific parameters.

Copyright © 2003 Swets & Zeitlinger B.V., Lisse, The Netherlands

7 CHEMICAL ANALYSIS OF GROUNDWATER QUALITY (JICA AND MGDM 2002)

In their comprehensive report, JICA and MGDM (2002) found that the total iron values mostly ranged between 1 to 10 mg/l and these exceeded the mandatory level of iron values specified in the Malaysian National Drinking Water Guidelines, i.e. 0.3 mg/l. This is possibly due to the nature of the soils particularly in residual soils formation. Its yellowish to red in color depicts the presence of ferrous and ferric irons in the soil.

The levels of arsenic, mercury, and chromium in some wells were also found higher than the standards. Three possible reasons of high arsenic levels can be identified, i.e. breakdown of pyrites and arsenopyrites in the soil, contribution from graveyards as formaldehyde is frequently used to replace blood in order to preserve the freshness of the dead, and from pesticides and herbicides. Mercury contamination can be traced back to left over from tin mines in which many tin mines areas were also similarly contaminated. Another possibility may be associated with fertilizer input. The excess chromium may be associated with industrial activities (waste disposal) and also related to soil chemical properties.

Only one sample out of 86 samples showed lead value above the standard while copper and zinc values do not exceed the standards at any wells (and surface water samples). Six organic compounds were detected in four wells. They were m-, p-, and o-xylenes, 1,2,4-trimethybenzene, napthalene, and 2-methylnapthelene. In terms of toxicity and carcinogenicity (requirements for standard) it must not be detected in drinking water. The detected compounds are commonly used in industries. However, they are not detected near any known industrial estates.

8 LAWS AND REGULATIONS

In Malaysia as a whole, water maters belongs to the state. Thus, the state of Selangor governs the issue of water in the Langat basin. The state of Selangor had established a body called the Selangor Water Management Authority (Lembaga Urus Air Selangor, LUAS) recently in 1999 through an enactment. This enactment specifically stated that this authority will provide the management and protection of river basins, water bodies, groundwater, coastal waters and wetlands, and for the sustainable development of water sources. However, specific law on groundwater is still not consolidated into a single comprehensive legislation. In addition to provisions in LUAS enactment on groundwater, there are also provisions in the Geological Survey Act. MGDM is the technical department responsible for groundwater in Malaysia. Its responsibility is to advise the federal and state government agencies on matters relating to policies and technical matters relating to minerals and geoscience (JICA and MGDM 2002).

The Dept. of Environment Malaysia (DOE) has power over many environmental issues. However with regard to groundwater, they have none. Still they are also in the position to advise any agencies over environmental quality in Malaysia. They also conduct routine groundwater monitoring throughout Malaysia since 1997 targeting at areas potentially vulnerable to contamination and area high in groundwater utilization.

Water treatment and supply is generally the duties of the Selangor Waterworks Department (Jabatan Bekalan Air Selangor, JBAS) which has now renamed itself as Selangor Water Management Corporation (Perbadanan Urus Air Selangor, PUAS). In some other states, the Waterworks Department ocasionally uses groundwater to meet demands, but in the Langat basin, no information is available. In any case, there are many departments involved in groundwater issues in the basin. Its timely that specific legislation for groundwater is developed to ensure groundwater supply and quality is not jeopardized.

9 INDICATORS OF GROUNDWATER POLLUTION AND THREATS TO THE GEOENVIRONMENT

Nasiman and Mohd Nazan (1997) reported on the alluvial aquifer in Selangor (near Kuala Langat) and the threats on the water resource. Their report was very relevant to groundwater resource as a whole. As previously mentioned, the alluvial aquifer has a high potential yield for fresh groundwater. Groundwater from the alluvial aquifer is suitable for use as a source of drinking water and for industrial uses. However, development in Selangor is threatening the quality of the groundwater. For example, tin mining, followed by sand mining from the alluvial deposits, could cause reduction in the aquifer yield through introduction of slime and clay particles into the aquifer. The use of mining lands and lakes as waste disposal grounds have introduced pollutants such as waste organics and toxic chemicals into the aquifer. Other sources or indicators of pollution which are threatening particularly groundwater in particular and the geoenvironment in general are described below.

9.1 *Waste generation*

It goes that the more waste generated, the more it threats the groundwater and the geoenvironment. Solid waste production in the Langat Basin for 1994 estimated at 345 tons per day with average percapita of 0.74 kg/head/day and out of this, industry contribute 53.29 ton per day of solid waste (Hasan et. al., 1998).

Copyright © 2003 Swets & Zeitlinger B.V., Lisse, The Netherlands

Table 2. Estimated total waste with time.

Year	Total amount of waste (tons/day)
2000	428
2005	514
2010	600
2015	686
2020	772

Table 3. Life-span of "unengineered" landfills in the Langat basin (modified from Hasan 1998).

"Unengineeered" landfills	Life-span (years)
Sg. Sedu (Kuala Langat)	10
Broga (Hulu Langat)	3
Ampar Tenang (Sepang)	6
Pajam (Seremban)	30
Sg. Kembong (Hulu Langat)	2

The amount of waste produced is expected to increased every year with average rate of 4% per year. The estimated total waste that would be generated in the basin with time is given in Table 2. Projections to the year 2020 is significant since the government has set a target for Malaysia to become a develop nation by then.

The numbers provided has included other contributors which are much more complicated to predict such as construction, shops, markets, institutional, landscaping and street sweeping. With respect to composition, in general waste characteristics depends on degree of affluence and urbanization of the served area. Organics forms a major composition followed by papers, plastics, metals, etc. Complete compositional data is unavailable since the relevant authorities could not provide them. Thus it is difficult to formulate new waste management plans and technologies. Accurate estimation of waste amount and its composition is essential to the design of resource recovery systems and waste minimization programs, estimation of life of landfills and evaluation of environmental impacts caused by certain types of wastes (Klee 1994). However, recycling activities in the basin is thriving albeit its full potential has not been capitalized yet. Main items sorted at collection and landfills (by collection staff and private parties) include papers, metals, and plastics. Rubber tires, batteries and used motor oils are also collected from shops and collection points. In addition to (eventually) reducing groundwater pollution, recycling serve to extend life of landfills, reduce usage and exploitation of raw materials, creation of new job opportunities and the development of new technologies (Hassan 1998).

9.2 *"Unengineered" landfills*

Although there is a landfill (engineered) just north of the basin, majority of waste as above mostly goes to 5 area "unengineered" landfill. Table 3 shows the landfills that is still in use and its life span. Most of these landfills are already close to its maximum capacity. However, there are no immediate plans to build other landfill sites to meet the demands although an incinerator construction is almost under way near Semenyih in the eastern border of the basin that the time of this writing.

Since the landfills are "unengineered" it pose major threats to the environment particularly groundwater. The domestic waste in Malaysia are also generally high with up to over 60% moisture content. This is due to high seasonal rainfall and eating habits (home cooking and food with gravies). Thus the amount of liquid flowing out of landfills is very high intensifying pollution.

Results from detailed investigation on surface water conducted near various landfills of similar type in the Kuala Lumpur area has revealed the following (Yusoff 1999)

- low water quality index (class III and IV)
- low dissolve oxygen, DO (0.29–6.5 mg/l, DO for with drinking water is about 8 mg/l)
- electrical conductivity high (139–7500 μmhos/cm, >1000 μmhos/cm indicating contaminated water).
- Turbidity high (6-401 Naphelometric Turbidity Unit [NTU], drinking water <5 NTU)
- High organic load, Chemical Oxygen Demand [COD] 26–201 mg/l compared to drinking water i.e. <10 mg/L, Biological Oxygen Demand [BOD] 16.5–39.4 mg/l compared to drinking water i.e. <1 mg/l).

The above results were complemented by Tan et al. (2002) who studied river water quality in the Linggi drainage basin (the southern border of the Langat basin). They concluded that 95% of rivers located nearby landfill sites are highly polluted with heavy metals and other related chemicals. Thus the rivers are not suitable for drinking and fishing activities.

It must be mentioned that in the Langat (and Linggi basins), water along the rivers are siphoned to treatment plants, and distributed to consumers to meet demands of the districts in and out of the basin. The above field measurements have shown that water drawn must be extensively treated before distributed to consumers. In some instances, the river water (as earlier mentioned) were too polluted to be treated thus the treatment plants were closed until the river water quality improves. These facts establish even further the importance of groundwater as streams and other surface water bodies are being continually polluted. It is thus crucial to maintain and preserve pristine nature of groundwater quality.

Copyright © 2003 Swets & Zeitlinger B.V., Lisse, The Netherlands

9.3 *Industrial activities*

Industrial and agricultural activities have been identified as the main pollution sources to groundwater in the Basin. These activities contribute towards non-point sources of pollution.

Industrial development activities in Langat Basin is intensive and predicted to continue to grow with time. This is not difficult to hypothesize since there are ever and overflowing of industrial and commercial activities from Kuala Lumpur and the on-going extensive development of Putrajaya and Cyberjaya. Currently, there are 30 industrial estates housing 337 factories located in the basin. Factories in the basin were engaged in 22 categories of industrial production, ranging from the manufacture of agricultural end-products to high-tech products such as consumer electronics (Mohamed and Jahi 2000). Electrical and electronic industries predominate followed by industries manufacturing industrial and engineering products, furniture, textiles and fabrics, and building materials and chemicals. Visits to various industries particularly to those of relatively medium to small scale industries revealed that in majority no or minimal waste management procedures are in place. For example, drums with chemicals were found to be abandoned in the backyards. Many are corroded and leaked into the ground and eventually to the groundwater. Abdul-Rahman (2000) found that groundwater quality at all nine industrial sites studied were more contaminated than those in other sites.

More control or monitoring of these industries are thus required to ensure industries maintain a proper standard of environmental system. In addition it must be highlighted that there are currently many regulations have to be met to open an industry. However, when one wishes to close his or her industry, they just need to shut them and move on, i.e. there is simply no requirement for closure.

9.4 *Agricultural activities*

In 1995 agriculture activities in the Langat Basin utilised an area of about 1735.83 km^2, which is about 60% of total land area of the Langat Basin (Agriculture Department 1995). The main activity for agriculture is dominated by oil palm plantation, followed by rubber, piggeries, poultry, aquaculture, cattle and orchards. According to PORLA (2000) there are 94 palm oil estates and 8543 small holders in the Basin. Agriculture activities have been known using various types of chemicals as pesticides and fertilizers (Singh *et al.* 1999). There are many types of pesticides being used and mainly to control weeds, insects, rats and other pests. However the amount and types of pollutants produced were unable to be determined exactly.

9.5 *Other contributing factors*

The quality of groundwater in the basin is also threatened by domestic wastewater and polluted stormwater discharges into mining pits or lakes, and rivers. Although new settlement or housing areas have sufficiently built oxidation ponds to cater domestic liquids waste, most old houses are by and large disposed of domestic wastewater into nearby streams. In addition individual liquid waste ponds with little or no lining and treatment system are also commonly available. This traditionally dig and dump facility are common worldwide and discharges directly into the ground. Natural attenuation is then expected to take over to solve the problem.

Underground gasoline tanks for road vehicle patrols can be a major source of groundwater pollution. Although it numbers about 100 in the basin and generally small in size, but when leak and couple with favorable geologic conditions, its influence area can significantly grow. There still no requirement to replace the tank anytime during its service life. Graveyards are also a threat if uncontrolled as arsenic poisoning have been detected around the world near cemetaries.

In order to meet demands, new housing areas are being developed in marginalized land. This may alter groundwater flow patterns, inject pollutants from construction sites, and drying-up some wells. Developments in highland areas are not without risk as uncontrolled flow of groundwater has been the main causes of many slope failures as earlier mentioned.

10 PRECAUTIONARY MEASURES

The need to maintain groundwater quality is essential for sustainable development of this basin. Once the groundwater or an aquifer is polluted, it is almost impossible to remediate them back to its original state. Although there are many well established techniques for cleanup, the procedures are mostly expensive, time consuming, no guarantee for success and unknown end result. This is particularly critical in the basin where remediation test results are not yet available and the soils are generally different from past experience.

Recognizing the importance of existing aquifers it is recommended that proper guidelines and mitigation measure be adopted order to protect the groundwater. This may include: (i) planning and construction of "engineered" waste disposal facilities, (ii) confinement and treatment of leachate from current "unengineered" landfills and factories, (iii) treatment of storm and other wastewaters to the level of quality acceptable for groundwater recharge, (iv) formulation of regulations on groundwater recharge, (v) maintaining former mining lands as groundwater recharge areas, hence keeping them as "green areas" without activities that may introduce pollutants, (vi) diversions of storm

Copyright © 2003 Swets & Zeitlinger B.V., Lisse, The Netherlands

water and other waters through conduits or surface drains that run directly into rivers to avoid discharging the wastewaters into lakes, (vii) regular monitoring of the lake water quality taking into consideration its biological and chemical properties, (viii) regular monitoring of groundwater quality and establishing pollution migration patterns from point-sources and non-point sources in the aquifer, (ix) making it a mandatory for industries to plan and strategize waste minimization and recycling programs, and (x) intensifying public education and promotion for good/clean environmental practices.

11 CONCLUSION

Groundwater in the Langat Basin is indeed an important resource which has yet to be exploited on a bigger scale so as to meet the ever increasing demand for water for various uses. The measurements conducted in this study showed that the groundwater quality is still generally good despite some elevated measurements of arsenic, mercury and chromium, and detection of toxic organics. However, sources of pollution are many and on the rise due to rapid development in the basin which threatens groundwater. These include mainly the ever increasing waste generation, "unengineered" landfill, extensive industrial and agricultural activities. Thus precautionary measures are essential in order to maintain groundwater and geoenvironmental quality in the Langat basin for its sustainable development.

ACKNOWLEDGEMENT

The author would like to acknowledge the members of the Institute of Environment and Development (LESTARI), Universiti Kebangsaan Malaysia for providing much of the resources for the publication of this material. In particular gratitude must go to Ahmad Fariz Mohamed, Shaharuddin Idrus, Sarah Aziz Abdul Ghani, and Lim Chiou Chuan. JICA and MGDM are also acknowledged for permission to extensively use their report.

REFERENCES

Abdul-Rahman, Z. 2001. Groundwater Quality Monitoring in Malaysia, *Brownfield 2001*, Institution of Engineers, Malaysia.

Agriculture Department 1995. *Landuse of Selangor and Negeri Sembilan*, Shah Alam.

Hasan, M.A. 1997. Groundwater resources: A neglected resource, *State of Environment in Malaysia*, Consumers Assoc. of Penang, Penang, Malaysia, pp. 146–153.

Hasan, M.H., Yusoff, M.K., Sulaiman, W.N.A., and dan Abdul-Rahman, R. 1998. Issues and Problems of Solid Waste Management in Malaysia in *National Review on Environmental Quality Management in Malaysia: Towards The Next Two Decades*. Hasan et al. Eds. Institute for Environment and Development (LESTARI), Universiti Kebangsaan Malaysia.

Hasan, M.N. (ed.). 2000. *Proceedings of the 1999 Langat Basin Research Symposium*, LESTARI, UKM Bangi, 271 p.

Hasan, M.N. 2000. Penyelidikan Ekosistem Lembangan Langat: Pendekatan Holistik Berlandas Konsep Kesihatan Ekosistem in *Proceedings of The 1999 Langat Basin Research Symposium. Mohd Nordin Hj. Hasan Ed*. Institute for Environment and Development, UKM, Bangi.

JICA and MDGM 2002. *The study on the Sustainable Groundwater Resources and Environmental Management for the Langat Basin in Malaysia*, Vol. 1–5, Japan International Cooperation Agency (JICA), Tokyo, and Minerals and Geoscience Department Malaysia, Kuala Lumpur.

Klee, A.J. 1994. *PROTOCOL: A Computerized Solid Waste Quantity and Composition Estimation System*, Engineering Laboratory, US Environmental Protection Agency (risk reduction), Ohio, Cincinnati.

Mohamed, A.F., and Jahi, J. 2000. Implication of Manufacturing Industries Within Langat Drainage Basin: Issues and Challenges. *Malaysian Journal of Environmental Management*, Vol. 1, pp. 143–161. Kuala Lumpur.

Mokhtar, M., Idrus, S., Mohamed, A.F., Shah, A.H.H., and Aziz, S.A.A.G. (ed.) 2001. *Proc. 2001 Langat Basin Research Symposium*, LESTARI, UKM Bangi, 374 p.

Nasiman, S. and Mohd Nazan, A., 1997. Alluvial Aquifer in Selangor: A Threatened Water Resource. *Journal of ENSEARCH*, 10(3/4), pp 195–201.

Palm Oil Registration and Licensing Authority (PORLA). 2000. *Palm Oil Plantation in Langat Basin*, Seremban.

Singh, G., Huan, L.K., Leng, T., and Kow, D.L. 1999. Oil Palm and The Environment. *Malaysian Oil Palm Grower's Council*, Kuala Lumpur.

Taha, M.R., Desa, H., and Kabir, H. 2002. The Use of Granite Residual Soil as a Material for Compacted Clay Liner, *World Engineering Congress (WEC 2002)*, Kuching, Univ. Putra Malaysia-Inst. Of Engineers Malaysia, pp. 264–268.

Taha, M.R., Hossain, M.K., Chik, Z., and Nayan, K.A.M. 1998. Geotechnical Behaviour of a Malaysian Residual Granite Soil, *Pertanika J. of Sci. and Technol*, 7(2), Univ. Putra Malaysia Press, Serdang, pp. 151–169.

Taha, M.R., Leng, T.O., Mohamad, A.B., and Kadhum, 2003. Batch Adsorption Tests of Phenols in Soils, *Bulletin of Engineering Geology and the Environment*, in print, Springer-Verlag, Berlin.

Tan, B.H., Jahi, J., Hassan, M.N., and Bidin, A.A. 2002. Impact of leachate from open dumping and municipal landfills on the environment-A perspective of policies in Linggi drainage basin. *Environmental Management: Ten Years after Rio*, Centre for Graduate Studies, Universiti Kebangsaan Malaysia, Bangi, pp. 82–89.

Yusof, M.K. 1999. Effects of solid waste landfill sites on surface water quality, Workshop on *Disposal of solid waste through sanitary landfill-Mechanisms, processes, potential, impacts, and post-closure management*, Universiti Putra Malaysia-Dept. of Environment, Malaysia, pp. 167–182.

Copyright © 2003 Swets & Zeitlinger B.V., Lisse, The Netherlands

Saline water intrusion into fresh groundwater aquifer at eastern area, Cheju Island, Korea

G.C. Jeong
Dept. of Earth & Environmental Sciences, Andong Nat'l Univ., Andong, Korea

S.A. Booh
Groundwater Research Lab., Rural Research Institute, Ansan, Korea

Y.S. Ko
Korea Water Resources Corporation, Daejeon, Korea

B.D. Ro
Korea Infrastructure Safety & Technology Corporation, Goyang, Korea

ABSTRACT: Based upon the groundwater level monitoring results for several years, the Cheju Island can be divided into four regions showing similar variation patterns of the groundwater table. The reason seawater is intruded more deeply into the inland direction in the East region can be summarized as follows; first, the groundwater level is declined by itself during the dry season and also by the excessive pumping due to the increasing water demand in the region; second, it has a favorable secondary geologic structure for the groundwater movement which is formed by the eruption of the Lath-Feldspar-Olivine-Basalt (FOB) of the low viscosity; third, the low permeable unconsolidated sediments (USF) underlying below 100 m in elevation can not effectively cut off the saltwater intrusion. These factors cause saltwater intrusion into the fresh groundwater aquifer and have influences on the saltwater intrusion into the deeper part of the inland.

1 INTRODUCTION

Many boreholes drilled for potable water and agriculture at the eastern part of the Cheju Island have been abandoned due to saline water intrusion. The contents of Cl^- ion more than 250 mg/l are distributed at very limited region at the northern and southern part of the island. However, the eastern area has many boreholes with saline water near the shoreline.

Rural Development Corporation (RDC) (1989) analyzed the reason that gentle and low level of groundwater table, geologic condition feasible for saline water intrusion and excessive pumping near the seashore area are the major reasons of saline water intrusion. Choi et al. (1991) also insisted the major reason as excessive pumping near the seashore. Yoon (1986) thought that salt in shellfish sandy layer is solved by rainfall, and then, intruded into subsurface. Koh (1997, 1992) reported that the saline water intrusion has been occurred by geologic strata such as alternation of fractured basalt layer and scoria layer. These geologic condition have induced saline water intrusion since the island have been formed.

Because most of water supply is dependent on groundwater in the island, saline water intrusion is very serious problem. In recent, north western area and south western area also have high concentration of saline in groundwater. This study analyzed the reason of saline water intrusion at eastern part of the island where the most serious damage is occurred.

2 REASON OF BRINE PHENOMENA

Reasons of brine phenomena can be chosen as (i) upward circulation of saline groundwater underlain by fresh water aquifer, (ii) destruction of aquifer by excessive pumping, (iii) distribution of high permeable geologic structures such as a cave or a lava tube dipping toward inland from seashore, (iv) dissolution of salt rock into an aquifer by rainfall or contact of salt rock to aquifer by an other reasons, (v) intrusion of Cl^- component from a fertilizer, (vi) CaCl or NaCl components from chemicals for snow removal in the winter season, (vii) spreading of chlorination in soil, leaking water from waste disposal sites.

Copyright © 2003 Swets & Zeitlinger B.V., Lisse, The Netherlands

According to the report of groundwater in the Cheju Island in 1971, well Dongbok W-001 at the eastern part of the island, had difference of salinity dependent on pumping. Elevation of the well was EL 28.95 m and depth of the borehole was 50 m, −21.05 m below the sea surface. Groundwater level was EL 13.04 m. Result of pumping test showed that the appropriate daily pumping amount was 1,230 m^3. Although pumping amount as 1,140 m^3 in a day showed salinity of 950 mg/l, the salinity was increased as much as 1,350 mg/l for the pumping amount as 1,230 m^3. The report conjectured that rise of mixed zone between brine and fresh water induced salt water intrusion due to the increase of pumping amount. Salinity data for other areas also revealed saline water intrusion into fresh water aquifer. The salinity was also detected from naturally erupted water before drilling.

Table 1 shows the comparison of TDS values from the boreholes bearing more than 100 mg/l in 1971. The numbers in parentheses are yearly mean value of Cl^-. Potential wells of salt water intrusion due to natural fluctuation of groundwater table are four boreholes such as W-011, W-019, W-015 and W-026.

3 CHANGES OF GROUNDWATER TABLE AT EACH AREA

3.1 *Area division*

Ministry of Agriculture and Forestry (MAF) (1971) divided the Cheju Island as six areas such as Cheju, West, Seoguipo, Namwon, East and High land. RDC (1985) also divided the island as four areas based on characteristics of geomorphology and geology which influences on budgets of water resources and their development. KOWACO (1993) determined four areas which are divided as sixteen sub areas considered with geomorphology, geology, groundwater table and contours. Koh (1997) divided the island on the basis of subsurface distribution of Seoguipo formation.

According to the MAF (1997), the areas are four such as North, East, South and West based on long term monitoring of groundwater table and its relationship to geology. Because of the areas, boundaries of the eastern area and the western area are moved westward from other studies. Son (1999) divided the island as four areas by co-kriging with groundwater table and elevation.

This study determined divides of groundwater as four areas on the basis of long term monitoring of groundwater level by RDC (Fig. 1). Koh et al. (1994) set Bugchon–Pyseon line (B–B′ in Fig. 1) revised from Gimyoung–Tosanri line (A–A′ in Fig. 1), because A–A′ line is similar to the absence line of Seoguipo formation. He designated the Bugchon–Pyoseon line as boundary between the eastern area and other areas. However, this study considered changing features of

Table 1. Monitoring wells showing saline water production from 1970 to 1971.

Area	Well number	Elevation (m)	Well depth (m)	Bottom elevation (m)	Water level (m)	Yield (m^3/D)	Distance From coast (m)	TDS(Cl^-) (ppm) '71	'93	'94	'95	'96	'97	Remarks
Eastern	W-011	28.95	50.0	−21.05	0.82	1,230	769	1,350	(39) 643	(178) 732	388		128	Monitoring well
	W-015	40.01	55.0	−14.99	1.16	1,230	1,841	187	(190) 290	(109) 419	388	(58) 404	(97) 349	Monitoring well
	W-019	38.50	45.5	−7.00	1.50	1,166	2,058	267						
	W-028	98.13	104.5	−6.37	12.88	838	5,201	250						
Western	W-022	19.14	34.0	−14.86	4.94	918	796	150						
Southern	W-026	18.42	27.5	−9.08	2.42	1,780	586	100						
	W-030	73.13	50.0	+23.13	38.13	450		150						Abandoned well
Northern	W-013	65.13	72.0	−6.87	13.04	812	1,527	150					(28) 267	Monitoring well

Copyright © 2003 Swets & Zeitlinger B.V., Lisse, The Netherlands

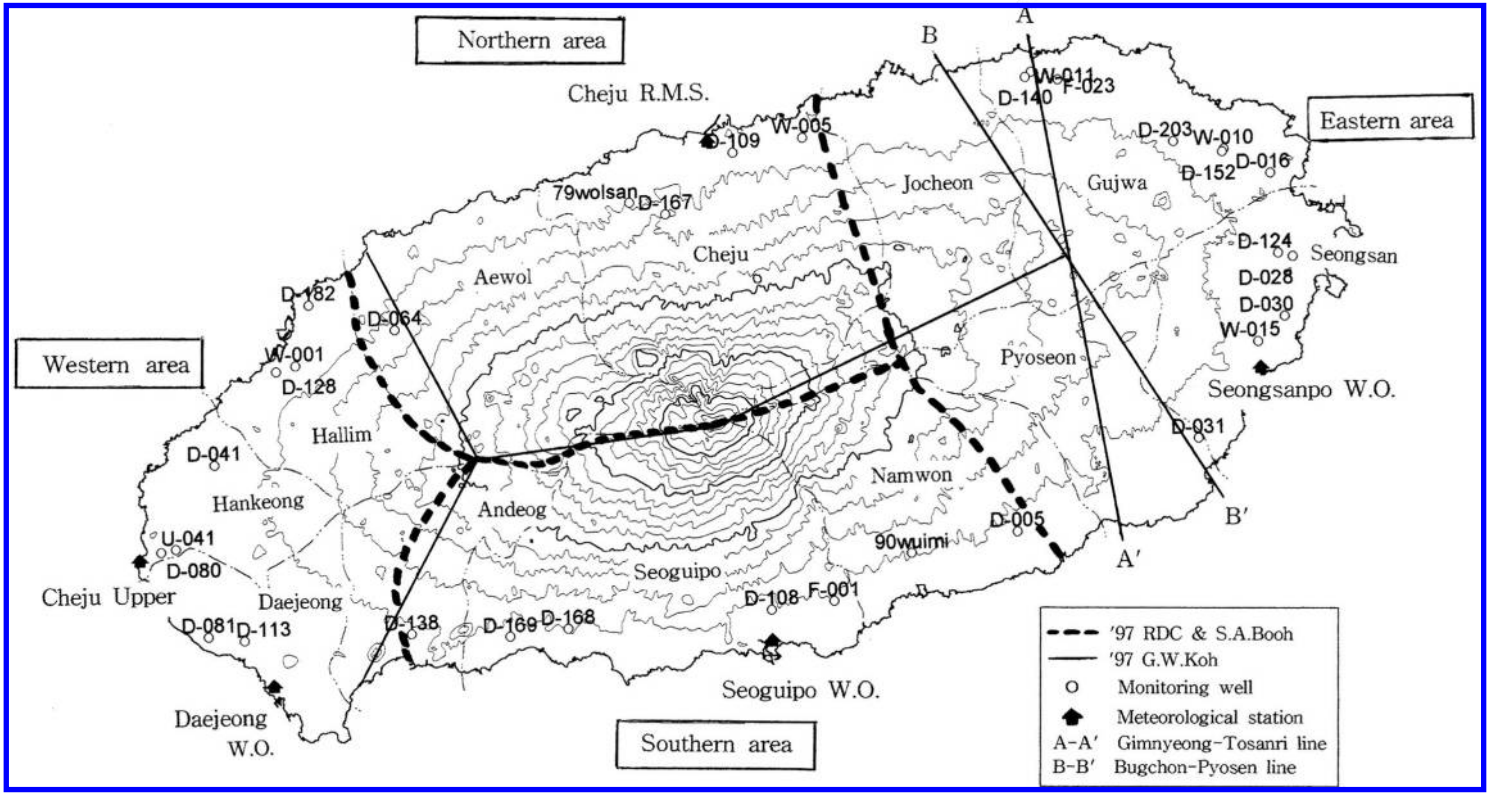


Figure 1. The groundwater divides of Cheju Island.

Copyright © 2003 Swets & Zeitlinger B.V., Lisse, The Netherlands

Table 2. List of the monitoring well in Cheju Island.

Area	Well name	Well number	Elevation (m)	Well depth (m)	Bottom elevation (m)	Start year	Average water level (m)	Maximum variation of water level (m)	Maximum water level variation per day (m)	Water level variation ratio (%)		Distance from coast (km)	Precipi-tation (mm)	X-Coord.	Y-Coord.
										Rain fall	Tidal				
Ave.	**4 areas**	**37 wells**	**51.41**	**87.06**	**−35.64**		**10.64**	**6.10**	**0.32**	**57**	**3**	**1.83**	**1483**		
Eastern	Dongbok	W-011	28.95	50.00	−21.05	93.02.	0.80	1.62		203		0.76	1846	175510	55730
	Gimnyeong2	D-140	35.85	60.00	−24.15	91.06.	1.16	1.46		126		1.15	1846	175150	55430
	Onpyeong	D-030	33.26	50.00	−16.74	94.01.	0.88	1.68	1.79	191	203	1.17	1846	190250	40860
	Jongdal	D-016	12.02	35.00	−22.98	91.06.	1.01	1.07		106		1.21	1846	189600	49390
	E.gimnyeong2	F-023	46.33	72.00	−25.67	91.06.	0.85	1.80		212		1.52	1846	177100	55230
	Hacheon	D-031	40.95	80.00	−39.05	92.10.	1.40	4.40	0.67	314	48	1.62	1846	184970	33730
	Pyoseon 2	Pyoseon 2-O	51.55	100.00	−48.45	96.04.	1.55	0.96	0.33	62	21	1.70	1846	177795	30185
	Goseong	D-028	28.24	41.00	−12.76	93.02.	0.90	1.15	0.39	128	43	1.82	1846	190820	44390
	Nansan	W-015	40.01	55.00	−14.99	93.02.	1.05	3.20		305		1.84	1846	188651	39379
	Jongdal	D-200	52.02	75.00	−22.98	91.06.	1.07	1.75	0.19	164	18	1.91	1846	188750	49055
	Sinchon 1	Sinchon 1-O	45.69	80.00	−34.31	96.05.	1.27	0.64	0.21	50	17	2.05	1846	164135	51285
	Sangdo	W-010	29.78	50.00	−20.22	93.02.	0.87	0.91	0.44	105	51	2.31	1846	186862	50870
	Jocheon 1	Jocheon 1-O	47.99	100.00	−52.01	96.05.	2.50	0.89	0.02	36	1	2.35	1846	169995	53195
	Sangdo	D-152	40.55	60.00	−19.45	92.08.	1.69	3.37	0.55	199	33	2.49	1846	186780	50700
	Susan 2	D-124	28.65	62.00	−33.35	93.03.	1.03	1.64	0.12	159	12	2.63	1846	189960	44610
	Haengwon 1	Haengwon 1-O	88.72	120.00	−31.28	96.04.	1.39	0.68	0.26	49	19	3.00	1846	179835	53060
	Peongdae	D-203	68.08	91.00	−22.92	92.08.	1.76	2.77	0.25	157	14	3.04	1846	183870	51400
	Subtotal	**17 wells**	**42.27**	**69.40**	**−27.19**		**1.24**	**1.72**	**0.43**	**139**	**35**	**1.91**	**1846**		

Copyright © 2003 Swets & Zeitlinger B.V., Lisse, The Netherlands

Western	Suwon	D-182	13.84	70.00	−56.16	91.06.	0.86	0.83		97		0.56	940	132270	42840
	Yeongrak 2	D-081	16.74	130.00	−113.26	92.09.	5.33	3.53	0.20	66	4	0.71	940	125920	23250
	Hyeopjae	D-128	26.13	82.00	−55.87	92.09.	9.53	3.75	0.07	39	1	0.72	940	130270	38910
	Gosan 2	D-080	18.86	82.00	−63.14	91.06.	2.39	3.68		154		0.81	940	123200	28350
	Illgwa	D-113	22.14	80.00	−57.86	92.09.	6.99	6.41	0.14	92	2	1.00	940	128020	22970
	Dongmyeong	W-001	25.05	60.00	−34.95	92.09.	8.48	6.50	0.06	77	1	1.25	940	131416	39252
	Gosan	U-041	35.32	61.00	−25.68	91.06.	1.98	3.15		159		1.70	940	124092	28499
	Panpo	D-041	35.32	61.00	−25.68	94.01.	18.23	18.18	0.09	100	0.5	2.44	940	126470	33480
	Subtotal	**8 wells**	**24.17**	**78.20**	**−54.07**		**6.72**	**5.75**	**0.11**	**86**	**2**	**1.14**	**940**		
Southern	Yeorye 2	D-169	59.41	170.00	−110.59	92.10.	22.41	1.64		7		0.90	1873	143810	22890
	Hwasun	D-138	67.21	90.00	−22.79	94.01.	37.35	11.16	0.08	30	0.2	1.38	1873	137950	23160
	Jungmun	D-168	113.17	130.00	−16.83	95.03.	73.12	11.62		16		1.70	1873	147260	23270
	Wuimi	’90Wuimi	102.00	130.00	−28.00	95.03.	28.02	9.43		34		1.89	1873	151340	47320
	Seohong 3	D-108	73.16	100.00	−26.84	92.10.	54.76	19.94		36		1.91	1873	159370	24130
	Sinhyo	F-001	53.51	130.00	−76.49	91.06.	14.95	24.57		164		2.14	1873	163090	24550
	Eugui	D-005	66.61	90.00	−23.39	94.01.	3.38	4.34	0.22	128	7	2.43	1873	174060	28440
	Subtotal	**7 wells**	**76.43**	**120.00**	**−43.56**		**35.26**	**11.81**	**0.15**	**33**	**0.4**	**1.76**	**1873**		
Northern	Samyang	W-005	33.84	42.50	−8.66	91.06.	3.89	4.27		110		1.22	1273	161830	52130
	Sinsan	D-109	68.28	122.00	−53.72	95.02.	17.29	6.74		39		1.45	1273	157710	51350
	Wolsan	’79wolsan	88.40	116.00	−27.6	92.09.	14.05	21.14		150		2.67	1273	167770	27230
	Eoum	D-064	111.75	124.00	−12.25	95.02.	8.52	4.71		55		4.13	1273	137360	41260
	Yeondong 3	D-167	153.13	170.00	−16.87	92.09.	41.26	30.30		73		4.25	1273	153620	47780
	Subtotal	**5 wells**	**91.08**	**114.90**	**−23.82**		**17.00**	**13.43**		**79**		**2.74**	**1273**		

Copyright © 2003 Swets & Zeitlinger B.V., Lisse, The Netherlands

groundwater level to divide areas. Therefore, some areas were included to the eastern area.

3.2 *Changes of groundwater level at each area*

Analysis of changes of groundwater level was performed to define the reason of saline water intrusion at the eastern area. Total number of monitoring wells is fifty one. Table 2 shows the results of monitoring for 37 wells from 1993 to 1997 among the 51 wells. Distribution of well is 17 at the eastern area, 8 wells at the western area, 7 wells at the southern area and 5 wells at the northern area.

According to the comparison result of the maximum variation of water level per day and distance of wells from the coast show, there are variations as 0.43 m on the well located about 1.91 km from the coast at the eastern area, variation as 0.11 m and distance as 1.14 km at the western area, and variation as 0.15 m and distance as 1.76 km at the southern area.

However, the northern area doesn't show the maximum variation of groundwater level per day. Average water level and the average maximum variation of annual water level due to rainfall are EL 1.24 m and EL 1.72 m, respectively. The variation ratio is 139% of water level in monitoring wells. The other areas have variation ratios as 86%, 33% and 79% for the western, the southern and the northern area, respectively. The variation ratios indicate that the eastern area has low value of average annual water level but the largest variation ratio. Fig. 2 shows the water level variation in the representative wells. Water level variations are similar between the eastern and the western areas. The southern and the northern areas also have similar pattern of water level variation each other. Fig. 3 is the maximum variation of water level due to tidal effect for well Pyoseon2, D-081 and D-005.

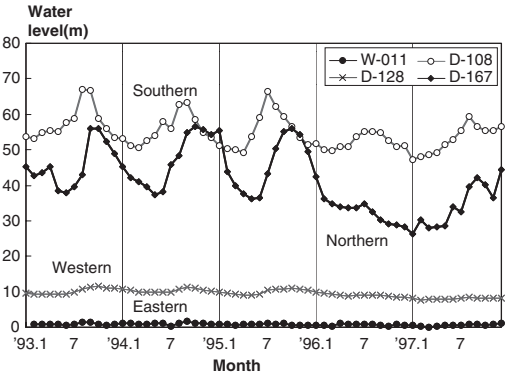


Figure 2. Water level variation at the monitoring well.

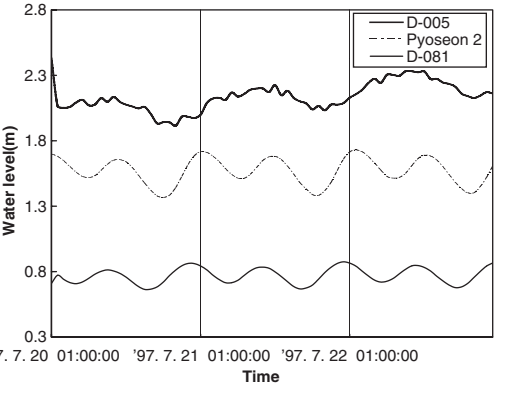


Figure 3. Maximum water level variation due to tide level change.

3.3 *The eastern area*

The seventeen monitoring well at the eastern area are located on EL 12.02–88.72 m. Depths of the wells are 31.0–120.0 m, in other words, (−)52.01 m below the sea level. Distance from the coast is 1.91 km in average. Two wells are located in sedimentary formation. D-124 has the sedimentary formations from (−)29.55 m below the sea level and Chocheon-1 has them from (+)11.99 m above the sea level.

Average monthly rainfall during 1993–1997 is 153 mm and average annual rainfall is 1,846 mm. Average water level is EL 1.24 m showing the highest value of average monthly level as EL 5.01 m and the lowest one as EL 0.03 m for five years. The maximum range of water level variation is 4.40–0.68 m meaning lower than 2 m variation for 76% of the monitoring wells.

Twelve monitoring wells among 17 wells reveals daily water level variation due to tidal effect. Range of daily water level variation is 0.02–1.79 m meaning 0.43 m in average during 1993–1997.

The maximum daily variation of water level is 0.43 m, 25% of monthly variation. D-030 is the only well showing larger maximum average daily variation of water level than the maximum average monthly variation. This indicates that the eastern area is affected by tidal effect stronger than the other areas. However, it doesn't mean that tidal effect influences more strongly on water level variation than rainfall.

3.4 *The western area*

Eight wells are located on the elevations between EL 13.84 and 35.32 m. Depth of them are 60.0–130.0 m meaning (−)113.26 m below the sea level. Average distance of the wells from the coast is 1.14 km. Five wells located in sedimentary formation. Well D-080 has the formation from EL 0.0 m. The other wells represent the formation below the sea level.

Copyright © 2003 Swets & Zeitlinger B.V., Lisse, The Netherlands

The average monthly rainfall is 75 mm and the average lowest value is 335 mm for five years. The average annual rainfall is 94 mm, the lowest value among the four areas. The average water level is EL 6.72 m for five years. The highest and the lowest levels are EL 18.23 m and EL 0.86 m, respectively. The maximum variation range of water level is 18.18–0.83 m, meaning 5.75 m in average. Most of the wells except D-041 show less than 7 m variation.

Five wells have daily variation of water level between 0.06 and 0.20 m among eight wells. The maximum average monthly variation of water level is 3.53 m which is longer than 1.76 times of water level variation due to the tidal effect. This means that the western area is influenced more strongly by rainfall than tidal effect.

The reason of the above phenomenon is as follows. The Seoguipo Formation (SGF), low permeable layer, is located at (−)100.71 m below the sea level in five wells. The lower parts of the wells are composed with the SGF and bed rocks. Therefore, it is difficult to be influenced by tidal effect. Moreover, the rainfall infiltrated into confined aquifer is ascended more fast than flow downward due to obstruction from low permeable or impermeable layer.

3.5 *The southern area*

Seven wells are located on the elevations between EL 53.51 and 113.17 m. Depth of them are 90.0–130.0 m meaning (−)110.59 m below the sea level. Average distance of the wells from the coast is 1.76 km. Five wells located in sedimentary formation between EL 10.0 and 40.0 m.

The average monthly rainfall is 156 mm and the average highest value is 790 mm for five years. The average annual rainfall is 1,873 mm. The average water level is EL 35.26 m for five years. The highest and the lowest levels are EL 73.12 m and EL 3.38 m, respectively. The maximum variation range of water level is 24.57–1.64 m, meaning 11.81 m in average. Fifty seven percent of the wells show more than 10 m variation.

Two wells have daily variation of water level between 0.08 and 0.22 m among seven wells. The maximum average monthly variation of water level is 4.34 m which is longer than 20 times of water level variation due to the tidal effect. This means that the southern area is influenced more strongly by rainfall than tidal effect.

The major reasons of the above phenomenon are distribution of the SGF above the sea level, no tidal effect except very close area to the coast and fast ascending of rainfall toward potentiometric surface than flow downward. The large variation range of water level is due to sensitive response of potentiometric surface to exterior condition.

3.6 *The northern area*

Five wells are located on the elevations between EL 33.84 and 153.13 m. Depth of them are 42.50–170.0 m meaning (−)53.72 m below the sea level. Average distance of the wells from the coast is 2.74 km. D-167 well is located in sedimentary formation from EL 12.63 m.

The average monthly rainfall is 106 mm and the average highest value is 578 mm for five years. The average annual rainfall is 1,273 mm. The average water level is EL 17.0 m for five years. The highest and the lowest levels are EL 41.26 m and EL 3.89 m, respectively. The maximum variation range of water level is 30.30–4.27 m, meaning 13.43 m in average.

Well D-167 is located on the highest elevations and its depth to the sea level is 20 m shallower than the average depth. Moreover, the low permeable layer is distributed above the sea level. These facts are the major reasons of high water level and large variation of water level.

4 REASONS OF SALINE WATER INTRUSION AT THE EASTERN AREA

4.1 *Low groundwater level and excessive pumping*

The major reasons of saline water intrusion at the eastern area are very low level of groundwater table and continuous ascending of saline water due to repetitive fluctuation of water table by rainfall and tidal effect. Moreover, excessive pumping of groundwater accelerates saline water intrusion.

As mentioned previously, the eastern area has very large annual variation ratio of water level. Although the average water level is EL 1.24 m for 17 monitoring wells during five years, variation of water level is 1.72 m in average and the average water level is $1.24\,\text{m} \pm 1.72\,\text{m}$. Therefore, the interface between fresh water and saline water is fluctuated up and down, resulting in partial exchange of fresh water to saline water.

Fig. 4 is a schematic diagram of depth of the theoretical G-H interface between fresh and saline water for well D-203 and D-028. Based on the G-H theory, water levels during drilling are EL 1.09 m and 1.04 m for D-203 and D-028, respectively. Therefore, the interfaces are located at (−)43.2, and (−)41.6 m below the sea level. They have extra depths as much as 20–28 m from the lower limits of drilling, (−)22.92 m and (−)12.76 m.

Fluctuation of water level becomes larger by the tidal effects. Fig. 5 is a schematic diagram of interface calculated by G-H theory. They included the highest and the lowest values of monthly average water levels and the maximum variation of daily water level for five

Copyright © 2003 Swets & Zeitlinger B.V., Lisse, The Netherlands

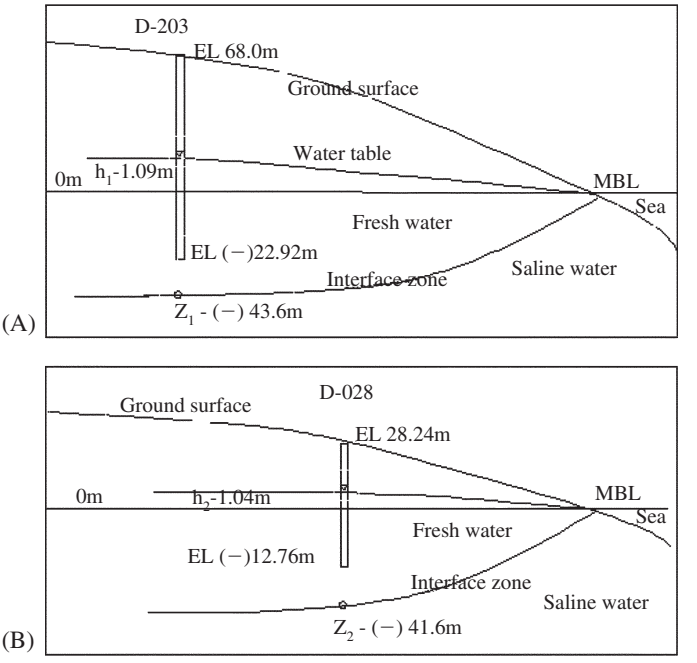


Figure 4. Depth to inferred interface zone between the fresh and the saline water.

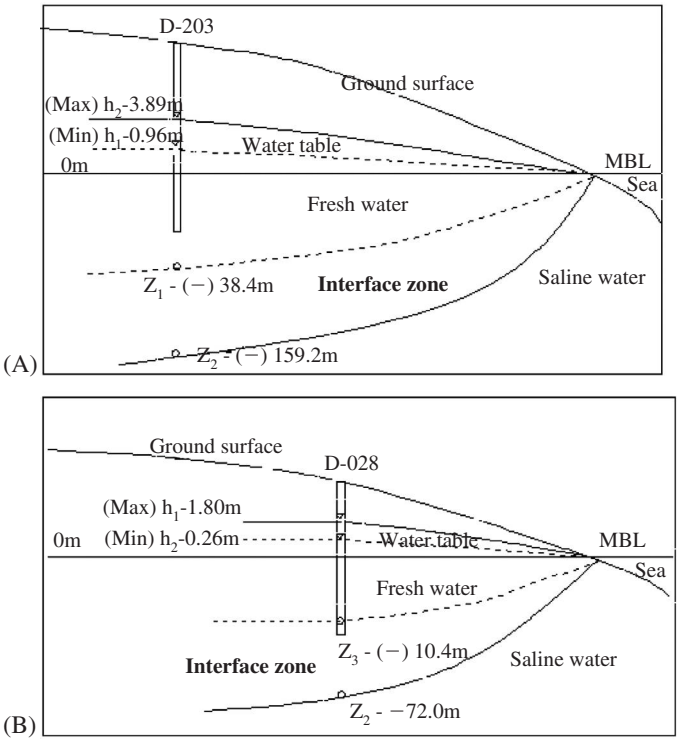


Figure 5. Elevation of the interface zone varying with rainfall and tidal change.

Copyright © 2003 Swets & Zeitlinger B.V., Lisse, The Netherlands

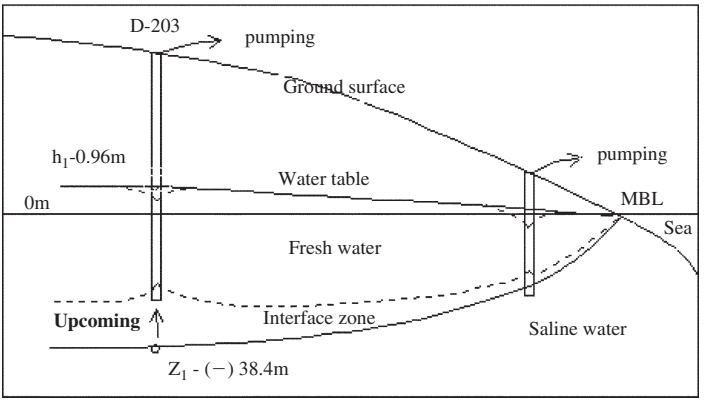


Figure 6. Upcoming of the saline water level due to simultaneous pumping of two wells.

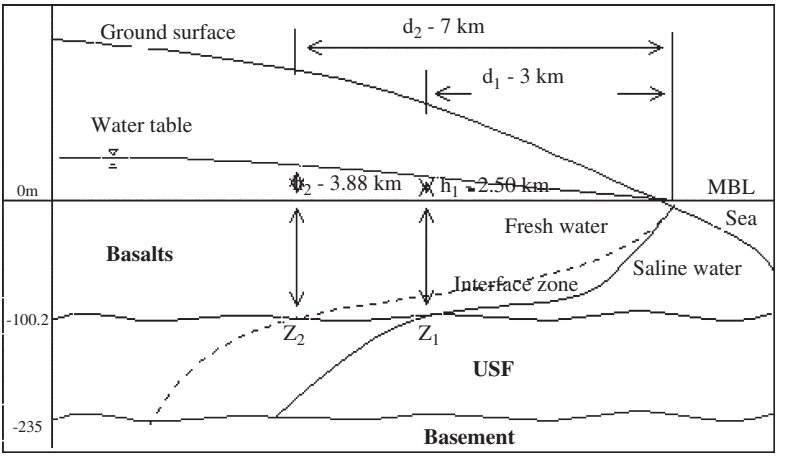


Figure 7. Schematic diagram on the distribution of the interface zone in eastern Cheju Island.

years. According to Fig. 5, saline water doesn't intrude into D-203 even at the low tide during the dry season. In case of well D-028, it is intruded by saline water at the bottom of well.

Although D-203 isn't intruded by saline water, abrupt increase of pumping rate and period during drought occur fast draw down of water level and acceleration of upcoming of interface zone. This mechanism induces intrusion and ascending of saline water (Fig. 6).

4.2 *Geologic structures of subsurface*

The wide distribution of basalt layer (FOB) at the eastern part is also one of the reasons of saline water intrusion. Since the FOB has low density, several horizontal lava tubes have been formed along the flow direction near the coast. The FOB also developed columnar joints and vertical joints. The interlayers between each lava unit contain pyroclastic layers, krinker, fracture zone and scoria layers. These layers play good roles to conduits of groundwater flow. Therefore, water level can not be ascended by fast infiltration to the subsurface along the primary and the secondary geologic structures and discharge of rainfall to the coast. The geologic structure can be a good conduit of horizontal intrusion of saline water toward inland.

4.3 *Distribution depth of low permeable sedimentary formation*

The distribution of uncemented sedimentary formation (USF) at (−)100.2 m below the sea level is one of the reasons of saline water intrusion. Although the USF which is composed with sandy silt, silty sand or muddy

Copyright © 2003 Swets & Zeitlinger B.V., Lisse, The Netherlands

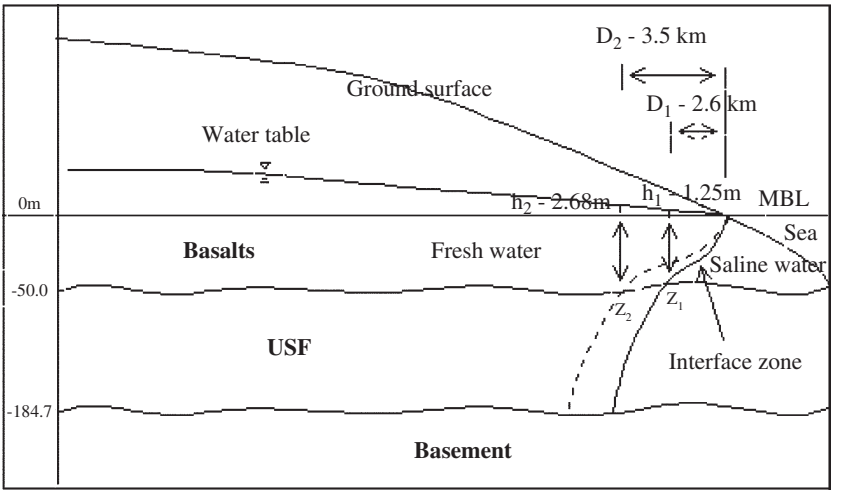


Figure 8. Schematic diagram on the distribution of the interface zone related to the depth of uncemented sediment formation (USF) in the eastern Cheju Island.

sand contains a lot of groundwater, it is a aquitard or aquiclude. Moreover, the eastern area doesn't contain the SGF, the low permeable formation at the upper part. In case of saline water intrusion area, most of the average water level is lower than EL 3m. Since they have low permeable sedimentary formation to present saline water, interface zone can be distributed up to the area of EL 2.5 m water level by G-H theory. According to the G-H theory, the interface zone is formed at the area of EL 3.89 m of the average water level, since water level of the area is drawn to the EL 2.50 m. Therefore, saline water can be intruded to the distance of 7 km from the coast based on the water level during drilling. If there is horizontal geologic structures, the intrusion can be propagated to more distant area.

Analysis of saline water intrusion was performed with assumption of more higher elevation of the USF than the present. Fig. 8 has assumptions deposition of the USF distribution around (−)50 below the sea level and no confining. In this case, the interface zone in formed at water level of EL 1.25 m and 2.6 km distance from the coast. There would also be intrusion up to 3.5 km from the coast with consideration of water level variation due to rainfall. Therefore, if the USF had been distributed near sea level or above the sea level without the SGF, the eastern area would not be intruded by saline water.

5 CONCLUSION

The Cheju island can be divided as four areas, north, south, east and west. The average water levels of monitoring wells of each area are EL 1.24 m for the east, EL 6.72 m for the west, EL 35.26 m for the south and EL 41.26 m for the north. The variation ratios of water levels are 139% for the east, 86% for the west, 33% for the south and 73% for the north. The eastern area has low level of groundwater table, while it has large range of water level variation, resulting in larger fluctuation of interface between fresh water and saline water than that of fresh water. The major reasons of saline water intrusion are as follows. First, since the very low level of groundwater table as much as below than EL 3 m near the coast, ascending of interface zone up to the bottom of wells is occurred due to draw down of water level during dry season and excessive pumping. Second, the secondary geologic structures formed by eruption of low density basalt act as good conduits of groundwater flow. Third, deep distribution of the low permeable USF around (−)100 m below the sea level doesn't prevent from saline water intrusion, although the thickness of the USF reaches up to 135 m.

REFERENCES

Booh, S. A., 1999, A study on the groundwater characteristics and use in Cheju Island, Master Thesis, Andong University (in Korean).

Booh, S. A., Chung, H. J., and Jeong, G. C., 2001, The studyt of Hamdeok-Pyoseon Graben in Cheju Island, In: Koh, H. J., Choi, Y. S. (Eds), The 3rd Joint Meeting of Japanese and Korean Structure and Tectonic Research Group.

Choi, S. H., Kim, Y. K., and Lee, D. Y., 1991, Sea Water Intrusion in the Coastal Area of Cheju Volcanic Island, Korea. J. Korea Inst. Mining Geol. 24(3), pp. 319–327.

Fetter, C. W., 1994, Applied Hydrogeology, Prentice Hall, 691.

Copyright © 2003 Swets & Zeitlinger B.V., Lisse, The Netherlands

Halaguchi, 1931, Geology of Cheju Island, GSK, vol. 10, No.1, p. 34 (in Japanese).
Koh, G. W., 1997, Characteristics of the groundwater and hydrogeologic implications of the Seoguipo Formation in Cheju Island, Ph.D. Thesis, Pusan University (in Korean).
KOWACO, 1992–1997, Groundwater Monitoring in Cheju Island (in Korean).
Minstry of Agriculture and Forestry (MAF), 1971, Report on groundwater of Cheju Island (in Korean).
Rural Development Corporation (RDC), 1985, 1989, Report on groundwater of Cheju Island (in Korean).
Yoon, J. S., 1986, A study on reason of brine phenomena of groundwater of Eastern Area, Cheju Island, Research of Cheju Island, vol. 3, pp. 43–53 (in Korean).

Copyright © 2003 Swets & Zeitlinger B.V., Lisse, The Netherlands

Operational systems for water management under extreme climatic conditions

P.-W. Graeber
Dresden University of Technology, Dresden, Germany

ABSTRACT: Storms, heavy rain falls and floods in the past time require water management more than ever for extreme conditions and long-term climatic changes. Hence new strategies are needed to requirements of society and environment. Comparable results and intergovernmental water management on an international level is required which means to learn from each other experience. To ensure sustainable water management strategies a holistic approach is emphasized. The bases of a modern water management system are computer based Decision Support Systems (DSS) including computer simulation tools with active graphical user interface. By using of modern mathematical solutions (e.g. Fuzzy-systems, GIS, Neuronal Networks) the prognosis of water level and flood prevention and control is possible. A DSS requires a coupled analysis of all kinds of data to describe the long-term scenario of global and local changes. To get measurable results benchmarks are defined to evaluate performance of the developed simulation tool. Water management needs will be set into a socio-economic context.

1 INTRODUCTION

A deficit of water resources, unfavorable distributions of water in time and space, increasing water use, polluted water resources, variability and instability of climate and change of socio-economic activities demand rational ways of water management.

The goal of the DSS OSMOW computer program system is to develop a methodology for effective operational water management under normal and extreme conditions of the water cycle.

On December 22nd 2000 the General European Guidelines for Water was enforced. This guideline forms the inter-European cooperation for water protection, water management and catastrophe prevention and ensures a controlled management of surface and ground water. The General Guideline for Water requests harmonization of actions for water protection and contributes to the further decrease of water pollution. But much needs to be done to fulfill this goal. The General European Guidelines can be used not only inside the European Union, but also is valid worldwide.

Consequent installation of a circumspect classification of water sources especially under hydrological, economical and ecological aspects is an excellent chance to improve water management in Europe. This does not neglect the unique aspects of single river or lake system. Both must be enabled through:

- a consequent, aerial and river-specific approach
- a specific approaches for every water course
- the monitoring of sufficient data and its compilation in data bases,
- a combined consideration of pollutants (emission and imission) and
- a single pollutant or complex pollutant cocktail specific approach.

Paragraph 3 of the guidelines is a central theme of the guideline and every national water management authority will have to cope with its demands. Until now the water management is under supervision of national or even local authorities with no interaction to each other. Water management was enabled within political or geographical borders. But 50% of the residential areas are situated aside international water course systems and all of the water authorities responsible for the supply of water and waste water management have one common interest: to nationalize the advantages of water and to internationalize the disadvantages of water.

Due to the introduction of the new guidelines water authorities will have to co-ordinate their actions on a broader and more international scale. Along international river courses international river water management and constructive plans must be introduced.

Copyright © 2003 Swets & Zeitlinger B.V., Lisse, The Netherlands

International river catchment areas must be handled adequately. In order to establish such a water management and such construction plans a huge amount of data for the evaluation, determination of management goals as well as action plans must be compiled. The interaction of climatic, social, agricultural, industrial, environmental and economical aspects have to be considered and controlled. An interactive decision for step must be taken according to all that information. Water pollution and the measures for water protection will have to be revised constantly. The management plan therefore must be reviewed every 6 years (prescribed by paragraph 4 of the guidelines) and effects caused by previous actions, improvements and damages have to be evaluated. The status of the necessity of exceptional regulations has to be evaluated all the time and, if the status has expired, the regulation must be withdrawn. All information must be stored and forms input data for an interactive decision support system for the European water management.

The co-ordination of an information exchange and a decision consulting is in the first place a management task, which challenges experts and which is the only way to ensure stable supply of water and to protect the environment. The living standard, the agricultural production and a modern industry depend on a stable supply of water and wastewater treatment.

Catastrophes caused due to absence or strong presence of water occurs with the highest probabilities. Natural catastrophes due to flooding or catastrophes caused by water such as slope sliding, dam failure or even the failure of concrete reservoir constructions due to flood impact as well as hygienic impacts, which come in the course of such events, are strongly burned into our mind. But also sneaking quiet catastrophes have a terrible and ugly face such as dry seasons. The more extreme a catastrophic event becomes the less probable becomes its occurrence. But this actually forms the danger of natural disasters. The danger that comes along with these events is difficult to predict and measures against such events are difficult to master. Prediction of such events, measures against floods and the planning of residential areas and industrial areas away from areas prone to floods is one effective measure. The construction of reservoirs for both flood protection and dry-out prevention becomes an international and inter-cultural task especially on river courses, which are situated in several countries. Water management for prevention of natural catastrophes must deal with

- the protection against catastrophes of high probability, but under economic considerations and with a calculable remaining risk,
- the remaining risk must be at a scale that the national economy is able to carry the damage and is not turned into long-term disaster.

Concerning the General European Guideline for Water much research demand exists for a variety of topics. The research proposed deals with the classification of water courses using a circumspect approach, deals with compilation and evaluation of ecological aspects and in the end prepares a tools for fast and efficient water management for both flood prevention, dry-out prevention and pollutant impact under economical, ecological and sustainable aspects.

The main problems to be interpreted in the proposal are delineated in connection with: Water Resources, Water Users and Operational Water Management. The scientific/technological objectives and the solution of these problems are outlined in general objectives and measurable targets are described in the specific problems, respectively.

The current research proposal deals with the adaptation of models and the development of management scenarios for catastrophe protection.

The addressed general objectives of the developed project include:

1. evaluate the danger of catastrophes,
2. evaluate the vulnerability for disasters of an area,
3. manage the catastrophe prevention and catastrophe protection,
4. improve the model output of interpolation and prognosis for managing tasks for water management based on circumspect data and its handling in an interactive data base,
5. consider hydrological, meteorological, biological, biochemical and ecological influences for decision-making,
6. furthermore the need for water supply and protection against dry seasons must be handled. Water resources therefore must be qualified regarding quantity and quality of the water reservoir. Decision support systems will be needed and therefore the development deals with:
   - coupled analysis of water supply safety and the safety of food supply. This involves the use of information and an integrated analysis method of water availability, water usage, food demand, and economical aspects for agriculture, and
   - improvement of respective development for decision support for the management of catchment areas with help of input data describing the long-term scenario of global climatic changes.
   - the decision support system must supply tools to help to improve the co-operation and communication of involved parties.
7. the decision support system also must help the governments and the private industries to decide and take action,
8. the decision support systems developed within the presented approach will help by the economical controlling and steering of water supply systems,

Copyright © 2003 Swets & Zeitlinger B.V., Lisse, The Netherlands

waste water treatment plants and help to evaluate the environmental impact of actions taken.

2 STATE OF ART

The motivation to submit the program system OSMOW is the necessity to develop tools – methods, programs, techniques, etc. – which will enable a decision support system for water management in Europe as requested by previously published guidelines. Present practices of many European countries may need considerable alterations. Water economy systems ensuring in general needs of different water users, are methodically and technically unfit in particular cases and cannot be operated in synchrony with user requirements, for example – during unexpected droughts and floods. The operation of systems managing groundwater flow for instance is in particular exposed to retardation. The response to user needs in large open channel systems and an inter-European approach is retarded as well.

The aim of the to developed OSMOW is to develop a methodology, contributing DSS for the sustainable water resources management. The methodology for water management under normal and extreme conditions of water cycle builds up on management of water resources for normal cases.

The approach to the solution of considered management problems combines the best available scientific knowledge and methodologies. On basis of existing and own-developed numerical and balance models of surface and ground water flows and other dynamic processes, a new simulation and controlling system on a regional scale is constructed. The controlling system is based on a hierarchical online closed-loop concept with two simulation levels. Water needs of different water users are reflected in the management methodology, thus achieving an integrated water management. Under a user-friendly interface a decision support system is formed that allows to control and predict possible actions for water management regarding environmental, agricultural, hydrological and socio-economic aspects.

The management process is realized by an integrated information system, performing cyclic processing and analysis of the information and transferring the commands for the next time step.

The selection of several water systems/subsystems is envisaged to be the starting point and the criterion for the development of different problems included in the DSS–OSMOW. These territories (catchments) will be equipped with information devices and monitoring will be organized for the detailed observation of water flow processes, as well as for other processes in the course of experiments with the developed methods.

The introduction of strategic methods for sustainable water resources management in the practice of European countries will be in direct connection with the recently adopted European Water Framework Directive. The introduction of management methods leads to a decrease of water losses, thus affecting favorably economic efficiency. The regulation of the water/air regime in the unsaturated soil zone influences environmental conditions. Vadose zone is functioning as buffer system for the mitigation of extreme conditions.

Water resources management methods are a technological progress for the population living and working in the corresponding territory. In this way significant social effects are achieved.

3 NEW ASPECTS OF WATER MANAGEMENT SYSTEMS

Traditionally water resources management till now has been practically performed for surface water flows. It has been realized mainly by reservoir operation for both ordinary water use and flood prevention. The management task is expressed in an optimized hierarchical distribution of water volumes between different water users for an annual or seasonal time interval. The operative management of an open channel system is connected with substantial problems concerning the water distribution in single nodes of the system. The solution of these problems leads to accurate supply of water volumes to end points of the system.

During the last two decades the problem of integrated water management has reached a certain level of development. Groundwater management for instance is very important because of observed trends of water supply deficiencies and of possibilities to use water for irrigation purposes more economically. Regulating groundwater table contributes to the solution of diverse ecological problems. The general concept of groundwater management is based on controlled drainage according to available water resources in the region. The classical drainage facilities are ditches, open channels, drainage pipes, mole drainage and vertical drainage wells, providing mainly subsurface drainage. Water management systems are set up in various configurations. The drainage facilities should be operated alternately for the management purposes.

Investigations on water management systems useable for subsurface irrigation have been carried out in different countries: Slovakia, Russia, the Netherlands, Poland, Bulgaria, Germany, the USA, the Ukraine and elsewhere. In most cases the attention has been focused on drainage equipment operation and on possibilities of maintaining a certain groundwater level, or on determining the drainage water amount under constant operation conditions. The results of investigations and practical applications clearly confirm the possibility of

Copyright © 2003 Swets & Zeitlinger B.V., Lisse, The Netherlands

regulating the groundwater level by means of drainage equipment. These results are only the basis for new research work on a complex of problems depending on requirements for control systems operating under dynamically changing conditions and still meeting the needs of water users.

The computer program system OSMOW comprises new investigations in following research topics:

1. harmonized modeling for strategic planning,
2. hydraulic processes connected with the structures for regulation of surface and groundwater flows under changing conditions,
3. regional and inter-regional performance of management systems under the effect of natural conditions and the needs of different competitive water users,
4. influence of groundwater table management on mitigation of extreme environmental conditions (floods and droughts) by water retention or water release in the aquifer and in the vadose zone as well,
5. technical-economic, social, hydrological, meteorological, biological, chemical and other problems related to development and operation of systems for water regime management,
6. evaluate the vulnerability of an area regarding disasters,
7. prevent or if it fails manage a catastrophic event,
8. coupled analysis of water supply, safety, food supply and environmental impact,
9. possible pollutant impact is involved for decision making.

The strategy under consideration (item 1) is set into a holistic approach, including definition of tasks and needs (visions, guidelines), water controlling (transformation of strategy into practice), use of selected or developed tools (workmanship) and interpretation of results. The loop is completed through the feedback of results with respect to the defined tasks (Fig. 1).

Investigations of item 2 are designated to formulate direct relationships between two types of parameters, describing the processes: “controlling” and “controlled” ones. These relationships are necessary for the quantitative process modeling for both surface and groundwater flows. The experience of the partners of the project consortium shows that it is possible to obtain these relationships by means of numerical modeling.

A new simulation and controlling system to achieve the transformation of strategies for the regional water-resources management will be developed in connection with the investigations in item 3. This system will be based on a hierarchical online closed-loop controlling system with two simulation levels, a detailed complex simulation tool and reduced block-models. The interaction between different processes in soil and groundwater zone is described by coupling different models to one detailed complex simulation package.



Figure 1. Strategic water resources planning approach.

Non-steady-state simulations can be performed. Substantial error reduction is achieved by introducing fine-mesh discretisation models. Detailed simulation requires the use of High-performance Computation (HPC) technique and parallel computers. The to developed project OSMOW emphasizes on the application of recently developed HPC tools in parallel codes for groundwater flow simulation to the Danube lowland and other groundwater dominated areas. On-line closed-loop control tools must be created for practical field application. These reduced models, the so-called block-models, are calibrated by the complex model. New methods will be used for calibration and sensitive analyses. In this way a hierarchical controlling system will be created. Elements of knowledge based system and mathematical methods for computation with inaccurate measurement values will be also incorporated in the block-models.

Research on groundwater pollution is included in the sphere of the regional management problems considered in this project OSMOW. In particular, the “pure zones” in the region will be defined by solving the so-called “inverse problems”, as well as places for discharge and disposal of polluted water will be determined.

Investigations in test fields related to item 4 would contribute to the proof or adaptation of theoretical concepts. Data for all observed water, soil and plant parameters with respect to the regulated groundwater regime will be analyzed.

There are no data available for holistic investigations related to item 5 on technical-economic and social problems of water systems with controlled operation. Such an analysis will be performed on basis

Copyright © 2003 Swets & Zeitlinger B.V., Lisse, The Netherlands

of quantitative characteristics both existing and new planned water systems.

OSMOW will advance the present situation by a holistic methodology for water resource planning under dynamic changing conditions.

Results of investigations envisaged in the DSS–OSMOW would represent a sound basis for further development and practical application of methods for water-resources management.

As a final conclusion the performance of these investigations will represent a stage in the acknowledgement of the general trend for rational use of water resources.

The OSMOW includes the development of a new method of modeling the diffuse pollution. The basis of the new method is the solution of "inverse problems". In this way the possibility is created to determine (manage) the flow path of disposed pollutant without aggravation of water quality in the rest part of the catchment.

4 THE CONCEPT OF OSMOW

The work planned is following the red line conception phase → implementation → application.

The conception phase comprises the harmonization of the modeling concepts within the consortium to achieve comparable results and data process identification for extreme conditions. All partners need to be actively involved in this part, because it is essential for the success of the proposal to establish a common starting point and a mutual understanding of problems each partner contributes to the research investigations. The consortium is formed by partners comprising knowledge in water resources management, groundwater flow simulations, drainage and irrigation, unsaturated flow, data base establishment as well as socio-economic and environmental issues. In this way most synergy effects of the different expertises may be gained for the project. The research work will be performed with a strong link to endusers. Members of the consortium include research institutes and water management institutions.

The implementation is a key action of the project. Hence first the selection, adaptation and when needed the development of new mathematical/numerical concepts will be performed. The participating partners have experiences with all kind of models related to all parts of the hydrological cycle. With these models a pool of mathematical concepts is formed and cross models are established. The pool of models includes in particular:

- Regional models for description of surface water flow: HBV and HBV-light (rainfall-runoff model), NLC, NONLIN, MODI (river water quantity and quality)
- Models for water balance in cross-sections of a main river
- Regional models for description of groundwater flows: MODFLOW, MOC, THEIS
- Local models for description of drainage system operation: DRAINMOD (simulation of shallow groundwater table), SEEP-CANAL (operation of an open drainage channel), SEEP-DRAIN (operation of pipe drainage), SEEP-WELL (drainage wells)
- Solute transport models: MODFLOW-MT3D, SWMS-3D, RPMOD (3D-model for reverse filtration problems), HYDRUS, COMBESICK, GLOBAL (1D-, 2D- and 3D-models for unsaturated flow in rigid soils), MACRO (2D-water and solute transport in macro porous soils), FLOCR (water flow in shrinking and swelling soils)
- Models for determining the relationships between "controlling" and "controlled" parameters
- Algorithms for inverse problems: MINPACK (LEVENBERG-MARQUARDT-Code), NL2SOL (Secant method for nonlinear least squares)
- Block models for simplification of the detailed models
- Models for water-economy balance in a catchment

The pool is not defined to be final during this phase; it may be extended with other models whenever needed.

The mathematical/numerical concepts are made useable by developing simulation models. The simulation tools are structured in two levels. Out of a detailed complex simulation model so-called block models are generated (Fig. 2). These models are related to a given task.

Block models are:

- simplifications of a detailed model. There are different methods to achieve simplifications, e.g. condition viewer or transfer functions
- designed for special regions and users
- designed for different hydrological conditions, that means for a region more than one block model is required, e.g. for spring or summer conditions, flood or low discharge

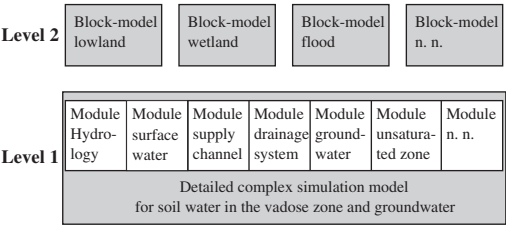


Figure 2. Hierarchical controlling system.

Copyright © 2003 Swets & Zeitlinger B.V., Lisse, The Netherlands

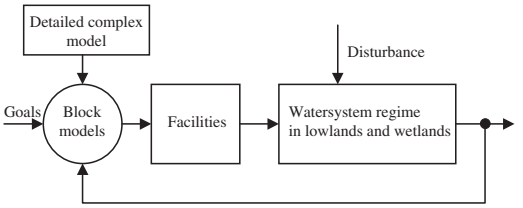


Figure 3. Loop for controlling components of water balance: surface water, vadose zone and groundwater.

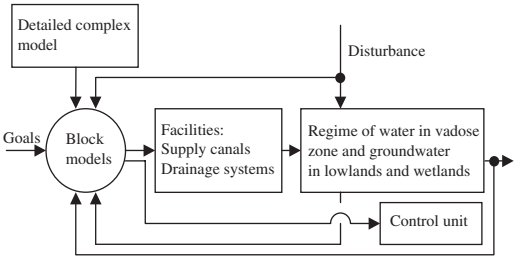


Figure 4. Multi-stage control system.

- calibrated by the complex model
- integrating a part of knowledge based rules. In this case a lot of expert experience exists.

The block-model level is a simplification, but enables the user to overcome the disadvantage that not all influences of the groundwater level can be described by mathematical equations. Block-models run not only on mainframes, but also on control computers, e.g. on a PC. Another aspect is inaccurate measurement values. In the state of art simulation tools take for granted accurate values, which are not available for practical working conditions. The innovative idea is the combination of mathematics of inaccurate values (e.g. Fuzzy set manipulation) with the block-models to achieve knowledge based Fuzzy controlled system.

Figure 3 shows the online closed-loop control system for a part of the regional water balance: surface water – vadose zone – groundwater.

The block model is online coupled with the control-loop comparing results with actual values. The goal function will be created in the computer or put in by the operator. Actual measurement values are made available online or with datalogger systems. The block-model calculates the input of regulation units. The transmission from the computer to regulation units is online. In this way a feedback between actual values and the regulation unit will be guaranteed. For the improvement of controlling effects multi-stage control loops will be used (Fig. 4). Such control loops take into consideration e.g. disturbance values (disturbance feed forward) and early warning condition values (controller feedback).

The best mathematical concepts will not be used if they are not set into a user-friendly simulation environment. Therefore it is intended to embed the simulation tools into a graphical user-interface.

The application phase starts with the establishment of benchmarks. Test regions are selected to cover most foreseen extreme conditions in Europe. Simulations in test regions serve to proof the applicability of the proposed simulation tool and to perform a feasibility study with the established benchmarks.

A diversity of European test sites, covering the extreme conditions as previously described before, including

The East Slovakia Lowland
Estimation of the characteristics of:

- Water-level regime in a river network and channels
- Water-level regime of groundwater
- Water-content regime of the unsaturated zone of soil
- and their both spatial and temporal interaction
- Estimation of the components of water balance in the system of atmosphere – plant canopy – unsaturated zone of soil – groundwater
- Comparison of the characteristics monitored in the test region with the results from the harmonised model.

Test field in Poland

- The catchment of the Gasawka river with drainage-subirrigation systems as main users of water, with other users as fish ponds, sugar plants, small towns and villages, environment (biological flows), wetlands, recreation and tourism
- The polder area in the north Poland with flood risk and mainly agriculture activity.

Test field in Bulgaria

- With subirrigation as characteristic component of water balance
- description of Iskar river basin up to Novi Iskar town, detail description of water resources system structure
- Methodology for short-term operation of water resources system.

Upper Tisza Region, Hungary

- Especially with respect to social, economic and environmental effects of integrated water resource management.

Marchfeld region in Lower Austria

- This region is supplied with water from Danube for irrigation purposes. The main channel serves

Copyright © 2003 Swets & Zeitlinger B.V., Lisse, The Netherlands

also as recipient for some small wastewater treatment plants.

should be representative for Europe.

After the establishment of the harmonized modeling concepts the following workpackages are embedded into a socio-economic context. Environmental issues, when not already included in water related topics, are attributed accordingly.

5 INTERNATIONAL ASPECTS

The European dimension of dynamic changes of the water cycle is reflected in the European Water Framework Directive. Global change effects are investigated in various research programs. The changing of climate is not only a European problem, but also more a worldwide challenge. OSMOW will take advantage of these results and is aimed to develop strategies to react to extreme conditions, like floods and water shortages. Water as a transboundary resource needs common attention of neighboring countries or of those who share river catchments. A harmonized modeling concept for strategic water resource planning will contribute to improvements of guidelines, standardization and regulations. It also ensures that the guidelines are applied accordingly.

Declining availability of water is a profound problem, which is not only a result of reduced water supply, but also exaggerated by the continuing increase of water use for agriculture, industry, municipal demand, nature conservation, etc. These problems become evermore significant in many regions of Europe and worldwide, especially in CEE countries (Central and Eastern Europe).

On the other side of the spectrum extreme conditions related to an excess of water due to an increase of annual return periods are observed in the western part of Europe. Most practices are related to surface water. An important aspect of the proposed research project is to investigate the controlling possibilities of groundwater and the storage capacities of the unsaturated zone.

Due to human activities water quality (pollution) became a key topic for water provision and environmental conservation.

The problems stated above (floods – draughts – pollution) occur in different regions and under different hydrological and environmental conditions, but to cope with the effects for all an efficient management strategy is needed. Hence exchange of information and expertise between the regions in Europe has to be enforced. In particular this will emphasize the role of integrated water measurements and efficient water use strategies.

- By developing a harmonized modeling tool results are comparable and synergy effects are easily passed on.
- The establishment of benchmarks should contribute to unbiased analyses of the performance of the proposed strategies.
- The proposed strategies are set into operation by simulation for test regions, which are representative for Europe.

The project will utilize existing experience whenever available and will establish a knowledge resource that will be continuing beneficial after the present research program is completed. For the dissemination of results CD-ROM and other electronic means are utilized. The information collected in the created knowledge base will be accessible through Internet.

The scale of the project impact is potentially very large. Regional development in water scarce areas is highly dependent on available water resources. The efficient allocation of water is important as it maximizes the potential returns on water use economically and environmentally.

The research partners also see particular promise for the commercial exploitation of European expertise around the World. Solving the problems of rational water use in Europe will enable European organizations to utilize or adapt the techniques for other parts of the world – particularly developing countries where water-shortage is steadily increasing and represents a profound threat to the stability of the local environment and society.

6 SOCIAL ASPECTS

The natural, economic and social conditions of most countries in Europe and worldwide confront the society with the challenge to solve the problem of sustainable water resources management under dynamic changing conditions. These changing conditions may be a result of global change effects or due to human impacts. Strategic water resource planning utilized by operational methods contributes to mitigate negative effects of droughts (water deficiencies) or an excess of water (floods) in other periods of the year. In general, according to quantity and quality, water is considered to be a deficient natural product.

Water resources management in modern practice represents already an instrument for solving water economic and ecological problems in a rational way. Management tasks are related to surface and groundwater. Emphasize has to be paid between both resources in a catchment. An important role plays the movement of water in the unsaturated zone. The resource water is under continuous pressure of pollutants, due to various points and diffuses sources.

Copyright © 2003 Swets & Zeitlinger B.V., Lisse, The Netherlands

Sufficient amount of water of good quality is essential for the quality of life and health.

This will only be achieved if the resource water is treated as an European concern.

In a broader sense "operational management" includes all activities leading to a sustainable water regime. More specific, operational water management has to deal with predictions of water resources use in a catchment, monitoring and data processing, analyses of water resources changes and identification of response actions.

This has to be seen in a socio/economic context and interactions with water policy statements are foreseen.

The results of OSMOW will directly effect European and worldwide international social objectives by:

1. Maintaining rural livelihoods. By providing mentoring advice to water and agricultural organizations, the project output will help to improve food and water availability; preserve/enhance the environment and to provide employment. Improvement of Quality of Life and Health and Safety can be expected. It has been recognized in the Fifth Environmental Action Program that the abandonment of farmlands can have negative effects on the environment.
2. Expansion of EU by promoting and developing links between leading organizations in the existing EU that are interested in efficient water resource management (especially in regions with water shortage) and similar organizations in Central and Eastern Europe. The network will encourage better intra-European co-operation. This will ensure that relevant results and experiences within the community can be utilized – hopefully to the advantage of the pre-accession states.
3. Improvements directly developed in the CEE, which will be utilizable in many regions of the EU. This is a step towards equality of information access and opportunity in all countries of EU. The compilation of all the information from the various sub-topic networks into one integrated system will provide specialized knowledge to be readily accessible by professional colleagues in partner countries, thereby adding to the EC's net overall knowledge.
4. Improving agricultural production and maintaining the agricultural nature of regions in Europe. Better availability of technical information across the range of irrigation and drainage topics will help participants to better contribute to European efforts to improve yields and to limit effect of external impositions of drought and associated difficulties.

The project results will enable researchers and practitioners across Europe to share experience and skills, and then apply/adapt the benefits to their own respective countries or regions.

From an indirect point of view, the wasteful use of water has financial and economic consequences including the loss of rural livelihoods. In water scarce regions farm incomes are often very marginal and livelihoods are delicately balanced.

7 CONCLUSION

A deficit of water resources, unfavorable distributions of water in time and space, increasing water use, polluted water resources, variability and instability of climate and change of socio-economic activities demand rational ways of water management. The main objective is a methodology for effective operational water management under normal and extreme conditions of the water cycle. The research supplies solutions and tools to: evaluate the danger and vulnerability of an area; prevent damage; handle water supply and ensure quantity and quality of water resources; consider hydrological, meteorological, biological, biochemical and ecological influences; generate sufficient data; handle an interactive data base for interpretation and prognosis. A DSS requires a coupled analysis of all kinds of data to describe the long-term scenario of global and local changes. DSS improves co-operation and communication of involved parties in order to take action for controlling and steering.

Main milestones and expected results are: harmonized modeling concepts and data base for simulation of extreme conditions, simulation models including a graphical user interface, benchmarks to ensure comparable results and to provide a check of simulation performance, socio-economic and environmental restrictions. The result is a DSS as required by the new General European Guidelines regarding the controlling and steering of the water cycle to provide help to evaluate possible impact of actions.

Copyright © 2003 Swets & Zeitlinger B.V., Lisse, The Netherlands

Characterization and modeling of hydraulic property of fractured rock mass

A. Kobayashi
Graduate School of Agricultural Science, Kyoto University, Kyoto, Japan

ABSTRACT: Flow problem in a fractured rock mass is controversial for the recent environmental subjects, e.g., radioactive waste disposal and deep underground usage at urban area. The hydraulic aspect of fractured rock mass is, however, very difficult to understand differently from the soil ground because of the discontinuities existing in the rocks. In this paper, a characterization method of the flow problem in the fractured media is introduced and then the inference method of permeability distribution with the other data is presented. Lastly, the treatment of the scale effect of the permeability is discussed.

1 INTRODUCTION

Flow problem in a fractured rock mass is controversial for the recent environmental subjects. For example, the performance assessment of high-level radioactive waste disposal in deep geology has to be carried out by considering the characteristics of the hydraulic property of the surrounding rock mass (JNC, 1999). Moreover, the deep underground usage at urban area will be extensively carried out in Japan. The environmental problem is very important for the projects because the impact for the surrounding circumstance such as the subsidence due to the decrease in groundwater level has a significant effect on the urban life. Therefore, the prediction of the groundwater flow in a fractured rock mass is very important and the accuracy of the prediction has to be examined so carefully.

It is, however, very difficult to predict the flow in fractured media in general. This is because the flow is restricted by the discontinuities like cracks and fractures, of which locations and properties are difficult to identify. If we can understand the geometry and the mechanical and hydraulic properties of all the discontinuities, the entire flow regime may be realized by numerical method with high accuracy. It is, however, impossible in fact to get the data to infer enough the characteristics of the fractured rock mass. This lack of the information is the important uncertainties related to the geotechnical problem.

In general, the hydraulic characteristic of the ground is investigated by the permeability tests. The fracture characteristic is examined by the observation at outcrops and core examination. Since the boreholes are used for the in-situ investigation, the amount of the information is very restricted as a matter of fact. Therefore, we need some interpolation technique to infer the hydraulic property at the place where no permeability test is carried out.

At present, two major approaches exist to analyze the flow problem in the fractured rocks. One is the continuous one and another is the discontinuous one. The continuous approach needs to make the equivalent property to the real phenomena, in which groundwater flows though the discontinuities. The averaged permeability can be, however, measured directly by the in-situ test. On the other hand, the discontinuous approach aims at the model of pore through which water flows (Dershowitz et al. (1991)). In many processes of the discontinuous approach, the statistical model of fracture geometry is used to construct the pore structure.

If the discontinuous approach is used for prediction, it is necessary to make a statistical model of fracture geometry for the interpolation of hydraulic property. This process is firstly based on the geological investigation results. Then, the classification and statistical modeling of the discontinuities are carried out. The objective method is required at this process because the classification of the information has a large effect on the final model. In this paper, some suggestion for the classification of the statistical information is firstly presented.

In the case when the continuous approach is used, the hydraulic conductivity is used for prediction. Differently from the soil ground, the anisotropy and heterogeneity of the permeability is significant for the fractured rock mass. There are major two ways for modeling of the anisotropy. One is to use the hydraulic

Copyright © 2003 Swets & Zeitlinger B.V., Lisse, The Netherlands

conductivity tensor equivalent to the discontinuous field, e.g., Oda (1985). The other is to use the heterogeneous isotropic permeability distribution with some directional trend. From the point of view related to the numerical stability, the latter treatment is easy to handle. It is, however, impossible to investigate the full distribution of hydraulic conductivity. In many cases, the statistical method is applied to infer the spatial distribution of the permeability. Geostatistics is a useful method to make a heterogeneous permeability distribution. Kriging, Cokriging, Gaussian Simulation and Indicator Simulation (Deutsch and Journel 1992) have been used for hydrogelogical problems. Kriging and Gaussian Simulation uses only hard data, i.e., permeability data, while Cokriging and Indicator Simulation can use many other attributes, which is called soft data. In the case when the number of hard data is small, the method using the other attributes is very useful, while the accuracy is very dependent on the soft data. In this paper, the method to improve the estimation using the soft data is secondly introduced.

In association with the flow problem though fractured rock mass, the scale effect is also very important subject to treat the model. This is because the heterogeneity and anisotropy is significant and then the variation of the flow path pattern in the ground is changed with the scale. This is the important problem for solute transport because the mechanical dispersion is derived from the variation of flow path pattern. Thus, the dispersion coefficient has a large dependency on the scale. In this paper, the treatment of the dependency of the permeability on the scale is finally discussed.

2 CHARACTERIZATION OF FRACTURE GEOMETRY INFORMATION

As mentioned above, for the discontinuous and continuous model using the fracture geometry information, the results of joint survey have been used to develop the flow path network for a numerical modeling. Each geometric property, i.e., direction, largeness and aperture, is treated independently in many cases. This is probably because the relation between properties is difficult to be clarified from the survey results. The hydraulic conductivity is, however, related to the entire system of flow path structure, i.e., the combination of the hydraulic aperture of each fracture and the geometry of fracture network. In this section, a method to infer the relation between hydraulic aperture and length is presented (Kobayashi et al. (2000))

Although it is impossible to grasp the full flow pattern in the ground, we can evaluate the flow pattern at the field by using the general flow model proposed by Barker (1988). This model considers the flow aspect by the real number dimension. In the procedure, the real number dimension is found by fitting the type curves of real number dimensions with the observed result and then the hydraulic conductivity and specific storage are calculated at the meeting point in the conventional way of the well problem. If high flow dimension close to three is obtained, water may flow homogeneously in the ground. On the other hand, the small dimension close to one shows the biased flow situation. By using this method, the relation between the hydraulic conductivity and the dimension can be obtained, which correlation is related to the geometry of the flow network and hydraulic properties of flow paths.

In this section, firstly an example of the result obtained from the general theory by Barker is introduced. Secondly the characteristics of hydraulic properties of fractures are examined with the discontinuous fracture network model. This model uses the statistical properties of fracture geometry. Through the parametric study for the aperture distribution, the variety in the relation between flow dimension and hydraulic conductivity is tested. The characteristics of the fracture properties to represent the real behavior is examined.

2.1 *General theory*

Firstly, the general theory by Barker is briefly introduced. The continuity equation of ground water flow in the rock mass from the injection hole is given as following by Barker:

$$\frac{1}{\alpha_1}\frac{\partial h}{\partial t} = \frac{1}{r^{n-1}}\frac{\partial}{\partial r}\left(r^{n-1}\frac{\partial h}{\partial r}\right) \tag{1}$$

where α_1 is K_f/S_{sf}, in which K_f is the hydraulic conductivity and S_{sf} is the specific storage of the fractured rock mass. n is the real number dimension between 1 and 3, h is the total head in the rock mass and r is the distance from the central point of the injection hole.

The conservation equation in the injection hole is given as

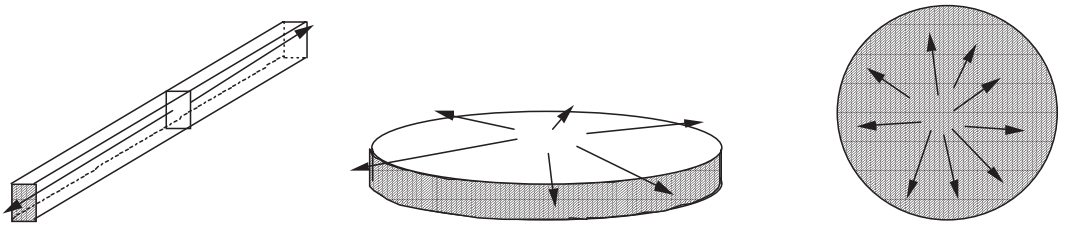
$$S_w\frac{\partial H}{\partial t} = Q + K_f b^{3-n}\alpha_n\, r_w^{n-1}\left.\frac{\partial h}{\partial r}\right|_{r=r_w} \tag{2}$$

where S_w is the storage capacity of the source which is given as πr_w^2, Q is the injection rate, H is the total head in the injection hole and r_w is the radius of the injection hole. α_n is given as

$$\alpha_n = \frac{2\pi^{n/2}}{\Gamma(n/2)} \tag{3}$$

where Γ is the gamma function. $b^{3-n}\ \alpha^n r^{n-1}$ implies the area through which the injected water goes in n dimensional way. Figure 1 shows the schematic view of the area given by this equation with some specific values of n.

Copyright © 2003 Swets & Zeitlinger B.V., Lisse, The Netherlands



(a) 1 dimension (b) 2 dimension (c) 3 dimension

Figure 1. Flow patterns of the different dimension.

Unfortunately, only the type curve for the limited condition of the constant rate test is introduced in the Barker's paper. The constant pressure test like Lugeon test is more popular in Japan than the constant rate test. The type curve has to be derived to analyze a constant head test. Kobayashi et al. (1998) introduced the type curve for the constant pressure test by using Laplace transform.

2.2 *In-situ hydraulic test and examination results*

Japan Nuclear Cycle Development Agency (JNC) has conducted the activities of geoscientific R&D program at Kamaishi mine in order to understand the deep geological condition (PNC (1996)). The bedrock in the area consists of Paleozoic sedimentary rock, Cretaceous sedimentary rock, and igneous complexes. The test site is located at the drift 550 m above the sea level in the Cretaceous-age Kurihashi granodiorite. The overburden thickness at the test site is about 260 m. 7 boreholes are set. The length of each borehole is 8 m. By using the boreholes, the constant pressure test is carried out at the several depths of each borehole. The constant rate test is also carried out for some boreholes.

Figure 2 shows the examination result of the relation between hydraulic conductivity and dimension. It is found from the figure that the flow dimension has the positive correlation to the hydraulic conductivity. The dimension and permeability obtained from the constant rate test are mostly similar to the ones by the constant pressure test.

2.3 *Numerical examination and results*

The discontinuous flow model is used to examine the characteristics of the fracture system. This model is fundamentally the same as the one like FracMan (Dershowitz (1994)). The statistical information of fracture geometry is used to realize the fracture network. The shape of the fracture plane is assumed to be a circle. The intersecting planes are obtained by geometric calculation, and the points connecting to the other fracture plane are gotten on each fracture plane. The finite element discretization of each fracture plane is

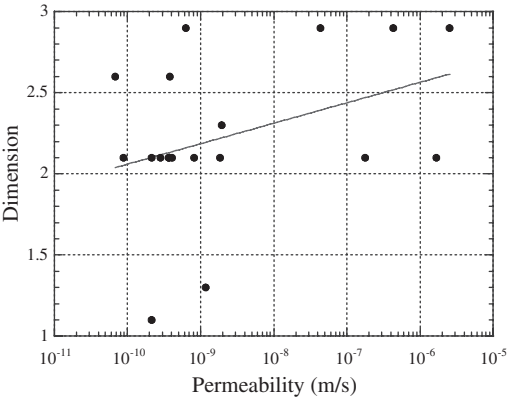


Figure 2. Relation between measured dimension and hydraulic conductivity.

carried out by Delaunay triangulation method (Sloan (1987)).

While the statistical information on the fracture length and direction can be obtained from the in-situ investigation, the aperture information is inferred from the hydraulic test in many cases. This is because of the difficulty to measure the aperture directly at the in-situ investigation. Thus, the parametric study on the aperture distribution is carried out to find the model realizing the relation between the dimension and permeability as shown in Figure 2. In the process, four cases are examined:

Case 1: Constant aperture case
Case 2: Lognormal distribution case
Case 3: Week exponential relation between aperture and length
Case 4: Strong exponential relation between aperture and length

The mean and standard deviation of the aperture are obtained from the permeability distribution by the single hole hydraulic test results. The permeability distribution is according to the lognormal one. The aperture is calculated by the cubic law from the

Copyright © 2003 Swets & Zeitlinger B.V., Lisse, The Netherlands

Table 1. Statistical data of fracture.

No. of set	1	2	3	4	5
Fracture density (No/m^3)	0.5847	0.2811	0.1455	0.3033	0.2637
Average fracture length (m)	1.50	1.65	1.86	2.18	1.81
Standard deviation	0.859	0.868	0.988	0.572	1.010
Average fracture aperture (m)	0.358E−4	0.358E−4	0.358E−4	0.358E−4	0.358E−4
Standard deviation	0.116E-3	0.116E−3	0.116E−3	0.116E−3	0.116E−3
Dip direction (°)	335.5	345.3	348.6	346.1	0.6
Standard deviation	57.4	91.9	168.9	129.2	48.3
Dip angle (°)	68.5	72.6	77.6	29.5	76.7
Standard deviation	11.7	13.6	7.1	18.1	13.4

measured permeability. Table 1 shows the statistical information obtained from the in-situ geological survey and hydraulic tests. The center of the fracture plane is located by Poisson's distribution, the fracture length is generated by the lognormal distribution, the direction is according to the normal distribution, and the aperture is according to the lognormal distribution in Case 2.

By using the statistical information shown in Table 1, the discontinuous model is produced with different random seeds. For the examination, about 30 realizations are generated. The region is 10 × 10 × 10 m. Water is injected at the constant rate of 10^{-4} m^3/s from the node that is located at the center of the region. All boundaries have a fixed total head of 10 m, which is mostly the same as the measured in-situ hydraulic pressure. The transient response at the injection node is calculated, and is used to determine the dimension and the permeability.

Thus, 30 values of the dimension and permeability are obtained for each case. By the assumption of the ergodicity, the fluctuations of 30 realizations mean the heterogeneous distribution of the region. Therefore, the relation between the dimension and permeability from 30 realizations is corresponding to the measured relation.

Figures 3 and 4 show the results of Cases 1 and 2. Case 1 has the constant aperture for each set. The aperture is the same as the mean values shown in Table 1. On the other hand, Case 2 has the lognormal distribution of the aperture. It is found that the dimension of Case1 is smaller than that of Case 2, and that the large negative correlation is shown in Case 2. The tendencies of both cases are different from the real one because both have negative correlation. In Case 3, the correlation between aperture and length (diameter) is assumed as

$$(\text{Aperture}) = (\text{Mean aperture}) \times \exp\left[2\frac{(\text{Diameter}) - (\text{Mean diameter})}{(\text{Mean diameter})}\right] \quad (4)$$

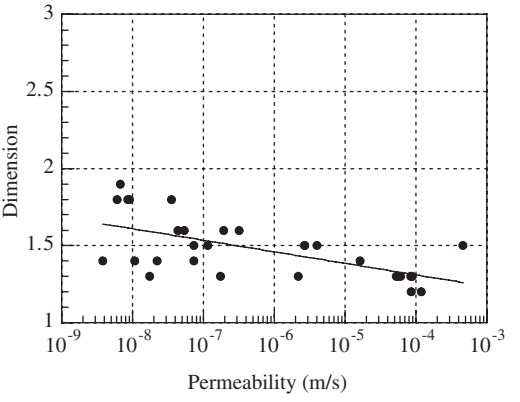


Figure 3. Result of Case 1.

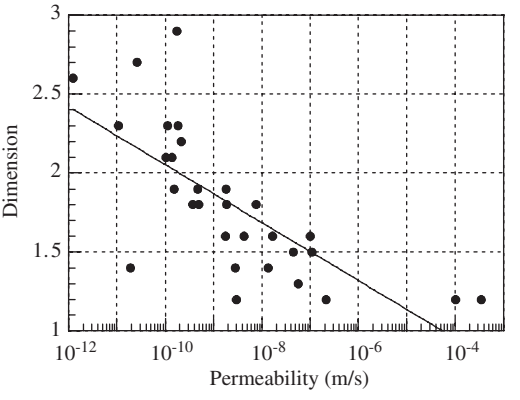


Figure 4. Result of Case 2.

For Case 4, the factor 2 in the exponent is replaced by factor 4. The maximum aperture is temporaly set at 1 mm. While the maximum value is truncated at 1 mm, the aperture under 1 mm is according to the lognormal distribution. Figures 5 and 6 show the relation between the aperture and length. The aperture of

Copyright © 2003 Swets & Zeitlinger B.V., Lisse, The Netherlands

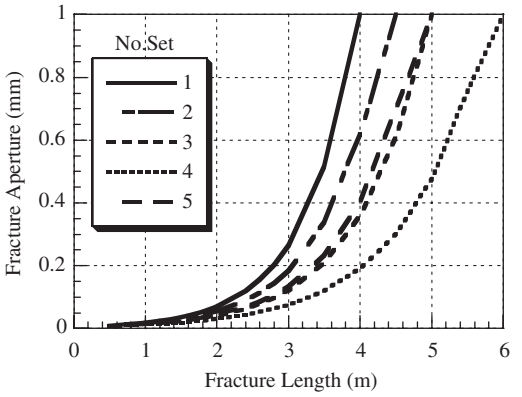


Figure 5. Relation between aperture and length of Case 3.

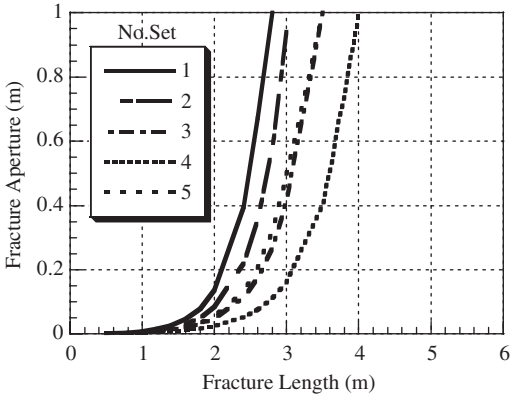


Figure 6. Relation between aperture and length of Case 4.

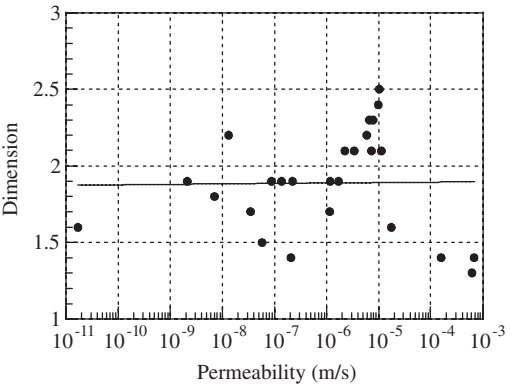


Figure 7. Result of Case 3.

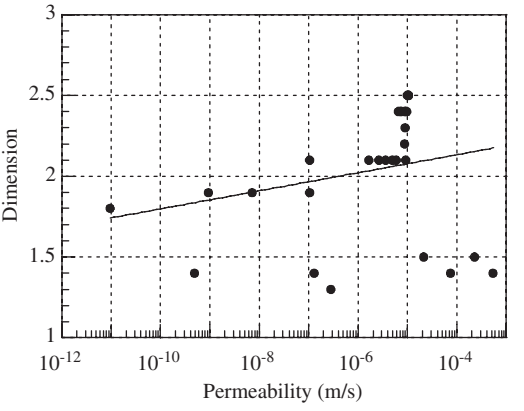


Figure 8. Result of Case 4.

Case 4 increases drastically with the fracture length. Figures 7 and 8 show the result of Cases 3 and 4, respectively. Both results have a positive correlation between the dimension and permeability. This is the same tendency as the measured one. It is found that the result of Case 4 has a larger positive correlation than that of Case 3, and the tendency of Case 4 is similar to the measured one.

2.4 *Conclusions*

In the case that the properties of fracture geometry have no correlation each other (Cases 1 and 2), the result has a negative correlation between dimension and permeability. This is the generally expected result. However, the measured relation shows the positive correlation. This indicates the possibility that the properties of fracture geometry have correlation each other. In the examination, the case that the aperture has a correlation with the fracture length is tested. This is because the other properties than the aperture can be measured at the in-situ survey, but the aperture is difficult to measure directly. The result shows that the correlation between dimension and permeability becomes realistic in the case that the aperture becomes large drastically with the increase in the length. Although the other factors to produce the positive relation between dimension and permeability may exist, it can be concluded that the properties of fracture geometry have a correlation each other in some way.

3 SOFT DATA TREATMENT

3.1 *Indicator simulation method*

In this section, the method of treatment of soft data is proposed. The soft data are used to infer the hard data at the point where the hard data, e.g., permeability, are not measured. Usually, the indicator simulation method is used for this purpose. Firslty, the method is

Copyright © 2003 Swets & Zeitlinger B.V., Lisse, The Netherlands

briefly introduced. In this method, indicator kriging is carried out to get the cumulative probability distribution function of the permeability at the non-measured point. This is a method of liner regression with indicator i of the measured hard data and indicator y of the measured soft ones, which is given by (Journel, 1989).

$$I_k^*(\mathbf{u}) = \left[\text{prob}\{z(\mathbf{u}) \le z_k(n+n')\}\right]_{IK} = \lambda_0 F(z_k) + \sum_{\alpha=1}^{n} \lambda_\alpha(\mathbf{u}; z_k)\, i(\mathbf{u}_\alpha; z_k) + \sum_{\alpha'=1}^{n'} \nu_\alpha(\mathbf{u}; z_k)\, y(\mathbf{u}_{\alpha'}; z_k) \quad (5)$$

in which the hard indicator data i originated from the hard data $z(\mathbf{u})$,which is the measured permeability in this paper, is written by

$$i(\mathbf{u}_\alpha; z_k) = 1 \quad \text{if } z(\mathbf{u}_\alpha) \le z_k$$
$$i(\mathbf{u}_\alpha; z_k) = 0 \quad \text{if not} \quad (6)$$

This means that if the measured permeability is greater than a value of permeability z_k, indicator i equals 1, if not, i becomes 0. z_k $(k = 1, \ldots, K)$ are called the cutoff values. K is the number of cutoff values, $F$is the mean of z_k, λ_0 is the weight of F, $\mathbf{u}$ is the position vector, n is the number of the hard data, and n' is the number of the soft data. The soft indicator $y(\mathbf{u}_\alpha; z_k)$ is given by

$$y(\mathbf{u}_\alpha; z_k) = \text{prob}\{Z(\mathbf{u}_\alpha) \le z_k\} \quad (7)$$

which is the probability that Z inferred from the soft data is smaller than cutoff value z_k. The probability is obtained from the scattergram, which is the plot between the hard and the soft data measured at the same point as shown in Figure 9. The soft data are divided into a few groups, and the probability y is calculated for each z_k in each group.

λ_α are the weights applied to the n permeability samples, and ν_α are the weights applied to the n' soft data. While these are obtained by minimizing the square error of estimated values by using the covariance matrix of hard and soft data, the covariance of the hard data is also used for soft data for simplicity.

In the indicator simulation, the probability at non-measurement point is estimated by the kriging of the equation (5). The probability that Z are smaller than the cutoff value z_k is put in order, so that the cumulative probability at the point is given (Figure 10). A random number is generated from 0 to 1, and the permeability corresponding to the random number is obtained from the cumulative probability distribution. Then the same processes are carried out at the next non-measurement point to estimate the permeability. Thus we can make multiple heterogeneous spaces by means of the way

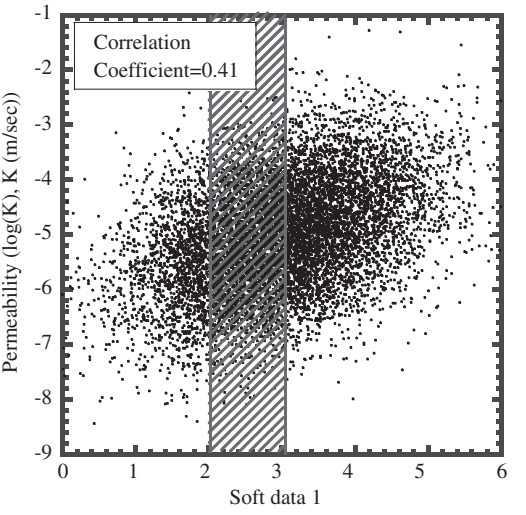


Figure 9. Example of scattergram.

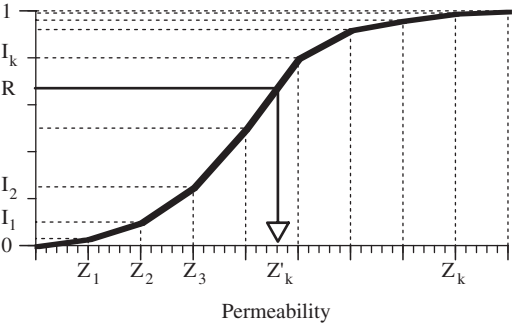


Figure 10. Cumulative probability distribution and estimation of the permeability.

to generate random number and the turn of the non-measurement points.

The method is clearly effective if the correlation between hard and soft data is high. In particular, it is important that the range of hard data in a group of soft data is small. This means that the range of permeability in Figure 10 is small. In that case, the range of the generated permeability is limited for the group of soft data. When the range is similar among the groups of soft data, the resultant permeability distribution is not so related to the value of soft data even if the probability distribution function of permeability for each group is different. Thus, the method to reduce the range of the hard data is important. In this section, the treatment of soft data is proposed for this purpose.

Copyright © 2003 Swets & Zeitlinger B.V., Lisse, The Netherlands

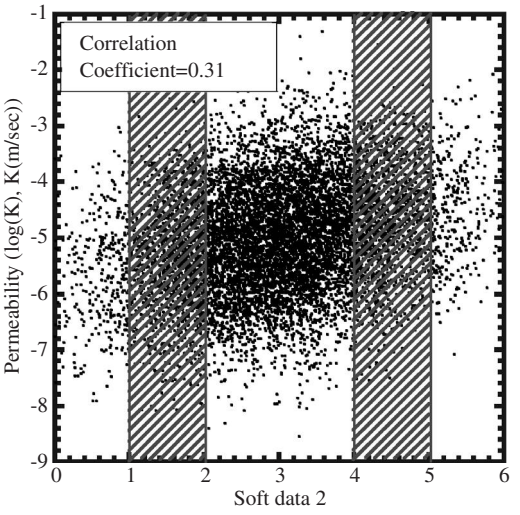


Figure 11. Scattergram of another soft data.

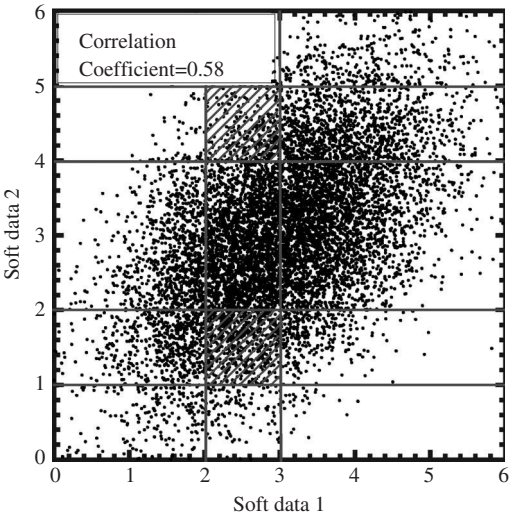


Figure 12. Correlation between soft data 1 and 2.

3.2 *Soft data treatment*

Figure 9 shows the exmaple of soft data, of which correlation coefficient is 0.41. As a matter of fact, the correlation coefficient between permeability and the other properties is not so high, and about 0.4 is the highest value of this. Figure 11 shows another hypothetical example of soft data, of which correlation coefficient is 0.31. Figure 12 shows the correlation between soft data 1 and soft data 2. In those examples, the correlation between soft data is assumed to be 0.58.

Usual indicator simulation uses the second soft data by adding the cumulative probability data as shown in Figure 10 to the location where the second soft data are measured (Deutsch and Journel, 1992). In this case, the range of the permeabililty of soft data 2 is the mostly same as that of soft data 1. Thus, the difference of generaged permeability for different soft data is very small. This kind of condition is a usual case because the permeability is measured at the same site. Moreover, since the properties are mostly obtained from the boreholes, the soft data are measured at the same location. As a usual case, the soft data having a higher correlation coefficient is selected.

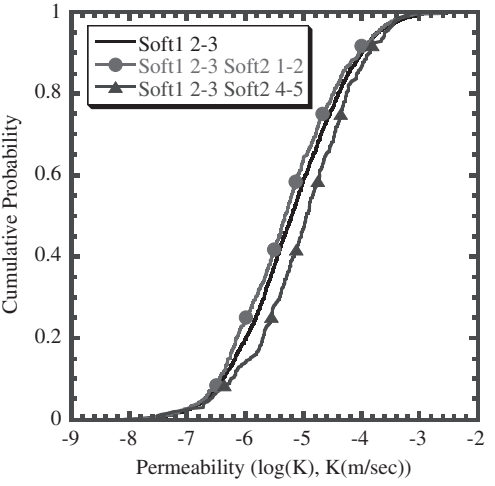


Figure 13. Cumulative probability of two soft data case.

In the examination, the soft data 1 and 2 are generated with the correlation as shown in Figures 10–12. Thus, the both data are assumed to be obtained at the same location. Firstly, the soft data 1 is divided by some groups. The example of cumulative probability of the group of soft data 1 of which range is from 2 to 3 is shown in Figure 13. In this case, the permeability, $\log(K)$, is from -2.20 to -8.55. To reduce the range of the permeability, the data of the group are selected by the group of soft data 2 as shown in Figure 12. Hatched area shows the group belonging to the soft data 1 between 2 and 3 and soft data 2 between 4 and 5 and between 1 and 2. By using the selected data, the cumulative probability is obtained as shown in Figure 13. For the group of soft data 1 between 2 and 3 and soft data 2 between 1 and 2, the permeability is from -2.51 to -8.07. That for the group of soft data 1 between 2 and 3 and soft data 2 between 4 and 5 is from -2.96 to -7.51. It is clearly found that the range of permeability of the group becomes narrow. This kind of treatment of soft data is very effective for the generation of the permeability distribution.

When the third soft data are obtained, the same treatment can be carried out and the range of permeability

Copyright © 2003 Swets & Zeitlinger B.V., Lisse, The Netherlands

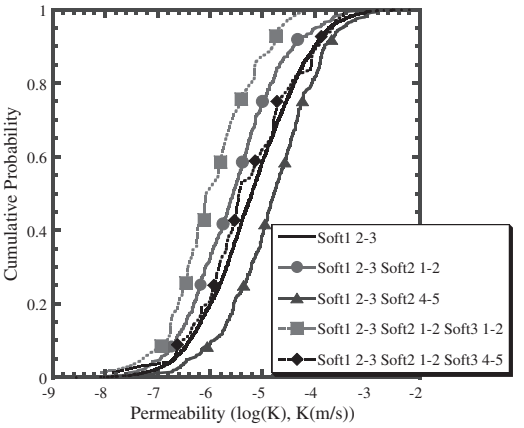


Figure 14. Cumulative probability of three soft data case.

can be reduced even if the correlation between third soft data and permeability is small. Figure 14 shows the cumulative probability for three soft data case. In this case, the third soft data has a correlation coefficient with permeability of 0.19. The range of permeability is from −4.18 to −8.07 and from −3.44 to −7.84.

By using this kind of treatment of soft data, the indicator simulation can generate the limited range of permeability at the point where no hydraulic test is carried out.

4 MODELING OF SCALE EFFECT

As information on hydraulic properties of rock mass, the statistical data on permeability and the geometric information of fractures can be used. The data are, however, related to the relatively small region, e.g., a few meters in a borehole. Thus, the hydraulic property of the large area has to be estimated when the flow in a large region has to be examined.

If the analysis region is small, the effects of the flow path geometry are very intensive, and so the location, direction and largeness of the fractures are necessary to be modeled concretely. When the area becomes large, it becomes difficult to give the concrete geometry of each fracture into the model. For a discontinuous approach, cutting off of small fractures is needed and relatively large fractures are modeled. For a continuous model, the property conformable to the region size has to be estimated. However, it is difficult to examine the behavior of analysis region with a homogeneous property. Thus, the analysis region is, in general, divided by the elements having heterogeneous property. The element size cannot be made small to express explicitly the effect of the fracture geometry. Then, the element property has to be obtained from some homogenization method. Moreover, the statistical treatment for homogenization is, in many cases, carried out because of the uncertainty of the parameter distribution. In a stochastic continuous model, the effect of spatial variation of the permeability is presented by many realizations of the possible distributions through the ergodic hypothesis. In this section, the stochastic continuous model is focused on. The relation between the effective parameter and heterogeneous model is examined for the flow through the fractured media.

As a homogenization method of the small region influenced by the fracture geometry, the two-dimensional pixel method is used in this section. This is because the pixel method can treat all the fracture from small to large ones in the same manner. However, the smallest area called pixel is decided arbitrarily. To obtain the homogenized property of the small area consisting of many pixels, the averaged property is calculated under some boundary condition. Dagan (1979) showed that the geometric mean best approximated the effective hydraulic conductivity in two-dimensional steady flow when the variance of permeability is small. The variance of the permeability is, however, determined from relation between the flow path system and the region size. In this section, it is examined by using the real fracture information if the effective parameter coincides with the geometric mean for each size and if the variance is changed with the size. Then, the method to express the size effect is discussed.

Firstly, the fractures are generated in 150 m cube according to the fracture geometry information. The center horizontal section is considered as a reference plane. The reference plane is divided by 0.2 m squares, i.e. pixel. The number of fracture crossing each pixel is counted and the permeability proportional to the number of fracture is provided to each pixel. The size of homogenized area, sub-region, is 5 m, 10 m, 15 m, 30 m, 50 m and 75 m square. The sample of the sub-region is derived from the reference plane. The original plane is divided by square finite element mesh, of which size is coincident with above sub-region size. For example of 5 m sub-region case, the number of the samples is 900 ($= 30 \times 30$) and averaging is carried out for 900 samples. The effect of the scale is examined by the variation of the average homogenized permeability for different size of sub-region.

4.1 *Scale effect of permeability*

4.1.1 *Fracture generation*

3-D fracture distribution is realized through the assumption that the circle fracture is distributed randomly. The fracture length is considered from the maximum length of 250 m to the minimum of 0.5 m. The geometric information is given in Table 2, which is obtained at the Sellafield site, UK (Nirex, 1997). The

Copyright © 2003 Swets & Zeitlinger B.V., Lisse, The Netherlands

Table 2. Fracture data for scale effect examination.

Set	Mean dip (°)	Dip direction (°)	Max spacing vertical (m)	Mean spacing vertical (m)
Set 1	8	145	5.35	0.29
Set 2	88	148	2.21	0.26
Set 3	76	21	2.01	0.28
Set 4	69	87	3.54	0.31

length, i.e., diameter L, is distributed by the following distribution function;

$$f(L) = \frac{4 \times 10^6}{7653570} L^{-2.2} \tag{8}$$

The region size is $150 \times 150 \times 150$ m. Then the fracture intersecting by the horizontal plane existing at the center of the region is searched and the intersecting length of the fracture is calculated. The 3-D fracture is generated until the total length of intersection on the plane coincides with the density, N_{21}, which is calculated firstly from

$$P_{21} = 2.4 \cdot L_{\min}^{-1} \, (1/m) \tag{9}$$

Above density function and distribution function of length is estimated from the in-situ investigation. The total length of the fracture of arbitrary area, $L_m \times L_m$ (m^2), is obtained by

$$N_{21} = (P_{21} \times L_m \times L_m) \tag{10}$$

L_m is 150 m in this paper. Figure 15 shows the distribution of the pixel having more than on fracture in the 150×150 m region, which is corresponding to the distribution of fracture on the reference plane.

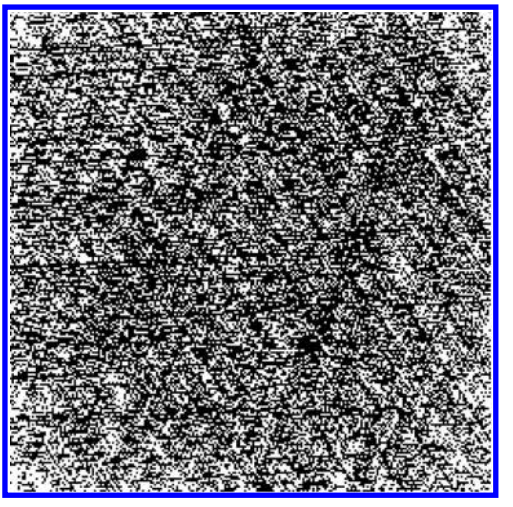


Figure 15. Distribution of pixel having more than one fracture.

4.1.2 *Conditions*

The plane is divided by the pixel of which side length is 0.2 m. The number of the fracture crossing each pixel, N_{frac} is counted. The hydraulic conductivity of each pixel, K_{Pixel} is calculated by

$$\log(K_{Pixel}) = \frac{N_{frac} - \mu_{frac}}{\xi_{frac}} \xi_{perm} + \mu_{perm} \tag{11}$$

where μ_{fac} is the average number of fractures in pixel, ξ_{frac} is its standard deviation, μ_{perm} is the average measured $\log(K)$ and ξ_{perm} is its standard deviation. The statistical information of permeability is given from the data of in-situ hydraulic tests. From this treatment, the distribution of the permeability of the pixel is mostly lognormal.

The hydraulic conductivity is assumed to be isotropic in a pixel and the value increases with the number of the fractures crossing the pixel. The region examined for scale-effect is 5 m, 10 m, 15 m, 30 m, 50 m and 75 m square, which is called sub-region in this paper. These sub-regions are derived from 150×150 m plane without superposition. The finite element mesh is, firstly, made for 150×150 m region with the same size as the sub-region. The sub-region coincides with an element as shown in Figure 16. The boundary condition is applied to realize the 1-D flow through the region, in which the side boundaries are set as no-flow condition. The vertical and horizontal flow is examined.

4.1.3 *Results*

The finite element simulation is carried out with 1-D flow condition. The pixel is treated as the element. For example, the case of 30×30 m sub-region has 22,500 ($= 150 \times 150$ pixels) elements. The equivalent permeability of a sub-region is obtained as an average velocity at the outlet boundary because of unit hydraulic gradient and the same element size.

Figure 17 shows the average horizontal hydraulic conductivity as a function of size. The standard

Copyright © 2003 Swets & Zeitlinger B.V., Lisse, The Netherlands

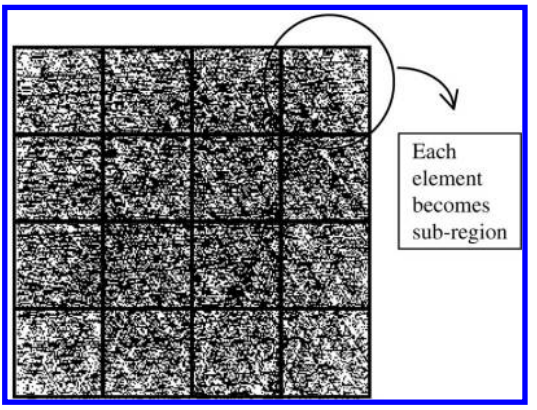


Figure 16. Sub-region is derived from a mesh of FEM.

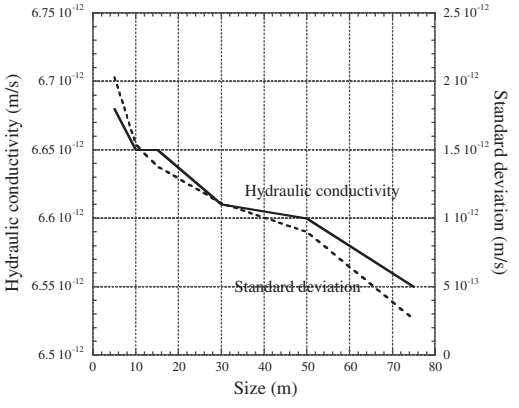


Figure 17. Horizontal directional hydraulic conductivity as a function of size. Dotted line; standard deviation, solid line; average.

deviation is also shown in the same figure. Figure 18 indicates the results for vertical direction. It is found from both figures that the hydraulic conductivity slightly decreases with size while the standard deviation decreases drastically. It is notable that the scale of the vertical axis is different between average and standard deviation. The small dependency of the average hydraulic conductivity on the scale is inferred from the fact that the average fracture length (diameter of the circle) is about 2 m. The scale dependency of the region larger than 2 m square may be caused from a small number of large fractures and heterogeneity of the fracture location.

While it is difficult that the size giving the stable hydraulic conductivity is determined from the present study, the scale effect of the hydraulic conductivity is very small in the case that the size is larger than 5 m square.

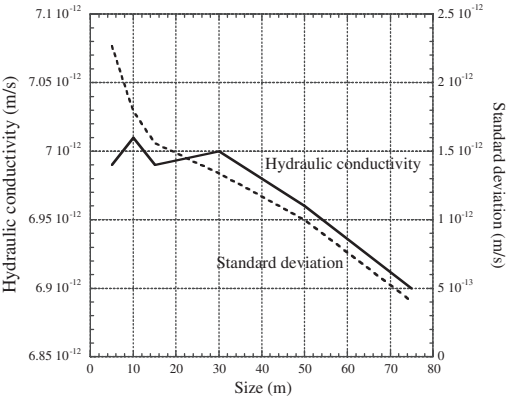


Figure 18. Vertical direction of hydraulic conductivity as a function of size. Dotted line; standard deviation, solid line; average.

4.2 *Effective parameter*

If the effective parameter can be defined as an equivalent parameter that produces an output variables that replicates the mean behavior of the system over the range of variability (Gomez-Hernandez and Gorelick(1989)), the permeability calculated for each sub-region is the effective parameter for each size. Moreover, it can be said from the above result that the effective parameter for each size is not so different for various sizes in this study.

The effective parameter is analytically examined for the steady two-dimensional flow by Dagan (1979). For low variance of hydraulic conductivity, the effective parameter coincides with the geometric mean. To check the pixel model, the results of 5 m and 30 m sub-regions are examined. Figure 19 shows the comparison between the effective hydraulic conductivity and the geometric mean of hydraulic conductivity of pixel for each element. For the case of 5 m sub-region, the effective parameter can be possibly presented by the geometric mean while the effective parameter of 30 m sub-region is larger than geometric mean. Table 3 shows the average and standard deviation of effective parameter and geometric mean of sub-region. It can be found that the average standard deviation of the effective parameter of 30 m sub-region is larger than that of 5 m sub-region.

4.2.1 *Modeling method of large region*

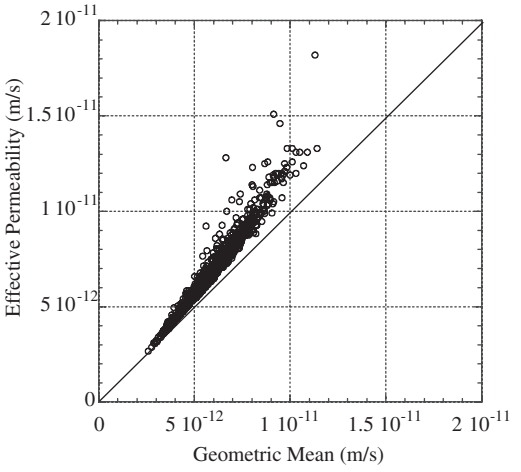
Then, the effective parameter of the large region consisting of sub-regions is considered. In general, the region is divided by elements and the element has a parameter value as a material property. In this process, the elemental value is decided from some homogenization method. The pixel method is one of the homogenization methods. There may be a scale

Copyright © 2003 Swets & Zeitlinger B.V., Lisse, The Netherlands

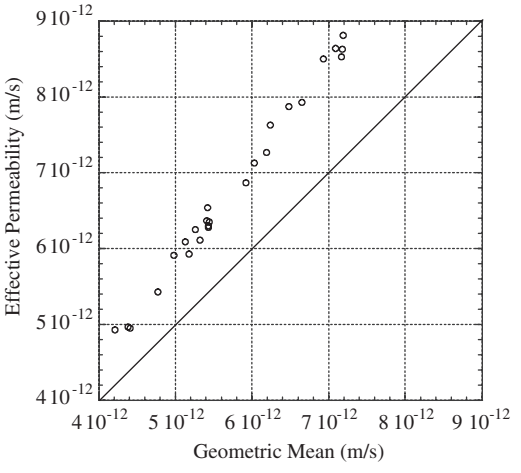
effect of parameter value, which scale effect is inherent for fracture system. However, the size of element is dependent on the size of structure and objective of the analysis, e.g., near or far field examination. Thus, the parameter value of an element has to be properly set for the size of element. Moreover, it is needed that the region divided by elements shows the property for its size.

In this section, the ability to represent the region as a group of elements is examined by testing the region consisting of sub-regions. The objective is to check if the effective parameter is represented by geometric mean. If the effective parameter is expressed by geometric mean, the region could be represented by the lognormal distribution of the elemental value because the average property is equivalent to the property of the entire region. The variation of the distribution can be realized by ergodic hypothesis.

Firstly, the entire region, 150×150 m, is divided by the sub-regions as shown in Figure 20. Each sub-region has an effective value corresponding to the location and size, which is obtained by the above



(a) 5m sub-region



(b) 30 m sub-region

Figure 19. Comparison between effective parameter and geometric mean for pixel model.

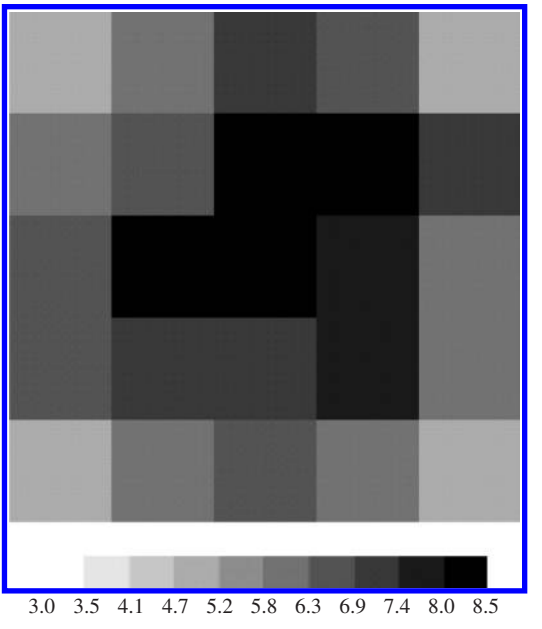


Figure 20. Entire region divided by sub-regions. Value is horizontal hydraulic conductivity ($\times 10^{-12}$ m/s). Examination is carried out with anisotropic hydraulic conductivity tensor.

Table 3. Average and standard deviation of pixel value.

Region size (m)	Average geometric mean K_g(m/s)	Average standard deviation of $-\log_{10}$ (K_{pixel}), $\sigma_{\log K}$	Average effective parameter (m/s)
5	5.86×10^{-12}	0.46	6.83×10^{-12}
30	5.75×10^{-12}	0.49	6.81×10^{-12}

Copyright © 2003 Swets & Zeitlinger B.V., Lisse, The Netherlands

Table 4. Effective value and various means ($\times 10^{-12}$ m/s) Kx; horizontal, Ky; vertical direction.

Sub-region size (m)	Direction	Effective value	Geometric mean	Harmonic mean	Arithmetic mean
5	Kx	6.46	6.39	6.12	6.68
	Ky	6.72	6.66	6.37	6.99
10	Kx	6.50	6.48	6.30	6.65
	Ky	6.80	6.79	6.57	7.00
15	Kx	6.52	6.50	6.35	6.65
	Ky	6.82	6.81	6.64	6.99
30	Kx	6.53	6.52	6.43	6.61
	Ky	6.87	6.88	6.76	7.00
50	Kx	6.54	6.54	6.48	6.60
	Ky	6.89	6.89	6.82	6.96
75	Kx	6.55	6.54	6.54	6.55
	Ky	6.89	6.88	6.87	6.90

Table 5. Geometric mean and its standard deviation.

Size (m)	Geometric mean $-\log_{10}(K)$ m/s	Standard deviation of $-\log_{10}(K)$ m/s
5	11.18	0.126
10	11.18	0.104
15	11.18	0.094
30	11.17	0.077
50	11.17	0.059
75	11.17	0.020

pixel method. The hydraulic conductivity of element is anisotropic, which is set with K_x and K_y from the pixel method and $K_{xy} = 0$. The same boundary conditions as the examination of sub-region are applied to the entire region. Table 4 shows the summarized examination results. Besides geometric mean, harmonic and arithmetic means are also indicated. The effective hydraulic conductivity in the case of 5 m sub-region is larger than the geometric mean. This is probably because of the large variance as shown in Figure 17. It is, however, concluded from the table that the geometric mean has a good agreement with the effective hydraulic conductivity. When the sub-region becomes large, the difference between various means becomes small because of the decreases of variance of hydraulic conductivity.

The correlation between elemental hydraulic conductivity is calculated as a function of distance. The correlation becomes zero at about 55 m for the cases of 5 m, 15 m, 30 m sub-region. Thus, the case of the size over 50 m sub-region shows no correlation between elements.

Table 5 shows the geometric mean of the mean hydraulic conductivity ($=(K_x+K_y)/2$) and its standard deviation for each case. It is found that the geometric mean is mostly constant for all the size while the variance becomes small with the increase of size. Thus, it can be said that the element smaller than 50 m square has the variance of hydraulic conductivity shown in Table 5 and the correlation length of 50 m, and the element larger than 50 m square has a constant hydraulic conductivity.

4.3 *Conclusions*

In this section, the method to provide the hydraulic conductivity to the element of the large region model is examined. As a result, the following procedure is recommended for a continuous model;

1. The effective hydraulic conductivity for a given size should have a distribution dependent on the fracture geometry. The entire region will be divided by the sub-regions having the effective hydraulic conductivity distribution. If the variance of the effective hydraulic conductivity is small, the geometric mean of the values of sub-regions is equivalent to the effective parameter of the entire region.

   In this process, the mean fracture length and fracture density are very important for giving the geometric mean equivalent to the effective parameter. If the mean fracture length is not so long and density is high as given in this study, the geometric mean of the pixel values coincides with the effective hydraulic conductivity of small sub-region.
2. The large entire region is divided by the elements for the finite element analysis. The statistical information of the effective hydraulic conductivity of the sub-regions is used to provide the hydraulic conductivity to the elements. Since the geometric mean coincides with the effective hydraulic conductivity, the lognormal distribution can be appropriate for the hydraulic conductivity distribution. Using a small size of element, the variance is large. Since the variance of the hydraulic conductivity and correlation between elements become small with the

Copyright © 2003 Swets & Zeitlinger B.V., Lisse, The Netherlands

increase of the size, the hydraulic conductivity for large element becomes constant.

5 CONCLUSIONS

In this paper, three topics related to the flow problem through a fractured medium are introduced. Firstly, the relation between geometric parameters of flow paths is examined by numerical analysis. Modeling of flow paths is to construct the hypothetical field conformable to the hydrogeological concept for the site. In such a process, the method tends to adjust the model for the measured data without physical ground. It is, however, very important for a model to conform to the various measured data. It is not admitted to make a model not backed by measured data even if the data are not enough. The first topic is an example of the way to consider the model from various points.

Secondly, the treatment method of soft data used for the indicator simulation is presented. This is not a new method, but a proper method to effectively use the soft data. This kind of methods reduces the cost of the in-situ investigation and makes the uncertainty of the data small.

Last topic is related to the concept of the modeling of large area. The answer for the scale effect is very difficult to verify. The method introduced in this paper is, however, probably reasonable one in two-dimensional field. For a three-dimensional problem, the effective parameter is shifted from the geometric mean. In this case, the variation from geometric mean has to be also modeled.

REFERENCES

Barker, J.A. (1988). Water Resources Research, Vol. 24, No.10: 1796–1804.

Dagan, G., Water Resources Research, Vol. 15, No.1, pp. 47–63, 1979.

Dershowitz, W., Wallmann, P. and Kindred, S. (1991). Stripa Project Technical Report 91–16, SKB.

Dershowitz, W., Lee, G., Geier, J., Hitchcock, S. and LaPointe, P. (1994). FRACMAN, User documentation, Golder Associates Inc., Redmond, WA.

Deutsch, D.V. and Journel, A.G. 1992. Geostatistical Software Library and User's Guide, *Oxford university Press*.

Gomez-Hernandez, J.J. and Gorelick, S.M. (1989). Water Resources Research, Vol. 25, No. 3, pp. 405–419,

JNC, (1999). H12: Project to Establish the Scientific and Technical Basis for HLW Disposal in Japan.

Journel, A.G. (1989). Fundamentals of geostatistics in Five Lessons, *Short Course in Geology*: Vol. 8.

Kobayashi, A., Fujita, T. and Chijimatsu, M. (1998). Soils and Foundations, Vol. 38, No. 4: 57–70.

Kobayashi, A., Hosono, K. and Fujita, T. (2000). Groundwater Updates, Sato and Iwasa (eds), pp. 381–386.

Nirex, (1997). Nirex Report SA/97/052.

Oda, M. (1985). Water Resources Research, Vol. 22, No. 13: 1845–1856.

PNC (1996). HYDRAULIC TESTS, PNC TN8410 96-058.

Copyright © 2003 Swets & Zeitlinger B.V., Lisse, The Netherlands

Dewatering at excavation sites

Copyright © 2003 Swets & Zeitlinger B.V., Lisse, The Netherlands

Construction management to secure the water sealing function of underground LPG storage cavern tanks

H. Megumi, K. Shibata & K. Baba
Japan Liquefied Petroleum Gas Storage Co., Ltd., Tokyo, Japan

T. Tobase
Electric Power Development Co., Ltd., Tokyo, Japan

ABSTRACT: National Liquefied Petroleum Gas (LPG) Reserved Bases, consisting of water sealing type underground LPG storage cavern tanks, are constructed at Namikata in Ehime Prefecture and at Kurashiki in Okayama Prefecture. A water sealing type underground LPG storage cavern tank stores LPG safely by preventing it from leaking by maintaining the groundwater pressure around the rock cavern that is higher than the internal pressure of the rock cavern. For this reason, both the Namikata and the Kurashiki bases were designed with an artificial water sealing system that forces the groundwater pressure to act on the rock around the rock cavern. In order for the water sealing to function normally, it is important to prevent the formation of an unsaturated zone around the rock cavern. The water sealing is performed at the construction stage and some items (Geological observation at the face, Groundwater level, Pore pressure, and Rate of seepage water) used to evaluate its effectiveness are monitored, and whenever these items are abnormal, countermeasures are taken immediately. This report presents an outline of the concept of construction management by integrating monitoring and countermeasures in order to secure the water sealing function of LPG storage cavern tanks.

1 INTRODUCTION

National Liquefied Petroleum Gas Reserved Bases consisting of water sealing type underground LPG storage cavern tanks are constructed at Namikata in Ehime Prefecture and at Kurashiki in Okayama Prefecture. Table 1 shows some specifications of these two bases.

The water sealing type underground storage cavern tanks stores LPG at normal temperature and high pressure in non-lining rock cavern, by preventing it from leaking by maintaining the groundwater pressure around the rock cavern at a level higher than the internal pressure of the rock cavern (water sealing principle, Figure. 1).

This report presents an outline of the concept of water sealing management during construction in order to secure the water sealing function of the LPG storage cavern tanks.

Table 1. Specifications of underground LPG storage cavern tanks.

Base name	Storage capacity (Rock cavern specifications)
Namikata base	Propane 300,000 tons (W26 m × H30 m × L490 m × 2) Butane 150,000 tons (W26 m × H30 m × L430 m × 1)
Kurashiki base	Propane 400,000 tons (W18 m × H22 m × L640 m × 4)

W: width, H: height, L: length

2 DESIGN OF THE WATER SEALING SYSTEM

To prevent the leakage of the LPG stored in the rock cavern, the water sealing system was designed so that the hydraulic gradient of the seepage towards the rock cavern satisfies the following condition of gas tightness and condition of liquid tightness.

- Condition of gas tightness: the vertical hydraulic gradient (Iv) at the cavern crown, that is the part of gas phase, is 0.5 or more.
- Condition of liquid tightness: the normal hydraulic gradient (In) at the cavern wall, that is the part of liquid phase, is 0 or more.

Copyright © 2003 Swets & Zeitlinger B.V., Lisse, The Netherlands

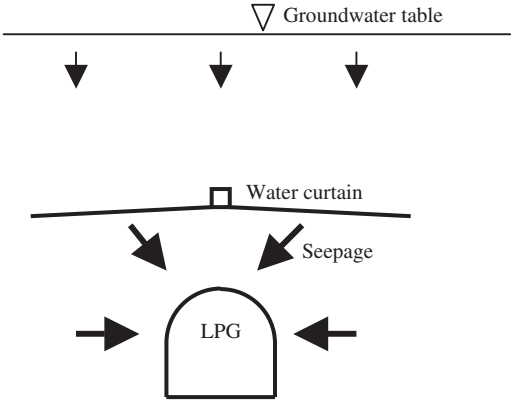


Figure 1. Water sealing principle.

At both the Namikata Base and the Kurashiki Base, an artificial water sealing system that satisfies the above conditions is used and a water gallery and water curtain boreholes are constructed. The role of the water curtain boreholes is to supply water to the joints around the rock cavern in order to generate the action of the stipulated water pressure. The water curtain boreholes are, therefore, designed so that it intersects the joints strike that are ascertained by a preliminary investigation. The hydraulic head of the water curtain and the critical groundwater level that satisfy the condition of gas tightness and the condition of liquid tightness are obtained by seepage analysis that modeled the rock cavern and the water curtain boreholes (here, critical groundwater level is the lowest groundwater level that can be permitted in order to satisfy the condition of gas tightness and condition of liquid tightness during operation).

In order for the water sealing system to function effectively, it is important to guarantee a stable groundwater level above the rock cavern and the necessary groundwater pressure around the rock cavern. However, during cavern excavation, the rock around the cavern is susceptible to become unsaturated. Once rock has become unsaturated, it is difficult to restore it to saturated condition by supplying water to the rock, and it is difficult to confirm its restoration. Therefore, during the construction work, a water gallery and a water curtain boreholes are installed to supply water before the excavation of the rock cavern in order to prevent the formation of an unsaturated zone around the rock cavern. Taking the Namikata Base as an example, Figures 2 and 3 show the results of performing vertical two-dimensional seepage analysis to judge how the groundwater levels differ when water sealing is and is not performed at the construction stage. As Figure 2 shows, when water sealing is not performed at the construction stage, the groundwater level is lower than the

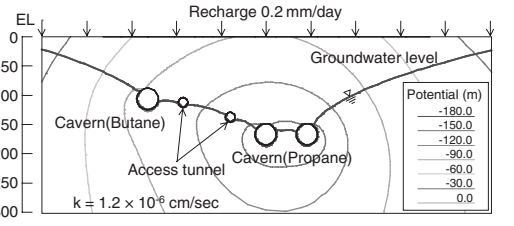


Figure 2. Ground water level without water sealing at the construction stage. (k; Average permeability coefficient).

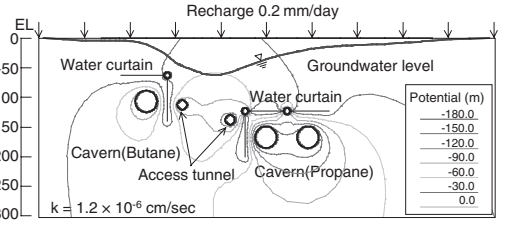


Figure 3. Ground water level with water sealing at the construction stage. (k; Average permeability coefficient).

rock cavern, and the rock around the rock cavern is in unsaturated condition. As Figure 3 shows, when water sealing is performed at the construction stage on the other hand, the rock around the rock cavern is covered with groundwater and its saturated condition is maintained.

3 MANAGEMENT OF WATER SEALING AT THE CONSTRUCTION STAGE

Water sealing management at the construction stage, which is necessary because the behavior of groundwater is known to be uncertain, is performed by monitoring some items that evaluate the effectiveness of water sealing at the construction stage and immediately taking countermeasures when these items are abnormal so that the water sealing system functions normally. Figure 4 shows the flowchart of water sealing at the construction stage.

3.1 *Monitoring*

3.1.1 *Geological observation at the face*

The actual joints strike and distributed density are confirmed by performing geological observations at the face of the water gallery, and reviewing the direction and interval of the water curtain boreholes whenever they differ from that hypothesized by the initial design. And the existence of a concentrated zone of fractures and the state of the seepage are confirmed by geological observations at the face of the construction tunnel and the rock cavern.

Copyright © 2003 Swets & Zeitlinger B.V., Lisse, The Netherlands

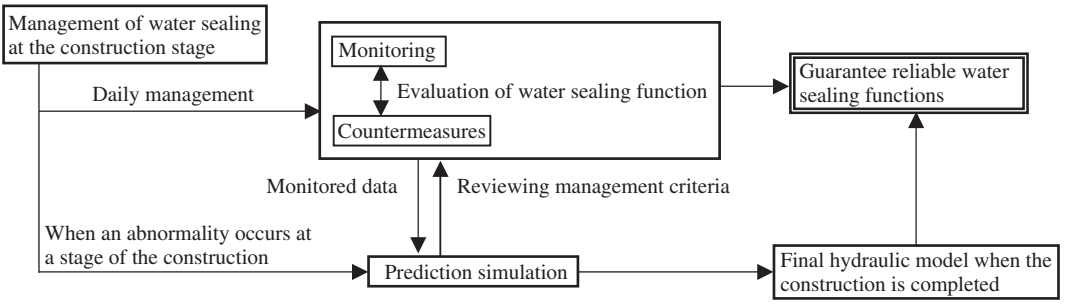


Figure 4. Concept of water sealing management at the construction stage.

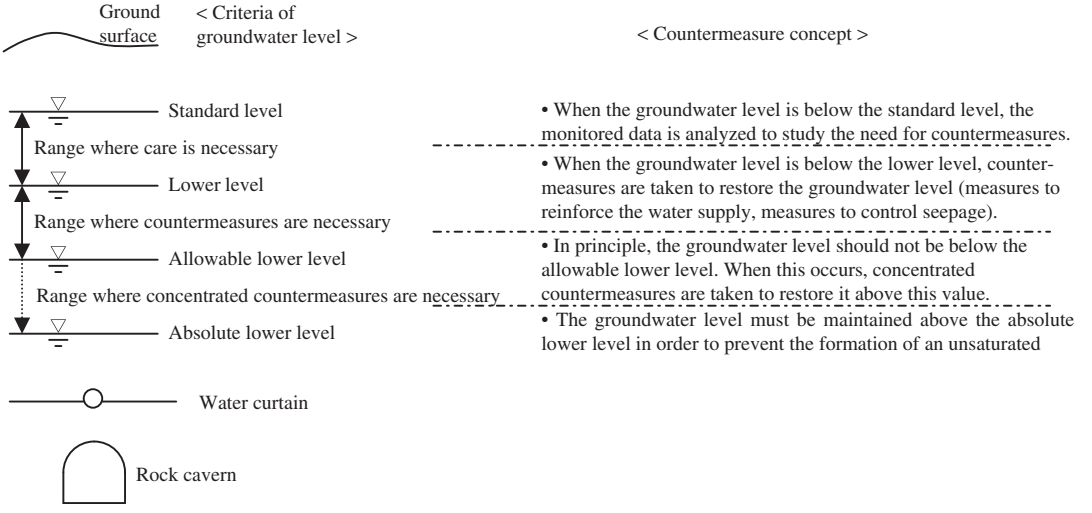


Figure 5. Criteria of groundwater level during construction.

3.1.2 *Groundwater level*

When the groundwater level is maintained at a high level during construction, the water sealing functions more effectively, but on the other hand, it worsens working conditions by, for example, increasing seepage into the rock cavern. The criteria of groundwater level during construction are set within a range where, even when the groundwater level has fallen at the construction stage, an unsaturated zone will not form around the rock cavern and it will be possible to quickly restore the groundwater level during operation. The criteria of groundwater level during construction are set at four levels: standard level, lower level, allowable lower level, and absolute lower level. Figure 5 presents the criteria of groundwater level during construction and the concept of the countermeasures to deal with each one.

3.1.3 *Pore pressure*

In contrast to the groundwater level that represents the water cover over a relatively wide area, the pore pressure represents the local groundwater pressure around concentrated zone of fractures and the rock cavern. Measuring pore pressure is, therefore, considered to be an effective way to monitor the state of the water sealing around a rock cavern. Pore pressure gauges were installed around the rock cavern to monitor changes in pore pressure accompanying the cavern excavation and to confirm that an unsaturated zone does not form.

3.1.4 *Rate of seepage water*

When a rock cavern or tunnel is excavated, seepage occurs, but if the rate of seepage water is excessive, the water balance might be disrupted lowering the groundwater level and obstructing the water sealing function. It is, therefore, important to clarify in advance if there is a concentrated zone of fractures or other location that will cause excessive discharge of seepage water. Therefore pilot boring from the face of a tunnel is done to confirm the state of the geology and seepage ahead.

Copyright © 2003 Swets & Zeitlinger B.V., Lisse, The Netherlands

Table 2. Construction management to secure the water sealing function during construction.

Monitoring items	Criteria	Countermeasures
Geological observation at face	When the joint strike or distributed density differs from the initial design	Optimizing the direction and interval of the water curtain borehole
Groundwater level measurement	When it is below the lower level (See Figure 5)	Hard-hitting measures for water supply (adding another water curtain borehole or raising the hydraulic head of the water curtain)
Pore pressure measurement	When localized pressure decline is observed	
Rate of seepage water measurement	When excessive discharge of seepage water from the pilot boring is observed (see Figure 6)	Restrictive measures for seepage water (pre-grouting)
	When excessive discharge of seepage water from the excavated section is observed	Restrictive measures for seepage water (post-grouting)

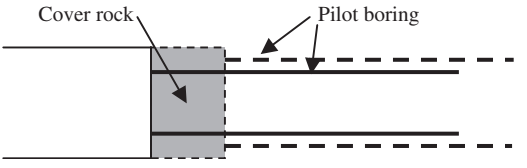


Figure 6. Pilot boring at the tunnel face.

The rate of seepage water in the tunnel is measured to designate locations where excessive discharge of seepage water will occur.

3.2 *Countermeasures at the construction stage to secure the water sealing function*

Countermeasures must be taken immediately if the results of the above monitoring conflict with the criteria shown in Table 2. Two types of countermeasures—hard-hitting measures for water supply and restrictive measures for seepage water—are considered, but it must be noted that these measures have contradictory characteristics. In sum, strengthening the water supply, by adding another water curtain boring for example, increases the seepage into the cavern, and grouting the joints to restrict seepage water reduces the effectiveness of supplying water to the joints. As basic concepts for countermeasures at the construction stage to secure the water sealing function, hard-hitting measures for water supply are applied to the water gallery and water curtain boreholes that are water sealing facilities, and restrictive measures for seepage water are applied to the construction tunnel and rock caverns that are on the side where seepage is discharged.

4 CONCLUSIONS

In order for the water sealing system to function effectively, it is important to guarantee a stable groundwater level above the rock cavern and to guarantee the necessary groundwater pressure around the rock cavern. Therefore, during the construction work, a water gallery and a water curtain boreholes are installed to supply water before excavation of the rock cavern in order to prevent the formation of an unsaturated zone around the rock cavern. Water sealing management at the construction stage is performed by monitoring some items (Geological observation at the face, Groundwater level, Pore pressure and Rate of seepage water) that evaluate the effectiveness of water sealing and immediately taking countermeasures when these items are abnormal so that the water sealing system functions normally.

When actual full-scale construction work begins, we will analyze and evaluate monitored data and take countermeasures at the same time as we work to expand the application of the concept of construction management to secure the water sealing function at the construction stage. This is to enable the construction of safer water sealing type underground LPG storage cavern tanks.

REFERENCE

Japan National Oil Corporation & Engineering Advancement Association of Japan (2000), Report on the study of the basic items included in construction management of water sealing type underground storage cavern tanks. (in Japanese)

Copyright © 2003 Swets & Zeitlinger B.V., Lisse, The Netherlands

Blow-out of soil particles during construction of a caisson type pile

T. Tanaka & S. Minami
Kobe University, Kobe, Japan

R. Matsuura
Dai Nippon Construction Co. Ltd., Osaka, Japan

ABSTRACT: This paper first reports a case history of blow-out of soil particles during construction of a caisson type pile. Countermeasures are also presented. Second, seepage flow analyses are carried out and stability with respect to boiling is investigated. Finally, the causes of the blow-out are considered, and the following results were then obtained: At the first-step excavation within sheet pilings, 11.0 m long, the safety factor with respect to boiling is equal to 3.43 and the base soil is very stable at the working platform level (G.L.-5.0 m). A caisson type pile was bored from the working platform. When the bottom of the bored hole approaches to the lowest level of the sheet piles (G.L.-11.0 m) and reaches the 8th ring (G.L.-9.0 m), seepage water concentrates in the bottom of the bored hole and the safety factor against boiling of the base soil becomes less than 1.0. It is thought that at this point boiling occurred and soil particles blew out.

1 INTRODUCTION

In an excavation of soil with a high ground water level, seepage failure of soil often occurs (Bauer 1984, Miura et al. 2000). There are still many questions to be solved in the seepage failure problem. Case studies on seepage failure of soil in real excavations are very important for understanding the seepage failure mechanism. This paper reports a case study on blow-out of soil particles during construction of a caisson type pile.

Figure 1 shows a plan view of the K-Line viaduct and piers in Kita-Kyushu District. Blow-out of soil particles occurred in the bottom of an excavation for caisson type piles for piers P2 and P3 (Fig. 1). Let us consider the pier P2, which stands on four caisson type piles A to D shown in Figure 2(a). For the caisson type pile C, excavation was made, liner plates of the 8th ring (or 4.0 m deep) were installed from the working platform level and the surrounding soil was improved with cement grouting with no trouble. During excavation for the 9th to 12th rings (or 4.5 to 6.0 m deep), bottom soil of the bored hole blew out. Figure 2(b) illustrates the section where blow-out of soil particles occurred at the bottom of the excavation for the P2(C) caisson type pile.

FEM seepage flow analyses are carried out for the conditions before and after the construction of the caisson type pile P2(C). Stability against boiling of the base soil during continuing excavation of the bore hole P2(C) is investigated precisely.

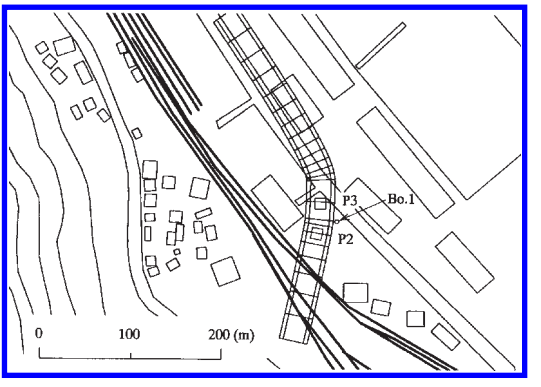


Figure 1. Plan view of the K-Line viaduct and piers in Kita-Kyushu District.

2 DETAILS OF EXCAVATION

A first-step excavation, 10.8 m wide, 10.8 m long and 5.0 m deep, was made within steel sheet pilings of type III (JIS A5528), 11.0 m long and with one level of a strut. From the base of the first-step excavation (or working platform level), a second-step excavation

Copyright © 2003 Swets & Zeitlinger B.V., Lisse, The Netherlands

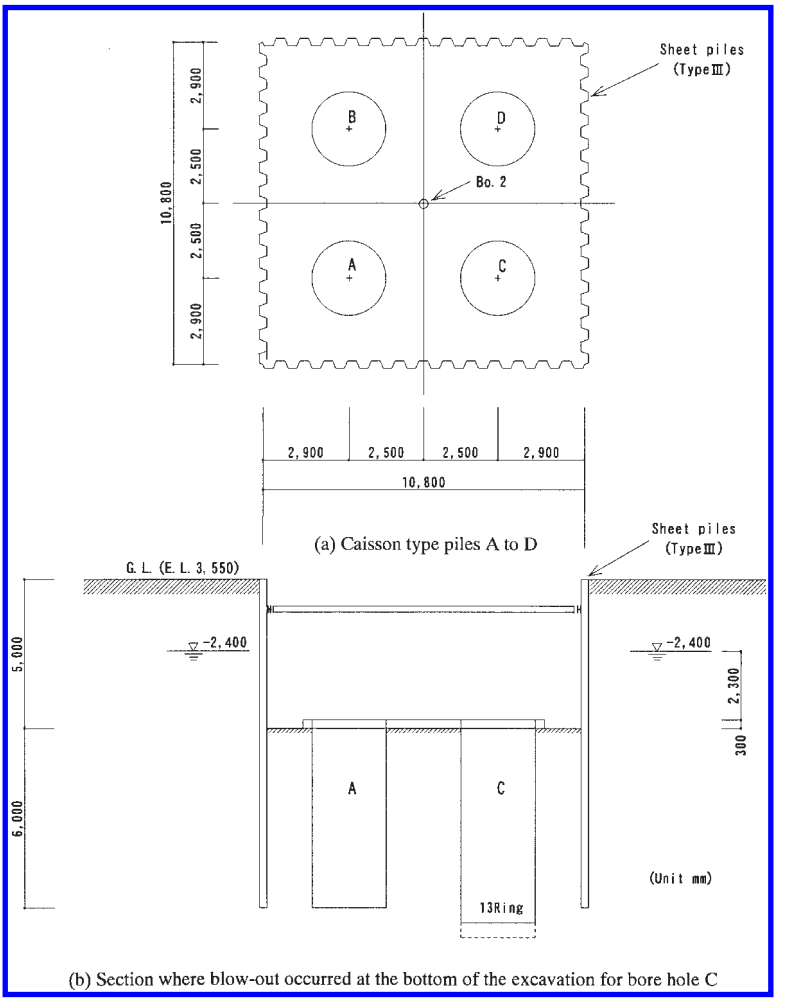


Figure 2. Bored holes for pier P2 and occurrence of blow-out.

(or a circular bored hole) for a caisson type pile was made with hand labor. Four bore holes were constructed by installing liner plates to the full depth of 27 rings (13.5 m deep). Each liner plate was 2.5 m in outer and 2.0 m in inner diameter, and 0.5 m high. These four bore holes with liner plates were then reinforced and concreted up to the working platform level.

A boring log obtained before construction showed that the soil was a weathered porphyrite with SPT N values (JIS A1219) greater than 50 and a coefficient of permeability of 2.53×10^{-7} m/s. The ground water table was 2.4 m below the ground surface. It should be noted that the boring pit was about 25 m distant from the pier construction site. It was judged from these values that construction of bore holes could be done easily by dewatering with a sump and using liner plates as a retaining structure. However, the soil was in fact weathered granite with SPT N values of 15–30 and blow-out of the soil particles occurred. Figure 3 shows the N values changing with depth before construction and after the occurrence of blow-out. It is observed from Figure 3 that the N values decrease from greater than 50 to 15–30 after excavation work for caisson type piles. It is thought that the soil surrounded by sheet piles was loosened due to concentration of upward seepage flow and the SPT N values dropped drastically. It should be noted that the boring logs before construction (Nov. 1992) and after the occurrence of blow-out (30 Dec. 1992) were obtained at locations 24.5 m (Bo.1 as shown in Figure 1) and 3.5 m (Bo.2 as shown in Figure 2(a)) distant from the center of P2(C), respectively.

Copyright © 2003 Swets & Zeitlinger B.V., Lisse, The Netherlands

3 OCCURRENCE OF BLOW-OUT OF SOIL PARTICLES AND COUNTERMEASURES

Figure 4 shows the excavation process, occurrence of blow-out of soil particles and rise of water level

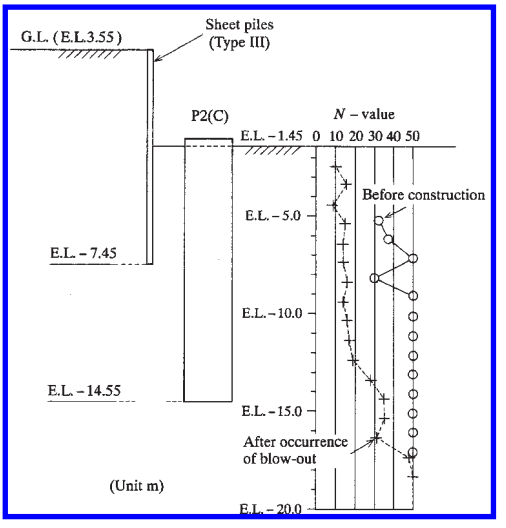


Figure 3. *N* values changing with depth before construction and after the occurrence of blow-out.

in continuing excavation of the caisson type pile P2(C). On 19th December 1992, P2(C) pile was excavated from the 9th to 12th rings and cement/water glass grouting (LW or Labiles Wasser-glass) was injected behind the liner plates. On 21st December 1992, the bottom of the excavation heaved up to about 1.5 m from the bottom. When the mechanical excavation for the 14th ring was finished and liner plates were installed, much water sprang out and successive excavation works had to be stopped.

Based on exploratory boring results, chemical grouting (or twin pipe grouting with flash setting solution) was adopted as a supplementary method with an improved width of 1.0 m and an injection rate of 32%.

On 19th January 1993, the excavation was made from the 14th to 20th rings, cement and water glass grouting (LW) was injected and the chemical grouting was made. On 20th January 1993, the bottom soil heaved up about 1.0 m and the depth of water was 2.0 m. Further excavation and chemical grouting were made between 21st and 22nd ring. But a lot of water sprang out. After completion of the 23rd to 25th rings and installation of the 26th ring, the soil behind the liner plates collapsed, the bottom soil heaved up seriously and the excavation work became impossible. The liner plates of the 14th to 19th rings were deformed. Dry mixing concrete of 40 cm thickness was installed. On 21st January 1993, the bottom soil

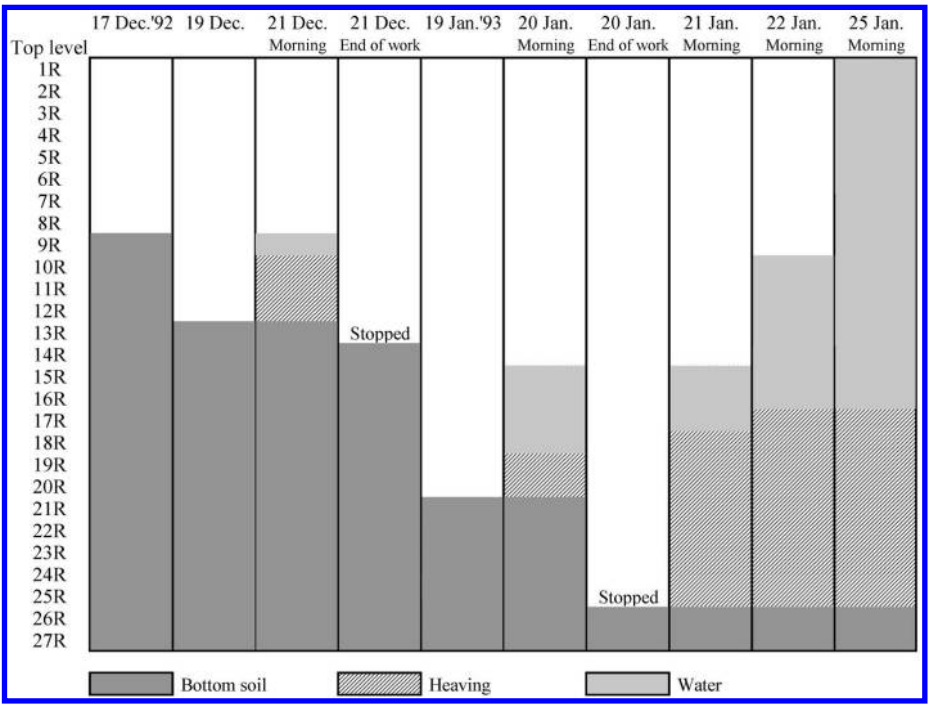


Figure 4. Excavation process, occurrence of blow-out and rise of water level in continuing excavation of caisson type pile P2(C).

Copyright © 2003 Swets & Zeitlinger B.V., Lisse, The Netherlands

heaved up 4.0 m and the water level rose 1.5 m above the bottom of the soil. On 22nd January 1993, the heaving of the bottom soil was 4.5 m and the depth of water was 3.5 m. On 25th January 1993, the water reached the first-step excavation level.

According to an engineering judgement, the bottom soil was improved with the CJG (Column Jet Grouting) method, the surrounding soil was reinforced with CCP (Chemical Churning Pile) method, and the caisson type pile was finally completed on 27th February 1993. Using the CJG method, the subsoil was improved 1.0 m deep and 2.0 m in diameter under the bottom of caisson type pile. Using the CCP method, the surrounding soil was also improved 1.0 m to 2.0 m thick from the outer boundary of the liner plates, and 1.0 m deep from the bottom of the pile with an injection rate of 28%.

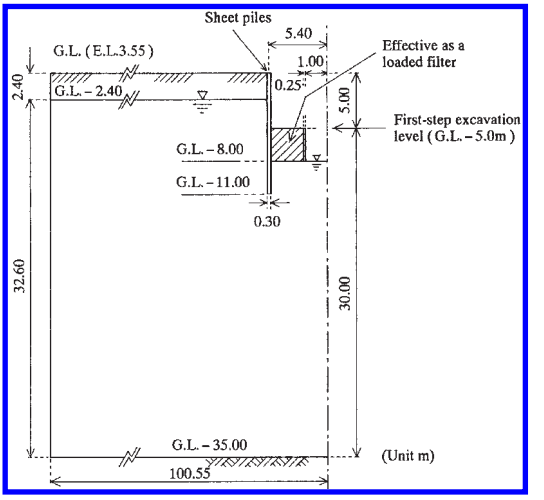


Figure 5. Region for analysis (the bored hole to the 6th ring).

4 SEEPAGE FLOW AND STABILITY ANALYSES

Now let us consider the seepage flow through soil during construction and the stability against boiling of the bottom soil in the first-step excavation and second-step construction of a bored hole.

4.1 *Seepage flow through soil during construction*

FEM seepage flow analyses were carried out and characteristics of seepage flow were discussed for the conditions of first-step excavation and second-step construction of a bored hole from the 1st to 12th rings. In the analyses, it is assumed that the construction site is in an axisymmetric condition and the circular hole for the caisson type pile is bored at the center of circular first-step excavation base as shown in Figure 5.

In construction of the liner plates, the surrounding soil between sheet piles and liner plates was loosened due to disturbance. Bored holes for P2(A), (B) and (D) were constructed somewhat after the P2(C) work of our interest. So it is thought that the ground water table decreased within the soil and was near the bottom level of excavation of bored holes for P2(C). In this paper, it is assumed that the water table within the soil surrounded by sheet piles of type III and liner plates was at the same level as the excavation bottom of the P2(C) bored hole. The coefficient of permeability of soil was 2.53×10^{-7} m/s, and the ground water table within the soil behind sheet pilings of type III was 2.4 m below the ground surface.

Figure 6 shows (a) finite element mesh with 5951 nodes and 5920 elements and (b) equi-potentials (each increment of potential 0.5 m from the base of the bored hole) for the first-step excavation. As shown in Figure 6(a), the mesh size is fine near the excavation where velocity vectors change drastically. Figures 7(a), (b), (c) and (d) show equi-potentials (each increment of potential 0.5 m from the base of the bored hole) for successive excavation of a bored hole to the 3rd, 6th, 9th and 12th ring, respectively. The hydraulic head drops between any two adjacent equi-potentials are equal to 0.5 m. So the closer the space of two adjacent equi-potentials comes, the larger the seepage velocity becomes. It is observed, from Figure 6 and Figures 7(a), (b), (c) and (d), that seepage flow concentrates more strongly in the excavation bottom of the bored hole with increasing depth.

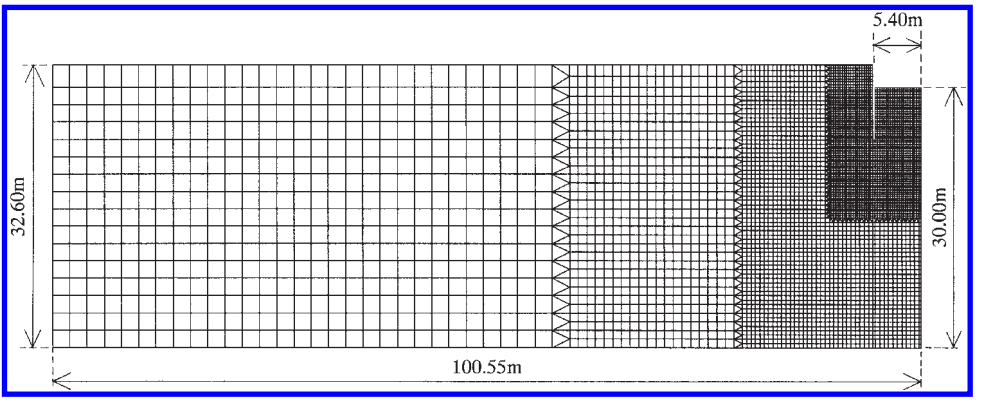
4.2 *Stability against boiling of bottom soil in excavation*

Stabilities against seepage failure of bottom soils in the first- and second-step excavation were analyzed and investigated. The drained soil surrounded by sheet piles and liner plates (or the portion illustrated by oblique lines in Figure 5) works effectively as a loaded filter. The soil under the portion is thus stable against an upward seepage flow. Only the bottom of a bored hole is susceptible to seepage failure. Here, we consider safety factors against seepage failure of the bottom soil of a bored hole, using Harza's method and the Prismatic failure concept.

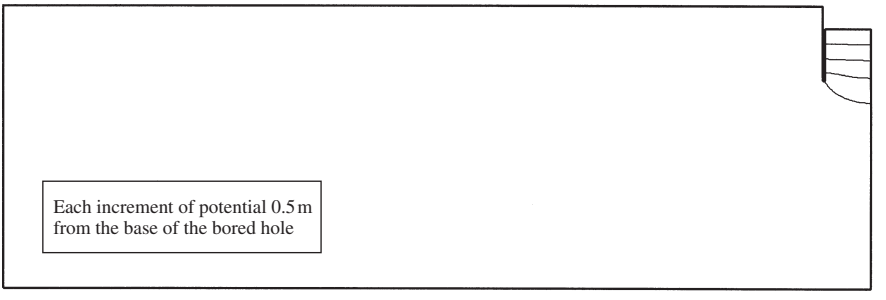
Harza (1935) thought the maximum exit hydraulic gradient is a problem at the downstream surface of seepage flow. The safety factor against boiling due to Harza F_H is defined as the ratio of the critical hydraulic gradient for boiling i_c to the maximum exit hydraulic gradient $i_{e\,\max}$, or

$$F_H = \frac{i_c}{i_{e\,\max}}. \tag{1}$$

Copyright © 2003 Swets & Zeitlinger B.V., Lisse, The Netherlands

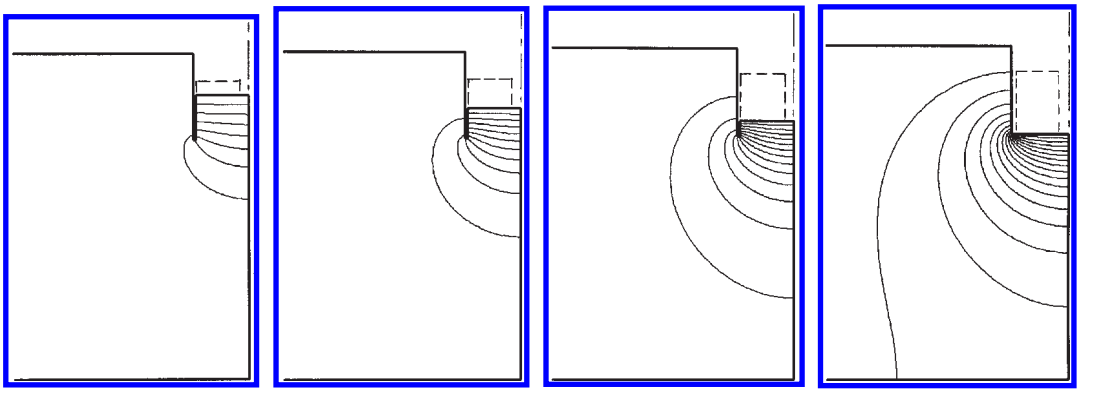


(a) Finite element mesh



(b) Equi-potentials

Figure 6. Finite element mesh and seepage flow through soil for the first-step excavation.



(a) 3rd ring (b) 6th ring (c) 9th ring (d) 12th ring

Figure 7. Equi-potentials for successive excavation (each increment of potential 0.5 m from the base of the bored hole).

The maximum exit hydraulic gradient $i_{e\,\max}$ occurs in an element adjacent to the inner surface of a liner plate.

According to the Prismatic failure concept (Tanaka & Verruijt, 1999), we assume that the body of soil lifted by seepage water has the shape of a prism with a certain height and width adjoining a sheet pile wall. The rise of a prism is resisted by the submerged weight W' and the frictions F_L and F_R on the left and right sides. The safety factor F_s with respect to the rise of the prism,

Copyright © 2003 Swets & Zeitlinger B.V., Lisse, The Netherlands

which is subjected to the excess pore water pressure on its base U_e, is given as

$$F_s = \frac{W' + F_L + F_R}{U_e}. \quad (2)$$

For a hydraulic head difference H between up- and downstream sides, safety factors F_s are calculated for all of the prisms in front of sheet piles. The safety factors F_s take a minimum value $F_{s\,\min}$ for a certain prism among all of the prisms. The calculation is iterated for another hydraulic head difference H until the condition that $F_{s\,\min}$ becomes equal to 1.0. $H = H_c$ at which the condition $F_{s\,\min} = 1.0$ is applied is defined as the critical hydraulic head difference. The prism giving a value of $F_{s\,\min} = 1.0$ is also defined as the critical prism. We could say the critical prism is separated from the underlying soil at its base when H exceeds H_c. Safety factors by the Prismatic failure concept are calculated for cases of considering no friction F_{PN} and considering friction F_{PF}. There was no difference between (No friction) and (Friction) for the case treated here. This is because the upward seepage flow through soil within sheet piles is nearly one dimensioned, so residual effective stresses vanish and no frictional resistances are exerted.

Figure 8 shows the relationship between the depth of excavation bottom of bored hole P2 (C) and safety factors with respect to seepage failure, according to Harza's method and the Prismatic failure concept. It is observed from Figure 8 that the two methods give just the same result. This is due to the one-dimensional upward seepage flow through soil within sheet piles as stated above. The bottom of the bored hole is stable against boiling for liner plates less than 7 rings, in which the depth of bored hole is 3.5 m under the first-step working platform level. When the excavation for the 8th liner plate is made, the safety factor becomes less than 1.0. This situation occurs a little bit earlier than that of the in-situ condition, where the bottom soil particles blew out during excavation for the 9th to 12th rings.

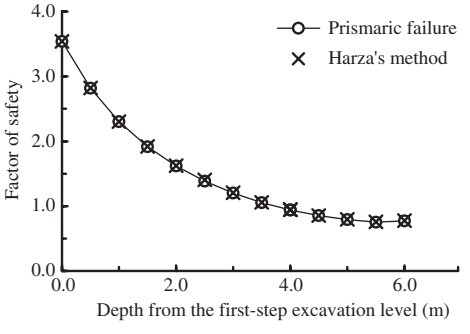


Figure 8. Relationship between the depth of excavation bottom of bored hole P2(C) and safety factor.

5 CONCLUSIONS

Blow-out of soil particles occurred at the bottom of an excavation for a caisson type pile at a K-Line Viaduct pier in Kita-Kyushu District. A first-step excavation was made with sheet piles with one level of a strut. From the base of the first-step excavation, a second-step excavation for a caisson type pile was made using hand labor. FEM seepage flow analyses were made and safety factors against boiling of bottom soils were investigated during successive excavations. The following results were then obtained:

1. At the first-step excavation, the safety factor with respect to seepage failure of base soil F_s is equal to 3.43 and so the first-step excavation base soil is very stable. As the bottom level of the bored hole becomes lower, the safety factor with respect to seepage failure F_s decreases.
2. When the excavation bottom of a caisson type pile approaches to the lowest level of the sheet piles and reaches the level of the 8th ring, seepage water concentrates in the bottom and the velocity grows large. The safety factor with respect to seepage failure of the bottom soil of the bored hole F_s then becomes less than 1.0. At this point, it might be thought that boiling occurred and soil particles blew out since the speed of soil-particle movement exceeds the speed of construction work of liner plates. The occurrence of the critical condition analyzed is a little bit earlier than that of the in-situ condition reported.
3. The in-situ soil properties are indeed quite different from the boring data obtained before construction, which means that it is difficult to comprehend soil properties correctly from a few bores.
4. It should be noted that the soil surrounded by sheet piles is loosened due to concentration of upward seepage flow and the SPT N values may drop drastically.

REFERENCES

Bauer, G.E. 1984. Dewatering, hydraulic failure and subsequent analysis of a sheeted excavation, *Proceedings of International Conference on Case Histories in Geotechnical Engineering*: 1415–1421.

Harza, L.F. 1935. Uplift and seepage under dams and sand. *Trans. of ASCE*, No.100: 1352–1406.

Miura, K., Supachawarote, C. & Ikeda, K. 2000. Estimation of three dimensional seepage force inside cofferdam regarding boiling type of failure, *Proceedings of the Geotech – Year 2000, Developments in Geotechnical Engineering*: 371–380.

Tanaka, T. & Verruijt, A. 1999. Seepage failure of sand behind sheet piles – The mechanism and practical approach to analyze –. *Soils and Foundations* 39(3): 27–35.

Copyright © 2003 Swets & Zeitlinger B.V., Lisse, The Netherlands

Three-dimensional numerical investigation of piping for excavations in cohesionless soils

F. Cai & K. Ugai
Gunma University, Kiryu, Japan

ABSTRACT: The stability against piping for excavations in cohesionless soils is usually predicted using Terzaghi & Peck's method. In this paper, three-dimensional finite element analysis of water flow through soils is used to predict the water pressure around excavations, and the calculated water pressure is used to evaluate the safety factor with respect to piping. Two case histories of piping are analyzed. The three-dimensional shape of excavations makes the water pressure higher than that of Terzaghi & Peck's method. Consequently, the excavations in cohesionless soils are on the dangerous side if the three-dimensional effect is not considered in design.

1 INTRODUCTION

Boiling is a common failure mode of retained excavations in cohesionless soils, and it occurs if the water head is sufficient to produce critical velocities. The safety factor with respect to piping is usually predicted using the method proposed by Terzaghi & Peck (1948). The method considered that hydraulic head linearly reduces on the two sides of the wall below the excavation base since the gravel rests on a bed of uniform sand, of which the level is the same as that of the excavation base. Symons (1983) proposed an equation to calculate the water pressure at the wall tip based on the assumption that the hydraulic head linearly reduces with distance around the wall from the water table position on the active side to the level of the excavation base on the passive side. These two methods did not consider the influence of the excavation shape on the water pressure. NAVFAC DM-7 (1971) supplies charts for determining whether piping may occur, where the excavation width is considered. Totally, the three methods were developed for two-dimensional situations. The three-dimensional effect of water flow around excavations increases the water pressure to make piping occur easily. Thus the water pressure of three-dimensional analysis of water flow around excavations should be used to predict piping in design if the excavation length is not large enough to consider the excavation as a two-dimensional case. Some case histories have indicated that piping occurred though it was considered to be safe based on the three above-mentioned methods for the two-dimensional situations.

In this paper, three-dimensional finite element analysis of water flow through soils is used to calculate the water pressure around excavations, and the calculated water pressure is used to evaluate the safety factor with respect to piping. The safety factor is defined as the ratio of the effective soil weight to the uplift load of the water pressure, which is identical to that in Terzaghi & Peck's method. Two case histories are analyzed using the three-dimensional finite element analysis of water flow through soils. The three-dimensional effect makes the water pressure higher than that of Terzaghi & Peck's method. This is just the reason why piping took place in the excavations that were considered to be safe based on Terzaghi & Peck's method.

2 FINITE ELEMENT ANALYSIS OF WATER FLOW THROUGH SOILS

The finite element analysis of water flow through unsaturated-saturated soils was used for the computations reported in this paper. Darcy's law has been shown to be valid for the water flow through unsaturated soils as well as the flow through saturated soils. The main difference is that the permeability is assumed to be constant for saturated soils, while it depends on the pore volume occupied by water for unsaturated soils.

The water flow in cohesionless soils is usually considered to be steady, so the soil-water characteristics and the specific moisture capacity of unsaturated soils are not necessary in the finite element analysis of

Copyright © 2003 Swets & Zeitlinger B.V., Lisse, The Netherlands

steady water flow through soils. The relative permeability, the ratio of the unsaturated permeability to the saturated permeability, of soils is assumed to be 0.001 if the ratio of the volumetric moisture content to the saturated volumetric moisture content, θ/θ_s, is smaller than 0.9, and to linearly increases to 1.0 with the increase in θ/θ_s from 0.9 to 1.0. The calculated results have indicated that such assumption for the permeability has neglect influence for the steady water flow through soils (Cai 2001). The assumption for the permeability is essentially identical to the constant mesh approaches (Desai 1976, Bathe & Khoshgoftaar 1979).

3 CASE HISTORIES

3.1 *Case one*

The case is reported in a Special Issue, Nikkei Construction (2001). The excavation has a length of 21.2 m, a width of 11.9 m, and a depth of 16.3 m, and the groundwater level is 4.8 m below the ground surface, as shown in Figure 1. The ground mainly consists of sand layer and sandy gravel layer, but the details are not reported in the Special Issue (2001). Sheet-piles are used as the retained wall, and are inserted 9.2 m below the excavation base. The length of sheet-piles is determined by the safety factor against piping, which is about 1.58 of Terzaghi & Peck's method. When the excavation is near the expected depth of 16.3 m, boiling occurred. The contractor had to use deep wells to draw down the groundwater level behind sheet-piles, and to stop boiling.

The three-dimensional finite element analysis is used to clarify the reason for boiling. Firstly, the water pressure in the ground is calculated, and then the safety factor with respect to piping is evaluated as in Terzaghi & Peck's method. Due to the symmetry, only 1/4 of the ground under the groundwater level is analyzed. The boundary conditions are as follows: the symmetrical faces and the faces close against the sheet-piles are impervious; the outer boundaries of the analyzed zone are of known hydraulic head; the excavation base is of known hydraulic head of which the pressure head is zero; the top surface of the mesh is also of known hydraulic head of which is the pressure head is assumed to be zero to compare with Terzaghi & Peck's method. The thickness of the soil layer under the wall, T, was assumed to be three times H for the soil layer of infinite depth. The distances from the outer boundaries to the center of the excavation are about 200 times the width, B, or the length, L, of the excavation, respectively, and they are consider to be enough to reflect the influence range of the groundwater. The two-dimensional analysis is firstly conducted for the cross section shown in Figure 1.

Figure 2 shows the contours of pressure head near the excavation for the two-dimensional analysis. The

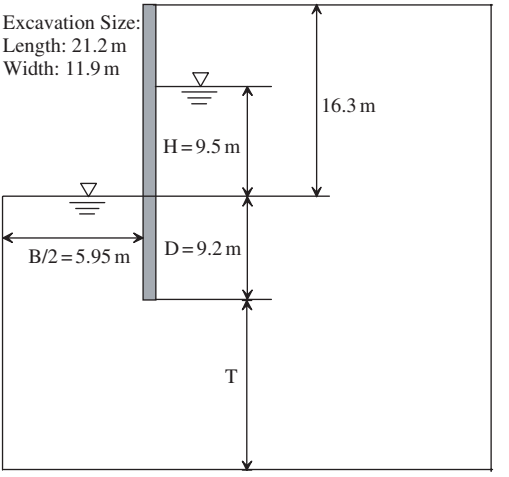


Figure 1. Geometry of Case 1.

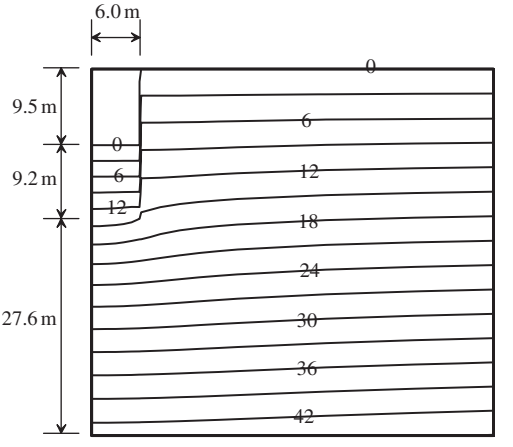


Figure 2. Contours of pressure head (m) for two-dimensional finite element analysis of the cross section shown in Figure 1.

maximum excess pore pressure, U_a, of 57.3 kPa is at the wall tip. Even for the two-dimensional analysis, U_a of finite element analysis is much larger than the value of Terzaghi & Peck's method and Symons' method. In Tergaghi & Peck's method, U_a is given by

$$U_a = \frac{\gamma_w H}{2} \tag{1}$$

where γ_w is the unit weight of water. Terzaghi & Peck's method implies that the loss of hydraulic head occurs only along the two sides of the wall inserted below

Copyright © 2003 Swets & Zeitlinger B.V., Lisse, The Netherlands

Table 1. U_a and safety factor against piping for Case 1.

Method	U_a (kPa)	Safety factor
Tergazhi	46.60	1.579
Symons	30.73	2.395
NAVFAC DM-7	–	1.49
FEM(2D)	57.27	1.285
FEM(3D)	76.71	0.959

the excavation base. The safety factor against piping is given by

$$F = \frac{\gamma' D}{U_a} \tag{2}$$

where γ' is the buoyant unit weight of soil.

In Symons' method, U_a is expressed as

$$U_a = \gamma_w \frac{HD}{H + 2D} \tag{3}$$

For Case 1, the calculated maximum excess water pressure U_a of the two-dimensional analysis by various methods and the corresponding safety factor against piping are listed in Table 1, where the buoyant unit weight of soil is 8.0 kN/m^3 (Special Issue 2001). The safety factor with respect to piping is larger than 1.0 for any two-dimensional methods, however, the safety factor is smallest when the maximum excess water pressure is calculated by the two-dimensional finite element analysis.

For Case 1, the thickness, T, of the soil layer under the wall tip, and the width, B, of the excavation is changed to clarify their influence on the water pressure around the excavation in two-dimensional situations. Figure 3 shows the influence of T and B on the maximum excess water pressure U_a at the wall tip. As shown by the open squares in Figure 3, the thickness, T, has slight influence on U_a when T is larger than $3H$ and when B is equal to the width of the excavation of 11.9 m. Thus the finite element mesh with $T = 3H$ used in analysis is large enough for cases where the pervious soil layer is of infinite depth. On the other hand, as shown by the solid squares in Figure 3, the smaller the width of the excavation, the higher the maximum excess water pressure U_a at the wall tip. Such influence is more significant when B is less than about $5H$. Even when B is about $10H$, U_a of the finite element analysis is still 1.3 times U_a of Symons' method. Thus the limited width of the excavation makes U_a increase. For Case 1, because the width of the excavation is only about $1.25H$, the two-dimensional finite element analysis gives a larger U_a than Terzaghi & Peck's method. As shown by the solid circles in Figure 3, U_a of the finite element analysis is approximately equal to Symons' method only when the thickness T is very small. The details of the influence of T on U_a for small thickness T are listed in Table 2.

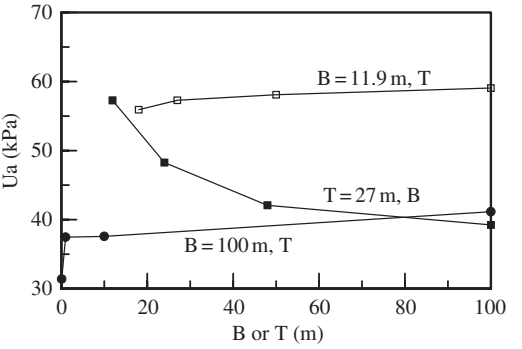


Figure 3. Influence of B and T on U_a of FEM(2D) for a fixed $H = 9.5$ m: open squares for $B = 11.9$ m and various T, soild squares for $T = 27$ m and various B, and solid circles for $B = 100$ m and various T.

Table 2. U_a (kPa) for various T and $B = 100$ m.

T(m)	Symons	FEM
1.0	30.73	37.47
0.5	30.73	37.28
0.2	30.73	35.32
0.1	30.73	31.39

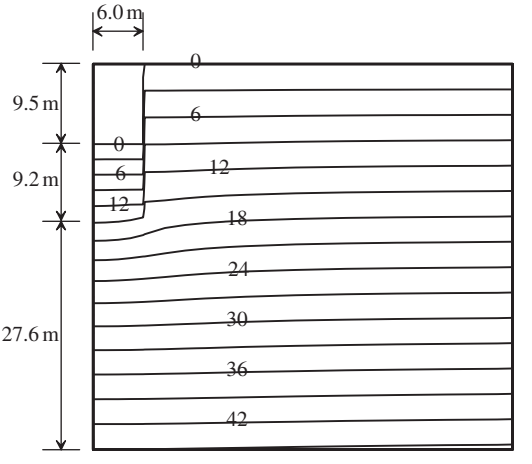


Figure 4. Contours of pressure head (m) for the symmetrical cross section of three-dimensional finite element analysis.

The three-dimensional finite element analysis of water flow around the excavation is conducted to consider the influence of the limited length of the excavation. Figure 4 shows the contours of the pressure

Copyright © 2003 Swets & Zeitlinger B.V., Lisse, The Netherlands

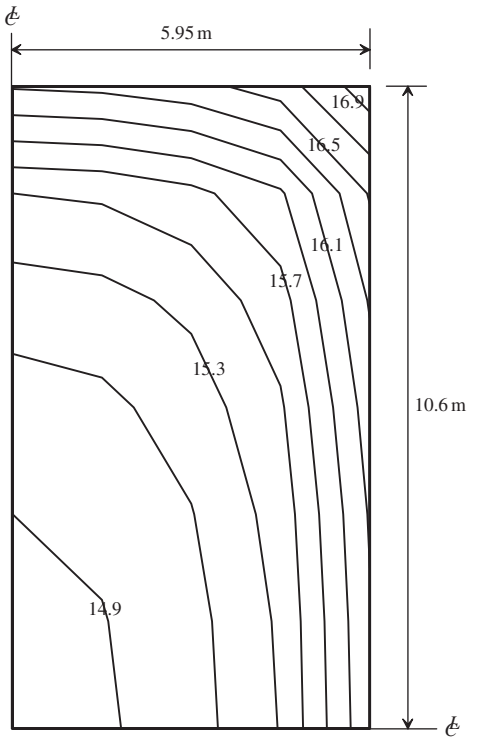


Figure 5. Contours of pressure head (m) for the horizontal section just below the excavation base at the level of the wall tip.

head for the symmetrical cross section. Comparing to that in Figure 2, the water pressure at the wall tip of the three-dimensional finite element analysis is significantly larger that of the two-dimensional finite element analysis. Figure 5 shows the contours of the pressure head of the horizontal section at the level of the wall tip. It is clear that the pressure head is highest at the corner of the wall.

The calculated safety factor with respect to piping for Case 1 is listed in Table 1. The safety factor of boiling is less than 1.0 only when the water pressure is calculated using the three-dimensional finite element analysis. This indicates that the three-dimensional finite element analysis of water flow through soils can reproduce the boiling that occurred in Case 1. Thus the three-dimensional effect on the water pressure around the excavation should be considered in design. For the present computers, the three-dimensional analysis of the water flow through soils does not take so long time, as an example, the three-dimensional finite element mesh has 11802 nodes and 9828 eight-nodal brick elements for Case 1, the calculation takes about ten minutes on the personal computer with a CPU speed of 1.8 GHz. There are now many commercial

Table 3. Physical properties of soils.

Soil	Gravel	Sandy silt
Specific gravity, G_s	2.657	2.659
Uniformity coefficient, U_c	21.84	7.02
D_{50} (mm)	3.87	0.219
Permeability, $k(10^{-4}$m/s)	2.82	0.463
Buoyant unit weight, γ'(kN/m^3)	11.49	9.17

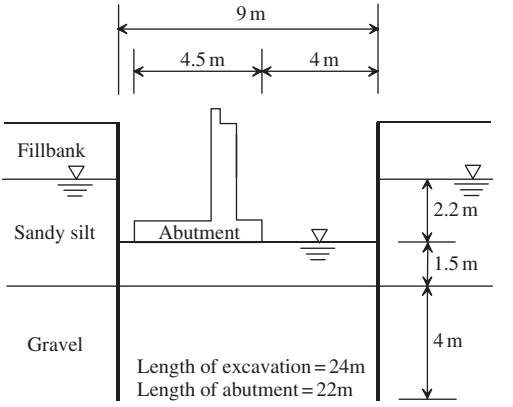


Figure 6. Geometry of Case 2.

programs that can calculate the water pressure around the excavation.

3.2 *Case two*

This case is reported by Tanaka et al. (1994). Piping occurred within a cofferdam for the construction of a bridge abutment along the left bank of the Isasa River. The excavation has a length of 24 m and a width of 9 m, and the abutment has a length of 22 m and a width of 4.5 m. The cantilever sheet-piles with a length of 9.8 m are used as the earth retaining wall. The site is located on an alluvial plain, and a gravel layer is overlaid with a sandy silt layer, of which the physical properties are listed in Table 3. The details of the excavation are shown in Figure 6.

Piping did not occur during excavation, but it occurred when the abutment was constructed within the cofferdam. It induced 4 cm settlement of the abutment within one week since fine soil particles were being washed out. Pumping water from the cofferdam had to be stopped, and the water level in the cofferdam increased to prevent piping. Grouting was used to improve the sandy silt layer, and to prevent piping.

The case has been studied by Tanaka et al. (1994) using the two-dimensional finite element analysis of water flow through soils. The size of the excavation and the abutment indicates that the three-dimensional finite element analysis is necessary to consider the

Copyright © 2003 Swets & Zeitlinger B.V., Lisse, The Netherlands

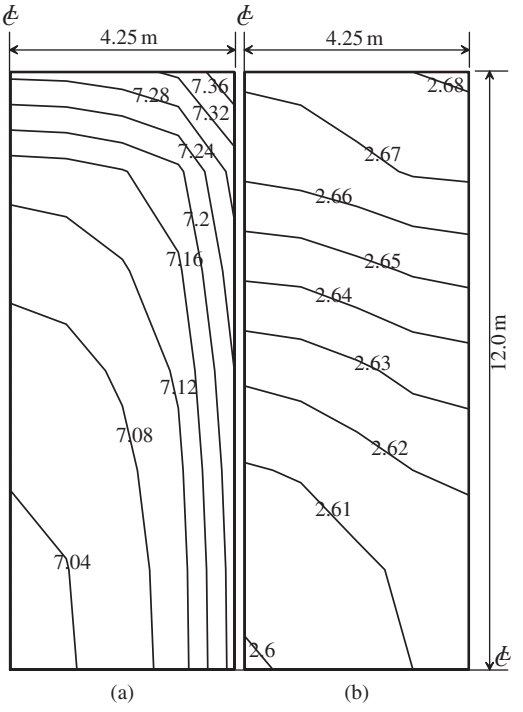


Figure 7. Contours of pressure head (m) for the horizontal section just below the excavation base: (a) at the level of the wall tip, and (b) at the level of the boundary between the two soil layers.

three-dimensional distribution of the water pressure around the excavation and the abutment. Because of the symmetry, one half of the excavation, the abutment, and the ground is analyzed, where the abutment and revetment on the excavation base is assumed to be impervious. The boundary conditions are similar to that in Case 1.

Firstly, the finite element analysis is conducted to calculate the water pressure before the construction of the abutment. Because of the symmetry before the construction of the abutment, only one half of the analyzed zone is used to show the results. Figures 7(a) and (b) show the contours of pressure head for the horizontal section just below the excavation base at the level of the wall tip, and at the level of the boundary between the sandy silt and gravel layers, respectively. Figure 7 shows that the difference of pressure head on the horizontal section is about 0.4 m at the level of the wall tip; however, it is about only 0.1 m at the level of the boundary between the two soil layers.

The maximum water pressure is at the corner of the wall, as in Case 1. The excess pore pressure at the corner of the wall at the level of the wall tip, U_a, and at the level of the boundary between the two soil layers, U_b, and, in turn, the safety factor with respect

Table 4. Safety factor of boiling for Case 2.

Method	U_a,U_A (kPa)	U_b, U_B (kPa)	F_a	F_b
Before the construction of the abutment				
Tergazhi	10.79		5.534	
FEM(3D)	18.56	11.60	3.217	1.186
After the construction of the abutment				
FEM(3D)	19.23	13.31	3.105	1.033

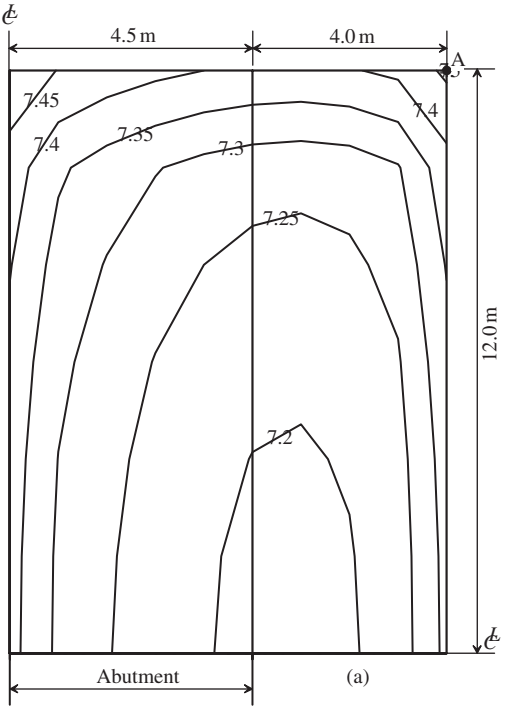


Figure 8a. Contours of pressure head (m) for the horizontal section at the level of the wall tip.

to piping are listed in Table 4, where the safety factor is calculated with Equation 2. It is indicated that the safety factor with respect to piping at the level of the boundary between the two soil layers, F_b, is much smaller than that at the level of the wall tip, F_a. This indicates that for two-layered ground the upper layer is much more dangerous for piping if its permeability is smaller than that of the lower layer. Terzaghi & Peck's method gives a much larger safety factor even for the lower layer than that of the three-dimensional finite element analysis because the three-dimesional effect is not considered in Terzaghi & Peck's method. The safety factor with respect to piping, F_b, is only 1.186, calculated with the water pressure of the three-dimensional finite element analysis. The safety factor

Copyright © 2003 Swets & Zeitlinger B.V., Lisse, The Netherlands

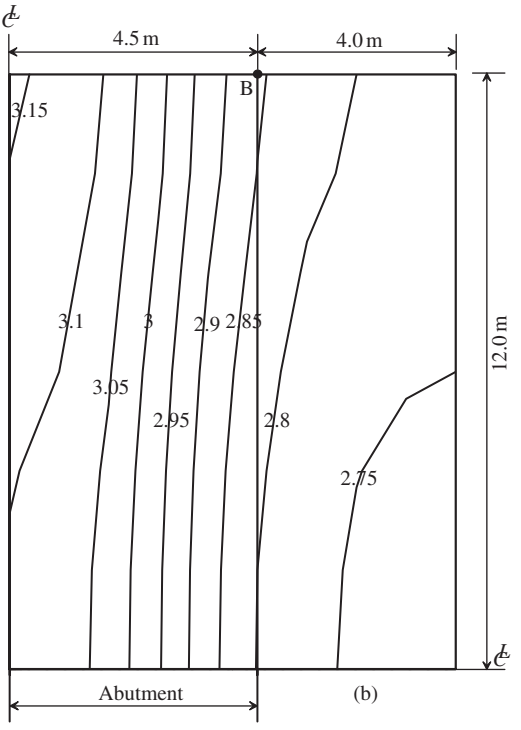


Figure 8b. Contours of pressure head (m) for the horizontal section at the level of the boundary between the two soil layers.

of 1.186 indicates that the excavation is near piping even before the construction of the abutment.

The abutment and the revetment are considered as impervious boundary condition for the three-dimensional finite element analysis of water flow after the construction of the abutment. Figure 8(a) shows the contours of pressure head for the horizontal section just below the excavation base and at the level of the wall tip. The maximum excess pore pressure within the zone where piping may take place is at point A, and U_A is 19.23 kPa. Thus the safety factor with respect to piping is 3.105. Figure 8(b) indicates the contours of pressure head for the horizontal section just below the excavation base and at the level of the boundary between the two soil layers. The maximum pore pressure within the zone where piping may occur is at point B, and U_B is 13.31 kPa, so the safety factor with respect to piping is 1.033. It is the safety factor with respect to piping very close to unity that explains the 4 cm settlement of the abutment within one week since fine soil particles were being washed out.

4 CONCLUSIONS

Two case histories where boiling or piping occurred in excavations in cohesionless soils are analyzed. The finite element analysis of water flow through soils is used to calculate the water pressure around the excavations. The safety factor with respect to piping is defined as in Terzaghi & Peck's method, and is evaluated using the water pressure calculated from the finite element analysis of water flow through soils. The boiling or piping of the two case histories are well reproduced only when the three-dimensional finite element analysis of water flow through soils is used to calculate the water pressure around the excavations. The three-dimensional effect on the water pressure and in turn on the safety factor with respect to piping is significant for the two case histories where the length is about two times the width of the excavation.

REFERENCES

Bathe, K.J. & Khoshgoftaar, M.R. 1979. Finite element free surface seepage analysis without mesh iteration. *Int. J. Numer. Anal. Methods Geomechanics*, 3: 13–22.

Cai, F. 2001. *Finite element analysis of groundwater and rainfall infiltration*, Text for Seminar on Application of FEM to Numerical Analysis of Landslides. Japan Landslide Society (in Japanese).

Desai, C.S. 1976. Finite element residual schemes for unconfined flow. *Int. J. Numer. Methods Eng.*, 10: 1415–1418.

NAVFAC DM-7. 1971. *Design Manual – Soil Mechanics, Foundations, and Earth Structures*. Department of the Navy, Naval Facilities Engineering Command. Washington, D.C.

Special Issue. 2001. The sheet-pile was not penetrated enough below the excavation base. *Nikkei Construction*, September, 37–39 (in Japanese).

Symons, I.F. 1983. Assessing the stability of a propped in situ retaining wall in overconsolidated lay. *Proc. Instn Civ. Engrs*, 75, Part 2, 617–633.

Tanaka, T., Toyokuni, E. & Ozaki, E. 1994. A case study on piping during excavation for bridge abutments. *Proc. Int. Symp. on Underground Construction in Soft Ground*, New Delhi, India, 159–162.

Terzaghi, K. & Peck, R.B. 1948. *Soil mechanics in engineering practice*. 2nd ed. John Wiley & Sons, New York.

Copyright © 2003 Swets & Zeitlinger B.V., Lisse, The Netherlands

An example of groundwater control measures in large-scale open-cut works

A. Ogata & N. Ikoma
Kumagaigumi Co. Ltd., Tokyo, Japan

ABSTRACT: Effects of river action, such as sedimentary deposition, have transformed the Fujitanishiki district in Okayama City. The project discussed in this paper was one of the main undertakings for the public sewerage system in Okayama City, and involved the construction of a junction pumping station for wastewater on the left bank of the Sasagase River. The target was to complete the project and start pumping operations at the end of 1994. This report presents the results of an analysis, carried out in advance, on the quality and situation of the improved ground, and monitoring procedures for field measurements.

1 PREFACE

The Fujitanishiki district in Okayama City is located approximately 7.5 km south of the urbanized area of the city proper. The area is in the southern part of Okayama Plain, which was built up by deposits from the Asahi River flowing through the central area of the city, and from the Sasagase River in the west end of the city and turning south. The bedrock is granite, with non-solidified layers of diluvium and alluvial deposits on top (Figure 1).

The Nishiki pumping station is a wastewater relay station. A cemetery and the Sasagase River are adjacent to the station shaft.

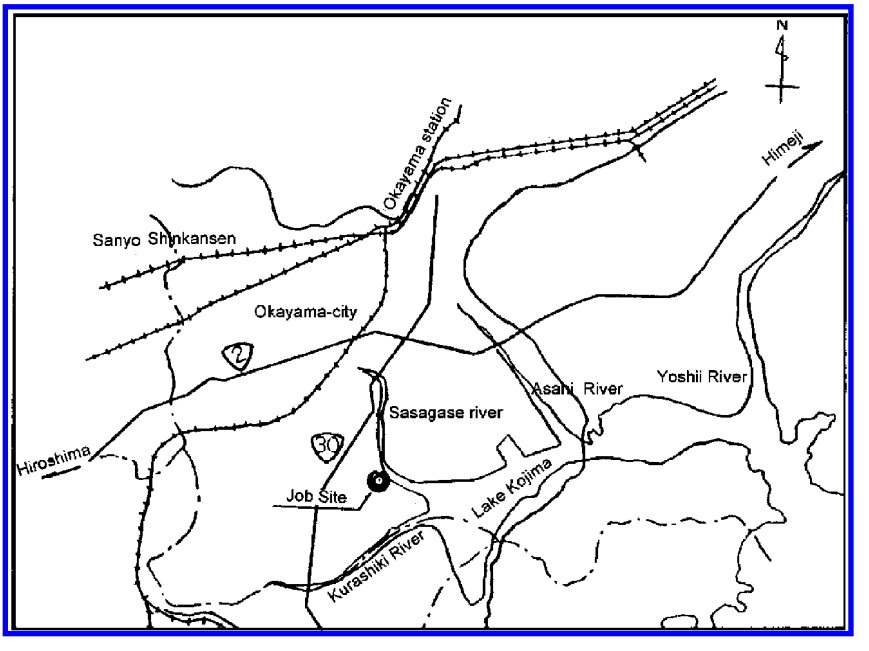


Figure 1. Location.

Copyright © 2003 Swets & Zeitlinger B.V., Lisse, The Netherlands

2 OUTLINE OF THE WORK

2.1 *Detail of works:*

Shaft Dimensions: 37.9 m × 20.9 m

Earth retaining wall with secant bored pile wall and soldier pile wall (ONS method)	ϕ 800, L = 24.5 m, 114 no.
SMW (Soil mixing wall)	2,373 m^2
Intermediate pile	32 no.
Shaft excavation depth	D = 20.9 m
Support	Six steps

2.2 *Geological outline*

The borehole data as shown in Figure 2. indicates the following soil layers. Top 1.5 m of soil is earth of N-value 9. From GL-1.5 m to GL-14.8 m is a cohesive alluvial soil (soft cohesive soil) with N-value from 0 to 2. From GL-14.8 m to GL-19.2 m is a sandy alluvial soil with N-value from 5 to 27. Layers below GL-19.2 m are of diluvia. From GL-19.2 m to GL-22.6 m is the first diluvium gravel layer. This layer shows an N-value of between 25 to 50, and coefficient of permeability of 10^{-2}cm/s. From GL-22.6 m to −23.5 m, is a diluvium clay layer. This layer has an N-value of around 4, but its adhesive strength is large. Below GL-23.5 m is the second layer of diluvium gravel with an N-value of more than 50. The coefficient of permeability of this layer is 10^{-2}cm/s. This layer contains diluvium clay from GL-29.5 m to GL-30.0 m.

The ground water level is at GL-1.5 m, but the artesian head of the gravel layer of the diluvium is as high as GL0.0 m.

3 IN-SITU TRIAL TESTS

Trial tests were carried out to confirm the quality of the improved ground, for two reasons.

Firstly, there are only a few precedents where ground improvement has been carried out in gravel layers using a JGC (jet grout column) method as a countermeasure against uplift in a large excavation, of size around 20 m × 30 m wide, and about 20 m deep. Secondly, there are some unknown parameters within the improved soil model that have effects on safety. In the tests, two types of soil improvement models were carried out in the neighborhood of the shaft. One model is the 'association' type where the raise speed of the grout tube executes the work at a rate of 16–20 min/m. Another model is the '14 minutes' type that improves speed to 14 min/m (Figure 3).

3.1 *Field tests*

To confirm the quality and dimensions of the soil-improvement slab using the JGC method, the following sampling was carried out on the treated soil.

1. Core boring
2. Permeability measurement
3. Rotary sounding

The results of permeability testing and rotary sounding are presented in Table 1 and Figure 4 respectively.

On the basis of the above-mentioned test results, the following were observed.

- We could not extract a good core sample when the soil was improved using the '14 minutes' type model.
- The 'association' type provided better results than the '14 minutes' type. However, the shape of the 'association' type in the gravel layers did not meet the required design criteria.
- The causes of the low quality in the gravel layer (in particular, the basement Dg2 layer), especially for the 'association' type, are as follows.
- It was found in the velocity-measuring test that the speed of ground water was 7 m/day in the Dg2 layer.
- Dissipation and dilution of bentonite slurry was found in a boring-hole at the Dg2 layer during the boring-work.
- During the improvement for test pile No. 1, the rate of dissipation was very rapid from 27.0 m to 28.5 m in the gravel layer. It took 1.5 hours to stop the dissipation using approximately 20 m^3 of adhesive material (This indicated the presence of bigger water fuse).

3.2 *Countermeasures and results*

3.2.1 *Countermeasures*

The countermeasures for the problems encountered above were as follows.

- Water infiltration:

It shuts off groundwater movement in the improved object (an open cut range) from the inside and the outside. It carries out setting the soil-cement part of an earth-retaining wall constructed by the ONS method at Dc2 layer at EL-29.50 m.

- Water fuse:

After ground-water interception, the susceptibility of an improved soil body to high permeability was a major concern during execution.

By this method, a SMW wall was installed in department of each sectional conjugation.

3.2.2 *Result of countermeasures*

The required design quality was achieved in the improved soil slab after carrying out the above countermeasures, as shown in Table 2.

Copyright © 2003 Swets & Zeitlinger B.V., Lisse, The Netherlands

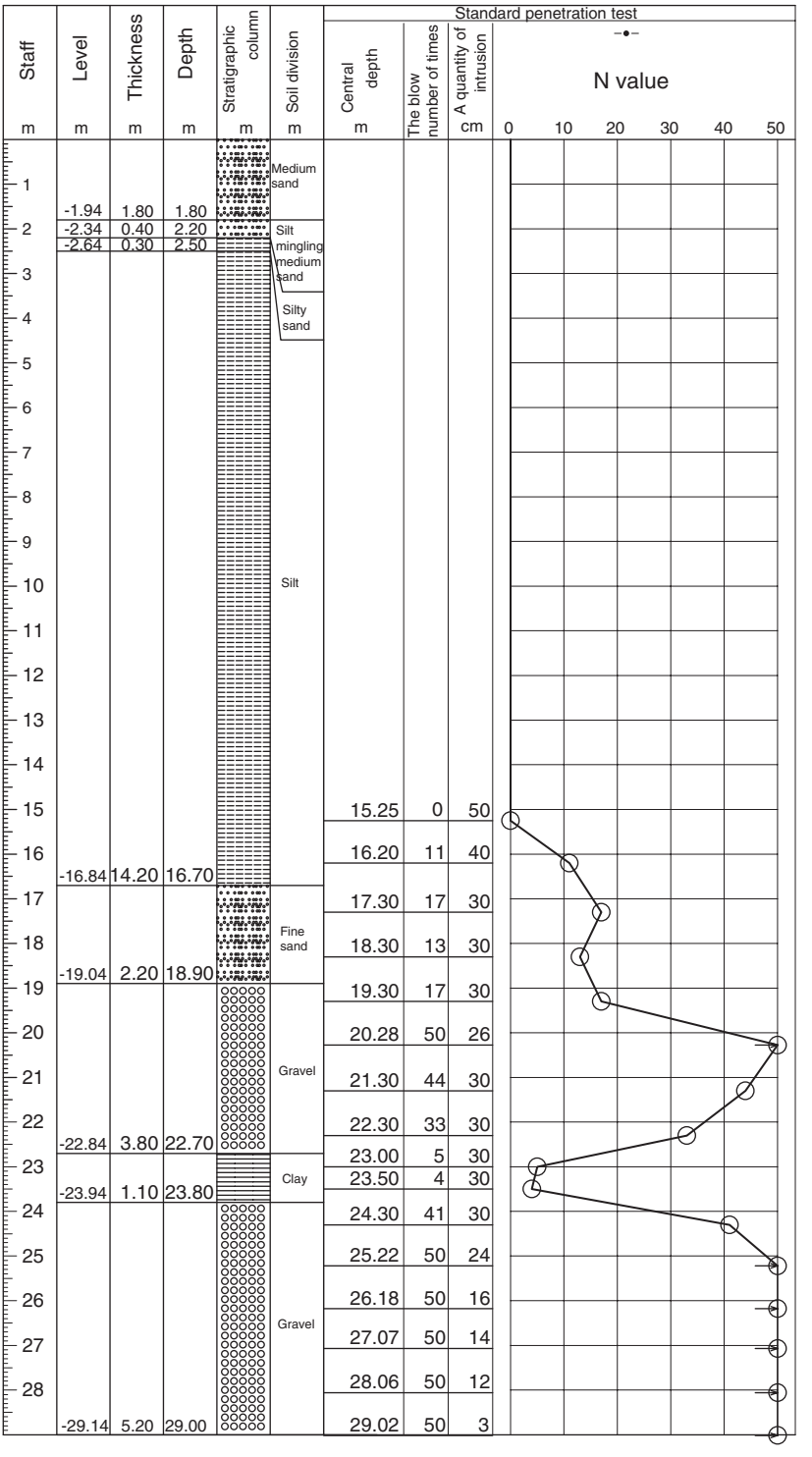


Figure 2. Soil stratigraphic column.

Copyright © 2003 Swets & Zeitlinger B.V., Lisse, The Netherlands

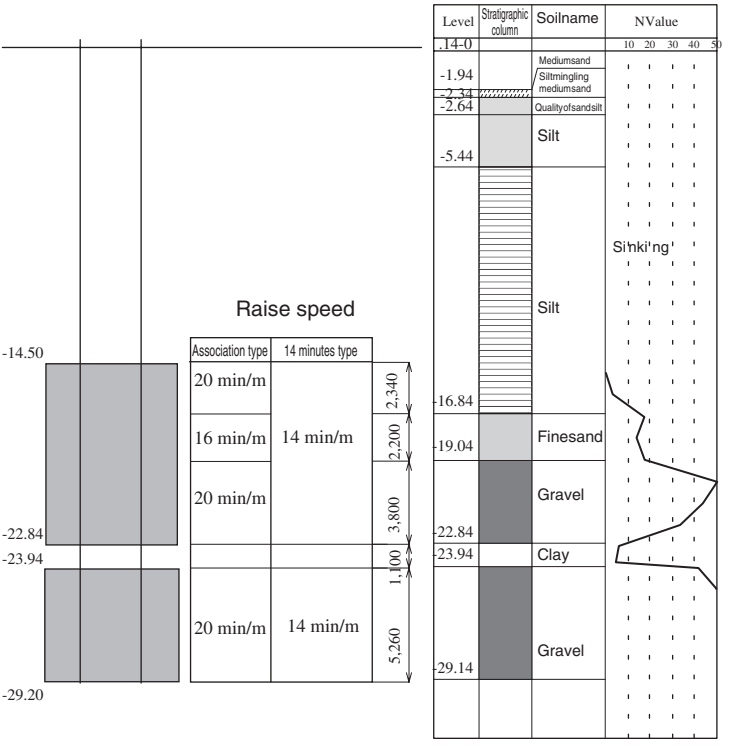


Figure 3. A figure of field trial.

Table 1. Field permeability test (cm/s).

EL-(m)	Before improvement	14 minutes type	The association type
24.50∼25.50	1.6×10^{-2}	4.27×10^{-3}	1.44×10^{-3}
26.00∼27.00	1.6×10^{-2}	5.42×10^{-3}	1.28×10^{-3}
27.20∼28.70	1.6×10^{-2}	7.84×10^{-4}	1.09×10^{-3}

4 OBSERVATIONAL MONITORING CONTROL

We carried out a monitoring program to review safety and to confirm the behavior of the improved soil slab, which was an uncommon structure, used to restrain the base against uplift caused by this large and deep excavation. As for the material strength of an improved body, the soil cement strength used for earth-retaining walls (a SMW wall and an ONS wall) is smaller than the CJG strength. On this account, the following strength confirmation tests for an existing soil-cement between an improved body and earth-retaining walls were carried out.

1. In-situ shear strength test
2. High tension triaxial test

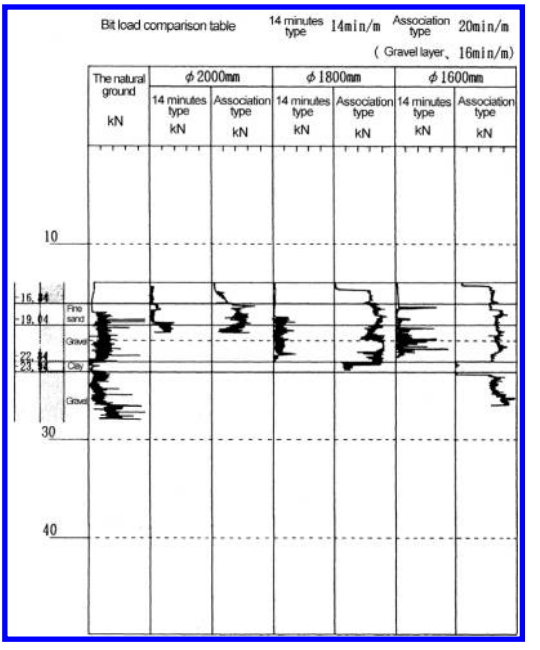


Figure 4. Rotary sounding.

Copyright © 2003 Swets & Zeitlinger B.V., Lisse, The Netherlands

Table 2. Compressive strength.

	Unconfined compressive strength (N/mm^2)	
Soil	Design	In situ
Gravel	3.0	22.9
Clay	1.0	3.7

In addition, FEM analysis was carried out to predict the behavior of the improved soil slab.

4.1 *Monitoring items and locations of equipment*

The monitoring items and location of equipment are shown in Table 3 and Figure 5 respectively.

Table 3. Monitoring items.

Item	Phenomenon monitored	Measuring equipment	Mark	Remarks
Behavior of the center of the improved soil slab	Vertical movement of the intermediate pile	Leveling settlement gauge	a1, a2, a3 b1, b2	Measurements are monitored on screen in real-time. Temperature effects on the gauge are also measured.
Behavior of the improved soil slab near the earth retaining wall	Vertical movement of the displacement steel wire	Displacement gauge	D1, D2	Measurements are monitored on screen in real-time. Measures the relative displacement between the steel pipe sheet pile head and the improved soil slab.
Behavior of SMW	Vertical movement of the top part of SMW	Leveling settlement gauge	S1, S2	Measurements are monitored on screen in real-time. Temperature effects on the gauge are also measured.
Change in uplift	Water head of confined aquifer	Pore water pressure gauge		Measurements are monitored on screen in real-time. Monitors the movement caused by seasons and leakage.
Detects a change of the improved soil slab	Leakage of the excavation inside	Visual information		See as a sign of a fracture event in the improved soil slab.

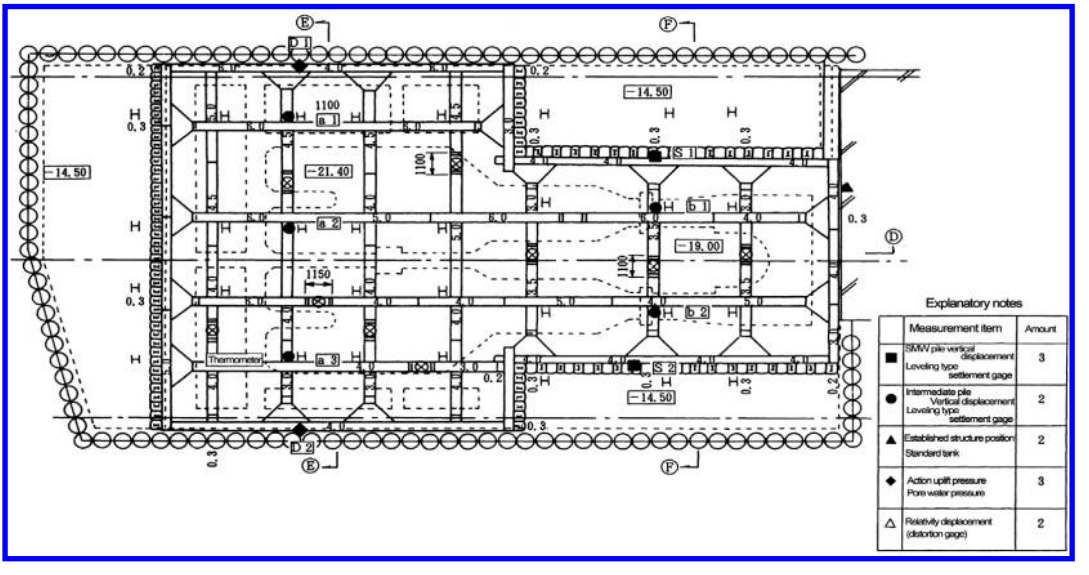


Figure 5. Measure layout.

Copyright © 2003 Swets & Zeitlinger B.V., Lisse, The Netherlands

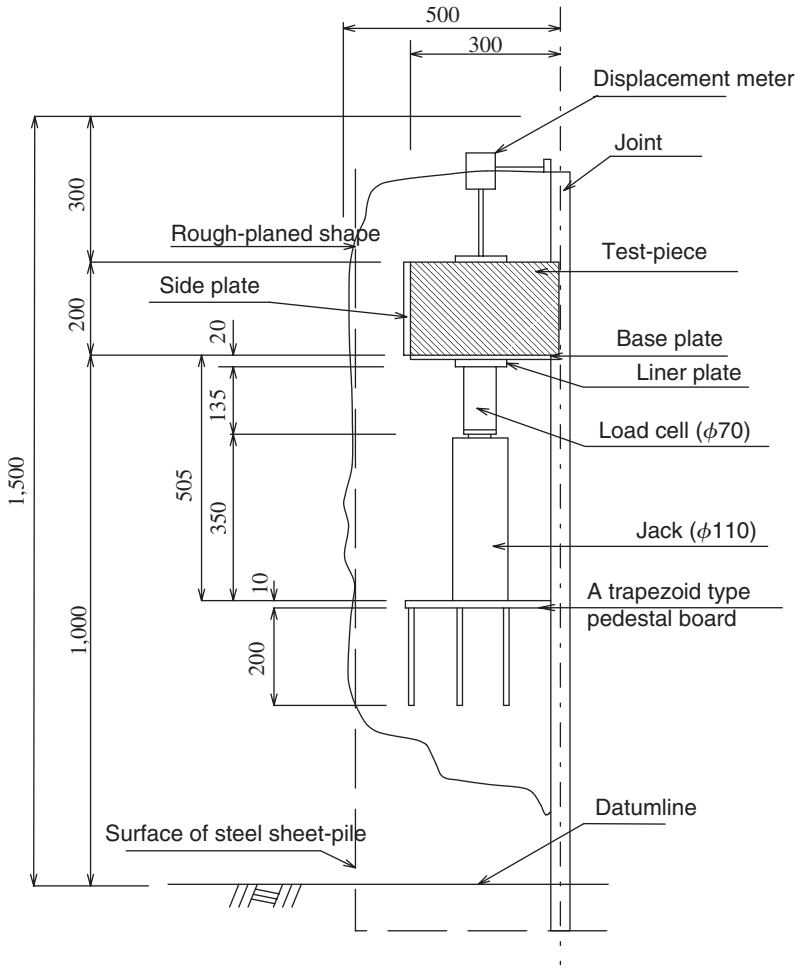


Figure 6. Test plant layout.

4.2 *In-situ shear strength test and high-tension triaxial test*

4.2.1 *In-situ shear strength test*

A test-piece was made from soil-cement adhering to steel pipe sheet pile in the ONS method.

We used a device to show in Figure 6 the existing position and tested shear strength of soil cement.

The method of the testing is shown in Figure 6.

The shear strength was 212.7 kN/m^2, as shown in Figure 7.

4.2.2 *High-tension triaxial test*

Based on the material strengths (VIZ. Young's modulus, adhesive strength, angle of internal friction) and compression strength of soil-cement, we analyzed the behavior of the improved soil slab by the FEM. Table 4 shows the results of the analysis.

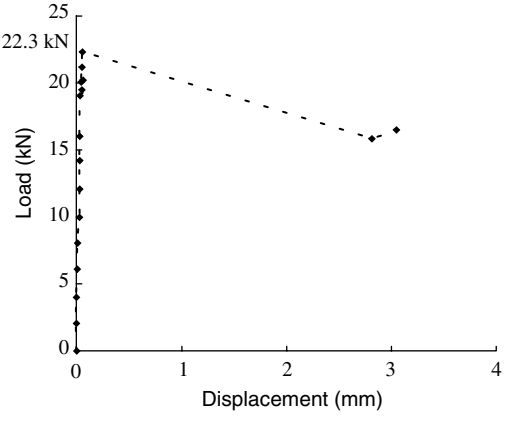


Figure 7. Load and displacement concerned.

Copyright © 2003 Swets & Zeitlinger B.V., Lisse, The Netherlands

4.3 *A measurement and an analysis result*

Figure 8 indicates the monitoring results of the A part (section E-E). The leveling type settlement gauge that was used to control the measurement was influenced by a difference in temperature between day and night. Results from measurement at 5:00 am, minimized influences from temperature. Therfore, the measurement at 5:00 a.m. for long-term monitoring of settlement effects was carried out. A further correction for temperature as measured by leveling settlement gage, was applied for a more accurate measurement.

We used two-dimensional FEM to model the behavior of the slab under loads. Table 5 shows the analysis cases for the section E-E shown in Figure 9. Results

Table 4. Physical properties of soil-cement.

	E (kN/m^2)	C (kN/m^2)	ϕ (°)
Range	7.83∼11.22×10^6	7490∼9500	32.5∼40.4
Average	9.52×10^6	8610	36.3

Compressive strength about 3.8 N/mm^2.

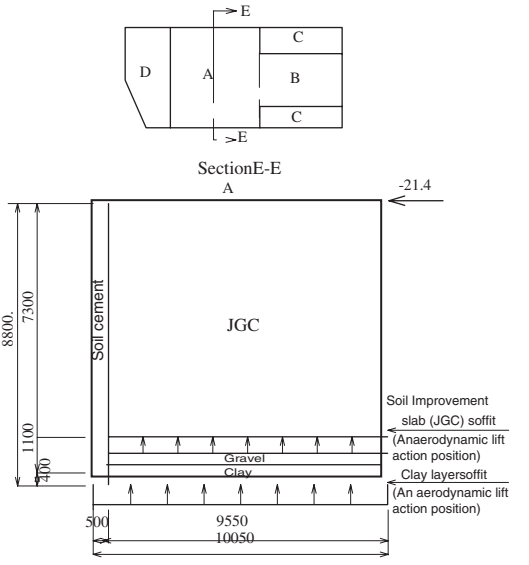


Figure 9. Analysis model.

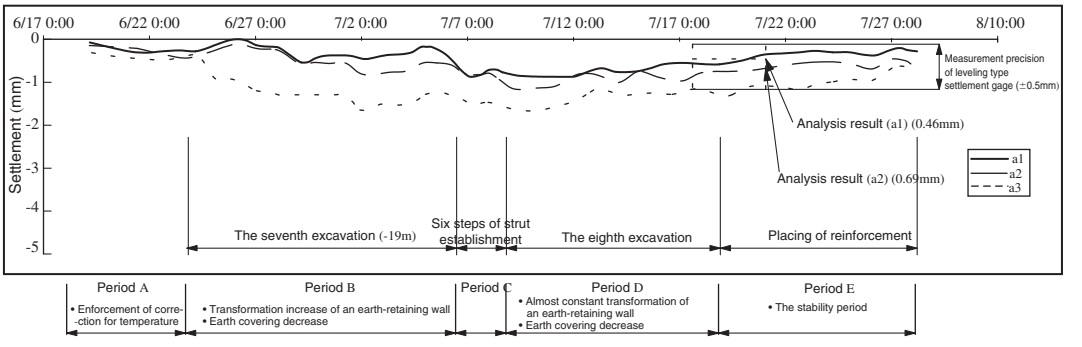


Figure 8. Hour change of A-part settlement after correction for temperature.

Table 5. An analysis case.

A case name	Physical property of soil-cement	An uplift pressure action position	An earth-retaining wall and adhesion side
Case 1	It is decided by a high pressure three axis examination	Cohesive soil soffit	All fixed
Case 2	It is decided by a high pressure three axis examination	Cohesive soil soffit	Only a part ahead of adhesive strength is free
Case 3	It is decided by a high pressure three axis examination	Improvement ground (JGC) soffit	All fixed
Case 4	It is decided by a high pressure three axis examination	Improvement ground (JGC) soffit	Only a part ahead of adhesive strength is free
Case 1′	It is a strength condition at first (Standard design strength)	Cohesive soil soffit	All fixed

Copyright © 2003 Swets & Zeitlinger B.V., Lisse, The Netherlands

Table 6. Generalized list of an analysis result.

	Vertical displacement in excavation bottom face (mm)		Tensile stress destruction and the situation of safety factor for shear fracture		
An analysis case	Settlement gage near a2	Settlement gage near a1, a3	Soil cement	JGC	Other
Case 1	−0.69 (Drop)	−0.46 (Drop)	Almost the whole area area $F_s > 1.0$	Almost the whole area $F_s > 1.0$	Only sand layer under JGC $F_s < 1.0$
Case 2	1.04 (Rise)	1.11 (Rise)	Almost the whole area $F_s > 1.0$	Almost the whole area $F_s > 1.0$	Only sand layer under JGC $F_s < 1.0$
Case 3	−0.67 (Drop)	−0.44 (Drop)	Almost the whole area $F_s > 1.0$	Almost the whole area $F_s > 1.0$	
Case 4	1.32 (Rise)	1.34 (Rise)	Almost the whole area $F_s > 1.0$	Almost the whole area $F_s > 1.0$	
Case 1′	1.00 (Rise)	0.50 (Rise)	Almost the whole area $F_s < 1.0$	Almost the whole area $F_s > 1.0$	Only sand layer under JGC $F_s < 1.0$

from the analysis are presented in Table 6. In order to calculate the shear stress between the soil-cement and the earth retaining wall, we used a simple beam model.

The analyzed shear stress was 188.2 kN/m^2 and the safety factor was $F_s = 212.7/188.2 = 1.13$.

In the actual state, the soil-cement showed partial unevenness, but the test-piece that was used was examined as being within the average for the material. The test was executed without lateral pressure, which would reduce the results of the shear strength. This indicates that the actual shear strength with lateral pressure should be higher. The shear strength in the test may have been weakened by other external forces (vibration, impact, etc.) that took place during the formation of the in-situ specimens. As a result, the safety factor, F_s for the shear strength between the improved soil slab and the retaining wall should be more than 1.13. Confident of obtaining a sufficiently high safety factor, we decided to continue the work with control by measurement.

4.4 *Assumed behavior of improved soil slab*

We examined the safety factor of the improved soil slab at each depth, and found the slab totally stable. However, there was a possibility of partial destruction at the neighborhood of the slab levee crown. Models to show assumed behavior of an improved soil are presented.

Model-1: The JGC is assumed to behave as a simple beam. In this case, the ends of the JGC would deform outward from the earth-retaining wall line by uplift pressure.

Model-2: In this case, the part that deforms outwards from the earth-retaining wall (line that occurred in Model–1) is restrained by an earth-retaining wall. On this account, the stress concentration is at the base of excavation and is shaped like an arch (It is called a 'weak arch' action henceforth).

Model-3: This model considers the deformation of the bracing wall with excavation. In this case, an earth-retaining wall deforms to the excavated side during excavation.

On this account, the stress concentration is at the base of the excavation and is arch shaped. Furthermore, greater forces exist together with an arch effect so that the restraint assumed in Model-2 is added on. When the restraint effect of the earth-retaining wall (in Model 2) is added to this deformation, the arch action is strengthened (it is called a 'strong arch' action henceforth).

The analysis and results using the above-mentioned three models are summarized.

The result of a 'weak arch' effect by Model-2 was smaller than those from Model-1 at the E-E section.

The quantity of rise (by transformation of central part) was reduced to about 48% in comparison with Model-1.

The tensile stress that occurred in the neighborhood of the central part within the levee crown was reduced to about 34% in comparison with Model-1.

If the physical properties of the improved soil slab were assumed homogenous, the applied stress by a 'weak arch' action and the reduced rate of deflection were constant.

The strong arch action causes downward deformation, and due to this, the stress at the upper part of the slab is changed from tensile to compressive.

Near the earth retaining wall of the slab, there is soil-cement, which is softer than the JGC. When we took this fact into consideration, the stress and the deformation of the slab was higher than in our analysis, where we do not consider the softer soil-cement. Stress and deformation of the slab by this influence became larger than the case that supposed that the whole improvement used a JGC method of

Copyright © 2003 Swets & Zeitlinger B.V., Lisse, The Netherlands

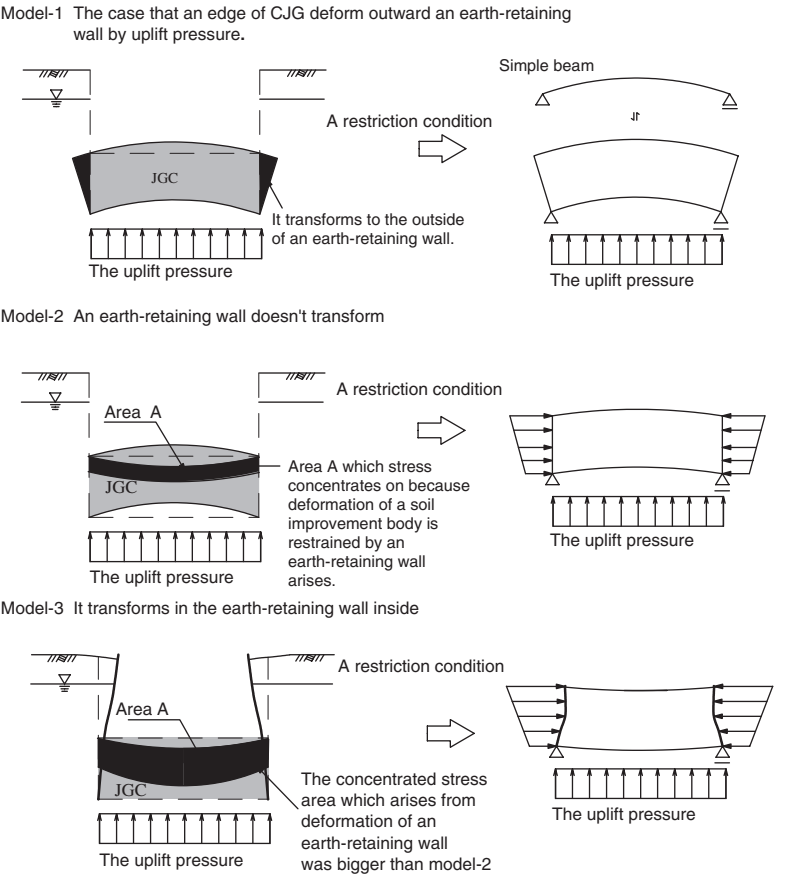


Figure 10. Behavior and internal stress of JGC part by uplift pressure.

construction. As a result, the stress increases up to 1.3 times while the deformation increases up to 2.3 times.

This FEM analysis used similar physical properties provided from in-situ tests as that used for analysis. The results from the analysis are almost identical to the site-measured values. We were not able to confirm the soil improvement slab internal real behavior by a measurement. However, it is hypothesized that the internal behavior of the soil improvement-slab inside is the same as the arching action result of Model-3.

5 CONCLUSION

Sufficient and uniform strength in the improved soil slab is required for large-scale ground improvement as a countermeasure against up-lift. The strength in design should be evaluated carefully as we must give consideration to the variation of strength within the slab. Prior to commencement of the actual construction work, it is important to carry out tests to confirm the in-situ strength, and measurements to ensure safety during the works. In this project, not only was the required strength of the slab made sufficient and uniform, but also a new type of behavior mechanism for the improved slab was suggested, namely an arching action due to excavation. However, further study and investigation on the function, mechanism, and application of this arch action are required.

REFERENCE

Japanese Jet Grouting Association, ‘Jet grout engineering data’, Japanese Jet Grouting Association, June 1992, pp. 15–18.

Copyright © 2003 Swets & Zeitlinger B.V., Lisse, The Netherlands

Simplified design method of deepwells placed in excavation area

N. Kohsaka & A. Ishikawa
Institute of Technology, Shimizu Corporation, Tokyo, Japan

ABSTRACT: A simplified design method for deepwells placed in an excavation area enclosed by cut-off wall in a multiple aquifer system is proposed. This method is based on the steady state well formula with the following three ideas: the number of deepwells is evaluated by the radius of a virtual large diameter well; drawdown curve in the excavation area has the equivalent influence radius considering the effect of the cut-off wall; and permeability of an interbedded aquitard is converted to the cut-off wall length. The procedure of this design method is described and results of this method are compared with 3-D FEM results. Discharge rate and the number of deepwells to provide required drawdown are calculated by this method, and these results agree well with the FEM results. Effectiveness of the proposed method is confirmed.

1 INTRODUCTION

As for excavation works deeper than groundwater level, dewatering method using both a cut-off wall penetrating in an aquitard (low permeable layer) and deepwells placed in the excavation area is adopted. According to this method, the discharge rate for dewatering is largely reduced because of low permeability of the aquitard and the cut-off wall. Then we can reduce the construction cost and environmental influence in the neighbor area.

Conventionally, the discharge rate and the number of deepwells is designed using a general well formula such as Thiem's equation that ignores the effect of the aquitard and the cut-off wall. In most of these cases, the possibilities to over design are high because the discharge rate reduction by the aquitard and the cut-off wall is not considered.

On a large site, detailed investigations of ground permeability is carried out and, based on this result, a numerical computation technique such as finite element method (FEM) is used for the design. But this method requires a great deal of time and expense.

In this paper, a simplified design method for the discharge rate and the number of deepwells is proposed. In this method we can consider permeability of both the interbedded aquitard and the cut-off wall, thereby the appropriate dewatering facilities are designed easily.

The validity of the proposed method is inspected by three dimensional groundwater flow analysis by FEM.

2 CONCEPTUAL IDEAS OF THE DESIGN METHOD

The proposed design method is based on the following three ideas:

- The number of wells is evaluated by means of the radius of a large diameter virtual well that has equivalent ability as the array of wells.
- The drawdown in an excavation area enclosed by a cut-off wall is calculated by the steady state well formula (Thiem's equation) with the equivalent influence radius R' considering the effect of the cut-off wall.
- The permeability of an interbedded aquitard is converted to the cut-off wall penetration length in multi-layered aquifer system.

2.1 *Design method for multiple well system*

Most dewatering systems for excavation consist of a number of deepwells to provide the required drawdown. One of the major problems in design such a system is to determine the number and spacing of deepwells. Where the deepwells in a system are spaced in a circular array (see Figure 1), discharge rate from one deepwell q and total discharge rate Q are calculated by Equation 1 and 2 respectively.

$$q = \frac{2\pi T s_w}{\ln\left(R^{n-1+(1/\eta)} \Big/ n l^{n-1} r_w^{1/\eta}\right)} \tag{1}$$

Copyright © 2003 Swets & Zeitlinger B.V., Lisse, The Netherlands

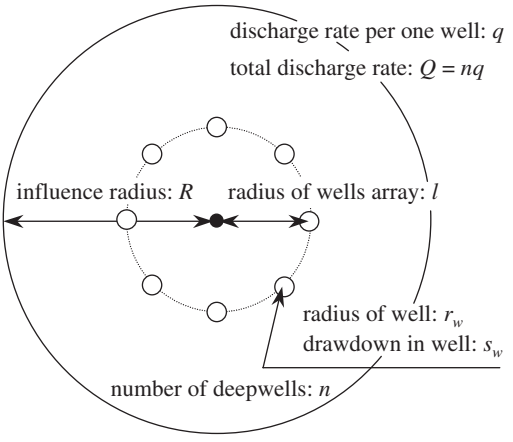


Figure 1. Schematic diagram of a multiple deepwell system.

$$Q = nq = n\frac{2\pi Ts_w}{\ln\left(R^{n-1+(1/\eta)}\Big/ nl^{n-1}r_w^{1/\eta}\right)} = n\eta'\frac{2\pi Ts_w}{\ln\left\{\dfrac{R}{\left(nl^{n-1}r_w^{1/\eta}\right)^{\eta'}}\right\}} \quad (2)$$

where n = the number of deepwells; T = transmissivity of aquifer; s_w = drawdown in well; R = influence radius by pumping; l = radius of wells array; r_w = effective radius of well; η = well efficiency by well loss; and η' = equilibrium well efficiency coefficient related to well loss and well interference.

$$\eta' = \frac{1}{n - 1 + (1/\eta)} \quad (3)$$

Equation 2 shows that the total discharge rate by deepwells of the number n is same as the discharge rate by one deepwell whose radius is r'_w presented by Equation 4 and whose efficiency is $n\eta'$.

$$r'_w = \left(nl^{n-1}r_w^{1/\eta}\right)^{\eta'} \quad (4)$$

According to the above, the pumping condition by the circular array of deepwells is converted to pumping from one large diameter well (Kohsaka 1995, 1999). Thereby this pumping condition is simulated by an axis symmetric analysis. The procedure for the calculation is follows. Firstly the equivalent well radius r'_w is calculated by Equation 4. Secondly, the total discharge rate Q is calculated by axis symmetric analysis giving the head constant condition equivalent to drawdown

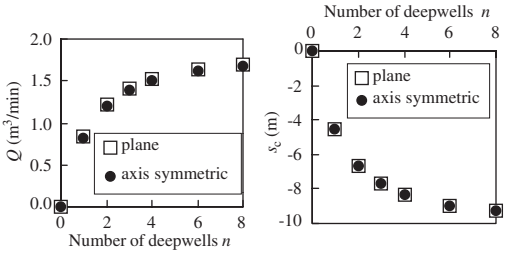


Figure 2. Comparison of proposed large diameter well analysis (axis symmetric) and plane flow analysis.

in the large diameter well $s'_w = n\eta' s_w$ internal the virtual well area. Finally drawdown adjacent to the well array is calculated by axis symmetric analysis giving the discharge rate Q constant condition at the point of the circular wells array radius.

Results from the proposed method are compared to 2-dimensional plane flow analysis results, which can evaluate the well layout. The total discharge rate Q and the drawdown at the center of the well array s_c are compared in Figure 2. The analytical conditions are $T = 10^{-1}$ m^2/min, $R = 1000$ m, $l = 30$ m, $r_w = 0.45$ m, $s_w = 10$ m, and $\eta = 1.0$. These results indicate that both methods agree very well. This means that the number of deepwells can be evaluated by axis symmetric analysis using the above-proposed method.

2.2 *Drawdown characteristics in excavation area enclosed by a cut-off wall in single aquifer system*

In excavation works larger than middle scale (about 10 m deep), the excavation area is enclosed by a cut-off wall, and groundwater level is lowered by pumping from deepwells placed inside the cut-off wall. Low permeability of the cut-off wall reduces the discharge rate to provide the required drawdown.

Figure 3 shows a schematic diagram of an excavation area. Equation 5 (Thiem's well formula) calculates drawdown s by pumping from a deepwell whose discharge rate is Q, when cut-off wall does not exist.

$$s = \frac{Q}{2\pi T}\ln\left(\frac{R}{r}\right) \quad (5)$$

where r = radius of the calculating point from the pumping well. When a cut-off wall, whose installation radius is r_0, thickness is d, and hydraulic conductivity is k_w, is constructed, the drawdown in excavation area enclosed by the cut-off wall is calculated by Equation 6.

$$s = \frac{Q}{2\pi T}\ln\left(\frac{R'}{r}\right) \quad (6)$$

Copyright © 2003 Swets & Zeitlinger B.V., Lisse, The Netherlands

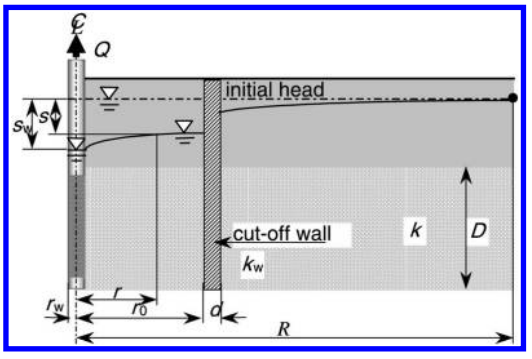


Figure 3. Schematic diagram of an excavation area enclosed by cut-off wall in a single aquifer system.

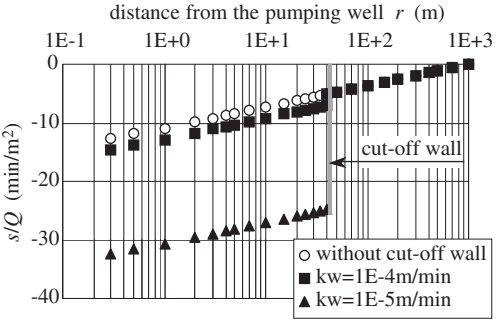


Figure 4. Distance drawdown curve calculated by axis symmetric FEM.

where R' = apparent influence radius calculated by Equation 7.

$$R' = R\left(\frac{r_0 + d}{r_0}\right)^{(T-T')/T'} = F_w R \tag{7}$$

$$F_w = \left(\frac{r_0 + d}{r_0}\right)^{(T-T')/T'} \tag{8}$$

where $T' = k_w D$ = transmissivity of the cut-off wall zone; and D = thickness of aquifer. F_w presented by Equation 8 is named the cut-off wall factor, and this factor expresses the effect of the cut-off wall to reduce the required discharge rate (Kohsaka 1997).

Comparison of Equation 5 and Equation 6 shows that the distance-drawdown curve in the excavation area has same slope and different intercept on the log scale graph. Thus the drawdown in the excavation area enclosed by the cut-off wall has a characteristic that the influence radius is F_w times larger than the condition without the cut-off wall.

Figure 4 shows the distance drawdown plot calculated by axis symmetric analysis. The value of s/Q is taken in vertical axis to compare the calculation results which has different discharge rate. The graph shows three case results: without cut-off wall, hydraulic conductivity of cut-off wall k_w is 1×10^{-4} m/min, and 1×10^{-5} m/min, which are 1/100 and 1/1000 of the hydraulic conductivity of the aquifer $k = 1 \times 10^{-2}$ m/min. This figure shows that the drawdown of the outside of the cut-off wall is the same, but the drawdown of the inside of the cut-off wall becomes larger as the permeability of the cut-off wall becomes smaller. The drawdown curves inside the excavation area are parallel, and the influence radius obtained by extending the plot are $R' = 3600$ m for $k_w = 1 \times 10^{-4}$ m/min and $R' = 3.0 \times 10^8$ m for $k_w = 1 \times 10^{-5}$ m/min. The cut-off wall factor calculated by equation 8 is $F_w = 3.4$ for $k_w = 1 \times 10^{-4}$ m/min and $F_w = 2.5 \times 10^5$ for $k_w = 1 \times 10^{-5}$ m/min. Since the influence radius R is 1000 m from the condition of analysis, it is proved that the proposed method expresses the drawdown characteristics in the excavation area with enough precision.

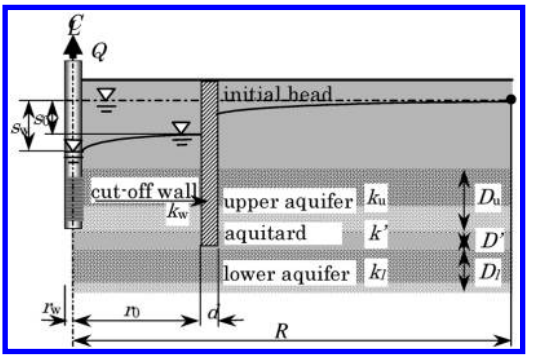


Figure 5. Schematic diagram of an excavated area enclosed by a cut-off wall in multiple aquifer system.

2.3 *Conversion of the interbedded aquitard permeability into the cut-off wall length in multi-layered aquifer system*

In multi-layered aquifer system, the cut-off wall penetrating the interbedded aquitard is constructed to reduce the discharge rate. Figure 5 shows a schematic diagram of an excavation work in a multi-layered aquifer. Under this condition, the groundwater flow into the excavation area has a horizontal component from the cut-off wall and a vertical component through the aquitard. To calculate the discharge rate in order to provide the required drawdown, the simplified calculation method that converts the aquitard permeability into the cut-off wall length is proposed (Kohsaka 1998). Thus, Equation 9 and 10 express the hydraulic resistance of the cut-off wall P_w and the aquitard P', and the aquitard permeability is converted into the

Copyright © 2003 Swets & Zeitlinger B.V., Lisse, The Netherlands

equivalent penetration length D_{eq} of the cut-off wall, as expressed by Equation 11.

$$P_w = 2\pi r_0 D_u k_w / d \tag{9}$$

$$P' = \pi r_0^2 k' / D' = 2\pi r_0 D_{eq} k_w / d \tag{10}$$

$$D_{eq} = d r_0 k' / 2D' k_w \tag{11}$$

where, D_u = thickness of the upper aquifer; k' = hydraulic conductivity of the aquitard; and D' = thickness of the aquitard. Then, the transmissivity of the cut-off wall zone T' is expressed by Equation 12.

$$T' = (D_u + D_{eq}) k_w \tag{12}$$

Steady state drawdown in the excavation area enclosed by the cut-off wall is expressed by the following equations.

$$s = \frac{Q}{2\pi T_u} \ln\left(\frac{r_0}{r}\right) + \frac{Q}{2\pi T'} \ln\left(\frac{r_0 + d}{r_0}\right) + \frac{Q}{2\pi T} \ln\left(\frac{R}{r_0 + d}\right)$$

$$s = \frac{Q}{2\pi T} \ln\left(\frac{F'_w R}{r}\right) \tag{13}$$

where T = total transmissivity of the ground ($= k_u D_u + k' D' + k_l D_l$); T_u = transmissivity of the upper aquifer; and F'_w = the cut-off wall factor in multi-layered aquifer system (expressed by Equation 14).

$$F'_w = \frac{(r_0 + d/r_0)^{(T-T')/T'}}{(r_0/r_w)^{(T_u-T)/T_u}} = \frac{F_w}{(r_0/r_w)^{(T_u-T)/T_u}} \tag{14}$$

3 SIMPLIFIED DESIGN METHOD FOR DEEPWELLS IN LEAKY MULTIPLE AQUIFER SYSTEM

A simplified design method for deepwells in leaky multiple aquifer system is proposed by Kohsaka (1999) based on above three ideas.

3.1 *Input parameters for design*

The input parameters for design are listed in Table 1. These parameters are classified in following five categories; information about cut-off wall; information about interbedded aquitard; information about aquifers; condition of excavation; and information about deepwells. Most of these must be assumed, because it is difficult to investigate them. Enough attention must be paid, when the parameters which have great effects to the design results are estimated.

Table 1. Input parameters for design.

Category	Input parameter
Cut-off wall	d: thickness k_w: hydraulic conductivity
Aquitard	D': thickness k': hydraulic conductivity
Aquifer	D_u: thickness of upper layer T_u: transmissivity of upper layer T: total transmissivity R: influence radius
Excavation	r_0: equivalent radius s_0: required drawdown
Deepwell	η: well efficiency by well loss l: radius of well array r_w: effective radius of well s_w: drawdown in a well

3.2 *Procedure of design*

The design procedure is separated into two steps: the step for calculation of the required discharge rate; and the step for determining the number of deepwells.

3.2.1 *Calculation of required discharge rate*

The calculation procedure for the required discharge rate is as follows:

1. Calculate the equivalent penetration length D_{eq} by Equation 11.
2. Calculate the transmissivity of the cut-off wall zone T' by Equation 12.
3. Calculate the cut-off wall factor in multi-layered aquifer system F'_w by Equation 14, but F'_w is simplified to F_w by substitution r_0 for r_w.
4. The required discharge rate is calculated by the following equation derived from Equation 13.

$$Q_0 = \frac{2\pi T s_0}{\ln(F_w R / r_0)} \tag{15}$$

where, Q_0 = required discharge rate; s_0 = required drawdown; and r_0 = equivalent radius of excavation area.

3.2.2 *Determination of the number of deepwells*

The determination procedure for the number of deepwells is as follows:

1. Assume the number of deepwells n.
2. Calculate the equilibrium well efficiency coefficient η' by Equation 3.
3. Calculate the equilibrium well radius r'_w by Equation 4.
4. Calculate the cut-off wall factor in multi-layered aquifer system F'_w by Equation 14 by substitution r'_w for r_w.

Copyright © 2003 Swets & Zeitlinger B.V., Lisse, The Netherlands

5. Total discharge rate Q_n by deepwells of the number n is calculated by the following equation derived from Equation 13.

$$Q_n = n\eta' \frac{2\pi T s_w}{\ln(F'_w R / r'_w)} \tag{16}$$

where, s_w = drawdown in the deepwells.

6. Drawdown at the center of the excavation area s_c is calculated by the following equation.

$$s_c = \frac{Q_n}{2\pi T} \ln\left(\frac{F_w R}{r_0}\right) \tag{17}$$

7. Comparing s_c and s_0, if s_c is bigger than s_0, n can be adapted to the possible number of deepwells.

4 VERIFICATION OF PROPOSED METHOD BY 3-DIMENSIONAL GROUNDWATER FLOW ANALYSIS

4.1 *Analytical conditions*

The analytical model is shown in Figure 6. It has two aquifers and an interbedded aquitard. The thickness of the aquifers (D_u and D_l) is 10 m each, and the thickness of the aquitard D' is 2 m. Influence radius R is 200 m, and the head at the boundary is fixed to $H_0 = 32$ m from the bottom of the lower aquifer. Then these aquifers are in confined condition. The excavation area is circular in shape with the radius $r_0 = 20$ m and enclosed by a cut-off wall of thickness $d = 0.5$ m and hydraulic conductivity $k_w = 1 \times 10^{-5}$ m/min. The deepwells are placed in a circular array of radius $l = 18$ m. In this calculation a quarter model is used to reduce the calculation time and capacity. The mesh size which is surrounding the nodes corresponding to the deepwells is 1m square, then the apparent radius of the deepwell r_w is set to 0.2 m. The drawdown in the deepwells s_w is 8 m, then the head at the nodes corresponding to the deepwells is fixed to $h_w = 24$ m. The well efficiency by well loss η is determined as 0.85 by drawdown curve of one deepwell pumping simulation.

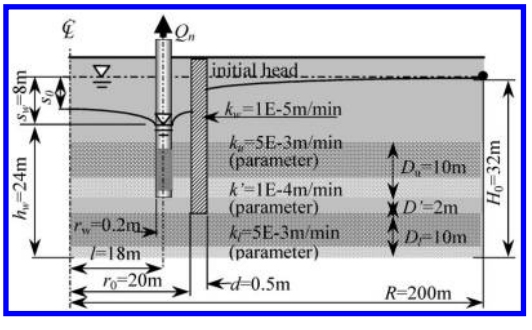


Figure 6. Analytical model of a multiple aquifer system.

The hydraulic conductivity of the aquitard k' is 1×10^{-4} m/min, and it is changed from 1/10 to 10 times of the original condition ($k' = 1 \times 10^{-5} \sim 10^{-3}$ m/min) in order to examine the influence of this parameter. The hydraulic conductivities of the aquifers k_u and k_l are 5×10^{-3} m/min, and they are changed from 1/5 to 4 times of the original conditions (k_u and $k_l = 1 \times 10^{-3} \sim 2 \times 10^{-2}$ m/min) in order to examine the influence of these parameters. The number of deepwells n is changed to 1, 2, 4, 6, and 8.

4.2 *Calculation results and discussions*

The design results from the proposed method are compared with the 3-dimensional analysis results in the following figures. In these figures, lines express results by the proposed design method (PDM) and marks express the computation results by 3-D FEM.

4.2.1 *Required discharge rate*

Figure 7 shows the relation between total discharge rate from the excavation area and drawdown at the center of the excavation. The hydraulic conductivities of the interbedded aquitard, the lower aquifer, and the upper aquifer are varied in each graph. It is clear from Equation 17 that the relation between the total discharge rate and the drawdown is linear in the proposed method, which is expressed by lines. The results by 3-D FEM, which is expressed by marks, show the same trend. The graphs show that the proposed design results are broadly consistent with the 3-D FEM results, but in the case of a high value of k' (□ and ▲ in graph a) and the case of a low value of k_l (● and ○ in graph b), the results don't agree well. The hydraulic conductivity of the aquitard has a great effect on the relation between s_0–Q_0, whereas the hydraulic conductivities of the aquifers have little effect.

The variation of the discharge rate to provide the required drawdown $s_0 = 6$ m with the hydraulic conductivities is shown in Figure 8. The required discharge rate which is calculated by the proposed method is consistent with that of 3-D FEM results. Some differences between the two results are recognized in the following parts: The hydraulic conductivity of the aquitard is high; that of the lower aquifer is low; and that of the upper aquifer is high. However, the differences are smaller than 30% and since the results of the proposed method are bigger than the FEM results, it provides the safety side.

4.2.2 *Deepwell number*

Figure 9 shows the relation between the number of deepwells and drawdown at the center of the excavation. In these graphs, the results by the proposed design method are consistent with the results of the 3-D FEM. The graphs show that the hydraulic conductivities of the aquitard and the upper aquifer have

Copyright © 2003 Swets & Zeitlinger B.V., Lisse, The Netherlands

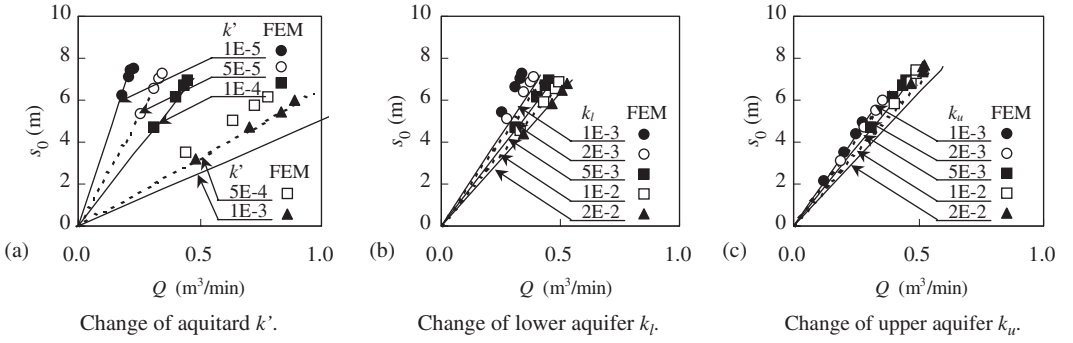


Figure 7. Comparison of calculation results of Q-s_0 relation with proposed design method (PDM) and FEM.

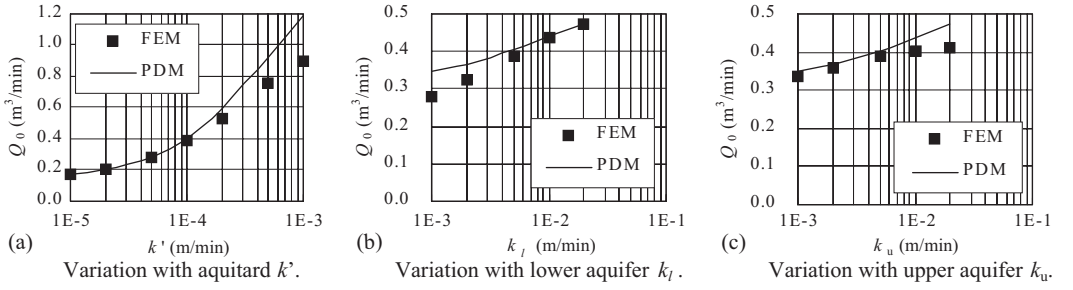


Figure 8. Variation of the required discharge rate with the hydraulic conductivities.

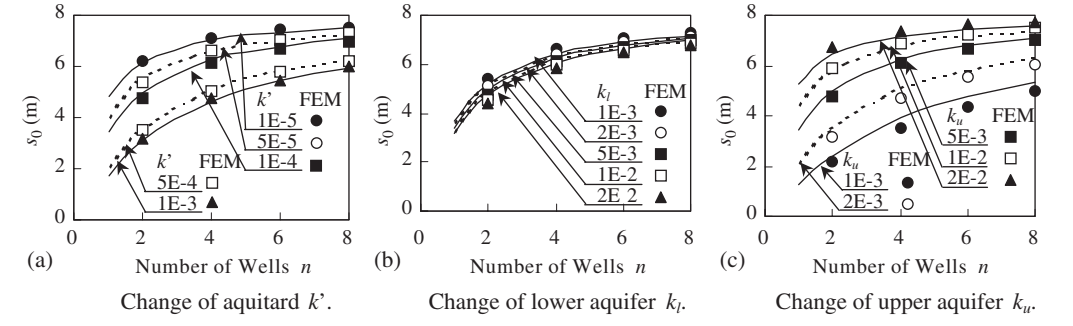


Figure 9. Comparison of calculation results of n-s_0 relation with proposed design method (PDM) and FEM.

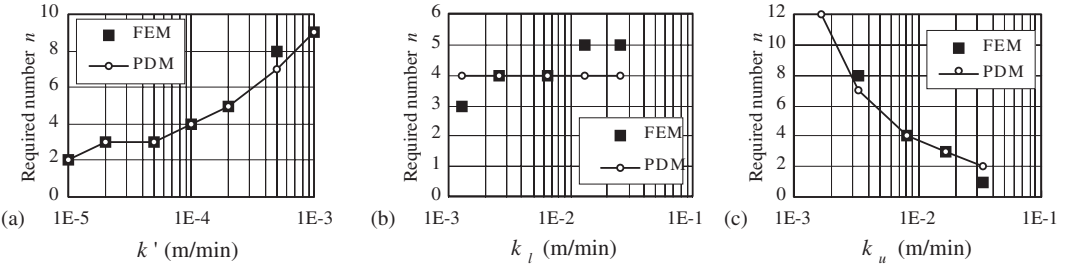
great influence on the number of deepwells, whereas the hydraulic conductivity of the lower aquifer has little effect.

The number of deepwells that provides the required drawdown of $s_0 = 6$ m is shown in Figure 10 with the variation of the hydraulic conductivities. The calculated results from the proposed design method agree well with the results of FEM. These graphs show that the hydraulic conductivities of the aquitard and upper aquifer have great effects on the estimation of the number of deepwells. As the hydraulic conductivity of the aquitard becomes large, and the hydraulic conductivity of the upper aquifer becomes small, more deepwells are required.

5 CONCLUSIONS

In this paper, a simplified design method for deepwells in a multiple aquifer system is proposed. A

Copyright © 2003 Swets & Zeitlinger B.V., Lisse, The Netherlands



Variation with aquitard k'. Variation with lower aquifer k_l. Variation with upper aquifer k_u.

Figure 10. Variation of the required number of deepwells with the hydraulic conductivities.

design procedure to calculate the required discharge rate and to determine the number of deepwells is shown and verification of this method is confirmed by the comparison with 3-D FEM results.

The differences between the results of the proposed design method and 3-D FEM for the required discharge rate are smaller than 30%. The calculated results of the number of deepwells that will provide the required drawdown by the proposed method agrees well with the FEM results. These results prove that the proposed method is useful for practical use.

REFERENCES

Kohsaka, N. 1995. Evaluation method for the number of deepwells in an axis symmetric analysis. *The proceedings of the 50th Japan society of civil engineers annual meeting*: III212–213.

Kohsaka, N. 1997. Drawdown characteristics in excavation area enclosed by cut-off wall. *The proceedings of the 52nd Japan society of civil engineers annual meeting*: III494–495.

Kohsaka, N. 1998. Evaluation method of cut-off wall effect in multiple aquifer system. *The proceedings of the 53rd Japan society of civil engineers annual meeting*: III624–625.

Kohsaka, N. 1999. Proposal of a simple calculating method for deepwells in multi-layered ground. *The proceedings of the 34th Japan national conference on soil mechanics and foundation engineering*: 1339–1340.

Copyright © 2003 Swets & Zeitlinger B.V., Lisse, The Netherlands

Effects of subsurface water on stability of slopes

Copyright © 2003 Swets & Zeitlinger B.V., Lisse, The Netherlands

Changes in strength characteristics of rock-powder under the action of carbonic acid

N.P. Bhandary
Graduate School of Science and Engineering, Ehime University, Matsuyama, Japan

K. Hirota
Nihon Kiso Engineering Consultants, Tokyo, Japan

R. Yatabe & K. Yokota
Ehime University, Matsuyama, Japan

ABSTRACT: A large number of landslides in Shikoku, Japan have been caused by tectonic activities along the fault lines that pass across east-west of the island. One of the major reasons for the activation of these landslides is weathering of rock minerals along the slip surface. Although a number of research studies relating to the mechanism of landslide activation and landslide properties have been carried out, the proper mechanism of rock mineral weathering and the strength characteristics of weathered mass are yet to be investigated in detail. This paper therefore makes efforts to introduce the action of carbonic acid on the rock minerals, and resulted changes in the strength properties of the rock minerals under the chemical action of the carbonic acid. So as to carry out the study strength and X-ray diffraction tests were performed on the rock powders obtained from some landslide sites in Shikoku, and comparisons were made among the strength properties and ion releases in the samples obtained. The test results revealed that the shear strength of rock powder decreases with the increase in period of action of carbonic acid, which is due to ion release by the rock minerals and changing into weaker clay minerals.

1 INTRODUCTION

Like many other mountainous countries, Japan with nearly 70% mountainous terrain has always become an active region for the geo-hazards like landslides, slope collapses, and debris or mudflows. In addition to rain-induced slope failures occurring every year, many active and potential landslides sites have been recognized in various parts of the country. One of such parts is Shikoku Island in western Japan, which is made of nearly 80% of steep mountainous terrain. For this reason most landslides in Shikoku Region are found to have steeper slopes as reported by Yagi et al. (1989). They report that the landslides in Shikoku have steeper angle of slip than the landslides in tertiary zone in northern Japan.

Figure 1 shows landslide distribution map of Shikoku including active and potential landslide sites prepared by the Ministry of Construction (1992). Investigations have shown that the geological condition of the Shikoku Island is comparatively fragile because three active fault lines pass across the island in east west direction (Yagi et al., 1989). One of these fault lines and the most active one is median tectonic line (better known as MTL), which has a total length of more than 2000 km. Adjacent to this on the south is second active fault line, which is known as Mikabu tectonic line (MiTL). As also seen in Figure 1, most landslides on Shikoku Island have occurred near these two fault lines. Geological investigations have revealed that the rock masses near the MTL and the MiTL are in fractured state due to ever continuing tectonic activity along the fault lines. This fractured state of the rock masses in Shikoku is supposed to be one of the main causes of landslide activation. For this, the landslides in Shikoku are often known as fracture zone landslides (Ministry of Construction, 1992).

Most landslides on the Shikoku Island possess a distinct layer of clayey soil weathered from rock minerals as their slip surfaces. Except for the case of hydrothermal clay formation, the reason for the formation of such clay layers in the landslides is supposed to be the physical changes due to failure of slope mass and tectonic movement followed by the decomposition of the rock minerals due to chemical action of the underground water. So far, the characteristics of

Copyright © 2003 Swets & Zeitlinger B.V., Lisse, The Netherlands

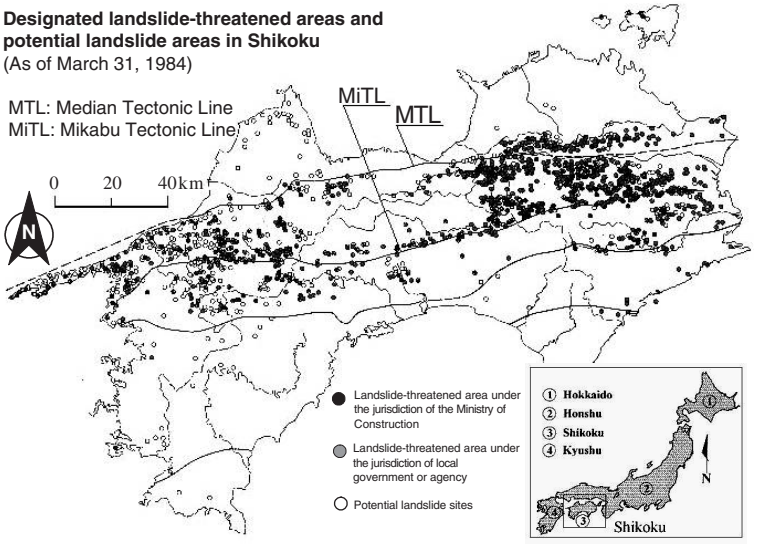


Figure 1. Distribution of landslides in Shikoku (from Ministry of Construction, 1992).

the landslide clay as well as the composed minerals have been studied (Yube, 2001), but the mechanism of formation of the minerals in the landslide clays is yet to be understood well. It has been widely accepted that the chemical decomposition of rock minerals is a result of the release of ions from the rock mineral structure under the action of groundwater. It is therefore obvious that the strength characteristics of the slip surface soil are greatly influenced by the chemical action of the underground water in addition to causing the chemical decomposition of the soil. Hence, efforts are made in this paper to study the changes in shear strength of powdered samples of dominant rock types obtained from some active landslide sites on Mikabu geological belt, which lies between the MTL and the MiTL in Shikoku under the action of carbonic acid.

2 MINEROLOGICAL ASPECTS

The importance of mineralogical study in evaluating the soil strength and its formation is very significant. Mineralogical analysis not only helps to recognize the soil type but also makes clear the mechanism of soil weathering and changes in strength properties of the soil. The study of mineralogical aspects of some major landslides on the Shikoku Island have revealed that a greater number of fracture zone landslides consist of expansive clay minerals in their slip surface soils (Yagi et al., 1999). The formation of the expansive clay minerals can be directly attributed to weathering or decomposition of the rock minerals under the chemical action of underground water. In the process of decomposition, minerals like mica and chlorite lose certain ions and turn into weaker minerals like smectites and expansive chlorite (Yatabe et al., 2000). Other minerals present in the slip surface soils of the landslide in Shikoku are feldspar, illite, vermiculite, serpentinite, etc. All these minerals undergo chemical decomposition under the action of underground water, and this process becomes one of the prominent factors that activate creeping landslides.

3 TESTS AND RESULTS

The tests conducted in the laboratory mainly consist of ring shear tests to evaluate the soil strength and X-ray diffraction tests to analyze the mineralogical composition of the soil samples. The ring shear tests were carried out under drained conditions and the state of the test samples was saturated. The particle size of the test samples at the beginning of the tests was below 425 μm. The shape of the specimen sheared was like a flat-ring with external diameter of 16 cm, internal diameter of 10 cm, and initial thickness of 2 cm. The shearing speed or the rate of shear in terms of angular measurement was set to be 0.44°/min (i.e., 0.5 mm/min along the center of the specimen width). It was preconfirmed that the development of pore water pressure due to shearing at this rate of deformation remains negligible making the shearing condition to be perfectly drained.

The test samples were obtained from various landslides sites in the Mikabu belt, where the dominant

Copyright © 2003 Swets & Zeitlinger B.V., Lisse, The Netherlands

Table 1. Physical and strength parameters for the rock powder samples employed in the test.

Test sample	Triaxial	Ring shear		LL	PL		Solid density	Initial particle size distribution		
								Clay	Silt	Sand
	$\phi'(^\circ)$	$\phi_d\,(^\circ)$	$\phi_r\,(^\circ)$	(%)	(%)	I_p	ρ_s (g/cm^3)	(<5 μm)	(5~75 μm)	(75~425 μm)
Black schist	32.9	26.7	22.4	23.5	16.3	7.2	2.81	14.3	34.7	51.0
Green schist	42.9	43.4	40.4	20.2	13.7	6.5	3.02	17.4	44.0	38.6
Serpentine	44.8	44.6	40.0	–	–	–	2.65	9.3	37.4	53.3
Mikabu greenstone	35.7	41.6	32.8	–	–	–	2.09	10.9	29.1	60.0

ϕ': effective angle of friction, ϕ_d: peak angle of friction, ϕ_r: residual angle of friction, LL: liquid limit, PL: plastic limit, I_p: plasticity index.

rock types are green schist, black schist, Mikabu greenstone, and serpentine. The samples obtained were not all fresh rocks but slightly weathered soft rocks composed of cemented and free particles. The powder samples employed in the tests were prepared by crushing the four types of rock samples and sieving through 425 μm sieve. The physical and strength parameters of each prepared sample are listed in Table 1.

While preparing the test samples with carbonic acid, 1800 ml of distilled water was first poured into four 3000 ml glass jars. Then, 900 gm of each powdered rock sample was added into the jars. Finally, CO_2 gas was passed into each jar at a rate of 50 ml/min until the pH of the solution came down to a level of 5.0. From this state of the crushed rock samples pH measurement, estimation of amount of ions released, X-ray diffraction tests, ring shear tests, particle size analysis, etc. were carried out for a period of three months. The former two observations were carried out in a two-week interval except for the very first week, whereas the X-ray diffraction and ring shear tests were conducted in one month interval. The amounts of ions released in terms of weight per volume of the liquid were estimated by spectroscopic analysis using ICP (Inductivity Coupled Plasma) instrument.

The measurements of the pH values for each solution in the jars are presented in Figure 2. It is clear that the pH values for all solutions have risen above 6.5, which is because the hydrogen ions present in the solution react with carbonates and form water and carbon dioxide gas, as exemplified below.

$$CaCO_3 + 2H^+ \rightarrow Ca^{2+} + CO_2 + H_2O \qquad (1)$$

Similarly, the results of spectroscopic analysis to estimate the amounts of ions released by the minerals in the tests samples are shown in Figure 3. It is seen that except for the serpentine sample, all three sample show a considerable release of calcium ions. However, the release of magnesium ions in case of green schist and Mikabu greenstone is significantly more than that from the black schist. The release of magnesium ions from these two rock samples is supposed to be due to presence of chlorite minerals in them. On the other hand, the black schist shows a notable release of potassium ions, which is because the black schist consists of mica and mica under the action of carbonic acid released potassium ions. It is supported by the results of X-ray diffraction tests for black schist sample, as shown in Figure 4. Here, the peak for mica is seen to have decreased notably with the passage of time, which clearly means that the amount of mica in the sample decreased after releasing the potassium ions. The release of calcium ions in the black schist can be attributed to the presence of feldspar in it, whereas that in the green schist and the Mikabu greenstone is due to presence of hornblende.

The release of magnesium ions in serpentine, on the other hand, is seen to be significantly more than that in other three samples. It may be considered that the serpentine consists of brucite layers, which under the action of carbonic acid might have released excessive magnesium. This means that the serpentine rock is much more prone to weathering than the green schist and Mikabu greenstone. Likewise, the decomposition of mica in black schist is very much notable. Although there was seen no significant difference in the amount of ions released by Mikabu greenstone and green schist in the lab, the field observation of the state of their weathering shows that the former is more decomposed than the latter.

The results of the strength tests in terms of peak (ϕ_d) and residual (ϕ_r) angles of shearing resistance are presented in Figure 5. Compared to almost negligible variation of the strength (i.e., in terms of angles of shearing resistance) for black schist, the strength for green schist has decreased significantly. Likewise, the strengths for Mikabu greenstone and serpentine under the action of carbonic acid seem to have decreased with the passage of time. The reason for the decrease in the strength of the test samples might be considered to be

Copyright © 2003 Swets & Zeitlinger B.V., Lisse, The Netherlands

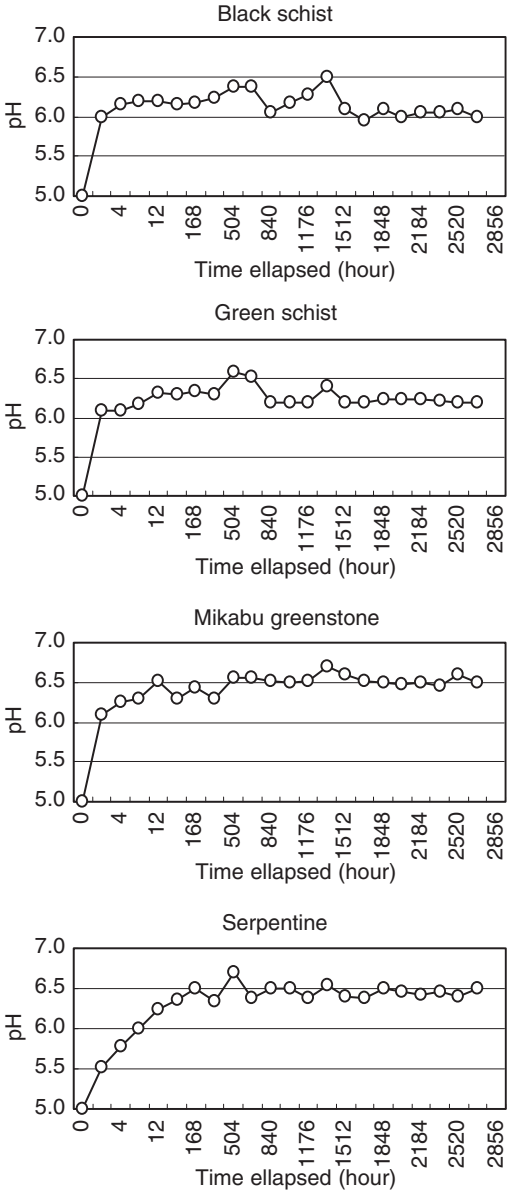


Figure 2. Measurement of pH during the test period.

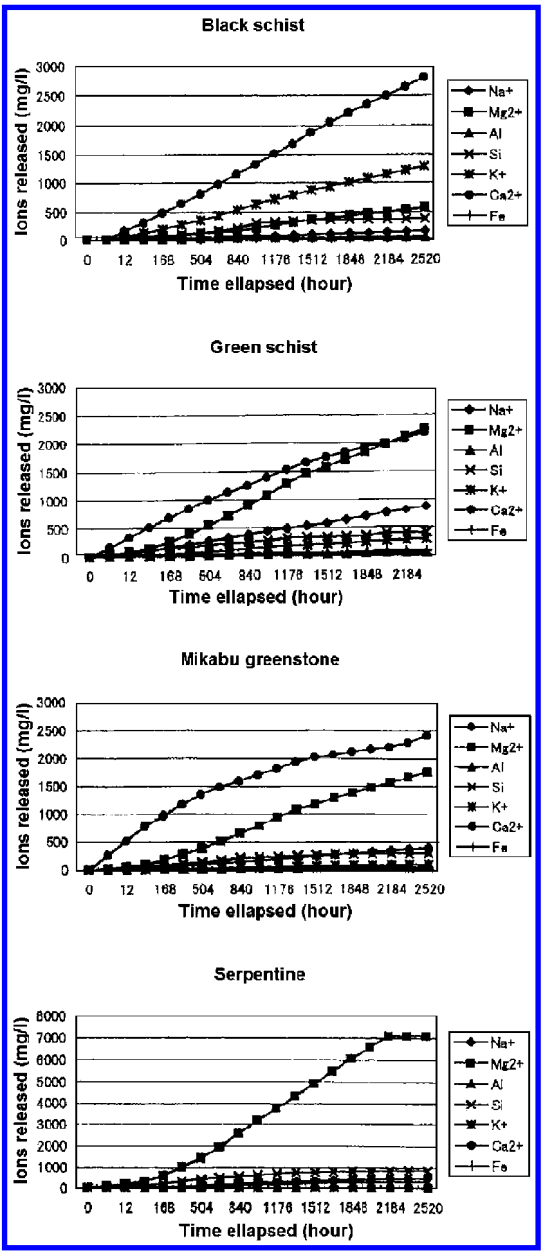


Figure 3. Amounts of ions released by the sample rocks.

formation of and increase in the clayey particles due to either mineral decomposition or particle crushing during the shear. It was therefore necessary to look into pre- and post-test particle size distribution of the samples.

Figure 6 shows the results of particle size analysis for each test sample. It is clear from the figure that except for the serpentine sample, the percentage of finer particles in case of other three samples has considerably increased in three months due to the action of carbonic acid. Serpentine sample, on the other hand, shows negligible change in particle size distribution even after three months. The decrease in strength of the serpentine sample might therefore be attributed to particle crushing during the shear deformation. Figure 7 shows results of the particle size analysis for

Copyright © 2003 Swets & Zeitlinger B.V., Lisse, The Netherlands

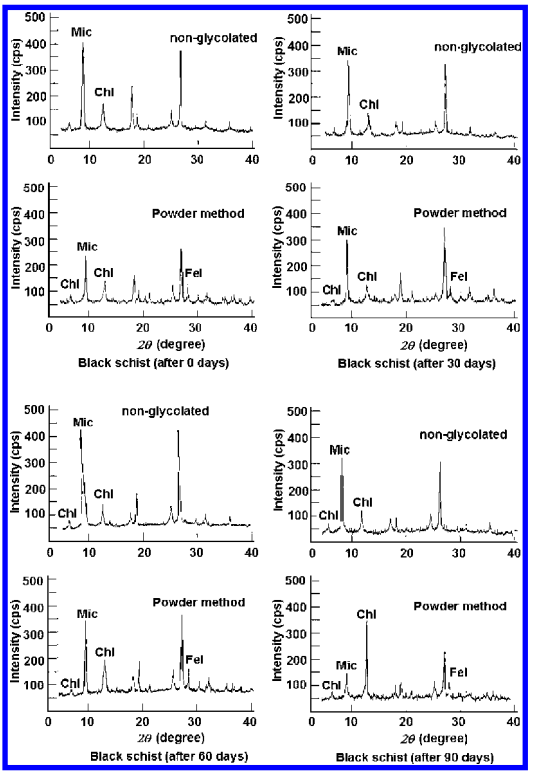


Figure 4. X-ray diffraction patterns for black-schist sample.

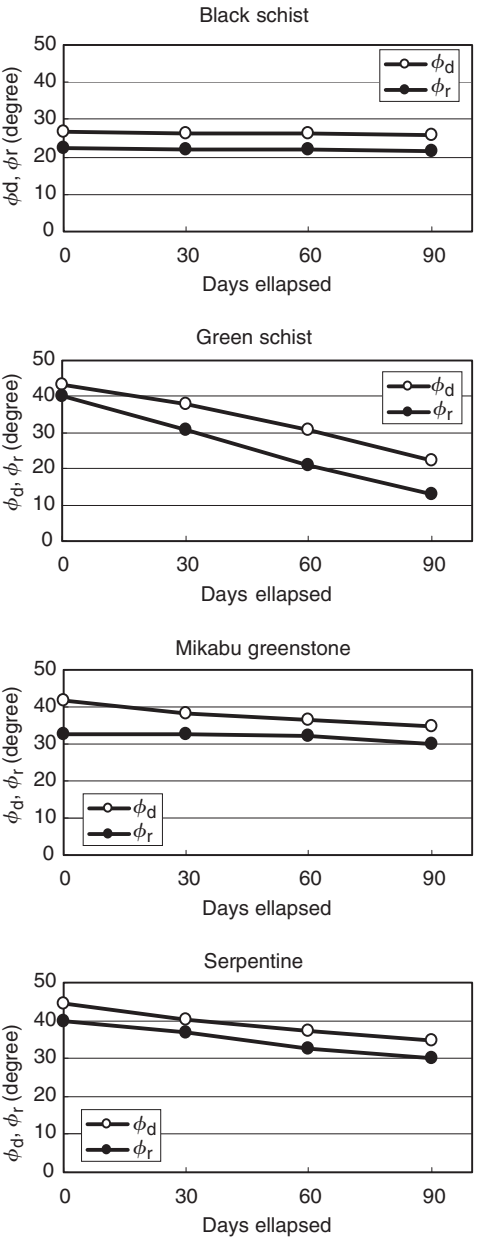


Figure 5. Variation in strengths in terms of angles of shearing resistance for all tested rock samples.

the serpentine sample before and after the shear tests, which indicates a clear increase in percentage of the finer particles.

Thus, the implications of the test results presented above can be summarized as follows. The increase in the pH values of the test solutions indicates a clear exchange of ions between the mineral compounds and the acid. The spectroscopic tests showed that the amount of ions released by the rock minerals in the carbonic acid is significant, which resulted in decrease of the shear strength of the samples as seen in ring shears tests. Except for the serpentine sample, the reason for the decrease in shear strength of the test samples was mineral structural weakening due to release of ions from the minerals. In serpentine sample, the decrease in the shear strength due to ion release was seen to be insignificant despite having released a significant amount of Mg^{2+} ion.

4 CONCLUSIONS

This paper briefly introduced the mineralogical aspects and the effect of ion release from the minerals on the strength of soil material involved in the landslides near the active fault lines on Shikoku Island of Japan. In addition to causing chemical decomposition of the soil minerals, the action of underground water greatly affects the strength properties of the soil. In an effort to investigate the action of underground water on the rock and soil minerals, the ring shear and X-ray diffraction

Copyright © 2003 Swets & Zeitlinger B.V., Lisse, The Netherlands

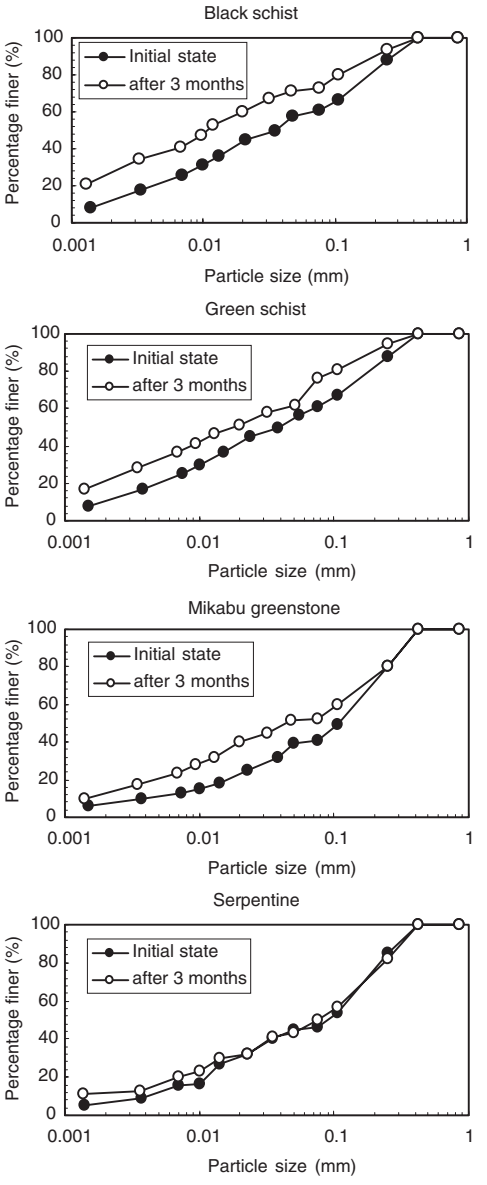


Figure 6. Particle size distribution curves for the tested samples indicating increase in finer particles with the passage of time.

tests conducted on powdered rock samples in carbonic acid revealed the following.

1. The pH value of the carbonic acid solution after reacting with the rock minerals increases with the passage of time, which is due to loss of hydrogen ions to form water and carbon dioxide from carbonates present in the rock minerals.

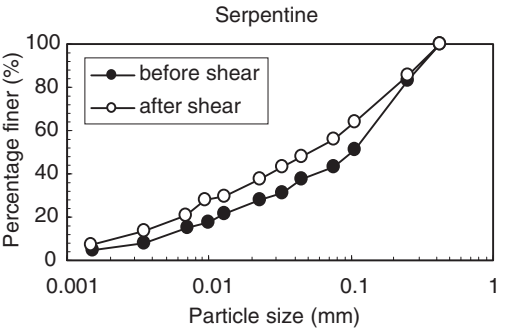


Figure 7. Particle size distribution curves for serpentine sample indicating increase in finer particles after the shear.

2. The major ions released by the test samples in the carbonic acid solution were magnesium (Mg), calcium (Ca), and potassium (K) along with some aluminum (Al), iron (Fe), and silica (Si).
3. The black schist, green schist, and Mikabu greenstone samples showed nearly equal amount of Ca^{2+} release, whereas the serpentine sample released a significant amount of Mg^{2+}. This makes it clear that rock minerals release their major ions under the action of carbonic acid.
4. The values of angles of shearing resistance decrease with the passage of time, which might be attributed to increase in finer particles in the test samples due either to chemical decomposition or particle crushing during the shear. The maximum decrease due to release of ions was found to be half after three months.
5. The chemical decomposition of the minerals causes structural weakening of the soil particles due to release of the ions by the minerals as understood from the laboratory tests.

REFERENCES

Ministry of Construction, 1992. *Landslides in Japan*, A booklet published by Sabo Publicity Center, Slope Conservation Division.

Yagi, N., Yatabe, R., & Enoki, M., 1989. Stability analysis on landslide in fracture zone, The Japan-China Symposium on Landslides and Debris Flows, Japan, p.147–152.

Yagi, N., Yatabe, R., Yokota, K., & Bhandary, N.P. (1999). Strength of landslide clay from mineralogical point of view, Proc. IS-Shikoku'99, Matsuyama, Japan, Vol. 2, p. 701–704.

Yatabe, R., Yokota, K., Yagi, N., & Bhandary, N.P., 2000. Influence of expansive chlorite on the strength of weathered green rock at Mikabu belt of Japan. Proc., Geoeng2000, Melbourne, Australia (CD version).

Yube, M., 2001. *Mineralogical and Geotechnical Considerations on Mechanism of Landslides in Mikabu Belt*, Doctoral Thesis, Ehime University, p. 116 (in Japanese).

Copyright © 2003 Swets & Zeitlinger B.V., Lisse, The Netherlands

Failure of cut slopes in the Izumi group and associated action of groundwater

J. Uchida
Takamatsu Technical Office, Japan Highway Corporation, Takamatsu, Japan

R. Yatabe, K. Yokota & N. Yagi
Ehime University, Matsuyama, Japan

ABSTRACT: A part of the geology of Shikoku Island in Japan is characterized by Izumi rock group composed primarily of inter-layered sandstone and shale rocks. The Izumi group is distributed on the north of median tectonic line on Shikoku, which is one of the prominent active fault lines in Japan. Construction of the expressways in Shikoku, especially over the Izumi group resulted in disturbance of the natural slope stability causing various patterns of cut slope failures. One of the patterns, as mentioned in this paper, is sliding failure of slope mass through the bedding planes where the shale rock has been weathered into clayey layers. It is considered that such a failure is caused by rise in pore-water pressure at the clay layers following a rainfall. Therefore, the variations of pore-water pressure at the shale-turned-clay layer are observed in-situ at a failure site in Itano-Naruto section of the expressway linking Takamatsu and Tokushima cities in Shikoku. The slope stability analysis results revealed that lowering the groundwater level by applying drainage borings could largely stabilize the cut slopes in the Izumi group.

1 INTRODUCTION

A significant number of cut slopes along the expressways linking Takamatsu, Tokushima, and Matsuyama cities in Shikoku region of Japan constructed over the Izumi geological group, which is distributed on the north of the median tectonic line (indicated as MTL in Figure 1), experienced plain failure through the bedding planes. The Izumi group of rocks in Shikoku is primarily composed of inter-layered sandstone and shale rocks, and the shale rock layers particularly near the MTL in most cases have turned into clayey layers under various favorable conditions for weathering of rock. In such geological formations, failure of cut slopes through interlayer dipping planes is considered to be caused by development of pore-water pressure at the clay layers following a rainfall. The developed pore-water pressure reduces the effective normal stress acting along the potential plane of failure, thereby resulting in reduction of the shear resistance.

This paper attempts to report field observations of rise in pore-water pressure at bedding plane clay layers of a failed cut slope along Itano-Naruto section of Takamatsu-Tokushima expressway. A relationship is established between amount of rainfall and rise in pore-water pressure, which is then employed in estimating the pore-water pressure at the time of failure. In addition, the strength parameters for the weathered shale in the form of clay are determined by carrying out the direct shear tests, and the stability aspects of a cut slope during the rise in pore-water pressure at the clay layers are studied. Finally, a proposal is made such that the most effective way to stabilize the cut slopes in the Izumi group is application of the drainage borings.

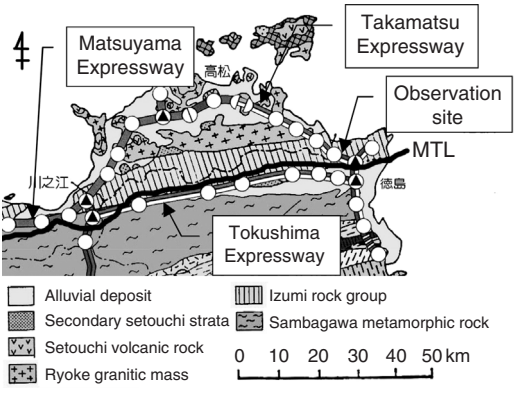


Figure 1. Geological map and the observation site.

Copyright © 2003 Swets & Zeitlinger B.V., Lisse, The Netherlands

2 STUDY SITE

As the Itano-Naruto section of the expressway has been aligned to pass through the lower hills of the south slopes of the Okusan Mountains on the north of Yoshinogawa River, it is quite close to a part of the median tectonic line near the Naruto fault. The site where the pore-water pressure observations and measurements were made is indicated in Figure 1.

The geology of the study site is characterized by the distribution of sandstone and shale rocks of the Izumi group. Due to tectonic activities through the median tectonic line, however, the shale rock layers in the alternately layered sandstone and shale rock masses with a domination of the latter have undergone decomposition turning into clay layers. The dip and strike of the bedding planes or the interlayer planes were observed to be N60° and E22°, respectively, and the cut slope plane is parallel to the interlayer planes with a dipping rock mass structure.

3 SLOPE FAILURE AND PLACEMENT OF THE PORE-WATER PRESSURE METER

The failed slope measured 70 m in width and 17 m in length. It was cut in three steps, and the step that failed was first from the bottom, which had an inclination of about 34° (i.e., a gradient of 1:1.5).

The slope failed after a continuous rainfall amounting 26.5 mm. At the beginning, a 10 cm crack measuring one meter in length was observed near the middle-bottom of the step, and one meter portion of the step was seen to have bulged. Finally, however, the failure of the same part of the slope went up to an extent measuring as big as 10 m wide and 8 m long (indicted as 'crack' at the bottom of the slope in Figure 2). A second slope failure measuring 30 m wide and 10 m long in similar dipping conditions of the rock mass occurred near the top of the slope step along a plane through the clayey layer of the weathered shale rock (indicted as 'crack' at the top of the slope in Figure 2).

To measure pore-water pressure developed due to rise in groundwater level, a pore-water pressure meter (indicated by No.1 in Figure 2) was placed at the level of failure plane in the developed deformation crack of the second slope failure.

4 RAINFALL AND DEVELOPED PORE-WATER PRESSURE

After having measured the pore water pressure at the clay layer formed as a result of shale rock weathering for about four months beginning July 2001, a relationship between the amount of rainfall and the developed pore water pressure could be established.

As per the rock classification (Miyashima, 1982) for the Izumi group, the rock mass at the site of slope deformation was found to have cracks of as big as 3 cm, and it was one of the most fractured rock masses.

The relationship between the amount of rainfall and the developed pore-water pressure is shown in Figure 3. As seen in the figure, there is no rise in the pore-water pressure at the level of plane of failure as long as the amount of a continuous rainfall remains below 6.5 mm. However, a representative amount of rainfall causing a rise in the pore-water pressure can be seen to be 10 mm. Based on the pattern of rise in groundwater level with the amount of continuous rainfall, a relationship between them can be established. If the amount of continuous rainfall causing maximum rise in the pore-water pressure is taken to be R (mm), the maximum groundwater level, W (GL-m) can be related with R as follows.

$$W = 0.002R - 0.36 \quad (1)$$

Moreover, the representative pattern of rise in the pore-water pressure with the amount of rainfall is shown in Figure 4.

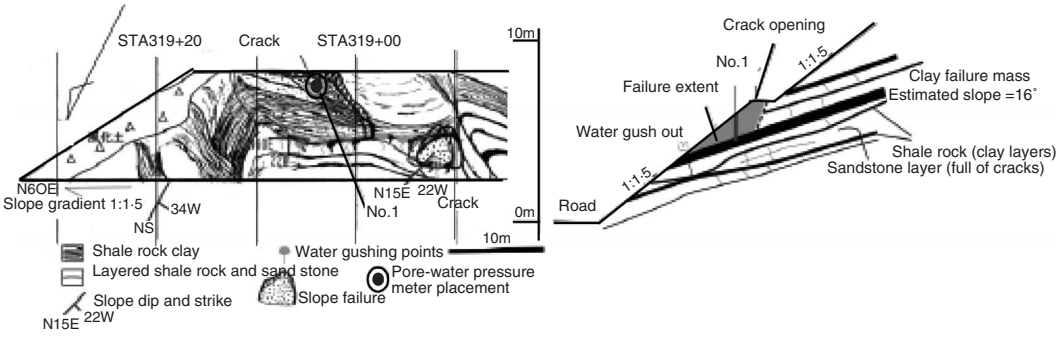


Figure 2. Slope failure conditions and placement of pore-water pressure meter (No.1).

Copyright © 2003 Swets & Zeitlinger B.V., Lisse, The Netherlands

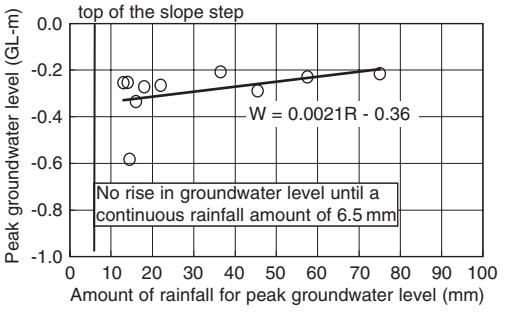


Figure 3. Relationship between continuous rainfall and the peak pore-water pressure (groundwater level).

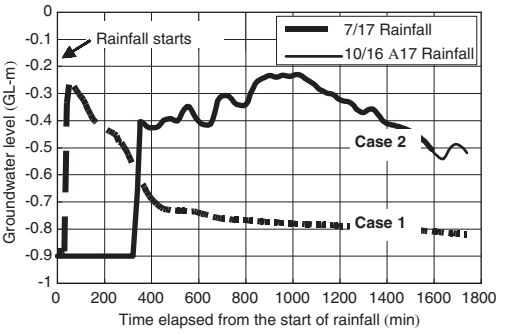


Figure 4. Variation of groundwater level after the beginning of rainfall.

Two cases were dealt in the study. Case 1 was taken to be the maximum rainfall intensity below 10 mm continuing for 1 to 2 hours, whereas Case 2 was taken to be the maximum rainfall intensity below 5 to 6 mm continuing for 4 to 7 hours. In both cases, the rise in pore-water pressure was observed to be abrupt, and immediately after the rainfall of amounts mentioned above the rise in groundwater level in 10 to 20 minutes was observed to be 50 to 70 cm. Thus, based on the observations as shown in Figures 3 and 4, the amount of continuous rainfall at the time of slope deformation was determined to be 26.5 mm, which caused a rise in groundwater level up to GL-0.3 m in the slope.

5 LABORATORY TEST RESULTS

The laboratory tests consisting of reversal box shear tests were carried out on disturbed soil samples collected from the failure planes of the deformed slopes. As a result of the tests, as shown in Figure 5, the peak angle of shearing resistance ϕ and the cohesion intercept c were obtained as 25.1° and zero respectively. These values of strength parameters were then compared with the values obtained from back

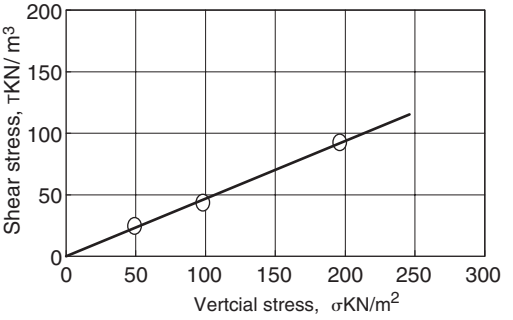


Figure 5. Result of direct ring shear tests.

analysis method so as to adopt closer values of strength parameters in the stability analysis.

6 SLOPE STABILITY ANALYSIS

So as to carry out the slope stability analysis at the time of failure under the action of rising groundwater level, the Fellenius method was employed.

The strength parameters in the field conditions were estimated by the back analysis method. The assumptions made in the back analysis were that the unit weight of the failed slope material was 19 kN/m^3 (1.9 tf/m^3) and the failure was a plain type failure through a layer consisting of shale rock clay with a horizontal inclination of 16°. At the time of failure the groundwater level was supposed to be GL-0.3 m based on the amount of continuous rainfall of 26.5 mm as obtained from Figure 3, and the factor of safety at the time of collapse was assumed to be $F_s = 0.95$.

From the back analysis of the failed slope and the laboratory tests, the adopted values of the strength parameters for the failed slope material, i.e. shale rock clay, were:

Drained cohesion, $c = 2.1$ kN/m^2 (0.21 tf/m^2)
Angle of shearing resistance, $\phi = 25°$

The values of the strength parameters thus obtained were then used in carrying out the stability analysis of the failed cut slope under the influence of groundwater level variation. The results of the analysis are presented in Figure 6, which indicates that the factor of safety for the slope goes up to 1.0 when the groundwater level comes down to GL-0.4. The figure also indicates that the factor of safety increases to as high as 1.2 if the groundwater level decreases below a level of GL-0.8.

7 PROPOSED STABILIZATION METHOD

A cut slope in dipping geological conditions is quite prone to plain failure through inter-bedding or

Copyright © 2003 Swets & Zeitlinger B.V., Lisse, The Netherlands

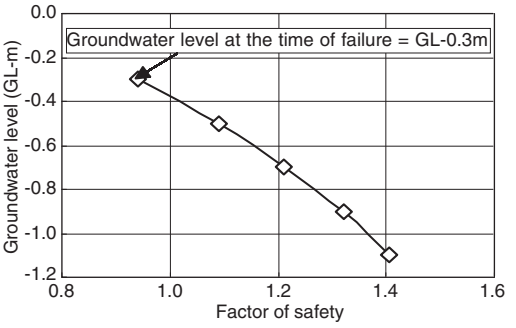


Figure 6. Relationship between the factor of safety and the groundwater level.

interlayer planes due to rise in groundwater level (i.e., pore-water pressure) following a rainfall. To overcome this problem, it is necessary to lower the groundwater level to GL-0.8 m, as indicated in Figure 6, which results in an increase of the factor of safety to as high as 1.2. According to Okuhara & Ogata (1984), the safe requirement of drainage boring to bring down the groundwater level in 100 m^2 of slope area by 1 m is 10 m. As per this the stability of the cut slope in Taima area with a total width of 60 m can be assured by applying 5 m long drainage borings with an inter-boring space of 10 m in one step of the cut slope.

Thus, as a control work for the cut slopes in above mentioned conditions, the application of drainage borings together with the ground anchors might result in an increased safety of the cut slopes, which could help lower the groundwater level prior to a condition that could cause the slope failure.

8 CONCLUSION

This paper briefly introduced the aspects of cut slope failures in the Izumi group of Shikoku due to the action of groundwater on interlayer planes of sandstone and shale rocks, especially the weathered layers of shale rock. The rise in the groundwater level following a rainfall was found to have resulted in an increased pore-water pressure at the weathered shale rock layers. It was particularly observed that the failure or the slope deformations occurred in the cut slopes that had a dipping rock mass with a gradient of 1:1.5. In addition, the failure spots had a dense distribution of cracks with a greater existence of clay layers weathered from the shale rock. The slope stability analysis after applying drainage borings so as to lower the groundwater level showed that the drainage borings of length 5 m effectively bring down the pore-water pressure, thereby increasing the factor of safety for the slope in geological conditions as mentioned in this paper. It is expected that a proposal on implementing such drainage borings so as to control cut slope failures in the Izumi group or the similar geological conditions will be made and verified by experimental studies as a follow up research work to this study.

REFERENCES

Miyashima, K. 1982. Geotechnical investigations for Naruto bridge (II), Oyo Chishitsu Corporation, Vol. 23, No.1, 46–56 (in Japanese).

Okuhara, M. & Ogata, H. 1984. A report on the problems and effects of groundwater collecting wells in the landslide sites, Japan Highway Corporation, Vol. 21, 13–20 (in Japanese).

Copyright © 2003 Swets & Zeitlinger B.V., Lisse, The Netherlands

The change in suction and water content in natural Masado slopes due to rainfall

Thi Ha, T. Moriwaki, Y. Sasaki & S. Kano
Hiroshima University, Hiroshima, Japan

A.K. Dissanayake
University of Peradeniya, Peradeniya, Sri Lanka

ABSTRACT: The Hiroshima Prefecture is mostly underlain by weathered granite soil called Masado and heavy rainfall had repeatedly caused slope failures and debris-flows that had led to severe damages to both life and property in this region. In order to study the mechanism of slope failure induced by rainfall infiltration and groundwater flow, a research was carried out by monitoring the suction, water content and groundwater level in natural Masado slopes nearby a debris-flow site on Hiroshima University premises, where a debris-flow had occurred due to heavy rainfall on June 29, 1999. From the monitoring results, the changes in suction, water content and groundwater level in the slopes with rainfall infiltration were investigated and then the water retention curves of the in-situ Masado were obtained. It was also found that the different conditions at each site such as topography and geological structure lead to different responses in suction and water content in the slopes.

1 INTRODUCTION

Masado, one of the typical residual soils in Japan, is sandy soil of heavily weathered granite and it is widely dispersed in the western part of Japan including the Hiroshima Prefecture (Figure 1). The Hiroshima Prefecture has many susceptible natural slopes to rain-induced failures and has repeatedly experienced such disasters. Among them, a remarkable series of slope failures and debris-flow occurred on June 29, 1999 causing severe damages to property and loss of 32 human lives.

It is difficult to predict when and where slope failures will occur, and by what amount and pattern of rainfall. Therefore, traffic restriction and public warnings against slope failure are generally established based on the past relational data of precipitation and disasters. One of the authors had already proposed a rainfall index (R_f) to evaluate the hazard of failure in the Masado slopes based on the analysis of rainfall data of the June 29, 1999 Hiroshima Prefecture Disaster. Detailed description of Rf has been presented in Sasaki et al. 2001, and so Rf will not be discussed in this paper. The advantages of this rainfall index expressing the amount of the accumulative and hourly precipitation by one variable, are the simplicity and good possibility to evaluate the hazard of failure for the broad range of region. On the other hand, from the

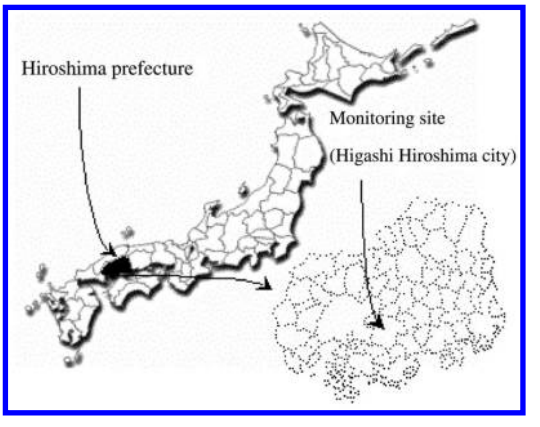


Figure 1. Location of monitoring site in Japan.

view of geotechnical engineering, rain-induced slope failure is a problem of water infiltration and stability. The critical rainfall should be reasonable from the view of geotechnical engineering, and therefore, it is essential to clarify the influences of several factors that are related to the infiltration process and the stability.

The mechanism of slope failure is understood as changes in driving forces and resistance forces with rainfall. When the rainwater infiltrate into the slope, the driving forces, such as bulk weight of soil (in the

Copyright © 2003 Swets & Zeitlinger B.V., Lisse, The Netherlands

case where slope inclination is greater than friction angle of soil) and seepage forces (in the case where the inclination of groundwater surface is greater than ones of the bed of slope or slip surface) increase. On the other hand, rainwater infiltration induces a reduction of suction in the unsaturated soil, thereby causing a reduction in shear strength of the soil, and pore water pressure increase with the increase in groundwater level, resulting in a decrease in effective stress. When the driving forces become larger than the resistance forces, the failure occurs. If the mechanism of rainwater infiltration and strength reduction in the Masado slopes during rainfall is clarified, it becomes possible to predict the amount of rainfall that causes slope failure.

In order to study the mechanism of rainfall infiltration and formation of groundwater in the subsoil of slope and reduction of suction during precipitation, a research was carried out by monitoring the suction, water content, groundwater level and precipitation in the Masado slopes near a debris-flow site on Hiroshima University premises. This event occurred due to heavy rainfall on June 29, 1999.

In this paper, it will be shown from the monitoring results that the different responses of suction and water content, the formation of groundwater level are linked with the different conditions of topography and geological structure at each measurement site and the pattern of rainfall.

2 FIELD INSTRUMENTATION

2.1 *Location of monitoring site*

The heavy rainfall on June 29, 1999 had caused slopes failures in and around the Hiroshima University. In this research, field measurement is carried out on a nearby debris-flow site that is one of the failure sites on university premises on the northern slope of Mount Gagara with elevation of about 330 m above mean sea level (MSL). The crest of this flow site rises up to about 300 m MSL. The flow length of the slide including the source area, main track, and depositional area was about 200 m, and the width varied from about 6 m to 21 m. The depth of failed mass varied from 2.2 m to 3.5 m and the slide inclination ranged from 25 degrees to 40 degrees at the source area. The amount of outflow of soil was 1200 m^3 to 1600 m^3 by eye measurements.

Sampling pits at the monitoring site showed that the slope consisted of extensively weathered Masado. The slope profile was basically composed of two layers: the top layer of silty sand with gravel up to a depth of about 2 m, and hard rock of weathered granite thereafter. Laboratory tests on soil samples from depths 50–80 cm indicate that the specific gravity is 2.59–2.62, the saturated coefficient of permeability was $1.33–4.72 \times 10^{-5}$m/s, and the

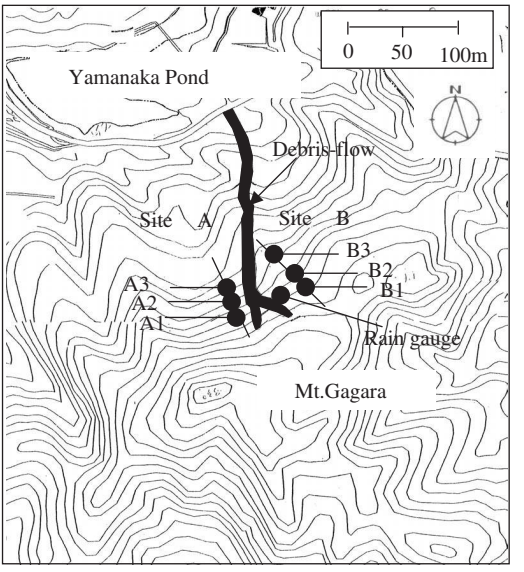


Figure 2. Topography of the monitoring site.

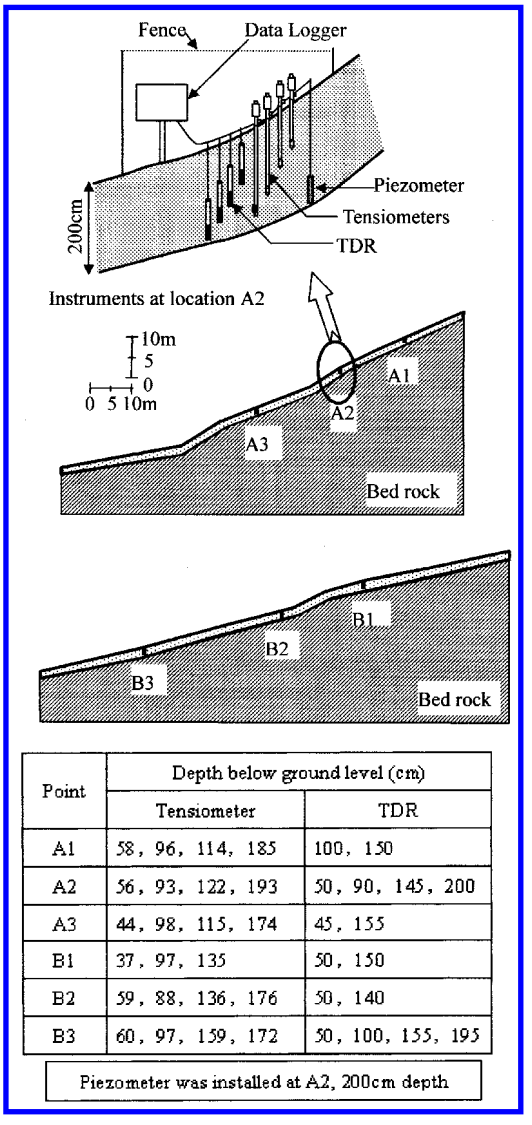
friction angle and cohesion were found to be 35–39 degrees and 5–8.5 kPa, respectively.

In this field measurement, two sites were selected near the debris-flow, namely sites A and B, as shown in Figure 2. Out of these, site A was steeper than site B whereas site B had a bigger catchment area than site A. Moreover, the topography showed that site B was in a valley while site A was located on a much planer slope. Six positions were instrumented having three at each site and the rain gauge was setup in an open space between the two sites, as shown in Figure 2.

2.2 *Measuring system*

The measuring system consisted of an array of tensiometers and TDR (Time Domain Reflectometry) to measure suction and volumetric water contents, a piezometer to measure groundwater level, a rain gauge, and an automatic data-acquisition system. The schematic layout diagram of the measuring system at location A2 and detail lists of instrumentations at each point are shown in Figure 3. The required power for functioning of the tensiometers and TDR is supplied by DC 12V batteries. The measuring data are filed into a data logger at each place and acquired by a personal computer. The data logger can store about 60,000 pieces of data and the sampling interval can be selected from 1 second to 60 minutes; it is actually set to be 10 minutes for all monitoring. This system is capable of continuous monitoring and the monitoring was started on April 2001. The detailed description of each instrument, the calibration method, installation,

Copyright © 2003 Swets & Zeitlinger B.V., Lisse, The Netherlands



Point	Depth below ground level (cm)	
	Tensiometer	TDR
A1	58, 96, 114, 185	100, 150
A2	56, 93, 122, 193	50, 90, 145, 200
A3	44, 98, 115, 174	45, 155
B1	37, 97, 135	50, 150
B2	59, 88, 136, 176	50, 140
B3	60, 97, 159, 172	50, 100, 155, 195

Piezometer was installed at A2, 200cm depth

Figure 3. Layout details of instrumentation.

and maintenance at this site has been presented in Thi Ha et al., 2001.

3 DISCUSSION OF THE RESULTS

3.1 *Variation of water content and suction*

Figure 4 shows the variation of the suction, volumetric water content and rainfall at point B3 on June 2001. It is clear from this figure that the suction decreases with increasing volumetric water content after rainfall. The amount of precipitation on June 18 and 19 were

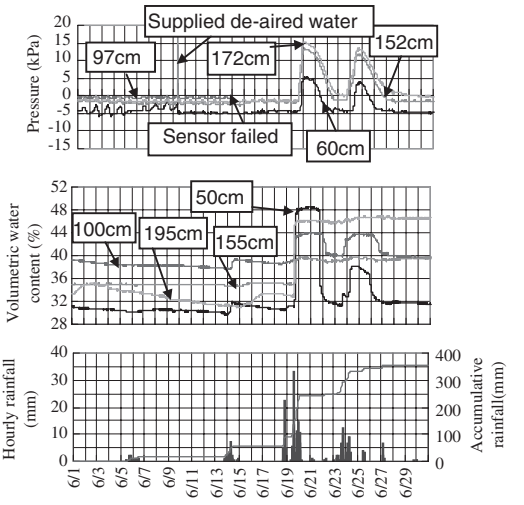


Figure 4. Measuring results at point B3 on June 2001.

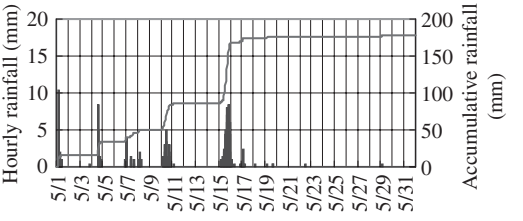


Figure 5. The precipitation on May 2002.

33.5 mm and 130 mm, respectively, and the positive pore water pressure had been recorded at location B3 on June 19.

As shown in Figure 5, 82.5 mm of daily rainfall was recorded on May 15, 2002. Positive pore water pressure was detected at point B2 and B3 during this rainfall. Monitoring results at point B3 from May 15 to May 18 are shown in Figure 6 and, Figures 6 (a) and 6 (b) are the change in the vertical distributions of the suction and the water content, respectively. The precipitation started from the early morning of May 15 and the TDR showed a little response at the depths of 50 cm and 100 cm at 20 hr of the same day as shown in Figure 6 (b-1). However, the depth of 195 cm also showed a rapidly increasing from nearly 37 to 43% of water content, at 20 hr of May 15. The saturated coefficient of permeability from laboratory test on soil samples from depth 80 cm of point B3, was 2.38×10^{-5} m/s. So, the rainfall started at 3 hr of May 15 and, infiltration rainwater will reach to the depth of about 145 cm at 20 hr, where it is assumed that the hydraulics head gradient is 1. Besides, from the amount of increasing volumetric water content,

Copyright © 2003 Swets & Zeitlinger B.V., Lisse, The Netherlands

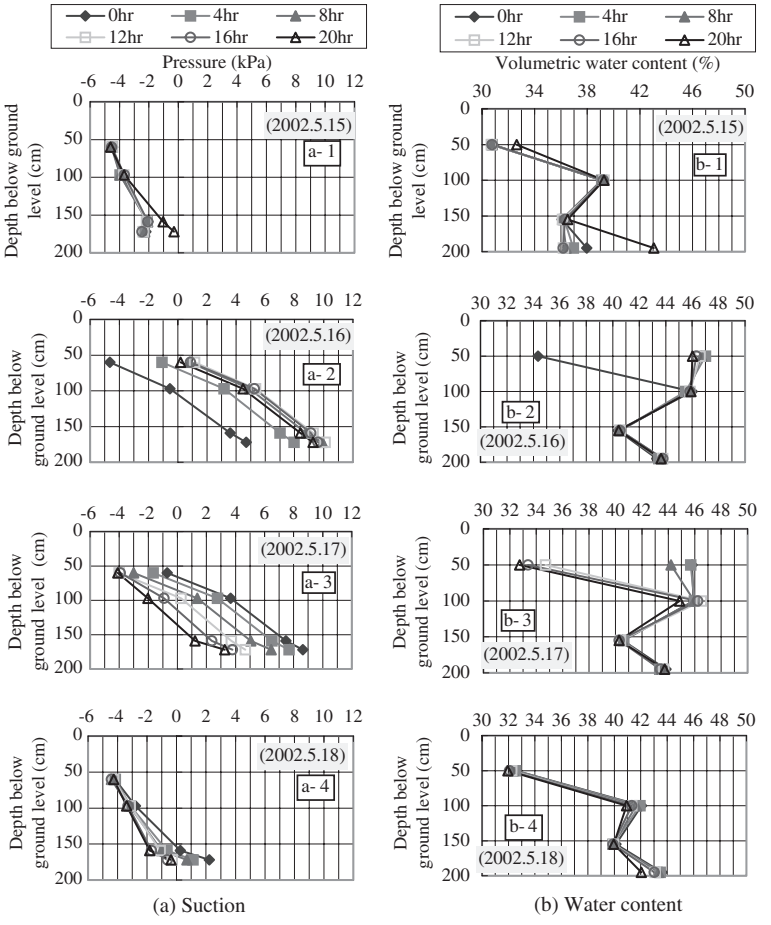


Figure 6. Change of suction and water content at point B3.

it can be considered that the increasing water content at 50 cm and 100 cm is due to the infiltration water from the ground surface but at 195 cm, it is also due to the groundwater flow from the upstream of the soil layer overlying the relatively impermeable bedrock. The suction of Figure 6 (a-1) at 172 cm, showed positive pressure at 20 hr. This indicates that the groundwater is generated from the subsoil surface at this point. On May 16, all the tensiometers show positive pore water pressures from 8 hr and the water content at all depths show no more increment from 4 hr. This means that the water content reached to the maximum value because the formation groundwater has occurred at this point (Figure 6 (a-2) and (b-2)). On May 16∼18, the precipitation was only a little amount and therefore, Figure 6 (a-3) showed the draw down of water level and also water content decreased at the depth of 50 cm at 4 hr and 100 cm at 16 hr (Figure 6(b-3)). On May 18, all the tensiometers showed negative pore pressure at 20 hr and the water content also decreased gradually (Figure 6 (a-4) and (b-4)).

3.2 *In-situ water retention curve of Masado*

Figure 7 shows the water retention curves obtained at the depth of 60 cm of point B3 on June 2001 and May 2002 and Figure 8 is at depth 97 cm of point B3, on May 2002. Both figures indicate that the suction decreased rapidly to zero at nearly 45–48% of volumetric water content (about 90 ∼ 95% in degree of saturation).

The next important fact obtained from these figures of in-situ water retention curves, is that the dry curve (drying process after rainfall ceases) is inside of the wet curve (wetting process during rainfall). But it is well known that the dry curve is outside of the wet curve in water retention curve obtained from the results of laboratory test and this is because of rain dropped effect or ink bottle effect (Bear 1979, Yanai 1987). It is

Copyright © 2003 Swets & Zeitlinger B.V., Lisse, The Netherlands

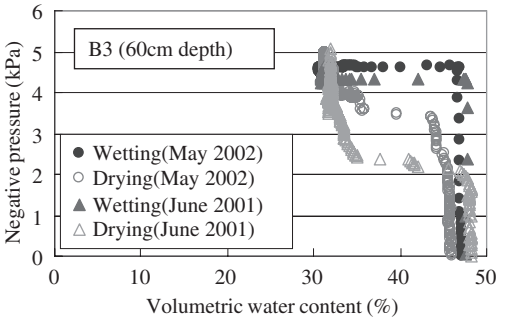


Figure 7. In-situ water retention curve of Masado.

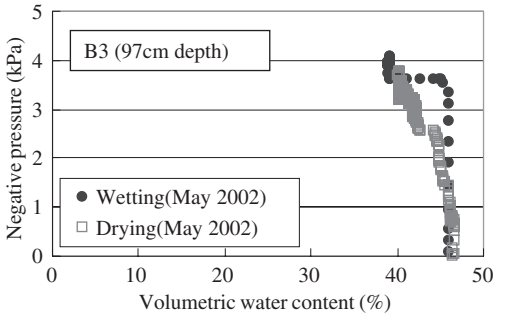


Figure 8. In-situ water retention curve of Masado.

necessary to clarify why the field measurement results differ from previous researches.

From April 2001, when the monitoring started, to June 2002, two water retention curves were obtained at depth 60 cm of point B3, as shown in the Figure 7. It is clear from this figure that the wet curves for both times are the same but the dry curves are different for June 2001 and May 2002. The different condition for these cases is only the amount of precipitation. In the former case of June 2001, the amount of precipitation from June 18 to 19 was 164 mm and the positive pore water pressure rose up to about 15 kPa. In the latter case of May 2002, the amount of precipitation on May 15 was 82.5 mm and the recorded positive pore water pressure was about 10 kPa. At present, it is difficult to make any concrete conclusion on the relation between rainfall pattern and the characteristics of the water retention curve and also why these two curves are not the same.

3.3 *The implications for groundwater modeling*

As mentioned above, 164 mm of rainfall had fallen on June 18 to19, 2001 and the data were obtained on June 19 from A3, B1, B2 and B3 where the positive pore water pressures had been recorded. Figure 9 shows the groundwater level from the bottom of the weathered

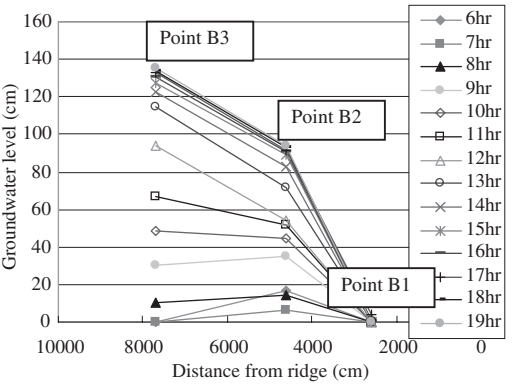


Figure 9. Rise up of groundwater level at site B.

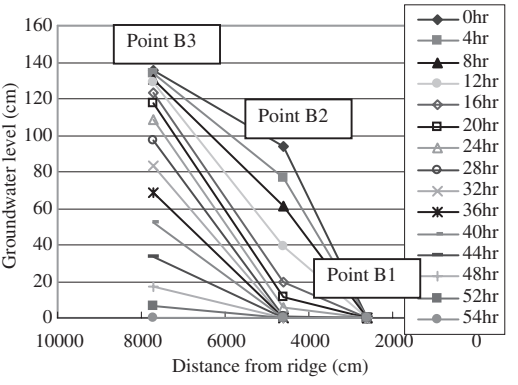


Figure 10. Draw down of groundwater level at site B.

granite layer at site B. The formation of groundwater level at point B1 (135 cm depth), B2 (136 cm depth) and B3 (159 cm depth) has occurred after 11 hr, 6 hr and 8 hr, respectively, from the start of precipitation on June 19. About 135 cm, 94 cm and 4 cm of the highest groundwater levels were recorded at points of B3, B2 and B1, respectively. After the intense rainfall (4 hr on June 20) the ground water levels became draw down and it needed 30 hr to be zero at point B2 and 54 hr at point B3 (Figure 10). The comparison of the rise up and draw down phenomena indicated that the rise up of groundwater levels was much faster than the draw down.

Figure 11 shows the variation of pressure and volumetric water content due to the precipitation of June 19, 2001. In this figure, the volumetric water content increases rapidly and then it becomes very narrow in range of variation. At nearly same time, the tensiometers show the positive pressure and so it is clear that the formation of groundwater has occurred at this point. It could be clearly noted from these figures that during the precipitation, the positive pressure starts

Copyright © 2003 Swets & Zeitlinger B.V., Lisse, The Netherlands

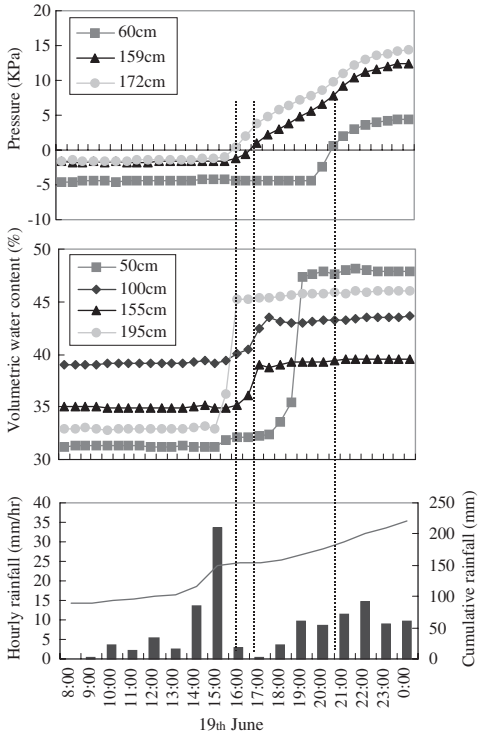


Figure 11. The variation of pore pressure and water content at point B3 on June 19, 2001.

to build up from the bottom of the weathered granite layer. It is also evident that the upper layers remain in an unsaturated state while the bottom of the soil layer is saturated first. This means that the groundwater rises from the bottom of the permeable layer while the upper layers remain in the unsaturated state. The same phenomena also occurred at the other points, B2 and A3. This observation at the site of the field measurement in Masado slopes leads to a very important conclusion on the mechanism of the formation of water level in highly permeable materials like Masado.

After the intense rainfall of June 19, 2001, the draw down of groundwater level was also analyzed. The draw down of water level also shows the similar pattern of behavior as the rise of water levels; that is, the topmost layers discharge the water much earlier than the bottom layers and a similar way of performance of volumetric water content is observed.

3.4 *The permeability parameter of in-situ Masado slope*

The flow of water in a saturated soil is commonly described using Darcy's law, as Equation 1.

$$v = k \cdot i \tag{1}$$

where v is flow rate of water; k is coefficient of permeability; i is hydraulic head gradient.

But, in the case of unsaturated soils, water flow at the area of pore-water with remaining of pore-air and the flowing area can be calculated as follow.

$$A_w = Sr \cdot n \cdot A \tag{2}$$

where, Sr is degree of saturation; n is porosity; A is total area. The actual flow rate can be described as,

$$v_s = \frac{Q}{A_w} = \frac{Q}{Sr \cdot n \cdot A} = \frac{v}{\theta} \tag{3}$$

where, θ is volumetric water content. Therefore, the unsaturated coefficient of permeability can be calculated as follow.

$$k_\theta = \frac{v_s}{i}\theta \tag{4}$$

The velocity of infiltrating water at the monitoring site can be calculated by the starting time of the precipitation from the rain gauge and the time taken to infiltrate from the response time of TDR. It was assumed that the hydraulic head gradient was 1. As a result, the unsaturated coefficient of permeability at the monitoring site is in the order of 10^{-5} m/s to 10^{-6} m/s. It should be noted that the effect of the initial water content, the groundwater flow from the upstream in the subsoil and the pattern of rainfall were not considered in this method.

The saturated coefficient of permeability (k_s) calculated by Irmay's Equation ($k_\theta = k_s(Sr)^3$), is in the order of 10^{-5} m/s. This value is the same to the result from laboratory tests.

4 CONCLUSIONS

The decrease of suction with the increase of the degree of saturation and the formation of groundwater level due to the precipitation make the slopes unstable and it is essential to clarify these characteristics by monitoring an actual site and hence, the instrumentation was done on the slopes nearby a debris-flow site. The following conclusions are drawn from the results.

1. The variation of suction and water content, and the formation of groundwater are different with the different conditions of topography, geological structure and the amount and pattern of precipitation.
2. In-situ water retention curves of Masado were obtained. From the results, the suction decreased rapidly to zero at about 90 ~ 95% in the degree of saturation and the dry curve in the water retention curves is inside of the wet curve. For the same soil, different water retention curves were obtained with the different precipitations.

Copyright © 2003 Swets & Zeitlinger B.V., Lisse, The Netherlands

3. The upper layers remain in an unsaturated state while the bottom of the soil layer is saturated first. Next, the groundwater level rises from the bottom of the permeable layer while the upper layers remain in the unsaturated state.
4. Even though the groundwater level rises rapidly, the draw down of the increased groundwater levels is much slower. It is also important to note the draw down phenomenon of the groundwater levels because the rising groundwater level is different with the initial conditions, that is, the groundwater level from the previous event of precipitation.
5. The coefficient of permeability at the monitoring site is in order of 10^{-5} m/s to 10^{-6} m/s. The order of in-situ coefficient of permeability can be estimated from the result of the laboratory test.

REFERENCES

Sasaki, Y., Moriwaki, T., Kano, S., & Shiraishi, Y. 2001. Characteristics of precipitation induced slope failure disaster in Hiroshima prefecture of June 29, 1999 and rainfall index for warning against slope failure disaster. Soils and Foundation 49-7:16–18.

Thi, Ha., Moriwaki, T., Sasaki, Y., Kano, S., & Dissanayake, A.K. 2001. Field measurements of moisture content and suction in Masa slope at Hiroshima University campus. Journal of Ground engineering 19-1:37–48.

Bear, J. 1979. Hydraulics of Groundwater: McGraw-Hill Inc.

Yanai, K. & Iitake, S. 1987. The applying of pF in engineering. Soils and Foundation 35-2:99–105.

Copyright © 2003 Swets & Zeitlinger B.V., Lisse, The Netherlands

Preservation of natural groundwater flow

Copyright © 2003 Swets & Zeitlinger B.V., Lisse, The Netherlands

Influence of spatial distribution of caves on salt-water intrusion in Ryukyu limestone aquifer in Komesu underground dam basin, Okinawa Island

M. Imaizumi, S. Ishida, T. Tsuchhara & M.A. Fazal
National Institute of Rural Engineering, Tsukuba, Japan

ABSTRACT: The spatial distribution of caves in Ryukyu Limestone has been identified on the basis of boring data in the Komesu Underground Dam Basin. The formation ages of caves estimated from the old sea level and the sea level curve of Japan are presumed to be 9,800 to 2,800 years B.C. Various forms of vertical distribution of electric conductivity (EC) are classified into six types, A to F. Types B, C and F are well known as a typical form of salt-water intrusion in an aquifer of a porous medium. Types D and E may be characteristic types in a karst aquifer because typical phenomena of karst aquifers, namely a brackish zone of several hundred meters width, are distributed around the areas of types D and E.

1 INTRODUCTION

The Ryukyu Limestone is a Quaternary elevated limestone distributed in the Southwestern Islands of Japan. Karst features, such as limestone caves and dolines are ubiquitously observed in the Ryukyu Limestone. Unsettled problems of the Ryukyu Limestone are the location and the distribution of caves and the relationship between the distribution of caves and the occurrence of groundwater.

Groundwater is closely related to the formation history of caves. From the general viewpoint, a shallow unconfined groundwater zone is considered to be suitable for the formation of caves. The sea level fell to more than 100 m below the present sea level in the last glacial age of Pleistocene. The Quaternary limestone was exposed above the old sea level. As a result, the outflow groundwater decreased, and precipitation could infiltrate deeper than the present level. It is thought that the infiltration of water is one of the reasons why the caves are distributed deeper than the recent sea level (Domienico and Schwartz, 1990).

Not all limestone, especially Quaternary limestone forms karst aquifers. A limestone aquifer goes through a process of evolution from the aquifer in the initial stage to the karst aquifer in the mature stage. There is no cave system in limestone in the initial stage where dispersion flow is dominant. The cave gradually develops as time passes, and the caves are progressively mutually connected to form a channel. Only channel flow is dominant in the karst aquifer in the mature stage.

In the Komesu underground dam basin (KUDB) of the southern part of Okinawa Island where typical The Ryukyu Limestone is underlain, national irrigation projects using underground dams are advancing. Many geological boring surveys and measurement of groundwater level and electric conductivity (EC) of wells have been carried out for the design and execution of these underground dams. A comprehensive analysis of these materials reveals that cave systems of several levels exist under the present groundwater level and related to the behavior of salt-water intrusion.

2 OUTLINE OF TOPOGRAPHY AND GEOLOGY

The study area is located in Itoman city, 25 km south of Naha city. Terraces and fringing reef, which exist around the coastline, characterize the topography of the area.

The integrated geologic column is shown in Figure 1. According to Kizaki (1985), the geology around the study area is as follows. Shimajiri Group and Tinen sand layer in Miocene to the lowest part of Pleistocene are hydrogeological bed rock. The Ryukyu Limestone, unconformably overlying the bed rock, is extensively distributed as terrace deposits. The area of limestone terraces is divided into 12 groundwater basins with boundaries of faults. Each groundwater basin is independent as a block. The study area belongs to KUDB with a catchment of 2.64 km^2 (Figure 2).

Copyright © 2003 Swets & Zeitlinger B.V., Lisse, The Netherlands

Age		Geological Colum	Stratum	Facies • Structure	Topography	Soil
Quatanary	Holocene		Recent Coral Limestone	Coral, Coral sand and silt, Coral gravel	Coral	No
			New dune sand	Calcareous and layer with old peat layer	Duen	Sandy immature soil
			Alluvium	Dark gray-brown mud, sand, gravel, with fragment of coral	Alluvial low land	Gray soil
	Pleistocene		Terrace Limestone	Brown clayly soil Sandy limestone	Terrace (Middle level terrace)	Brown soil
			Red brown clay	Shimajiri marge (Weathering)	Limestone Terrace	Red brown-yellow brown clayly soil
			Tinen L.	Calcareous sand		
Tertiary	Pliocene	Shimajiri	Sinzato F.	Altenation S/M	no terrace	Gray soil
			Yonaba -ru F.	Mainly mudstone with sand and tuff layers		
	Miocene		Tomigu -suku F.	Upper: Oroku sandston Lower: mudstone		

Figure 1. Schematic geological column. From Kizaki et al. (1985).

The upper surface of the bed rock is distributed 10 to 20 m above sea level in the northern part of the study area. However, it is submerged below sea level in the southern part because it inclines to the south. The altitude of the deepest upper surface of the bed rock is −70 m above sea level. Two faults, Faults A and B in KUDB, are presumed from the altitude discrepancy of the upper surface of the bed rock. Average thickness of the Ryukyu Limestone is 30 to 40 m. The maximum thickness is 100 m. The Ryukyu Limestone is distributed at higher levels on the east side of Okinawa Island and at lower levels on the west side. Terrace limestone unconformably overlying The Ryukyu Limestone, which is not distributed in the study area, has the same distribution pattern as The Ryukyu Limestone. These distribution patterns show a continuing tilting by tectonics after the time of sedimentation of The Ryukyu Limestone. Figure 2 shows the already known locations of the large caves and spring. Suu-gah and Urusu-gah are costal springs.

The Komesu underground dam with 69.4 m in dam height, 2,489 m in crest length, 62,400 m^3 in volume, and 2,062,000 m^3 of reservoir capacity, is a continuous soil-cement cut-off wall for storage of groundwater and prevention of salt-water intrusion. It was constructed along the coast from 1994 to 2001.

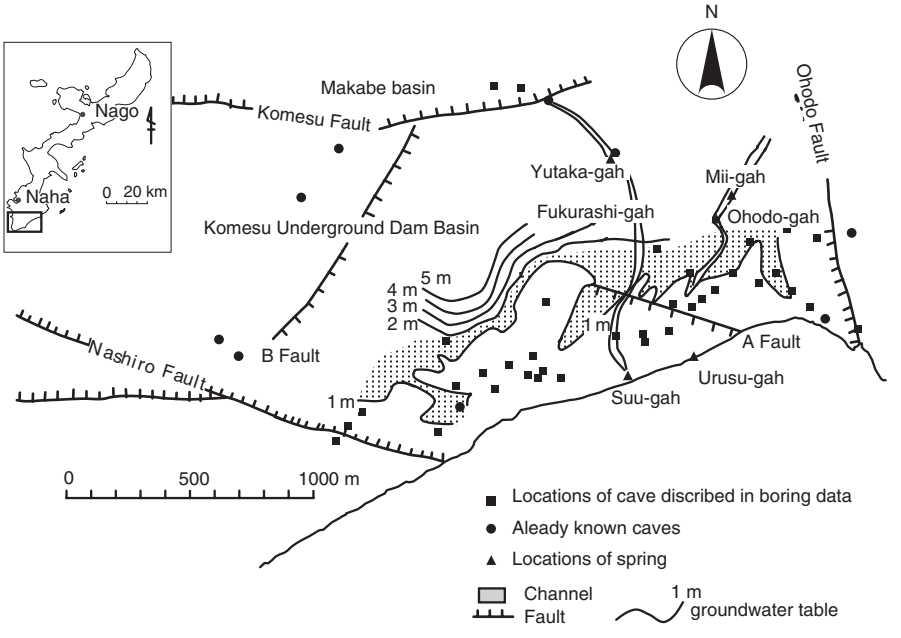


Figure 2. Relationship between distribution of caves and groundwater level in the Komesu underground dam groundwater basin.

Copyright © 2003 Swets & Zeitlinger B.V., Lisse, The Netherlands

3 INVESTIGATION METHOD

Data of geologic columns with a total length of 7,542 m in 52 sites was reexamined in order to clarify the distributions of rock faces and caves. The Ryukyu Limestone is classified into a sandy/muddy limestone, a calcareous algae ball limestone, and a coral limestone. The parts without sampling cores and described as inflow clay are classified as caves. Measurement of groundwater level and EC in the vertical direction of depth at every 2 hours for 10 hours was carried out for evaluation of salt-water intrusion control of underground dam. Measurements were carried out at 22 wells in 1994 when the progress rate of work was 4.6% of the finished cut-off wall, and at 40 wells in 199 when the progress rate was 65%. Figure 3 shows the locations of observation wells.

4 RELATIONSHIP BETWEEN ROCK FACES AND DISTRIBUTION OF CAVES

Figure 4 shows four geological cross sections parallel to the direction of coastline. The locations of sections are shown in Figure 3. Generally, much coral limestone tends to be distributed on the east side of Fault A. Figure 2 shows the locations of the cave described as the no-sampling part or the inflow clay filling part. The size ranges from several 10 cm to 1.5 m in length. The caves are distributed within the range from the coastline to 500 m inland.

5 RELATIONSHIP BETWEEN DISTRIBUTION OF CAVES AND GROUNDWATER TABLE

Figure 2 shows the relationship between the average groundwater table on June 16, 1994 and the distribution of caves (■). The groundwater table shows a harmonizing shape with topography at 500 m or more away from the coastline. However, the shape of the iso-1m contour of the groundwater table shows a complex shape within 500 m from the coastline. The iso-1 m contour deeply enters the inland side near the Ohodo Fault on the east side and Nashiro Fault on the west side of the basin. On the other side, a ridge of iso-1 m contour projects to the seaside in the west and central parts. The caves are distributed in the valley where the groundwater level is 1m or less above sea level (outside of the hatch area). The distribution of these caves in the valley of the groundwater table suggests that at least some of the caves connect with the sea.

6 RELATIONSHIP BETWEEN CAVES AND SALT-WATER INTRUSION

The form of groundwater flow in a Karst aquifer with preferential paths such as channel systems is

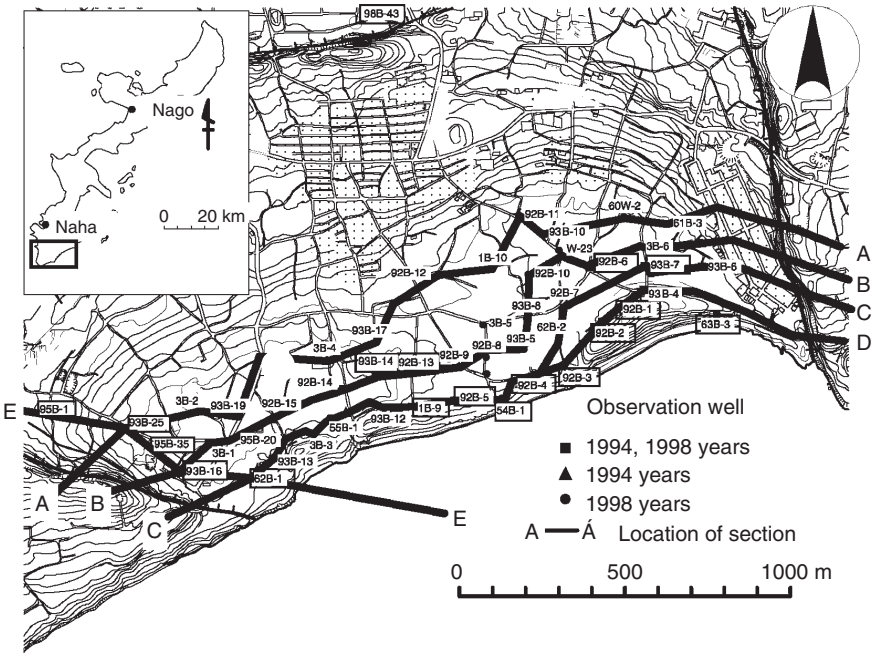


Figure 3. Location map of investigated wells and geological sections.

Copyright © 2003 Swets & Zeitlinger B.V., Lisse, The Netherlands

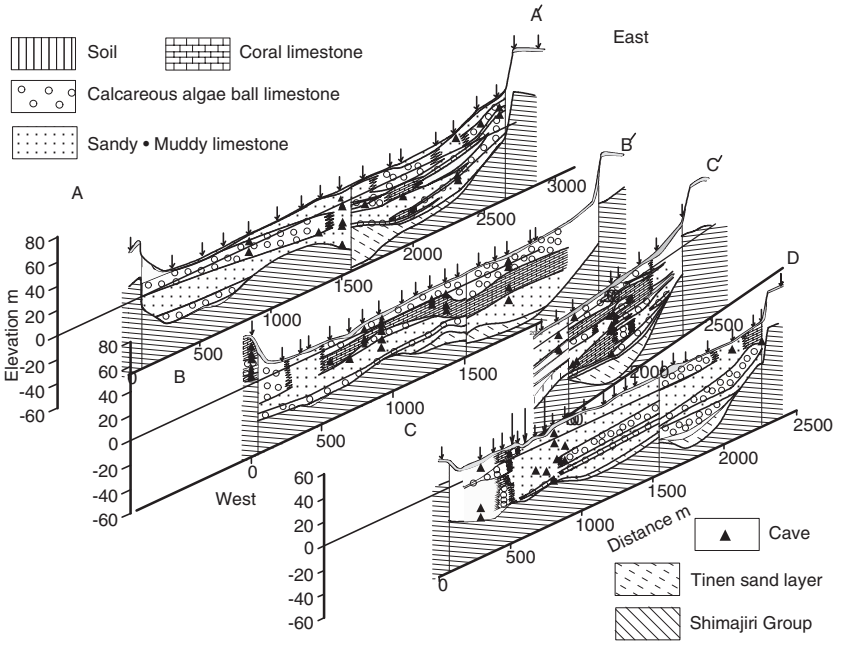


Figure 4. The geological cross sections near seashore in study area.

quite different from that in other aquifers. The law of Ghyben-Herzberg that applies to the fresh water-salt water interface in porous media only partially applies in a karst aquifer (Milanovic, 1981).

The distribution of EC in the direction of depth at wells (as described in the next section) changes hourly accompanied with ebb and flow. In order to gain a general view of salt-water intrusion, sections of the distribution of EC value in 1994 were examined (Figure 5). The EC value, which is an average of five measurements at each depth is divided into four classes in Figure 5; 2.0 mS/cm or less, 2.0–20.0 mS/cm, 20.0–40.0 mS/cm, 40.0 mS/cm or more.

The shape of the boundary of 2.0–20.0 mS/cm shows an upward bulge on the west side of section C–C′ which is 50–100 m away from the coastline. Salt-water intrudes from a comparatively shallow position where caves are densely distributed. On the other hand, the upward bulge on the east side of section C–D is pushed into the bed rock in section C–C′. Fresh-water of 2.0 mS/cm or less is extensively distributed in section B–B′ which is 200–300 m away from the coastline. Caves tend to be distributed in the vicinity of the boundary of 2.0–20.0 mS/cm. The fresh water area extends throughout section A–A′ which is 500 m away from the coastline except in an isolated part of 40.0 mS/cm or more which is located in the vicinity of Fault A. The cave is distributed over the isolated high EC part. The reason why the area of 2.0–20.0 mS/cm is distributed in the center part of sections B–B′ and C–D is considered to be that the fresh water flowing through the channels to the Suu-gah and Urusu-gah springs influences the distribution of EC.

7 VERTICAL DISTRIBUTION OF EC IN OBSERVATION WELLS

7.1 *Classification of form and change pattern of EC*

The form of the vertical distribution of EC can be classified into six types, A to F (Figure 6). The pattern of fluctuation of EC with time can be classified into six patterns of a to f (Figure 6). Types B, C and F are well known as typical forms of salt-water intrusion in an aquifer of a porous medium. Types D and E may be characteristic types in a karst aquifer because typical phenomena of karst aquifers, namely a brackish zone of several hundred meters width, are distributed around the areas of types D and E (see next section).

7.2 *Distribution of character of the vertical distribution of EC*

The character of the vertical distribution of EC can be expressed by a combination of type and pattern such as “Aa”. Figure 7 shows the distribution of the combination in 1994. Two or more types and patterns are needed to express the character for some wells. These characters may be related with a complex structure of

Copyright © 2003 Swets & Zeitlinger B.V., Lisse, The Netherlands

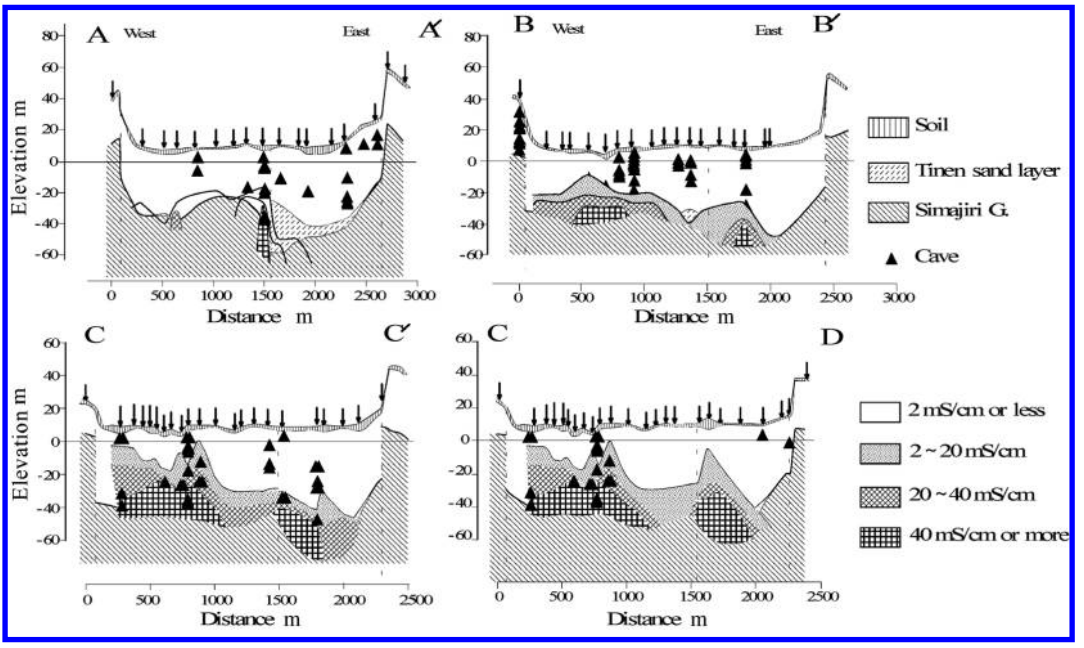


Figure 5. Relationship between salt-water intrusion and distribution of caves.

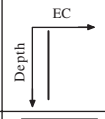
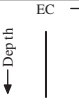
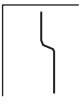
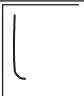
Type	Form	Explanation	Pattern	Fluctuation of EC	Explanation
A		The value of EC is under 1.0 mS/cm. This type is the form of non-intrusion.	a		The distribution form of the EC hardly changes. This pattern is a pattern not influenced by tidal change.
B		EC rapidly rises from a certa in depth (a discontinuous point) of fresh water/salt water interface. This type has a narrow brackish water zone.	b		The form of EC is hardly changes except a brackish zone from a discontinuous point to the EC of seawater. This pattern has a narrow fluctuation zone.
C		EC gradually rises from a certain depth (a discontinuous point) offresh water/salt water interface. This type has a wide brackish water zone	c		The depth of a discontinuous point changes and a wide of brackish water zone fluctuates accompanied with the ebb and flow of the tide.
D		EC gradually increased from a small fresh water zone to the EC of seawater (50 mS/cm).	d		A stable width of brackish zone. The depth of discontinuous point fluctuates with time.
E		A comparatively high EC (5.0 mS/cm or more) zone is distributed from the surface of groundwater table. This type has a homo-geneous brackish water zone and occasionally has another higher EC brackish zone.	e		A whole form of EC fluctuates with time, particularly, a part of shallow depth remarkably changes.
F		EC increase at a discontinuous point of EC but doesn't reach to the EC of seawater. This type is an incomplete type of B or C types.	f		A little change of EC.

Figure 6. Classification of distribution types and fluctuation patterns of vertical electric conductivity.

Copyright © 2003 Swets & Zeitlinger B.V., Lisse, The Netherlands

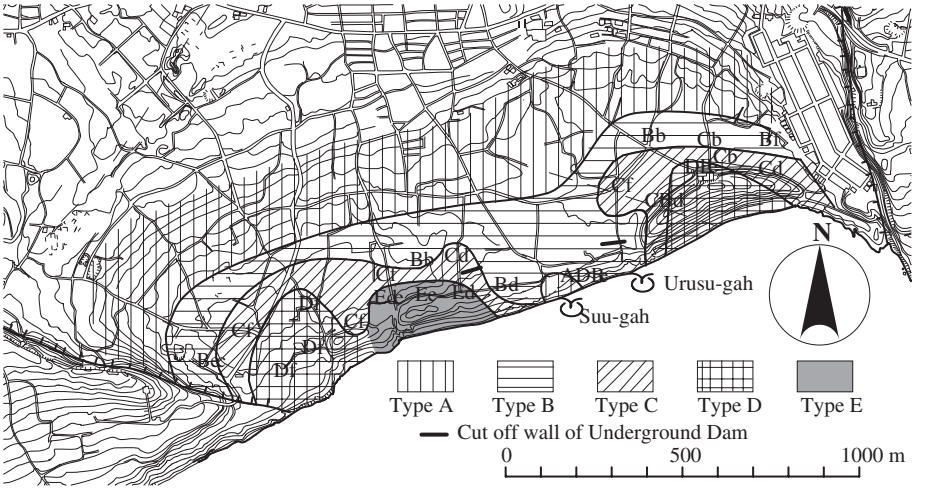
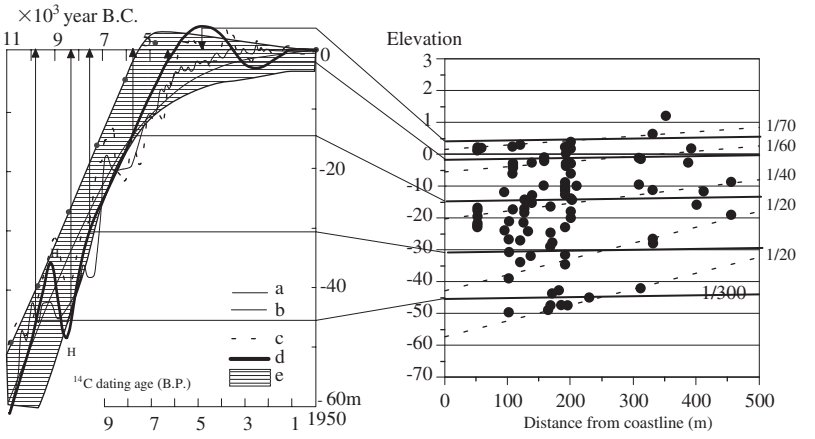


Figure 7. Distribution map of types and patterns and estimated zoning of types of vertical electric conductivity in 1994.



Sea level curve in a postglacial age (Ohota and Naruse, 1977) a: Morner (1969) from the data in Southern Scandinavia, b: Shepard (1963), c: Fairbridge(1961), d: Kaizuka et al. (1977) from the data around Tokyo Bay. e: Horiand Kayane (2000)

Figure 8. Sea level curves and the relationship between levels of cave and distance from seashore. Sea level curves edited by Ohta and Naruse (1977) and range of sea level curves reviewed by Hori and Tine (2000).

permeability. Figure 7 shows a zonal distribution map of type in 1994. This figure shows the zonal structure of type in the natural condition because the progress rate of construction of the cut-off wall in 1994 was only 4.6%. The zonal distribution shows Type A→ Type B→ Type C→ Type (D or E) in accessing the coastline. The zonal structure is disturbed in the vicinity of the coastal springs where type B projects to the coastline. Type A is locally distributed in the vicinity of the Suu-gah spring.

8 CONSIDERATION

8.1 *Formation age of caves*

There is a possibility that caves were formed in the vicinity of the groundwater level during late Pleistocene, if the groundwater level maintained around a certain level for a certain period during the rising of sea level. The caves that were formed by this mechanism may be arranged along an old groundwater level in the diagram with distance from coastline on

Copyright © 2003 Swets & Zeitlinger B.V., Lisse, The Netherlands

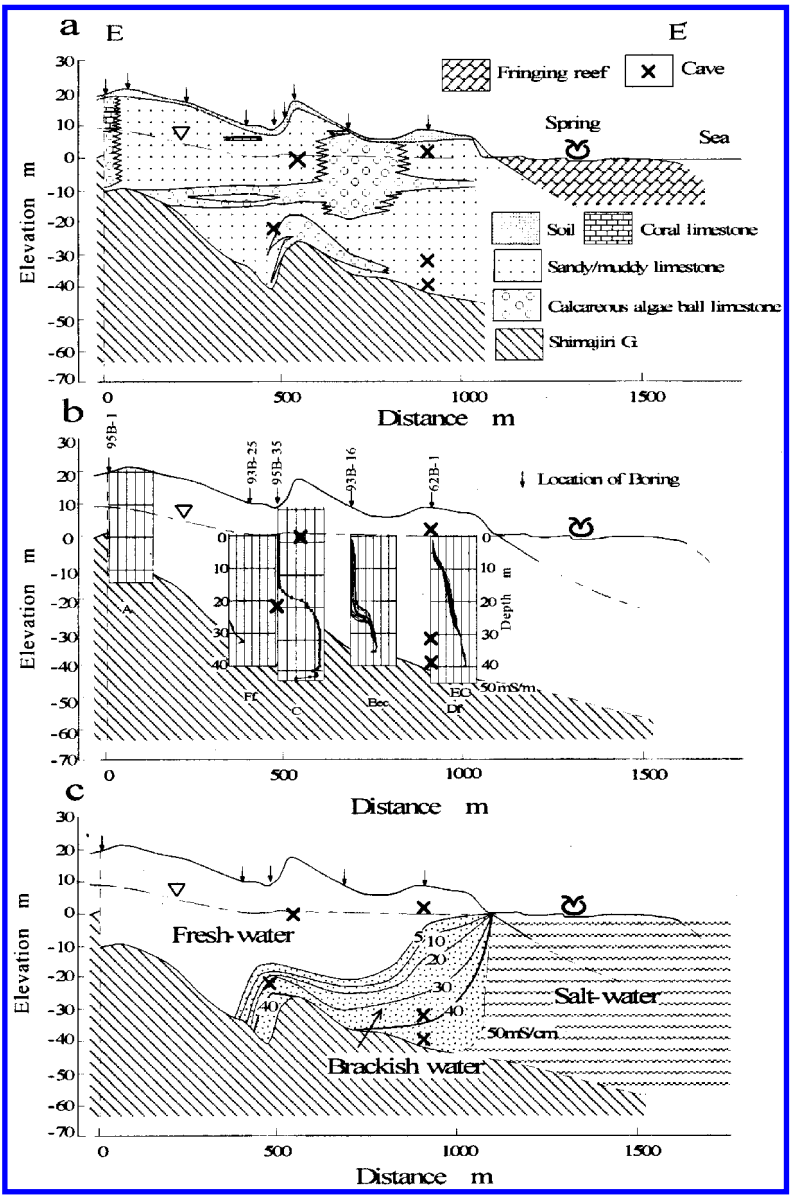


Figure 9. Cross sections of geology (a), vertical electric conductivity (b) and zoning of salt-water intrusion (c) along EE′.

the x-axis and distribution level of the caves on the y-axis (Figure 8). The array lines of the lowest and highest altitude in Figure 8 have gradients of 1/20 and 1/70, respectively. Other array lines with gradients of 1/20, 1/40, and 1/60 in ascending elevation order are recognized between these lines. That is, the higher the array line is, the gentler gradient the array line has. The gradient of the old groundwater level is too steep compared with the present gradient of the groundwater level. It is considered that the tectonic tilting is related to this, on the basis of a study on the distribution level of notches around Okinawa Island (Kizaki, 1985).

The sea level curve is one method of determining the old sea level. Figure 8 shows the sea level curves edited by Ohota and Naruse (1977) and the range of sea level curves from all over the world collected by Hori and Kayane (2000). The sea level curve of Japan is shown as the curve “d”. The formation age of the caves can be estimated from the sea level curve of Japan, if we can find out the old groundwater levels at the coastline

Copyright © 2003 Swets & Zeitlinger B.V., Lisse, The Netherlands

which are related to each array line of caves. The old sea levels are estimated by the following method. Let us assume that the gradient of the groundwater level was 1/300. Here, it is thought that the middle depth between the deepest and shallowest depths is an old sea level. In this method, an array line of caves is compensated to the line with 1/300 that goes through the point where 250 m on the x-axis and the array line of cave intersect. The altitude of the compensated line at 0 m distances from the coastline gives the elevation of the old sea level. According to age determinations from sea level curve "d" around Tokyo bay and the altitude of old groundwater levels presumed from arrays of caves, the formation of caves is follows (Figure. 8), the lowest level −45 m: 8300–9800 B.C., −31 m: 7600 B.C., −15 m: 5800 B.C, −2 m: 4300B.C., +4 m: 2800 B.C. Because the formation ages estimated by this method contain many assumptions, the formation ages are not the absolute ages, however, the results show that the caves were formed after 10,000 B.C.

8.2 *Brackish water zone*

Milanovic (1981) explained the characteristics of fluctuation patterns of salinity in karst aquifers with data of investigations at fixed points in wells or long-term records of fluctuations of salinity at springs. Kohout and Klein (1967) suggested that a wide brackish water zone is a characteristic phenomenon of the karst aquifers.

From the definition of type, the distribution area type E (Figure. 7) shows a broad brackish water zone, width of 200 m or more. In order to examine the width of the brackish water zone of the distribution area of type D, a geological cross section (Figure. 9a), a vertical distribution diagram of EC at wells (Figure. 9b), and the figure of salt water intrusion (Figure. 9c) along section E–E′ were made. The value of 5.0 mS/cm or less is defined as fresh water and 5.0 mS/cm–50.0 mS/cm is defined as brackish water in Figure. 9c. Figure. 9c shows that the width of the brackish water zone is 500 m or more in a straight line. The iso-line of 40.0 mS/cm enters 400 m inland from the coastline. A cave is distributed near the iso-line of 40.0 mS/cm at 95B–35. It is thought that this phenomenon of deep inland intrusion of the brackish water zone is caused by connections between the caves and seawater. It is thought that types D and E are characteristic of karst aquifers due to the wide brackish water zone.

9 CONCLUSION

The spatial distribution of caves in The Ryukyu Limestone has been identified on the basis of boring data in the Komes Underground Dam Basin. The formation ages of caves estimated from the old sea level and sea level curve of Japan are presumed to be 9,800 to 2,800 years B.C. The distribution of caves are closely related to the behavior of salt-water intrusion.

REFERENCES

Domienico P.A. and Schwartz F.W., 1990, *Physical and Chemical Hydrogeology*, John Wiley & Sons, 824.

Hori K. and Kayane H., 2000, Submarine Morphology of the Island shelf off the middle and south Ryukyu Island, Southwest Japan, *Geographical Review of Japan*, 73A-3, 161–181 (in Japanese).

Kizaki K. (eds), 1985, Geology of Ryukyu Arc, *Okinawa Times*, 278. (in Japanese).

Kohout, F. A., and Klein, H. (1967): Effect of pulse recharge on the zone of diffusion in the Biscayne aquifer: *Inter. Assoc. Sci. Hydrol. Symp*. Haifa, Pub. 72, 252–270.

Milanovic, P. T (1981): Karst Hydrogeology, Water Resources Publicatons, 434p.

Naruse H., 1982, *Quatanary*, Iwanami-shoten 193–220.

Ohota Y. and Naruse H. (977): Japanese coastal terrace–glacial eustasy in circum-Pacific region, *Kagaku*, 47, 281–292. (in Japanese).

Copyright © 2003 Swets & Zeitlinger B.V., Lisse, The Netherlands

Soil structure and change of free groundwater in the Kanto Loam formation

H. Narioka
Okayama University, Okayama, Japan

M. Komamura
Tokyo University of Agriculture, Tokyo, Japan

ABSTRACT: This paper aims to investigate the environmental preservation of the groundwater in Tokyo, Japan where the relationship between rainwater infiltration and soil physical characteristics is considered. The main parameters studied were physical characteristics of soil layers, precipitation, evaporation, water inflow, soil moisture, free groundwater level and pore structure using the soft X-ray imaging method. Specifically, the relationship between rainwater and free groundwater, and the actual state of underground water preservation were looked into.

1 INTRODUCTION

The relationship between infiltration by rainwater and soil physical properties was investigated during 1985–1995. The investigation area was located on the Musashino Plateau in Tokyo, Japan. In this area, urbanization is very high and there is a decrease of rainwater infiltration in the area. In such a situation, characteristics of the fluctuation of the free surface groundwater was analyzed and the actual state elucidated (Narioka et al., 2000a,b,c).

To observe the change of the groundwater level is one of the effective means of understanding the complicated phenomenon. Therefore, the observation of the act of groundwater at fixed sites was done. The investigation stations were the shrine precinct and the residential land site in Setagaya, Tokyo. The relationship between rainwater and the free groundwater level and the actual state of groundwater preservation were analyzed. In addition, it was considered that the structure of soil macropores influenced water flow velocity in the soil and the fluctuation velocity of the groundwater level.

2 MATERIALS AND METHODS

2.1 *Research area*

The investigation sites were the shrine precinct ("Hachiman" as site 1) and the residential land site ("Daikan" as site 2) in Setagaya, Tokyo. Setagaya is located on the "Yamanote-Daichi" which is a residential plateau, on which urban development is advancing at a high rate. Therefore rainwater infiltration into the soil is decreasing, and the conservation of rainwater is non-existent. In such conditions, there is the need to study the changes the free groundwater level and elucidate the mechanism for the preservation of groundwater.

2.2 *Measured parameter*

The main investigation parameter were the physical characteristics of soil layers, precipitation, evaporation, water inflow, soil moisture, free groundwater level etc. The observation and analysis devices were automatic rain gauge, automatic water level meter, automatic tensiometer (from 10 to 200 cm; nine depth) and soft X-ray device (SOFTEX, Japan; CMB-3 special model). The soft X-ray imaging device was used for the analysis of the pore structure of the soils (Narioka, 1989).

3 RESULTS AND DISCUSSION

3.1 *Basic physical characteristics of soils*

3.1.1 *Soil profiles* (Figure 1)

At Hachiman (site 1), the soil from the surface layer to 95 cm deep was Andosol that was rich in humus and blackish brown in color. The aggregate structure

Copyright © 2003 Swets & Zeitlinger B.V., Lisse, The Netherlands

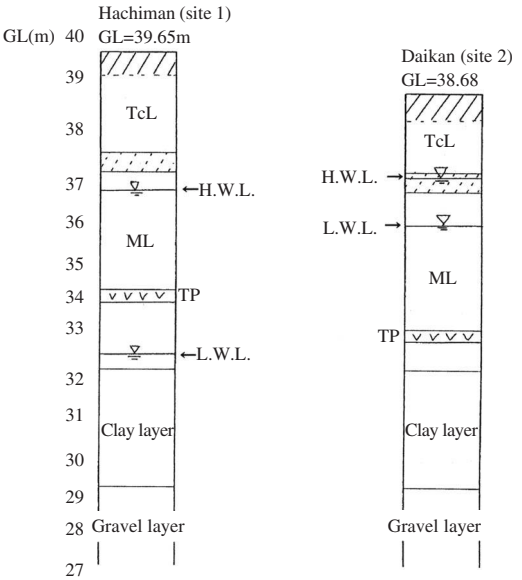


Figure 1. Soil profiles.

was mainly of surface layer, and soil texture was Light Clay (LiC). The volcanic ash layer was of mainly bright brown color. Less than 95 cm deep were soil texture of Heavy Clay (HC) or Clay Loam (CL). The Tachikawa Formation (TcL) and Musashino Formation (ML) were accumulated from the top, and tubular macropores developed in soil layers. The higher limit (H.W.L.) and lower limit (L.W.L.) of the groundwater level went up and down in the TcL layer.

In the Daikan (site 2), there was much humus to depth of 130 cm and Andosol soil structure has developed. The soil texture was LiC in surface layer, and HC or CL in subsoil layer. The groundwater level went up and down in the upper part of the ML layer from the lower part of the TcL layer.

3.1.2 *Soil physical characteristics* (Tables 1 and 2)
The specific gravity (Gs) of the surface layer was small and included rich organic matter but large in the subsoil layer. The mean value of dry bulk density (ρ_d) was 0.56 Mg/m^3 in the Hachiman and 0.64 Mg/m^3 in the Daikan. All are characteristic values of the Kanto Loam Formation. The porosity value was large around 80%.

Figure 2 shows the distribution of three phases in soil layers. In the pore space, both macropores ($\leqq$pF1.8) and micropores (>pF1.8) were shown. At the border between the liquid phase and gas phase, the liquid was distributed in micropore, and gas was filled in macropore.

Table 1. Basic characteristics of soil profile at "Hachiman" (site 1).

Depth (cm)	Specific gravity (Gs)	Water content w (kg/kg)	Dry bulk density ρ_d (Mg/m^3)	Porosity n (%)
10	2.44	1.00	0.46	81.2
20	2.45	0.69	0.62	74.7
30	2.41	0.71	0.65	73.0
40	2.43	0.71	0.63	74.1
50	2.48	0.68	0.63	74.6
70	2.49	0.92	0.50	80.0
100	2.58	1.08	0.51	80.2
150	2.68	1.36	0.47	82.5

Table 2. Basic characteristics of soil profile at "Daikan" (site 2).

Depth (cm)	Specific gravity (Gs)	Water content w (kg/kg)	Dry bulk density ρ_d (Mg/m^3)	Porosity n (%)
10	2.48	0.51	0.80	67.1
20	2.52	0.59	0.70	72.6
30	2.51	0.66	0.71	72.2
40	2.53	0.88	0.67	77.7
50	2.48	0.80	0.61	76.7
70	2.69	0.88	0.51	81.1
100	2.74	0.93	0.58	78.5
150	2.78	1.21	0.56	79.3

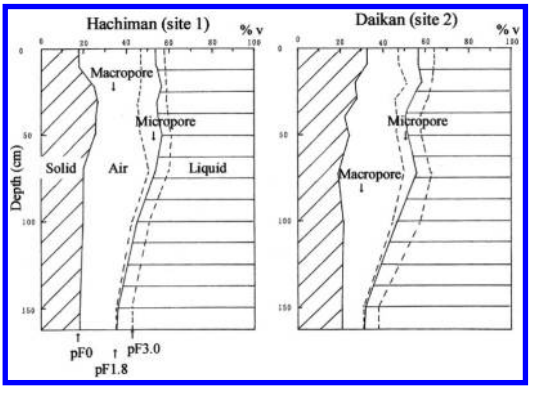


Figure 2. Three phase distribution in soil profiles.

3.2 *Groundwater level*

The groundwater level was changing in the Kanto Loam Formation (mainly, the Musashino Formation; ML) that is situated in the range from 1 to 7 m depth from the surface. This was low in winter and high in summer. Also, the water level began to rise immediately after the onset of rainfall and reached

Copyright © 2003 Swets & Zeitlinger B.V., Lisse, The Netherlands

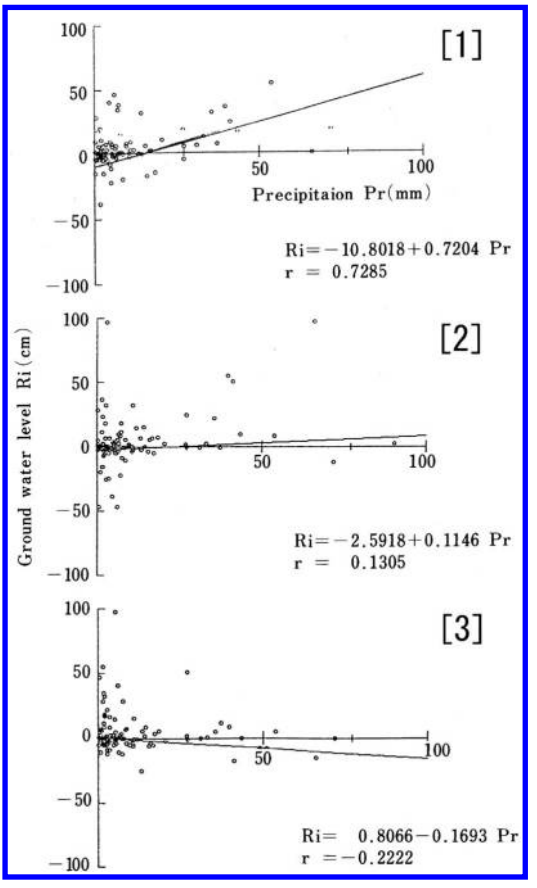


Figure 3. Relationship between precipitation and groundwater level.

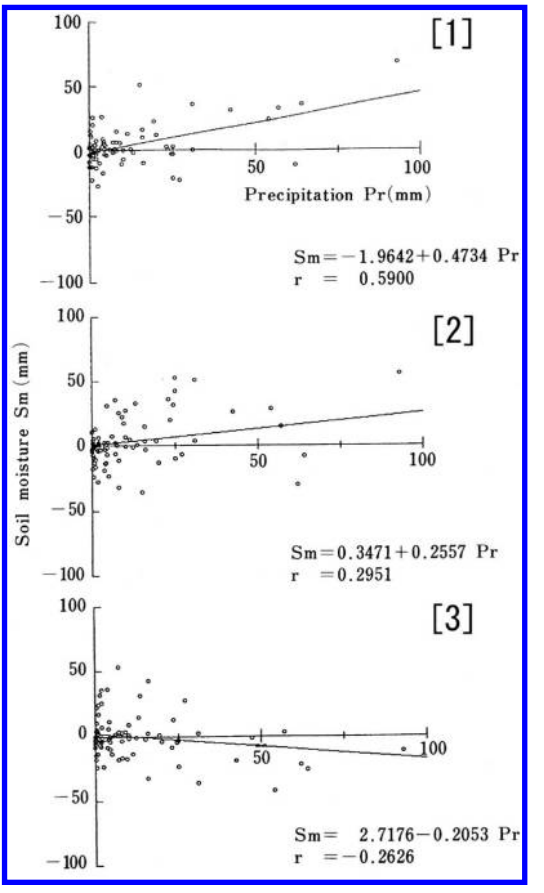


Figure 4. Relationship between precipitation and soil water content.

the maximum water level within ranging from 2 to 6 hours. The altitudes of observed the groundwater levels were about ranging from 32 to 38 m. The distribution of the groundwater level inclined with the landform inclination.

The relationship between the rainfall and groundwater rise is shown in Figure 3. For the measurement time of groundwater rising during 24 hours, three kinds of period were selected. They were,

1. Since rain day before to rain day.
2. Since rain day to rain next day.
3. Since rain next day to rain day after next day.

An incline of regression line of Figure 3 is small in order of [1], [2] and [3]. And a rise of ground-water in rain day is the largest. But the correlations of the three examples were not so high. The continuation rain gave correlation influence. After the start of rain, the groundwater level began to rise within a short time and fell after having reached a peak. The average time difference was 4 hours from the start of rain, for the groundwater level to start rising. If rain intensity was large, a peak of a graph and a quantity of rise were large.

3.3 *Soil water content*

Soil water content in the range from 0 to 150 cm depth changes in the range of 30–70% of the volumetric water contents through the year. This was the sensitive response to the rainfall. In the sub-soil, the maximum soil water content was attained the range from 1 to 2 days from the end of rainfall.

The relationship between the rainfall and soil water increase is shown in Figure 4. Three examples [1], [2] and [3] were made in the same way as the analysis period shown in Figure 3.

The coefficient of correlation is not high. As for the incline of regression curve, [1] is the largest. The soil water reaches a peak after the rain within 24 hours. In addition, an incline of [3] becomes negative. When two days passed after rain, the soil water content decreased.

Copyright © 2003 Swets & Zeitlinger B.V., Lisse, The Netherlands

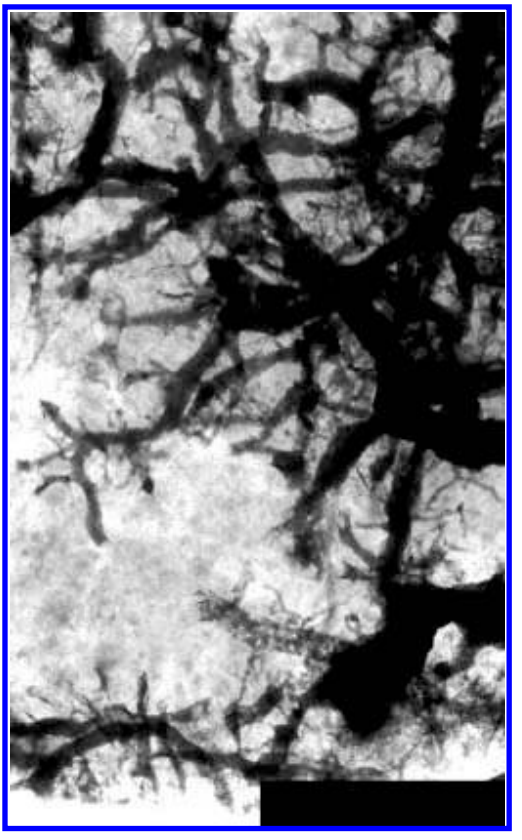


Figure 5. Soft X-ray radiograph of tubular pores in the Tachikawa Formation (TcL) (film No.D108 (FR), 60 kV, 3 mA, 120 s, FFD = 500 mm, thickness = 30 mm, scale = 10 mm).



Figure 6. Soft X-ray radiograph of tubular pores in the Musashino Formation (ML) (film No.M118 (FR), 60 kV, 3 mA, 120 s, FFD = 500 mm, thickness = 33 mm, scale = 10 mm).

3.4 *Soil macropore and infiltration*

Porosity in the soil layer of 0–150 cm depth was about 80%. The non-capillary pore (≦pF1.8) accounted for about 20% of the porosity. Especially, a lot of macropores with the equivalent diameter of 0.05–0.15 mm contributed to the ground infiltration of rainwater.

The structure of the subsoil was identified through the soft X-ray radiographs (Figures 5 and 6). The tubular macropores formed by plant roots developed solidly. A lot of macropores were thick with the vertical direction. The inside diameter of tubular macropore of a plumb direction was the range from 1.2 to 2.4 mm (equivalent pF value was the range from 0.4 to 0.1). The maximum inside diameter included 3.1 mm, too. Therefore, it was considered that rainwater propagate in tubular macropores and reached the groundwater level rapidly.

Schematic diagrams of the processes on the infiltration of rainwater through the soil layer during the early period of rainfall (Case-A) and during the latter period (Case-B), which also shows the rise in the groundwater level, are presented in Figure 7.

In Case-A, tubular macropores of a plumb direction can become the main channel for bypass flow.

In addition, a network with thin the tubular macropores in the horizontal direction is made. When water flows, the downward gas pressure rises. The tubular macropores that do not become an approach course of rainwater becomes an exhaust channel. The exhausted gas is evaded in ground direction or a horizontal direction.

In Case B, the level of the groundwater rises as rainwater infiltrates downward. With increased rise in groundwater level over an area, a phenomenon resembling the principle of a piston occurs. Soil gas is pushed up from the groundwater level and pass through the tubular pores. With the evolution of the gas, the speed in the rise of the groundwater level increases.

Copyright © 2003 Swets & Zeitlinger B.V., Lisse, The Netherlands

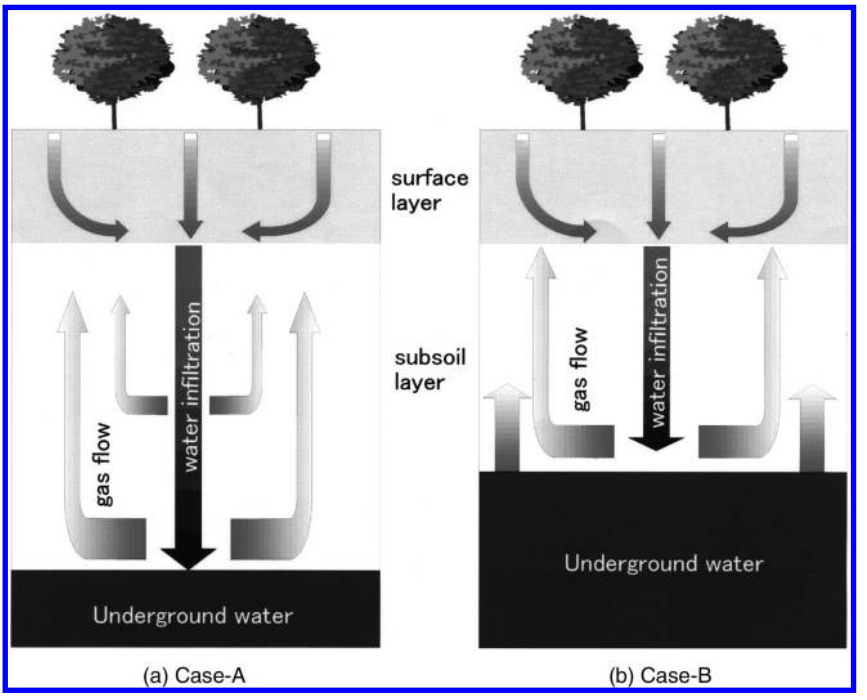


Figure 7. (Case-A) An infiltration process of rainwater (early period), (Case-B) An infiltration process of rainwater (latter period) and rising period of the groundwater level.

3.5 *Hydrologic cycle in the shallow layer* (Table 3)

As for precipitation, 1,112 mm as minimum were observed in 1987. The maximum was nearly twice the minimum value with 2,061 mm observed in 1991. The average precipitation in the observation period was about 1,500 mm. The average groundwater preservation quantity was about 35% of the annual precipitation of the range from 30 to 39%. In the daily average, it was about 1.5 mm. This value as the groundwater preservation quantity was evaluated. The surface outflow percentage was the range from 4 to 27% (an average of 15%) and reflected the large infiltration characteristic of the Kanto Loam Formations (the Musashino Formation; ML).

During rainfall:

$$R = ET + SM1 + G1 + F + L \quad (1)$$

End of rainfall:

$$SM2 = ET + G2 \quad (2)$$

During dry weather conditions:

$$SM3 = ET \quad (3)$$

$$SM1 = SM2 + SM3 \quad (4)$$

Table 3. Annual precipitation in investigation site and preserved groundwater.

Year	R (mm)	G2 (mm)	Daily output (mm)	RCG (%)
1985	1,635	615	1.7	37.6
1986	1,423	160	1.3	32.3
1987	1,112	335	0.9	30.1
1988	1,329	435	1.2	32.7
1989	1,585	545	1.5	34.5
1990	1,582	545	1.5	34.5
1991	2,061	715	2.0	34.7
1992	1,741	645	1.8	37.6
1993	1,731	630	1.7	36.4
1994	1,162	395	1.1	34.0
1995	1,144	445	1.2	38.9

where R: precipitation(mm); ET: evapotranspiration (mm); SM1: soil water increase (mm); G1: direct preserved groundwater by rainfall (mm); F: surface outflow (mm); L: loss precipitation (mm); SM2: soil water decrease (mm); G2: preserved groundwater (mm); SM3: soil waterdecrease (mm).

$$RCG = (G2/R)100 \quad (5)$$

where RCG: ratio of preserved groundwater (%).

Copyright © 2003 Swets & Zeitlinger B.V., Lisse, The Netherlands

The rainwater infiltration areas such as the green land were about 30% in the whole of Setagaya and situated on the flat part. In the infiltration area, the rainwater was supplied to underground and became the source of supply for the other difficulty infiltration area.

4 CONCLUSIONS

Rain does not fall and infiltrate uniformly in the area of study because buildings and other obstructions cover certain portions of the ground surface. Hence, the role of macropores in the maintenance of the groundwater resources at the Musashino Plateau in Southwest Tokyo was examined.

Rainwater falling on the surface of the plateau was found to infiltrate rapidly to the groundwater level through the tubular macropores as the main route and further to the micropores or soil matrix. In the vertical direction, tubular macropores were large while they are thin and winding in the horizontal direction.

Macropores oriented horizontally could be filled by rainwater transmitted through the macropores in the vertical direction and eventually displace air in the soil layer which evolves through macropores where water did not pass through. The air displacement hastens rainwater infiltration. Such process give the macropores specialized functions as either the course for rainwater infiltration or for gas evolution.

REFERENCES

Narioka, H. 1989. Study on the physical functions of soil macropores and the instrumentation for their measurement, *Bulletin of NODAI Research Institute*, TUA, (1): 1–58 (in Japanese).

Narioka, H. & M. Komamura. 2000a. Tubular macropores formed in the Kanto Loam Formations of the Musashino plateau, *Trans. of JSIDRE* (208): 99–105 (in Japanese).

Narioka, H., Y. Iwata & M. Komamura. 2000b. Permeability and drainability of macropores in volcanic ash subsoil of the Kanto Loam Formation, *Trans. of JSIDRE*, (208): 63–71 (in Japanese).

Narioka, H. & M. Komamura. 2000c. Macropore properties of Andosols in the Kanto Loam Formation by physical anal ysis of soil structure and drainability, *Trans. of JSIDRE*, (210): 19–27 (in Japanese).

Copyright © 2003 Swets & Zeitlinger B.V., Lisse, The Netherlands

Instability of foundations undergoing rise in groundwater level

K. Yasuhara, S. Murakami & S. Mitsuyama
Ibaraki University, Hitachi, Japan

ABSTRACT: The paper outlines the methods which are proposed for evaluating the instability of foundations due to rise in groundwater level: decrease in bearing capacity and increase in settlements. It has been indicated from the results calculated using the proposed methods that:

1. The decrease in bearing capacity of sand becomes marked after the h_w/D_f is beyond 1.0 where GWL reaches above the bottom of foundations. In the case of clay foundations, bearing capacity does not decrease considerably before the h_w/D_f becomes unity. However, once h_w/D_f exceeds the unity, then the decrease in bearing capacity is more pronounced with increasing D_f/B. In other words, this proves the importance of foundation depth on maintenance of bearing capacity.
2. Using the hyperbolic load vs. settlement relation, an empirical method for evaluating immediate settlements of foundations undergoing the rise in groundwater level is proposed. This method requires the degradation in strength and stiffness, and the safety factor of bearing capacity.

1 INTRODUCTION

In the large cities in Japan such as Tokyo and Osaka, land subsidence has seemingly been terminated due to regulation of groundwater abstraction since around 1980, although they suffered severe damage due to land subsidence by groundwater abstraction after the World War II. On the other hand, as a consequence in these cities, groundwater level has been recovering and this results in inducing the instability of foundations such as increase in settlements and a decrease in bearing capacity. Besides, building structures under rise of groundwater may sometimes be lifted up by buoyant force in the case when the rise in groundwater is severe. This instability may be accelerated by possible increase in GWL due to sea level rise due to global warming. It is, therefore, important for maintaining the infrastructures to make countermeasures against increased instability due to rise in groundwater level, based on the knowledge obtained from geotechnical engineering.

After reviewing the problems related to changes in groundwater level, the methods are proposed for evaluating the instability of foundations due to rise in groundwater level.

2 MECHANISM OF INSTABILITY OF FOUNDATIONS AND GROUND DUE TO RISE IN GROUNDWATER LEVEL

Although lowering of groundwater level (GWL) triggers land subsidence, rising in GWL induces the instability in foundations and ground as is summarized in Table 1. In the present paper, however, the floating of building structures due to buoyant force followed by rise in ground water level is eliminated from the listed problems in Table 1, although we should tackle it for maintaining the safety of infrastructures in the large cities such as Tokyo and Osaka. Let us start by considering an arbitrary soil element under the center of foundation of structures as is shown in Fig. 1. In

Table 1. Stress condition before and after rise in GWL.

	p'	q
Before	$p'_c = (\sigma'_{vc} + 2\sigma'_{hc})/3$	$q_c = \sigma'_{vc} - \sigma'_{hc}$
After	$p' = p'_c - \gamma_2 \cdot h_w$ Decrease Swelling	$q = q_c = \sigma'_{vc} - \sigma'_{hc}$ Constant Shear def.

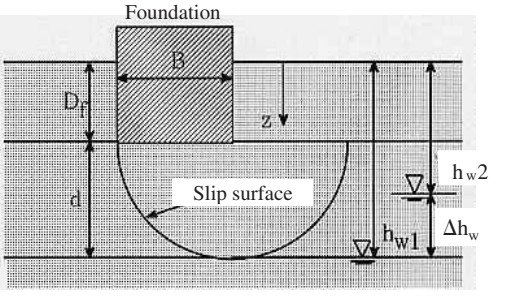


Figure 1. Model for foundation and ground.

Copyright © 2003 Swets & Zeitlinger B.V., Lisse, The Netherlands

this case the location of GWL is assumed to exist at a location with h_w in depth from the ground surface or with z_w from the base of the foundation. The severity of increased instability depends upon a magnitude of risen groundwater level, Δh_w. As a first approximation, z_w is assumed to be equal to, d, which is a distance from the bottom of the slip surface of circle failure, as shown in Fig. 1. In estimating the instability, the location of GWL after rising up is assumed to be two cases: one, between point A and point B which is below the bottom of foundations, another, between point A and point C which is beyond the bottom and within the depth in foundations. The stress states corresponding to these two cases before and after rise in GWL are summarized in Table 1. Judging from the fact that the mean effective principal stress, p', decreases and the principal stress difference, q, is kept constant, inducing the increase in shear stress ratio, q/p', settlements of foundations are governed by both the volume change the shear deformation depending on the decrease in p' and the increase in q/p'. Thus, settlements, S_T, due to rise in GWL yield:

$$S_T = S_E - S_S \tag{1}$$

where S_E is settlement due to shear and S_S is rebound due to swelling, respectively.

3 DECREASE IN BEARING CAPACITY DUE TO RISE IN GROUNDWATER LEVEL

3.1 *Procedure for evaluating the decrease in bearing capacity*

Bearing capacity of the foundation ground decreases with increasing rise in GWL because of the decrease in effective stress. The way how the bearing capacity should decrease depends upon the magnitude of rise in GWL or where GWL rises beneath or above the bottom of the foundation as given by the following two cases:

(1) $D_f < D_f + B$ or $0 < (z_w/B) < 1$
According to Vesic (1975), unit volume weight, $\gamma*_{ave}$, of foundation soils in this case, is given by

$$\begin{aligned}\gamma*_{ave} &= \gamma' + (z_w/B)(\gamma_t - \gamma') \\ &= \gamma' + (1 - \Delta h/B)(\gamma_t - \gamma')\end{aligned} \tag{2}$$

Bearing capacity of foundations subjected to rise in GWL, whose situations are schematically illustrated in Fig. 1, is given by:

$$q_u^* = (1/2)\gamma_{ave}^* B N_\gamma + \gamma_t D_f N_q\text{: for sand} \tag{3a}$$

$$q_u^* = c_u N_c + \gamma_t D_f N_q\text{: for clay} \tag{3b}$$

The normalization of these bearing capacities by those not subjected to rise in GWL yields:

$$\frac{q_u^*}{q} = \frac{(\gamma_{ave}^*/\gamma_t)N_\gamma + 2(D_f/B)N_q}{N_\gamma + 2(D_f/B)N_q} \tag{4a}$$

$$\frac{q_u^*}{q_u} = \frac{m(OCR)^{\Lambda_0}(\gamma_t^* B + \gamma_{tc} D_f)N_c + \gamma_{ts} D_f N_q}{m(\gamma_{tc} B + \gamma_{tc} D_f)N_c + \gamma_{ts} D_f N_q} \tag{4b}$$

These equations are based on the following relation:

$$\frac{(c_u/p')_{OC}}{(c_u/p')_{NC}} = (OCR)^{\Lambda_0} \tag{5}$$

where Λ_0 is empirical constant equal to $1 - C_s/C_c$.

(2) $D_f > h_w$
Let us consider the situation where the GWL rises above the bottom of the foundation. The bearing capacities in this case are given by:

$$q*_u = \frac{1}{2}\gamma' B N_\gamma + p_0' N_q \tag{6a}$$

$$q*_u = m(OCR)^{\Lambda_0}(p_0' + \gamma_{tc} B)N_c + p_0' N_q \tag{6b}$$

where p_o' is given by:

$$p_0' = \gamma_t D_f + \gamma_w (D_f - h_w) = \gamma' D_f + \gamma_w h_w \tag{7}$$

and

$$m = \left(\frac{c_u}{p'}\right)_{NC}\text{: undrained strength increment ratio} \tag{8}$$

As well as Eq. (5), the bearing capacity ratio is given by:

$$\frac{q_u^*}{q_u} = \frac{\gamma^* B N_\gamma + 2p_0' N_\gamma}{\gamma_t B N_\gamma + 2\gamma_t D_f N_q}\text{ for sand} \tag{9a}$$

$$\frac{q_u^*}{q_u} = \frac{m(OCR)^{\Lambda_0}(p_0' + \gamma_{tc} B)N_c + p_0' N_q}{m(\gamma_{ts} D_f + \gamma_{tc} B)N_c + \gamma_{ts} D_f N_q}\text{ for clay} \tag{9b}$$

Let us describe examples of calculation on the decrease in bearing capacity of foundations resting on sand and clay grounds, respectively, using Eq. (9a) and Eq. (9b). The results are expressed in the form of the bearing capacity ratio, q_u^*/q_u, plotted against the normalized rise in GWL, h_w/B, as shown in Fig. 2 for sand ground and in Fig. 3 for clay ground, respectively. Fig. 2 and Fig. 3 correspond to the model foundations as shown in Fig. 4 and Fig. 5, respectively. Comparison between results in Fig. 2 and Fig. 3 proves:

i) The decrease in bearing capacity of sand is more marked than that of clay.

Copyright © 2003 Swets & Zeitlinger B.V., Lisse, The Netherlands

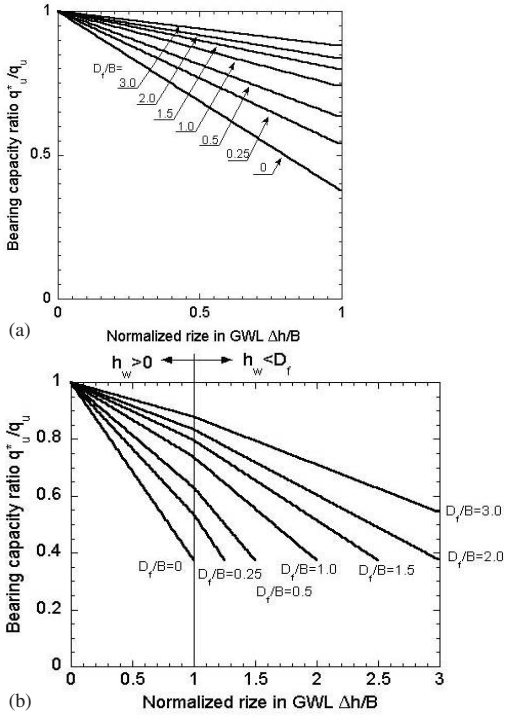


Figure 2. Decrease in bearing capacity (Sand).

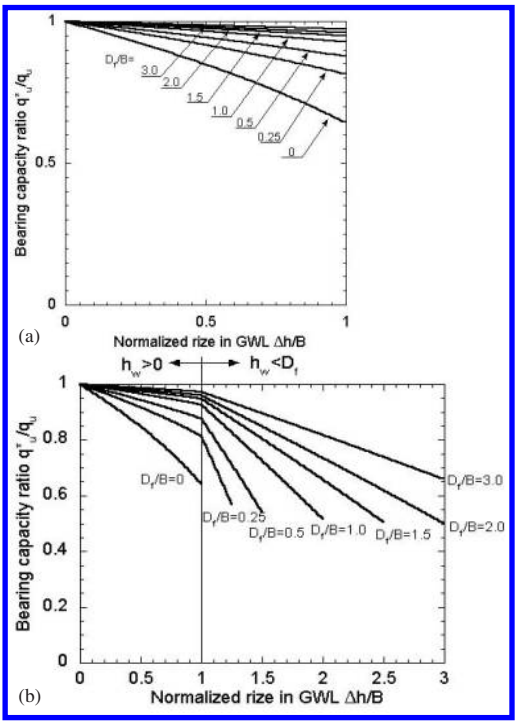


Figure 3. Decrease in bearing capacity (Clay).

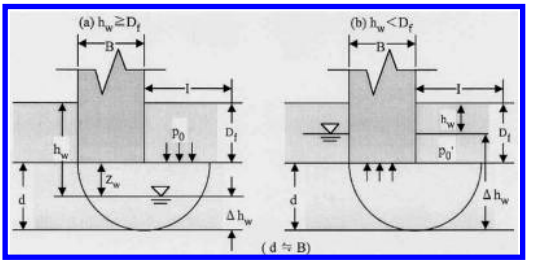


Figure 4. Situations in GWL (Sand).

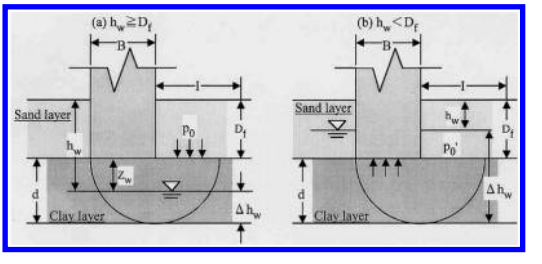


Figure 5. Situations in GWL (Clay).

- ii) The decrease in bearing capacity of sand becomes marked after the h_w/D_f is beyond 1.0 where GWL reaches above the bottom of foundations.
- iii) In the case of clay foundations, bearing capacity does not decreases significantly before the h_w/D_f becomes unity. However, once h_w/D_f exceeds the unity, then the decrease in bearing capacity is more pronounced with increasing D_f/B. In other words, this proves the importance of foundation depth on maintenance of bearing capacity.

4 SETTLEMENTS OF FOUNDATIONS DUE TO RISE IN GROUNDWATER LEVEL

4.1 *A method for evaluating the settlements of foundations*

For demonstrating the method proposed for evaluating the settlements of foundations, let us consider here the case where a building structure with foundations with B in width is applied with q (= q_f/F_s, F_s: safety factor in bearing capacity) as load intensity on ground with q_f as ultimate bearing capacity. The load vs. settlement curve in this case is assumed to follow curve A in Fig. 6. Generally speaking, when ground consists of normally consolidated clay or loose sand, this type of curve can empirically be represented by the hyperbolic function as (Yamaguchi, 1977; Kusakabe and Kawai, 1989).

$$S_{i,NC} = \frac{q_{f,NC}\, q}{K_{i,NC}(q_{f,NC} - q)} \tag{10}$$

Copyright © 2003 Swets & Zeitlinger B.V., Lisse, The Netherlands

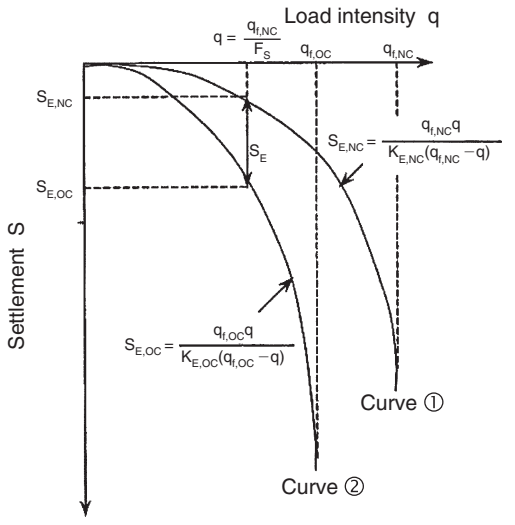


Figure 6. Load vs. setlement curve.

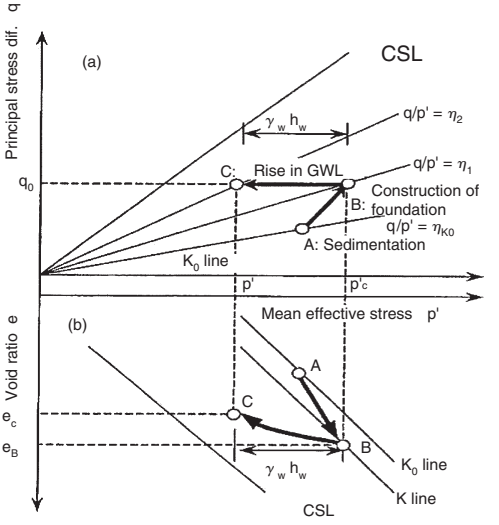


Figure 7. Stress path and state path due to rise in GWL.

where K is coefficient of subgrade reaction and is given by:

$$K_{i,NC} = \frac{E_{i,NC}}{(1-\nu^2)BI_\sigma} \tag{11}$$

where $E_{i,NC}$ is secant modulus, B; width of loading plate, Is: influencing factor, m; Poisson ratio, and $q_{uf,NC}$ is Terzaghi's ultimate bearing capacity which yields in the case of ground consisting of NC clay:

$$q_{f,NC} = (2+\pi)s_{u,NC} \tag{12}$$

where s_{uNC} is undrained strength.

When groundwater level rises up from point P to Q in Fig. 1, the mean principal effective stress, p', in a soil element below the center of foundations must decrease along the line with the constant, q_o, in p' vs. q space. Both the stress path and the state path in this case are schematically represented in Fig. 7. Behaviour of a soil element undergoing the change in p' is relatively complex because shear deformation is caused by increased effective stress ratio, q/p' and swelling takes place due to decreased p'. This leads to increase in displacement of foundations, although whether settlements or rebounds occur in foundations on ground depends on which effect gives the more severe, q/p'-increase or p'-decrease to increased displacement of foundations. Thus, the total settlements due to rise in groundwater level is given by Eq. (1):

On the other hand, by referring to Fig. 3, settlements due to rebound induced by decrement in p' is given by:

$$S_S = HC_S \log\left(\frac{p'_c - \gamma_w \Delta h_w}{p'_c}\right) \tag{13}$$

However, the relative settlements in the present study refer to immediate settlements only in the present paper. In other words, the swelling displacement is neglected.

The settlement vs. load relation of the foundation ground undergoing the rise in groundwater level as shown in Fig. 1 may become Curve B in Fig. 7 because of the decrements in strength and stiffness of soil elements beneath the foundation that are situated under overconsolidation. Following the same manner as the empirical Eq. (10), the curve B can be expressed by:

$$S_{E,OC} = \frac{q_{f,OC}q}{K_{i,OC}(q_{f,OC}-q)} \tag{14}$$

where

$$K_{i,OC} = \frac{E_{i,OC}}{(1-\nu^2)BI_\sigma} \tag{15}$$

$q_{f,OC}$ is bearing capacity of the ground after rising up of GWL and $E_{i,OC}$: deformation modulus of overconsolidated soils.

Combination of Eq. (1) with Eq. (14) gives:

$$\frac{s_E}{S_{E,NC}} = \frac{R_q}{R_K}\left[\frac{1-\frac{1}{F_s}}{R_q - \frac{1}{F_s}}\right] - 1 \tag{16}$$

which may be used for predicting the cyclic-induced settlements of fine-grained soils. Strength ratio and stiffness ratio included in Eq. (16) are respectively given by:

$$R_q = (OCR_q)^{1-\Lambda_0} \tag{17}$$

Copyright © 2003 Swets & Zeitlinger B.V., Lisse, The Netherlands

$$R_K = \frac{1 + C \ln (OCR_q)}{OCR_q} \tag{18}$$

where OCR_q is defined by:

$$OCR_q = (OCR)^{1/1-\lambda} \tag{19}$$

where Λ_o and C are empirical constants regarding decrements in strength and stiffness of overconsolidated soils respectively given by:

$$\Lambda_0 = \frac{\ln \left\{ \frac{(s_u/p')_{OC}}{(s_u/p')_{OC}} \right\}}{\ln OCR} \tag{20}$$

$$C = \frac{\left\{ \frac{(E/p')_{OC}}{(E/p')_{NC}} \right\}}{\ln OCR} - 1 \tag{21}$$

4.2 *Determination of overconsolidation due to rise in GWL*

In the case of $D_f < zw < d + D_f$, OCR is given by:

$$OCR = \frac{\gamma_t (B + D_f)}{\gamma_{ave} B + \gamma_t D_f} \tag{22a}$$

ii) In the case of $zw < D_f$, OCR yields:

$$OCR = \frac{\gamma_t (B + D_f)}{\gamma' (B + D_f) + z_w (\gamma_t - \gamma')} \tag{22b}$$

4.3 *Parametric study*

It is required for forecasting settlements/rebound of foundations due to rise-up in groundwater level to determine soil parameters and OCR depending on the magnitude of rise in groundwater level. To demonstrate an example, the successive footing with the same configuration of $L/B = 100$ as is shown in Fig. 8 is assumed to be built on the clay whose index properties are: unit weight is 14.0 kN/m^3, $q_{f,NC}$ is 145 kPa, Poisson ratio $\nu = 0.34$, Λ_o is 0.596, and $C = 0.26$ which correspond to the prediction of typical clay soils. The results from numerical computation using Eq. (16) and Eq. (13) are illustrated in Fig. 8 in the form of settlement, $\Delta S_{i,NC}$, plotted against the rise in groundwater level, Δh_w, as a parameter of stiffness index, E/s_u. Fig. 8 indicates that:

i) immediate settlements increase with increasing the rise in GWL normalized by the width of foundations, h_w/B, particularly the increase in settlements is marked when $\Delta h_w/B$ exceeds unity, where Δh_w reaches above the bottom of foundations.
ii) the settlement under the undrained shear increases with decreasing the value of E/s_u.

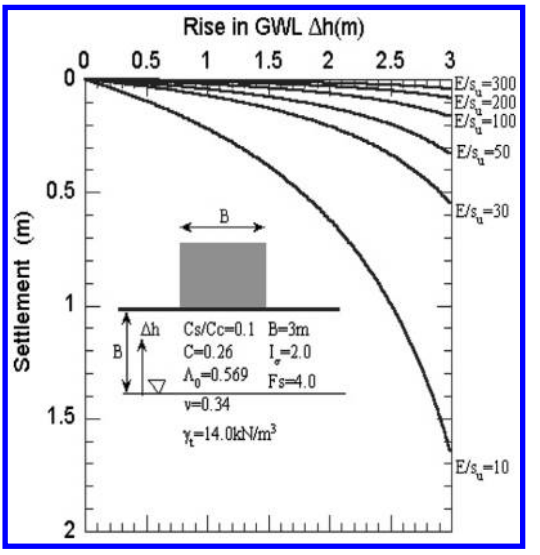


Figure 8. Settlement due to rise in GWL.

5 CONCLUSION

1. The decrease in bearing capacity of sand is more marked than that of clay. The decrease in bearing capacity of sand becomes marked after the h_w/D_f is beyond 1.0 where GWL reaches above the bottom of foundations. In the case of clay foundations, bearing capacity does not decreases significantly before the h_w/D_f becomes unity. However, once h_w/D_f exceeds the unity, then the decrease in bearing capacity is more pronounced with increasing D_f/B. In other words, this proves the importance of foundation depth on maintenance of bearing capacity.
2. Using the hyperbolic load vs. settlement curve, an empirical method for evaluating immediate settlements of foundations undergoing the rise in groundwater level is proposed. This method requires the degradation in strength and stiffness and the safety factor of bearing capacity.
3. The results calculated by using the proposed method, indicates:
   i) immediate settlements increase with increasing the rise in GWL normalized by the width of foundations, h_w/B, particularly the increase in settlements is marked when $\Delta h_w/B$ exceeds unity, where Δh_w reaches above the bottom of foundations.
   ii) the settlement under the undrained shear increases with decreasing the value of E/s_u.

Copyright © 2003 Swets & Zeitlinger B.V., Lisse, The Netherlands

ACKNOWLEDGEMENT

This research has been financially supported by the Nissan Science Foundation, Tokyo, Japan.

REFERENCES

Brand, E. W. and Brenner, R. P.: Soft Caly Engineering, Development in Geotechnical Engineering 20, Elsevier Scientific Pub. Co. Ltd., pp. 82–84, 1981.

Kusakabe, O. and Kawai, N.: Reduction in bearing capacity and increase in settlement of a footing due to an upward seepage flow, J. of Japan Geotechnical Society (Tsuchi-to-Kiso), 37(6), 57–62, 1989 (in Japanese).

Mitachi, T. and Kitago, S.: Change in undrained shear strength characteristics of saturated remoulded clay, Soils and Foundations, 16(1), 45–58, 1976.

Vesic, A. S.: Bearing Capacity of Shallow Foundations, Foundation Engineering edited by H. Winterkorn, Van Nostrand Co. Ltd., 1975.

Yamaguchi, H.: Panel discussion, Proc. 9th ICSMFE, 3, 382–384, 1977.

Copyright © 2003 Swets & Zeitlinger B.V., Lisse, The Netherlands

Simulations on the effects of tillage on pressure head, subsurface drainage, and groundwater recharge

T. Moroizumi
Okayama University, Okayama, Japan

ABSTRACT: The objective of this study is to precisely evaluate the effects of tillage on pressure head, subsurface drainage discharge, and groundwater recharge, using the experimental data and the numerical simulations. A controlled comparative experiment was conducted under natural weather conditions, using tilled and untilled columns. The observed results were analyzed by a standard water movement model (Richards equation) and the van Genuchten's functions for hydraulic properties. The model was solved numerically with a finite difference method and a Picard iterative solution scheme. The performance of the model was quite satisfactory, and the differences between the tilled and the untilled soils for pressure heads, subsurface drainage, and ground water recharge were simulated well.

1 INTRODUCTION

Tillage practice is one component of the best management tool of farmland to control groundwater recharge and contamination, because the tillage practice greatly influences the movement of both water and solutes. To evaluate the effect of tillage on water movement and solutes quantitively is extremely difficult. This difficulty is mainly due to spatial variability of hydraulic properties.

In general, the soil tillage increases porosity and reduces bulk density, leading to changes in hydraulic properties such as water retention curve and hydraulic conductivity. Wu et al. (1992) indicated that the no-tillage treatment had greater numbers of continuous macropores and equal or greater saturated hydraulic conductivity than the moldboard plow tillage. Benjamin (1993) reported that the no-till system had as great and greater hydraulic conductivity as both the mold board plow and chisel plow systems owing to either a greater conductivity of pores or to water flow through a few very large pores. Kribaa et al. (2001) showed that the tillage increased hydraulic conductivity, especially at water potentials close to saturation.

Hill et al. (1985) and Hill (1990) reported that conventionally tilled soils drained more rapidly than conservation tilled soils. Recently tilled soil also has rapid infiltration until settled by rainfall and irrigation. However, the effects of tillage on soil hydraulic properties, infiltration rate, and drainage discharge generally should vary with time and space. Infiltration rates under no-tillage compared with tillage may be faster, slower, or not significantly different (Logsdon et al., 1993). The influences of tillage on surface pond and tension infiltration were transient and dependent on the tillage and subsequent rain. For this reasons, measurement of long-term tillage management effects on surface soil properties requires some well documented measurements. If possible, the measurements should be conducted soon after rainfall events to quantify accurately the tillage effects on subsurface drainage (Logsdon et al., 1993).

Several research studies examining the modeling of the effects of tillage on water movement in tilled soil have been conducted. Most of them included heat transport and were aimed at finding the effects of tillage on soil moisture, soil temperature, and evaporation, using the coupled water and heat transport model (e.g., Hammel et al., 1981; Yang and Zeng, 1988; Benjamin et al., 1990; Moroizumi et al., 2002).

The objective of this study is to evaluate the effects of tillage on pressure head, subsurface drainage, and groundwater recharge experimentally and numerically. The controlled comparative experiment was carried out with the two columns before and after tillage of one of the columns in order to exclude spatial variability and estimate precisely the influences of tillage. The one-dimensional water flow model, HYDRUS version 6.0, was used to analyze the experimental data. The model solves the Richards equation, and was tested by comparing the model simulations with the experimental data. Finally, the influence of tillage on groundwater recharge was simulated using the model.

Copyright © 2003 Swets & Zeitlinger B.V., Lisse, The Netherlands

2 NUMERICAL SOLUTION

2.1 *Governing equation*

The one-dimensional vertical water movement in variably saturated soil is described by the following mixed form formulation of Richards equation:

$$\frac{\partial \theta}{\partial t} = \frac{\partial}{\partial z}\left(K\frac{\partial h}{\partial z} + K\right) \tag{1}$$

where θ is the volumetric water content $[L^3L^{-3}]$, h is the soil water pressure head $[L]$, t is time $[T]$, z is the vertical space coordinate $[L]$, and K is hydraulic conductivity $[LT^{-1}]$.

The soil water retention property and hydraulic conductivity were expressed by the van Genucthen (1980) function with the Mualem pore size distribution model:

$$\theta(h) = \theta_r + \frac{\theta_s - \theta_r}{[1 + |\alpha h|^n]^{1-1/n}} \quad h < 0$$

$$\theta(h) = \theta_s \quad h \geq 0 \tag{2}$$

$$K(S_e) = K_s S_e^l \left[1 - (1 - S_e^{n/(n-1)})^{1-1/n}\right]^2 \tag{3}$$

where θ_r is the residual soil water content $[L^3L^{-3}]$, θ_s is the saturated soil water content $[L^3L^{-3}]$, K_s is the saturated hydraulic conductivity $[LT^{-1}]$, α is the fitting parameter in the soil retention curve $[L^{-1}]$, n is also the fitting parameter in the soil retention curve [dimensionless], and S_e is the effective water content. The α and n were calculated to fit the laboratory water retention data using Powell's conjugate direction method (Powell, 1964).

Nonlinear partial differential Equation (1) was solved numerically by the computer code HYDRUS version 6.0, which is a free software revised and updated by Simunek et al. (1998). In this code, Equation (1) was solved with a mass-lumped linear finite element scheme for the spatial discretization of the flow domain and a Picard iteration procedure at each time step. The time derivative was approximated by a fully implicit difference scheme. The element lengths were shorter when approaching the soil surface where pressure head values varied rapidly because of rainfall, irrigation, and evaporation.

2.2 *Initial and boundary conditions*

A surface boundary condition was specified by the Neumann condition which was given by precipitation and the maximum potential rate of evaporation under atmospheric conditions. A seepage face at the bottom was used as a bottom boundary condition. This boundary condition often applies to a finite lysimeter, such as the one used in this study, which is allowed to drain under gravity (Simunek et al., 1998).

The initial conditions for the pressure head were given based on their measured profiles at the start of the experiment (0:00 a.m. on day 247). They already included the effects of tillage on pressure heads in the drying process before the experiment.

3 EXPERIMENTAL DESIGN

Field experiments were carried out on a 10 × 20 m bare soil area at the School of Veterinary and Animal Sciences, Kitasato University, in Aomori prefecture, Japan. This area is located in the northeastern part of the main island of Japan. The soil at this site is volcanic ash soil or andosol which is called "Kuroboku" soils in Japanese soil classification system. The apparent soil texture ranged from sandy loam to sand. Two soil columns were buried in the area to estimate the effects of tillage on subsurface drainage and water potential.

Each soil column was 49.2 cm in diameter, 110.8 cm in depth, and had a drain pipe at the bottom. The diameter of this pipe was 3.0 cm. The columns were packed from the surface with sand soil material between 50 and 100 cm depths and sandy loam from 0 to 50 cm; this layering was the same as the soil profile in the field around each column. The columns were also packed with coarse sand and gravel, as a filter material, below a depth of 100 cm. Water potential values were measured at depths of 5, 10, 25, 45, 65, 80, and 100 cm, using tensiometers with pressure transducers, and were recorded automatically at five-minute intervals with a data-logger controlled by a portable computer. The subsurface drainage discharge at the bottom was measured manually at appropriate time steps, using a graduated cylinder. The rainfall was measured with a tipping-bucket rain gauge(Moroizumi, 1998).

The field experimental data for subsurface drainage discharge and water potential values were measured intensively from day 247 to 255 of 1993. one of the two columns (called Column 2) was tilled crosswise by hand, using a small hand-plow which was a kind of hoe. The depth of tillage was at an approximate tillage depth of 4.5 cm. Tillage was conducted during 1010 h to 1050 h on day 244.

The results of laboratory tests for the basic physical properties of the soils are presented in Table 1.

4 RESULTS AND DISCUSSION

4.1 *Pressure head*

Figure 1 shows simulated and measured pressure head values at depths of 5, 10, 25, 45, 65, 80, and 100 cm for the tilled and the untilled column. Several pressure head values (e.g., during the 16:00 on day 249 to the 15:00 on day 250 and the 0:00 to the 24:00 on day 253)

Copyright © 2003 Swets & Zeitlinger B.V., Lisse, The Netherlands

Table 1. Physical properties of soils.

	Depth (cm)	Soil texture*	Soil particle density ($g\,cm^{-3}$)	Dry bulk density ($g\,cm^{-3}$)	Porosity (%)	Saturated hydraulic conductivity ($cm\,s^{-1}$)
Untilled	0–50	Sandy loam	2.47	0.890	63.6	3.68×10^{-4}
	50–100	Sand	2.53	0.746	61.3	3.06×10^{-4}
Tilled	0–5	Sandy loam	2.47	0.681	71.8	4.52×10^{-2}

* Classification by the International Soil Science Society.

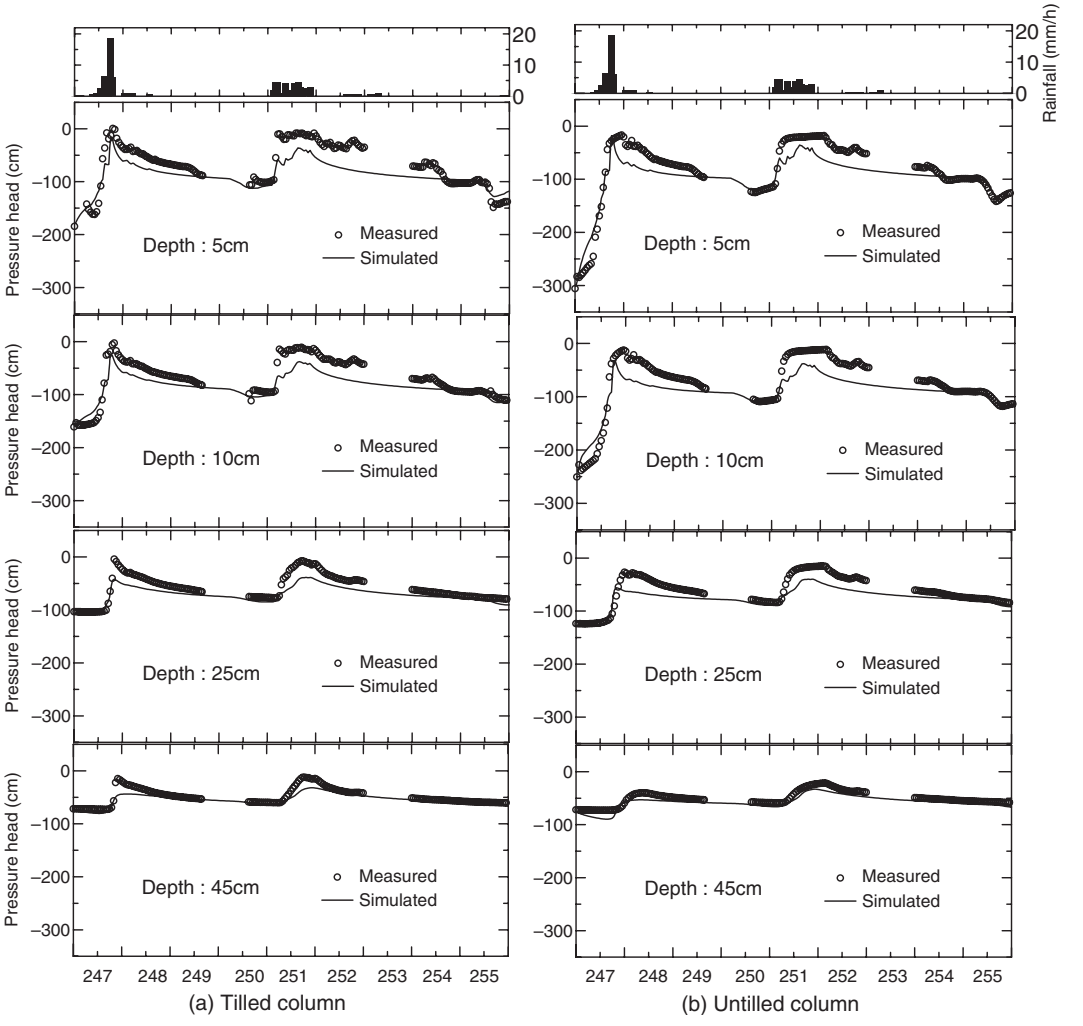


Figure 1. Simulated and observed values of the temporal changes in pressure head at depths of 5, 10, 25, and 45 cm, from day 247 to day 255 in 1993.

Copyright © 2003 Swets & Zeitlinger B.V., Lisse, The Netherlands

could not be detected because of a temporary failure in the data logging system.

As a whole, the variations in simulated head values tended to be similar to the variations in the measured ones, although the simulated values for the increase in pressure head values influenced by rainfall were slightly lower than the measured values. One reason is thought to be a hysteresis in the water retention curves that was not included in the numerical analysis in this study; therefore, the simulated data did not show the increase in pressure head values by rainfall, the impact of rainfall on the pressure head values at depths of 5, 10, 25, and 45 cm were well reproduced. The model is satisfactory for evaluating pressure head values in the same way as the subsurface drainage discharge.

4.2 *Subsurface drainage*

Figure 2 shows a comparison between the tilled column (Column 2) and the untilled column (Column 1) for the cumulative drainage water from precipitation. There were two main occurrences of precipitation on days 247 to 248 and days 251 to 253. The total amount of each precipitation was 45.5 mm for days 247 to 248 and 52.0 mm for days 251 to 253. Runoffs and crusts at the two columns were not observed.

The onset of drainage for the tilled column was at 1700 h on day 248, namely, 11 hours earlier than that for the untilled column. It can be inferred that this result was caused by an increase of the infiltration rate at the tilled column due to a rise of the saturated hydraulic conductivity and porosity in the tilled layer, as shown in Table 1.

The total amount of subsurface drainage discharge was 55.2 mm for the tilled column and 38.8 mm for the untilled column. Its difference was 16.4 mm. The results indicate that the tillage induced the onset of drainage to occur earlier and the amount of drainage water to increase.

Figure 2 also presents simulated values for the cumulative amount of drainage water in each column. Both simulated values were slightly higher than the measured values after day 252. The simulated value for the tilled column at the end of the experiment was 60.5 mm, which was 5.3 mm higher than that for the measured value. Similarly, the simulated value for the untilled column was 45.7 mm, which was 6.9 mm higher than the measured value. The results indicate that the model used here is working satisfactorily to evaluate the effect of tillage on subsurface drainage discharge.

4.3 *Groundwater recharge*

Figure 3 shows a temporal change of groundwater recharge per hour. The groundwater recharge was larger in the tilled column than in the untilled after the first rainfall (day 247 to 248), and the start of the recharge for the tilled column was earlier than that for the untilled column. The difference between the tilled and the untilled column, however, became smaller after the second rainfall (day 251) than after the first rainfall. The maximum of the difference was about 0.1 mm h^{-1}. After day 253, the groundwater recharge in tilled column was approximately identical with that in the untilled column.

The difference after the first rainfall was due to not only the change of the water retention curve and hydraulic conductivity but also the effect of tillage on the initial pressure head profile at the beginning of the experiment. We, however, inferred that those effects diminished after the second rainfall.

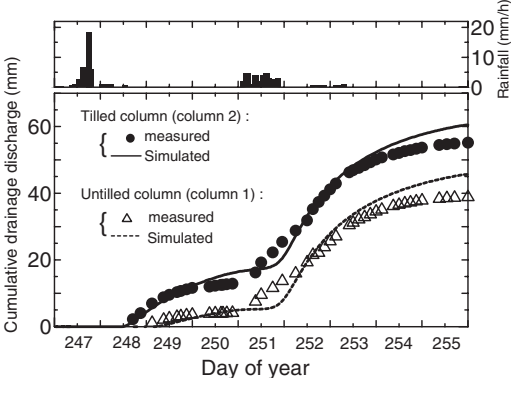


Figure 2. Simulated and observed values for cumulative sub-surface drainage discharge for Column 1 (solid circle) and Column 2 (open triangle) during the preliminary experiment from day 239 to day 243.

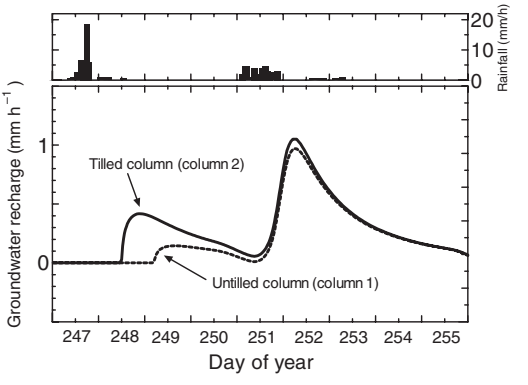


Figure 3. Simulated values for groundwater recharge for Column 1 (solid circle) and Column 2 (open triangle) during the preliminary experiment from day 239 to day 243.

Copyright © 2003 Swets & Zeitlinger B.V., Lisse, The Netherlands

5 CONCLUSION

A controlled comparative experiment was conducted using a tilled and an untilled column to evaluate the effects of tillage on pressure head, subsurface drainage discharge, and groundwater recharge. Measured pressure heads and subsurface drainage discharges were analyzed by a numerical model, HYDRUS version 6.0 code (Simunek et al., 1998), and the model performance was tested. Additionally, the effect of tillage on groundwater recharge was simulated. The following conclusions were drawn from this study:

As a result, the model used in this study reproduced the measured values very well for pressure heads and subsurface drainage discharge. The numerical results indicated that the differences between the tilled and the untilled soil were brought about by the changes in hydraulic properties and by the difference of the initial condition of pressure head.

REFERENCES

Benjamin, J.G., Blaylock, A.D., Brown, H.J. & Cruse, R.M., 1990. Ridge tillage effects on simulated water and heat transport. Soil Tillage Res., 18: 167–180.

Benjamin, J.G., 1993. Tillage effects on near-surface soil hydraulic properties. Soil Tillage Res., 26: 277–288.

Hammel, J.E., Papendick, R.I. & Campbell, G.S., 1981. Fallow tillage effects on evaporation and seedzone water content in a dry summer climate. Soil Sci. Soc. Am. J., 45: 1016–1022.

Hill, R.L., Horton, R. & Cruse, R.M., 1985. Tillage effects on soil water retention and pore size distribution of two mollisols. Soil Sci. Soc. Am. J., 49: 1264–1269.

Hill, R.L., 1990. Long-term conventional and no-tillage effects on selected soil physical properties. Soil Sci. Soc. Am. J., 54: 161–166.

Kribaa, M., Hallaire, V., Curmi, P. & Lahmar, R., 2001. Effect of various cultivation methods on the structure and hydraulic properties of a soil in a semi-arid climate. Soil Tillage Res., 60: 43–53.

Logsdon, S.D., Jordahl, J.L. & Karlen, D.L., 1993. Tillage and crop effects on ponded and tension infiltration rates. Soil Tillage Res., 28: 179–189.

Moroizumi, T., 1998. The effects of tillage on the temperature and water in an unsaturated soil zone. J. Japan Soc. Hydrol. & Water Resour., 11: 61–66 (in Japanese with English abstract).

Moroizumi, T. & Horino, H., 2002. The effects of tillage on soil temperature and soil water. Soil Sci., 167: 548–559.

Powell, M.J.D., 1964. An efficient method for finding the minimum of several variables without calculating derivatives. Computer J., 155–162.

Simunek, J., Huang, K. & van Genuchten, M.Th., 1998. The HYDRUS code for simulating the one-dimensional movement of water, heat, and multiple solutes in variably-saturated media. Research Report No. 144, 1–142.

van Genucthen, M.Th., 1980. A closed-form equation for predicting the hydraulic conductivity of unsaturated soils. Soil Sci. Soc. Am. J., 44: 892–898.

Wu, L., Swan, J.B., Paulson, W.H. & Randall, G.W., 1992. Tillage effects on measured soil hydraulic properties. Soil Tillage Res., 25: 17–33.

Yang, B.J. & Zeng, D.C., 1988. Simulation of seedbed soil moisture and temperature behavior as effected by tillage operations. Proc. 11th International Conference, Soil and Tillage Research Organization, Edinburgh, Scotland, 433–438.

Copyright © 2003 Swets & Zeitlinger B.V., Lisse, The Netherlands

Basic concept on preservation natural groundwater flows from intercepting by underground structure

M. Tambara
Hanshin Consultant Co. Ltd., Kobe, Japan

M. Nishigaki
Okayama University, Okayama, Japan

T. Hashimoto
Geo-Research Institute, Osaka, Japan

Y. Shinshi
Konoike Construction Co. Ltd., Osaka, Japan

K. Daito
Daido Institute of Technology, Nagoya, Japan

ABSTRACT: This paper discusses the influence of earth retaining walls on natural groundwater flow and countermeasures for it. A basic concept for a countermeasure is proposed: a collecting facility, a passing-through facility and a recharging facility. A collecting facility will be set up on the upper side of the groundwater flow, nearby an earth retaining wall. A recharging facility will be set up on the lower side of the groundwater flow nearby, an earth retaining wall. A passing-through facility is connected above both of the facilities in a space surrounded with pierced walls. The influence of natural groundwater flow on the environment also is summarized in this paper, and a flow chart for discussion of the countermeasure is proposed. Last, detailed considerations of the facilities for site investigation, design, construction, monitoring and maintenance are included in subsequent papers in this conference.

1 CONDITIONS WHICH CURRENTLY SURROUND UNDERGROUND CONSTRUCTION

Because of the sudden rise in the price of land accompanying increased economic growth, underground infrastructure maintenance in cities in Japan has been a major factor in developing public sites, mainly under public roads. In recent years, new underground structures often have been set deeply to avoid existing structures. In response to the continued growth of cities, and because of remarkable developments in construction technology, the tendency is for underground infrastructure to become more and more deep. Concern and discussions, however, about increased cost and environmental impact have created a review of present construction practices.

In May 2000, policies involving deep subterranean construction were defined and strengthened by laws aimed at more effectives and expanded underground land use, especially below privately owned an principally undeveloped top-side properties. Prior to this, in 1997, assessments of the environmental impact created by large-scale construction projects had become codified and mandated under the guidance of national law. With this in mind, it seems that promotion will continue for further utilization of underground resources and that the number of underground structure will increase.

On the other hand, the case where the structure is constructed underground increases for not only underground use for effective use for land but also consideration to the noise, the vibration, air pollution and the spectacle deterioration, etc. This tendency extends even to the surrounding of the city part and the provinces.

In general, the underground structure is constructed by the cut and cover construction, shield method, and the NATM method. Recently, shield method is often adopted in the construction of a deep underground structure in the line like the railway, drainage, and the

Copyright © 2003 Swets & Zeitlinger B.V., Lisse, The Netherlands

telecommunication equipment, etc. However, when the underground structure in a large section like the subway station, the channel road, and the approach to the tunnel etc. are constructed, the cut and cover construction is often adopted.

2 INFLUENCE ON GROUNDWATER BY UNDERGROUND STRUCTURE

In the cut and cover construction, earth retaining walls are constructed more deeply than the main body structures for the prevention of the ground collapse under digging and the groundwater interception. And, after construction is completed, the earth retaining wall is left in the earth with the structure in case of almost. When long line structure is constructed with the open-cut method like the railway and road. The main body structure and left earth retaining wall give groundwater widely terrible influence. The influence reaches widely for a long term after completing the underground structure.

The influence that the underground structure gives the groundwater flow immediately is as follows.

(a) The amount of the groundwater flow changes by the change of the groundwater level around the underground structure.
(b) The water level of upstream side of groundwater rises by the underground structure.
(c) The water level of downstream side of groundwater lowering by the underground structure.
(d) The bleeding channel along the underground structure is generated. And, the groundwater flow changes the direction at the edge of this structure.

As a result, there is a possibility that the deformation of the structure by the hydraulic pressure increase and the water leak to the underground structure and the lowering of the well abilities etc. are generated for the short term. Moreover, the subsidence by the change in strength of the soil, the influence on the ecosystem such as the plant and the animal, and the change in water qualities, etc. might occur for the long term. The influence by the groundwater flow obstruction is shown in Table 1. The problem caused by the interception of the subterranean stream is shown in Figure 1. The cases with a concrete influence and damage by the change in the groundwater level are shown in Figures 2 and 3.

When the construction of the underground structure is planned, it is important to forecast and to evaluate what influence and damage occur by the groundwater flow obstruction.

3 PRESERVATION METHOD OF GROUNDWATER FLOW

The preservation method of groundwater flow is a method for avoiding the groundwater flow obstruction by the main body structure and the earth retaining wall. This is a method of securing the flow of groundwater after the main body structure and the earth retaining wall are constructed (Daito, K et al., 1996). First, the intercepted groundwater is collected in the aquifer on the upstream side of the structure and the earth retaining wall. Next, the passing pipe and the gravel zone in the part of the main body structure and the earth retaining wall pass groundwater, and groundwater is recharged to the ground on the downstream side at the end. The concept chart of preservation method of groundwater flow is shown in Figure 4.

In a past case, the groundwater flow preservation countermeasure has been executed while trying and erring in allopathy after the problem occurs at each construction. Few groundwater flow preservation countermeasures were systematically planned from the plan stage of the underground structure. Moreover, there are few cases verified whether to have achieved the effect for a long term after measures.

Table 1. Influence of groundwater flow obstruction.

	Change in groundwater Change in groundwater level, hydraulic gradient and bleeding channel	
Event	Water level rise on the upstream side	Water level lowering on the downstream side
1. Gruondwater use	• Breakdown of pump	• Lowering of the pumping ability of well
2. Groundwater level	• Lowering of water quality because of stay	• Water salination
3. Ground environment	• Making of ground moist • Increase in liquifaction risk	• Subsidence of ground
4. Structure	• Increase in buoyancy • Increase in groundwater leak	• Subsidence by lowering of pore water pressure
5. Ecosystem	• Damage of the tree by root rot • Influence on underground living thing	• Standing decayed of tree • Influence on aquatic life

Copyright © 2003 Swets & Zeitlinger B.V., Lisse, The Netherlands

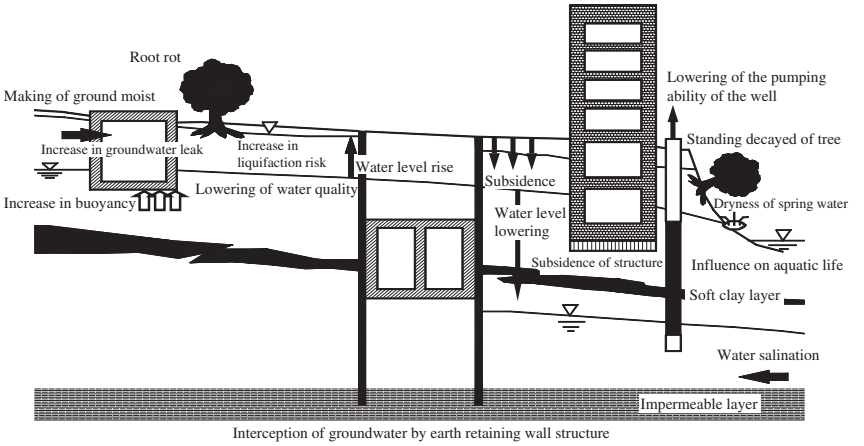


Figure 1. Image of problems that occur by interception of groundwater.

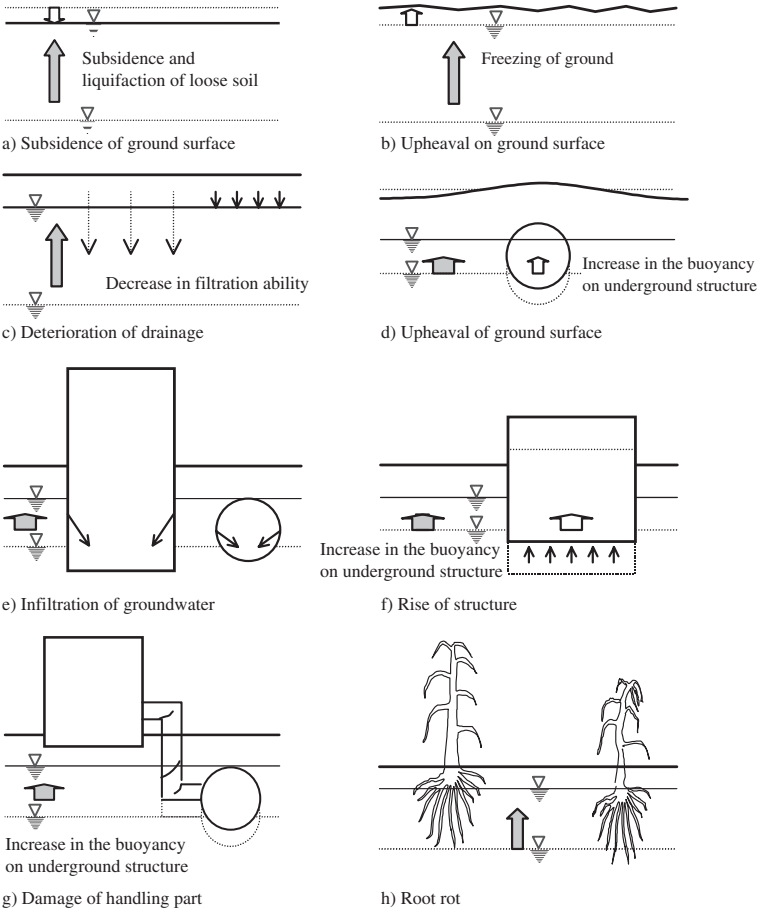


Figure 2. Examples of damage by rise of water level.

Copyright © 2003 Swets & Zeitlinger B.V., Lisse, The Netherlands

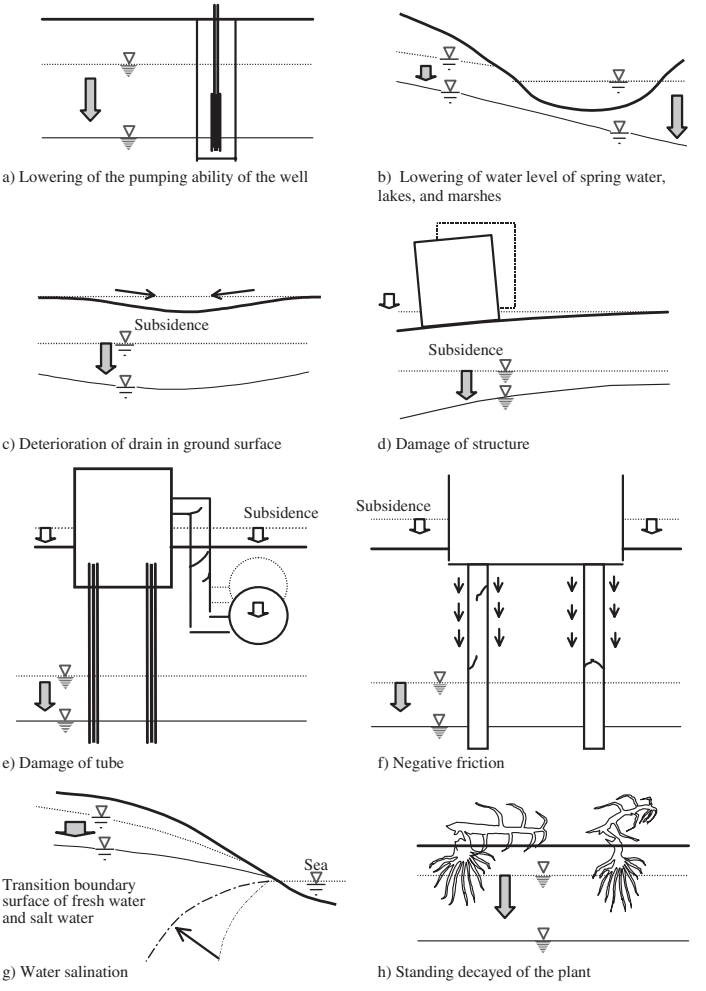


Figure 3. Examples of damage by lowering of water level.

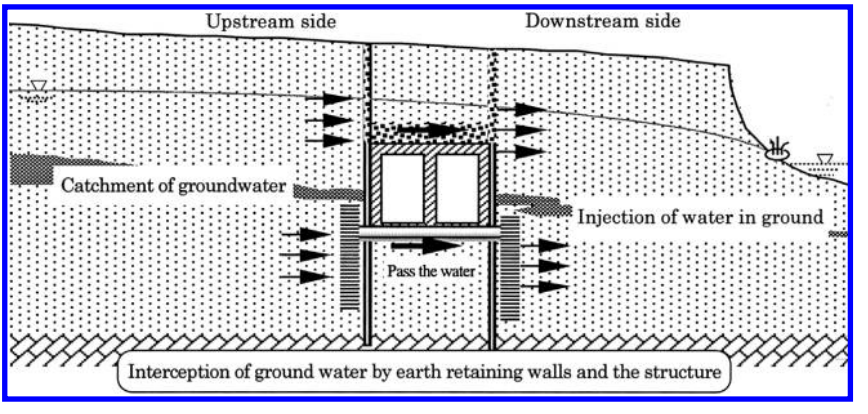


Figure 4. The concept chart of preservation method of groundwater flow.

Copyright © 2003 Swets & Zeitlinger B.V., Lisse, The Netherlands

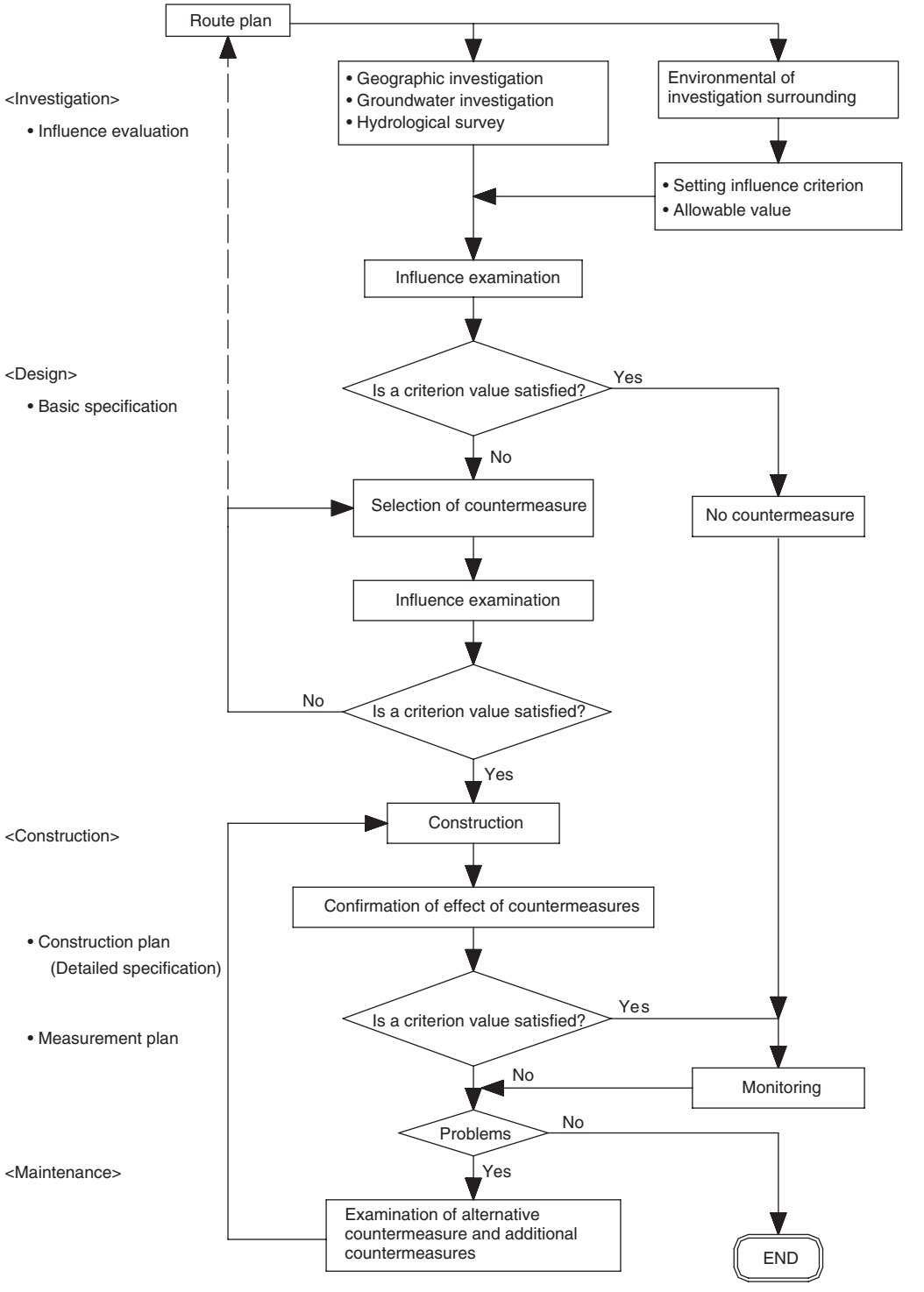


Figure 5. Examination flow of the preservation of groundwater flow.

Copyright © 2003 Swets & Zeitlinger B.V., Lisse, The Netherlands

Thus, a lot of problems that should be solved in the future have been left in the application of the method though the component of the method is a simple mechanism.

The problems that groundwater flow preservation countermeasure is examined are as follows.

(a) A systematic examination technique over the investigation, the design, and maintenance is not set up.
(b) It is easy to obtain wide-ranging, three dimensional neither ground nor groundwater information in the investigation.
(c) In the influence evaluation, the selection of an index, an allowable value, and an analytical model is difficult. Especially, there is no simple analytical technique to do an outline evaluation. Moreover, when the criterion is decided, it takes time to explain and to form mutual agreement to the outsider such as a resident in the surrounding.
(d) In the design and construction, the water interception is requested while constructing the earth retaining wall, and after the earth retaining wall is constructed, permeability is demanded for the groundwater flow preservation. Thus, the development of the earth retaining wall with the conflicting performance.
(e) After adopting the groundwater flow preservation countermeasure, the confirmation of the long-term effect is difficult because it takes cost and time.

The case where the groundwater flow preservation countermeasure is adopted will increase in the construction plan of the underground structure for the groundwater preservation and environmental preservation in the future. And, this method comes to occupy the corner of an important method in the construction technology.

It is important to analyze a past construction case collecting to solve the above mentioned problem, to clarify the problem, and to bring what should be examined at each stage of the investigation, the design, construction, and maintenance together. Basic examination flow of the groundwater flow preservation countermeasure is as shown in Figure 5.

4 CONCLUSIONS

This paper discussed the influence of earth retaining walls on natural groundwater flow and countermeasure for it. A basic concept for a countermeasure was proposed: a collecting facility, a passing-through facility and a recharging facility. A collecting facility will be set up on the upper side of the groundwater flow, nearby an earth retaining wall. A recharging facility will be set up on the lower side of the groundwater flow nearby, an earth retaining wall. A passing–through facility is connected above both of the facilities in a space surrounded with pierced walls.

The influence of natural groundwater flow on the environment also was summarized in this paper, and a flow chart for discussion of the countermeasure was proposed.

Last, detailed considerations of the facilities for site investigation, design, construction, monitoring and maintenance are included in subsequent papers in this conference.

REFERENCE

DAITO, K., UESHITA, K. & ICHIKAWA, E. 1996. Study on Preservation of Groundwater Flow around Excavated Linear Facilities, *Journal of Geotechnical Engineering*, JSCE, No. 535, III-34, 13–21 (in Japanese).

Copyright © 2003 Swets & Zeitlinger B.V., Lisse, The Netherlands

Investigation procedure for preserving groundwater flows

T. Hashimoto
Geo-Research Institute, Osaka, Japan

Y. Ando
Okiko Corporation Co. Ltd., Osaka, Japan

K. Noda
Tokyo Construction Consultants Co. Ltd., Osaka, Japan

J. Miyagawa
Kawasaki Geological Engineering Co. Ltd., Osaka, Japan

ABSTRACT: The method of preserving groundwater flows prevents groundwater flows from being intercepted in construction of underground structures in aquifer stratum. In order to arrange planning, designing, construction and maintenance, using the method, it is important to comprehend the geological condition, the groundwater conditions, the surroundings including the ecosystem and the legislation in the targeted area. Although investigations to comprehend these are carried out at each stage from planning to maintenance, investigations before designing need to be regarded as the most important.

1 METHOD OF INVESTIGATION

1.1 *Procedure of investigation*

The flow chart of the investigation is shown in Figure 1. The investigations are roughly classified into preliminary investigations and detailed investigations.

1.2 *Preliminary investigation*

In the preliminary investigation, the information on the legislation and the surroundings, including the ecosystems, are collected based on the existing documentation or results of simple investigations. Using the investigation results, the investigation area is set and the necessity of detailed investigations is judged by a rough prediction of construction influences, while investigation items are set and appropriate locations and degrees of detailed investigations are studied. An example of an investigation area is shown in Figure 2. The investigation areas are decided from a comprehensive perspective, in consideration of past cases, results of calculations, and topographic, geographical and social conditions of the surroundings. An investigation area consisting of the recharge source to the outflow point is ideal, taking the water balance into consideration.

1.3 *Detailed investigation*

The detailed investigations are classified into the main investigations emphasizing on the groundwater flow and the investigations on the surroundings. The main investigations are carried out to obtain the necessary data to set analytical models, boundary conditions or conditions of external forces in the detailed study on the influences of the interruption in the groundwater flow. The characterization and the basic flow chart of the main investigation are shown in Figure 3. The most important thing in the investigation is how accurately the water path is understood. Figure 4 shows an example of a multi-point temperature logging in gravel.

The construction of the lining structures in the areas where groundwater is flowing continues to influence the surrounding communities for a long time, whether the method of preserving groundwater flows is employed or not. The first phenomenon is a rise or a drop of the water level, and the change of the water level causes the secondary phenomenon, changes of

Copyright © 2003 Swets & Zeitlinger B.V., Lisse, The Netherlands

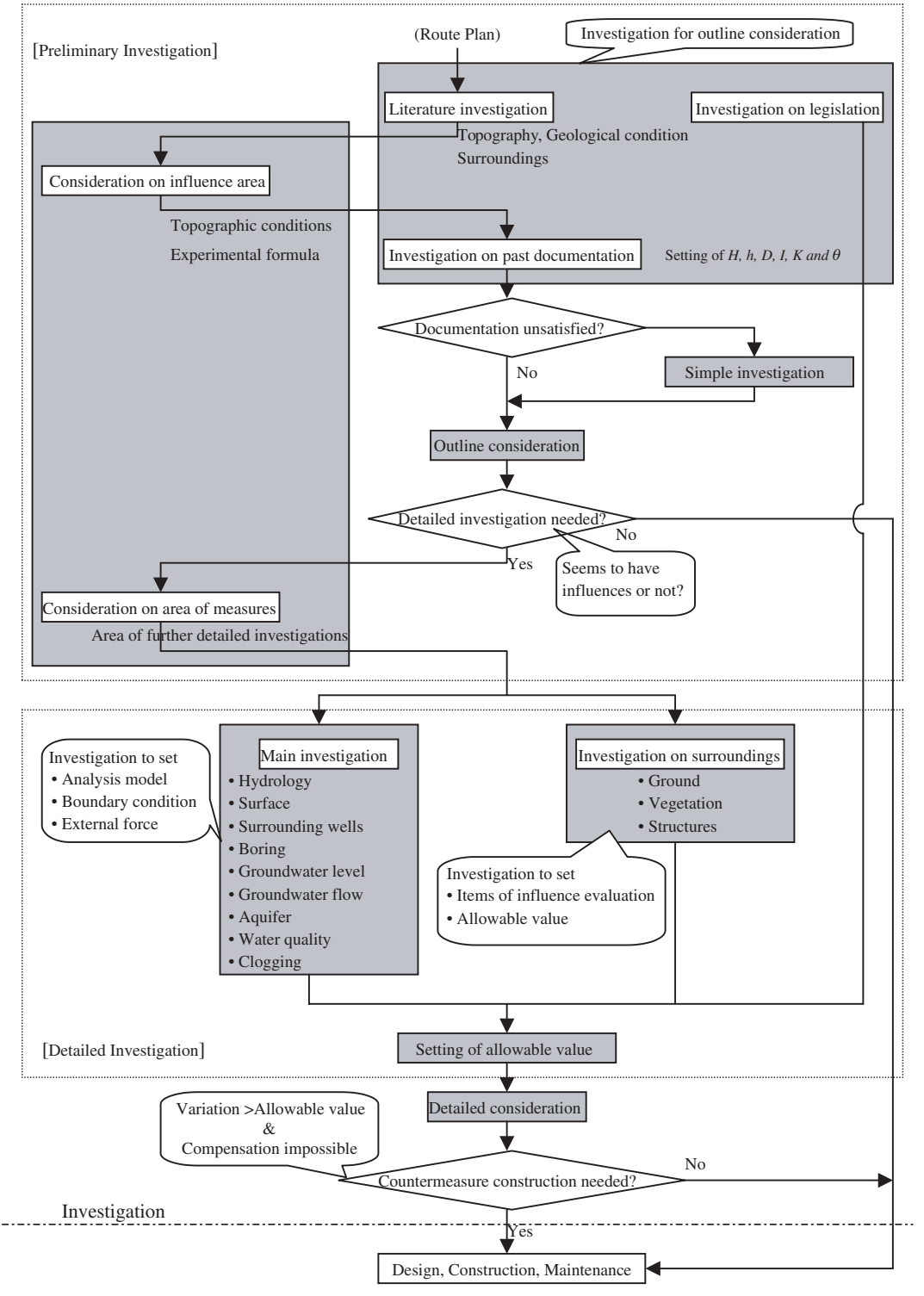


Figure 1. Investigation flow chart.

Copyright © 2003 Swets & Zeitlinger B.V., Lisse, The Netherlands

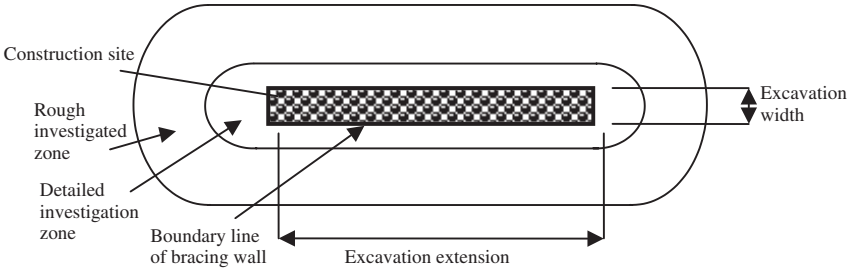


Figure 2. Example of investigation area.

Table 1. Groundwater investigation zone by geologic stratum.

Geologic stratum	Detailed investigation zone	Rough investigation zone
Stratum corresponding to loamy layer of the Kanto district	Within 100–150 m	Within 200–300 m
Stratum corresponding to gravel layer	Within 150–300 m	Within 300–500 m

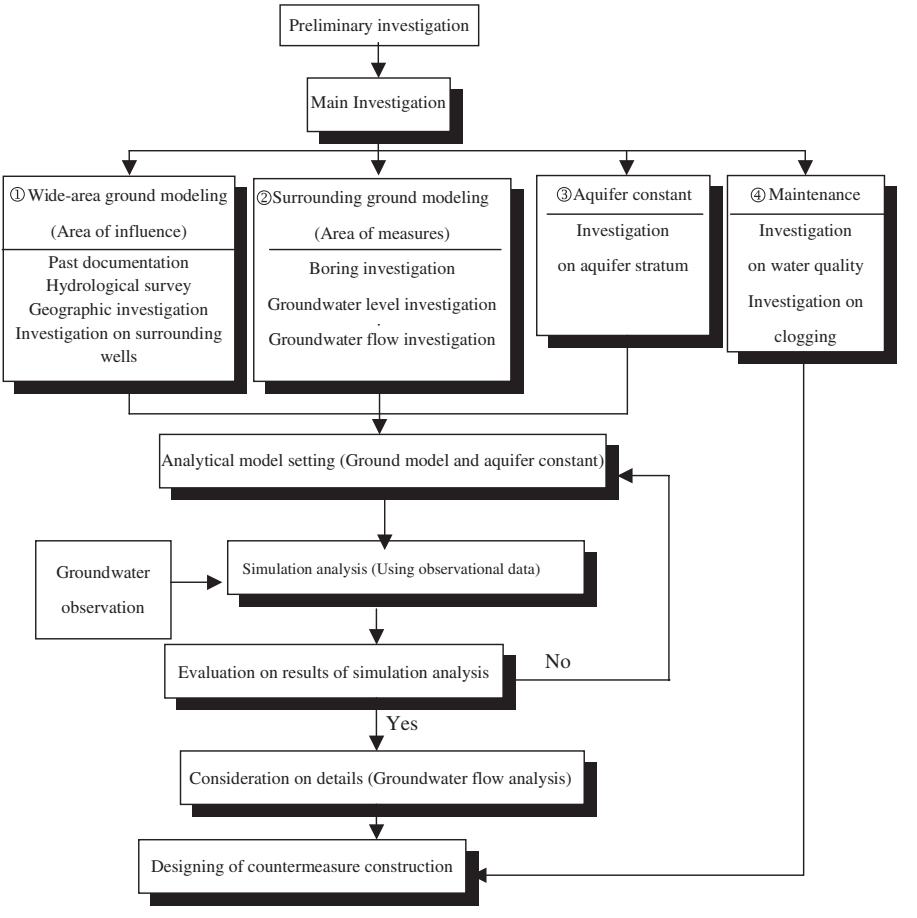


Figure 3. Basic flow chart of main investigation.

Copyright © 2003 Swets & Zeitlinger B.V., Lisse, The Netherlands

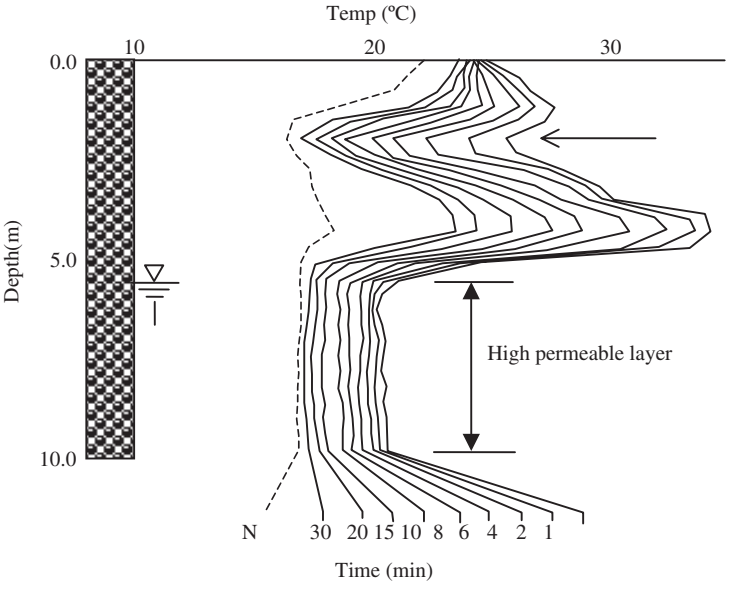


Figure 4. Example of a multi-point temperature logging in gravel.

the surroundings over time. The investigations on surroundings are carried out in order to investigate and observe the secondary changes of surroundings caused from "before" and "after" the construction.

The influences on the surroundings are:

- Ground: land subsidence, liquefaction, waterlogging, aridification, soil depletion
- Groundwater: spring depletion, pollution widening, salinization, change of water quality
- Vegetation (Crop): root rot, loss of trees
- Structures: uneven settlement, negative friction, lift of buildings and underground structures, damage on surface and underground pipes, water leakage into basement, dried-up wells, useless wells, deterioration of water of wells, cave-in in pavement, deterioration of facilities accompanying decline
- Surroundings; oxygen deficiency, deterioration.

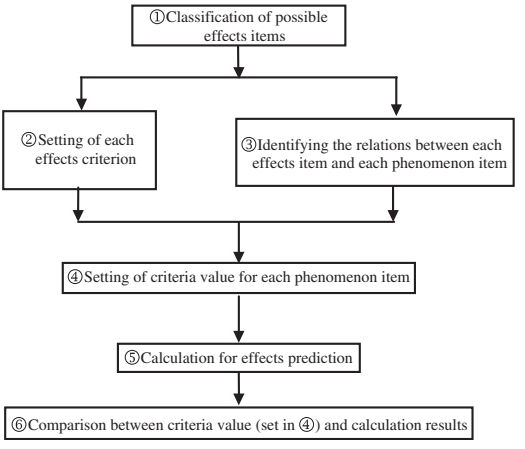


Figure 5. General process of effects evaluation.

2 EVALUATION OF EFFECTS

In the valuation of effects, in the effects of the interruption in the groundwater flow accompanying construction are estimated quantitatively, based on the data obtained in the preliminary investigations or the detailed investigations. The general process of the evaluation of effects is shown in Figure. 5.

3 SUMMARY

The general method of investigations in employing the method of preserving groundwater flows is described in this paper. In the investigations, the comprehension of the water paths is important and it is necessary to investigate the influences caused by the groundwater flow interception, taking the ecosystems and cultural aspects into consideration. There are few experiences

Copyright © 2003 Swets & Zeitlinger B.V., Lisse, The Netherlands

of this method as it is completely new. However, the importance of this method, which preserves the groundwater flow and even the environment, will be growing from now on.

REFERENCES

Tokyo Construction Bureau 1997. *Outline of environmental research associated with construction* (in Japanese).

Shinshi, Y., Kano, H., Wada, T., and Hashimoto, T. 1999. Simplified calculation method for influence of groundwater flow interruption and design of its measures. *The proceeding of symposium on groundwater and ground environment in '99:* 97–114 (in Japanese).

Takeuchi, A. 1996. *Investigative approach of flowing groundwater*, Kokon Shoin: 303 (in Japanese).

Copyright © 2003 Swets & Zeitlinger B.V., Lisse, The Netherlands

Design on groundwater flow preservation measures

I. Komatsu
Hanshin Expressway Public Corporation, Osaka, Japan

T. Sugimura
Kobe City Transportation Bureau, Hyogo, Japan

K. Namikawa
Metropolitan Expressway Public Corporation, Tokyo, Japan

N. Imai
Ministry of Land, Infrastructure and Transport Government, Osaka, Japan

T. Ogata
Fukuoka City Transportation Bureau, Fukuoka, Japan

Y. Sakayama
Dainichi Consultant Inc., Osaka, Japan

N. Kohsaka
Shimizu Corporation, Tokyo, Japan

Y. Matsuda
Yachiyo Engineering Co., Ltd., Tokyo, Japan

ABSTRACT: An outline about the design of groundwater flow preservation measures, which is attracting a lot of attention as measures of groundwater flow interruption problems occur from the construction of long underground structures, is given.

A basic design idea is shown. After that, a determination procedure for criteria evaluation for design is discussed. The design procedure is shown in a flow chart, and outlined according to this. Some kinds of measures are described and the points of method selection are shown. The design articles are listed, and it is stated that the installation interval of facilities is the main design factor. As for the calculation technique of design, the method by numerical computation such as finite element method and the method by simplified calculation are compared. Finally, the optimum design of facilities interval, which evaluates the total cost considering the maintenance required for performance deterioration by long-term clogging, is commented on.

1 INTRODUCTION

Because of environmental issues such as noise, vibration and landscape, transportation systems like railway or highway are sometimes constructed underground in urban areas. However, these long underground structures may cause other environmental problems. If the underground structure is constructed by cut and cover method, long and deep cut-off walls are built and left at the site even after the completion of the construction. This long deep wall and the underground tunneling itself may interrupt the flow in aquifers at the site, causing the rise and drawdown of groundwater levels at upstream and downstream, respectively. This change of groundwater regime leads to various environmental problems, for example, leakage of groundwater from basement and death of plants upstream, and land subsidence and drawdown of water in wells downstream.

In order to prevent the above mentioned problems associated with groundwater flow interruption, groundwater flow preservation measures are applied.

Copyright © 2003 Swets & Zeitlinger B.V., Lisse, The Netherlands

But most past cases of groundwater flow preservation measures were adopted after problems occurred, and they have been carried out making trial and error conditions. There are few examples where prior design was performed, and design techniques on groundwater flow preservation measures are not established.

From the viewpoint of environmental influence evaluation and consensus building among neighborhood inhabitants, prior evaluation of the influence and prior design of measures are required. Therefore, the establishment of design for groundwater flow preservation measure is an important theme.

2 A BASIC IDEA FOR DESIGN

When groundwater flows through an aquifer interrupted by a structure or cut-off walls, a groundwater flow preservation measure is applied to maintain the conditions before construction. In these measures, the interrupted water is collected at the upstream side, passed using pipes or permeable zones and recharged at the downstream side. Such facilities are installed at an appropriate interval. The conceptual diagram is shown in Figure 1. The design of the groundwater flow preservation measure is to determine the specifications and installation intervals of the facilities so that the influence of the construction of the structure does not cause a substantial defect. Even if the groundwater flow preservation measure is adopted, the influence will not be zero. As a result, it is an important point of the design to set evaluation criteria on how much change is permitted.

3 EVALUATION CRITERIA

The following evaluation criteria are set to examine the necessity and propriety of the measures when the groundwater flow preservation measure is designed. After this, the groundwater level is used as an index of environmental influence evaluation.

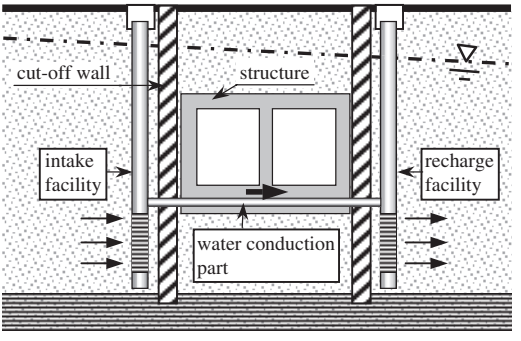


Figure 1. Conceptual diagram of a groundwater flow preservation measure.

3.1 *Limit criterion:* ε_0

The limit criterion is the value that some environmental problem occurs, when a groundwater level change more than this. That is to say, the limit criterion is the value that groundwater level changes of more than this is not permitted.

3.2 *Permission criterion:* ε_1

The permission criterion is the value of groundwater level changes permitted in the object area. The permission criterion is set by the limit criterion with consideration of allowance for uncertainty of site investigation. If the investigation precision is high, the permission criterion can be set as almost equal value to the limit criterion. And if investigation precision is low, a large difference is required between the permission criterion and the limit criterion. The necessity of a groundwater flow preservation measure is determined by comparing the permission criterion with the predicted groundwater level change without measures.

3.3 *Monitoring criterion:* ε_2

The monitoring criterion is the value to check the performance of the groundwater flow preservation measure by observing its long-term operation. When a groundwater level change of more than the monitoring criterion occurs, maintenance is carried out and the performance of measures are recovered. It is a long-term performance objective value of the groundwater flow preservation measure.

3.4 *Design criterion:* ε_3

The design criterion is the objective value of a groundwater level change at the early stage after the start of operation of the groundwater flow preservation measure. The groundwater flow preservation measure is designed to achieve the design criterion. As for groundwater flow preservation measures, performance deterioration by clogging due to continuous operation is predicted. Hence, the design criterion is determined with estimation of the performance deterioration on the monitoring criterion. It is a short-term performance objective value of the groundwater flow preservation measure.

4 DESIGN PROCEDURE

A flow chart of groundwater flow preservation measures examination that focused on design is shown in Figure 2. Initially a predicted change of groundwater level is compared with the permission criterion, and the necessity of measures is evaluated. When the measures necessity is confirmed, suitable measures are selected (refer to Figs 3–4). At this time, a basic method

Copyright © 2003 Swets & Zeitlinger B.V., Lisse, The Netherlands

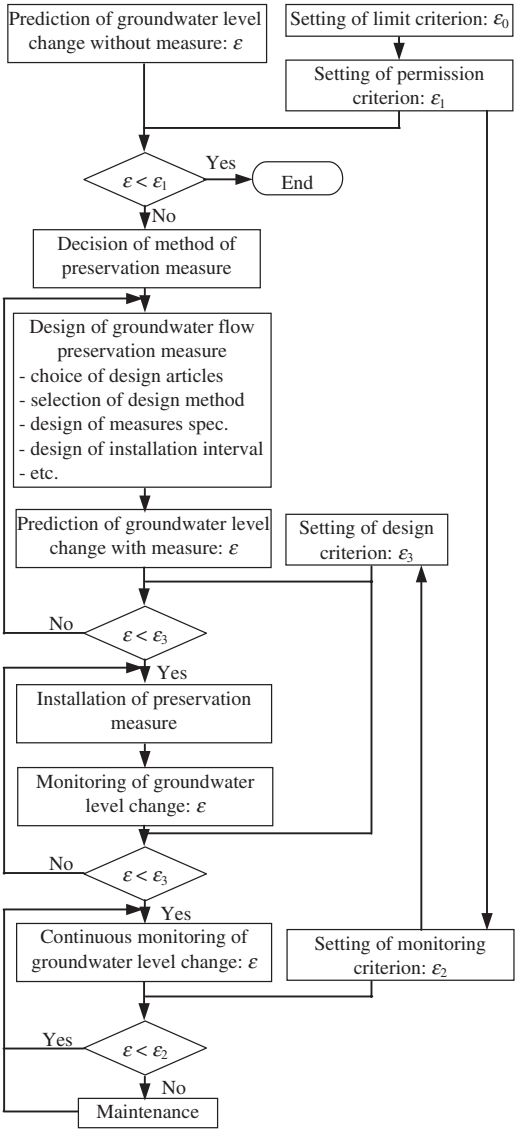


Figure 2. Flow chart of examination process of groundwater flow preservation measure.

of intake-recharge facilities and water conduction part are chosen by considering field and site conditions. Next, the design criterion (a short-term performance objective value) is determined, after long-term performance deterioration by clogging is considered on the monitoring criterion (a long-term performance objective value), which is derived from the permission criterion. The groundwater flow preservation measure is designed to achieve the design criterion. Specific design tasks are the choice of design parameters, the selection of a design method, decision on specifications of measures, determination of installation interval of measures, and so on. After the measures are designed, predicted groundwater level change with measures is calculated and compared with the design criterion and the design condition is confirmed to be sufficient. The designed measures are installed on the site. The groundwater level change is monitored, and it is confirmed that the design criterion is satisfied at the initial stage. Furthermore, long-term continuous monitoring is carried out to confirm sufficiency of the monitoring criterion.

5 KINDS OF MEASURES METHOD AND POINTS OF THE METHOD SELECTION

Methods for intake-recharge are shown in Figure 3 and water conduction methods are shown in Figure 4.

5.1 *Methods for intake and recharge*

When a method of groundwater flow preservation measures is chosen, the most important parts are the intake and recharge facilities. For the intake and recharge facilities, it is important to make the contact surface with the ground as large as possible. In addition, it is required that flushing and clogging prevention work effectively at this contact surface.

5.1.1 *A method to remove the cut-off wall*

After the completion of the underground structure, parts of the cut-off walls are removed to recover the transmissivity of the aquifer.

5.1.2 *A method to install intake and recharge pipes in drilled holes*

After the completion of the underground structure, horizontal holes are drilled through the cut-off walls, and intake and recharge pipes are installed into the aquifer from the holes.

5.1.3 *A method to provide intake and recharge function in cut-off walls*

During the construction of the cut-off walls, functions of intake and recharge of groundwater are provided in the wall.

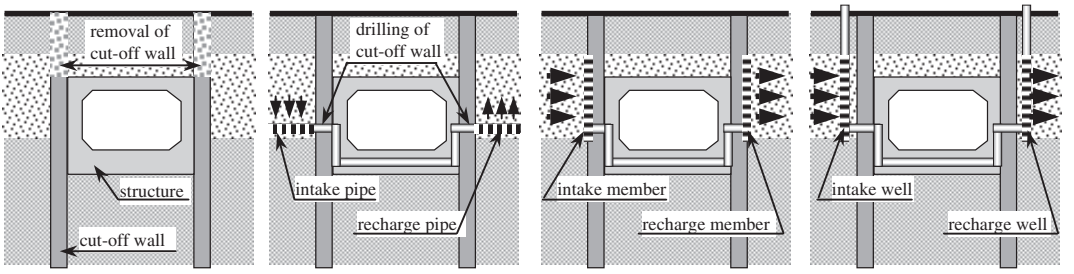
5.1.4 *A method to install intake and recharge wells*

The intake and recharge wells are installed outside the cut-off walls, which require some place for the wells. The installation of the wells is possible at any time.

5.2 *Methods for water conduction*

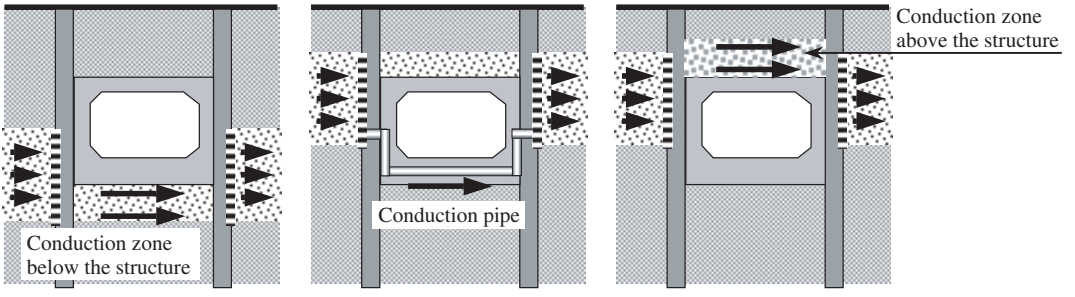
The water conduction part is a substitute for an interrupted aquifer. It is required that the head loss in the water conduction part be as small as possible.

Copyright © 2003 Swets & Zeitlinger B.V., Lisse, The Netherlands



(a) Removal of cut-off wall (b) Intake and recharge pipes installed in drilled hole (c) Intake and recharge functions provided in cut-off wall (d) Intake and recharge wells

Figure 3. Methods for intake and recharge of groundwater flow preservation measure.



(a) Water conduction below the structure (b) Water conduction using pipes (c) Water conduction above the structure

Figure 4. Methods for water conductino of groundwater flow preservation measure.

5.2.1 *Water conduction method below the structure*

It is a method that uses the lower part of the structure as water conduction zone. The aquifer that is original ground is used, or gravel material with high conductivity is substituted for the water conduction zone.

5.2.2 *Water conduction method using pipes*

It is a method that conducts groundwater by pipes laid in or beneath the structure.

5.2.3 *Water conduction method above the structure*

It is a method that uses the upper part of the structure as water conduction zone. Gravel material with high conductivity is usually used to fill up the water conduction zone.

5.3 *Points of method selection*

The following subjects should be considered in the selection of a method of intake-recharge and water conduction.

– The ground condition such as the relation between the depth of an interrupted aquifer and structure.
– The site condition concerning the space available for the installation of facilities outside the cut-off wall.
– The condition of installation time of measures in accordance with the necessity of measures during the construction period.

Some combinations of the intake-recharge methods and water conduction methods are good, but some of these are not so good. In considering these, the method whose total system shows high performance should be chosen. The suitable combinations of intake-recharge methods and water conduction methods are shown in Table 1.

6 DESIGN ARTICLES

The main design parameters of each method are shown in Table 2. The design articles are classified roughly into the following three items, which are installation intervals, individual specifications and depth of an aquifer that needs measures. Among these, articles about depth of the target aquifer are determined by the ground condition. The articles concerning individual specifications are not so flexible because they

Copyright © 2003 Swets & Zeitlinger B.V., Lisse, The Netherlands

Table 1. Suitable combinations of intake–recharge methods and water conduction methods.

Water conduction method	Intake and recharge method			
	Cut-off wall			
	Remove cut-off wall	Intake and recharge pipe	Intake and recharge member in wall	Intake and recharge wall
Water conduction below the structure	◯	△	△	△
Water conduction pipe	◯	◎	◎	◎
Water conduction above the structure	◎	△	△	△
Timing of installation	After completion of underground works	During excavation works	During construction of cut-off wall	Anytime

◎: Good combination; ◯: Combination with actual examples; △: Possible combination without example.

Table 2. Design parameters for method of groundwater flow preservation measures.

	Method	Design parameters		
		Interval	Specifications	Depth
Intake and recharge part	Removal of cut-off wall	Interval of removal zone: a	Width of removal zone: b	Depth of removal zone: z
	Intake and recharge pipes through cut-off wall	Interval of installation: a	Diameter of pipe: r_w Length of pipe: l	Installation depth: z Installation angle: ϕ
	Intake and recharge member installed in cut-off wall (line shape)	Interval of installation: a	Equivalent radius of member: r_w	Depth of intake and recharge member: z
	Intake and recharge member installed in cut-off wall (plain shape)	Interval of installation: a	Width of member: b Thickness of filter zone: d Hydraulic conductivity of filter zone: K_f	Depth of filter zone: z
	Intake and recharge wall	Interval of installation: a	Well radius: r_w	Depth of intake and recharge screen: z
Water conduction part	Water conduction zone	Interval of water conduction zone: a	Width of water conduction zone: b Hydraulic conductivity of water conduction zone: k	–
	Water conduction pipe	Interval of installation: a	Diameter of water conduction pipe: D	–

are determined by site conditions and construction machines. Consequently, the installation interval is the main design article of groundwater flow preservation measures.

7 DESIGN CALCULATION

7.1 *Methods of design calculation*

Numerical computation such as finite element method and simplified calculation techniques are proposed for the methods of design calculation. By numerical computation such as finite element method, complicated boundary conditions and ground conditions can be considered. Consequently, we can evaluate the intake-recharge facilities and water conduction part totally. In addition, groundwater level changes at arbitrary points are evaluated quantitatively. It is a universal technique. But the necessity for the enormous time needed to make a model is the greatest limitation of this technique. There is no point to use this technique on sites where the boundary conditions and ground conditions are not adequately known.

Copyright © 2003 Swets & Zeitlinger B.V., Lisse, The Netherlands

On the other hand, the simplified calculations are design methods that can be applied to sites where the ground conditions and boundary conditions are supposed to be a simple model. The method of using monographs (Shinshi et al. 1999) and the method of applying the well equation (Kohsaka, 1999) have been developed until now. In simple conditions, it has been confirmed that good results are obtained. On sites where information such as boundary conditions and ground conditions are not enough, these techniques are effective as approximate calculation.

7.2 *A procedure of design calculation*

An outline procedure of design calculation is shown in Figure 5. Initially the individual specifications of intake and recharge facilities (diameter, device type, depth, etc.) are determined. According to the design conditions, the flow rate per unit width which satisfies the design criterion and the limiting speed at which clogging does not occur are given. From these, the maximum installation interval is calculated. The installation interval is assumed in smaller range than the maximum interval, and the satisfaction of the design criterion of groundwater level change and discharge flow rate is calculated by trial and error. When it is confirmed that the calculated installation interval is a practical value, that installation interval is finally accepted.

This calculation procedure is an outline of a simplified calculation method, but is basically similar to the numerical computation.

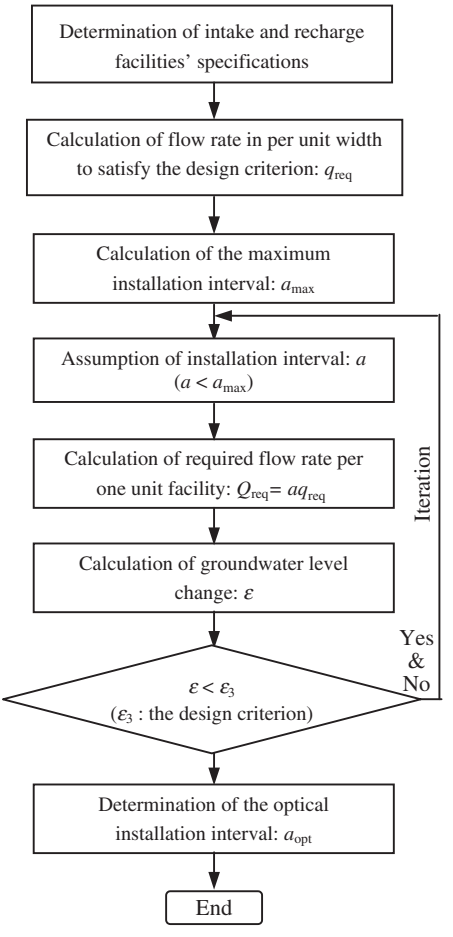


Figure 5. Outline procedure of design calculation.

8 CONSIDERATION OF LONG-TERM CLOGGING

A groundwater flow preservation measure should be operated without maintenance basically. But maintenances at an appropriate time interval are required when a long-term clogging reduces the performance of the intake and recharge facilities. In this case, the facilities should be designed so that the total cost, which is composed of initial cost for facilities installation and running cost for maintenance, becomes small. Figure 6 shows the relation between the installation interval of facilities and the installation cost, maintenance cost, and total cost (Kohsaka, 2000). When the installation interval is small, the installation cost is high because many facilities are required. But the small installation spacing makes the maintenance interval longer and the maintenance cost cheaper, because the flow rate per unit is small. On the contrary, when the installation interval is large, the installation cost of facilities is low, but the maintenance cost becomes high because of the

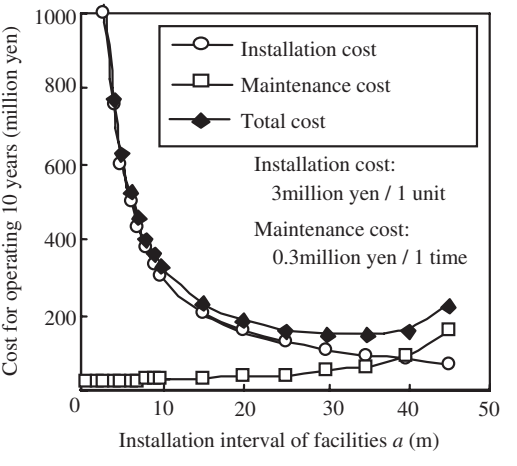


Figure 6. Relation between installation interval and installation cost, maintenance cost, total cost.

Copyright © 2003 Swets & Zeitlinger B.V., Lisse, The Netherlands

need for frequent maintenance. The optimum design of the installation interval is determined by consideration of the total cost the lowest. Consequently, the biggest installation interval calculated in the design is not always the most suitable one. The installation interval should be determined in some range with consideration to uncertainty.

9 SUMMARY

In this report, an outline of a design technique for groundwater flow preservation measures is discussed. In major projects, numerical computation such as finite element method is frequently used as a design technique. Numerical computation techniques are universal, but involves a great deal of work. In consideration of balance with precision of investigation of the input side and of construction of the output side, an appropriate design technique should be chosen.

REFERENCES

Shinshi, Y., Kano, H., Wada, T. and Hashimoto, T. 1999. Simplified calculation method for influence of groundwater flow interruption and design of its measures. *The proceeding of symposium on groundwater and ground environment in '99*: 97–114 (in Japanese).

Kohsaka, N. 1999. Design method for groundwater preservation measures. *The proceeding of symposium on groundwater and ground environment in '99*: 115–134 (in Japanese).

Kohsaka, N. 2000. Installation interval of intake and recharge facilities for a groundwater preservation measures. *The proceeding of the 12th symposium Chubu branch of the Japanese geotechnical society*: 15–22 (in Japanese).

Copyright © 2003 Swets & Zeitlinger B.V., Lisse, The Netherlands

Construction of preservation facilities on natural groundwater flows

S. Kusumoto
Osaka Branch Office, Penta-Ocean Construction Co. Ltd., Osaka, Japan

H. Omae
Kansai Branch, Taisei Corporation, Osaka, Japan

T. Sato
The Zenitaka Corporation, Tokyo, Japan

M. Watanabe
Kansai Branch, Kajima Construction Co. Ltd., Osaka, Japan

N. Kobayashi
Tobishima Construction Co. Ltd., Tokyo, Japan

K. Nishida
Obayashi Corporation, Tokyo, Japan

ABSTRACT: This paper describes the general requirements in constructing water-collecting/recharging and passing equipments firstly, and then introduce an example of adopting these system in an actual project.

1 CONSIDERATION TO BE MADE FOR THE CONSTRUCTION OF WATER-COLLECTING/RECHARGING FACILITIES AND WATER-PASSING FACILITIES

1.1 *Water-collecting/recharging facilities*

The water-collecting/recharging facilities should be able to collect the ground water on the upstream side of the aquifer (collecting facilities) and to recharge the water into the ground on the downstream side (recharging facilities).

Therefore great care should be taken both in choosing material types and in determining the methods of installation. General notes for applying individual types are as follows.

1.1.1 *Types of materials*

(1) Screen

This equipment comprises of a screen and filter material to be filled in it.

1. *Screen*: The fine-grained soil material such as silt and fine sand may easily be collected with water and be transferred to the recharging side. Therefore, the proper cleaning and finishing should be required to prevent the deterioration of well efficiency.
2. *Filter material*: The filter material stabilizes the well wall, prevent inflow of the silt from the aquifer, and prevent a radical change in flow rate. Therefore, the material should be selected to suit the screen size that will prevent silt inflow.

This type of material is will be adopted in conjunction with installation methods of, "retaining wall boring, water-collecting/recharging pipe installation method," and "water-collecting/recharging well method".

(2) Drain

1. The drain installation should be carried out by the excavation method to secure its water-passing properties.
2. Due to decreased permeability of the contact surface with the drain accompanying the excavation and change in flow rate caused by the difference in coefficient of permeability between the drain material and the natural ground, the washing-out of soil particles and clogging tend to occur on the water-collecting side and the recharging side, respectively.

Copyright © 2003 Swets & Zeitlinger B.V., Lisse, The Netherlands

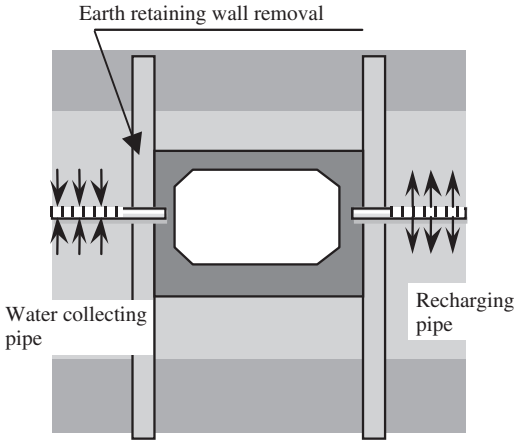


Figure 1. Earth retaining wall removal and wall-collecting/recharging pipe installation.

It is, therefore, preferable to adopt such a structure as to allow the cleaning/flushing of the water-passing on surface and the drain.

3. Where crushed concrete or processed coal-ash material is proposed as drain material, the effect on water quality such as high alkalinization of the groundwater should be examined prior to actual installation.

This type of material is adopted in conjunction with the installation methods of, "retaining wall removal/partial destruction method" and "retaining wall method with water-collecting/recharging function".

1.1.2 *Methods of installation*

(1) *Earth retaining wall removal, water-collecting/recharging pipe installation method* (Fig. 1)

This method can be applied to all earth retaining walls. Since the pipes are installed at the time of cut & cover excavation, this method is also applicable to the remedy work against encountered trouble at construction stages.

The considerations that have to be made for this method are as follows.

1. Since the effective area of collecting/recharging ground water is smaller than those for other methods, a large number of pipe installation should be required to ensure sufficient capacity.
2. Since long penetration into the surrounding aquifer may be required for horizontal pipes to ensure the efficiency of total system, the site condition, such as possibility of encroaching on boundary should be examined prior to the actual installation.
3. Due attention should be paid to the difference in water pressure between inside and outside the earth retaining wall while piercing the wall. The examination of countermeasure against water ingress should be required prior to the actual installation.

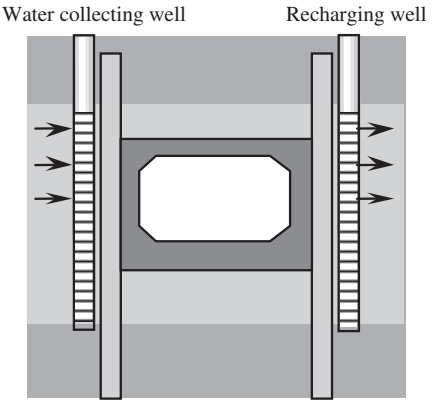


Figure 2. Water-collecting/recharging well installation.

(2) *Water-collecting/recharging well installation method* (Fig. 2)

This method installs wells outside the earth retaining wall. Although this method has the merit that the number of installation can easily be controlled depending on actual site condition, an additional area (outside of retaining wall) is required for the installation of the collecting/recharging well.

Open hole well type and cased hole wall type are normally employed in this method.

The considerations that have to be made for the construction of each well type are as follows.

1. *Open hole well*: Since mud slurry is to be used as wall support during excavation, the mud cake formed in the well wall should be completely removed before the installation of filter material.
2. *Cased hole well*: Since casing is to be employed as wall support during excavation, the permeability at interface with surrounding strata may be kept to the original state, however, great care is required in operating casing (jacking and vibration) in order to minimize the disturbance of the surrounding ground.

For both of the above well types, the most suitable cleaning method is the combination of horizontally continuous V slot screen and jetting.

(3) *Earth retaining wall removal and partial destruction method* (Fig. 3)

Although this method has normally been applied to sheetpile wall and soil mixing wall which can easily be extracted or destroyed after the completion of cut & cover structure, the examination of application to other type of retaining wall such as diaphragm wall has recently been started.

Copyright © 2003 Swets & Zeitlinger B.V., Lisse, The Netherlands

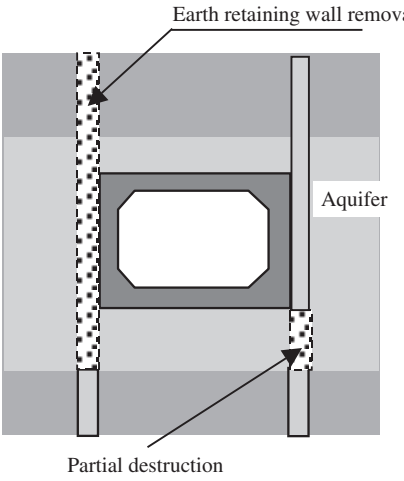


Figure 3. Earth retaining wall removal and partial destruction.

The considerations that have to be made for this method are as follows.

1. *Crushing system*: Destroyed retaining wall portion should completely be replaced with drained material in order to ensure the efficient capacity of the collecting/recharging ground water. In addition, a protective work such as backfilling with impermeable material at the undrained portion should be undertaken in order to prevent the mixing of different water flow.
2. *Removal system*: There is the need to minimize the disturbance to the surrounding ground. Where the removal of the retaining wall is be carried out before the completion of cut & cover structure, protective work to prevent ground water ingress is required prior to the commencement of the removal work.

(4) *Earth retaining wall system with water-collecting/recharging function* (Fig. 4)
In this method, the earth retaining wall is partially attached with linear or sheet members having water-collecting/recharging functions. This method may cover very large water-collecting/recharging systems.

The considerations that have to be made for this method are as follows.

1. Since the water collecting/recharging capacity is difficult to increase after the completion of installation, the spacing quantity and the individual capacity of components should carefully be examined prior to the actual installation.
2. *For soil wall*: The removal of soil cement in the ground, complete replacement with drain material, and cleaning of the porous wall are required.

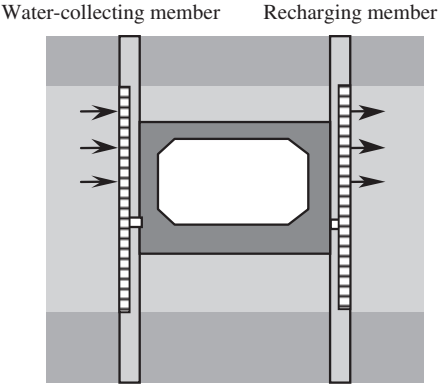


Figure 4. Earth retaining wall with water-collecting/recharging function.

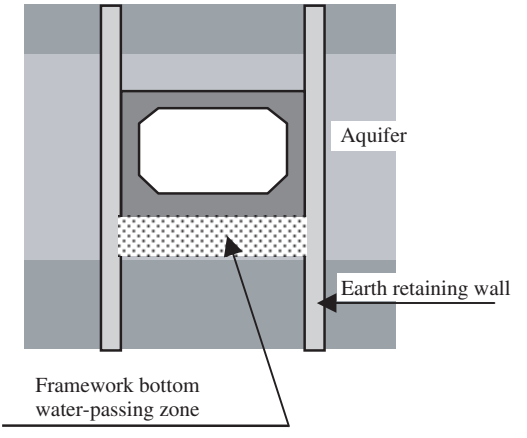


Figure 5. Framework bottom water-passing system.

3. *For RC diaphragm wall*: The preparatory work to prevent concrete flow into porous member is required.

For the portion where permeability is expected to be reduced due to the use of a stabilizing slurry, careful cleaning and finishing of the porous member is required to secure the original permeability.

1.2 *Water-passing facilities*

The water-passing facilities are installed between the water-collecting and recharging facilities, and they transfer the collected groundwater toward the recharging point downstream. The water pipe type or filter type of granular material is usually adopted as water-passing facilities.

1.2.1 *Filter type system* (Fig. 5–6)

Crushed stone, sand, material produced at the site or permeable mat will be applied in this system, and

Copyright © 2003 Swets & Zeitlinger B.V., Lisse, The Netherlands

where the resident layer has a sufficient permeability, this layer may be utilized as the water-passing facility.

The considerations that have to be made for this system are as follows.

1. Where the resident layer is utilized as the water-passing portion, great care in excavation work should be taken to prevent the mixing of clay material into a permeable layer.
2. Where the settlement of the filter material is expected, sufficient allowance should be provided in the collecting/recharging facilities.
3. Compaction of the material should be controlled in order to secure the required bearing capacity and permeability.

1.2.2 *Water pipe system* (Fig. 7)

The water-passing pipe will be installed inside the structure or be embedded in the structure. Cast iron, polyethylene, etc. will be adopted as the water-passing facility depending on the site condition.

The considerations that have to be made for this system are as follows.

1. Where the settlement of the water pipe is expected, a flexible joint, etc. should be used so as to cope with the level difference between the earth retaining wall and the water-passing portion.
2. Where pipes are embedded in the structure, proper reinforcing measures are required so as not to decrease the strength of the structure.
3. Where pipes are installed inside the structure, enough space for maintenance work (pipe cleaning and replacing) and adequate waterproofing treatment should be undertaken.

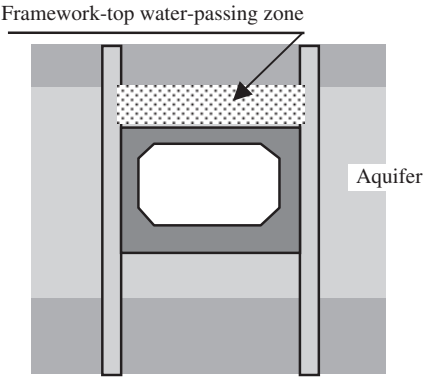


Figure 6. Framework top water-passing system.

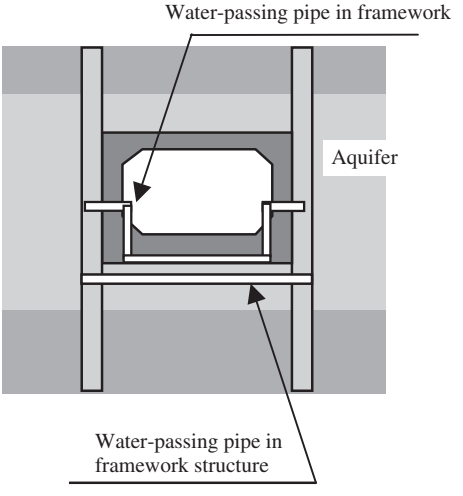


Figure 7. Water-passing pipe system.

2 EXAMPLE ADOPTED IN ACTUAL PROJECT

2.1 *Outline of water-passing facilities*

We introduce an actual example done by combinig a water-collecting/recharging well system and water-passing pipe system.

The specifications of the earth retaining work and water-passing facilities are shown in Table 1 and the general plan and typical section are shown in Figure 8.

2.2 *Outline of each facility*

2.2.1 *Well construction*

(1) *Open hole well*

Considering the easiness of cleaning the excavated wall surface, organic slurry agent, whose viscosity

Table 1. Earth retaining and water-passing facilities specifications.

Earth retaining	Column strip type continuous wall Wall thickness 600 mm
Water-collecting/ recharging system	Open hole well: Pitch 96 m × 9 sets, Diameter 400 mm Excavation depth 8 m Screen: Structure: Horizontal continuous V slot Screen length 4 m Slot size 2 mm Material: stainless steel (SUS-304)
Water-passing system	Water-passing pipe: ϕ 75 mm Material: PVC Connecting pipe: ϕ 150 mm Material: stainless steel (SUS-304)

Copyright © 2003 Swets & Zeitlinger B.V., Lisse, The Netherlands

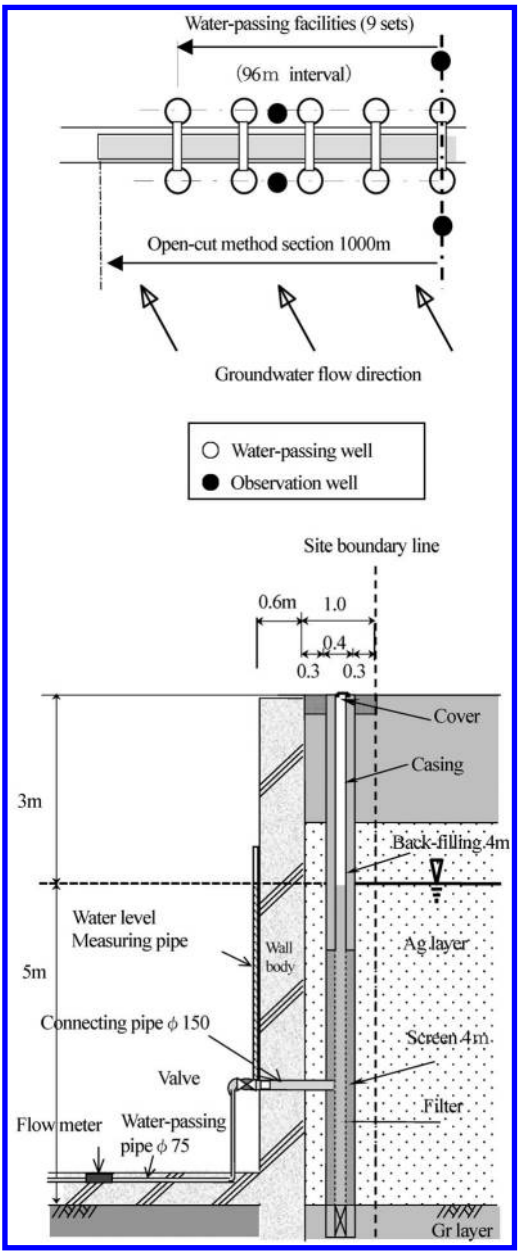


Figure 8. Position drawing, cross-sectional drawing.

is quite high during construction and subsequently disappears in short period, was applied as the wall support material, and well excavation was carried out by using a rotary boring.

Since the organic slurry agent tends to breed bacteria and capture fine soil particle (causing clogging), thorough cleaning of the wall surface was carried out after excavation.

Table 2. The cleaning specifications.

Pressure pump	Number of nozzles	Cleaning speed
2 Mpa	4	3 times at the cleaning speed of 0.5 cm/sec

(2) *Filter material*

The filter material was selected so as to have sufficient grain size distribution corresponding to the grain size of surrounding layers and the slot size of the screen.

The fine-grained fraction of the filter material was removed by washing with water, and the filling around the screen and back-filling around the casing were carefully carried out to eliminate voids.

(3) *Well cleaning*

There are many methods for cleaning the well, and the result greatly differs depending on the combination of the screen to be used and the cleaning method. In this project, since the screen was of horizontal continuous V slot structure, we adopted a cleaning method by jetting which has the highest cleaning effect.

The features of this method are the jet directly acts on a local portion, the jet works in a swirling way so as to allow the fine-grained fraction to be taken into the well, and cleaning specifications can be set easily to meet the conditions, etc. of the aquifer.

During the cleaning, the well water level was set about 1 m lower than the peripheral groundwater level for draining, and the cleaning was done until the turbid drain water and fine-grained fraction disappeared.

2.2.2 *The water-passing pipe*

The installation of the water-passing pipe consisted of connecting the pipe with the well and installing the pipe line inside the cut & cover structure.

(1) *Connecting with well*

Details of the connecting portion is shown in Figure 9. Boring for the installation of connecting pipe was carried out from the excavated area (inside the retaining wall).

The connecting pipe is filled with filter material in order to prevent the inflow of soil particles.

The water heads inside the collecting/recharging walls were temporally lowered during the connecting work in order to prevent the inflow of ground water, soil particle and filter material.

(2) *Installation of water-passing pipe inside of the Cut & Cover structure*

A typical section is shown in Figure 8. After the installation of the connecting pipe, the pipeline for ground water-transfer was installed inside of the Cut & Cover structure.

Copyright © 2003 Swets & Zeitlinger B.V., Lisse, The Netherlands

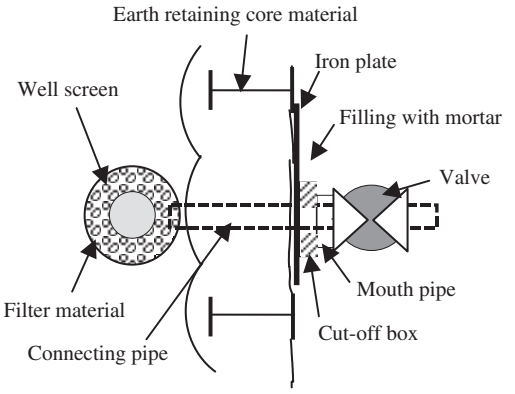


Figure 9. Connecting portion with well.

An air vent valve, water level indicator, and flowmeter were also installed on the pipeline in order to monitor the efficiency of the total system.

2.2.3 *Consideration made at temporary stage before the completion of Preservation System*

(1) *Preservation measures before the completion of the collecting/recharging system*

Two to three years were estimated to be required for the completion of Cut & Cover structure excavation. Therefore, the following measures were taken at each excavation stages in order to prevent any drop in ground water table at down stream side.

1. Stage 1 (bottom of excavation is higher than ground water table)
   Wells on the downstream side were planned to be utilized for "Forced recharging system".
   The operation of the well pumps were automatically controlled to maintain the original ground water table, and in order to prevent the bubbling of dissolved oxygen due to increase in water temperature, the continuous pipe system was employed to avoid direct blaze from sunbeams.
2. Stage 2 (bottom of excavation is lower than ground water table)
   The installation of temporary pipeline in the excavation area was adopted.

(2) *Performance tests after completion*

After the installation of all the facilities, performance tests were carried out to confirm the capacity of each facilities.

1. *Water-passing test for total system*: Confirmation of water-passing capacity of the entire system
2. *Test for individual facilities*: Confirmation of water-passing capacity of each facilities.
   (water-collecting facility – water-passing facilities – water-recharging facilities).
3. Remedial works to rectify defects at pipe connection and repetition of performance tests

In order to obtain an effective ground water preservation system, different considerations to suit the actual conditions (such as retaining wall type, soil condition, depth of Cut & Cover structure, construction schedule, and type/combination of preserving facilities) are required at the construction stage.

On the basis of above points, further examination, especially into applicability to various site conditions and cost evaluation, is required.

Copyright © 2003 Swets & Zeitlinger B.V., Lisse, The Netherlands

Methods on observing groundwater flow and maintaining facilities for preserving natural groundwater flows

S. Hamate
Pacific Consultants Co., Ltd., Osaka, Japan

Y. Hanaoka
Keisoku Techno Co., Ltd., Osaka, Japan

T. Kozato
Construction Project Consultants, Inc., Osaka, Japan

T. Sugimoto
Tokyo Metropolitan Government, Tokyo, Japan

ABSTRACT: Passing-through facilities, using groundwater preservation of the natural groundwater flow industrial method, are basically to be designed as maintenance free. However, it is necessary to examine their maintenance methods in order to cope with unavoidable long-term stopped-up.

As for the relationship between the performance and the maintenance of the passing-through facilities, the recognition of an initial performance, a long-term performance, and a necessary performance, in particular, is of great significance.

1 MAINTENANCE

1.1 *Concepts of maintenance*

1.1.1 *Directions*

A conventional well with compulsory pumping or pouring water is fundamentally different in its use from a well using groundwater preservation of the natural groundwater flow industrial method. By its nature, the conventional well focuses mainly on how to pump or pour water in large quantity. This puts a heavy load on the well, thus requiring frequent maintenance as a stopped-up measure associated with the load. Whereas a well using groundwater preservation of the natural groundwater flow industrial (catchment and training facilities) is aimed at securing the current underground water flows, permitting neither a large change of water level nor flowing quantity: this requires the pass as close as possible to its current state. Thus, the load on the well using groundwater preservation of the natural groundwater flow industrial method is significantly small, compared with a conventional well, and the necessity of its maintenance is small. Moreover, such pass-through facilities limit their applicable maintenance methods because they are usually constructed under the road, and under these circumstances they are not easily maintained.

Therefore, the pass-through facilities using groundwater preservation of the natural groundwater flow industrial method are basically designed, aimed at maintenance free. However, it is necessary to examine their maintenance methods in order to cope with unavoidable long-term stopped-up.

1.1.2 *Relation between the performance and the maintenance of pass-through facilities*

The performance of the facilities can be roughly divided into two in the light of the use process. The performance of the catchment and the training facilities for a comparatively short period is assumed to be an initial performance after the pass facilities are used; and a long series of afterwards performance is assumed to be a long-term performance. An initial performance includes the well loss caused by the conditions of the digging method, the washing method, and the finish situation when catchment and the training facilities are constructed, and stopped-up which occurs at a relatively earlier use stage. A long-term performance is subject to stopped-up in progress by which a chemical change of the material in under ground water according to the change in water quality, water temperature, and pressure, and the generation of the microorganism.

Copyright © 2003 Swets & Zeitlinger B.V., Lisse, The Netherlands

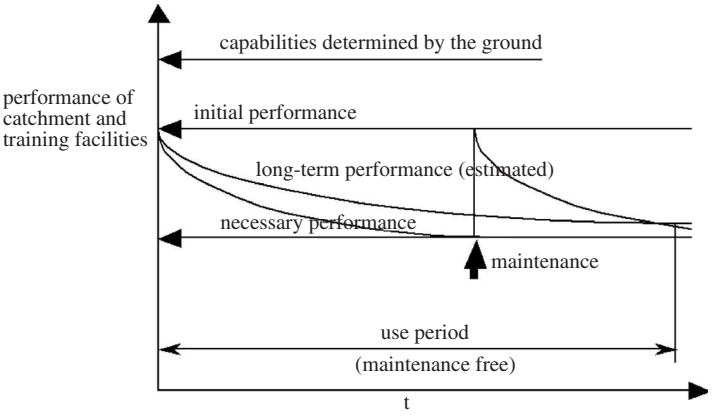


Figure 1. Relation between the performance and the maintenance of catchment and training facilities.

In general, an initial performance of the catchment and the training facilities is smaller than that of the well ability calculated from the ground investigation result. The long-term performance gradually decreases an initial performance to the maximum value thereafter. Therefore, the ability of the catchment and the training facilities used to design by the concept of maintenance free (initial performance) should be set for the long-term performance forecast for the use period to make more than a necessary performance. It is necessary to implement maintenance at the appropriate time in the case when a long-term performance are lower than expected. The relation between these performances is shown in Figure 1.

It is necessary to raise an initial performance as much as possible, assuming that it can be used without losing its function for a long term. However, even if measures of the stopped-up prevention are given, and an initial performance is set high, it is impossible with the stopped-up phenomenon to the nil. Enough investigations of the site situation (change and extent of the underground water quality and the underground water environment) and other implementation examples, etc. are necessary for the setting of an initial performance.

1.2 *Maintenance methods*

It is necessary to execute maintenance of the performance recovery when the performance decreases for a long term. The maintenance method can be divided into two cases: in the case where maintenance from the ground is possible; and in the case when maintenance from the ground is impossible.

1.2.1 *When maintenance from the ground is possible*

For catchment and training facilities (in the form of well), separated from soil detainment wall and its structure, washing from the upper structure is possible, using the same method as applied to an ordinary well. (1) re-array by the movement of soil particle; and (2) chemical reaction in the aquifer, and an increase in the microorganism, are chiefly thought as stopped-up factors in the catchment and training facilities by the natural flowing method: for (1), the reverse-washing method through drain with the pumping pump is effective; and for (2), the removal which uses the chemical reaction material is effective.

1.2.2 *When maintenance from the ground is impossible*

Because washing from the ground is impossible for catchment, training facilities, and the horizontal bore etc. with soil detainment wall, it is suggested that the reverse-washing method through drain in which connected tubes, shown in Figure 2, be used.

2 MONITORING

2.1 *Measurement purpose of each stage*

The measurement purpose of each stage is roughly as follows:

Stage	Measurement purpose
Measurement before construction	Understanding of current state (water level etc.) and examination of countermeasures
Measurement during construction period	Understanding (water level etc.) and interim evaluation of countermeasures during construction period
Measurement after construction	Understanding (water level etc.) and evaluation of countermeasure after construction

Copyright © 2003 Swets & Zeitlinger B.V., Lisse, The Netherlands

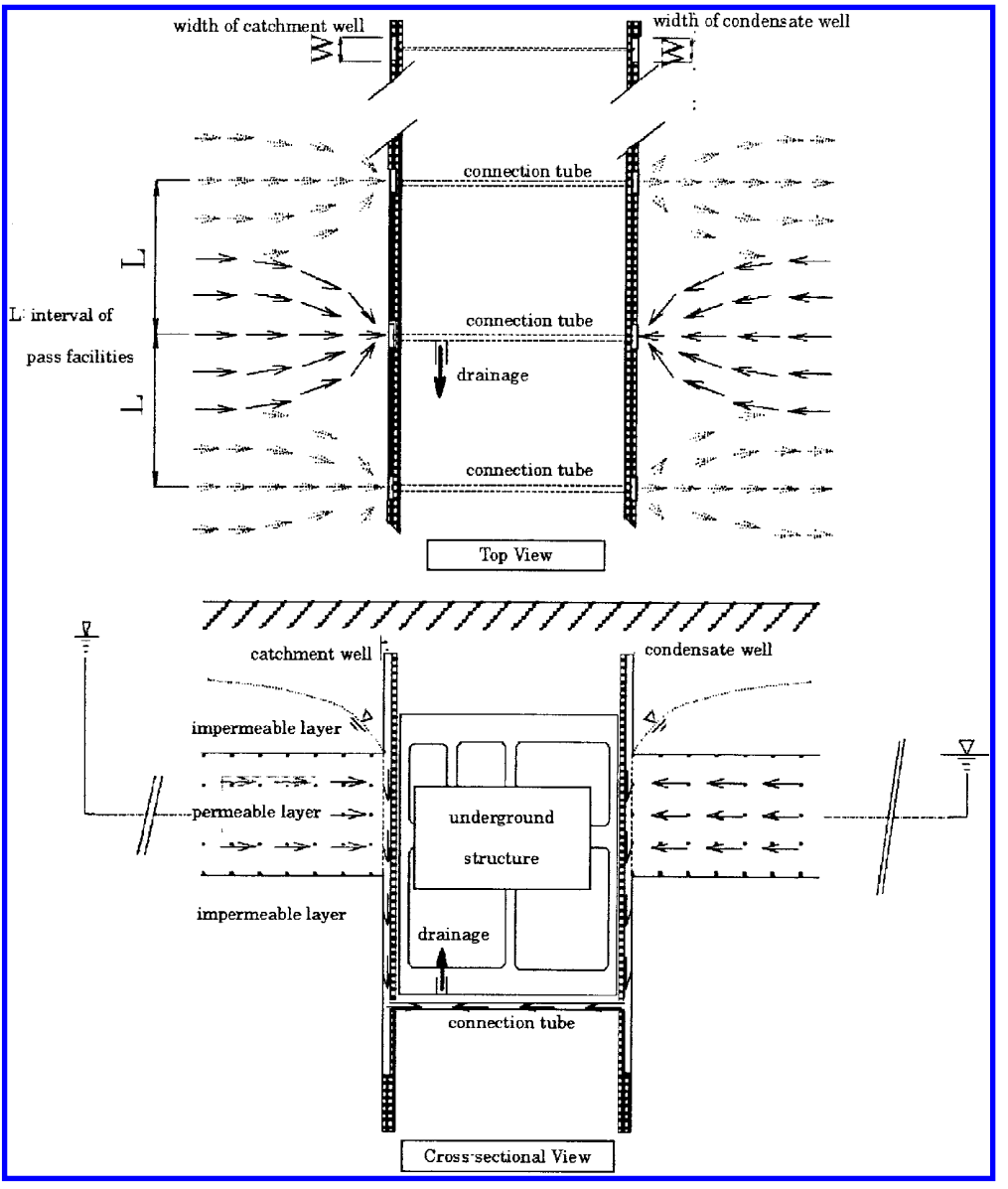


Figure 2. Maintenance method using connection tubes.

Measurement after construction is explained in detail in the next paragraph.

2.2 *Measurement after construction (examination, measurement, and management of pass facilities)*

2.2.1 *Confirmation of initial performance*

The pass facilities, when its installation was completed, shall be confirmed that the initial ability (catchment ability, pass ability, and training ability) set by the design is secured.

2.2.2 *Measurement and management of pass situation*

It is considered that the ability of the pass facilities decreases by the progress of stopped-up if passing continues for a long term. Management by which measurement and its result are to confirm that a prescribed function is obtained are necessary from the

Copyright © 2003 Swets & Zeitlinger B.V., Lisse, The Netherlands

viewpoint of groundwater preservation of the natural groundwater flow industrial method.

2.2.3 *Measures after construction*

It is necessary to add the industrial method as measures after construction when performance shortages of the following groundwater preservation of the natural groundwater flow industrial method are recognized by the measurement management.

- Though the necessity of groundwater preservation of the natural groundwater flow industrial method are recognized by the examination before construction when the water level changes at a level more than expected after the structure is constructed.
- When an initial performance of the pass facilities cannot satisfy a water level and flowing quantity which is insufficient.
- The pass facilities: when the ability decreases by stopped-up in case where ability recovery means of facilities (maintenance technique) are not available.
- When the pass facilities' ability decreases by stopped-up; when an enough ability cannot be fully recovered despite its treatment; and when frequent maintenance is necessary.

An applicable industrial method becomes limited by the problem of the construction condition, the work place, and the site as measures after construction. Especially, after the beginning to use the structure, the industrial method, which can be added as measures after construction, becomes limited. By this viewpoint, it is preferable to confirm the function of groundwater preservation of the natural groundwater flow industrial method at the earliest possible stage. The following are thought as industrial methods which can be applied. These are industrial methods applied to date as the measures when an unexpected problem of the underground water flow obstruction occurs after construction.

- The installation of the horizontal water pulling-out pipe: the structure and the soil detainment wall are set up and the water pulling-out pipe for diagonal horizontal direction of grinding hole is set up.
- Destruction and pulling-out of the soil detainment wall: permeability is secured by destroying and pulling out the soil detainment wall in the part which corresponds to the aquifer.
- The catchment and the training well are set up outside the wall: when there is room in the site, this is made by setting up of the catchment well and the training well outside of the soil detainment wall and is made to pass .

This shall be operated immediately after facilities are set up when ability shortage of the pass facilities is supplemented with measures after construction (pass), and the increase is examined while confirming the effect. Consideration is necessary lest facilities where an enough function cannot be expected are randomly set up.

Copyright © 2003 Swets & Zeitlinger B.V., Lisse, The Netherlands

Groundwater flow preservation measures for linear underground structures in urbanized areas

S. Noda
Japan Highway Public Corporation, Chiba, Japan

M. Nishigaki
Okayama University, Okayama, Japan

M. Terashima & T. Yamashita
Japan Highway Public Corporation, Tokyo & Chiba, Japan

T. Kisanuki
Expressway Technology Center, Tokyo, Japan

ABSTRACT: In linear underground structure construction projects in urbanized areas, the study of groundwater flow preservation measures is imperative in these days. The methods of analysis of groundwater flow have been established but the methods of assessment corresponding to the current level of knowledge in numerical analysis are not. In this paper, a rational assessment method and criteria are proposed for a linear underground structure in an urbanized area around Tokyo. The objective of this assessment method for groundwater flow preservation is to prevent the detrimental effects caused by the blocking of groundwater flow on the environment from occurring. In this paper, a practical application of the assessment method is presented and its feasibility discussed.

1 INTRODUCTION

1.1 *Environmental impacts caused by blocking groundwater flow*

Environmental impact studies and assessment are evolving as technology advances and social requirements for engineering change. Until recently, major groundwater problems were related to construction safety. In these days, project administrators are required to put into place feasible measures that would minimize environmental impacts. The new Japanese Environmental Assessment Act proclaimed in 1997 requires that detrimental environmental impacts of projects are minimized. To establish a rational and feasible ground water preservation system and an assessment method are some of the critical issues facing the construction industry today.

In urbanized areas, many infrastructures are constructed underground. For example, because of high land price and environmental considerations, transportation systems such as highways and railways are constructed underground. When such large-scale linear underground structure construction projects are undertaken, groundwater preservation measures are required to minimize the detrimental effects of blocked groundwater flow on the environment.

As it is generally known, blocking the flow of groundwater causes many problems in the surrounding area. So the appropriate groundwater flow preservation systems should be prepared at the planning stage. However, once a large-scale structure is set in the earth, the groundwater flow is affected in greater or less degree. So, to prevent any detrimental effect to both the residents and the natural environment, comprehensive social and natural environment studies are inevitable.

1.2 *The need for an assessment method*

The phenomenal problems caused by blocking groundwater flow have been well studied for several decades. These include the drying up of wells and land subsidence. However, few practical studies on large-scale linear underground structures have been conducted.

In this report, the results of a practical study conducted on the assessment method of a large-scale linear underground structure (i.e. expressway) in an urbanized region around Tokyo are presented under the following themes.

Copyright © 2003 Swets & Zeitlinger B.V., Lisse, The Netherlands

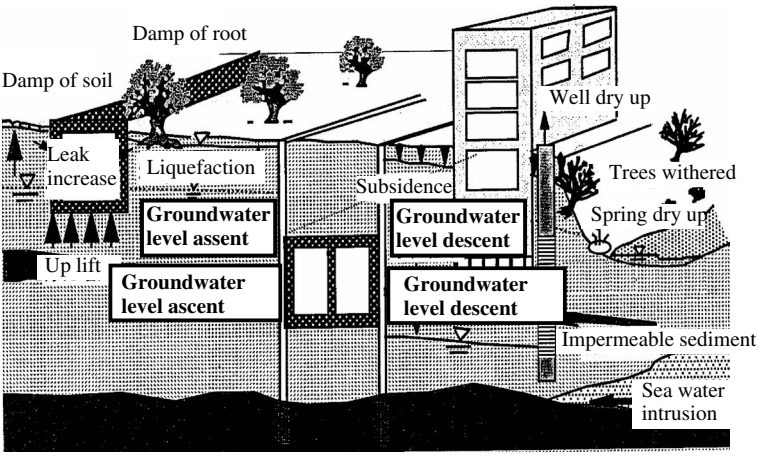


Figure 1. Possible bad effects of groundwater blocking.

Table 1. Phenomena caused by the blocking of ground water flow.

	Groundwater fluctuation	
Objects	Ascent	Descent
Ecosystem	Damp of root Effects for underground organisum	Plant wither up Effects for underground organisum
Geological environment	Damp of soil Liquifaction	Subsidence
Surrounding structures	Up lift Leak increase	Settlement
Groundwater usage		Well dry up

First, the basic concept of the assessment method is discussed. Then, the search for the assessment criteria is described. Finally, the methods for the assessment criteria are detailed.

1.3 *Assessment in a project*

Different phenomena arise from blocking the flow of groundwater. The major ones are summarized in Table 1. The purpose of a groundwater flow preservation system is to avoid and/or reduce the possible detrimental effects on the natural and social environments.

Usually, a large-scale linear underground construction project involves several steps, such as planning, design, construction, and maintenance. The assessment at each stage of the project has the following objectives.

At the design stage, quantitative requirements of each phenomenon as shown in Table 1 are determined, so that the existence of the underground structure would not cause any detrimental effects on the natural and social environments. For the planned route and structure, whether the constructed structure would result in any bad phenomena or not should be checked, using numerical analysis. If a groundwater preservation system is required, then the detailed system requirements are to be determined from the numerical analysis and the preservation system designed. It should be noted that the preservation system is designed not only for the intended underground structure, but also for every stage of the construction process.

At the construction and maintenance stages, the causal relations between the detrimental effects and the observed criteria have to be verified.

2 BASIC CONCEPT OF THE ASSESSMENT METHOD

2.1 *Requirements for assessment method*

If large-scale underground linear structures are constructed without proper design, groundwater is blocked and the groundwater level either goes up or goes down. The detrimental influences listed in Table 1 are all caused by the fluctuation of groundwater level. Therefore, quantitative assessment criteria for groundwater flow preservation system can be determined from the groundwater level, i.e. the head of the aquifer.

The assessment criteria defined by the assessment method are to serve as guides for the design, construction, and maintenance stages of projects. So, the criteria and the critical values for the criteria ought to be established in a consistent manner for projects,

Copyright © 2003 Swets & Zeitlinger B.V., Lisse, The Netherlands

including the preparatory investigations, analysis, design, and evaluations to validate design results.

The same criteria should be used in evaluating the design of the groundwater preservation system and the observations made during construction and maintenance (defined as verifiable observations). Then, it should be confirmed by the verifiable observations that the blocking of the groundwater by the underground structure does not cause any detrimental effect on the environment. This confirmation procedure is essential for this assessment system because no analysis and design can be perfect.

2.2 *Criteria for causal relation*

When the details of the assessment criteria are described, the causal relations between the criteria and the detrimental effects due to the blocking of groundwater have to be established. To analyze the situation during the validation stage, four possible situations may be considered.

The first possible situation is that the criteria are fulfilled and no detrimental phenomena are observed.

The second possible situation is that the criteria are not fulfilled and no detrimental phenomena are observed.

The third possible situation is that the criteria are not fulfilled and no detrimental phenomena are observed.

The fourth possible situation is that the criteria are fulfilled and detrimental phenomena are observed.

If the actual situations are only the first and second, then the criteria have good causal relation with the phenomenon. However, these are not the actual cases.

The third situation has little possibility of occurring, because the observations are conducted in such a manner that the criteria are fulfilled. In other words, if there is something wrong with the observations, some measures are taken to correct them. If the safety factor for the criteria is too high, the third situation may happen. However, the safety factor has to be determined so as to cope with a more serious situation such as the fourth situation mentioned above.

The fourth situation is possible and it is the important situation that determines the details of the criteria. In this situation, the project administrator has to be certain that the existence of the underground structure is not the cause of the detrimental phenomena, based on meeting the set criteria. The ways by which the causal relations are established are different for effects on society and the natural environment. In the case of the influences on society, the causal relations are determined on legal bases. On the other hand, in the case of the influences on the natural environment, it is a matter of accountability of the project administrator to the public.

Details of the design and observation criteria are to be established with careful considerations given to the causal relations stated above.

2.3 *Allowable range of hydraulic head of aquifer*

There are several possible ways to establish the criteria for groundwater flow preservation. The verifiable observations are conducted by using these criteria and the projects are controlled so that the observations fulfill the set criteria.

One conservative method is to use the past maximum and minimum head as the criteria. However, since we assumed the possible detrimental effects shown in Table 1, it is possible and more rational that the criteria are established to prevent the unwanted influences of these phenomena.

To prove that the groundwater level fluctuation is not the cause of the detrimental phenomena when the criteria are fulfilled, the criteria are to be determined on the basis of established theoretical relations between the criteria and the phenomena. In this case, the appropriate safety factor has to be employed to cope with the uncertainty inherent in the established theory.

3 AN EXAMPLE OF ASSESSMENT METHOD

3.1 *Introduction*

An example of an assessment method for a large-scale linear underground structure is presented below. When the detailed method was established, an effort was made so that the criteria for the design and validation were the same.

3.2 *Preparatory observations and investigations*

The first thing to do for the assessment is preparatory observations of the aquifer. The period of the observations should be long enough and the observations should cover the influence area of the groundwater level fluctuation caused by the structure with the required density.

Concurrently, the effects on the natural and social environment are studied. Then, the phenomena are selected for the criteria. Based on the study conducted, the allowable range of hydraulic head for each phenomenon is determined at the designated points where each phenomenon is occurring. Using the established theory, the range of hydraulic head (defined “allowable range of hydraulic head”) is set to prevent the detrimental effects caused by the groundwater level fluctuation.

3.3 *Analysis and design of the groundwater preservation system*

The present pattern of analysis should reproduce the highest and the lowest water level situation in each aquifer.

Copyright © 2003 Swets & Zeitlinger B.V., Lisse, The Netherlands

The margins of the hydraulic head between the range of fluctuation and the allowable range of head for a phenomenon can be determined at each designated location by using the results of the analytical procedure stated above. The margins are called "allowable fluctuations" and they are shown in Figure 2.

The ground water flow preservation system is designed on the basis of the present pattern of reproduction models. At each designated location of the phenomenon, the allowable range of hydraulic head should be fulfilled with the designed groundwater flow preservation system.

3.4 *Validation and criteria*

The validation process should be conducted at the construction and maintenance stages of the project. The criteria for each observation well are to be determined on the basis of the sum of the historical highest or lowest hydraulic head and the allowable fluctuation as shown Figure 3.

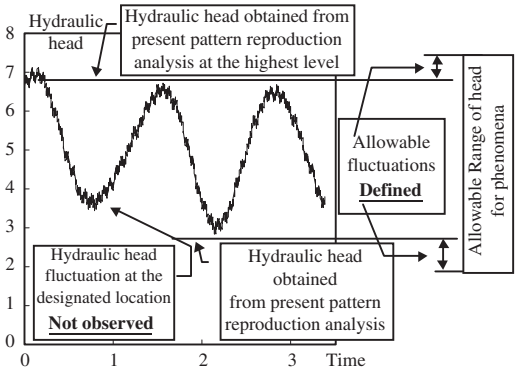


Figure 2. Concept of allowable fluctuation of hydraulic head.

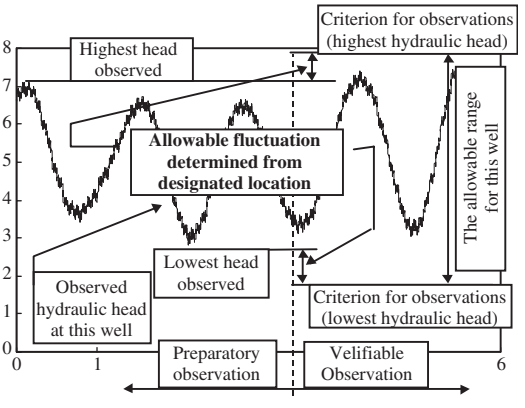


Figure 3. Concept of criteria at the observations wells.

Usually, an observation well and a designated location of the phenomena are different. So, the appropriate observation wells are to be selected. A selected well should be near the designated location and it should be closer to the constructed underground structure than the designated location.

4 DETAILS OF INVESTIGATIONS AND CRITERIA

4.1 *Study area*

Generally, the urban areas in Japan are located on alluvial plains. The urban area around Tokyo is a typical example.

We conducted a practical study on groundwater flow preservation assessment criteria in the east bank of Edogawa River where the east of Tokyo metropolitan area is located. The planned underground structure has a length of 10 km, and the structure and sheath for construction block the aquifers in alluvial and diluvial sand sediments.

There is a newly developed residential area which, basically, consists of traditional wooden houses in the north of the area; and an industrial area which mainly consists of small factories in the south of the area. Throughout the area, wells are used for industrial production and residential utility.

The terrain of the area, as shown in Figure 4, consists of diluvial bank and alluvial low land such as buried wave cut terrace and valley. The aquifers exist in the alluvial and diluvial sand sediments that make up alternating strata with clay sediments.

4.2 *Groundwater observations*

For the assessment system mentioned in this paper, groundwater observations have to be planned with the following in mind.

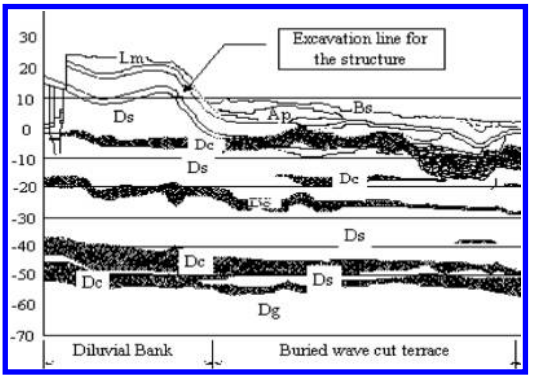


Figure 4. Geological profile of the north part of study area.

Copyright © 2003 Swets & Zeitlinger B.V., Lisse, The Netherlands

The precipitation of the area is one of the major factors for groundwater level fluctuation. Therefore, the preparatory observations should be conducted for a long enough period in order to relate the fluctuation of each aquifer to the precipitation.

In our study, the observations have been conducted since 1998. Based on the observations and the precipitation records, a clear relation between groundwater level and precipitation has been established. This area's diluvial aquifers correlate well with the amount of annual maximum monthly precipitation.

The observation wells are set approximately 200 m interval along the linear underground structure. This interval is less than the influence radius determined by pumping tests conducted in the area. The density is therefore good enough to detect the groundwater fluctuation caused by the underground structure.

The observation area covers a radius of 800 m or more from the linear underground structure. The distance is almost the same as the distance to the influence radius determined by the pumping test.

4.3 *Phenomena of allowable fluctuations*

In this region, the following major phenomena are studied with reference to the groundwater level fluctuations. They are the drying up of wells and springs, effects of subsidence on existing structures and effects on vegetation.

The relationship between the drying up of wells and groundwater level fluctuations can be easily formulated based on the condition that such groundwater level changes would not affect the water supply system. In the same way, the relationship between the drying up of springs and groundwater level fluctuations can be formulated.

The following sections discuss the effects of groundwater level fluctuations on existing structures, and vegetation.

4.4 *Effect of subsidence on existing structures*

This is one of the major problems that the blocking of groundwater flow by structures cause to the society.

In studying this phenomenon, the area was zoned, on the basis of its geological characteristics and land usage. Using architectural standards, the allowable settlement for each structure is plotted. As an example of these standards, the architectural design standards for wooden houses are listed in Table 2 (Architectural Institute of Japan 2001).

Once the allowable settlement is determined at each designated location, the allowable range of hydraulic head is deduced using established consolidation theory.

Consolidation tests were conducted for clay and peat sediments in the region and the characteristics were studied. The study has shown that diluvial clay sediments of confined aquifers are in over-consolidated state.

Table 2. Design standards for wooden houses.

Object structure	Type of deformation	Allowable value
Wooden houses	Maximum settlement	30 mm
	Deformatno angle of ground surface	2×10^{-3} radian
	Relative settlement	22.5 mm

The cause of this over consolidation has been attributed to the fact that the aquifers in the diluvial sand under the clay sediments had been over-pumped for industrial use. The lowering of the ground water level had caused large areas to subside in the 1960's and 1970's. To cope up with the situation, strict regulations have been introduced for pumping the groundwater since the 1970's. In recent times, the groundwater levels have recovered. Due to these historical experiences, the diluvial clay sediments are over consolidated. On the other hand, the alluvial clay and peat sediments are in their normal consolidated states. Therefore, these sediments can be sensitive to groundwater level fluctuations.

The relationship between the groundwater hydraulic head and the amount of settlement is formulated by using established consolidation theory. However, as it is well known, the method of analysis is based on many assumptions and the calculated value is not very accurate. Therefore, we employ a safety factor of two when the allowable range of hydraulic heads that are used for assessment criteria are calculated.

However, even if we fulfill the allowable settlement standards, the existing structures may suffer because of groundwater level fluctuation caused by the constructed underground structure. In such a case, there is the possibility that the project administrator could be liable for prosecution. Therefore, it is important that preparatory studies are carried out on existing buildings prior to the construction of structures that would block groundwater flow.

4.5 *Effects on vegetation*

The region where we conducted the study is urbanized, but mangroves remain around the edge of the diluvial bank where the land is steep. The mangroves are important for the ecosystem of this region.

The vegetation is one of the most important components of the ecosystem and groundwater level fluctuation may affect it. The effect of groundwater level fluctuation on the vegetation is one typical case of natural environmental consequences.

However the groundwater fluctuation is only one of several factors that affect vegetation. Thus, there are

Copyright © 2003 Swets & Zeitlinger B.V., Lisse, The Netherlands

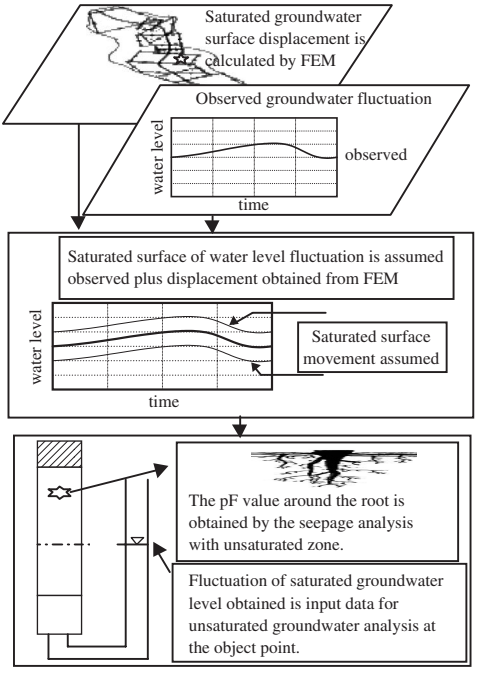


Figure 5. Calculation method for pF using hydraulic head fluctuation.

other possible causes and detrimental effects. In such a case, the project administrator has to be certain that the groundwater fluctuation caused by the constructed structure has little or no effect on the vegetation. To cope up with such a situation, the allowable range of hydraulic head on the vegetation is formulated.

The health of the vegetation depends on the condition of soil around the root. One major soil condition factor is osmotic potential, which is influenced to a large extent by the water content of the soil. The osmotic potential can be indicated as the power of free energy (i.e. pF). If the pF is less than 1.5, then there is the possibility of root decay. On the contrary, if the pF is greater than 3.0, then plants wilt till they die. Therefore, the pF value should be from 1.5 to 3.0 around the roots of plants. (Japan society of soil physics 1979).

Since the osmotic potential in the soil can be calculated by seepage analysis with non-saturated elements using hydraulic head fluctuations as shown in Figure 5, so can the allowable range of hydraulic head be determined by the reverse analysis. A safety factor of two is employed for this criterion.

4.6 *The determined criteria for this region*

The determined criteria for this region are summarized in Table 3. According to this study, a groundwater flow preservation system is required for the vegetation

Table 3. Results of allowable fluctuations of hydraulic head (Unit: TP+m).

Geological block	Diluvial bank	Buried wave cut terrace
Historical highest hydraulic head	9.5	5.4
Allowable fluctuation for high level head		
Structures	(9.9)	1.1
Vegetation	2.7	(1.2)
Allowable highest level	12.2	6.5
Historical lowest hydraulic head	8.9	4.1
Allowable fluctuation for low level head		
Subsidence	N/A	0.0
Vegetation	−2.7	(−2.6)
Allowable lowest level	6.2	4.1

growing on the diluvial bank. In the alluvial lowland, the hydraulic head should be almost at the same level, as before, at the designated locations where wooden houses are sited. This is to prevent or reduce any detrimental effect arising from the existing underground structures. To cope up with the situation, very accurate analytical methods are required.

5 CONCLUSION

In this report, a practical method of assessment for groundwater flow preservation system is presented. The following are the important guidelines of the practical assessment method:

1. The assessment method should be defined in a consistent system that includes preparatory investigation, analysis, design, and validation.
2. The criteria should represent the causal relationships of possible detrimental effects. In other words, based on the fulfillment of the set criteria, it should be proved that groundwater level fluctuations are not the cause of the detrimental effects in the region.
3. It is rational to determine the criteria in terms of hydraulic head and the strictest range for all possible influences should be employed in each area.
4. Based on the concept of the assessment method, detailed methods for two criteria are presented. One is for detrimental influences to existing structures caused by subsidence. The other is the effect on vegetation. All the important components in the methods have been established some decades ago. Therefore, when an assessment method is constructed, these components should be used in the total system with due consideration given to the assessment system's function in the project.

At present, the project is on-going. Construction is being carried out with observations to validate the

Copyright © 2003 Swets & Zeitlinger B.V., Lisse, The Netherlands

assessment method are also being taken. The observation criteria are fulfilled and no major difficult situation related to groundwater level fluctuation has been encountered.

ACKNOWLEDGEMENT

We are grateful to Dr. Takao Sugimoto of the Civil Engineering Research Institute, Tokyo Metropolitan Government Office and, Professor Tamotsu Sakura of Chiba University for their important suggestions during the study.

REFERENCES

Architectural Institute of Japan 2001. *Guideline for foundation design*. Tokyo: Maruzen Co., Ltd.

Japan society of soil physics 1979. *Soil physics*. Tokyo: Morikita Shuppan Co., Ltd.

Copyright © 2003 Swets & Zeitlinger B.V., Lisse, The Netherlands

Preservation countermeasures for groundwater flow against the linear open cut tunnel in low alluvial plain with dissected valley

Y. Arai & M. Ohnishi
Japan Highway Public Corporation, Tokyo Construction Bureau, Tokyo, Japan

G. Imai
Researcher and professor, Graduate School of Engineering, Yokohama National University, Yokohama, Japan

T. Kisanuki
Expressway Technology Center, Tokyo, Japan

M. Hirayama
Taisei Kiso Sekkei Co., Ltd., Tokyo, Japan

ABSTRACT: The authors planned a linear open cut tunnel for a district where there is a thick layer of deposited alluvial clay and where the ground is still settling. In such a district, there is a high possibility of the constructed linear underground structure blocking the groundwater flow and lowering the groundwater level, encouraging the settlement of the surrounding ground as a result. In order to select countermeasures against this obstruction of the underground flow by predicting the way of ground water flow after completion of the underground structure, it is most important to validate the analytical result of the present condition model by comparing the real condition of the site including the state of development and the situation of land use. This report describes a method for evaluating the validity of seepage flow analysis in the ground with the topography of this kind.

1 INTRODUCTION

It is required to estimate the effect of road tunnel construction on the groundwater flow in the case that it is planned by the open cut (cut and cover) method. In such cases, FEM groundwater analysis is often carried out not only for estimating the effect but also planning the countermeasures. One of the most important steps in such study is to evaluate the validity of the analysis model in order to obtain more precise predictions. To improve on the suitability of the wide area model that reproduces present conditions, the authors performed the inverse analysis to obtain the appropriate values on seepage flow by means of fitting the simulated contour lines to the observed elevations of groundwater at the observation wells. At the same time, the authors estimated the present condition model from the following 3 points; (1) the research results from the past, (2) studying land use pattern, and (3) performing a tank model analysis. Based on the results of FEM groundwater analysis using a quasi-3-dimensional model, the infiltration constant was 2.7%. The infiltration constant from (1) to (3) ranged from 3.0% to 3.5%. Because these generally comformed each other, the authors confirmed the suitability of the wide area groundwater analysis model based on results of the quasi-3-dimensional analysis. These results are described below(Arai, Y. et al. 2002).

2 STATE OF THE GEOLOGY AND THE GROUNDWATER

The map of the area analyzed is shown in Figure 1, and the geological profile of the planned route is shown in Figure 2.

The planned route crosses alluvial plain formed along a river with hillocks of various sizes scattered on the surrounding land. In the district, the bedrock is Kazusa Group mudstone formed in the Pleistocene, and it is covered by alternating soft clay layer and sandy soil layer which distribute in the district.

The principal aquifers are the As1 layer and As2 layer, the confined groundwater levels of both layer are equally high, and their annual fluctuation range is small at about 50 cm.

Copyright © 2003 Swets & Zeitlinger B.V., Lisse, The Netherlands

3 ANALYSIS METHOD, AREA, MODEL, AND CONDITIONS

3.1 *Analysis method*

The quasi-3-dimensional groundwater analysis was used for the following reasons.

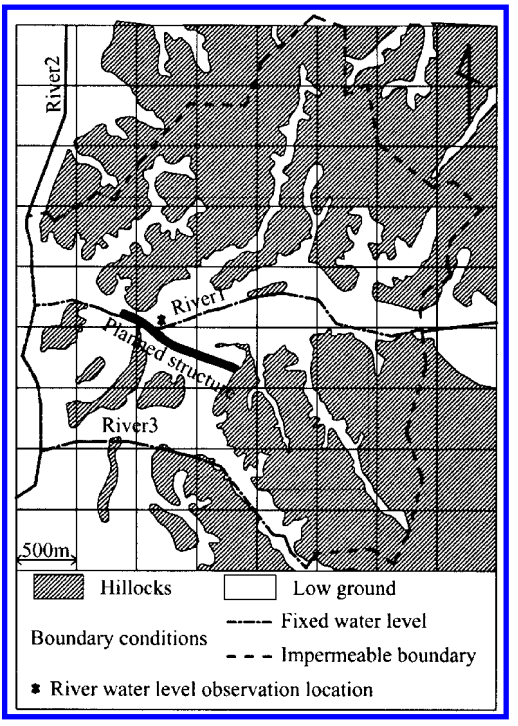


Figure 1. Analysis area map.

(1) Because the tunnel was planned to be embedded in the mudstone stratum that is presumed to be an aquiclude, the tunnel completely blocked the aquifer, and it is adequate to consider only the horizontal flow.
(2) The results of the geological survey, water quality survey, and the groundwater level observations revealed that the As1 and As2 aquifers were both linked by the same recharge source, and could be handled as a single aquifer in the seepage analysis.
(3) The quasi-3-dimensional model was prepared by evaluating the coefficient of transmissivity at each point by Σ (stratum thickness × coefficient of permeability).

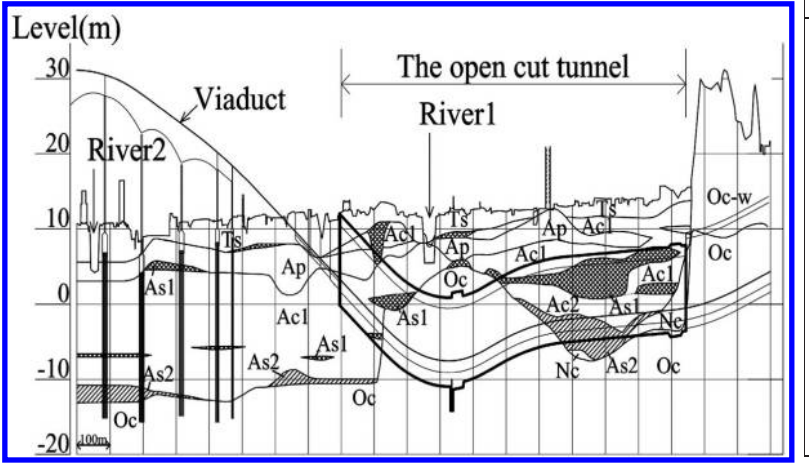
3.2 *Study area and model*

The areas for the analysis are shown in Figure 1, and the analysis models of the two aquifers, As1 and As2, are shown in Figure 3.

The analysis area is the catchment boundary, and the north side and the east side of the analysis boundary in the model are now housing areas where the original topography has disappeared, but the boundaries were set based on the catchment boundaries of the former topography. And the elements were, in principle, divided into 50 m parts, but close to the planned structure, the elements were 25 m in order to clarify the detailed water level distribution.

3.3 *Analysis conditions*

Table 1 shows the coefficients of permeability for each stratum used for the analysis. Table 2 shows the results of field permeability test of the aquifer.



Geological stratigraphy table

Geological Age			Stratigraphy	Code
Quaternary	Holocene	Alluvium	Surface soil, enbankments, landfill	Ts
			Organic clay stratum	Ap
			First clay stratum	Ac1
			Second clay stratum	Ac2
			First sandy stratum	As1
			Second sandy stratum	As2
	Pleistocene	Sagami Group, Naganuma formation	Sandy stratum	Ns
			Clay stratum	Nc
		Kazusa Group, Koshiba formation	Sandy stratum	Ks
			Sandy mudstone	Kc
		Ofuna formation	Weathered mudstone	Ocw
			Mudstone and sandy mudstone	Oc

Figure 2. Geological profile of the planned route.

Copyright © 2003 Swets & Zeitlinger B.V., Lisse, The Netherlands

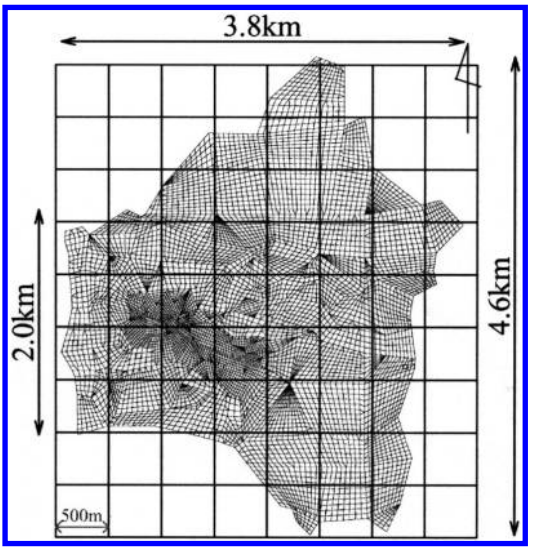


Figure 3. Analysis model.

Table 1. Coefficient of permeability.

Stratum code	Coefficient of permeability (cm/sec)	Stratum code	Coefficient of permeability (cm/sec)
Ts	1×10^{-5}	Ns	3×10^{-4}
Ap	1×10^{-5}	Nc	1×10^{-5}
Ac1	2×10^{-6}	Ks	3×10^{-4}
Ac2	2×10^{-6}	Kc	5×10^{-5}
As1	9×10^{-4}	Ocw	1×10^{-5}
As2	1×10^{-3}	Oc	1×10^{-5}

Table 2. Results of field permeability test of the aquifer.

Code	Range (cm/sec)	Number	Average (cm/sec)
As1	1.0×10^{-4} to 6.6×10^{-3}	20	9×10^{-4}
As2	3.5×10^{-4} to 5.3×10^{-3}	10	1×10^{-3}

The coefficients of permeability of the aquifers were set at 9×10^{-4} cm/sec for As1 and at 1×10^{-3} cm/sec for As2 with reference to the results of field permeability test. The coefficients of permeability for the other layer were set with reference to field permeability test results, the results of grain size analysis, and documents.

The boundary conditions were the boundary with fixed water level of the river and the impermeable boundary for the catchment boundary. These conditions are shown in Figure 1. And as underground blockage conditions, the blockage rate of the revetment pile foundation was considered according to the equivalent coefficient of permeability by equation (1). Table 3 shows the equivalent coefficient of permeability.

Table 3. Equivalent coefficient of permeability.

Stratum code	River 1 (cm/sec)	River 2 (cm/sec)
As1	6×10^{-4}	–
As2	6×10^{-4}	8×10^{-4}

$$K' = \frac{(L_1 k_1 + L_2 k_2)}{(L_1 + L_2)} \quad (1)$$

where K' = equivalent coefficient of permeability; L_1 = pile diameter; L_2 = (pile pitch – pile diameter); k_1 = coefficient of permeability of the precast concrete piles (hypothesized to be 1×10^{-7} cm/sec); and k_2 = coefficient of permeability of the sand layer.

In the analysis, groundwater supply quantity was supposed to multiply the precipitation by infiltration constant with the sharing area of each node. The analysis was carried out in each layer, and total infiltration constant was obtained by adding each infiltration constant of As1 and As2.

The annual average precipitation was set at 1500 mm based on data obtained during the past 3 years from 1998 to 2000 at a nearby meteorological observation station. The average precipitation for the past 23 years (1978–2000) is also 1500 mm.

4 RESULTS

The contour lines of the present groundwater level in As1 are shown in Figure 4 and the analytic contour lines of the groundwater level are shown in Figure 5. Because the shapes of the two contour lines are almost identical, the analysis results based on conventional methods were judged to be satisfactory. Table 4 and Table 5 shows the infiltration constant based on the analysis results. In this table, the infiltration constant based on the quasi-3-dimensional analysis was 2.7%. The infiltration constant in the low ground was 1.0% in the As1 aquifer: the rate in the urban district where pavement rate is high. It is hypothesized that the infiltration constant in the As2 aquifer is 0%, because the Ac2 layer above it acts as an aquiclude.

5 RESULTS VERIFICATION METHOD AND VALIDITY EVALUATION

5.1 *Results verification method*

5.1.1 *Results of past research based on a water budget*

The results of a study of Hofu Plain in Yamaguchi Prefecture performed by Yuhara (Yuhara, K. 1967) using

Copyright © 2003 Swets & Zeitlinger B.V., Lisse, The Netherlands

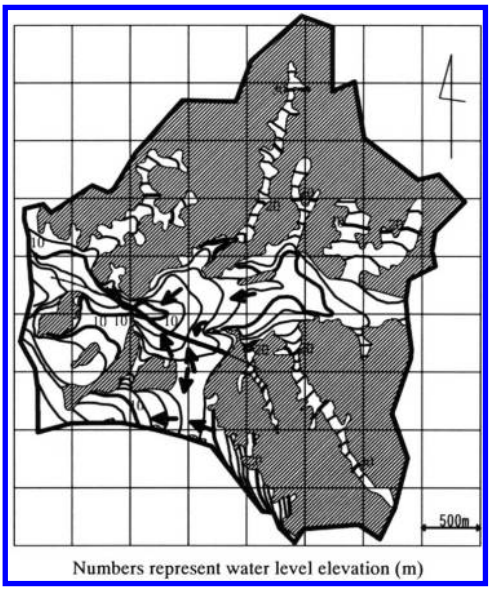


Figure 4. Present contour lines of the groundwater level in the As1 layer.

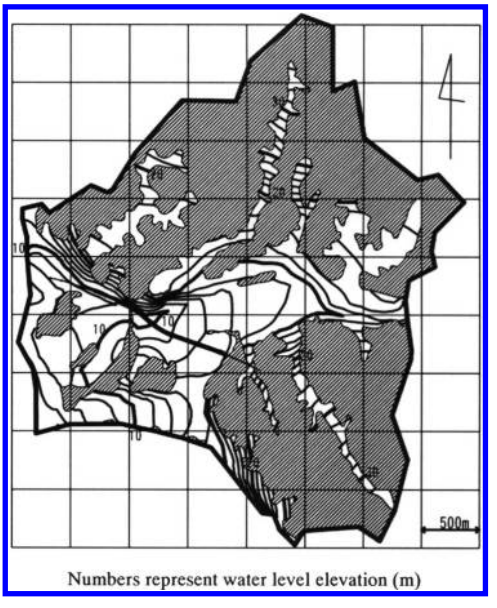


Figure 5. Analytic contour lines of the groundwater level in the As1 layer.

a water budget revealed that under topographical conditions identical to those in this district, the infiltration constant was 3.5% (Yuhara, K. 1967). The following is the water budget used by Yuhara (Yuhara, K. 1967).

$$F + P - G - Q + HAS = 0 \quad (2)$$

Table 4. Results of quasi-3-dimensional groundwater flow analysis (Infiltration constant).

Category	Low ground (%)	Hillocks (%)
As1 Layer	1.0	1.8
As2 Layer	0.0	1.2
Total	1.0	3.0

Table 5. Infiltration constant taking account of the area ratio.

Category	Area ratio, a	Infiltration constant, b (%)	Infiltration constant taking account of the area ratio, c* (%)
Low ground	0.15	1.0	0.15
Hillocks	0.85	3.0	2.55
Total	1.00	–	2.7

*c = a · b.

where F = infiltration from the river; P = infiltration from rainfall; G = groundwater runoff; Q = ground surface runoff; H = groundwater level decline; S = coefficient of storage; and A = related surface area.

So rewriting equation (2) assuming that G = 0, the following equation is obtained.

$$lW + mpA - Q + HAS = 0 \quad (3)$$

where l = coefficient; W = infiltration from the river; m = infiltration from rainfall; and p = rainfall.

There are three unknowns, W, m, and S, and based on data for 3 years, they were obtained as $W = 62.90 \times 10^6$ m^3/year, m = 0.035 (3.5%), and S = 0.177.

5.1.2 *Rainfall infiltration taking account of the state of land use*

Figure 6 shows the present state of land use.

The rainfall infiltration was computed by the following equation taking account of this figure.

$$Q = Q1 - Q2 - Q3 \quad (4)$$

where Q = rainfall infiltration; Q1 = annual average precipitation; Q2 = ground surface runoff; and Q3 = evaporation.

Here, Q1 was assumed to be 1500 mm based on Section 3.3. The area was divided into urban (83%) and forest etc. (17%), and the value of Q2 was calculated for each area based on their respective surface area ratios assuming that the runoff coefficient was 0.75 (Japan Road Association 1987) for the urban part and 0.6 (Japan Society of Civil Engineers 1985) for the forests etc. The calculation results are shown in Table 6.

Copyright © 2003 Swets & Zeitlinger B.V., Lisse, The Netherlands

Q3 was obtained by the Thornthwaite Method shown in the following equation. The monthly average temperature was data from 1998 to 2000 at a nearby meteorological observation station.

$$E_T = 1.6\left(\frac{10Ti}{I}\right)^a \quad (5)$$

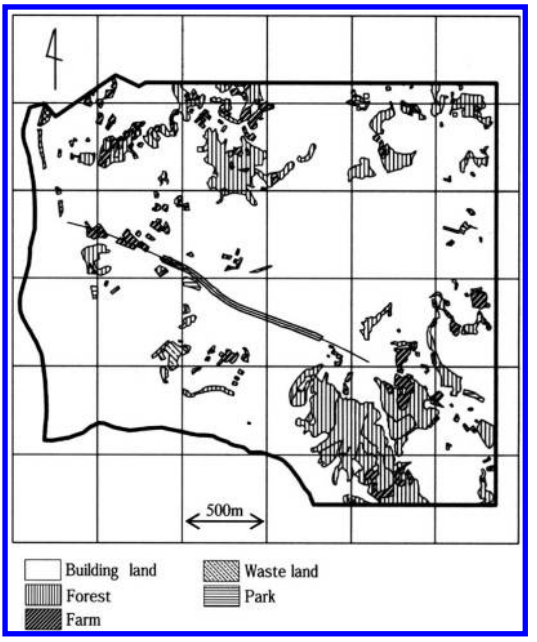


Figure 6. Outline of the state of surrounding land use (1999).

Table 6. Ground surface runoff.

Category	Surface area ratio, a	Runoff coefficient, b	Ground surface runoff, Q2* (mm/y)
Urban district	0.83	0.75	930
Forest etc.	0.17	0.60	150
Total	1.00	–	1080

*$Q2 = a \cdot b \cdot Q1$.

where E_T = evaporation (cm/month); Ti = monthly average temperature (°C); $I = \Sigma(Ti/5)^{1.514}$; and $a = (0.675I^3 - 77.1I^2 + 17920I + 492390) \times 10^{-6}$.

The results of the above calculations are shown in Table 7. The infiltration constant taking account of land use was 3.0% based on the table.

5.1.3 *Rainfall infiltration based on the tank model*

A conceptual diagram of the tank models shown in Figure 7. The tank model method is a method of modeling the rainfall – river flow volume response in a preset drainage basin. In particular, a long-term runoff hydrograph obtained from the tank model method consists of two components. One is the ground surface runoff that occurs immediately after rainfall. The other is the base flow: rain water that infiltrates the ground, then reappears on the ground surface as groundwater runoff. This study focused on the infiltration volume that is the source of supply for this base flow runoff. In sum, it is a method of obtaining the rainfall infiltration from the flow volume component of river flow.

Figure 8 shows the parameter constants of a tank model. In this figure, the first tank to the third tank are ground surface flow and the fourth tank is the base flow runoff (rainfall infiltration). In this case, a tank model consisting of a row of four tanks was used and the study point was the catchment area above the river water level observation station (catchment area: 14.0 km^2).

The verification of the tank model constants treated the three years period from April 1998 to March 2001

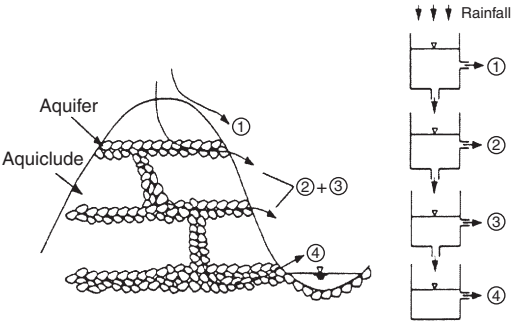


Figure 7. Outline of the tank model (Japan River Association 1997).

Table 7. Results of study of infiltration constant based on the state of land use.

Annual average precipitation, Q1 (mm/y)	Ground surface runoff, Q2 (mm/y)	Evaporation, Q3 (mm/y)	Rainfall infiltration, Q* (mm/y)	Infiltration constant, Q/Q1
1500	1080	375	45	0.030

*$Q = Q1 - Q2 - Q3$.

Copyright © 2003 Swets & Zeitlinger B.V., Lisse, The Netherlands

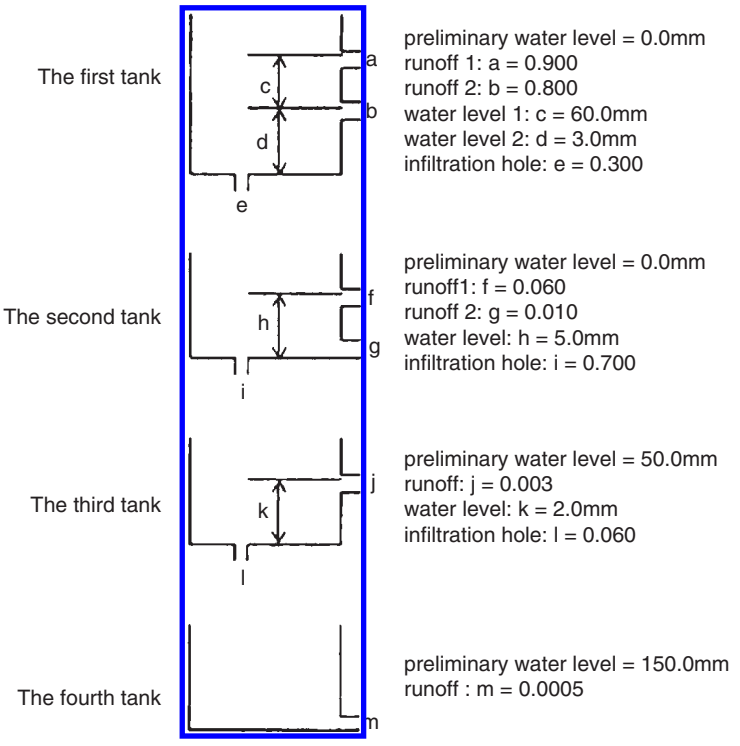


Figure 8. Parameter constants of the tank model.

as the historical matching period. The water level – flow volume properties were hypothesized based on the planned flood flow volume (90 m^3/sec). The daily precipitation and the river flow volume at the water level observation point are shown in Figure 9, and the river section is shown in Figure 10.

Table 8 shows the results of the calculations. The infiltration constant based on the tank model was an average of 3.3% (3.2 to 3.6%).

5.2 *Validity evaluation*

Table 9 summarizes the results of the above study.

The result from the quasi-3-dimensional model analysis obtained by varying the infiltration constant in each aquifer, As1 and As2, the water level distribution in assuming the permeability 2.7% was similar to the observed ground water level. The measured values and the results of the study based on the present state of land use and the tank model ranged from 3.0 to 3.5%, that are values a little larger than the former, but which generally conform with them. The authors have, therefore concluded that the wide area groundwater analysis model based on the results of quasi-3-dimensional analysis are appropriate.

6 CONCLUSION

In the past, the suitability of the present status reproduction model in wide area groundwater analysis has often been evaluated by performing reverse analysis of hydrological constants so that the model matches the contour lines of the present groundwater. For this study, the authors focused on the infiltration constant in the wide area groundwater analysis and used three methods to evaluate the suitability of the analysis model, obtaining similar values in all three cases to confirm the suitability of the model. In future, when a study of groundwater problems in low ground with basin structures is performed, a method that focuses on the parameters for the infiltration constant in the tank model etc. will also play a role in improving the precision of analysis models.

The model verified by the above method is now being used for earth retaining wall effects prediction analysis and flow countermeasure work analysis based on quasi-3-dimensional groundwater flow analysis, and the flow countermeasure work is now being executed, then in the future, the suitability of analysis models will be verified based on the results of groundwater observations now being carried out.

Copyright © 2003 Swets & Zeitlinger B.V., Lisse, The Netherlands

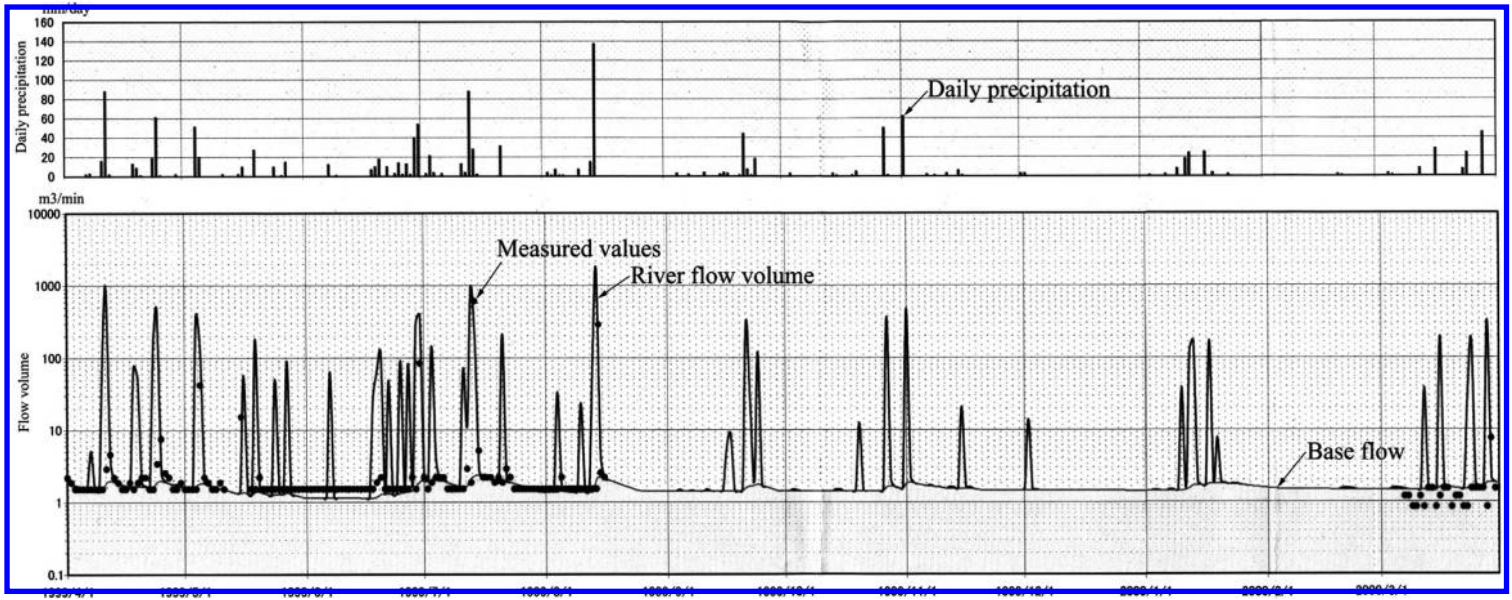


Figure 9. Daily precipitation–river flow volume relationship.

Copyright © 2003 Swets & Zeitlinger B.V., Lisse, The Netherlands

Table 8. Results of the study based on the tank model.

Period	Annual precipitation (mm)	Evaporation (%)	Ground surface runoff (%)	Infiltration constant (%)
1998.4–1999.3	1615	24.1	72.3	3.6
1999.4–2000.3	1348	30.2	66.6	3.2
2000.4–2001.3	1531	25.7	71.1	3.2
Average	1498	26.7	70.0	3.3

Table 9. Summary of infiltration constant.

Study method	Quasi-3-dimensional groundwater flow analysis	Measured values	State of land use	Tank model
Infiltration constant (%)	2.7	3.5	3.0	3.3

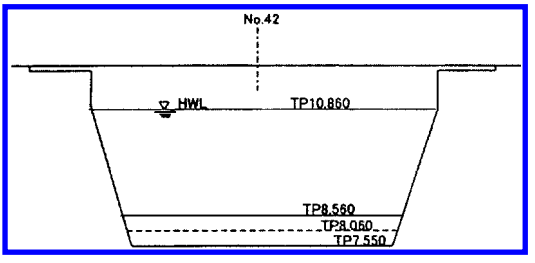


Figure 10. River cross section.

REFERENCES

Arai, Y. et al. 2002. *Estimation of the validity of a FEM model to predict the effects on groundwater.* 57th Annual Technical Conference. Japan Society of Civil Engineers.

Japan River Association 1997. *Ministry of Construction river and sediment control technical guidelines (proposed) and commentaries Surveying volume*: 99.

Japan Road Association 1987. *Road earthwork and drainage work guideline*: 21.

Japan Society of Civil Engineers 1985. *Collected hydrological equations*: 155.

Yuhara, K. 1967. The water budget of shallow groundwater of Hofu Plain in Yamaguchi Prefecture. *Bulletin of the geological survey of Japan* 18(8).

Copyright © 2003 Swets & Zeitlinger B.V., Lisse, The Netherlands

Contamination of soil and groundwater: investigation, prediction and remediation

Copyright © 2003 Swets & Zeitlinger B.V., Lisse, The Netherlands

A monitoring technique of remediation of groundwater using resistivity cones

M. Fukue & K. Kita
Marine Science & Technology, Tokai University, Shimizu, Japan

T. Minato
Aoki Marine Co., Osaka, Japan

K. Makito & T. Chida
Koa-Kaihatsu Co., Tokyo, Japan

ABSTRACT: In this study, the resistivity cone developed previously was examined to develop a monitoring system during remediation of soil and/or groundwater. Hazardous substances, such as heavy metals and NAPLs, influence the resistivity or electrical conductivity of soils or pore water. During remediation of soils or groundwater, the resistivity of the soil changes with the change in concentration of the hazardous substances.

Previous studies showed that the reduction of cation will increase the resistivity, while the reduction of the amount of NAPLs in pores will decrease the resistivity. These imply that the in-situ resistivity measurement can be used for monitoring the remediation effect.

In this study, laboratory tests were performed to examine the feasibility of the resistivity cone technique for the application to field. The resistivity cone was installed in sand layer in a container. Resistiviy was measured when sodium chloride solution and standard heavy metal solutions (Zinc, Nickel and lead) permeated horizontally through the sand layer, respectively. The experimental results showed that the resistivity of the sand decreased to some extent, depending on the initial concentration of the electrolytes. After the resistivity reached the minimum value, drinking water was permeated to remove the electrolytes in pore water. Consequently, the resisitivity was increased up to the original value of the sand. Therefore, the movement of plume or contaminated zone can be monitored with the technique developed in this study.

1 INTRODUCTION

For soil-remediation works using extraction wells, evaluation is usually made using chemical analyses on extracted groundwater. Even if a good result is obtained on the extracted groundwater, it does not necessarily mean that the surrounding soils or groundwater is clean. The result only says that the extracted ground water is clean. To ensure that the surrounding soils are clean, a large number of samples of soils and groundwater is required at different positions and depths. A large number of chemical analyses are also needed. To reduce these procedures, a resistivity-cone technique is proposed in this study.

The remediation of contaminated land has been performed with various methods. Besides the removal of contaminated soils, the evaluation of the effects of remediation is often difficult. For example, the quality of soils contaminated with TCE has been examined on the water sample extracted from the well. However, even if the water is clean, the soil is not necessarily clean, because of the remnants in the pore spaces. The remnants of TCE will gradually dissolve with time. Note that TCE is one of non-aqueous liquids, NAPLs and only 0.11 percent will dissolve in water.

In order to evaluate the effects of remediation works, it is needed to monitor the behaviour of plume or contaminated zone. Therefore, in this study, a monitoring technique of contaminated zone is developed using resistivity cones.

2 CONCEPTS

Cone penetration has been used to identify soil type in terms of hardness. On the other hand, piezometric cone has been used to measure water pressure, i.e., water head. Therefore, the measurements of water head from a number of piezometric cones will provide the

Copyright © 2003 Swets & Zeitlinger B.V., Lisse, The Netherlands

gradient of water head. This will give the direction of the movement of plume or contaminated zone.

The resistivity is primarily dependent on the soil type. For example, the water content of soils strongly affects the resistivity (Fukue et al., 1998). Furthermore, the resistivity of soils depends on the type and concentration of electrolytes in the pore water (Fukue et al., 2001). If the pore liquid is NAPLs, the resistivity shows an extremely high value.

The electrolytes in pore water will decrease the resistivity of soils. Therefore, the change in electrolyte concentration in groundwater can be observed by the change in resistivity measurements.

With the combination of a water pressure gauge and electrodes attached on a cone or rod, the change in water head and resistivity can be measured. Therefore, installation of a number of the cone instruments at different locations, the movement of plume or contaminated zone can be monitored. This technique can be suitable in evaluating the effects of remediation. The present objective is, therefore, to examine the feasibility of the resistivity cone technique in field application.

3 EXPERIMENTS

3.1 *Resistivity cone*

The resistivity cone used in this study is similar to those developed by Campanella and Weemees (1990). Four electrodes are located within a given interval, as shown in Figure 1. The spacing r_M can be changed using different height of the plastic rings for electric insulation. The thickness of electrodes is 5 mm. The diameter of the cone rod, d is 42 mm. The maximum diameter of the cone part is 35.7 mm and the angle of the cone tip is 60 degree. The distance between the cone tip and the top electrode indicated by A in Figure 1, is indicated by D, which is 250 mm.

A constant square current AC source, set at 1000 Hz, is applied to build the electric field in soil and the voltage yielded between the inner two electrodes located between the current and grounded electrodes (M and N), as shown in Figure 1, is measured. This is a potential difference.

The electric field developed around the cone rod is complicated, because of the complicated boundary condition. For cone penetration, Fukue et al. (1998) obtained the following theoretical relationship, based on the Ohm's law.

$$\rho = \pi^2 \Delta V/(CI) \tag{1}$$

where

$$C = 1/(d + r_M) - 1/(d + r - r_M) - 1/(d + r_N) + 1/(d + r - r_N) \tag{2}$$

where p is the resistivity of the soil, ΔV is the potential difference to be measured and I is the current supplied. Eq. (1) was examined comparing with one dimensional -current flow experiments (Fukue et al., 1998).

3.2 *Dispersion test*

The monitoring of the resistivity cone was examined with horizontal seepage test, as shown in Figure 2. The resistivity cone was installed in a sand layer. The sand used has a density of 2.646 g/m^3 and uniform grain size distribution, i.e., $D_{10} = 0.22$ mm and $D_{60} = 0.36$ mm.

The electrolyte solution with heavy metal ions was permeated from the inlet (left side) to the outlet (right side), when the hydraulic gradient was 4/15. After adequate seepage was performed with drinking water, the liquid in the inlet side was rapidly changed from drinking water to a given concentration of solution by adding heavy metal solution. After that, a solution with the constant concentration was poured in the inlet until

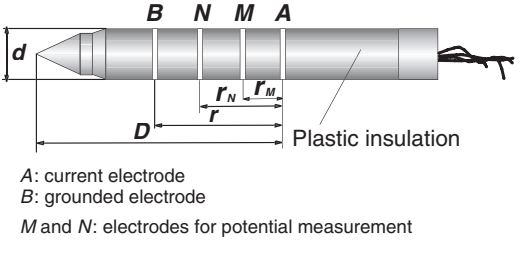


Figure 1. Resistivity cone used in this study.

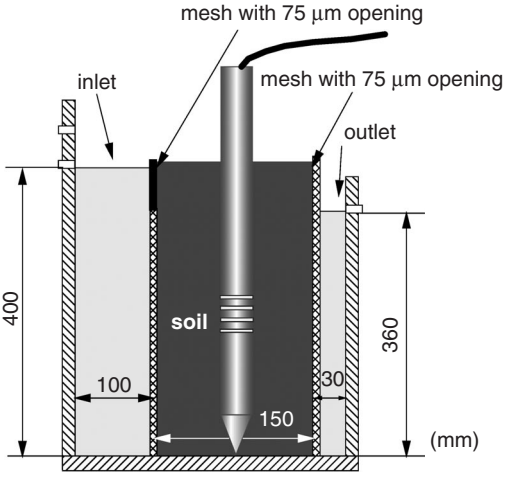


Figure 2. Apparatus used for the experiments.

Copyright © 2003 Swets & Zeitlinger B.V., Lisse, The Netherlands

the resistivity became the minimum value. When the resistivity reached the minimum value, drinking water was added to the inlet side during permeation. The overflow was allowed to keep the constant water level. By adding water, the concentration of the solution in the inlet is gradually decreased.

As standard solutions, reagents of Ni, Zn and Pb standard solutions were used. NaCl solution was also used as a typical electrolyte. During the permeation of solution, the potential difference was measured with the resistivity cone.

A frequency of 1 kHz and an AC current of 0.1 mA were used (Fukue et al., 1998), as mentioned earlier. The separation between electrodes, r_M, was 1 cm. The measurements of potential difference, ΔV, were recorded every two seconds. The resistivity was calculated from (1).

4 RESULT AND DISCUSSION

The results obtained are presented in Figures 3–5. Figure 3 shows the changes of resistivity during migration of Ni. The resistivity starts decreasing when the Ni ions reach the electric fields in the sand layer, because of the low resistivity of the electrolyte solutions. The time required to reach the minimum resistivity value slightly varies with the concentration used. When the initial concentration is higher, the time required to reach the minimum resistivity value is a little shorter. This is because of the diffusion of ions towards the back. Note that diffuison depends on the concentration gradient. The minimum value of resistivity can be obtained when the ions permeate through total sand layer, and corresponds to the maximum concentration of ions in the middle part. The increase in the resistivity beyond a certain time was exerted from the adding of water. When all the ions were discharged from the sand layer to the outlet, the resistivity was completely recovered, as seen in Figure 3.

Figures 4 and 5 show the change in resistivity for the cases of Zn and Pb, respectively. The trends of both are similar to the case of Ni. The time required to reach the minimum values is approximately 10 minutes and slightly varies with the concentration and the type of elements.

The unsymmetric figures of resistivity-time curves in Figures 3–5 are attributed to the initial and boundary conditions in the inlet, as described earlier. It is natural that the slow decrease in concentration in the inlet provides the relatively slow recovery of the resistivity.

Figure 6 was obtained from the results shown in Figures 3–5. The maximum change in resistivity means the difference between the maximum (original) and minimum resistivities. The result with Na Cl solution is also presented in Figure 6. The figure shows that

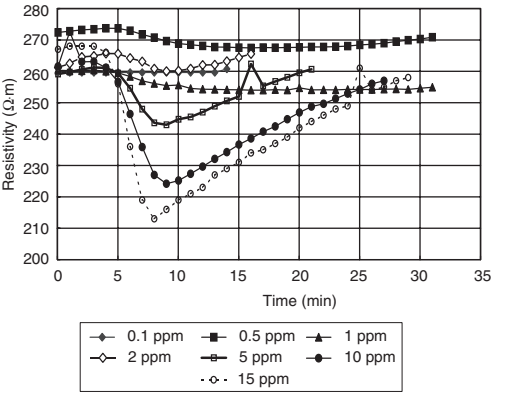


Figure 3. Change in resistivity during migration of Ni solution.

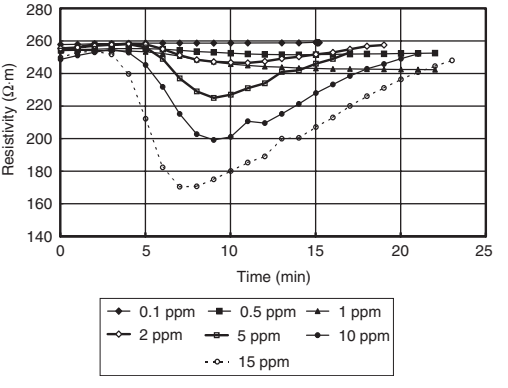


Figure 4. Change in resistivity during migration of Zn solution.

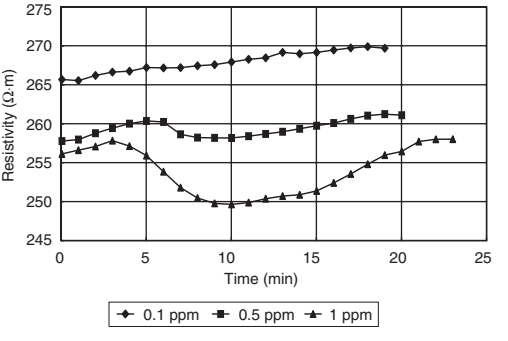


Figure 5. Change in resistivity during migration of Pb solution.

the higher maximum resisitivity is obtained for higher concentration of ions. It seems that the relationships between the maximum change in resistivities and the concentration of ions are linear to some extent. With

Copyright © 2003 Swets & Zeitlinger B.V., Lisse, The Netherlands

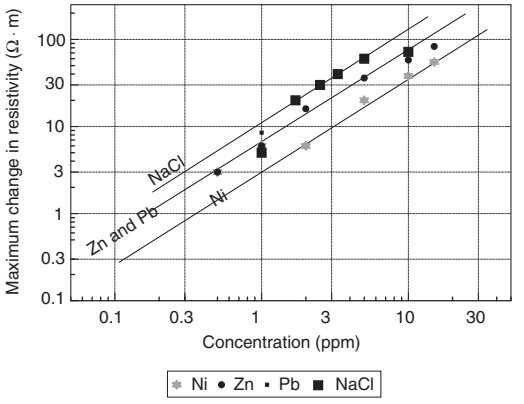


Figure 6. Maximum change in resistivity with concentration of solution.

these linear relationships, lower concentrations can be estimated from the resistivity to be measured.

5 APPLICATION TO FIELDS

There are several problems for the application to fields. These are:

1. Not only single contaminant in soils, but plural elements – this leads difficulty for determining laboratory calibration curve, because of many combinations with type of substances.
2. Lower environmental standards in comparison to measurement level – this may concern accuracy of measurement. At present, it is found that measurement of 1 Ω · m is still possible. However, the change in groundwater flow, i.e, velocity and level, may affect measurements in this range.
3. Variation of background value in resistivity resulting from groundwater quality – if ground water contains salts and other ions, the resistivity of the soil is very low. In this case, the effect of heavy metals will become relatively small. In fact, some groundwater contains high concentration of Ca, Mn, Fe and/or Na ions.

These problems may be partially solved using the following technique.

5.1 *In-situ calibration*

Firstly, it is assumed that the extraction well is built at heavily contaminated zone and that the substances are specified. This assumption is valid, because remediation works are performed against known substances. The in-situ calibration for a relationship between concentration and resistivity can be demonstrated as

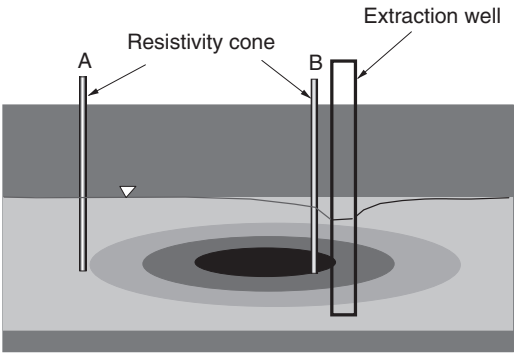


Figure 7. Interpretation for obtaining in-situ calibration curve.

follows:

1. One or some resistivity cone(s) should be installed (penetrated) near extraction well, as shown in Figure 7.
2. The chemical analyses of extracted water should be made on extracted groundwater.
3. The measurement of resistivity should be made during extraction of ground water.
4. From the results, a relationship between concentration and resistivity should be obtained, which is not dissimilar to Figure 6. The time lag between measurements of water sampling and resistivity measurement should be taken into account.

This is regarded as the in-situ calibration curve. If data for low concentration can't be obtained, the water should be poured into an adjacent well.

5.2 *In-situ measurement and monitoring*

For remediation works using extraction wells, the results are usually evaluated using chemical analyses on extracted groundwater. Even if a good result is obtained on the extracted groundwater, it does not necessarily mean that the surrounding soils and groundwater became clean. It should be realized that the result only says "the extracted ground water is clean".

To ensure if the surrounding soils and groundwater are clean, the resistivity-cone technique proposed in this study can be used. The monitoring can be made as the following procedure.

1. The piezometric resistivity-cones should be installed at different site locations and depths, as shown in Figure 8.
2. Pore water pressure and resistivity should be measured with a certain time interval.
3. Equi-concentration should be obtained using measured resistivity values using the calibration. "Equi-concentration"means a calibrated concentration.

Copyright © 2003 Swets & Zeitlinger B.V., Lisse, The Netherlands

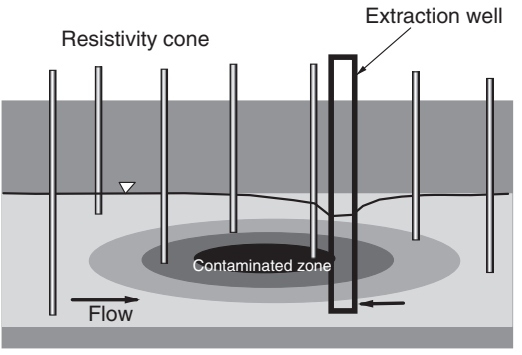


Figure 8. In-situ monitoring system using piezometric resistivity-cones.

This can be defined for non-specified elements or more than two elements.

Pore water pressure measurements provide the distribution of water head, which will give information on the advection. The movement of plume, therefore, is monitored with change in equi-concentration.

The technique proposed in this study will provide cost down, because the number of chemical analyses will be reduced. Furthermore, some other information, such as permeability of soils, can possibly be obtained using the monitoring results.

6 CONCLUSIONS

This study examined the feasibility of resistivity cone in order to apply for monitoring of contaminated soils during remediation works. The results of the laboratory tests showed that the electrolyte solutions containing heavy metals provide significant changes in resistivity. Therefore, the change in the heavy metal concentration can be monitored with the change in resistivity.

In-situ calibration curve for monitoring can be obtained using resistivity measurements and chemical analyses. Using the calibration curve, monitoring of plume or contaminated zone can be achieved using the results of piezometric resistivity-cones at different locations.

ACKNOWLEDGEMENT

This study was financially supported by Grant-In-Aid for Scientific Research (C), No. 40119699.

REFERENCES

Campanella, R.G. and Weemees, I. 1990, Development and use of an electrical resistivity cone for groundwater contamination studies, *Can. Geotech. J.* 27, 557–567.

Fukue, M., Taya, N., Matsumoto, M. and Sakai, G. 1998, Development and application of cone for measuring the resistivity of soil, *Journal of Geotechnical Engineering*, Japanese Society of Civil Engineers, No. 596/3–43, 283–293, (Text in Japanese).

Fukue, M., Minato, T., Matsumoto, M., Horibe, H. and Taya, N. 2001, Use of resistivity cone for detecting contaminated soil layers, *Engineering Geology* 60, 361–369.

Copyright © 2003 Swets & Zeitlinger B.V., Lisse, The Netherlands

Groundwater studies and mitigation programs for arsenic contamination in Bangladesh

M.A. Fazal, M. Imaizumi, S. Ishida & T. Tsuchihara
National Institute of Rural Engineering, Tsukuba, Japan

T. Kawachi
Graduate School of Agricultural Science, Kyoto University, Kyoto, Japan

ABSTRACT: Arsenic contamination in Bangladesh is the biggest calamity in the world, where many organizations are working on this issue. However, research methodologies, sampling strategies and objectives of each organization are not unique. Therefore, the research findings cannot give any conclusive result about the severity and the cause of contamination. Major problems of survey are lack of coordination, improper sampling and survey using field-kits. Field-kits violate 33.43% in accurate detection of arsenic contamination. Two hypotheses pyrite oxidation and oxy-hydroxide reduction are prevailing in Bangladesh to describe the cause of contamination. However, none of them have been studied thoroughly with accurate field data. Therefore, actual cause of contamination is still unknown. Programs that are taken for the arsenic mitigation also not out of the controversy. Because most of them either economically or technically or both are not feasible. To cope with these problems, some recommendations are put forward in this paper.

1 INTRODUCTION

In Bangladesh over 97% populations are reported to have access to drinking water from tubewells. In recent years, however, it is believed that tubewell-water in Bangladesh is not safe, rather arsenic-polluted, causing health hazards to the million of people. Groundwater arsenic contamination was at first discovered in West Bengal, India, in 1983 and then in Bangladesh in 1993. The Department of Public Health Engineering (DPHE), Bangladesh, started creating awareness of the problem to the people and the issue came in limelight in 1995. To save the lives of the million of people, the Government of Bangladesh formed a National Steering Committee in 1996.

The priority areas for action, by the committee, are:

(i) Investigation of the extent of the affected areas and sources of the arsenic.
(ii) Development of appropriate technologies for water treatment.
(iii) Treatment of affected populations.
(iv) Development of public awareness.

Arsenic contamination in Bangladesh is the biggest calamity in the world and in the history, where millions of people are now under the direct threat of it. As a result, many international donor agencies became interested to save the people of Bangladesh as well as to know the fundamental process of natural or man-made groundwater pollution by arsenic. Some of them are: United Nations Development Program (UNDP), World Health Organization (WHO), Japan International Cooperation Agency (JICA), Governments of the Netherlands (GON) and Danish International Development Agency (DANIDA). The government of Bangladesh through the Ministry of Health and Family Welfare took mitigation programs, and many governmental and nongovernmental organizations started working on Bangladesh groundwater arsenic contamination issue. The organizations which are working on arsenic are: Department of Public Health Engineering (DPHE), Grameen Bank (GB), Non Government Organization (NGO) Forum, Dhaka Community Hospital (DCH), School of Environmental Studies (SOES) of Jadavpur University, India, Bangladesh University of Engineering and Technology (BUET), Bangladesh Council for Scientific and Industrial Research (BCSIR), NRECA (a US consulting firm working for Rural Electrification Board of Bangladesh), DANIDA (Official Danish aid agency), Bangladesh Rural Advance Committee (BRAC), British Geological Survey (BGS) and so on. A long time has already past from the first groundwater arsenic detection in Bangladesh. Therefore,

Copyright © 2003 Swets & Zeitlinger B.V., Lisse, The Netherlands

it would not be unwise to assess the amount of works done by the different organizations and the quality of works to fulfill commitments of the Government of Bangladesh to its people. It is also needed to find out the cause of delay for achieving goals.

2 EXTENT OF GROUNDWATER ARSENIC CONTAMINATION

There are 64 districts, 490 thanas and 68,000 villages in the country. Though the first job of every organization that is working on arsenic contamination was to identify the contaminated tubewells, till February 2000, only 50,000 tubewells have so far been surveyed by different organizations. Till now only two reports describing the spatial extent of arsenic contamination in Bangladesh are available. One is the British Geological Survey Report (BGS, 1999) and the other is the Survey Report of School of Environmental Studies and Dhaka Community Hospital (SOES-DCH, 2000). In the BGS report, two separate figures are presented, one based on field tests and another on laboratory tests to describe the extent of groundwater arsenic contamination in Bangladesh (BGS, 1999). Though in both figures the index of arsenic contamination is percentage of wells contaminated, they are not unique. Therefore, it is difficult to say what the accurate extent of arsenic contamination in each district is. The reason may be the difference between the field-kits' results and the laboratory tests. Moreover, comparison of the two methods is not possible for all locations, since some locations are covered by either field tests or laboratory analyses. Therefore, a combination of field and laboratory test results would give a better picture of the extent of groundwater arsenic contamination in Bangladesh (Figure 1). From Figure 1, it could be seen that 61 districts out of 64 have been surveyed by all organizations and all the surveyed districts show the presence of arsenic contamination. In terms of thana, 270 out of 411 surveyed thanas were found contaminated having arsenic above Bangladesh standard (0.05 mg/L).

In April 2000, SOES and DCH jointly published a report on Bangladesh groundwater arsenic contamination, which shows different figures than those published in the BGS report. They found that in 47 districts out of all the 64 surveyed districts, arsenic concentration in groundwater was above 0.05 mg/L (SOES-DCH, 2000). In terms of thanas, they could cover 222 thanas out of 490 thanas by February 2000 and found 147 contaminated. In terms of villages, they could cover 1,063 out of 68,000 villages and found 918 contaminated. Therefore, if they would cover all the thanas, there is possibility of increasing number of districts contaminated by arsenic. Another limitation of SOES-DCH survey is that their samples are biased towards the arsenic affected areas. Figure 2 shows arsenic affected districts according to the SOES-DCH survey.

2.1 *Arsenic detection by field and laboratory tests*

There are many methods for arsenic detection; some of them can be categorized as two main groups: Field-kits and Laboratory test. Sophisticated laboratory facilities are required to accurately detect arsenic in groundwater, which are very limited in Bangladesh. Moreover, the laboratory method of arsenic detection is expensive and time consuming. Therefore, many organizations started groundwater arsenic detection using the field-kit method. 'Field-kit' is an instrument which is designed to identify the presence of arsenic with >0.05 mg/L concentration in drinking water. It is a 'Yes–No' type instrument that cannot detect absolute concentration of groundwater arsenic. A performance evaluation of field-kits was done jointly by SOES and DCH using 2,866 water samples collected from those tubewells which were colored red (contaminated; arsenic concentration >0.05 mg/L) or green (safe; arsenic concentration <0.05 mg/L) after testing with field-kits. For comparison, SOES-DCH used FI-HG-ASS system laboratory analysis, which can determine arsenic up to 0.002 mg/L with 95% confidence level. In the SOES-DCH analyses it can be seen that contaminated and safe wells identified by field-kits are 60.12% and 39.88%, respectively. When these contaminated (red) wells are rechecked by FI-HG-ASS system laboratory analysis, 50.73% of the contaminated (red) wells show safe (green), meaning that from red wells truly contaminated wells are 49.27%. Thus, if we represent violation (over-estimation) in the field kits in terms of truly contaminated wells identified from the red wells, it would be 102.97%. On the other hand, when safe (green) wells are rechecked by FI-HG-ASS system laboratory analysis, 7.35% of the safe (green) wells show contaminated (red), meaning that from green wells truly safe wells are 92.65%. Thus, if we represent violation (under-estimation) in the field-kits in terms of true safe wells identified from the green wells, it would be 7.93%. Therefore, by combined analysis for all of the 2,866 samples, we could say that instead of 60.12% contaminated wells truly contaminated wells are 32.55%, and instead of 39.88% safe wells truly safe wells are 67.45% (Figure 3), meaning that field-kits significantly violate identifying actual status of tubewells. Therefore, the percent of wells contaminated estimated from field-kits tests is not dependable at all. However, BGS report shows that out of 31,651 samples 22,777 (72%) were tested by field-kits. Therefore, we can gauge the dependability of field-kits results that were used to show the extent of arsenic contamination in Bangladesh.

Copyright © 2003 Swets & Zeitlinger B.V., Lisse, The Netherlands

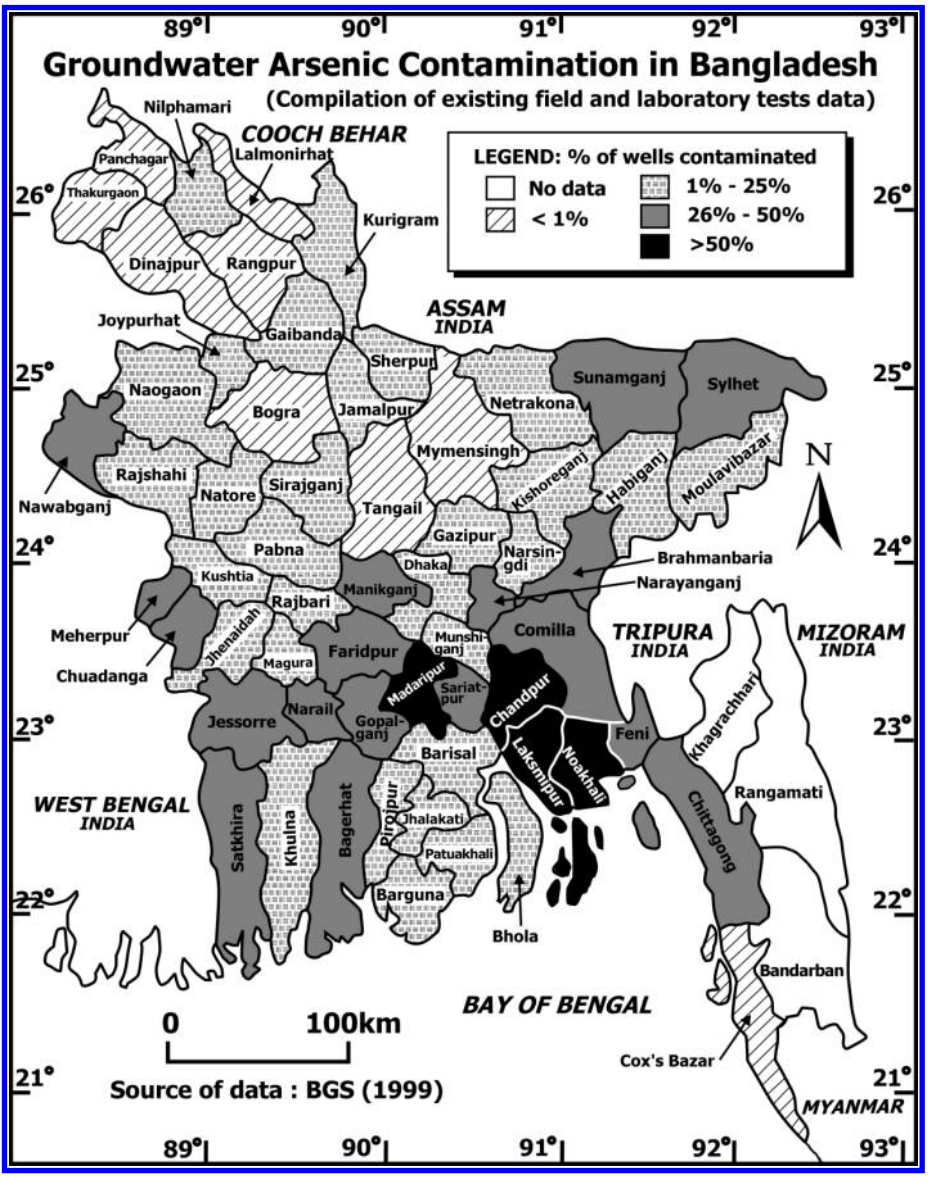


Figure 1. Groundwater arsenic contamination in different districts of Bangladesh based on compilation of field and laboratory test data (after Fazal et al., 2001a).

3 POPULATION EXPOSED TO ARSENIC CONTAMINATION

Before implementing any arsenic mitigation program, it is important to know the actual extent of arsenic contamination, population exposed and actual arsenic patients in different regions of the country. About population exposed to arsenic contamination, in different articles, different figures are presented ranging from 20 to 90 million out of the total about 130 million people. Only two reports, BGS (1999) and SOES-DCH (2000), estimated this figure and found to be 21 million and 25 million, respectively. However, SOES-DCH estimated the population exposed to arsenic contamination for 43 contaminated districts where 85 million people live. Therefore, if we consider all the 64 districts of the country, the population exposed to arsenic concentrations above the

Copyright © 2003 Swets & Zeitlinger B.V., Lisse, The Netherlands

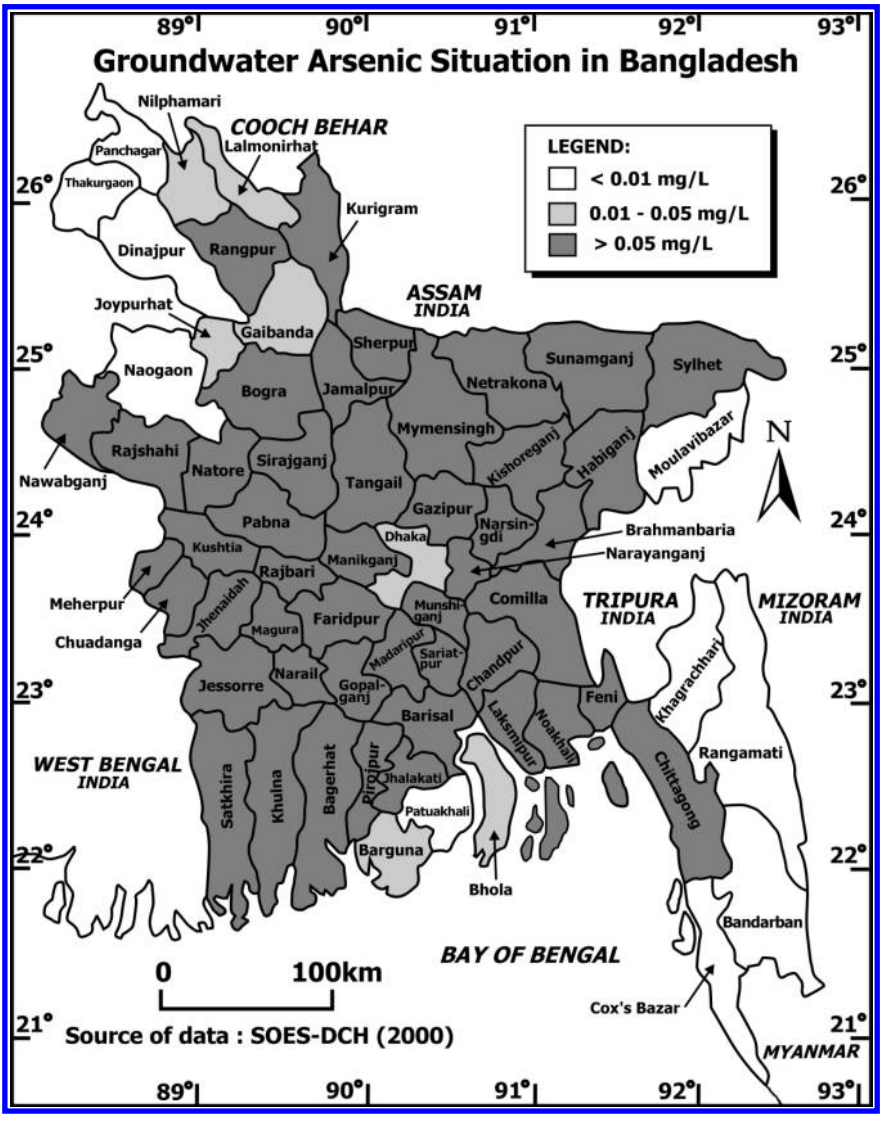


Figure 2. Groundwater arsenic contamination in different districts of Bangladesh (after SOES-DCH 2000).

Bangladesh standard may be as much as around 40 million.

3.1 *Number of arsenic patients*

Dhaka Community Hospital jointly with the School of Environmental Studies and separately worked on this issue. Till February 2000, the water samples from 22,003 hand tubewells of Bangladesh, around 11,000 randomly selected hair, nail, urine and skin scale samples from 1,063 affected villages were analyzed in laboratory under the SOES-DCH survey. The presence of high-level arsenic was detected in 53.47% samples of water, 83.15% samples of hair, 93.77% samples of nail and 95.11% samples of urine. People identified having skin lesions were 20.6% (SOES-DCH, 2000). Altogether some thousands of arsenic patients and 40 deaths due to arsenic related diseases were identified by the SOES-DCH survey only from the 241 affected villages. There are altogether 68,000 villages in the country of which at least 25,000 may be arsenic affected. The percentage of identified arsenic patients seems to be higher than the national average, since the selected villages were biased towards more

Copyright © 2003 Swets & Zeitlinger B.V., Lisse, The Netherlands

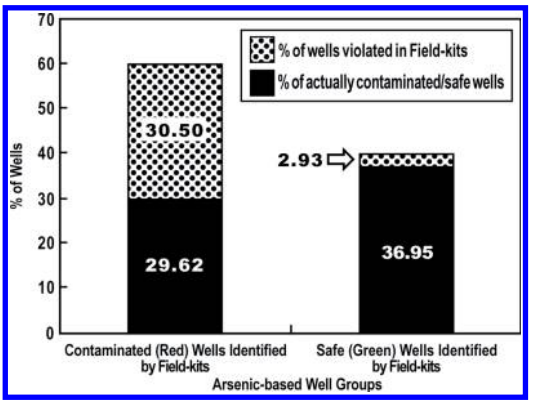


Figure 3. Comparison between actual percent of wells contaminated and percent of wells violated by field-kit measurement (after Fazal et al., 2000b).

affected areas. But the true situation may be different; as described in the report, only a small percentage of the true patients in the affected areas were possible to be identified as patients due to many social constraints. Another detailed survey of DCH which covered 500 arsenic affected villages of Bangladesh shows that 52.17% tubewells are contaminated, 56.15% of the total population (of affected 500 villages) is at risk and identified arsenic patients are 0.28% of the total population of surveyed villages (DCH, 2000). Therefore, there is a large variation in the arsenic patients, and it is very hard to gauge how many actual arsenic patients are present in the country. Only a detailed survey of all of the affected regions can give the answer.

3.2 *Treatment of affected population*

Unfortunately there is no specific treatment for chronic arsenicosis. Stopping further intake of arsenic contaminated water and taking arsenic free water improve the cases. Recent report of DCH (2000) states that chronic arsenicosis do not cure, but the symptoms are reversible up to certain point. Though the Bangladesh Government takes steps to identify affected populations, the government is not providing medical assistance to the identified patients. The first advice to the identified patients should be to stop taking arsenic contaminated water. However, wrongly detecting arsenic contaminated tubewells by the field-kits method may worsen the condition of arsenic patients.

4 CAUSES OF ARSENIC CONTAMINATION IN BANGLADESH

It is recognized that the source of arsenic in Bangladesh is naturally occurring geological deposits. Two main hypotheses are prevailing to describe the cause (mobilization) of arsenic into groundwater. These are: (a) pyrite oxidation and (b) oxy-hydroxide reduction.

4.1 *Pyrite oxidation hypothesis*

Arsenic is assumed to be present in certain sulphide minerals (pyrites) that are deposited within the aquifer sediments. Due to the lowering of water table below deposits, arseno-pyrite oxidized in the vadoze zone releases arsenic as arsenic adsorbed on iron hydroxide. During the subsequence recharge period, iron hydroxide releases arsenic into groundwater. According to this hypothesis the origin of arsenic rich groundwater is man-made.

4.2 *Oxy-hydroxide reduction hypothesis*

Arsenic is assumed to be present in alluvial sediments with high concentration in sand grains as a coating of iron hydroxide. The sediments were deposited in valleys eroded in the delta when stream base level was lowered due to sea level drop during the last glacial advance. The organic matter deposited with the sediments reduces the arsenic bearing iron hydroxide and releases arsenic into groundwater. According to this hypothesis, the origin of arsenic rich groundwater is due to a natural process, and seems that the arsenic in groundwater has been present for thousands of years without being flushed from the delta.

Using the 'Oxy-hydroxide Reduction' hypothesis to describe the mobilization of arsenic from the source to the groundwater for Bangladesh basin was first proposed by Nickson et al. (1998). Nickson was highly criticized for showing an unrealistic high percentage of organic carbon content (6%) in the aquifer sediments of the Bangal basin to support oxy-hydroxide reduction. The British Geological Survey (BGS) made an investigation to identify the cause of groundwater arsenic contamination in Bangladesh. Based on their findings they rejected pyrite oxidation and accepted oxy-hydroxide reduction hypothesis. However, they have neither studied pyrite oxidation nor oxy-hydroxide reduction properly with accurate field data. They have used space–dependent relationships to reject pyrite oxidation. Space–dependent relationships of different hydro-geological parameters for the heterogeneous aquifer system are not valid to represent time–dependent phenomenon. For example, for a particular location there is no doubt that the relationship of aquifer water level and water abstraction would be significant positive, but it is possible to have the significant negative relationship for these same parameters in spatial-domain. Moreover, the key parameter of their analysis, percentage of wells contaminated, is erroneous due to field-kits measurements. On the other hand, to support oxy-hydroxide reduction hypothesis they used the relationships of some parameters

Copyright © 2003 Swets & Zeitlinger B.V., Lisse, The Netherlands

(for example, pH, Eh data), which were not collected while sampling. Therefore, several experts are opposing their research findings. Other reasons of opposing oxy-hydroxide reduction are: (a) no prior reported arsenic patients before intensive irrigation development period in the country and (b) districts which were arsenic free just few years ago are now becoming contaminated. Though, pyrite oxidation gets more preference, due to long debate on this issue, the actual cause of arsenic contamination in Bangladesh remains dubious.

5 DEVELOPMENT OF PUBLIC AWARENESS

Up to now three international conferences in Bangladesh, and some local and international seminars have been organized by governmental and non-governmental organizations to develop public awareness about the groundwater arsenic contamination. Through these the issue has come into the limelight. In addition to these, some articles have been published in different journals, daily news papers and internet, but mostly in English. No steps were taken to create large-scale public awareness through the mass media like TV and Radio. Therefore, though only a few percentages of people know about this natural disaster while surveying their tubewells, majority are still in the dark.

6 ARSENIC MITIGATION PROGRAMS

The main challenge of the Bangladesh Government is how to provide the millions of arsenic affected people with arsenic free, bacteriologically as well as chemically safe, and aesthetically acceptable alternative source of drinking water. To achieve this goal, the Ministry of Health and Welfare has initiated some action plans. These are:

(a) Identification of arsenic free tubewells in the affected areas.
(b) Identification of arsenic free aquifer basins.
(c) Extent of the potential alternative sources, namely, surface water and rainwater.
(d) Treatment of arsenic contaminated water where no other safe source exits.

However, now we know the extent and nature of works that have been done for the identification of arsenic free tubewells. Identification of arsenic free aquifers require more intensive works, because only some pockets of the upper shallow aquifers are now arsenic free. Whereas, consideration of arsenic free tubewells and aquifers should get more preferences, because the potentiality of surface water and rain-water is limited and treatment of arsenic contaminated water is expensive.

The limitation of the availability of surface water during the dry season and spreading of different water borne diseases through the untreated surface water should be taken into consideration. About rain-water harvesting, Khalequzzaman (2000) mentioned that rainwater is not completely pollution free; to make it drinkable treatment is necessary. Moreover, at present, there are no extra facilities in the houses of Bangladeshi people that are needed to harvest rainwater, and the scope of rainwater harvesting during the dry season is limited due to the non uniform rainfall pattern. He also mentioned that to cope with the arsenic contamination, Bangladesh would have to develop an integrated water resources development plan. The development of a rainwater harvesting plan that is economically and technically feasible for the majority of the people in Bangladesh should be given high consideration as a part of the integrated water resources management plan.

Treatment of arsenic contaminated water may be of different types; small-scale and large-scale. Some small-scale arsenic removal filters that would be affordable for everyone are now under development. But it is expected that a reliable and low-cost filter could be developed. Large-scale arsenic removal plant is expensive and has several merits and demerits. Before implementing any water treatment plan, the assessments of technical as well as economical feasibility for different agro-ecological regions are needed.

The Bangladesh Government is going to implement small water purification plant called Community-based Water Systems (CWS) in rural areas of Bangladesh, which requires a water source; our government is going to dig one pond in every village for this purpose. However, researches on pond water hydraulics, utilization status and feasibility of runoff water harvesting (Islam et al., 1994 and Fazal et al., 1996) show that ponds without any runoff water harvesting facility cannot be used as a man-made source of water, because even in ponds having good soil characteristics pond-water gain (direct rainfall) and pond-water loss (evaporation, seepage & percolation) are just in equilibrium (Figure 4). So if any extra loss (say, 18,000 m^3 per year for a CWS system) is imposed, the pond will be totally empty just after one year. So we have to seek or dig pond with runoff water harvesting facility. Runoff water harvesting depends on many factors: the important one is topographical situation. Survey results of different districts in Bangladesh show that in 25% of ponds runoff water harvesting is impossible, 22% of ponds receive runoff water naturally and in the remaining 53% of ponds runoff water harvesting is possible by making extra facilities (Fazal, et al., 1996). Therefore, in many

Copyright © 2003 Swets & Zeitlinger B.V., Lisse, The Netherlands

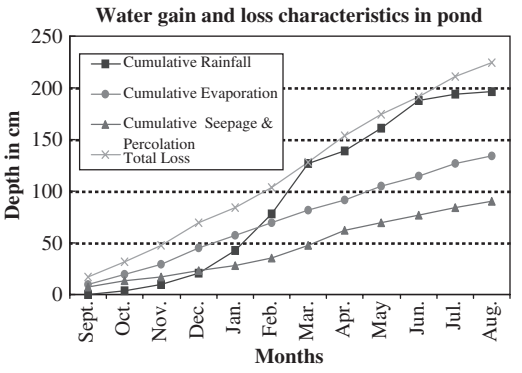


Figure 4. Rainfall received and water losses in the Teknagpara pond of Bangladesh for the period from July 1988 to June 1991 (after Fazal et al., 1994).

places of Bangladesh even if we want to harvest runoff water in pond, it would not be possible. Hence, technically pond is not a feasible water supply source for the community-based water system. Moreover, for runoff water harvesting, deep ponds are required. The average area and depth of ponds in Bangladesh range between 100–150 m^2 and 3–4 m, respectively. If we want to keep 18,000 m^3 runoff water in an average size pond, the depth should be 7–8 m. The net loss or gain in a pond does not depend on area of the pond, for example, in a large area pond, the gain is high and the loss is also high. So, for a very deep pond (i) the excavation cost is high, (ii) there is a possibility of seepage of arsenic contaminated water from the upper shallow aquifer to the pond and (iii) there is a possibility of land subsidence. To prevent arsenic contaminated groundwater intrusion and land subsidence, the banks and bottom of the pond should be lined with concrete. In this case, a very high cost will be required and the system may not be economically feasible. Therefore, before implementing this program the Government should consider these important factors.

7 CONCLUSIONS

The groundwater of Bangladesh is highly contaminated with arsenic. The Government of Bangladesh took different necessary actions to provide safe water to its millions of affected people and to remedy this natural disaster. Many organizations are working on this issue. However, due to the lack of coordination among the different organizations, compared to the extent and severity of the problem, little works have been done. Moreover, the quality of works is questionable. To cope with this problem, coordination among the different organizations that follow the same objectives and methodologies is strongly needed.

8 RECOMMENDATIONS

To mitigate groundwater arsenic contamination problem in Bangladesh, the following factors should be taken into consideration:

(a) To get a clear and accurate picture of groudwater arsenic contamination in Bangladesh, a coordinated nation-wide survey of all drinking wells water and some sampled irrigation wells water is necessary. Adequate member of samples should be collected without any biasness and they should be analyzed accurately in the laboratory. Since field-kits results are erroneous, these should be avoided. Mitigation of arsenic contamination depends on accurate identification of the contaminated wells.
(b) The cause of arsenic contamination should be investigated thoroughly using reliable field data.
(c) To get the number of patients suffering from arsenic related diseases, intensive survey works in all the contaminated regions are necessary.
(d) In the arsenic affected regions, the identification of the arsenic free tubewells as well as aquifers should be given priority.
(e) As in most of areas of the country deep aquifers are almost arsenic free, low-cost, small capacity deep tubewells could be installed as an alternative water source, after investigating the possibility of leaching arsenic contaminated water from the upper shallow aquifer.
(f) Before implementing any arsenic mitigation program, studies on its reliability, and technical as well as economical feasibility for different environmental regions of the country should be done.

REFERENCES

B.G.S. (British Geological Survey), 1999. Groundwater Studies for Arsenic Contamination in Bangladesh, *Main Report*, Government of the Peoples Republic of Bangladesh, Ministry of Local Government, Rural Development and Cooperatives; Department of Public Health Engineering, Dhaka, Bangladesh and Mott MacDonald International Ltd., UK.

D.C.H. (Dhaka Community Hospital), 2000. Arsenic in Bangladesh: *Report on the 500-Villaee Rapid Assessment Project*, Dhaka, Bangladesh.

Fazal, M.A., M.H. Rashid, M.S. Islam and M.A.K. Mridha, 1996. Utilization of Ponds in Bangladesh: A Case Study. *Bangladesh Journal of Agricultural Research*, 21(1), 80–88.

Fazal, M.A., T. Kawachi and E. Ichion, 2001a. Extent and Severity of Groundwater Arsenic Contamination in Bangladesh. *Journal of Water International*, 26(3), 370–379.

Fazal, M.A., T. Kawachi and E. Ichion, 2001b. Validity of the Latest Research Findings on Causes of Groundwater Arsenic Contamination in Bangladesh, *Journal of Water International*, 26(3), 380–389.

Copyright © 2003 Swets & Zeitlinger B.V., Lisse, The Netherlands

Islam, M.S., M.H. Rashid, M.A. Fazal and N.N. Karim, 1994. An Assessment of Pond-water Availability in Joydebpur Area, *Journal of Institution of Engineers*, Bangladesh, 22(2), 47–52.

Kalequzzaman, M., 2000. Can Rainwater Harvesting be a Solution to Drinking Water Problem in Bangladesh?, Article published in the Website: http ://www. damichi-consul.co.jp/english/ arsenic/article/rain-water.htm

Nickson, R., J. McArther, W. Burgess, K.M. Ahmed, P. Ravenscroft and M. Rahman, 1998. Arsenic Poisoning of Bangladesh Groundwater, *Nature*, 395, 338.

SOES-DCH, 2000. Groundwater Arsenic Contamination in Bangladesh. *A. Summary of 239 Days Field Survey from August 1995 to February 2000, B. Twenty Seven Days Detailed Field Survey Information from Apri1 1999 to February 2000.* School of Environmental Studies, Jadavpur University, Calcutta 700 032, India and Dhaka Community Hospital, Dhaka 1217, Bangladesh.

Copyright © 2003 Swets & Zeitlinger B.V., Lisse, The Netherlands

Nitrate pollution in groundwater in the lower reach of the Yellow River, case study in Shandong Province, China

J. Chen
Graduate School of Science and Technology, Chiba University, Japan
Institute of Geographic Sciences and Natural Resources Research, Chinese Academy of Sciences, China

C. Tang, Y. Sakura & Y. Shen
Graduate School of Science and Technology, Chiba University, Japan

ABSTRACT: Yucheng and Qihe counties in the lower reaches of the Yellow River tended to be an important agricultural area after the Yellow River water was diverted in 1972. Field surveys and sampling were implemented in the area to examine the nitrate pollution of groundwater, which is recharged dominantly by the diverted water. Nitrate pollution was found to have occurred in the shallow layer of less than 8 m in depth with the highest concentration of more than 200 mg/l. Though nitrate content was found in the Yellow River ranging from 16.3 to 37.1 mg NO_3/l, it was not found in the canal, ditch and pond used to convey and store the diverted water, excluding the N source from the Yellow River. ^{15}N was measured to identify the nitrogen of anthropogenic and fertilizer/soil organic sources. The upward potential gradient of the saturated zone observed in the piezometers at Yucheng Experimental Station, the occurrence of ZFP at 120 cm depth, and denitrification process deduced from the change in $\delta^{15}N$ and SO_4 concentration helped explain why NO_3 was found only in the shallow layer of the aquifer.

1 INTRODUCTION

Nitrate pollution in groundwater is a big concern in the world due to its toxicity to the human health, especially to the newly born baby, and the standard of 45 mg NO_3/l (or 10 mg N/l) was established for the drinking water by WHO (Follet, 1989). Nitrogen from either natural source (rainfall, geologic deposit, forest, forage, pastoral agriculture and etc.) or anthropogenic source (fertilizer, waste material and etc.) may undergo the following processes (Komor and Anderson, 1993).

Mineralization–immobilization: the process between soil organic N and NH_4^+

Fixation: Symbiotic and non-symbiotic N_2 fixation by plant

Nitrification: the microbial oxidation of ammonium to nitrite NO_2^- and further to nitrate NO_3^-, and

Denitrification: combined N returns to the atmosphere as gaseous N (N_2, nitrous oxide N_2O, nitric oxide NO, nitrogen dioxide NO_2).

Stable isotopes, such as ^{18}O and ^{15}N are useful in identifying the sources and the above processes (Shearer, Kohl and Chien, 1978; Mariotti, Landreau & Simon, 1988; Börrcher et al., 1990).

The study area, including Qihe and Yucheng counties, is located in the semi-arid zone to the north of the Yellow River in between 116°22′–117°37′E and 36°24′–37°12′ N with an area of about 2500 km^2. This area is a discharge zone in terms of groundwater flow system and the crop could not be grown due to the high salinity on top of soil. It was reclaimed by diverting the Yellow River in 1972, and became an important agricultural area for winter wheat and summer maize. About $6–9 \times 10^8$ m^3 of water is diverted annually from the Yellow River, which was found to have a nitrate concentration of 16.8 mg/l (Chen et al., 2001). Fertilizer is applied at an average rate of about 300 kg N/ha for the growing season of wheat. The excessive application of fertilizer, as well as the nitrate content in the water from the Yellow River increases the risk of nitrate pollution in the groundwater, which is taped mostly in the depth of about 5–20 m and used by local farmers as drinking water without any treatment.

The objective of the study is to examine the sources and the depth of nitrate-polluted groundwater in the lower reach of the Yellow River based on the field surveys and observations in situ in the study area.

Copyright © 2003 Swets & Zeitlinger B.V., Lisse, The Netherlands

2 MATERIAL AND METHODS

Surface water and groundwater samples were collected seasonally from the study area from May 2000 to April 2001 with the help of GPS (global position system). 63 groundwater samples from wells with depths from 3.5 to 70 m and four surface water samples collected in Dec. 2000 were used for the subsequent analyses (Figure 1). Four surface water samples were from the Yellow River near the entrance to the diversion canal, a pond used for storing diverted water, the ditch near Yucheng Experimental Station and the Tugai River, which is located about 100 km to the north of the Yellow River. The electrical conductivity (EC), pH, temperature and groundwater depth were measured in situ.

Chemical components of NO_3^-, SiO_2, Cl^-, and SO_4^{2-} were analyzed by ion chromatography (Shimadzu), Na^+, K^+, Mg^{2+}, Ca^{2+} by Inductively Coupled Plasma (ICPS-1000 III C, Shimadzu), and HCO_3^- by titration (pH 4.8 alkalinity). ^{15}N was analyzed by using the Delta S in Chiba University following a standard procedure, i.e., transformation of NO_3 to $(NH_4)_2SO_4$, the speciation of N_2 from the reaction of KOBr and $(NH_4)_2SO_4$ and the purification of N_2 gas through a vacuum glass line. Information such as groundwater usage, well depth, screen depth, land use etc was collected by interviews with well managers or farmers.

A series of piezometers (wells) with depths of 4, 5, 6, 8 and 10 m respectively were set at Yucheng Experimental Station in Sept. 2000 to determine the groundwater movement. Water samples were collected since then every month. Soil water samples with depths of 30, 50, 70, 90, 120, 150 and 200 cm were collected twice per month by means of the vacuum method. These samples were analyzed for the chemical components indicated above. The water table or potential (zero at surface datum, negative downward) was measured every three days manually in the piezometers, as well as soil water suction in tensiometers located adjacent to porous cups for collecting soil water samples.

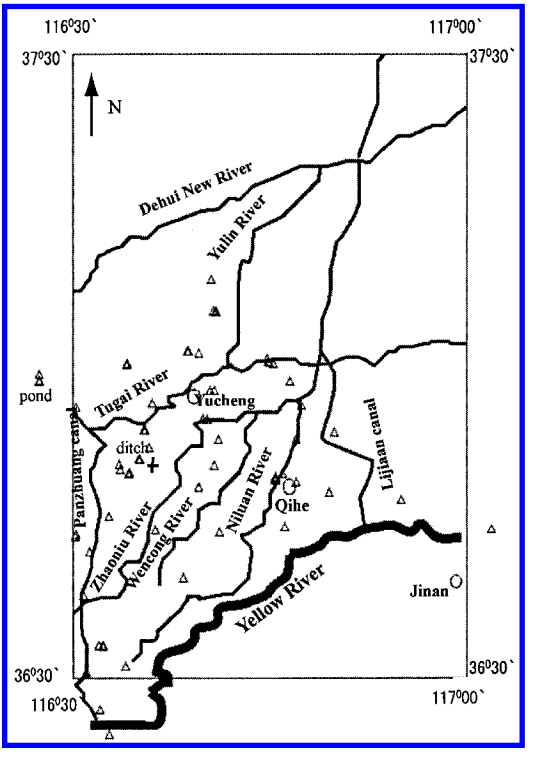


Figure 1. Sampling locations (Δ) in the study area (+ Yucheng Experimental Station of Chinese Academy of Sciences).

3 RESULTS

Four samples of different seasons from the Yellow River were found to have a concentration of NO_3 ranging from 14.7 to 37.1 mg/l (Table 1). On the other hand, the surface water samples from the pond and ditch were found to be free of nitrate. The denitrification process along the diversion canal was the possible cause of this phenomenon. Thus, the sources of the nitrate pollution in groundwater in the study area may come from the manure, fertilizer and etc rather than the diverted water from the Yellow River. The Tugai River, now mainly used as the drainage of domestic and industrial wastewater from Liaocheng City, was found to have a high NO_2 concentration of 126.4 mg/l, and a similar level of NO_3 concentration of 31.5 mg/l as that in the Yellow River.

The contents of major ions in groundwater were found stable within the period from May 2000 to April 2001, in contrast to the fluctuation in soil water, reflecting the attenuation effect of the unsaturated zone. Nitrate pollution in the groundwater of the study area occurred only in the shallow layer of less than 8 m in depth (Figure 2). Among 32 wells of this depth, 10 wells were found polluted by nitrate ranging from

Table 1. Concentrations of major ions in the Yellow River near the entrance to Panzhuang Canal (in mg/l).

Time	HCO_3	Cl	NO_3	SO_4	Na	Ca	Mg	K
May 2000	196.7	91.1	16.8	148.5	89.3	56.2	26.1	1.8
Sept. 2000	187.0	89.5	14.7	159.7	78.1	60.6	24.7	8.0
Dec. 2000	224.6	78.5	37.1	179.4	72.7	71.4	29.9	5.3
April 2001	242.9	109.6	16.3	163.5	100	82.0	34.2	5.6

Copyright © 2003 Swets & Zeitlinger B.V., Lisse, The Netherlands

12.6 to 210.3 mg NO_3/l, i.e., about one third of shallow wells were polluted. The average nitrate concentration of the groundwater from the polluted wells is 89.5 mg/l, two times as high as the WHO standard.

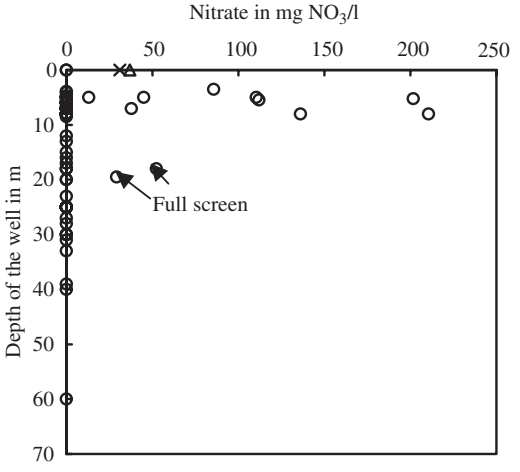


Figure 2. Nitrate concentrations fro the varied well depth in the study area (Δ–the Yellow River, x–the Tugai River, the other two samples of the surface water are shown in (0,0)). Two wells of about 20 m in depth as indicated by the arrow were found to have nitrate because the whole depth was taped.

Several polluted wells are still used by the farmers as the drinking water.

Figure 3 shows the nitrate concentration and δ^{15}N for the wells under the varied land use or background. Groundwater beneath the vegetable garden within the residence area was found to have the highest NO_3 because manure and urine was intensively applied to grow vegetables. δ^{15}N for this source was found to be in the range of 10–20‰ which was close to the range of 10–22‰ given by Kreitler (1975) for final isotopic composition of nitrates resulting from the decomposition of animal waste. The enrichment of ^{15}N for two groundwaters beneath the poultry farm and cattle field reaches a high level of 27.0‰ and 32.5‰ respectively, which was presumed to be the result of denitrification and/or ammonia volatilization of animal waste. However, this enrichment is much higher than that of $^{15}N_{NO_3-N_2} = 20‰$ given by Wada et al. (1975) and 15.9‰ by Börrcher et al. (1990). Commercial fertilizers have generally δ^{15}N close to 0‰, as they originate from the atmosphere. Gormly and Spalding (1979) observed the resultant nitrate with δ^{15}N of -1.1 ± 1.0‰. Natural soil organic-N in the field was found to have δ^{15}N ranging from 2 to 9‰ (Heaton, 1986; Kreitler, 1975). Thus, groundwaters and soil waters with δ^{15}N less than 10‰ in the study area were assumed to have the nitrogen sources from either fertilizers or soil organic-N, which is to be

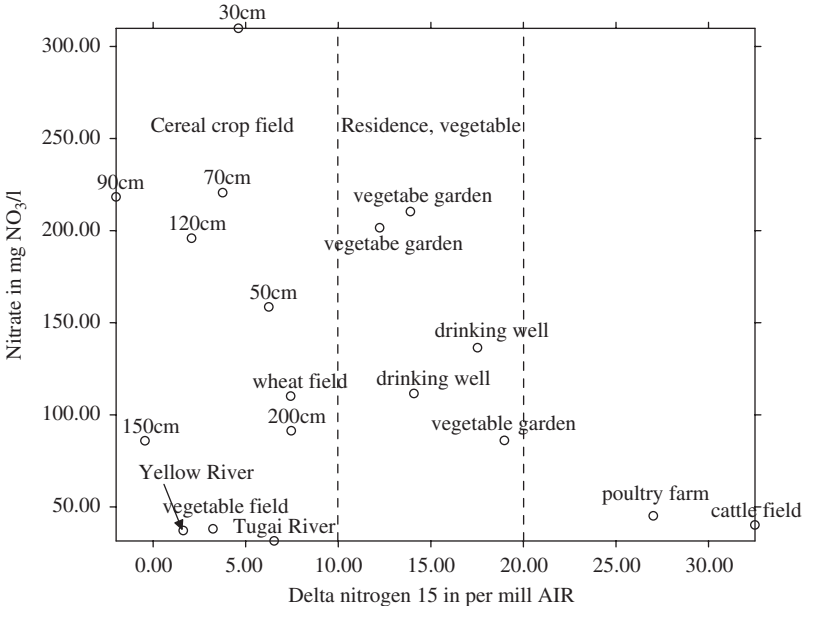


Figure 3. Nitrate concentration and δ^{15}N (delta nitrogen 15) for different nitrogen sources and land use. δ^{15}N for the anthropogenic waste ranges in between 10‰ and 20‰ AIR, it is less than 10‰ AIR for soil organic N and fertilizer, and it is very high for the two wells just beneath the poultry farm and cattle field. Two drinking wells are close to the waste drainage. 30 cm, 50 cm . . . are referred to the soil water at the depths of 30 cm, 50 cm . . . respectively.

Copyright © 2003 Swets & Zeitlinger B.V., Lisse, The Netherlands

discussed in details in the vertical profile of the subsequent section. Surface water from the Yellow River and the Tugai River was found to have a low $\delta^{15}N$, which may come from the combination of fertilizers and soil organic-N.

4 DISCUSSIONS

Nitrogen cycle, i.e., N circulation in different N-bearing compounds through various environments, is closely related to water movement in the continuum of ground water, soil, plant and atmosphere. Nitrate pollution in the study area mainly occurs in the shallow layer of less than 8 m with the highest content of NO_3 more than 200 mg/l as shown in Figure 2. The reasons that nitrate concentrates in the shallow layer are to be examined with the vertical profile of concentrations of major ions and $\delta^{15}N$, and the change of the potential in both the unsaturated and saturated zones from 0.3 to 10 m at Yucheng Station of Chinese Academy of Sciences.

The groundwater table fluctuates due to rainfall and/or diverted water from the Yellow River in this region, enabling strong interaction between groundwater and soil water that is high in nitrate content. The diverted water is pumped directly for irrigation from widely distributed canals, and the groundwater is supplied either from percolation due to the irrigation or seepage from the canals and reused when there is no water available from the Yellow River. Water inputs from the Yellow River speeds up the water movement in this zone. Even though nitrate is rather high in the shallow layer, it does not go down further due to the upward water head gradient, i.e., groundwater of the deep layer is moving up in the discharge zone, which can be verified by the measured groundwater potential of different layer at Yucheng Station (Figure 4). On the other hand, a zero flux plane (ZFP) of conversion was found frequently at a depth of 120 cm (Chen et al., 2002), which functions to keep the solute from flowing generally down to the deeper layer. As a result, nitrate was not detected for the layers of deeper than 5 m at Yucheng Station (Figure 5).

There are two peaks for SO_4 concentration at the depth of 120 cm and 200 cm as given in Figure 5, while there is only one for NO_3 at the depth of about 70–90 cm, reflecting the different order of ion absorption. The high concentration of SO_4 at the depth of 120 cm corresponds well to the frequent occurrence of ZFP at this depth. When the conversion type of ZFP occurs, soil water above ZFP moves down while it moves up beneath ZFP, i.e., ZFP acts as a barrier for the downward movement of solute. The profile of $\delta^{15}N$ shows that the source of soil organic N occurs at 30–70 cm and 200 cm depth, while the source of fertilizer at the depths of 90–150 m. It is shown in

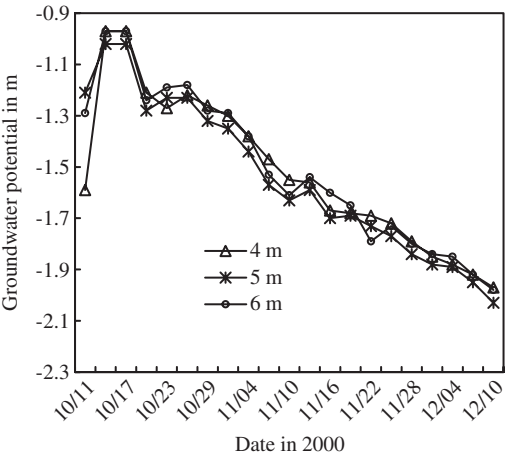


Figure 4. Change of water potentials of the piezometers at the depth of 4, 5 and 6 m at Yucheng Station. (The potential is set to be zero at surface and negative downward, and groundwater moves from high to low potential.)

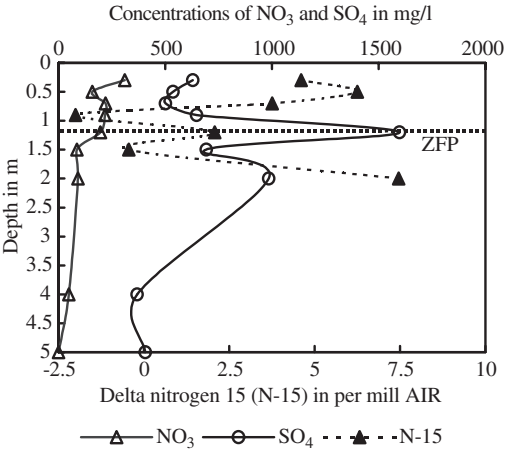


Figure 5. Concentrations of NO_3, SO_4 and $\delta^{15}N$ VS the depth of the sampled water (in Oct., 2000) along the vertical profile at Yucheng Station.

Figure 5 that $\delta^{15}N$ decreases generally as soil moisture moves either downward for the layer above ZFP or upward for the layer beneath ZFP, implying that the fertilizer source N could move in an easier way than soil organic N. Shallow groundwater depth and high soil moisture content near ZFP indicate an environment of limited oxygen suitable for the reduction of NO_3 to gaseous N. The concentration of SO_4 increases from 90 cm to 120 cm depth, and 150 cm to 200 cm depth, forming two peaks along the vertical profile. That both SO_4 and $\delta^{15}N$ increase for the intervals of the above depth is a good evidence for denitrification,

Copyright © 2003 Swets & Zeitlinger B.V., Lisse, The Netherlands

which may occur according to (Börrcher et al., 1990; Korom, 1992; Clark and Fritz, 1997):

$$5FeS_2 + 14NO_3^- + 4H^+ = 7N_2 + 10SO_4^{2-} + 5Fe^{2+} + 2H_2O \quad (1)$$

This reaction is mediated by the bacteria known as Thiobacillus denitrificans (Kölle et al., 1985). That the groundwater in the study area is rich in Fe^{2+}/Fe^{3+}, which can easily be observed from the rusty surface of local hygiene apparatus, confirms on the other hand this process. Nitrate content at 200 cm did not decrease as expected from the above reaction, indicating that the profiles of nitrate and $\delta^{15}N$ were formed as a comprehensive result of moisture and solute movement derived from the change of potential, and denitrification derived from the chemical and microbiological activity.

5 CONCLUSION

The excessive application of commercial fertilizers, manure, and etc in the study area caused the nitrate pollution in the shallow groundwater of less than 8 m depth with the highest concentration of more than 200 mg NO_3/l. ^{15}N was used for identifying the anthropogenic and fertilizer/soil organic N sources, while two wells just beneath the poultry farm and cattle field showed an extreme enrichment of ^{15}N, which was assumed to be the result of denitrification and/or ammonia volatilization of animal waste. No nitrate was found in the ditch and pond, which are used to convey and store the water from the Yellow River though it was found in the river water. Thus, nitrate from the Yellow River was excluded from possible sources of nitrate pollution in the groundwater. Denitrification process along the vertical profile from the evidence of ^{15}N and SO_4 in the soil water, the occurrence of ZFP at 120 cm depth, and the upward potential gradient are the main reasons that NO_3 was found only in the shallow layer of the aquifer.

ACKNOWLEDGEMENT

The authors gratefully acknowledge grant-in-aid for scientific research from the Ministry of Education, Culture, Sports, Science and Technology of Japan, (B)(2) 12480146, 2000 and (B)(2) 13480152, 2001 and fund from the Ministry of Sciences and Technology of China, G19990436-01 (National 973 project). They are also grateful to the constructive advice and the help in the field survey from Yucheng Experimental Station, Chinese Academy of Sciences, which also provided a special fund for this study.

REFERENCES

Börrcher, J., Strebel, O., Voerkelius, S., & Schmidt, H.L. 1990. Using Isotope fraction of nitrate-nitrogen and nitrate-oxygen for evaluation of microbial denitrification in a sandy aquifer. *J. of Hydrology*, 114: 413–424.

Chen, J.Y., Tang, C.Y., Sakura, Y., Kondoh, A., & Shen, Y. 2002. Measurement and analysis of redistribution of soil moisture and solute in a maize field in the lower reach of the Yellow River. Unpublished.

Chen, J.Y., Tang, C.Y., Sakura, Y., Kondoh, A., Shen, Y.J., & Ouyang, Z. 2001. The impacts of diversion from the Yellow River on the local aquifer – case study in Shandong Province, China. In: Seiler, K.P., Wohnlich, S. (eds). *New Approach Characterizing Groundwater Flow*: 1143–1147, A.A. Balkema Publishers, Lisse.

Clark, I.D., & Fritz, P. 1997. 148–154. *Environmental Isotopes in Hydrogeology*. Lewis Publishers: Boca Raton, New York.

Follett, R.F. 1989. Ground water quality concerns about nitrogen, In Follett, R.F. (ed): *Nitrogen Management and Ground Water Protection*: 1–34, Elsevier.

Gormly, J.R., & Spalding, R.F. 1979. Sources and concentrations of nitrate-nitrogen in groundwater of the Central Platte region, Nebraska. *Groundwater*, 17: 291–300.

Heaton, T.H.E. 1986. Isotopic studies of nitrogen pollution in the hydrosphere and atmosphere: a review. *Chem. Geol*., 59: 87–102.

Komor, S.C., & Anderson, H.W. Jr. 1993. Nitrogen isotope as indicators of nitrate sources in Minnesota sand-plain aquifers. *Groundwater*, 31: 260–270.

Korom, S. 1992. Natural denitrification in the saturated zone, a review. *Water Resources Research*, 28: 1657–1668.

Kreitler, C.W., & Jones, D.C. 1975. Natural soil nitrate: the cause of the nitrate comtamination of groundwater in Runnels County, Texas. *Groundwater*, 13: 5–13.

Kölle, W., Streble, O., & Börrcher, J. 1985. Formation of sulfate by microbial denitrification in a reducing aquifer, *Water Supply*, 3(1): 35–40.

Mariotti, A., Landreau, A., & Simon, B. 1988. ^{15}N isotope biogeochemistry and natural denitrification process in ground water: Application to the chalk aquifer of northern France. *Geochimica et Cosmochiimica Acta*, 52: 1869–1978.

Shearer, G., Kohl, D.H., & Chien, S.H. 1978. The nitrogen-15 abundance in a wide variety of soils. *Soil Sci. Soc. AM. J*., 42: 899–902.

Wada, E., Kadonaga, T., & Matsuo, S. 1975. ^{15}N abundance in nitrogen of naturally occurring substances and global assessment of denitrification from isotopic view point. *Geochemical Journal*, 9: 139–148.

Copyright © 2003 Swets & Zeitlinger B.V., Lisse, The Netherlands

Some considerations on the restorative effectiveness and efficiency of the groundwater pumping in impervious wall

K. Aoki
Osaka Institute of Technology, Osaka, Japan

K. Hioki, K. Harada & M. Yamamoto
Fudo Construction Co., Ltd., Tokyo, Japan

ABSTRACT: In order to find a simple way to estimate the restorative effect of pumping ground water in a section of ground sealed with an impervious wall of steel sheet piles and so on, unsaturated seepage column tests using a solution of TCE solvent or salt water were carried out and various observations made. The results showed that the restorative effect of pumping ground water is dependent on the degree of saturation of the contaminated ground and may be evaluated quantitatively from the water retention curve of the ground. Further, as a measure to improve the restorative effectiveness in clayey ground, the formation of 'water courses' using a sand pile method of ground improvement (sand drain method) was considered, and improvement in restorative effectiveness was estimated from a saturated–unsaturated seepage analysis. The results showed that the restorative efficiency was improved by the groundwater pumping method with sand piles.

1 INTRODUCTION

To extract and eliminate contaminants such as volatile organic compounds from disused industrial sites and other contaminated land, the groundwater pumping method or soil vapor extraction method, for saturated or unsaturated ground respectively, are frequently used. However, their restorative effectiveness (extraction/elimination degree of contaminants) and efficiency are greatly influenced by the ground conditions.

In order to suggest a simple method to estimate the restorative effectiveness of groundwater pumping in an impervious wall (steel sheets and so on) creating the unsaturated condition, unsaturated seepage column tests using TCE solvent solution as a non-electrolyte contaminant and salt water as an electrolyte one were carried out. This method, however, is limited to condition where the contaminated concentration is uniform and the existence of the plume is left out of consideration. In addition, from a two-dimensional saturated–unsaturated seepage analysis, a quantitative evaluation of restorative effectiveness and efficiency was attempted for a range of different ground conditions. Furthermore, the forming of 'water courses' in clayey ground through the installation of sand pile (sand drain method) was considered as a means to improve restorative efficiency in such ground, and the degree of improvement in restorative efficiency was studied using the same analytical method.

2 A SIMPLE METHOD TO ESTIMATE THE RESTORATIVE EFFECTIVENESS OF USING THE GROUNDWATER PUMPING IN IMPERVIOUS WALL

2.1 *Outline of unsaturated seepage column tests*

When groundwater is pumped from contaminated ground enclosed by an impervious wall, there can be no inflow from the outside and so the ground will be transferred from a saturated to an unsaturated state. Thus, the restorative effectiveness in such a case may be considered dependent on the saturation degree of the ground. In order to verify this, unsaturated seepage column tests were undertaken using the following procedure:

1. Seepage columns 15 cm in diameter and 5 cm in height were filled with soil samples to a determined density, and after injection of carbon dioxide gas, the specimens were saturated with TCE solvent solution (concentration: 10 mg/liter) or salt water (concentration: 10,000 mg/liter).
2. The seepage columns were transferred to an unsaturated state through the application of a set level of suction over a 24-hour period.
3. In the test with TCE solvent solution, the TCE concentration in the unsaturated seepage column was measured according to official law (JIS K 0125 5.1), and its TCE content was determined. In the test

Copyright © 2003 Swets & Zeitlinger B.V., Lisse, The Netherlands

Table 1. Physical properties of used materials.

	Soil A	Soil B	Soil C
Specific density, ρ_s (g/cm^3)	2.75	2.63	2.54
Fines content, F_c (%)	4	20	53
Clay content, C_c (%)	1	6	21
Hydraulic conductivity, k (cm/sec)	1.3×10^{-2}	8.8×10^{-3}	7.2×10^{-5}
Porosity, n	0.460	0.512	0.605

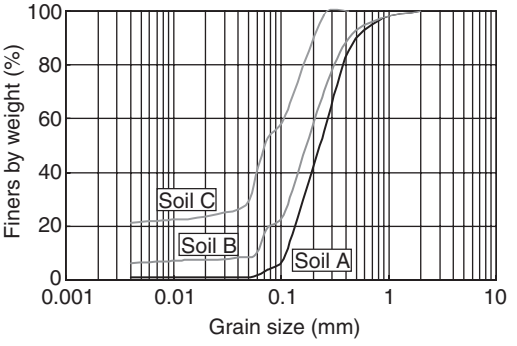


Figure 1. Grain size distribution curves of used materials.

using salt water, pure water was added to the unsaturated specimen, and after forced mixing, sucking and filtrating the salt content was determined from its electric conductivity. The three types of soil used in the column tests are shown in Table 1. They were A: natural sand from Kisarazu, often used as filling in sand drains, B: silty sand, taken from a Tokyo coastal area, C: Kanto loam collected from Sashima-gun, Ibaragi Prefecture. The grain size distribution curves and water retention curves of the used materials are shown in Figures 1 and 2.

2.2 *Test results and considerations*

Figures 3 and 4 show comparisons of the results drawn from the unsaturated seepage column tests and theoretical values based on the assumption that restorative effectiveness is dependent on the saturation degree of contaminated ground, for the TCE and salt tests respectively. The theoretical values were calculated from TC $[SC] = C_{TCE}\,[C_{salt}] \cdot S_r \cdot V \cdot n/100{,}000$, where TC is the TCE content (mg), SC is the salt content (mg), C_{TCE} is the TCE concentration (mg/liter), C_{salt} is the salt solution concentration (mg/liter), S_r is the saturation degree (%), V is the column volume (cm^3) and n is the porosity.

Both TCE content and salt content are shown to correlate well with the saturation degree, but overall the test result values are lower than the theoretical

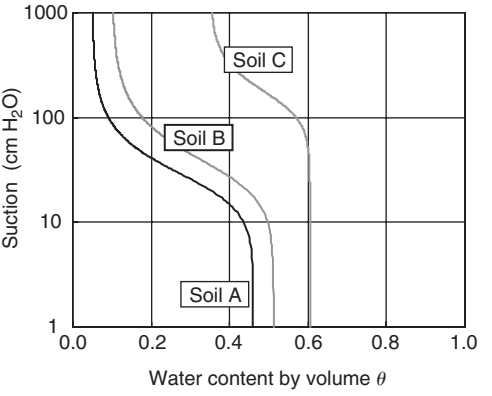


Figure 2. Water retention curves of used materials.

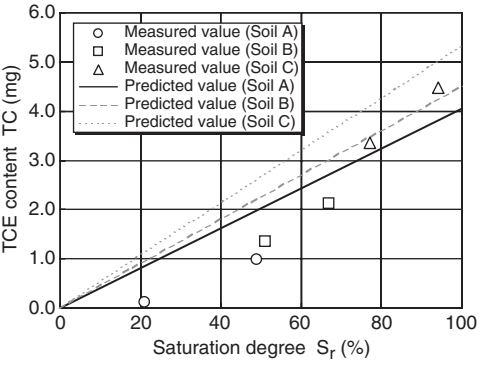


Figure 3. Relationship between TCE content and saturation degree.

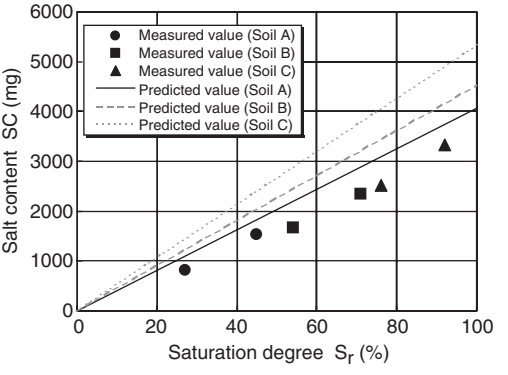


Figure 4. Relationship between salt content and saturation degree.

values. The fact that the volatilizing of TCE is accelerated according to the vapor-liquid equilibrium or the suction may be one factor in this, an explanation backed up by the fact that the difference between the

Copyright © 2003 Swets & Zeitlinger B.V., Lisse, The Netherlands

theoretical values and test results increases as the saturation degree decreases. With regard to the salt content, the adsorption to the soil particles may be one factor because of the fact that the difference between the theoretical values and test results increases for specimens with higher water retention. (In this case, as pure water was used as the cleaning agent, the sodium ion (Na^+) and chlorine ion (Cl^-) adsorbed chemically to the soil particles weren't measured.) In general the greater the retention of the soil, the higher its adsorptive capacity and this can be clarified by undertaking an ion analysis to evaluate the ion adsorption effect.

From this it is clear that the restorative effectiveness of pumping groundwater depends on the saturation degree of the contaminated ground and may be evaluated simply from the water retention curve for that contaminated ground. However the problems of evaluating quantitatively the effect on acceleration of volatilizing and the adsorption to the soil particles are left, for TCE solvent solution and salt water respectively.

3 ESTIMATION OF RESTORATIVE EFFECTIVENESS AND EFFICIENCY THROUGH SATURATED–UNSATURATED SEEPAGE ANALYSIS

3.1 *Estimation of restorative effectiveness and efficiency for different ground conditions*

As has been noted, the restorative effectiveness of pumping groundwater is dependent on the ground's saturation degree and may be evaluated simply from its water retention curve. That being so, the restorative effectiveness can be estimated from saturated–unsaturated seepage analysis. A study was made using two-dimensional saturated–unsaturated seepage analysis, of restorative effectiveness and efficiency for ground samples enclosed by the installation of an impervious wall where the water table is assumed lowered by 10 m (the contaminated concentration is uniform and not taking into account rainwater seepage from the ground surface), as shown in Figure 5(a).

For the analysis, the van Genuchen model (van Genuchen 1980) was used for the water retention curves and the Mualem model (Mualem et al. 1979) for the coefficients of unsaturated permeability. The parameters used in the study are shown in Table 2. Since the restorative effectiveness is dependent on the saturation degree after lowering the water table, the restorative effectiveness in ground C (steady state) for example can be expressed as the oblique line part in Figure 6. Thus, the restorative effectiveness for the ground samples can be estimated as ground A: approx. 80%; ground B: approx. 70%; ground C: approx. 30%. Obviously, the greater the ground's water retention characteristics, the smaller the restorative effectiveness.

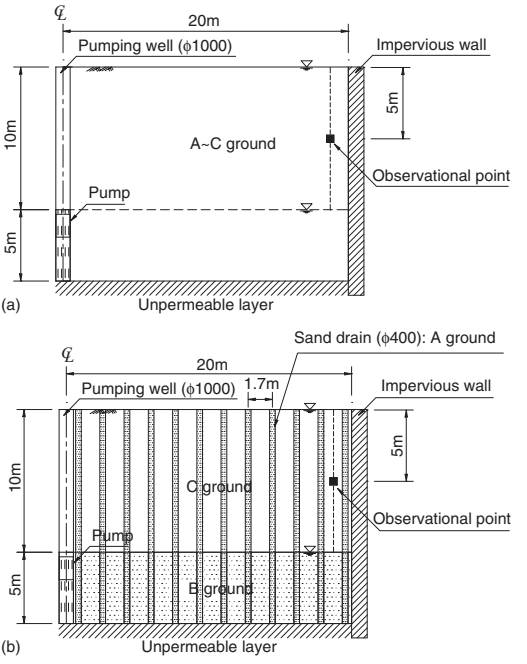


Figure 5. Analytical model.

Table 2. Parameters used in analysis.

	A ground	B ground	C ground
α (cm^{-1})	0.0422	0.0323	0.0058
n	2.60	2.40	2.86
θ_{sat}	0.460	0.512	0.605
θ_r	0.050	0.100	0.350
k (cm/sec)	1.3×10^{-2}	8.8×10^{-3}	7.2×10^{-5}
S_s	1.0×10^{-3}	1.0×10^{-3}	1.0×10^{-3}

θ_{sat}: Saturated water content by volume; θ_r: Minimum water-holding capacity; α, n: Constants; k: Hydraulic conductivity; S_s: Specific storage coefficient.

The restorative efficiency for the ground samples is shown in Figure 7. The restorative efficiency, α, is here assumed to be the 'reduction in the saturation degree at a particular time as a proportion of the maximum reduction in the saturation degree', and α is expressed as

$$\alpha = \frac{(100 - S_r)}{(100 - S_{r(ss)})}$$

where $S_{r(ss)}$ is the saturation degree under steady state. From the figure it is apparent that not only restorative effectiveness but also restorative efficiency is dependent on the ground's water retention characteristics: the

Copyright © 2003 Swets & Zeitlinger B.V., Lisse, The Netherlands

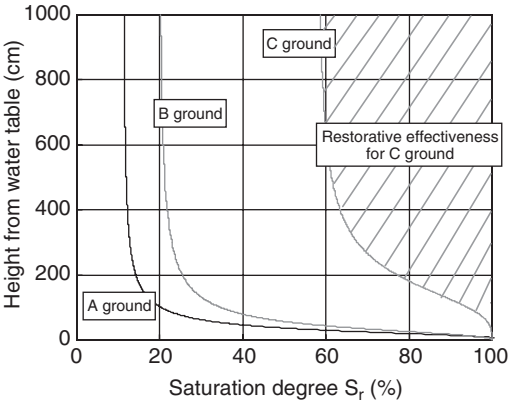


Figure 6. Conceptional figure of restorative effectiveness under steady state.

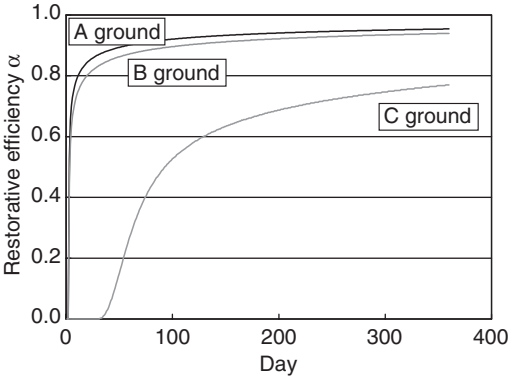


Figure 7. Restorative efficiency for each ground (G.L.−5.0 m).

greater the ground's water retention characteristics, the poorer the restorative efficiency becomes.

3.2 *Measures to improve restorative effectiveness for clayey ground*

As shown in Figure 7, in clayey grounds such as ground C (Kanto loam), restorative efficiency is extremely low. However, in clayey ground where sand piles had been installed (composite ground), existing results of site pumping tests (Achiwa et al. 1996), an inverse analysis based on those results (Hioki et al. 2002), and a saturated–unsaturated seepage analysis from this inverse analysis that took into account identified aquifer parameters, served to confirm the effectiveness of installing sand piles. This conclusion, however, is limited only to ground condition where the sand layer exists below the clayey layer. The following points

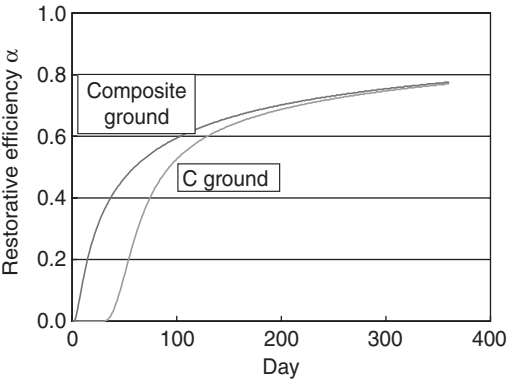


Figure 8. Improvement degree of restorative efficiency (G.L.−5.0m).

were established (Achiwa et al. 1996; Harada et al. 2002; Hioki et al. 2001; Hioki et al. 2002):

1. When the dewatering (deep well) method is applied to composite ground, pumping water from the wells first lowers the water head in the sand layer, and linked to this the water level falls in turn in the sand piles and then the clay layer.
2. As the water level is lowered in the sand piles, a large water level difference (hydraulic gradient) occurs between the sand piles and the clayey layer. The occurrence of this water level difference is thought to be the main factor in the lowering of the water level in the clayey layer.
3. The effect of installing sand piles is considerable, but the effect resulting from differences in the sand pile pitch (in the range 1.4–2.0 m in square arrangement), or in the permeability coefficients of the pile (in the range $k = 1.0 \times 10^{-1}$–1.0×10^{-3} cm/sec) is small.
4. The route of the contaminated water during extraction/elimination is: clayey layer → sand pile → sand layer → pumping well.

From this, the authors considered the formation of 'water courses' by means of a sand drain method of ground improvement, as shown in Figure 5(b), as a means to improve the restorative efficiency in clayey ground, and studied its validity. In order to verify the degree of Improvement in restorative efficiency resulting from (1) the existence of a sandy layer below the clayey layer, and (2) the installation of sand piles in the clayey ground, two-dimensional saturated–unsaturated seepage tests were carried out. (The displacement ratio of the sand piles was small, thus having negligible effect on restorative effectiveness.) A comparison of restorative efficiency in ground C and the composite ground is shown in Figure 8. The elapsed time of the saturation degree due to

Copyright © 2003 Swets & Zeitlinger B.V., Lisse, The Netherlands

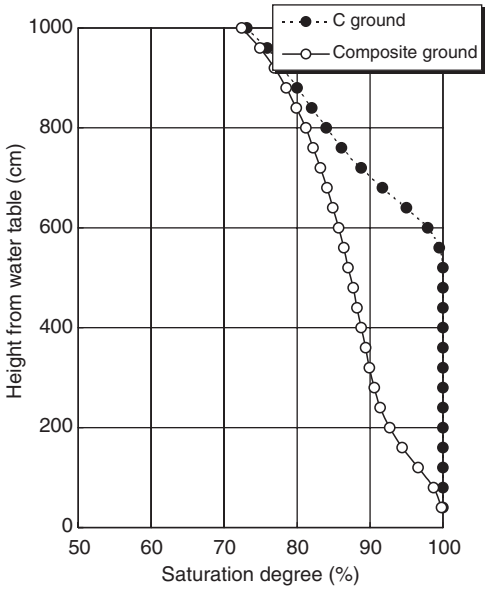


Figure 9. Change of saturation degree due to dewatering (After 30 days).

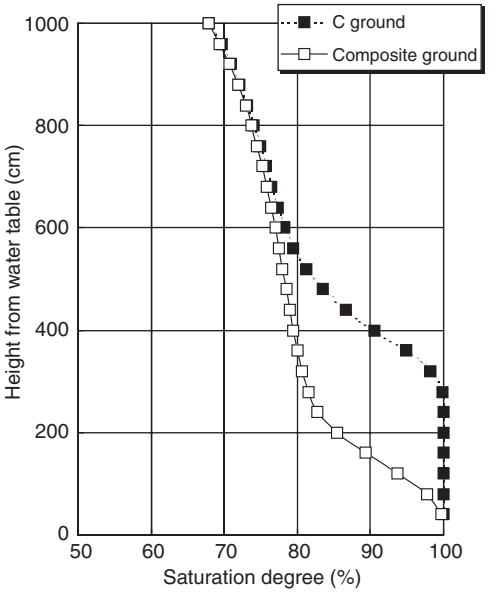


Figure 10. Change of saturation degree due to dewatering (After 90 days)

dewatering is shown in Figures 9–12. These figures show that, the effect of conditions (1) and (2) above, accelerates dewatering within impervious walls and the restorative efficiency is improved.

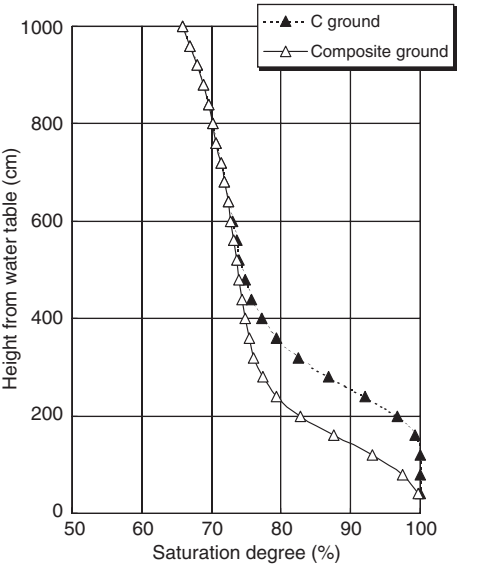


Figure 11. Change of saturation degree due to dewatering (After 180 days)

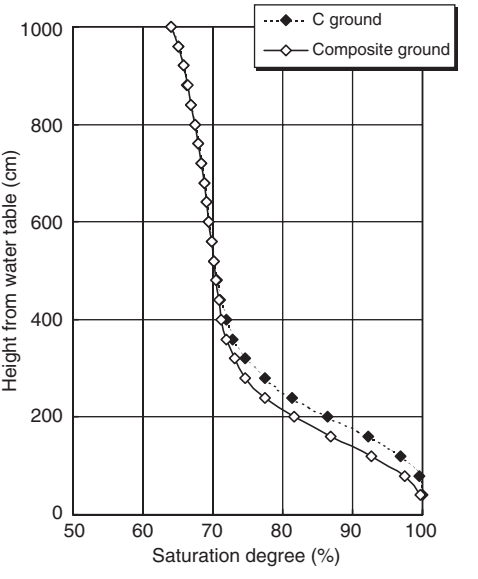


Figure 12. Change of saturation degree due to dewatering (After 360 days)

4 CONCLUSIONS

A study comprised of site tests and theoretical analysis was undertaken to examine the restorative effectiveness and efficiency of transferring a contaminated ground from a saturated to an unsaturated state by

Copyright © 2003 Swets & Zeitlinger B.V., Lisse, The Netherlands

pumping out groundwater in impervious wall. Summaries of the results obtained are given below:

1. It was established that the restorative effectiveness of groundwater pumping in impervious wall creating the unsaturated condition is dependent on the saturation degree of the contaminated ground, and may be evaluated simply from the ground's water retention curve.
2. It was established that the restorative effectiveness and efficiency of groundwater pumping in impervious wall can be estimated quantitatively from a saturated–unsaturated seepage analysis, and is greatly affected by the water retention characteristics of the contaminated ground.
3. As measures to improve the restorative efficiency in clayey grounds, the formation of 'water courses' through the installation of sand piles was considered, and a saturated–unsaturated seepage analysis was carried out. The results showed that the groundwater pumping method with sand piles accelerates dewatering within impervious walls and the restorative efficiency is improved.

However the restorative effectiveness and efficiency shown in this study is based on the results of the simple estimation method and not on detailed study. In order to study in detail, evaluating quantitatively the effect on volatilizing of acceleration according to the vapor-liquid equilibrium or suction and adsorption, for electrolyte contaminants such as TCE and non-electrolyte contaminants such as salt water respectively, must be studied in future.

Finally the restorative effectiveness and efficiency of most restorative technologies are greatly affected by the ground conditions. Thus, to forecast the restorative effectiveness and efficiency, an understanding of the ground conditions is vital. There is therefore a need to carry out adequate ground surveys in the same way as contamination surveys. In some cases, ground improvement by mixing with quicklime would be effective in improving the restorative effectiveness and efficiency of a restorative technology (Ujike et al. 1997).

REFERENCES

Achiwa, F., Yamaguchi, H. and Matsuo, M. (1996) 'Ground Improvement Field Test using a Sand Pile Method Combined with Dewatering', *Japan Society of Civil Engineers*, Paper no. 534/VI-30, pp.31–44 (in Japanese).

Harada, K., Aoki K. and Hioki, K. (2002) 'Identifying Aquifers in Composite Ground and Approach for Design (part 2)', *37th Japan Geotechnical Society Meeting*, Papers, pp.1223–1224 (in Japanese).

Hioki, K., Aoki, K. and Harada, K. (2001) 'Some Observations on the Suitability of the Groundwater Pumping Method for Clayey Ground', *Japanese Association of Groundwater Hydrology, Autumn 2001 Meeting*, Paper Summaries, pp.130–135 (in Japanese).

Hioki, K., Aoki, K. and Harada, K. (2002) 'Identifying Aquifers in Composite Ground and Approach for Design (part 1)', *37th Japan Geotechnical Society Meeting*, Papers, pp.1221–1222 (in Japanese).

Mualem, Y. and Miller, E.E. (1979) 'A Hysteresis Model Based on an Explicit Domain Dependence Function', *Soil Sci. Soc. Am. J.*, Vol.43, pp.1067–1073.

Ujike, M., Higaki, K., Nagafuji, T., Ishii, M. and Okada, K. (1997) 'In Situ Decontamination of Soil Contaminated with Volatile Organic Compounds using Quicklime', *2nd Symposium on Environmental Geotechnology*, Papers, pp.31–34 (in Japanese).

Van Genuchten, M.Th. (1980) 'A Closed-form Equation for Predicting the Hydraulic Conductivity of Unsaturated Soil', *Soil Sci. Soc. Am. J.*, Vol.144, pp.892–898.

Copyright © 2003 Swets & Zeitlinger B.V., Lisse, The Netherlands

Numerical simulation of impact by precipitation on bioremediation process of hydrocarbon-contaminated groundwater

D.J. Song
Chubu-Branch, Kiso-Jiban Consultants Co., Ltd., Nagoya, Japan

A. Katayama
ResCWE, Nagoya University, Nagoya, Japan

ABSTRACT: The biodegradation of organic contaminants in the subsurface has attracted great attention as inexpensive remediation technologies such as *in situ* biodegradation and natural attenuation. Larger variations in the biodegradation rate have been often observed in field than in the laboratory experiments. One of the reasons attributes to this is the inaccurate evaluation of aerobic and/or anaerobic conditions of aquifer, which influences the biodegradation rate greatly. We have simulated the impacts of precipitation pattern on the aerobic and/or anaerobic conditions in aquifer by constructing a three-dimensional transport model and on the bioremediation process of contaminated groundwater with TEXN (Toluene, Ethylbenzene, Xylene and Naphthalene) in a lysimeter. The model described the bioremediation process with Monod nonlinear equations that were the functions of microbial growth and multiple electron acceptors. Based on the results of groundwater analysis, the populations of strict aerobes, facultative nitrate reducers, and anaerobic sulfate reducers were estimated. The Monod parameters were extracted from literature. Precipitation data for four months was inputted into the model in the following patterns: 1) no precipitation, 2) a constant daily precipitation as averaged precipitation value, 3) actual daily precipitation. Without precipitation, dissolved oxygen were soon utilized and depleted, the aquifer became anaerobic, and the nitrate, which had a high concentration of 70 mg/L, became the predominant electron acceptor. When using the constant daily precipitation as input impact, although oxygen was supplied continuously, the surface layer could not maintain an aerobic state because of insufficient supply of oxygen compared to the microbial respiration. But with actual daily precipitation, the change of aerobic/anaerobic state became more dynamic, and even deeper layer became aerobic temporarily. The results demonstrated that the interval and intensity of precipitation were key factors that affect the biodegradation rates in aquifer and these have to be considered in order to achieve a reliable simulation of bioremediation process in field.

1 INTRODUCTION

1.1 *General introduction*

For evaluation of natural attenuation or when designing cost effective and reliable bioremediation technology of contaminated groundwater, the accurate estimation of biodegradation rate of organic contaminants is necessary. However, the biodegradation rate estimated from measured data in field varies widely. For example, Aronson & Howard (1997) reported wide ranges of first-order rate constants of selected petroleum hydrocarbons: 0∼0.0036 day^{-1} for benzene, 0.00099∼0.059 day^{-1} for toluene, 0.00082∼0.021 day^{-1} for *o*-xylene, respectively. This variation results in an uncertainty in the prediction of the period and cost for bioremediation of a contaminated aquifer, or in planning of the monitoring intervals of natural attenuation. The variation of biodegradation rate is mainly due to complex microbial processes and physicochemical properties of aquifer and their temporal changes during the biodegradation. One of the most important reasons of the wide variation is considered to be inaccurate evaluation of aerobic and/or anaerobic conditions in aquifers. Because the respiration rate of aerobes is orderly higher than that of anaerobic microbes, an inaccurate evaluation will lead to a large difference from the actual degradation rate.

In hydrocarbon-contaminated aquifers, the existing dissolved oxygen is rapidly depleted by high respiration rate of aerobes, so that anaerobic state is established in the aquifer. In a typical aquifer, after the depletion of dissolved oxygen, denitrification occurs

Copyright © 2003 Swets & Zeitlinger B.V., Lisse, The Netherlands

first, followed by Mn(IV) reduction, Fe(III) reduction, sulfate reduction and methanogenesis (Wiedemeier et al., 1999). However, when there is precipitation infiltration water, the aquifer may become aerobic temporally and the anaerobic state would not be established.

For shallow aquifers, precipitation influences the aerobic/anaerobic condition by supplying dissolved oxygen, but the influence would not be stable because of the discontinuity and varied intensity in precipitation. The aerobic/anaerobic state in aquifer then would be a function of precipitation interval, intensity, the advective and dispersion influx, and the utilization rate of O_2 in aerobes.

1.2 *Objective of this research*

The objective of this paper is to assess the impacts of precipitation pattern on the aerobic and/or anaerobic conditions in aquifer by constructing a three dimensional transport model and on the bioremediation process of contaminated groundwater with TEXN (Toluene, Ethylbenzene, Xylene and Naphthalene) in a lysimeter. The model described biodegradation processes with Monod nonlinear equations that were the function of microbial growth and multiple electron acceptors. A numerical simulation was carried out using MODFLOW (McDonald, G. & Harbaugh, A. W., 1988) and SEAM3D (Waddill, D.W. & Widdowson, M.A., 1998) for the transport and biodegradation of contaminants, and transport and utilization of the electron accepters.

2 THEORY AND FORMULATION DETAILS

2.1 *Mathematical modeling*

When hydrocarbons such as gasoline leak into subsurface environments, the components like BTEX will be dissolved into groundwater. Considering linear sorption on aquifer material, and neglecting the dissolution, the aqueous phase transport and biodegradation in an aquifer can be described by the advection-dispersion equation, which may be written for each hydrocarbon component as

$$\left(1+\rho_b\frac{K_d}{n}\right)\frac{\partial C_k}{\partial t} = -\frac{\partial}{\partial x_i}(V_i C_k)+\frac{\partial}{\partial x_i}\left(D_{h,ij}\frac{\partial C_k}{\partial x_j}\right)+\frac{Q}{n}C'_k - R_{bio,k} \tag{1}$$

where ρ_b = bulk density of aquifer [ML^{-3}]; K_d = distribution coefficient [L^3M^{-1}]; n = porosity of aquifer; t = time [T]; x_i = distance [L]; C_k = concentration [ML^{-3}] of the hydrocarbon component $k, k = 1, 2, \ldots$ NS (number of components); V_i = pore-water velocity [LT^{-1}]; D_{ij} = tensor for hydrodynamic dispersion coefficient [L^2T^{-1}]; Q = volumetric flux of water per unit volume of aquifer [T^{-1}]; C' = concentration of source/sink term Q [ML^{-3}]; R_{bio} = biodegradation sink term [$ML^{-3}T^{-1}$], considering that microbial populations use hydrocarbons as substrate, which are described by the following relationship,

$$R_{bio,k} = \sum_x \frac{M_x}{n}\sum_{le} v_{x,k,le} \tag{2}$$

$$v_{x,k,le} = v^{max}_{x,k,le}\left[\frac{C_k}{K^S_{x,k,le}+C_k}\right]\left[\frac{E_{le}}{K^S_{x,le}+E_{le}}\right]N_x I_{le,li} \tag{3}$$

where, M = the biomass content [ML^{-3}] of microbial population x, $x = 1, 2, \ldots$ NM (number of microbial population); $v_{x,k,le}$ = specific rate [$M_k M_b^{-1} T^{-1}$] (M_k denotes mass of substrate k, M_b denotes mass of microbial biomass) of substrate utilization for microbial population x growing on substrate k and electron accepter le, $le = 1, 2, \ldots$ NE (number of electron acceptors); $v^{max}_{x,k,le}$ = maximum specific rate [$M_k M_b^{-1} T^{-1}$] of substrate utilization for microbial population x growing on substrate k and electron accepter le, $K^S_{x,k,le}$ = half saturation constant [ML^{-3}] for substrate k utilizing electron accepter le, $K^S_{x,le}$ = half saturation constant [ML^{-3}] for electron accepter le, E_{le} = concentration [ML^{-3}] of aqueous electron accepter le, N_x denotes a function describing nutrient limitations, and $Nx = 1$ when considering no nutrient limitation, respectively. The symbol $I_{le,li}$ = an inhibition function (Widdowson et al., 1988), which is defined by:

$$I_{le,li} = 1 \quad \text{for} \quad le = 1$$
$$I_{le,li} = \prod_{li=1}^{le-1}\left[\frac{\kappa_{le,li}}{\kappa_{le,li}+E_{li}}\right] \quad \text{for} \quad le = 2, 3, \ldots NL \tag{4}$$

where $\kappa_{le,li}$ = electron acceptor inhibition coefficient [ML^{-3}], showing inhibition of use of electron acceptor le by li. It is the concepts that the availability of any electron acceptor (li) may inhibit utilization of others (le) that provide less Gibbs free energy to the microbes.

Neglecting the effects of sorption, the transport of electron acceptor le in aquifer is influenced by the processes of advection, dispersion and utilization of microbial population as represented by

$$\frac{\partial E_{le}}{\partial t} = -\frac{\partial}{\partial x_i}(V_i E_{le})+\frac{\partial}{\partial x_i}\left(D_{h,ij}\frac{\partial E_{le}}{\partial x_j}\right) + \frac{Q}{n}E'_{le} - R^{EA}_{bio,le} \tag{5}$$

Copyright © 2003 Swets & Zeitlinger B.V., Lisse, The Netherlands

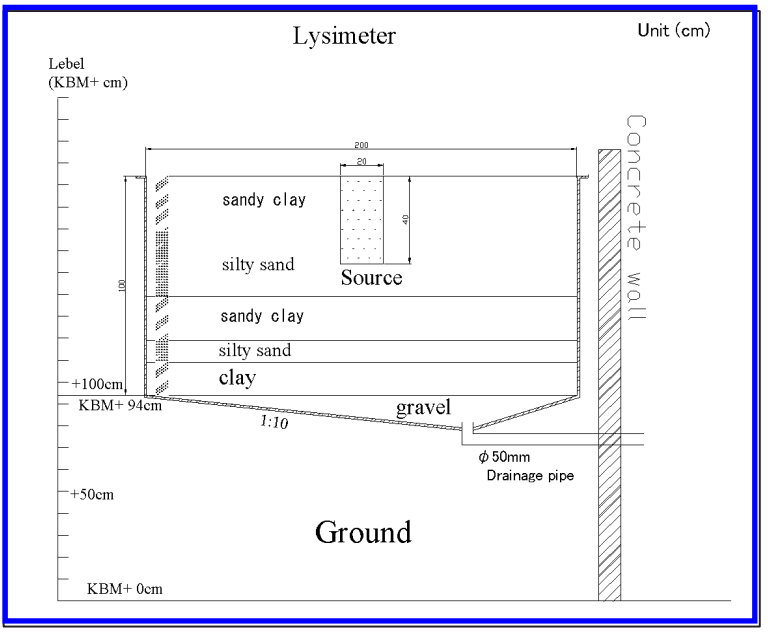


Figure 1. A cross-section view of the lysimeter.

where, $R^{EA}_{bio,le}$ = sink term of electron acceptor *le* for utilization of microbial population [$ML^{-3}T^{-1}$], which are considered as the following relationship

$$R^{EA}_{bio,le} = \sum_{x} \frac{M_x}{n} \sum_{le} \gamma_{x,k,le} v_{x,k,le} \tag{6}$$

where $\gamma_{x,k,le}$ = elector acceptor use coefficient [M_{le} M_k^{-1}] (M_{le} denotes the mass of electron acceptor *le*; M_k is the mass of substrate *k*).

Hydrocarbons in aquifer cause biomass growth accompanied by depletion of electron acceptors and nutrients. Neglecting the transport of microbes, the mass balance equation for growth and death of microbial population x may be written as

$$\frac{1}{M_x}\frac{dM_x}{dt} = \sum_{le}\sum_{k} Y_{x,k,le} v_{x,k,le} - k_{d,x} \tag{7}$$

where $Y_{x,k,le}$ = biomass yield coefficient [$M_b M_k^{-1}$]; representing the mass of microbial population *x* produced per unit mass of substrate *k* while using electron acceptor *le*, and $k_{d,x}$ = microbial death rate [T^{-1}].

2.2 *Description of numerical model*

A three-dimensional numerical model containing MODFLOW module and SEAM3D module was used to solve the set of governing equations given by Eqs. (1)–(7) and associated boundary and initial conditions. The MODFLOW module is a finite-difference method that simulates groundwater flow in three dimensions with external stresses such as wells and precipitation recharges, evapotranspiration and etc. The SEAM3D module is a numerical model for subsurface solute transport with aerobic and sequential anaerobic biodegradations. In this study, hydrocarbon contaminants are simulated as substrates for microbial growth, with available electron acceptors utilized in sequence according to the Gibbs free energy.

2.3 *Characterization of lysimeter*

The lysimeter (Figure 1) used in this research is located in Nagoya University Farm, Togo-cho, Aichi Prefecture, with the dimensions of 200 cm in length, 100 cm in width and 115 cm in depth. The sides are made of impermeable materials, at the bottom a drainage pipe of 5 cm in diameter was set to allow the precipitation infiltration to flow out.

The water head in the lysimeter was 39 cm from the ground level (GL-39 cm). This water head was maintained by opening the bulb at the height equivalent to GL-39 cm. Figure 2 shows the precipitation during the period from Sep–Dec 2001. The total precipitation was 404 mm, so the average was 1.7 mm/day. Based on the relation between the precipitation and the increase of water table in lysimeter, the infiltration ratio was estimated as 0.5.

Copyright © 2003 Swets & Zeitlinger B.V., Lisse, The Netherlands

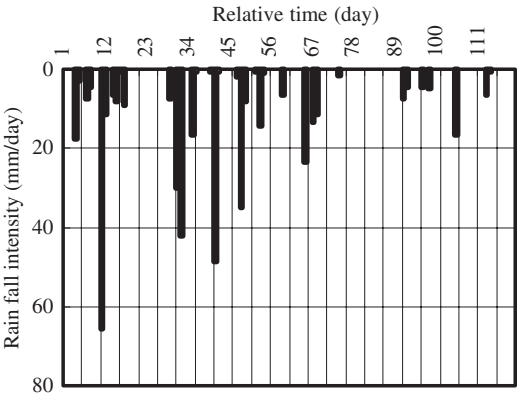


Figure 2. Daily precipitation observed during Sep.–Dec., 2001.

Table 1. Properties of aquifer materials in lysimeter.

Property	Value	Description
Hydaulic conductivity (K)		Measured
Horizontal (K_H)	0.006 cm/s	
Vertical (K_V)	0.0015 cm/s	
Source material	0.01 cm/s	e.g. Freeze &
Gravel layer	0.1 cm/s	Cherry, 1979
Specified yield (n_e)	0.17	Field drianage test
Porosity (n)	0.45	Measured
Bulk density (ρ_b)	1.39 g/cm3	
Organic carbon content (f_{oc})	0.34%	Measured by CHN corder
Longitudinal dispersivity (α_L)	2.0 cm	Fetter, 1993
Transverse dispersivity (α_T)	$0.1\alpha_L$	

Based on the analytical results of soil samples from the lysimeter, the aquifer material consisted of silty sand and sandy silt with an average grain size of 0.2–0.5 mm. A set of soil tests and field tests were carried out to determine the hydraulic conductivity, porosity, and bulk density and sorption properties. The properties of the aquifer materials are showed in Table 1.

2.4 *Properties of Hydrocarbon components*

The hydrocarbon components Toluene, Ethylbenzene, Xylene and Naphthalene (TEXN) were used as contaminants. The contaminant plume is assumed to range from water table (GL-39 cm) to GL-100 cm. Table 2 shows the chemical properties and the initial concentrations of TEXN.

Table 2. Chemical properties and initial concentrations of TEXN.

	Toluene	Ethylben	Xylene	Naphtha
$\text{Log}(K_{oc}^*)$	2.13	1.98	2.38	3.04
K_d	0.459	0.325	0.816	3.728
Initial C_0	30 mg/L	10 mg/L	5 mg/L	2 mg/L

* Widemeier et al., 1999.

Table 3. Types of microbial populations and the concentrations of electron acceptors.

Microbial population		Electron acceptors		
x	Types	*le*		Concentration (mg/L)
1	Strict aerobes	1	O_2	3.3
	Faculative	1	O_2	3.3
2	NO_3 reducers	2	NO_3	70.0
3	SO_4 reducers	3	SO_4	30.0

The distribution coefficient K_d was defined by the following relationship

$$K_d = f_{oc} K_{oc} \tag{8}$$

where f_{oc} = fraction total organic carbon [MM^{-1}]; K_{oc} = soil sorption coefficient normalized for total organic carbon content [$L^{-3}M$]; the initial concentrations of TEXN in plume were determined based on a dissolution test of a hydrocarbon mixture.

2.5 *Biodegradation parameters*

Biodegradation parameters (Tables 3, 4) were based on laboratory measurements, published values and theoretical estimates. For simplicity, parameter values were not allowed to vary in the aquifer.

The microbial population and the concentrations of electron acceptors were determined by an analysis of lysimeter water with DO meter and ion chromatography. The initial concentration of electron acceptors in the lysimeter were set to the values shown in Table 3, as the same were contained in infiltration except oxygen, which was set to 8.0 mg/L.

For aerobes, the maximum specific rate of substrate utilization for TEX was set based on the published values (Bekins et al., 1998). For naphthalene, the parameters were excerpted from the result of Knights & Peter (2000). For anaerobes, the value of $\nu_{x,k,le}^{max}$ were set over an order of magnitude lower than the aerobic biomass. The electron acceptors use coefficients $\gamma_{x,k,le}$ were estimated from the stoichiometric relationship between each electron acceptor and substrate. For

Copyright © 2003 Swets & Zeitlinger B.V., Lisse, The Netherlands

Table 4. Biodegradation parameters for substrates, electron acceptors, and inhibition.

	Toluene	Ethylbenzene	Xylene	Naphtha
$\nu^{max}_{1,k,1}$	1.0	1.0	1.0	1.5
$\nu^{max}_{2,k,1}$	0.05	0.05	0.05	0.075
$\nu^{max}_{2,k,2}$	0.02	0.02	0.02	0.03
$\nu^{max}_{3,k,3}$	0.01	0.01	0.01	0.01
$K^{S}_{1,k,1}$	10.0	11.8	10.0	0.57
$K^{S}_{2-3,k,1-2}$	5.0	5.0	5.0	5.0
$\gamma_{1,k,1}$	3.1	3.2	3.2	3.0
$\gamma_{2,k,1-2}$	4.8	4.9	4.9	4.6
$\gamma_{3,k,3}$	4.7	4.8	4.8	4.5
$\kappa_{2-3,1}$	0.1	0.1	0.1	0.1
$\kappa_{3,2}$	0.5	0.5	0.5	0.5

inhibition by oxygen, numerous values have been reported, and $\kappa_{le,li}$ values vary between 0.01 and 0.1 mg/L (e.g. Chen et al., 1992). For inhibition by other electron acceptors, $\kappa_{le,li}$ values were set at a high value based on the theoretical estimates (Waddill, D.W. & Widdowson, M.A., 1998).

The yield coefficient $Y_{x,k,le}$ for aerobes was set at 0.5 gg^{-1} (e.g. Chen et al., 1992). For anaerobes, $Y_{x,k,le}$ is usually lower than for aerobes, and set at 0.2 gg^{-1} (Edwards et al., 1992). The death terms k_{dx} was calculated by SEAM3D module according to the background concentration of the substrates and the electron accepters. Finally, for estimating the advection and dispersion, a conservative tracer was used, which had the same properties as toluene but was not biodegradable.

3 RESULTS AND DISCUSSION

Toluene was used as a representative to estimate the concentration decrease due to the biodegradation. A nonbiodegradable tracer with the same properties was specified in the simulation model. The variation in concentration of toluene is compared to that of tracer, and the difference is taken as the biodegradation term. A first-order decay rate is used to investigate the relationship between the biodegradation and aerobic/anaerobic state in aquifer. The decay rate is written

$$\frac{dC}{dt} = -\lambda t \quad \text{or} \quad C = C_0 \, \boldsymbol{exp}[-\lambda t] \tag{9}$$

where $C =$ the concentration of substrate [MT^{-1}], $\lambda =$ the first-order decay rate [T^{-1}], and $C_0 =$ the initial concentration of substrate.

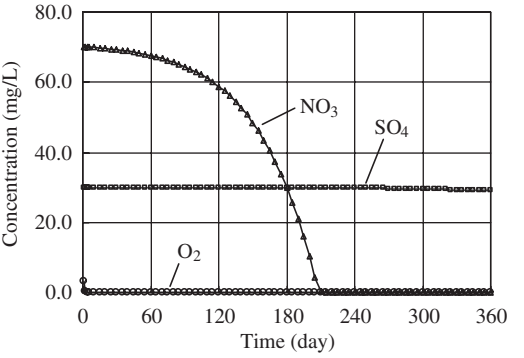


Figure 3. Temporal variation in concentration of electron acceptors in simulation under no precipitation condition.

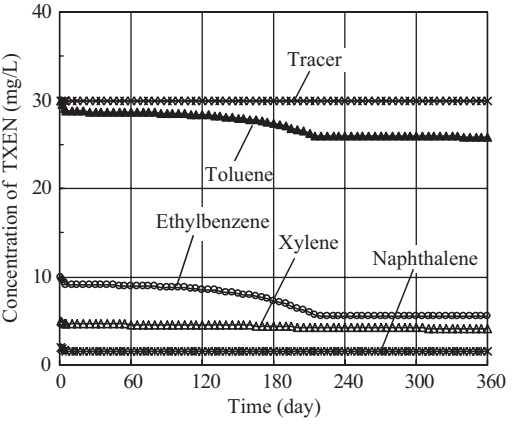


Figure 4. Temporal variation in concentration due to biodegradation in simulation under no precipitation condition.

3.1 *Decay in no precipitation*

Without precipitation, the existing dissolved oxygen in aquifer was utilized by aerobes and soon depleted (Figure 3), the nitrate became the predominant electron acceptor. NO_3 was utilized and depleted after about 220 day. In sequence, sulfate became predominant. In the simulation period of one year, the degradation rate of TEXN was nearly 0.13 to 0.43 day^{-1} for aerobes, was increased from 0.00015 day^{-1} to 0.003 day^{-1} for NO_3 reducers, but was maintained at 0.00003 day^{-1} for SO_4 reducers. The increase in the decay rate of NO_3 reducers was due to the high concentration of nitrate, which allowed the increase in microbial biomass.

3.2 *Decay in constant precipitation*

In the case of constant precipitation, the aquifer was divided into two zones: the infiltration affected zone and anaerobic zone. The affected zone was limited to

Copyright © 2003 Swets & Zeitlinger B.V., Lisse, The Netherlands

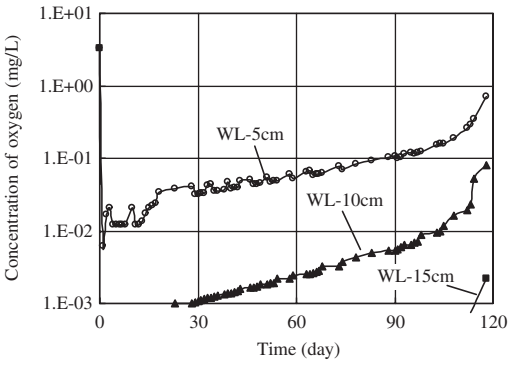


Figure 5. Temporal variation in concentration of dissolved oxygen in simulation under constant precipitation condition.

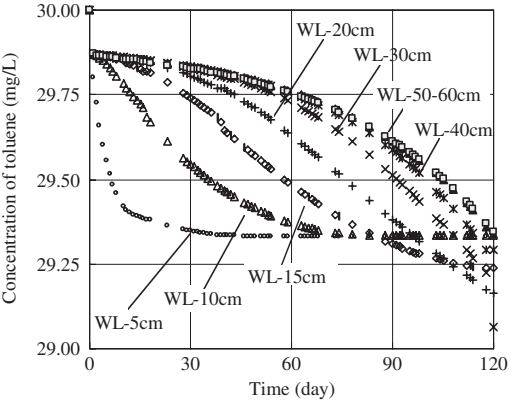


Figure 6. Concentration decreases of toluene due to the bio-degradation in simulation under constant precipitation condition.

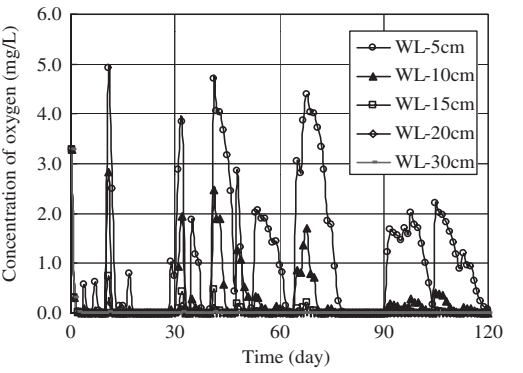


Figure 7. Temporal variation in concentration of dissolved oxygen in simulation under actual daily precipitation condition.

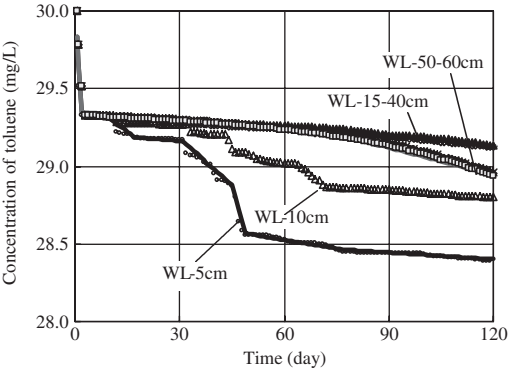


Figure 8. Concentration decreases of toluene due to the bio-degradation in simulation under actual daily precipitation condition.

the layer of 10 cm below water table level (WL-10 cm), and the concentration of dissolved oxygen maintained at a very low level (Figure 5). After about 100 days, oxygen concentration increased sharply because the substrates decreased to a level below 1 mg/L due to downward advection. The lower layer remained as an anaerobic zone because no oxygen was supplied.

The concentration of toluene decreased due to biodegradation as shown in Figure 6. A significant difference was confirmed between the infiltration affected zone and the anaerobic zone. In the infiltration affected zone, the decay rate was 0.02 day^{-1} for WL-5 cm layer before substrate decreased below 1 mg/L due to downward advection, and increased from 0.002 day^{-1} to nearly 0.02 day^{-1} for WL-10 cm. It was considered that although oxygen concentration was not sufficient for the active respiration of aerobes, the oxygen concentration still remained at an inhibitory level for NO_3 reducers and SO_4 reducers. While in the anaerobic zone, with no inhibition of oxygen, the decay rate was at a level of 10^{-4} day^{-1}, but soon increased sharply as in the case of no precipitation.

3.3 *Decay in actual daily precipitation*

In the case of actual daily precipitation, the rainfall duration and intensity changed greatly, resulting in a random dissolved oxygen supply. From the temporal variation of nonbiodegradable tracer, a long-term rainfall with high intensity even affects the layer as deep as 40 cm below water table, but the significant oxygen only appeared up to the layer of 20 cm below water table (Figure 7). This suggested that the aerobes in the upper layer utilized the most of recharge oxygen before they reached to lower layers. While, the layer of WL-50–60 cm maintained in an anaerobic state during the simulation period.

The concentration variation of toluene due to biodegradation is shown in Figure 8. In the top layer, although sufficient oxygen was supplied randomly, the

Copyright © 2003 Swets & Zeitlinger B.V., Lisse, The Netherlands

decay rate changed from 0.003 day^{-1} to 0.6 day^{-1} corresponding to the precipitation duration and intensity. In the layer below the top layer, the degradation rate was the slowest, for example, 10^{-5}–10^{-4} day^{-1} in the layer of WL-15 cm–40 cm, This is considered to be due to the inhibition of low oxygen concentration, like the case of constant daily precipitation. In the lower anaerobic zone, the decay rate showed the same tendency as the two cases discussed. Denitrification is the predominant biodegradation process, and the decay rate was of 10^{-5}–10^{-4} day^{-1} at early step, and increased to a level of 0.002 day^{-1} at later step.

4 SUMMARY

The impact of precipitation infiltration on the biodegradation process of hydrocarbon-contaminated groundwater was simulated. Examining three different scenarios of precipitation, the following conclusions are drawn.

1. The impact of actual daily precipitation changed the aerobic/anaerobic state of the aquifer dynamically, and resulted in the variation of biodegradation rate. In the surface layer of the contaminated plume, the aquifer became aerobic, and achieved a high biodegradation rate temporally. But in the lower layer, insufficient oxygen supply results in a very low biodegradation rate.
2. When using constant daily precipitation as precipitation value, insufficient supply of oxygen could not maintained an aerobic state even in surface layer of aquifer. So this precipitation pattern is not suitable to simulate the actual situation.
3. In the lower anaerobic zone, normally low biodegradation rate is maintained. But in this site, decay rate for NO_3 reducers increased because of the high concentration of nitrate. Further works remains to be done in order to confirm the results from field experiments.

It is shown that the intervals and intensity of precipitation were key factors that affect the biodegradation rates in aquifers. These have to be considered in order to achieve a reliable simulation of bioremediation process in field. It is misleading to predict the aerobic/anaerobic state of aquifer by using constant daily precipitation as the average precipitation.

REFERENCES

Aronson, D. & Howard, P.H. 1997. Anaerobic biodegradation of organic chemicals in groundwater: A summary of field and laboratory studies, Draft final report, *American Petroleum Institute*, Washington, DC.

Bekins, B.A., Warren, E., & Godsy, E.M. 1998. A comparison of zero-order, first-order, and monod biotransformation models, *Ground Water*, Vol. 36, No. 2, pp. 261–268.

Chen, Y.M., Abriola, L.M., Alvarez, P.J.J., Anid, P.J. & Vogel, T.M. 1992. Modeling transport and biodegradation of benzene and toluene in sandy aquifer material: comparisons with experimental measurements. *Water Resour. Res.*, 28, 1833–1847.

Edwards, E.A., Wills, L.E., Reinhard, M. & Grbic-Galic, D. 1992. Anaerobic degradation of toluene and xylene by aquifer microorganisms under sulfate-reducing conditions. *Appl. Environ. Microbiol.*, 58(3), 794–800.

Fetter, C.W. 1993. Contaminant hydrogeology, New York: Macmilla Publishing Company, 66–68.

Freeze, R.A. & Cherry, J.A. 1979. *Groundwater*, London: Prentice-Hall, Inc., 29–37.

Knightes, Christopher, D. & Peters, Catherine, A. 2000. Statistical Analysis of Nonlinear Parameter Estimation for Monod Biodegradation Kinetics Using Bivariate Data, *Biotecnology and Bioengineering*, 69(2).

McDonald, G. & Harbaugh, A.W. 1988. A modular three-dimensional finite-difference ground water flow model, *U.S. Geological Survey Techniques of Water Resources, Investigations*, Book 6, Chapter A1.

Waddill, D.W. & Widdowson, M.A. 1998. A numerical model for three-dimensional solute transport and sequential electron acceptor based bioremediation in groundwater. *Technical report of Virginia Polytechnic Institute and State University*, 1998.

Wiedemeier, T.H., Rifai, H.S., Newell, C.J. & Wilson, J.T. 1999. *Natural Attenuation of fuels and chlorinated solvents in the subsurface.* 198–199. New York: John & Sons.

Copyright © 2003 Swets & Zeitlinger B.V., Lisse, The Netherlands

Copper adsorption by decomposed granite soil and its effect on the breakthrough curve

S. Sasaki
Wakayama National College of Technology, Gobo, Japan

R. Lynch
Cambridge University, Cambridge, UK

ABSTRACT: This study is to examine the influence of the degree of weathering on the breakthrough curve of a copper contaminant plume when passing through decomposed granite soil. The copper concentration is measured in real time in soils by means of a fibre-optic sensor buried in the soil, operating in reflective mode with yellow light, and the resulting breakthrough curve is compared with FEM analysis using the advection-dispersion equation. From the result, it is shown that the curve of severely weathered sample is characterized by the parameters such as R_d, α_L and D_L, which is dependent on the degree of weathering.

1 INTRODUCTION

To study contaminant transport through soil, it is useful to be able to measure the contaminant concentration by some in-situ device buried in the soil under experiment.

In previous experiments at Cambridge, we have used a simple fibre-optic sensor method for monitoring the copper concentration in the soil column experiments (Lynch et al., 2000).

The technique makes use of the fact that the light absorbency of a solution is proportional to the concentration of light absorbing species.

In this research, the reflective type sensor was applied to the tracking of a copper plume moving through samples, and also the adsorption properties were studied by batch testing. The data from the copper adsorption tests and breakthrough curve from the sensor measurement were compared with the FEM simulated curve of 2 (%) in order to examine the plume properties.

2 SAMPLES AND EXPERIMENTAL PROCEDURE

The samples used in the experiment are the saturated sand and decomposed granite soil, which were sieved into fractions below 2000 μm.

The ignition loss has been adopted as an index for estimating the degree of weathering. The ignition loss of alluvial sand and decomposed granite soil was found to be 1.944 and 4.226 (%) respectively.

2.1 *Copper adsorption batch test*

The copper adsorption properties of the sample were determined by a series of copper solution batch experiment.

A known weight, 0.004 kg of sample adsorbent and a series of copper solution, 40 m*l* of 0.1, 0.2, 0.4, 0.6, 0.8 (%) of $CuSO_4$ were placed in polyethylene bottles. They were shaken for several hours. The amount of sorbed copper was determined by measuring the concentration remaining in solution after the sample had been immersed for 24 hours using a copper selective electrode and meter.

2.2 *Sample column experiment*

The dimensions of the sample column were 100 mm inner diameter and 250 mm deep, which is contained in a rigid Perspex tube. The soil sample is introduced into the column by keeping it fully saturated from a bucket containing soil and de-aired water.

The fibre-optic sensor was buried at 100 mm below the surface as shown in Figure 1. In the experiment, the copper solutions were prepared at the concentrations 4, 2, 1 (%) of $CuSO_4$, and the sensor was buried in the saturated sample during the column construction, which was prepared with de-aired water.

Copyright © 2003 Swets & Zeitlinger B.V., Lisse, The Netherlands

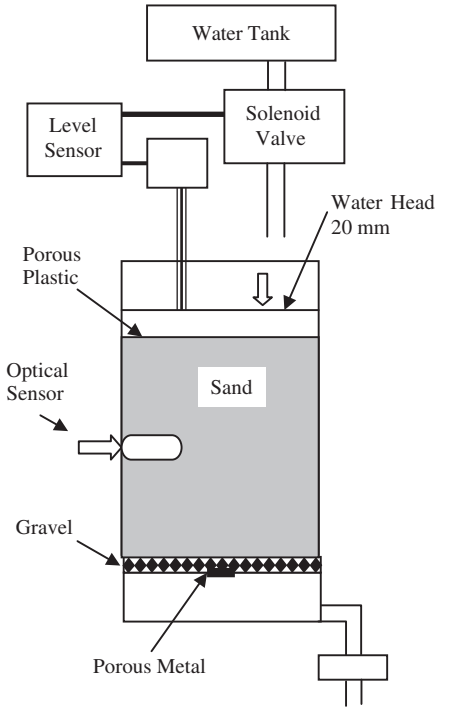


Figure 1. Sand column experiment.

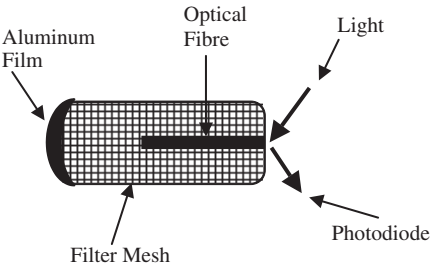


Figure 2. Layout of reflective type sensor.

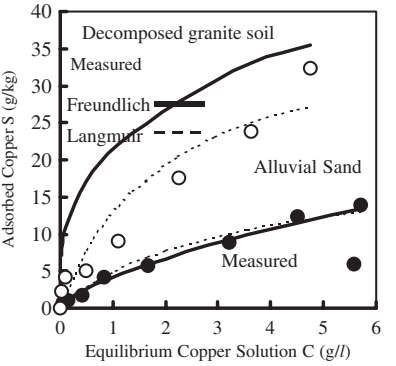


Figure 3. Relationship between experimental and analytical values.

A hydraulic gradient ($i = 1$) was maintained across the sample surface, apart from the application of the copper solution to the sample surface. The water level was maintained 20 mm above the soil throughout the experiment by a level sensor controlled by a solenoid valve.

One hundred milliliters of copper are then applied to the sample surface, which is protected from disturbance by a filter paper. When the copper solution has almost disappeared into the sample, the water level is returned quickly to the original height of 20 mm (see Figure 1), and maintained there until the copper has passed out of the bottom.

2.3 *Fibre optic sensor*

The type of sensor shown by Figure 2. is the reflective type, previously used by (Sentenac, 2001) in which both fibres enter the cell from the same side, and light is reflected back from a miniature aluminum reflector, having passed twice through the pore fluid. In this experiment, yellow light, at peak wavelength 590 nm was used. The reason that we used yellow light is that this wavelength is adsorbed by the blue-green color of copper ions in solution.

3 RESULTS AND DISCUSSIONS

The adsorption characteristics curves of a copper contaminant on the samples were determined by the batch experiments mentioned earlier. The experimental results are shown in Figure 3. In this figure, the sorbed copper concentration increases in a parabolic manner. In considering the relations between the sorbed copper and the degree of weathering, the curve for decomposed granite soil takes a form of steep gradient, comparing with that of alluvial sand, and the amount of adsorbed copper for decomposed granite soil increases, showing a nonlinear behavior with increasing the copper concentration than the alluvial sand. But, this may mean that there are more sites available for adsorption yet. The amount of adsorbed copper for decomposed granite soil is remarkably larger than that of alluvial sand due to severely weathering sample.

The two adsorption models of Freundlich and Langmuir are given in Equations 1 and 2. Figure 3 show the fitting of these models to the experimental results obtained from the batch tests.

$$S = K_f C^{m_f} \tag{1}$$

$$C/S = 1/bK_l + C/b \tag{2}$$

Copyright © 2003 Swets & Zeitlinger B.V., Lisse, The Netherlands

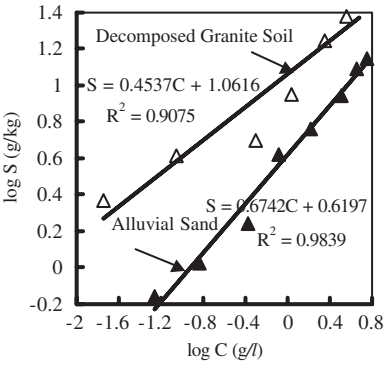


Figure 4. Fitting of Freundlich model.

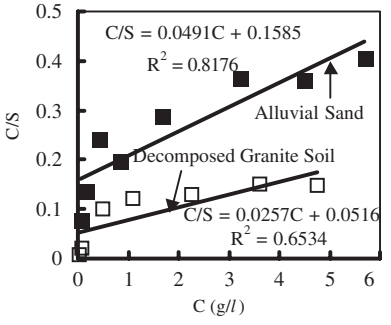


Figure 5. Fitting of Langmuir model.

where, S: mass of ion i adsorbed by the soils per unit mass of dry soil (g/kg); K_f: sorption coefficient (l/kg); C: solute concentration at equilibrium (g/l); m_f: Freundlich constant; K_1: sorption coefficient, equal to the ratio of adsorption and desorption coefficients (l/g); b: Langmuir parameter, equal to the maximum sorption capacity (g/kg).

Applying the Equations 1 and 2 for the measured data in Figure 3 in order to get the parameters in the equations, the relations in Figures 4 and 5 were determined. The results (the curved line) for the samples calculated by the above equations are shown again in Figure 3.

On these samples, the measured values of adsorbed copper correspond well with the calculated values by Langmuir model equation.

The copper solution breakthrough curves are shown in Figures 6 and 7, for different degrees of weathering. These concentrations versus time plots were obtained by applying the calibration equation 3 to the voltage-time data collected from the fibre-sensor.

$$C = kln(V/V_o) \quad (3)$$

where, C: copper concentration (%), V: sensor volts (V), V_o is the output voltage at 0% concentration

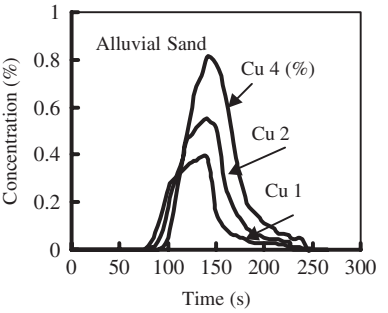


Figure 6. Breakthrough curves of copper plums.

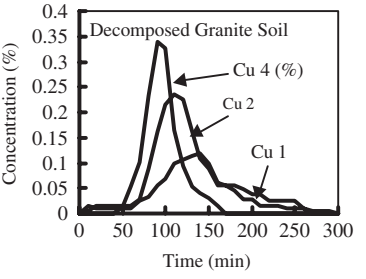


Figure 7. Breakthrough curve of copper plums.

(V), k(=−0.369) is a coefficient that depends on the physical dimension of the sensor.

It is observed that the plume shapes in the alluvial sand and decomposed granite soil are almost of a Gaussian distribution. But, on examining the data in detail, it appeared that the patterns are quiet different between Figures 6 and 7. That is, the decomposed granite soil such as the severely weathered sample shows a time lag of peak concentration when compared to the alluvial sand. Moreover, the breakthrough curves show irregular shapes as the initial copper concentration decreases.

As an example, at initial copper concentration of 4 (%), the concentration of decomposed granite soil is smaller than that of the alluvial sand.

This could be due to the copper being adsorbed in the intragranular voids caused by increasing degree of weathering.

Figure 8 shows that the area of the plume increases as the copper concentration increases. It is evident from the figure that the plume area for decomposed granite soil is smaller than that of alluvial sand because of the copper adsorption effects.

The retardation factor $\boldsymbol{R}_d$ is a measure of the metal mobility in the soils. This represents the retardation of the solute movement compared to the movement of water in which it is dissolved. When the adsorption is nonlinear, the relationship between $\boldsymbol{R}_d$ and

Copyright © 2003 Swets & Zeitlinger B.V., Lisse, The Netherlands

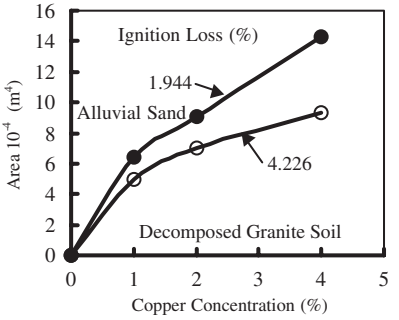


Figure 8. Relations of breakthrough curve area and copper concentration.

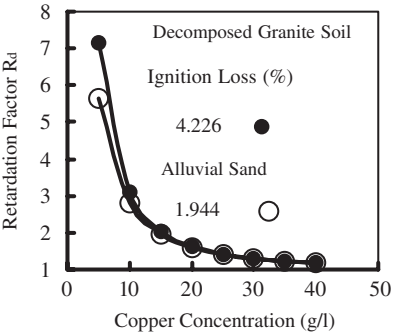


Figure 9. Retardation factor versus copper concentration.

Table 1. Copper solution (2%) example of input parameters for calculations.

Symbol	Unit	Parameter	Alluvial sand	Decomposed granite soil
Ig. loss	%	Ignition loss	1.944	4.226
K_f	m/s	Coefficient of permeability	1.27×10^{-3}	1.46×10^{-5}
$\boldsymbol{\theta}$	m^3/m^3	Volumetric water content	0.356	0.491
$\boldsymbol{R}_d$	–	Retardation factor	1.58	2.0
α_L	m	Longitudinal dispersivity	0.0045	0.102
D_L	m^2/s	Longitudinal dispersion coefficient	5.70×10^{-6}	1.5×10^{-6}
t_o	s	Input contaminant pulse duration	32	1860

$\boldsymbol{C}$ are governed by Equation 4 for the Langmuir model (Schrijver et al., 1999).

Figure 9 is a plot of the retardation factor calculated as a function of equilibrium copper concentration using Equation 4 from the batch test data.

$$\boldsymbol{R}_d = 1 + \frac{\boldsymbol{\rho}_d \boldsymbol{b} \boldsymbol{K}_l}{\boldsymbol{\theta}(1 + \boldsymbol{K}_l \boldsymbol{C})^2} \tag{4}$$

where, $\boldsymbol{\rho}_d$: dry density of soil (g/cm^3), $\boldsymbol{\theta}$: volumetric water content (m^3/m^3).

It is seen that $\boldsymbol{R}_d$ of both samples varies significantly below a copper concentration of 20 (g/l). Above this value, there is no difference in the values of two samples, i.e., $\boldsymbol{R}_d$ is almost constant. But, $\boldsymbol{R}_d$ for the decomposed granite soil is still high than that of the alluvial sand under 20 (g/l). It is thought that the degree of weathering affects the $\boldsymbol{R}_d$ due to copper adsorption.

It is possible to estimate the contaminant concentration distribution of a sand column using FEM analysis (Dtransu Soft), which calculates the advection-dispersion in saturated or unsaturated porous media (Nishigaki et al., 1994).

In the analysis, a 5-mm mesh size was used. If the soil is subjected to a pulse input of contaminant, the following boundary and initial conditions are considered.

Total head h = 250 (mm) at x = 0 (mm), h = 250 (mm) at $x = 250$ (mm). Surface concentration $C = C_o$ for $0 < t \leqq t_o$, C = 0 for $t > t_o$.

The value of $\boldsymbol{R}_d$ in the FEM analysis has been determined from Equation 4 driven for Langmuir model using experimental data.

In order to confirm the effect of $\boldsymbol{R}_d$ on the plumes, a FEM simulation (finite element model) was carried out. The FEM analysis was carried out using the transport parameters given in Table 1. In Table 1, the longitudinal dispersivity α_L and the longitudinal dispersion coefficient D_L are calculated from Equations 5 and 6, using the measured breakthrough curve (Freeze et al., 1979).

$$\boldsymbol{C}/\boldsymbol{C}_o = \frac{1}{2}\boldsymbol{erfc}\left[\frac{\boldsymbol{x} - \boldsymbol{V}_f \boldsymbol{t}}{2(\boldsymbol{\alpha}_l \boldsymbol{V}_f \boldsymbol{t})^{1/2}}\right] \tag{5}$$

$$\alpha_L = \frac{D_L}{V_f} \tag{6}$$

where, $\boldsymbol{x}$: position (mm), $\boldsymbol{t}$: time (s), $\boldsymbol{V}_f$: pore water velocity (m/s).

From these results, the calculated values of the alluvial sand in Figure 10 are in relatively good agreement

Copyright © 2003 Swets & Zeitlinger B.V., Lisse, The Netherlands

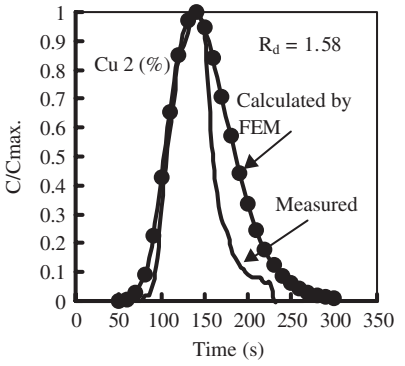


Figure 10. Calculated and measured breakthrough curve of alluvial sand.

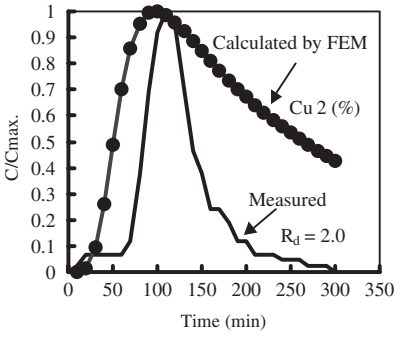


Figure 11. Calculated and measured breakthrough curve of decomposed granite soil.

with the measured values. But, on the decomposed granite soil, there is some difference with the calculated values. Moreover, the peak time between the calculated and the measured plumes is not quite close. Moreover, the peak time between the calculated and the measured plumes is not quite close. The discrepancy with the results between Figures 10 and 11 may be due to the adsorption effect, which is dependent on the degree of weathering.

4 CONCLUSIONS

The results of the studies on the influence of the degree of weathering on copper breakthrough curve lead to the following conclusions.

It was found that the Langmuir model could also be applied to the sample. Especially, it is confirmed that the breakthrough curve of severely weathered sample is characterized by the parameters such as $\boldsymbol{R}_d$, α_L and D_L which is dependent on the degree of weathering.

REFERENCES

Lynch, R.J., Treadaway, A.C.J., Bailey, G., Bolton, M.D., Chandler, S.G., Collison, C.H., Sentenac, P., Garrett, J.A., Santos, C.A. & Silva, MAG 2000. Fibre-optic photometric probes for tracking ground water pollutant tracers in geotechnical centrifuge studies, *Int. Symp. on Physical Modeling a Testing in Environmental Geotechnics, La* Bavle: 35–42.

Nishigaki, M. & Hishiya, M. 1994. *Manual of Dtransu-2DEL, Dia consultant*: 1–97 (in Japanese).

Schrijver, R.R. & Weststrate, F.A. 1999. Preliminary experimental research on the time effects in sorption processes, Technical report CO-368190/80 Delft Geotechnics: 1–30.

Sentenac, P. & Lynch, R. J. 2001. Measurement of a sidewall boundary effect in the soil columns using fibre-optics sensing, *Int. Journal Physical Modeling in Geotechnics, 4*: 35–41.

Copyright © 2003 Swets & Zeitlinger B.V., Lisse, The Netherlands

Centrifuge modeling of LNAPL infiltration in sand deposits with an impervious sheet

Y. Hayashi
Kumamoto University, Kumamoto, Japan

H.G.B. Allersma
Delft University of Technology, Delft, The Netherlands

ABSTRACT: Centrifuge model tests were performed to examine the mechanism of light nonaqueous liquid (LNAPL) transportation in an unsaturated sand deposit. The experiments simulated the effect of a floating-type vertical barrier wall to delay the LNAPL transportation. The LNAPL was transported along the streamlines, and the wall could not stop the LNAPL transportation. However, the LNAPL accumulated on the upstream side of the wall. The installation of the wall delayed and decreased the LNAPL transportation to the downstream.

1 INTRODUCTION

The geoenvironmental damage caused by the release of liquid forms of hazardous chemical substances into the subsurface is a major public concern. Mathematical and physical modeling has been developed to quantify the transport of such contaminants in soil and ground water. A convenient and efficient physical modeling technique for these problems involves the use of a geotechnical centrifuge. Arulanandan et al. (1988) developed one of the earliest applications of centrifuge modeling for studying contaminant transport problems. They showed that the length scale and modeling time could be reduced by subjecting models to centripetal acceleration. Scaling laws already developed by other researchers (e.g., Cooke and Mitchell, 1991; Mitchell and Stratton, 1988) were used to establish the model dimensions.

Knight and Mitchell (1996) modeled the release of 1,000 L of light nonaqueous phase liquid (LNAPL) into unsaturated fine sand. Their paper describes the use of a centrifuge modeling technique to study the release of an LNAPL from a localized zone into unsaturated fine sand. Two different rates of release and their influence on the penetration of the LNAPL into a sand layer were examined. Esposito et al. (1999) simulated a 2D spill of LNAPL in unsaturated sand prepared at two values of porosity. The experiment presents details of the experimental methodologies and the measuring techniques used to evaluate the final distribution of water and LNAPL content in the soils. In addition, Esposito and Allersma (2000) conducted a pilot test of the removal of a viscous LNAPL by means of a forced ground water flow. They succeeded in showing a cleaning process of LNAPL. However, their test also shows the risk of contaminant advection due to ground water flow.

Miki et al. (1999) carried out an experimental study by enclosing a pollutant in floating-type double-barrier wall. Model tests and numerical analysis with 1g of material were conducted. The walls inserted at both sides of the pollutant were effective in preventing the diffusion of the pollutant.

In this study, a floating type barrier wall was inserted into an unsaturated sand deposit. LNAPL was used as the contaminant. The transportation of LNAPL by a water flow around the barrier was simulated in a centrifuge test. The experiment was observed with on-board video camera.

2 CENTRIFUGE MODELING

The tests were carried out at the Geotechnical Centrifuge Facility at Delft University of Technology, The Netherlands. The centrifuge, shown in Photo 1, has a diameter of 2.5 m, and samples with a weight of 300 N can be subjected to acceleration of up to 300 times the Earth's gravity field (Allersma, 1994a,b).

The model container used in this research is shown in Figure 1. The container consists of a metal frame on which two Perspex sheets are attached at a distance of

Copyright © 2003 Swets & Zeitlinger B.V., Lisse, The Netherlands

0.04 m from each other. The sand deposit was located at the center of the container and was included between two porous rigid plastic walls. The plastic walls were covered by filters, which prevented the loss of sand. Two outlet taps located at both sides of the base of the container permitted drainage of the sand sample in flight. An electric pump, which was variable in capacity by a given voltage, was placed on a swinging basket of the centrifuge. The voltage could be adjusted in flight in order to keep the water in the reservoirs at the desired level. The dimensions of the container are given in Table 1.

An impermeable plastic sheet was used in Model B as a barrier wall in order to examine the expected delay of the LNAPL transportation. The tip of the barrier wall was inserted below the water table in the sand deposit (Figure 1).

Dutch sand with a D_{50} of 0.20 mm and a coefficient of uniformity of 1.58 was used, and was prepared at a porosity of 0.36. The water level in the reservoirs was 70 mm from the bottom. At 1 g, the water table in the sand deposit reached the surface of the sand due to the capillary suction pressure.

The LNAPL used in the experiments was motor oil with a density of 910 kg/m^3 and a dynamic viscosity of 0.14 Pa·s. The hydrocarbon was colored with Sudan III, a dye made by coupling diazotized *p*-phenylazoaniline to 2-naphthol.

The layout of the LNAPL supply container, which was developed by Allersma (1998), is shown in Figure 2. In the first instance, the LNAPL was stored in a closed tank-A, which was connected with a thin canal with an open tank-B. The container was placed on the sand deposit, and, when the infiltration process was started, tank-A was pressurized so that LNAPL started to flow to tank-B with a split in the base. It was possible to control the LNAPL infiltration by the air pressure in tank-A in combination with a nozzle. In this case, the LNAPL of tank-A was moved in a short period to tank-B.

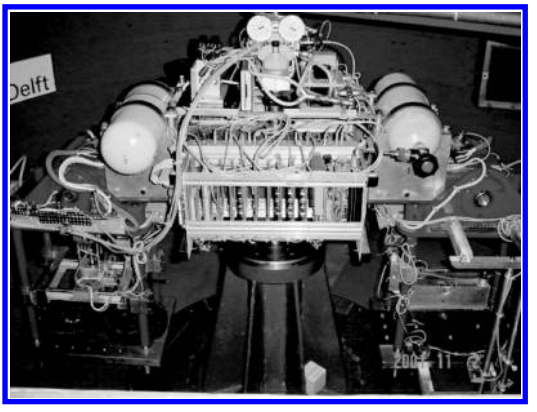


Photo 1. Geotechnical centrifuge.

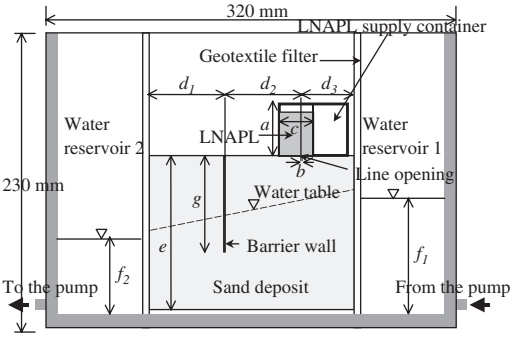


Figure 1. Dimensions of models.

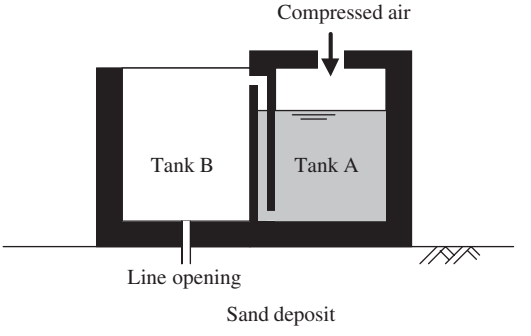


Figure 2. LNAPL supply container.

Table 1. Dimensions of models.

Model		Unit	a	b	c	d_1	d_2	d_3	e	f_1	f_2	g
A	Centrifuge scale	mm	40	1.5	35	0	80	80	120	62	95	0
	Prototype model	m	1.20	0.05	1.05	0.00	2.40	2.40	3.60	1.86	2.85	0.00
B	Centrifuge model	mm	40	1.5	35	60	45	55	120	60	88	75
	Prototype scale	m	1.20	0.05	1.05	1.80	1.35	1.65	3.60	1.80	2.64	2.25

Copyright © 2003 Swets & Zeitlinger B.V., Lisse, The Netherlands

3 LNAPL RELEASE AND TRANSPORTATION

3.1 *LNAPL transportation in the sand deposit without a barrier wall (Model A)*

The model container, shown in Figure 1, was placed in the centrifuge and was accelerated to 30 g without activating the pump. The water table in the sand was lowered and stabilized at about 10 mm above the water level of the water reservoir due to the capillary suction. The LNAPL was then supplied into the sand deposit in a few minutes.

Figure 3 shows the plume obtained by the images recorded by the on-board camera at an elapsed time of 50 min (prototype time of 31.3 days) after the supply of LNAPL. The behavior of the plume after activating the supply container is described in the following:

1. The LNAPL was added through the line opening at the bottom of the LNAPL supply container.
2. It diffused between the surface of the sand deposit and the bottom of the container due to the lack of a perfect fitting.
3. The LNAPL was then gradually transported downward due to the gravity.
4. The LNAPL diffused widely in a lateral direction along the water table.

In 55 min, the pump was started to force a groundwater flow. The LNAPL was transported gradually in a horizontal direction due to this action. Figure 4 shows the plume after 60 min.

Figure 5 shows the superimposed LNAPL plumes at elapsed times. The equivalent times of the prototype are also written in parentheses. The area of the plume became larger because the displacement of the plume front at the left-hand side along the water table was more than the movement of the plume front at the upstream. In 120 min, the LNAPL reached the boundary of the model container, and the test was terminated. The image after 120 min is shown in Figure 6; the concentration difference in the plume is visibly good.

An image processing technique was used to determine the concentration change with the elapsed time. Figure 7 shows a subtraction using the images at

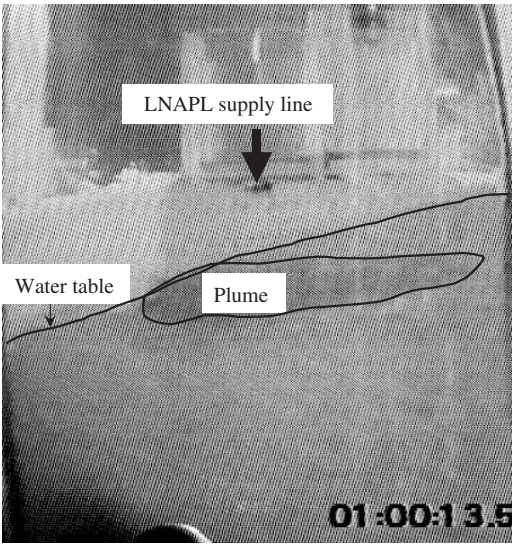


Figure 4. Plume at time = 60 min (Model A).

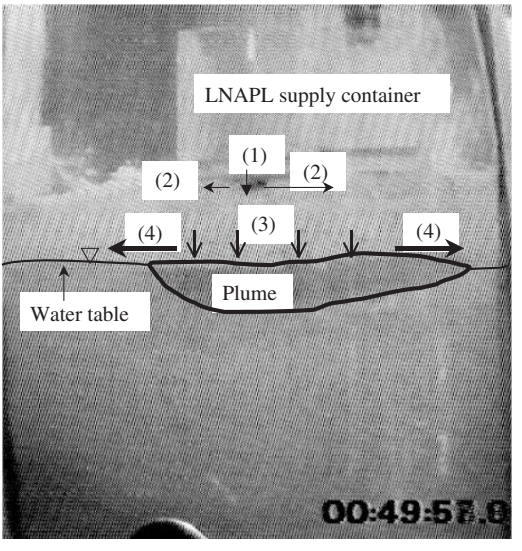


Figure 3. Plume at time = 50 min (Model A).

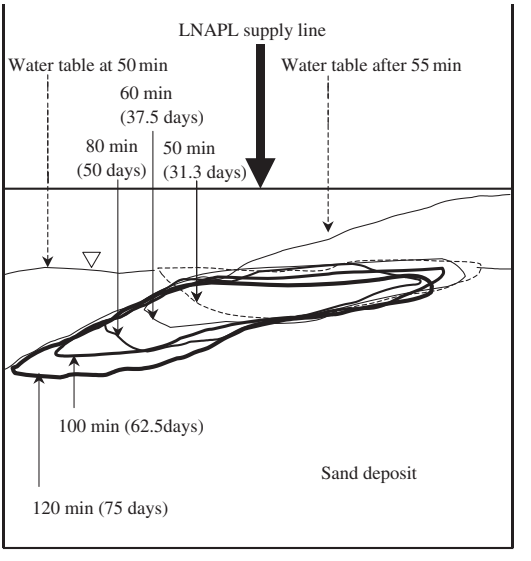


Figure 5. Plumes of LNAPL (Model A).

Copyright © 2003 Swets & Zeitlinger B.V., Lisse, The Netherlands

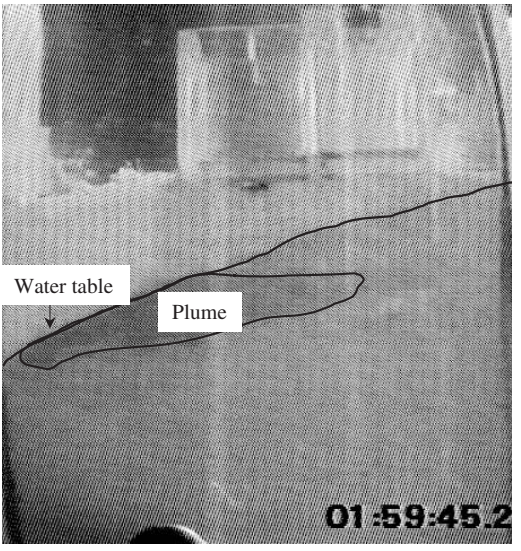


Figure 6. Plume at time = 120 min (Model A).

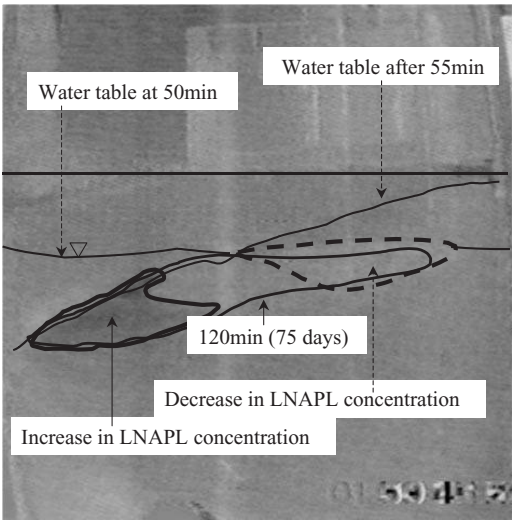


Figure 7. Concentration variation in the plume (Model A).

120 min and at 60 min. It shows the concentration variation in the LNAPL plume at the end of the test. In Figure 7, the plume at 120 min is also drawn. The darker and lighter areas indicate an increase and decrease in the LNAPL concentration between 120 min and 60 min (prototype elapsed time of 37.5 days), respectively. The concentration in the upstream plume decreased. The LNAPL was transported downward along the inclined water table.

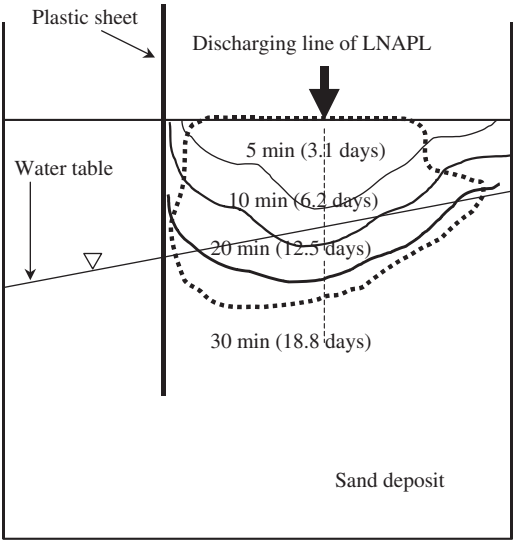


Figure 8. LNAPL plumes at 5–30 min (Model B).

3.2 *The LNAPL transportation of Model B*

Soon after the model container was accelerated to 30 g in the centrifuge, the pump was started to force a groundwater flow. The LNAPL was supplied after 40 min when the water table was stable.

Figure 8 shows the progress of the infiltration fronts of the LNAPL. The time intervals after LNAPL suppletion were 5, 10, 20, and 30 min, which were equivalent prototype times of 3.1, 6.2, 12.8, and 18.8 days, respectively. The area between the fronts and the surface of the sand deposit was wetted with LNAPL. The water table is also drawn in the figure; the streamline around the sheet, however, could not yet be confirmed.

The deepest part of the front of the plume after 5 min was below the supply line of LNAPL. Later, the lowest part moved with the elapsed time toward the left downward due to the water flow and gravity.

Figures 9 and 10 show the plume at durations of 30–60 min and of 60–360 min, respectively. The upper boundary of the plume was moved downward with the elapsed time after the LNAPL supply finished. The plume was transported in a downstream direction, and the front reached the tip of the plastic sheet in 120 min. The LNAPL was transported by the water flow to the left side of the sheet via the sand below the tip of the sheet and then reached the water table again. The position of the lowest plume boundary was almost fixed in 180 min; it is believed that the boundary was along the streamline. The barrier wall delayed the infiltration of the contaminant to the lateral direction; however, the contaminated area spread to a deeper area.

Figure 11 shows the subtracted images using the images at 360 and 120 min. The darker and lighter

Copyright © 2003 Swets & Zeitlinger B.V., Lisse, The Netherlands

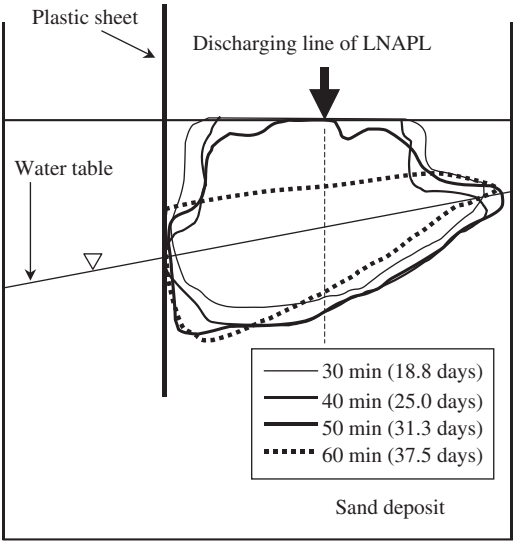


Figure 9. LNAPL plumes at 30–60 min (Model B).

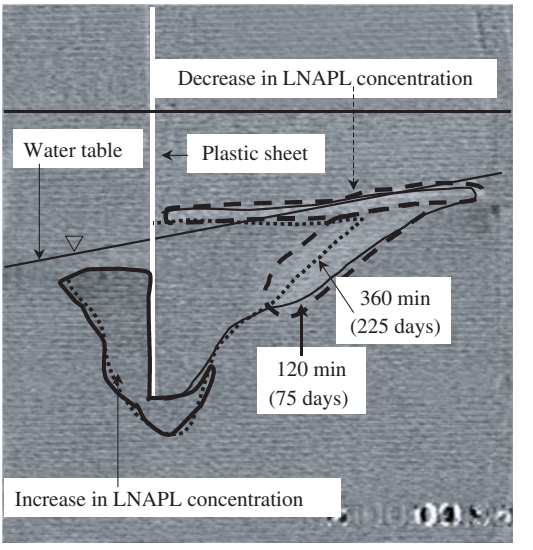


Figure 11. Concentration variation in the plume (Model B).

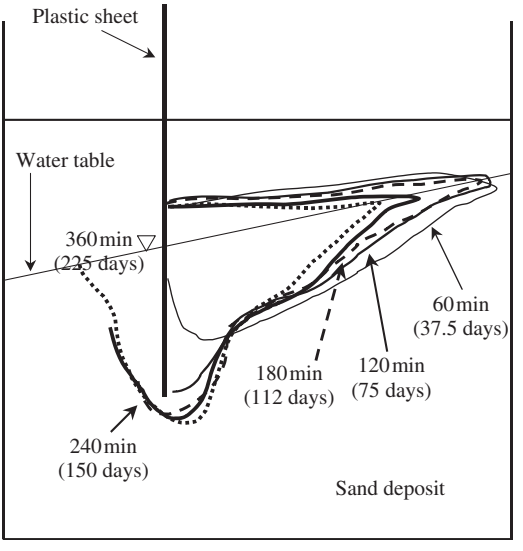


Figure 10. LNAPL plumes at 60–360 min (Model B).

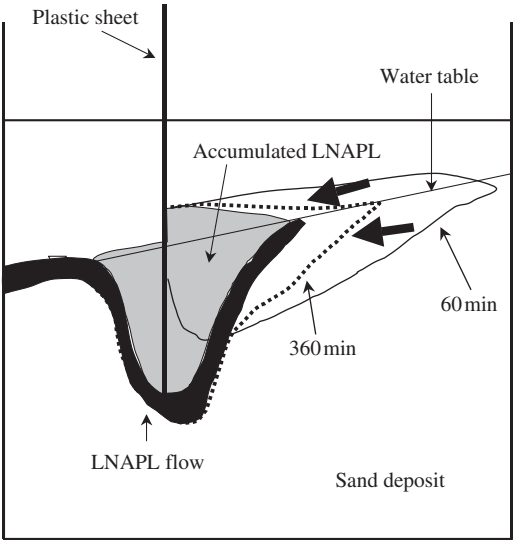


Figure 12. Schemes of LNAPL accumulation (Model B).

areas indicate an increase and decrease in the LNAPL concentration at 360 and 120 min, respectively. The prototype elapsed time was 150 days. An area with decreased concentration can be seen in the right-hand side in the plume. This observation makes it plausible for the plume to be transported further.

Figure 12 illustrates the progress of the LNAPL transportation of this experiment. The LNAPL is transported in the black area along the streamline. A part of the LNAPL, however, temporarily accumulates in the gray areas. This delays the transportation of the LNAPL. Much more LNAPL might accumulate if the barrier wall were inserted deeper.

4 CONCLUSIONS

Two centrifuge model tests were conducted; the major difference was the existence of a barrier wall in one of the model tests. The main effect of the barrier was

Copyright © 2003 Swets & Zeitlinger B.V., Lisse, The Netherlands

that the LNAPL transportation in a partially saturated sand deposit with a water flow was delayed. From the observations, the following conclusions can be drawn:

- The LNAPL supplied from the surface of the partially saturated sand deposit infiltrated toward the water table for a short time and was slowly transported downstream due to the water flow.
- The LNAPL was transported underneath the impermeable barrier wall and reached the water table in the opposite side of the sheet. Apparently, the sheet could not stop the LNAPL transportation.
- The barrier allowed some of the LNAPL to accumulate upstream and delayed and decreased the downstream transportation of the LNAPL.

The transportation mechanism depends on many parameters, such as the density of the sand deposit, the velocity of the water, the amount and kind of contaminant, and the depth of the barrier. Further research will be necessary.

ACKNOWLEDGEMENT

The first author wishes to acknowledge Nishida Tekko Inc., which founded this research.

REFERENCES

Allersma, H. G. B. 1998. Development of cheap equipment for small centrifuge, *Centrifuge 98*, Kimura T., Kusakabe, O. and Takemura, J. (ed.), A.A. Balkema, Rotterdam: 85–90.

Allersma, H. G. B. 1994. The University Delft geotechnical centrifuge, *Centrifuge 94*, Leung, C. F., Lee, F. H. and Tan, E. T. S. (ed.), A.A. Balkema, Rotterdam: 47–52.

Allersma, H. G. B. 1994. Development of miniature equipment for a small geotechnical centrifuge, *Transportation Research Record*, No.1432: 99–105.

Arulanandan, K., Thompson, P. Y., Kutter, B. L., Meegoda, N. J., Muraleetharan, K. K. and Yogachandran, C. 1988. Centrifuge modeling of transport process for pollutants in soils, *Journal of Geotechnical Engineering*, ASCE, 114, 2: 185–205.

Cooke, B. and Mitchell, R. J. 1991. Physical modeling of a dissolved contaminant in an unsaturated sand, *Canadian Geotechnical Journal*, 28: 829–833.

Esposito, G. and Allersma, H. G. B 2000. Centrifuge simulation of in-situ contamination removal, *Proceedings of the International Symposium on Physical Modelling and Testing in Environmental Geotechnics*, Garnier, J., Thorel, L. and Haza, E. (eds), La Baule: 141–148.

Esposito, G, Allersma, H. G. B. and Selvadurai, A. P. S. 1999. Centrifuge modeling of LNAPL transport in partially saturated sand, *Journal of Geotechnical and Geoenvironmental Engineering*, ASCE: 1066–1071.

Knight, M. A. and Mitchell, R. J. 1996. Modeling of light nonaqueous phase liquid (LNAPL) releases into unsaturated sand, *Canadian Geotechnical Journal*, 33: 913–925.

Miki, H., Furumoto, K., Kuwabara, M., Harada, K., Ishida, H., Yoshihara, S., Kubo, M., Saragai, A., Morita, H, Okamoto, S., Iwata, H. and Yamamoto, C. 1999. Experimental study on enclosing effect of floating type barrier wall, *Third Symposium on Environmental Geotechnics*, Tokyo: 277–282 (in Japanese).

Mitchell, R. J. and Stratton, B. C. 1994. LNAPL penetration into porous media *Centrifuge 94*, Leung, C. F., Lee, F. H. and Tan, E. T. S. (ed.), A.A. Balkema, Rotterdam: 345–349.

Copyright © 2003 Swets & Zeitlinger B.V., Lisse, The Netherlands

In-situ electrokinetic and hydraulic remediation of saturated aquifer contaminated by heavy metal

S. Shiba, K. Yamaberi & Y. Hirata
Graduate School of Engineering Science, Osaka University, Toyonaka, Japan

T. Seno
Graduate School of Engineering, Shizuoka University, Hamamatsu, Japan

ABSTRACT: In order to investigate the electrokinetic and hydraulic remediation technique for polluted soil, which is considered to be a promising method for aquifers contaminated by especially heavy metals, a mathematical model has been developed. The model is based on the physico-chemical transport process of heavy metals in pore water under an electric field. The electrokinetic and hydraulic method is theoretically proved to be an effective remediation for aquifers polluted by heavy metals. The results of the numerical simulation show that: (1) Heavy metal is removed from the upstream anode region and accumulated in the downstream cathode region; (2) To carry away the heavy metal from aquifers, the hydraulic flow by purge water is essential; and (3) Electromigration contributes mainly to the local removal (rebuild of heavy metal distribution in the aquifer).

1 INTRODUCTION

The shortage of water resources is increasingly serious in not only developing countries but also developed countries. This forces us to exploit more groundwater which has been utilized for a long time as one of the good quality water resources. However, in many aquifers groundwater has been seriously contaminated by the migration of various hazardous organic and inorganic chemicals from the disposal of municipal and industrial wastes. Increase in water demand makes it urgent to clean up contaminated groundwater and soil immediately.

Many new techniques have been presented for remediation of groundwater and soil. Among them, one of the most cost-effective in-situ technologies is the electrokinetic and hydraulic remediation. This method utilizes electromigration of the charged pollutants in an electric field and hydraulic flow by purge water in soil pore. However, understanding the electromigration of the pollutants in pore water is not only experimentally but also theoretically quite insufficient. This is because the technique is relatively new and innovative for decontamination, although in civil engineering the electrokinetic method (electroosmotic flow) has been utilized for soil dewatering.

This paper aims to develop a mathematical model based on physico-chemical mass transport theory and to simulate the nonsteady characteristics of the transport of heavy metals by the electromigration and hydraulic flow in pore water of aquifers. However, only a few studies (Alshawabkeh & Acar 1992, Eykholt & Daniel 1994, Rodsand et al. 1995, Segall & Bruell 1992, and Shapiro 1989) can be utilized for construction of such a mathematical model as takes the electromigration of heavy metals into consideration.

2 ELECTROMIGRATION

The electrokinetic remediation of aquifers utilizes the electromigration of pollutants, especially heavy metals. It is accomplished by: (1) installing electrodes (anode and cathode) into the contaminated zone, which should be saturated with groundwater or purge water, (2) injecting purge water into the anode well and taking out contaminated water from the cathode well, and (3) applying a fixed low voltage direct current between the electrodes, as shown in Figure 1.

Compounds of heavy metal are typically ionized into cation (e.g. Cu^{2+}, Pb^{2+}, Cd^{2+} and so on) in groundwater. In electric fields an electrokinetic driving force acts on the ionized heavy metal (cation) and causes the electromigration of the heavy metal in pore water. The force is directed toward the cathode and superposed on the hydraulic force due to purge water. Therefore, the heavy metals are accelerated and

Copyright © 2003 Swets & Zeitlinger B.V., Lisse, The Netherlands

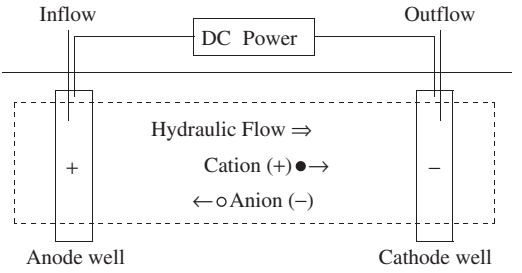


Figure 1. Schematic representation of electrokinetic and hydraulic remediation. Cationized heavy metals and anions are transported by the hydraulic flow caused by purge water in conjunction with electromigration caused by the applied voltage.

migrate to the cathode well where they are swept out through the drainage of waste water.

On the other hand, because the electrokinetic driving force on anions (e.g. CO_3^{2-}, SO_4^{2-} and so on) is directed toward the anode, i.e. in the opposite direction to the hydraulic flow, the migration of the anions is retarded or even driven in opposite to the hydraulic flow. Then, the cationized heavy metals are separated from anions and transported with increasing speed to the downstream well.

3 CHEMICAL REACTIONS

Three kinds of chemical reactions are treated in this model. The first one is the homogeneous liquid-phase reaction, which generates the molar rate R_k^{aq} and is included in the governing equation as the reaction term. The second one is the heterogeneous interface reaction (adsorption and desorption) between the pore water and the soil surface, which generates the molar rate R_k^{sp} and is considered by introducing the retardation factor. The third one is the electrode reaction, which generates the flux J_{ek}^* and is combined with the boundary conditions.

3.1 *Homogeneous liquid-phase reaction*

The heavy metal treated here is copper sulfate, $CuSO_4$. Then, homogeneous liquid-phase chemical reactions are dissociation and can be expressed as follows:

$$CuSO_4 \rightleftharpoons Cu^{2+} + SO_4^{2-} \quad (K_1) \tag{1}$$

$$H_2SO_4 \rightleftharpoons H^+ + HSO_4^- \quad (K_2) \tag{2}$$

$$HSO_4^- \rightleftharpoons H^+ + SO_4^{2-} \quad (K_4) \tag{3}$$

$$H_2O \rightleftharpoons H^+ + OH^- \quad (K_W) \tag{4}$$

where K_1, K_2, K_4 and K_W are the dissociation constants.

The concentrations of chemical species in the above reactions (mol/L), C_k, are defined as:

$$(C_1, C_2, C_3, C_4, C_5, C_6) = ([CuSO_4], [Cu^{2+}], [SO_4^{2-}], [HSO_4^-], [H^+], [OH^-]) \tag{5}$$

From Equations 1–4, the reaction rate for species k, R_k^{aq}, is given as:

$$R_1^{aq} = -(k_{1+}C_1 - k_{1-}C_2C_3) \tag{6}$$

$$R_2^{aq} = k_{1+}C_1 - k_{1-}C_2C_3 \tag{7}$$

$$R_3^{aq} = k_{1+}C_1 - k_{1-}C_2C_3 + k_{4+}C_4 - k_{4-}C_3C_5 \tag{8}$$

$$R_4^{aq} = k_{4+}C_4 - k_{4-}C_3C_5 \tag{9}$$

$$R_5^{aq} = k_{4+}C_1 - k_{4-}C_3C_5 + k_{W+} - k_{W-}C_5C_6 \tag{10}$$

$$R_6^{aq} = k_{W+} - k_{W-}C_5C_6 \tag{11}$$

where $k_{1+}, k_{1-}, k_{4+}, k_{4-}, k_{W+}$, and k_{W-} are reaction rate constants satisfying the next equations:

$$(K_1, K_4, K_W) = (k_{1+}/k_{1-}, k_{4+}/k_{4-}, k_{W+}/k_{W-}) \tag{12}$$

Equations 6–11 are included in the governing equation as the reaction term.

3.2 *Heterogeneous interface reaction*

Adsorption and desorption of chemical species k at soil surface is represented by:

$$C_k + \text{Soil site} \rightleftharpoons S_k \quad (Kd_k) \tag{13}$$

where S_k = chemical species k in soil phase (mol/g); and Kd_k = distribution coefficient (L/g). This reaction is included in the governing equation.

3.3 *Electrode reaction*

At the electrodes, electrode reactions occur by passage of the electric current which is caused by the application of electric potential between the electrodes. At the anode, water gives electrons to the electrode and generates oxygen gas and H^+. At the cathode, water takes electrons from the electrode and releases hydrogen gas and OH^-. These reactions are described by:

$$2H_2O - 4e^- \rightarrow O_2(g) + 4H^+ \tag{14}$$

$$2H_2O + 2e^- \rightarrow H_2(g) + 2OH^- \tag{15}$$

where e^- = electron. These reactions are combined with the boundary conditions of the governing equation.

Copyright © 2003 Swets & Zeitlinger B.V., Lisse, The Netherlands

4 MATHEMATICAL MODEL

4.1 *Governing equation*

The model developed here is described by: (1) advective diffusion equation with homogeneous and heterogeneous chemical reactions and (2) its boundary conditions with electrode reactions. Under steady uniform flow, the equation of conservation of mass (diffusion equation), which considers the advection, dispersion, chemical reaction and sorption for chemical species k in saturated homogeneous isotropic media, can be described as follows (Shapiro et al. 1989):

$$\frac{\partial}{\partial t}(\mathrm{nRd_k}C_\mathrm{k}) + \frac{\partial}{\partial z}\{(u_\mathrm{s} + u^*_\mathrm{ezk})C_\mathrm{k}\} = \mathcal{D}^*_\mathrm{k}\frac{\partial^2 C_\mathrm{k}}{\partial z^2} + \mathrm{n}R^\mathrm{aq}_\mathrm{k} \tag{16}$$

where C_k = concentration of species k(mol/L); D^*_k and u^*_ezk = effective diffusion coefficient ($\mathrm{cm^2/s}$) and effective electromigration velocity of species k (cm/s), respectively; u_s = pore flow velocity (cm/s); n = porosity of soil (−); $\mathrm{Rd_k}$ = retardation factor (−) defined by Equation 18 mentioned later; and R^aq_k = molar rate due to liquid-phase chemical reactions (mol/L/s). D^*_k and u^*_ezk are defined by:

$$(\mathcal{D}^*_\mathrm{k},\ u^*_\mathrm{ezk}) = \left(\frac{\mathrm{n}}{\tau^2}\mathcal{D}_\mathrm{k},\ \frac{\mathrm{n}}{\tau^2}u_\mathrm{ezk}\right) \tag{17}$$

where τ = tortuosity obtained experimentally (−); D_k = diffusion coefficient of chemical species k in pore water ($\mathrm{cm^2/s}$); and u_ezk = electromigration velocity of species k (cm/s) defined by Equation 19.

It is seen from Equation 16 that we can operate hydraulic flow velocity (u_s) by pumping rate and electromigration velocity (u^*_ezk) by applied voltage, respectively.

4.1.1 *Retardation factor*

Chemical reactions in the governing equation are homogeneous liquid-phase reaction, which generates the molar rate R^aq_k in pore water, and heterogeneous reaction between pore water and soil (adsorption and desorption), which generates the molar rate R^sp_k. The retardation factor $\mathrm{Rd_k}$ is introduced to consider R^sp_k satisfactorily (Inoue & Kaufman 1963) as:

$$(\mathrm{Rd_k},\ \mathrm{Kd_k}) = \left(1 + \frac{(1-\mathrm{n})\rho}{\mathrm{n}},\ \frac{\partial S_\mathrm{k}}{\partial C_\mathrm{k}}\right) \tag{18}$$

where p = density of soil solids ($\mathrm{g/cm^3}$); $\mathrm{Kd_k}$ = distribution coefficient (L/g); and S_k = absorbed species per unit mass of soil solid (mol/g).

4.1.2 *Electromigration velocity*

The electromigration is the core of this model and the electromigration velocity u_ezk plays an important role in the remediation of aquifers and is given by:

$$u^*_\mathrm{ezk} = -\frac{\mathrm{F}}{\mathrm{RT}}\mathrm{z_k}\mathcal{D}^*_\mathrm{k}\frac{\partial \phi}{\partial z} \tag{19}$$

where F = Faraday's constant (C/mol); R = universal gas constant (J/K/mol); T = water temperature (K); $\mathrm{z_k}$ = charge number of species k(−); ϕ = electric potential (V); and the potential gradient $\delta\phi/\delta z$ is given by:

$$\frac{\partial \phi}{\partial z} = -\frac{\mathrm{RT}}{\mathrm{F}}\,\mathrm{f}(t,z) \tag{20}$$

where f (t,z)is a function of C_k and the electric current density i^*_s. As the current density is estimated by summing up all products of the ion charge number $\mathrm{z_k}$ and the ion flux J^*_k defined by Equation 27, from Equations 19, 20 and 27 f(t, z) is obtained as:

$$\mathrm{f}(t,z) = \frac{\left[\sum(\mathrm{z_k}\mathcal{D}^*_\mathrm{k}\frac{\partial C_\mathrm{k}}{\partial z}) + 10^3\frac{i^*_\mathrm{s}}{\mathrm{Fn}}\right] - u_\mathrm{s}\sum(\mathrm{z_k}C_\mathrm{k})}{\sum(\mathrm{z_k^2}\mathcal{D}^*_\mathrm{k}C_\mathrm{k})} \tag{21}$$

The factor 10^3 multiplying i^*_s is introduced since C_k is specified in mol/L as usual practise. As $i_\mathrm{s}(t) = I(t)/A\ i^*_\mathrm{s}$ is calculated from the electric current as:

$$i^*_\mathrm{s}(t) = \frac{\mathrm{n}}{\tau^2}\,i_\mathrm{s}(t) = \frac{\mathrm{n}}{\tau^2}\,\frac{I(t)}{A} \tag{22}$$

where $I(t)$ = electric current from power unit (A); and A = cross sectional area of soil column ($\mathrm{cm^2}$).

4.1.3 *Electric potential*

Integrating Equation 20, electric potential $\phi(t,z)$ along the experimental soil column is estimated by:

$$\phi(t,z) = \phi(t,0) - \frac{\mathrm{RT}}{\mathrm{F}}\int_0^z \mathrm{f}(t,z)\,\mathrm{d}z \tag{23}$$

Then the applied voltage E (Volts) between the anode ($z = 0$) and the cathode ($z = L$) is obtained as follows:

$$E(t) = \phi(t,0) - \phi(t,L) \tag{24}$$

4.2 *Initial condition*

The initial condition for the governing equation (Equation 16) is simply given by:

$$C_\mathrm{k} = C_\mathrm{k0} \qquad \text{at} \qquad t = 0 \tag{25}$$

This equation specifies the initial concentration distributions in pore water. C_k0 is not necessarily uniform.

Copyright © 2003 Swets & Zeitlinger B.V., Lisse, The Netherlands

4.3 *Boundary conditions*

At electrodes boundary conditions are given as the continuity of the flux of chemical species (J_k^*). Because electrode reactions occur by passage of the electric current, the flux due to electrode reactions (J_{ek}^*) must be taken into account in the boundary conditions in addition to the convective flux.

The production rate of H^+ at the anode and of OH^- at the cathode can be expressed in terms of their flux J_{eH}^* and J_{eOH}^*, respectively, as follows:

$$(J_{eH}^*,\ J_{eOH}^*) = \left(10^3 \frac{i_z^*}{z_H F},\ 10^3 \frac{i_z^*}{z_{OH} F}\right) \tag{26}$$

where i_z^* = effective electric current density (A/cm^2). J_{eH}^* and J_{eOH}^* are superposed on J_H^* (for H^+) and J_{OH}^* (for OH^-), respectively.

As $i_z^* = i_s^*/n$; $z_H = +1$; and $z_{OH} = -1$, the boundary conditions in terms of flux (J_k^*) can be stated as:

$$J_k^* = -\frac{\partial(\mathcal{D}_k^* C_k)}{\partial z} + (u_s + u_{ezk}^*) C_k = \left[\begin{array}{ll} \left(\begin{array}{ll} u_s C_k^{IN} + 10^3 \frac{i_s^*}{Fn}, & \text{for } H^+ \\ u_s C_k^{IN}, & \text{for others} \end{array} \right) & \text{at } z = 0 \\ \left(\begin{array}{ll} u_s C_k - 10^3 \frac{i_s^*}{Fn}, & \text{for } OH^- \\ u_s C_k, & \text{for others} \end{array} \right) & \text{at } z = L \end{array} \right] \tag{27}$$

Governing equation can be solved numerically under the boundary conditions.

5 NUMERICAL SIMULATION

Numerical simulations were done under the conditions shown in Tables 1 and 2. Table 1 represents the assumed values for the bench scale soil column experiments. Table 2 shows the values of the operational variables for the electromigration and the purge water.

Table 1. Characteristics of soil column.

Property	Value
Soil column length (L)	0.40 m
Cross sectional area of soil column (A)	0.01 m^2
Porosity of soil (n)	0.4
Tortuosity of pore (τ)	1.5
Initial acidity of pore water (pH)	6.0

Table 2. Operational variables of electromigration.

Variable	Value
Flow rate of purge water (Q)	0.0010 and 0.0015 ml/s
Applied Voltage (E)	2 and 3 V
Acidity of purge water (pH)	7.0

5.1 *Distribution of pH*

As is mentioned earlier, by the electrode reactions at the anode and the cathode, hydrogen ion (H^+) is produced at the anode and hydroxyl ion (OH^-) is generated at the cathode (see Eqs 14 and 15). Therefore, it is supposed that, with the passage of time, pH at the anode should decrease and pH at the cathode should increase in their values. Then, pH distribution curves are expected to have an ascending gradient. And the gradient considered to become steeper and steeper with the passage of time.

Time variation of the distribution of pH between the anode and the cathode is shown in Figure 2. The abscissa is the dimesionless distance from the anode (z) and the ordinate is pH value. As usual pH is defined as $-\log([H^+])$. Curves are plotted parametrically in time (hour). The initial pH of pore water is 6.0 and is represented by the horizontal thick line.

As is supposed from the electrode reaction, pH distribution curves obtained by the model have an ascend ing gradient with respect to the distance from the anode, although the gradient varies greatly with the distance. Furthermore, they have a sharp increase of pH value (pH jump) in the distribution (acid front) with respect to the anode. On the other hand, with respect to the cathode they have a sharp decrease of pH value (pH drop) in the distribution (base front).

5.2 *Distribution of total copper*

Electrokinetic driving force acting on Cu^{2+} is directed toward the cathode. This makes Cu^{2+} concentration of the cathode higher and that of the anode lower, even if the hydraulic flow is very small. Then, denoting that $\widehat{C}_1$ and $\widehat{C}_2$ = dimensionless copper sulfate concentration and dimensionless copper ion concentration, respectively, it is supposed that the distribution curve of total copper concentration X_1 in the soil column has an ascending gradient with respect to the distance

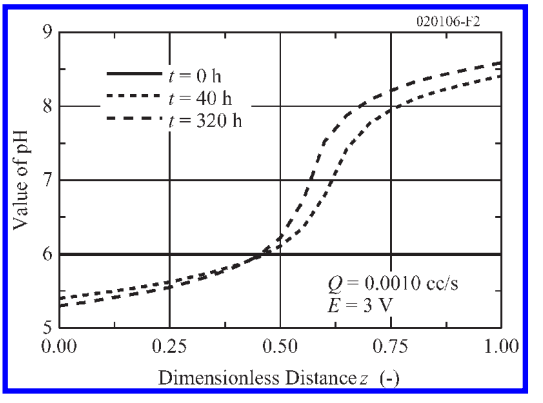


Figure 2. Distribution of pH in soil column.

Copyright © 2003 Swets & Zeitlinger B.V., Lisse, The Netherlands

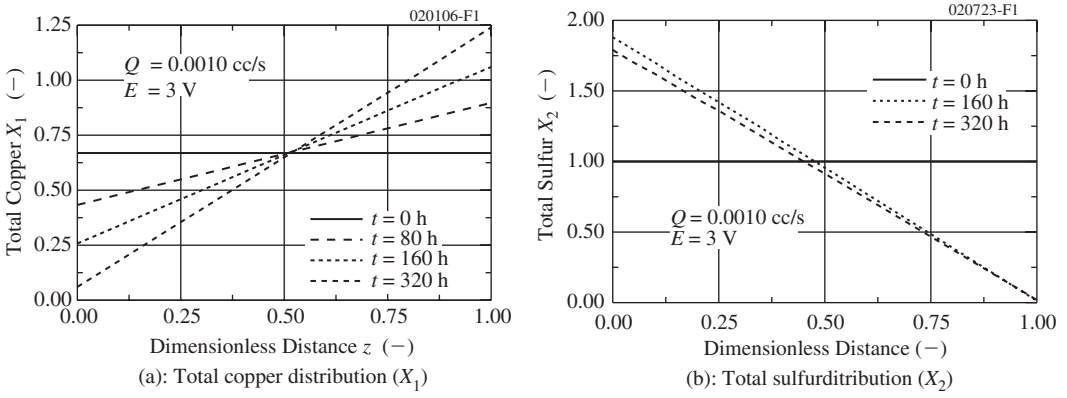


Figure 3. Time variation of total copper ($X_1 = \hat{C}_1 + \hat{C}_2$) and total sulfur ($X_2 = \hat{C}_1 + \hat{C}_3 + \hat{C}_4$) distributions in soil column.

from the anode, since $\widehat{C}_2 \gg \widehat{C}_1$. The total copper concentration (X_1) is defined as:

$$X_1 = \hat{C}_1 + \hat{C}_2 \tag{28}$$

The time variations of the total copper distribution in the soil column are plotted in Figure 3 (a). As is supposed, at any time the distributions of total copper concentration $X_1(=\widehat{C}_1 + \widehat{C}_2)$ in the soil column are almost linear with respect to the distance from the anode ($\hat{z}$). Curves have an ascending gradient except for the initial distribution (horizontal thick solid line). This figure suggests that copper is removed from the anode (upstream end) and that it is transported and accumulated near the cathode (downstream end). The remediation (local removal of copper) in the soil column advances from the anode to the cathode with the passage of time. This tendency of distributions of copper concentration accords qualitatively with the results for the heavy metals obtained by Nekrasova & Korolev (1997) in a one-dimensional column experiment.

5.3 *Distribution of total sulfur*

Sulfate ion (SO_4^{2-}) is an anion and the electrokinetic driving force is directed toward the anode. Therefore, the distribution of total sulfur X_2 defined by Equation 29 is supposed to be descending curve with respect to the distance from the anode ($\widehat{C}_3 \gg (\widehat{C}_1, \widehat{C}_4)$). The total sulfur concentration (X_2) is defined as:

$$X_2 = \hat{C}_1 + \hat{C}_3 + \hat{C}_4 \tag{29}$$

where $\widehat{C}_1, \widehat{C}_3$ and $\widehat{C}_4$ = dimensionless copper sulfate concentration, dimensionless sulfate ion concentration and dimensionless bisulfate ion concentration, respectively.

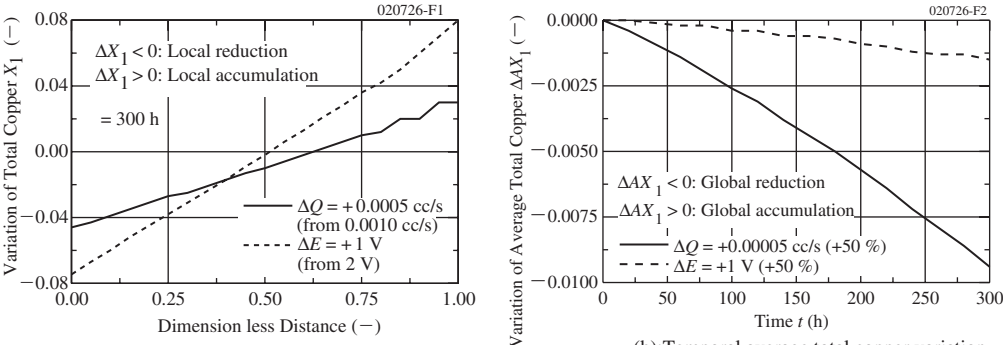
Simulated time variation of total sulfur distributions is shown in Figure 3 (b). At any time the curves have a descending gradient except for the initial distribution (horizontal thick solid line). This means that by electromigration sulfate ion is removed from the cathode (downstream end) and that it is transported to the anode against the hydraulic flow. Therefore, sulfur is accumulated near the anode (upstream end) and the concentration at the anode is higher than the initial concentration. As the effluent concentration is very low compared with the anode concentration and as the flow rate of purge water is small, the global reduction of sulfur from the soil column (carry away through the effluent) is very slow.

5.4 *Effect of applied voltage and purge flow on the distribution of total copper* X_1

The global reduction of copper, which is carried away from the soil column through the effluent, is small compared with the so excellent local removal near the anode region [global residual is estimated as the average total copper concentration (AX_1) by Equation 30 mentioned later]. This is because the carry away is caused not by the electromigration but by the hydraulic flow (hydraulic flow velocity u_s is dependent on the flow rate of purge water Q) which is rather small as is seen from Table 2.

From Figure 3 (a), it can be seen that the electromigration contributes much to the rebuilding of the copper distribution (local removal and local accumulation) in pore water of the soil column but not so much to the global reduction (carry away from the column) and that the aid of the purge water is essential to the electrokinetic remediation. The local separation of copper sulfate and copper ions near the anode region and their accumulation near the cathode region due to electrokinetic forces in the soil column is demonstrated in Figure 4 (a). Apart from the electrokinetic driving force, there is a hydraulic flow in the pore due to the purge water, which may also affect copper distributions.

Copyright © 2003 Swets & Zeitlinger B.V., Lisse, The Netherlands



(a): Distribution of total copper variation

(b):Temporal average total copper variation

Figure 4. Effect of applied voltage and hydraulic flow on local variation (ΔX_1) and global variation (AX_1) of total copper.

The applied voltage (E) and the purge flow (Q) are increased by 50% from their values in the standard condition of numerical simulations ($E = 2$ V and $Q =$ 0.0010 ml/s) to 3 V and 0.0015 ml/sec in other operations, respectively. The effects of the increments on the distributions of total copper concentration (X_1) are shown in Figure 4 (a). The effects are described by the variation of total copper concentration (ΔX_1) against operations of E and Q . It is distinctly clear from the figures that the applied voltage operation is more effective to separate and accumulate copper ions than the purge water operation. The local removal at the anode increases by 11% for 1 V increment in the applied voltage (solid curve), where this increment is 6.9% when the purge flow rate is increased from 0.0010 ml/s to 0.0015 ml/s (broken curve).

5.5 *Effect of purge flow and applied voltage on global reduction of total copper (*AX_1*)*

The decrease in average total copper (AX_1) in the column for 50% increment in the purge flow rate (Q) and applied voltage (E) is shown in Figures 4 (b). The average total copper concentration is defined as:

$$AX_1 = \int_0^1 (\hat{C}_1 + \hat{C}_2)\, d\hat{z} \tag{30}$$

After the 300 hours' remediation, 50% increment of purge water flow reduces AX_1 by 2.9% (solid curve). On the other hand, 50% increment of applied voltage reduces AX_1 by only 0.23% (broken curve).

Figure 4 (b) demonstrates the importance of the purge water in the electrokinetic remediation. The total copper in the soil column is carried away with the purge water effluent (evaluated by the reduction in AX_1), where the electromigration greatly contributes to local removal from the anode region. It should be noted here that the injection of purge water is essential to carry away the locally separated heavy metal.

6 CONCLUSIONS

The results of the numerical simulations show that: (1) Electromigration is effective especially for the local removal of heavy metals near the anode; (2) Heavy metal is removed from the anode region (upstream region) and transported to be accumulated in the cathode region (downstream region); (3) For the carry away of the heavy metal through the effluent, the hydraulic flow by purge water is essential, because electromigration contributes mainly to the local removal (redistribution); and (4) The pH distribution, which is characterized by the pH jump with acid and base fronts, is well reproduced by the mathematical model.

REFERENCES

Alshawabkeh, A. N. & Acar, Y. B. 1992. Removal of Contaminants from Soils by Electrokinetics: A Theoretical Treatise. *Environ. Science Health* A27(7): 1835–1861.

Bruell, C. J., Segall, B. A. & Walsh, M. T. 1992. Electroosmotic Removal of Gasoline Hydrocarbons and TCE from Clay. *J Environmental Engineering ASCE* 118(1): 68–83.

Eykholt, G. R. & Daniel, D. E. 1994. Impact of System Chemistry on Electroosmosis in Contaminated Soil. *J Geotechnical Engineering ASCE* 120(5): 797–815.

Inoue, Y. & Kaufman, W. J. 1963. Prediction of Movement of Radionuclides in Solution through Porous Media. *Health Physics* 9(7): 705–715.

Nekrasova, M. A. & Korolev, V. A. 1997. Electrochemical Cleaning of Polluted Soils. In P. G. Marinos et al. (eds), *Engineering Geology and the Environment* 2: 2047–2052. Rotterdam: Balkema.

Rodsand, T., Acar, Y. B. & Breedveld, G. 1995. Electrokinetic Extraction of Load from Spiked Norwegian Marine Clay. In Y. B. Acar & D. E. Daniel (eds), *Geoenvironment 2000* 2: 1518–1534. New York: ASCE.

Shapiro, A. P., Renaud, P. C. & Probstein, R. F. 1989. Preliminary Studies on the Removal of Chemical Species from Saturated Porous Media by Electroosmosis. *Physico Chemical Hydrodynamics* 11(5/6): 785–802.

Copyright © 2003 Swets & Zeitlinger B.V., Lisse, The Netherlands

A designing method for in-situ bioremediation of TCE contaminated groundwater with cometabolic degradation

T. Kawai, J. Kawabata, M. Goto & S. Otuka
Kajima Corporation, Technical Research Institute, Tokyo, Japan

ABSTRACT: A field study was demonstrated to remediate TCE contaminated groundwater with in-situ bioremediation using cometabolic TCE degradation by methanotrophs. A design method using solute transport analysis is proposed to determine the effective injection scheme and injection pattern for the effective bioremediation, based on the characterization of various parameters from laboratory and in-situ experiments. The solute transport calculation showed that one-point intermittent injection was more effective for the prevention of biofouling than multi-point simultaneous injection.

1 INTRODUCTION

It has been recognized that pump-and-treatment method may need long operation time for the clean-up of contaminated aquifers, which could increase the remediation cost. The in-situ bioremediation, which uses microbes and remediates polluted soil and groundwater without excavation, is expected as a technology that can remediate low-concentration contamination of soil and groundwater at lower cost. However, the in-situ bioremediation of contaminated groundwater of chlorinated hydrocarbon is not popular in Japan. Then, the granted research "In Situ Soil Bioremediation Project" (December, 1995–March, 2001) of the Ministry of International Trade and Industry (the present Ministry of Economy, Trade and Industry) aiming at new industrial training was carried out at the Research Institute of Innovative Technology for the Earth (RITE), and Ebara, Kajima Co., Kurita Water Industries, Organo, Shimizu Co., the Marine Biotechnology Research Institute, etc. participated in the joint research project. In this project, the efficiency of in-situ bioremediation, elucidation of a remediation mechanism, influence evaluation to the ecosystem, etc. were performed through the field experiment in the trichloroethylene (TCE) polluted site.

The objectives of this study were to evaluate the solute transport characteristics of targeted aquifer, such as retardation factor, and to evaluate the nutrients mixing methods for developing the designing method of in-situ bioremediation.

2 OVERVIEW OF THE FIELD TEST

The field experiment was conducted at the TCE pollution site in Kimitsu-city, Chiba, 1989. At this site the pump & treatment were performed and TCE concentration was reduced to the value about ten times the concentration of the Japanese environmental quality, but the remediation efficiency felt with time.

The aquifer to be treated is an unconfined aquifer (permeability coefficient is about 2.1×10^{-3} cm/s) composed of diluvial fine sand ($d_{50} = 0.019$ cm).

The remediation process considered here is in-situ biostimulation, which is one of bioremediation methods. Biostimulation is a technique that stimulates indigenous microbes to degrade contaminants. The condition is created by injecting electron donor, electron acceptor, and nutrients into aquifer and by mixing them with the contaminated groundwater at the proper concentration. The remediation system applied to this site is based on groundwater circulation in which contaminated water is pumped up from a well and mixed with the nutrients and oxygen, methane, and then water is reinjected through injection wells (Figure 1). Many

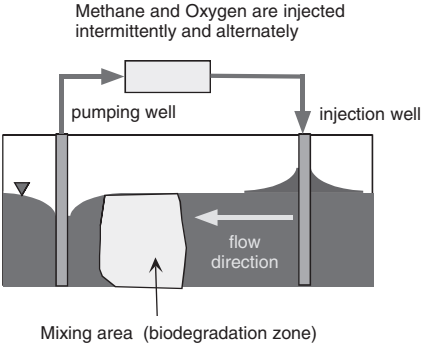


Figure 1. Schematic diagram of in-situ circulation bioremediation.

Copyright © 2003 Swets & Zeitlinger B.V., Lisse, The Netherlands

investigators have demonstrated biodegradation of TCE using methanotrophs. Some methanotrophs can degrade TCE aerobically with cometabolism, because their enzyme (methane monooxygenase) has a wide range of degradation activities.

3 EVALUATION OF SOLUTE TRANSPORT CHARACTERISTICS

3.1 *Hydrogeological parameter*

In order to investigate the hydrogeological characteristic of the aquifer, soil analysis and in-situ examination were performed. In drilling investigation, while having grasped the stratum distribution in detail, parameter values, such as the aquifer length or static head, were acquired. In the in-situ examination hydrogeological characteristic parameters, such as permeability and radius of influence, were obtained as shown in Table 1.

3.2 *Evaluation based on laboratory column test*

The laboratory column test was conducted using solutes that should be actually injected in an aquifer (oxygen, methane, nutrients, TCE, DCE). The purpose of this test is to determine the retardation factor that should be applied in the design analysis (Figure 2).

3.3 *Retardation factor*

The primary substrate and nutrients required for the multiplication of microbes may adsorb to the surface of the particles of an aquifer, and delay may arise in the movement of the substance in the aquifer. Then, in order to grasp the retardation characteristic of each substance required for biostimulation, a soil column test was conducted. The objects of the test were TCE, methane, oxygen, and nutrients (each ion of nitrate, nitrite, sulfate, and phosphate). In this test, sand was taken from the site where the field test was performed. The sand was packed in a column with the same density as the targeted aquifer. The solute transport characteristics were evaluated by examining the breakthrough curve observed at the downstream end of the column. The concentration of nutrients was measured by ion chromatograph method and oxygen was measured by dissolved oxygen meter. TCE and methane were measured by the head space gas chromatograph method. Moreover, the chlorine, bromine, and iodine ion, which are nonreactive tracers, were measured as contrast. The retardation factor of each substance is shown in Table 2.

The value of retardation factor of chlorine and bromine, which are nonreactive tracers, showed as 1.0. Although the retardation factor of chlorine or bromine with same nitric acid, nitrous acid, and sulfuric acid was 1.0, the retardation factor of phosphate was 2.9. However, since a sufficient quantity (160 mg/kg) of phosphate was contained in soil, it was guessed that the supply of phosphate would not be necessary. Moreover, although oxygen and methane did not show retardation, TCE and DCEs showed 1.2 and about 1.1 delay respectively. The movement of organic compounds, such as TCE, is thought to receive much influence from the organic matter content in the aquifer. From the value of the factors, it is thought that it originates in the low organic matter content of the aquifer at the concentration of 200 mg/kg. Moreover, the calculated value of retardation factor of TCE and DCEs from the equation 1 and the measurement data were comparatively

Table 1. hydrogeological parameters of the field test aquifer.

Parameter	Value
Permeability (cm/s)	2.0×10^{-3}
Static head (m)	5.0
Radius of influence (m)	10
Groundwater flow rate (cm/sec)	$1–5\times10^{-5}$

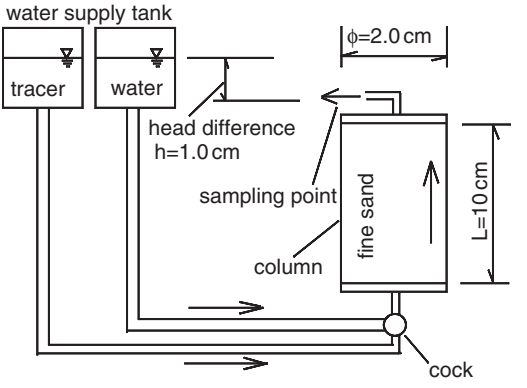


Figure 2. Schematic diagram of laboratory column test.

Table 2. Retardation factors of primary substrates, nutrients, and contaminants.

Substance	Retardation factor
Chlorine	1.0
Bromine	1.0
Iodine	1.0
Nitrate	1.0
Nitrite	1.0
Sulfate	1.0
Phosphate	2.9
Oxygen	1.0
Methane	1.0
TCE	1.2
DCEs	1.1

Copyright © 2003 Swets & Zeitlinger B.V., Lisse, The Netherlands

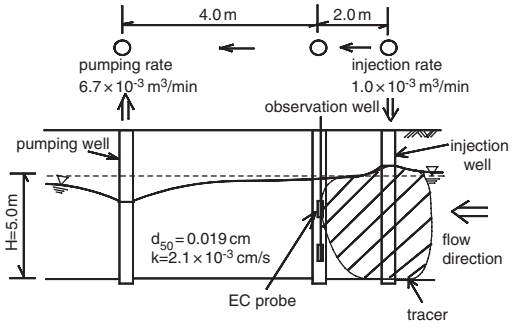


Figure 3. Outline of the in-situ tracer test.

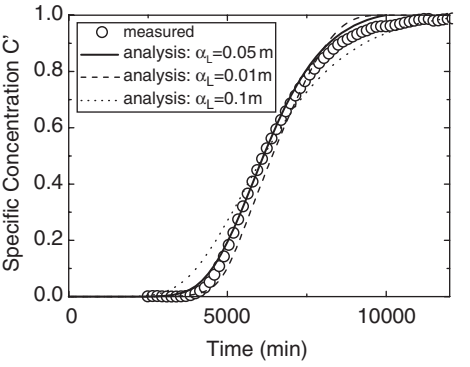


Figure 4. Breakthrough curve of tracer test.

well in agreement (Table 2). The dispersivities of TCE and chlorine are very close, 8.5×10^{-3} cm^2/s and 8.2×10^{-3} cm^2/s, respectively.

$$R = 1 + (0.63 \times f \times K_{ow} \times \rho)/n \quad (1)$$

where f = fraction of organic carbon, K_{ow} = octanol–water partition coefficient, ρ = dry bulk density, n = porosity.

3.4 *Evaluation based on in-situ tracer test*

An in-situ tracer test was conducted using the additives (methane solution, oxygen solution) to be used in an actual groundwater in-situ bioremediation system.

An advective–dispersive analysis was performed to estimate dispersivity from the test results. The numerical code used here was based on the upwind finite element method. The same analysis code was used in the remediation system study described in the following chapter.

In the tracer test, automatic pumping and injecting system was used, which is able to keep a constant injecting tracer flow rate. Figure 3 illustrates the concept of the system. The test procedure was as follows. At first, groundwater was pumped up from pumping wells at a rate of Q = 6.7 l/min (which is 80% of the maximum pumping capacity for the well) to create an artificial groundwater flow field. Then, when the groundwater level stabilized, 100 ppm NaCl solution was injected continuously into the injection wells at a rate of 1.0 L/min. Finally, electrical conductivity is measured with time at the observation well located downstream of the injection well.

Figure 4 shows the test results. The time required for the specific concentration (the ratio assuming the concentration at a time of injection as 1.0) of tracer to become 0.5 was used to calculate the actual flow velocity and effective porosity. Two-dimensional advective–dispersive analysis was conducted to determine dispersivities that fit the breakthrough curves. The calculated values of effective porosity obtained from breakthrough curves were typical value of fine sand's aquifer (around 30%). Longitudinal dispersivity (an indicator of dispersion in the direction of flow) was about 0.05 m.

Table 3. The parameters for the solute transport analysis.

Parameter	Value
Permeability (cm/s)	2.0×10^{-3}
Static head (m)	5.0
Radius of influence (m)	10
Longitudinal dispersivity (m)	0.05
Transverse dispersivity (m)	0.005
Effective porosity (%)	30
Pumping rate (m^3/min)	1.5×10^{-3}
Injection rate (m^3/min)	1.5×10^{-3}

4 SYSTEM DESIGN

4.1 *Analysis model*

Solute transport analysis was conducted in order to investigate the conditions under which a methane solution and an oxygen solution are to be well mixed with using characteristic values defined on the basis of the solute transport evaluation in the preceding chapter. The parameters of the analysis are shown in Table 3.

4.2 *Mixing region*

It is pointed out that the rapid multiplication of microorganisms would cause clogging and serious lowering of permeability at the injection well if nutrients are injected continuously and simultaneously from one injection well. In order to prevent this clogging, methane and oxygen required for multiplication of the microbe should be injected separately to avoid mixing in a well. As shown in Figure 5, two methods can be considered to solve this problem.

Copyright © 2003 Swets & Zeitlinger B.V., Lisse, The Netherlands

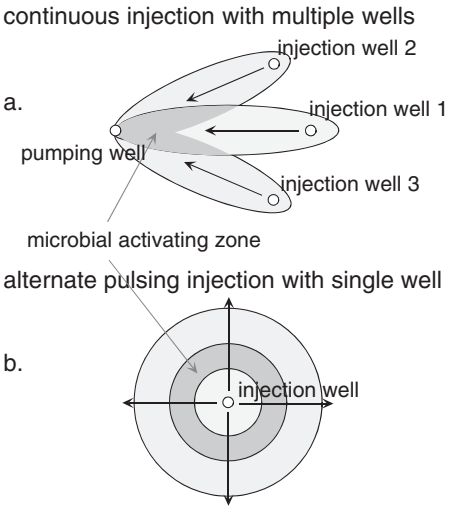


Figure 5. Well schemes for biofouling prevention.

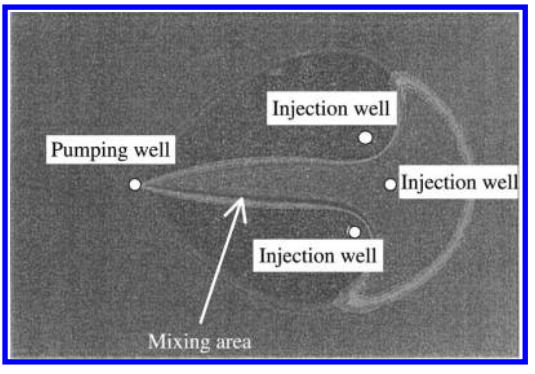


Figure 6. Primary substrates distribution with multi-point simultaneous injection.

In the former method, water with nutrients is injected simultaneously from two or more wells (a. multi-point simultaneous injection), and in the latter method, water with nutrients is injected intermittently from one well (b. one-point intermittent injection).

In order to remediate TCE contaminated groundwater effectively by biostimulation, the methane and oxygen, which were injected separately, should be mixed well in the aquifer, and it is necessary to form the microbe activation region where TCE is decomposed. The solute transport analysis was carried out to obtain the result of the concentration distribution of the methane and oxygen in each method. The result is shown in Figures 6 and 7.

From the result of the analysis, it became clear that the mixing region by the one-point intermittent injection method is wider than that by the multi-point simultaneous injection method. It is suggested

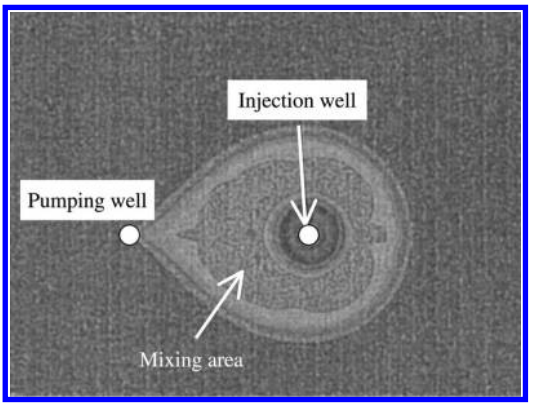


Figure 7. Primary substrates distribution with one-point intermittent injection method.

Table 4. Designing conditions.

	Injection time (min)			
Case	Methane solution	Water	Oxygen solution	Water
Case 1	500	500	500	500
Case 2	500	250	500	250
Case 3	250	250	250	250

that mixing by using transverse dispersion along a streamline would not be enough for efficient mixing. Since the permeability coefficient of this field test site was almost $2–5\times10^{-3}$ (cm/sec) and the comparatively low, the one-point intermittent injection method is applied to the test. Although it is thought that the one-point intermittent injection method is more effective, it is presumed that a multi-point simultaneous injection system is also applicable at the site where the permeability coefficient is very big.

4.3 *Injection pattern*

A simulation analysis was used for examining the optimal condition for the injection pattern of methane and oxygen in the one-point intermittent injection method. The condition of injection pattern used for analysis is shown in Table 4. In order to avoid mixing in an injection well, water was poured in after injection of methane and oxygen.

Figure 8 shows the changes with time of methane and oxygen concentrations at the observation wells A, B, and C. The wells are installed 0.75 m intervals away from the injection well. A is the nearest to the injection well and C is the most distant from the injection well. The two solutions in Case 2 tend to be mixed

Copyright © 2003 Swets & Zeitlinger B.V., Lisse, The Netherlands

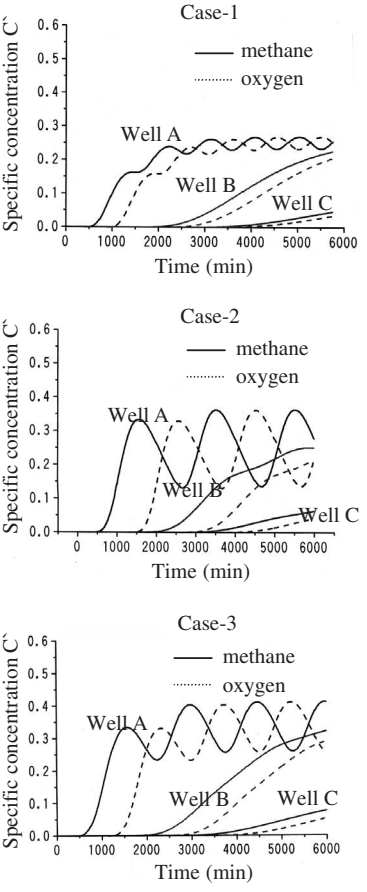


Figure 8. Breakthrough curve of methane and oxygen in Cases 1–3.

together at higher concentrations than in Case 1. It also shows that the concentration of both methane and oxygen in Case 3 is smaller than that in Case 1. These results indicate that the analysis model is capable of predicting the location of the mixing zone with required values of each substance's concentration. Hence, it is possible to decide the required intervals among methane, oxygen and water injection and the required concentration of each substance when injecting, from the analysis shown here.

4.4 *Flow pattern*

An injection and pumping well system and their flow patterns were shown in Figure 9. In this case, well A and well B are the injection wells with a flow rate 1.5l/min each, and the well C is the pumping well with a flow rate 3.0l/min. Most of streamlines out of both injection wells enter the pumping well except 2

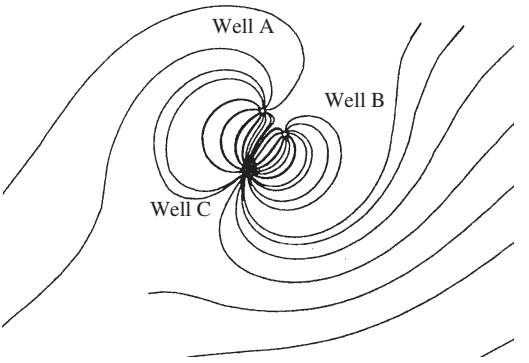


Figure 9. Flow pattern of injection and pumping well system.

streamlines to the downgradient. From the ratio of entering streamlines into the pumping well to sum of streamlines from the injection wells, the circulation factor *R* can be assumed. The streamlines connecting the injection and pumping wells are the circulation flows in which contaminants would be biodegraded. The injection and pumping well system is analogous to the bioreactor, such as a biological wastewater treatment.

In the case of cometabolic degradation of TCE, the biodegradation rate is so slow compared to that of aerobic treatment of wastewater. This means that the cometabolic degradation of TCE needs more retention time to clean up so that the circulation factor *R* should be higher. The circulation factor, *R*, is affected by the regional hydraulic gradient, flow rate of the injection and pumping wells, and the angle of well line to the regional flow. In the case of Figure 9, the circulation factor, *R*, is 85–90%. From this flow pattern analysis, well spacing and number for the in-situ system can be determined for the optimum well configuration design.

5 CONCLUSIONS

In this study, the laboratory column test indicated that both oxygen and TCE are transported in aquifer in almost the same manner as typical conservative solutes. The mixing of oxygen, methane, and nutrients were quantitatively evaluated by using a solute transport analysis on the basis of precise evaluation of transport characteristics. This analysis makes it possible to predict an optimum intermittent injection time and the required concentration of each substance to be injected, which can create an effective condition to degrade TCE in groundwater efficiently. Furthermore, from the flow pattern analysis, well spacing and number for the in-situ system can be determined for the optimum well configuration design. These

Copyright © 2003 Swets & Zeitlinger B.V., Lisse, The Netherlands

methods, therefore, should be useful in designing a biostimulation system for groundwater contaminated with TCE.

In addition, a part of result in this paper is obtained from the Industry's soil remediation technology development project implemented by the Research Institute of Innovative Technology for the Earth (RITE). This project is under a contract with the New Energy and Industrial Technology Development Organization (NEDO) of the Ministry of Economy, Trade and Industry of Japan.

REFERENCES

Brett T. Kawakami et al. 1998. Design of an In-situ Injection/Extraction Bioremediation System. The First International Conference on Remediation of Chlorinated and Recalcitrant Compounds (C1-6): 33–38.

John T. Cookson, JR. 1995. Bioremediation Engineering. McGraw-Hill, Inc: 272–273.

Kawabata et al. 1998. The design Method using Transport Analysis for In-situ Bioremediation of Groundwater. Bibliography 1 The Kajima Technical Research Institute annual report. 46: 183–188.

L. Semplini et al. 1991. Between model simulations and field results for in-situ biorestoration of chlorinated aliphatics. Ground Water. 29: 365–374.

Robert S. 1989. In-situ Aquifer Restoration of Chlorinated Aliphatics by Methanotrophic Bacteria. 172–196.

U.S. EPA. 1998. Technical protocol for evaluation natural attenuation of chlorinated solvents in ground water. EPA/600/R-98/1998: 25–28.

William J. Dentsch. 1997. Groundwater Geochemistry. Lewis Publishers: 54–55.

Xu & Eckstein. 1995. Use of least-Squares Method in Evaluation of Relationship between Dispersivity and Field Scale. Groundwater. 33(6): 905–908.

Copyright © 2003 Swets & Zeitlinger B.V., Lisse, The Netherlands

Subsurface environmental change after HRC injection

M. Nakashima & X. Wu
Kokusai Kogyo Co. Ltd., Tokyo, Japan

M. Nishigaki
Okayama University, Okayama, Japan

ABSTRACT: A field study on hydrogen release compound (HRC) enhanced in-situ bioremediation barrier was performed. The bio-barrier was designed to remediate chlorinated contaminants in groundwater at the site to prevent further spreading of contaminated groundwater plume. With one injection, HRC has substantially accelerated the natural reductive dechlorination process and marked decrease of contaminant concentrations were obtained within a one-year period. Detailed subsurface environmental change after HRC injection was investigated by comparing bio-barrier downgradient monitoring well (W2) result with upgradient monitoring well (W1) result. Possible organic acids of lactic acid, pyruvic acid, butyric acid, propionic acid and acetic acid from microbiologically metabolizing of HRC were measured from W2. DO, pH, ORP, TOC, EC, temperature, sulfate concentration and chloride concentration in W1 and W2 were measured to evaluate the subsurface environmental change after HRC injection. Monitoring data show that DO in groundwater decreased a little bit. There was no obvious change in pH and EC were measured, decreasing of ORP and sulfate were consistent well with organic acid concentration and TOC changes in groundwater.

1 INTRODUCTION

Environmental investigation of a plant shows that its groundwater is contaminated by chlorinated organic compounds. The plant once used the organic solvent of tetrachloroethylene (PCE) for many years. Besides PCE, trichloroethylene (TCE) and cis-1.2-dichloroethylene (cis-DCE) were also detected from groundwater samples, both TCE and cis-DCE are believed to be daughter products of PCE at this site. Because the plant is still under operation and it is hard to remediate the source of the contaminants, which are located under the plant building. However, at groundwater downgradient boundary of the plant, contaminant concentrations exceeded the Environmental Quality Standards (EQS). Evaluating on natural attenuation result of the site showed, though relatively high concentrations of daughter products were detected at downgradient, contaminated groundwater plume is still under enlarging stage. In order to prevent further spreading of contaminated groundwater to outside of the plant, a bio-barrier was decided to be set up for accelerating the natural attenuation process, and monitoring result will be used to decide if any further actions need to be taken. Hydrogen Release Compound (HRC) from Regenesis was selected as the hydrogen donor and nutrient to be injected since its long term and slow hydrogen release features. Two monitoring wells were set up one in upgradient of the bio-barrier and another one at downgradient. After HRC was injected into the aquifer through the injection wells, water samples were taken basically once a month for analyzing contaminant concentration change in groundwater for evaluating enhanced bioremediation effect, geo-environmental parameters as dissolved oxygen (DO), oxidation-reduction potential (ORP), sulfate concentration, pH, electric conductivity (EC), temperature and total organic carbon (TOC) were closely monitored as well. These detailed field parameters were used for evaluating geo-environmental change and future remediation design.

2 FIELD APPLICATION

2.1 *On HRC*

HRC^{TM} (produced by Regenesis) is a food quality, polylactate ester specially formulated for the slow release of lactic acid (an organic acid) upon hydration (Koenigsberg 1999). The lactic acid in HRC will be converted to several other acids as pyruvic acid, butyric acid, propionic acid and acetic acid. Along this hydration process, the hydrogen will be produced

Copyright © 2003 Swets & Zeitlinger B.V., Lisse, The Netherlands

simultaneously, and produced will be used by reductive dechlorinators, which have capability of dechlorinating contaminants, such as PCE, TCE, dichloroethylene (DCE) and vinyl chloride (VC) (Cornuet et al. 2000). The injected HRC not only serves as a hydrogen source as an electron donor, but also as an essential nutrient source when it changes to a series of organic acids, which are ideal for stimulating and sustaining rapid microbial growth. Several studies show that HRC has capacity of releasing hydrogen as long as about one year, and this can dramatically reduce operation and maintenance costs compared to the repeated and continuous injections associate with other substrate. Because it offers an in-situ treatment, and no any above ground equipment is required after injection, daily business and commercial activities can be continued as usual.

2.2 *Field condition*

The aquifer of the field site is about 3 to 6 m below the ground surface and it has an average thickness about 2.1 m. The aquifer is mainly composed of gravel with some boulder. Since exist of boulder in aquifer formation, it is hard to drill the borehole again and again to inject HRC through direct injection method, 2 rows of injection wells were designed for HRC injection. The layout of HRC injection wells is given in Figure 1. All together, 7 wells (4 at upgradient and 3 at downgradient) were constructed, the width of contaminated groundwater plume is about 8 m, 2.5 m interval between injections wells was chosen. Originally, boreholes were drilled with rotary-percussion machine, which made the diameter of borehole as 146 mm, thick-type PVC pipe was used as well casing, which has inner diameter of 48.6 mm and the slot of well screen is 2 mm. Around the injection well screen, 15 mm to 20 mm small stone was filled as package.

2.3 *HRC injection*

For calculating HRC injection amount, highest history monitored contaminant concentration values were used, and on other water quality data, result of W2 before injection well construction were used. Based on these conditions, the estimated minimum requirement of HRC was 218 kg, and this amount was estimated by assuming that all sulfate ion of 110 mg/l in groundwater would be reduced. However, it is hard to estimate at first time that how much sulfate should be reduced. Supposing only 50 mg/L sulfate would be reduced through HRC consumption, then required amount of HRC would be about 116 kg. Because of the high sulfate concentration in groundwater, HRC injection amount evaluation shows that sulfate reduction is a very sensitive factor at this site. No nitrate and iron were detected from groundwater, and as Bouwer (1994) has pointed out (USEPA 1998) that the most

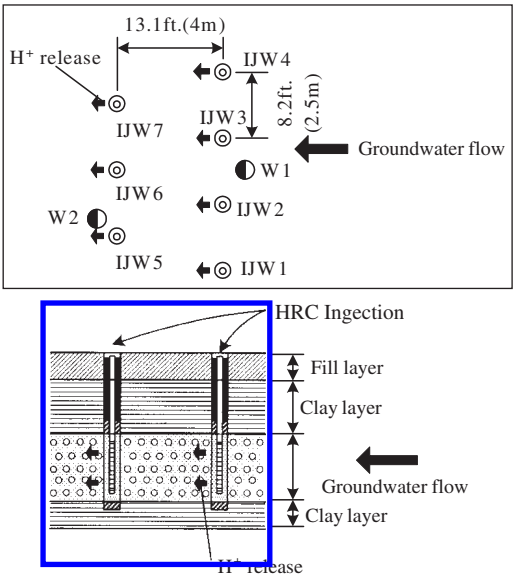


Figure 1. Site layout and injection wells.

rapid reductive dechlorination occurs under sulfate-reducing condition, sulfate reduction situation can be a good indicator at this site for reductive dechlorination process.

HRC was firstly heated with 60°C hot water to decrease its viscosity, and then injected into each well through injection pump. For seeking high safety and considering field management, 272 kg HRC was injected at last for first injection.

3 RESULT AND DISCUSSION

3.1 *Decreasing of chlorinated organic compounds*

After HRC injection, more than one year has passed. Concentrations of PCE, TCE, cis-1,2-DCE, trans-1,2-DCE, 1,1-DCE and VC in well W1 and W2 were measured and the result are shown in Figure 2.

It is clear that within whole period, contaminant concentrations in W1 have not changed too much, which indicates a relatively stable high concentration groundwater flowing into the HRC barrier. However, after HRC injection, data in W2 show that concentrations of PCE and TCE have been decreased very rapidly, and within one year period, no apparent TCE accumulation was measured from W2. The result can be clearly seen from Figure 3, which is calculated and depicted on molar concentration of contaminants. Enhanced biodegradation of chlorinated contaminants can be obviously observed from total contaminant molar concentration change. Average contaminants molar concentration in W1 was

Copyright © 2003 Swets & Zeitlinger B.V., Lisse, The Netherlands

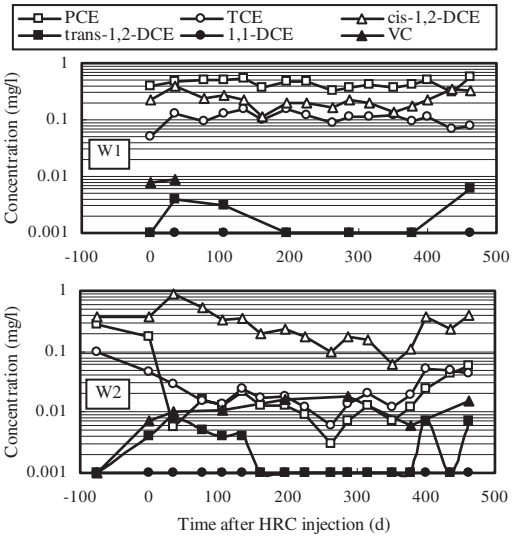


Figure 2. VOCs concentration change in W1 and W2.

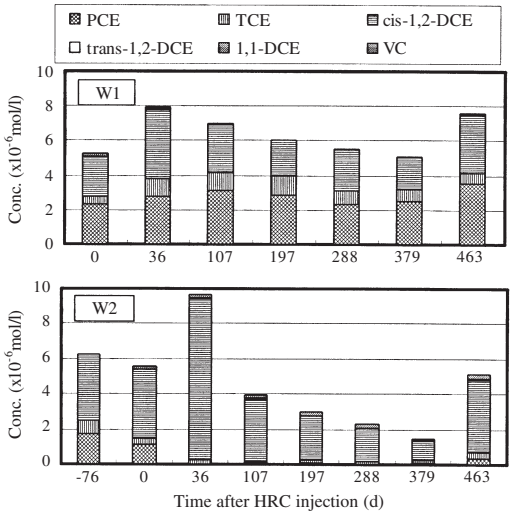


Figure 3. Contaminant molar concentration change in W1 and W2.

about 6×10^{-6} mol/l, and they are mainly composed of PCE, TCE and cis-DCE, after HRC injection, PCE and TCE concentrations decreased to a very low level and the main contaminant had been changed to cis-DCE, which can be seen from the result of W2. In W2, 36 days after HRC injection, cis-DCE reached the highest concentration and after that it began to decrease as well. After one year, the total contaminant molar concentration had been decreased to lower than 2×10^{-6} mol/l.

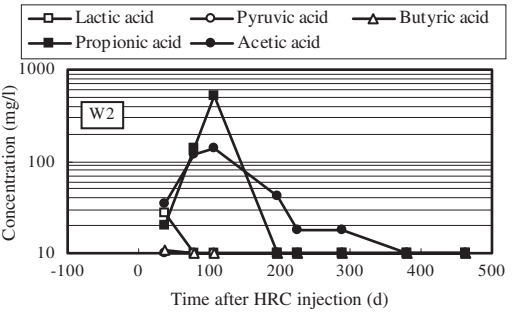


Figure 4. Organic acid concentration in W2.

The results show that HRC injection had accelerated biodegradation of main PCE contaminant at this site substantially, just very low concentrations of PCE and TCE were detected from downgradient monitoring well. cis-DCE accumulation was observed after 36 days and though cis-DCE turned to decrease after that, degradation of cis-DCE was slower than PCE and TCE. Detailed discussion can be found in Nakashima et al. (2002). Rebound of contaminants occurred about 400 days after HRC injection, this result is consistent well with the expected one year HRC life for one injection as designed. Depends on good monitoring result, second HRC injection was conducted 423 days after first injection.

3.2 *Concentration of organic acid*

After HRC injection, concentration of organic acids in W2 were measured for following injected HRC change in subsurface, the results are shown in Figure 4. Pyruvic acid and butyric acid were almost not detected from water samples, and lactic acid was detected only at first sampling after HRC injection. However, after HRC injection propionic acid and acetic acid concentrations in groundwater increased very quickly and reached the highest concentrations simultaneously at 107 day. After that, propionic acid concentration decreased very quickly within one month to undetectable level (<10 mg/L). Acetic acid concentration turned to decreasing too, and in sample of 379 days late, no any acetic acid was detected, which is believed to indicate that all HRC has been exhausted in the aquifer. Measured result of organic acid concentrations change is consistent with contaminant concentration decreasing, both of them indicate that injected HRC has lasted for about one year to be dissolved into water and microbiologically metabolized to different form of organic acid and release hydrogen for accelerating reductive dechlorination process.

3.3 *DO and pH*

DO has been used as the main indicator to show that subsurface environment is suitable for anaerobic

Copyright © 2003 Swets & Zeitlinger B.V., Lisse, The Netherlands

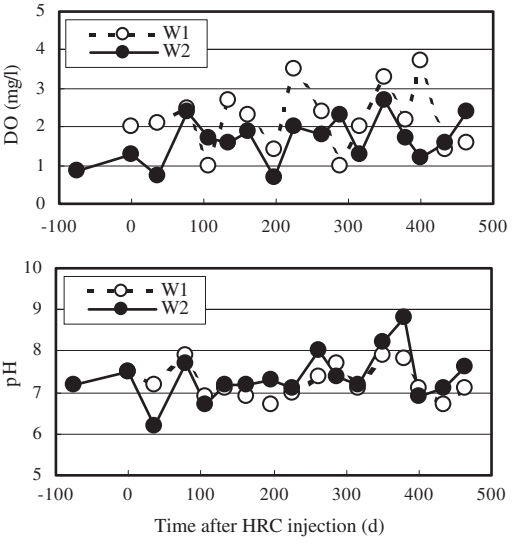


Figure 5. Measured DO and pH in W1 and W2.

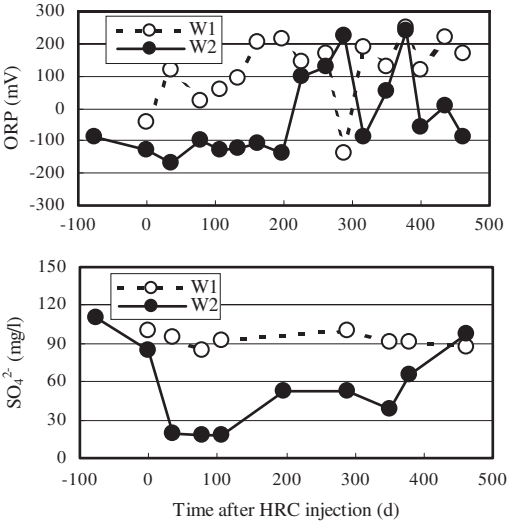


Figure 6. Measured ORP and sulfate concentration.

reductive dechlorination process, and it is said that anaerobic bacteria generally cannot function at DO concentration greater than about 0.5 mg/l (USEPA 1998). DO was well monitored at this site before and after HRC injection, the result is given in Figure 5. At this site, because of relatively high cis-DCE concentration in groundwater, and the plant never used any kind of dichloroethylene, it is believed cis-DCE in groundwater is the daughter product of PCE, which means reductive dechlorination process had been happening before HRC injection, though DO in groundwater is not lower than 0.5 mg/l. After HRC injection, DO from two monitoring wells were measured. The data show that DO in W2 is generally lower than DO in W1, however, the average DO concentrations in W1 and W2 are not so different and both of them are about 2 mg/l. If considering measured result in W2 before HRC injection that DO concentration in W2 was a little bit lower than in W1, it is hard to say that HRC injection has caused obvious DO deduction. It is considered that because of not uniform condition in subsurface, a relatively high DO concentration in groundwater sample doesn't necessarily mean that the whole area in aquifer is under aerobic condition. Well accelerated PCE degradation at this site has proved that reductive dechlorination process can be well enhanced even field measured DO concentration is as high as about 2 mg/l or a little bit more.

pH is not only an important parameter affecting microorganism activities, but also a very sensitive parameter at combined contamination site, particularly if the site is contaminated by heavy metals as well. Since the change of pH may cause heavy metals in soil to dissolve into groundwater and transport to downgradient. Measured pH data after HRC injection is also given in Figure 5. The data show that except two times, pH in W2 were almost same as in W1. First difference was measured one month after HRC injection, which gave the pH in W2 was about 1 unit lower than in W1, and the second apparent difference was appeared one year late which shows that pH in W2 was conversely a little bit higher than in W1. Because of hydrogen release from HRC, there is possibility for pH decreasing at HRC application site, however, the released hydrogen will be utilized by reductive dechlorination and other subsurface reactions. The measured results show that at this site HRC injection had not caused obvious pH change in subsurface.

3.4 *ORP and sulfate concentration*

ORP of groundwater is a measure of electron activity and is an indicator of the relative tendency of a solution to accept or transfer electrons. Oxidation-reduction reactions in groundwater containing organic compounds are usually biological mediated and therefore, ORP of a groundwater system depends upon and influences rates of biodegradation (USEPA, 1998). ORP is also important because some biological processes operate only within a prescribed range of ORP conditions.

Measured ORP data is shown in Figure 6, at the beginning of 200 days, ORP in W2 was obviously reduced to a lower level than in W1, and after that reincreasing tendency was measured, which basically is consistent with organic acids measurement result. At the beginning of 200 days, high organic acids concentrations were measured, and these organic acids

Copyright © 2003 Swets & Zeitlinger B.V., Lisse, The Netherlands

supplied carbon sources for microorganism activities. So it can be deduced that at this stage since abundant existing of nutrients, active microorganism activities can be expected and consequentially, ORP in subsurface was reduced obviously. However, when organic acid concentration was undetectable, ORP data showed obvious increase also.

One feature of this site is that sulfate concentration in groundwater is quite high (about 110 mg/l). Reductive dechlorination has been demonstrated under nitrate and iron-reducing conditions, however, the most rapid biodegradation rates, affecting the widest range of chlorinated aliphatic hydrocarbons, occur under sulfate-reducing and methanogenic conditions (USEPA, 1998). In order to get optimal degradation condition, it is necessary to reach sulfate-reducing condition, which means more HRC should be injected to reduce sulfate in groundwater. First injected amount of HRC was estimated on exhausting all sulfate in groundwater and actual sulfate concentration change in groundwater is also given in Figure 6. Measured data show that after HRC injection, sulfate in groundwater was rapidly decreased to about 20 mg/l. However, after 200 days, sulfate concentration in W2 increased to about 50 mg/l level and maintained for nearly 100 days. One year late after HRC injection, obvious sulfate concentration increase in W2 was measured. Sulfate concentration change are consistent well with ORP data, when sulfate concentration turned to increase, ORP data increased either, which shows that ORP is a very good indicator to reflect subsurface environment change. Additionally, in last 100 days, though sulfate concentration in groundwater kept at about 50 mg/l level, continuous decreasing of contaminant concentrations (Fig. 3) showed reductive dechlorination processed well. So for second injection, HRC amount was calculated for assuming reducing sulfate to 30 mg/l other than zero as in first injection.

Which has been pointed out previously that at this site, though HRC injection has accelerated the biodegradation of cis-DCE in groundwater, but estimated degradation rate from field data (Nakashima et al. 2002) show that half-life of cis-DCE is obviously longer than half-lives of PCE and TCE, and even after one year, a relatively high concentration of cis-DCE was measured from downgradient monitoring well. This result can be explained as, since the rate of reductive dechlorination decreases as the degree of chlorination decreases (USEPA 1998), it is not strange that field measured data had given a relatively longer half-life of cis-DCE than PCE and TCE. However, up to date researches show that dehalogenation of DCE and VC generally are restricted to sulfate reducing and methanogenic conditions (USEPA, 1998), measured result of ORP and sulfate concentration show that at the beginning 200 days, both of ORP and sulfate concentration decreased distinctively, however, after 200 days, when organic acids were almost undetectable, both of ORP and sulfate concentration increased, particularly the ORP data increased to near to upgradient ORP level, which may indicate apparent subsurface environment change. So another reason of small degradation rate of cis-DCE at the site maybe related to the high ORP and sulfate concentration in aquifer.

3.5 *Other environmental parameters*

Besides DO, pH, ORP and sulfate concentration, total organic carbon (TOC), chloride concentration, electrical conductivity (EC) and temperature were also measured and result of these parameters are given in Figure 7. After HRC injection, TOC in W2 was apparently higher than in W1 and it maintained until 300

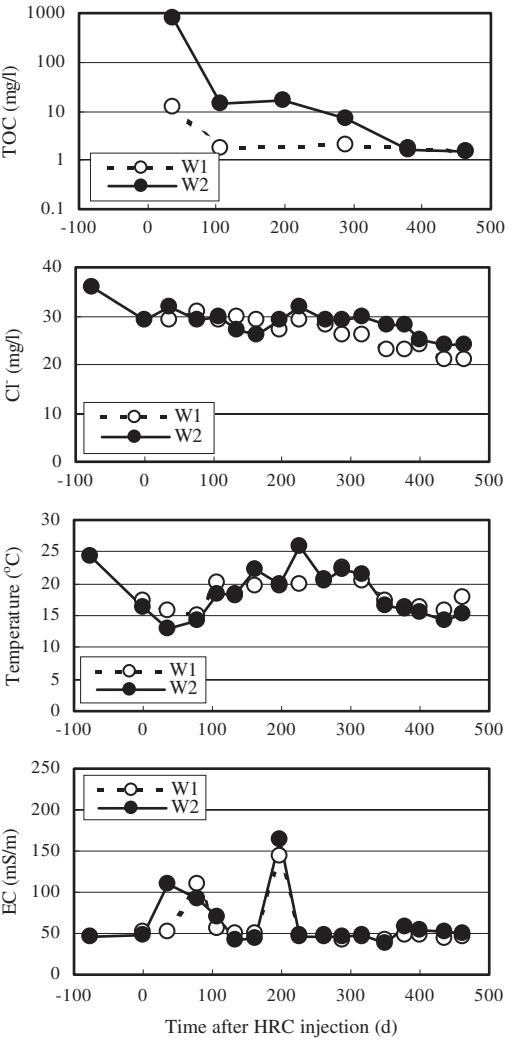


Figure 7. Measured TOC, Cl^-, temperature and EC in W1 and W2.

Copyright © 2003 Swets & Zeitlinger B.V., Lisse, The Netherlands

days late as expected in designing stage. Chloride concentration data showed that in W2 it was a little bit higher than in W1, it is clear that dechlorination process should have increased chloride ion concentration in downgradient groundwater, however, within whole study period, chloride concentration change in upgradient monitoring well was as large as about 10 mg/l, it is hard to distinguish how much of chloride comes from dechlorination process and how much was caused by chloride difference in coming groundwater.

Measured data show that HRC injection had not caused any obvious change in groundwater temperature and EC, temperature and EC data in W2 are almost equal to data in W1.

4 CONCLUSIONS

By HRC injection, natural biodegradation of chlorinated organic contaminants at this site had been dramatically accelerated. For first injection, accelerated degradation process had been lasted for about one year.

Environmental parameter changes after HRC injection have been closely investigated. ORP and sulfate in groundwater have been rapidly and distinctively decreased after HRC injection, however, 200 days late, both of them again increased to some-extent, which is consistent well with measured organic acid concentration change in groundwater. Site result show that it is not necessary to reduce sulfate to zero for enhancing bioremediation, at sulfate concentration of about 50 mg/l, contaminant concentrations of PCE and TCE greatly decreased in this research. However, field data show that degradation of cis-DCE is lower than PCE and TCE, no any accumulation of TCE was measured within one year period, other than obvious cis-DCE accumulation was measured about one month late. One reason can be considered is that reductive dechlorination decreases as the degree of chlorination decreases, which says that cis-DCE has a relatively longer half-life than PCE and TCE, it can be used to explain this field result. Additionally, when cis-DCE concentration reached the peak, it turned to decreasing rapidly, however, a relatively high concentration was continuously measured. Another reason can be considered is because of relatively high ORP and sulfate concentration data, particularly 200 days late, maybe the subsurface environment is not too good to degrade cis-DCE rapidly. After one year, when accelerated reductive dechlorination process stopped, both ORP and sulfate concentration increased to original levels.

Though DO data in downgradient monitoring well was a little bit lower than in upgradient monitoring well generally, no obvious DO change has been measured in this research. Further more, a relatively high DO concentrations (1–3 mg/l) were field measured in both monitoring wells, no matter field reductive dechlorination process had been well enhanced. This result suggests that, for field DO data, it is not necessary to be lower than 0.5 mg/l to show suitable reductive dechlorination condition.

Measured pH data show that before and after HRC injection, the site was almost under neutral condition and HRC injection did not cause obvious change of subsurface pH.

TOC in downgradient monitoring well was obviously increased after HRC injection, and it decreased gradually until one year late, when it is almost equal to the concentration in upgradient well. This result is consistent well with organic acid result in this research. Because organic acid analysis is quite expensive, for generally monitoring carbon source situation in subsurface after HRC injection, maybe TOC analysis can give adequate information.

Generally, chloride concentration in downgradient monitoring well was higher than in upgradient monitoring well, however, three lower data were also measured and particularly since chloride concentration in coming groundwater showed a wide change range. If contaminant concentration is low, such as at this site, even reductive dechlorination processed very well, it is hard to evaluate reductive dechlorination process indirectly through chloride concentration analysis.

REFERENCES

Cornuet, T. S., Sandefur, C., Eliason, W. M., Johnson, S. E. & Serna, C. 2000. Aerobic and Anaerobic Bioremediation of cis-1,2-Dichloroetene and Vinyl Chloride. In Koenigsberg, S. S. (ed.), *Accelerated Bioremediation of Chlorinated compounds in groundwater.* Regenesis Bioremediation Products, 41–49.

Koenigsberg, S. S. & Farone, W. A. 1999. The Use of Hydrogen release compound (HRC^{TM}) for CAH Bioremediation. In Leeson, A. & Alleman, B. C. (eds), *Engineered Approaches for In Situ Bioremediation of Chlorinated Solvent Contamination.* Proceedings from the Fifth International In Situ and On-Site Bioremediation Symposium held April 19–22, San Diego, California.

Nakashima, M., Wu, X., Okada, R. & Nishigaki,M. 2002. Enhanced bioremediation of chlorinated solvents by HRC injection in Japan. *The third international conference on remediation of chlorinated and recalcitrant compounds*, May 20–23, 2002. Monterey, California. Sponsored by Battelle.

US Environmental Protection Agency, 1998. *Technical Protocol for Evaluating Natural Attenuation of Chlorinated Solvents in Ground Water.* EPA/600/R-98/128.

Copyright © 2003 Swets & Zeitlinger B.V., Lisse, The Netherlands

Remediation of hydrocarbon contamination in groundwater using in-situ biosparging

K.R. Reddy
University of Illinois, Chicago, Illinois, USA

J.A. Adams
ENGEO Consultants, San Ramon, California, USA

ABSTRACT: As an alternative to the use of coupled in-situ air sparging and soil vapor extraction (SVE), in-situ biosparging is increasingly being implemented to remediate hydrocarbon-contaminated groundwater. This paper presents the results of a laboratory investigation performed to assess and quantify the removal and degradation of hydrocarbon contamination within saturated soils and groundwater. A series of batch reactor tests were performed to determine the kinetics and stoichiometry of benzene degradation using a benzene enrichment culture. The resulting data were used to develop a modified Monod kinetics model to describe the rate of degradation as a function of biomass and benzene concentration. Additionally, a series of column tests were performed to determine the contribution of biodegradation to overall benzene remediation during air sparging in bioaugmented sand profiles. The tests revealed that biodegradation contributed significantly to overall benzene remediation. Substantial biodegradation occurred during periods between air injection until dissolved oxygen concentrations were depleted. The rates of degradation appeared to be independent of initial benzene concentration and biomass concentration for the range of concentrations used during testing. These results indicate that dissolved oxygen is the rate-limiting factor for aerobic biodegradation.

1 INTRODUCTION

In-situ air sparging has emerged as a popular remedial alternative to traditional pump and treat for the remediation of hydrocarbon-contaminated saturated soils and groundwater (Marley et al., 1992; Johnson et al., 1993; Ahlfeld et al., 1994; Reddy et al., 1995; Bass & Brown, 1997). During the use of air sparging, a gas, usually air, is injected into the subsurface below the lowest known point of contamination. Due to the effect of buoyancy, the injected air will begin to rise toward the soil surface. During this migration, the air will, through a variety of mass transfer and transport mechanisms, induce vapor-phrase portioning of NAPL- and aqueous-phase contamination. As the contaminant-laden air continues to migrate toward the surface, it will enter into the vadose zone, where collection and treatment can be performed using a soil vapor extraction (SVE) system.

When designing and implementing an air sparging system, the use of a complementary soil vapor extraction system to capture volatilized contaminants can add substantial cost to the remedial project. An alternative strategy known as biosparging is becoming a popular option to avoid the use of a soil vapor extraction system. Biosparging is essentially the same as air sparging except that air is injected strategically with the purpose of enhancing in-situ aerobic degradation of hydrocarbons instead of or in addition to vapor-phase partitioning and subsequent removal using soil vapor extraction. Biosparging differs from standard air sparging in that a lower air injection flow rate is used during implementation. Air is pulsed into the subsurface with a long period of air cessation, allowing biodegradation to take place and reducing remedial costs. When air is injected during biosparging, the subsurface dissolved oxygen concentration increases, stimulating native microbial populations and leading to aerobic biodegradation of hydrocarbon contamination.

A comprehensive research program has been underway at the University of Illinois at Chicago (UIC) to systematically investigate air sparging. Previous investigations were performed to investigate the effect of soil grain size and grain size distribution, air flow, the use of pulsed air injection, the synergetic effects of co-contaminants, and the effect of NAPL type on air sparging performance efficiency (Semer & Reddy,

Copyright © 2003 Swets & Zeitlinger B.V., Lisse, The Netherlands

1997; Semer et al., 1998; Reddy & Adams, 1998; Adams & Reddy, 1999; Reddy et al., 1999). Studies were also performed to investigate the effect of aquifer heterogeneity, groundwater flow, and the efficiency of air sparging to remediate NAPL contamination (Adams & Reddy, 2000; Reddy & Adams, 2000; Reddy & Adams, 2001).

While these studies have provided valuable results regarding parameters critical to the success of air sparging, previous testing had been performed using clean, sterile soils, eliminating the contribution of biodegradation to overall contaminant remediation. However, because biodegradation can substantially contribute to air sparging performance and biosparging is emerging as an option to standard air sparging, laboratory testing is necessary to study the contribution of biodegradation during air sparging use. Therefore, the objectives of this study are (1) to determine the kinetics of benzene biodegradation during the use of biosparging, and (2) to determine the contribution of biodegradation to overall contaminant removal during biosparging. To accomplish these objectives, a series of batch reactor tests and soil column tests were performed. This paper summarizes the results of this study. The detailed test procedures and analysis of the test results are given elsewhere (Adams, 1999).

2 EXPERIMENTAL METHODOLOGY

2.1 *Batch reactor tests*

The first series of tests were performed to determine the oxygen uptake rate with respect to initial benzene concentration within a benzene enrichment culture. A benzene enrichment culture was created from a supply of return activated sludge. The return activated sludge was spiked with benzene on a daily basis to promote the selection and enrichment of benzene degrading microbes.

For testing, a portion of the benzene enrichment cultures was aerated to achieve near-saturation dissolved oxygen probe to determine the rate of oxygen uptake. A total of 12 trials with benzene concentrations ranging from 0.14 mg/l to 102 mg/l were performed. The rates were plotted versus initial benzene concentration. The data was linearized to determine the necessary parameters for the Monod kinetic rate form (Adams, 1999).

The second series of tests were performed to determine the rate of benzene degradation as a function of initial benzene concentration. As before, a benzene enrichment culture was used for testing. 1000-mg/l cultures were placed into 250-ml amber bottles and spiked with benzene. The benzene concentration with respect to time was determined through culture sampling and analysis using gas chromatography at pre-determined times throughout the test. A total of six trials were performed using initial benzene concentrations ranging from 9.3 mg/l to 74.1 mg/l. The data was linearized to determine the necessary parameters for the Monod kinetic rate form (Adams, 1999).

Both series of batch tests were conducted at room temperature of 25°C.

2.2 *Soil column tests*

To determine the effect of biodegradation during the use of biosparging, six soil column tests were performed (Adams, 1999). All the tests were performed using a uniform coarse sand as a test soil in a column test setup shown in Figure 1.

To provide a basis for comparison, the first test was performed in a sterile soil subjected to a dissolved benzene contaminant plume. The soil profiles in the other tests were augmented with the benzene enrichment culture to simulate the enrichment of benzene-degrading microorganisms that occurs at gasoline-contaminated sites. For comparison, low and high concentrations of microorganisms in the soil were used. Two dissolved benzene concentrations were used: 100 mg/l and 300 mg/l. Five tests were subjected to a pulsed air injection regime consisting of five minutes of air injection followed by 24 hours of injection cessation. A sixth test was performed with only one five-minute air injection period to determine the effect of dissolved oxygen probe built into the soil column. Pore water samples were analyzed using gas chromatography to monitor aqueous benzene concentrations during the course of the test, and the portion of the initial benzene mass removed through volatilization was determined by analyzing the carbon filer tubes used to remove vapor-phase benzene from the effluent air. All column experiments were conducted at room temperature of 25°C.

3 RESULTS

3.1 *Oxygen uptake rate and benzene degradation*

Several benzene concentrations were utilized in the batch tests, ranging from approximately 0.1 to 100 mg/l. As shown in Figure 2, the oxygen uptake rate ranges from a low value of 0.459 mg/l/min to a peak uptake rate of 1.44 mg/l/min corresponding to initial benzene concentrations of 0.1 and 10.2 mg/l, respectively.

After the maximum uptake rate was reached, however, the oxygen uptake rate began to decline with higher initial benzene concentrations. The higher initial benzene concentrations began to have an inhibitory effect on the benzene enrichment culture, thus reducing the oxygen uptake rate at higher concentrations. These data were linearized to determine the necessary

Copyright © 2003 Swets & Zeitlinger B.V., Lisse, The Netherlands

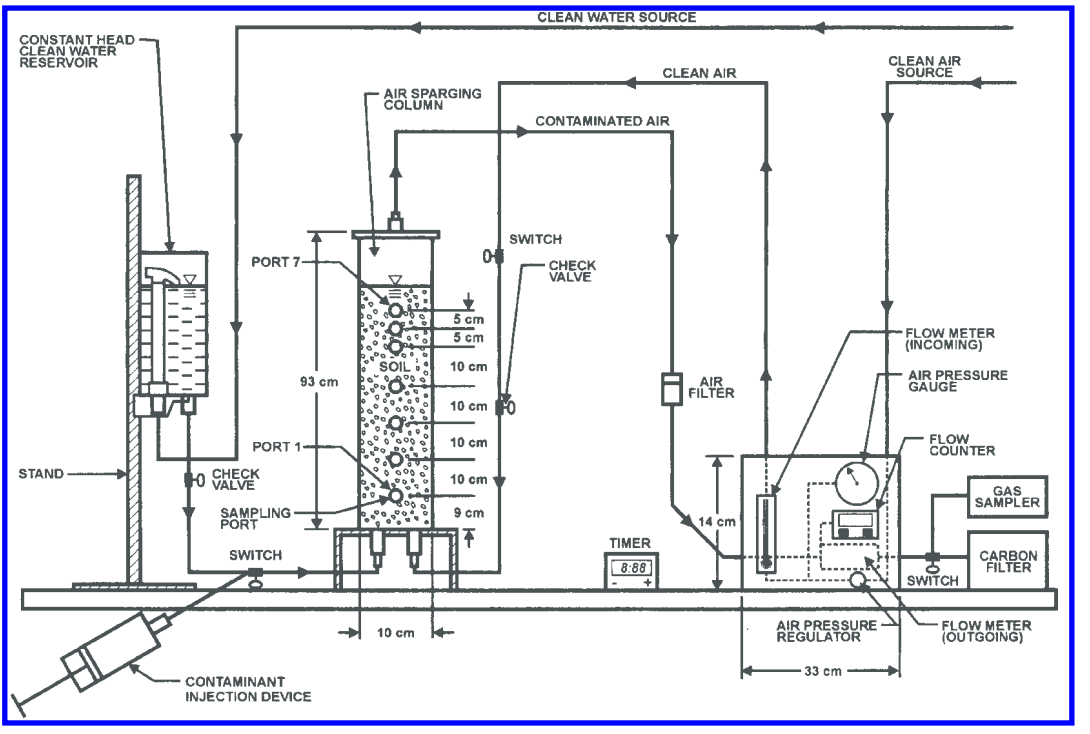


Figure 1. Schematic of biosparging column test setup.

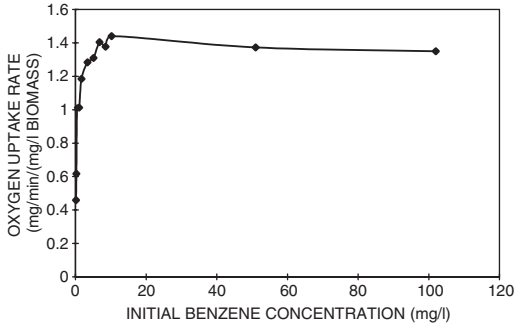


Figure 2. Oxygen uptake analysis.

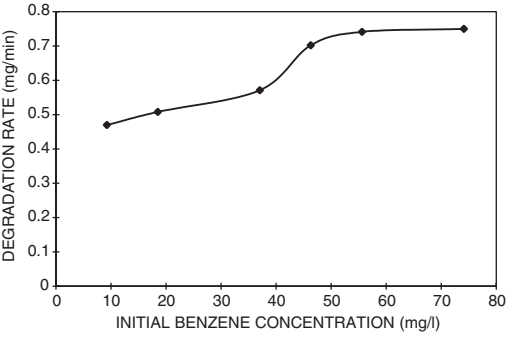


Figure 3. Benzene degradation rate.

parameters for a Monod-form kinetic model. A maximum uptake rate ($k = 0.049$/hour) and half saturation constant ($K_I = 0.293$ mg/l) were determined from the linearized data (Adams, 1999).

In addition to the oxygen uptake rate study, batch tests were performed to determine the degradation rate of benzene with respect to the initial benzene concentration. As shown in Figure 3, increased initial benzene concentration resulted in a greater degradation rate.

This rate of increased degradation rate, however, begins to lessen as higher initial benzene concentrations are used. As in the previous test, this attenuation of the benzene degradation rate is attributed to an inhibitory effect on the degradation capability of the benzene enrichment culture due to high benzene concentration. These data were linearized and maximum uptake rate (k) of 0.045/hour and a half saturation constant of 6.369 mg/l were determined from the plot.

To determine the rates of oxygen uptake and benzene degradation with respect to initial benzene concentration, a modified saturation kinetics model was developed. Due to the time frame of sampling and analysis during testing and assumptions made for this study, a number of simplifications were made.

Copyright © 2003 Swets & Zeitlinger B.V., Lisse, The Netherlands

Since the tests are of short duration (on the scale of approximately an hour), cell growth and decay were not considered important factors. Additionally, the rates of oxygen uptake and benzene degradation were measured during the initial stages of the test. During this time of measurement, oxygen concentrations were high compared to its half saturation constant. As discussed before, both the benzene degradation rate and the oxygen uptake rate reached a limiting peak where further increases in benzene concentration decrease both the rate of benzene degradation and the oxygen uptake rate. This behavior warrants the inclusion of an inhibition term. By applying the appropriate experimentally-measured parameters, the modified Monod kinetics model becomes:

$$r = \frac{0.045[\text{Benz.}][\text{Biomass}]}{6.369(1 + [I]/K_I) + [\text{Benz.}]} \quad (1)$$

where r = benzene degradation rate (mg/l/hr); [Benz.] = concentration of benzene (mg/l); [Biomass] = concentration of biomass (mg/l); $[I]$ = concentration of inhibitor (benzene) (mg/l); and K_I = half saturation constant for inhibitor (benzene) (mg/l).

This model could be used to predict the rate of oxygen uptake or benzene degradation for a given benzene concentration and biomass concentration. The inhibitor half saturation constant, however, was unknown. An iterative procedure was used to determine an appropriate value. Four predictions were performed with four different values of K_I: infinity (no inhibition), 100 mg/l, 15 mg/l, and 10 mg/l.

When a K_I of 10 mg/l is used, the corresponding generated data accurately predicted the experimental data, especially at higher concentrations of benzene.

3.2 *Contribution of biodegradation during biosparging*

When a test was performed using sterile coarse sand contaminated with an initial benzene concentration of 100 mg/1, substantial removal occurred during the period of air injection, but no removal occurred during periods of injection cessation, as expected. However, in bioaugmented soils, a substantial portion of benzene removal occurred due to biodegradation. In one test, only 37% of the initial benzene mass was removed through volatilization, while the remainder has been removed through biodegradation. However, the efficient removal of a substantial portion of the initial benzene mass from the soil profile during limited air injection indicates that volatilization is the dominant removal mechanism.

Remedial performance in all of the tests subjected to bioaugmentation and pulsed air injection was compared to determine the effect of biomass concentration on the rate of degradation. Over the range of biomass concentration used for testing, it was found that the rate of degradation was independent of biomass concentration. Additionally, it was found that the rate of benzene mass reduction was independent of initial dissolved benzene concentration for the range of benzene concentration used for this study.

When a test was performed using a single five-minute injection period, the rapid depletion of dissolved oxygen prevented biodegradation from occurring. Once the dissolved oxygen was depleted, biodegradation was not detected. Therefore, dissolved oxygen depletion was the rate-limiting factor for aerobic degradation within the subsurface; without adequate subsurface dissolved oxygen, degradation rates become prohibitive for efficient remediation.

Additionally, in tests subjected to the pulsed air injection regime, the concentration of dissolved oxygen within the soil profile was found to correlate to the rate of biodegradation. When the dissolved oxygen was depleted, the dissolved oxygen curve attenuated, indicating that the rate of oxygen utilization is greatly reduced. These time periods corresponded to periods of little or no benzene concentration reduction, indicating that biodegradation rates became negligible. Therefore, the measurement of the dissolved oxygen concentration within the soil can be useful in determining the extent of biodegradation during the use of air sparging.

The rates of biodegradation within the column tests were not as fast as those achieved within the suspended batch reactor tests performed to study the oxygen uptake rate and benzene degradation rate. Within the batch reactor tests, the biomass maintained intimate contact with dissolved oxygen, aqueous-phase benzene, and nutrients at all times. Within the column tests, however, the nature of the soil structure and fabric prevented this contact from occurring. As a result, especially at later stages of testing when benzene mass in the vicinity of microbial populations was depleted, the uneven distribution of benzene mass and biomass within the soil profile prevented the occurrence of maximum degradation rates. Therefore, as biosparging progresses, bioavailability may contribute to reduced biodegradation rates due to the non-homogeneous distribution of microorganisms and contaminant.

4 CONCLUSIONS

An experimental study was performed to determine the rate of oxygen uptake and benzene degradation with respect to initial benzene concentration. Additionally, the relative contribution of biodegradation to contaminant removal during the use of air sparging was studied. A modified saturation kinetic model was developed to determine the rate of oxygen uptake and benzene concentration. To help determine the applicability of this

Copyright © 2003 Swets & Zeitlinger B.V., Lisse, The Netherlands

model in predicting air sparging-induced biodegradation, a series of column tests were performed utilizing homogeneous coarse sand subjected to different biomass and contaminant conditions.

An increase in initial benzene concentration led to a greater oxygen uptake rate and a greater rate of degradation. Eventually, however, a peak uptake rate was reached where further increases in benzene concentration led to reduced oxygen uptake rates and an attenuation in the rate of degradation. This indicated that high benzene concentrations had an inhibitory effect on the benzene enrichment culture and the resulting rates of oxygen uptake and degradation. The results of these investigations were used to develop a modified Monod Kinetics model. Once the necessary parameters for the saturation kinetics model were determined and inserted into the model, it was found that a $K_I = 10\,\text{mg/l}$ yield the best fit to the experimental data.

Biodegradation accounted for a substantial portion of benzene remediation during the application of biosparging. During air injection, removal through volatilization was the dominant removal mechanism. In order for substantial aerobic biodegradation to occur, however, adequate amounts of dissolved oxygen must exist within the subsurface to serve as an electron acceptor. During testing, it was shown that benzene biodegradation ceased to occur in the absence of adequate dissolved oxygen levels. Additionally, the rates of biodegradation within the column tests were not as fast as those achieved within the batch reactor tests performed to study the oxygen uptake rate and benzene degradation rate. Within the batch reactor tests, the biomass maintained intimate contact with dissolved oxygen, aqueous-phase benzene, and nutrients at all times. Within the column tests, however, the nature of the soil structure and fabric prevented this contact from occurring.

Within the range of initial benzene concentrations used for this study, the observed rates of biodegradation were independent of the initial aqueous-phase benzene concentration. Additionally, the rate of biodegradation observed were independent of the biomass concentration within the range used for this study. As a result, the biomass concentration within the subsurface may not as important as its ability to degrade the contaminant of interest, provided the contaminant does not exist at levels that are toxic to the microbial population and sufficient dissolved oxygen is supplied.

5 ACKNOWLEDGMENTS

This study was performed as part of National Science Foundation Grant CMS-9813466. The support of this agency is gratefully acknowledged. The assistance of John Gramsas in fabricating the test setup is also highly appreciated.

REFERENCES

Adams, J.A. 1999. *System effects on the remediation of contaminated saturated soils and groundwater using air sparging*, Ph.D. Dissertation, University of Illinois, Chicago.

Adams, J.A. & Reddy, K.R. 2000. Removal of dissolved and NAPL-phase benzene pools from groundwater using in-situ air sparging. *Journal of Environmental Engineering*, ASCE 126(8): 697–707.

Adams, J.A. & Reddy, K.R. 1999. Laboratory study of air sparging of TCE-contaminated saturated soils and ground water. *Ground Water Monitoring and Remediation* 19(3): 182–190.

Ahfeld, D.P., Dahmani, A. & Ji, W. 1994. A conceptual model of field behavior of air sparging and its implications for application. *Ground Water Monitoring Review* 14(4): 132–139.

Bass, D.H. & Brown, R.A. 1997. Performance of air sparging systems – a review of case studies. In: *Proceedings of the Fourth International Symposium on In-Situ and On-Site Bioremediation* 1: 117–122. Columbus, Ohio, Batelle Press.

Johnson, R.L., Johnson, P.C. Mc Whorter, D.B., Hinchee, R.E. & Goodman, I. 1993. An overview of in situ air sparging. *Ground Water Monitoring Review* 13(4): 127–135.

Marley, M.C., Hazebrouck, D.J. & Walsh, M.T. 1992. The application of in situ air sparging as an innovative soils and ground water remediation technology. *Ground Water Monitoring Review* 12(2): 137–145.

Reddy, K.R., Kosgi, S. & Zhou, J. 1995. A review of in-situ air sparging for the remediation of VOC-contaminated saturated soils and groundwater. *Hazardous Waste and Hazardous Materials* 12(2): 97–118.

Reddy, K.R. & Adams, J.A. 1998. System effects on benzene removal from saturated soils and ground water using air sparging. *Journal of Environmental Engineering* 124(3): 288–299.

Reddy, K.R., Semer, R. & Adams, J.A. 1999. Air flow optimization and surfactant enhancement to remediate toluene-contaminated saturated soils using air sparging. *Environmental Management & Health* 10(1): 52–63.

Reddy, K.R. & Adams, J.A. 2000. Effect of groundwater flow on remediation of dissolved-phase VOC contamination using air sparging. *Journal of Hazardous Materials* 72(2–3): 147–165.

Reddy, K.R. & Adams, J.A. 2001. Effects of soil heterogeneity on air flow patterns and hydrocarbon removal during in-situ air sparging. *Journal of Geotechnical and Geoenvironmental Engineering*, ASCE 127(3): 234–247.

Semer, R. & Reddy, K.R. 1997. Mechanisms controlling toluene removal from saturated soils during in situ air sparging. *Journal of Hazardous Materials* 57(1–3): 209–230.

Semer, R., Adams, J.A. & Reddy, K.R. 1998. An experimental investigation of air flow patterns in saturated soils during air sparging. *Geotechnical and Geological Engineering Journal* 16(1): 59–75.

Copyright © 2003 Swets & Zeitlinger B.V., Lisse, The Netherlands

Nitrogen contamination from fertilizer in tea plantation, Kiku River basin, Japan

H. Ii, K.Yamano & T. Hirata
Wakayama University, Wakayama, Japan

T. Tanaka
Osaka Gas, Osaka, Japan

M. Nishikawa
National Institute for Environment Studies, Tsukuba, Japan

ABSTRACT: The relationship between the amount of fertilizer used and concentrations of nitrate and metals in well and river waters was studied on a Japanese tea plantation. The amount of nitrogen fertilizer used decreased from 112 kg N/10a in 1993 to 65 kg N/10a in 2000. Nitrate and metal concentrations of some heavily contaminated well water decreased considerably. However reduced concentrations were still high and concentrations in most contaminated wells were unchanged. Therefore, a greater reduction of nitrogen fertilizer used is still needed. Irrigation water from the Ohi River basin flows into the Kiku River basin. Delta ^{18}O and delta D values were used for estimating the mixing rate between the two basin waters. Average irrigation water was calculated to be more than 40% of total flow in the Tanno River of the Kiku River basin. Therefore irrigation was very effective to reduce nitrate and metal concentrations in the Kiku River basin.

1 INTRODUCTION

Groundwater and river water nitrate contamination caused by nitrogen fertilizer is an important issue because nitrate is a harmful substance in drinking water (Hirata 1996). In particular, the use of nitrogen fertilizer in tea plantations per unit area is highest of all Japanese agricultural lands and excess fertilizer resulted in metal and nitrate contamination of groundwater with acidification (Tanaka et al. 2001, Yamano et al. 2001, Ii et al. 2000, Ii et al. 1997a, b). Sometimes mass and sudden death of fish in ponds near tea plantations has been reported in newspaper (Heisei 1998) and pond eutrophication near tea plantations was also reported (Ii et al. 1997a, b). Acidification or Al contamination was thought to kill fish in ponds (Tanaka et al. 2001, Yamano et al. 2001, Ii et al. 2000). Excess fertilizer and inflow from groundwater caused eutrophication of rivers recharged from tea plantations (Ii et al. 1997a, b).

The Japanese government has widely investigated nitrogen contamination of groundwater and has set out guidelines for local governments (Ministry of Environment 2002). Some prefectures, following the guidelines of the Ministry of Environment, have made an effort to reduce the amount of fertilizer used by farmers. Resultantly, the use of nitrogen fertilizer per unit area of tea plantation decreased from 1997 in the Kiku River basin, Shizuoka prefecture. The area is very widely covered by tea plantations. Therefore, the influence of reduced amounts of fertilizer on groundwater near tea plantations was studied at the basin. In the basin, the use of water from the Ohi River for irrigated agriculture is very common and the irrigation runoff water flows into the Kiku River basin. Therefore, the influence of dilution caused by irrigation from the Ohi River on river water quality near tea plantation in the basin also was studied.

2 INVESTIGATION

2.1 *Study area*

Figure 1 shows the study area located at Kikukawa Town in central Honshu. This area, where the plains are used for rice fields and housing, and plateaus and hillsides are used for tea plantations is famous for its green tea. Tea plantations comprised the major land use of the basin. Geologically, Quaternary terrace deposits

Copyright © 2003 Swets & Zeitlinger B.V., Lisse, The Netherlands

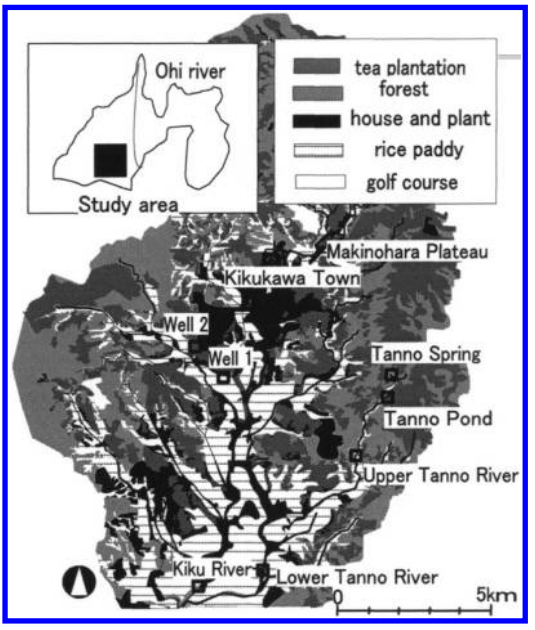


Figure 1. Sampling sites and land use of study area.

covering Tertiary rocks such as mudstone and siltstone are distributed on the plateaus and hillsides. Alluvial sediments are distributed on the plains.

Irrigation water from the Ohi River is supplied by private pipelines to tea plantations on the plateau and flows upstream into the Kiku River directly. Irrigation using the Ohi River is widely practiced at both the studied area and the surrounding areas. It was very difficult to estimate the used flow rate of the irrigation water. However, there are great differences in altitude of the plateau of the Kiku River basin and the Ohi River. The former is 100 to 200 m while the catchment altitude of the latter is over 3000 m. The difference between the annual average temperatures of both catchments is 6°C. Therefore, because stable isotopic ratios of oxygen and hydrogen of precipitation depend on altitude or temperature, using these ratios was thought to be an effective method for estimating the mixing rate of the Ohi River water.

2.2 *Method*

Water samples were taken from two wells, a spring, a pond and three rivers once a month, from April 1998 to April 2001. Two serious nitrogen contaminated wells denoted Well 1 and Well 2 within the tea plantation are located in the west of the Kiku River basin. The Tanno River is one of the eastern branch rivers of the Kiku River basin. The sample point of the Tanno Spring is upstream of the Tanno River and it flows into the Tanno Pond. The sample points of the upper Tanno River and lower Tanno River are located downstream of the Tanno Pond. The upper Tanno River is 2.5 km down from the Tanno Pond and lower Tanno River is 7.5 km down from the upper Tanno River. The sample point of the Kiku River is located in the center of the basin.

The pH values of the sampled waters were measured in situ using portable field kits (D-24/Horiba). Water samples were filtered (0.45 μm) before chemical analysis. Samples were stored at 4°C and concentrations of NO_3^- and Cl^- were measured by ion exchange chromatography (DX-AQ/DIONEX) in the laboratory. HCO_3^- concentrations were measured by titration in laboratory. Stable hydrogen isotopic ratios of H_2 gas were measured by mass spectrometer (DELTA PLUS/Finnigan Mat) after the H_2 gas had equilibrated with the sampled water. Stable oxygen isotopic ratios of CO_2 gas were measured by mass spectrometer after the CO_2 gas had equilibrated with the sampled water. After samples for heavily metal analysis were acidified (pH > 3) with HNO_3 solution, heavily metal concentrations were measured by ICP-AES method (SPS1700HVR/Seiko Instruments). Then the measured Al, Zn, Ni, and Mn shows total metal concentrations in water.

3 RESULTS AND DISCUSSIONS

3.1 *Changes in amount of nitrogen fertilizer used*

Recent media reports cited a sudden kill off of fish in the pond derived from the tea plantation catchment due to nitrate and Al contamination of groundwater. Nitrogen fertilizer used in Japan is usually $(NH_4)_2SO_4$ which transforms into NO_3^-, H^+, and SO_4^{2-} by the following nitrification process (Ii et al. 2000, Ii et al. 1997a, b).

$$(NH_4)_2SO_4 + 4O_2 = 2NO_3^- + 4H^+ + SO_4^{2-} + 2H_2O \quad (1)$$

In addition, Ca and Mg carbonates are also added into soil in order to neutralize acidic soil (Ii et al. 2000, Ii et al. 1997a, b).

$$2H^+ + (Ca, Mg)CO_3 = CO_2 + (Ca^{2+}, Mg^{2+}) + 2H_2O \quad (2)$$

In order to control nitrate contamination caused by nitrogen fertilizer, the amount of nitrogen fertilizer used has been decreased from 110 kg N/10a in 1993 to 65 kg N/10a in 2000. On the other hand, the amount of carbonates increased from 80 kg CO_3/10a in 1993 to 130 kg CO_3/10a in 2000. Therefore, Ca^{2+}, Mg^{2+}, NO_3^- and SO_4^{2-} values were very high in the spring and upper stream of tea plantation catchment (Ii et al. 2000, Ii et al. 1997a, b).

Copyright © 2003 Swets & Zeitlinger B.V., Lisse, The Netherlands

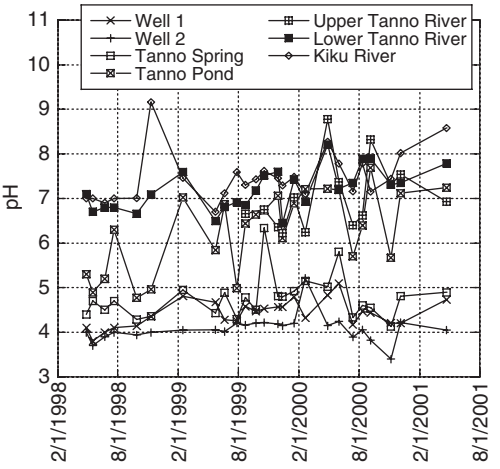


Figure 2. The time series of pH values of each type.

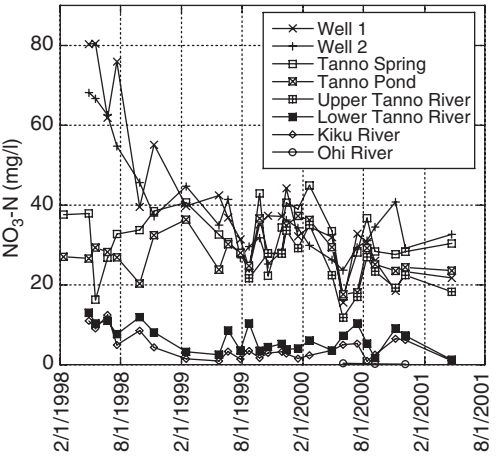


Figure 3. The time series of NO_3-N concentration of each type.

3.2 *pH values*

Figure 2 shows the time series of the pH values of the sampled waters. pH values ranged remained unchanged from 4 to 5 in heavily contaminated wells and Tanno Spring. pH values of Tanno Pond gradually increased from 5 to 7. pH values of river waters remained unchanged and mainly ranged from 6 to 8. Therefore, excluding Tanno Pond, pH values were not influenced by decrease of used nitrogen fertilizer. pH values of Tanno River increased down the stream.

3.3 *Nitrate concentration*

Figure 3 shows the time series of NO_3–N concentration of each type. NO_3–N concentrations in heavily contaminated wells decreased remarkably with the reduction in the amount of nitrogen fertilizer used. However, the NO_3–N concentrations of the wells, the Tanno spring and the upper stream of Tanno River still exceeded 10 mg/L (Japanese drinking water standard). Nitrate concentrations in the Tanno River and Kiku River sometimes exceeded 10 mg/L. Nitrate concentrations in the Kiku River and the lower stream of Tanno River stabilized at less than 10 mg/L. Therefore, nitrate concentrations of heavily contaminated wells were influenced by the decrease of used nitrogen fertilizer, but nitrate concentrations of river water were not. These concentrations decreased down the stream. In contrast, nitrate concentrations in the Ohi River were very small.

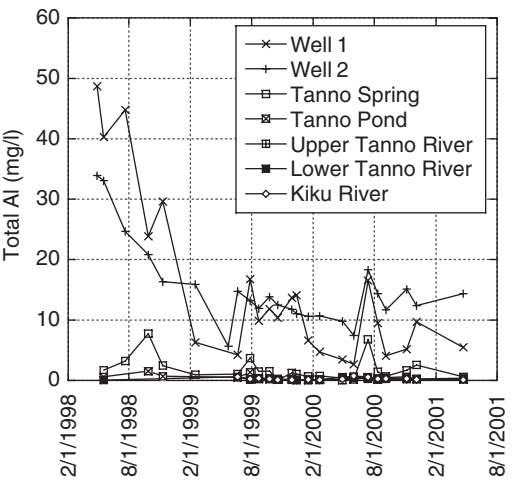


Figure 4. The time series of total Al concentrations of each type.

3.4 *Total Al*

Generally, Al minerals are stable under neutral pH conditions. However, Al may be dissolved from Al minerals of kaolinite ($Al_2Si_2O_5(OH)_4$) and Al(OH) by weathering at low pH conditions by the following process (Ii et al. 2000).

$$Al_2Si_2O_5(OH)_4 + 6H^+ = 2Al^{3+} + 2H_4SiO_4 + 2H_2O \quad (3)$$

$$Al(OH)_3 + 3H^+ = Al^{3+} + 2H_2O \quad (4)$$

The equations indicate that Al minerals dissolve with an increase of hydrogen ion concentrations. Figure 4 shows the time series of total Al concentrations of each type of water. Total Al concentrations in water are thought to depend on pH values according to

Copyright © 2003 Swets & Zeitlinger B.V., Lisse, The Netherlands

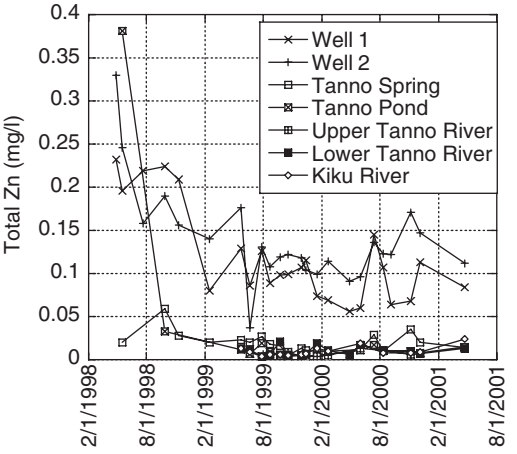


Figure 5. The time series of total Zn concentrations of each type.

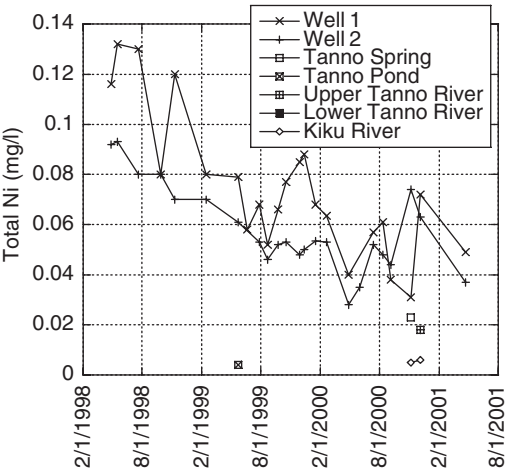


Figure 6. The time series of total Ni concentrations of each type.

the equations. Therefore, the heavily contaminated wells with low pH values show high concentrations of total Al and they contained more than 0.2 mg/L Al (the agreeable maximum concentrations for Japanese drinking water). Total Al concentrations of rivers with high pH values kept low concentrations. Total Al concentrations in the heavily contaminated wells decreased remarkably with the reduction in the amount of nitrogen fertilizer used in the same way as nitrate concentrations, although pH values were stable. Therefore, the reduction of nitrogen fertilizer and increase of carbonates used was effective for reducing total Al concentrations.

3.5 *Total Zn*

ZnO is a production of weathered rock. ZnO easily dissolves into Zn ion under neutral to acidic condition and also ZnO dissolves into Zn hydrate ions under alkaline condition by the following equations (Taga & Nasu 1996).

$$ZnO + 2H^+ = Zn^{2+} + H_2O \quad (5)$$

$$ZnO + 2H_2O = Zn(OH)_3^- + H^+ \quad (6)$$

Therefore, minimum concentrations of soluble Zn reached under neutral area. Figure 5 shows the time series of total Zn concentrations of each type. Total Zn concentrations in water are thought to depend on pH values. The heavily contaminated wells with low pH values show high concentrations of total Zn. Rivers with high pH values kept low concentrations. Total Zn concentrations in the heavily contaminated wells decreased remarkably with the reduction in the amount of nitrogen fertilizer used in the same way as nitrate and total Al concentrations. Therefore, the reduction of nitrogen fertilizer used was effective for reducing total Zn concentrations.

3.6 *Total Ni*

Ni ions are easily precipitated as $Ni(OH)_2$ produced by weathering. Thus it is important to understand that the stable condition of $Ni(OH)_2$ is dissolved into Ni ion by the following equation (Yamada 1996).

$$Ni(OH)_2 + 2H^+ = Ni^{2+} + 2H_2O \quad (7)$$

According to the equation, Ni dissolves with an increase of hydrogen ion concentrations. Figure 6 shows the time series of total Ni concentrations of each type. Total Ni concentrations in water are thought to depend on pH values. The heavily contaminated wells with low pH values show high concentrations of total Ni and they contained in excess of 0.01 mg/L Ni (the guiding concentrations of Japanese drinking water). Rivers with high pH values kept low concentrations. Total Ni concentrations in the heavily contaminated wells decreased remarkably with the reduction in the amount of nitrogen fertilizer used in the same way as nitrate. Therefore, the reduction of nitrogen fertilizer used was effective for reducing total Ni concentrations.

3.7 *Total Mn*

As Mn is a redox-sensitive element in groundwater, Mn ion concentrations depends on both pH and Eh values and Mn ions are easily precipitated as various kinds of Mn oxides, and Mn oxides are dissolved into Mn ion by the following equations (Shikazono 1997).

Copyright © 2003 Swets & Zeitlinger B.V., Lisse, The Netherlands

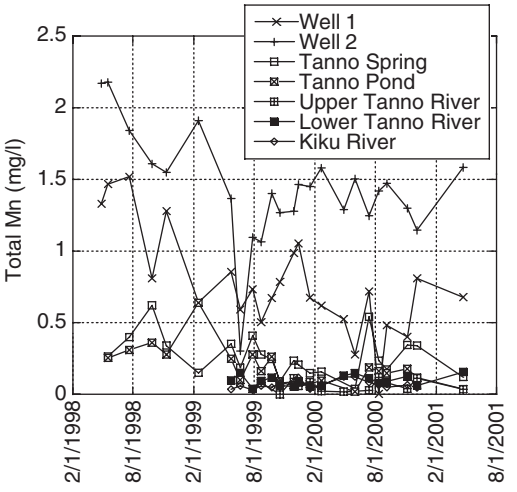


Figure 7. The time series of total Mn concentrations of each type.

$$MnO_2 + 4H^+ + 2e^- = Mn^{2+} + 2H_2O \quad (8)$$

$$Mn_2O_3 + 6H^+ + 2e^- = 2Mn^{2+} + 3H_2O \quad (9)$$

$$Mn_3O_4 + 8H^+ + 2e^- = 3Mn^{2+} + 4H_2O \quad (10)$$

$$Mn(OH)_2 + 2H^+ = Mn^{2+} + 2H_2O \quad (11)$$

According to the equations, Mn dissolves with an increase of hydrogen ion concentrations in a reductive condition. Figure 7 shows the time series of total Mn concentrations of each type. Total Mn concentrations in water are thought to depend on pH values. The heavily contaminated wells with low pH values kept over 0.5 mg/L which was much more than 0.05 mg/L Mn (the guiding concentrations of Japanese drinking water). Rivers with high pH values also often reached 0.05 mg/L. Total Mn concentrations in the heavily contaminated wells did not decrease remarkably with the reduction in the amount of nitrogen fertilizer used in the same way as nitrate. Therefore, the reduction of nitrogen fertilizer used was not effective for reducing total Mn concentrations.

3.8 *Nitrate concentrations with pH and Al*

As reduction of nitrogen fertilizer is effective for reducing metal concentrations, Figure 8 shows the relation between nitrate and total Al concentrations. The wells and spring waters indicated that total Al concentrations increased with nitrate concentrations. However, total Al concentrations in the rivers were very low even if high nitrate concentrations and Al concentrations of the Tanno River decreased down the stream. As Al concentrations depend on pH, Figure 9 shows that the relation between pH and nitrate concentrations. pH values in the wells and spring were

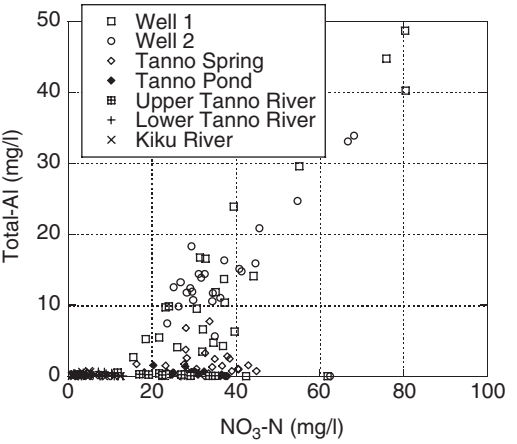


Figure 8. The relation between nitrate and total Al concentrations.

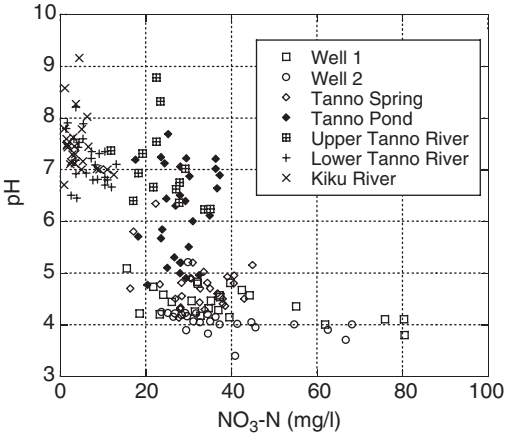


Figure 9. The relation between nitrate and pH values.

4 to 5 and NO_3-N concentrations were over 20 mg/L. But nitrate concentrations decreased with an increase of pH values down the stream in the Tanno rivers. Especially, from the Tanno spring to the Tanno Pond, pH values increased remarkably with nitrate concentration decrease. As the Tanno spring is a main source of the Tanno Pond and dilution caused by another branch river water is very small, an increase of pH values and decrease of nitrate concentrations were thought to be caused by either denitrification or photosynthesis by the following equations (Ii et al. 1997a, b).

$$2H^+ + 5H_2 + 2NO_3^- = N_2 + 2H_2O \quad (12)$$

$$106CO_2 + 138H_2O + 16NO_3^- = (CH_2O)_{106}(NH_3)_{16} + 138O_2 + 16OH^- \quad (13)$$

Copyright © 2003 Swets & Zeitlinger B.V., Lisse, The Netherlands

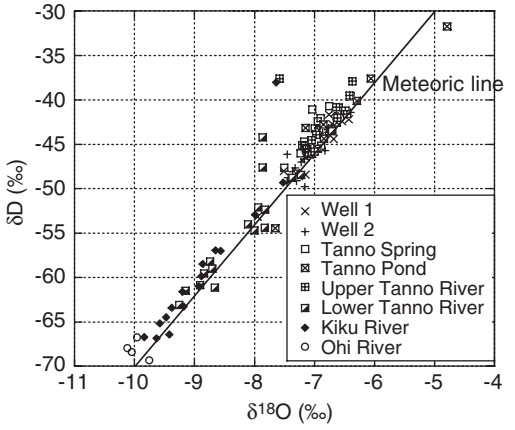


Figure 10. The relation between delta D and delta ^{18}O.

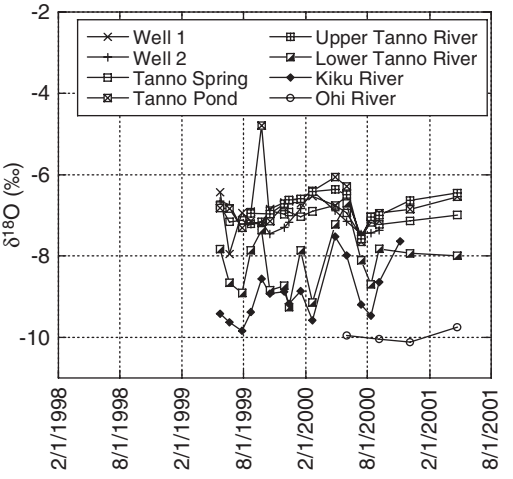


Figure 11. The time series of delta ^{18}O values of each type.

3.9 *Delta D and delta ^{18}O*

Stable oxygen and hydrogen isotopic ratios are good indicators of water origin. River water originates from two sources. Irrigation water from the Ohi River originates from precipitation in mountainous areas where the summit reaches more than 3000 m in altitude. The Kiku River basin is a low altitude plateau area. Figure 10 shows the relation between delta D and delta ^{18}O values. Most waters were on the meteoric line. This indicated that evaporation was not active. The delta D and delta^{18}O values of the Ohi River were very low and the delta D and delta ^{18}O values of two wells and Tanno Spring were very high. The difference of delta D and delta ^{18}O values were thought to depend on the difference of source altitude. Therefore, well and spring water originates mainly from precipitation in-situ. However, down the stream, the delta D and delta ^{18}O values of river decreased indicating the mixing of the Ohi river irrigation.

3.10 *Mixing ratio*

Figure 11 shows the time series of delta ^{18}O values. The delta ^{18}O values of wells and spring were constantly about 7 per mill. Similarly, delta ^{18}O values of the Ohi River were constantly about 10 per mill. However, delta ^{18}O values of the Kiku River and the lower stream of Tanno River were changeable and indicated mixing rate changes of irrigation. If the delta D and delta ^{18}O values of well and spring waters were representative of precipitation in the catchment, calculated mixing rate of irrigation by delta D and delta ^{18}O values were 25 to 95% in the Kiku River and about 40% in the lower stream of Tanno River. Similarly, mixing rate of irrigation was calculated at 75% from nitrate in the Kiku River. As the difference of nitrate concentrations between the upstream and downstream of Tanno River was very large and nitrate concentrations of the Ohi River was very low, mixing rate reached a high value. The difference was attributed to denitrification and photosynthesis. Therefore, denitrification and photosynthesis is thought to have caused the gap between mixing ratios calculated from stable isotope and nitrate. The high mixing ratio indicated that dilution was important for reducing metal and nitrate concentrations of contaminated water.

4 CONCLUSION

Well and river water chemistries near tea plantations were studied to investigate the relationship between amount of fertilizer used and concentrations of nitrate and metal. Acidification caused by nitrogen fertilizer increased Al, Ni, Zn and Mn concentrations of groundwater and they reached 50, 0.1, 1.0 and 5 mg/L respectively. Therefore, the amount of nitrogen fertilizer used was decreased from 112 kg N/10a in 1993 to 65 kg N/10a in 2000. Nitrate and metal concentrations of some heavily contaminated well water decreased effectively. However reduced concentrations were still high and concentrations in contaminated wells unchanged. Therefore a greater reduction in nitrogen fertilizer use is needed.

Irrigation water from the Ohi River basin flowed into the Kiku River basin. Delta ^{18}O and delta D values of river water between the two basins were very different because the Ohi River basin has a high mountainous area and delta ^{18}O and delta D values are very low. Therefore, delta ^{18}O and delta D values were used for estimating the mixing rate between the two basin waters. Average irrigation water was calculated at over

Copyright © 2003 Swets & Zeitlinger B.V., Lisse, The Netherlands

40% of total flow in the Tanno River of the Kiku River basin. Thus irrigation was very important to reduce nitrate and metal concentrations and increase pH values of river water in the Kiku River basin because of low nitrate concentrations in the Ohi River. Down the stream, nitrate concentrations decreased with an increase of pH values. Biological reaction such as denitrification and photosynthesis was thought to also be important for controlling pH and metal and nitrate concentrations.

REFERENCES

Heisei Chakou 1998. *News in August 1*. Shizuoka: Shizuoka Shimbun.

Hirata, T. 1996. *Soil and groundwater contamination and its countermeasure*. Tokyo: Japan Environmental Measurement and Analysis Community.

Ii, H., Hirata, T., Matsuo, M., Nishikawa, M. & Tase, N. 1997a. Surface water chemistry, particularly concentrations of NO_3^- and DO and *f* Â^{15}N values, near a plantation in Kyusyu, Japan, *Journal of Hydrology* 202: 341–352.

Ii, H., Hirata, T., Matsuo, M., Nishikawa, M. & Tase, N. 1997b. Nitrate nitrogen due to fertilizer application to tea plantation and its effect on ambient surface water, *Annual Journal of Hydraulic Engineering* 41: 575–580.

Ii, H., Hirata, T., Tanaka, M., Nishikawa, M., Nakajima, T. & Umehara, K. 2000. Spring, pond and river water chemistries derived from a tea plantation central Shizuoka prefecture, *Annual Journal of Hydraulic Engineering* 44: 1155–1160.

Ministry of Environment 2002. *The guideline about countermeasure of nitrogen contamination of groundwater*. Tokyo: Environmental Research and Control Center.

Shikazono, N. 1997. *Chemistry of the Earth System*. Tokyo: Tokyodaigaku Press.

Taga, M. & Nasu, S. 1996. *Chemistry and Environment of the Earth*. Tokyo: Sankyo Press.

Tanaka, T., Ii, H., Hirata, T., Nishikawa, M., Nakajima, T., Umehara, K. & Ogawa, Y. 2001. Groundwater chemistry near a tea plantation in the center of Shizuoka prefecture, Japan, *Annual Journal of Hydraulic Engineering* 45: 355–360.

Yamada, T. 1996. *A small amount metal and the living body operation*. Tokyo: Japan Chemical Society.

Yamano, K., Ii, H., Hirata, T., Tanaka, T., Nishikawa, M. & Ogawa, Y. 2001. The effect of fertilizing from tea plantation and water conveyance from Oigawa river upon nitrogen contamination in Kikugawa basin, central Shizuoka prefecture, *Environmental Engineering Research* 38: 197–205.

Copyright © 2003 Swets & Zeitlinger B.V., Lisse, The Netherlands

Electro-chemical remediation of VOCs contaminated groundwater

T. Miura & H. Kubo
Technical Research Institute, Obayashi Co. Ltd., Tokyo, Japan

ABSTRACT: Volatilization loss and adsorption with activated carbon are generally used for the remediation of water contaminated with volatile organic compounds (VOCs). Recently, decomposition treatment by oxidation-reduction has been developed. Electric dechlorination (EDEC) also decomposes and makes VOCs innocuous by oxidation-reduction at the surfaces of electrodes. The authors have studied the fundamental decomposition characteristics of EDEC by batch and column tests using trichloroethylene (TCE) as a VOC. The results show that EDEC decomposes TCE and the reaction is controlled by the quantity of electricity for still water, and by electric current and water velocity for flowing water. We made a composite electrode comprising of conductive porous fillers between electrode parts, and performed column tests. It was thus shown that the decomposition rate increased when using the composite electrode, and this effect was verified by a full size experiment.

1 INTRODUCTION

In recent years, with redevelopment of abandoned factory sites, the soils contaminated with volatile organic chlorine compounds (VOCs) have been discovered, and this has become a big social problem. Development of remediation technology has been furthered in many construction companies and other companies. New, cheap technologies need to be developed, depending on the contaminated form.

Volatilization loss technology which makes VOCs gasify, and the adsorption with activated carbon are generally used for the remediation of water contaminated with VOCs. These methods are simple and well established. However, they simply collect VOCs, but do not decompose them. Thus, when highly contaminated water is treated, running cost tends to increase to burden of recovery material, such as activated carbon.

Technologies for decomposition of VOCs by oxidation–reduction reaction are proposed as a method that does not use recovery material. A method using iron powder has been promoted (Senzaki and Kumagai, 1988). Although this method is cheap and simple, it has the disadvantage that the decomposition speed is slow and the reaction may be unmaintainable, depending on soil environment.

The authors carried out basic research on electric dechlorination technology (EDEC), which is use to decompose VOCs into innoxious substance by electrolysis. This paper reports the principle of EDEC, basic decomposition characteristics by batch and column tests and improvement in decomposition efficiency by porous filler composite electrodes, and summarizes the EDEC treatment conditions.

2 PRINCIPLE OF EDEC

When a direct current is passed through water containing a little electrolyte, the following three phenomena mainly happen. (1) Cations and anions move to the cathode and the anode, respectively, by electrophoresis. (2) The anode side becomes acidic and cathode side becomes alkaline due to electrolysis of water. (3) Joule heating occurs and the water temperature rises.

The decomposition of VOCs by EDEC is a phenomenon similar to (2). Figure 1 illustrates these

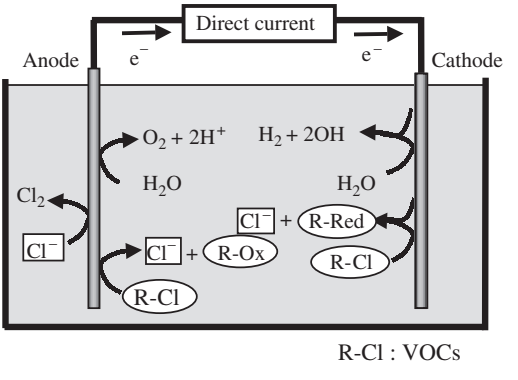


Figure 1. Principle of EDEC.

Copyright © 2003 Swets & Zeitlinger B.V., Lisse, The Netherlands

Cathode (Reduction)

$CHCl{=}CCl_2$ (TCE) → CHCl=CHCl (dichloroethylene) →
$CHCl{=}CH_2$ (chloroethylene) → $CH_2{=}CH_2$ (ethylene) →
CH_3CH_3 (ethane), CH_4 (methane)

Anode (Oxidation)

$CHCl{=}CCl_2$ (TCE) → $Cl_2CHCOOH$ (dichloroacetic acid) →
HCOCOOH (glyoxylic acid) → HOOCCOOH (oxalic acid)
→ CO_2 (carbon dioxide)

Figure 2. Decomposition process of TCE.

principles. Since VOCs are prone to the oxidation-reduction reaction, they are electrolyzed like water. Specifically, chlorine in the VOCs is replaced with hydrogen by reduction at the cathode, and oxidation at the anode replaces chlorine with hydroxyl and carboxyl group compounds. These are fundamentally the same reactions as reduction, using iron powder, and oxidization decomposition using fault manganese acid potassium or light (Sequeira, 1998).

Figure 2 shows the presumed decomposition process of trichloroethylene (TCE) by EDEC. Since oxidization and reduction take place simultaneously, it is difficult to clarify the EDEC decomposition process. Various organic matters may be generated by decomposition, but detrimental organic matter is not been generated by a dechlorination process.

3 BATCH TEST

3.1 *Experimental method and cases*

The change of TCE concentration by EDEC in still water was investigated. The factor that affects the decomposition efficiency and the optimal treatment conditions were studied.

The batch test device is shown in Figure 3. Four liter of TCE solution was put into a glass tank and titanium electrodes were set at 10 cm intervals. The anode was plated with platinum. The electrical conditions were as follows. Electric current: direct current 0.02–0.1 A, time of turning on electricity: 4–240 hour, initial concentration: 1–100 mg/L, electrical conductivity: 0.2 dS/m.

In order to investigate the reaction at each of the cathode and the anode, an experiment was conducted in which the solution of the two electrodes was separated by a salt bridge. Figure 4 shows the experimental device. 0.5 Litter of TCE solution was put into a glass tank, and the same electrodes as above were set at 5 cm intervals. The electrical conditions were as follows. Electric current: direct current 0.02–0.1 A, time of turning on electricity: 24 hour, initial concentration: 100 mg/L, electrical conductivity: 0.2 dS/m.

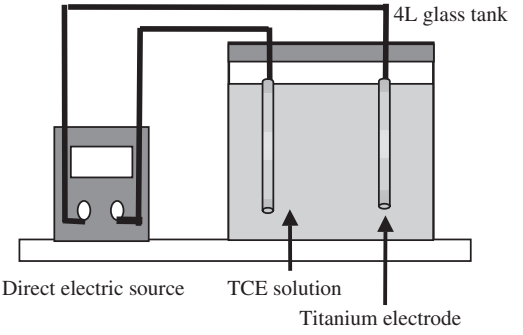


Figure 3. The device of batch test.

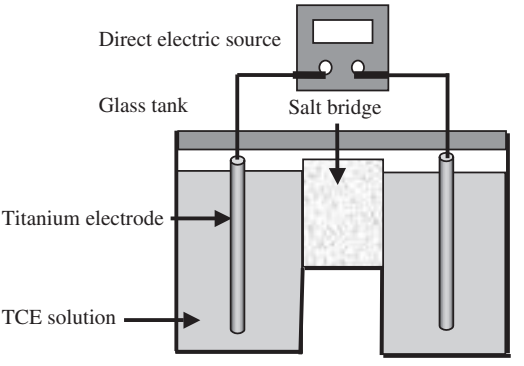


Figure 4. The device of batch test with salt bridge.

The TCE solution was made by mixing an electrolyte that do not contain chlorine and with a fixed quantity of TCE. In order to prevent loss by volatilization, the device was put into a pyrostat and maintained at 4°C. After treatment, the solution was collected and TCE and chloride concentrations were measured.

3.2 *Results and discussion*

Figure 5 shows the relations between the quantity of electricity and TCE residual rate and chlorination rate. The TCE residual rate is the ratio of concentration in treated water to initial concentration. The chlorination rate is the rate at which the quantity of chloride ion in treated water is converted from the quantity of TCE, and is expressed by the ratio of initial concentration. The residual rate decreases as the quantity of electricity increases. Therefore, EDEC can decrease TCE and a fixed expression of relations can be established between TCE residual rate and the quantity of electricity. The TCE chlorination rate increases as the quantity of electricity increases. This indicates that the reduction in TCE depends on dechlorination. By calculating the input and output of TCE, the sum of the residual

Copyright © 2003 Swets & Zeitlinger B.V., Lisse, The Netherlands

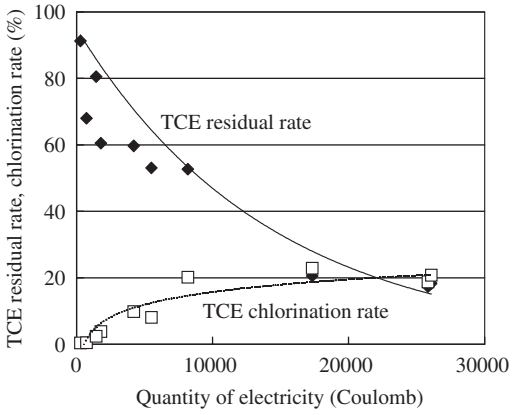


Figure 5. Relation between quantity of electricity and TCE residual rate.

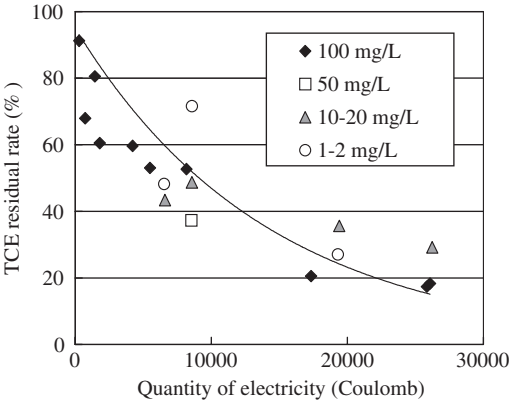


Figure 6. Influence of TCE initial concentration.

rate and chlorination rate corresponding to each was determined as 40–100%. This loss is considered to be the main cause of chlorine gas generation in the anode.

Figure 6 shows the TCE residual rate when initial concentration was changed from 1–100 mg/L. The relation between the TCE residual rate and the quantity of electricity was almost fixed in spite of the changes in initial concentration. This means that the decomposition of TCE per unit quantity of electricity increases as the initial concentration is high.

From these results, the relation between the TCE residual rate and the quantity of electricity can be expressed by the following empirical equation.

$$\ln \frac{C}{C_0} = -KE \tag{1}$$

where $C/C_0 =$ TCE residual rate; $K =$ experimental constant; and $E =$ quantity of electricity.

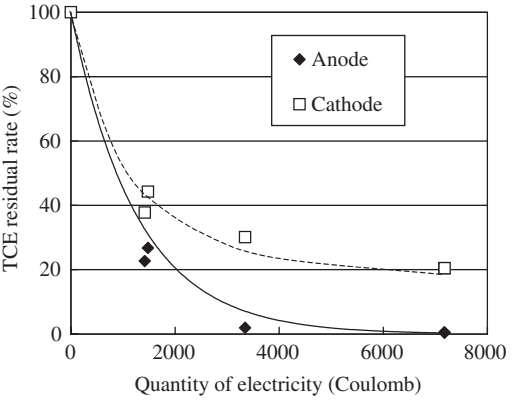


Figure 7. Change of TCE residual rate.

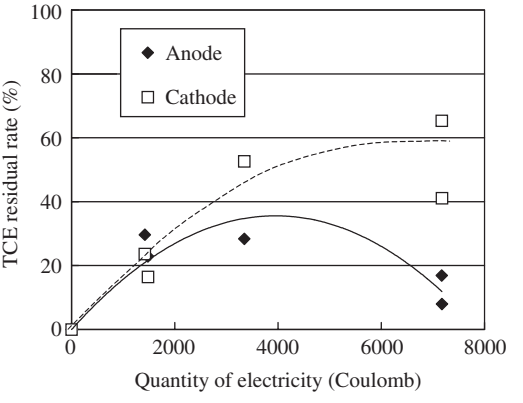


Figure 8. Change of TCE chlorination rate.

Figures 7 and 8 show the relation between TCE residual rate, chlorination rate and the quantity of electricity when the cathode and anode were separated by a salt bridge. TCE residual rate decreased at both electrodes as the quantity of electricity increased. Therefore, EDEC decreased TCE at both electrodes. TCE chlorination rate increased with increase in the quantity of electricity, and showed that dechlorination of TCE had occurred. On the anode side, after the TCE chlorination rate increased to 40%, it decreased a little. This is considered to be due to the chlorine in the water volatilizing as chlorine gas. Compared with the above-mentioned previous case, TCE residual rate decreased for a small quantity of electricity. This is so because the quantity of the TCE solution is small and the electric current differs from that of the previous case.

After treatment, a part of the solution was extracted and the concentration of environmentally regulated VOCs having two chlorine were checked (dichloromethane, 1,2-dichloroethane, 1,1-dichloroethylene, cis-1,2-dichloroethylene, 1,3-dichloropropene). The

Copyright © 2003 Swets & Zeitlinger B.V., Lisse, The Netherlands

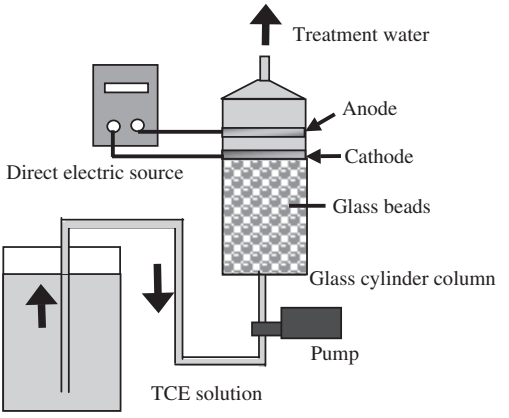


Figure 9. The device of column test.

results were all below the environmental standard values (0.02 mg/L, 0.004 mg/L, 0.02 mg/L, 0.04 mg/L, 0.002 mg/L, respectively).

4 COLUMN TEST

4.1 *Experimental method and cases*

The effect and characteristics of EDEC on water flow conditions were investigated.

Figure 9 shows the device of the column test. The cathode and anode were set at a 1 cm intervals in the glass cylinder column (diameter: 100 mm, height: 200 mm). A mesh made of stainless steel and a platinum plated mesh were used as cathode and anode, respectively. The TCE was mainly used as a VOC, but tetrachloroethylene (PCE) and 1,1,1-trichloroethane were also used. The electrical conditions were as follows. Electric current: direct current 0.05–0.8 A, flow velocity: 3–12 mL/min from bottom to top of the column, initial concentration: 5–200 mg/L, electrical conductivity: 0.2 dS/m. After passing through the electrodes, the water was collected at fixed intervals, and the VOC and chloride concentrations were measured.

4.2 *Results and discussion*

Figure 10 shows the TCE residual rate and chlorination rate when the initial concentration was 50 mg/L, the current was 0.8 A and the flow velocity was 3 mL/min. On passing electricity, the TCE residual rate decreased and it approached a constant low value as time passed. Thus, EDEC can also remove TCE under flowing conditions. The TCE chlorination rate increased because of dechlorination.

Figures 11, 12 and 13 show the relations between current, flow velocity, initial concentration, and TCE residual rate. From Figures 11 and 12, the TCE residual

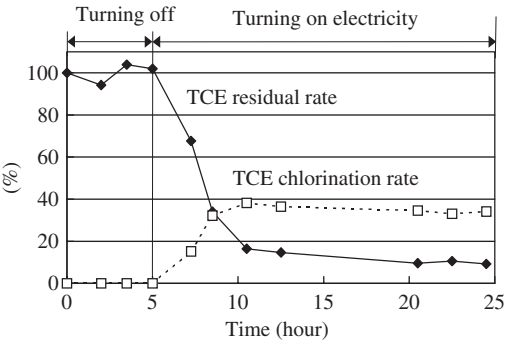


Figure 10. Change of TCE residual rate.

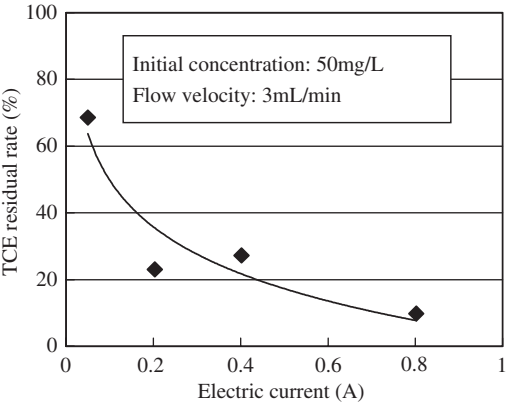


Figure 11. Relation between electric current and TCE residual rate.

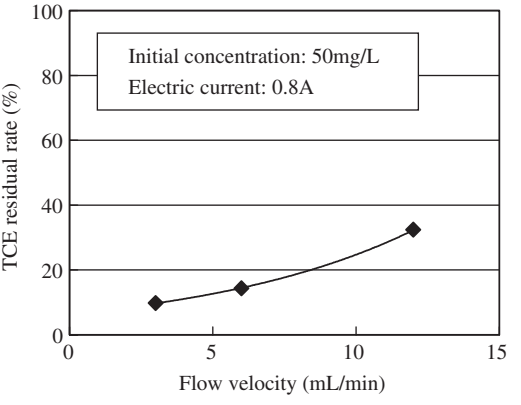


Figure 12. Relation between the flow velocity and TCE residual rate.

rate decreased as flow velocity decreased and current increased. The lowest residual rate was about 10% with treatment at 0.8 A and 3 mL/min. PCE and 1,1,1-trichloroethane showed the similar result (the

Copyright © 2003 Swets & Zeitlinger B.V., Lisse, The Netherlands

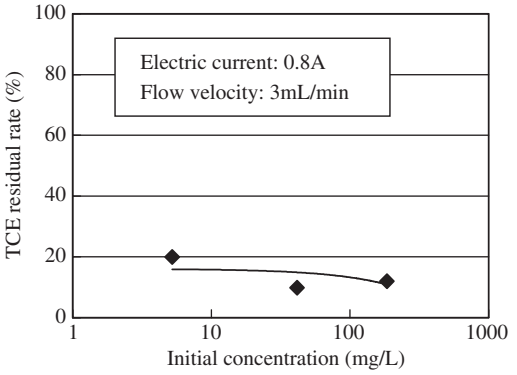


Figure 13. Relation between the initial concentration and TCE residual rate.

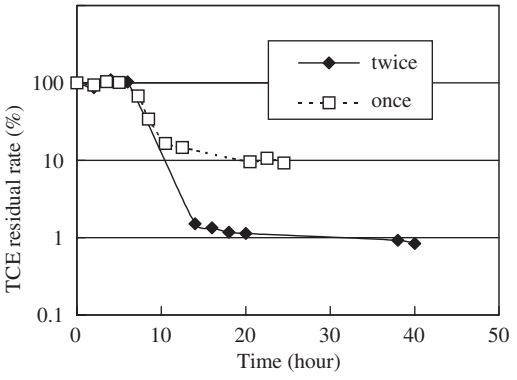


Figure 14. TCE residual rate of the water passed to electrodes twice.

figure for this result is omitted). From Figure 13, TCE residual rate was almost fixed in spite of the change of initial concentration. This tendency has been seen by the results of previous batch tests, and it indicates that the quantity of decomposition increases as the initial concentration increases.

In this experiment, the lowest TCE residual rate was about 10%. Thus, depending on the initial concentration, the environmental groundwater quality value (TCE: 0.03 mg/L) may not be satisfied in some cases. In order to lower the residual rate further, an experiment was conducted in which the water passed the electrodes twice. The results of this experiment are shown in Figure 14. The current value and the flow velocity were 0.8 A and 3 mL/min, respectively. The TCE residual rate in the solution that passed the electrodes twice was smaller than that passing only once, and attained a residual rate of 1% or less. It is thus shown that the residual rate can be decreased by increasing the number of times that the solution passes the electrodes.

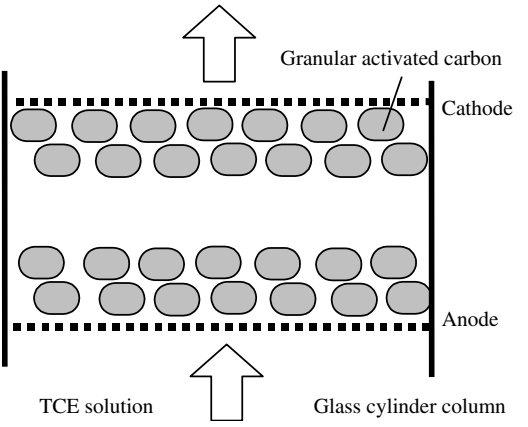


Figure 15. Structure of porous filler composite electrode.

5 IMPROVEMENT TEST USING POROUS FILLER COMPOSITE ELECTRODES

5.1 *Experimental method*

The EDEC reaction occurs when VOCs in water contact with the electrode surface (Schmal, 1987). Thus, in order to reduce the TCE residual rate further, a porous filler composite electrode was made, and the remediating effect was investigated using TCE solution. The porous filler composite electrode comprised a mesh electrode with an electrically conductive porous filler inside it. This increased the contact opportunity between the electrode surface and the VOCs. Figure 15 illustrates the structure of the composite electrode. Small- and large-scale equipment were used for this experiment.

1) In the small-scale experiment, the same small column as in section 4 (diameter: 100 mm, height: 200 mm) was used, and the insides of both electrodes were filled with about 40 g of granular activated carbon. The electrical conditions were as follows. Electric current: direct current 0.1 A, flow velocity: 3 mL/min, TCE initial concentration: 2 mg/L, electrical conductivity: 0.2 dS/m.

2) In the large-scale experiment, the electrodes were put into a steel pipe (diameter: 600 mm, height: 600 mm), and the insides of both electrodes were filled with about 3 kg of granular activated carbon. The electrical conditions are as follows. Electric current: direct current 6.4 A, flow velocity: 0.2, 0.8, 2 L/min (3 cases), TCE initial concentration: 2 mg/L, electrical conductivity: 0.2 dS/m. Figure 16 shows the large-sized experiment equipment. Treated water was collected at regular intervals, and TCE concentration was measured.

Copyright © 2003 Swets & Zeitlinger B.V., Lisse, The Netherlands



Figure 16. Large-sized experiment equipment.

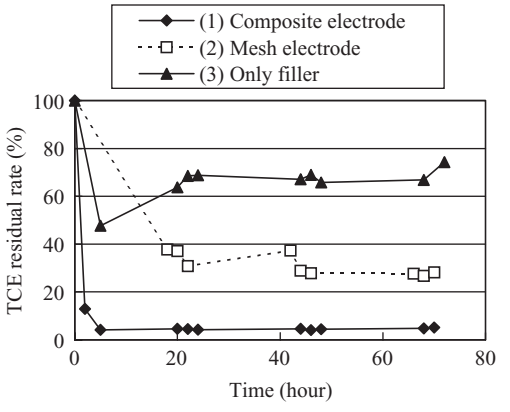


Figure 17. Change of TCE residual rate (small-scale experiment).

5.2 *Results and discussion*

Figure 17 shows the change of TCE residual rate in the small-scale experiment. There were three experimental cases: (1) porous filler composite electrode, (2) mesh electrode (aforesaid electrode), and (3) only filler. The TCE residual rate using composite electrode (1) decreased to about 3%, and showed remarkable removal compared to (2) and (3). It is thought that the increase in the contact opportunity between the TCE in solution and the electrode surfaces by using composite electrodes led to this excellent decomposition efficiency. When using only filler (3), the TCE residual rate decreased to about 70%. This decrease is attributed to adsorption by the activated carbon. (1) is not the result of only uniting effects (2) and (3).

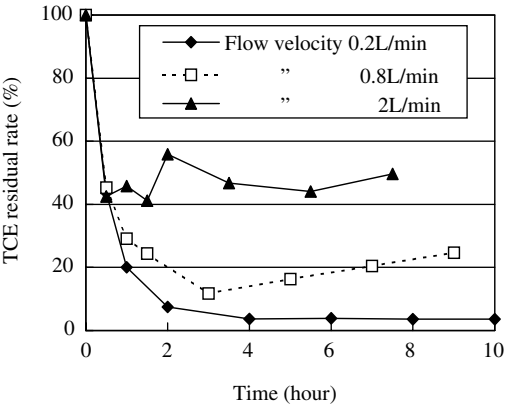


Figure 18. Change of TCE residual rate (large-scale experiment).

It is because that the TCE residual rate becomes 21% ($0.7 \times 0.3 = 0.21$) and is not attained to 3%, if the remainder was electrolyzed after adsorption removal is carried out by activated carbon.

The result of the large-scale experiment in three cases of the flow velocity, 0.2, 0.8, and 2 L/min, is shown in Figure 18. The TCE residual rate decreased to about 3% when the flow velocity was 0.2 L/min. It was thus proved that the remediating effect was equivalent to that of the small-scale experiment. The TCE residual rate increased so that the flow velocity became large, and it showed about 50% reduction at 2 L/min. When the flow velocity reached 2 L/min or more, there was no difference in the remediating effect of EDEC and adsorption by the filler. Consequently, the range of flow velocity that can be treated by EDEC is 2 L/min or less.

6 DESIGN OF ELECTRIC AND WATER FLOW CONDITIONS IN EDEC

When EDEC is applied for treating VOC-contaminated water, the following input conditions should be set: treatment conditions: flow velocity of the contaminated water and target residual rate (decomposition rate), device and operation conditions: type of electrode (mesh electrode or porous filler composite electrode), electrode area, and electric current. The decision on these conditions determines the number of times of electrode passage that is required for remediation. Figure 19 indicates the concept of design of electrical and water flow conditions for EDEC.

The application restrictions of these conditions depend on the usage. For example, when using a composite electrode, the maximum flow velocity is 2 L/min, because the effect of EDEC will almost be lost when the flow velocity becomes 2 L/min or more.

Copyright © 2003 Swets & Zeitlinger B.V., Lisse, The Netherlands

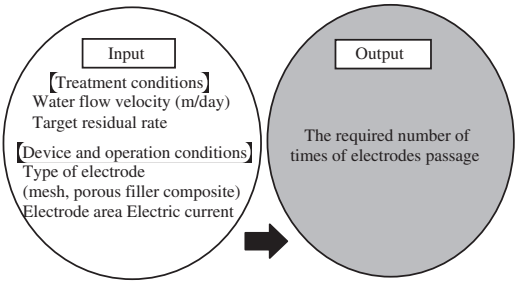


Figure 19. The concept of electric and water flow conditions.

When EDEC is used with simple underground equipment, the voltage may be restricted to less than 60 V, because the standard of an electrical corrosion protection institution will be applied. When setting the electrode area at 0.5 m^2, the maximum current is about 10 A (current density is about 20 A/m^2). However, when it is applied to a water treatment plant at ground level, it is thought that current density can be set higher.

7 CONCLUSIONS

Batch and column test were performed to investigate the basic characteristics of VOCs contaminated water remediation by electric dechlorination technology (EDEC). Moreover, an experiment was carried out on a porous filler composite electrode designed to increase the effect of EDEC, and its remediation capability was investigated. The results are summarized below.

1. EDEC can dechlorinate and decompose TCE in solution under still and flow water conditions.
2. The reaction of EDEC is mainly controlled by the quantity of electricity for still water, and by the current and flow velocity for flowing water.
3. With a mesh electrode, EDEC can decrease the TCE residual rate to about 10% without regard to initial concentration. By passing the solution by the electrodes two or more times, the residual rate can be decreased further.
4. When a porous filler composite electrode is used, compared with the case where the mesh electrode and only the porous filler (activated carbon) are used, a very high treatment effect is achieved and the residual rate can be decreased. This tendency was shown not only in a small-scale experiment but also in a large-scale experiment, thus proving that the scale up of equipment was satisfactory.
5. The number of times required for the solution to be passed by the electrode for remediation is determined from the flow velocity, target residual rate, type of electrode, electrode area and current.

Compared with the other water remediation technologies, the amount of water that can be treated per unit time by EDEC is small. However, EDEC has the following three advantages. 1) It can decompose VOCs. 2) It easily responds to change of VOCs concentration. 3) It is advantageous when treating highly contaminated water. Research will continue on ways to efficiently utilize the characteristics of EDEC in the future.

REFERENCES

Senzaki T. & Kumagai Y. 1988. Removal of chloroorganic compounds in waste-water by reductive treatment – Reductive degradation of chlorinated organic hydrocarbons with iron powder. *Industrial water* 357: 2–7 (in Japanese).

Sequeira CAC. 1998. Electrochemical approach to pollutants removal and destruction. In G.P. Gallios and K.A. Matis (eds.), *Mineral Processing and the Environment*: 111–128. Netherlands: Kluwer Academic Publishers.

Schmal D. 1987. Electrochemical treatment of organohalogens in process waste waters. *Environmental Technology*: 284–293.

Copyright © 2003 Swets & Zeitlinger B.V., Lisse, The Netherlands

Evaluation of remedial actions for a contaminated site using risk assessment approaches

M. Kamon, T. Inui & T. Katsumi
Graduate School of Global Environmental Studies, Kyoto University, Japan

A. Doi
Department of Civil Engineering, Kyoto University, Japan (Currently, MIT Corporation, Japan)

D. Miyagi
Department of Civil Engineering, Kyoto University, Japan

ABSTRACT: Contaminant transport in and around a site contaminated by illegal dumping of waste is evaluated to assess the effectiveness of a containment disposal facility (CDF) as a remedial action in terms of human health risk. PCDDs and PCBs are the contaminants of concern. Analytical and numerical models are used to evaluate contaminant transport through the groundwater and atmosphere. This paper mainly presents the results of numerical analysis on the transport in groundwater with or without a CDF, which is composed of vertical cut-off wall and capping system. Furthermore, human health risk assessment approaches are applied to quantify the effectiveness of a remedial action by comparing calculated health risk before and after constructing a CDF. Analytical results indicate that this CDF could significantly prevent the contaminants transport as well as potential human health risk.

1 INTRODUCTION

Risk based remediation program for soil and groundwater contamination has recently been focused based on the fact that it can make the remedial action more effective and results in the cost reduction in a process of remediation activities (e.g. American Society for Testing and Materials 1996, DEFRA & Environment Agency 2002). It was developed to determine the remediation goal and choose the most cost-effective remedial option in terms of environmental and/or human health risk. In Japan, however, the remediation goal is generally fixed upon the prescribed environmental criteria. Consequently, it takes a long time to complete remediation activities, because most contaminated sites are forced to apply a remedial method for the contaminant source reduction and it is very difficult to reduce to the environmental criteria.

This paper examines the adequacy of a remedial action in terms of human health risk reduction, based on the analysis regarding contaminant transport, mainly in groundwater. A site concerned in this study was contaminated due to illegal dumping of waste. It was considered that polychlorodibenzo-p-dioxins (PCDDs) and polychlorinated biphenyls (PCBs) are the contaminants of potential concern. Several media (e.g. air, groundwater, and soil) are regarded as transport/exposure pathways for these contaminants. Contaminant transport through groundwater is examined using the finite element method for groundwater flow with mass transport, and potential human health risk of contaminants in groundwater at the boundary on this site is estimated before or after the construction of the containment disposal facility (CDF). In addition, results of contaminant transport through the air and related human health risk are also introduced. Finally, by comparing the calculated human health risk before and after remediation, the effectiveness of this CDF as a remedial action is discussed.

2 BACKGROUND

2.1 *General aspects of risk assessment*

Risk of an adverse health impact, such as cancer, respiratory illness, and birth defects, on a population caused by the contaminant intake is quantified in the risk assessment related to soil/groundwater contamination

Copyright © 2003 Swets & Zeitlinger B.V., Lisse, The Netherlands

problems. A general procedure is as follows: (i) identify the contaminant source and concentration in each concerned medium, (ii) evaluate the contaminant transport and intake rate for each exposure scenario (e.g. inhalation of contaminated dust, ingestion of groundwater) based on site specific parameters, and (iii) summarize contaminant intake and assess risk levels based on toxicological data. Cancer risk can be generally estimated using Equation (1):

$$Risk = C \times SF \times \frac{CR \times EFD}{BW \times AT} \quad (1)$$

where $Risk$ = a unitless probability (e.g. 2×10^{-5}) of an individual developing cancer, C = chemical concentration (mg/m^3), SF = slope factor; a plausible upper-bound estimate of the probability of a response per unit intake of a chemical over a lifetime ((mg/kg-body-weight/day)$^{-1}$), CR = contact rate; the amount of the contaminated medium contacted per unit day (m^3/day), EFD = exposure frequency and duration; the product of exposure frequency, EF (days/year) and exposure duration, ED (years), generally, BW = body weight (kg), and AT = averaging time; period over which exposure is averaged (days) (USEPA 1989).

2.2 *Uncertainty of parameters in risk assessment*

The parameters used in Equation (1) are divided into three categories; a site specific parameter, C, a parameter based on the toxicological data, SF, and parameters related to human activity, CR, EFD, BW, and AT. Uncertainties in parameters related to human activity are generally described as the normal or lognormal distributions, whose mean values and standard deviations are reported by USEPA (1997). In this study, in order to integrate these uncertainties, the Monte Carlo simulation was introduced. 20,000 sets of related parameters for the health risk by each human exposure pathway (e.g. drinking intake ratio, EF, ED, BW, and AT for the health risk by drinking contaminated water) were simulated according to their probability distributions reported by USEPA (1997), and then a probability distribution for $(CR \times EFD)/(BW \times AT)$ was estimated (Katsumi et al. 2002). This is equivalent to the distribution of $Risk/C/SF$, which means a variety of risk in a population for a chemical concentration. Figure 1 shows these distributions calculated for the risk by drinking or dermal contact of contaminated water.

3 CONTAMINATED SITE

3.1 *Site description*

Figure 2 shows a schematic view of a contaminated site. The site is located in a retarding basin for two rivers and contaminated by illegal dumping of waste. The volume of the contaminated soil, which mostly exists in 0.2 to 3.0 m of surface layer, is approximately 110,000 m^3.

In situ investigations at this site comprised hydrogeological investigations such as geotechnical log boring and infiltration tests, and detections of contamination level in waste, groundwater, atmosphere and its surrounding soil. Laboratory triaxial permeability tests on foundation materials were also conducted. Contaminants detected in this site were PCDDs, PCBs, and several kinds of heavy metals. In particular, the concentrations of PCDDs and PCBs are much higher than the Japanese environmental criteria (1,000 pg-TEQ/g and "Not detected", respectively). Therefore, they were regarded as the contaminants of potential concern.

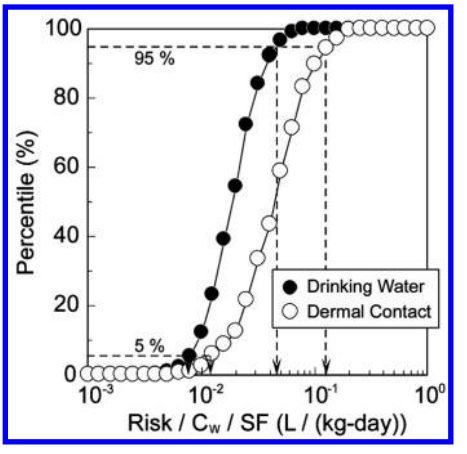


Figure 1. Distributions of human health risk by drinking and dermal contact of contaminated water.

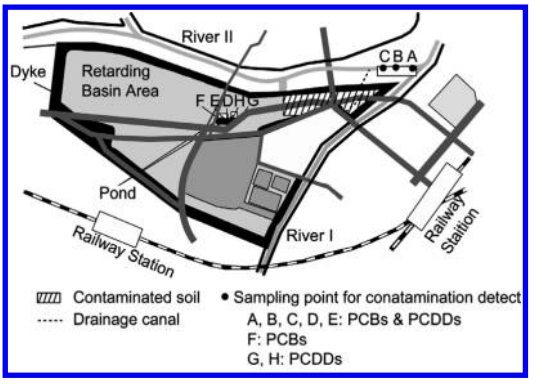


Figure 2. Schematic view of a contaminated site.

Copyright © 2003 Swets & Zeitlinger B.V., Lisse, The Netherlands

3.2 *Containment disposal facility (CDF)*

As a remediation program, the contaminated soil was isolated in a CDF, which is newly constructed in this site. This containment system is composed of a vertical cut-off wall and capping system. A schematic and specifications of this CDF are shown in Fig. 3. The vertical cut-off wall consists of a 2 mm thickness geomembrane sheet and cement stabilized soil mixing wall, and is keyed 2.5 m into an alluvial clay layer to prevent leakage flow.

3.3 *Exposure pathway*

Contaminants exposure pathways considered in the human health risk assessment are shown in Table 1. It was assumed that the CDF can absolutely prevent the contaminants exposure through soil and airborne dust by a capping layer constructed. In the following section, contaminant transport through groundwater is mainly examined, and the potential human health risk caused by contaminants in groundwater at the boundary of this site, as well as in contaminated soil itself and airborne dust was estimated before or after the construction of the CDF.

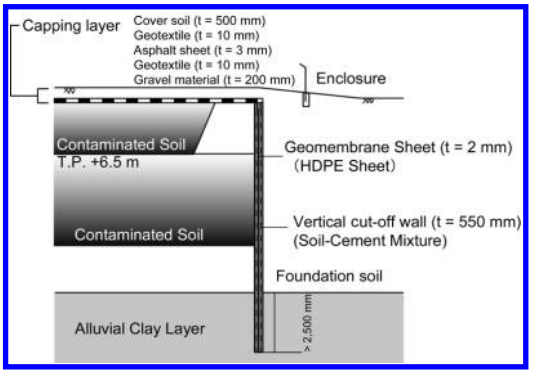


Figure 3. Cross section of the containment disposal facility.

4 ANALYSIS OF CONTAMINANT TRANSPORT IN GROUNDWATER

4.1 *Modeling of groundwater flow*

Groundwater flow pattern at this site, based on the hydrogeological conditions, is modeled numerically using the finite element method. Hydrogeological conditions include the foundation profile, groundwater level, and hydraulic properties of foundation materials such as their porosities and hydraulic conductivities. The foundation layers of this site consist mainly of two alluvial clay layers and fill-up layer on the impermeable layer. Considering the foundation profile, groundwater level and the fact that the upper alluvial clay layer had a relatively higher permeability, as shown in Table 2, it could be predicted that horizontal groundwater flow in the upper alluvial clay layer was dominant at this site. Therefore, two dimensional analysis was conducted to model the horizontal groundwater flow. In this analysis, constant water head conditions based on the groundwater levels investigated in geotechnical log boring tests and average water levels of two rivers were applied at the boundary of this site.

Figure 4 shows an analytical result of velocities of groundwater flow at this site. It indicates that the dominant pathway of contaminant leakage is predicted to be the horizontal groundwater flow from a CDF to the two rivers which run along this site.

4.2 *Modeling of contaminant transport*

As shown in the previous section, modeling of groundwater flow confirms that horizontal groundwater flow in the direction of the two rivers from the CDF is most dominant at this site. Therefore, two cross sections shown in Fig. 4, which are parallel to the dominant direction of groundwater flow, were analyzed. The finite element advection–dispersion chemical transport model, DTransu–2D·EL, which was developed by

Table 1. Pathways of contaminants transport/exposure considered in this study.

Medium, transport pathways	Exposure	Before construction	Under construction	After construction
Atmosphere				
Dust	Inhalation	○	○	–
	Dermal contact	○	○	–
Volatized gas	Inhalation	○	○	○
Groundwater	Intake	○	○	○
Soil	Dermal contact	○	○	–
	Intake	–	–	–

○, considered; –, not considered.

Copyright © 2003 Swets & Zeitlinger B.V., Lisse, The Netherlands

Table 2. Material properties used in numerical analysis.

Parameters		Unit	Fill-up layer	Upper alluvial clay layer	Lower alluvial clay layer	Contaminated soil	Cut-off wall
Hydraulic conductivity	k	cm/s	1.0×10^{-5}	5.0×10^{-5}	2.0×10^{-7}	1.0×10^{-4}	1.0×10^{-11}
Effective porosity	n_e	–	0.55	0.60	0.65	0.50	0.01
Transversal dispersivity	α_T	cm	10	10	10	10	10
Longitudinal dispersivity	α_L	cm	1	1	1	1	1
Effective diffusivity	D_{me}	cm^2/s	1.0×10^{-5}	1.0×10^{-5}	1.0×10^{-5}	1.0×10^{-5}	1.0×10^{-5}
Retardation factor	R	–	10	10	10	10	10

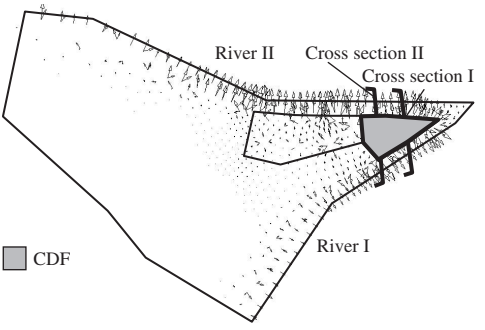


Figure 4. Results of groundwater flow analysis – steady state.

Nishigaki et al. (1995), was used to analyze the concentration and mass flux of a contaminant released from the contaminated soil. This model provides an analytical solution for contaminant concentration with time by solving the governing equation for fluid-density dependent groundwater flow with mass transport (Nishigaki et al. 1995).

Figure 5 shows one of the cross sections for contaminant transport analysis. The area for the analysis is 190 m in width and 30 m in height. Contaminated soil is disposed inside the vertical cut-off wall on the foundation layer. The parameters for each material used in the analysis are shown in Table 2. It was assumed that a vertical cut-off wall is a material of very low permeability, considering that there is a possibility that a geomembrane sheet allows the leakage caused by defects during its service life. At this site, soil contamination due to waste dumping is reported to have occurred about 30 years ago. Accordingly, contaminant transport in 30 years without a CDF was firstly simulated, then transport in another 30 years was analyzed with or without a CDF. Furthermore, only PCBs is regarded as a contaminant of concern, for no previous study has reported that PCDDs in contaminated soil is transported by groundwater flow in soluble form.

The retardation factor, R, is generally estimated based on many factors such as the octanol–water partition coefficient of chemical, K_{ow}, and the organic carbon content in soil, f_{oc}, etc. Previous research confirms that the R values of clay materials for PCBs are very high (e.g. 10^3 to 10^4, Schnoor 1996). However, this value is easily and significantly affected by many factors. In this study, the R value for each foundation material is set at 10, considering that it is better to assume a worst case scenario in human health risk assessment, as well as the measured organic carbon content of the soil.

As the boundary conditions in the analysis, constant water head were assumed based on the groundwater level investigated inside the CDF (before and after the construction of the CDF; 400 cm and 650 cm, respectively) and the average water level of two rivers. Contaminant transport was analyzed under the steady-state hydraulic head distribution and saturated water flow condition. Unitless initial contaminant concentration, C_0, of 100 was set for the mesh corresponding to contaminated soil. For the human health risk assessment, an initial concentration of 100 was assumed equal to a solubility of PCBs, 0.34 mg/L (Spitz & Moreno 1996).

Figure 6 shows the hydraulic head distributions analyzed in case of before and after construction of the CDF. From these results, the vertical cut-off wall makes most of hydraulic head loss occur only in the lower alluvial clay layer, whose hydraulic conductivity is relatively low as shown in Table 2. On the other hand, in the case of before construction of the CDF, the hydraulic head loss occurs in relatively high permeable layers (fill-up layer and upper alluvial clay layers) as well as in the lower alluvial clay layer. These observations indicate that the vertical cut-off wall can significantly reduce horizontal groundwater flow and advective contaminant transport in aquifer.

Figure 7 shows one of the analytical results of a contaminant concentration change with time normalized by C_0 at the boundary of this site. In the case of before the construction of the CDF, the groundwater which contains a very low concentration of contaminant reached the boundary of this site after about 10 years. However, a vertical cut-off wall allows almost no contaminant to reach the boundary of the site.

Copyright © 2003 Swets & Zeitlinger B.V., Lisse, The Netherlands

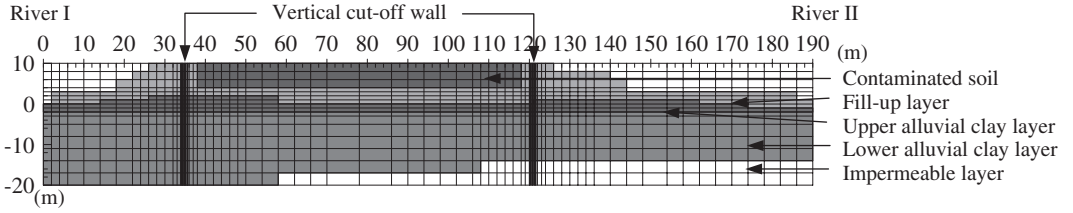


Figure 5. Cross section and finite element mesh used in transport analysis in case of cut-off wall construction.

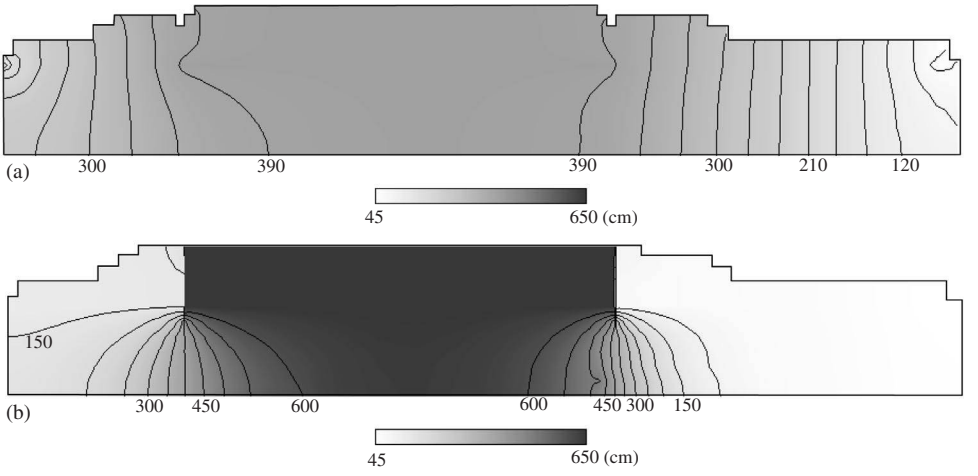


Figure 6. Hydraulic head distribution: (a) before construction of cut-off wall; (b) after construction of cut-off wall.

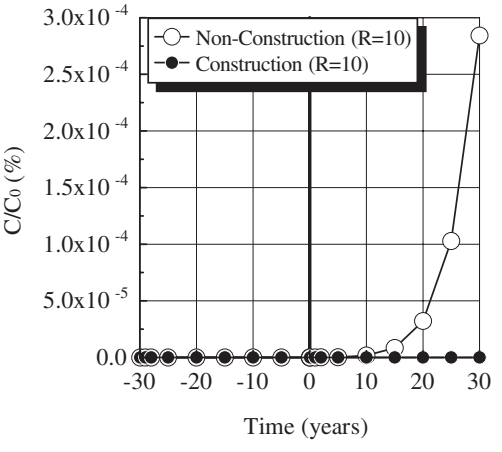


Figure 7. Example of contaminant transport analysis – chemical concentration with time on the boundary in the site.

5 HUMAN HEALTH RISK ASSESSMENT

Using the analytical results of the contaminant transport in groundwater, human health risk caused by intake of groundwater is calculated with the assumption that the contaminant exposure by groundwater intake continues for 50 years. In fact, the groundwater at this site and its surrounding area is not utilized as drinking water, and therefore human health risk caused by groundwater intake will not occur. However, in this study, the potential human health risk of groundwater is evaluated in order to discuss the effectiveness of the CDF as a remedial action.

Figure 8 shows the potential human health risk caused by groundwater at the boundary of the site (along two rivers shown in Fig. 2 and a drainage canal inside the site), before and after construction of the CDF. *SF* used in calculations is according to the accumulated data by USEPA (1996, 2001). In addition, 5% to 95% values in a risk distribution shown in Fig. 1, based on a variety of risk in a population for a chemical concentration, are applied in order to represent the range of the health risk. The results obtained indicate that CDF can significantly reduce the potential human health risk by about 10^{-4} to 10^{-6} times at the boundary of the site, and by about 10^{-1} time at the drainage canal.

Furthermore, the potential human health risk caused by other exposure pathways at this site,

Copyright © 2003 Swets & Zeitlinger B.V., Lisse, The Netherlands

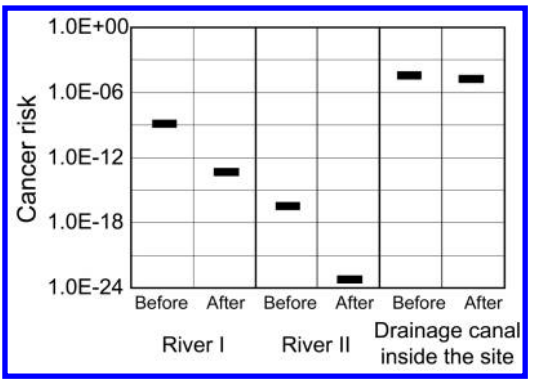


Figure 8. Calculated human health risk caused by PCBs and dioxins exposure through groundwater.

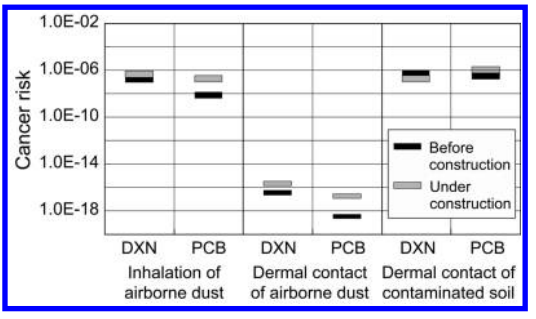


Figure 9. Calculated human health risk caused by PCBs and dioxins exposure through air and soil.

including inhalation of airborne dust, dermal contact of airborne dust, and the dermal contact of the contaminated soil, was also evaluated as shown in Fig. 9 (Kamon et al. 2002). In the assessment of health risk under construction of the CDF, health risk for a person who worked in this site for 1 year was estimated. From these results, the calculated values of potential health risk through these pathways are relatively higher than by contaminant transport in groundwater. In particular, the inhalation of airborne dust, which occurs most usually and frequently even in a neighborhood, results in a relatively high health risk. On the basis that a capping layer in the CDF is considered to prevent almost absolutely the generation of contaminated airborne dust, this containment system can reduce human health risk to the level much lower than the accepted level (generally, 10^{-6}).

6 CONCLUSIONS

This paper presents a case study performed with numerical and analytical models, in order to assess the effectiveness of a containment facility as a remedial action in terms of human health risk. Contaminant transport in aquifer at a contaminated site was analyzed using the numerical model, and then human health risk, mainly caused by groundwater contamination, is calculated in case of before/after construction of the CDF. The results can be summarized as follows:

1. Distributions of human health risk due to the uncertainties in parameters related to human activity, which indicates a variety of risk in a population for a chemical concentration, were summarized using Monte Carlo simulation method.
2. Contaminant transport analyses confirm that a vertical cut-off wall in the CDF can significantly reduce the horizontal groundwater flow rate and advective contaminant transport in aquifer.
3. The CDF constructed at this site proved to be so effective based on the analytical result that it can significantly reduce the potential human health risk caused by ground water intake as well as by inhalation of airborne dust, dermal contact of airborne dust, and dermal contact of contaminated soil.

Human health risk calculated in this study are based on the given input parameters and several simplifications, in particular, relate to inter-phase mass transfer for contaminants such as contaminant sorption on solid phase. Therefore, further studies should include modeling inter-phase mass transfer for contaminants as well as identifying the dominant factors in human health risk calculations.

ACKNOWLEDGEMENT

This research has been carried out with valuable information provided by Keihin Work Office, Kanto Regional Development Bureau, Ministry of Land, Infrastructure and Transport.

REFERENCES

American Society for Testing and Materials. 1996. Standard guide for risk-based corrective action applied at petroleum release sits, *ASTM Designation:* E1739-95.

DEFRA & Environment Agency. 2002. *Assessment of Risks to Human Health from Land Contamination*: *An overview of the development of guideline values and related research*, R&D Publication CLR7.

Kamon, M., Inui, T., Katsumi, T., Doi, A. & Miyagi, D. 2002. A risk based approach for the evaluation of the contaminated land remediation, *Proc. 37th Japan National Conference on Geotechnical Engineering*, 2329–2330 (in Japanese).

Katsumi, T., Yamada, K., Inui, T., Doi, A. & Kamon, M. 2002. Evaluating the environmental risks induced by soil and groundwater contamination, *Proc. 37th Japan National*

Copyright © 2003 Swets & Zeitlinger B.V., Lisse, The Netherlands

Conference on Geotechnical Engineering, 2327–2328 (in Japanese).
Nishigaki, M., Hishiya, T., Hashimoto, N. & Kohno, I. 1995. The numerical method for saturated–unsaturated fluid-density-dependent groundwater flow with mass transport. *J. Geotech. Engrg*., JSCE 511: 135–144 (in Japanese).
Schnoor, J.L. 1996. *Environmental Modeling*, John Wiley & Sons, Inc.
Spitz, K. & Moreno, J. 1996. *A practical guide to groundwater and solute transport modeling*, A Wiley-Interscience Publication, John & Wiley Sons, Inc., 356–361.
USEPA. 1989. *Risk Assessment Guideline for Superfund; Volume I; Human health evaluation manual*, EPA/540/1-89/002, Washington, D.C.
USEPA. 1996. *PCBs: Cancer Dose-Response Assessment and Application to Environmental Mixtures*, EPA/600/P-96/011, Washington, D.C.
USEPA. 1997. *Exposure Factors Handbook*, Update to Exposure Factors Handbook (EPA/600/8-89/043 – May 1989), EPA/600/ P-95/002Fa, Washington, D.C.
USEPA. 2001. *Integrated Risk Information System (IRIS)*, http://www.epa.gov/iris/index.html.

Copyright © 2003 Swets & Zeitlinger B.V., Lisse, The Netherlands

DNAPL contaminant mass outflux rate and its relation to remediation cleanup level

J.W.E. Page, K. Soga & N.S. Gowers
University of Cambridge, Cambridge, UK

ABSTRACT: The mass flux-based source zone remediation assessment method was used to assess the effect of ground water flow rate on mass flux of aqueous-phase DNAPL exiting a source zone. A stochastic model for the permeability field was used to generate permeability fields and 0.5 m^3 of PCE was spilled in the model subsurface. Various remediation levels were simulated by uniform volumetric reductions of DNAPL. Dissolution was then modelled with the single resistance model at different flow rates. Numerical results show that source zone geometry perpendicular to the flow, the flow rate itself and the volumetric content of DNAPL are the dominant parameters controlling the mass flux exiting the source zone. Following the development of a modified non-dimensional mass flux that takes into account the major factors affecting the source zone mass flux, an approximate relationship between the modified non-dimensional mass flux and the volume of remaining DNAPL is developed.

1 INTRODUCTION

Dense Non-Aqueous Phase Liquids (DNAPLs) are a class of chemicals characterised by their low solubility in water. Their accidental release and improper disposal is widely recognised as one of the largest contributing causes of subsurface chemical contamination. After the spill, free-phase DNAPL generally migrate downwards and the migration path is dependent on the structure and permeability of the soil (e.g. Kueper & Frind, 1991). The DNAPL may collect and pool on lower permeability layers (e.g. at the bottom of an aquifer). The resultant DNAPL distribution in the subsurface is very complex, consisting of fingering and pools, which is shown in Figure 1.

The zone in which the DNAPL is found in the free phase is known as the source zone. As ground water flows past the DNAPL in the source zone, a small amount of chemicals in the DNAPL dissolves into the aqueous phase forming a downstream dissolved contaminant plume. The plume can transport the DNAPL contaminants significant distances downstream as shown in Figure 1. The source zone is likely to persist for many years due to the low solubility of the DNAPL.

Risk assessment of contaminated land is concerned with identifying the risk of adverse effects in humans due to exposure to a contaminant. Exposure is determined by the pathways by which a person may come into contact with the contaminant (e.g. inhalation, dermal contact, and ingestion), concentrations of the contaminant in the various phases and the length of time over which exposure occurs. Quantitative risk assessment is based on the temporal concentration of contaminant at the receptor (see Figure 1) and various models are necessary to perform this quantification as shown in Figure 2. Plume fate and transport models (i.e. advection, dispersion, retardation, biological transformation, chemical transformation) are

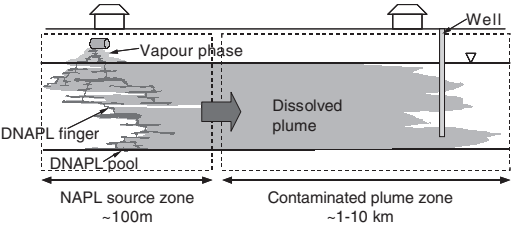


Figure 1. Source zone and plume zone.

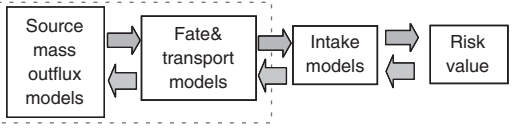


Figure 2. Quantitative Risk Assessment.

Copyright © 2003 Swets & Zeitlinger B.V., Lisse, The Netherlands

used to predict future concentrations at the receptor point in order to ascertain future risk via intake models. The plume development depends not only on the subsurface conditions but the concentration of contaminant within the plume itself, which is ultimately dependent on the concentration and quantities of contaminant leaving the source zone. This is calculated from a source zone mass out flux model. Therefore, the assessment of risk at a downstream site is dependent on the mass flux of dissolved contaminant leaving the source zone, which itself is likely to be dependent on characteristics of the source zone.

This paper uses the mass-flux method and seeks to assess what effect the ground water flow rate, volumetric content of DNAPL and subsurface heterogeneity has on the mass flux of DNAPL exiting the source zone. The implications for risk assessment are then discussed.

2 FIELD SCALE MASS OUTFLUX

2.1 *Source zone remediation and mass outflux*

In practice, attention of source zone remediation is focused on the actual reductions of NAPL source and the effectiveness of the chosen technique in the specific conditions. Remediation efficiency (quantified in terms of volumetric reduction) of up to 99.9% is achieved for small-scale tests (e.g. in laboratory columns). This is reduced to 70–80% or less in larger-scale heterogeneous field tests (see Soga et al., 2002 for more details).

The relationship between volumetric reduction of NAPL source and the source zone exit mass flux is not known. For example, a remediation strategy may recover 85% of the source zone DNAPL. However, it may be the case that the remaining 15% generates a similar mass flux as the initial 100% case. If so, the remediation has failed. Therefore, it has been suggested by Soga et al. (2002) that a mass-flux approach needs to be adopted to assess the efficiency of source zone remediation technologies. The approach considers the mass flux of NAPL contaminants from the free phase to the aqueous phase to be of greater importance than the amount of NAPL in the source zone itself. By considering the mass flux pre- and post-remediation and over a sufficiently large time scale the effectiveness of the remediation can be assessed.

2.2 *Field heterogeneity and mass outflux*

The mass outflux from the source zone is expected to be influenced largely by the DNAPL morphology in the field due to the complex migration and entrapment patterns. Sale & McWhorter (2001) showed analytically that the source-zone geometry is a primary factor governing bulk mass transfer and persistence of the source. They concluded that the advective-dispersive transport of dissolved chemical away from the DNAPL subzone governs the overall mass transfer process of chemicals from DNAPL to aqueous phase. Brusseau et al. (2002) conducted intermediate-scale dissolution experiments and to these results correlated quantitative 3-D mathematical models of varying complexity. They concluded that larger scale factors such as non-uniform immiscible-liquid distribution, permeability variability, and sampling-associated dilution control dissolution behaviour and that local-scale mass transfer processes are generally of secondary importance.

The conclusions of Sale & McWhorter (2001), and Brusseau et al. (2002) are especially relevant to field scale spills. In the field the DNAPL distribution is very much determined by the heterogeneity of the subsurface. Field scale flow rates are very slow (0.5 metres per day represents an upper bound) so large aqueous-phase NAPL concentrations can be expected. Therefore, in the field scale, it is very likely that heterogeneity and NAPL distribution effects are dominant over local mass transfer effects.

3 NUMERICAL ANALYSIS OF FIELD SCALE MASS OUTFLUX

To test the above hypothesis, numerical analysis is used in this study to model various source zones and determine the aqueous-phase mass fluxes at the exit. By considering non-dimensional (or normalised) mass fluxes the dependence on local-scale mass transfer can be determined. Ideally field scale experiments need to be carried out with typical NAPL volumes. However, in order to investigate ground water flow rate, heterogeneity effects and remediation efficiency, multiple field scale experiments are neither practical nor possible.

3.1 *DNAPL spill simulation*

A finite-difference compositional simulator, UTCHEM (Delshard et al., 1996), was used to model the complex DNAPL source zone architecture and multiphase flow. The subsurface model is based on a log-normal distribution in field hydraulic conductivity. A 50 m by 10 m (by 1 m wide) two-dimensional permeability field was created using a correlated stochastic model by Tompson et al. (1989). Restricted by computing power and for simplicity, the analyses considered in this paper are for two-dimensional source zones. Considering that the complex DNAPL entrapment is affected by small scale changes in soil stratigraphy (Pankow & Cherry, 1996), each element had the dimensions 0.5 m by 0.1 m thus making 10,000 elements in total. The parameters

Copyright © 2003 Swets & Zeitlinger B.V., Lisse, The Netherlands

Table 1. Parameters used to generate permeability field.

Mean, μ, of ln[k (millidarcy)]	9.21
Variance, σ, of ln[k (millidarcy)]	0.6
Vertical correlation length (m)	0.5
Horizontal correlation length (m)	5.0

Table 2. Aquifer and chemical properties.

PCE density	1.623 g/cm^3
Water viscosity	1.0 mPa · s
PCE viscosity	0.89 mPa · s
PCE-water interfacial tension	45 dynes/cm
PCE equilibrium concentration	0.00015 vol. frac. (∼243 mg/l)
Constant reservoir porosity	0.34
Sherwood no. constant β_0	4.79
Reynold's no. exponent β_1	0.6
Oil content exponent β_2	0.87
Schmidt no. exponent β_3	0.5
Capillary pressure endpoint	3 $psi\sqrt{darcies}$
Capillary pressure exponent	−0.52

used in the generation of the field are summarised in Table 1 and the values used simulate a sandy glacial aquifer. The z-direction permeability was modelled as half the x-direction permeability (given by the permeability field generation). Three different realisations of the stochastic parameters were generated for the investigation. The parameters for the Brooks-Corey capillary saturation relationship were also scaled according to the permeability value assigned to each block.

Tetrachloroethene (PCE) was released from a point source at the top of the aquifer and 15 m from the upstream boundary. The release rate was 0.005 m^3 per day over a period of 100 days. A further 900 days were then allowed for the PCE to migrate downwards and redistribute itself in the aquifer. This was carried out under natural hydraulic conditions with a mean groundwater velocity of 0.1 m/day for most cases (0.1, 1.0 and 5.0 m/day for Realisation 3). Table 2 summarises the aquifer and chemical properties used for the multiphase flow simulations. The computed DNAPL entrapment conditions are shown in Figure 3.

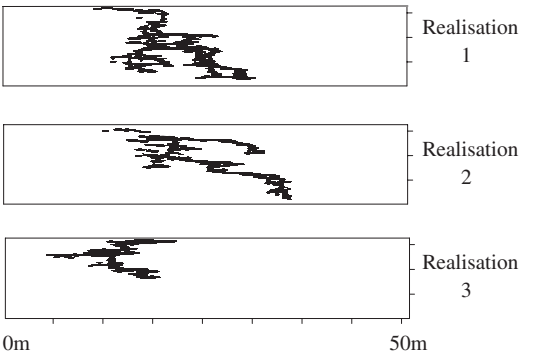


Figure 3. Simulated DNAPL spil profiles (shaded area where DNAPL saturation exceeds 0.00016).

3.2 *Mass transfer simulation*

If the effect of flow velocity and/or contact time between the mobile water and the stationary NAPL is neglected, then equilibrium mass transfer of NAPL into the aqueous phase can occur. The solubility limit (C_s) thus sets an upper bound for the concentration of DNAPL. At the REV level, the rate, at which mass is transferred from the DNAPL to the aqueous phase, $\dot{M}$ (MT^{-1}L^{-3}), is modelled by a single resistance model expressed in Eq. 1. It is an example of a rate-limited model of mass transfer whereby equilibrium concentration is not immediately attained.

$$\dot{M} = K_L(C_s - C) \tag{1}$$

where C_s (ML^{-3}) is the solubility limit and C is the current bulk aqueous phase concentration of the contaminant. K_L (T^{-1}) is the mass transfer coefficient, determined empirically and thought to be directly proportional to the molecular diffusion coefficient in the aqueous phase and the interfacial area between the two phases. K_L can be related to a modified Sherwood number *Sh*.

$$Sh = \frac{K_L d_p^2}{D_m} \tag{2}$$

where d_p (L) is the mean particle size and D_m (L^{2}T^{-1}) is the molecular diffusion coefficient for the contaminant in the aqueous phase.

The modified Sherwood number is correlated empirically to other non-dimensional numbers such as Reynolds number, NAPL content and Schmidt number. In UTCHEM, a general equation is given by

$$Sh = \beta_0 \mathrm{Re}^{\beta_1} \theta_n^{\beta_2} Sc^{\beta_3} \tag{3}$$

where β_0, β_1, β_2, β_3 are input parameters determined by best fit to the experimental data. Re ($= d_p v\rho/\mu$) is the Reynold's number, v is the aqueous velocity, ρ is the aqueous density, μ is the aqueous viscosity, θ_n is the volumetric content of NAPL, and Sc ($= \mu/D_m\rho$) is the Schmidt number. The parameters used in the present analysis are listed in Table 2.

Allowing non-equilibrium mass transfer of DNAPL, the output from the spill stage was subject to groundwater flow conditions to create a downstream aqueous-phase contaminant plume. Parameters and governing

Copyright © 2003 Swets & Zeitlinger B.V., Lisse, The Netherlands

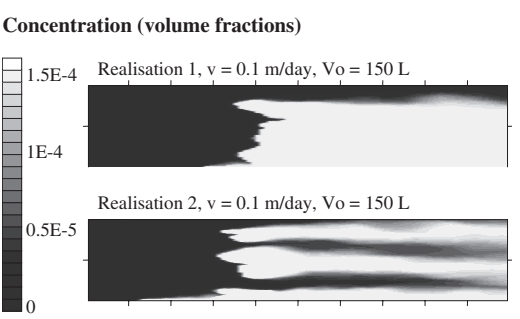


Figure 4. Simulated aqueous phase concentration profiles.

equations for this analysis were as for the spill stage but with the addition of Equation 1 to model the non-equilibrium mass transfer. The dissolution stage was allowed to run for 1000 days.

Simulated remediation was achieved by multiplying the output saturation profile of free-phase DNAPL from the spill stage by a factor representing a level of remediation. Five different values were used: zero, 70%, 90%, 95% and 99% remediation respectively. The uniform reduction is for demonstration purposes only and does not seek to reproduce the activity of remediation; the activities of remediation may result in a change in the characteristics of the source zone. The particular remediation levels considered were chosen because it is expected that significant volumetric reduction is required in order to achieve useful mass flux reductions.

Figure 4 shows the contaminant plumes at the instance of peak mass flux for the 70% remediation case (i.e. 0.150 m^3 of PCE in the subsurface). Most of the plume is at, or close to, the equilibrium concentration of 0.00015 volume fractions. Hence, the plume is carrying close to the maximum possible amount of aqueous phase PCE.

3.3 *Data interpretation*

Using the dissolution stage result, the mass flux of dissolved DNAPL out of the source zone (or model downstream boundary) can be determined. The 1-D mass flux of aqueous phase contaminant, $\dot{m}_x$, in a saturated elemental block (as shown in Figure 5(a)) is given as:

$$\dot{m}_x = a\rho v_x C_{vf} \tag{4}$$

where a is the cross sectional area of the elemental block perpendicular to the flow, ρ is the density of the contaminant (in this case PCE), v is the Darcy velocity and C_{vf} is the concentration in volume fractions. The subscript x indicates the flux in the x-direction in a Cartesian co-ordinate system where mean flow velocity is in the x-direction.

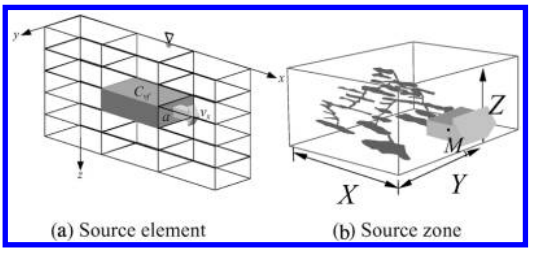


Figure 5. Mass outflux calculation parameters.

For a saturated m wide by n deep uniform grid of blocks the total mass flux of dissolved contaminant through a vertical slice is given as the sum of the mass flux through each block in the vertical stack (see Figure 5(b)). This is shown in Equation 5, where the subscript i indicates the value of the parameter at the given grid block.

$$\dot{M}_x = a\rho \sum_{i=1}^{m\times n} v_{xi} C_{vfi} \tag{5}$$

4 SIMULATION RESULTS AND DISCUSSION

4.1 *Effect of flow velocity and rate-limited mass transfer on source zone mass outflux*

In the dissolution analysis, four different mean groundwater flow velocities were considered for each remediation level of spilled DNAPL. 0.1 m/day represents a typical in-field ground water flow rate, whereas 5.0 m/day represents a typical upper bound to elevated flow conditions achieved during pump and treat remediation.

In order to ascertain the effect of rate-limit behaviour, a non-dimensional source zone exit mass flux, $\dot{M}_{ND}$ was used:

$$\dot{M}_{ND} = \frac{\dot{M}_x}{C_s \bar{v} A} \tag{6}$$

where C_s is the solubility limit, $\bar{v}$ is the mean Darcy's velocity, and A is the cross sectional area of the downstream source zone boundary.

Figure 6 shows the relationship between normalised mass flux and volume of PCE remaining for Realisations 1 with 90%, 95% and 99% remediation level. For each remediation level, there is one distinct curve of normalised mass flux against volume remaining. Therefore the rate of mass transfer, on the macroscopic scale, is dependent only the flow velocity and not limited by local scale mass transfer as given by Equation 1.

Copyright © 2003 Swets & Zeitlinger B.V., Lisse, The Netherlands

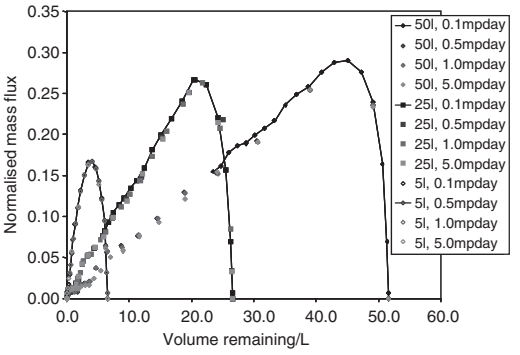


Figure 6. Normalised mass flux of Realisation 1.

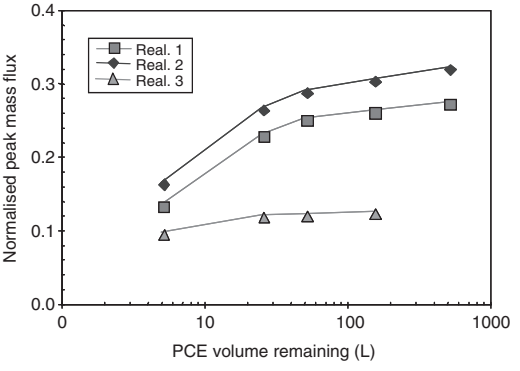


Figure 7. Normalised peak flux for given PCE volume.

4.2 *Effect of DNAPL distribution on source zone mass outflux*

The peak normalised mass flux for each remediation level and realisation at 0.1 m/day is plotted against initial volume of PCE, as shown in Figure 7. There is significant variation in peak mass flux between the different realisations. The only distinguishing feature between the various models is the distribution of DNAPL due to the realisations themselves. This suggests that distribution of DNAPL significantly affects the mass flow rate of DNAPL leaving the source zone. Referring back to Figure 3, the DNAPL spills in Realisations 1 and 2 occupy a similar vertical extent of the aquifer, which is roughly twice the extent contaminated in Realisation 3.

Figure 8 shows the normalised mass flux against remaining volume of PCE for 70% and 95% remediation of Realisation 3. In the light of the previous discussion it would be expected that the mass-flux curves for different flow rates would combine when normalised according to Equation 6 and this is the case for flow rates of 0.1 m/day and 0.5 m/day (they have a very similar spill saturation profile). However,

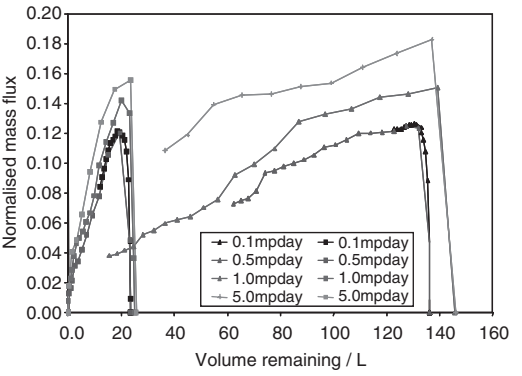


Figure 8. Normalised mass flux of Realisation 3 (two source volumes and four different flow velocities).

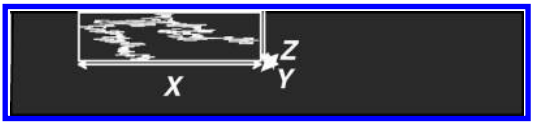


Figure 9. Definition of source size (X, Y and Z).

elevated normalised mass flux is observed at flow rates of 1.0 and 5.0 m/day. The most likely reason is different distributions of the DNAPL at the spill stages as shown in Figures 3(c), (d) and (e).

It seems therefore that the peak mass flux is not dictated by macroscopic rate limited behaviour but by source zone geometry and ground water flow rate. This is also in agreement with Sale & McWhorter (2001) in suggesting that source zone architecture is a primary factor governing bulk mass transfer out of the source zone and that local rate-limited mass transfer is a secondary effect (at least at the volumes examined in this study).

4.3 *Modified normalization of mass outflux*

As the mass flux out of the source zone seems to be strongly dependent on the DNAPL distribution, the non-dimensional mass flux was multiplied by the average saturation of DNAPL in the "distribution zone". A general form of normalization can be expressed as follows:

$$\dot{M}'_{ND} = \frac{\dot{M}_x}{C_s \bar{v} A} \frac{V_0^{\beta_1}}{X^{\alpha_1} Y^{\alpha_2} Z^{\alpha_3}} \tag{7}$$

where X, Y and Z are defined as shown in Figure 9, α_1, α_2, and α_3 are exponents of X, Y and Z respectively, and β_1 is the exponent of the initial volume of DNAPL. For dimensional consistency, $\beta_1 = (\alpha_1 + \alpha_2 + \alpha_3)/3$. It was found that the most satisfactory correlation for

Copyright © 2003 Swets & Zeitlinger B.V., Lisse, The Netherlands

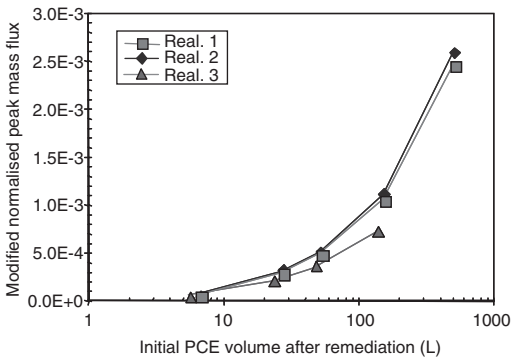


Figure 10. Modified normalised peak mass flux.

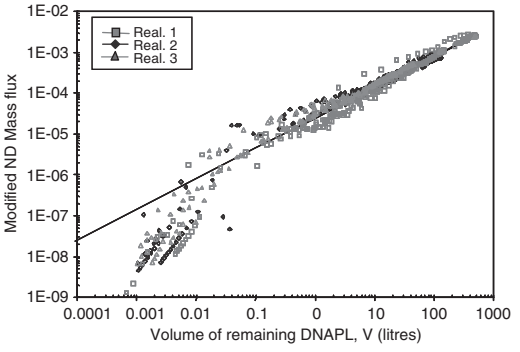


Figure 11. Modified normalised mass flux vs PCE volume.

the combination of all data was $\beta_1 = 2/3$, $\alpha_1 = 0$, and $\alpha_2 = \alpha_3 = 1.0$.

The peak values for this correlation are shown in Figure 10 and the post-peak data follows a general curve. The fit between the data is still not perfect, implying that there are other factors that affect the bulk mass flux of contaminant out of the source zone. However, the closeness of the data to the general trend suggests that the dominant factors have been considered.

The dominance of Y and Z can be explained with reference to Sale & McWhorter (2001); they show that the greatest mass transfer of DNAPL into the aqueous-phase occurs at the leading edge of a DNAPL pool or finger. Thus the distribution of DNAPL perpendicular to the flow is going to be a dominant factor in the dissolution of DNAPL into the aqueous phase.

Applying the modified non-dimensional mass flux (MNDMF) to the complete set of data gives on a log-log scale gives Figure 11. A suitable curve fit is as follows (where V is in L):

$$\dot{M}'_{ND} = 1 - \exp\left\{-2.5 \times 10^{-5} V^{0.75}\right\} \quad (8)$$

This represents a reasonable model because the MNDMF can never go above unity since it is a product of the proportion of the maximum possible mass flux and the average saturation perpendicular to the flow.

As shown in Figure 11, there is a large variation in MNDMF (up to one order of magnitude) at the lowest volumes. This could be due to one of two factors: numerical errors or rate limited behaviour as expressed by Equation 1. However, the latter is probably more dominant, suggested by the shape of the curve for volumes below 0.1 L where the volume remaining is tending to zero but less rapidly. At very small volumes the "interference" between subzones may be less due to complete depletion of some subzones and so geometric effects are likely to be less significant. Therefore the distribution of results, and the drop away from the curve-fit suggests some sort of microscopic rate limited behaviour that is affecting the macroscopic mass flux. Alternatively, the drop away from the curve could be as a result of significant volumetric depletion of the source zone such that it can no longer be considered to be made up of one "distribution zone" perpendicular to the flow but needs to be considered as individual isolated zones with significant areas of clean soil between them.

Assuming that source zone geometry (Y and Z) does not change, a simple calculation using Equation 8 shows that a 90% reduction in initial volumetric content of NAPL (500 L to 50 L) achieves only a 13% reduction in mass flux. This implies that current remediation technology is unlikely to be able to reduce the mass flux considerably in the short term. Hence, focus needs to be brought to what happens to the mass flux after the "post remediation peak". However, it should also be noted that the 13% reduction in peak mass flux can be cancelled out by a 10% increase in the distributed area of DNAPL perpendicular to the flow. Hence, the DNAPL redistribution during remediation stage may have a significant effect on source zone mass outflux.

5 CONCLUSIONS

The mass flux of aqueous phase DNAPL exiting the source zone is shown to be strongly dependent on the source zone geometry and the volumetric content of DNAPL and directly proportional to the flow velocity. Microscopic rate limited mass transfer is shown to not be significant at the volumes considered. This confirms the observations of Sale & McWhorter (2001) and Brusseau et al. (2002). Hence, the ratio of post- to pre-remediation peak mass flux is strongly dependent on the post- to pre-remediation DNAPL distribution zone area ratio and only weakly dependent on the volumetric reduction.

Current remediation technology is unable to achieve the remediation efficiencies required to reduce the volumetric DNAPL content such that immediate

Copyright © 2003 Swets & Zeitlinger B.V., Lisse, The Netherlands

significant mass flux reduction is achieved. Attention needs to be diverted to temporal mass flux behaviour after remediation. Remediation technology needs to focus on volumetric content reduction and redistribution to maximise mass transfer in the short term such that natural dissolution will result in mass flux levels falling to acceptable levels.

Further investigation is currently being carried out to verify the results found here using intermediate scale test experiments and to make the analysis more applicable to field situations.

REFERENCES

Brusseau, M.L., Zhang, Z., Nelson, N.T., Cain, R.B., Tick, G.R. & Oostrom, M. 2002. Dissolution of non-uniformly distributed immiscible liquid: Intermediate-scale experiments and mathematical modelling. *Environ. Sci. Technol.* 36: 1033–1041.

Delshad, M., Pope, G.A. & Sepehrnoori, K. 1996. A compositional simulator for modeling surfactant enhanced aquifer remediation, *J. of Cont. Hydrology*, 23: 303–327.

Kueper, B.H. & Frind, E.O. 1991. Two-phase flow in heterogeneous porous media. 2- Model application. *Water Resour. Res*. 27: 1059–1070.

Pankow, J.F. & Cherry, J.A., Eds. 1996. *Dense Chlorinated Solvents and Other DNAPLs in Ground Water*. Waterloo Press, Portland, Oregon.

Sale, T.C. & McWhorter, D.B. 2001. Steady state mass transfer from single-component dense nonaqueous phase liquids in uniform flow fields, *Water Resour. Res.*, 37: 393–404.

Soga, K., Page, J.W.E. & Gowers, N.S. 2002. NAPL source zone remediation-mass flux approach, Proceedings of the 4th International Congress on Environmental Geotechnics, de Mello and Almeida (Eds.), Balkema, Vol. 2, pp. 1069–1081.

Tompson, A.F.B., Ababou, R. & Gelhar, L.W. 1989. Implementation of the three-dimensional turning bands random field generator. *Water Resour. Res.*, 25: 2227–2243.

Copyright © 2003 Swets & Zeitlinger B.V., Lisse, The Netherlands

Contaminant migration from a line source: a mathematical model

A.P.S. Selvadurai
Department of Civil Engineering and Applied Mechanics, McGill University, Montreal, QC, Canada

ABSTRACT: This paper presents a mathematical study of the problem of advective migration of a chemical from a line source that is located in a porous medium of infinite extent. The solution is developed by considering potential flow from a cavity with the shape of a prolate spheroid. The solution to the advective transport problem for a prolate spheroidal region is obtained through the application of a Laplace transform technique. The critical parameter that governs the solution to the line source problem is determined through an expansion technique involving the *aspect ratio* of the dimensions of the prolate spheroid. The numerical results also consider the influence of a natural attenuation component.

1 INTRODUCTION

The study of the movement of contaminants such as pollutants and other toxic chemicals in porous media has received considerable attention over the past three decades, particularly in view of the potential importance of the studies to geoenvironmental engineering and environmental geomechanics (Bear and Verruijt, 1990; Philips, 1991; Bear and Bachmat, 1991; Banks, 1994; Sun, 1996; Domenico and Schwartz, 1998; Charbeneau, 2000). The modelling of processes that govern the transport of contaminants in fluid saturated porous media is a problem of considerable complexity, which is influenced by a variety of factors applicable to the porous medium, the fluid saturating the porous medium, the chemical composition of the contaminant, the chemical interactions between the porous medium and the contaminant and the attendant time influences. For example, consider the problem of a porous medium that will experience structural shrinkage as a result of the interaction between the migrating chemical and porous solid. In such a situation the volume change can be influenced by the chemical concentration, which in turn can alter the hydraulic conductivity of the porous medium. Such an alteration in the hydraulic conductivity will influence the advective fluid velocities and the corresponding advective transport pattern. The resulting model will involve a nonlinear advective transport problem with spatial and time dependent inhomogeneity in the fluid transport characteristics and in the chemical transport. The continued provision of a hydraulic potential and the reduction in the hydraulic conductivity are an ideal combination for the generation of hydraulic fracture of the porous medium.

The ensuing modelling of the advective transport from a line source should be regarded as an elementary model of a very complicated problem. The basic transport mechanisms that dominate movement of contaminants in porous media can be classified according to whether the processes are either advection-dominated or diffusion-dominated. In reality both processes will occur, but in certain situations the advection can dominate. The conditions for the advection-dominated contaminant migration can be deduced by examining the *Peclet Number* for the transport process, which is defined by $Pe = VL/D$, where V is a characteristic velocity, L is a characteristic length and D is a diffusion coefficient. When Pe exceeds unity, the advective phenomena will dominate; similarly, when Pe is less than unity, the diffusive processes are expected to dominate. This paper deals with a problem of some interest to the advective transport of a chemical in a porous medium. The problem specifically deals with the advective migration of a contaminant from a line source that is located in a porous medium of infinite extent. The practical situation can be visualized as an unlined section of a deep borehole into which a chemical is introduced at a time-dependent concentration. The advective flow is maintained by a potential difference between the line source and the far field and the flow velocities are determined by Darcy's law. There are several ways in which this particular problem can be approached. In this study, the mathematical analysis is accomplished by first considering the potential problem for a prolate spheroid, which defines the flow

Copyright © 2003 Swets & Zeitlinger B.V., Lisse, The Netherlands

velocities in the infinite domain. The advective transport problem is then solved by appeal to a Laplace transform technique. The analysis also takes into consideration the influences of natural attenuation within the porous domain. The solution to the problem of the line source is obtained as limiting case where a dimension ratio (diameter/length) of the prolate spheroid approaches a limiting value.

2 GOVERNING EQUATIONS

The partial differential equation governing advective flow of a contaminant in a porous medium can be derived through fundamental considerations (Selvadurai, 2000, 2002a,b). The dependent variable is the chemical concentration $C(\mathbf{x},t)$ which is measured per unit total volume of the porous medium, $\mathbf{x}$ is a position vector and t is the time variable. We assume that advective flow takes place with advective velocity **v(x)**, which is determined from a steady state Darcy flow maintained by gradients of the hydraulic potential $\phi(\mathbf{x})$ and determined from

$$\mathbf{v} = -k\nabla\phi \tag{1}$$

where k is the hydraulic conductivity of the porous medium. We also note that the velocity $\mathbf{v}(\mathbf{x})$ represents a measure averaged over an entire cross section of the porous medium. If the fluid within the porous medium is incompressible

$$\nabla \cdot \mathbf{v} = 0 \tag{2}$$

and the potential satisfies Laplace's equation

$$\nabla^2\phi(\mathbf{x}) = 0 \tag{3}$$

We define the *flux* as the mass of the chemical species either *entering* or *leaving* a unit total surface area in unit time. The flux vector, defined as the mass being transported by advection, per unit total area per unit time, is given by

$$\mathbf{F}_a = \mathbf{v}C(\mathbf{x},t) \tag{4}$$

The total mass of the chemical species being transported into an arbitrary control volume V of surface S is given by

$$m_i = -\iint_S \mathbf{F}_a\mathbf{n}\,dS \tag{5}$$

where $\mathbf{n}$ is the outward unit normal to the elemental surface area dS. Applying the divergence theorem, we can rewrite (5) as

$$m_i = -\iiint_V \nabla\cdot\{\mathbf{v}C\}\,dV \tag{6}$$

The species is assumed to accumulate in the fluid within the void space of the porous medium. It can be shown that the rate of accumulation of the species is given by

$$m_a = \frac{d}{dt}\iiint_V C\,dV = \iiint_V \frac{\partial C}{\partial t}\,dV \tag{7}$$

The rate of production/loss of the chemical species due to either generation (+) or natural decay (−) processes within the porous medium is given by

$$m_p = \pm\iiint_V n^*\xi\tilde{C}\,dV = \pm\iiint_V \xi C\,dV \tag{8}$$

where ξ is a generation/decay factor measured per unit time; n^* is the porosity and $\tilde{C}$ is the local concentration. For conservation of mass of the contaminant species we require $m_a = m_i + m_p$, which when combined with the *Dubois-Reymond Lemma* for the existence of a local equation, gives the partial differential equation governing advective transport of a chemical species as follows:

$$\frac{\partial C}{\partial t} + \nabla\cdot(\mathbf{v}C) = \pm\xi C \tag{9}$$

It may be noted that since the concentration is measured per unit total volume of the porous medium and since the velocity represents a quantity averaged over the entire cross section of a flow surface, the partial differential equation (9) governing the contaminant concentration is independent of the porosity of the porous medium. The equations (3) and (9) represent the partial differential equations governing the advective transport problem, which is a weakly coupled set of partial differential equations, with a second-order elliptic equation governing $\phi(\mathbf{x})$ and a first order hyperbolic equation governing $C(\mathbf{x},t)$. The term weakly coupled is intended to emphasize the fact that the potential can be solved independent of the advective transport problem. The formulation of the boundary value problem requires the specification of Dirichlet and Neumann boundary conditions for $\phi(\mathbf{x})$ for $\forall\mathbf{x}\in S$ and the specification of (i) $C(\mathbf{x},t)$ on $\forall\mathbf{x}\in S_D$ and/or (ii) $\mathbf{n}\nabla C$ on $\forall\mathbf{x}\in S_N$ where S_D and S_N are subsets of S with the requirement $S_D \cup S_N \neq S$. This latter requirement is both necessary and sufficient to ensure uniqueness of solution of the classical advective transport problem (Selvadurai, 2003).

3 THE POTENTIAL PROBLEM

We first consider the problem of a porous medium of infinite extent that is bounded internally by a prolate spheroidal cavity. The prolate spheroidal coordinates are such that the parametric surfaces α = const.,

Copyright © 2003 Swets & Zeitlinger B.V., Lisse, The Netherlands

say α_0, $\beta = \beta_0$, and $\gamma = \gamma_0$, form a triple orthogonal confocal family of prolate spheroids, hyperboloids of two sheets and meridional half-planes respectively. The cylindrical polar coordinates for the axisymmetric state (r, θ, z) are now defined by

$$r = c_p \sinh\alpha \sin\beta; \quad z = c_p \cosh\alpha \cos\beta \tag{10}$$

where (r, θ, z) refers to the cylindrical polar coordinate system. Every point in space is represented by restricting the ranges of the prolate spheroidal coordinates (α, β, γ) as follows:

$$0 \le \alpha < \infty; \quad 0 \le \beta \le \pi; \quad 0 \le \gamma \le 2\pi \tag{11}$$

The metric or local scale coefficients are given by (see e.g. Selvadurai, 2000)

$$\begin{aligned} h_1^p = h_2^p &= \left[c_p^2 (\sinh^2\alpha + \sin^2\beta) \right]^{-1/2} = h_p \\ h_3^p &= (c_p \sinh\alpha \sin\beta)^{-1} \end{aligned} \tag{12}$$

The focal distance c_p can be expressed in terms of the dimensions of the semi-major axis and the equatorial radius of the prolate spheroid conforming to the internal boundary of the porous medium, which is assumed to be defined by $\alpha = \alpha_0$, such that

$$\begin{aligned} &a_p^2 = c_p^2 \cosh^2\alpha_0; \quad b_p^2 = c_p^2 \sinh^2\alpha_0; \\ &c_p = \sqrt{a_p^2 - b_p^2} \end{aligned} \tag{13}$$

We first consider the flow problem where the axis $\beta = 0$ coincides with the z-axis, the axis of symmetry of the prolate spheroidal cavity. For axisymmetric problems, the hydraulic potential is independent of the azimuthal coordinate γ and in terms of the curvilinear coordinates (α, β), Laplace's equation (11) takes the form

$$\begin{aligned} &\nabla^2 \phi(\alpha, \beta) \\ &\quad = h_p^2 \left(\frac{\partial^2}{\partial\alpha^2} + \frac{\partial^2}{\partial\beta^2} + \coth\alpha \frac{\partial}{\partial\alpha} + \cot\beta \frac{\partial}{\partial\beta} \right) \\ &\qquad \times \phi(\alpha, \beta) = 0 \end{aligned} \tag{14}$$

The partial differential equation is to be solved, subject to the boundary and regularity conditions

$$\begin{aligned} &\phi(\alpha, \beta) = \varphi_0 \quad \text{on} \quad \alpha = \alpha_0 \\ &\phi(\alpha, \beta) \to 0 \quad \text{as} \quad \alpha \to \infty \end{aligned} \tag{15}$$

where $\alpha = \alpha_0$ corresponds to the boundary of the cavity. Considering *Lamé* product solution to this boundary value problem, it can be shown that the relevant solution is given by

$$\phi(\alpha) = \frac{\varphi_0}{\ln\xi_0} \ln\xi \tag{16}$$

where

$$\xi = \left(\frac{\cosh\alpha + 1}{\cosh\alpha - 1} \right); \quad \xi_0 = \xi(\alpha_0) \tag{17}$$

The solution to the potential problem is now formally complete, in the sense that the velocity vector $\mathbf{v}(\alpha, \beta, \gamma)$ can be obtained in explicit closed form by using (16) in (1); the non-zero velocity component is

$$\mathbf{v}(\alpha, \beta) = \frac{2k\phi_0}{c_p \ln\xi_0 \sinh\alpha \sqrt{\sinh^2\alpha + \sin^2\beta}} \mathbf{i}_\alpha \tag{18}$$

4 THE ADVECTIVE TRANSPORT PROBLEM

Considering (18) and in view of the divergence free constraint (2) imposed by the incompressibility of the fluid, the partial differential equation (9) for advective transport of the contaminant now reduces to the form

$$\frac{\partial C}{\partial t} + \frac{2k\phi_0}{c_p^2 \sinh\alpha (\sinh^2\alpha + \sin^2\beta) \ln\xi_0} \frac{\partial C}{\partial \alpha} = \pm \xi C \tag{19}$$

The initial and boundary conditions applicable to the problems are as follows: we assume that the porous medium is initially free of the contaminant and that the entire boundary of the prolate spheroidal cavity, $\alpha = \alpha_0$ is subjected to a contaminant charge with an arbitrary time variation. These give

$$C(\alpha, \beta, 0) = 0; \quad C(\alpha, \beta, t) = C_0 F(t) \tag{20}$$

where C_0 is a constant concentration and $F(t)$ is an arbitrary function of time. In the context of the present problem it is convenient and sufficient to consider a method of solution that is based on the application of Laplace transforms. We define the Laplace transform of $\hat{C}(\alpha, \beta, t)$ with respect to the time variable as (Sneddon, 1972) such that

$$\begin{aligned} \bar{c}(\alpha, \beta, t) &= L\{C(\alpha, \beta, t)\} \\ &= \int_0^\infty \exp(-st) C(\alpha, \beta, t)\, dt \end{aligned} \tag{21}$$

and since the initial chemical concentration in the porous medium is zero (see e.g. (29)), we have

$$L\left\{ \frac{\partial C}{\partial t} \right\} = s\bar{c}(\alpha, \beta, s) \tag{22}$$

Applying the Laplace transform to (19) we obtain a first-order ordinary differential equation for the transformed dependent variable $\bar{c}(\alpha, \beta, s)$; further restricting attention to *attenuation processes in the porous medium*, we obtain the solution as follows:

$$\bar{c}(\alpha, \beta, s) = C_0 f(s) \exp[-(s + \xi)\Omega_p(\alpha, \beta, \lambda)] \tag{23}$$

Copyright © 2003 Swets & Zeitlinger B.V., Lisse, The Netherlands

where

$$\Omega_p(\alpha,\beta,\lambda) = \frac{c_p^2 \ln \xi_0}{6k\varphi_0}[\cosh^3\alpha - \cosh^3\alpha_0 + 3\cos^2\beta\,\{\cosh\alpha - \cosh\alpha_0\}] \quad (24)$$

and $f(s)$ denotes the Laplace transform of $F(t)$, which is assumed to exist. We can express the functions in (24) in terms of coordinates (r,z) and the geometric aspect ratio of the prolate spheroid:

$$\cosh\alpha = \left[\frac{\sqrt{\rho_p^2 + (\eta_p + \sqrt{1-\lambda^2})^2}}{2\sqrt{1-\lambda^2}}\right] + \left[\frac{\sqrt{\rho_p^2 + (\eta_p - \sqrt{1-\lambda^2})^2}}{2\sqrt{1-\lambda^2}}\right] \quad (25)$$

$$\cos\beta = \left[\frac{\sqrt{\rho_p^2 + (\eta_p + \sqrt{1-\lambda^2})^2}}{2\sqrt{1-\lambda^2}}\right] - \left[\frac{\sqrt{\rho_p^2 + (\eta_p - \sqrt{1-\lambda^2})^2}}{2\sqrt{1-\lambda^2}}\right] \quad (26)$$

$$\cosh\alpha_0 = \frac{1}{\sqrt{1-\lambda^2}};$$
$$\ln\xi_0 = \ln\left[\frac{1+\sqrt{1-\lambda^2}}{1-\sqrt{1-\lambda^2}}\right] \quad (27)$$

$$\lambda = \frac{b_p}{a_p} < 1; \quad \rho_p = \frac{r}{a_p}; \quad \eta_p = \frac{z}{a_p} \quad (28)$$

The advective transport problem is now reduced to the Laplace transform inversion of the expression for $\bar{c}(\alpha,\beta,s)$; the formal result can be written as follows:

$$\frac{C(\alpha,\beta,t)}{C_0} = L^{-1}\{f(s)\exp[-(s+\xi)\Omega_p(\alpha,\beta,\lambda)\} \quad (29)$$

where L^{-1} refers to the inverse Laplace transform. This general result for the advective transport in a porous medium of infinite extent due to contaminant loading applied at the boundary of the prolate spheroidal cavity can be evaluated by specifying plausible time variations defined by $F(t)$, along with the use of the convolution theorem for Laplace transforms defined by

$$L^{-1}\{f(s)g(s)\} = F \times G = \int_0^t F(u)G(t-u)\,du \quad (30)$$

Alternatively, the inversion can be carried out by appeal to Tables of Integral Transforms (see e.g. Erdelyi et al., 1954) or through the use of symbolic mathematical manipulation software such as MAPLE® or MATHEMATICA® or through the use of numerical inversion techniques. As an illustrative example, consider the case where the boundary of the prolate spheroidal cavity is subjected to a contaminant concentration, which is in the form of a Heaviside step function: i.e.

$$F(t) = \begin{cases} 0; & -\infty > t \geq 0 \\ 1; & 0 \leq t < \infty \end{cases} \quad (31)$$

For this case the result (29) gives

$$\frac{C(\alpha,\beta,t)}{C_0} = \exp\left[-\xi\,\Omega_p(\alpha,\beta,\lambda)\right] \times H\left[t - \Omega_p(\alpha,\beta,\lambda)\right] \quad (32)$$

where $H\lfloor t - \Omega_p(\alpha,\beta,\lambda)\rfloor$ is the Heaviside step function with the time shift $\Omega_p(\alpha,\beta,\lambda)$. In the case when $\xi = 0$, (32) gives the result for the problem of contaminant migration from the prolate spheroidal source in the absence of any *natural attenuation*.

5 THE LINE SOURCE PROBLEM

The problem of the advective transport of a contaminant migration from a line source can be obtained in a variety of ways. The first approach is to consider the Green's function for the potential problem that involves the potential flow from a source of constant strength. This can then be utilized to generate the integro-partial differential equation governing the advective transport from the point source. This equation is not amenable to an exact solution in a convenient form that can be integrated to generate the line source problem. Recourse has to be made to some form of numerical scheme involving either boundary integral equations or finite element schemes. The numerical difficulties associated with the solution of the integro-partial differential equation are further compounded by the fact that the velocity field at the extremities of the line source will exhibit large gradients. For these reasons, the development of a numerical solution to the advective transport from a line source cannot be regarded as a routine exercise.

The solution developed for the problem of the advective transport from a prolate spheroidal cavity

Copyright © 2003 Swets & Zeitlinger B.V., Lisse, The Netherlands

can be utilized to develop an approximate solution to the line source problem. This is done by letting the relative cavity dimensions parameter λ approach a small value. In theory this can be set to zero, but a more convenient and realistic approach is to allow this parameter to be a small quantity and to represent the parameter Ω_p in a power series in terms of λ. It can be shown that the relevant power series approximation, valid to $O[\lambda^4]$, is given by

$$\begin{aligned}
&\frac{\Omega_p(\rho_p,\eta_p,\lambda)}{a_p^2/6k\varphi_0} \\
&= \frac{1}{8}\Delta(-8+(\zeta_1+\zeta_1)^3+3(-2+\zeta_2+\zeta_3) \\
&\quad\times(\zeta_2+\zeta_3)^2)+\left(\frac{1}{8}\left(-\frac{1}{2}-\Delta\right)(-8+(\zeta_1+\zeta_2)^3\right. \\
&\quad\left.+3(-2+\zeta_2+\zeta_3)(\zeta_2+\zeta_3)^2\right) \\
&\quad+\frac{3}{16}\Delta(-8+(\zeta_1+\zeta_2)^3+(\zeta_1+\zeta_2)^2 \\
&\quad\times\left(-\frac{\eta_p^4}{\zeta_1}-\frac{1+\eta_p^2}{\zeta_2}\right)+4\left(\frac{1}{4}(\zeta_2+\zeta_3)^2\right. \\
&\quad\times\left(-2+\zeta_2+\zeta_3+\frac{-1+\eta_p^2}{\zeta_3}-\frac{1+\eta_p^2}{\zeta_2}\right) \\
&\quad\times\left((-2+\zeta_2+\zeta_3)(\eta_p^8+\rho_p^2(1+\zeta_2\zeta_3+\rho_p^2)\right. \\
&\quad\left.\left.\left.+\eta_p^4(-1+\zeta_2\zeta_3+2\rho_p^2)\times\frac{1}{\zeta_2\zeta_3}\right)\right)\right)\lambda^2+O[\lambda^4]
\end{aligned} \tag{33}$$

where

$$\zeta_1=\sqrt{\eta_p^4+\rho_p^2};\quad \zeta_2=\sqrt{(\eta_p^2+1)^2+\rho_p^2}$$

$$\zeta_3=\sqrt{(\eta_p^2-1)^2+\rho_p^2};\quad \Delta=\ln 4-2\ln\lambda \tag{34}$$

The result (34) can be used in (32) to develop the appropriate analytical result. For the purposes of the paper it is sufficient to consider computational results for the case where the advective transport takes place from a prolate spheroidal region where λ is considered to be a small parameter.

Since the analytical results are presented in explicit forms these expressions can be evaluated quite conveniently. The purpose here is to present some typical numerical results that demonstrate the pattern of time-dependent contaminant migration from the line source. The advective time parameter $a_p^2/6k\varphi_0$ encountered in the expression for Ω_p is set equal to 10 days. This value can be identified, for example, with the case of a line source of length $2a_p \approx 6$ metres, embedded in a porous medium of hydraulic conductivity $k \approx 0.05$ metres/day and subjected to a flow potential $\varphi_0 \approx 6$ metres. (Note that the value of φ_0 represents the potential difference between the cavity surface and the far field, which initiates the advective flow.) The attenuation coefficient is assigned the value $\xi = 0.005$/day. The results for the time-dependent advective transport of the contaminant from a line source of aspect ratio $\lambda = b_p/a_p = 1/100$, are presented in Figures 1–3.

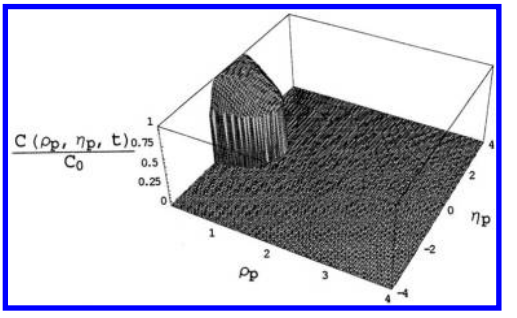


Figure 1. Contaminant distribution around the line source [Time: *100 hours*].

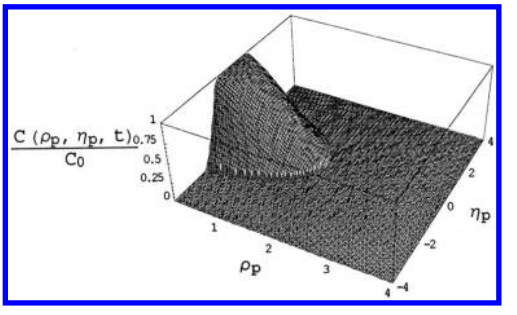


Figure 2. Contaminant distribution around the line source [Time: *500 hours*].

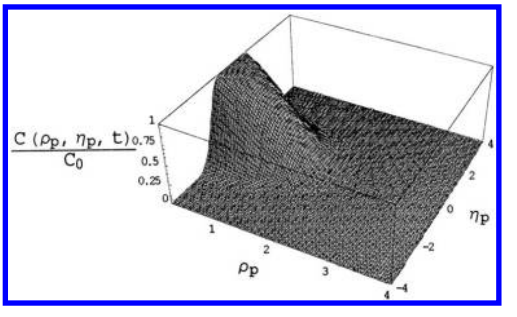


Figure 3. Contaminant distribution around the line source [Time: *10,000 hours*].

Copyright © 2003 Swets & Zeitlinger B.V., Lisse, The Netherlands

6 CONCLUSIONS

The advective transport equation represents an elementary representation of the complex process of contaminant migration in a porous medium where the diffusive processes are of secondary importance. The weakly coupled nature of the governing equations lends itself to the development of a wider class of analytical and numerical solutions. The analytical solutions in particular can be developed for geometries that can represent a range of practical situations of interest to contaminant migration in porous media. This particular paper presents a compact analytical solution for the case of a line source from which a contaminant is continually being released at a fixed concentration to the source from which a contaminant is continually being released at a fixed concentration to the surrounding porous medium.

The analytical procedure takes into consideration the geometrical aspect ratio of the geometrical aspect ratio of the line source. Here, the pressure potential is applied at a given surface and the chemical is released at the same surface. This specified geometrical interpretation of a line source is a departure from the solution schemes that consider the line source as a continuous distribution of point sources, both for the hydraulic potential and the released contaminant. In such an approach there is no provision for interpreting the strengths of these sources, particularly in relation to the dimension over which they are prescribed. The present solution alleviates some of these difficulties and introduces the geometric aspect ratio of the line source as a further variable. This work has been extended to cover the case of the oblate spheroid and the limiting case of the penny-shaped crack from which the contaminant is released (Selvadurai, 2002a, 2003). From these solutions it would appear that at distances remote from the contaminant source, the exact nature of the source configuration is less important. This is analogous to "*Saint-Venant's Principle*" in elasticity, which indicates that for equipollent force systems, the far-field stress state is independent of the exact nature of the distribution of the forces. Extension of this argument to the contaminant migration problem is self-evident.

REFERENCES

Banks, R.B. 1994. *Growth and Diffusion Phenomena: Mathematical Frameworks and Applications*, Berlin, Springer-Verlag.

Bear, J. and Bachmat, Y. 1991. *Introduction to the Modelling of Transport Phenomena in Porous Media*, The Netherlands, D. Reidel Publ. Co.

Bear, J. and Verruijt, A. 1990. *Modelling of Groundwater Flow and Pollution*, The Netherlands, D. Reidel Publ. Co.

Charbeneau, R.M. 2000. *Groundwater Hydraulics and Pollutant Transport*, NJ, Prentice-Hall.

Domenico, P.A. and Schwartz, F.W. 1998. *Physical and Chemical Hydrogeology*, New York, John Wiley.

Erdelyi, A. et al. 1954. *Tables of Integral Transforms* Vols. 1 and 2, New York, McGraw-Hill.

Philips, O.M. 1991. *Flow and Reactions in Permeable Rocks*, Cambridge, Cambridge University Press.

Selvadurai, A.P.S. 2000. *Partial Differential Equations in Mechanics: Vols. 1 and 2*, Berlin, Springer-Verlag.

Selvadurai, A.P.S. 2002a. Certain analytical solutions for advective transport in a porous medium, in*: Environmental Geomechanics* (L. Vulliet, L. Laloui and B.A. Schrefler, Eds.) Lausanne, EPFL Press, 69–82.

Selvadurai, A.P.S. 2002b. Advective transport of a chemical from a cavity in a porous medium, *Computers and Geotechnics*, **29**: 525–546.

Selvadurai, A.P.S. 2003. Advective transport from a penny-shaped crack and an associated uniqueness theorem (submitted).

Sneddon, I.N. 1972. *Applications of Integral Transforms*, New York, McGraw-Hill.

Sun, N.-Z. 1996. *Mathematical Modelling of Groundwater Pollution*, Berlin, Springer-Verlag.

Copyright © 2003 Swets & Zeitlinger B.V., Lisse, The Netherlands

Influence of the kinematic viscosity of oil contaminants in the compaction and hydraulic conductivity in certain type of soils

J.C. Rojas, L.M. Salinas & I.D. Garnica
Laboratorio de Geotecnia, Universidad Mayor de San Simón, Cochabamba, Bolivia

ABSTRACT: This paper presents the influence of the kinematic viscosity of different oil components in the compaction and hydraulic conductivity of clay, silt and sand. As a consequence of oil spills, besides the environmental damage, the geotechnical properties of the soil present variations. Bolivian crude oil, engine oil and gear oil, with kinematic viscosities of 1.61 E-6, 84.95E-6 and 4810.11E-6 m^2/s at 20°C, respectively, were selected as soil contaminants. The soil specimens used in the research program correspond to a lean clay (CL), silt (ML) and silty sand (SM). The modified compaction tests were carried on following ASTM D1557-91, the hydraulic conductivity was assessed from variable head permeability tests in remoulded specimens compacted at its γ_{dmax} value. The tests were performed in all the samples with different concentrations of each contaminant. It was maintained a constant temperature of 20°C during the execution of the set of probes. It is presented the properties of the contaminants and soils used in the investigation, a summary of the procedure, compaction and hydraulic conductivity in function of kinematic viscosity and the conclusions of the program. The results of the performed tests exhibits that the soil compaction characteristics change among the presence of different soil contaminants and are also function of the applied compaction energy. The increase of the quantity of soil contaminant or their kinematic viscosity follows a decrease in the soil hydraulic conductivity.

1 INTRODUCTION

Oil products are one of the main contaminants all over the world. When a spill occurs the physical and mechanical soil properties change, like the hydraulic conductivity. If the spill is in a large area the recharge system of the aquifers can be seriously affected.

For a good evaluation of consequences and how the contaminant can modified the hydrological cycle of this regions, it is necessary to know how the hydraulic conductivity changes in contaminated soils.

A parameter commonly used to perform the comparison between oil product is the kinematic viscosity (Puri et al. 1994; Shin & Das 2000; Shin et al. 2002).

2 LITERATURE REVIEW

Several papers related with the change of the physical properties of contaminated sands have been published in the last years. Puri et al. (1994) conduced Proctor standard tests in Mississippi sand and they found out that the maximum dry unit weight for a given compactive effort occurred approximately at the same degree of saturation, independent of whether oil or water was used as the pore fluid. The same authors found that the hydraulic conductivity depends on the viscosity of the oil contaminant when other factors remain constant.

Shin & Das (2000) presented an article related to the physical properties of unsaturated contaminated sand. Proctor standard compaction and hydraulic conductivity parameters were determined in a Jumoonjin contaminated sand. From the tests, they concluded that the maximum dry unit weight of a compacted sand increases with the increase in kinematic viscosity of oil, for a similar compaction effort. This is accompanied by a decrease in the degree of saturation. Furthermore, an increasing of oil content and kinematic viscosity leads to a decrease in the hydraulic conductivity of a soil.

3 TESTED SOILS AND OILS

The samples used in the research program were obtained in Cochabamba, Bolivia. Table 1 presents their properties.

Three different hydrocarbons; Bolivian crude, engine and gear oils, were used as soil contaminants, Figure 1 shows the variation of kinematic viscosity with temperature.

Copyright © 2003 Swets & Zeitlinger B.V., Lisse, The Netherlands

Table 1. Physical properties of the soils.

Properties	Silty sand	Silt	Clay
Unified soil classification	SM	ML	CL
Effective size, D_{10}	0.06 mm	UD	UD
Liquid limit, *LL*	NP	NP	36
Plastic index, *PI*	NP	NP	15
Specific gravity, G_S	2.73	2.71	2.74

UD = undeterminated, NP = non plastic.

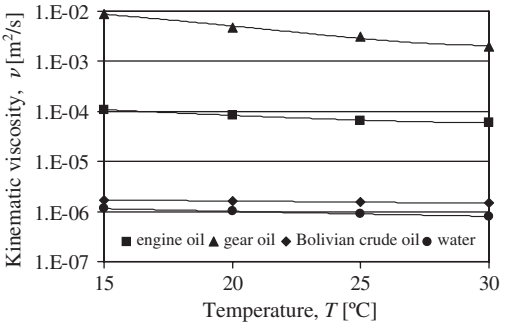


Figure 1. Variation of kinematic viscosity with temperature for the three oils and water used in the program.

The Bolivian crude oil was classified as a very light crude oil following the American Petroleum Institute recommendations.

4 COMPACTION TESTS

Modified Proctor tests, following ASTM D1557, were performed in the uncontaminated and contaminated soils, in order to determine the compaction parameters (i.e. maximum dry unit weight, γ_{dmax}, and optimum water/oil content, w_{opt}). All the study was carried out at a constant ambient temperature of 20°C.

The following procedure was used for the three soils. First, a common modified Proctor compaction test was carried out. Different degrees of contaminant content were reached mixing each one of the soils with different quantities of hydrocarbons. Table 2 presents the test results.

Figure 2 shows the compaction curves obtained for the silty sand used in the study. A slight reduction of the dry unit weight for the contaminated soils can be appreciated. The curve shape corresponds to a typical sand curve (i.e. one and one half peaks), and it does not change with the contaminants addition.

The compaction curves obtained for the silt specimen show a high decrease of the dry unit weight for the

Table 2. Modified Proctor compaction test results.

		Contaminant		
Soil	Water	Crude oil	Engine oil	Gear oil
Silty sand	20.16	19.50	20.10	20.04
	9.3	8.2	6.8	7.9
Silt	18.67	16.20	17.00	16.67
	12.4	4.6	8.2	10.1
Clay	18.61	16.29	17.28	16.62
	12.9	6.9	13.6	8.8

Upper row is maximum dry unit weight, γ_{dmax} [kN/m^3]. Lower row is optimum water/oil content, w_o/w_w [%].

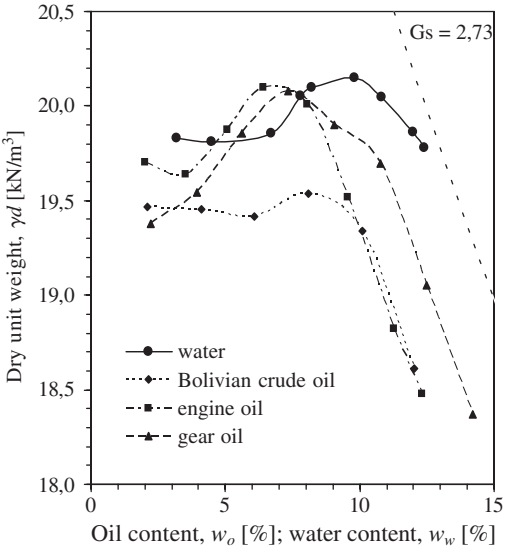


Figure 2. Variation of dry unit weight with oil/water content for a silty sand (SM).

contaminated soils. The shape of the uncontaminated soil compaction curve reproduce a single peak, but, for the contaminated condition the compaction curves have flattener shapes (Fig. 3).

Typical clayey-soils-compaction curves (i.e. bell shaped) were obtained from the compaction of the uncontaminated clay. For the contaminated clay, the bell shape curve is not clearly observed (Fig. 4). In the same way, for all the previous mentioned soils, the maximum dry unit weight decreases with the increase of oil content (Fig. 4).

Figure 5 indicates the variation of the maximum dry unit weight with the kinematic viscosity. No clear relation can be observed.

Copyright © 2003 Swets & Zeitlinger B.V., Lisse, The Netherlands

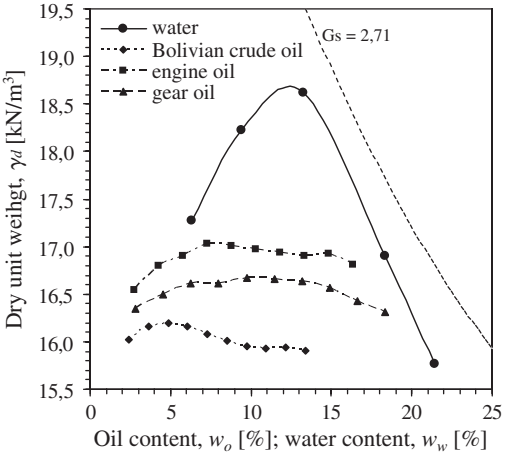


Figure 3. Variation of dry unit weight with oil/water content of silt (ML).

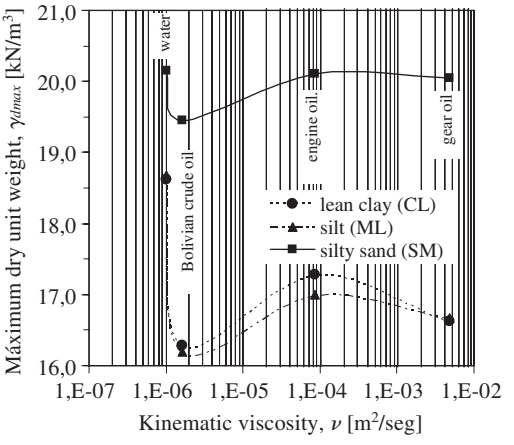


Figure 5. Variation of maximum dry unit weight with kinematic viscosity.

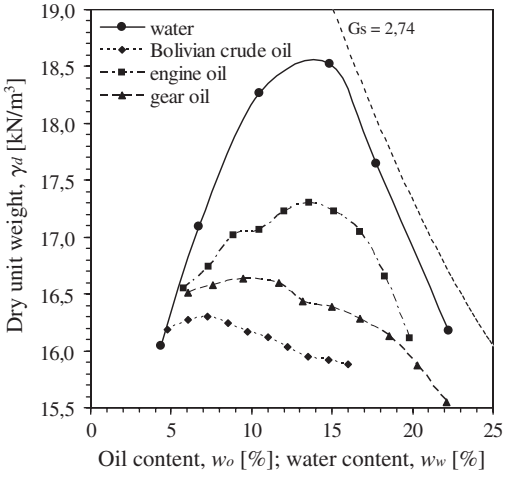


Figure 4. Variation of dry unit weight with oil/water content of lean clay (CL).

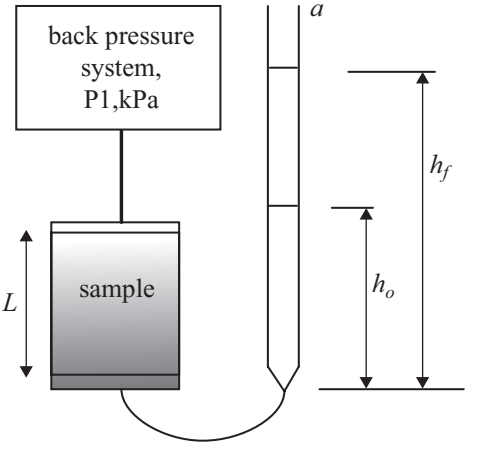


Figure 6. Diagram of the falling head permeability tests equipment.

5 HYDRAULIC CONDUCTIVITY TESTS

Hydraulic conductivity tests were carried out in all type of soil specimens selected for the study. They were compacted at the maximum dry unit weight value obtained from the Modified Proctor test for each uncontaminated soil.

Each specimen was mixed with 2, 4, 6% of each contaminant before being recompacted.

Falling head permeability tests were performed in one back pressure system with de-aired water; a diagram of the used equipment is presented in Figure 6, and the corresponding equation is Equation 1. The variation of measured values for all the contaminants, contaminant rates, and soils are presented in Table 3 and Figures 7, 8 and 9:

$$k = 3.84\left[\frac{aL}{At}\log_{10}\left(\frac{102P1 - h_o}{102P1 - h_f}\right)\right] \times 10^{-5} \qquad (1)$$

where k = hydraulic conductivity, [m/s]; a = cross section area of the burette, [mm^2]; L = length of the soil specimen, [mm]; A = soil area, [mm^2]; t = time, [min]; $P1$ = incoming pressure, [kPa]; h_o = initial height at the burette, [mm]; and h_f = final height at the burette, [mm].

Copyright © 2003 Swets & Zeitlinger B.V., Lisse, The Netherlands

Table 3. Permeability test results expressed in [m/s].

Soil	Water	Contaminant		
		Crude oil	Engine oil	Gear oil
Silty sand	1.88E−7	1.28E−7	9.76E−8	3.05E−8
		1.16E−7	2.99E−8	1.04E−8
		1.12E−7	2.31E−8	3.69E−9
Silt	1.95E−9	2.25E−9	1.12E−9	3.73E−10
		1.80E−9	6.33E−10	1.05E−10
		1.48E−9	5.41E−10	5.99E−11
Clay	3.30E−9	2.14E−9	1.69E−9	7.21E−10
		2.07E−9	6.33E−10	1.80E−10
		1.77E−9	4.03E−10	8.88E−11

For the oils: Upper row is for a 2% contaminant content, middle row is for a 4% contaminant content, lower row is for a 6% contaminant content.

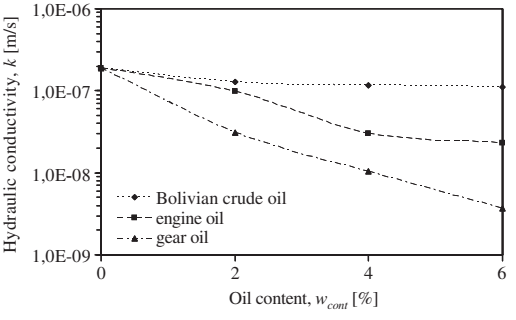


Figure 7. Variation of the silty sand conductivity hydraulic with the oil content.

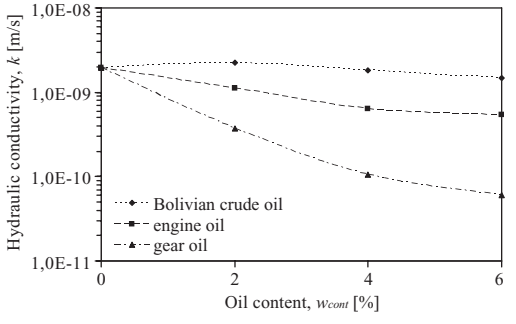


Figure 8. Variation of the silt conductivity hydraulic with the oil content.

Hydraulic conductivity values decrease when the oil content increase. When kinematic viscosity increases the values of the hydraulic conductivity decreases. This is valid for all the samples except the silt with 2% of Bolivian oil crude content (Fig. 7).

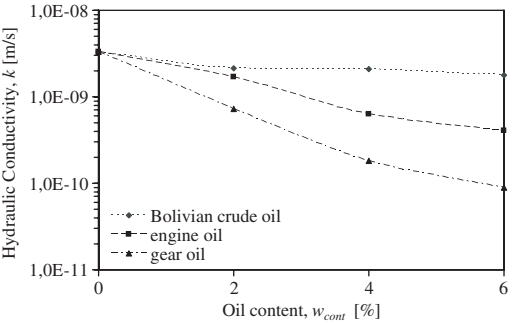


Figure 9. Variation of the hydraulic conductivity of clay with the oil content.

6 DISCUSSION

The value of maximum dry unit weight did not occur at the same degree of saturation, independent of whether oil or water was used as the pore fluid, as it was claimed by Puri et al. (1994) for Mississippi sand compacted with the standard Proctor test (Figs. 2, 3 and 4). Initially, it was stated that it did not depend on the compaction effort, because Shin & Das (2000), working on a sand with the standard effort, did not found this pattern, either. However, some tests using standard effort were performed in silty sand (SM) in order to prove this difference (Fig. 9). Finally, for the standard effort, it was concluded that the value of maximum dry unit weight occurred at the same degree of saturation (i.e. S = 63.5%, approximately), independent of whether oil or water was used as the pore fluid as it was claimed by Puri et al. (1994) (Fig. 10).

Shin & Das (2000) and Shin et al. (2002) found an increase in maximum dry unit weight with the increase in kinematic viscosity of oil for a sand. The results of this study show that there is no relationship between these parameters. In addition, due to the possibility that this no-relation is due to the energy of compaction utilized in the tests, the same program of analysis was conducted for the sand, with the same compaction effort that Shin & Das (2000) used (i.e. standard Proctor tests following ASTM 698). In the same way the results carried out with the standard Proctor tests show that there is no relationship between these parameters (Fig. 11).

Puri et al. (1994), Shin & Das (2000) and Shin et al. (2002) found out that the hydraulic conductivity of a soil decreases with an increase of oil content and kinematic viscosity. The last theory has been confirmed for the sand and extended to clays and silts as a result of this work.

Due to the inconsistency of the hydraulic conductivity value for silt with a 2% of Bolivian oil crude

Copyright © 2003 Swets & Zeitlinger B.V., Lisse, The Netherlands

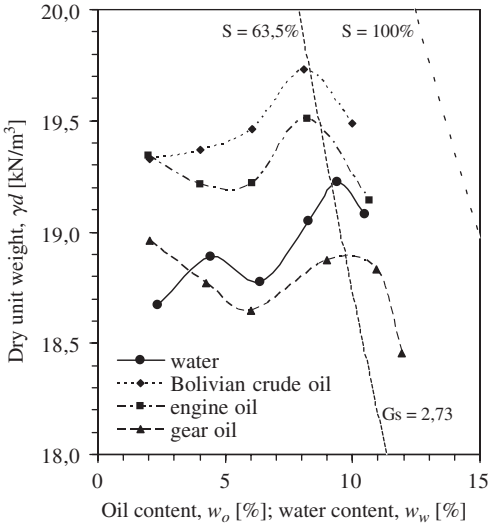


Figure 10. Variation of dry unit weight with oil/water content of silty sand (SM) for standard effort.

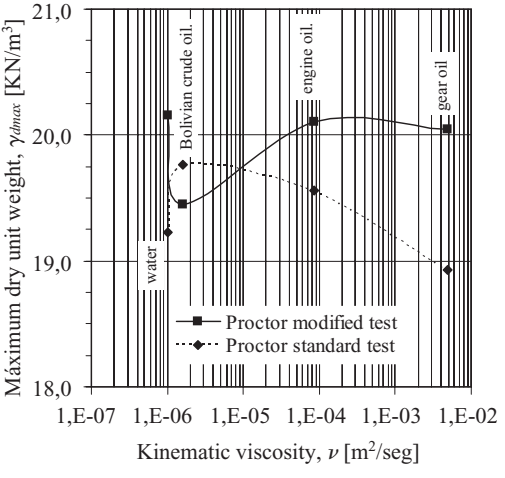


Figure 11. Comparison between the maximum dry unit weight vs. kinematic viscosity values obtained from Proctor standard and Proctor modified test for sand.

content, this sample was retested and the new value (i.e. $k = 2.21\text{E-}9$) was almost the same.

Figure 12 shows the variation between the hydraulic conductivity ratio (i.e. ratio of contaminated hydraulic conductivity, k_c, and uncontaminated hydraulic conductivity, $k_{c=0}$). From this figure, it can be observed that the hydraulic conductivity ratio is about the same for all soils when the kinetic viscosity of the oil used is higher than 4810.11 E-6 m^2/s.

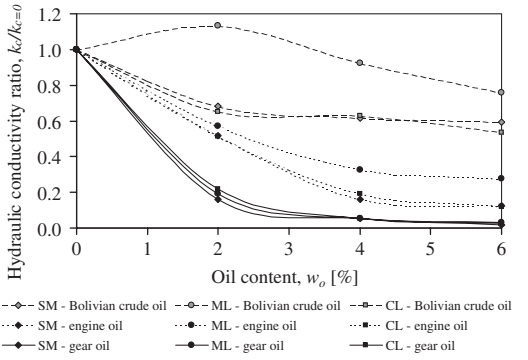


Figure 12. Comparison between the hydraulic conductivity ratio, $k_c/k_{c=0}$, with the oil contents tested.

7 CONCLUSIONS

This paper presents the variation of hydraulic conductivity and compaction properties of three different soils (i.e. clay, silt and sand) of Cochabamba, Bolivia, with different oil contaminants and also investigating the influence of their kinematic viscosity in the studied parameters.

Figures 2, 3 and 4 present the variation of maximum dry unit weight as a function of water/oil content. It can be observed that the peaks (i.e. maximum dry unit weight) using the modified effort are given at different degrees of saturation of the sample, in contradiction with Puri et al. (1994) conclusions. However, from Figure 10 it can be stated that the value of the maximum dry unit weight occurred at the same degree of saturation (i.e. S = 63.5%, approximately), independent of whether oil or water was used as the pore fluid.

Figures 5 and 11 present the maximum dry unit weight as a function of the kinematic viscosity for a modified and standard Proctor tests, respectively. No clear relationship between these parameters was observed as Shin & Das (2000) and Shin et al. (2002) proposed.

Hydraulic conductivity decreases in magnitude when the oil content increases (Fig. 7). For high viscosity values this decrement is similar for all types of soil.

ACKNOWLEDGEMENTS

The authors gratefully acknowledge the financial support from the IUC – UMSS project.

REFERENCES

Puri, V.K., Das, B.M., Cook, E.E. & Shin, E.C. 1994. Geotechnical properties of crude oil contaminated sand.

Copyright © 2003 Swets & Zeitlinger B.V., Lisse, The Netherlands

In Tracey O'shay & Keith Hoddinott (eds.), *Analysis of soils contaminated with petroleum constituents; STP 1221*. U.S.A.: ASTM.

Shin, E.C. & Das, B.M. 2000. Some physical properties of unsaturated oil-contaminated sand. In Cássia de Brito Galvao & Hilary Inyang (eds.), *Environmental geotechnology and global sustainable development*; *Proc. fifth intern. symp., Belo Horizonte, 17–23 August 2000*.

Shin, E.C., Omar, M.T., Tahmaz, A.A., Das, B.M. & Atalar, C. 2002. Shear strength and hydraulic conductivity of oil – contaminated sand. . In Luiz Guilherme de Mello & Márcio Almeida (eds.), *Environmental geotechnics: Vol. 1; Proc. fourth intern. cong., Rio de Janeiro, 11–15 August 2002*. Lisse: Balkema.

Copyright © 2003 Swets & Zeitlinger B.V., Lisse, The Netherlands

Large-scale model test of ethanol-bentonite slurry cutoff wall

M. Asada, A. Ishikawa & S. Horiuchi
Shimizu Corporation, Tokyo, Japan

ABSTRACT: In the use of cutoff walls, continuity, long-term stability and flexibility are crucial to minimize the permeability. Soil-bentonite mixtures meet such requirements, if more than 70 kg of bentonite per 1 m^3 soil could be homogeneously mixed with soil in-situ. Bentonite should be added to soil in a slurry state for homogeneous mixing; however, 20 kg/m^3 of bentonite would be the largest amount by bentonite-water slurry. To achieve increasing the bentonite content, the utilization of hydrophilic organic solvent was studied. In this paper, large-scale model was tested in order to investigate the cutoff property of ethanol-bentonite slurry wall and the geo-environmental effect of ethanol. The wall had enough cutoff ability ($k = 4.0 \times 10^{-10}$ m/s), and pumping the groundwater properly could minimize the ethanol effect on the ground.

1 INTRODUCTION

Several types of cutoff walls have been developed and used for the following applications in Japan; (1) containment for waste disposal facilities, (2) measure for liquefaction by lowering the area's groundwater level surrounded by the cutoff wall, (3) earth retaining for excavation. Non-permeable walls are made of clay, bentonite, soil-cement, mortar, asphalt, concrete, reinforced concrete, grouting chemicals, and sheet piles. In the use of cutoff walls mainly to contain waste disposal facilities, continuity, long-term stability and flexibility to the earth deformation are crucial in order to minimize the permeability and the environmental risk.

Soil-bentonite (SB) walls are commonly constructed as seepage barriers mainly in the United States (D'Appolonia 1980). A narrow trench, typically, 0.6 to 1.5 m wide, is excavated using bentonite/water slurry. The trench is subsequently backfilled with soil-bentonite mixtures that forms a barrier of very low permeability (Panjan et al. 1995). This method, however, is rarely used in Japan, because the walls have low strength and they may cause the settlement of the surrounding areas. Sheet piles with sealant for their connections are used for seepage barriers, but they could hardly keep the adequate permeability.

The mixed in place (MIP) walls are used for earth retaining in Japan. Cement/bentonite (CB) slurry is used as the material to harden the MIP walls. This method uses three or five-axis hollow stem augers that churn and mix the soil in-situ with the CB slurry introduced through the base of the augers. The hydraulic conductivity of the CB-MIP walls is higher than that of the SB walls (Oweis & Khera 1998), however, the CB-MIP walls have no flexibility to earth deformation, and have no self remediation.

If the MIP walls could be constructed by bentonite slurry, instead of CB slurry, and an enough amount of bentonite could be homogeneously mixed, they could have high flexibility and their hydraulic conductivity could be lower than 10^{-9} m/s. The minimum amount of bentonite required for the non-permeable wall, $k < 1 \times 10^{-8}$ m/s, would be more than 70 kg per 1 m^3 soil (Chapuis 1990, Kenney et al. 1992). Constructing walls by MIP method, the bentonite should be added to the soil in a slurry state for homogeneous mixing; however, 20 kg/m^3 of bentonite in the wall would be the largest amount by a conventional slurry additional volume.

To increase the bentonite content in the MIP soil, the use of ethanol was studied. When a pore fluid has a low dielectric constant, such as ethanol, it will have the tendency to curtail bentonite swelling. Therefore, the slurry's viscosity decreases, if ethanol is used for the bentonite slurry. The viscosity of the ethanol bentonite slurry changes gradually, as the ethanol in placed slurry is replaced by water in the ground. The strength of the soil-slurry mixtures could increase to almost the same strength as the surrounding soil by the swelling pressure of the bentonite in the mixtures. Some experimental works were reported on mechanical properties of soil/solvents mixtures (Sridharan & Venkatappa 1973, 1979), in which the soil strength and consolidation properties significantly influenced by the dielectric properties of the pore medium; i.e. hexane, heptane, carbon tetrachloride, benzene, ethyl acetate, acetone, methanol, and ethanol.

Copyright © 2003 Swets & Zeitlinger B.V., Lisse, The Netherlands

In the previous studies, the advantages of ethanol usage for bentonite slurry preparation were reported; (1) bentonite content in the slurry can be increased up to 625 kg/m^3 using 60% ethanol, (2) ethanol in the slurry or slurry mixed soil can be easily replaced by permeating water, (3) water-replaced mass shows hydraulic conductivity of less than 10^{-9} m/s and shear strength of 0.01 MPa (Asada et al., 2001a, 2001b). This information gives us an idea of its applications for impermeable wall by in-situ mixing method. It is very attractive to use ethanol in civil engineering works, because a large amount of ethanol is produced via agricultural process and is thought to be a material friendly to environment. However, to gain the proper cutoff ability, the pore ethanol must be replaced by water, and bentonite must be swelled. In order to replace the pore ethanol with water, certain water level difference must be supplied to the ethanol/bentonite slurry cutoff wall. Its applicability needs to be confirmed in large-scale tests prior to actual construction including, (1) cutoff ability improvement of the ethanol/bentonite slurry wall due to the replacement of pore ethanol to water, (2) influence on the underground environment of ethanol diffused from the slurry walls, (3) settlement and displacement of the surface, (4) soil mechanics characteristics of the slurry wall.

In this paper, a large-scale model test results are reported. The objective is to ascertain the cutoff property of the ethanol bentonite slurry wall, such as its enough cutoff ability ($k = 4.0 \times 10^{-10}$ m/s), and its safety to the ground with pumping the groundwater properly.

2 EXPERIMENTS

2.1 *Materials*

Na-Bentonite: Kunigel V1 (Kunimine Industries Co., Ltd., Japan) was selected and used. Its characteristics are given in Table 1. Ethanol: Reagent grade of 92.5 wt% ethanol, $\rho = 0.82$(g/cm^3), was used.

The model ground was prepared using a well washed sandy soil. Groundwater collected from Tokyo metropolitan area construction site was used throughout of this study.

2.2 *Procedures*

Figure 1 schematically shows the model SB cutoff wall. The size of the model tank is 2 by 6 by 2 m, and the 60 cm wide cutoff wall was set at the center.

The test procedure is as follows: (1) two separate iron plates were set 60 cm apart at the place for the cutoff wall (Photo 1), (2) gravels were spread all over the outside plates up to 5 cm height. Washed sand was spread on the gravel up to 185 cm height including the gravel layer, (3) sandy soil was spread over the gravel layer, compacted and kept at a given dry density.

The dry density of the model sand ground was 1.56 Mg/m^3, the soil particle density was 2.75 Mg/m^3, water content was 25%, void ratio was 0.76, the degree of saturation was 90%, and the coefficient of permeability was 4.2×10^{-5} m/s.

Table 1. Properties of bentonite

Property	
Water content (%)	7.3
Swelling potential (mL/g)	20
pH	10.3
Conductivity (μS/cm)	424
Surface area (m^2/g)	16.9
50% particle size (μm)	6.6
Particle density (g/cm^3)	2.79
Liquid Limit (%)	370
Metyrene-blue Adsorbing Capacity (mmol/100 g)	74
Cation exchange capacity (meq/100 g)	72.1

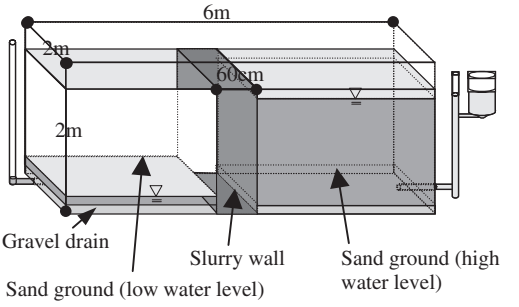


Figure 1. Model SB cutoff wall tank.



Photo 1. Separation iron plates.

Copyright © 2003 Swets & Zeitlinger B.V., Lisse, The Netherlands



Photo 2. Mixing bentonite and soil in voltex mixer.

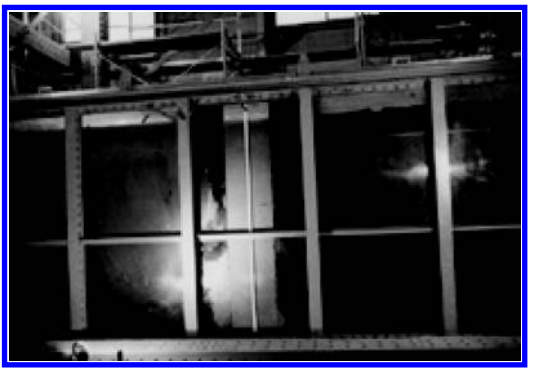


Photo 3. Model SB cutoff wall.



Photo 4. Pore water sampling.

In the sand layer, a sampling tube of ϕ 1 mm were placed to collect the void water or void air in order to measure the concentrations of ethanol and the other materials formed through biological decomposition. Diffusion coefficient was calculated to figure out the ethanol diffusion towards the surrounding ground from the slurry wall. The samples were collected at 20, 70, 120, 170 cm height apart from the bottom, and at 5, 10, 20, 50, 100, 180 (200) cm apart from the slurry wall.

The cutoff wall was installed by the following procedure:

1. The ethanol/bentonite slurry was prepared by mixing bentonite with 123% ethanol solution by weight, 100 kg of bentonite was mixed with 80 kg pure ethanol and 43 kg water. Pore ethanol concentration is 60 wt%.
2. Sandy soil of water content 20% was mixed with the ethanol/bentonite slurry, in which the weight ratio of the bentonite to the dried sand was adjusted to be 10%. The voltex mixer was used for the mixing (Photo 2).
3. The mixed soil was put into the void space supported by the two iron plates up to the same height as the surrounding sand ground 185 cm.
4. The iron plates were then pulled up by the crane.

The mixture placed was 2.4 m^3 in volume and 4 Mg in weight. The wet density of the slurry wall was 1.80 Mg/m^3, and the water content was 29.3% and the ethanol concentration of the pore water was 20 wt%.

Photo 3 shows the model SB cutoff wall. The central part is the cutoff wall. Black rubber gaskets were attached on both sides of the wall, and the sand ground on both outer sides.

Just after the placement of the slurry wall, the groundwater collected from the construction site was immersed into both sides of the sandy soil portions from the gravel layers, and the water level was raised up to the 180 cm. For the prevention of evaporation, a polymer sheet was placed on the surface of the cutoff wall, and a transparent acryl board was put over the model ground. The water level was kept at the same height for 12 days, and pore water samples were collected to determine the ethanol diffusion in the sandy soil. Then the groundwater of one portion of the sand ground was drained to 20 cm, and 160 cm water level difference was exerted on the slurry wall, in order to accelerate the replacement of pore ethanol with water. The pore media samples were collected every week for three months (Photo 4) to measure the ethanol concentration. The ethanol concentration of the pore water was determined by high performance liquid chromatography (HPLC), and that of the pore air was analyzed using a portable gas detector tube (Gastec Inc). Using the diffusion data, a series of parametric and analytical studies were carried out.

After three months, the model ground was investigated with the core sampling. The ethanol concentration of the pore liquid was measured. One dimensional compression tests, tri-axial compression tests, and permeability tests were conducted. The strength distribution of the cutoff wall was measured using a hand vane.

Copyright © 2003 Swets & Zeitlinger B.V., Lisse, The Netherlands

3 RESULTS

3.1 *Distribution of ethanol concentration*

Figures 2–4 show the distribution of ethanol concentration. Within 12 days after the placement, the water level on both sides were kept high, and ethanol diffusing from the model cutoff wall went up along the surface on the both sides of the wall by density difference. For example, 5% ethanol solution's density is 0.99 g/cm^3 at 15°C. On the 12th day, the groundwater on the left side of the sand ground was drained in order to increase the water pressure on the wall and to accelerate the exchange of the pore ethanol with water. As a result, ethanol diffused out from the wall mainly to the right-hand side of the sand ground, and increased near the surface. On the drainage side (left side), the ethanol concentration in the bottom water increased, and that of the pore air near the wall also increased gradually.

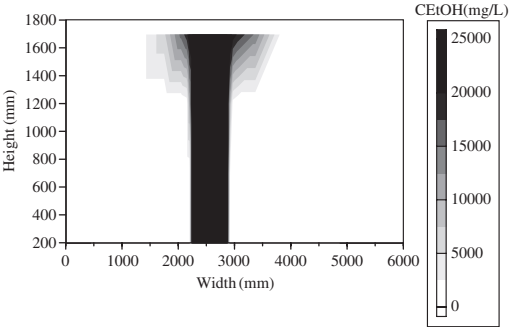


Figure 2. Ethanol diffusion after 12 days.

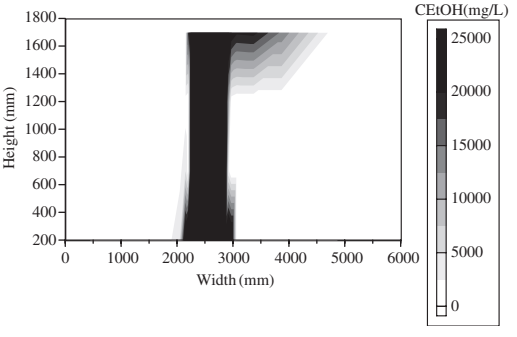


Figure 3. Ethanol diffusion after 47 days.

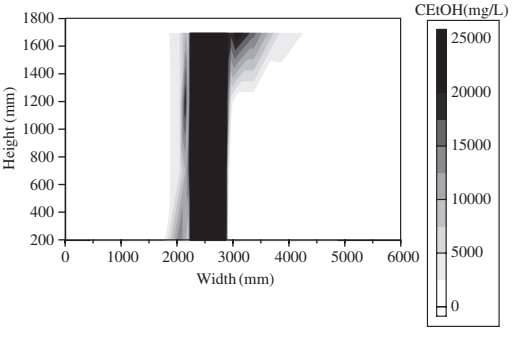


Figure 4. Ethanol diffusion after 97 days.
Note: in figures 2–4, CEtOH expresses pore ethanol concentration. Initial ethanol concentration in the cutoff wall was 20 wt% (200,000 mg/L).

Comparing Figures 2–4, the ethanol diffusing area enlarged until the 47 days, then began to shrink afterwards, because the ethanol was degraded by the high activity of the microbe contained in the groundwater from the construction site. On the 47th day, ethanol diffused further (1.5 m) apart from the cutoff wall. After 3 months, the ethanol concentration on the right-hand side surface water near the wall decreased to 2% from that of the maximum (2.5%).

From the parametric study, the value of the molecular diffusion coefficient, a_m, is estimated to be 3.7×10^{-10}(m^2/s), which is one-third of that of the water-ethanol two component system ($1.1–1.2 \times 10^{-9}$(m^2/s)). The value of bio decomposition rate (λ) is estimated to be 0.018 (1/d), which is similar to that of the anaerobic condition. Using these data, the ethanol diffusion from a 60 cm width cutoff wall of 20 m depth was predicted. The water level difference that will accelerate the replacement of pore ethanol to water was set to 18 m. Ethanol diffusing area was enlarged along the water surface up to 12 m apart from the wall until 60 days, then, began to shrink afterwards by biodegradation. It was verified that the ethanol diffusion can be minimized by pumping the groundwater properly, and that the ethanol diffusing out from the cutoff wall can be easily degraded by biomass underground.

3.2 *Distribution of ethanol concentration, water content, shear strength, and dry density in the cutoff wall*

Figures 5–8 show the distribution of dry density, water content, ethanol concentration, and shear strength in the cutoff wall after 3 months. The right-hand side is adjacent to the groundwater, and the left side to the pore air.

The ethanol concentration adjacent to the right-hand side model was lowered to less than 10% (100,000 mg/L) because of water intake into the wall. The ethanol concentration adjacent to the model ground (left side) also decreased slightly because the ethanol diffused to the pore air.

The water content of the lower and right-hand side attached to the groundwater increased up to 30%, though that of other portion was 27%. This is because

Copyright © 2003 Swets & Zeitlinger B.V., Lisse, The Netherlands

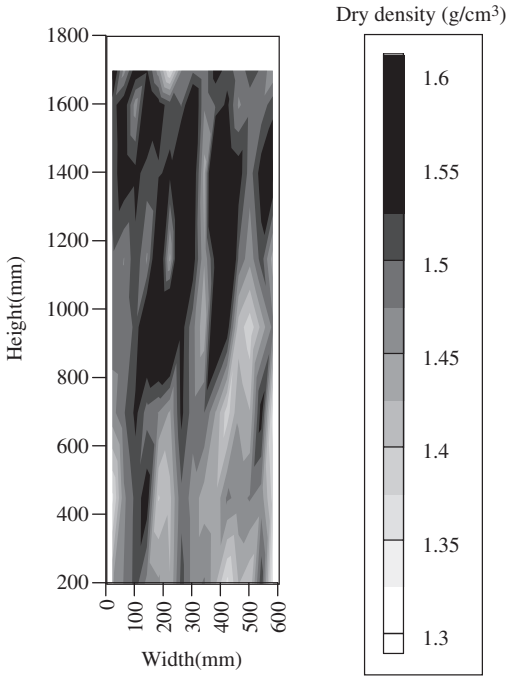


Figure 5. Dry density in the wall.

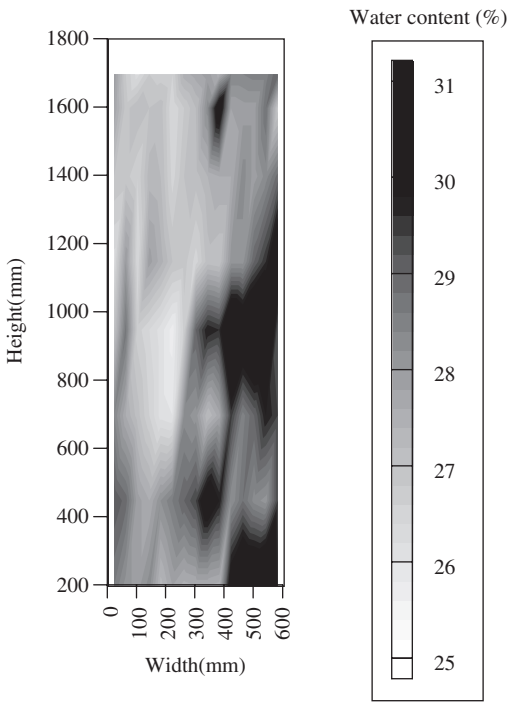


Figure 6. Water content in the wall.

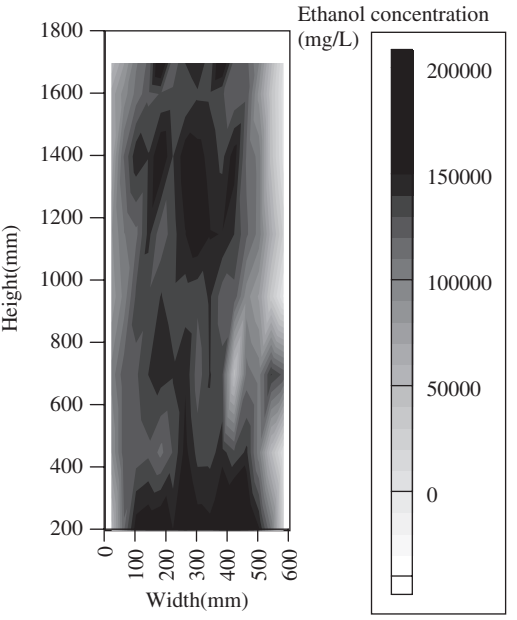


Figure 7. Ethanol concentration in the wall.

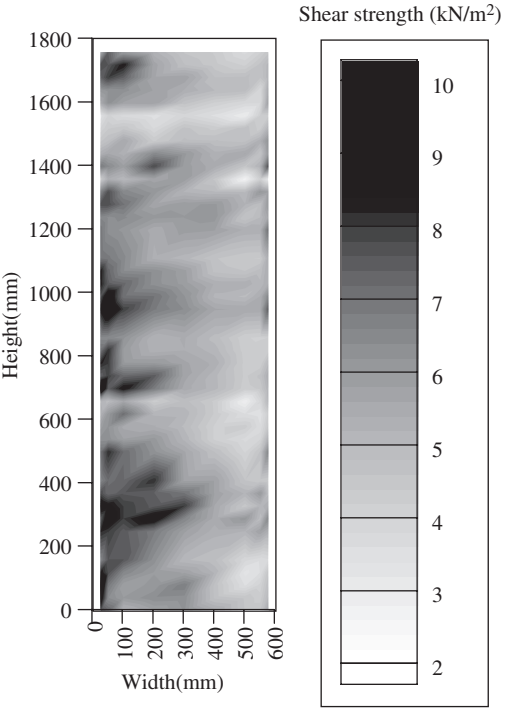


Figure 8. Shear strength in the wall.

Copyright © 2003 Swets & Zeitlinger B.V., Lisse, The Netherlands

replacing the ethanol with water occurred at the right side and the bentonite began swelling.

Shear strength increased on the left side unexpectedly, though shear strength was expected to increase on the right side because the bentonite began to swell and increased the pressure (Asada et al., 2001b). This may be one of the reasons why the pore liquid attached to the air evaporated, reducing the water content and thus resulting in strength improvement.

Dry density increased from the center to the top, though dry density was expected to increase at the bottom because of consolidation. From the consolidation test results, the void ratio of the bottom part should be 1.0, but it was 0.8, as shown in Figure 5. It is thought that the pore ethanol of the bottom part was exchanged for water, and that bentonite began swelling and this minimized consolidation. The top central portion was consolidated by both its own weight, because the ethanol exchange with water did not occur and the bentonite did not swell at that time.

The maximum ethanol concentration of the drain water from the left side was 730 mg/L.

The hydraulic conductivity of the wall was 4.0×10^{-10} m/s, calculated from the amount of the permeation water through the wall. This value is very close to 5.0×10^{-10} m/s, obtained by tri-axial hydraulic conductivity test using cutoff wall samples. Only 14% of ethanol contained in the cutoff wall was replaced with water during the 102 days. However, even the hydraulic conductivity was low enough if the replacement of ethanol with water was not complete. The time to exchange all the pore ethanol with water of a 60 cm width cutoff wall of 20 m depth was predicted by the calculation. The water level difference needed to accelerate the replacement of pore ethanol with water was set at 18 m. It is estimated that 400 to 600 days is needed to exchange all the pore ethanol with water.

3.3 *Settlement and displacement of the surface*

Figures 9–12 show the change of the surface settlement and displacement after 1 hour and 3 months (just before the digging) of the wall view from just above the surface. When the iron plates were pulled out from the model ground just after the cutoff wall placement, the sand ground near the wall displaced 10 mm to the wall and settled 10 mm. According to the settlement distribution, the upper mass of the model ground started to slide, and the sliding failure was observed as shown in Photo 5. The cutoff wall, however, remained stable against earth pressure. Small settlement and displacement were then observed, but they were the results of consolidation of the wall by the weight itself, earth pressure, and water pressure. The surrounding ground moved towards the wall gradually. The sand surface just near the wall settled 15 mm

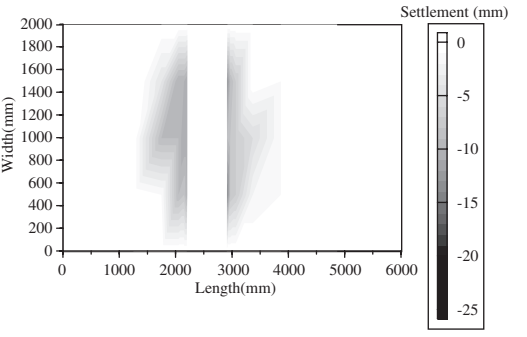


Figure 9. Surface settlement after 1 hour. Surface near the cutoff wall settled 5–10 mm.

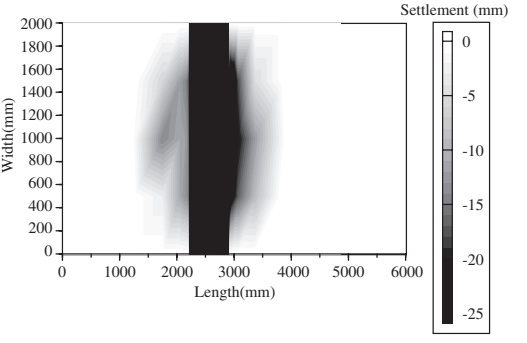


Figure 10. Surface settlement after 103 days. Cutoff wall settled 25 mm and the right side of the wall settled 20 mm.

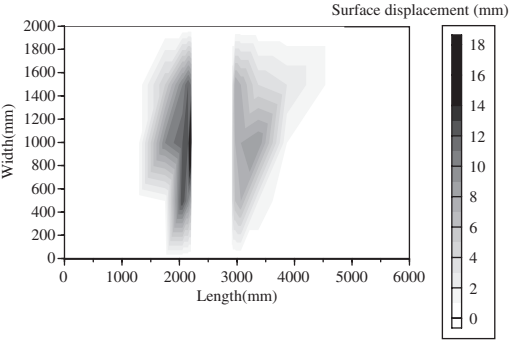


Figure 11. Surface displacement after 1 hour.

after 19 days, and 25 mm after 3 months. It also displaced towards the wall 15 mm after 19 days, 20 mm after 3 months. A large settlement of 200 mm was suspected from the pre-studies, but this was not observed actually. The settlement of the wall subsided to 25 mm, due to the swelling of the bentonite.

Copyright © 2003 Swets & Zeitlinger B.V., Lisse, The Netherlands

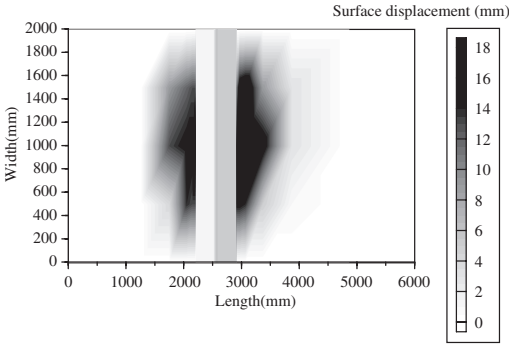


Figure 12. Surface displacement after 103 days. Surface near the cutoff wall moved 10–15 mm towards the wall. Note: in Figures 11 & 12, the positive value on the surface of sandy soil expresses the displacment toward the slurry wall. The positive value on the cutoff wall means the displacement to the left.

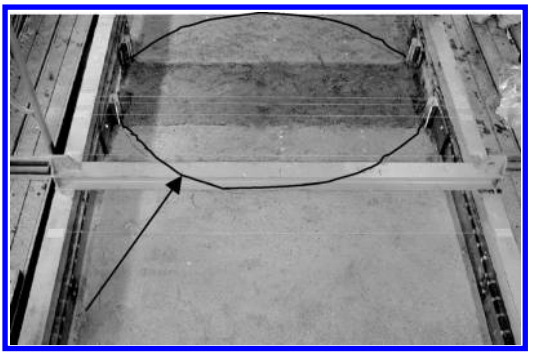


Photo 5. Sliding failure on the surface.

4 CONCLUSIONS

In this paper, large-scale model was tested to investigate the cutoff property of ethanol-bentonite slurry wall and the geo-environmental effect of ethanol based on the following test results; (1) cutoff wall made by ethanol/bentonite slurry had enough barrier ability of hydraulic conductivity 4.0×10^{-10} m/s, (2) ethanol diffusion area was limited within 1.5 m from the wall, (3) pore ethanol was easily exchanged with water in 1 or 2 years, (4) bentonite swelling prevented the wall consolidation. From these results, ethanol/bentonite slurry was concluded to be a suitable material for the soil-bentonite cutoff walls.

REFERENCES

Asada, M., Ishikawa, A. & Horiuchi, S. 2001a. Cutoff wall construction using bentonite/ethanol slurry, Clay Science for Engineering, Rotterdam, A. A. Balkema: 511–516.

Asada, M. & Horiuchi, S. 2001b. Applicability of Ethanol/bentonite Slurry for Seepage Barriers, *Geo-environmental Engineering*, London, Tomas Telford: 159–164.

Chapuis, R. P. 1990. Sand-bentonite liners: predicting permeability from laboratory tests, *Can. Geotech. J.* 27: 47–57.

D'Appolonia, J. 1980. Soil-bentonite slurry trench cutoffs, *Journal of the Geotechnical Engineering Division, Proceedings of the Americal Society of Civil Engineers* 106 GT4 (April): 399–417.

Kenney, T. C., van Veen, W. A., Swallow, M. A. & Sungaila, M. A. 1992. Hydraulic conductivity of compacted bentonite-sand mixtures, *Can. Geotech. J.* 29: 364–374.

Oweis, I. & Khera, R. 1998. *Geotechnology of waste management*, Boston, PWS Publishing Company.

Panjan, N. S. et al. 1995. Permeability and compressibility behavior of bentonite-sand/soil mixes, *Geotechnical Testing Journal* 18(1): 86–93.

Sridharan, A. & Venkatappa Rao, G. 1973. Mechanisms controlling volume change of saturated clays and the role of the effective stress concept, *Geotéchnique* 23(3): 359–382.

Sridharan, A. & Venkatappa Rao, G. 1979. Shear strength behaviour of saturated clays and the role of the effective stress concept, *Geotéchnique* 29(2): 177–193.

Copyright © 2003 Swets & Zeitlinger B.V., Lisse, The Netherlands

Field investigation of groundwater contamination due to nitric acid in Matsumoto Basin, Nagano, Japan

S. Nakaya, A. Ikeuchi, I. Ohmiya, & H. Komiya
Department of Civil Engineering, Shinshu University, Nagano, Japan

H. Masuda
Department of Geosciences, Osaka City University, Osaka, Japan

M. Kusakabe
Institute for Study of the Earth's Interior, Okayama University, Tottori, Japan

ABSTRACT: We investigated the stable isotope of oxygen and hydrogen, and the water quality of groundwater in order to identify the flow paths and groundwater contamination due to nitric acid in the Matsumoto Basin, Japan. The spatial distributions of the oxygen and hydrogen stable isotopic ratios, water quality and altitude effect against oxygen stable isotope of groundwater indicated that the flow systems of shallow groundwater, deep groundwater, and seven flow paths are distinguishable in the study region. The NO_3^-–N from three contamination sources partially exceeded the WHO standard migrates and spreads toward the urban area along the flow paths in both the shallow and deep groundwater system. After monitoring NO_3^-–N for three years, it became apparent that NO_3^-–N of groundwater maintains a constant concentration in a shallow groundwater system, while it increases in a deep groundwater system.

1 INTRODUCTION

The Matsumoto Basin, which is surrounded by 2,000 m to 3,000 m high mountains in central Japan, depends considerably on groundwater for domestic, agricultural, industrial and urban use. An understanding of the groundwater contamination from nitric acid provides important information for strategy into the resource management as well as the prevention of groundwater contamination. Since nitric acid is usually transported by groundwater flow, it is essential to find the flow paths in the study region. For example, previous researchers investigated the stable isotopic ratios of oxygen (δ^{18}O) and hydrogen (δD) and of groundwater in order to study the groundwater recharge and flow (eq., Mizutani & Oda 1983, Mizutani & Satake 1997, Mizutani et al. 2001).

We investigated δ^{18}O and δD, and the water quality of groundwater in order to identify flow paths and to understand the transportation of nitric acid in the Matsumoto Basin. The first purpose of this study is to show the applicability of stable isotope data to the identification of groundwater flow paths from the spatial distributions of δD and δ^{18}O. The second is to evaluate the groundwater contamination by nitric acid in the groundwater system.

2 HYDROGEOLOGY

Aquifers in the Matsumoto Basin mostly consist of several conglomerate layers (CL) which are supplied from the western mountains composed of Paleozoic–Mesozoic formations, while the granite and eastern mountains are composed of Miocene formations and diorite. These sediments are classified into the Enrei formation, Nashinoki CL, Kataoka CL, Akagiyama CL, Nakayama peat layer, Hata CL, Moriguchi CL and the alluvial layer (Sakai et al. 1982). The Itoigawa–Shizuoka tectonic line (ISTL) extends in the north and south direction and several faults derived from ISTL are inferred under the Matsumoto Basin.

3 METHOD

Ninety-eight groundwater and several surface water samples were collected from domestic, agricultural, industrial and urban wells (0–200 m depth) and springs during 1999–2001 (Figure 1). The 21 monitoring points were chosen for temporal variation of NO_3^-–N and the groundwater samples were collected once a month from June to November of 2001.

Copyright © 2003 Swets & Zeitlinger B.V., Lisse, The Netherlands

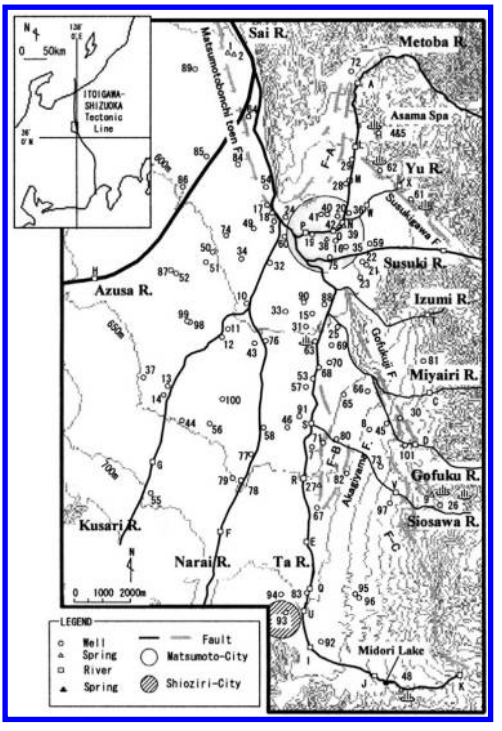


Figure 1. Locations of wells in study region.

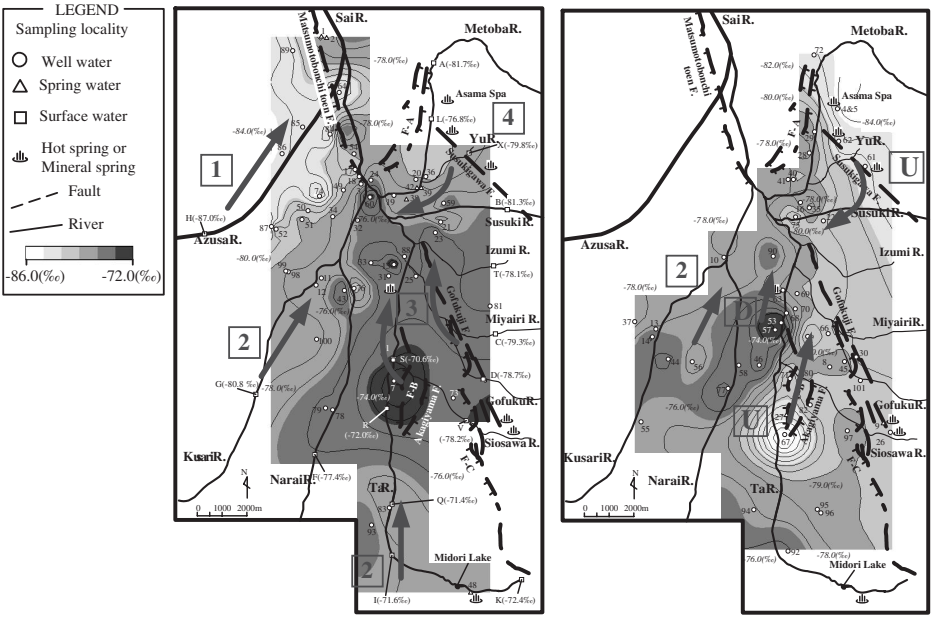
The water quality of the samples were measured: HCO_3^- as 4.8 alkalinity (*in situ*), Cl^-, SO_4^{2-} and NO_3^-–N (by ion chromatography), Na^+ and K^+ (atomic absorption spectrometry), and Ca^{2+} and Mg^+ (titration).

The D/H analysis of the groundwater sample was carried out by the preparation of hydrogen from the water by an uranium reduction technique (Friedman & Smith 1958), followed by hydrogen isotope mass spectrometry. The $^{18}O/^{16}O$ ratio of groundwater samples was determined using the automated CO_2–H_2O equilibration technique (Epstein & Mayeda 1953, Chiba et al. 1985), followed by hydrogen isotope mass spectrometry. The results were expressed as a common δ notation, which was a permil deviation from those of the Vienna Standard Mean Ocean Water (V-SMOW, (Coplen et al. 1983)). The analytical errors of the isotopic measurements are ± 1.5 and ± 0.1‰ for δD and δ^{18}O, respectively.

4 RESULTS AND DISCUSSION

4.1 *Spatial distribution of δD and δ^{18}O values*

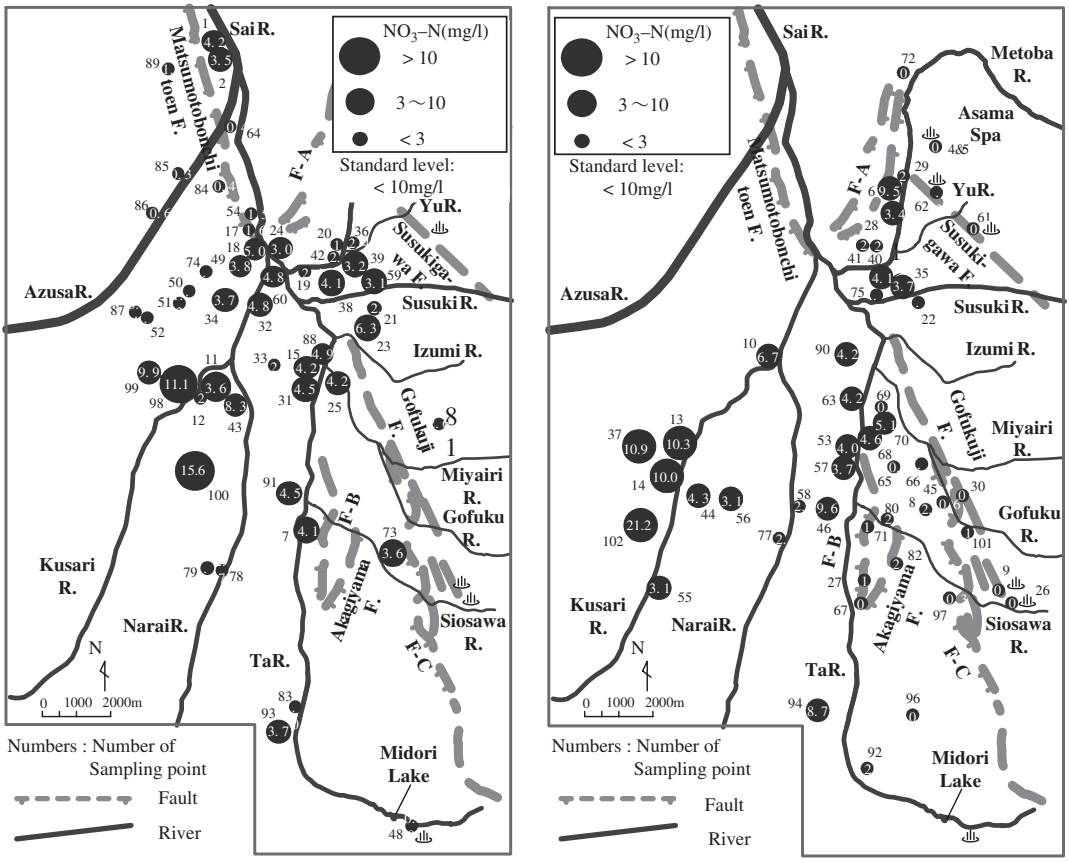
The values of δD and δ^{18}O for meteoric and surface waters, and the altitude effect in central Japan are reported (Waseda & Nakai 1983, Mizota & Kusakabe 1994). The values of δD and δ^{18}O of groundwater and



(a) Shallow groundwater flow system (b) Deep groundwater flow system

Figure 2. Spatial distribution of δD in (a) the shallow groundwater flow system and (b) the deep groundwater flow system.

Copyright © 2003 Swets & Zeitlinger B.V., Lisse, The Netherlands



(a) Shallow groundwater flow system

(b) Deep groundwater flow system

Figure 3. Spatial distribution of NO_3^-–N in (a) the shallow groundwater flow system and (b) the deep groundwater flow system.

surface water samples in the Matsumoto Basin and the surrounding mountains agree with the results and are plotted widely between two meteoric water lines, $\delta D = 8\delta^{18}O + 10$ (Craig 1961) and $\delta D = 8\delta^{18}O + 17$.

From the spatial distributions of the oxygen and hydrogen stable isotopic ratios and water qualities, the two flow systems, namely the shallow groundwater flow system and the deep groundwater flow system, are distinguishable in the study region as shown in Figure 2. The water quality of the samples also supports the distinction of the two flow systems because groundwaters in a shallow system and a deep system are almost always a Ca–HCO_3 type and a multiple type (Ca–HCO_3, Na–(Cl)–HCO_3, Na–SO_4 and Ca–HCO_3–SO_4 types), respectively. In a shallow groundwater flow system, at least four flow paths are distinguishable based on the spatial distribution of δD and δ^{18}O values. They also seem to be undercurrent along the rivers, mixing with each other. In a deep groundwater flow system, in addition to flow paths in a shallow system, three flow paths are distinguishable in relation to inferred faults (Akagiyama F., Susukigawa F. and F-B fault). The low δD and δ^{18}O groundwater is observed at the Akagiyama fault and Susukigawa fault, while the high value is observed at the F-B fault. In our understanding, the low δD and δ^{18}O at faults means that the deeper groundwater discharges along the faults as a preferential flow path while the high δD and δ^{18}O at faults means that the shallow groundwater flows to deep system in downward aquifer toward the footwall along the normal fault.

4.2 *Spatial distribution of NO_3^-–N*

The seven groundwater samples from 98 sampling points exceeded the WHO standard for NO_3^-. Figure 3 shows the spatial distribution of NO_3^-–N. It indicates that the NO_3^- migrates and spreads toward the urban

Copyright © 2003 Swets & Zeitlinger B.V., Lisse, The Netherlands

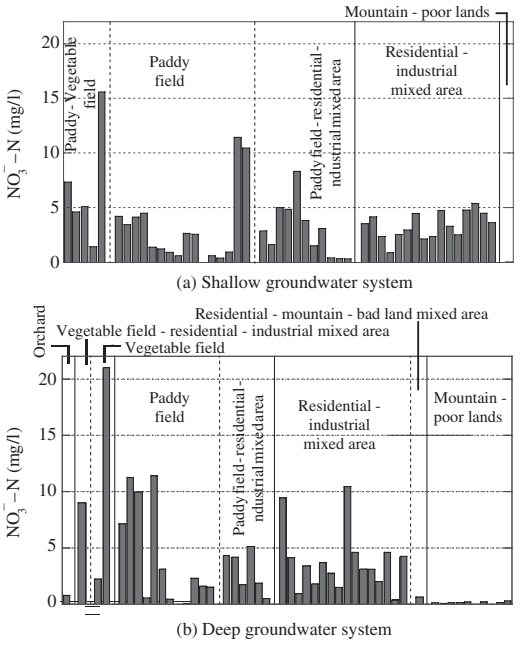


Figure 4. Relationship between NO_3^-–N and land use at different groundwater systems.

area along the flow paths in both the shallow and the deep groundwater system.

Figure 4 shows the relationship between NO_3^-–N and land use at different groundwater systems. In the forest and poor lands, NO_3^-–N is very low because of the rare effect of anthropogenic activities. The NO_3^-–N is less than 1.0 ppm which nearly equals the rain water. In an agricultural system, NO_3^- pollution is extremely high in vegetable fields and paddy–vegetable mixed fields. Since the correlation coefficients of Ca^{2+}–SO_4^{2-}, Ca^{2+}–Mg^{2+} and Na^+–Cl^- are 0.64, 0.77 and 0.18, respectively, the contamination must come from ammonium sulfate fertilizer. From the flow path, the contamination sources are estimated to be the fertilizer from some vegetable fields behind the paddy fields. Furthermore, they partially include NO_3^- from the chicken farming and cattle shed as a spot source. Another contamination source is estimated from the drainage of residential–industrial mixed area which is located mainly along the Ta River between Matsumoto City and Shiojiri City, because the relationship between Na^+ and Cl^- are plotted along the line of $Na^+/Cl^- = 1.0$ and there is a good correlation between NO_3^-–N and Cl^-.

4.3 *Temporal variation of NO_3^-–N*

We monitored the NO_3^-–N of 21 sample points during June to November of 2001. The average changes

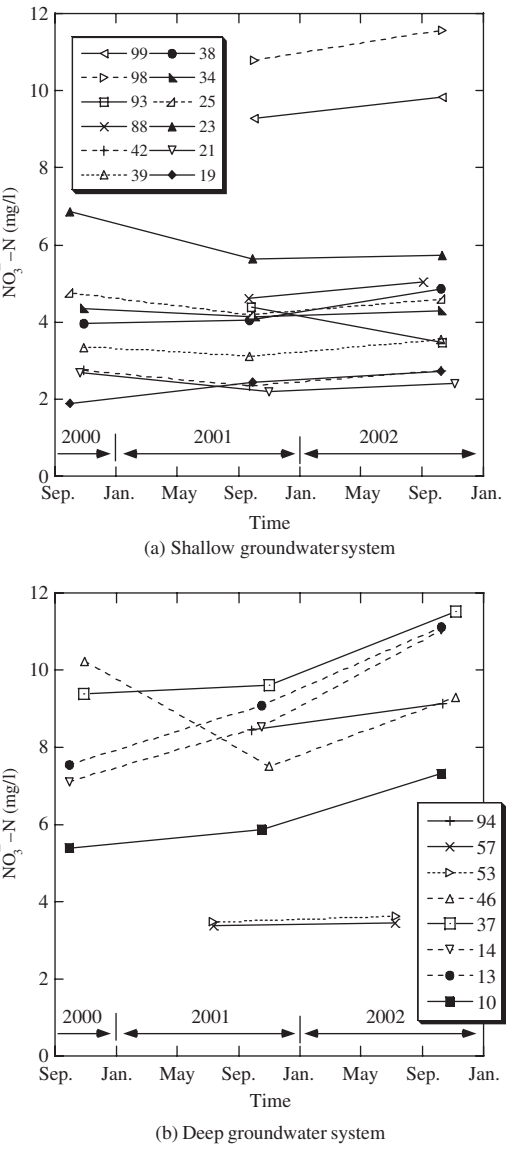


Figure 5. Temporal changes of NO_3^-–N for three years.

of NO_3^-–N for six months in an agricultural area and in a residential–industrial mixed area are 1.5 ppm and 0.8 ppm, respectively. The monitoring points in an agricultural area belong to the paddy field. The monitored results of NO_3^-–N in a paddy field indicate that the NO_3^-–N of groundwater increases just after periods of drainage in paddy fields. This suggests that NH_4^+–N changes to NO_3^-–N under an O_2 rich condition by the bacteria in the soil, and then NO_3^-–N is leached through an unsaturated zone into a groundwater table

Copyright © 2003 Swets & Zeitlinger B.V., Lisse, The Netherlands

without absorption during and just after periods of drainage in paddy fields [eq., Tsurumaki, 1992]. After monitoring NO_3^-–N for three years (Figure 5), NO_3^-–N of groundwater maintains a constant concentration in a shallow groundwater system, while it increases in a deep groundwater system.

5 CONCLUSIONS

We investigated stable isotopes of oxygen and hydrogen, and the water quality of groundwater in the Matsumoto Basin, Japan. The followings are drawn:

(1) The spatial distributions of the oxygen and hydrogen stable isotopic ratios and water quality indicate that flow systems of shallow groundwater and deep groundwater, and seven flow paths are distinguishable in the study region.
(2) The NO_3^-–N from three contamination sources partially exceeded the WHO standard, which then migrates and spreads toward the urban area along the flow paths in both the shallow and the deep groundwater system.
(3) In an agricultural system, NO_3^- pollution is remarkably high in vegetable fields and paddy–vegetable mixed fields. From the flow path, the contamination sources are estimated to be the fertilizer from some vegetable fields behind paddy fields. Furthermore, they partially include NO_3^- from the chicken farming and cattle shed as a spot source.
(4) Another contamination source is estimated from the drainage of residential–industrial mixed area.
(5) In forest and poor land systems, NO_3^-–N is very low because of a rare effect of anthropogenic activities. The NO_3^-–N is less than 1.0 ppm which nearly equals that of rain water.
(6) According to the results from monitoring NO_3^-–N for three years, NO_3^-–N of groundwater maintains a constant concentration in a shallow groundwater system, while it increases in a deep groundwater system.

ACKNOWLEDGEMENTS

We would like to thank all the owners of the wells that helped us with our collection of groundwater samples.

REFERENCES

Chiba, H., Sakai, H. & Yasutake, M. 1985. Automatic measurement of oxygen isotope ratio of water samples. *Pap. Inst. Thermal Spring Res. Okayama Univ.* 56: 27–34 (in Japanese).

Coplen, T. B., Kendall, C. & Hopple, J. 1983. Comparison of stable isotope reference samples. *Nature* 302: 236–238.

Craig, H. 1961. Isotopic variations in meteoric waters. *Science* 133: 1702–1703.

Epstein, S. & Mayeda, T. K. 1953. Varidation of O18 content of waters from natural sources. *Geochim. Cosmochim. Acta* 4: 213–224.

Friedman, I. & Smith, R. L. 1958. The deuterium content of water in some volcanic glasses. *Geochim. Cosmochim. Acta* 15: 218–228.

Mizota, C. & Kusakabe, M. 1994. Spatial distribution of δD-δ^{18}O values of surface and shallow groundwaters from Japan, south Korea and east China. *Geochemical J.* 28: 387–410.

Mizutani, Y. & Oda, M. 1983. Stable isotope study of ground water recharge and movement in the Shogawa Fan, Toyama. *Chikyukagaku* 17: 1–9 (in Japanese).

Mizutani, Y. & Satake, H. 1997. Hydrogen and oxygen isotope compositions of river waters as an index of the source of groundwaters. *J. Groundwater Hydrology* 39(4): 287–297 (in Japanese).

Mizutani, Y., Satake, H., Yamabe, A., Miyachi, H., Mase, N. & Yamamura, K. 2001. Hydrogen and oxygen isotope ratio of groundwaters in shallow aquifers beneath the alluvial fan. *J. Groundwater Hydrology* 43(1): 3–11 (in Japanese).

Sakai, J. 1982. Matsumoto-daira ground map. Architecture asso. *Nagano architects & Building Engineers Associations Matsutiku branch Nagano Japan*. 175p.

Tsurumaki, M. 1992. Nitrate nitrogen in shallow groundwater. *J. Groundwater Hydrology* 34(3): 153–162 (in Japanese).

Waseda, A. & Nakai, N. 1983. Isotopic compositions of meteoric and surface waters in central and north-east Japan. *Chikyukagaku* 17: 83–91 (in Japanese).

Copyright © 2003 Swets & Zeitlinger B.V., Lisse, The Netherlands

On predicting the effects of hexavalent chromium leached from cement treated soil

N. Tsuneoka & H. Mori
Public Works Research Institute, Tsukuba, Japan

T. Obata
Origawa Dam Office, Ministry of Land, Infrastructure and Transport, Yamaoka-machi, Gifu, Japan

ABSTRACT: This is a report on the results of testing of input values and parameters needed to perform numerical analysis to predict the effects of hexavalent chromium leached from cement treated soil on the surrounding environment. A column water pass-through test was performed to find the leaching value of hexavalent chromium that is a value input to the numerical analysis, confirming that it is possible to define the relationship between the leaching value and seepage quantity. As for the retardation coefficient that is a parameter for the numerical analysis, a comparison of the numerical analysis results and the large soil tank experiment revealed that the results of both conform closely if the retardation factors are equal.

1 INTRODUCTION

There is fear that hexavalent chromium is leached from cement treated soil that is made by mixing cement with soil. This study considers a type of cement treated soil used for shallow layer improvement. Where shallow layer improvement has been done, rainwater seeping through the cement treated soil leaches the hexavalent chromium from the soil and carries it through the surrounding ground. Numerical analysis based simulations are done to predict the effects of such hexavalent chromium on the surrounding environment.

The concentration of the hexavalent chromium leached from the cement treated soil is input to the numerical analysis performed to simulate its distribution through the surrounding ground that is the model. The analysis can be done using an existing analysis program, but the hexavalent chromium leaching value that is a value input to the numerical analysis must be set. So to obtain this leaching value, columns were filled with cement treated soil whose hexavalent chromium leaching had been confirmed and used for water pass-through tests. The leaching value of hexavalent chromium from cement treated soil is usually obtained by the leaching test in Environmental Agency Notification No. 46. This test is performed by crushing a specimen, using a solvent to prepare the test fluid with a solid–liquid ratio of 1:10, and agitating it for 6 hours to leach the hexavalent chromium. Below, the values based on this test method are called the JLT46 values. In shallow layer improvement, the hexavalent chromium concentration in the seepage water that is a value input to the numerical analysis is the result of passing seepage water through cement treated soil with a certain JLT46 value formed with varying thickness. So for the water pass-through tests, each of the columns was filled with cement treated soil with a different JLT46 value and the testing done varying the filling length, pass-through speed, and the pass-through direction.

A large soil tank test was also conducted in model ground made by placing a layer of cement treated soil with confirmed leached hexavalent chromium above a thick sandy layer on the tank's bottom. It was done to study the hexavalent chromium leached from cement treated soil in a condition more like that of actual ground and to compare it with the numerical analysis. Rain water was poured on it, seepage water taken from the sandy ground at various depths below the cement treated soil, and its hexavalent chromium concentration measured. The numerical analysis was done with the large soil tank as the model to study the setting of the retardation factor. Figure 1 shows an outline of this research.

Obata et al. 2002 have performed a detailed study of the leaching characteristics of hexavalent chromium from soil treated for deep layer improvement.

Copyright © 2003 Swets & Zeitlinger B.V., Lisse, The Netherlands

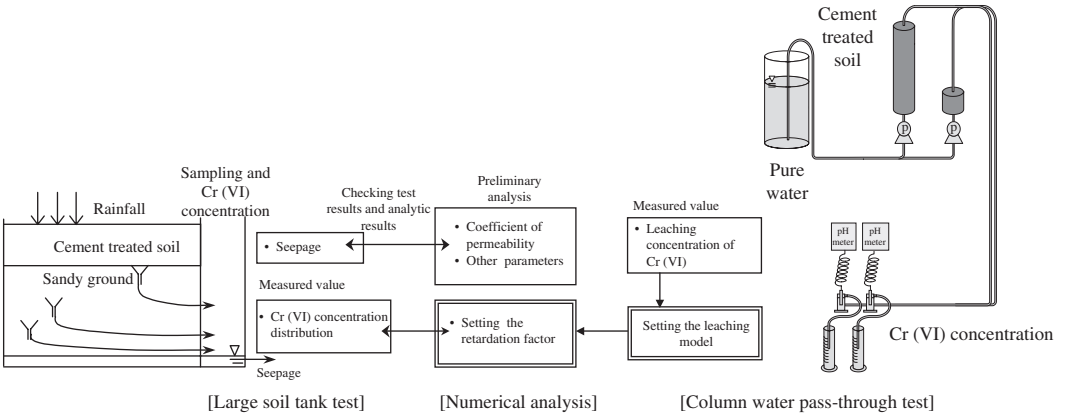


Figure 1. Schematic drawing of experiment and numerical analysis.

2 LEACHING OF HEXAVALENT CHROMIUM FROM CEMENT TREATED SOIL

2.1 *Cement treated soil*

The cement treated soils used are shown in Table 1, Volcanic ash clay was mixed with cement at a different rate, making three types of treated soil of different JLT46 values.

2.2 *Column water pass-through experiment*

Figure 2 shows the experimental system. This experiment was done by filling acrylic columns with internal diameter of 10.4 cm with cement treated soil, then using a pump to pass water through each column from either the top or the bottom of the column at a constant flow volume. The pH of the water passing through the column was measured with a pH meter at the same time as the water that had passed through the cement treated soil was collected and its hexavalent chromium content was measured by the diphenylcarbazide spectrophotometric method at fixed intervals.

The test cases are shown in Table 2. A total of 6 cases were performed by varying the filling length for three types of cement treated soil. And when the coefficient of permeability of the cement treated soil was measured for case 1–1 after the test had continued for seven days, a value of 1×10^{-5} cm/s was obtained.

2.3 *Experimental results*

Figures 3 and 4 show the results of the test. The horizontal axis represents the quantity of water passing through the cement treated soil, and the vertical axis represents the concentration of the hexavalent chromium in the water that has passed through the cement treated soil. During the experiment, the concentration of the hexavalent chromium in the water that has passed through the cement treated soil peaked when the water started to pass through, but tended to gradually decline afterwards. The pH of the water that had passed through the cement treated soil had high values between 10 and 12, because it was caused by alkali produced by the cement.

As shown in Figure 3, regardless of the JLT46 value of the cement treated soil, the concentration of the hexavalent chromium in the water that passed through the cement treated soil early was plotted around 0.3 mg/l. Later, the smaller the JLT46 value of the cement treated soil, the more rapid the decline of the concentration of hexavalent chromium in the water. Judging from the results, the JLT46 value of the cement treated soil influences the duration of the hexavalent chromium concentration, but has no effect on the initial (maximum) concentration of hexavalent chromium in the water that has passed through the cement treated soil.

Table 1. Cement treated soil adjustment method.

Cement treated soil	JTL46 Value Cr (VI) Leached concentration (mg/l)	Adjustment method
1	0.06	Blended by adding cement hardener to volcanic ash clay (passed through a 2 mm sieve) at a rate of 50 kg/m^3 (powder addition), curing the mixture for 7 days, then passing the product through a 2 mm sieve.
2	0.38	Above at a rate of 300 kg/m^3
3	0.89	Above at a rate of 300 kg/m^3 done in a different year.

Copyright © 2003 Swets & Zeitlinger B.V., Lisse, The Netherlands

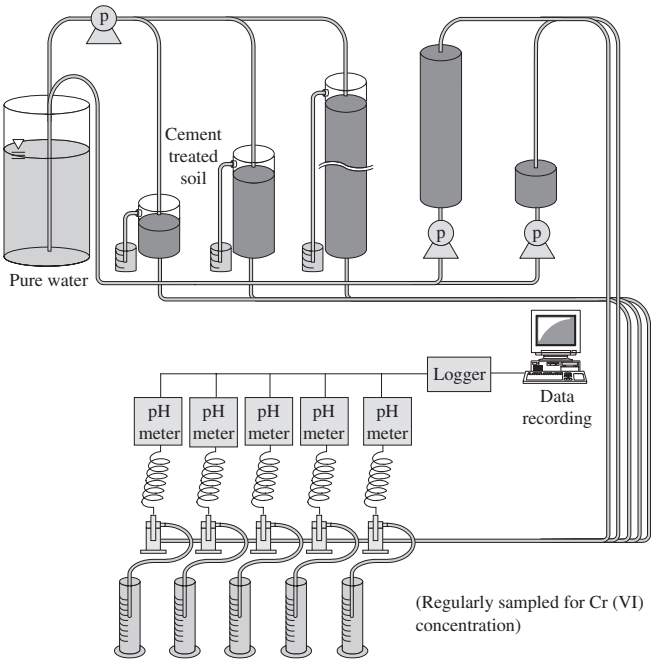


Figure 2. Experimental system.

Table 2. Column water pass-through test cases.

	Cement treated soil used				
Case	Length (cm)	Filled density (g/cm^3)	JTL46 Value Cr (VI) Leached concentration (mg/l)	Pass-through method (Injection end) (ml/min)	Type of cement treated soil
1–1	10	1.2	0.06	0.5 (bottom)	1 Volcanic ash clay
1–2	10	1.2	0.38	0.5 (bottom)	2 Volcanic ash clay
1–3	10	1.2	0.89	0.1 (bottom)	3 Volcanic ash clay
2–1	10	1.2	0.89	0.5 (top)	3 Volcanic ash clay
2–2	40	1.2	0.89	0.5 (top)	3 Volcanic ash clay
2–3	100	1.2	0.89	0.5 (top)	3 Volcanic ash clay

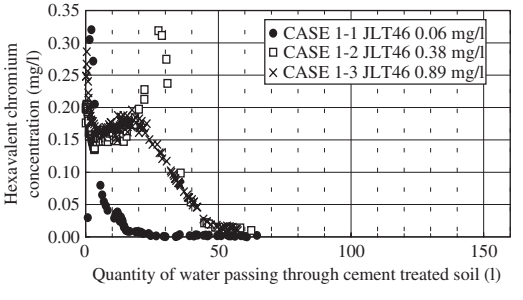


Figure 3. Effects of different JLT46 values of cement treated soil.

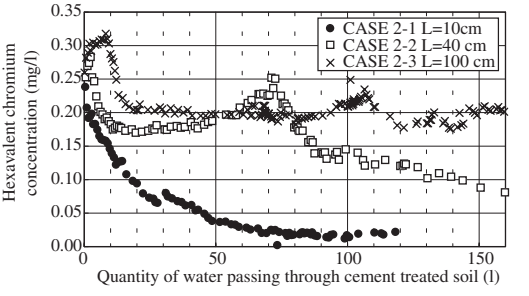


Figure 4. Effects of different lengths of cement treated soil.

Copyright © 2003 Swets & Zeitlinger B.V., Lisse, The Netherlands

As shown in Figure 4, like the different JLT46 values of the cement treated soil, variations in the length of the cement treated soil had no effect on the initial concentration of the hexavalent chromium in the water that had passed through the cement treated soil, which was around 0.3 mg/l. As the experiments continued, the shorter the length of the cement treated soil, the faster the decline in the concentration of the hexavalent chromium in the water that had passed through the cement treated soil. This result shows that the length of the cement treated soil influenced the duration of the hexavalent chromium concentration, but had no effect on the initial (maximum) concentration of hexavalent chromium in the water that passed through the cement treated soil. The pass-through speed and direction had almost no effects in this experiment (see Mori et al. 2002).

Table 3 shows the total quantity of hexavalent chromium leached from the cement treated soil. The experimental values were obtained by adding the quantity of residual hexavalent chromium in the columns to the results obtained by totaling the concentration of hexavalent chromium in the water that passed through the cement treated soil. The calculated values were obtained by equation (1) based on the JLT46 values. The experimental values were between 1 and 2 times the calculated values. One of the reasons of the difference between the experimental and calculated values is the different ways of leaching hexavalent chromium from cement treated soil.

$$\begin{aligned}&\text{Total quantity of leached hexavalent chromium}\\&\text{(calculated value) (mg)}\\&\quad = \text{JLT46 value (mg/l)}\\&\qquad \times \text{quantity of cement treated soil (kg)}\\&\qquad \times 0.5(\text{l})/0.05(\text{kg})\end{aligned} \tag{1}$$

Based on the above results, it has been proposed that the leaching value that is input to the numerical analysis be set as explained below in the light of the characteristics of leaching from the cement treated soil in the experiment.

1. The maximum leaching concentration is 0.3 mg/l regardless of the JLT46 value and thickness of the cement treated soil.
2. The total quantity leached is double the calculated value obtained by equation (1).

Figure 5 shows the leaching curve that is proposed. It is necessary to define the parts of the curve where the leaching concentration begins to fall from its maximum value and where leaching stops, but because it does not have a big influence on the results of the analysis performed to predict the first half of its effects over time, it is represented as the rectangle shown by the dotted line in Figure 5.

3 MOVEMENT OF HEXAVALENT CHROMIUM FROM CEMENT TREATED SOIL

3.1 *Soil layer preparation*

The method used to prepare each layer is shown in Table 4. A 30 cm layer of cement treated soil with confirmed leached hexavalent chromium was placed above an 80 cm thick sandy layer and a 10 cm thick gravel layer on the tank's bottom. The cement treated soil was made by mixing volcanic ash clay with cement.

3.2 *Large soil tank experiment*

A soil tank experiment was performed as shown in Figure 6 by applying rain water to cement treated soil

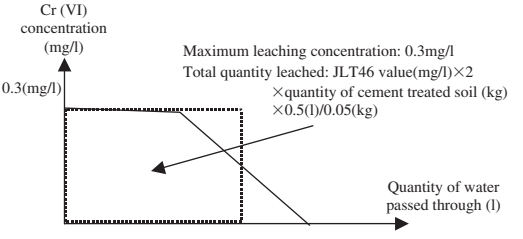


Figure 5. Model of leaching from shallow layer cement treated soil.

Table 3. Total quantity of leached hexavalent chromium.

	Item	Unit	1–1	1–2	2–1
Experimental value	Cumulative quantity of water passed through	l	65.2	62.4	120.6
	Cumulative quantity of leached hexavalent chromium	mg	1.4	7.54	6.13
	Quantity of residual hexavalent chromium in columns	mg	0	0	3.23
	Total quantity of leached hexavalent chromium	mg	1.4	7.54	9.36
Calculated values	Quantity placed in column	g	1018.9	1018.9	1018.9
	No. 46 value	mg/l	0.065	0.38	0.89
	Total quantity of leached hexavalent chromium	mg	0.662	3.87	9.07
Ratio			2.1	1.95	1.03

Copyright © 2003 Swets & Zeitlinger B.V., Lisse, The Netherlands

Table 4. Layer preparation methods.

	Preparation methods
Cement treated soil layer	Cement treated soil made by adding cement hardener to volcanic ash clay (passed through a 10 mm sieve) at a rate of 300 kg/m^3 (powder addition) is compacted to obtain the stipulated density, then it is finished to a thickness of 30 cm. JLT46 value: 0.33 mg/l Coefficient of permeability: approx. 1×10^{-3} cm/sec Density: 1.2 g/cm^3
Sandy soil layer	Natural sandy soil from Miho in Ibaraki is finished every 20 cm, to form four layers with total thickness of 80 cm. Coefficient of permeability: approx. 1.5×10^{-2} cm/sec Density: 1.6 g/cm^3
Water storing gravel layer	Gravel is spread to a thickness of 10 cm, and the lower 5 cm part stores water.

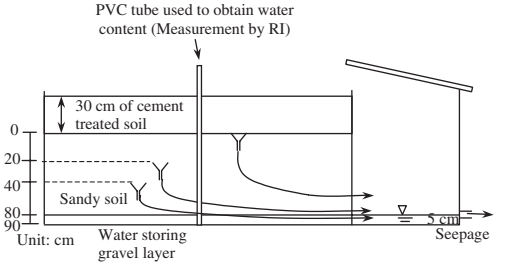


Figure 6. Outline of large soil tank experiment.

in conditions close to that in actual ground in order to clarify the state of leaching from cement treated soil and the way that it is diffused under the ground. From the bottom of the tank, a layer of water storing gravel, a layer of sand, and a layer of cement treated soil were formed. A sprinkler installed above the tank supplied rainfall at a rate of 30 mm/h continuously for 43 days. Beginning 2 days after the rainfall started, part of the rainwater was retained on the surface of the cement treated soil, with the result that about 50% of the total rainfall seeped into the ground, reaching the water storage layer. To clarify the state of the leaching and diffusion of the hexavalent chromium and the alkali, water was sampled at three depths – directly at the bottom of the cement treated soil layer, 20 cm below it, and 40 cm below it – and the hexavalent chromium concentration and the pH of each sample were measured.

3.3 *Experimental results*

Figure 7 shows the experimental results. The hexavalent chromium concentration at the sampling point at the bottom of the cement treated soil layer varied between 0.1 and 0.5 mg/l when the rainwater started, then after the fourth day, it fell to between 0.05 and 0.15 mg/l. The leaching value tendencies observed were similar to those seen in the results of the column water pass-through tests. The pH directly below the cement treated soil layer was high between 10 and 12 throughout the experiment period.

The hexavalent chromium concentration in the water sampled 20 cm below the cement treated soil layer was identified by numerical analysis. The numerical analysis was done using a two-dimensional finite element method, the Eularian–Lagragian saturated–unsaturated advection dispersion analysis program (Dtransu2D•EL) (see Nishigaki 1991). Table 5 shows

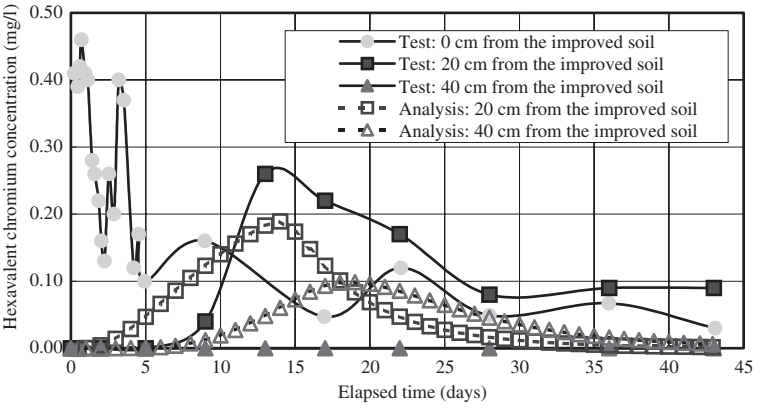


Figure 7. Comparison of test results with numerical analysis results.

Copyright © 2003 Swets & Zeitlinger B.V., Lisse, The Netherlands

Table 5. Parameters used for the analysis.

Coefficient of permeability	1.52×10^{-2} cm/s
Longitudinal dispersion length	0.1 m
Lateral dispersion length	0.01 m
Effective porosity	0.2
Retardation factor	Variable

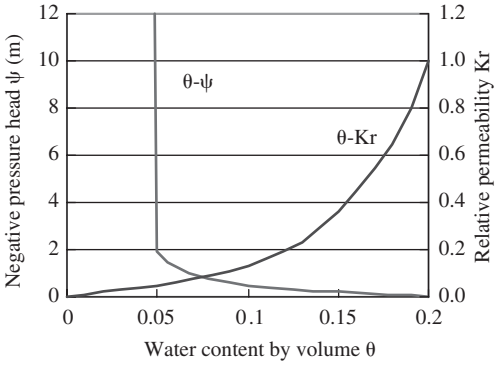


Figure 8. Unsaturated flow characteristics (River Bureau 2000).

the parameters that were used. The longitudinal dispersion length was determined by the size of the model, and the lateral dispersion length was set to a tenth of that value (see Japanese Geotechnical Society 2002). Figure 8 shows the flow characteristics in the unsaturated domain. A simulation using the leaching curve in Fig. 5 as an input value under the same conditions as the soil tank experiment defined the retardation factor of hexavalent chromium that moved through the sandy layer as 125. The results of the numerical analysis with a retardation factor of 125 are shown in Fig. 7. At 40 cm below the cement treated soil, the results of numerical analysis with the retardation factor set at 125 were higher than the experimental results. It is assumed that this occurs because near 40 cm below the cement treated soil, the retardation factor is even higher in actual sandy soil. This is explained based on the concentration dependency of the retardation factor. The pH at 20 cm and 40 cm below the cement treated soil shows the initial low values of the sandy soil, but the rise in the hexavalent chromium concentration was accompanied by high values caused by the cement.

Figure 9 shows the results of the relationship between the concentration in equilibrium and the retardation factor by performing a batch experiment using soil identical to the sandy soil in the soil tank experiment. For this batch test, 300 ml of a solution with its hexavalent chromium adjusted to stipulated concentrations (100, 10, 1, 0.1, 0.01 mg/l) were placed in a flask, 30 g of the sandy soil described above

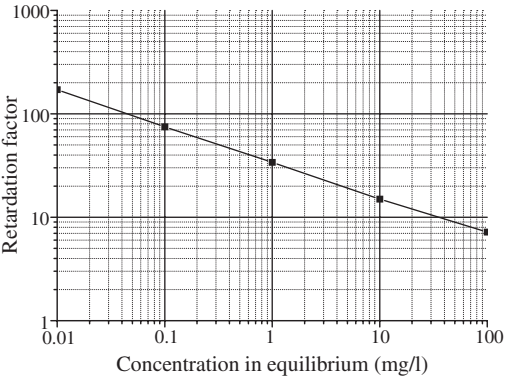


Figure 9. Relationship of the concentration in equilibrium with the retardation factor.

were placed in the flask and agitated for 4 hours, then the hexavalent chromium concentration in the filtered fluid (concentration in equilibrium) was measured and the quantity adsorbed by the sandy soil was calculated. The retardation factor can be calculated from the coefficient obtained by using Fruendlich's adsorption formula to approximate the quantity adsorbed and the concentration in equilibrium (see Yong 1992). In the batch experiment, it was assumed that the specimen soil placed in the flask was dispersed in particles, but it was revealed that with a relatively loosely formed sandy layer such as that formed in the soil tank experiment, the retardation factor obtained by a batch experiment is fairly usable. The retardation factors of 75 and 171 were calculated with the concentration in equilibrium of 0.1 mg/l and 0.01 mg/l respectively. The above concentration dependency trend was also observed.

4 SUMMARY

The leaching test in Environmental Agency Notification No. 46 is an ordinary method used to clarify the contaminant concentration of soil. In cases where there is danger of leaching from cement improved soil, the first step is to obtain the JLT46 value. Linking the value input to numerical analysis with the widely used JLT46 value to predict the effects of hexavalent chromium leached from a shallow layer of cement treated soil increases the practical applicability of numerical analysis. This report has proposed a leaching curve that considers the total quantity of hexavalent chromium leached from cement treated soil to be double a value calculated using the JLT46 value and assumes that the maximum value of the leaching concentration is 0.3 mg/l.

Regarding the retardation factor used for the same numerical analysis, the applicability to actual ground

Copyright © 2003 Swets & Zeitlinger B.V., Lisse, The Netherlands

of the value obtained by the batch experiment was confirmed by the large soil tank experiment. The ability to obtain parameters based on a batch experiment that can produce numerous data quickly using a simple method is welcome progress.

Cement treated soil is made by mixing soil and cement, and the possibility of leaching of hexavalent chromium is highest when the soil used is volcanic ash clay. This report, therefore, put priority on the use of volcanic ash clay, but more experiments must be done using cement treated soil made with soils other than volcanic ash clay to set input hexavalent chromium values to be used for numerical analysis.

It is also necessary to explain that the maximum value of the leaching concentration is not dependent upon the conditions of the specimen. Regarding this question, it is assumed that while seepage is passing through the specimen soil placed in a column, repeated desorption and adsorption of the hexavalent chromium occurs, achieving a constant balanced concentration.

REFERENCES

Japanese Geotechnical Society. 2002. Surveys, Predictions and Measures for Soil and Groundwater Contamination: 104–107.

Mori H., Tsuneoka N. & Ono M. 2002. Experiment concerning characteristics of the leaching of hexavalent chromium from cement treated soil, Proceedings of the 57th JSCE Annual Meeting, Sapporo, 25–27 September 2002.

Nishigaki M. 1991. Lecture published in a journal, Groundwater numerical calculation methods (13)2–4, Material transport and other analysis methods – Eularian–Lagragian Method (EL method), Journal of the Japan Association of Groundwater Hydrology, 33 (4): 265–276.

Obata T., Tsuneoka N. & Kohashi H. 2002. Research on the leaching characteristics of solidified soil, 4th International Congress on Environmental Geotechnics, Rio de Janeiro, 11–15 August 2002.

River Bureau, Ministry of Construction of Japan. 2000. Design Guideline for River Levees: 67–73.

Yong, R.N., Mohamed A.M.O., & Warkentin, B.P. 1992. Principles of Contaminant Transport in Soils, B.V. Elsevier Science Publishers.

Copyright © 2003 Swets & Zeitlinger B.V., Lisse, The Netherlands

Field survey and determination of hydraulic properties

Copyright © 2003 Swets & Zeitlinger B.V., Lisse, The Netherlands

A study on evaluating hydraulic conductivity of soil with numerical analysis of groundwater flow and resistivity investigation

Y. Sun & M. Inoue
Kiso-Jiban Consultants Co., Ltd., Tokyo, Japan

ABSTRACT: A method of evaluating the hydraulic conductivity of soil mass only using the data of electrical resistivity investigation is presented. The relationships of $\theta-\rho$ and $\theta-\phi$ of ground mass are assumed as the Van Genuchten function. The resistivity variation is used to calculate the degree of saturation S_r^{obs} of soil, the value of test coefficients α_i and β_i of $\theta-\phi$ curve can be determined by inverse analysis of groundwater flow F.E.M in reference of data S_r^{obs}. The analysis results of an example showed the suitability of this method.

1 INTRODUCTION

In ground water analysis, how to get the correct geophysical properties (especially, hydraulic conductivity) of soil is an important problem for raising the analysis accuracy. In other words, how to lower the cost of investigation has become a more important thing in civil engineering investing works. As it is known, resistivity investigation is a very convenience method of getting much information of ground in a short time and a cheap cost. However how to obtain more information about the geophysical properties of the ground from the data of resistivity investigation is still a problem that need to be resolved in future research work.

Many have researched the relationships between resistivity variation and geophysical properties of soil. For example, Archie (1942) had given the relationship between the degree of saturation and the resistivity of rock. Nishda et al. (1993) had researched the relationship between resistivity variation and volumetric moisture content. Wada & Inoue (1995) had used the resistivity variation of soil to estimate the water content variation of ground-foundation when it is rain. It showed that a series of resistivity method can be used to measure the water content change of soil-structure during rain or other watering process. But in this kind of investigation it is very important that establishes the relationship between the resistivity and degree of saturation of soil, which needs a lot of laboratory tests.

In the investigation of resistivity method, it is usually difficult to divide the soil or rock sorts only depending on resistivity data, because the resistivity values of soil or rock material have no obvious difference in many states.

As known there is an obvious difference of permeability in the soil and rock usually. It means that the water seepage behavior in different soil layer has obvious different during watering test or rain process. Therefore, we consider if the groundwater flow analysis and a series investigation of resistivity can be connected to measure the water content change of soil-structure during rain or other watering process, so that it will be able to increase the accuracy of soil layer distinction. In this paper, firstly we present a union analysis method of resistivity and water seepage analysis for raising the investigation accuracy of soil layer, and also research a method of determining the unsaturated hydraulic conductivity. Finally, an example has been analyzed. The results of analysis showed that this method is suitable in determining the hydraulic conductivity of ground.

2 CALCULATING METHOD

In this section, a union analysis method including saturated-unsaturated groundwater flow analysis and resistivity analysis for estimating the hydraulic conductivity has been presented. The flow chart of this method is shown in Figure 1. The analysis steps can be explained as following.

1. For an investigating area, a series resistivity measurement is performed during the watering or rain process.
2. Making a F.E.M model of investigated area for the resistivity analysis and groundwater flow analysis.

Copyright © 2003 Swets & Zeitlinger B.V., Lisse, The Netherlands

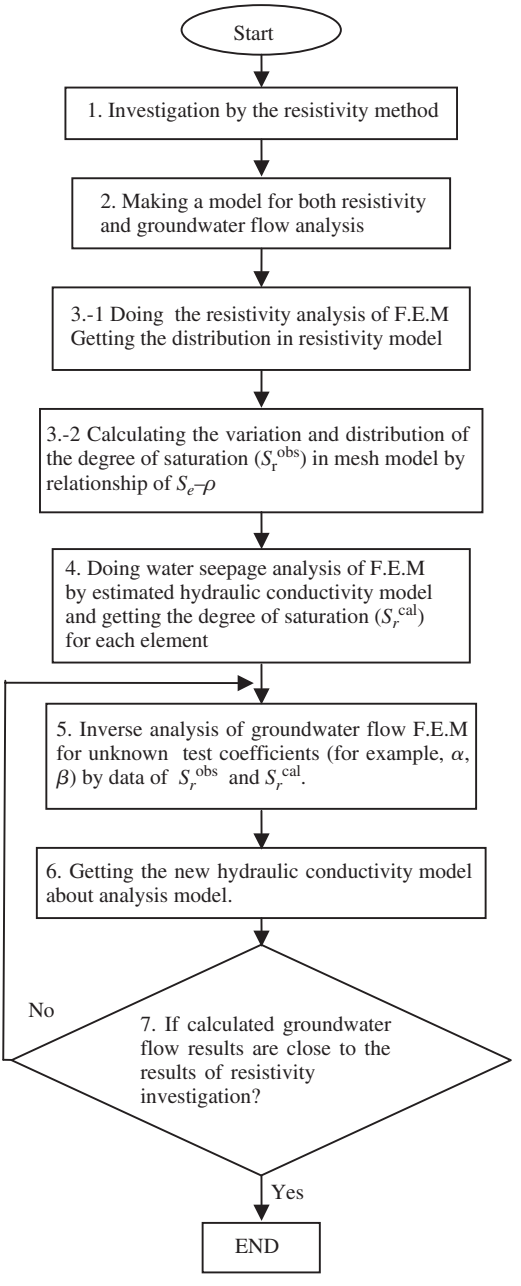


Figure 1. Flow chart of union analysis including saturated-unsaturated groundwater flow and resistivity analysis.

And giving the initial hydraulic conductivity in referencing of other investigation results for groundwater flow analysis.

3. Performing the resistivity analysis according to a series resistivity measurement data and getting the resistivity variation distribution. And calculating the degree of saturation (S_r) by the relationship of S_r–ρ.
4. Performing the groundwater flow analysis by initial hydraulic conductivity model. And getting the distribution of the degree of saturation.
5. Calculating the parameters α_i, β_i ($i = 1, 2, \ldots,$ n, n is numbers of unknown hydraulic conductivity in analysis model) by inverse analysis of groundwater flow F.E.M according to data of step 3.
6. According to the results of step 5 (distribution of test coefficients α and β), re-establishing a new hydraulic conductivity model for groundwater flow analysis.
7. Doing groundwater flow analysis using new hydraulic conductivity model again, if calculated groundwater flow results is close to the investigation results of the resistivity method, the hydraulic conductivity model used in last groundwater flow analysis can be considered as a reasonable model so that it can increase the accuracy of soil layer distinction.

3 BASIC EQUATIONS

The basic equations of union analysis method presented above section included the groundwater flow control equation and resistivity forward and inverse analysis equations that had been introduced in other papers. Here, we mainly introduce the parties of equations that have been used in calculating the degree of saturation of soil in resistivity analysis and groundwater flow analysis repetitively.

3.1 *Water content curve*

The many equations had been presented to describe the pF test curves or soil-water characteristic curves in the past (Fredlund (1993)). It had been verified that the equation presented by van Genuchten (1980) is very reasonable for several kinds of soil. Therefor, the van Genuchten model (called as VG model simply) was used to describe the soil-water characteristic curve in this paper. The equations are written as following.

$$\frac{\theta - \theta_r}{\theta_s - \theta_r} = \left\{1 + |\alpha \cdot \psi|^{\beta}\right\}^{1/\beta - 1} \tag{1}$$

$$K(\theta) = K_s \cdot S_e^{1/2} \left\{1 - (1 - S_e^{\beta/\beta-1})^{1-1/\beta}\right\}^2 \tag{2}$$

where the effective degree of saturation S_e is defined as

$$S_e = \frac{\theta - \theta_r}{\theta_s - \theta_r} \tag{3}$$

Copyright © 2003 Swets & Zeitlinger B.V., Lisse, The Netherlands

θ: volumetric water content of soil;
θ_s: volumetric water content of saturated state;
θ_r: residual volumetric water content of soil;
ψ: matrix suction of soil;
α, β: soil coefficients;
$K(\theta)$: unsaturated soil permeability;
K_s: saturated soil permeability.

When two soil coefficients α and β have been determined, the effective degree of saturation S_e of soil can be calculated by Eq. 1, 2, the water pressure or suction of soil of Eq. 1, 2 can be easily achieved from the results of groundwater flow analysis.

3.2 *Relationship of the degree of saturation (Se) and resistivity (ρ)*

In unsaturated state, the resistivity of soil can be written as Eq. 4. It means that the reverse of resistivity is equal the sum of ratio of air volume and resistivity of air, ratio of the volume and the resistivity of water, ratio of the volume and the resistivity of soil particle

$$\frac{1}{\rho} = \frac{V_a}{\rho_a} + \frac{V_w}{\rho_w} + \frac{V_s}{\rho_s} \tag{4}$$

$$V_a + V_w + V_s = 1 \tag{5}$$

where ρ is resistivity; ρ_a, ρ_w, ρ_s are the resistivity of air, water and soil particle repetitively; V_a, V_w, V_s are the volume of air, water and soil particle in soil block repetitively.

From Eq. 4 and 5, we can know that the degree change of saturation of soil is also able to cause the change of resistivity. Therefore, it is possible to establish a relationship between the apparent resistivity and the effective degree of saturation. Archie (1942) had suggested a equation between the apparent resistivity and the effective degree of saturation

$$\frac{\rho_{unsat}}{\rho_{sat}} = \frac{1}{(S_r^{dc})^m} \tag{6}$$

where ρ_{sat} is the resistivity of saturated state; ρ_{unsat} is the resistivity of unsaturated state; m is a test coefficient and usually $m = 2.0$.

In other way, the variation ratio of resistivity has been calculated easily in continuity measurement of resistivity, and the variation ratio of resistivity can be indicated as

$$C_s = \frac{(\rho_{unsat} - \rho_{sat})}{\rho_{sat}} = \frac{\rho_{unsat}}{\rho_{sat}} - 1 \tag{7}$$

Therefore, Eq. 6 can be also rewritten as the function of C_s and S_r.

A test set used to measure the relationship of resistivity and volumetric water content or the effective degree of saturation has been showed in Figure 2 (Takeshita, Y. & Inoue, M. et al. 1993).

For the TOYOURA sand, a pF test of soil column was used to measure the variation of the apparent resistivity with water drying process. Test results showed that the relationship between the degree of saturation

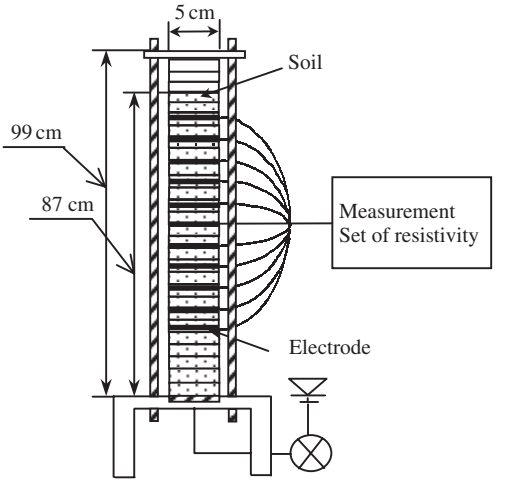


Figure 2. Test set of soil column for measuring the variety of resistivity with draining (Takeshita, Y. & Inoue, M. et al. 1993).

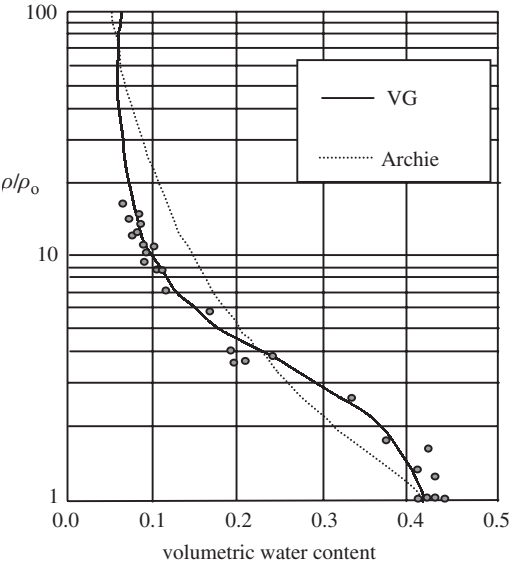


Figure 3. Relationships of apparent resistivity and volumetric water content (Takeshita, Y. & Inoue, M. et al. 1993).

Copyright © 2003 Swets & Zeitlinger B.V., Lisse, The Netherlands

and the apparent resistivity is fitted goodly by VG equation (Takeshita, Y. & Inoue, M. et al. 1993).

$$\frac{\theta-\theta_r}{\theta_s-\theta_r}=\left\{1+\left|\alpha\left(\frac{\rho_{unsat}}{\rho_{sat}}\right)\cdot\right|^{\beta}\right\}^{1/\beta-1} \tag{8}$$

Although Eq. 8 is much better than Eq. 6 in fitting the measured results, it is convenient to use Eq. 6 for calculating the degree of saturation from apparent resistivity.

3.3 *Inverse analysis method for determining the coefficients α and β*

The inverse analysis method is an effective method in determining the unknown parameters using filed observation data. We will use Non-linear Least squares method to estimate the test coefficients α and β in this paper. The degree of saturation S_r obtained from resistivity measurement is used as the observation value of objection function. The sum of residual squares about the degree of saturation can be calculated by

$$R(b)=\sum_{i=1}^{n} W_j\{S_i^{dc}-S_r\}^2 \tag{9}$$

where S_i^{dc} is observation data of the degree of saturation; S_r is calculated the degree of saturation; W_j is a set of weighting coefficients; **n** is total number of observation for S_i^{dc} ($i=1,2,3,\ldots,$ n); **b** is a **m** order vector of unknown parameters; **m** is total number of unknown parameters ($j=1,2,3,\ldots,$ m).

The Gauss-Newton optimization method (Sun 1994) is used to minimize Eq. 9. The matrix form can be obtained as

$$A^{T(0)}\cdot A^{(0)}\cdot \Delta b^{(0)}=A^{T(0)}(dS_r)^{(0)} \tag{10}$$

where

$$(dS_r)^{(0)}=(S_r^{dc})_{j^i}-f_j(b)^{(0)} \tag{11}$$

b presents all unknown parameters; Δb is a increase vector of unknown parameters (α and β); $A^{[\mathrm{n}\times\mathrm{m}]}$ is called the sensitivity matrix which consist of the derivatives of functions $f_1(b)$, $f_2(b),\ldots,$ $f_n(b)$ with respect to the variation of each parameters $b_1, b_2,\ldots,$ b_m ($\partial f_i(\mathrm{b})/\partial b_j$). The subscript (0) is used to denote a set of time.

Since **n** is usually much large than **m**, it is not a square matrix. And Δb can be represented in matrix form as following

$$\Delta b^{(0)}=(A^{T(0)}\cdot A^{(0)})^{-1}A^{T(0)}(dS_r)^{(0)} \tag{12}$$

Therefore, the modified unknown parameters vector can be obtained directly from Eq. 12, it can be written as

$$b^{(\mathrm{k}+1)}=b^{(\mathrm{k})}+\Delta b^{(\mathrm{k})} \tag{13}$$

In this paper, unknown parameter vector b can be replaced as

$$b=\{\alpha_1,\beta_1,\alpha_2,\beta_2,\ldots,\alpha_m,\beta_m\} \tag{14}$$

Therefore, a set of $(S_r^{dc})_i^{t0}$ $(t_0,t_1,t_2,\ldots,t_{\max};\ i=1,2,\ldots,n)$ can be used to calculate a set of the test coefficients α_j and β_j ($j=1,2,\ldots,m$).

4 APPLICATION AND ANALYSIS EXAMPLE

4.1 *Application problem*

It can be considered this method can be used in following ways.

One is used to estimate or determine the soil coefficients of water characteristic curve by the resistivity variation of soil mass during rain process or watering process. It means that the resistivity variation of soil mass can be easily measured with groundwater change or unsaturated flow in all positions and in any time. Usually, the rainfall or pumping well can cause the ground water changes in ground model.

If the velocity variation of ground water is also able to cause the variation of resistivity in soil layer, this method is used to detect a hollow in saturated clay layer. In general, due to the resistivity values of saturated clay and the water stored in the hollow are very low and have not obvious difference, it is difficult to inquiry the place of a hollow in saturated clay layer only using the resistivity inquiry method now. As we known, because the permeability of both saturated clay party and the hollow party in soil layer have obvious difference, when pumping well test is performed the velocity of ground water flow in both party of hollow and other clay party have also obvious difference. In according to this characteristic, it is able to give a permeability distribution about soil layer by the union analysis method. With this help of permeability distribution in soil layer, the place of hollow can be determined more accurately. Therefore we think that it is impossible for researching the relationship among hydraulics behavior and resistivity of soil. In other paper, we will continue to discuss the application case about this method, and a lot of filed data will be applied to insure the reasonableness of this method.

4.2 *Analysis example*

For showing the application of union analysis method presented in this paper, a pF test process showed in

Copyright © 2003 Swets & Zeitlinger B.V., Lisse, The Netherlands

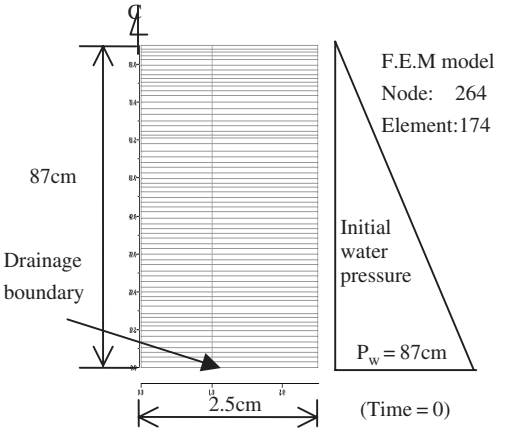


Figure 4. Calculation model for inverse analysis of groundwater flow F.E.M.

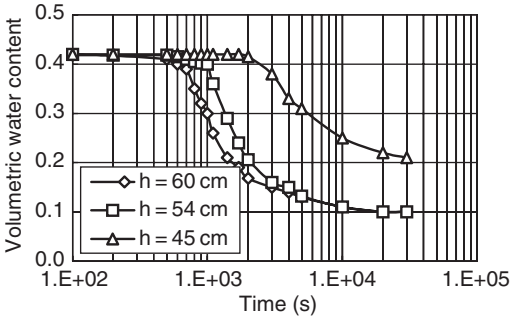


Figure 5. Curve of volumetric water content with time change by $\rho_{unsat}/\rho_{sat} - \theta$.

Figure 2 has been analyzed. The height of the test sample has 87 cm, and diameter is 5 cm. The measurement points about resistivity have been set between the 24 cm and 60 cm high. Test sample is TOYOURA sand, its saturated permeability K_s is 2.3×10^{-3} cm/s, the volumetric water content θ_s in saturated state is 0.42, and $\theta_r = 0.05$. Eq. 8 is used to calculate the volumetric water content change with time. The two soil coefficients α and β in Eq. 8 are 0.38 and 3.80 which were determined by test results. The soil column set is considered as an axis-symmetry model shown in Figure 4 for groundwater flow analysis.

The curves of volumetric water content with time in each measurement points of resistivity (electrodes of Figure 2) have been achieved, the part results of which is shown in Figure 5. And those curves can be used as measured data in inverse analysis of water seepage F.E.M to estimate the two coefficients α and β of Eq. 1 and 2. The average calculating results of α and β in the model are 0.038 and 7.38. The test results of

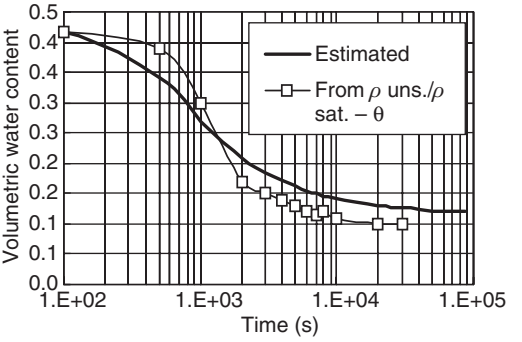


Figure 6. Curves of volumetric water content with time (h = 60 cm).

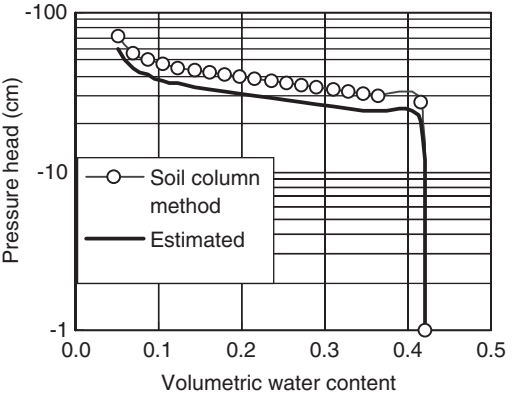


Figure 7. Water characteristic curve.

α and β by soil column are 0.027 and 8.0. The comparison about the curve of volumetric water content with time in height 60 cm is shown in Figure 6, and the comparison about the water characteristic curve is shown in Figure 7. By those comparison results we can think that it is suitable to estimate the test coefficients of water characteristic curve only by resistivity measurement.

5 CONCLUSION

The research results above can be concluded as following:

1. It is considered that an union analysis method included resistivity analysis and groundwater flow F.E.M presented in this paper can be used to raise the investigation accuracy and low the cost in many investigating projection.
2. Analysis results about a pF test example showed that is suitable to estimate the test coefficients of

Copyright © 2003 Swets & Zeitlinger B.V., Lisse, The Netherlands

water characteristic curve only by the resistivity measurement.

In future, there are many analysis works need to be performed in verifying the suitability of this method.

REFERENCES

Archie, G.E. 1942. The electrical resistivity log as an aid in determining some reservoir characteristics. AIME, 146: 54–62.

Fredlund, D.G. & Rahardjo, H. 1993. *Soil mechanics for unsaturated soils*. John Wiley & Sons, Inc.

Nishida, N. & Aoyama, C. 1993. The Characteristics of resistivity of the unsaturated soil and the application of electric prospecting for evaluation of seepage flow through the ground. *J. of Geotechnical Enginering* 475: 1–9 (in Japanese).

Takeshita, Y., Inoue, M., Ono, T. & Kohno, I. 1993. Properties of resistivity on the unsaturated seepage flow. Proceeding of the 88th SEGJ conference: 217–220 (in Japanese).

Van Genuchten, M.T. 1980. A closed-form equation for predicting the hydraulic conductivity of unsaturated soils. *Soil Sci. Soc. Am. J*. 44: 892–898.

Sun, N.Z. 1994. *Inverse problems in groundwater modeling.* Kluwer academic publisher 15–37.

Wada, T. & Inoue, M. et al. 1995. Downward infiltration of rain water by using continuous electric prospecting within Pyroclastic Plateau (Shirasu-Daichi) in southern Kyushu, Japan. *J. of the Japan society of engineering geology* 36(5): 29–38 (in Japanese).

Copyright © 2003 Swets & Zeitlinger B.V., Lisse, The Netherlands

A study on clogging characteristics of recharge well depended on hydraulic gradient

T. Shimizu & M. Aoki
Takenaka Corporation, Chiba, Japan

ABSTRACT: The objective of this study is to gain an understanding of the clogging characteristics of a recharge well. In-situ step recharge test was performed to obtain the capacity of a recharge well. Test result at step intervals of 1 hour was compared with the result at step intervals of 24 hours. Using the test results, we examined the method of step recharge test, capacity of a recharge well, hydraulic conductivity in recharge condition and critical hydraulic gradient to avoid the clogging of a well. Last, we measured sand-extraction at pumping. Measurements at continuous pumping were compared with measurements at cyclic pumping. Using the results, we examined effective washing of a recharge well in order to avoid clogging.

1 INTRODUCTION

Recharge well method is a procedure for injecting ground water into the aquifer with recharge wells, which have the same construction as deep wells. The main objective is to avoid drawdown of the surrounding groundwater. Recent years have seen increasing applications for the recharge well method, such as the remediation of contaminated groundwater or aquifer thermal energy storage system (ATES). Its use is no longer limited to short-term temporary applications during engineering work, as needs for the long-term use of recharge installations grow.

No clear design methodology has been established for planning an application of the recharge well method, and in many cases the design is based on the same procedures as the deep well method. But the design of a recharge well method installation involves many undetermined factors aside from the hydrogeological properties of the ground. So in practice much is decided on the basis of the engineers' experience. Most difficult problem is a prediction of the loss of recharge capacity that may result from the clogging of the recharge well. Possible causes of clogging are reported to be the quality of the water injected into the well, the quality of the well installation work, and the pressure at which the water is injected (PWRI et al. 1993), but the reports are mostly based on specific cases, and very few give quantitative evaluations. This study reports the procedure used for in-situ recharge tests carried out to ascertain the clogging characteristics depended on the injection water pressure, and the knowledge gained from the test results.

2 CLOGGING CHARACTERISTICS OF RECHARGE WELLS

A conceptual diagram for the clogging of a recharge well is shown in Figure 1. In cases where clogging is caused by the injection water pressure, a decrease of hydraulic conductivity has been reported as resulting from the realignment of soil particles in the aquifer around the well during injection (PWRI et al. 1993).

Step-recharge tests were proposed as a method to investigate this phenomenon (PWRI et al. 1993). A conceptual diagram of a step-recharge test is shown in Figure 2. The water level inside the recharge well

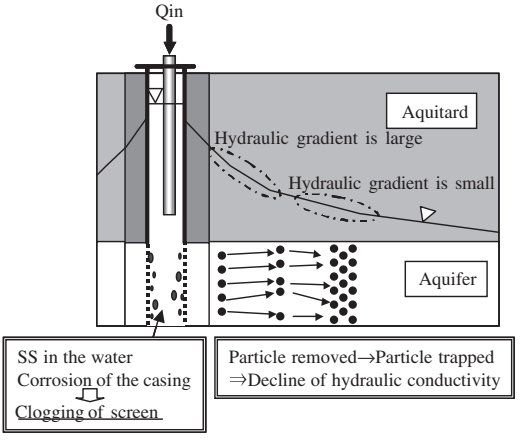


Figure 1. Concept of clogging for recharge well.

Copyright © 2003 Swets & Zeitlinger B.V., Lisse, The Netherlands

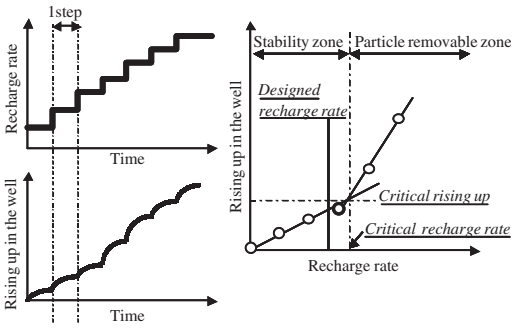


Figure 2. Concept of step-recharge test.

is rise in steps, and the recharge rate and the water level in the well are measured in order to determine critical recharge rate and critical rising up. But the step-recharge tests proposed are very time-consuming because they are based on obtaining a steady state water level and steady state recharge rate at each step. Also, under conditions where a large volume of water is injected, it is possible that clogging may occur during the test, and making it impossible to obtain a steady state water level.

For this study, the clogging characteristics of recharge wells were investigated through past step-recharge tests in-situ, and also through carrying out shortened step-recharge tests, in which the risk of clogging occurring during the tests is small, and examining the validity of the test results. Further, for washing, which is carried out to counter any gradual loss of recharge well capacity over time, an effective method with pumping method was examined.

3 OUTLINE OF TESTS

The constitution of the test ground is shown in Figure 3. From the surface to a depth of 6.4 m there are cohesive soil sediments, and below them fine sandy layers reach a depth of 45 m. The sands change gradually in their characteristics and can be divided into 4 types. The specifications of the test wells and their layout are shown in Figure 4. Two deep wells had 32 m depth, with boreholes 0.6 m in diameter. The diameter of the casing pipes was 0.35 m, and the screens were installed between the depths of 14 m and 30 m. Stainless steel casing pipes were selected because of steel's excellent corrosion resistance. A coarse sand filter material was used between the depths of 5.5 m and 32 m. Two deep wells (DW1, DW2) were drilled at positions 20 m apart. In addition, five observation wells were drilled around DW1 and one observation well was drilled near DW2.

A pump was installed in each deep well, and the ground water pumped from one well was then injected

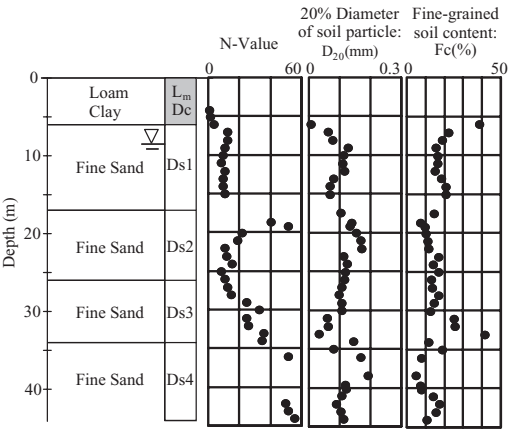


Figure 3. Constitution of ground.

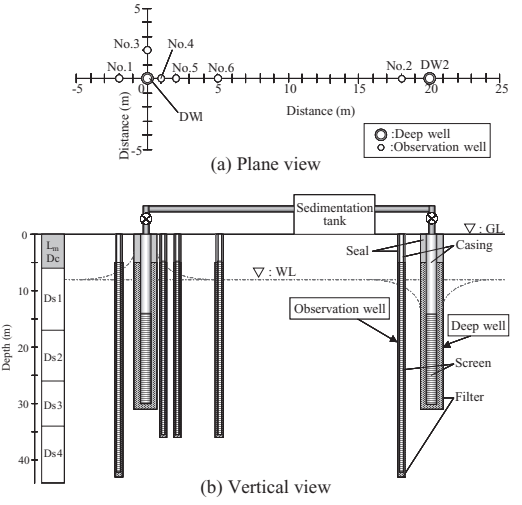


Figure 4. Specifications and layout of wells.

into the other. Both wells were equipped for both pumping and injecting, and the flow rate was controlled. The fine-grained soil in the pumped ground water was prevented from being injected into the recharge well by installing a sedimentation tank in the piping to remove it. Measurements were taken automatically using a water pressure transducer to measure the groundwater level in each well and an electromagnetic flow gauge to measure the flow rate. Measurements were made at one-minute intervals.

In order to check whether or not the ground water contained material that could possibly lead to clogging, the quality of the ground water was analyzed.

The results of groundwater quality analysis are shown in Table 1.

The tests performed are listed in Table 2.

Copyright © 2003 Swets & Zeitlinger B.V., Lisse, The Netherlands

Table 1. Results of water quality analysis.

Item	Unit	Value
pH		6.4
BOD	mg/L	27
COD	mg/L	25
SS	mg/L	35
Dissolved Iron	mg/L	0.11
Total Iron	mg/L	2.52
Iron Bacterium		ND
Langelier Index		−1.2
Temperature	°C	15

Table 2. List of tests.

Test	DW	Objective
Step-Drawdown Test	1,2	Pumping Capacity
Pumping Test	1	Hydraulic Conductivity
Step-Recharge Test		Recharge Capacity
*1step-per-hour	1,2	(Clogging Characteristics)
*1step-per-24hours	1	
Sand Extraction Test	1	Washing Method for a Well

4 TEST RESULTS

First, pumping tests were carried out to ascertain the hydrogeological properties. The coefficient of hydraulic conductivity, calculated by Thiem's method (Wenzel, 1932, 1936), was found to be 3.09×10^{-3} cm/sec. Results of Step-drawdown test are shown in Figure 5 and Table 3. Steady state water level was almost shown with each stage as well in one hour.

Results of 1step-per-hour step-recharge test are shown in Figure 6 and Table 4. As well as the result of step-drawdown test, steady state water level was almost shown with each stage as well in one hour.

The results of 1step-per-24hours step-recharge test are shown in Figure 7 and Table 5.

A steady state water level was confirmed to STEP4. But, water level rose gradually, and steady state water level was not confirmed in STEP5 and STEP6. It is expected that clogging occurred and progressed. So the resistance against the injecting water increased. Therefore, it considers having the possibility not to confirm steady state water level when test time is extended on the condition which the amount of recharge rate.

Figure 8 shows the results of step-recharge tests of 1step-per-hour and 1step-per-24hours for DW1. From both tests, the relation between the rising up in the well and the recharge rate can be approximated to bilinear lines. The lines on the left are considered to indicate the stability zone where the recharge rate is smaller than the recharge well's capacity. The points at which the gradients are large can be considered that the recharge

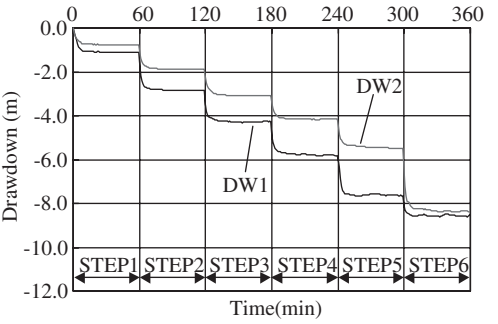


Figure 5. Results of step-drawdown tests.

Table 3. Results of step-drawdown test (1step-per-hour).

Step	DW1 Qout	dh	DW2 Qout	dh
1	0.098	−1.10	0.095	−0.75
2	0.198	−2.85	0.199	−1.90
3	0.295	−4.30	0.293	−3.10
4	0.393	−5.85	0.385	−4.15
5	0.484	−7.65	0.483	−5.50
6	0.512	−8.60	0.661	−8.40

Qout: Pumping rate (m^3/min); dh: Drawdown (m).

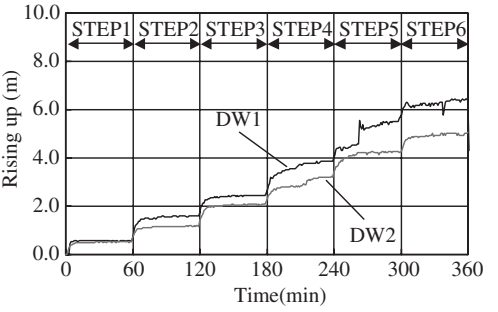


Figure 6. Results of step-recharge test (1step-per-hour).

Table 4. Result of step-recharge test (1step-per-hour).

Step	DW1 Qin	dh	DW2 Qin	dh
1	0.053	0.60	0.049	0.55
2	0.104	1.60	0.099	1.15
3	0.150	2.45	0.150	2.10
4	0.199	3.85	0.200	3.20
5	0.245	5.50	0.251	4.25
6	0.278	6.45	0.290	5.00

Qin: Recharge rate (m^3/min); dh: Rising up (m).

Copyright © 2003 Swets & Zeitlinger B.V., Lisse, The Netherlands

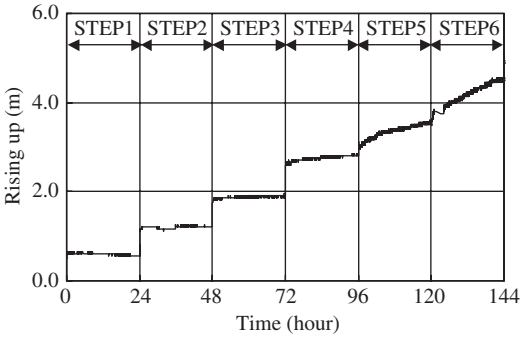


Figure 7. Results of step-recharge tests (1step-per-24 hours).

Table 5. Result of step-recharge test (1step-per-24hours).

Step	Qin	dh DW1	No. 1	No. 3	No. 4	No. 5	No. 6
1	0.050	0.55	0.40	0.15	0.30	0.25	0.00
2	0.104	1.21	0.88	0.40	0.72	0.61	0.23
3	0.150	1.91	1.37	0.70	1.12	0.94	0.39
4	0.202	2.80	1.99	1.05	1.63	1.35	0.59
5	0.244	3.56	2.27	1.35	1.93	1.59	0.83
6	0.266	4.89	2.81	1.54	3.20	2.07	1.12

Qin: Recharge rate (m^3/min); dh: Rising up (m).

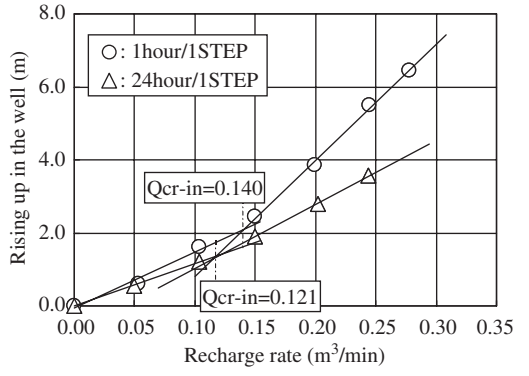


Figure 8. Results of step-recharge tests.

rate exceeds the recharge well's capacity. For both tests, as in the evaluation of results for step-drawdown tests (JGS, 1995), the intersections of the two lines were taken as indicating the critical recharge rate and critical rising up. The critical recharge rate was found to be 0.140 m^3/min from the 1step-per-hour step-recharge test, and 0.121 m^3/min from the 1step-per-24hours test. These are relatively close values.

Comparisons of the results of 1step-per-hour step-recharge tests and step-drawdown tests for DW1 and

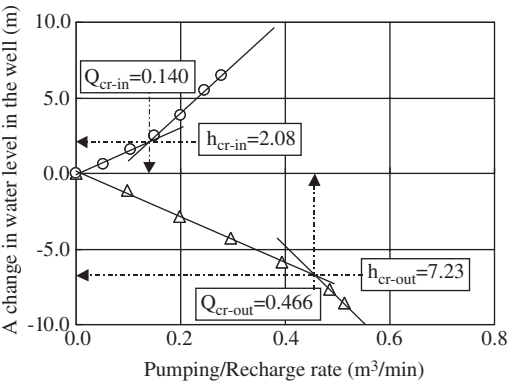


Figure 9. Comparison critical pumping rate with critical recharge rate (DW1).

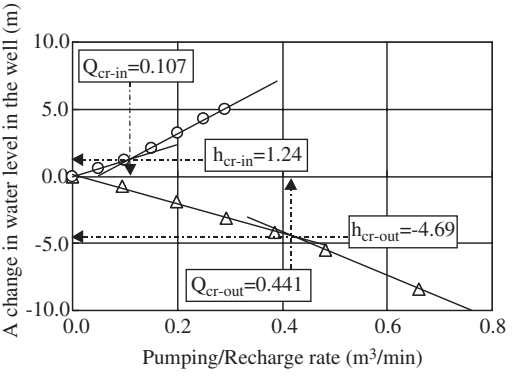


Figure 10. Comparison critical pumping rate with critical recharge rate (DW2).

DW2 are shown in Figure 9 and Figure 10. For both wells, the critical recharge rate is smaller than the critical pumping rate. And the former is between 1/3 and 1/4 the value of the latter. This is thought to be due to a removal of the fine-grained soil, which affects its hydraulic conductivity, in the ground close to the well, because of the large hydraulic gradient. When water is pumped, the fine-grained soil is sucked into the casing pipe and does not impede hydraulic conductivity. But when water is injected, the removed fine-grained soil is trapped in the ground and adversely affects the hydraulic conductivity.

Figure 11 shows that the critical recharge rate and critical rising up depend on the fine-grained soil content. It indicates that the lower the fine-grained soil content, the higher the critical recharge rate and critical rising up.

Next, from an earlier evaluation formula based on the results of 1step-per-24hours step-recharge tests, the clogging zone and the coefficient of hydraulic conductivity in the clogging zone were calculated.

Copyright © 2003 Swets & Zeitlinger B.V., Lisse, The Netherlands

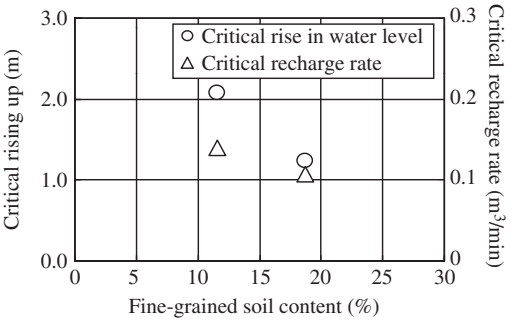


Figure 11. Relation between fine-grained soil content and recharge capacity.

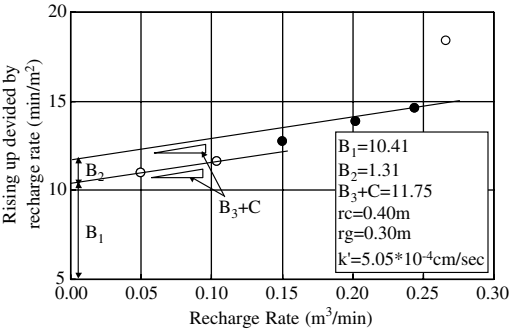


Figure 13. Determination of clogging zone.

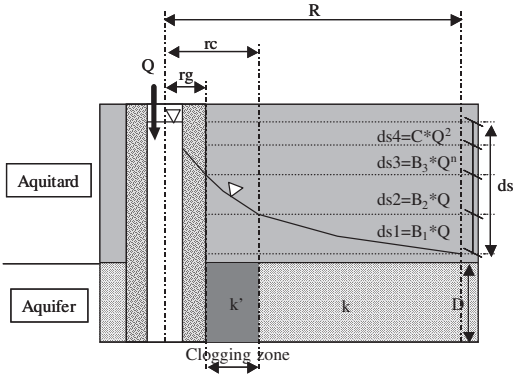


Figure 12. Calcualtion model for clogging of recharge well.

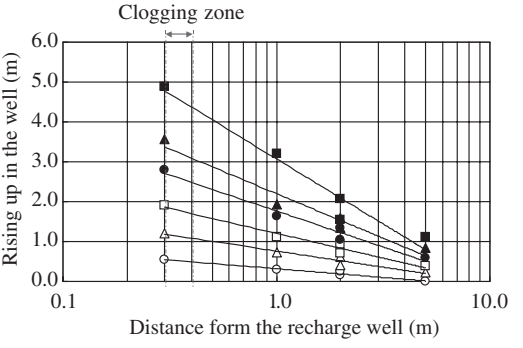


Figure 14. Distribution of water levels around recharge well.

How to calculate this is shown in the following (PWRI et al. 1993).

$$B_1 = \frac{\log\left(\frac{R}{rc}\right)}{2\pi Dk} \quad (1)$$

$$B_2 = \frac{\log\left(\frac{rc}{rg}\right)}{2\pi Dk'} \quad (2)$$

where ds1 = aquifer loss; ds2 = clogging loss, ds3 = turbulent flow loss; ds4 = well loss; ds = total loss; B_1 = aquifer loss coefficient; B_2 = clogging loss coefficient; B_3 = turbulent flow loss coefficient; n = Parameter to change in the range of 2 from 1, C = Well loss coefficient; Q = recharge rate; R = radius of influence; rc = radius of clogging zone; D = thickness of aquifer; k = hydraulic conductivity coefficient of aquifer; rg = radius of filter zone; k' = hydraulic conductivity coefficient of clogging zone.

The results, shown in Figure 13, indicate that the clogging zone is an extremely narrow 10 cm width extending from the outer edge of the well's filter. Further, the coefficient of hydraulic conductivity in the clogging zone is 5.05×10^{-4} cm/sec. It is about 1/6 times as high as the coefficient of hydraulic conductivity in original ground, which is 3.09×10^{-3} cm/sec.

Figure 14 shows the rising up measured at the observation wells, during the 1step-per-24hours step-recharge tests.

Using Thiem's method, the average coefficient of hydraulic conductivity was found to be 1.13×10^{-3} cm/sec. This is lower than the 3.09×10^{-3} cm/sec coefficient of hydraulic conductivity that was determined through pumping tests. This low value can be attributed to the effect of the clogging zone around the well.

Taking the clogging zone as a width of 10 cm around the well, the relation between the hydraulic gradient in the clogging zone and the recharge rate is shown in Figure 15. As with the relation between the rising up and the recharge rate, the relation between the hydraulic gradient in the clogging zone and the recharge rate can be approximated to bilinear lines. From this, the hydraulic gradient corresponding to the critical recharge rate was determined to be 1.24. This

Copyright © 2003 Swets & Zeitlinger B.V., Lisse, The Netherlands

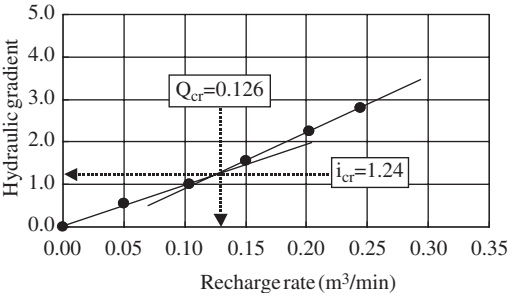


Figure 15. Relation between hydraulic gradient and recharge rate.

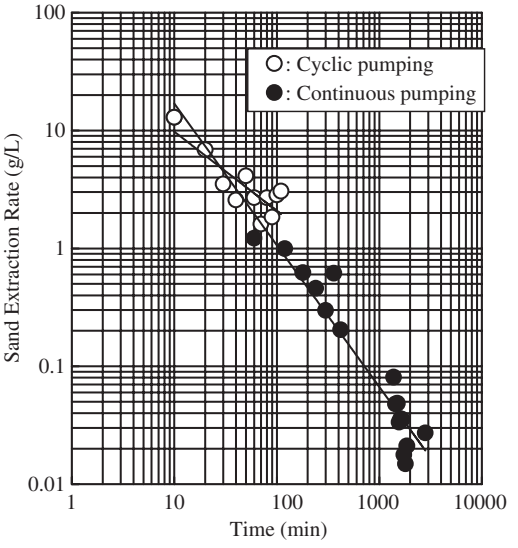


Figure 16. Change over time in sand-extraction.

is comparatively close to the value of 1.0 for the minimum hydraulic gradient in fine sand (the hydraulic gradient at which fine particles begin to remove) determined through laboratory tests, which was reported in an earlier paper (Nishigaki, 1991).

Figure 16 shows the sand-extraction changed with time during the well washing that took place after the recharge tests. Two methods were used for the well washing. One was the cyclic pumping the other was the continuous pumping. For the cyclic pumping, the pump was stopped and started at 10 minutes intervals. The time parameter was the accumulated time, not including the periods of pump inactivity. It was found that in both cases, the sand-extraction declined over time. And fine sand was extracted more with cyclic pumping than with continuous pumping. This indicates that for washing a recharge well, cyclic pumping is expected to be more effective than continuous pumping, at extracting the fine-grained soil that causes clogging.

5 CONCLUSION

Using two deep wells installed in the fine sand layers, in-situ tests were carried out to ascertain the clogging characteristics caused by the injection water pressure during the operation of the recharge well method. And knowledge was gained that can be applied to the designing and operation of the recharge well method.

The following knowledge could be obtained from in-situ step-recharge test.

1. The critical recharge rate can be found by the 1step-per-hour step-recharge test.
2. The critical recharge rate was smaller than the critical pumping rate, and it was about 1/4 from 1/3.
3. The lower the fine grain content, the higher the critical recharge rate and the critical rising up.
4. At the ground composed of fine sand, the hydraulic gradient corresponding to the critical recharge rate was determined to be 1.24.
5. Hydraulic conductivity in recharge condition was lower than that in pumping condition, because of the clogging zone around the recharge well.
6. Fine sand was extracted more with cyclic pumping than with continuous pumping.

To prevent the clogging of a recharge well which was dependent on the hydraulic gradient, it is effective that designed recharge rate is set less than the critical recharge rate. If the water level in the well reaches the critical rising up, it should be washed the well with cyclic pumping.

In the future, using accumulated data from step-recharge tests and long-term recharge, it is hoped that a methodology is established for the designing and operating of the recharge well method in a way that assure long-term durability.

Finally, the data from in-situ tests was measured as a part of the research commissioned for 'Development of hybrid HVAC and hot water supply system using regenerable energy' in 2001, as a part of 'Recyclable Housing Technology Development Project' by Ministry of Economy, Trade and Industry.

REFERENCES

PWRI, et al. 1993. A technological manual for groundwater environment in the underground space construction, Design and Construction Practice of Recharge well method, *Public Works Research Institute (PWRI) of The Ministry of Construction, Government of Jalan*, 14–28.

Copyright © 2003 Swets & Zeitlinger B.V., Lisse, The Netherlands

Wenzel, L.K. 1932. Recent investigations of Thiem's method for determining permeability of water-bearing materials, *Trans. Amer. Geopys. Union*, HY. 313–317.
Wenzel, L.K. 1936. The Thiem's method for determining permeability of water-bearing materials, *USGS Water-Supply Paper*, 679–A.
JGS 1995. Standard of Japanese Geotechnical Society for ground survey method, *Japanese Geotechnical Society*, 296–304.
Nishigaki, M. 1991. A study on clogging characteristics of recharge well method, Proceedings of 46th JSCE Annual Conference, *Japanese Society of Civil Engineers*, 912–913.

Copyright © 2003 Swets & Zeitlinger B.V., Lisse, The Netherlands

Studies on natural and artificial recharge mechanisms in diluvial upland using ^{222}Rn concentration in groundwater as tracer

S. Ishida, M. Imaizumi, T. Tsuchihara & M.A. Fazal
National Institute of Rural Engineering, Tsukuba City, Japan

ABSTRACT: Long-term monitorings of ^{222}Rn concentration in groundwater in the upper part of a saturated zone are carried out to clarify the recharge mechanisms caused by rainfall and artificial recharge in diluvial upland. In the case of artificial recharge, the unsaturated water is pushed out by recharge water, then recharge water reaches the saturated zone. In the case of natural rainfall, ^{222}Rn concentration right under the groundwater table fluctuates from 2 to 12 Bq/l due to seasonal precipitation. Infiltration velocity of natural rainfall is slower than that of saturated downward flow even when unsaturated downward flow occurs.

1 INTRODUCTION

The ^{222}Rn concentration in groundwater is a useful hydrogeological tool for analyzing groundwater flow because ^{222}Rn concentration in groundwater is tens or thousands times higher than that in surface water and there is a unique concentration due to ^{226}Ra content in each aquifer (Hamada & Komae 1996). Hamada & Komae (1998) extended the scope of utilization of ^{222}Rn concentration in groundwater as a tracer to studies on water movement in unsaturated zones. They showed that ^{222}Rn concentration in groundwater in the upper part of a saturated zone is a useful indicator for detecting the existence of downward movement of water (unsaturated downward flow) to the saturated zone through an unsaturated zone in lowland paddy fields, where irrigation water moves downward for several months. A detailed understanding of the recharge mechanisms is needed for the protection and conservation of groundwater against contamination from nitrogen fertilizer in agricultural upland areas. However, studies on recharge mechanisms in upland areas are rare. When the rainfall infiltrates from surface of the earth, water reaches at the groundwater table while changing the amount of moisture of the unsaturated zone (Shiozawa 1997). Andersen & Sevel (1974), Imaizumi et al. (2000) clarified infiltration velocity of natural rainfall is very slow in the unsaturated zone by natural rainfall.

In this paper, the authors discuss how water infiltrates underground in the case of artificial recharge and natural rainfall in diluvial upland from the distribution of ^{222}Rn concentration in groundwater.

2 ARTIFICIAL RECHARGE

2.1 *Study area*

The district of Uonuma, Nagaoka city, Niigata prefecture, Japan, is 4 km from the Shinano river (Fig. 1).

The study area is situated in diluvial upland at the elevation of about 100 m above sea level. The geological structure of the upland consists of surface loam of about 2 m thick, sand and gravel of about 8 m thick, sandy silt of 30 cm thick, coarse sand of 1 m thick, and silt basement (Fig. 2). Aquifers are found in the sand and gravel and coarse sand. Groundwater exists 10–11 m below the surface. The hydraulic conductivity of the sand and gravel is on the order of 10^{-3} cm/sec and that of loam is of the order of 10^{-4} cm/sec by analysis of grain size and permeability tests.

2.2 *Artificial recharge*

Ministry of Agriculture, Forestry and Fisheries (MAFF) had experimented on artificial recharge of groundwater several times in the past (Ishida et al. 1993). In this time artificial recharge is carried out for 5 days by Hokuriku Regional Agricultural Administration Office, MAFF, Japan. 10 hours of continuous recharging is carried out per day. River water is pumped up and allowed to flow through a recharge pond (drain pit) of 200 cm (diameter) × 230 cm (depth) to the field. A gravel layer of about 9 m in depth is placed in the unsaturated zone beneath the drain pit. Groundwater is collected at 1-hour intervals from observation wells using sampling tubes. The distance

Copyright © 2003 Swets & Zeitlinger B.V., Lisse, The Netherlands

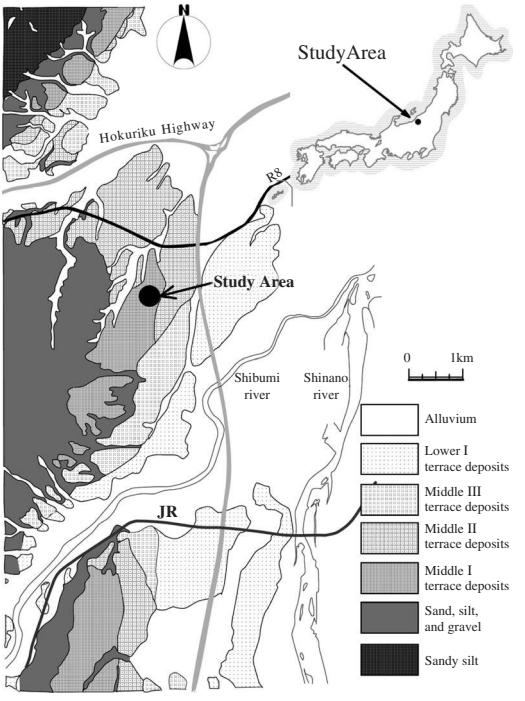


Figure 1. Geological location map of the study area.

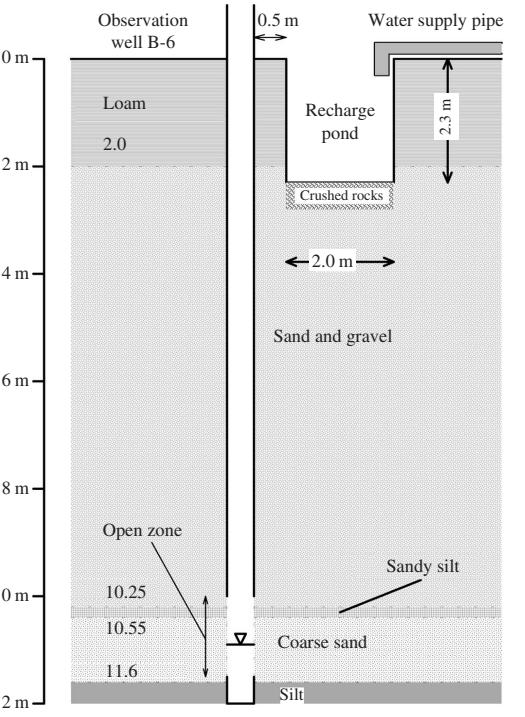


Figure 2. Geological section of the study area with artificial recharge mechanism.

between the observation wells and recharge pond is about 50 cm (B-6) and 65 cm (B-6III).

To measure ^{222}Rn, the extraction method with toluene is used. Radioactivity is measured with a liquid scintillation counter (Packard 2250CA). The detection limit is 0.1 Bq/l.

2.3 *Results*

The maximum initial recharge speed is found to be 1.2 m^3/hour but decreases during the recharge period due to clogging. The average recharge speed is 0.7 m^3/hour (Table 1). During the artificial recharge, the precipitation is only 5 mm.

The ^{222}Rn concentration of recharged water (river water) varies from 0.00 to 0.18 Bq/l. This differs from the original ^{222}Rn concentration of groundwater, which is over 10 Bq/l.

Figure 3 shows the fluctuation of ^{222}Rn concentration of the groundwater collected from B-6 on the first day of artificial recharge. From the start of recharge to 6 hours after, ^{222}Rn concentration is found to be about 10–12 Bq/l. Then after 7 hours from the start of recharge, ^{222}Rn concentration decreases to about 7 Bq/l and after that becomes about 6–7 Bq/l.

Figure 4 shows the fluctuation of ^{222}Rn concentration of the groundwater collected from B-6III from the start of recharge to 70 hours. ^{222}Rn concentration decreases during the artificial recharge period, at 60 hours the minimum value of about 2 Bq/l is obtained, then reaches about 2–3 Bq/l.

Table 1. Results of artificial recharge.

Day	Average recharge speed (m^3/hour)	Total volume (m^3)
1	1.2	11.2
2	0.8	8.4
3	0.6	5.5
4	0.4	4.1
5	0.4	4.0
Average	0.7	6.6

3 NATURAL RAINFALL

Long-term monitoring of recharge ^{222}Rn concentration in groundwater in the upper part of a saturated zone clarifies the recharge mechanisms caused by rainfall.

3.1 *Study area*

The study was carried out on the site of the National Institute of Rural Engineering, Tsukuba city, Ibaraki

Copyright © 2003 Swets & Zeitlinger B.V., Lisse, The Netherlands

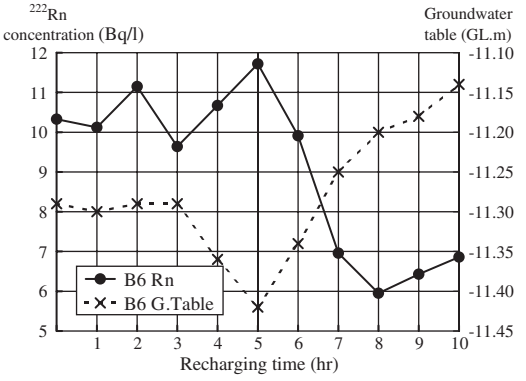


Figure 3. Fluctuation of ^{222}Rn concentration in B-6 observation well (0–10 hr).

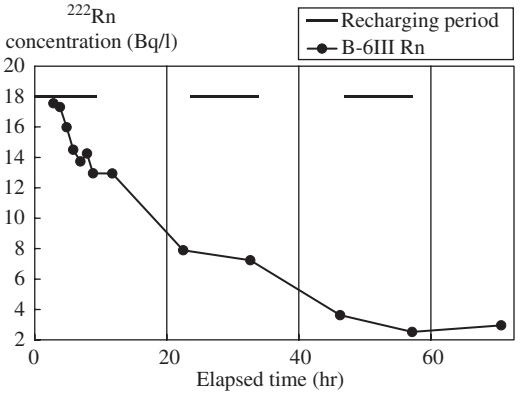


Figure 4. Fluctuation of ^{222}Rn concentration in B-6III observation well (0–70 hr). B-6III is away from the recharge pond by 65 cm.

prefecture, Japan, which is situated in diluvial upland (Fig. 5).

The elevation is about 23 m above sea level. The geological structure of the upland consists of surface loam of about 2.6 m thick, tuffaceous silt of about 2 m thick, and sand basement (Fig. 6). Aquifers are found in the sand and groundwater exists 9–10 m below the surface.

3.2 *Methodology*

To measure ^{222}Rn, the extraction method with toluene is used. Groundwater is collected every week for over 1 year from observation well using a sampling tube, at three sampling points: right under the groundwater table, 15 m depth from the surface and 20 m depth from the surface. The groundwater level, pH, EC, groundwater temperature and precipitation are also measured.

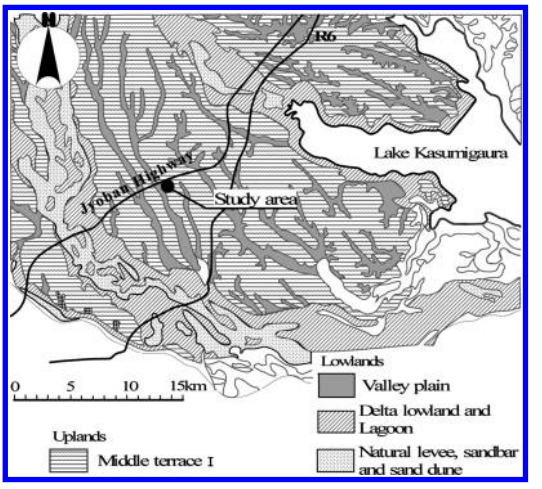


Figure 5. Geological location map of the study area.

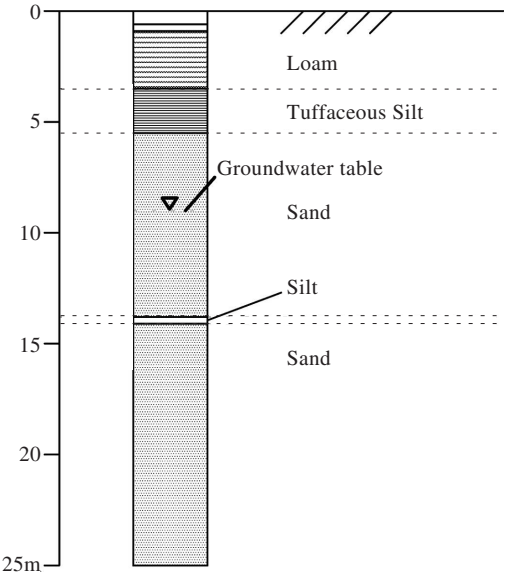


Figure 6. Geological section of the study area.

3.3 *Results*

The ^{222}Rn concentration of groundwater at depths of 15 m and 20 m, are about 8–9 Bq/l and do not fluctuate much, whereas ^{222}Rn concentration right under the groundwater table fluctuate from 2 to 12 Bq/l (Fig. 7).

The fluctuation pattern of ^{222}Rn concentration right under the groundwater table shows that ^{222}Rn concentration decreases after about two months of rainfall in the rainy season in 2000 when much precipitation was recorded. After the rainy season (June and July),

Copyright © 2003 Swets & Zeitlinger B.V., Lisse, The Netherlands

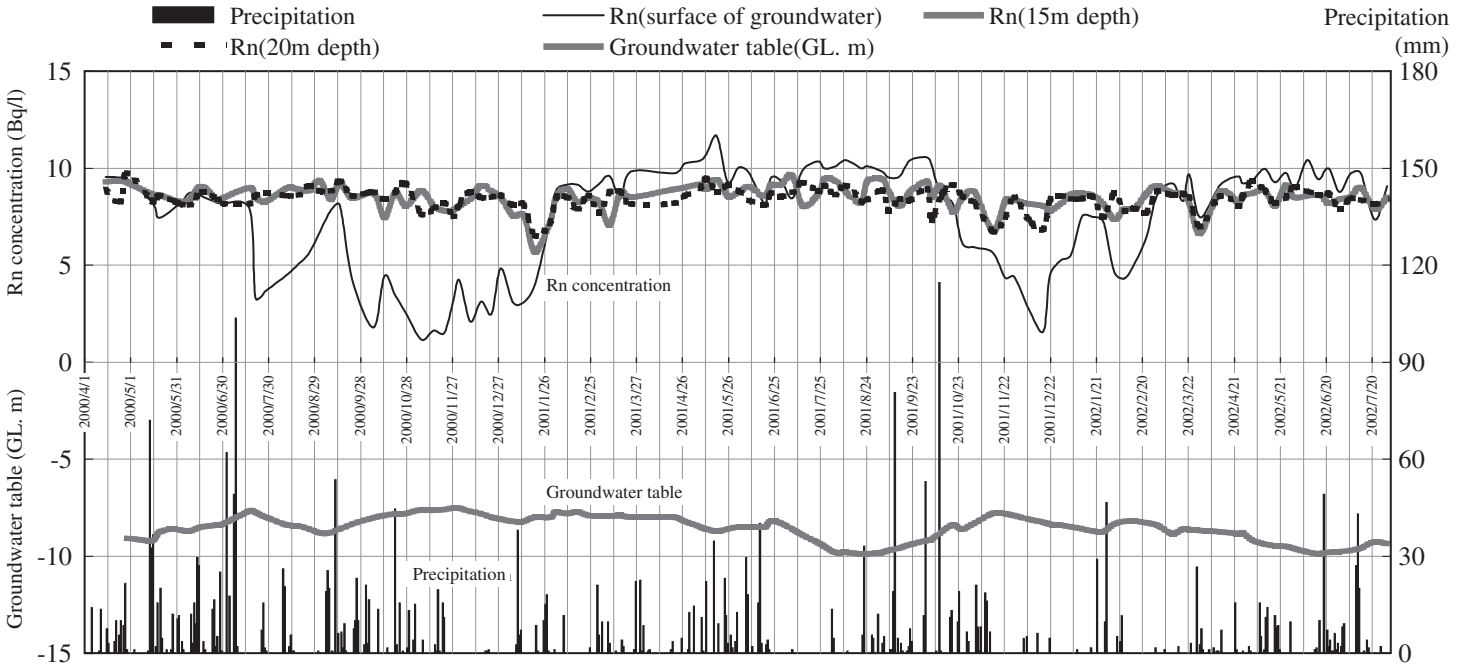


Figure 7. Fluctuation of ^{222}Rn concentration, groundwater table and precipitation.

Copyright © 2003 Swets & Zeitlinger B.V., Lisse, The Netherlands

the concentration is sensitively influenced by rainfall, and after less precipitation (about 1.5 months) the concentration increases remarkably.

In 2001 less precipitation compared with the precipitation in 2000 was recorded in the rainy season, and the concentration does not decrease after the rainy season. But there was much precipitation in August and September and the concentration decreases from the end of October and reaches about 2 Bq/l. After that, the precipitation was 22.5 mm for 68 days, and the concentration increase.

In 2002 less precipitation was recorded in the rainy season too. The concentration does not decrease after the rainy season.

4 DISCUSSION

Figure 3 shows that the ^{222}Rn concentration of groundwater decreases after about 7 hours from the start of recharge, but the ^{222}Rn concentration does not decrease until the recharging of the surface water. So at that time recharged water did not reach the saturated zone directly; it is considered that the downward flow of recharged water pushed out unsaturated water.

Figure 4 shows that the ^{222}Rn concentration decreased to a low level after 60 hours, so it is considered that recharge water reached the saturated zone.

The phenomenon leads to a conceptual model of the recharge mechanism in upland areas that saturated downward flow with a comparatively fast velocity occurs under artificial recharge conditions.

On the other hand, Figure 7 shows that the occurrence of unsaturated downward flow is influenced by the amount of precipitation under natural recharge conditions and infiltration velocity is slower than that of saturated downward flow even when unsaturated downward flow occurs. Moreover, once unsaturated downward flow occurs, the amount of infiltration from the unsaturated zone to the saturated zone by rainfall is higher compared with the amount of infiltration without the occurrence of unsaturated downward flow.

5 CONCLUSION

In this paper, the analysis method using ^{222}Rn in groundwater in the upper part of a saturated zone is proposed to clarify the recharge mechanisms caused by rainfall and artificial recharge. The results obtained are as follows:

1. In the case of artificial recharge, unsaturated water is pushed out by recharge water, then recharge water reaches to the saturated zone.
2. In the case of natural rainfall ^{222}Rn concentration of groundwater at depth of 15 m and 20 m, do not fluctuate so much. On the other hand ^{222}Rn concentration right under the groundwater table fluctuates from 2 to 12 Bq/l by seasonal precipitation.
3. Infiltration velocity of natural rainfall is slower than that of saturated downward flow even when unsaturated downward flow occurs.

REFERENCES

Andersen, L.J. & Sevel, T. 1974. Six years' environmental tritium profile in the unsaturated and saturated zones, Grohoj Denmark, *Isotope Technique in Groundwater Hydrology Vol. 1, IAEA*, 3–20.

Hamada, H. & Komae, T. 1998. Analysis of recharge by paddy field irrigation using ^{222}Rn concentration in groundwater as an indicator, *Journal of Hydrology, 205:* 92–100.

Hamada, H. & Komae, T. 1996. Investigation on Shallow Groundwater in Small Basin Using Natural Radioisotopes, *RADIOISOTOPES, 45*: 71–81.

Ishida, S., Inamoto, A., Kobayashi, I., Nakagawa, K., Fujinawa, K. & Yokoyama, T. 1993. Artificial Recharge of Groundwater in Dune Sand for Use of Thermal Energy, *International Association of Hydrogeologists, Volume 4*, 205–213.

Imaizumi, M., Komae, T. & Nihira, S. 2000. Evaluation of Recharge Mechanism of Confined Groundwater Using Long Term Concentration Records in the Metropolis of Tokyo, *Jour. Japan Soc. Eng. Geol., 41(2):* 87–102.

Shiozawa, S. 1997. Infiltration of rainfall in field. *Hydrology, 27(2):* 117–124.

Copyright © 2003 Swets & Zeitlinger B.V., Lisse, The Netherlands

Estimation method of permeability distributions of rock mass with fracture frequency

A. Kobayashi, S. Aoyama, K. Inoue & I. Fukushima
Kyoto University, Graduate School of Agricultural Science, Kyoto, Japan

ABSTRACT: The data on fracture frequency is easy to get at an in-situ investigation, while permeability tests are not carried out so often because of financial limitation. Thus, it is very valuable to establish a technique to estimate the permeability distribution by using a data easily obtained like the fracture frequency. In this paper, an indicator simulation technique of the geostatistics is tried by using the fracture frequency as a soft data. To improve and develop the technique, the discrete fracture network generation method is applied to estimate the fracture frequency distribution. Which parameter among the statistical information of geometry of fracture is important to estimate the permeability distribution is examined. It is found as a result that the density distribution of fracture is most important.

1 INTRODUCTION

It is a very important subject for geoenvironmental and groundwater pollution problems to grasp the permeability distributions of the ground. The estimation of the permeability distribution has a large effect on the prediction of solute transport because mechanical dispersion occurs due to heterogeneous velocity distribution. If many in-situ permeability tests are carried out, the accuracy of the estimation becomes high. However, in-situ permeability tests are not carried out so often because of financial limitation. Thus, if other kinds of data can be used to estimate the permeability distribution, it is very useful for geoenvironmental problems.

In general, the permeability of ground is distributed with a given spatial correlation. Geostatistics is a useful method to make a heterogeneous permeability distribution according to such a correlation. Kriging, Cokriging, Gaussian Simulation and Indicator Simulation (Deutsch and Journel 1992) have been used for hydrogeological problems. Kriging or Gaussian Simulation uses only hard data, i.e., permeability data, but Cokriging or Indicator Simulation can use many other attributes, which are called soft data. In the case when the number of hard data is small, the method using the other attributes is very useful while the accuracy is very dependent on the soft data.

The problem solved in this paper is the groundwater flow through a fractured rock mass. This problem has become very controversial recently because the high level radioactive waste disposal is planned in deep geology. In this paper, fracture frequency observed in a borehole is used as soft data because the fracture frequency is easily measured. However, the correlation between fracture frequency and permeability is not so high in general. Thus the cumulative probability of permeability for each threshold value of the fracture frequency might not be distinctive. In this case, the fracture frequency does not work effectively as soft data. In this paper, the correlation is emphasized by using the tendency and a given variance. The difference of the range of permeability estimated from the soft data is made clear for each threshold value of fracture frequency. The effectiveness of such a treatment of soft data is examined.

Moreover, the generation method of fracture geometric system has been developed in recent years (Dershowitz 1991). At the test site for this study, many fracture data are obtained, e.g., orientation, trace length and spacing. By making the statistical model of each geometric datum, the fracture system can be realized and the fracture frequency is counted for each element. The cumulative probability functions used in Indicator simulation are applied for each element to estimate the permeability according to the fracture frequency. As a continuous approach, it is examined which parameter among the fracture data is important for the estimation of the permeability distribution.

The interference test is simulated by using the generated permeability distributions and then the calculated hydraulic pressure responses at observation points are compared with the measured ones. The effectiveness of the method is judged by the accuracy of the calculated responses.

Copyright © 2003 Swets & Zeitlinger B.V., Lisse, The Netherlands

2 INDICATOR SIMULATION METHOD

In this method, indicator kriging is carried out in order to get the cumulative probability distribution function of the permeability at the non-measured point. This is a method of linear regression with indicator i of the measured hard data and indicator y of the measured soft ones, which is given by (Journel 1989).

$$I_k^*(\mathbf{u}) = [\text{Prob}\{z(\mathbf{u}) \le z_k(n+n')\}]_{IK} = \lambda_0 F(z_k) + \sum_{\alpha=1}^{n} \lambda_\alpha(\mathbf{u}; z_k) i(\mathbf{u}_\alpha; z_k) + \sum_{\alpha'=1}^{n'} \nu_\alpha(\mathbf{u}; z_k) y(\mathbf{u}_{\alpha'}; z_k) \quad (1)$$

in which the hard indicator data i originated from the hard data $z(\mathbf{u})$,which is the measured permeability in this paper, is written by

$$i(\mathbf{u}_\alpha; z_k) = 1 \quad if\ z(\mathbf{u}_\alpha) \le z_k$$
$$i(\mathbf{u}_\alpha; z_k) = 0 \quad if\ not \quad (2)$$

This means that if the measured permeability is greater than a value of permeability z_k, indicator i equals 1, if not, i becomes 0. z_k $(k = 1, \ldots, K)$ are called the cutoff values. K is the number of cutoff values, F is the mean of z_k, λ_0 is the weight of F, $\mathbf{u}$ is the position vector, n is the number of the hard data, and n' is the number of the soft data. The soft indicator $y(\mathbf{u}_\alpha; z_k)$ is given by

$$y(\mathbf{u}_\alpha; z_k) = \text{prob}\{Z(\mathbf{u}_\alpha) \le z_k\} \quad (3)$$

which is the probability that Z inferred from the soft data is smaller than cutoff value z_k. The probability is obtained from the scattergram, which is the plot between the hard and the soft data measured at the same point. The soft data are divided into a few groups, and the probability y is calculated for each z_k in each group. In this paper, the scattergram is obtained from the relation of the permeability to the fracture density as shown in Figure 1.

λ_α are the weights applied to the n permeability samples, and ν_α are the weights applied to the n' soft data. While these are obtained by minimizing the square error of estimated values by using the covariance matrix of hard and soft data, the covariance of the hard data is also used for soft data for simplicity.

In the indicator simulation, the probability at non-measurement point is estimated by the kriging of the equation (1). The probability that Z is smaller than the cutoff value z_k is put in order, so that the cumulative probability at the point is given (Figure 2). A random number is generated from 0 to 1, and the permeability corresponding to the random number is obtained from the cumulative probability distribution. Then, the same processes are carried out at the next non-measurement point to estimate the permeability. Thus, we can make multiple heterogeneous spaces by means of the way to generate the random number and the turn of the non-measurement points. In this paper, 30 realizations are generated and the results are examined with the averaged values.

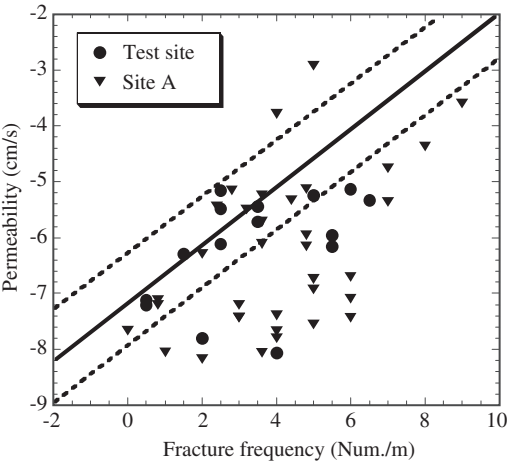


Figure 1. Scattergram of permeability and fracture frequency.

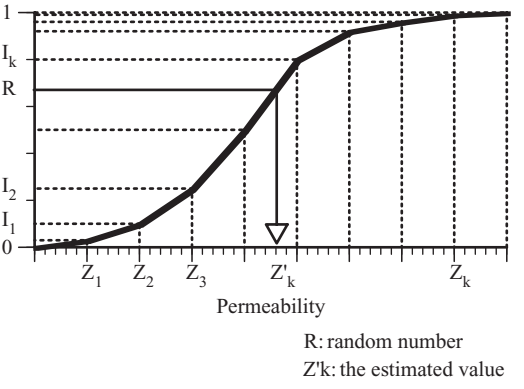


Figure 2. Cumulative probability distribution and estimation of the permeability.

3 IN-SITU TEST

The method examined in this paper is applied to in-situ hydraulic tests. The in-situ experiment was carried out at Kamaishi mine by JNC (Yokoi, et al. (1991), Figure 3). The fracture observation was carried out at each borehole by BHTV, and the fracture density was

Copyright © 2003 Swets & Zeitlinger B.V., Lisse, The Netherlands

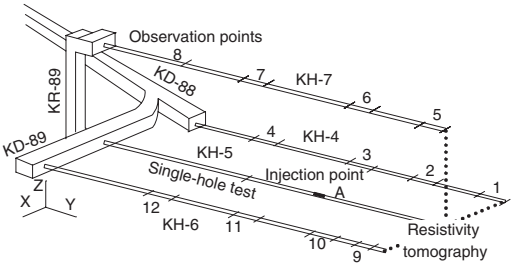


Figure 3. Schematic view of test site.

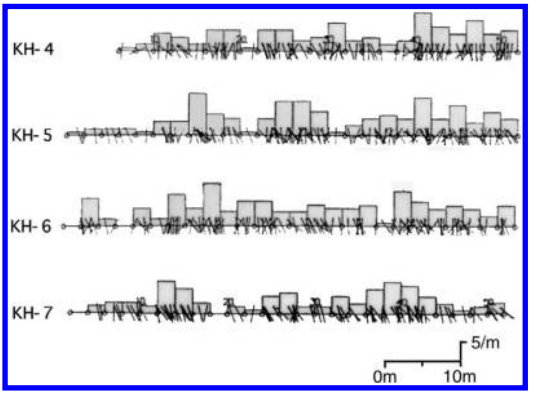


Figure 4. Measured fracture frequency.

obtained at each hole. Further more, the single-hole hydraulic tests are carried out at 15 points of KH-5, and the interference tests are also carried out by injecting from A of KH-5 and observing the 12 points of KH-4, KH-6, and KH-7 as shown in Figure 3 (Okuno 1994).

Figure 4 is the result of the fracture frequency observation. The number of measurement points where both permeability and fracture frequency are investigated is only 15. A (in Figure 5) is added to make the scattergram (Yokoi, et al. (1991)).

To overcome the shortage of the information, the data obtained at the other site in the same mine are also included. From the scattergrams, the cutoff permeability values are set by every one order from $10^{-8} \sim 10^{-3}$ cm/sec. The fracture density is classified by the threshold values of 2, 4, 5.5 and 6.5/m. y of the equation (3) is calculated in each group of the soft data. Using the above information, the indicator simulation is carried out.

The other distribution methods, which are explained in the following section, are also examined. The comparison among the methods is carried out between calculated and measured transient responses at 10 observation points, at which the clear responses were monitored. The analysis region is 44 m $\times$ 60 m $\times$ 32 m rectangular solid containing the margin of about 10 m

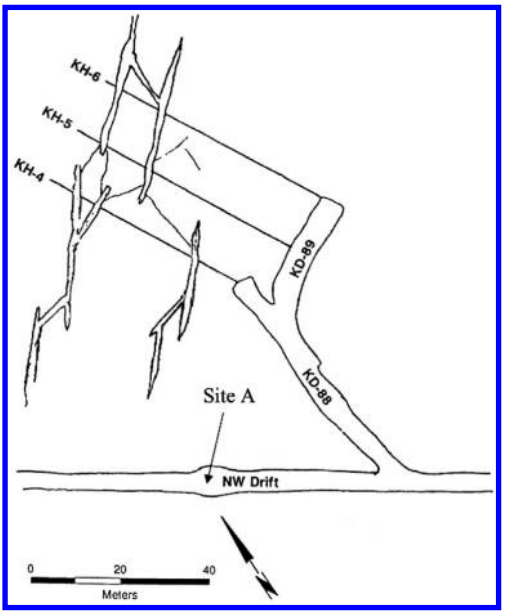


Figure 5. Test site and sampling point of additional data.

from the edge of the boreholes. The region is divided into cube elements whose sides are 2 m. The total pressure at all the boundaries is fixed at 400 KPa. The boundary conditions are decided from the in-situ survey results. The injection rate at the point A is fixed at 4.446×10^{-6} m^3/sec, and the interference test is simulated.

4 PERMEABILITY DISTRIBUTION

4.1 *Strategy*

Based on the indicator simulation technique mentioned above, the permeability distribution is examined. However, as shown in Figure 1, the variance at each threshold value of fracture frequency is relatively large. This means that the realization of permeability at a threshold value is in a large range of permeability and the difference between the realized permeability and the threshold values are very small. To emphasize the effect of soft data, the tendency of the relation between both values is constructed as shown in Figure 1 by solid and dotted lines, in which solid line indicates the mean relation and dotted line shows the range of standard deviation. The gradient is inferred from the entire relation, and the mean relation is decided so that the mean measured fracture frequency has the mean measured permeability. The standard deviation is obtained from the measured permeability data. By using this emphasized relation between the permeability and fracture frequency, the indicator of y at the points having the

Copyright © 2003 Swets & Zeitlinger B.V., Lisse, The Netherlands

Table 1. Stochastic data of fracture geometry.

Cluster Number	1	2	3	4	5
Area/Volume	0.846	0.743	0.404	0.625	0.515
Mean length	1.67	1.64	1.92	2.13	1.86
St. dev. of length	1.36	0.62	1.3	0.675	1.13
Mean Dip direction	316.8	248.9	178.5	179.7	353.1
Mean Dip	70.1	88.5	77.3	15.8	76.2
Fisher k	14.23	7.44	31.2	7.82	13.32

Table 2. Examination cases.

Case	Method
1	Ordinary indicator simulation using scattergram and conditioned permeability data
2	Indicator simulation using emphasized relation between permeability and fracture frequency and conditioned permeability data
3	Indicator simulation using emphasized relation between permeability and fracture frequency without conditioned permeability data
4	Permeability generated by using emphasized relation between permeability and fracture frequency and generated fracture frequency with discontinuous fracture network technique

measured fracture frequency shows the clear distribution according to the fracture frequency. The variation of the indicator at the measurement holes is similar to that of the indicator at the permeability measurement hole, KH-5.

Moreover, the fracture geometry information is obtained at site A, shown in Figure 5. Table 1 shows the inferred fracture stochastic data. By using the information, the fracture can be generated with discontinuous fracture network approach for the test site and the fracture frequency at each element can be estimated from the generated fracture distribution. The permeability at each element can be generated with the estimated fracture frequency and the emphasized relation between the permeability and fracture frequency, while the spatial correlation of hard and soft data is neglected. In this case, the measured permeability is difficult to be conditioned. Thus, the indicator simulation without conditioned permeability data is also examined in order to compare with the case using the discontinuous fracture network approach. Therefore, four cases, as shown in Table 2, are examined in this study.

4.2 *Examination results*

Figure 6 shows an example of the permeability distributions for each case. The value is a logarithm of permeability of cm/s. The plane is a horizontal one through the KBH-4, 5 and 6. The cases using the indicator simulation approach, Cases 1, 2 and 3, show similar distribution, while Case 4 indicates quite different distribution. This is because Case 4 does not take into account any spatial correlation of permeability and fracture frequency. The similarity among Cases 1 to 3 is caused by the spatial correlation of fracture frequency because the measured permeabilities exist on only KH-5.

By generating about 30 patterns for each case, the 95% confidence range of averaged value is compared with the measured responses. Figure 7 shows the comparison of responses at typical measurement points of three different boreholes. As shown in this figure, the measured response at point 10 is relatively high and shows a quick response. This is probably because the path from the source to point 10 has a high permeability. To examine the accuracy of the numerical calculation, the square error between the measured and calculated transient responses at 10 observation points is investigated. For Case 1, the square error was $0.011\,m^2$.

Considering the entire tendency of the numerical simulations, the responses at KH4 and 7 are relatively well simulated, while the responses at KH-6 are underestimated as shown in Figure 7(c). Although the area from the source to point 10 is realized with higher permeability distribution than the area between the source and point 1 in Case 1, as shown in Figure 6(a), it is necessary to realize more permeable paths in this area.

In Case 2, the emphasized relation between permeability and fracture frequency is used. Since a little higher permeability is induced from the relation than the scattergram as shown in Figure 1, the resultant distribution, Figure 6(b), shows the lighter color than (a). Figure 8 shows the response at point 10 by Case 2. While the response appeared quickly than Case 1, the final pressure rise is smaller than that in Case 1. The square error is $0.012\,m^2$. Thus, the accuracy is not improved by this treatment.

In Case 3, the measured permeability is neglected in generating the permeability distribution, but the measured fracture frequency is conditioned. As in Case 2, the emphasized relation between permeability and fracture frequency gives a little high permeability distribution. Therefore, the number of the part having light color becomes larger than Case 2, as shown in Figure 6(c). Figure 9 shows the response at point 10 by Case 3. While the quick response and small pressure rise similar to Case 2 are observed, the square error in this case is $0.0046\,m^2$. The accuracy for the entire region is much improved.

For Case 4, the permeability distribution is quite random as shown in Figure 6(d) in spite of the fact that the measured fracture frequency is conditioned. Figure 10 shows the result of point 10 by this case.

Copyright © 2003 Swets & Zeitlinger B.V., Lisse, The Netherlands

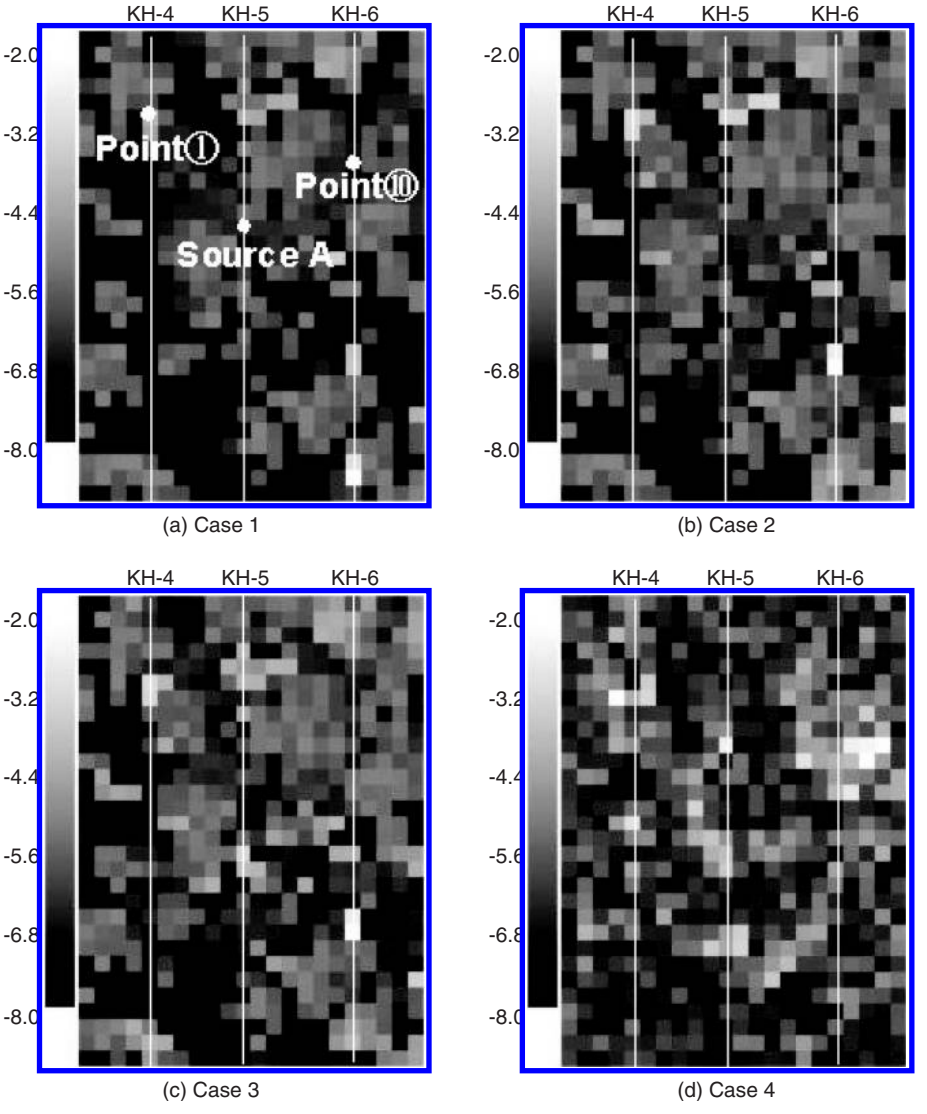


Figure 6. Examples of permeability distribution.

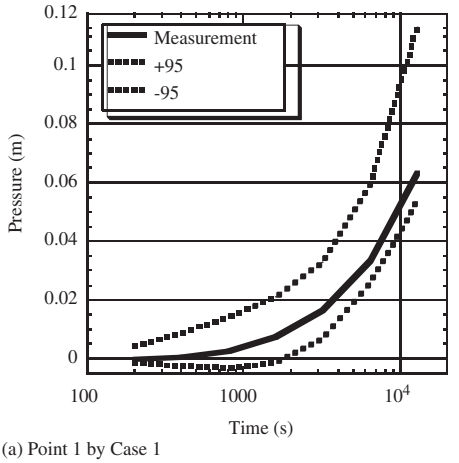
While the accuracy for point 10 is the best among the examined cases, the square error is 0.0083 m^2. Thus, the entire accuracy is improved from the ordinary indicator simulation approach.

5 CONCLUSIONS

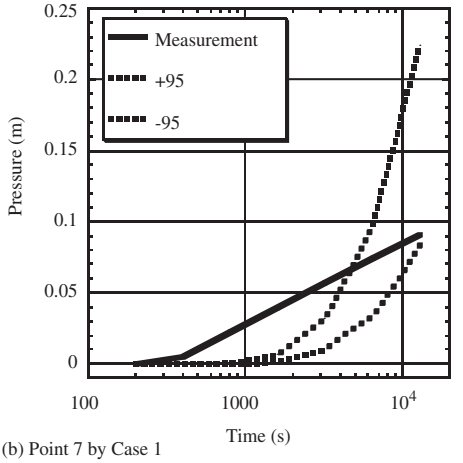
For the case where the permeability measurement is few, the ability to use the fracture frequency as soft information to infer the permeability distribution is examined in this study. As a conclusion, the followings are made;

(1) When the number of soft data is much larger than that of hard data, the generated distribution from neglecting the hard data is similar to that of conditioning the hard data.
(2) The fracture frequency does not correlate with permeability. Even if the relation is emphasized arbitrarily in order to have a good correlation, the generated result is not improved.

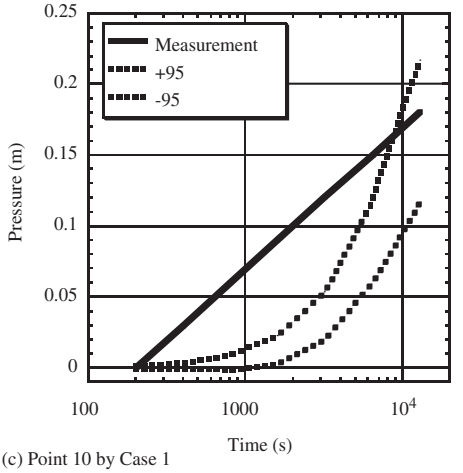
Copyright © 2003 Swets & Zeitlinger B.V., Lisse, The Netherlands



(a) Point 1 by Case 1



(b) Point 7 by Case 1



(c) Point 10 by Case 1

Figure 7. Examples of comparisons of responses by Case 1.

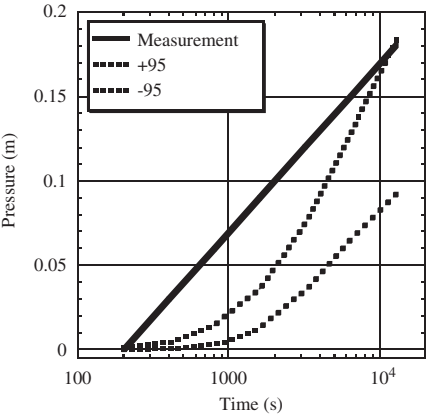


Figure 8. Response at point 10 by Case 2.

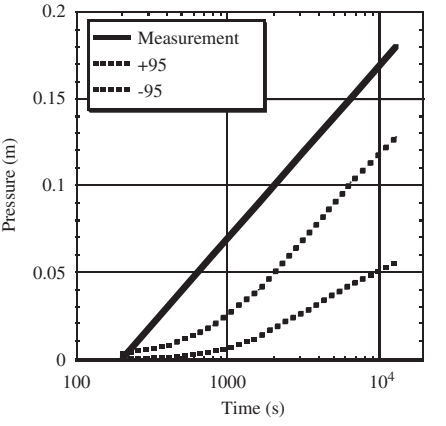


Figure 9. Response at point 10 by Case 3.

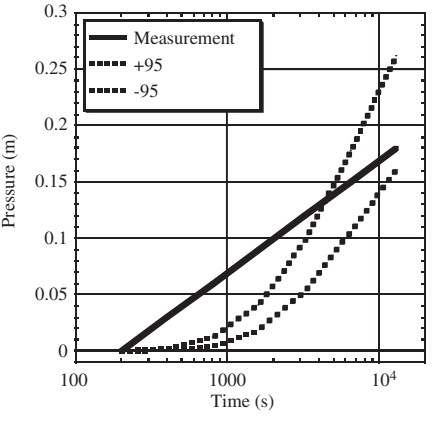


Figure 10. Response at point 10 by Case 4.

Copyright © 2003 Swets & Zeitlinger B.V., Lisse, The Netherlands

(3) When the permeability data is very few and the soft data are relatively large, it is effective to generate the permeability distribution by using only the soft data. This is probably because the spatial correlation induced from the measured permeability data may be wrong.
(4) While a discontinuous fracture network approach gives the distribution of fracture frequency, it is difficult to realize the distribution having the inferred spatial correlation from the measured fracture frequency. Among the stochastic parameters, the fracture density distribution, which corresponds to the fracture frequency, is most important for the estimation of the permeability distribution.

REFERENCES

Deutsch D.V., and Journel A.G., 1992, Geostatistical Software Library and User's Guide, *Oxford university Press*.

Journel A.G., 1989, Fundamentals of geostatistics in Five Lessons, *Short Course in Geology*: Vol. 8.

Okuno T., 1994, Study on the estimation of 3 dimensional distribution of permeability and calculation of ground water flow, *Nagoya University Dr. dissertation.*

Yokoi K., Noguchi Y., Choh H., and Hamabe S., 1991, Geophysical methods applied in underground investigation programs at the Kamaishi Mine, *BUTURI-TANSA*, Vol. 44, NO. 6, 350–361.

Dershowitz W., Wallmann P., and Kindred S., 1991, Stripa Project Technical Report 91–16, SKB.

Copyright © 2003 Swets & Zeitlinger B.V., Lisse, The Netherlands

Application of directional core drilling system to geological evaluation of liquefied petroleum gas underground storage base at Kurashiki site

K. Kojima
Geospace Labo, Professor Emeritus, Tokyo Univ., Tokyo, Japan

T. Otake
Japan National Oil Corporation, Tokyo, Japan

T. Tani
Nikko Exploration and Development Co., Ltd., Tokyo, Japan

Y. Moriguchi
Kawasaki Geological Engineering Co., Ltd., Tokyo, Japan

ABSTRACT: Construction of liquefied petroleum gas storage caverns is planned in deep underground granite body at Kurashiki City, Okayama Prefecture, Japan. Liquefied petroleum gas will be stored in caverns sealed by groundwater pressure system. Therefore it's important to clarify fracture systems, fractured zones and the rock permeability characteristics in the area before construction. Directional core drilling system was used for the first time in Japan to clarify underground geological features effectively. This system enables to control the borehole direction and to recover the core continuously with special wireline, which operates steerable core barrel by using a specially designed drill head. By applying this directional core drilling system to geological investigations, it is now possible to clarify the nature of high angle fracture systems which was difficult by conventional vertical drilling. This system is being continuously improved and has become very efficient and effective. Multipurpose use of the directional core drilling in the future are expected in various fields including rock evaluation.

1 INTRODUCTION

A national liquefied petroleum gas storage base with underground caverns is being planned at Kurashiki City, Okayama Prefecture, Japan. It will be capable of storing 400,000 tons of liquefied propane. This area stands on a reclaimed ground with surface facilities of an oil refinery complex. Underground caverns will be constructed in a solid Cretaceous granite body extending to deeper zones. These underground facilities will be maintained by a water-sealing system same as underground oil storage base (Hoshino, 1997). Therefore it is important to clarify the geologic environment of the site, particularly fracture systems and the rock permeability characteristics through geological investigation. The methods for clarifying geological characteristics of deep subsurface zones are based on experiences of underground oil storage base together with new advanced techniques are applied at Kurashiki site. Directional core drilling system was used for the first time in Japan for clarifying underground (between −100 m and −200 m a.s.l.) geological features. Here we will report on the distinctive features and results of directional core drilling.

2 GEOLOGICAL FEATURES AND PREVIOUS SURVEYS OF THE SURVEY AREA

The survey area is located in the Mizushima area, Kurashiki City in the southern part of Okayama Prefecture, Japan. The area stands at the mouth part of the Takahashi River which is one of three large rivers in Okayama Prefecture. The area is reclaimed ground facing the Mizushima-Nada of the Setonaikai (Seto Inland Sea). Many oil-refinery/petrochemical complexes are widely spread in Mizushima area, and there are few geologic outcrops to confirm the geological features. Therefore, many holes have been drilled mainly for geologic investigation.

Cretaceous granite body forms the basement which is overlain by late Tertiary-Quaternary sedimentary

Copyright © 2003 Swets & Zeitlinger B.V., Lisse, The Netherlands

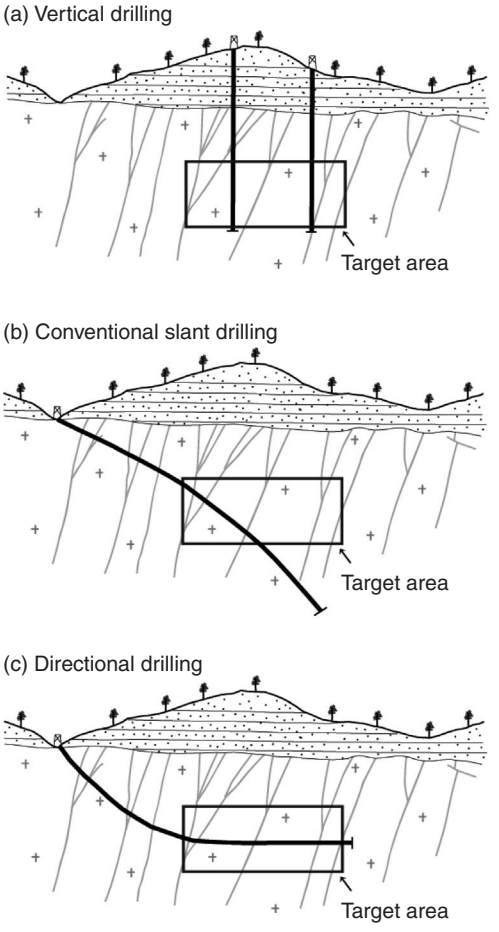


Figure 1. Characteristics of directional drilling (Hoshino et al., 1998).

rocks. The sedimentary layers consist mainly of sand, silt, and conglomerate. The thickness of the layers is about 70 m. The rock caverns will be constructed in the granite basement. The upper part of the granite is weathered, and transitional zone occurs between the weathered and fresh granite. The depth of weathering is irregular, but is generally about EL-100 m. Fault and fractured zone in the granite were recognized by many vertical drillings. Moreover, hydrothermal alteration zone accompanied by white clay veins were also found. These fault, fractured zone, and clay veins are inferred to have high angle dip.

The above geological features are inferred from the results of more than 30 drill holes in the past. Of these, three holes are directional drilling that we report in this paper. Directional drilling was used for evaluating fault/fracture systems parallel to or intersecting the caverns during the final stage of the detailed survey.

The surface of the study area is an oil refinement industrial complex and places available for drilling were very limited. Thus directional drilling was the important method for acquiring geological information of the area where drilling at necessary places was very difficult.

The effectiveness of directional drilling for evaluating laterally broad subsurface targets such as underground storage caverns is conceptually shown in Figure 1.

3 DESCRIPTION OF DIRECTIONAL DRILLING SYSTEM

The directional drilling has been successful for large-scale drilling such as oil-production wells using down hole motor system. The down hole motor system needs a large-scale drilling machine, and cores are not collected as a rule.

On the other hand, in the geological investigation for metallic deposits and for construction, cores are basically collected by using comparatively small drilling machine. The drilling diameter is generally smaller than 100 mm. And directional drilling system for small borehole was rarely used.

However, recent development of electronic equipments enabled the miniaturization of controlling tools for drilling. This resulted in the development of small-diameter-core directional drilling system.

The directional core drilling system used in this investigation was developed by DEVICO in Trondheim, Norway. It has been used for various projects in not only Norway but also Sweden, Canada, South Africa, and other areas. The purposes of drilling are explorations for coal mine, metallic deposit, undersea tunnel, construction of underground institution, pipeline and so on (Dowdell et al., 1999). Figure 2 shows the outline of this wireline directional core drilling assembly.

The characteristics of this system are as follows

- Direction of drilling can be controlled using conventional wireline and drilling machine system.
- Drilling direction can be easily set by electronic multishot device.
- Coring continuously by conventional and directional drilling is possible.
- Drilling can be controlled at high drilling speed by wireline system for directional drill head.
- Direction can be modified as necessary by checking during each drilling process with built-in survey device.
- Drilling can be controlled under varying geological condition from soft to hard rocks by changing the bit.

A special bit for directional drilling is fixed eccentrically out of the outertube. The conventional

Copyright © 2003 Swets & Zeitlinger B.V., Lisse, The Netherlands

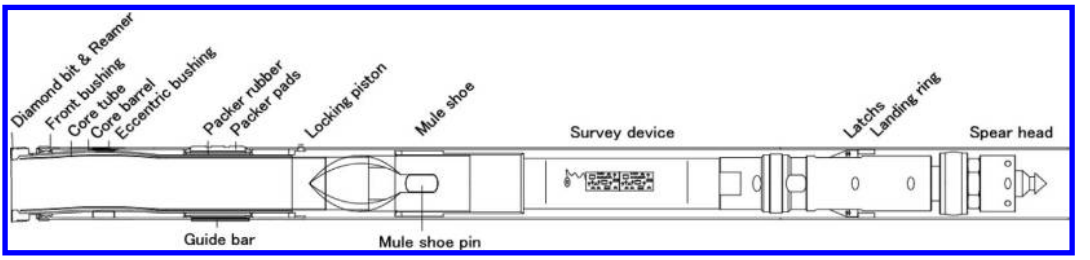


Figure 2. Outline of wireline directional core drilling head assembly.

Table 1. The summary of directional core drilling at Kurashiki site.

No. (year)	Length	Diameter	Directional drilling section	Rate of bending	Core recovery (%)	
					Directional	Conventional
No. 25 (1997)	430 m	BQ (60 mm)	207.9–354.0 m (146.1 m)	−40° to −1° (2.7°/10 m)	72	98
No. 31 (1998)	650 m	NQ (76 mm)	169.5–317.0 m (147.5 m)	−35° to −3° (2.2°/10 m)	88	99
No. 32 (1998)	450 m	NQ (76 mm)	167.2–351.3 m (184.1 m)	−45° to −2° (2.3°/10 m)	93	99

wireline drill head is replaced by a drill head with a bit for directional drilling. The outertube is fixed to the borehole wall by packer expanded by the circulating water pressure. This system allows continuous core sampling during steering with its special wireline operated steerable core barrel. The core barrel and bit rotate with the rods. The survey device is equipped to directionally drill in the aimed direction, and the eccentric bushing installed inside the outertube is set at the precise location to turn the bit to the aimed direction.

Drill strings are pushed by feed force and slide forward with expanded packer for directional drilling. Filled core tube is collected by a wireline system. After collecting the cores, the core tube is set again in the borehole and directional drilling restarts after checking direction with the survey device. Ordinary rate of bending is 3° per 10 m in BQ (60 mm), 2° per 10 m in NQ (76 mm), rods strength being taking into consideration.

4 SURVEY OF DIRECTIONAL CORE DRILLING

Three directional core drillings were made in 1997–1998 at the planned location for cavern construction. Each drilling length of the directional core drillings were 430 m, 650 m, and 450 m respectively. Table 1 shows the summary of each hole. Figure 3 shows cross section of the 650 m long drilling path and Table 2 shows calculation result of the drilling path.

The purpose of these directional drillings is the investigation of rock characteristics around the planned cavern in granite. Thus, each drilling path was planned to be horizontal in the planned carven position. Drilling of each hole was started at −40, −35, and −45-degree angle respectively. Conventional or standard wireline system was used in thick sedimentary rocks overlying the granite. Casing pipe was inserted after reaching fresh granite. Directional core drilling was started from fresh granite in NQ size (BQ size in 1997).

Because directional core drilling system was originally developed in a steady hardrock region in the Scandinavia peninsula, the improvements of the device were needed to drill the rocks with many cracks and repetition of hard and soft parts in Japan. These improvements included, inter alia; the shape and location of the expanded packer, shape of bits, and circulation mechanism of drilling water. These adjustments and improvements made it possible to drill each hole, according to the plan.

At first, the drill head was a single tube, so the cores rotated with bit and innertube in the directional drilling section. Thus soft cores were broken and core recovery declined. To prevent this, triple tube system and the use of bearing on coretube were adopted in 1998. Consequently, the core recovery in the directional section was improved from 72% to 88–93%.

Continuous curved cores were collected by the directional drilling in the hard parts of fresh granite, and it was possible to distinguish between the upper and lower parts of the cores.

Copyright © 2003 Swets & Zeitlinger B.V., Lisse, The Netherlands

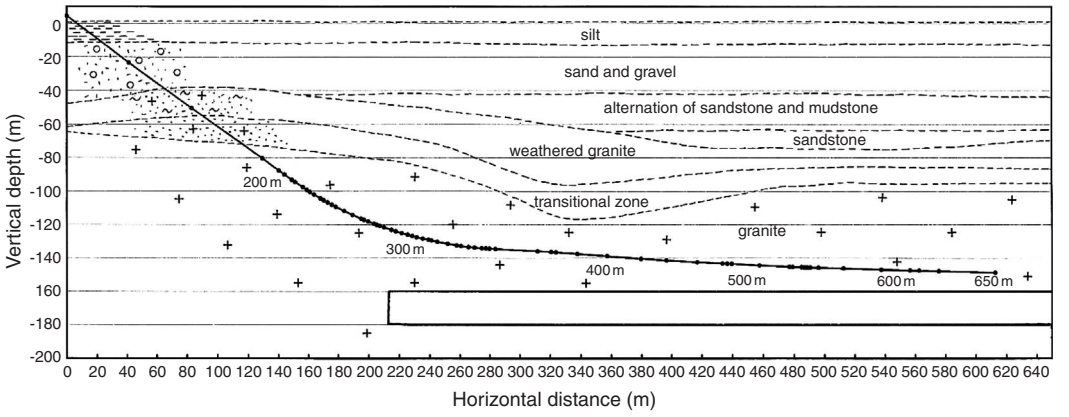


Figure 3. Cross-section of directional core drilling at Kurashiki site (No. 31 hole).

Table 2. Survey data of directional core drilling (No. 31 hole). (Surveyed data, calculated trajectories coordinates Hole: 31 (ind.: 1).)

Depth	Direction	Inclination	X-value	Y-value	Z-value
0.00	235.000	−35.000	0.000	0.000	4.560
50.00	235.000	−33.000	−23.775	−33.954	−23.398
100.00	235.000	−33.000	−47.827	−68.304	−50.630
155.00	235.000	−33.000	−74.284	−106.089	−80.585
160.00	235.000	−33.000	−76.689	−109.524	−83.309
200.00	234.000	−28.000	−96.703	−137.568	−103.604
224.00	232.500	−22.000	−109.716	−154.984	−113.743
235.00	232.000	−19.000	−116.024	−163.129	−117.595
246.00	231.000	−18.000	−122.518	−171.293	−121.085
250.00	231.000	−16.000	−124.925	−174.265	−122.254
300.00	228.500	−6.000	−156.608	−211.663	−131.784
317.00	229.000	−3.000	−167.781	−224.404	−133.118
321.00	228.000	−3.000	−170.428	−227.396	−133.327
349.00	228.000	−2.500	−189.142	−248.180	−134.671
350.00	228.000	−3.000	−189.810	−248.922	−134.719
358.00	228.500	−3.750	−195.128	−254.880	−135.189
361.00	229.000	−4.000	−197.102	−257.130	−135.392
375.00	229.000	−4.000	−206.264	−267.670	−136.369
394.50	229.000	−4.000	−219.026	−282.351	−137.729
400.00	229.500	−3.750	−222.608	−286.509	−138.101
417.00	229.500	−3.500	−233.627	−299.410	−139.176
434.00	229.500	−3.500	−244.647	−312.312	−140.213
450.00	229.000	−3.000	−255.074	−324.414	−141.121
454.50	229.500	−2.500	−258.008	−327.819	−141.336
471.00	229.000	−2.250	−268.769	−340.308	−142.020
474.00	229.500	−2.500	−270.726	−342.579	−142.144
477.00	229.000	−3.000	−272.682	−344.849	−142.288
495.00	228.000	−3.000	−284.593	−358.311	−143.231
500.00	228.500	−3.000	−287.917	−362.036	−143.492
514.50	228.000	−2.000	−297.563	−372.844	−144.125
516.60	228.500	−2.000	−298.961	−374.410	−144.198
522.30	227.500	−1.750	−302.773	−378.643	−144.384
524.00	228.000	−1.750	−303.915	−379.901	−144.436
526.00	228.000	−2.000	−305.253	−381.386	−144.502
528.00	228.000	−1.750	−306.590	−382.872	−144.567
533.50	226.000	−1.250	−310.340	−386.893	−144.711

(*Continued*)

Copyright © 2003 Swets & Zeitlinger B.V., Lisse, The Netherlands

Table 2. (*Continued*)

Depth	Direction	Inclination	X-value	Y-value	Z-value
550.00	226.000	−1.750	−321.798	−398.758	−145.143
575.00	226.000	−1.500	−339.157	−416.734	−145.852
594.00	226.000	−1.500	−352.351	−430.397	−146.349
600.00	226.000	−1.500	−356.518	−434.711	−146.507
613.00	226.000	−1.500	−365.545	−444.060	−146.847
650.00	226.000	−1.000	−391.241	−470.669	−147.654
650.00	226.000	−1.000	−391.241	−470.669	−147.654

Direction in Degrees, length unit Metre, inclination in Degrees, zero is horizontal.

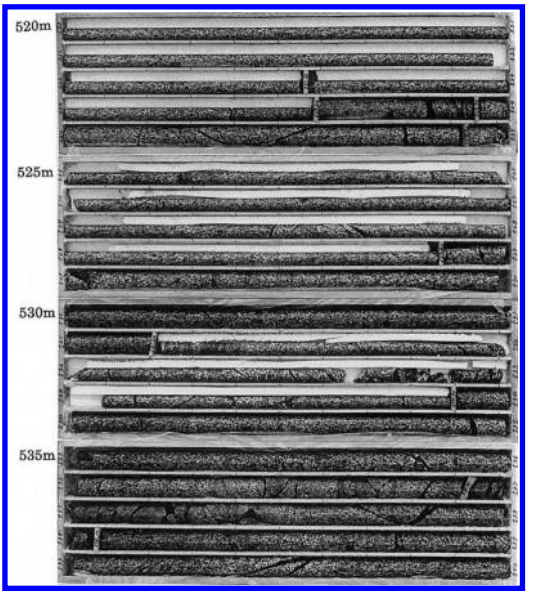


Figure 4. Photograph of core sample (No. 31 hole).

Normal wireline system was used in the horizontal section after the directional section, and the core recovery was almost 100% for the 3 holes. Various kinds of information, such as the widths of high angle fractures zones and frequency of zones, could be obtained by horizontal drilling. The nature of these high angle fracture system could not been clarified by the vertical drilling which is commonly used in geological surveys. The drilling direction was checked every 30 m during horizontal drilling and any deviation was corrected by directional drilling.

Figure 4 shows a photograph of a core sample in the horizontal section. Slender cores are collected by directional drilling, because the bits for the directional drilling have small inner diameter.

Regarding borehole tests, permeability and JFT (Johnston Formation Tester) were carried out in No. 25 hole by using the improved device during test section (drilling length 272 m–430 m) in 1997. Moreover,

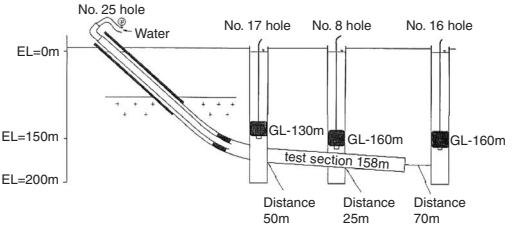


Figure 5. Outline of permeability test in directional hole.

after permeability test, water with 1MPa pressure was injected into No. 25 hole, and the variation of water pressure was measured in three vertical holes (No. 8, 16, and 17 hole). Figure 5 shows the outline of this test. An obvious pressure change in No.8 hole was recognized in two minutes after injection.

In 1998, permeability tests in directional holes (No. 31 and No. 32 hole) were carried out every 20 m. Packer was descended to the test section with the help of a special device because inclinations of these directional holes were very low – almost horizontal. This special device attached to the packer for a conventional wireline could make packer descend smoothly by water pressure.

As these results, continuousness of the permeability and the pervious layer was three-dimensionally evaluated in the investigation of the directional holes together with the vertical holes.

Drilling data such as the penetration rate, feed force, and torque were obtained by mechanical measuring system that was installed in this directional drilling system. The relation between these data and the geology was also studied. It is believed that these data will be used in various fields for geological analyses and rock mechanics.

5 FUTURE OUTLOOK

Directional core drilling system was used for the first time in Japan for the survey of a national petroleum gas storage base at Kurashiki. Three holes were drilled

Copyright © 2003 Swets & Zeitlinger B.V., Lisse, The Netherlands

satisfactorily along planned drill paths. By the introduction of this directional core drilling system, it is now possible to clarify the nature of high angle fracture systems. The technical knowledge necessary for applying the directional drilling technology to geological environment peculiar to Japan was sufficiently accumulated by this successful investigation.

The directional drilling system has become more effective as a result of many improvements undertaken subsequent to the above survey. This system is expected to be used in a broad field related to rock evaluation.

Various *in situ* tests were carried out in directional drilling holes. There are currently difficult *in situ* tests such as observation of the borehole wall using a borehole camera in the horizontal section. Therefore, it is necessary to develop devices which can be used in low angle holes in order to use directional drilling holes effectively as measurement holes. In the future, we hope to expand the multipurpose use of the directional drilling holes in weaker grounds by developing *in situ* measurement equipments.

6 CONCLUSIONS

Directional core drilling system was used for the first time in Japan to clarify geological features of granite at a national liquefied petroleum gas storage base. The directional core drilling system was originally developed in a steady hardrock region, so it was necessary to improve upon the devices for the application of the system to the rocks peculiar to Japan. We were able to obtain continuous cores by using special bit and steerable wireline system while changing the direction. Three directional drillings running parallel with or crossing the planned cavern positions were carried out as planned. The horizontal section of the directional drilling clarified high angle fracture systems which control underground water flow. Permeability test and JFT were carried out as *in situ* tests. By the improvement of the wireline system, directional drilling became more efficient and multipurpose uses are expected in the future.

REFERENCES

Dowdell, R., Kaplin, J. & Tokle, V. 1999. Directional core drilling used to explore rock conditions for water supply, Proceedings of the World Tunnel Congress: 51–59.

Hosino, K. 1997. Geomechanics and site investigation for underground works in Japan, Proceedings of 30th International Geological Congress, Vol. 14: 304–311.

Hosino, K., Hishikawa, A., Shiomi, T. & Matsumoto, T. 1998. Geological techniques applied for new project on underground storage of liquefied petroleum gas, Journal of the Japanese Geotechnical Society, 46(6): 25–27. (in Japanese)

Copyright © 2003 Swets & Zeitlinger B.V., Lisse, The Netherlands

Strong evidence for permeability scale effect in fractured rock

W.A. Illman
Department of Geoscience, University of Iowa, Iowa City, IA, USA;
Department of Civil & Environmental Engineering, University of Iowa, Iowa City, IA, USA;
IIHR – Hydroscience & Engineering, University of Iowa, Iowa City, IA, USA

S.P. Neuman
Department of Hydrology and Water Resources, University of Arizona, Tucson, AZ, USA

V.V. Vesselinov
Earth and Environmental Sciences Division, Los Alamos National Laboratory, Los Alamos, NM, USA

A.G. Guzman
Water Management Consultants, Tucson, AZ, USA

ABSTRACT: Permeability controls mass and energy transfer through rocks and soils. Several studies have suggested that the permeability of geologic materials tends to vary with scale. Whether this scale effect is real or an artifact of inadequate observation and analysis remains an open question. We present strong field evidence for a pronounced air permeability scale effect in fractured tuffs partially saturated with water at a study site in central Arizona, USA.

1 PERMEABILITY AND ITS IMPORTANCE

Permeability is a key parameter controlling mass and energy transfer in geologic media. Its magnitude and spatial distribution are important for the design of well fields and underground works, oil and gas extraction (*Raghavan*, 1993), geologic disposal of waste (including nuclear, *Macilwain*, 2001), subsurface energy storage, assessment and remediation of soil and groundwater contamination (*Fetter*, 1999; *Kersting et al*., 1999), and the understanding of catchment hydrology (*Kirchner et al.*, 2000), earthquake occurrence (*Davies*, 1999), and hydrothermal fluid circulation within the sea floor (*Fisher and Becker*, 2000).

Several studies have suggested that the permeability of geologic materials tends to vary with scale. Whether this scale effect is real or an artifact of inadequate observation and analysis remains an open question. We present strong field evidence for a pronounced air permeability scale effect in fractured tuffs partially saturated with water at a study site in central Arizona, USA.

2 DETERMINATION OF PERMEABILITY IN GEOLOGIC MEDIA

Permeability is commonly determined by means of laboratory permeameter measurements and field methods such as pressure tests involving single or multiple boreholes (*Freeze and Cherry*, 1979). Such tests are commonly interpreted on the assumption that the medium has uniform properties, including permeability. On rare occasions the analysis considers composite media containing a few layers, segments of layers and/or structural features such as dykes, faults and fractures within each of which the permeability is uniform. The analysis thus yields equivalent values of permeability for components of the subsurface that it considers being uniform. In reality, the subsurface is highly nonuniform (*Dagan and Neuman*, 1997; *Zhang*, 2001) and varies spatially on a wide range of scales (*Cushman*, 1990; *Sposito*, 1998). Therefore, it is reasonable to expect that equivalent properties, determined in the above manner, would vary with the scale of measurement. This scale ranges from millimeters to a few meters in the laboratory, from a few meters to tens of meters in single-hole pressure tests, and from tens to hundreds of meters in pressure interference tests between boreholes.

3 VARIATION OF PERMEABILITY WITH SCALE

Variations of permeability with scale have been reported in a variety of geologic settings (*Brace*, 1984;

Copyright © 2003 Swets & Zeitlinger B.V., Lisse, The Netherlands

Bradbury and Muldoon, 1990; *Schad and Teutsch*, 1994; *Rovey and Cherkauer*, 1995; *Tidwell and Wilson*, 1997; *Sánchez-Vila et al*., 1996; *Geldon*, 1996; *Samper-Calvete and Garcia-Vera*, 1998; *Schulze-Makuch et al*., 1999; *Martínez-Landa et al*., 2000; *Zhang et al.*, 2000).

There is, however, disagreement whether this effect is real or illusory. Among various artifacts cited as giving rise to an apparent scale effect one counts inadequate development of borehole intervals (*Butler and Healey*, 1998a–b), turbulence in boreholes (*Lee and Lee*, 1999), and interpretive errors stemming from the use of disparate methods to gather and analyze field data (*Zlotnik et al.*, 2000). Some authors (*Brace*, 1984; *Bradbury and Muldoon*, 1990; *Clauser*, 1992; *Neuman*, 1994) have relied on data collected at a variety of sites, under diverse fluid flow regimes, to conclude that the permeability scale effect is real. It remains unclear whether their conclusion applies to individual sites. Observations of permeability scale variations at individual sites have been attributed to composite structure such as the juxtaposition of various stratigraphic units and facies or the superposition of fractures and porous rock matrix (*Rovey and Cherkauer*, 1995; *Schulze-Makuch and Cherkauer*, 1998; *Rovey*, 1998).

To our knowledge, there has not been a systematic documentation of a permeability scale effect within a well-defined hydrogeologic unit that is not attributable to any of the above factors.

4 PERMEABILITY SCALE EFFECT AT THE ALRS

We present strong field evidence for a pronounced air permeability scale effect in a geologically homogeneous mass of fractured tuffaceous rocks at a study site in central Arizona, USA. The porous matrix at our Apache Leap Research Site (ALRS) is virtually saturated with water and so effectively impermeable to air (*Chen et al.*, 2000). Fractures tend to be open to airflow under conditions of pneumatic pressure tests.

Two types of pneumatic tests were conducted: single-hole tests during which air is injected into, and pressure is monitored in, a single borehole segment isolated from the rest of the hole by inflatable packers (*Guzman et al.*, 1994, 1996); and cross-hole interference tests during which air is injected into one isolated borehole interval while pressure is monitored simultaneously in numerous other such intervals within this and surrounding boreholes (*Illman et al.*, 1998; *Illman and Neuman*, 2001).

The site included 22 vertical and inclined (at 45°) boreholes completed to a maximum vertical depth of 30 m. Among numerous single-hole tests, 184 were conducted in 6 of these boreholes (V2, W2a, X2, Y2, Y3, Z2) within isolated segments of 1 m length whose center locations are indicated by dark circles in Figure 1.

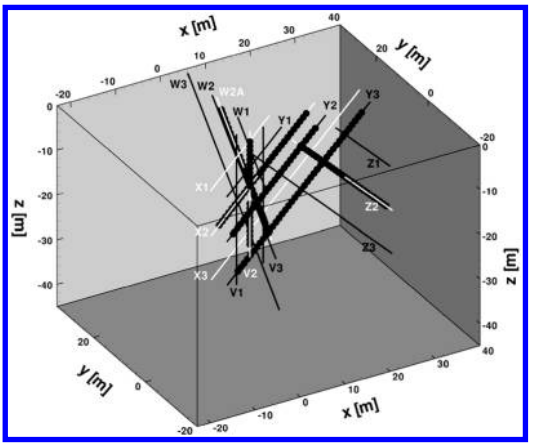


Figure 1. Center locations of 1-m single hole pneumatic test intervals; overlappig circles indicate retested locations (after *Vesselinov and Neuman*, 2001).

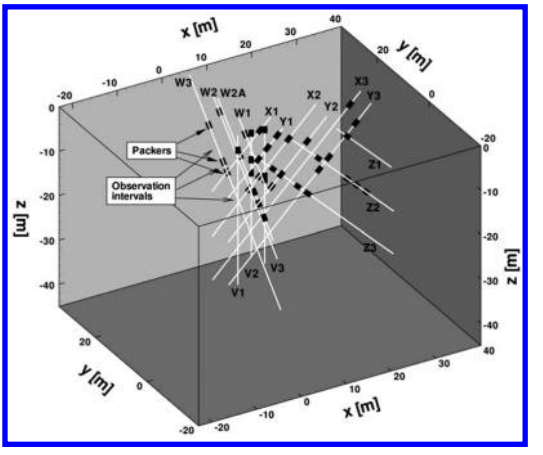


Figure 2. Locations of packers during cross-hole tests PP4-7 (after *Vesselinov et al.*, 2001a).

44 cross-hole tests were conducted in 16 of the 22 boreholes, including the 6 subjected previously to single-hole tests. A typical cross-hole test arrangement is depicted in Figure 2.

The results of the single-hole tests (primarily spatial distribution of air permeabilities and local flow geometry) together with other site information (primarily borehole televiewer images) served as a guide in designing the cross-hole tests. Among numerous phenomenological results revealed by these tests (*Guzman et al.,* 1994 and *Chen et al*., 2000), the following two are most directly relevant to this paper: (a) the pneumatic pressure behavior of fractured tuff at the site is

Copyright © 2003 Swets & Zeitlinger B.V., Lisse, The Netherlands

Table 1. Summary statistics of $\log_{10} k[m^2]$ estimated in various ways.

	Direct estimates			Kriging estimates		
Source	Sample size	Mean	CV	Sample size	Mean	CV
Single-hole tests (*steady-state analysis*)	227	−15.22	−0.061	53176	−15.20	−0.044
Cross-hole tests						
Uniform (equivalent) estimates						
PP4 (*type-curve analysis*)	30	−13.46	−0.043		—	
Cross-hole tests (*numerical inversion*)						
Uniform (equivalent) estimates						
PP4	32	−13.57	−0.056		—	
PP4-6	76	−13.70	−0.048		—	
Nonuniform (tomographic) estimates						
PP4: 32 pilot points		—		53176	−15.23	−0.085
PP4: 64 pilot points		—		53176	−14.77	−0.086
PP4-6: 72 pilot points		—		53176	−15.69	−0.089

amenable to analysis by treating the rock as a single (as opposed to dual or multiple) porous continuum on scales ranging from meters to tens of meters, and (b) this continuum is representative primarily of interconnected fractures (rock matrix having little effect on observed pneumatic behavior). Both the single-hole and cross-hole test results have proven to be virtually free of skin effect (*Illman and Neuman*, 2000, 2001), implying that they represent rock conditions unperturbed by the presence of boreholes.

Spatially distributed log air permeability data obtained from a steady state interpretation of the 184 single-hole tests in 1-m borehole intervals were subjected to geostatistical analysis by *Chen et al.* (2000). The authors determined that these data can be viewed as a sample from a random field that lacks a unique variance or correlation scale. Instead, the field constitutes a random fractal characterized by a large variance and a wide range of spatial correlation scales, both theoretically infinite. Using geostatistical interpolation (kriging) Chen et al. were able to estimate the way that log permeability varies in three-dimensional space between and around the boreholes. Their estimate is based on an augmented database of 227 values including the original 184 values corresponding to 1-m long test intervals, and 43 values obtained earlier by *Rasmussen et al*. (1990, 1993) from single-hole tests in 3-m intervals within boreholes X1, X3, Y1, Z1 and Z3, which have not been tested by *Guzman et al.* (1994, 1996). Statistics of the original data, and of the kriging results, are summarized in Table 1.

Illman and Neuman (2001) used a graphical method to interpret the results of a cross-hole test labeled PP4. The method relies on type curves based on a mathematical formula that treats the fractured rock as a uniform porous continuum. Their analysis yielded a set of equivalent directional air permeability (and air-filled porosity) estimates for each pair of borehole injection and monitoring intervals. The corresponding log permeability estimates are summarized statistically in Table 1.

Vesselinov et al. (2001a–b) used a three-dimensional numerical inverse model to interpret several cross-hole pneumatic tests at the ALRS. They analyzed pneumatic cross-hole test data by treating the rock as being either (a) spatially uniform or (b) a random fractal. The first approach yielded a series of equivalent log air permeability (and log air-filled porosity) estimates analogous to the type-curve estimates of *Illman and Neuman* (2001). The second approach yielded a high-resolution estimate of how log air permeability (and air-filled porosity), defined on grid blocks having a length scale of 1 m, vary spatially throughout the tested rock volume. The approach entailed geostatistical inversion of the cross-hole test data to yield estimates at "pilot points." Projecting these estimates onto the simulation domain by kriging yields a "tomographic" image of rock heterogeneity. Results obtained by the authors for tests labeled PP4-6, using both approaches, are summarized statistically in Table 1.

Table 1 reveals a steep increase in the mean value of log permeability estimates with the scales of observation and/or resolution. The smallest scale, on the order of 1 m, corresponds to single-hole test results and to tomographic (kriged) inverse estimates based on the cross-hole tests. The largest scale, on the order of tens of meters, corresponds to type-curve results and to inverse estimates of equivalent log permeability obtained from cross-hole tests upon treating the rock as being uniform. Mean values obtained by different methods at any given scale of estimation are generally comparable. Yet mean values obtained from cross-hole tests under the uniform rock assumption are consistently larger than those obtained by allowing

Copyright © 2003 Swets & Zeitlinger B.V., Lisse, The Netherlands

pneumatic properties to vary spatially over distances of 1 m.

For example, the mean of inverse log permeability estimates obtained from cross-hole tests PP4, 5, 6 when treating the rock as being spatially uniform (−13.70) exceeds the mean of simultaneous tomographic estimates from the same three tests (−15.69) by 1.99. This represents a 98-fold increase in the associated values of permeability. The mean of log permeability estimates obtained by inverting cross-hole test PP4 when treating the rock as being uniform (−13.57) exceeds the average of mean tomographic estimates obtained from this test using 64 pilot points (−14.77) by 1.20. This represents an increase in the associated values of permeability by a factor of about 16. The average of all uniform inverse mean estimates in Table 1 (−13.64) exceeds that of all tomographic mean estimates (−15.23) by 1.59, which corresponds to an increase in the associated value of permeability by a factor of 39. It is thus clear that estimates of air permeability increase markedly with scale at the ALRS.

5 DISCUSSION

We see that treating the rock as being uniform on the scale of cross-hole tests yields higher mean estimates of permeability than are obtained upon resolving smaller-scale spatial variations in these bulk fracture properties. A similar finding was recently reported by *Martinez-Landa et al.* (2000) in the context of cross-hole tests in saturated fractured granites at the Grimsel site in Switzerland, interpreted by means of a numerical inverse model. Both findings are in line with an earlier conclusion by *Neuman* (1990, 1994) that the scale effect diminishes as one improves the degree to which spatial variability is explicitly resolved by the model that one uses to estimate these parameters.

The permeability scale effect we have observed at the ALRS is clearly unrelated to the method of testing: there is consistency between single-hole and cross-hole test results corresponding to a wide range of injection rates and to steady state as well as transient flow regimes. The scale effect is likewise unrelated to the method of test interpretation: there is consistency between results obtained by means of steady state analytical formulae from single-hole test data (*Guzman et al.*, 1996), which are shown elsewhere to compare well with transient type-curve (*Illman and Neuman*, 2000) and inverse (*Vesselinov and Neuman*, 2001) analyses of the same data, and type-curve (*Illman and Neuman*, 2001) as well as numerical inverse (*Vesselinov et al.*, 2001a–b) interpretations of cross-hole test data. Contrary to a recent suggestion in the literature (*Butler and Healey*, 1998a–b), the observed scaling behavior is not an artifact of rock conditions around the injection borehole: neither the single-hole (*Illman and Neuman*, 2000) nor the cross-hole (*Illman and Neuman*, 2001) test results have been affected by any skin effect of consequence.

The pronounced permeability scale effect observed at the ALRS appears to be real.

A theoretical interpretation of the observed permeability scale effect at the ALRS has recently been published by *Hyun et al.* (2002). Their approach is based on a stochastic scaling theory due to *Di Federico and Neuman* (1997) and *Di Federico et al.* (1999), which views log permeability as a truncated random fractal.

6 CONCLUSIONS

a. Analysis of air injection test data conducted in a geologically homogeneous mass of fractured tuffaceous rocks revealed a strong evidence of pronounced air permeability scale effect.
b. The permeability scale effect is unrelated to the method of testing, test interpretation, and is not an artifact of rock conditions around the injection borehole.
c. The permeability scale effect may be large enough to justify including stochastic scaling theories in analyses of subsurface flow and transport.

ACKNOWLEDGMENTS

This work was supported by the 2002 Old Gold Fellowship from the University of Iowa, the U.S. Nuclear Regulatory Commission under contract NRC-04-97-056, and NSF/ITR Grant EAR-0110289.

REFERENCES

Brace, W. F. 1984. Permeability of crystalline rocks: New in situ measurements: *Journal of Geophysical Research,* 89(B6): 4327–4330.

Bradbury, K. R., & Muldoon, M. A. 1990. Hydraulic conductivity determinations in unlithified glacial and fluvial materials, In Nielson D.M. and Johnson, A. I., eds., *Ground Water and Vadose Zone monitoring*, *ASTM STP* 1053, 138–151.

Butler, J. J., Jr., & Healey, J. M. 1998a. Relationship between pumping-test and slug-test parameters: Scale effect or artifact?, *Ground Water*, 36: 305–313.

Butler, J.J., Jr., & Healey, J. M. 1998b. Discussion of papers: Authors' reply, *Ground Water*, 36: 867–868.

Chen, G., Illman, W. A., Thompson, D. L., Vesselinov, V. V., & Neuman, S. P. 2000. Geostatistical, type curve and inverse analyses of pneumatic injection tests in unsaturated fractured tuffs at the Apache Leap Research Site near Superior, Arizona, 73–98, in *Dynamics of Fluids in Fractured Rocks*, edited by B. Faybishenko et al., Geophysical Monograph 122, AGU, Washington, DC.

Copyright © 2003 Swets & Zeitlinger B.V., Lisse, The Netherlands

Clauser, C. Permeability of crystalline rocks. 1992. *Eos Transactions*, American Geophysical Union, 73(21): 233.

Cushman, J. H. 1990. *Dynamics of Fluids in Hierarchical Porous Formation*, Academic Press, London, United Kingdom.

Dagan, G., & Neuman, S. P. 1997. *Subsurface Flow and Transport: A Stochastic Approach*, Cambridge University Press, Cambridge, United Kingdom.

Davies, J. W. 1999. The role of hydraulic fractures and intermediate-depth earthquakes in generating subduction-zone magmatism, *Nature*, 398: 142–145.

Di Federico, V., & Neuman, S. P. 1997. Scaling of random fields by means of truncated power variograms and associated spectra, *Water Resour. Res.*, 33(5): 1075–1085.

Di Federico, V., Neuman, S. P., & Tartakovsky, D.M. 1999. Anisotropy, lacunarity, upscaled conductivity and its covariance in multiscale fields with truncated power variograms, *Water Resour. Res.*, 35(10): 2891–2908.

Fetter, C. W. 1999. *Contaminant Hydrogeology*, 2nd ed., Prentice Hall.

Fisher, A. T., & Becker, K. 2000. Channelized fluid flow in oceanic crust reconciles heat-flow and permeability data. *Nature*, 403: 71–74.

Freeze, R. A., & Cherry, J. A. 1979. *Groundwater*, Prentice-Hall, Englewood Cliffs, New Jersey.

Geldon, A. L. 1996. Results and interpretation of preliminary aquifer tests in boreholes UE-25c #1, E-25c #2, and UE-25c #3, Yucca Mountain, Nye County, Nevada, U.S. Geological Survey Water-Resources Investigations Report 94–4177.

Guzman, A., Neuman, S. P., Lohrstorfer, C., & Bassett, R. 1994. Chapter 4, in *Validation Studies for Assessing Flow and Transport Through Unsaturated Fractured Rocks*, edited by Bassett, R. L., Neuman, S. P., Rasmussen, T. C., Guzman, A., Davidson, G. R., & Lohrstorfer, C. F., NUREG/CR-6203, U. S. Nuclear Regulatory Commission, Washington, D. C.

Guzman, A. G., Geddis, A. M., Henrich, M. J., Lohrstorfer, C. F., & Neuman, S. P. 1996. *Summary of Air Permeability Data From Single-Hole Injection Tests in Unsaturated Fractured Tuffs at the Apache Leap Research Site: Results of Steady-State Test Interpretation*, NUREG/CR-6360, U.S. Nuclear Regulatory Commission, Washington, D.C.

Hyun, Y., Neuman, S. P., Vesselinov, V. V., Illman, W. A., Tartakovsky, D. M., & Di Federico, V. 2002. Theoretical interpretation of a pronounced permeability scale-effect in unsaturated fractured tuff, *Water Resour. Res*. in press.

Illman, W. A., & Neuman, S. P. 2000. Type-curve interpretation of multi-rate single-hole pneumatic injection tests in unsaturated fractured rock, *Ground Water*, 38: 899–911.

Illman, W. A., & Neuman, S. P. 2001. Type-curve interpretation of a cross-hole pneumatic injection test in unsaturated fractured tuff, *Water Resour. Res.*, 37: 583–603.

Illman, W. A., Thompson, D. L., Vesselinov, V. V., & Neuman, S. P. 1998. Single-Hole and Cross-Hole Pneumatic Tests in Unsaturated Fractured Tuffs at the Apache Leap Research Site: Phenomenology, Spatial Variability, Connectivity and Scale, *Rep. NUREG/CR-5559*, prepared for U.S. Nuclear Regulatory Commission, Washington, D.C.

Kersting, A. B., Efurd, D. W., Finnegan, D. L., Rokop, D. J., Smith, D. K., & Thompson, J. L. 1999. Migration of plutonium in ground water at the Nevada Test Site, *Nature*, 397: 56–59.

Kirchner, J. W., Feng, X., & Neal, C. 2000. Fractal stream chemistry and its implications for contaminant transport in catchments, *Nature*, 403: 524–527.

Lee, J.-Y., & Lee, K.-K., 1999. Analysis of the quality of parameter estimates from repeated pumping and slug tests in a fractured porous aquifer system in Wonju, Korea. *Ground Water*, 37: 692–700.

Macilwain, C. 2001. Out of sight, out of mind? *Nature*, 412: 850–852.

Martínez-Landa, L., Carrera, J. Guimerà, J., Vazquez-Suñé, E., Vives, L., & Meier, P. 2000. Methodology for the hydraulic characterization of a granitic block, 340–345, in *Calibration and Reliability in Groundwater Modelling; Coping with Uncertainty*, ModelCARE 99, edited by Stauffer, F., Kinzelbach, W., Kovar K. & Hoehn, E. IAHS Publication 265, IAHS Press, Wallingford, Oxfordshire, UK.

Neuman, S. P. 1990. Universal Scaling of Hydraulic Conductivities and Dispersivities in Geologic Media. *Water Resour. Res.*, 26: 1749–1758.

Neuman, S. P. 1994. Generalized Scaling of Permeabilities: Validation and Effect of Support Scale, *Geophys. Res. Let.*, 21: 349–352.

Raghavan, R. 1993. *Well Test Analysis*, Prentice Hall Petroleum Engineering Series, Prentice-Hall Inc.

Rasmussen, T. C., Evans, D. D., Sheets, P. J., & Blanford, J. H. 1990. *Unsaturated Fractured Rock Characterization Methods and Data Sets at the Apache Leap Tuff Site*, NUREG/CR-5596, U. S. Nucl. Regul. Comm., Washington D.C.

Rasmussen, T. C., Evans, D. D., Sheets, P. J., & Blanford, J. H. 1993. Permeability of Apache Leap Tuff: Borehole and Core Measurements Using Water and Air, *Water Resour. Res.*, 29: 1997–2006.

Rovey II, C. W., & Cherkauer, D. S. 1995. Scale dependency of hydraulic conductivity measurements, *Ground Water*, 33: 769–780.

Rovey II, C. W. 1998. Digital simulation of the scale effect in hydraulic conductivity, *Journal of Hydrology*, 6: 216–225.

Samper-Calvete, F. J., & Garcia-Vera, M. A., 1998. Inverse modeling of groundwater flow in the semiarid evaporitic closed basin of Los Monegros, Spain, *Hydrogeology Journal*, 6(1): 33–49.

Sanchez-Vila, X., Carrera, J., & Girardi, J. P. 1996. Scale effects in transmissivity, *Journal of Hydrology* 183: 1–22.

Schad, H., & Teutsch, G. 1994. Effects of the investigation scale on pumping test results in heterogeneous porous aquifers. *Journal of Hydrology*, 159: 61–77.

Schulze-Makuch, D., & Cherkauer, D. S. 1998. Variations in hydraulic conductivity with scale of measurements during aquifer tests in heterogenous, porous carbonate rock. *Hydrogeology Journal*, 6: 204–215.

Schulze-Makuch, D., Carlson, D. A., Cherkauer, D. S., & Malik, P. 1999. Scale dependency of hydraulic conductivity in heterogeneous media, *Ground Water*, 37: 904–919.

Sposito, G. 1998. *Scale Dependence and Scale Invariance in Hydrology*, Cambridge University Press, Cambridge, United Kingdom.

Tidwell, V. C., & Wilson, J. L. 1997. Laboratory method for investigating permeability upscaling, *Water Resour. Res.*, 33: 1607–1616.

Copyright © 2003 Swets & Zeitlinger B.V., Lisse, The Netherlands

Vesselinov, V. V., & Neuman, S. P. 2001. Numerical inverse interpretation of single-hole pneumatic tests in unsaturated fractured tuff, *Ground Water*, 39: 685–695.

Vesselinov, V. V., Neuman, S. P., & Illman, W. A. 2001a. Three-dimensional numerical inversion of pneumatic cross-hole tests in unsaturated fractured tuff: 1. Methodology and borehole effects, *Water Resour. Res.*, 37: 3001–3017.

Vesselinov, V. V., Neuman, S. P., & Illman, W. A. 2001b. Three-dimensional numerical inversion of pneumatic cross-hole tests in unsaturated fractured tuff: 2. Equivalent parameters, high-resolution stochastic imaging and scale effects, *Water Resour. Res.*, 37: 3019–3041.

Zhang, D., 2001 *Stochastic Methods for Flow in Porous Media*, Academic Press, San Diego, California, U.S.A.

Zhang, D., Zhang R., Chen S., & Soll W. E. 2000. Pore scale study of flow in porous media: Scale dependency, REV, and statistical REV, *Geophys. Res. Let.*, 27: 1195–1198.

Zlotnik, V. A., Zurbuchen, B. R., Ptak, T., & Teutsch G. 2000, Support volume and scale effect in hydraulic conductivity: experimental aspects, *in* Zhang, D., and Winter, C.L., eds., *Theory, Modeling, and Field Investigation in Hydrogeology: A Special Volume in Honor of Shlomo P. Neuman's 60th Birthday*: Boulder, Colorado, Geological Society of America Special Paper 348, 191–213.

Copyright © 2003 Swets & Zeitlinger B.V., Lisse, The Netherlands

Subsurface structure and groundwater of the Takamatsu crater (cauldron) by CSAMT method and boring data

S. Hasegawa
Kagawa University, Takamatsu, Japan

S. Kanayama
Shikoku Research Institute, Takamatsu, Japan

T. Kozato
Construction Project Consultant, Osaka, Japan

H. Ishii
Naiba Corporation, Takamatsu, Japan

ABSTRACT: The Takamatsu crater is a buried depression structure identified by a low gravity anomaly in the southern part of the Takamatsu Plain, northeast Shikoku, southwest Japan (Kono et al., 1994). The CSAMT survey suggests that the crater is composed of low resistivity material, while the surrounding bedrocks have high resistivity. The depth of the crater is estimated to be about 700–900 m in depth. The surface geology and boring cores in and around the crater have confirmed that the Takamatsu crater consists mainly of rhyolitic tuff and tuff breccia, and bedrocks are granitic rocks. The resistivity structure and abundant pyroclastic flow deposits strongly support the idea that the Takamatsu carter is a cauldron. In the cauldron, most of the water is confined in the voids of the tuffaceous rocks and cannot be pumped up. The fissure water is the only available water resource in the cauldron. Limited pumping tests in the cauldron have shown that the pumping capacity is 100–150 t/day. Therefore the Takamatsu crater cannot be a huge underground water reservoir.

1 INTRODUCTION

Takamatsu city is located on the northeast part of Shikoku Island, southwest Japan. Takamatsu has been often suffered from a shortage of water, because the area has one of the lowest rainfalls in Japan.

The Takamatsu crater is a buried depression structure identified by a low gravity anomaly in the southern part of the Takamatsu Plain, northeast Shikoku, southwest Japan (Kono et al., 1994; Figure 2). Its diameter and depth are estimated to be about 4 km and 1 km by gravity surveying. The buried depression structure were proposed to be of impact origin (Kono et al., 1994, Miura et al., 1995), but Hasegawa and Ishii (1994) asserted that it is one of the cauldrons (volcanic subsidence structures) in the Setouchi Volcanic Belt from geological evidences.

Another argument is on the estimation of groundwater. Kono et al. (1994) have proposed that the Takamatsu crater contains 2 billion m^3 of groundwater. But Hasegawa and Ishii (1994) also pointed out that the depression structure is composed of rhyolitic tuff and cannot be said to be an aquifer. If the Takamatsu crater was a huge aquifer, frequent water shortage might be solved. Takamatsu city have been surveyed with CSAMT (Controlled Source Audio-frequency Magneto-Telluric) in order to estimate the subsurface structure and groundwater of the Takamatsu crater. This paper describes the results of the CSAMT survey and discusses the subsurface structure and the groundwater of the Takamatsu crater.

2 GEOLOGICAL SETTING

2.1 *Topography*

The Takamatsu crater is a buried depression structure identified by a low gravity anomaly in the southern part of the Takamatsu Plain. In the area of the Takamatsu no crater topography is observed and small conic hills are

Copyright © 2003 Swets & Zeitlinger B.V., Lisse, The Netherlands

distributed on the plain (Figure 1). These conic hills are buttes of Middle Miocene volcanic rocks.

2.2 *Geology*

The Takamatsu Plain is covered by thick Quaternary fluvial sediments. They are composed of the Plio-Pleistocene Mitoyo Group, late Pleistocene and Holocene alluvium.

The bedrock of the Takamatsu Plain consists of Late Cretaceous granitic rocks. They are distributed outside of the Takamatsu crater (Figure 2). The conic hills in the Takamatsu crater are buttes of Middle Miocene volcanic rocks which are named the Sanuki Group. The tops of hills are covered by biotite dacite lava, and the foot of the hills are composed of rhyolitic tuff and tuff breccia which originated from pyroclastic flow deposits. The glass and associated rhyolite dated by K-Ar method are estimated to be 14 Ma (million years) (Yamada & Sato, 1998).

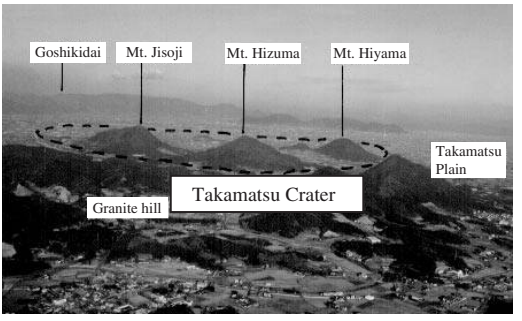


Figure 1. Topography of the Takamatsu crater (cauldron).

3 CSAMT SURVEY

3.1 *CSAMT method*

The CSAMT method is a frequency domain Electromagnetic (EM) method, and a frequency range of 1.25–5120 Hz is used to investigate deep subsurface structures. This method is usually applied to detect large-scale geologic structures where the electrical resistivity survey can not be applied.

As the depth of the Takamatsu crater is estimated to be about 1.5 km by gravity surveying, the CSAMT method is applied to estimate the geologic structure and groundwater of the Takamatsu crater.

3.2 *Field measurements*

The arrangement of the transmitter and receivers is shown in Figure 3. Twelve receivers are arranged north and south across the Takamatsu crater along the main

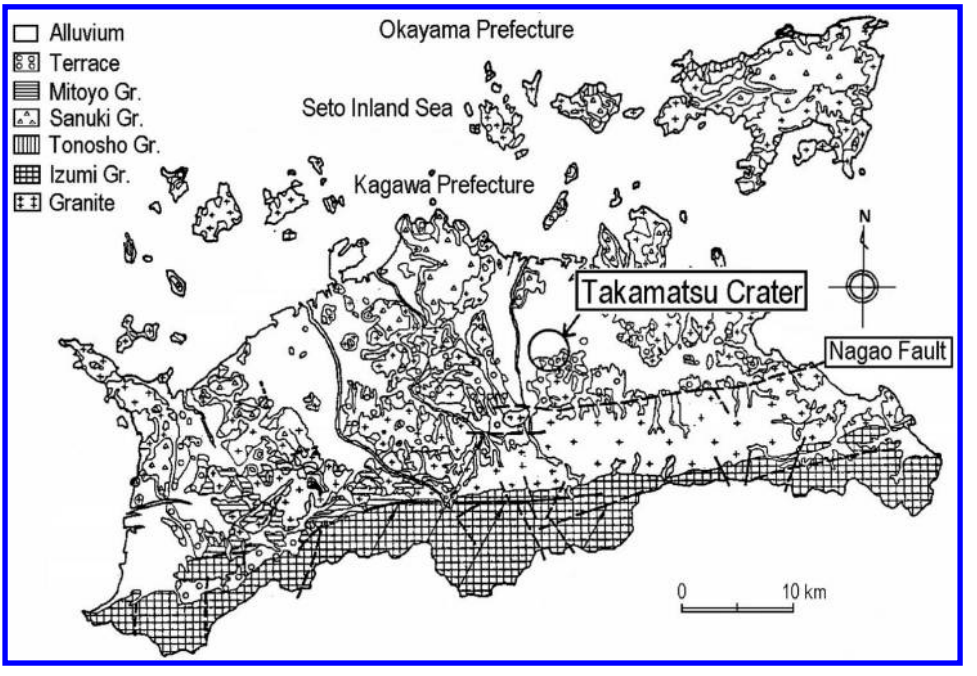


Figure 2. Locality of the Takamatsu crater (cauldron).

Copyright © 2003 Swets & Zeitlinger B.V., Lisse, The Netherlands

survey line, and five receivers are arranged east and west across the crater. The outline of the survey is as follows:

Receiver:	16 points
Direction:	N12W (Electric field)
	N78E (Magnetic field)
Frequency (Hz):	5120, 2560, 1280, 640, 320, 160, 80, 40, 20, 14, 10, 7.8, 5, 2, 1.25

3.3 *Data processing*

3.3.1 *Resistivity column*

The resistivity column of each receiver point is calculated by non-linear method of least squares, by assuming three to five resistivity layers. The resistivity columns of the Takamatsu crater are shown in Figure 4.

3.3.2 *Resistivity profile*

The resistivity profiles are obtained by using topological smoothing theory. The north-south resistivity profile is shown in Figure 5.

3.3.3 *FEM 2D inversion*

The resistivity profiles obtained from FEM 2D inversion is shown in Figure 6. In FEM 2D inversion, the ground is divided into cells and resistivity of each cell is computed. Initial resistivity is given by Figure 5.

3.4 *Results*

The CSAMT survey suggests that the crater is composed of low resistivity material, while the surrouding bedrocks have high resistivity. The surface margins of the low resistivity material are located between receiver No. 3 and 4, and between receiver No. 10 and 11. Both boundary points coincide with the margin of the Takamatsu crater by gravity surveying.

The depth of the crater is estimated to be 700–900 m below ground level. This indicates the bottom of the Takamatsu crater, but the depth is merely an approximate value because of near field effects. The low resistivity structure which inclines from the bottom margin to the outside is characteristic of the crater.

4 BORING DATA

4.1 *Geologic logs*

Figure 3 shows the boring locality and Figure 8 shows their geologic logs. At the location of the B-1 log, which is outside the crater, the bedrock is confirmed as granitic rock. At B-3, 4, and 5 logs which are inside

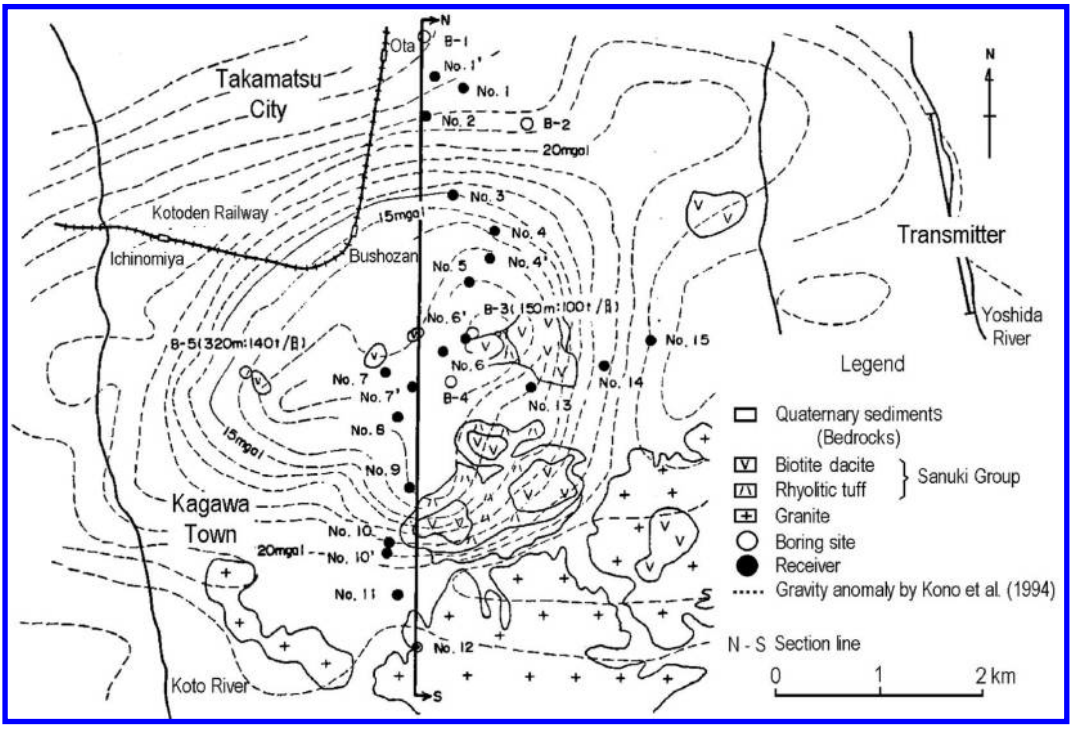


Figure 3. Gelology and CSAMT survey of the Takamatsu crater.

Copyright © 2003 Swets & Zeitlinger B.V., Lisse, The Netherlands

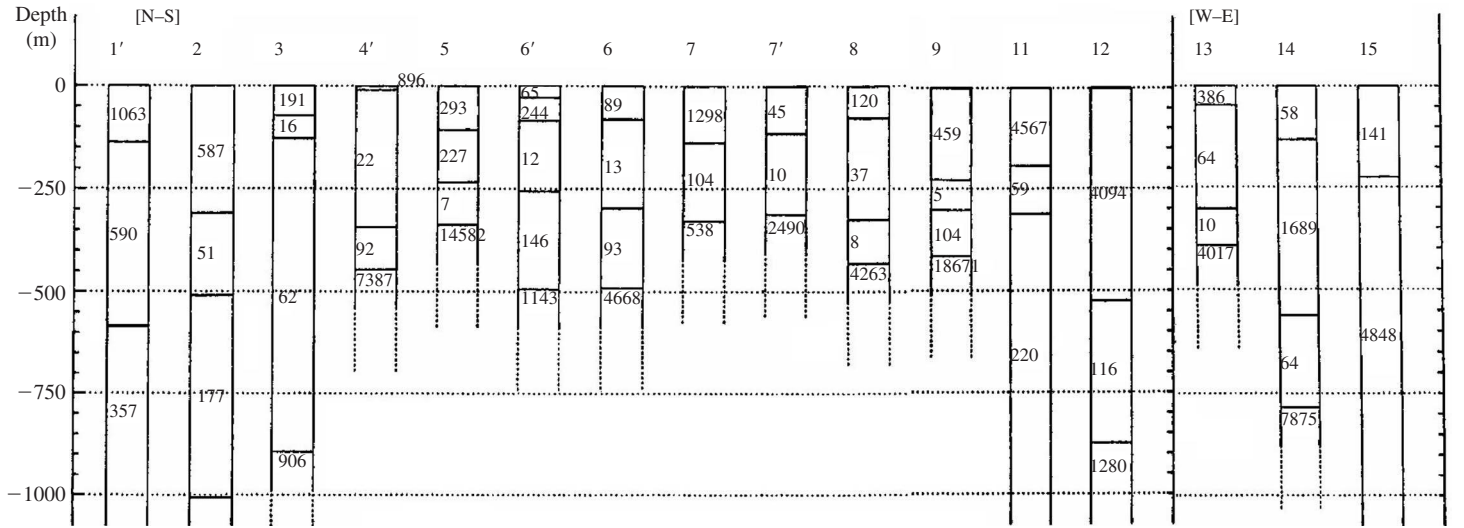


Figure 4. Resistivity columns of the Takamatsu crater.

Copyright © 2003 Swets & Zeitlinger B.V., Lisse, The Netherlands

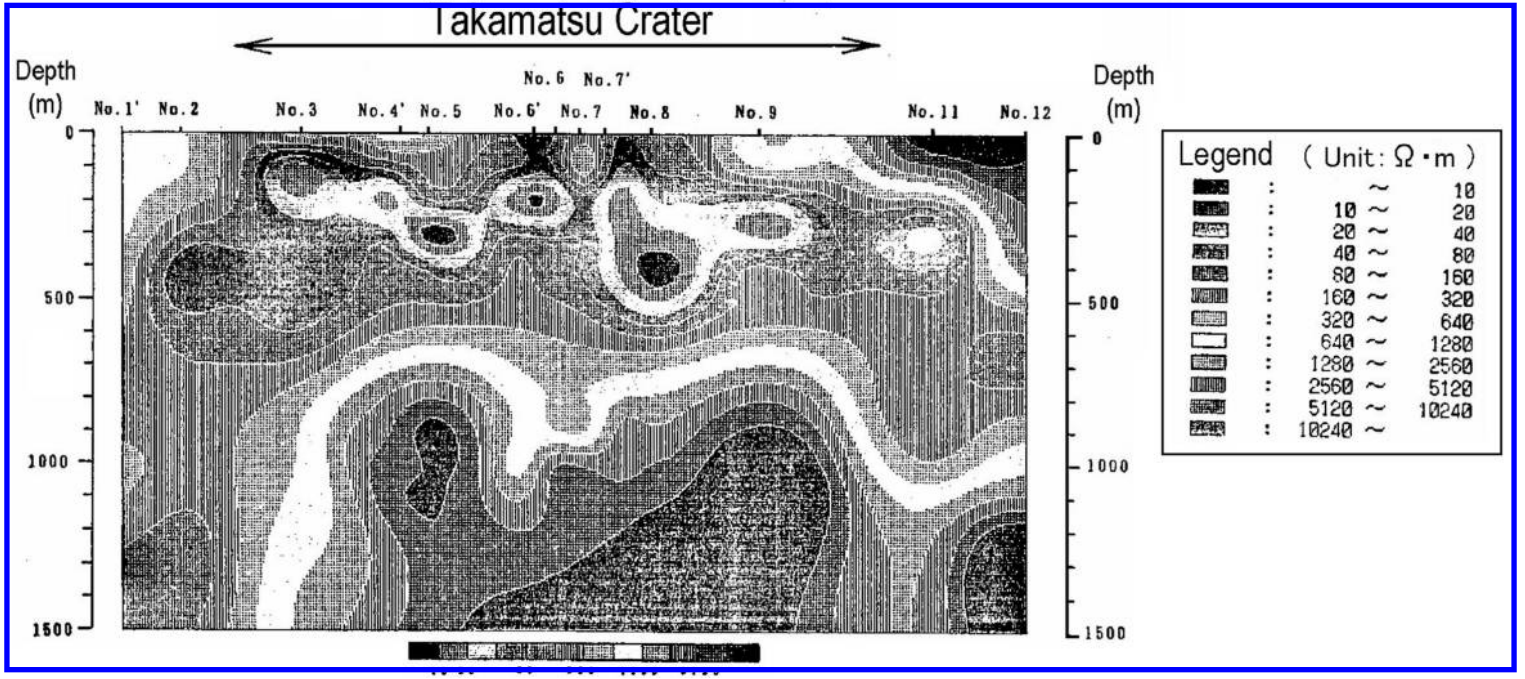


Figure 5. Resistivity profile of the Takamatsu crater (N-S direction).

Copyright © 2003 Swets & Zeitlinger B.V., Lisse, The Netherlands

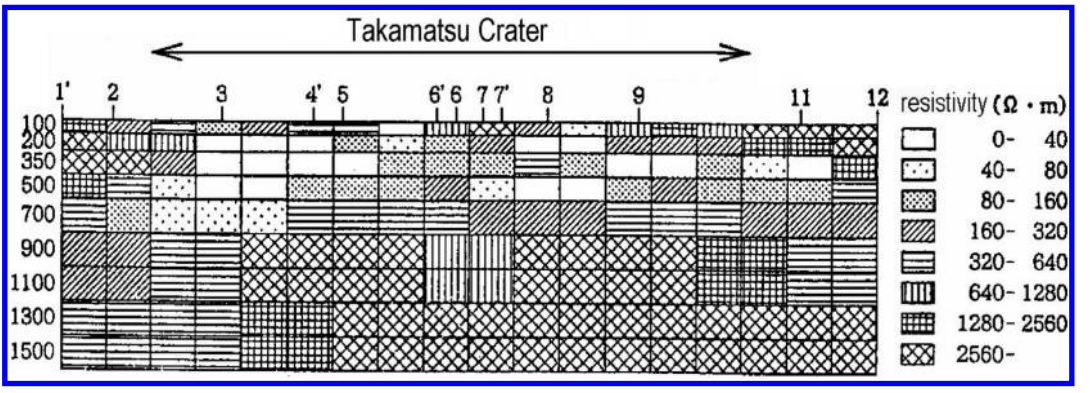


Figure 6. The resistivity profiles are obtained by FEM 2D inversion.

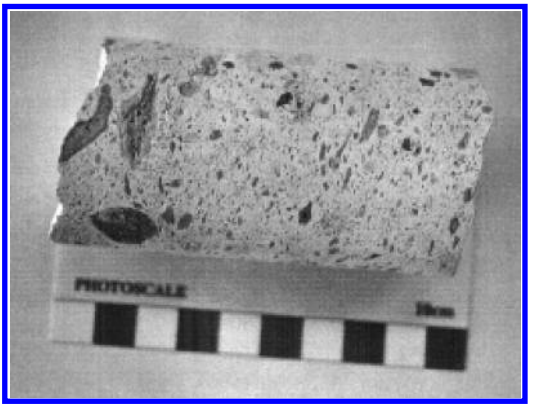


Figure 7. Boring cores of rhyolitic welded tuff sampled from 320 m under the ground at B-5.

the crater, the bedrock is confirmed as tuff and tuff breccia.

At B-5, boring cores of rhyolitic welded tuff were sampled from 320 m under the ground (Figure 7). This indicates that the Takamatsu crater is filled with thick rhyolitic tuff and tuff breccia.

4.2 *Physical properties of tuff*

The specific gravity of tuff sampled from the B-5 boring cores was measured. The saturated apparent specific gravity is 2.055, and true specific gravity is 2.450. Water absorption of tuff is 15.0%. This indicates that the tuff has abundant porosity.

The resistivity of tuff sampled from the B-5 boring cores was measured. The resistivities of tuff in the saturated condition and in the dry condition are 44.3 Ωm and 65252 Ωm respectively.

The sample measurement of specific gravity and resistivty confirm the low gravity anomaly and the low resistivity measured in the field study.

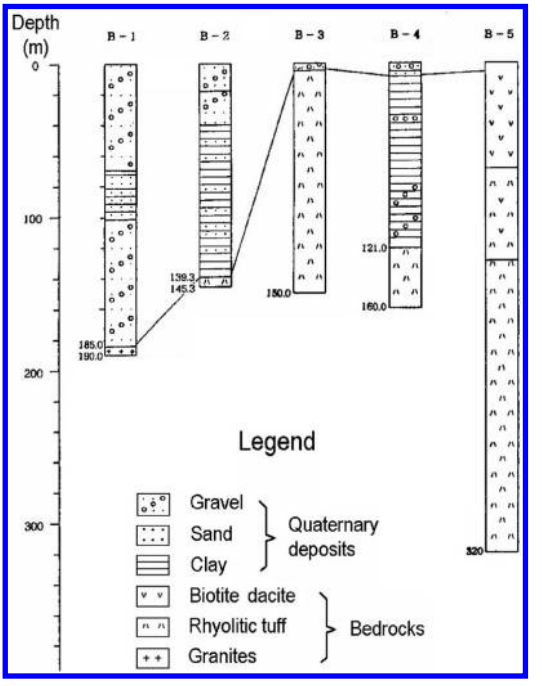


Figure 8. Geologic logs of the Takamatsu crater.

5 DISCUSSION

5.1 *Geologic structure*

The surface geology and boring cores in and around the crater have confirmed that the Takamatsu crater consists mainly of rhyolitic tuff and tuff breccia, and bedrocks are granitic rocks (Figure 9). The specific gravity of tuffs sampled from 300 m below ground level is around 2.1, and their water absorption is about 15%. The resistivity is under 100 Ωm in water-saturated condition. The constituent materials of the

Copyright © 2003 Swets & Zeitlinger B.V., Lisse, The Netherlands

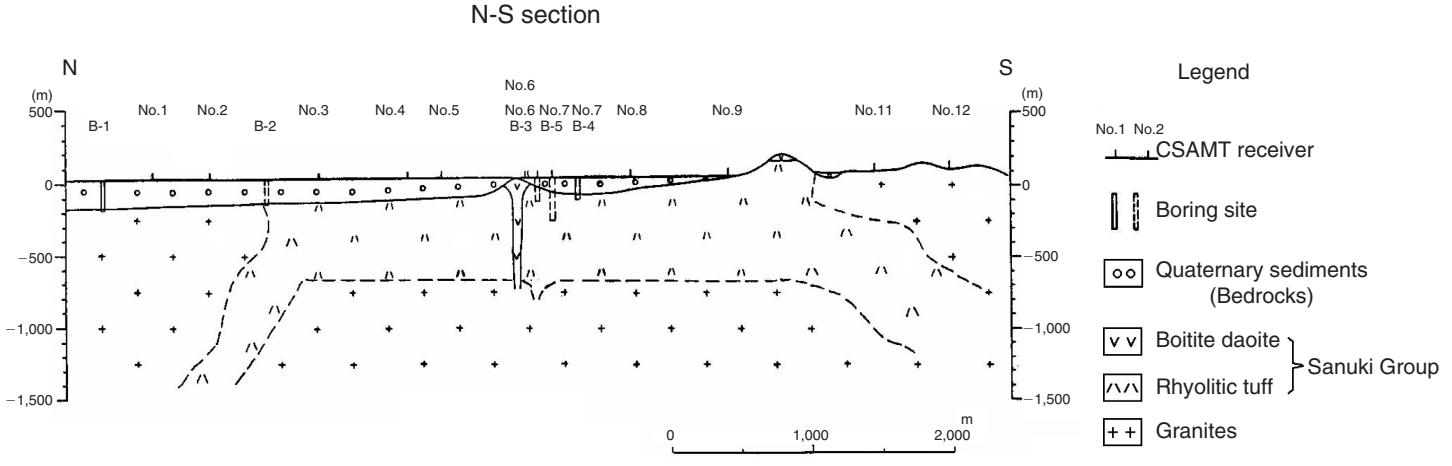


Figure 9. Geologic profile of the Takamatsu crater (N-S direction).

Copyright © 2003 Swets & Zeitlinger B.V., Lisse, The Netherlands

Takamatsu crater are considered to be water-saturated tuff and tuff breccia which are of pyroclastic flow origin. The depth to the bottom of the crater, which is the boundary between tuff and the granitic rocks is estimated to be 700–900 m.

Abundant pyroclastic flow deposits strongly support the idea that the Takamatsu carter is a cauldron. The low resistivity structures which incline from the bottom margin to the outside are inferred to be dikes or hydrothermal alteration zones caused by rhyolitic volcanism. This structure resembles that of the cauldron.

Unconsolidated Quaternary sediments unconformably cover both the tuff and granitic rocks. The depth of the sediments gradually increases towards the north and does not increase inside the crater. Thus, the Takamatsu crater is not composed of unconsolidated sediments.

5.2 *Groundwater*

The Takamatsu crater is not composed of unconsolidated sediments but of Miocene tuff and tuff breccia which are treated as a rockmass. In porous tuffaceous rocks most of the groundwater is confined in the void of rocks and cannot be pumped up. The fissure water is the only available water resource in the cauldron. Therefore, the Takamatsu crater is not a huge aquifer.

A limited number of pumping tests in the cauldron have shown that the pumping capacity is 100–150 m^3/day. This indicates that the Takamatsu crater can be used for a small source of water supply but cannot be a huge underground dam as proposed by Kono et al. (1994).

In addition, there is no risk of ground subsidence due to pumping from the cauldron, because available ground in the cauldron is pumped only from fissure water in taffceous rockmass.

6 CONCLUSIONS

Conclusions of this research are as follows:

1. The CSAMT survey suggests that the crater is composed of low resistivity material, while the surrouding bedrocks have high resistivity. The depth of the crater is estimated to be 700–900 m below ground. The resistivity structure resembles that of a cauldron.
2. The surface geology and boring cores in and around the crater have confirmed that the Takamatsu crater consists mainly of rhyolitic tuff and tuff breccia, and bedrocks are granitic rocks.
3. The specific gravity of tuffs sampled from 300 m below ground is around 2.1, and their water absorption is about 15%. The resistivity is under 100 Ωm in water-saturated condition. The constituent materials of the Takamatsu crater are explained by pyroclastic rocks. Abundant pyroclastic flow deposits strongly support that the Takamatsu carter is a cauldron.
4. The Takamatsu crater is composed of porous Miocene tuffaceous rocks. The fissure water is the only available water resource in the cauldron. Therefore, the Takamatsu crater is not a huge aquifer. Few pumping tests indicate that the Takamatsu crater can be used as a small source of water supply but cannot be a huge underground dam as proposed by Kono et al. (1994).

ACKNOWLEDGEMENT

This research was commissioned by the Takamatsu City Office. The authors would like to express their sincere gratitude to Mrs. Noboru Hayashi and Michitsugu Yoshida of Takamatsu City Office and Mr. Shouzo Tamura of Tamura Boring Co. Inc. for their help. We also thank Prof. W.D. Liam Finn of Kagawa University for advice on English expression of the manuscript.

REFERENCES

Hasegawa, S. & Ishii, H. 1994. Hydrogeological structure of the Takamatsu crater. *Proc. Annual Meeting of Chugoku-Shikoku Branch Jap. Soc. Eng. Geol.*, 31–34.

Hasegawa, S., Kanayama, S., Kozato, T. & Ishii, H. 2000. Subsurfacel structure and groundwater of the Takamatsu cauldron by CSAMT method. *Proc. Annual Meeting of the Jap. Soc. Eng. Geol.*, 109–112.

Kono, Y., Furumoto M. & Nagao, T. 1994. Gravity anomaly of Takamatsu crater. *ISAS Lunar and Planetary Symp.*, 67–70.

Yamada, R. & H. Sato 1998. Petrology of glassy rocks from Takamatsu crater, Kagawa Prefecture, Japan. *Gankou, Vol. 93*, 279–290.

Miura, Y., Okamoto, M., Fukuchi, T., Sato, H., Kono, Y. & M. Furumoto 1995. Takamatsu crater structure, Preliminary report of impact crater in active orogenic region. *Slope Lunar Planet. Sci., XXVIS(LPI, Houston)*, 987–988.

Copyright © 2003 Swets & Zeitlinger B.V., Lisse, The Netherlands

Discrimination of shallow and deep permeable zones by time-series electric prospecting in a rock mass slope

E. Tamura
Yonden Consultants Co., Inc., Takamatsu, Japan

S. Hasegawa
Kagawa University, Takamatsu, Japan

S. Tsuruta & S. Kanayama
Shikoku Research Institute, Inc., Takamatsu, Japan

ABSTRACT: The infiltration zones of groundwater in bedrock are very complex. Some infiltration zones are located near the ground surface and allow water to infiltrate rapidly into bedrock. Others are located deep in bedrock, where groundwater flows slowly. It is usually difficult to distinguish such complex permeable zones in bedrock by the borehole investigations alone. The authors explored permeable zones in a rock mass slope by time-series electrical prospecting and verified the results by continuous observation of groundwater in boreholes. This technique of time-series electrical prospecting can be utilized in designing sealing works for bedrock of dams, etc. and the design of drainage works for the prevention of landslides.

1 INTRODUCTION

The infiltration zones of groundwater in bedrock have extremely irregular structure; it is difficult to map the distribution of groundwater by borehole investigations alone. This paper presents a technique for making effective use of physical prospecting to complement the investigation by boring.

Electrical prospecting is one of the most effective physical methods of prospecting the ground for groundwater. This technique measures the resistivity of the ground in order to describe the distribution of groundwater. Besides, the changes of water contents of various zones in the ground can be investigated by carrying out time-series measurements of resistivity in the ground.

Kojima et al. (1989) revealed high-permeability zones in bedrock by using resistivity tomography, when brine was used as a tracer. Wada et al. (1995) elucidated the process of infiltration of rainwater into a plateau of sirasu by using continuous high-resolution electrical prospecting.

In the present study, high- and low-permeability zones under a bedrock slope were visualized by using resistivity tomography during and after rainfall. In addition, the continuous measurement of water levels and pore water pressures in groundwater under the slope was conducted to verify the infiltration process elucidated by the electrical prospecting.

2 TOPOGRAPHY AND GEOLOGY OF PROSPECTED SLOPE

The electrical prospecting was conducted on a slope to the south of the River Omogo, in Ehime Prefecture, Shikoku Island, South-west Japan (Fig. 1). The prospected slope is concave slightly and faces the east. The average gradient of the slope is from 30° to 40°. The slope is composed of slate containing lenticular rocks of chert, green rock, and sandstone in Chichibu Belt (CRIEPI, 1994). The bedrock is covered with deposited rock rubble from 3 m to10 m in thickness.

3 PROSPECTING METHOD

3.1 *Measuring method*

Resistivity imaging automatically make many measurements of the apparent resistivity in the two-dimensional section under a straight traverse and performs automatic two-dimensional analysis (Shima et al. 1995).

Copyright © 2003 Swets & Zeitlinger B.V., Lisse, The Netherlands

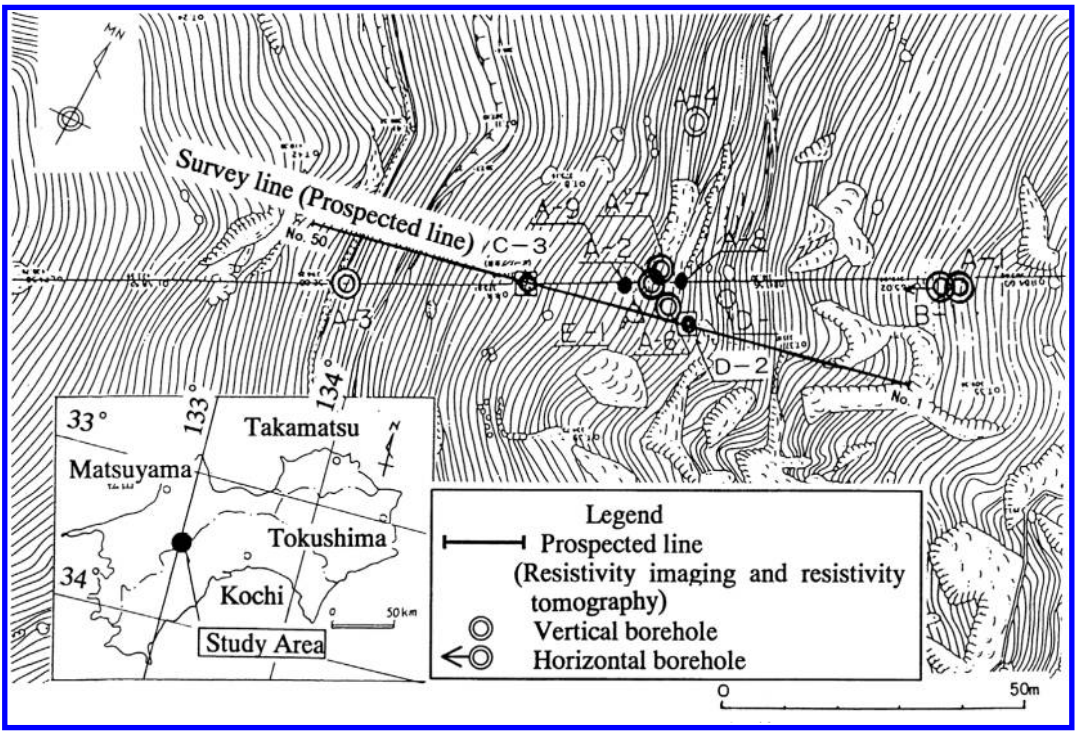


Figure 1. Location of prospected slope and prospected line.

Table 1. Arrangement of electrodes for resistivity tomography.

	Borehole D-2	Ground surface	Borehole C-3
Length of traverse	About 13 m	98 m (horizontal distance)	About 14.6 m
Spacing between electrodes	1.9 m	2.0 m	2.4 m
Number of electrodes	8*	50	7*

*Below the groundwater level.

Resistivity tomography arranges electrodes around an area to be prospected and reproduce the distribution of resistivity in the ground from obtained data (Sasa et al. 1993). Resistivity tomography is more effective deep in the ground than resistivity imaging.

In this study, electrical prospecting by resistivity imaging and by resistivity tomography were performed on the prospected line that we would call is a survey line shown in Figure 1. The length of the prospected line was 98 m and the electrodes were arranged at regular intervals of 2 m (Table 1). For resistivity tomography, vertical boreholes D-2 and C-3 were used as observation holes (Figure 1). The electrodes were arranged at regular intervals of 2 m below the groundwater level in the boreholes (Table 1). An electrical-prospecting device Mcohm-21 from Oyo Corporation, Japan was used.

3.2 *Method of analysis*

The analysis was performed with a workstation (Sun OS4/10) by the α-center method. This method is able to calculate the distribution of electric potentials of the structure from resistivities without constraints (Shima et al. 1995).

Difference analysis of the resistivity in the bedrock measured on the same survey line by resistivity tomography before, during, and after rainfall was performed in order to visualize the infiltration zones of groundwater. In difference analysis, the resistivity during

Copyright © 2003 Swets & Zeitlinger B.V., Lisse, The Netherlands

rainfall was divided by that of before rainfall and the ration of change of the resistivity was obtained. Similarly, the ration of change of the resistivity between during rainfall and after rainfall also was obtained by dividing the resistivity after rainfall by the resistivity during rainfall.

4 COMPARISON BETWEEN RESISTIVITY IMAGING AND RESISTIVITY TOMOGRAPHY

Before the time-series measurement of resistivity beneath the slope, resistivity imaging using only ground electrodes and resistivity tomography using both ground and underground electrodes were tested on the same survey line in order to compare and evaluate their prospecting capabilities.

The nature of resistivity described by resistivity imaging in the vicinity of the ground surface is similar to that by resistivity tomography. Both methods revealed a high-resistivity zone under the upper side of the slope below the borehole D-2 and the upper side of the slope above the borehole C-3 (Figure 2). In addition, both methods revealed low-resistivity zones under the section of the slope between D-2 and C-3 (Figure 2).

However, the structure of resistivity become more monotonous in the deeper prospecting area by the resistivity imaging (Fig. 2a). On the other hand, resistivity tomography describes the complex structure of resistivity to the depths of the ground (Fig. 2b). Thus, resistivity tomography can prospect the ground more deeply and accurately than resistivity imaging.

5 TIME-SERIES MEASUREMENT BY RESISTIVITY TOMOGRAPHY

5.1 *Purpose*

Time-series measurement of resistivity using resistivity tomography was carried out in order to analyze the relation between rainfall and resistivity, and visualize the process of infiltration of rainwater into the ground.

5.2 *Rainfall and measurement*

Three measurements were carried out on the survey line of Figure 1; i.e., on November 7 and 8 and December 1, 1995 (Figure 3). During-rainfall data were obtained three hours later after the beginning of rainfall on November 7. Post-rainfall data were obtained 10 hours later after the end of rainfall on November 8. The resistivity was measured on December 1, too, and the obtained data were treated as pre-rainfall data. It began to rain about 9 a.m. on

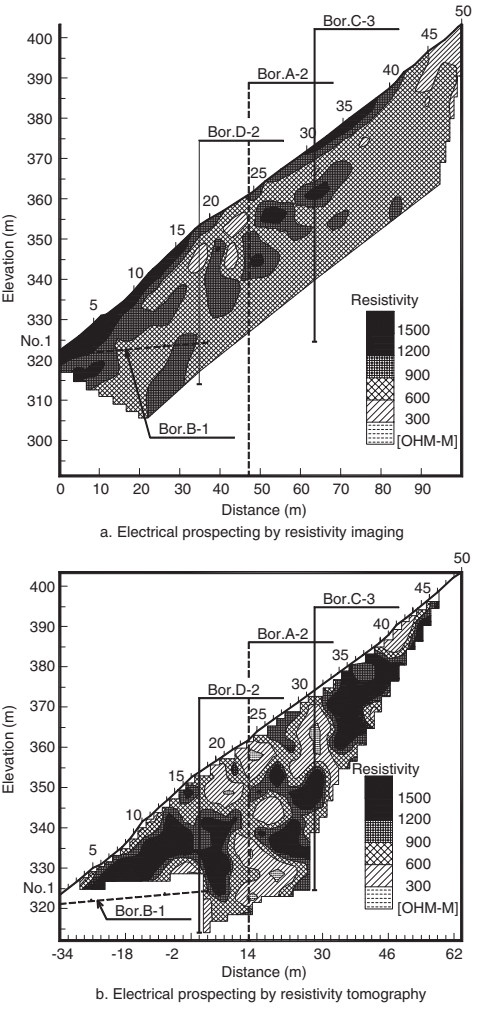


Figure 2. Result of test for composition between resistivity imaging and resistivity tomography.

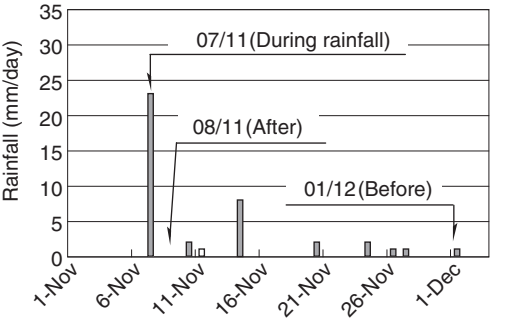


Figure 3. Rainfall at slope and date of test of resistivity tomography.

Copyright © 2003 Swets & Zeitlinger B.V., Lisse, The Netherlands

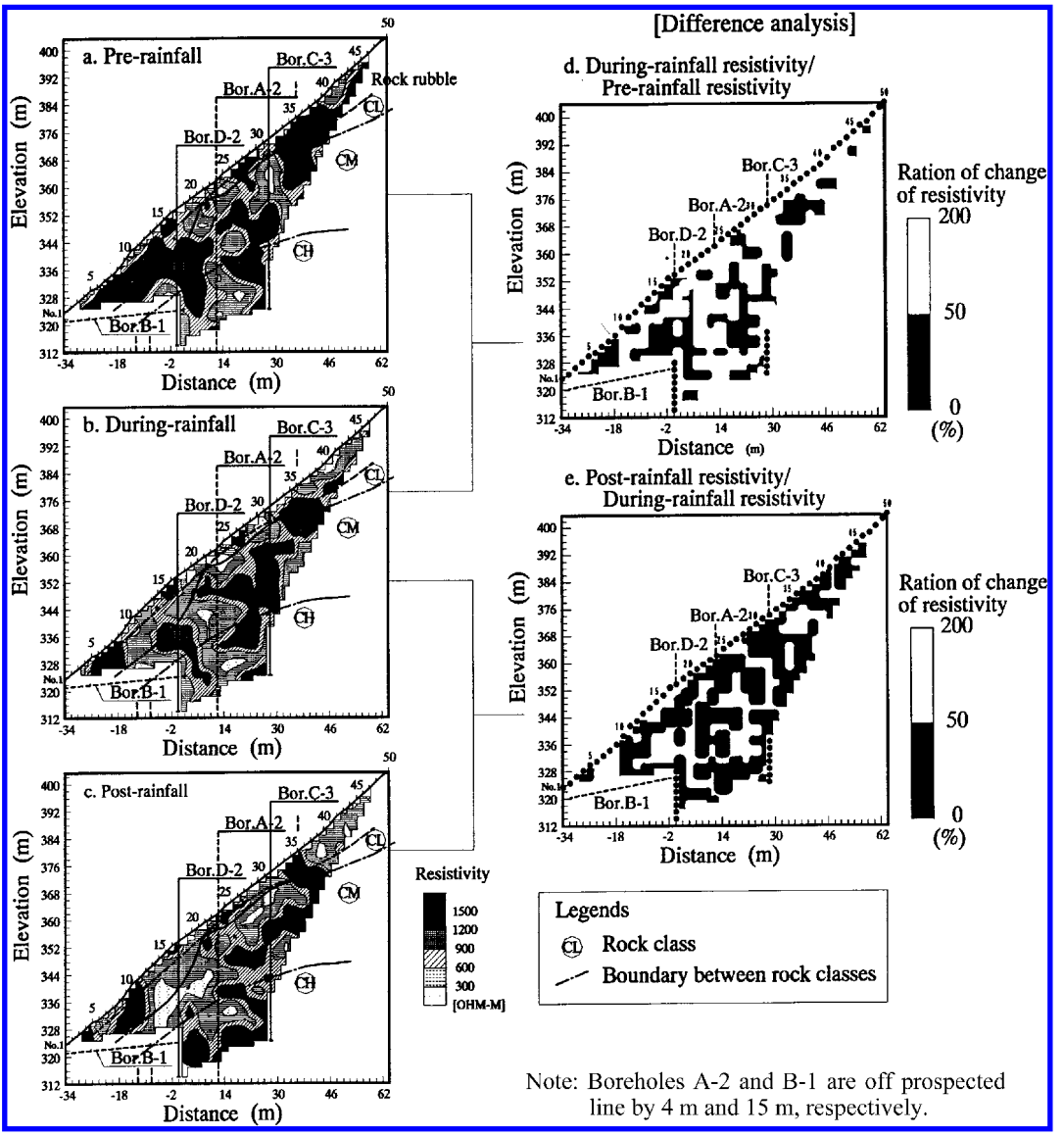


Figure 4. Results of analyses of time-series measurements.

November 7 and the cumulative rainfall at 10 p.m. on the day was 23 mm. The groundwater levels in the boreholes could not be measured during the measurement of resistivity, because the electrodes were set in the boreholes. The groundwater level during the three measurements was about 25 m in depth.

The ration of change of resistivity in analysis was expressed on a scale of 0% to 200%. 100% means no change of resistivity. 50% or less of the change becomes small in the resistivity and it is shown that many groundwater infiltrated into the ground.

5.3 *Result of analysis*

5.3.1 *Comparison of distributions of resistivity before, during, and after rainfall*

The distributions of resistivity before, during, and after rainfall were characterized by the following points.

(a) The distributions of resistivity during and after the rainfall differed remarkably from that before the rainfall. There was no remarkable difference between the distributions of resistivity during and after the rainfall (Figure 4a,b,c).

Copyright © 2003 Swets & Zeitlinger B.V., Lisse, The Netherlands

(b) The resistivity of the zone about 10 m thick under the lower side of the slope than the point of the borehole D-2 was over 900 Ω-m before the rainfall. The resistivity fell rapidly below 600 Ω-m during the rainfall and increased again after the rainfall (Figure 4a,b,c).

Although the total rainfall was as little as 23 mm, the general resistivity fell rapidly during the rainfall. There were some areas where the resistivity decreased further after the end of the rainfall. The about 10 m thick zone under the lower side of the slope below the borehole D-2 has a high permeability and responded very rapidly to the rainfall, its resistivity falling remarkably.

5.3.2 *Process of groundwater infiltration ascertained by difference analysis*

The rations of change of resistivity were found by difference analysis. The zones of change rations of 50% and less are indicated by shading in Figure 4d,e (Resistivity during-rainfall divided by pre-rainfall resistivity and post-rainfall resistivity divided by during-rainfall resistivity).

The distribution of the change ration caused by the rain and the distribution of the change ration caused by the ceasing of the rain were quite different from each other, indicating that the rainwater infiltrated rapidly into some zones during the rainfall and more gradually into other zones after the rainfall.

5.3.3 *Relation between bedrock classification and resistivity*

The bedrock classification estimated from the well logs of boreholes D-2 and C-3 and the resistivity measured by the time-series measurement were compared (Fig. 4a,b,c). The resistivity of the zone under the survey numbers 3–17 was over 1,500 Ω-m but fell below 600 Ω-m during the rainfall. The zone is composed of very loose CL-class rock. The zone is usually in an unsaturated state, presenting a high resistivity, but once it rains, the zone allows rainwater to infiltrate rapidly through its fissures and thereby reduce its resistivity. After the rain has stopped, the zone, having a poor water retentivity, returns rapidly into an unsaturated state.

6 VERIFICATION OF WATER-INFILTRATION PROCESS BY CONTINUOUS MEASUREMENT OF GROUNDWATER

The groundwater levels in the vertical boreholes A-1 to A-4 shown in Figure 1 were continuously measured with water-pressure sensors. The inside of the horizontal borehole B-1 at the bottom of the slope was divided into three chambers by a packer in order to measure the water-inflow pressure at three different depths beneath the slope. In addition, the flow rate of a nearby stream below the slope was measured (Figure 5, Tamura & Matsuka 1999).

There were observed time differences among the increase of the flow rate of the stream and the rise of groundwater levels and the increase of pore water pressure in the vertical boreholes halfway up the slope, while it was raining continuously. Rainfall was 671 mm during the period of July 26–30, 1993 (Figure 5, Tamura & Matsuka 1999). The rainfall at the time of continuous observation of groundwater in 1993 and the rainfall at the time of electrical prospecting in 1995 were different. However, since the changes of groundwater and the changes of resistivity occurred at the same places, the electrical prospecting appeared to have properly distinguished between the filtration zones near the ground surface where groundwater flows rapidly and infiltration zones deep in the ground where groundwater flows slowly. The early rise of the groundwater level in the borehole A-2 is indicative of high-permeability zones near the ground surface. The late rise of water-inflow pressure at the deepest portion (31–40 m deep) of the horizontal borehole B-1 is indicative of low-permeability zones in the depths of the ground. The topography and geologic structure of the region suggest that the deeply and slowly infiltrating groundwater is fed from the mountain behind the slope.

7 CONCLUSIONS

The results of electrical prospecting of the slope are as follows.

1. Resistivity tomography was capable of prospecting the nature of resistivity in deep bedrock more accurately than resistivity imaging. High- and low-permeability zones were visualized by applying difference analysis to the changing resistivity in the bedrock due to the rainfall.
2. The high-permeability zones near the ground surface are composed of very loose weathered rock. They are usually in an unsaturated state, presenting a high resistivity, but when it rains, they allow the rainwater to infiltrate rapidly into them through their fissures and thereby lower their resistivity.
3. The time lag between the rise of groundwater levels and the rise of pore water pressure and the changes of resistivity in the bedrock indicated that the groundwater could be classified into groundwater flowing near the ground surface and groundwater flowing deep the ground. The latter seemed to be fed from the mountain behind the slope.
4. The continuous observation of groundwater in the boreholes revealed a time lag between the rise of groundwater level and the increase of pore water pressure during rainfall. Discrimination of shallow

Copyright © 2003 Swets & Zeitlinger B.V., Lisse, The Netherlands

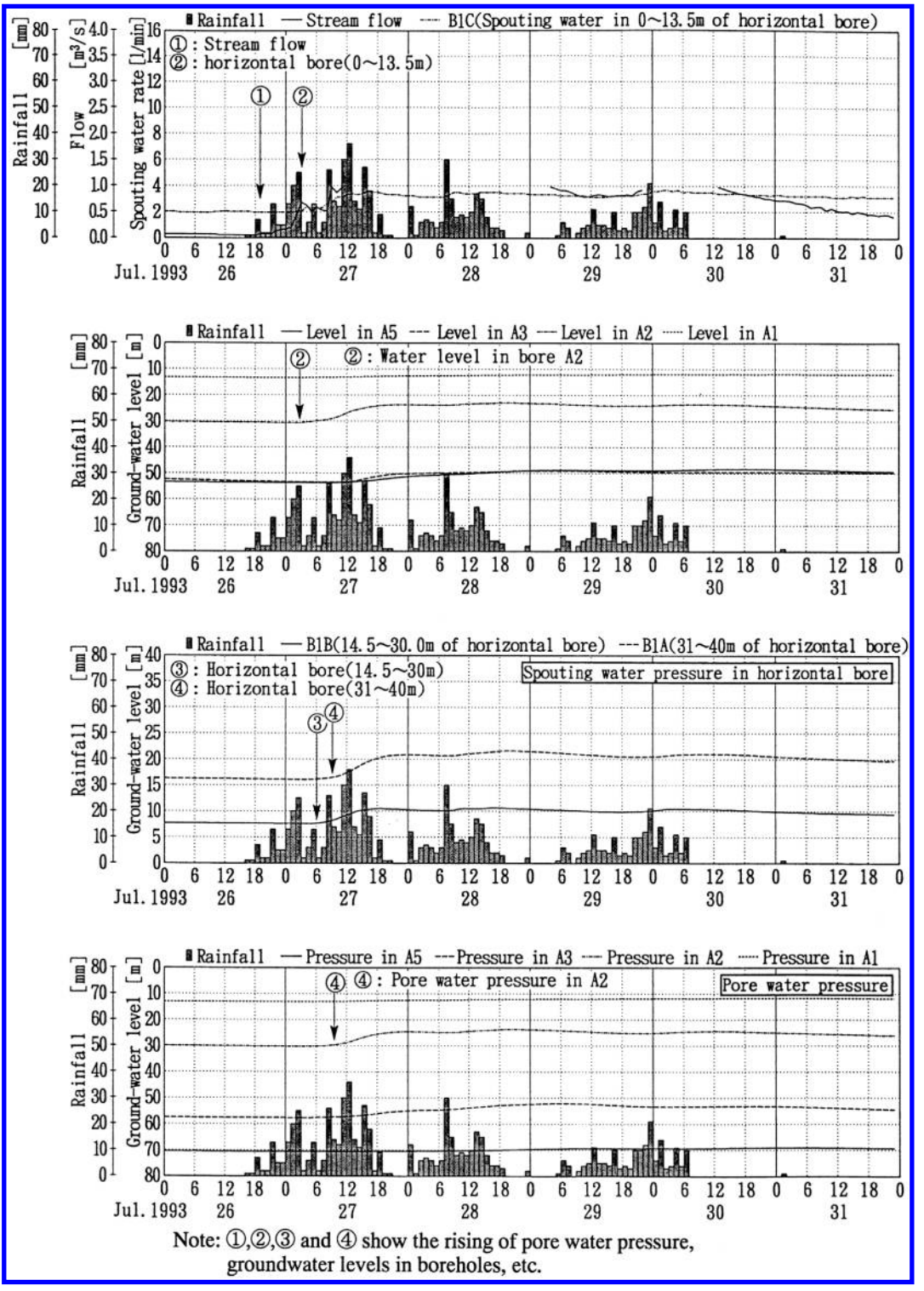


Figure 5. Automatic measurement of pore water pressure and groundwater levels in boreholes in bedrock slope.

Copyright © 2003 Swets & Zeitlinger B.V., Lisse, The Netherlands

and deep permeable zones by time-series electric prospecting was verified by the continuous measurement of underground water.

It was ascertained in this study that the ration of change of resistivity found by time-series electrical prospecting was effective in determining the process and zones of infiltration of rainwater into bedrock. This technique can be utilized for the study of sealing works for bedrock of dams, etc. and the design of drainage works in measures against landslides.

REFERENCES

Central Research Institute of Electric Power Industry 1994. *Report on case studies of hard-rock slopes*.

Kojima, K., Kamio, S., Ishibashi, H., Uchiyama, N., Saitoh, H. & Shima, H. 1989. Imaging of bedrock by geotomography (Part 2): Imaging of groundwater flows in bedrock. *Jour. Japan Soc. Engineering Geology*, 30(4): 1–10.

Oyo Corporation 1992. Measurement to analysis by resistivity imaging: Examples of application. *19th OYO Corporation technical seminar*.

Oyo Corporation 1996. *Report on work on evaluation test for bedrock by resistivity tomography*.

Sasa, K., Ashida, Y. & Kayano, T. 1993. *Physical prospecting for construction and disaster-prevention engineers*, p. 186. Tokyo: Morikita Shuppan.

Shima, H., Kajima, K. & Kamiya, H. 1995. *New electrical prospecting for construction, disaster prevention, and environment: Resistivity imaging*, p. 206. Tokyo: Kokon Shoten.

Wada, T., Inoue, M., Yokota, S. & Iwamatsu, H. 1995. Infiltration of rainwater into sirasu plateau observed by automatic continuous electrical prospecting. *Jour. Japan Soc. Engineering Geology*, 36(5): 29–38.

Tamura, E. & Matsuka, S. 1999. Automatic measurement of pore water pressure under hard-rock slope and sliding weathered-rock slope: Field survey in mountainous region in Shikoku Island, Japan. *Slope Stability Engineering*, N. Yagi, T. Yamagami & J. Jiang (eds), Balkema, 135–140.

Copyright © 2003 Swets & Zeitlinger B.V., Lisse, The Netherlands

Investigations and tests for evaluating the permeability of pyroxene andesite

T. Kakue & H. Kishi
Tokyo Electric Power Company, Kannagawa Power Plant Construction Office, Takasaki City, Japan

ABSTRACT: The permeability of dam foundations is generally evaluated by Lugeon water test. Lu values obtained by the test can be converted to coefficient of permeability, which would be needed in evaluating the amount of leakage from the reservoir, only in the case of laminar flow condition. For the jointed rock with open fissures, Lu values are liable to be underestimated, compared to those obtained under laminar flow condition, due to turbulent flow in testing. In this paper, examining the various kinds of field test methods such as investigations by analyzing a model of water balance in the river basin and conducting tracer tests, we have shown that these methods are useful to evaluate the permeability under laminar flow condition.

1 INTRODUCTION

Fewer sites with hard, highly impermeable rock masses have recently been available for dam construction. Dams are therefore constructed in many cases on foundations of volcanic rock, which is hard but jointed and highly permeable. For constructing dams on such highly permeable rock foundations, not only the stability of dam foundations but also the leakage from the rock masses around the regulating reservoir may be a critical issue. Thus, evaluating the permeability of the rock mass becomes important to the design of foundation treatment and the economic value of the dam.

This paper describes the usability of investigating and testing methods for evaluating the permeability of open jointed rock mass that can be substituted for the Lugeon test that is used generally but has some limitations.

2 GEOLOGICAL CHARACTERISTICS AT THE TEST SITE AND JOINTS IN PYROXENE ANDESITE

Investigations and tests were conducted in the rock mass around the upper dam of a pump storage power station. The geology at the dam site consists of the quaternary volcanic eruptive rock mainly composed of pyroxene andesite distributed over the base of Neogene tuff (Figures 1). The lapilli tuff at the bottom layer of the volcanic eruptive rock is relatively impermeable. Tabular joints and open joints, which are unique to lava, however, developed in the pyroxene andesite. The pyroxene andesite is therefore highly permeable. A stratum of loam containing relatively impermeable silicious volcanic ashes in its lower layer covers the pyroxene andesite.

The groundwater flows through the stratum of pyroxene andesite to a group of downstream springs (Figure 1).

The tabular joints that developed in the pyroxene andesite are hardly sloped. The open joints are found perpendicular to the tabular joints. Five boreholes along the grout curtain at the left bank rim of the reservoir (total length 253 m) were watched using borehole TV (BTV) cameras (Figure 1 (a)). The distribution of the probability of crack width exceeding the designated level is shown in Figure 2. Joints with a crack width exceeding 5 mm and 10 mm accounted for about 5% and 2%, respectively. The average number of open joints per stage (Lugeon test section; interval length 5 m) was about 20. At least one joint with a width of 5 mm or larger existed in a stage on the average. The distribution of the frequency of the maximum crack width in a stage is shown in Figure 3. The maximum crack width observed was 35.2 mm. The average maximum crack width was 11.5 mm. The porosity per stage (combined total of crack widths divided by 5 m) was 1.1% on the average and the maximum porosity was 3.6%. (Figure 4). In the grouting tunnel on the left bank of the reservoir, nearly vertical steep-sloped open

Copyright © 2003 Swets & Zeitlinger B.V., Lisse, The Netherlands

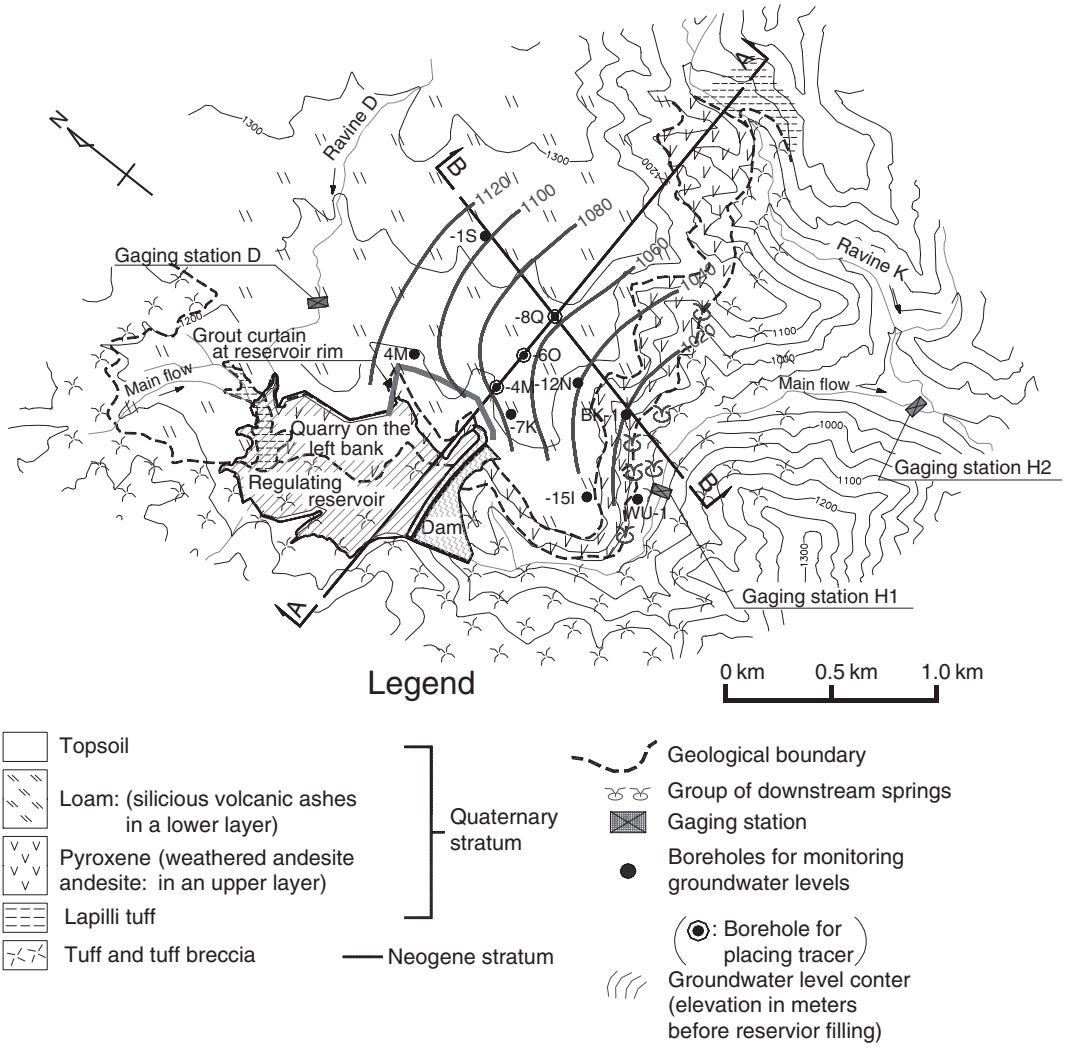


Figure 1. (a) Geological settings of study area.

joints were found to be predominant but strikes were diversely observed (Figure 5).

Numerous open joints developed densely that could affect permeability, but no predominant strikes were found. It was then assumed that the pyroxene andesite stratum at the site had a dense network of open joints over a wide area and areawide anisotropy was considered low macroscopically.

For the rock mass described above, Lugeon tests were conducted in the exploratory boreholes (identical to the groundwater monitoring boreholes shown in Figure 1 (a)) in the mountain on the left bank of the reservoir and along the grout line at the left-bank reservoir rim. The test results are shown in Figure 6. Permeability was high at 31.3 Lugeons (Lu) on the average (except in nine stages where no Lugeon values could be estimated). It exceeded 50 Lu in more than 10% of stages.

Open joints developed and increased the permeability in some stages where water filling pressure could not be increased during the Lugeon test. A grout curtain was therefore constructed along the reservoir rim on the left bank of the reservoir (Figure 1 (a)).

When filling of the reservoir was started after the construction of the grout curtain, it was found that seepage through the left bank of the reservoir would be several times greater than expected.

To identify the cause, various investigations and tests were therefore conducted for evaluating the permeability of pyroxene andesite.

Copyright © 2003 Swets & Zeitlinger B.V., Lisse, The Netherlands

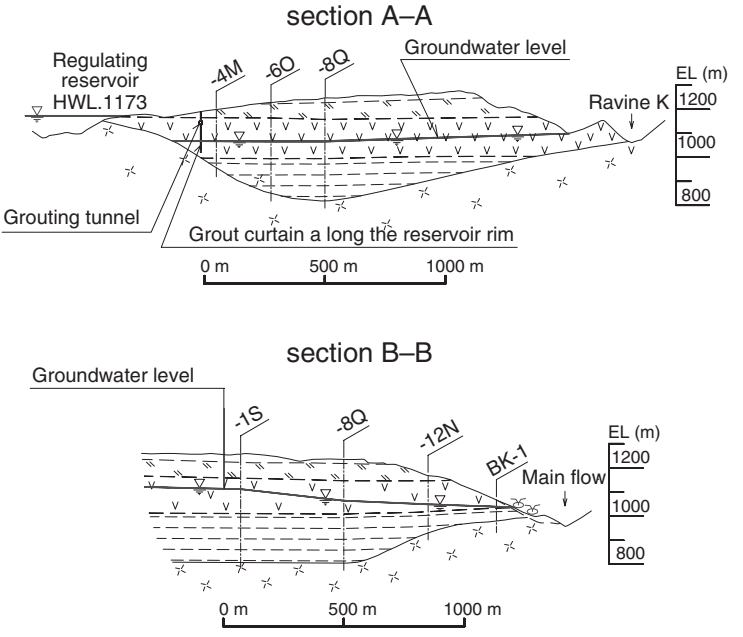


Figure 1. (b) Geological settings of study area (section A–A and B–B).

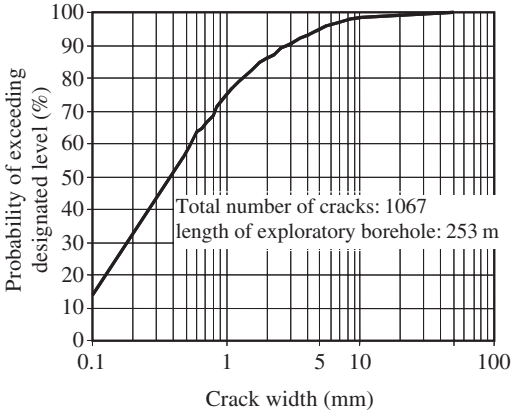


Figure 2. Probability of crack width exceeding the designated level.

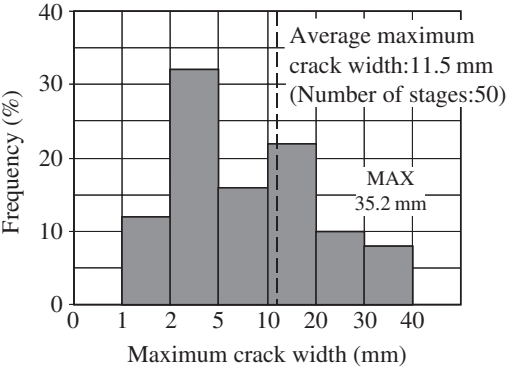


Figure 3. Distribution of frequency of the Maximum crack width in a stage (interval length:5 m).

3 INVESTIGATIONS AND TESTS FOR EVALUATING THE PERMEABILITY OF PYROXENE ANDESITE

The permeability of pyroxene andesite was estimated by a Lugeon test at about 30 Lu on the average (except in the stages where no estimation was possible). During a Lugeon test in an open jointed rock mass of high permeability, high velocity and turbulent flow occurs in the joints and a high flow resistance is likely to be created. Under such a condition, a smaller quantity of water is supplied than in a laminar flow condition even where the same filling pressure is applied. The Lugeon value obtained by the test tends to be lower than that in a laminar flow condition (Yamaguchi et al. 1987, 1989 & 1992). The flow in the pyroxene andesite after reservoir filling was considered to be in a laminar flow condition because the Reynolds number

Copyright © 2003 Swets & Zeitlinger B.V., Lisse, The Netherlands

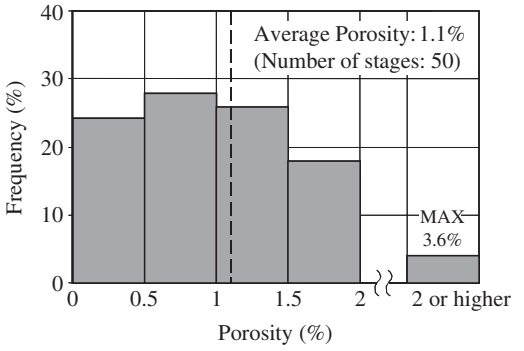


Figure 4. Distribution of frequency of Porosity.

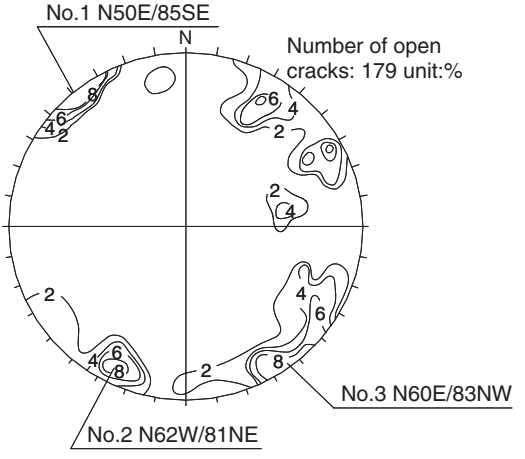


Figure 5. Frequency of open crack on Schmit net.

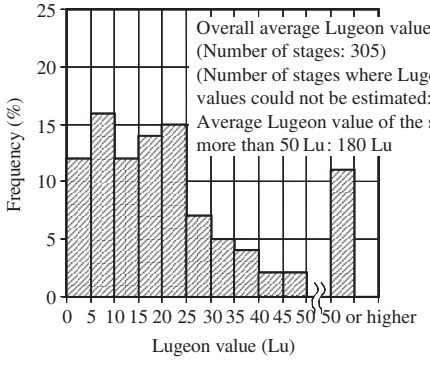


Figure 6. Distribution of frequency of the Lugeon values of the test stages mainly composed of pyroxene andesite (above the ground water level).

was estimated approximately at several dozens by the following equation.

$$\mathrm{Re} = 2Vt/\nu = 2Vt\rho/\mu = 5\sim30 \quad (1)$$

where V = velocity of groundwater (0.05 through 0.1 cm/sec based on tracer test results); t = crack width (mean: 1 cm, maximum: 3 cm based on BTV monitoring results); ν = dynamic viscosity of groundwater (0.01 cm^2/sec); ρ = fluid density; and μ = viscosity of fluid.

In a laminar flow condition, the permeability of pyroxene andesite was evaluated based on macro investigations by analyzing a model of water balance in the river basin and conducting tracer tests. A permeability test using highly viscous fluids, which is considered effective for evaluating permeability in a laminar flow condition, was also conducted (Watanabe et al. 1985, Matsumoto et al. 1988, Iwamoto et al. 1990).

The procedure and result of the permeability test using highly viscous fluids are discussed in a separate paper (Kishi et al. 2003) submitted to this symposium.

3.1 *Permeability estimated from a model of water balance in the river basin*

A model of water balance was established based on the hydrogeological structure at the site (Figure 7).

In the figure, P is the annual precipitation, E is the annual evapotranspiration, F_S is the surface runoff, F_1 is the runoff from a stratum at a small depth (loam), F_2 is the runoff from a stratum at a great depth (pyroxene andesite), R_1 is the groundwater charge

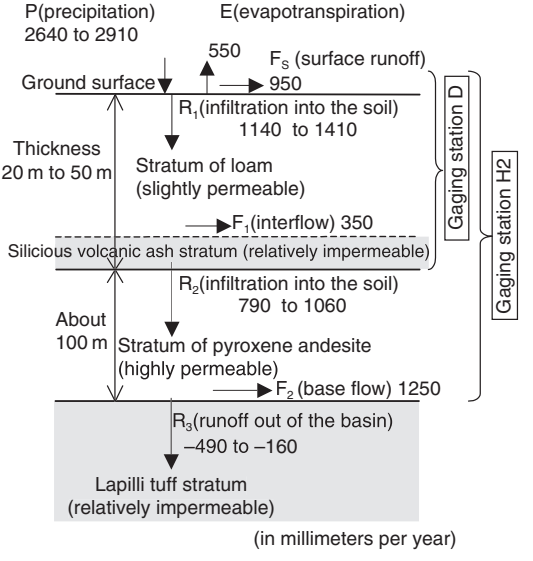


Figure 7. Model of water balance in basin.

Copyright © 2003 Swets & Zeitlinger B.V., Lisse, The Netherlands

in the loam stratum, R_2 is the groundwater recharge in the pyroxene andesite stratum, and R_3 is recharge in the loam stratum, R_2 is the groundwater recharge in the pyroxene andesite stratum, and R_3 is the runoff from the basin (negative value represents inflow from other basin).

The basic annual water balance equations at the site are listed below (Water balance reserch group. 1998).

On the ground surface: $P = E + F_S + R_1$
In the loam stratum: $R_1 = F_1 + R_2$
In the pyroxene andesite stratum: $R_2 = F_2 + R_3$

Based on the above water balance equations, groundwater recharge R_2 and runoff from the pyroxene andesite stratum F_2 were obtained using the hydrological and meteorological records.

The data collected while monitoring at the dam site in the five-year period between 1978 and 1982 were used.

3.1.1 *Precipitation and evapotranspiration*

- Annual precipitation (P)
- Average annual rainfall: 1280 mm (April through November)
- Average annual snowfall: 13.6 m (December through March, density of snow was assumed at 0.1 to 0.12)
- Annual precipitation (P): 2640 mm to 2910 mm per year
- Annual evapotranspiration (E)
- Annual evapotranspiration was calculated based on the average monthly temperature using Thorn thwaite's equation.
- Annual evapotranspiration (E): 550 mm per year

3.1.2 *Runoff*

Runoff was obtained based on the flow data collected at gaging station D in the basin on the left bank upstream of the dam, gaging station H2 downstream of the dam.

Gaging station D was installed on the impermeable subgrade in the silicious volcanic ash stratum, which is in the lower layer in the loam stratum, to gage F_S and F_1 in the water balance model. Gaging station H2 was installed on the impermeable subgrade in tuff below the stratum of pyroxene andesite for collecting data on the base flow (F_2) in addition to the flow identified at gaging station D. The five-year average annual runoff was 1300 mm (0.041 m^3/sec/km^2) at gaging station D and 2550 mm (0.081 m^3/sec/km^2) at gaging station H2. According to the water balance equations, $Fs + F_1 = 1300$ mm per year, and $Fs + F_1 + F_2 = 2550$ mm per year.

Then, F_2 (runoff from the stratum of pyroxene andesite) was 1250 mm per year (0.040 m^3/sec/km^2).

The base flow at gaging station D (355-day flow rate) was 350 mm per year (0.011 m^3/sec/km^2), which was considered the flow from the loam stratum (F_1).

Thus, surface runoff Fs was 950 mm per year, and runoff from the loam stratum F_1 was 350 mm per year.

The results are shown in the water balance model in Figure 7.

The relationship of a runoff of 0.040 m^3/sec/km^2 from the pyroxene andesite and the difference in specific runoff between gaging stations D and H2 was examined. The specific base flow estimated from the data collected at gaging station H2 was 0.055 m^3/sec/km^2 on the average, therefore the above difference was almost equal to the runoff obtained based on the annual water balance.

3.1.3 *Evaluation of permeability of pyroxene andesite*

The average permeability coefficient of pyroxene andesite K_a is expressed by the following equation.

$$K_a = Q/AI \quad (2)$$

where Q = the runoff; A = the area of flow section; and I is the hydraulic gradient.

A runoff of 0.21 m^3/sec was obtained by multiplying a base flow (specific runoff) of 0.040 m^3/sec/km^2 obtained from the water balance model by the area of the river basin on the left bank.

The hydraulic gradient I was assumed 0.1 based on the average hydraulic gradient in the distance from a groundwater monitoring borehole (-6O) in the mountain on the left bank to the group of downstream springs. The area of flow section A was obtained based on the assumption that the width of flow ranged from 500 m in the watershed surrounding the group of downstream springs to a maximum of 1500 m where downstream springs existed sporadically, and that the average groundwater depth was about 40 m.

Then, the permeability of pyroxene andesite K was estimated at 3.5×10^{-3} to 1×10^{-2} cm/sec based on the above equation.

3.2 *Permeability estimated from groundwater velocity*

A Tracer was placed in the groundwater in the pyroxene andesite through the groundwater monitoring boreholes (-4M, -6O and -8Q in Figure 1 (a)) in the mountain on the left bank. Then permeability coefficient was calculated based on the time required for the groundwater to reach downstream springs. The tracers: sodium fluorescent (Fl–Na), rhodamine B (Rh-B), potassium chloride (KCl), magnesium chloride ($MgCl_2$) and lithium chloride (LiCl) were tested. Fl–Na was found most effective at the site because it was hardly adsorbed to the rock or settled and could be easily detected, so it was used in the tracer test. At

Copyright © 2003 Swets & Zeitlinger B.V., Lisse, The Netherlands

Table 1. Results of tracer test.

Borehole for placing tracer	① Distance (m)	② Hydraulic gradient	③ Initial arrival time (in days)	④ Peak arrival time (in days)
-4M	800	0.11	13	24
-6O	750	0.11	12	23
-8Q	740	0.11	12	22

Table 2. Permeability coefficient of pyroxene andesite.

	Permeability coefficient (cm/sec)	
Actual velocity	n = 1%	n = 3%
V = 0.04 cm/sec (①/④)	3.6×10^{-3}	1.1×10^{-2}
V = 0.07 cm/sec (①/③)	6.4×10^{-3}	1.9×10^{-2}

the point of the spring where the tracer was detected (sampling for detection was conducted everyday), its concentration gradually increased and reached a peak in about ten days. Then the concentration decreased.

The results of the tracer test are shown in Table 1. The permeability coefficient of pyroxene andesite is shown in Table 2. If the porosity (n) of pyroxene andesite is assumed to be 1% to 3%, based on the results of BTV monitoring, the permeability of pyroxene andesite is estimated at 10^{-3} to 10^{-2} cm/sec on the average in the pyroxene andisite stratum where the tracer test was conducted.

3.3 *Results of evaluation of permeability of pyroxene andesite*

A permeability test using highly viscous fluids is discussed in a separate paper (Kishi et al. 2003). Only the results are described here. The relationship between the Lugeon values obtained by the Lugeon test and those obtained by highly viscous fluid test in a laminar flow condition is shown in Figure 8. A value of 30 Lu in the Lugeon test was equivalent to about 1000 Lu in a laminar flow condition.

The results of the permeability evaluation are listed in Table 3.

The permeability obtained by a test using highly viscous fluids was almost identical to that obtained by macroscopic investigations and tests. The permeability of open jointed pyroxene andesite was assumed to be 10^{-2} cm/sec macroscopically.

4 CONCLUSION

In open jointed, highly permeable rock masses, the Lugeon test can hardly be applied to the laminar flow

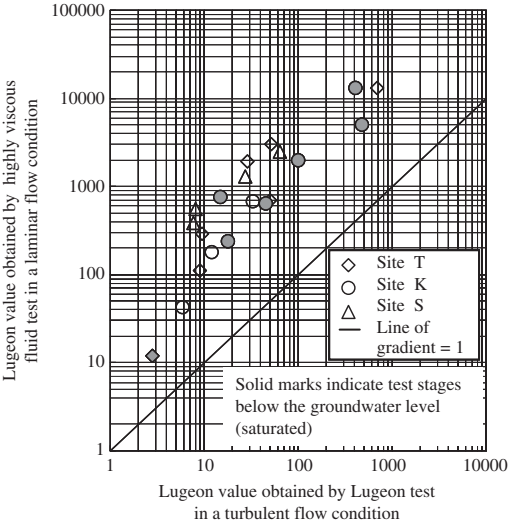


Figure 8. Relationship between Lugeon values obtained by Lugeon test and those obtained by highly viscous fluid test (Kishi et al. 2003).

Table 3. Results of evaluation of permeability of pyroxene andesite.

Method	Result
Permeability test using highly viscous fluids	31 Lu (turbulent flow) ~1,000 Lu (laminar flow)
Use of water balance in the river basin	400~1,000 Lu
Tracer test	400~2,000 Lu

1 Lu ≒ 1×10^{-5} cm/sec.

condition. Combining various investigations and tests described in this paper are important for comprehensive evaluation of rock permeability. Evaluating permeability may greatly affect the design of foundation treatment and the cost of dam construction. At dam sites with highly permeable rock masses, the validity of the Lugeon test should be reviewed carefully at the outset of the project.

REFERENCES

Iwamoto, T., Sonomoto, H., Arimoto, H. & Dotsuma, M. 1990. Measurement of coefficient of rock permeability using highly viscous fluids: Lugeon tests on welded tuff. *Engineering Geology* 31(2): 1–10.

Kishi, H., Kakue, T. & Nishigaki, M. 2003. Application of highly viscous fluid tests to jointed rock masses and evaluation of test results. *Proc. IS-OKAYAMA 2003*.

Matsumoto, N. Yamaguchi, Y. & Shibuichi, H. 1988. Permeability test using highly viscous fluids. *Proc. The 23rd*

Copyright © 2003 Swets & Zeitlinger B.V., Lisse, The Netherlands

meeting of the Japanese Society of Soil Mechanics and Foundation Engineering: 125–126.
Watanabe, K. & Ashikawa, R. 1985. A study on the effect of laminar flow during permeability tests in a jointed rock mass. *Proc. The 17th symposium on rock mechanics*: 161–165.
Water balance research group. 1998. *Groundwater resources and the environment*: 96–99. Tokyo: Kyoritsu-shuppan.
Yamaguchi, Y., Hiromatsu, F. & Matsumoto, N. 1987. Interpretation of Lugeon test results, *Proc. The 19th symposium on rock mechanics*: 156–160.
Yamaguchi, Y., Shibuichi, H. & Matsumoto, N. 1989. Effect of turbulent flow during Lugeon tests and corrective measures. *Proc. The 21st symposium on rock mechanics*: 401–405.
Yamaguchi, K. & Matsumoto, N. 1992. Lugeon values and permeability coefficients of rock masses. *Proc. Japan Society of Civil Engineers* (454): 123–126.

Copyright © 2003 Swets & Zeitlinger B.V., Lisse, The Netherlands

Laboratory column test for measuring long-term partial saturation in sand

A. Ishikawa, N. Kohsaka, N. Miyake & M. Amari
Institute of Technology, Shimizu Corporation, Tokyo, Japan

ABSTRACT: Laboratory column tests were conducted to investigate the degree of saturation (Sr) of sand by dewatering and recovering pore water. Two types of sands having different grain distribution curves were used as test samples and the following results were obtained. (1) The initial Sr just after the recovery of the water is 87–93%. The water showered from above the specimens gives a 2.5–4.3% lower Sr than a flow of water at the bottom. (2) The increase in Sr after about one month from the beginning of the tests is 1.8–2.0%. (3) The rates of Sr change are different for the two sands. The above results indicate that dewatering and recovering groundwater is an effective method in creating an unsaturated zone to prevent liquefaction.

1 INTRODUCTION

Previous studies have shown that liquefaction resistance increases with a reduction in the degree of saturation. When the degree of saturation (Sr) drops to a level of 90%, the liquefaction resistance increases to roughly twice as much as that at full saturation. When the Sr drops to 75%, the liquefaction resistance increases to three times (Yoshimi et al. 1989).

Shamoto and Goto (2002) looked into a mechanism for increasing liquefaction resistance under partially saturated conditions. Their hypotheses are (1) under the cyclic shear stress, a cushion of air bubbles prevents water pressure from increasing and (2) these stresses increase the soil's liquefaction resistance. Based on these hypotheses, they proposed a shear stress estimation model for sand under partially saturated conditions.

The above studies indicate that making and maintaining unsaturated zones is an effective method to prevent liquefaction.

Nishigaki and Komatsu (1998, 2002) have continued research into efficient methods of making partial saturation zones. They tested various methods of decreasing the Sr in the ground, i.e., groundwater drawdown and recovery methods, air injection and dissolved air injection methods.

In the current study, we have also examined the initial Sr just after dewatering and recovering pore water and the duration of the Sr. Features of our tests are as follows:

1. Using large columns and measuring the water pressure inside the specimens, Sr was calculated in different ways.
2. Using different types of sands as specimens (Toyoura and Shiodome sand), the effect of gradation in trapping air bubbles was investigated.

2 EXPERIMENTAL MEASUREMENTS

2.1 *Test procedure*

Figure 1 shows the set of system used in this study. The system consists of four parts. (1) Two columns hold the specimens in and saturate or partially saturate them. The columns are 200 cm in length and 6.76 cm in diameter. (2) An air tank store the air which floats up through the specimens. (3) A water supply tank supplies distilled water to the specimens. (4) Pressurized water in two manometers measures the degree of saturation of the specimens.

The Sr is obtained by the following equations.

$$Sr = \frac{1}{1-H} - \frac{\Delta V(P_0 + \Delta P)}{V_v \cdot \Delta P} \tag{1}$$

where Sr is the saturation ratio, H is the Henry constant, V_v is the void volume of the specimen, P_0 is the initial pressure to the pore water, ΔP is the increase in pressure in the manometer and ΔV is the change in volume by ΔP. The average saturation ratio $\bar{S}_r$, which integrates Equation (1) along the length of column, stands for the Sr at the middle of the column.

$$\begin{aligned}\bar{S}_r &= \frac{1}{a}\int_0^a \left[\frac{1}{1-H} - \frac{\Delta V(P_0 + \Delta P)}{V_v \cdot \Delta P}\right] dz \\ &= \frac{1}{1-H} - \frac{\Delta V}{V_v \cdot \Delta P}\left[\frac{a}{2} + P_{\text{atm}} + Z_0 + \Delta P\right]\end{aligned} \tag{2}$$

Copyright © 2003 Swets & Zeitlinger B.V., Lisse, The Netherlands

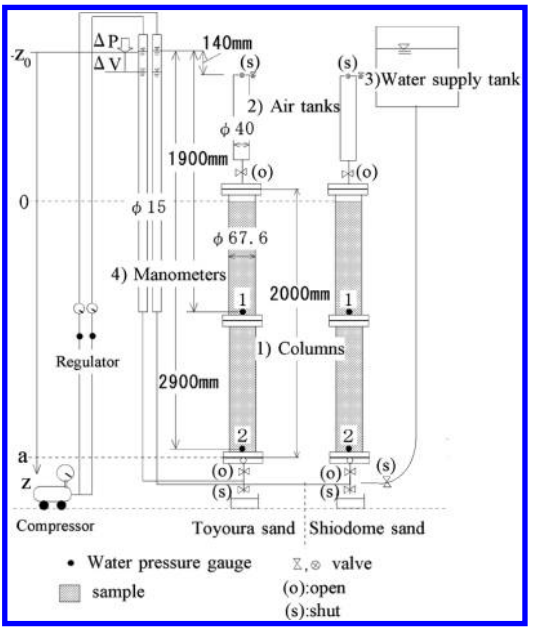


Figure 1. Experimental setup for laboratory test.

where P_{atm} (=1 atm) is the atmospheric pressure, Z_0 is the distance from the water level in the manometer to the top of the specimens, and a is the length of the column (see Figure 1).

The testing procedure was as follows. The columns were filled with sand through a funnel. The void in the sand was fully filled with CO_2. Deaerated distilled water (DO = 2.0 mg/l) was gradually made to flow into the bottom side of the column. The above operations were done in order to fully saturate the sand before dewatering. The Sr at this time was confirmed to be more than 99%. Then the valves at the bottom of the columns were opened in order to release the pore water. After three days, the columns were filled with distilled water which was not deaerated (DO = 5.9 mg/l). In the case of Toyoura-1 and Shiodome-1, water was made to flow into the bottom of the column. In the case of Toyoura-2 and Shiodome-2, water was showered from the top of the column. The purpose of the above operations was to create an artificially unsaturated zone.

As shown in Figure 1, the initial water level in the manometer was set 190 cm higher than the level of water pressure gauge No. 1. The air tanks were filled with water. The increase in pressure ΔP was set to 9.8 kPa.

2.2 *Testing materials*

Two types of sands were used in these tests, Toyoura sand and Shiodome sand. The condition of the materials is shown in Table 1. The relative density (Dr) was 50% for Toyoura sand and 42–45% for Shiodome sand. The grain size distribution curves, which affect the size of trapped air bubbles, were different for the two sands. As shown in Figure 2, Shiodome was better-graded than Toyoura. As shown in Figure 2, both grain size distribution curves were in the range of high risk of liquefaction which was prescribed for the design of harbor facilities foundation in Japan.

Table 1. Testing materials.

Sample	Dry density (g/cm^3)	Void ratio	Relative density, Dr (%)	Length (cm)
Toyoura-1	1.47	0.80	50	196.3
Toyoura-2	1.47	0.79	50	196.3
Shiodome-1	1.42	0.86	42	197.3
Shiodome-2	1.43	0.85	45	196.8

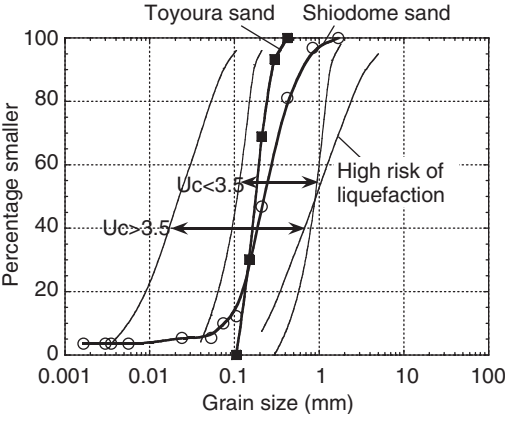


Figure 2. Grain size distribution curve of test sand.

3 TEST RESULTS

3.1 *Time series of saturation ratio*

Table 2 and Figure 3 show the time series of the degree of saturation of the specimens. The points plotted for $\overline{S}_r$ were obtained by Equation (2) with the measured volume change due to the pressure of the water in the manometer, while the solid lines for $\overline{S}_r$ were obtained from the changing water level in the manometer. When the air bubbles dissolved in the pore water, water flowed into the column from the manometer. (As the valve of the air tank was shut when testing, no water was supplied from the air tank.) So the lines for

Copyright © 2003 Swets & Zeitlinger B.V., Lisse, The Netherlands

Table 2. Average saturation ratio.

Sample	$\overline{S}_r$ ($t=0$) (%)	$\overline{S}_r$ (after 35–92 days) (%)	$\Delta\overline{S}_r$ (%)
Toyoura-1	92.9	94.9 ($t=92$)	2.0
Toyoura-2	88.6	90.6 ($t=84$)	2.0
Shiodome-1	89.9	91.7 ($t=92$)	1.8
Shiodome-2	87.4	89.4 ($t=35$)	2.0

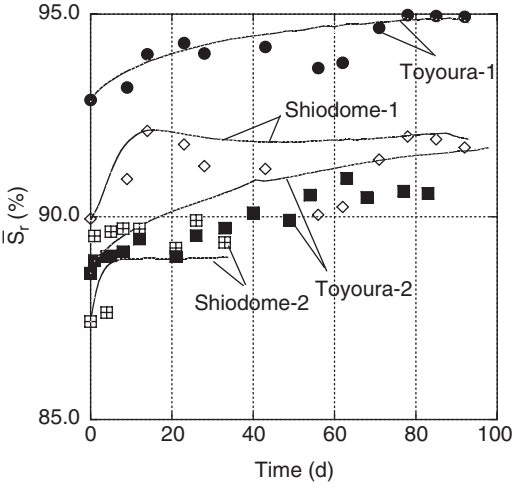


Figure 3. Time series of saturation ratios in the specimens.

$\overline{S}_r$ obtained from the water level in the manometers should be almost equal to the plotted $\overline{S}_r$. Although about 1% difference was seen, both $\overline{S}_r$ agree well.

Just after the water was recovered ($t=0$), the $\overline{S}_r$ of Toyoura-1 was 92.9%, Toyoura-2 was 88.6%, and Shiodome-1 was 89.9%. After 84–92 days, the $\overline{S}_r$ increased to 94.9% for Toyoura-1, 90.6% for Toyoura-2 and 91.7% for Shiodome-1. For Shiodome-2, with a testing period of 35 days, the $\overline{S}_r$ at $t=0$ was 87.4%; it increased to 89.4%. On each specimen the increase in $\overline{S}_r$ was 1.8–2.0%. Water showered from the above specimens gave a 2.5–4.3% lower Sr than the flow of water from the bottom. The difference between the two sands was the incremental rates of the $\overline{S}_r$. The $\overline{S}_r$ for Toyoura sand increased gradually, while the $\overline{S}_r$ for Shiodome sand increased rapidly and reached a steady state or began to decrease after about two weeks.

The above facts indicate that unless the groundwater DO is significantly low (initial DO of the pore water was 5.9 mg/l in this test), an artificial unsaturated zone (where $\overline{S}_r$ = 90–95%) is easy to make and once this unsaturated zone has been created, it will remain for at least several months.

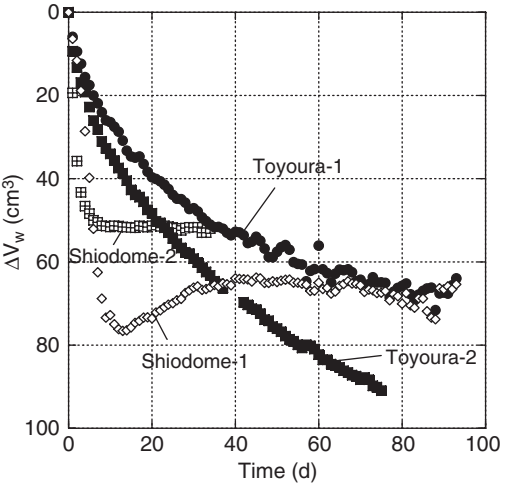


Figure 4. Time series of water volume change.

Stored air did not exist in the air tank. Air bubbles were kept trapped in the void of the sand and did not float through the sand. This fact indicates that the reason for the increase in $\overline{S}_r$ was the dissolution of trapped air bubbles in the pore water and the reason for the decrease in $\overline{S}_r$ was the reforming of dissolved air into air bubbles.

3.2 *Water changes in the manometer*

Figure 4 shows the time series of water volume changes (ΔV_w) in the manometers from the initial state. These values were calculated by measuring the pore water pressure at Pressure Gauge 2. The difference between the two sands was clear. The water volume changed slowly in Toyoura sand, while in Shiodome sand it rapidly decreased. We consider that this difference was caused by the difference in the grain size distribution. In Shiodome sand the diameter of trapped air bubbles varied, and the trapped air bubbles dissolve easily in the pore water.

3.3 *Formation of trapped air bubbles*

Photo 1 shows Toyoura-1 after 28 days. Black points represent trapped air bubbles. These black points were not observed in the initial stage of the test (at least in the first week). We consider that the trapped air bubbles in the void of the sand were attached to each other to form large air bubbles with diameters of 0.2–1.0 mm. The same phenomenon was observed in Shiodome sand. The diameters of the air bubbles were 0.5–4.0 mm, much larger than those in Toyoura sand. The air bubbles were formed in uniform distributions throughout the specimens.

Copyright © 2003 Swets & Zeitlinger B.V., Lisse, The Netherlands

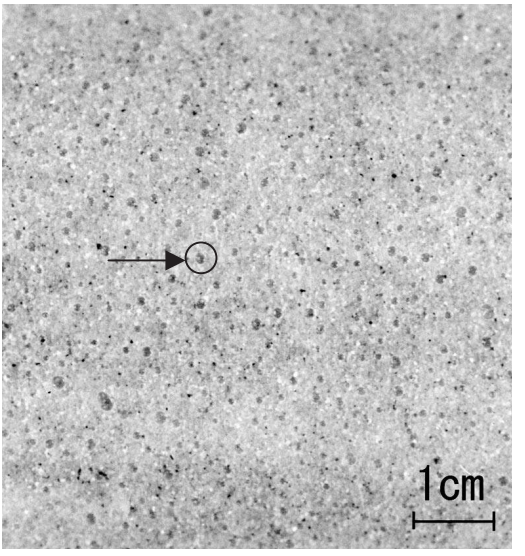


Photo 1. Toyoura-1 after 28 days. (Black points indicate trapped air bubbles.)

4 CONCLUSIONS

In this study, we investigated the degree of saturation of two sands after dewatering and recovering pore water. The following results were obtained.

1. After the recovery of the water, the $\overline{S}_r$ was 87–93%. Showering water from above the columns gave a $\overline{S}_r$ 2.5–4.3% lower than the $\overline{S}_r$ achieved with water flowing from the bottom.
2. The increase in $\overline{S}_r$ was 1.8–2.0% after 35–92 days. These facts indicate that once an unsaturated zone has been formed by dewatering and recovery methods, the zone remains unsaturated for several months.
3. The rates of Sr change between the two sands were different. Grain size distribution affected the size of bubbles formed. The diameters of air bubbles which could be observed by the human eye were 0.2–1.0 mm in Toyoura sand and 0.5–4.0 mm in Shiodome sand.

REFERENCES

Kodaka, T. & Akira, A. 1994. Formation of air bubbles in sandy soil during seepage process (in Japanese), *Journal of JSCE* 487(3): 129–138.

Nishigaki, M., Komatsu, M., Yamamoto, H. & Tajiri, N. 1998. A study of the holding rate of bubbles in saturated sandy soil for liquefaction prevention (in Japanese), *the 33rd annual conference for geo-technical engineering*: 1821–1822.

Nishigaki, M., Komatsu, M. & Ogawa, Y. 2002. Development of a method to prevent liquefaction by creating unsaturated conditions (in Japanese), *the 37th annual conference for geo-technical engineering*: 1227–1228.

Shamoto, Y. & Shigeru, G. 2002. Estimation method for the liquefaction strength of unsaturated sandy soil estimation considered by stress history during cyclic loading (in Japanese), *the 37th annual conference for geo-technical engineering*: 1985–1986.

Yoshimi, Y., Yanaka, K. & Tolimatsu, K. 1989. Liquefaction resistance of a partially saturated sand, *Soils and Foundation* 29(2): 157–162.

Copyright © 2003 Swets & Zeitlinger B.V., Lisse, The Netherlands

Comparison of analysis methods of slug test data sets: usage of Hvorslev and Cooper et al. methods

Y. Shinshi & H. Kano
Konoike Construction Co. Ltd., Osaka, Japan

S. Takeuchi & K. Nakano
Nuclear Cycle Development Institute, Toki, Japan

ABSTRACT: Of in-situ hydraulic tests, slug tests are popular worldwide. Hvorslev and Cooper et al. methods are the two that are often used for analyzing test data. However, these methods have different theoretical backgrounds and their ranges of applicability are not known. This paper explains the characteristics of these methods and reports the following two main conclusions. The first is that the range of applicability depends on the α value, which is the ratio of aquifer storativity to wellbore storage. Roughly speaking, the Hvorslev method is applicable for the range of roughly $\alpha < 10^{-3}$ and the Cooper et al. method for roughly $\alpha > 10^{-3}$. Secondly, α is an unknown parameter in the Cooper et al. method; this must be estimated from the test data analysis. This is a dilemma because the parameter α is one result of the Cooper et al. analysis to be judged. The authors propose that analysis of slug test data be done using both methods, then compare the hydraulic conductivities estimated by each method. In doing so, the smaller value of the two hydraulic conductivities is closer to the actual value of the investigated aquifer than the other.

1 INTRODUCTION

Slug testing is one of the most popular methods of in-situ hydraulic testing using a single borehole because it is simple and inexpensive. The method is explained using Figure 1. In a single borehole, the water level is instantaneously changed, either drawn down or raised up, and the recovering water level is observed. In Japan, slug tests are commonly conducted in a borehole logging investigation work. Moreover, since the test does not necessarily require a large amount of the groundwater discharge, it is very useful at sites with contaminated groundwater.

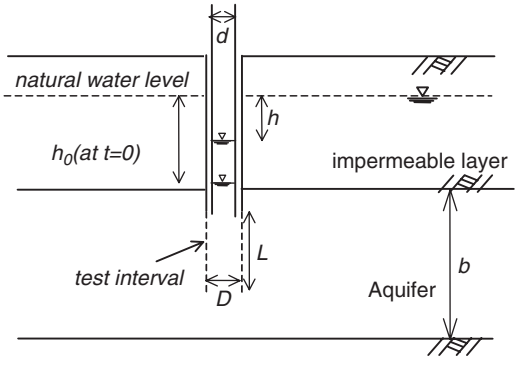


Figure 1. Schematic of slug test.

Although the data from slug tests can be analyzed using several methods, the methods recommended by Hvorslev (1951) and Cooper et al. (1967) are commonly used. These methods have different theoretical backgrounds and it is not known which method is better for a given test data. This paper intends to summarize the theoretical backgrounds of the two methods of slug test analysis and to propose an applicable range for each method and available usage.

The symbols used in this paper are summarized in the end of the paper.

2 THEORETICAL BACKGROUNDS

A comparison of the Hvorslev and Cooper et al. methods based on their theoretical background indicates that these methods differ from each other in terms of flow dimension, flow state, storativity of aquifer, analyzed parameters and basic approach for analysis. These features are summarized in Table 1. The features of the Hyder et al. (1994) method are also presented

Copyright © 2003 Swets & Zeitlinger B.V., Lisse, The Netherlands

Table 1. Features of slug test analysis methods.

	Hvorslev	Hyder	Cooper
Flow dimension	3D	3D	2D-radial
Flow state			
Aquifer	Steady	Unsteady	Unsteady
Wellbore	Unsteady	Unsteady	Unsteady
Storativity (aquifer)	Negligible	Considered	Considered
Penetration in aquifer	Partial	Partial	Full
Analysis parameters	K	K, S_s (penetration)	K, S_s
Analysis based on	Slope of straight line	Curve fitting	Curve fitting

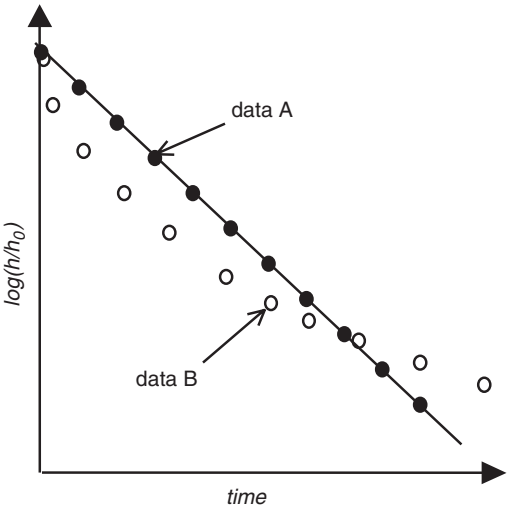


Figure 2. Hvorslev method.

in this table. The Hyder et al. method has some common features to both the Hvorslev and Cooper et al. methods.

The Hvorslev method is very often used in groundwater engineering. One reason is its simple application. The method uses the slope of a straight line of data plotted on semi-logarithm axis graph as shown in Figure 2 (data A) and does not need a high performance computer. The Japanese Geotechnical Society recommends this method (1995).

The method is based on the assumption that groundwater flow in an investigated aquifer is in a steady state, but the recovering water table in a borehole is unsteady. That is, the storativity of the aquifer is negligible. In some cases, however, the test data on the semi-logarithmic graph do not indicate a straight line as shown in Figure 2 (data B). It might be difficult to

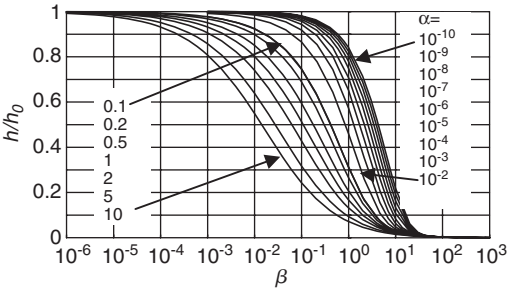


Figure 3. Type curves in Cooper et al. method.

determine which part of the data is the best to use to draw a straight line. Some reasons can be postulated for such as data B. If one of the reasons is the role of storativity on the aquifer, we can use the Cooper et al. method for the data set.

Cooper et al. developed a method considering storativity of the aquifer. The major difference from the Hvorslev method is the analysis process. The Hvorslev method is based on the straight line of test data and its slope, while the Cooper et al. method is based on type-curve-fitting, that is, fitting test data to one of several type curves as shown in Figure 3. Although the Cooper et al. method is more complicated than Hvorslev's, it can be adapted to data such shown in Figure 2 (data B) if its behavior is due to storativity of the aquifer.

Although the Cooper et al. method seems to be more accurate than the Hvorslev method with regard to storativity of aquifer, it is not certain that the Cooper et al. method can be exclusively used for any slug test data and the Hvorslev method can be abandoned. This issue is the main discussion in this paper.

In addition, the Hyder et al. theory is more mature than the others because it can explain a real situation of slug testing better than the others. However, it may not be applicable in practice since the penetration ratio of the test interval to an aquifer must be known in the method. In most slug tests, a tester can recognize the length of the interval, but the thickness of the aquifer will be unknown. Otherwise the penetration ratio must be included in the parameters to be estimated, and the approach might require too much effort for curve-fitting. Therefore, this theory is not investigated in this research, but it can be used in order to simulate our slug test data.

3 STORATIVITY EFFECT

Comparing the Hvorslev and Cooper et al. methods, their differences are penetration of testing interval and consideration of storativity in an aquifer. By discussing as follows, these differences were related with each other.

Copyright © 2003 Swets & Zeitlinger B.V., Lisse, The Netherlands

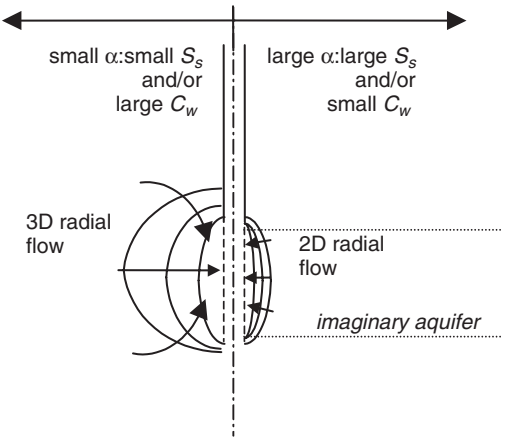


Figure 4. Flow and head contours near test interval with different storage ratio α.

Figure 4 explains the difference of flow and head contours in the left side and the right side. When a large amount of water inflow of the borehole from the aquifer, the groundwater flow is shown as the left side of Figure 4. Even if the amount is small and if storativity of an aquifer is small, its amount is large enough it to affect groundwater flow far away. This flow is 3D radial and seems suitable to the Hvorslev theory.

On the other hand, when a small amount of water inflow to the borehole from the aquifer, the groundwater flow is shown as the right side of Figure 4. Even if the amount is large and if storativity of an aquifer is large, its amount is as small as it can affect groundwater flow just near the interval. This flow is 2D radial and seems suitable to the Cooper et al. theory.

The storage ratio, α, is useful to explain the characteristics above, where $\alpha = \pi r_w^2 S_s L / C_w$, (Cooper et al. 1976). The S_s shows a storage ability of an aquifer. The C_w shows a storage ability of a test borehole and the amount of water during a slug test. Thus, "small α" means "small S_s" and/or "large C_w (large amount of water)". And "large α" means "large S_s" and/or "small C_w (small amount of water)". Based on this discussion, the suitable analysis method of slug test data can be selected by the storage ratio, α.

4 DIRECTION OF INVESTIGATION

4.1 *Conditions of slug test simulations*

Sets of slug test data were simulated by using the Hyder et al. theory. The input data are the followings.

$\alpha = 10^{-9}, 10^{-7}, 10^{-5}, 10^{-3}, 10^{-1}, 10$
$n(= L/b) = 100, 50, 25, 10, 1(\%)$
Hydraulic conductivity is assumed isotropic.
Interval is located at the center of an aquifer.

4.2 *The Hvorslev method*

To avoid human errors in selecting the data for a straight line, all data within $0.1 \leq h/h_0 \leq 1.0$ are selected. In this research, even though the plotted data on the semi-logarithmic graph seems a curve, these data are analyzed as a straight line. To regress the straight line for the plots, the least-square regression scheme was used.

4.3 *The Cooper et al. method*

In the Cooper et al. method, a set of data must be fitted to a type curve. The fitting scheme is a computational automatic scheme (Shinshi, 1996). Although the type curves of the original method are commonly given for the α in form of an order magnitudes ($10^N : N$ is integer) as shown in Figure 3, the automatic scheme can select arbitrary value of the α and fit the data to a type curve with a minimum residuals. The residuals are expressed as a summation of square residuals as for fitting to a type curve and the summation is the convergence index.

5 RESULTS AND DISCUSSION

5.1 *Cooper analysis for small α*

In the automatically fitting scheme, when the convergence indices show a minimum value, the corresponding α is given and fitting is recognized completed. If the data to be estimated are suitable to the Hvorslev method, the data are not affected by storativity of an aquifer, and the α is zero. It was investigated how the Cooper et al. method estimates such as the data. The convergence indices of this trial show in Figure 5. Thus, the indices were not converged even if the α decreased as small as an impractical condition. This feature is one of criteria for choosing not the Cooper et al. method but the Hvorslev method.

5.2 *Discussion*

The results of analyses by the Hvorslev and Cooper et al. methods are shown in Figure 6. In the figure, the horizontal axis is α and vertical axis is a ratio of the estimated value, K_{est}, to the input value, K_{inp}, which is for Hyder's simulation. The K_{inp} is considered as a real value of investigated aquifer. The n in each graph means penetration ratio of the test interval. From these results, some interesting features were found.

a) In the range of roughly $\alpha \geq 10^{-3}$, the Cooper et al. method suitably worked although the test interval was partially penetrated into an aquifer, which is

Copyright © 2003 Swets & Zeitlinger B.V., Lisse, The Netherlands

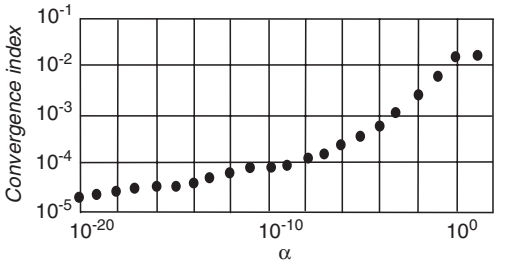


Figure 5. Relationship between α and convergence index for non-storativity data using Cooper et al. method.

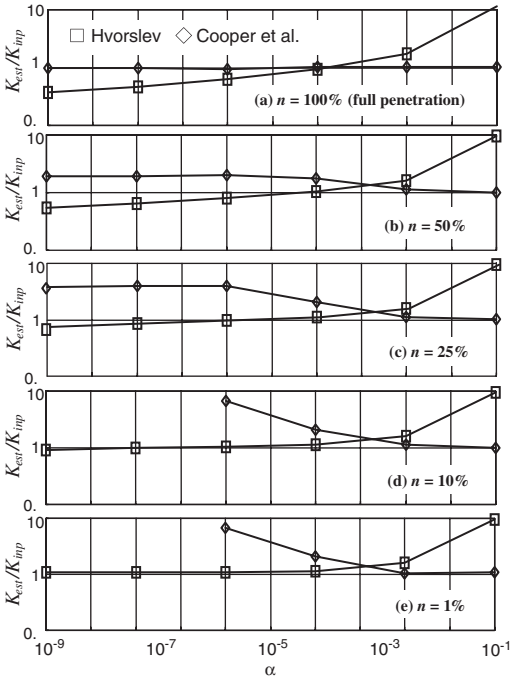


Figure 6. Comparison between estimated values of *Ks*.

not consistent with one of the conditions of Cooper et al. method. This feature is explained in the "STORATIVITY EFFECT" section.

b) In the range of roughly $\alpha \leq 10^{-3}$, the Hvorslev method suitably worked. As stated beforehand, the case of a small α is equivalent to a situation where storativity of an aquifer is negligible, which agrees with the Hvorslev's theory.
c) In the case of a fully penetrating interval, $n =$ 100%, the Hvorslev method did not work well.
d) Roughly speaking, by comparing the estimated K_s from both methods, the smaller a value of K, the closer it is to the real one.

6 RECOMMENDATION

From the result of the research, we recommend the following instruction for analyzing a set of slug test data.

1. The set of slug test data should be analyzed using both Hvorslev and Cooper et al. methods.
2. Comparing the estimated hydraulic conductivities, K, the smaller K should be reported as the result of the slug test.
   There are some additional considerations.
   a) In using the recommended scheme, the Hvorslev method should adapt the data with $0.1 \leq h/h_0 \leq 1.0$, which are recognized as a straight line, even if they do not fall on a straight line in a semi-logarithmic graph.
   b) If the fitting does not converge in the direction of smaller α, the data should be analyzed by using the Hvorslev method.

REFERENCES

Cooper, H.H. Jr., Bredehoeft, J.D. & Papadopulos, I.S. 1967. Response of a finite-diameter well to an instantaneous charge of water., Water Resources Research, 3(1): 263–269, 1967.

Hvorslev, M. 1951. Time lag and soil permeability in groundwater observations, Waterways, Experiment St. Corps of Eng., U.S. Army, No. 26, 1951: 50.

Hyder, Z., Butler, J.J., McElwee, C.D. & Liu W. 1994., Slug test in partially penetrating wells., Water Resource Research, 30(11): 2945–2957, 1994.

Japanese Geotechnical Society 1995 (JGS). Method for measuring Permeability in Single Borehole, JKGS1314–1995 (in Japanese), 1995.

Shinshi,Y. et al. 1996. An automatic analysis scheme of slug test with storage effect of an aquifer. JSCE the 51st annual conference, III: 608–609, 1996 (in Japanese).

SYMBOLS

b: thickness of aquifer, [L].
C_w: wellbore storage, [L^2].
d: diameter of borehole casing, [L]
D: diameter of test interval, [L]
h: drawdown in welbore from natural water level, [L].
h_0: induced drawdown in wellbore by slug, [L].
K: hydraulic conductivity of aquifer, [L/T].
K_{est}: estimated I from slug test analysis, [L/T].
K_{inp}: input K for slug test simulation, [L/T].
L: inflow interval length, [L].
n: penetration of interval into aquifer($= L/b$), [%].
r_w: radius of test interval($= D/2$), [L].
r_c: radius of borehole casing($= d/2$), [L].
t: time after inducing slug, [T].
S_s: specific storage of aquifer, [1/L].
α: storage ratio($= \pi r_w^2 S_s L/C_w$), [–].
β: dimensionless time($= KLt/r_c^2$), [–].

Copyright © 2003 Swets & Zeitlinger B.V., Lisse, The Netherlands

Determination of unsaturated hydraulic conductivity taking account of in-situ test

T. Sugii
Department of Civil Engineering, Chubu University, Aichi, Japan

T. Okumura
Thohou Chisui Co., Ltd., Gifu, Japan

ABSTRACT: The authors have proposed a permeability test for unsaturated soils in the laboratory. It is an improved type of the original instantaneous profile method, and is able to measure the permeability of many kinds of soils. In this study, an application of this method to in-site tests was considered, and two kinds of permeability test were performed: in the case of high groundwater level, and in the case of low groundwater level. The method of draining is used when the groundwater level is high, and the method of permeating is used when the groundwater level is low. These methods were used to determine the permeability of unsaturated soils the in-situ tests. The results show that the wetting test is more effective than the drainage test.

1 INTRODUCTION

Various methods of determining the hydraulic conductivity of unsaturated soils in the laboratory have been proposed, however, there are few methods of measuring the hydraulic conductivity of unsaturated soils in the field directly because it is difficult to control moisture and pore water pressure (matric suction) in the field. In this work we set out to develop a method for measuring the hydraulic conductivity of unsaturated soils in the field directly.

An experiment method has been developed in Chubu University to estimate hydraulic conductivity of unsaturated soil in the laboratory (Sugii et al. 2000). It is an improved type of the original instantaneous profile method (Watson 1966), and is able to measure the permeability of many kinds of soils directly. The method is characterized by the unsteady condition of the water profile and the linear approximation of moisture distribution. In this paper, the method is applied to a compacted sandy ground model taking account of an in-situ test. Two experiments, the method of draining when the groundwater level is high, and the method of permeating when the groundwater level is low, were conducted to examine the permeability of unsaturated soils in the field.

2 LABORATORY TEST

The improved instantaneous profile method (Approximated Profile Method; A.P.M.) is characterized by the unsteady condition of the water profile and the linear approximation of moisture distribution. In the original instantaneous profile method volumetric water contents are measured at several points, whereas: the improved method volumetric water content is measured at the top of the specimen only. The amount of drainage from the specimen is measured over time. After the measurement is finished, the water content of the bottom of the specimen is measured using the oven-dried method. If the vertical distribution of moisture is assumed to be linear, the volumetric water content at the bottom of the specimen can be estimated as follows. The amount of drainage through the specimen, q, between time t_{n-1} and time t_n is given by the hatched area in Figure 1.

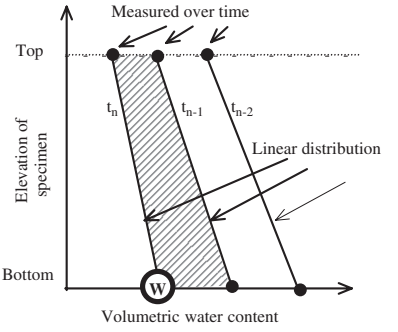


Figure 1. Distribution of volumetric water content in specimen over time.

Copyright © 2003 Swets & Zeitlinger B.V., Lisse, The Netherlands

The volumetric water content at point W is determined from the water content after the measurement is finished. Since the volumetric water content at the top of the specimen is measured over time, the volumetric water content in the previous time at the bottom can be calculated from the area of the trapezoidal section (the amount of drainage per unit area of specimen).

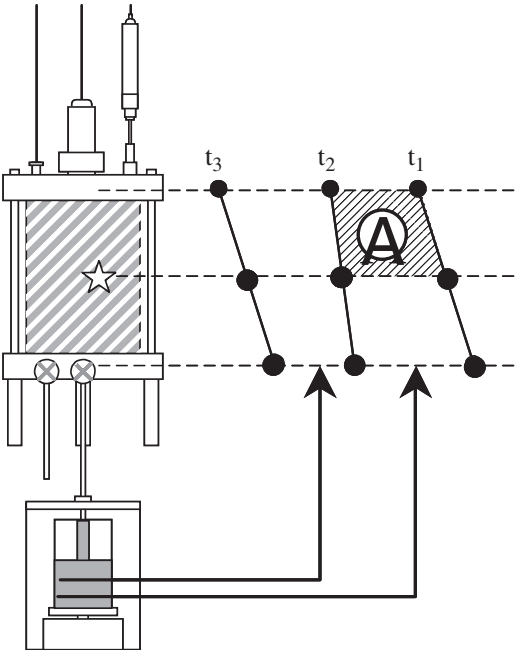


Figure 2. Amount of flow through the specimen.

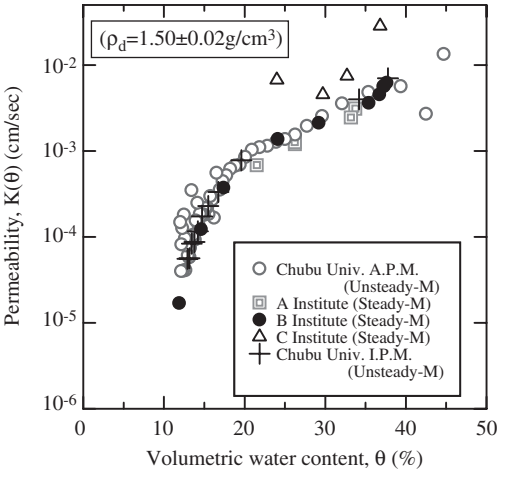


Figure 3. Permeability versus volumetric water content (suction method).

The amount of flow from t_1 to t_2 through the middle of the specimen is calculated as shown in Figure 2.

Figure 3 gives the relationship between permeability and volumetric water content of Toyoura sand.

3 DRAINAGE TEST IN CONSIDERATION OF IN-SITU TEST

3.1 *Experiment apparatus*

This test is performed when the groundwater level is high, using the experiment apparatus shown in Figure 4. The ground model is made of Toyoura sands (Table 1) in a columnar tank of 50 cm in diameter and 90 cm in height. At the surface and the undersurface, Amplitude Domain Reflectometry (ADR) sensors and tensiometers are set, respectively. The former measures volumetric water content, and the latter measures the pore water pressure of unsaturated soils.

The interval of these sensors is varied (20 cm, 30 cm and 40 cm) in order to investigate the influence of the interval of the installation position of a sensor. A well is dug in a foundation model, water is pumped up, and the groundwater level is reduced.

3.2 *Principles of measurement (drainage test)*

Fundamentally, the same principle as the original instantaneous method (Watson (1966)) is used which is

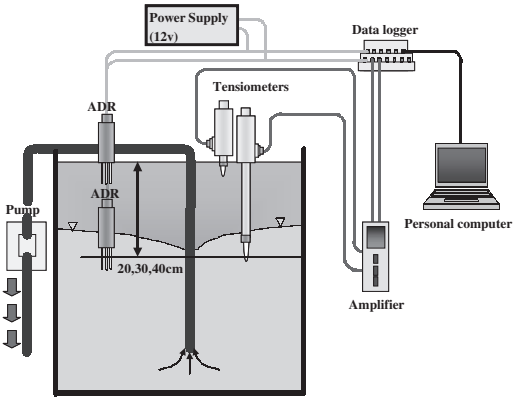


Figure 4. Experiment apparatus (Type 1).

Table 1. Toyoura sand.

Property		Value
Grain size	D	105–300 μm
Density of soil particles	ρ_s	2.65 g/cm^3
Dry density	ρ_d	1.50 g/cm^3
Permeability of saturated soil	k_{sat}	1.10E–2 cm/s

Copyright © 2003 Swets & Zeitlinger B.V., Lisse, The Netherlands

characterized by the piercing and installing of sensors from the ground surface. From the change of distribution of volumetric water content over time, the flow velocity at the midpoint between two sensors (ADR ① and ADR ② in Figure 5) is computed using the section area as follows.

$$v = \frac{A}{t_{n+1} - t_n} \tag{1}$$

where v is velocity, A is section area and $t_{n+1} - t_n$ is elapsed time. The change of pore water pressure over time is measured as shown in Figure 6.

The hydraulic gradient in the middle of these sensors is given by

$$i = \frac{\partial h_T}{\partial z} = \left(\frac{\Psi_1 - \Psi_2}{z_1 - z_2}\right) + 1 \tag{2}$$

where z_1, z_2 are the heights of the tensiometers. The hydraulic conductivity of unsaturated soil is calculated from equations (1) and (2) using Darcy's law.

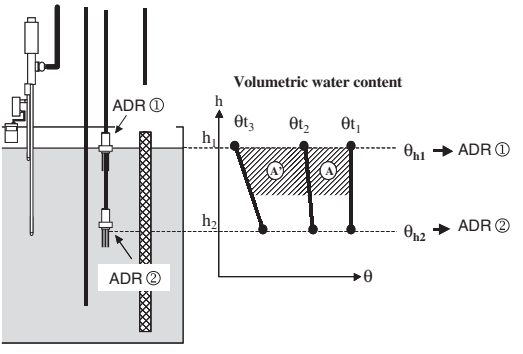


Figure 5. Distribution of volume water content.

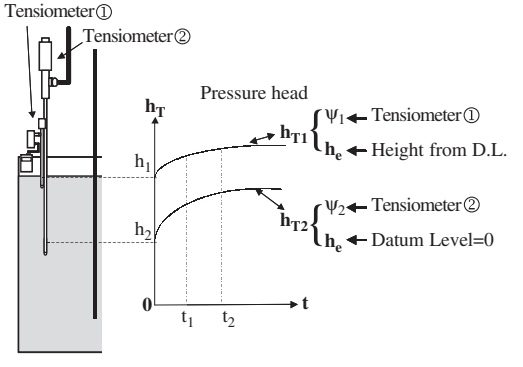


Figure 6. Pore water pressure (Type 1).

3.3 *Experimental results (drainage test)*

The experiment results when the sensor interval was varied for 20 cm, 30 cm, and 40 cm are shown in Figure 7. The result of the steady-sate method in the laboratory is also shown for comparison. Except for case-3 (interval, 40 cm), the influence of sensor interval is low at 20% or less of volumetric water content. On the contrary, when 20% volumetric water content is exceeded, the variation in data is large. The reason for this is assumed to be as follows from Figure 8 showing the change of the degree of saturation over time. The soil does not become unsaturated and a linear

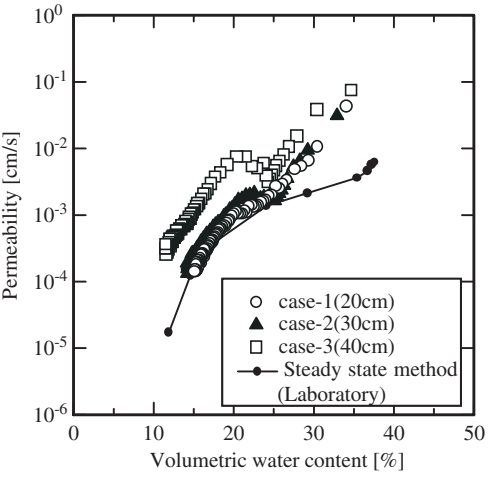


Figure 7. Permeability versus volumetric water content (influence of the interval of the installation position of a sensor).

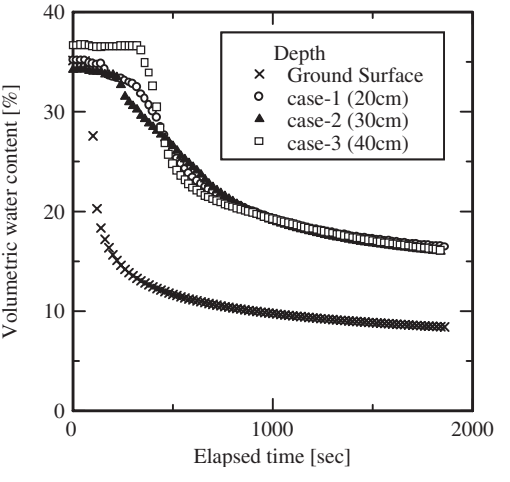


Figure 8. The change of the volumetric water content.

Copyright © 2003 Swets & Zeitlinger B.V., Lisse, The Netherlands

approximation of volumetric water content cannot be performed unless 300–600 seconds have passed for an interval of 20–40 cm underground, although drainage progresses and the surface is in the unsaturated state. This is considered to be the origin of the air entry value (A.E.V.) of Toyoura sand, which is about 20 cmH_2O (2 kN/m^2). It is considered that a linear approximation of volumetric water cannot be approximated at an interval larger than the A.E.V. of soils when the degree of saturation is high.

Figure 9 showing the change of the permeability of unsaturated soil over time supports this assumption.

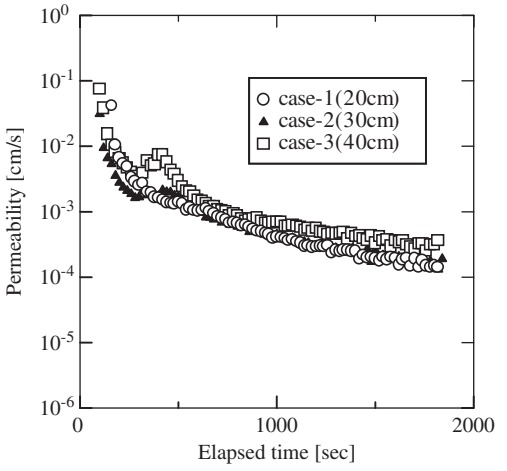


Figure 9. The change of permeability over time.

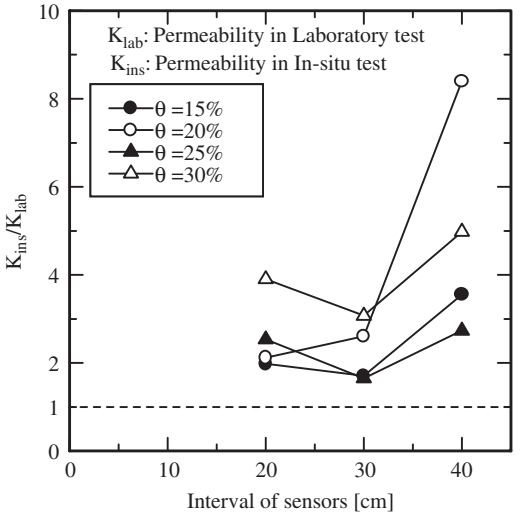


Figure 10. The ratio of the permeability versus intervals of the sensor.

Figure 10 shows the ratio of the permeability of unsaturated soil, k_1, obtained by the experiment in the laboratory, and the permeability of unsaturated soil, k_2, obtained by experiment for various intervals of the sensor in the ground. Approximating the influence of the dry density of the experiment in the laboratory and this experiment, and assuming a one-dimensional stream, about 20 cm is the maximum value of sensor interval for Toyoura sand. It is necessary to shorten the sensor interval when measuring the permeability of unsaturated soils in regions of high saturation.

4 PERMEATION TEST IN CONSIDERATION OF IN-SITU TEST

4.1 *Experiment apparatus*

The foregoing section considered the case when the groundwater level was high. However, generally the groundwater level is much lower than the ground surface in many cases. Therefore, part of the experimental equipment was improved and permeation tests by watering were performed.

The experiment apparatus is shown in Figure 11. The sensor (PR1) using the same dielectric constant principle is used for measuring the amount of moisture. The soil moisture at four depths can be simultaneously measured by PR1.

PR1 and two tensiometers are inserted in the dry ground model from the ground surface. Water is scattered using a sprinkler near the circumference of the sensors from the ground surface. Four volumetric water contents and two pore water pressures are measured over time.

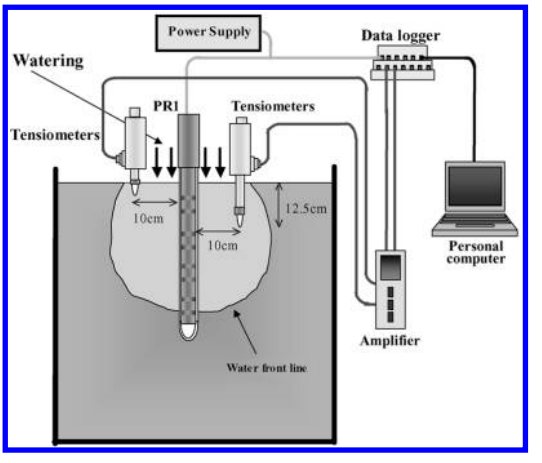


Figure 11. Experiment apparatus.

Copyright © 2003 Swets & Zeitlinger B.V., Lisse, The Netherlands

4.2 *Principle of measurement*

It was difficult to measure the amount of seepage flux per unit time and the flow velocity in this permeation test. Therefore, the amount of seepage flux can be calculated directly as shown in Figure 12.

Suppose that the moisture distribution, I, changes to the next moisture distribution, II, $\Delta t(=t_{\mathrm{II}}-t_{\mathrm{I}})$ hour after watering. The amount of seepage flux that permeated through the measurement point (MP) at this time is equal to the area shown in A. The velocity of seepage flux through the MP is given by

$$v=\frac{A}{\Delta t}=\frac{A}{t_{\mathrm{II}}-t_{\mathrm{I}}} \tag{3}$$

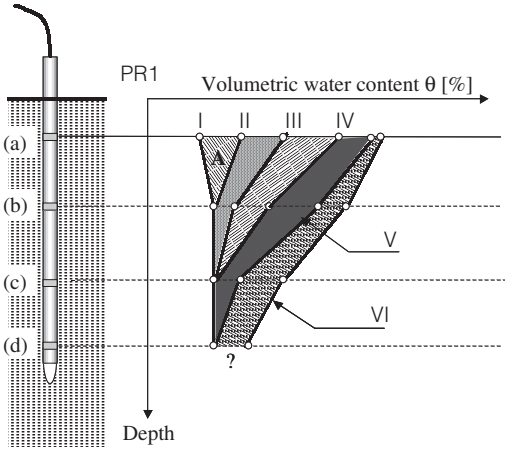


Figure 12. Time change of distribution of volumetric water content.

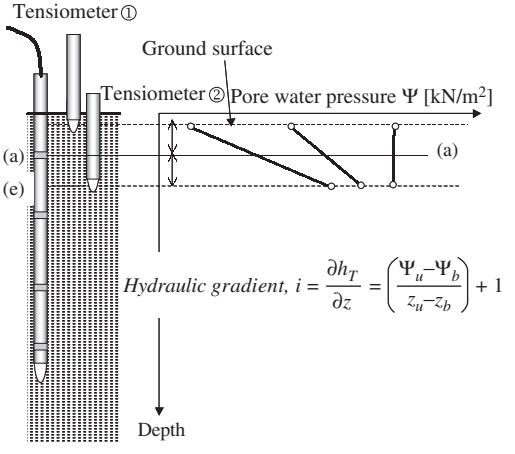


Figure 13. Calculation of hydraulic gradient.

Although the amount of seepage flux can be calculated in the time of I to V, since the amount of moisture of the deepest (at point 'd') is changing, from about V to VI, it cannot be calculated at this measurement value.

The pore water pressure of two points is needed for calculating a hydraulic gradient. This time, pore water pressure is measured at point (e) that is the ground surface and an object on both sides of point (a) as shown in Figure 13. The hydraulic conductivity of unsaturated soil is calculated using Darcy's law.

4.3 *Discussion of results*

Figures 14 and 15 show the change of volumetric water content and pore water pressure during the experiment. Watering was performed from 0 to 160 seconds. Since the strength of watering became almost the same as the permeability of saturated soil at 360 mm/h, watering was stopped at 160 seconds. When watering stopped, the amount of moisture in the surface soil begins to

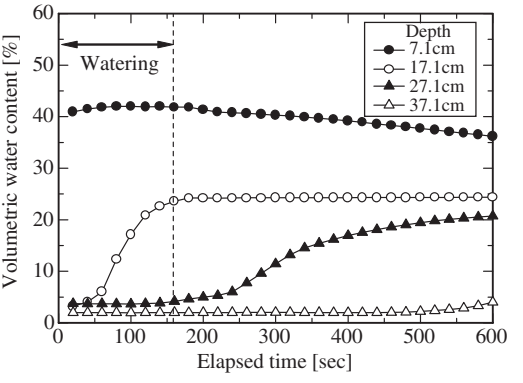


Figure 14. The change of volumetric water content over time.

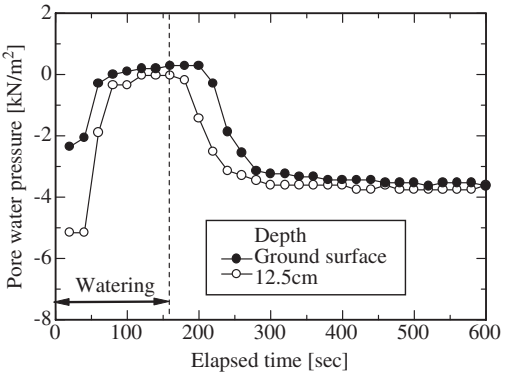


Figure 15. The change of pore water pressure over time.

Copyright © 2003 Swets & Zeitlinger B.V., Lisse, The Netherlands

decrease, and the amount of moisture at deeper points increases. It was found that the amount of moisture of the deepest point began to increase after about 500 seconds.

The change of distribution of volumetric water content is shown in Figure 16. Since the amount of moisture at the deepest point (point (d)) has not changed, the amount of seepage flux can be calculated.

Figure 17 shows three experiment results including the laboratory test (steady-state method). Since the permeation test had too high watering intensity, the permeability in the range of low saturation could not be taken, and the result was in agreement with the laboratory test. If watering intensity is controlled, it is guessed that it is measured from the degree of high saturation to the degree of low saturation. Generally, the groundwater level is below the ground surface, and the permeation test can measure the hydraulic conductivity for high degree of saturation. It is expected that by controlling the pore water pressure of the ground surface, or by adding a device which estimates lower pore water pressure from the value in the upper part, that permeability tests of unsaturated soil in the field can be performed.

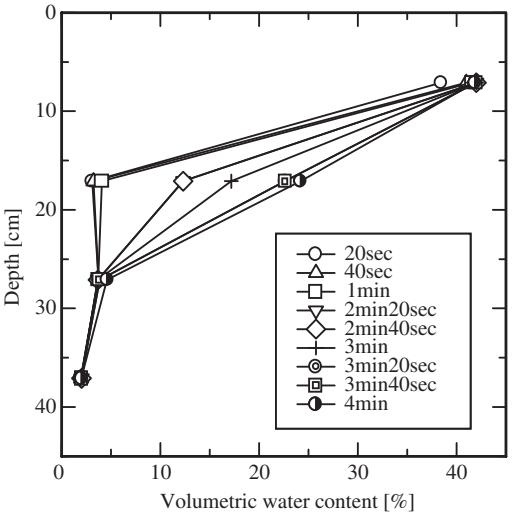


Figure 16. The change of distribution of moisture with overtime.

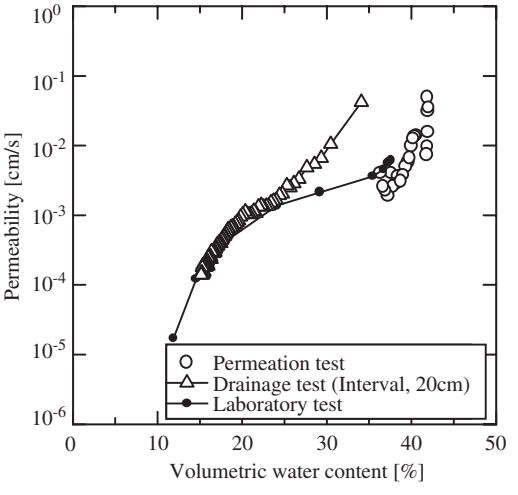


Figure 17. Comparison of experiment results.

5 SUMMARY

The following results were obtained from drainage tests and permeation tests, in consideration of application to in-situ tests of unsaturated soils.

- The measurable range of saturation reduces as that the sensor interval is increased.
- With the draining method, the permeability of unsaturated soils can be estimated accurately, but the result depends strongly on sensor interval, so the sensor interval should be set to be short taking into account of the air entry value of the soils.
- Generally, groundwater level is below the ground surface, therefore the permeation test for measuring the hydraulic conductivity under high saturation is more practical.
- The approximated profile method may be applicable to the measurement of hydraulic conductivity in the field.

ACKNOWLEDGEMENTS

The authors thank graduate students of Chubu University, Mr. T. Shibagaki and Y. Mizuguchi for their support in carrying out the experiments.

REFERENCES

Gaskin, G.J. & Miller, J.D. 1996. Measurement of soil water content using a simplified impedance measuring technique, *J. Agric. Engng Res.*, 63: 153–160.

Sugii, T., Yamada, K. & Uemura, M. 2000. Measuring hydraulic properties for unsaturated soils with unsteady method, *Proc. Asian Conf. on Unsaturated Soils* "UNSAT-ASIA2000", 439–444.

Sugii, T., Yamada, K., Umeda, Y. & Uemura, M. 2001. Permeability test of unasaturated soil approximating moisture distribution, *Proc. Int. Symp. on Suction, Swelling, Permeability & Structure of Clays.*

Topp, G.C., Yanuka, M., Zebchuk, W.D. & Zegelin, S. 1998. Determination of electrical conductivity using time

Copyright © 2003 Swets & Zeitlinger B.V., Lisse, The Netherlands

domain reflectometry: soil and water experiments in coaxial lines, *Water Resources Research*, 24(7): 945–952.
Uno, T. Sato, T. & Sugii, T. 1995. Laboratory permeability measurement of partially saturated soil: Alonso & Delage (eds.), *Unsaturated Soils, Proc. Intern. Symp., Paris, 6–8 September*, 573–578.
Watson, K.K. 1966. An instantaneous profile method for determining the hydraulic conductivity of unsaturated porous materials, *Water Resources Research*, 2: 709–715.
Whalley, W.R. 1993. Considerations on the use of time-domain reflectometry (TDR) for measuring soil water content, *J. Soil Science*, 44: 1–9.

Copyright © 2003 Swets & Zeitlinger B.V., Lisse, The Netherlands

Application of highly viscous fluid tests to jointed rock masses and evaluation of test results

H. Kishi & T. Kakue
Tokyo Electric Power Company, Kannagawa Power Plant Construction Office, Takasaki City, Japan

M. Nishigaki
Faculty of Environmental Science and Technology, Okayama University, Okayama City, Japan

ABSTRACT: Lu values obtained from Lugeon test are liable to be underestimated, compared to those obtained under laminar flow condition, due to turbulent flow during the test. To overcome this, we carry out Lugeon tests using highly viscous fluids (highly viscous fluid test) to evaluate the permeability of jointed rock masses. The test results show clearly the difference between the Lugeon values of highly viscous fluid test and those of Lugeon test.

1 INTRODUCTION

Permeability evaluated by Lugeon tests is often underestimated in jointed rock masses with high permeability because flows in cracks tend to become turbulent (Lancaster-Jones 1975, Houlsby 1976 & Kutzner 1985). Because suitable sites for dam construction are becoming less available recently, adequate evaluation of rock permeability is very important in ensuring the hydraulic stability of dam foundations and improving the cost efficiency of dam construction.

An approach to address this challenge is to carry out Lugeon tests using highly viscous fluids to evaluate the permeability of rock masses when there are laminar flows in cracks (Watanabe & Ashikawa 1985, Matsumoto et al. 1988, Yamaguchi et al. 1989 & Iwamoto et al. 1990) (such tests are called highly viscous fluid tests in this paper). In the present study, highly viscous fluid tests were applied to jointed rock masses with high permeability, the obtained results were compared to those of a Lugeon test, and the hydraulic properties of rock masses were evaluated.

2 METHODS OF HIGHLY VISCOUS FLUID TESTS AND ANALYSIS OF TEST RESULTS

2.1 *Test method*

A flowchart of the tests is shown in Figure 1, and the configuration of the test equipment is shown in Figure 2.

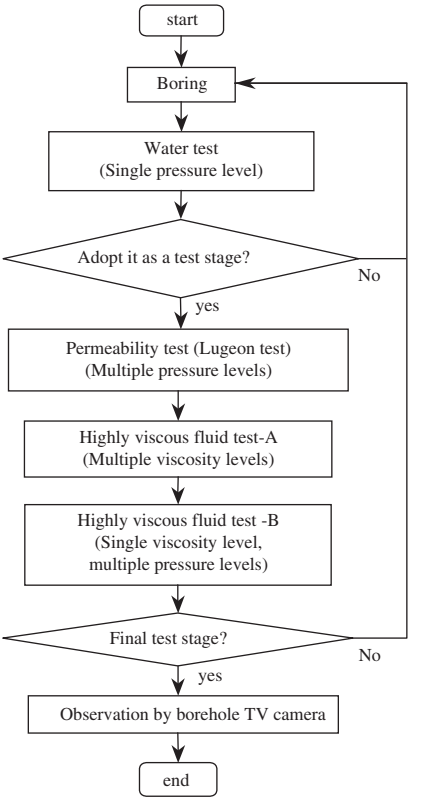


Figure 1. Test flowchart.

Copyright © 2003 Swets & Zeitlinger B.V., Lisse, The Netherlands

The Lugeon permeability test was carried out with a test section (one stage) of 5 m according to the "Technical guidance and explanation of Lugeon tests" (River Bureau, Ministry of Construction 1984). Pressure during the test was controlled so as not to exceed the expected critical pressure so that no rock deformation would occur during the test. Measurements were made mainly at low pressures to control the occurrence of turbulent flow. To improve upon the precision of measuring at low pressures, the pressure in the borehole was measured directly by using a pressure sensor attached to the tip of a rod. Because the effective capacity of pumping was limited to about 100 l/min, intended pressure could not be achieved and the number of measuring points was limited in high permeability stages. To cope with this problem, the flow rate was also controlled. The pressure and flow rate levels used in the permeability test are shown in Table 1. Each measurement was carried out for 10 min after confirming the stability of pressure and flow rate.

Based on the results of the Lugeon test, fluid injection pressures in the highly viscous fluid tests were selected in consideration of the viscosity of the fluid (methylcellulose-based solution). The viscosity was set at 1000 cP or lower in order to ensure Newtonian fluid condition. The viscosity was measured with a B-type viscometer.

In highly viscous fluid test A, the flow rate of the injected liquid was measured at a constant pressure while raising the viscosity progressively; the viscosity values in the test are listed in Table 2. In highly viscous fluid test B at site K for selected stages, the flow rate of the injected liquid was measured while changing the pressure progressively at a constant viscosity.

After completing the final stage of each test, the borehole was observed by using a borehole TV camera to investigate crack distribution, crack strike and dip, crack width, crack fills, and weathering.

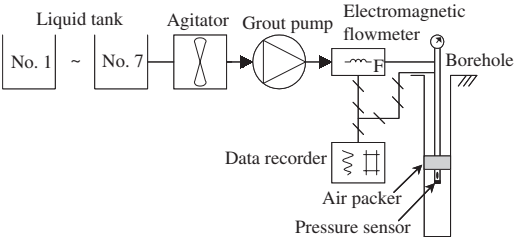


Figure 2. Configuration of test equipment.

2.2 *Method of test result analysis*

The relationship between the injection pressure (P_o) and flow rate (Q) obtained from a highly viscous fluid test in a laminar flow condition is given by

$$Q = \frac{C_1}{\mu} P_o \quad (1)$$

where μ = viscosity; and C_1 = a constant.

In the case of highly viscous fluid test A, where pressure was constant, the relationship between P_o and Q in a laminar flow condition is given by

$$\log Q = C_2 - \log \mu \quad (C_2 = \log C_1 P_o) \quad (2)$$

where C_2 = a constant.

The results of highly viscous fluid test A are summarized in Figure 3, whose horizontal and vertical axes, both on a logarithmic scale, represent fluid viscosity and the measured flow rate (l/min in a stage), respectively. In general, the data is plotted along

Table 2. Viscosity levels for highly viscous fluid test (Unit [cP]).

	Concentration No.									
Site	1	2	3	4	5	6	7	8	9	10
T	10	20	40	80	160	320	640	–	–	–
K	3	5	10	20	40	80	160	320	640	1000
S	10	20	40	80	160	320	640	–	–	–

Table 1. Pressure levels for permeability test.

		Test stage									
Site		1	2	3	4	5	6	7	8	9	10
T	Pressure (MPa)	0.05	0.10	0.15	0.20	0.25	0.30	0.40	0.50	0.10	0.05
	Flow rate (l/min/m)	3.0	5.0	6.0	8.0	9.0	10.0	13.0	20.0	3.0	5.0
K	Pressure (MPa)	0.02	0.05	0.10	0.15	0.20	0.30	0.50	1.0	0.3	0.1
	Flow rate (l/min/m)	3.0	5.0	6.0	8.0	9.0	10.0	13.0	20.0	10.0	5.0
S	Pressure (MPa)	0.05	0.10	0.15	0.20	0.25	0.30	0.20	0.10	–	–
	Flow rate (l/min/m)	3.0	5.0	6.0	8.0	9.0	10.0	8.0	5.0	–	–

Copyright © 2003 Swets & Zeitlinger B.V., Lisse, The Netherlands

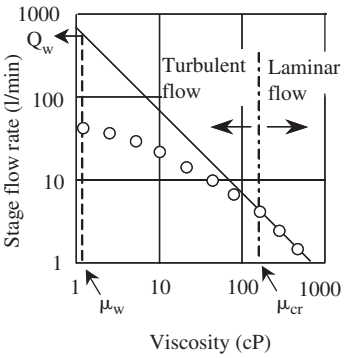


Figure 3. Results of highly viscous fluid test A.

a curve when the viscosity is low and along a straight line with a slope of −45 degrees when the viscosity is high. The straight line, obtained by the best fitting of linearly plotted data, is extrapolated to deduce an intercept (C_2 constant in equation (2)).

Now that the relationship between viscosity and flow rate in a laminar flow condition is given for the stage of concern, the flow rate of water is obtained by substitution of the viscosity of water.

$$Q_w = 10^{(C_2 - \log \mu_w)} \tag{3}$$

where Q_w = flow rate in a laminar flow condition; and μ_w = the viscosity of water.

With the flow rate of water, a Lugeon value is obtained from

$$Lu_2 = \frac{0.98 Q_w}{P_o L} \tag{4}$$

where Lu_2 = the Lugeon value in a laminar flow condition; and P_o = the injection pressure in MPa.

The Lugeon value obtained by the above procedure should indicate the permeability of a rock mass with laminar water flow. As described later, the Reynolds number at which laminar flow changes to turbulent flow is called a critical Reynolds number. This is obtained from the measured flow rate at the point of lowest viscosity (μ_{cr}) on the straight line of Figure 3.

Equation (1) is applicable to the results of highly viscous fluid test B because the viscous liquid whose laminar flow condition had been confirmed in highly viscous fluid test A was used in test B. The results of test B are therefore plotted on a diagram whose horizontal and vertical axes represent flow rate and injection pressure, respectively. Based on this diagram, a viscosity ratio-based conversion was carried out to deduce the Lugeon value of water from the measured or extrapolated flow rate at the injection pressure of 0.98 MPa. The result was compared to the value obtained from test A.

3 RESULTS

3.1 *Geology of the in-situ test sites*

The tests were carried out at sites T, K, and S, which are all dam sites in Japan.

Quaternary andesite is distributed at site T. According to borehole observation, the rock is hard and has 10–20 cracks/m, most of which are open cracks associated with cooling joints.

Conglomerate consisting of Neogene granodiorite and andesite is distributed at site K. According to borehole observation, the rock is hard and has about 5 cracks/m, about half of which are sharp open cracks associated with cooling joints.

Tertiary fine tuff is distributed at site S. According to borehole observation, the rock is hard and has been subjected to hydrothermal alteration. Cracks are difficult to discriminate from cores in fractured zones, which are abundant. Only 2–3 cracks/m can be clearly recognized, about half of which are open cracks.

3.2 *Results of the tests*

The in-situ test results reported in this paper are those of 20 stages, consisting of seven stages at site T, nine stages at site K, and four stages at site S. Highly viscous fluid test B was also carried out in three stages at site K. Some of the results are shown in Figures 4, 5, 6 and 8. The results of the Lugeon test are shown in Figure 4. The results of the highly viscous fluid test A are shown in Figure 5. Histograms of open crack width observed by using borehole TV camera are shown in Figure 6. The results of the highly viscous fluid test B are shown in Figure 8.

The Lugeon test results show a gradual decrease in the increment of flow rate with increased injection pressure. This is probably due to turbulent flow in rock during the test.

4 DISCUSSION OF RESULTS

4.1 *Relationship between the results of Lugeon test and highly viscous fluid tests*

The relationship between the Lugeon values obtained from the Lugeon test in a turbulent condition and those obtained from highly viscous fluid test A in a laminar condition is shown in Figure 7; the latter values are greater than the former by a factor of about 5 to 50. The difference becomes greater as the Lugeon value becomes greater but is nearly unchanged at a Lugeon test value of 20 or greater. Because the increase in pressure is restricted by the pumping capacity at Lugeon test values exceeding 20, the Lugeon values are obtained through a conversion from equation (4) based on the flow rate measured at an injection pressure of 0.98 MPa or less; 0.98 MPa is

Copyright © 2003 Swets & Zeitlinger B.V., Lisse, The Netherlands

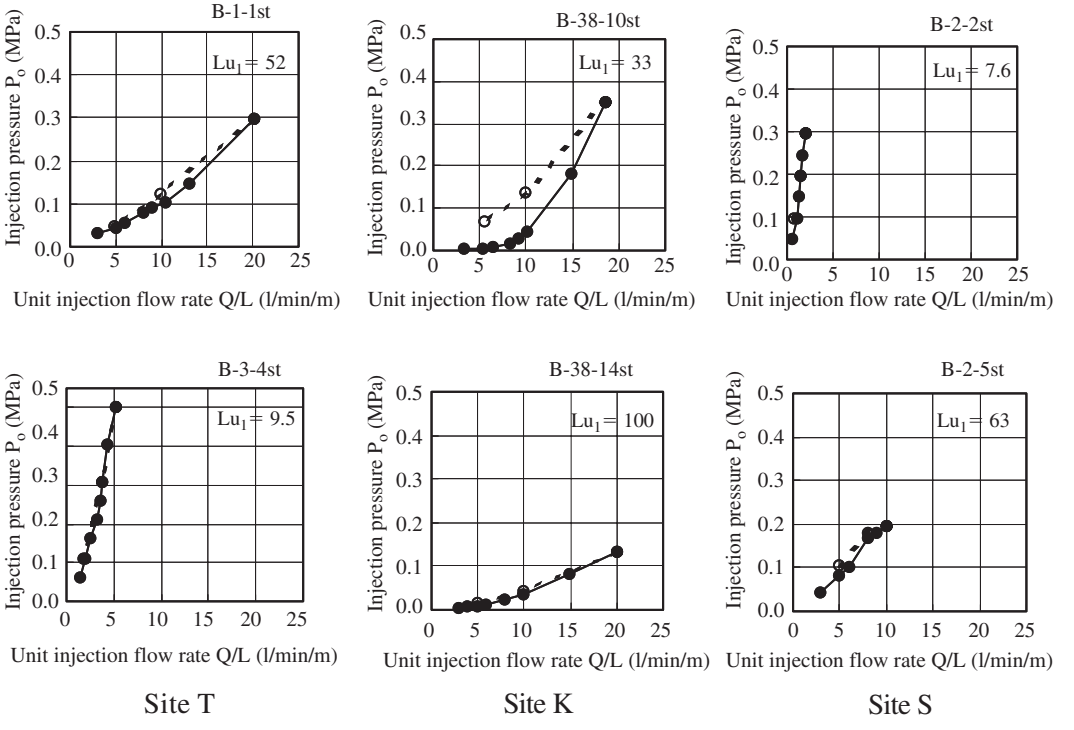


Figure 4. Lugeon test results.

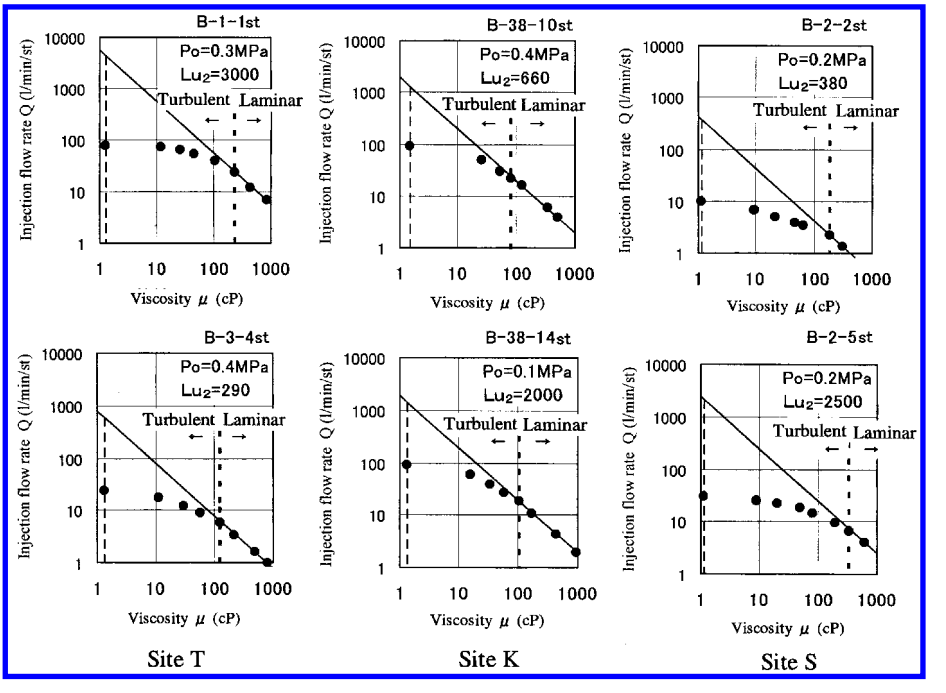


Figure 5. Highly viscous fluid test A results.

Copyright © 2003 Swets & Zeitlinger B.V., Lisse, The Netherlands

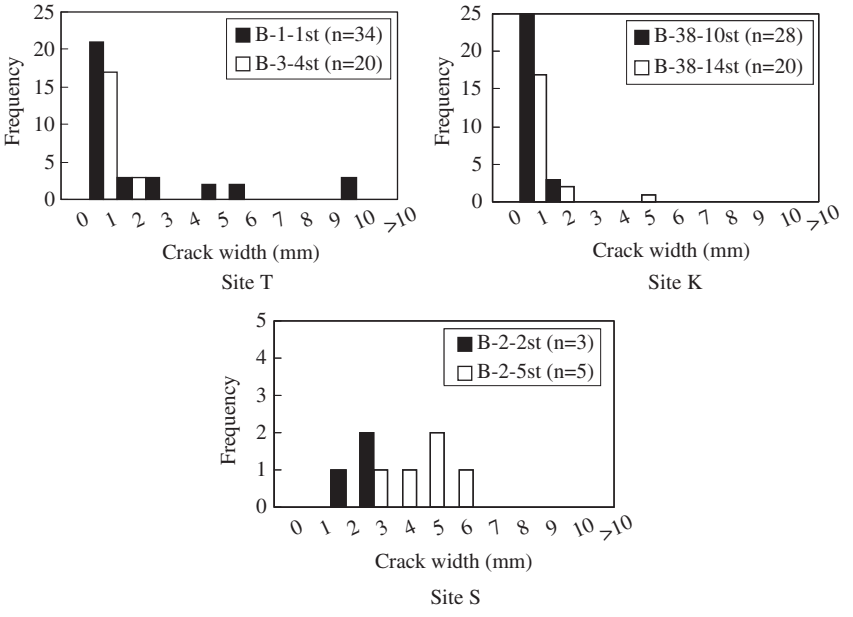


Figure 6. Histogram of open crack width.

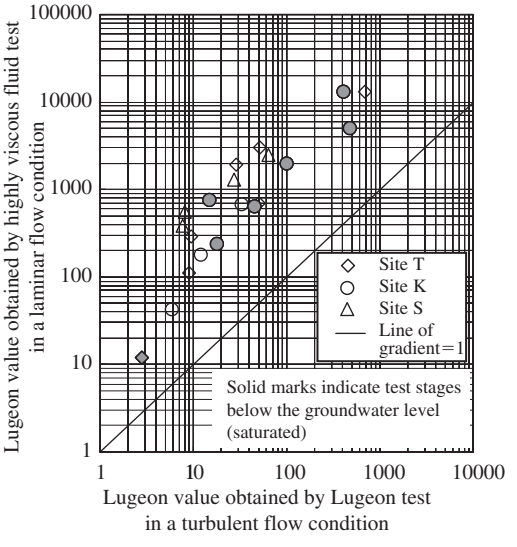


Figure 7. Relationship between Lugeon values obtained by Lugeon test and those obtained by highly viscous fluid test.

a standard value for Lugeon tests. Also, because measurements at low pressures are used for the calculation, the effect of turbulent flow may become relatively small.

While test stages below the groundwater level (saturated condition) are discriminated from those above

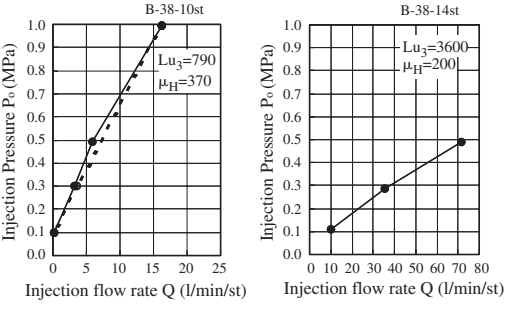


Figure 8. Results of highly viscous fluid test B.

the groundwater level (unsaturated condition) in Figure 7, no significant difference is found between the test results of the two conditions at site K. While a seepage flow in an unsaturated rock mass does not become a potential flow, the situation around a test stage could be viewed as a saturated condition because measurements were carried out after confirming the stability of the injection pressure and flow rate. This may explain why no significant difference was found between the results of the two conditions.

The results of highly viscous fluid test B show a nearly linear relationship between injection pressure and flow rate (Figure 8), and the Lugeon values of highly viscous fluid test B are nearly the same as those of test A (Figure 9). It is therefore considered that measurements in test B were carried out in a laminar flow condition.

Copyright © 2003 Swets & Zeitlinger B.V., Lisse, The Netherlands

The above results indicate that highly viscous fluid tests are useful for evaluating the permeability of rock masses in a laminar flow condition.

4.2 *Evaluation of critical Reynolds number*

The viscosity and flow rate at the turbulent–laminar boundary measured in highly viscous fluid test A were used to evaluate the critical Reynolds number. The relationship between viscosity and flow rate departs from linearity as viscosity decreases. This can be explained by the successive transition from laminar to turbulent flow in cracks starting from wider cracks in each stage.

Focusing on the widest open crack in each stage, the condition of the occurrence of turbulence is given by

$$\mathrm{Recr} = \frac{2t_{max}V_{o(tmax)}}{\nu} \tag{5}$$

where Recr = critical Reynolds number; t_{max} = the width of the widest open crack; $V_{o(tmax)}$ = flow velocity into the widest open crack; and ν = the coefficient of kinematic viscosity.

The flow velocity into the widest open crack is given by

$$V_{o(tmax)} = \frac{q_{(tmax)}}{2\pi r_o t_{max}} \tag{6}$$

where $q_{(tmax)}$ = flow rate in the widest open crack; and r_o = the radius of the borehole.

Because the permeability of a parallel plate crack is proportional to the third power of the crack width, the flow rate in an open crack is assumed to be proportional to the third power of the observed crack width. Then, the flow rate in the widest open crack is given by

$$q_{(tmax)} = \frac{t_{max}^3}{\sum t_i^3} Q_{cr} \tag{7}$$

where t_i = the width of each crack in the stage; and Q_{cr} = the stage flow rate at the turbulent–laminar boundary.

From equations (5) to (7), the critical Reynolds number is given by

$$\mathrm{Recr} = \frac{Q_{cr}}{\pi \nu r_o} \frac{t_{max}^3}{\sum t_i^3} \tag{8}$$

The critical Reynolds numbers obtained from equation (8) are shown in Figure 10; all of them are less than

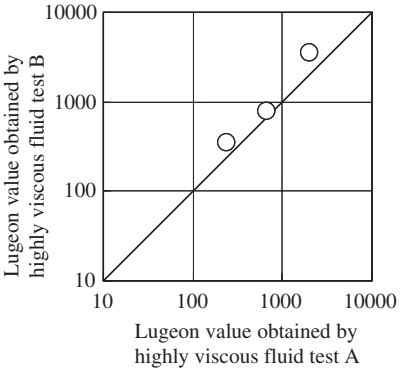


Figure 9. Relationship between highly viscous fluid test A and B.

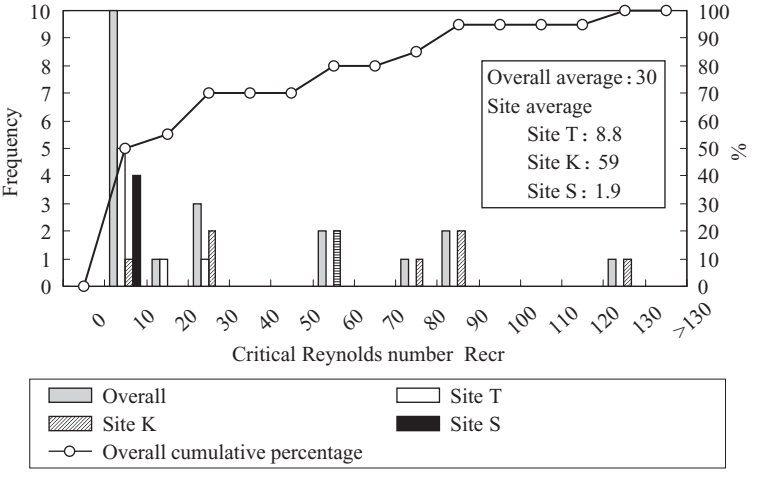


Figure 10. Histogram of critical Reynolds number.

Copyright © 2003 Swets & Zeitlinger B.V., Lisse, The Netherlands

130, and many of them are less than 10. These numbers are much smaller than a critical Reynolds number of 2000, which is typical of flows between parallel plates (Murota 1969). An explanation for this is that flows in rock masses easily change into turbulence because they are affected by complicated channels involving crack roughness, branching, merging, and local clogging (Watanabe 2001).

5 CONCLUSION

To evaluate the relationship between Lugeon test results and rock mass permeability, highly viscous fluid tests were carried out to obtain Lugeon values in a laminar condition. These Lugeon values are found to be greater than those obtained by the Lugeon test by a factor of about 5 to 50.

The critical Reynolds numbers obtained from the results of the highly viscous fluid tests are much smaller than those typically found in flows between parallel plates. This implies that turbulence easily occur in flows in rock mass cracks.

The fact that the Lugeon values obtained from the Lugeon test are smaller than those obtained from the highly viscous fluid tests can be explained by the occurrence of turbulence. Transition from laminar to turbulent flow in cracks (critical Reynolds number) is likely to be affected by crack surface roughness and network development.

REFERENCES

Houlsby, A.C. 1976. Routine interpretation of the Lugeon water-test. *Journal of Engineering Geology* 9: 303–313.

Iwamoto, T., Sonomoto, H., Arimoto, H. & Dotsuma, M. 1990. Measurement of coefficient of rock permeability using highly viscous fluids: Lugeon tests on welded tuff. *Engineering Geology* 31(2): 1–10.

Kutzner, C. 1985. Considerations on rock permeability and grouting criteria. *Proc. The 15th Congress on Large Dams* 58(17): 315–328.

Lancaster-Jones, P.F.F. 1975. The interpretation of the Lugeon water-test. *Journal of Engineering Geology* 8: 151–154.

Matsumoto, N., Yamaguchi, K. & Shibuichi, H. 1988. Permeability tests using highly viscous fluids. *Proc. The 23rd Meeting of the Japanese Society of Soil Mechanics and Foundation Engineering*: 125–126.

Murota, A. (ed.) 1969. *Applied Fluid Mechanics*: 43–45. Tokyo: Kyoritsu-shuppan.

River Bureau, Ministry of Construction (ed.) 1984. *Technical guidance and explanation of Lugeon tests*, Japan Institute of Construction Engineering.

Watanabe, K. & Ashikawa, R. 1985. An attempt to evaluate the effect of turbulent flow on permeability tests in a jointed rock mass. *Proc. The 17th Symposium on Rock Mechanics*: 161–165.

Watanabe, K. et al. (eds) 2001. *Geological surveys and evaluation of groundwater in a rock mass: Importance of geological surveys*: 99–118. The Japan Institute of Systems Research.

Yamaguchi, K., Shibuichi, H. & Matsumoto, N. 1989. Effects of turbulent flow on Lugeon tests and corrective measures. *Proc. The 21st Symposium on Rock Mechanics*: 401–405.

Copyright © 2003 Swets & Zeitlinger B.V., Lisse, The Netherlands

Modeling and analysis of groundwater flow

Copyright © 2003 Swets & Zeitlinger B.V., Lisse, The Netherlands

A new three-dimensional analysis system for seepage problem applying a meshless method

H. Sakurai
Nuclear Group, Institute of Technology, Shimizu Corporation

M. Kawahara
Department of Civil Engineering, Chuo University

ABSTRACT: A new three-dimensional (3D) seepage flow analysis system applying the element-free Galerkin method (EFGM) is presented. The EFGM is a meshless method that is expected to totally eliminate the mesh generation task. However, an analysis system by EFGM for complex and composite 3D objects has not been developed yet. In our system, a unique mesh data called consistency-free mesh assembly (CMA) is introduced to achieve a practical analysis system. A CMA is a simple assembly of meshes permitting incompatibility between adjacent meshes and overlap of meshes. The CMA circumvents the difficulty of the mesh generation of complex and composite domains such as geological structure consisting of several geological formations and underground facilities. This paper shows that the CMA is easy to generate and brings great advantages to the EFGM. Some 3D numerical examples are presented to demonstrate the usefulness of CMA and to discuss the accuracy of solutions.

1 INTRODUCTION

To plan a geological disposal repository of nuclear waste, it is very important to evaluate the groundwater flow field around the repository. Data available at the initial stage of the disposal project, however, is not sufficient to allow precise estimation of the groundwater flow field. Permeability and other physical parameters are not well known, and different models of geological structures may have to be studied if there are different interpretations on geological data. Against this background, the computer aided engineering (CAE) for groundwater flow analysis need to satisfy the following requirements, in order that the CAE actively contribute to the progress of the disposal project.

- Analysis data can easily be modified according to differences in geological interpretation or progress in geological surveys.
- Analysis data can easily be modified according to changes in the forms and orientations of underground facilities.

These requirements are very difficult to satisfy with CAE based on the conventional finite element method (FEM) because of difficulty in the three-dimensional (3D) mesh generation. The element-free Galerkin method (EFGM) proposed by Belytschko et al. (1994) is a meshless method that is expected to totally eliminate the mesh generation task. The EFGM have been applied to many problems (Belytschko et al. 1996), but a complete CAE system that can handle composite 3D domains consisting of several materials of complex shapes, such as geological structures, has not yet been developed.

In our system, a unique mesh data called a consistency-free mesh assembly (CMA) has been introduced to achieve a practical CAE system for 3D groundwater seepage flow analysis based on the EFGM (Sakurai & Kawahara 2002a, b). A CMA, which is a combination of independent meshes created for each geological formation and underground facility, is much more flexible than consistent meshes for FEM analyses because it allows incompatibility between adjacent meshes and overlap of meshes. This paper shows that the CMA is easy to generate and brings great advantages to the EFGM. Some 3D numerical examples are presented to demonstrate that the groundwater flow analysis system introducing the CMA into the EFGM can satisfy the aforementioned two requirements, and to discuss the fundamental performance.

Copyright © 2003 Swets & Zeitlinger B.V., Lisse, The Netherlands

2 ELEMENT-FREE GALERKIN METHOD

The EFGM uses the moving least square method (MLSM) to construct shape functions and discretize weak-form governing equations of continuum by using only nodes.

2.1 *Moving least square method*

In the MLSM, an unknown function, $\phi(\mathbf{x})$, at an arbitrary evaluation point, $\mathbf{x}$, in the domain is approximated by

$$\phi^h(\mathbf{x}) = \{P(\mathbf{x})_m\}^T \{a(\mathbf{x})_m\} \tag{1}$$

Here, $\{P(\mathbf{x})_m\}$ is a basis, which is given in the present system as a 3D linear basis:

$$\{P(\mathbf{x})_m\} = \{1 \quad x \quad y \quad z\}^T, \quad m = 4 \tag{2}$$

The coefficients $a(\mathbf{x})_m$ are obtained by minimizing the following a weighted, discrete L_2 norm at the evaluation point, $\mathbf{x}$.

$$J = \sum_i^N w(r_i) \left[\{P(\mathbf{x}_i)_m\}^T \{a(\mathbf{x})_m\} - \phi_i\right]^2 \tag{3}$$

Here, $\mathbf{x}_i$ is the coordinate value of node i, ϕ_i is the node value of ϕ at $\mathbf{x} = \mathbf{x}_i$, and r_i is the distance between the evaluation point $\mathbf{x}$ and the node i. N is the number of nodes present within the domain set around the evaluation point, is called a domain of influence (DI) with radius d_I. A quartic spline weight function (Beissel & Belytschko 1996) is adopted in the present system.

$$w(r) = 1 - 6\left(\frac{r}{d_I}\right)^2 + 8\left(\frac{r}{d_I}\right)^3 - 3\left(\frac{r}{d_I}\right)^4 \tag{4}$$

The stationarity of J in equation (3) with respect to $\{a(\mathbf{x})_m\}$ leads to shape function of ϕ, as follows:

$$\phi^h(\mathbf{x}) = \{G_N\}^T \{\phi_N\} \tag{5}$$

where

$$\{\phi_N\} = \{\phi_1 \quad \phi_2 \quad \ldots \quad \phi_N\}^T \tag{6}$$

$$\{G_N\}^T = \{P_m\}^T ([D_{mN}]^T [W_{NN}] [D_{mN}])^{-1} [D_{mN}]^T [W_{NN}] \tag{7}$$

$$[D_{mN}] = [\{P(\mathbf{x}_1)_m\} \quad \{P(\mathbf{x}_2)_m\} \ldots \{P(\mathbf{x}_N)_m\}] \tag{8}$$

$$[W_{NN}] = diag[w(r_1) \quad w(r_2) \ldots w(r_N)] \tag{9}$$

2.2 *Variational form*

The governing equation of groundwater flow in a domain V, is assumed to be given by a seepage flow equation:

$$\nabla(k\nabla\phi) = 0 \ \text{ in } V \tag{10}$$

Here, k is the permeability, ∇ is the linear differential operator and ϕ is the velocity potential. The boundary conditions are

$$\phi = \hat{\phi} \ \text{ on } S_\phi \tag{11}$$

$$k\frac{\partial\phi}{\partial n} = \hat{q} \ \text{ on } S_n \tag{12}$$

where the superscript "ˆ" indicates a prescribed value and n is a unit normal vector at the boundary of the domain V. The approximation function $\phi^h(\mathbf{x})$ generated by the MLSM does not satisfy Kronecker delta property. In a variational form, the essential boundary conditions of equation (11) and the C^0 continuity of ϕ at each formation interface S_i are also need to be taken into consideration. The C^0 continuity on S_i, however, was found by Sakurai & Kawahara (2002a, b) to have minimal effect in several numerical tests and was not taken into account in the present system. Therefore, a functional corresponding to the governing equations can be written as

$$\Pi(\phi) = \sum_e \left\{ \int_{V_e} \frac{1}{2} k_e (\nabla\phi)^2 dV - \int_{(S_n)_e} (\phi\hat{q})\, dS + \int_{(S_\phi)_e} \frac{\alpha}{2}(\phi - \hat{\phi})^2\, dS \right\} \tag{13}$$

Here, a subscript "e" to indicate a value related to each formation. α is a sufficiently large, positive, penalty number to enforce equation (11).

2.3 *Domain integration*

Numerical integration using cell structures is currently adopted for the domain integration in this system, as shown in Figure 1. Gauss quadrature is applied to each cell. The DI does not cross any boundaries, such as the domain boundary or material boundaries. If a boundary crosses a cell, a higher-order quadrature was applied to such a cell. The DI size is variable depending on nodal density introduced by Sakurai & Kawahara (2002a).

3 CONSISTENCY-FREE MESH ASSEMBLY

Solid modeling (Requicha & Voelcker 1982), which is one of the most advanced techniques of 3D geometry modeling, is widely used in geometry definition for

Copyright © 2003 Swets & Zeitlinger B.V., Lisse, The Netherlands

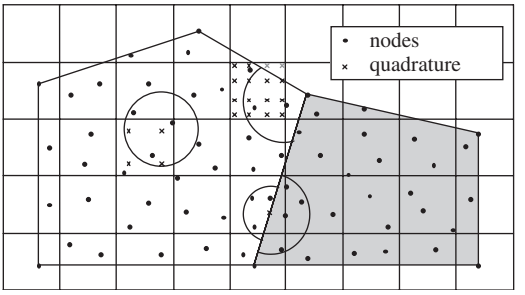


Figure 1. Cell structure for domain integration.

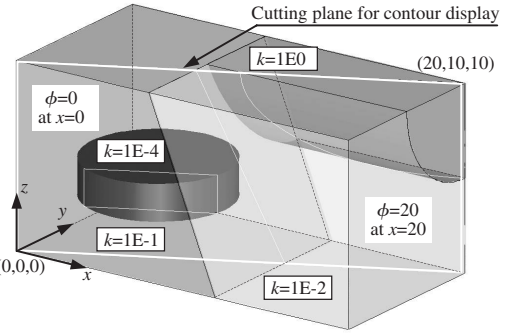


Figure 2. Model 1 consisting of simple geometries.

mesh generation in FEM analyses. Objects of groundwater flow analysis are geological structures that are composite domains consisting of several geological formations and underground facilities. The greatest factor that makes mesh generation in composite objects difficult is solid modeling so that mesh compatibility is ensured at each domain interface. If a group of meshes generated from solid models independently created without keeping such compatibility can be used in groundwater flow analysis, the solid modeling is therefore much easier. This inconsistent mesh group, which is termed a consistency-free mesh assembly (CMA), is used for EFGM analyses in our system. The CMA is a simple assembly of meshes. The CMAs not only allow incompatibility between adjacent meshes but also overlap of meshes. The CMAs may be used for:

– defining geometry of analysis objects,
– providing cells for numerical integration,
– visualizing analysis results,
– computing differential values with FEM shape functions, and so on.

Sakurai (2002) gave a full detail of computation using the CMA.

4 NUMERICAL EXAMPLES

To demonstrate the usefulness of the CMA, two sets of numerical example are presented in this paper.

4.1 *Composite consisting of simple geometries*

An analysis model consisting of three geological formations and one columnar underground structure was prepared as shown in Figure 2. These permeability values have differences up to four orders of magnitude as noted in the figure. The boundary conditions are $\phi = 0$ on a $y - z$ plane at $x = 0$, $\phi = 20$ on a $y - z$ plane at $x = 20$, and zero flux on the other boundary surfaces. To investigate the solution accuracy, a consistent finite element mesh, as shown in Figure 3,

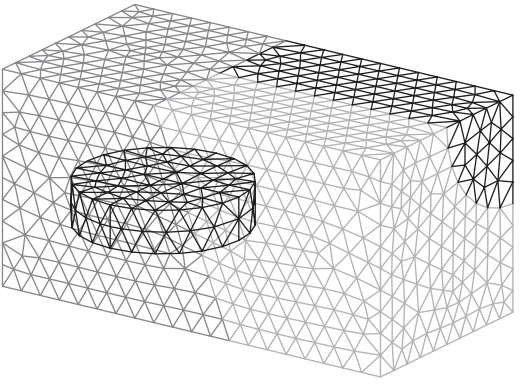


Figure 3. Mesh 1-A: a consistent mesh for Model 1.

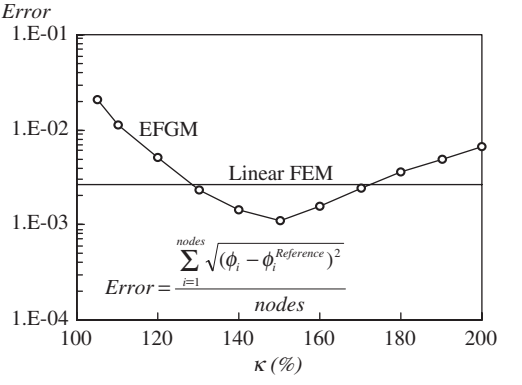


Figure 4. Solution accuracy and sensitivity to d_1.

was first computed and its solutions were compared with FEM solutions. Analysis results are shown in Figure 4, whose abscissa κ represents the normalized size of DI introduced by Sakurai & Kawahara (2002a). The ordinate represents the error norm denoted in the

Copyright © 2003 Swets & Zeitlinger B.V., Lisse, The Netherlands

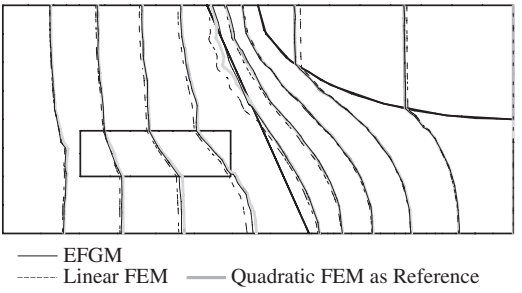


Figure 5. Comparison of solutions with Mesh 1-A.

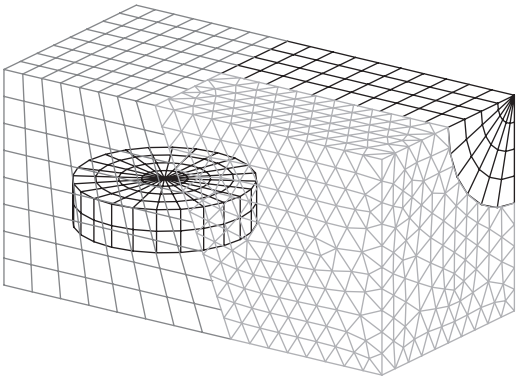


Figure 6. Mesh 1-B: a CMA for Model 1.

Figure 4. Reference solution was deduced by FEM analysis using quadratic tetrahedral elements obtained by adding intermediate nodes to the mesh of Figure 3. The results show that the solution accuracy is sensitive to the size of DI. However, precisions comparable to or better than that of linear FEM analysis were obtained within wide range of DI size. Figure 5 shows distributions of potential for the cross section illustrated in Figure 2. The solid lines are EFGM solution ($\kappa = 150\%$), the broken lines represent linear FEM solution, and the pale, thick lines are reference FEM solution. The EFGM solution is in good agreement with the reference.

To demonstrate the usefulness of the CMA in this problem, meshes were generated independently for each of the geological formations and the underground structure as shown in Figure 6, Mesh 1-B. Meshes were incompatible between formation boundaries, and the mesh of the underground structure completely overlapped the mesh of a geological formation. Figure 7 shows distributions of potential on the cutting plane denoted in Figure 2. The EFGM solution is in good agreement with the reference FEM solution computed by using a consistent mesh shown in Figure 3. The location and the shape of the mesh of the underground structure in this CMA can easily be changed because

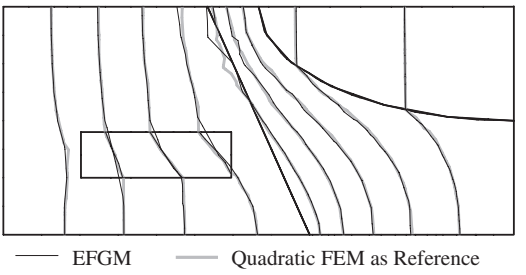


Figure 7. EFGM solution with Mesh 1-B.

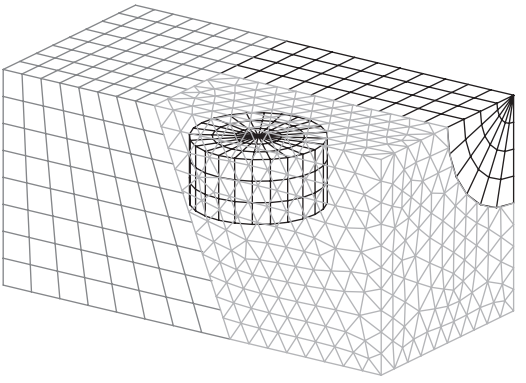


Figure 8. Mesh 1-C: a CMA with different repository.

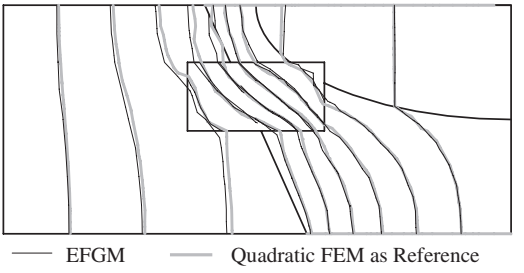


Figure 9. EFGM solution with Mesh 1-C.

the mesh is completely independent of other meshes. In another CMA, Mesh 1-C, presented in Figure 8, the underground structure with different dimensions has been moved to near the center of the model with no changes in the meshes of the geological formations. Figure 9 shows a potential distribution on the cutting plane obtained by an EFGM analysis. The EFGM solution is in good agreement with a reference FEM solution computed by using another consistent mesh. As shown, it is clear that CMAs can be easily changed to compare several underground facility plans having different forms and orientations.

Copyright © 2003 Swets & Zeitlinger B.V., Lisse, The Netherlands

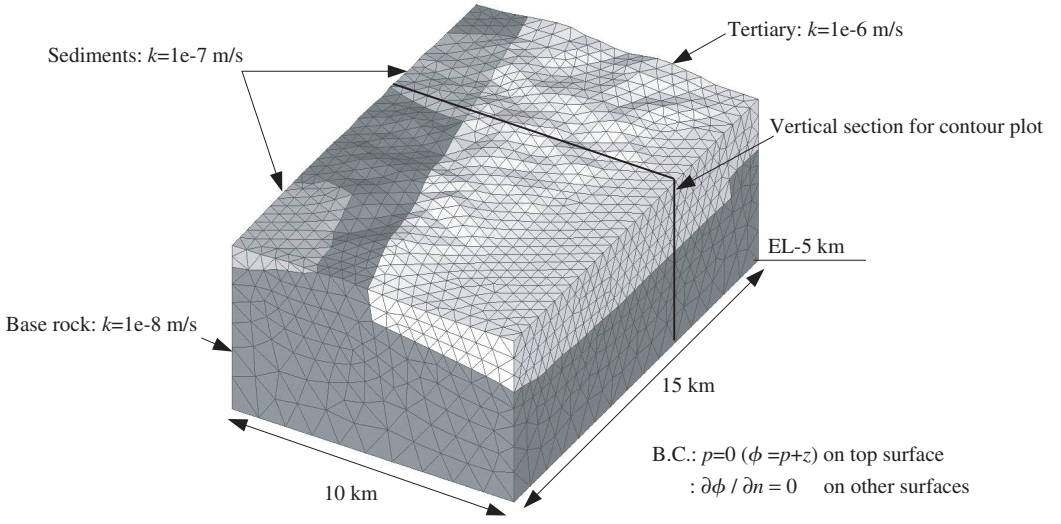


Figure 10. Model 2: an imaginary geological structure and a consistent finite element mesh, Mesh 2-A.

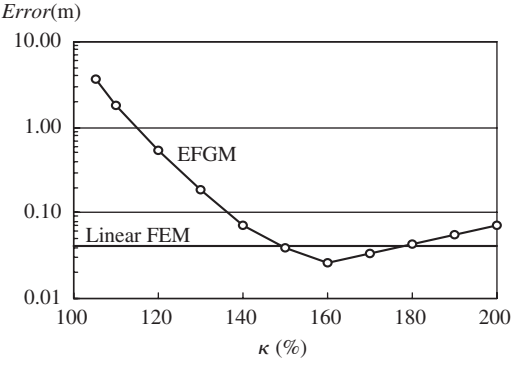


Figure 11. Solution accuracy and sensitivity to d_I.

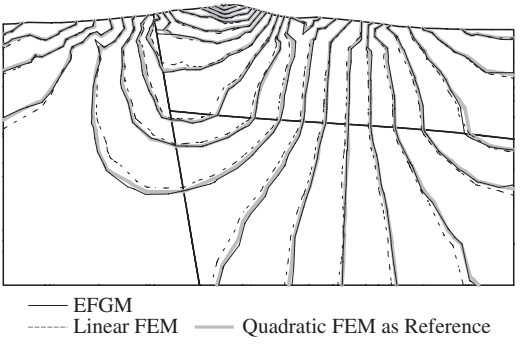


Figure 12. Comparison of solutions with Mesh 2-A.

4.2 *Fictitious geological structure*

An imaginary geological structure consisting of three types of formation was prepared as illustrated in Figure 10. The analyses were carried out by assuming that the groundwater level matches with the ground surface with boundary conditions of zero pressure on the ground surface ($\phi = z$) and zero flux on the other boundary surfaces. To investigate the solution accuracy, a consistent mesh named Mesh 2-A as shown in Figure 10 was first computed and its solution was compared with FEM solutions. Figure 11 shows the relationship between the size of DI and the error norm. In abscissas, the size of DI is represented by normalized value κ (Sakurai & Kawahara 2002a). Reference solution was computed by a FEM analysis using quadratic tetrahedral elements obtained by adding intermediate nodes to Mesh 2-A. A solution of FEM analysis using linear tetrahedral elements is also shown for comparison. As is the case with Model 1, although the solution accuracy is sensitive to the size of DI, it is acceptable within wide range, compared with linear FEM solution. Figure 12 shows the distributions of potential on a vertical section transecting the highest summit of the model, indicated in Figure 10. The solid lines represent EFGM solution ($\kappa = 160\%$), the broken lines represent FEM solution based on linear elements, and the pale, thick lines represent reference FEM solution. The EFGM solution is in good agreement with the reference solution. To demonstrate the usefulness of CMAs in this problem, meshes were generated independently for each of the geological formations as shown in Figure 13, Mesh 2-B. Meshes were incompatible between formation boundaries. Figure 14 shows distribution of potential on the same cross section as

Copyright © 2003 Swets & Zeitlinger B.V., Lisse, The Netherlands

Figure 12 obtained by EFGM analysis with $\kappa = 160\%$. The solid lines represent EFGM solution, and the pale, thick lines represent reference FEM solution as in Figure 12. The EFGM solution is in good agreement with the reference solution. In the CMAs, geological structures can be updated very easily because CMAs also permit overlaps of meshes. In another CMA, named Mesh 2-C, presented in Figure 15, a new layer with higher permeability has been added with no changes in the meshes of the original geological formations. Figure 16 illustrates the potential distribution on the same cross section as Figure 12 obtained by EFGM analysis with $\kappa = 160\%$. The figure shows that the new layer has a significant influence on the groundwater flow field. As shown, for example, a thin formation newly found by an additional borehole survey can easily be accommodated by adequately placing a mesh separately generated for the formation. The analyses can be carried out without changing the original CMA of the geological structures.

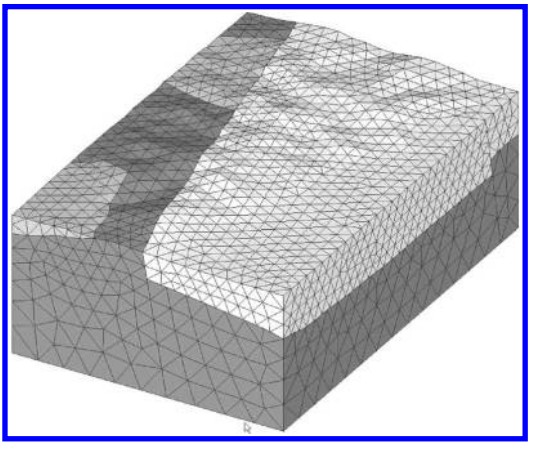


Figure 13. Mesh 2-B: a CMA for Model 2.

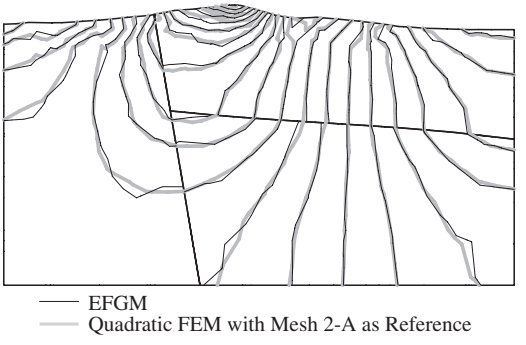


Figure 14. EFGM with Mesh 2-B and a reference result.

5 CONCLUSIONS

The most laborious task in 3D FEM analyses is solid modeling as geometry definition, which is carried out mainly through interactive operations. This means mitigating the restriction of geometry definition is a key to efficient 3D analyses. CMAs, which allow incompatibility between adjacent meshes and the overlap of meshes, circumvent the difficulty of the geometry definition of complex composite domains. The usefulness of CMAs has been demonstrated in this paper by 3D numerical examples. The two requirements mentioned at beginning of this paper can be achieved by introducing the CMA into the EFGM. Other than composite domains, CMAs may be applied to a complex shape consisting of a single material by modeling the shape as a combination of simple shapes.

The numerical examples showed that the solution accuracy of EFGM is sensitive to the size of the DI. However, it can be considered that the sensitivity is not significant for practical use. This is because the solutions are acceptable within wide range of the DI size.

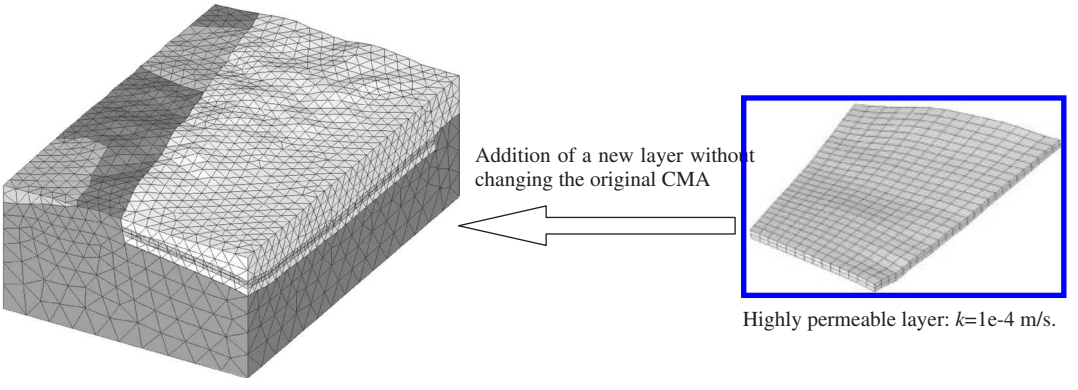


Figure 15. Mesh 2-C: CMA including newly found layer.

Copyright © 2003 Swets & Zeitlinger B.V., Lisse, The Netherlands

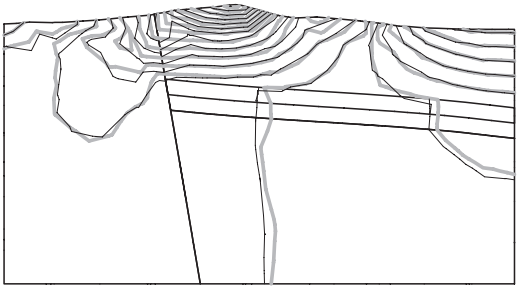


Figure 16. EFGM with Mesh 2-C and a reference solutions.

In our experience, we may always use 1.5 through 1.7 of the normalized DI size κ introduced by Sakurai & Kawahara (2002a).

There are discontinuous and duplicative contour lines in Figures 7, 9, 14 and 16 because they were drawn for each element by using a FEM post-processor. This problem can be overcome by using appropriate visualization software, if necessary.

REFERENCES

Beissel, S. and Belytschko, T. 1996. Nodal integration of the element-free Galerkin method. *Comput. Meth. Appl. Mech. Eng.*, 139: 49–74.

Belytschko, T., Lu, Y.Y. and Gu, L. 1994. Element-free Galerkin methods. *Intern. J. Num. Meth. Eng.*, 37: 229–256.

Belytschko, T., Krongauz, Y., Organ, D., Fleming, M. and Krysl, P. 1996. Meshless methods: An overview and recent developments. *Comput. Meth. Appl. Mech. Eng.*, 139: 3–47.

Requicha, A.A.G. and Voelcker, H.B. 1982. Solid Modeling: A historical summary and contemporary assessment. *IEEE Comput. Graphics Appl.*, 2: 9–24.

Sakurai, H. and Kawahara, M. 2002a. The element-free Galerkin method for three-dimensional groundwater flow analysis. *WCCM V, 5th World Congress Comp. Mech., Vienna, 8–12 July 2002* (publ. on congress website).

Sakurai, H. and Kawahara, M. 2002b. Three-dimensional groundwater flow analysis system using the element-free Galerkin method. *Proc. 6th. Japan-US Intern. Symp. Flow Sim. Modeling, Fukuoka, 29–31 May 2002*.

Sakurai, H. 2002. A new three-dimensional groundwater flow analysis system applying the element-free Galerkin method. *J. JSCE*, 720/7-25: 63–75, in Japanese.

Copyright © 2003 Swets & Zeitlinger B.V., Lisse, The Netherlands

A groundwater flow analysis at coastal area considering regression and transgression

M. Tanaka, J. Kawabata & M. Toida
Kajima Technical Research Institute, Tokyo, Japan

T. Hishiya & E. Sugimoto
DIA Consultants, Saitama, Japan

M. Nishigaki
kayama University, Okayama, Japan

T. Hasegawa
Central Research Institute of Electric Power Industry, Abiko, Japan

ABSTRACT: The authors performed numerical analysis of groundwater flow at coastal area considering ten thousand years of sea level changes. The analyzed area is a model site for high-level radioactive waste disposal. The original numerical code is used for the analysis, which can express dispersion of salt-water in groundwater and density driven flow by salt-water. The authors set up the boundary conditions (sea level changes) for the analysis by considering the geological map at the site and general idea of geological history. The analytical model is also made from the geological map without enough boring log etc., which is the same situation as the feasibility study stage for radioactive disposal site screening. The salt-water distribution that should occur in the past is evaluated and the distribution that may occur in the future is evaluated through sensitivity analysis. Some parameters are identified that may have strong influences on the groundwater situation, which should be essential of the feasibility stage of high-level radioactive waste.

1 INTRODUCTION

Coastal area as a high-level radioactive waste (H.L.W.) disposal site has some merits. One is that the hydraulic gradient of groundwater flow compared to inland area, the other is that no habitation area should generally exist in the down stream of groundwater flow. On the other hand, there should be a fresh and seawater interface in the ground, which location should change with sea level changes for a long period. The chemical environment of groundwater should affects H.L.W. sealing system. It is, therefore, very important to evaluate the brine distribution and its location changes for a long period.

The feasibility study of H.L.W. geological disposal proceeds gradually from literature survey stage followed by outline survey stage, detailed survey stage and facility construction. Through that process, the consideration above should start from outline survey stage, as it is necessary for screening proposed sites. It is likely that we need to depend on existing data (Figure 1) as analytical input, that is, without any boring data etc. In situ more detailed measuring data may become available at later stages. This paper discuss the analytical method and result evaluation method that should be adopted in this situation.

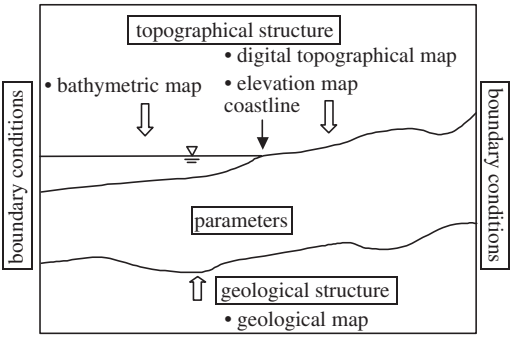


Figure 1. Schematic diagram showing existing information used for analysis.

Copyright © 2003 Swets & Zeitlinger B.V., Lisse, The Netherlands

The following analytical approach was taken: (1) the location of fresh and sea groundwater interface and groundwater flow situation is predicted for a targeted site in this paper under limited information. (2) The location of interface between fresh and sea groundwater is evaluated after 0.1 million years of sea level changes which is predicted from the geological map at the targeted site and from general idea of geological history. The feasibility as H.L.W. site can be discussed for the targeted site adopted in this paper.

2 PURPOSE OF ANALYSIS

The analysis in this study aims at investigating the influence of groundwater level in the land area and sea level changes for groundwater flow field and for brine concentration distribution. The following analyses are performed in this study, (1) steady flow analysis with fixed boundary conditions, those are, maximum and minimum groundwater level on both mountain and sea sides, and (2) unsteady flow analysis considering 0.1 million sea level changes of transgression and regression.

In this study, it is ideal to choose various ground parameters from the range as wide as possible and to consider sea level changes as long as possible. However, it is difficult to determine the geological structures and recharge conditions over period. It would therefore be impossible to cover all the possible parameter combinations especially when using three-dimensional analysis. To overcome this difficulty, steady flow analyses with constant boundary conditions are performed and the possible groundwater flow situation that may occur in that period is considered, and then unsteady analysis with variable sea levels is carried out only for the important cases.

3 ANALYTICAL STRATEGIES

Analytical conditions need to be set based, on existing data the reliability of which has been ensured. The types of data used here are (1) unbiased data, (2) data with homogeneous quality and quantity, and (3) data whose criteria and bases as analytical conditions are clear. The following points, which are required for analysis, are set from this point of view.

1) Analytical code: A two-dimensional analytical code was used for the sensitivity analysis. Dtransu 2D EL (Hishiya et al. 1996), Eularian-Lagrangerian method, was used as the analytical code.
2) Analyzed areas: Based on existing data, land areas (plain and mountain areas) can be defined by the span and topographic gradient of each area, and a sea area can be defined by sea bed gradient. The setting shown in Figure 1 was adopted without assuming a specific area.
3) Geological structures: Geological structures such as basement depth and distribution can be modeled based on existing geological maps. The analytical model with constant sea level case and variable sea level case shown in Figures 2 and 4 were used in the present study.
4) Topographic conditions: While topography can also be set based on existing multi-purpose data such as digital maps, no specific area was assumed in the present setting, as shown in Figure 1.
5) Hydraulic conductivity: 1×10^{-8} m/sec (for water) was adopted although different values can be set for different formations based on existing data.

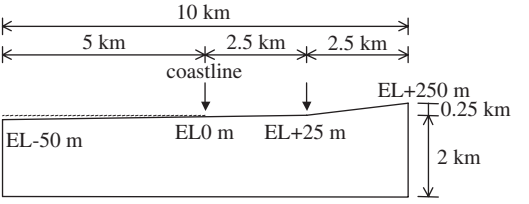


Figure 2. Analytical model (with constant sea level).

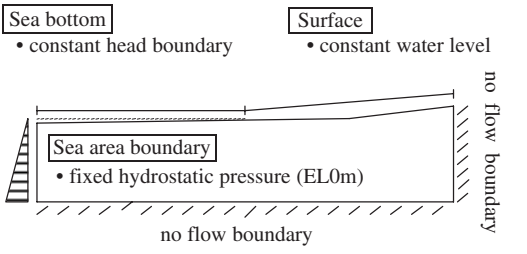


Figure 3. Boundary conditions: Hydraulic conductivity 1×10^{-8}(m/sec), Effective porosity 0.05, Specific storage 1×10^{-5}(l/m).

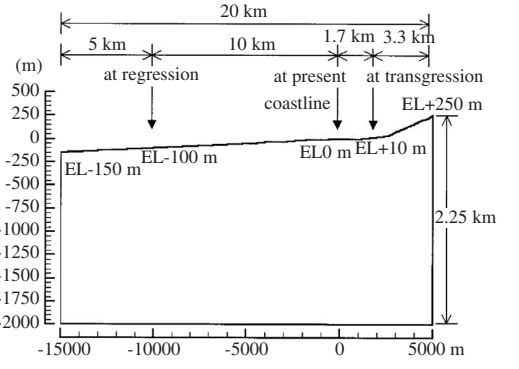


Figure 4. Analytical model (considering sea level changes).

Copyright © 2003 Swets & Zeitlinger B.V., Lisse, The Netherlands

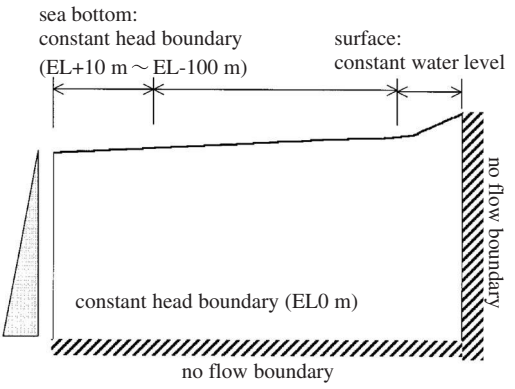


Figure 5. Boundary conditions for the analysis with variable sea level: Hydraulic conductivity 1×10^{-8} (m/sec), Effective porosity 0.05, Specific storage 1×10^{-5} (l/m).

6) Boundary conditions: The land area groundwater level was set to the ground surface level, and the lowest groundwater level was set to the elevation of river headwater at the time of base runoff. Generally it is assumed that the edge of a land area is a constant head boundary or no flow boundary, depending on the case, and the edge of a sea area is constant head boundary. Sea levels during transgression and regression can also be modeled based on the existing data. The model with constant sea level case and variable sea level case shown in Figures 3 and 5 were adopted in the present study.

4 ANALYTICAL CONDITIONS

4.1 *Analytical conditions*

While the behavior of groundwater under the sea bed of coastal areas has been studied by some researchers (Hathaway et al. 1979, Groen et al. 2000), a broad model was prepared in this study considering the purpose of this analysis.

4.1.1 *Analytical conditions of constant sea level case*

The model analyzed in this study has a sea area extending across 5 km and a land area extending across 5 km, the latter consisting of a 2.5 km plain area and a 2.5 km mountain area (Figure 2). The elevations of the deepest part of the sea bed, the highest part of the plain, and the highest part of the mountain area are −50 m, +25 m, and +250 m, respectively. While each area has a constant topographic gradient, it is possible to set a gradient for each 50 m square grid area by using commercially available digital map data in the case of a three-dimensional model. To make the computation simple, geological structures were simplified with an impermeable basement layer overlain by 1.95 to 2.25 km thick layer. Existing geological maps and gravity anomaly maps may be used to estimate the depth and distribution of the basement in more detail. As boundary conditions, a constant head is assumed for the sea area and the following two cases are assumed for the groundwater level in the land area.

4.1.2 *Analytical conditions of variable sea level case*

As shown in Figure 4, another analytical model has a sea area extending across 15 km and a land area extending across 5 km, the latter consisting of a plain area and a mountain area same as Figure 2. The elevations of the deepest part of the sea bed, and the highest part of the mountain area are −150 m, and +250 m, respectively. Each area has a constant topographic gradient. As for geological structures, an impermeable basement layer is overlain by a permeable layer having thicknesses of 1.85 to 2.25 km. The elevations of the coastline during transgression and regression were roughly set to −100 m and +10 m, respectively by taking past studies into account.

4.2 *Analytical cases*

Two groundwater level cases analyzed by using this model are described below.

Case 1: the highest groundwater level (ground surface level)
Case 2: the lowest groundwater level

As a procedure to determine the lowest groundwater level, river headwater elevations may be read from existing topographic maps, and this data may be used, together with digital topographic data, to draw groundwater contour lines three-dimensionally. The coefficient of permeability was assigned to only the upper layer. It may be worth using different values of different orders of magnitude for the calculation based on available data. These two groundwater cases are combined with constant sea level case and variable sea level case. The three combined cases analyzed by using this model are described below.

Analysis 1: Analysis with constant sea level for a transgression period

This is an analysis with constant sea level for a constant coastline elevation of +10 m. The boundary conditions are shown in Figure 5. Two cases of groundwater levels in the land area were analyzed: the highest level (ground surface level) and the lowest level (river headwater level). The initial elevation of coastline was +10 m, and pressure distribution was obtained from the results of seepage analysis. Freshwater was distributed on the land area above the elevation of the coastline at the time of transgression (+10 m),

Copyright © 2003 Swets & Zeitlinger B.V., Lisse, The Netherlands

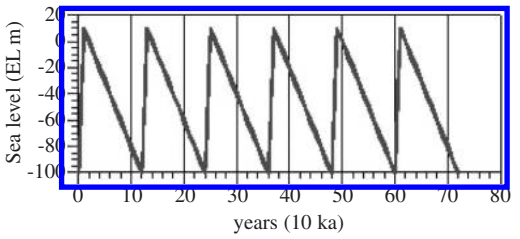


Figure 6. Modeling of sea level changes.

and brine was distributed on the sea area below this elevation.

Analysis 2: Analysis with constant sea level for a regression period

This is an analysis without sea level changes for a constant coastline elevation of −100 m. The boundary conditions are shown in Figure 4. As is the case with section 4.1, two cases of groundwater levels in the land area were analyzed. The initial elevation of the coastline was −100 m, and pressure distribution was given from the results of seepage analysis. Freshwater was distributed on the land area above the elevation of the coastline at the time of regression (−100 m), and brine was distributed on the sea area below this elevation.

Analysis 3: Analysis with variable sea level

Unlike the above two cases, this is an analysis with variable sea level in which the elevation of coastline changes cyclically. The elevation of the coastline in each cycle changed from −100 m to +10 m and vice versa and the whole computation was carried out over six cycles until the distributions of salt concentration and flow velocity were stabilized after each movement of the coastline. The cyclic movement and the speed of sea level changes are shown in Figure 6. During a regression period, the coastline elevation drops gradually from +10 m to −100 m over 110,000 years. During a transgression period, the coastline elevation rises relatively quickly from −100 m to +10 m over 10,000 years. The analytical results of the above analysis 2 were used for the initial conditions of analysis 3.

5 RESULTS

5.1 *Analyses with constant sea level*

The results (relative concentration) of the analyses with constant sea level for transgression and regression periods are summarized in Figure 7, with the results of the highest and lowest groundwater levels shown in the upper and lower parts of the figure, respectively.

The distributions of relative concentration obtained by advective diffusion analysis for cases 1 and 2, which

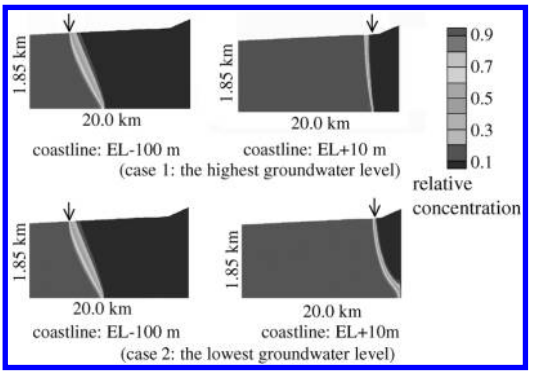


Figure 7. Results of the analyses with constant sea level for regression and transgression periods.

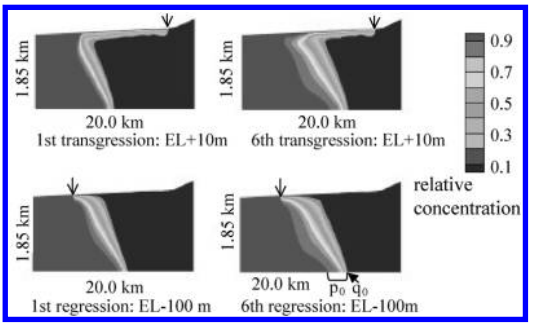


Figure 8. Results of the analysis with variable sea level (case 1: the highest groundwater level).

indicates that the fresh and sea groundwater interface is more moved toward the land area in case 2 (the lowest groundwater level) than in case 1 (the highest groundwater level). Because actual groundwater levels lie between the levels of both cases, the fresh and sea water interface is expected to lie between the interfaces of the two cases.

5.2 *Analyses with variable sea level*

Figures 8–9 show the analytical results of the 1st and 6th cycle (from elevation of +10 m to −100 m) for the highest and lowest groundwater levels. Also, the distribution of Darcian velocity at the initial and final stages are compared in Figures 10–11. Figure 13 shows the time variation of Darcian velocity associated with variable sea level at three evaluation points in the ground. Figure 14 summarizes the results of velocity obtained by the analyses with variable sea level and with constant sea level for the lowest groundwater level at three evaluation points in the ground. The evaluation points of Darcian velocity are as follows: (I) 2 km inland from the 0-m elevation point, (II) 0-m elevation point, (III) 2 km offshore from the 0-m elevation point. The elevation of each point is −500 m (Figure 12).

Copyright © 2003 Swets & Zeitlinger B.V., Lisse, The Netherlands

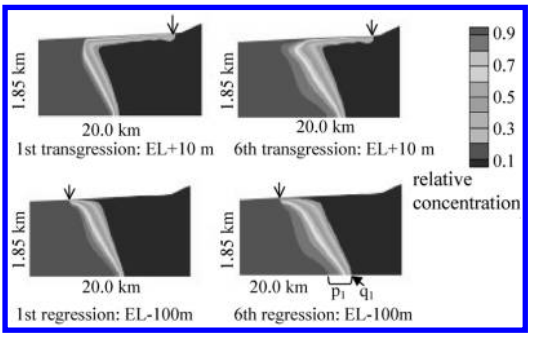


Figure 9. Results of the analysis with variable sea level (case 2: the lowest groundwater level).

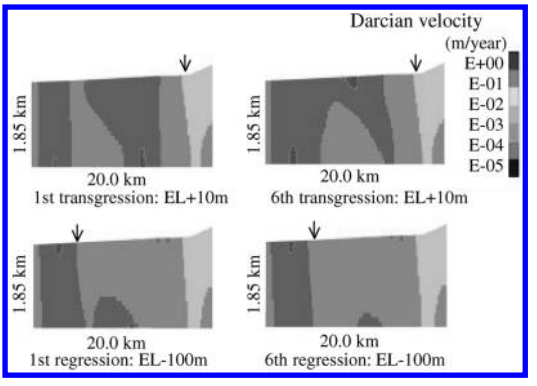


Figure 10. Darcian velocity of the analysis with variable sea level (case 1: the highest groundwater level).

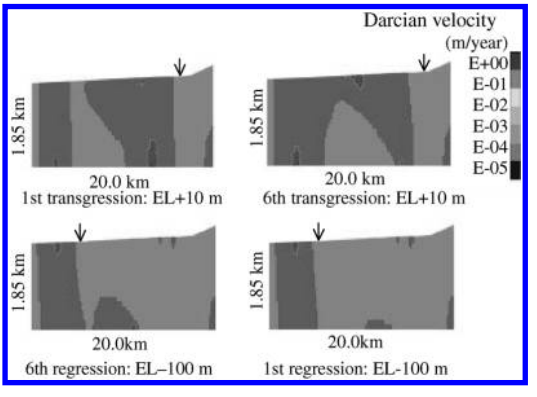


Figure 11. Darcian velocity of the analysis with variable sea level (case 2: the lowest groundwater level).

6 DISCUSSION

6.1 *Use of analyses with constant sea level*

As shown in Figure 14, the velocity obtained by the analysis with variable sea level is mostly bracketed

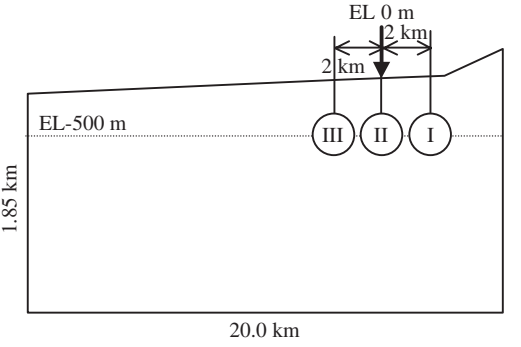


Figure 12. The evaluation points of Darcian velocity from analysis (Roman numerals).

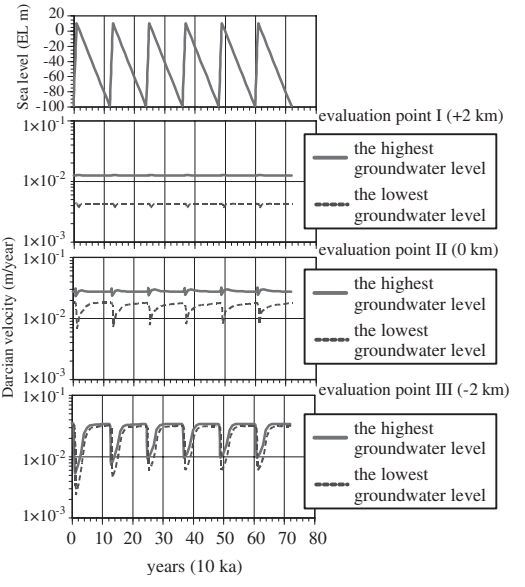


Figure 13. Darcian velocity obtained by the analysis with variable sea level.

by the flow velocities obtained by the analyses with constant sea level for transgression and regression. It is therefore possible to roughly estimate the extent of change in hydraulic fields considering sea level changes.

6.2 *Effect of the groundwater level in the land area*

– The results of analysis with constant sea level for transgression indicate that sea water penetrates farther toward land area as the groundwater level is low (Figure 7).

Copyright © 2003 Swets & Zeitlinger B.V., Lisse, The Netherlands

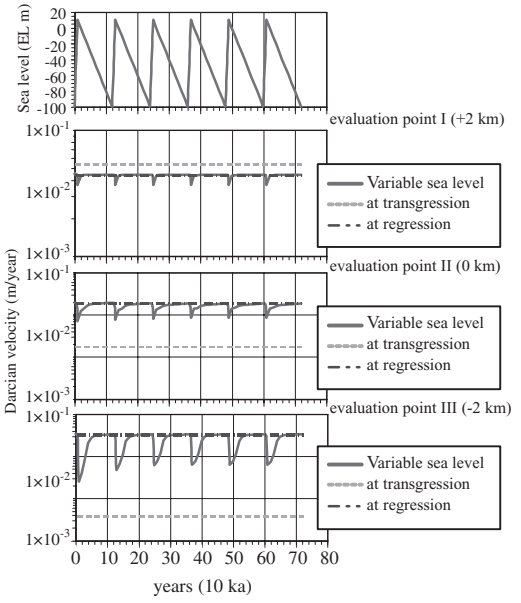


Figure 14. Darcian velocity obtained by the analyses (with variable sea level and constant sea level (at transgression, at regression), Case 2: the lowest groundwater level).

– The results of analysis with constant sea level for regression indicate that the location of the fresh and sea water interface is nearly independent of the groundwater level of the land area (Figure 7).
– In the analysis with variable sea level, the sea water front does not depend on the groundwater level but the width of the transition zone increases as the groundwater level drops for regression (width $p_0 = 2.5$ km, $p_1 = 2.8$ km in Figures 8–9).
– In the analysis with variable sea level, brine penetrates further toward the land area when the groundwater level is low (distance $q_0 - q_1 = 0.5$ km in Figures 8–9).
– The effect of land area groundwater level on salt concentration becomes negligible as the offshore distance from the coastline increases (Figures 8–9).
– Similarly, the effect of land area groundwater level on velocity becomes negligible in all the analyses as the offshore distance from the coastline increases (Figures 10–11).

The obtained reconnaissance can be summarized as follows.

(1) The results of the analyses with constant sea level (Figure 7) indicate that the hydraulic field near the present coastline is affected by the groundwater level in the land area. The analysis with constant sea level for transgression indicates that sea water penetrates farther toward inland as the groundwater level is low. On the other hand, the analysis with constant sea level for regression shows no effect of the groundwater level in the land area.
(2) The results of the analysis with variable sea level for the highest and the lowest groundwater levels (the 6th regression in Figures 8–9) indicate that the groundwater level in the land area does not affect the freshwater front on the sea area but affects the brine front on the land area.
(3) Figure 13 shows that the difference in velocity between the highest and lowest groundwater levels decreases as the offshore distance from the evaluation point I of +2 km increases. The difference nearly disappears at the evaluation point III of −2 km below the coastline.
(4) Hydraulic fields are strongly influenced by regression, whose duration is about ten times that of transgression. Because the fresh and sea groundwater interface during regression is mostly independent of the groundwater level in the land area, the fresh and sea groundwater interface is not much affected by the groundwater level even when sea level changes are taken into account.

The analytical results provide the following inputs to the discussion of H.L.W. disposal at the stage when available information is limited.

(1) The effect of the groundwater level in the land area is very small in the area between the present coastline and 2 km offshore in the case of the studied model.
(2) The difference in velocity between the highest and lowest groundwater levels in the land and coastal areas is less than an order of magnitude.

A similar numerical analysis study carried out (Kooi & Groen, 2000) associated local replacement of freshwater with brine in regard to the relationship between the impermeable layer near the sea bed and the velocity of coastline movement. These are among the subjects to be studied in the future.

7 SUMMARY

The useful results for the feasibility study on H.L.W. disposal site at coastal area are obtained. The change of the fresh and sea groundwater interface and velocity distributions for 0.1 million years was predicted with limited ground information. The effect of topographic and sedimentary changes in the time scale that requires consideration of sea level changes will further be investigated, together with the effect of geochemical factors. The scope and limit of evaluation when analyzing groundwater flow and advective diffusion from existing information will also be investigated.

Copyright © 2003 Swets & Zeitlinger B.V., Lisse, The Netherlands

ACKNOWLEDGEMENT

The authors are grateful to Dr. Soheil Razavi Darbar for useful discussion.

REFERENCES

Groen, G., Velstra, J. & Meesters, A.C.C.A. 2000. Salinization processes in paleowaters in coastal sediments of Suriname: Evidence from δ^{37}Cl analysis and diffusion modeling. *J.Hydorol.* 234: 1–20.

Hathaway, J.C., Poag, C.W., Miller, R.E., Schultz, D.M., Manheim, F.T., Kohout, F.A., Bothner, M.H. & Sangrey, D.M. 1979. U.S. Geological Survey core drilling on the Atlantic shelf. *Science* 206: 515–527.

Hishiya, T., Nishigaki, M., Hashimoto, N. & Yageta, M. 1996. The numerical method for saturated-unsaturated fluid density-dependent groundwater flow with mass. *Model-CARE96, Calibration and Reliability in Groundwater Modeling*: 90–98.

Japan Nuclear Cycle Development Institute 2000. *H12: Project to establish the scientific and technical basis for H.L.W disposal in Japan – Second progress report on research and development for the geological disposal of H.L.W in Japan*.

Kooi, H. & Groen, J. 2000. Modes of seawater intrusion during transgressions. *Water Resources Research* 36: 3581–3589.

Copyright © 2003 Swets & Zeitlinger B.V., Lisse, The Netherlands

Numerical analysis for seepage of rainwater and evaporation of pore water in unsaturated soil

K. Sako & R. Kitamura
Kagoshima University, Kagoshima, Japan

Y. Miyamoto
Kagoshima Prefecture, Kagoshima, Japan

ABSTRACT: A numerical model for seepage behavior of rainwater into unsaturated soil is proposed based on some mechanical and probabilistic consideration on the scale of soil particle size. The soil–water characteristic curve and unsaturated–saturated permeability coefficient are calculated by the proposed model, where the surface tension and viscous coefficient of pore water, grain size distribution, density of soil particle and void ratio are only needed as input parameters. The distribution of water content in unsaturated soil is calculated by using this model in the rainy days. Another numerical model for the phase change of pore water due to the change in temperature and pressure is also proposed in order to investigate the evaporation behavior of pore water in unsaturated ground. The distribution of water content in unsaturated ground is calculated by using this model on fine days. These two numerical models are combined to estimate the change in water content in unsaturated ground with the cycles of rainy and fine days. The numerical results are shown as the distribution of water content at a given time and the change in water content with time at a given point.

1 INTRODUCTION

The Kagoshima Prefecture is located in the southern part of the Kyushu Island and belongs to the Aso-Kirishima volcanic zone where there are some active volcanoes. The ground is consequently covered with volcanic products such as falling ash, pumice and pyroclastic flow deposits. Shirasu, which means white sand in Japanese, is geologically defined as the non-welding part of pyroclastic flow deposits. Shirasu is the most popular geomaterial which covers the soil surface in the Kagoshima Prefecture. Shirasu particle is porous and its density is smaller than common sandy soil. Also, Shirasu slopes are easy to fail due to heavy rainfalls in the rainy season. Sako et al. (2002) proposed a research strategy for predicting slope failure due to rainfall and introduced the updated numerical and experimental results obtained in Kitamura's laboratory.

In this paper a numerical model for seepage and evaporation in unsaturated soil is proposed. This extends the previous numerical model (Kitamura et al. 1998, Miyamoto et al., 1999) for seepage behavior in unsaturated soil, i.e., the evaporation behavior is modeled in the fine day and the previous model is modified to simulate the water content distribution in unsaturated soil.

2 MODELING OF SEEPAGE BEHAVIOR IN UNSATURATED SOIL

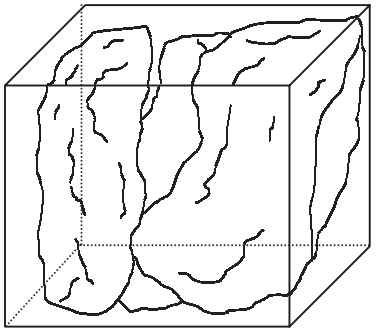
Kitamura et al. (1998) proposed the numerical model that simulates the seepage behavior in unsaturated soils. Figure 1 shows the modeling of voids and soil particles in soil mass. Based on Fig. 1(b) the void ratio, volumetric water content, suction and unsaturated–saturated permeability coefficient can be derived as follows.

$$e = \int_0^{\infty} \int_{-\frac{\pi}{2}}^{\frac{\pi}{2}} \frac{V_p}{V_e - V_p} \cdot P_d(D) \cdot P_c(\theta)\, d\theta\, dD \tag{1}$$

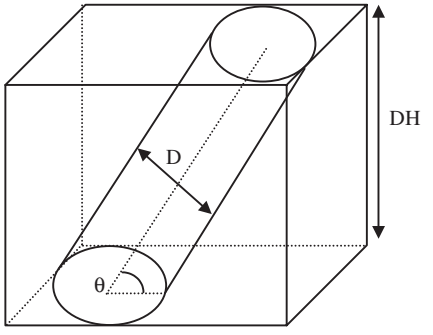
$$W_v = \frac{e(d)}{1+e} = \frac{1}{1+e} \int_0^{d} \int_{-\frac{\pi}{2}}^{\frac{\pi}{2}} \frac{V_p}{V_e - V_p} \times P_d(D) \cdot P_c(\theta)\, d\theta\, dD \tag{2}$$

$$s_u = \frac{4 \cdot T_s(T) \cdot \cos\alpha}{d} \tag{3}$$

Copyright © 2003 Swets & Zeitlinger B.V., Lisse, The Netherlands



(a) A few soil particles in element



(b) Modeling of soil particles and voids

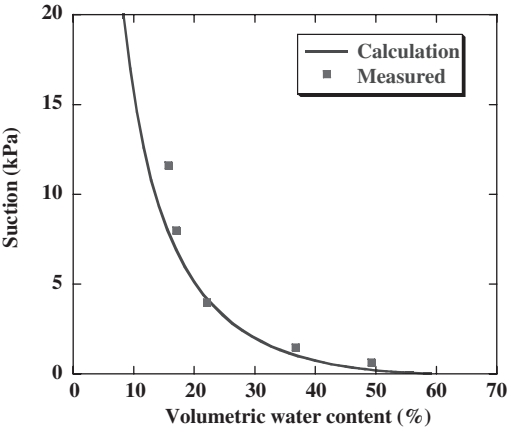
Figure 1. Modeling.

$$k = \int_0^d \int_{-\frac{\pi}{2}}^{\frac{\pi}{2}} \frac{\pi \cdot \rho_w(T) \cdot D^3 \cdot \sin\theta}{128 \cdot \mu_w(T) \cdot (D/\sin\theta + DH/\tan\theta)} \times P_d(D) \cdot P_c(\theta)\, d\theta\, dD \quad (4)$$

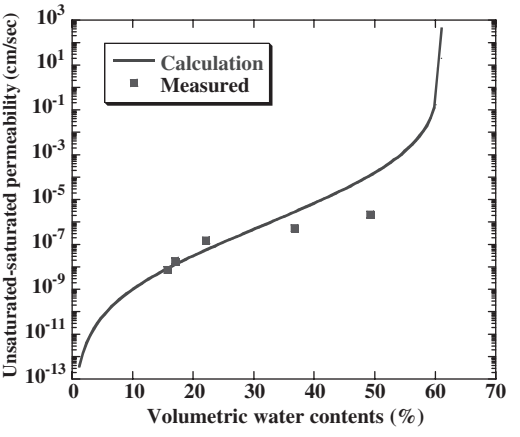
where,

V_p : Volume of pipe in Fig. 1(b),
V_e : Volume of container in Fig. 1(b),
$P_d(D)$: Probability density function of D,
$P_c(\theta)$: Probability density function of θ,
DH : Height of container in Fig. 1(b),
d : Maximum diameter of pipe which can retain water,
$T_s(T)$: Surface tension,
T : Temperature,
α : Contact angle between water and pipe,
$\rho_w(T)$: Density of water,
$\mu_w(T)$: Viscous coefficient of water,

By using these equations, the physical quantities mentioned above are obtained from the grain size distribution, density of soil particles and surface tension.



(a) Soil-water characteristic curve.



(b) Relation between permeability coefficient and volumetric water content.

Figure 2. Variations in moisture characteristics and permeability coefficient.

Table 1. Input parameter for the numerical model.

Sample	Shirasu
Density of soil particle (g/cm^3)	2.37
Surface tension (N/m)	73.48×10^{-3}
Coefficient of viscosity (Pa·S)	1.138×10^{-3}
Void ratio	1.567
Diameter finer than 10% D_{10}(cm)	7.45×10^{-4}
Coefficient of variance	−0.531

The numerical results for the soil–water characteristic curve and unsaturated–saturated permeability coefficient are shown in Fig. 2. The values of input parameters are listed in Table 1.

Copyright © 2003 Swets & Zeitlinger B.V., Lisse, The Netherlands

3 MODELING OF EVAPORATION IN UNSATURATED SOIL

Unsaturated soil is composed of soil particles and voids filled with air and water, i.e., the multi-phase material. The pore water in unsaturated soil is usually evaporated through the ground surface to the atmosphere as vapor (gas phase) on the fine day. The amount of vapor depends on the intensity of sunshine and wind, humidity of air and the water content in unsaturated soil. In the proposed model the amount of evaporation is simply assumed calculating the thermal flux by the temperature gradient in unsaturated soil. Figure 3 is a schematic condition that shows the heat transfer and evaporation near the surface ground. In Fig. 3 the energy conservation is expressed by the following equation.

$$q_x = q_{Tx} + q_{Px} \tag{5}$$

where,

q_x [J/sec]: Thermal flux flowing into the x-th layer,
q_{Tx} [J/sec]: Consumed thermal flux for change in temperature in the x-th layer,
q_{Px} [J/sec]: Consumed thermal flux for evaporation in the x-th layer.

The thermal flux between adjacent layers is calculated by the following equation.

$$q_i = \lambda_i \cdot \Delta T \cdot \frac{A_i}{h} \tag{6}$$

$$q_x = \sum q_i (= q_{soilparticle} + q_{water} + q_{air}) \tag{7}$$

where,

q_i [J/sec]: Thermal flux of phase i (i = soil particle, pore water and pore air),
λ_i [J/(k*cm*sec)]: Coefficient of heat conduction of phase i,
ΔT [K]: Temperature increment between adjacent layers,
A_i [cm^2]: Section area of phase i which can be obtained by void ratio and degree of saturation,
h [cm]: Distance between adjacent layers.

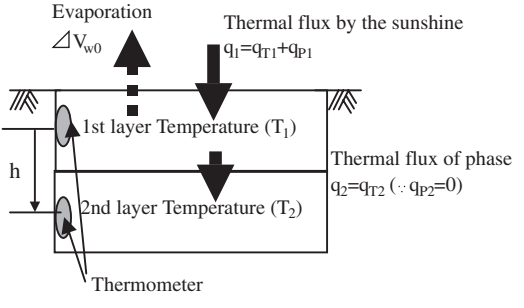


Figure 3. Schematic condition of one-dimensional thermal flux and evaporation.

The change in temperature in the x-th layer between time (t) and ($t+\alpha$) can be expressed as the following equation.

$$T_x(t+\alpha) = T_x(t) + \frac{\Delta q_{Tx}}{\sum c_i \cdot \rho_i \cdot V_i} \tag{8}$$

$$\Delta q_{Tx} = q_{Tx} - q_{Tx+1} \tag{9}$$

where,

Δq_{Tx} [J/(k*sec)]: Supplied thermal flux in the x-th layer,
c_i [J/(g*K)]: Specific heat of phase i (i = soil particle, pore water and pore air),
ρ_i [g/cm^3]: Density of phase i (i = soil particle, pore water and pore air),
V_i [cm^3]: Volume of phase i (i = soil particle, pore water and pore air).

The thermal flux of the first layer, q_1 is calculated by assuming to be 80% of the total amount of thermal flux as follows.

$$q_{p1} = \beta' \cdot q_1 \tag{10}$$

where,

β': Coefficient depending on the radial energy (=0.8).

Substituting Eq. (10) to Eq. (5), the following equation is derived.

$$q_{p1} = \beta \cdot q_{T1} \tag{11}$$

where,

$\beta = \beta'/(1-\beta')$ (=4.0 for $\beta' = 0.8$).

Figure 4 is the flow chart of the procedure for calculating the thermal flux of the first layer, q_1 supplied by the sunshine.

Figure 5 shows the relation between the latent heat of evaporation and temperature. Using the relation in Fig. 5 the amount of evaporation is calculated by the following equation.

$$\Delta V_w = \frac{q_{p1}}{\rho_w \cdot Q_w} \tag{12}$$

where,

ΔV_w [cm^3]: Volume of evaporation of water,
Q_w [sec*g/J]: Latent heat of evaporation.

Copyright © 2003 Swets & Zeitlinger B.V., Lisse, The Netherlands

4 FIELD MEASUREMENT AND NUMERICAL SIMULATION

4.1 *Field measurement of suction, temperature and precipitation*

Figure 6 schematically shows the field measuring system of suction, temperature and precipitation. The suction is measured with tensiometers which are installed 20, 40, 60, 80 cm in depth. The temperature is also measured with thermometer type devices installed 10, 20, 30, 40 cm in depth. The precipitation is measured with tipping type's rain gauge. Figure 7 shows an example of field measuring results. In Fig. 7 the temperature cyclically changes and the amount of change

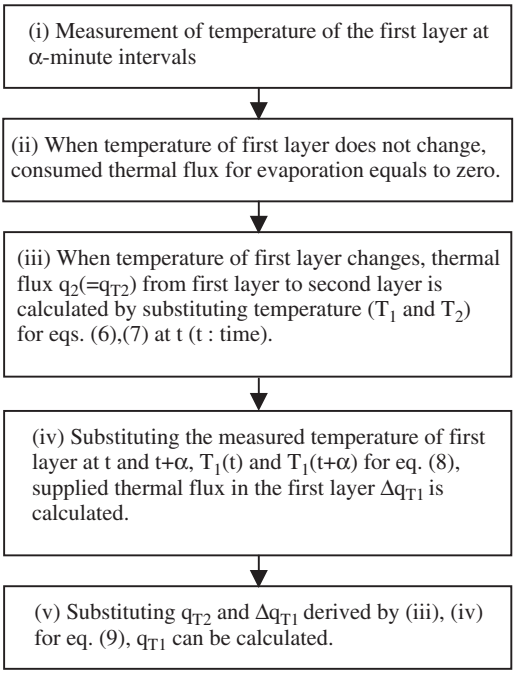


Figure 4. Calculation procedure of thermal flux flowing into unsaturated soil due to sunshine.

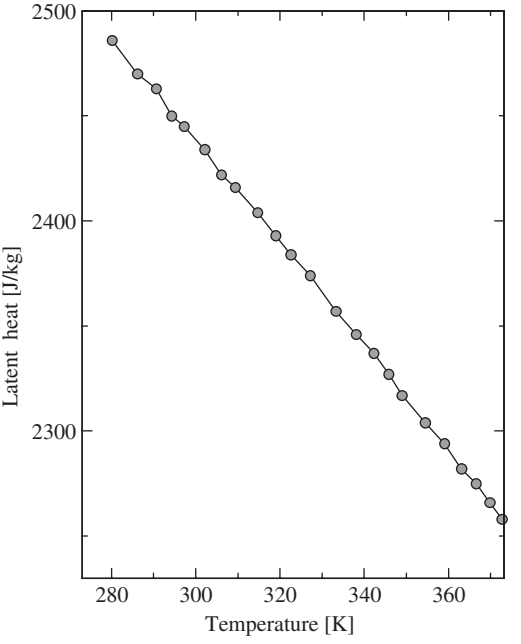


Figure 5. The relation between the latent heat of evaporation and temperature.

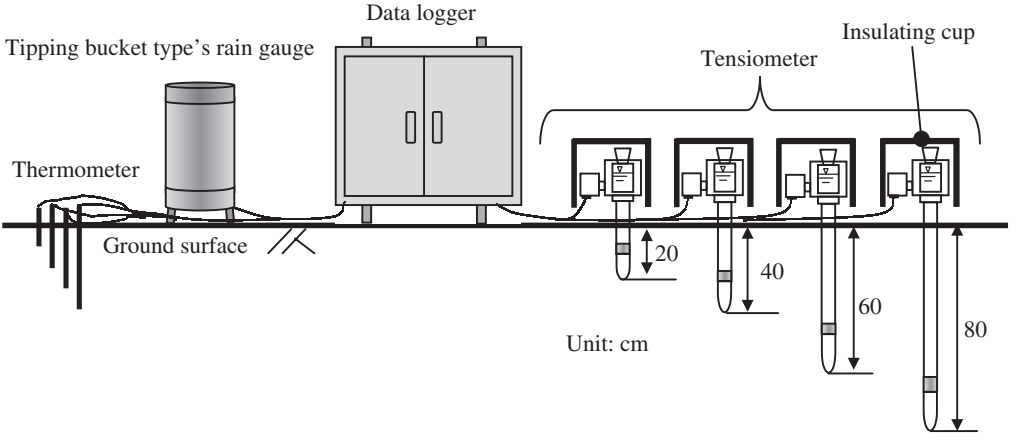


Figure 6. Field measuring system of suction, temperature and precipitation.

Copyright © 2003 Swets & Zeitlinger B.V., Lisse, The Netherlands

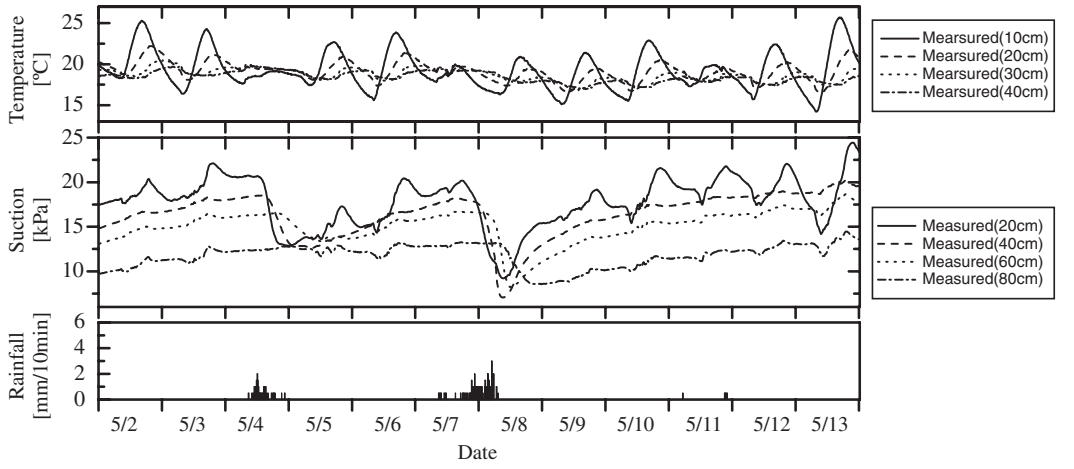


Figure 7. Example of field measuring results.

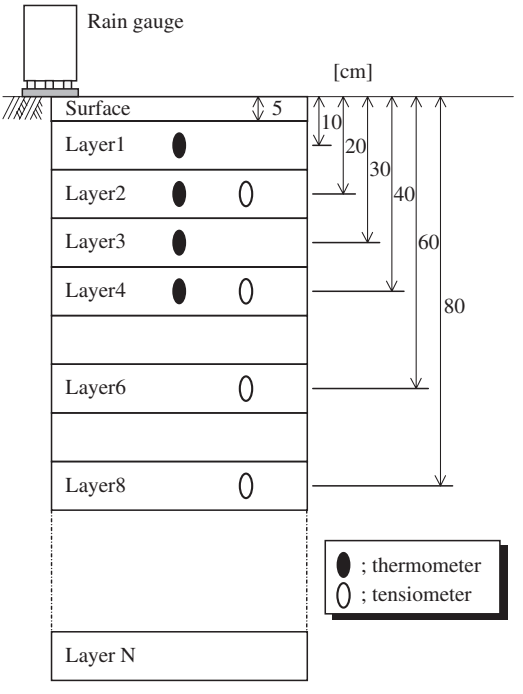


Figure 8. One-dimensional ground model.

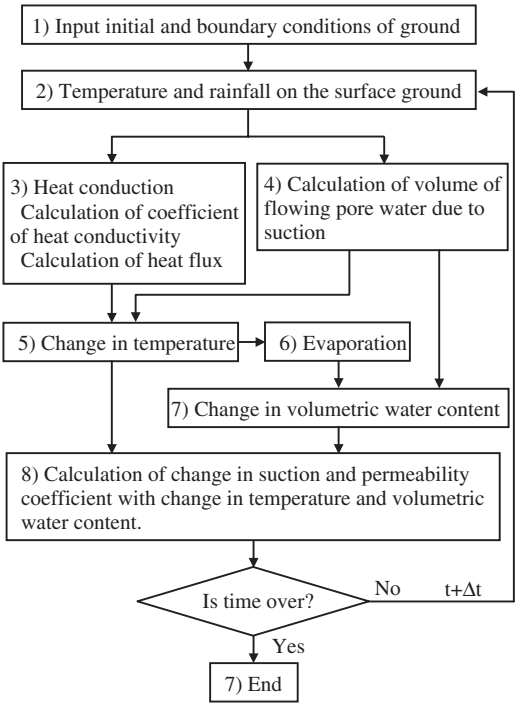


Figure 9. Calculation procedure.

is smaller with the depth in the fine days. In the rainy days the temperature changes smaller and the lowest at 10 cm in depth. The suction at 20 cm in depth is the highest and lower with the depth in the fine days. When the rainfall starts, the suction at 20 cm in depth is initially decreased and followed by 40, 60, 80 cm.

4.2 *Numerical simulation*

Figure 8 shows the one-dimensional model ground where the numerical simulation is carried out by using the input parameters in Table 2. The values of input parameters in Table 2 are selected to simulate the

Copyright © 2003 Swets & Zeitlinger B.V., Lisse, The Netherlands

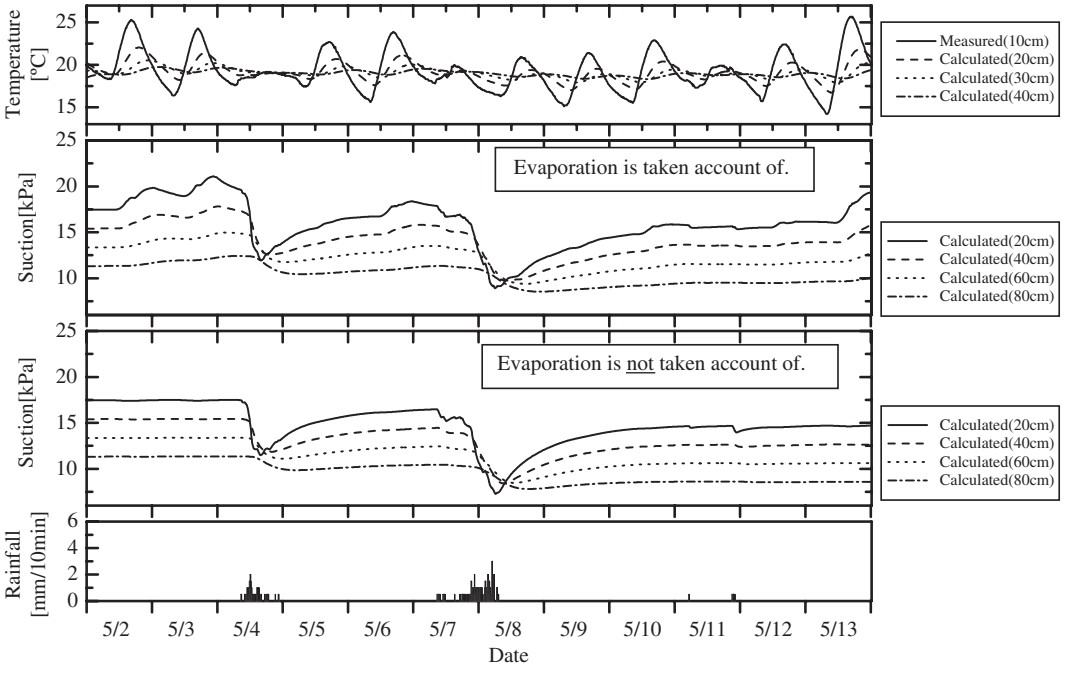


Figure 10. Results of numerical experiment.

Table 2. Values of physical quantities used ground model.

Number of layer	30
Cross sectional area	100 [cm^2]
Thickness of layer	10 [cm]
Density of soil particle	2.401 [g/cm^3]
Specific heat (solid)	0.8 [J/(g·K)]
Coefficient of heat conductivity	3.0 [J/(m·K)]

* IJ ≒ $2.8*10^{-7}$ kW*h

data shown in Fig. 7. The calculation procedure is shown in Fig. 9. Two calculation flows in Fig. 9 are adopted to examine the effect of evaporation, i.e., the evaporation is taken account of (flows of items 2)→(3) 4))→5)→6)→ 7)→8)) and not taken account of (flows of items 2)→4)→7)→8)). The temperatures at 20, 30 and 40 cm in depth are calculated by using the measured one at 10 cm as shown in Fig. 10. It is found that the simulation can follow the field condition by comparing the calculated temperatures at 20, 30 and 40 cm in depth with measured ones in Fig. 7. The calculation of suction is started by inputting the measured suction as the initial condition. In Fig. 10 the results of two cases are shown, i.e., the evaporation is taken account of (case 1) and not (case 2). It is found that the change in suction in the fine days are simulated better in case 1 than case 2 by comparing the results shown in Figs. 7 and 10.

5 CONCLUSIONS

The numerical model that can simulate the change in suction in unsaturated soil is proposed, taking account of the heat transfer through soil and the evaporation of pore water. The precipitation and the temperature are used as input data for the cases of rainfall and no rainfall, respectively. It is found from the comparison of numerical results with the field measurement that the proposed model is promising in simulating the change in water content in unsaturated ground with rainfall and evaporation of pore water.

ACKNOWLEDGEMENT

This research was supported by the grant-in aid of regional connected researches (Project No. 12792009) of the Ministry of Education, Culture, Sports, Science and Technology.

REFERENCES

Sako, K., Matsuo, K. & Kitamura, R. (2002): A research strategy for prediction of slope failure due to rainfall, Proc. Int. Conf. on Physical Modeling in Geotechnics, pp. 771–776.

Kitamura, R., Fukuhara, S., Uemura, K., Kisanuki, J. & Seyama, M. (1998): A numerical model for seepage

Copyright © 2003 Swets & Zeitlinger B.V., Lisse, The Netherlands

through unsaturated soil, *Soils and Foundations*, Vol. 38(4), pp. 261–265.

Kitamura, R., Miyamoto, Y. & Shimizu, Y. (2000): Numerical simulation for pore fluid flow through unsaturated soil, Asian Conference on Unsaturated Soils (Unsat-Asia 2000), pp. 409–413.

Miyamoto, Y., Jomoto, K. & Kitamura, R. (1999): Application of mechanical model for voids to unsaturated Shirasu ground, J. of Applied Mechanics JSCE, Vol. 2, pp. 593–598. (in Japanese)

Copyright © 2003 Swets & Zeitlinger B.V., Lisse, The Netherlands

Groundwater modelling of the Triassic Sandstone aquifer in the Selby area, North Yorkshire, UK

K. Yoshida
Water Resources Research Center, University of Hawaii at Manoa, USA

L.J. West & S.H. Bottrell
School of Earth Sciences, University of Leeds, UK

ABSTRACT: Groundwater from the Triassic Sherwood Sandstone aquifer has been used for industrial purposes and public water supply. The abstraction from Selby wellfield in Yorkshire, UK has caused decline of the water level in the Triassic Sandstone aquifer and groundwater quality problems such as high chloride and sulphate concentrations. Groundwater modelling of a 30 by 30 km area around Selby was carried out to understand the present groundwater flow conditions. Steady state modelling demonstrates that increased groundwater head difference between the overlying glacial sequence (drift) and the Triassic Sandstone due to the abstraction of the Selby wellfield causes higher leakage rates in the Selby wellfield than that in the rest of drift covered area. The groundwater flow model also shows that majority of groundwater inflow to the sandstone in the modelled area derives from is rainfall recharge and inflow from northern boundary. Capture zone analysis of the Selby wellfield abstraction boreholes indicates that the individual well capture zones had different shapes and the wells collect water from various directions. It also shows that the four abstraction boreholes contaminated by saline water collect the groundwaters from the north to north-east (i.e. from the direction of the boundary between the Sherwood Sandstone and the Mercia Mudstone), which suggests that the source of salinity is the dissolution of Mercia Mudstone evaporates.

1 INTRODUCTION

Groundwater is an important water resource. In the UK 80% of the total groundwater abstraction is from only two aquifers, the Cretaceous Chalk (54%) and the Triassic Sandstone (26%) (Owen et al. 1991). Groundwater from the Triassic Sherwood Sandstone aquifer of the Selby area has been used for industrial purposes and public water supply. There are 16 abstraction boreholes in the Selby wellfield and the total abstraction reached approximately 6700 Trillion Cubic Metres Per Annum (TCMA) (1997). Groundwater gradients in the sandstone aquifer indicate a general groundwater movement from the topographically high area near the north west boundary towards the south-east.

Chloride contamination has occurred at several abstraction boreholes. High concentrations of sulphate also occur in certain abstraction boreholes in the wellfield. In an area of sandstone that is not covered by glacial deposits at Brayton Barff, approximately 4 km south east of Selby, see Figure 1, groundwater quality has been reduced by high nitrate (Yoshida 2000). In order to understand the present groundwater flow condition and identify a saline water source the groundwater modelling was carried out using MODFLOW code (McDonald & Harbaugh 1988).

2 GEOLOGY AND HYDROGEOLOGY OF STUDY AREA

The geology of the study area is shown in Figure 1. The Triassic Sherwood Sandstone is covered by Quaternary drift deposits except for a small sandstone outcrop area at Brayton Barff. The area where drift is absent is relatively high ground. The ground elevation of the study area rises from 10 m AOD to over 30 m AOD in the NW and at Brayton Barff. To the east of study area the Sherwood sandstone is overlain by the Mercia Mudstone (approximately 14 km from the Selby town). The Sherwood sandstone is underlain by the Permian Marls and the Permian Magnesian Limestones which crop out to the west of study area. The sandstone dips towards east at a regional angle of about 2–4 degrees and increases in thickness from its feather-edge in the west to 400 m in the east. The thickness at Selby is

Copyright © 2003 Swets & Zeitlinger B.V., Lisse, The Netherlands

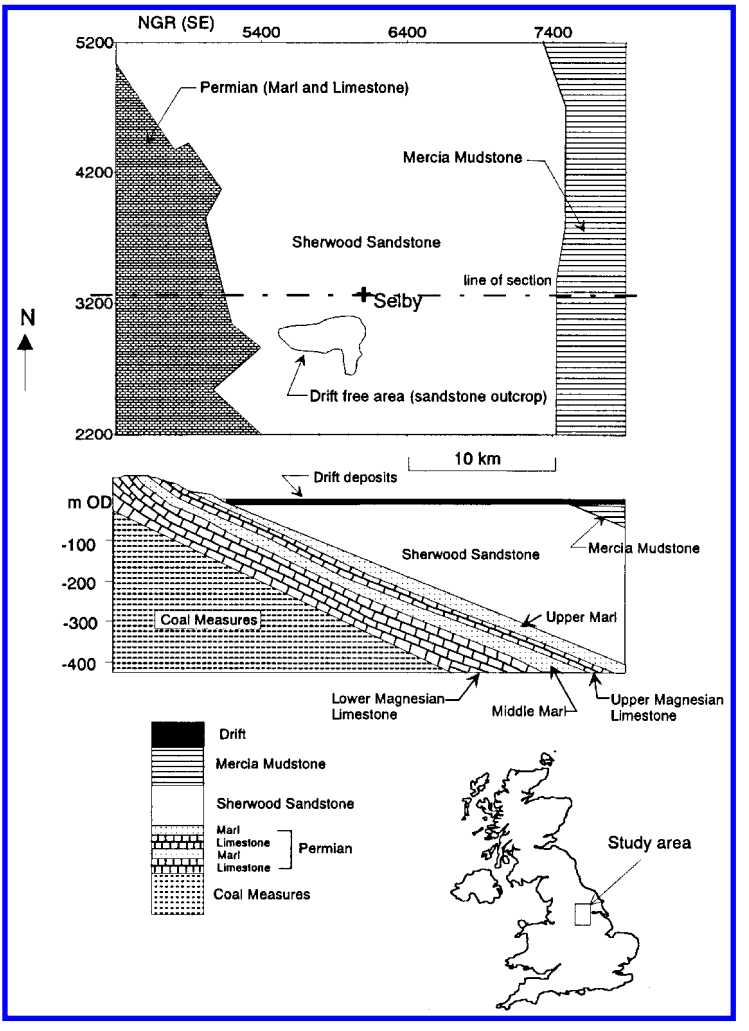


Figure 1. Geology of study area.

around 180 m. The sandstone aquifer is confined below by the Upper Permian Marl. The pumping test transmissivity values of the sandstone aquifer of the York, Selby and Goole area were 50–400 m^2/day (Allen et al. 1997). The hydraulic conductivity value estimated from core samples of the sandstone of the Yorkshire area ranges from 0.18 to 2.2 m/day (Lovelock 1977, Reeves et al. 1975).

Due to heavy abstraction in the Selby wellfield, water levels have fallen significantly in recent decades (Figure 2). The groundwater head dropped more than 8.0 m between 1984 and 1992. As a result, a huge cone of depression has been created by the abstraction at Selby, which appears to influence the groundwater flow direction within the whole study area.

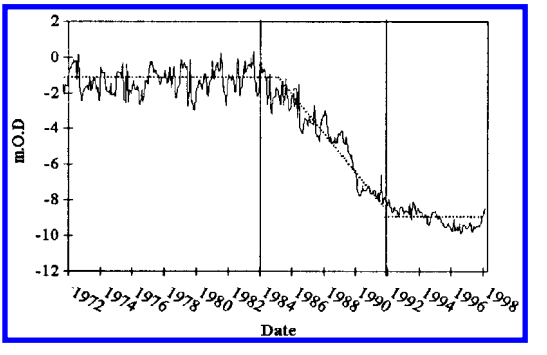


Figure 2. Hydrograph of an observation borehole in Selby.

Copyright © 2003 Swets & Zeitlinger B.V., Lisse, The Netherlands

3 GROUNDWATER MODELLING

3.1 *Conceptual model*

For mathematical modelling, the area was divided into two model layers. Model layer 1 represents glacial drift which covers the Sherwood Sandstone, and the sandstone itself where it crops out in the Brayton Barff area. The drift is composed of clay with sand and gravel, although in the model area the drift has a high proportion of clay. Layer 1 is assumed to be unconfined. Layer 2 everywhere represents the sandstone and is considered as confined.

Direct recharge is assumed to occur at the upper boundary of layer 1. However the locations and amounts of rainfall recharge water lost to the field drainage system, and thus not entering the aquifer, are difficult to estimate. Therefore initially it was assumed that direct recharge to the upper boundary of the drift is small because most water enters the drains rather than the aquifer. Later this was varied to calibrate the model, with different recharge rates specified according to the thickness of clay in the drift sequence. Hence waters which discharge into field drains did not need to be explicitly modelled. In contrast direct recharge to the sandstone of layer 1 in the outcrop area was assumed to be rainfall minus evaporation, i.e. available water flows into the sandstone. As the drift sequence usually contains at least several metres thickness of clay it is considered that rivers crossing the area are not hydraulically connected to the aquifer. The hydraulic conductivity of the sandstone aquifer is assumed to be uniform. Its transmissivity is calculated from the thickness of sandstone and the hydraulic conductivity. Calculated transmissivity values were then assigned to each cell of the model grid.

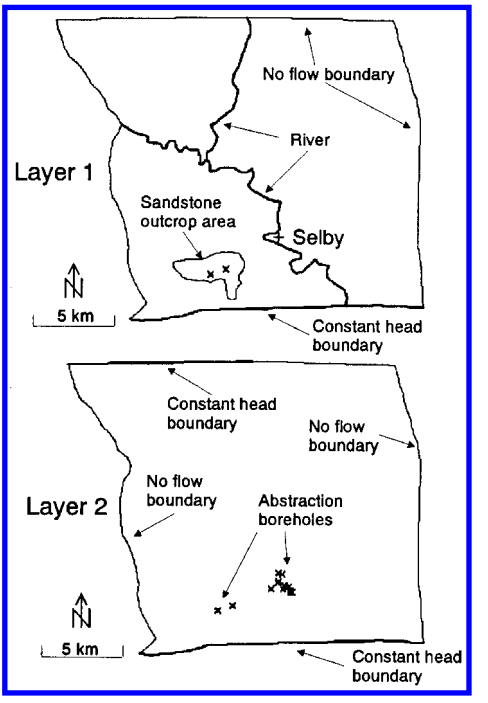


Figure 3. Model boundary conditions.

3.2 *Boundary conditions*

Figure 3 shows the model boundaries. The northern boundary is in the area where the highest groundwater level is observed and the boundary is thought to be a groundwater divide. In layer 1, the boundary is assumed to be a no flow boundary. This means that there is no drift water inflow across the northern boundary. The boundary is assumed to be a constant head boundary in layer 2. The eastern boundary is the area where the aquifer becomes confined by the overlying Mercia Mudstone. Although the sandstone extends beneath the Mercia Mudstone to the east, it is considered that groundwater flow across this boundary is minor (i.e. it is assumed to be a no flow boundary) because of the deep confined nature of the aquifer to the east.

The western boundary is the "feather edge" contact between the Sherwood Sandstone and the underlying Upper Permian Marl. Therefore, the western boundary is assumed to be a no flow boundary. The southern boundary is where the lowest groundwater head occurs. The actual flow rate through the southern boundary is difficult to determine. Hence, constant heads are applied for this boundary in both layer 1 and 2.

3.3 *Model description*

The groundwater level of the sandstone aquifer dropped more than 8 m between 1984 and 1992. Then it seems to have reached a steady state condition. There was not enough data available to construct the model to simulate the pre-1984 water level condition. Hence a steady state model was developed to simulate the post-1992 condition.

Abstraction data for 1992 was supplied by the UK Environment Agency, and rainfall and evaporation data was supplied by the UK Meteorological Office. Hydraulic conductivity value was estimated from the pumping test data.

An interaction between river and drift sequence was simulated using the river package of MODFLOW. The river package of MODFLOW requires the river bed conductance to be specified to simulate river–aquifer interactions. The conductance determines the amount of water that flows in or out of the model due to a river

Copyright © 2003 Swets & Zeitlinger B.V., Lisse, The Netherlands

and is described as

$$C = \frac{k}{m} wL \quad (1)$$

where C is the conductance of river bed, k is the hydraulic conductivity of the river bed sediments, m is the thickness of the riverbed sediments, w is the width of the river and L is the length of the river over the aquifer.

In this model, it was assumed that k is 0.001 m/day and m is 1.0 m. The rate of leakage between the river and the aquifer depends on the head difference between them and is described as:

$$QRIV = C(HRIV - h) \quad (2)$$

where QRIV is the rate of the leakage, C is the river conductance, HRIV is the head of the river and h is the head of aquifer. Positive QRIV means flow into the aquifer system and negative indicates flow out of the aquifer system. The shift from recharge of the aquifer to discharge to the river occurs at the point where the head in the aquifer equals the head in the river.

HRIV value was estimated from river gauge station data supplied by the UK Environment Agency.

In layer 1, three zones (A, B and C) were specified based on the proportion of clay in the drift and zone D represents the sandstone outcrop area (Figure 4). The proportion of the thickness of the drift sequences that were clay in zones A, B and C were 25–50%, 70–100% and 25–50%, respectively.

Initial values of hydraulic conductivity for the drift sequence and areal recharge were assumed to vary according to the proportion of clay in each zone. Zone B has a higher proportion of clay than the zone A and C. Hence the lowest recharge and hydraulic conductivity values were used for zone B.

MODFLOW's performance is primarily dependent on the application of a sufficiently fine grid (Haitjema et al. 2001). In this model fine grid spacing was used around wells so that the groundwater head near wells was simulated accurately. The grid spacing ranges from 50 m in the near wells to 500 m in the edge of the model. The total number of cells was 79,279 and the total model area was approximately 574,000,000 m^2.

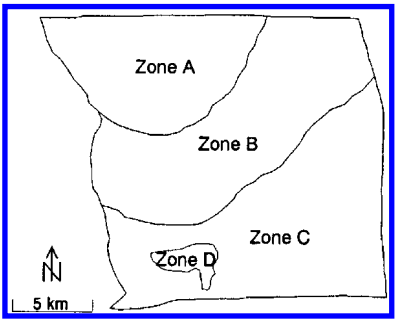


Figure 4. Model parameter zones for layer 1.

3.4 *Model calibration*

Calibration was done using measured water level in the observation boreholes, which are 9 boreholes in layer 1 and 15 boreholes in layer 2. In this study, a trial and error calibration was carried out to match the observed water level values. The result of the calibration is shown in Figure 5.

There is a discrepancy between the observed and computed head values in some boreholes. This could be due to water level measurement error or to problems of those boreholes construction. In general, most of the data fall near the 45 degree line of perfect calibration. Thus it is considered that the model can represent the aquifer system.

4 RESULTS AND DISCUSSION

4.1 *Water budget*

The total water budget for the final steady state model are summarised in Table 1. In layer 1, the source of most inflow was direct rainfall recharge and the amount was 9636 m^3/day. The main discharge source was leakage to layer 2 and the amount was 9445 m^3/day. In layer 2, water sources were the leakage from layer 1 and the inflow from north boundary and the proportion of total inflow into the aquifer system were 57% and 43%, respectively. The main discharge from layer 2 was abstraction by wells and the well abstraction accounted for 82% of total discharge.

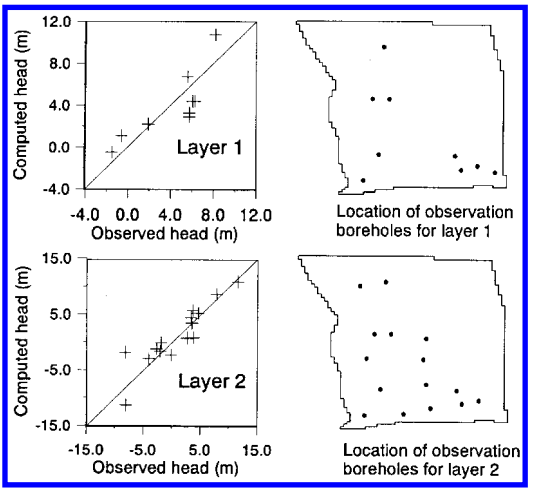


Figure 5. Relation between observed and computed head.

Copyright © 2003 Swets & Zeitlinger B.V., Lisse, The Netherlands

The recharge entering layer 2 (sandstone aquifer) from layer 1 in both the drift covered area and the sandstone outcrop area was estimated by ZONEBUDGET (Harbaugh 1990). ZONEBUDGET uses the cell-by-cell flow results created by MODFLOW to construct the water budgets of individual zones. The result showed that 78% of total recharge occurred in the sandstone outcrop area and 22% of total recharge occurred in the drift covered area. This indicates that a significant proportion of recharge into the sandstone aquifer occurs in the drift covered area although most recharge into the sandstone aquifer comes from the sandstone outcrop area.

In order to investigate the induced leakage from drift in the Selby wellfield the leakage rate at around the Selby wellfield area and the rest of the drift area were calculated. The calculated rate in the wellfield area and the rest of the area were 2.7 and 1.3 mm/year, respectively. The result clearly shows the induced leakage effect in the Selby wellfield area due to increased head difference between the drift and the sandstone aquifer.

4.2 *Well capture zone*

To identify the zone of contribution of abstraction boreholes, capture zone analysis was carried out using MODPATH (Pollock 1989) particle tracking code. The MODPATH code uses the cell-by-cell flow terms which are created by the MODFLOW simulation. (The cell-by-cell flow means the flow between each pair of adjacent cells.)

Table 1. Water balance for steady state model.

	Volume (m^3/day)	%
Layer-1 IN		
Direct recharge	9636	99.7
Inflow from river	26	0.3
Total	**9662**	**100.0**
Layer-1 OUT		
Discharge to river	−166	1.5
Boundary	−51	0.5
Leakage	−9445	98.0
Total	**−9662**	**100.0**
Layer-2 IN		
Leakage from upper layer	9445	57.0
North boundary	7099	43.0
Total	**16544**	**100.0**
Layer-2 OUT		
South boundary	−2957	18.0
Abstraction	−13587	82.0
Total	**−16544**	**100.0**

The result shows that the shape of capture zones of individual borehole varies. In general the shape of a capture zone is a function of the average linear groundwater velocity, the quantity of water being pumped from the aquifer and the distribution of hydraulic conductivity (Fetter 1999). The hydraulic conductivity of the sandstone layer is uniform in the model. Therefore, the boreholes which have high pumping rate tend to have wide capture zones.

In contrast the result indicates that the length of the capture zones varies little. The length (upgradient extent) of a capture zone is a function of groundwater velocity and time interval specified. The time interval is the same for all boreholes. Hence the observed pattern indicates that flow velocity is very similar within the area. In addition, the analysis shows that the direction of each of the capture zone is different. This suggests that the Selby wellfield boreholes collect the groundwaters from various directions.

4.3 *Source of saline water*

Several abstraction boreholes have been contaminated by saline groundwater in the Selby wellfield. The chloride concentration has reached about 900 mg/L.

The capture zones of the abstraction boreholes contaminated by saline groundwater clearly show that the groundwaters pumped in these boreholes are derived from the east or north-east, where the boundary between the Sherwood Sandstone and the Mercia Mudstone is located (Figure 6). The isotopic evidence, especially, the ^{34}S and ^{18}O of the saline groundwaters suggests that the source of saline water is the dissolution of evaporite derived from the Mercia Mudstone (Yoshida 2000).

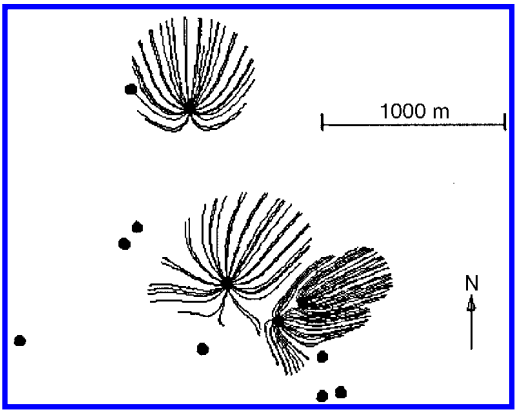


Figure 6. 20 year flowpath capture zones for boreholes contaminated by saline water.

Copyright © 2003 Swets & Zeitlinger B.V., Lisse, The Netherlands

5 CONCLUSIONS

Groundwater modelling of the Selby area demonstrated that water sources of the sandstone aquifer were the leakage from drift layer and the inflow from north boundary and the proportion of total inflow into the aquifer system were 57% and 43%, respectively. The model also showed that leakage from upper drift increased near the wellfield than the rest of the model area. The leakage rate in the wellfield area was 2.7 mm/year and that in the rest of the area was 1.3 mm/year. Well capture zone analysis using MODPATH suggested that the Selby wellfield boreholes collect the groundwaters from various directions and the source of saline water is from the Mercia Mudstone.

REFERENCES

Allen, D.J., Brewerton, L.J., Coleby, L.M., Gibbs, B.R., Lewis, M.A., MacDonald, A.M., Wagstaff, S.J. & Williams, A.T. 1997. *The physical properties of major aquifers in England and Wales*. BGS Technical Report WD/97/34.

Fetter, C.W. 1999. *Contaminant hydrogeology*. Prentice Hall.

Haitjema, H., Kelson, V. & Lange, W. 2001. Selecting MODFLOW cell sizes for accurate flow field. *Groundwater* 39: 931–938.

Harbaugh, A.W. 1990. *A computer program for calculating subregional water budgets using results from the U.S. Geological Survey modular three-dimensional finite-difference ground-water flow model*. U.S. Geological Survey Open File Report 90-392.

Lovelock, P.E.R. 1977. *Aquifer properties of the Permo-Triassic sandstones of the United Kingdom*. Bulletin of the Geological Survey of Great Britain No. 56.

McDonald, M.G. & Harbaugh, A.W. 1988. *A modular three-dimensional finite-difference ground-water flow model*. U.S. Geological Survey Techniques of Water-Resources Investigations Book 6, Chapter A1.

Owen, M., Headworth, H.G. & Morgan-Jones, M. 1991. Groundwater in basin management. In Downing, R.A. & Wilkinson, W.B. (eds), *Applied Groundwater Hydrology*: 17–34. Clarendon Press.

Pollock, D.W. 1989. *Documentation of computer programs to complete and display pathlines using results from the U.S. Geological Survey modular three-dimensional finite-difference ground-water model*. U.S. Geological Survey Open File Report 89-381.

Reeves, M.J., Skinner, A.C. & Wilkinson, W.B. 1975. The relevance of aquifer flow mechanisms to exploration and development of groundwater resources. *Journal of Hydrology* 25: 1–21.

Yoshida, K. 2000. Groundwater vulnerability of the Triassic Sandstone aquifer in the Selby area, North Yorkshire. unpubl. Ph.D. thesis, Univ. of Leeds.

Copyright © 2003 Swets & Zeitlinger B.V., Lisse, The Netherlands

VRML modeling of subsurface and groundwater movement

K. Yamada
Chiba Chigaku Ltd., Chiba, Japan

ABSTRACT: VRML is applied to the modeling of subsurface and groundwater movement to make world file to be viewed through internet or intranet by user's easy access. Ground surface, subsurface geological structure, element mesh and nodes, flow vector, flowpath and contour faces are placed in the virtual reality three dimensional world.

1 VRML

1.1 *Introduction*

The Virtual Reality Modeling Language (VRML) is a file format for describing interactive 3D objects and worlds (R. Carey et al. (1997)). The file based on VRML is named as world file (*.wrl). World file is a text file and therefore can be edited by editors and can be constructed using any other computer languages. The author uses Fortran language to construct world file which converts Fortran output text files into world files.

Computer simulation model is an interpretation of the process of real world by use of program which is to be loyal to the natural law, and data which is to be loyal to natural phenomena and observations. The interpretation which includes modeling concepts such as analyzed area, its subdivision, element, node, distribution of parameters, boundary condition, vector, and contour are not real objects in the real world, but they help us understand the process of the real world. VRML world is a representation of objects in the real world, and, in addition it can include a presentation of the process and modeling concepts. Recently visually based computer-graphical approach using GIS (geographic information system) has been introduced into modeling and it is referred as GMA (geographic modeling approach) (G.F. Pinder (2002)). Vrml modeling is one of GMA. In near future, GIS technology and vrml modeling would be unified and they would contribute to the construction of infra-structure related to geo-environment for E-Government (Electronic Government).

1.2 *Plugin-viewer of vrml world files*

There are several VRML plug-in viewers distributed by the members of VRML Consortium which are plug-in into internet viewers. The VRML plugin-viewer allows users to view the 3D world, walk through, fly and examine the objects. By specifying 'viewpoints' users can view from the fixed viewpoint in the world space. The 'walk' command allows the user to go around as if he is walking on the topographic surface keeping his viewpoint near the ground surface if it is defined. The 'examine' command allows the user to see, handle, move and overturn the object. The world file is interactive through links because objects in the vrml world can be linked to other files such as html files, wrl files or any other files for download.

2 DESCRIPTIVE WORDS AND PROCESSING PROGRAM

2.1 *Descriptive words*

There are some vrml words (underlined & italic) which describe the objects and movement of the objects.

Anchor: to make hyperlink
Appearance: to give color to the object
Background: to give background color to the vrml world
Billboard: to keep showing information of letters always facing to the viewer
Color: to give selected color to the object
ColorInterpolator: to change color time-dependently
Cone: to make a part of vector
CoordinateInterpolator: to move contour smoothly
ElevationGrid: to make topographic surface etc. together with bitmaps
IndexedFaceSet: to construct contour faces etc.
IndexedLineSet: to construct element framework etc.
Material: to make object appearance
PositionInterpolator: to move a particle along flowpath

Copyright © 2003 Swets & Zeitlinger B.V., Lisse, The Netherlands

ScalarInterpolator: to change scalar value such as transparency
Shape: to construct element frame etc.
Sphere: to make a particle
Text: to give information by letters in the Vrml space
TimeSensor: to give time-transient value
Transform: to give movement to objects
Viewpoint: to give fixed viewpoints

2.2 *Writing vrml words on the world file, and processing program*

In the processing programs vrml words are written on the world file on the platform of Fortran language, using Fortran 'write' and format command. The processing program prepares data for the viewing and then reads element and node information, and outputs for conversion into vrml format. Vrmlmake-Fem3dmesE.exe is a processing program for finite elements with six faces and eight corner nodes, and this is applicable to Acunsaf3d (K. Akai et al. (1979)), a three dimensional finite element program for saturated–unsaturated groundwater flow. PTCVrmlmake.exe is a processing program customized for PTC (G.F. Pinder (2002)), a three dimensional finite element/difference flow program for saturated groundwater flow and contaminant transport with variable mesh height for free water table. Here the surface of mesh frame is dependent on free water table.

Both programs describe information as follow:

1. coordinates
2. viewpoints and lighting
3. information words
4. element and its framework
5. flowpath
6. contour

2.3 *Element type and nodes*

For the processing program elements are of three dimensional with six faces and eight corner nodes. Coordinates in the VRML space are as shown in Figure 1, where (X,Y,Z) in the VRML space corresponds to (x,y,z) coordinates in the analyzed space as follows: X corresponds to x-coordinate, Y corresponds to z-coordinate and Z corresponds to y-coordinate.

Node numbering in one element is as shown in Figure 2.

2.4 *Viewing information*

For the viewing of the vrml world, coordinate system, lighting, viewpoint, and information words are to be prepared.

Heading for the world file should be the following:

#VRML V2.0 utf8

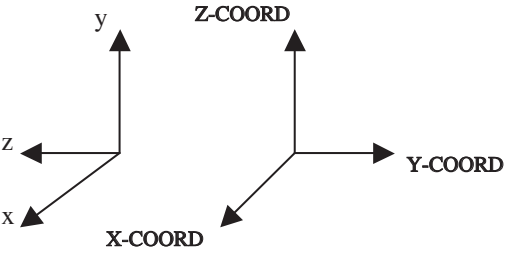


Figure 1. Coordinates in the VRML space (left) and analyzed space (right).

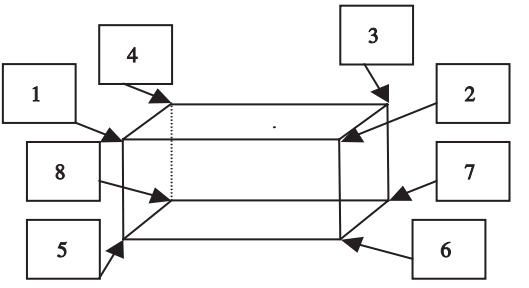


Figure 2. Element and node numbering.

Background color is given as follows:

Background {skyColor .70 .70 .70}

Color is defined by specifying three components of red[0.0–1.0], green[0.0–1.0], and blue[0.0–1.0]. Lighting is by headlight and/or directional parallel light.

```
DirectionalLight {
  color 0.5 0.5 0.5
  direction .5 −.7 −.5}
NavigationInfo {
  headlight TRUE}
```

Viewpoints give the user fixed points and orientations to see the world. The program creates viewpoints with parallel orientation to the three coordinate axes. The same literature can be used for any vrml files by replacing only position. To find the best viewpoints trial and error is required for the value of position.

```
DEF near1 Viewpoint {
fieldOfView 1.0
orientation 1 0 0 −1.57
position 75.00 300.00 −75.00
jump TRUE
description "parallel to Z axis"}
```

Information words such as element numbering, and node numbering can be placed in the space using *billboard* which keep the words always facing to the

Copyright © 2003 Swets & Zeitlinger B.V., Lisse, The Netherlands

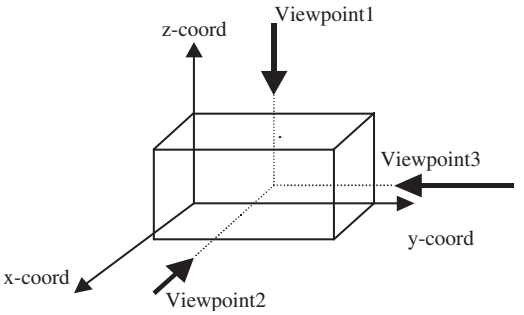


Figure 3. Coordinates and viewpoints.

viewer. The following specifies a word 'X 10.00' with font size of 3 on the x-coord axis located at (x,y,z) = (10.0,0.0,0.0) in the vrml space.

```
Transform {children [Billboard {
  children [Shape {
  geometry Text {string "X 10.00"
  fontStyle FontStyle {size 3.00}}
  appearance Appearance {material Material {
  }}}]}]
  translation 10.0 0.0 0.0}
```

2.5 *Element, node and framework*

Element faces are described as *IndexedFaceset* with high transparency. *IndexedFaceset* specifies a face by a group of points which make up the four corners of one of element six faces. The element frameworks are described as *IndexedLineset* which is a group of lines connecting every two corner nodes. In order to minimize the file size, the duplication of faces and lines are to be avoided. If faces and lines are described on element basis, duplication would occur, because one face is common between two elements, and one line is common among three, four or more elements.

The element and framework are fixed if the element shape is independent of the water table etc. They depend on the free water table if the program adopts variable element thickness depending on free water table.

The numbering of elements and nodes can be placed in the vrml space for reference using *billboard*.

2.6 *Bitmap on the surface or in the subsurface*

Topographic surface and subsurface geology are described by *ElevationGrid* and bitmap. The following sample shows a surface topography of test.jpg gridded 6 by 5 of 62.5 m by 50 m area. This literature can be used to show various kinds of bitmaps by replacing subdivisions, spacings, elevation data and maps such as topographic map, geological map, texture map and design drawings. In one vrml space more than two sets of elevation grid and bitmap can be placed. One geological formation can be shown by a pair of upper and lower surfaces.

```
#VRML V2.0 utf8
  Shape {
    geometry ElevationGrid {
      xDimension 6
      xSpacing 12.5
      zDimension 5
      zSpacing 12.5
     height [0.1 0.2 0.3 0.4 0.5 0.3
             0.2 0.3 0.5 0.4 0.3 0.4
             0.3 0.5 0.4 0.2 0.5 0.7
             0.2 0.4 0.3 0.5 0.3 0.4
             0.4 0.5 0.3 0.2 0.7 0.6]
     solid FALSE
     }
     appearace Appearance {
     material Material {}
     texture DEF tex1 ImageTexture {
      url "test.jpg"}
      textureTransform TextureTransform {
      scale 1 −1
     }}}
```

3 FLOWPATH ROUTINE

3.1 *Vector*

Vector is described as a combination of a line and a cone with the same orientation as the specified vector on one element. To visualize a vector, scale factor is to be specified. The following shows a sample of vector:

```
Shape {
   geometry IndexedLineSet {
   coord Coordinate {point [
    25.000 5.000 −25.000 5.000 25.000 −5.000]}
  coordIndex [0 1 −1]
  color Color {color [1 0 0,0 1 0,0 0 1]}
  colorIndex [2 2 2 2 −1 2 2 2 2 −1]}}
  Transform {
  children [Shape {geometry Cone {
  bottomRadius 2.165064
  height 8.660254}
  appearance Appearance {
  material Material {} }}]
  rotation .71 .00 .71 −2.19
  translation 25.00 5.00 −25.00}
```

3.2 *Flowpath routine*

Flowpath is calculated based on vectors given in each element from the specified starting point to the calculated ending point. Vectors are for steady-state. Attention is to be paid for vectors if they are Darcy's

Copyright © 2003 Swets & Zeitlinger B.V., Lisse, The Netherlands

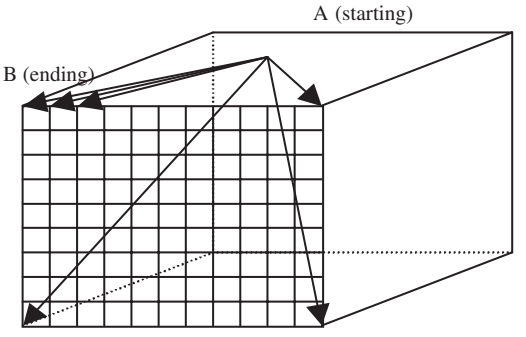


Figure 4. Ending point is checked for subdivision points on all six element faces.

average flow velocity or real flow velocity, because the routine calculates based on only velocity value. Coordinates, and traveltime are calculated and recorded to make flowpath of a particle in the vrml space. The routine makes another flowpath data html file which is hyperlinked from the particle in the vrml space using *anchore*. In one element the flowpath is defined as the line from the starting point to the ending point. The starting point (A) can be anywhere in the element or on one of element surface, and the ending point (B) may be on one of element faces, on one of twelve rim line or on one of eight corner nodes. Here vector AB is required to have the same direction with the specified vector (V) for the element. In the routine, the ending point (B) is assumed to be on the subdivided mesh points of 100 by 100 (by default) on one element face and all the six faces are surveyed for the direction of vector so that it has the nearest direction.

$$p(i,j,k) = \frac{\overrightarrow{AB} \times \overrightarrow{V}}{\left|\overrightarrow{AB}\right| \times \left|\overrightarrow{V}\right|} \cong 1 \qquad (1)$$

where k is the k-th face among 6 faces on the element and (i, j) are the i-th and j-th point of subdivision of the face ($0 \le I \le N, 0 \le J \le N, N = 100$).

When $p(i,j,k)$ is much smaller than 1, other elements are surveyed in case the starting point is on the rim line or on the corner nodes. Prior to this flowpath routine, every face of elements is checked for the facing elements. And also, every node is checked for common elements.

When there is no face with ending point on any element, the flowpath routine terminates. As shown in the following sample, flowpath of moving particle is described by key value of *PositionInterpolator* to make smooth movement on time. Here, *anchor* is used to make hyperlink from the moving particle to an outside html file which lists up the flowpath information.

```
Anchor {url "Fem3dmeshEpathfile001.htm"
children DEF Obj1 Transform {
children Shape {geometry Sphere {radius 5.0}
appearance Appearance {material DEF Mat1
 Material {} }
}}}
DEF Polatorc1 ColorInterpolator {
   key [0, .09, 0.1, 1]
   keyValue [0 1 0, 0 1 0, 0 0 1, 1 0 0]}
DEF Sensor1 TimeSensor {
   loop TRUE
   cycleInterval 22.22
   stopTime −1}
ROUTE Sensor1.fraction_changed TO
 Polatorc1.set_fraction
ROUTE Polatorc1.value_changed TO
 Mat1.set_diffuseColor
DEF Polator1 PositionInterpolator {
   key [.000, .100, .550, 1.000,]
   keyValue [.0 30. .0, .0 30. .0, 30. .0 −30.,
 60. −30. −60.]}
ROUTE Sensor1.fraction_changed TO
 Polator1.set_fraction
ROUTE Polator1.value_changed TO
 Obj1.set_translation
```

4 CONTOUR ROUTINE

4.1 *Construction of contour*

When the contour value is specified, all the faces of elements are to be surveyed for the possible cross points of contour surface.

1. Every one of six element faces is divided into two triangles and all twelve triangles are checked for intersection on three lines connecting the three vertices of the triangle. In one survey, a set of intersections are found and called as A and B. Next points are found till E and F. For example, A and B, B and C, C and D, D and E, E and F, F and G, G and H, H and A. In many cases the points are found randomly, so they must be re-arranged.
2. All the intersections on the contour surface in one element is arranged so that it makes a good order to finally come back to the starting point for example A, B, C, D, E, F, G, H, A.
3. *IndexedFaceset* is used to describe the contour face. The number of intersection points differs on the situations ranging from 3 to 11 in one element.

Lines connecting the intersections in 12 triangles on six faces of an element can be shown as a framework structure of contour using *IndexedFaceset*.

A contour consists of many small contours. Contour can be constructed within one element. However, in order to construct continuous contour surface, the continuity among adjacent elements must be considered. For example the subdivision of triangles for

Copyright © 2003 Swets & Zeitlinger B.V., Lisse, The Netherlands

the common face among two elements are not the same, i.e. if one element has triangles of the type 125 and 256 and adjacent element has another type 237 and 276, contours for the same face does not coincide with each other, because the triangles are crossing.

In order to solve this problem, the routine arranges the vertices for one contour survey in order to find any closed cycle of vertices after all the elements are calculated for the vertices. Even though there might be some gaps among adjacent elements, the routine finds closed cycle of vertices including both vertex points that make a continuous looking contour surface.

4.2 *Moving contour*

Here are shown two methods that describe the moving contours on time step.

1. Showing the contour for only the specified time and otherwise keeping it invisible by *transparency* on *timesensor*.
2. Moving all intersections on one contour using *PositionInterpolator* on *Timesensor*.

In the first method, all the contours on specified numbers of timesteps are calculated once, and then given *transparency* depending on timesteps using *timesensor*. The movement of the contour is discrete.

The following example shows a contour which is visible between the time 50.0 and 66.7 in the cycle interval of 100.0 seconds when *transparency* is controlled by the key value of *ScalarInterlolator* 0.0, and otherwise invisible when transparency is controlled by key value of *ScalarInterlolator* 1.0.

```
Shape {
  geometry IndexedFaceSet {
    coord Coordinate {point [
    30.00 .00 −50.00
    22.50 .00 −52.50
    .00 .00 −60.00
    30.00 3.33 −60.00
    30.00 2.50 −57.50]}
color Color {color [1 0 0, 0 1 0, 0 0 1]}
coordIndex [0 1 2 3 4 −1]
colorIndex [2 2 2 2 2 −1] solid FALSE}
appearance Appearance {
material DEF Matcontour1 Material {} }}
DEF Polators1 ScalarInterpolator {
key [0,.167,.167,.333,.333,.500,.500,.667,
 .667,.883,.883,1]
keyValue [1.0,1.0,1.0,1.0,1.0,1.0,0.0,
 0.0,1.0,1.0,1.0,1.0]}
DEF Sensor1 TimeSensor {
  loop TRUE
  cycleInterval 100.0
  stopTime −1}
ROUTE Sensor1.fraction_changed TO
 Polators1.set_fraction
ROUTE Polators1.value_changed TO
 Matcontour1.set_transparency
```

The same number of contours as the timesteps appear visible one by one just on time steps, therefore, the moving of contour is not smooth but is discrete.

In the second method, the vertices of one contour in one element are specified for the starting, and end points to make a smooth movement using *CoordinateInterpolator*. This is not easy because the number of vertices of one contour changes when the contour passes through one corner node. This is analyzed as follows:

1. In the subdivision of 6 contour faces into 12 triangles, one corner node has 3 or 5 bonds connecting the nodes. The number of bonds depends on the way of subdivision, and in the case node1(5), node2(5), node3(5), node4(3), node5(5), node6(3), node7(5), and node8(5). Node1 has five bonds to 2, 3, 4, 5 and 8. Node4 has three bonds to 2, 4 and 7 as shown in Figure 5.
2. For example, at a time one contour has one intersection on one bond near node1 and after passing node1 the number of intersections on bonds changes to $5-1=4$. In this case number of vertices changes by addition of 3.
3. When one simple flat contour face comes from outside and then passes through one element and then goes out, it should pass through all the 8 nodes. Therefore, the number of vertices changes starting from 1 (corner node) then to 5 or 3 and then by passing one element some addition or subtraction of vertices occurs. Then finally it comes to one corner node to go out of the element.
4. The process is analyzed into small steps which do not include times when it just passes on the corner nodes. Until the contour passes the next corner

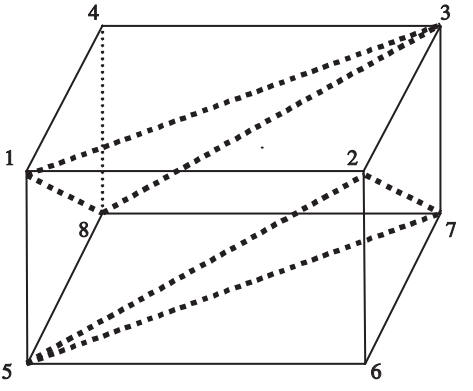


Figure 5. Complementary subdivision on 6 faces to make 12 triangles.

Copyright © 2003 Swets & Zeitlinger B.V., Lisse, The Netherlands

node, the number of vertices is not changed, therefore, *CoordinateInterpolater* is applied only for this small time step.

Here, it is to be noted that the movement of the contour surface is always not constant even if the values at the 8 corner nodes change linearly on time. However, *CoordinateInterPolator* creates constant movement of the contour. This may cause some differences in contour surfaces among adjacent elements because the time steps for the contour depend on each element and the times are decided by the time of passing contour through the corner nodes of each element. So it is recommended to take time step length as small as a few seconds so that the differences may not be clear even if they exist when the contour is moving.

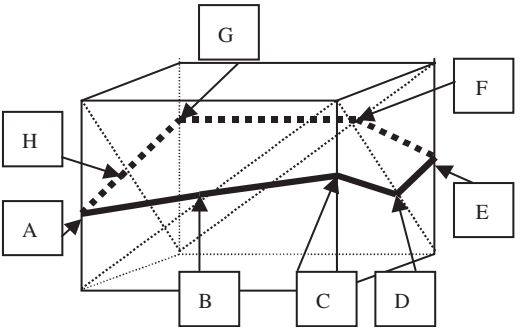


Figure 6. Typical eight intersections making one contour in one element.

5 EXAMPLES

Processing program was applied in order to test the processing program and performance of the world file. In the test, several points for improvements come clear.

5.1 *PTC*

Vrml sample is shown in Figure 7. Vector, moving particles and concentration contour are shown.

5.2 *Acunsaf3d*

Here, the element framework, vector, contour and moving particles are shown in Figure 8.

6 CONCLUSIONS

1. VRML modeling enables not only representation of real objects in the real world but also presentation of process and modeling concepts in the subsurface and groundwater movement.
2. There remain developments, improvements and experiments to be worked and to be studied

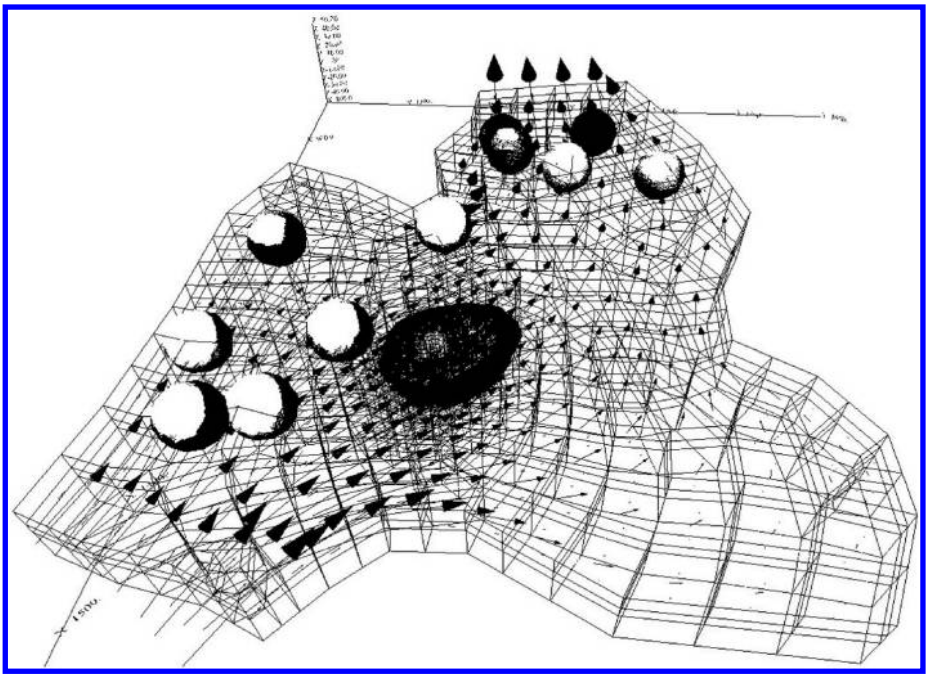


Figure 7. Application to PTC.

Copyright © 2003 Swets & Zeitlinger B.V., Lisse, The Netherlands

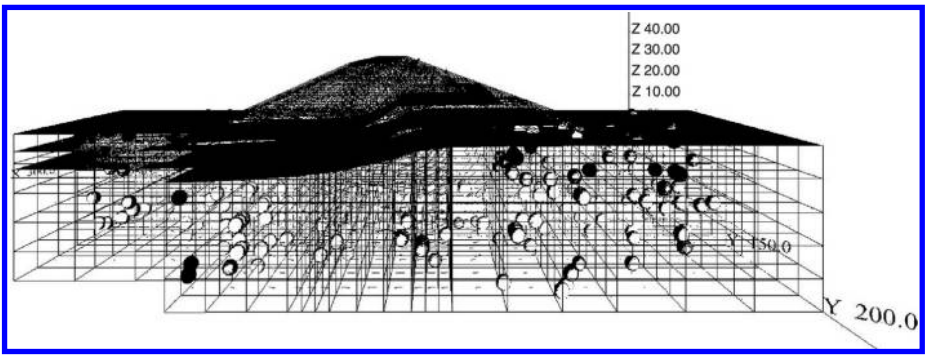


Figure 8. Application to Acunsaf3d.

furthermore as listed below:

developments

(a) flowpath routine in the transient vector field
(b) extension to various types of elements
(c) real time operation of the world file

improvements

(d) moving contour routine for better performance
(e) decreasing world file size
(f) decreasing calculation time

experiments

(g) multi-user environment
(h) web-site management

REFERENCES

Rikk Carey et al. (1997) ISO/IEC 14772-1:1997 Virtual Reality Modeling Language (VRML), VRML Consortium Incorporated.

George F. Pinder (2002) Groundwater Modeling Using Geographical Information Systems, Wiley, New York.

K. Akai et al. (1979) Finite Element Analysis of Three-Dimensional Flows in Saturated–Unsaturated Soils, 3rd Int'l Conf. On Numerical Methods in Geomech., Aachen, pp. 227–239.

Copyright © 2003 Swets & Zeitlinger B.V., Lisse, The Netherlands

An integrated stream and groundwater model for simulating groundwater-stream exchange in an alluvial plain, Kofu basin

X.-W. Zhang, X.-H. Zhang, K. Takeuchi & H. Ishidaira
Department of Civil and Environmental Engineering, Yamanashi University, Japan

ABSTRACT: Frequently, the water exchange between stream and aquifer is estimated with an integrated model, which consists of the two-dimensional (2D) groundwater model and stream flow routing model. However, in many cases, the stream flow and the shallow groundwater are usually closely interlinked, and the water exchange between shallow and confined groundwater exists. The use of an integrated multi-layer groundwater and stream flow routing model is thus necessary to simulate the water exchange between stream and multi-layer groundwater. In this paper, an integrated quasi three-dimensional (Quasi-3D) groundwater and Kinematic wave routing model is proposed, and applied to the alluvial plain between Fuefuki River and Ara River located in Kofu basin, Japan. The simulation for the period from February 1990 to December 1991 is performed and compared with the measurements. The results indicate that the integrated model can reasonably describe the actual process of water exchange between stream and multi-layer groundwater.

1 INTRODUCTION

The hydrologic interactions between stream and groundwater play an important role in stream ecosystem structure and function. Simulation of the stream-groundwater interaction is a coupled process, which consists of the groundwater flow as well as the stream flow. Since 1970s, the stream-aquifer interaction has been studied by a number of researchers. The study of Pinder et al. (1971) and Cunningham et al. (1979) were conducted by using a coupled numerical model for canal flow and 2D groundwater flow. Illangasekare et al. (1986) developed special distributed parameter surface-groundwater models for stream-aquifer management. Furthermore, Swain et al. (1993) proposed a stream-aquifer-interaction model based on the MODBRANCH, which couples 2D groundwater model and the St. Venant equation. Other approaches reported include the 2D groundwater flow numerical simulation as well as a kinematic wave model through a streambed leakage (Yan et al., 1994; Perkins et al., 1996; Lal et al., 1999).

However, all of the above models are limited to 2D shallow groundwater flow. In Kofu basin, the stream flow and the shallow groundwater are closely interlinked, and the water exchange between the shallow and confined groundwater exists. Thus the use of an integrated multi-layer groundwater and stream model is necessary for regional stream-groundwater management. In this study, an integrated multi-layer groundwater and stream model is developed to estimate the water exchange between stream and the multi-layer groundwater.

A quasi-3D groundwater model simulates the multi-layer groundwater flow. Because of the irregularity of the stream, the finite element scheme is often considered to solve the quasi-3D groundwater model. The coordination of time steps of stream-flow routing and groundwater flow simulation is important for solving the integrated model (Perkins et al., 1996; Querner, 1997). For example, the stream flow routing model has a small time step, of the order of several minutes to hours, conversely, the time step of several weeks to one month for multi-layer groundwater modeling is usually considered. In order to effectively couple both of these models, the multi-layer groundwater model often adopts the time step of one week to as much as 10 days. Unfortunately, the spurious oscillation solution may occur in the case of relatively small time step (Zhang et al., 2001). This difficulty restricts the use of the quasi-3D groundwater flow finite element scheme for practical stream-aquifer water exchange simulation. In this study, therefore, the triangular mesh finite difference scheme is used to solve quasi-3D groundwater flow model.

In addition, the Kinematic wave model is adopted to simulate the stream flow. The model in general is discretized by a classical upwind difference scheme with

Copyright © 2003 Swets & Zeitlinger B.V., Lisse, The Netherlands

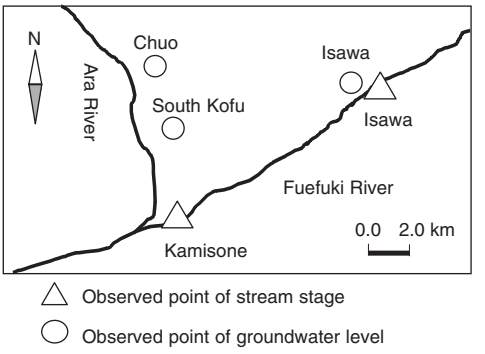


Figure 1. Location of the study reach.

the first-order accuracy. In order to have a mass conserving numerical approximation, the Koren upwind scheme (Holstad, 2000) with the third-order accuracy is employed to discretize Kinematic wave equation, in this paper.

Finally, the model is applied to the alluvial plain between Fuefuki River and Ara River located in Kofu basin, Japan. The simulation for period from February 1990 to December 1991 is performed and tested against the measurements, and the results can well describe the actual process of unconfined groundwater recharge from stream, as well as the water exchange between unconfined and confined groundwater from February 1990 to December 1991.

2 STUDY SITE

The study area shown in Figure 1 consists of a 9.8 km reach between Isawa and Kamisone in Fuefuki River, which is associated with the multi-layer aquifer located in Kofu basin. The unconfined aquifer is formed from deposit with thickness of 15∼40 m. In the confined aquifer, the thickness is 10∼80 m and the geology is in the finer texture than that of unconfined aquifer. Clay layer between the unconfined and confined aquifers is semi-pervious layer with a thickness of 0∼30 m.

The annual mean discharge of Fuefuki River is about 4.8 m^3/s at Isawa. The river has an average width of 24.1 m, and there are impervious dikes on both banks. The interface between the streambed and aquifer is semi-pervious layer of clay.

3 GOVERNING EQUATIONS

Equations describing quasi-3D groundwater flow and 1D stream flow are considered to be the principal relationships that govern the stream-aquifer interaction.

3.1 *Quasi-3D groundwater flow model*

3.1.1 *The unconfined groundwater flow*

$$\mu\frac{\partial h}{\partial t} = \frac{\partial}{\partial x}\left(T_1\frac{\partial h}{\partial x}\right) + \frac{\partial}{\partial y}\left(T_1\frac{\partial h}{\partial y}\right) + \frac{k'}{m'}(H-h) + \delta(x,y)Q_r + q_1 \quad (1)$$

where h = groundwater level of unconfined aquifer; H = the confined head; x, y = distance along horizontal x- and y-axes; T_1 = transmissivity of unconfined aquifer; μ = storage coefficient; m', k' = thickness and hydraulic conductivity of aquitard; Q_r = water exchange between stream and aquifer during groundwater model time step; q_1 = pumping water. $\delta(x,y)$ is coupled function between stream and unconfined aquifer, that is

$$\delta(x,y) = \begin{cases} 1 & (x,y) \in \textit{node is on stream} \\ 0 & (x,y) \notin \textit{node is not on stream} \end{cases} \quad (2)$$

3.1.2 *The confined groundwater flow*

$$S\frac{\partial H}{\partial t} = \frac{\partial}{\partial x}\left(T_2\frac{\partial H}{\partial x}\right) + \frac{\partial}{\partial y}\left(T_2\frac{\partial H}{\partial y}\right) + \frac{k'}{m'}(h-H) + q_2 \quad (3)$$

where T_2 = transmissivity of unconfined aquifer; S = storage coefficient; q_2 = pumping water.

3.2 *Stream flow routing equation*

Kinematic wave model is adopted to simulate stream flow.

$$\begin{cases} \dfrac{\partial A}{\partial t} + \dfrac{\partial Q}{\partial x} = q_d \\ Q = \alpha A^m \end{cases} \quad (4)$$

where A = stream cross-section area; Q = discharge in the stream; q_d = lateral flow discharge per unit length of stream; $\alpha = s_0^{1/2}/(nR^{2/3})$, S_0 = bottom slope; n = Manning roughness coefficient; R = wetted perimeter.

3.3 *Water exchange between stream and aquifer*

To couple groundwater flow and stream flow routing equations, the water exchange between the stream and aquifer at the aquifer-stream interface must be defined. As indicated in Pinder (1971), the water exchange is based on Darcy's law and is written as the following form (Figure 2)

$$q_r = k_m R\frac{Z-h}{m} \quad (5)$$

Copyright © 2003 Swets & Zeitlinger B.V., Lisse, The Netherlands

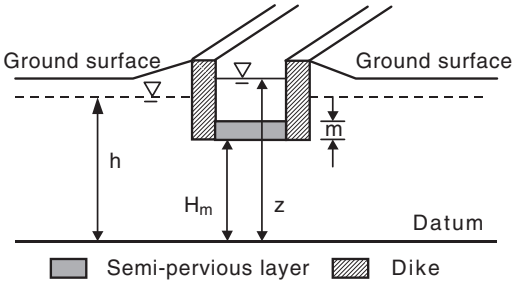


Figure 2. Aquifer and stream with sediment layer.

where k_m = hydraulic conductivity of the semi-pervious layer between stream and aquifer; m is thickness of the semi-pervious layer; R is wetted perimeter and Z is stream stage.

4 NUMERICIAL SOLUTION

The accuracy of the integrated stream-groundwater model depends on the reliability and stability of numerical scheme. Unfortunately, small time step (Δt) of groundwater flow model is often selected in the integrated surface-subsurface water modeling because Δt for flood routing is small (Querner, 1997). In this case, the quasi-3D groundwater flow finite element scheme is perhaps unstable, and the oscillation solution may occur (Zhang et al., 2001). Hence, in order to avoid oscillation, the triangular mesh finite difference scheme is used to solute quasi-3D groundwater model due to the scheme being more stable than the finite element scheme.

For stream flow routing, the Koren upwind scheme with the third-order accuracy is used to discretize the Kinematic wave equation.

4.1 *The discrete formulation of the quasi-3D groundwater flow model*

The triangular mesh finite difference scheme is used to discretize the quasi-3D groundwater flow models of equations (1) and (2) (Zhang et al., 2001)

4.1.1 *The discretization of equation (1)*

$$\sum_e \frac{T_1^e}{4A^e}[(b_ib_i + c_ic_i)h_i + (b_ib_j + c_ic_j)h_j + (b_ib_m + c_ic_m)h_m] - \sum_e \frac{k'\rho^e}{m'}(H_i - h_i) + \sum_e \mu^e\rho^e\frac{h_i^{k+1} - h_i^k}{\Delta t_g} = \delta(x,y)\cdot Q_n + q_{li} \qquad (6)$$

The discretization of equation (2) is:

$$\sum_e \frac{T_2^e}{4A^e}[(b_ib_i + c_ic_i)H_i + (b_ib_j + c_ic_j)H_j + (b_ib_m + c_ic_m)H_m] - \sum_e \frac{k'\rho^e}{m'}(h_i - H_i) + \sum_e \mu^e\rho^e\frac{H_i^{k+1} - H_i^k}{\Delta t_g} = q_{2i} \qquad (7)$$

where $\rho^e = -\frac{1}{16A^e}[(b_m^2 + c_m^2)(b_ib_j + c_ic_j) + (b_j^2 + c_j^2)(b_jb_m + c_ic_m)]$; Δt_g = time step of groundwater flow simulation.

4.2 *The discrete formulation of Kinematic wave model*

Consider equation (4),

$$\frac{\partial A}{\partial t} + \frac{\partial Q}{\partial x} = q_d \qquad (8)$$

In order to have a mass conserving numerical approximation, equation (8) is discretized in space using a cell-centered finite-volume method, giving

$$\oint_{\Omega_i}\frac{\partial A}{\partial t}dx + \oint_{\Omega_i}\frac{\partial Q}{\partial x}dx = \int_{\Omega_i} q_d dx \qquad (9)$$

where Ω_i = the ith solution domain.

Flux item in equation (9) can be discretized as

$$\oint_{\Omega_i}\frac{\partial Q}{\partial x}dx = Q_{i+1/2} - Q_{i-1/2} \qquad (10)$$

Koren upwind difference (Holstad, 2001) is used to discrete flux items in equation (9), hence, a numerical scheme is conservative such that the scheme can be written as

$$Q_{i+1/2} = Q_i + \frac{1}{4}(Q_{i+1} - Q_i) + \frac{1-k}{4}(Q_i - Q_{i-1}), \quad k \in (-1, 1) \qquad (11)$$

and similarly for $Q_{i-1/2}$.

The numerical experiments carried out by Holstad (2000) have shown that the flux difference $Q_{i+1/2} - Q_{i-1/2}$ is third order accuracy for steady linear and nonlinear problems when choosing $k = 1/3$. Thus equations (11) can be rewritten as

$$Q_{i+\frac{1}{2}} = Q_i + \frac{1}{3}(Q_{i+1} - Q_i) + \frac{1}{6}(Q_i - Q_{i-1}) \qquad (12)$$

In order to keep the monotomicity, equation (12) is reformulated as follows (Sweby, 1984),

$$Q_{i+\frac{1}{2}} = Q_i + \frac{1}{2}\varphi(r_{i+1/2})(Q_i - Q_{i-1}) \qquad (13)$$

Copyright © 2003 Swets & Zeitlinger B.V., Lisse, The Netherlands

where $\varphi(r_{i+1/2})$ is the limiter function. That is

$$\varphi(r_{i+1/2}) = \max\left(0, \min\left(2r, \min\left(\frac{1}{3} + \frac{2}{3}r, 2\right)\right)\right) \tag{14}$$

$$r_{i+1/2} = (Q_{i+1} - Q_i)/(Q_i - Q_{i-1}) \tag{15}$$

Substituting equations (11)–(15) into equation (8), the discrete formulation of Koren upwind difference for kinematic wave model can be written as

$$\begin{cases} \frac{A^{t+1}_{i+\frac{1}{2}} - A^t_{i+1/2}}{\Delta t_r} + \left[\frac{Q^t_{i+1/2} - Q^t_{i-1/2}}{\Delta x}\right] = \frac{q^{t+1}_{d_{i+1/2}} + q^t_{d_{i+1/2}}}{2} \\ Q_{i+1/2} = Q_i + \frac{1}{2}\varphi(r_{i+1/2})(Q_i - Q_{i-1}) \\ r_{i+1/2} = (Q_{i+1} - Q_i)/(Q_i - Q_{i-1}) \\ \varphi(r_{i+1/2}) = \max(0, \min(2r, \min(\frac{1}{3} + \frac{2}{3}r, 2))) \end{cases} \tag{16}$$

Lateral discharge q_{d_i} at node i can be calculated as

$$q_{di} = q_{Li} + q_{ri} - q_{si} \tag{17}$$

where $q_{L_i}, q_{s_i}, q_{e_i}$ = the discharge of lateral stream and the pumping discharge from stream and the water exchange between the stream and groundwater at node i.

4.3 *Coordination of time scales*

As stated above, the flow of water in the stream can change in a short time whereas the groundwater flow changes relatively slower. Because of their linkage, the two processes should be ideally calculated with the same time step so as to capture the coupling effects of rapidly varying stream flow. Therefore, the key numerical difficulty in modeling stream-aquifer interaction is in coordinating the difference time scales of the stream and groundwater equations (Querner, 1997). In this study, each time step Δt_g is divided into an integer number of stream flow routing time step Δt_r. During time step Δt_g, the groundwater heads of unconfined and confined aquifer are assumed to remain constant, and the water exchange between groundwater-stream is accumulated during groundwater time step by the following equation,

$$Q_{ri} = \sum_{\mathrm{d}} q_{ri}/R_i \tag{18}$$

where $\mathrm{d} = \Delta t_g/\Delta t_r$.

4.4 *Flow chart for solving the integrated model*

To solve the integrated model an iterative procedure is used. Firstly, the necessary physical parameters of the stream and semi-pervious layer of streambed (e.g. Manning roughness coefficient and mean width of stream, thickness and hydraulic conductivity of the semi-pervious layer) are defined.

Secondly, the hydraulic conductivities of unconfined and confined aquifers at each node are estimated by Kriging method (Sun, 1999).

Thirdly, the stream flow routing equation (8) is solved for steady flow conditions, the groundwater flow equations (1) and (3) are then solved for steady flow using the calculated groundwater level and stream stages. The stream equation must be solved once again because the water exchange term q_d has been modified by the new head distribution in the unconfined aquifer. The above iterative cycle is continued until the calculation values of the groundwater level and stream stage at validation locations are within a predetermined error tolerance.

5 APPLICATION

The model was applied to the alluvial plain between Fuefuki and Ara River. The study region has an area of 63.8 km^2, and it is divided into triangular meshes with 75 elements and 51 nodes (Figure 3). The simulation for the period from Feburay 1990 to December of 1991 is performed with the time step of 1 hour for stream and the time step of 10 days for groundwater.

5.1 *Data preparation*

On the basis of the geological cross section of-streambed at Nakamichi and Isawa in Fuefuki River, the semi-pervious formation between stream and aquifer is formed from clay with an average thickness of 1.5 m in study stream reach. We assume that the hydraulic conductivity of the semi-pervious formation is same as that of semi-pervious layer between unconfined and confined aquifers, i.e. $k_m = k' = 8.64 \times 10^{-5}$ m/d.

The hydraulic conductivities of two aquifers were estimated using Kriging method based on the field

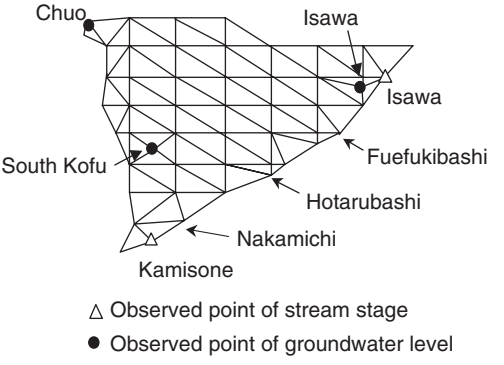


Figure 3. Net of triangular element for the study area.

Copyright © 2003 Swets & Zeitlinger B.V., Lisse, The Netherlands

permeability test of hydraulic conductivities of unconfined and confined aquifers at 46 locations. The results are shown in Figure 4. The storage coefficients of the unconfined and confined aquifers are 0.1 and 0.05, respectively.

In addition, the discharges pumped from groundwater and stream were obtained by investigating the water supply in Yamanashi Prefecture, and the estimate of recharge from precipitation was calculted based on the water balance analysis in this prefecture i.e. recharge from direct precipitation was estimated as 17% of total.

5.2 *Boundary and initial conditions*

The prescribed head boundary was assigned along Ara River. Due to the lack of records for the water levels along the Ara River, the water level at each node was interpolated on the basis of the slope of the river's bed and the water level at the confluence of Fuefuki River and Ara River. The mountaineous area at the northern part was treated as a flow boundary.

Because the water depth and stage in the stream were given in the initial conditions, the stage-discharge relationship at each section was employed to calculate discharge crossing the section.

5.3 *Calibration and validation*

Due to the lack of hydraulic head records, the calibration and validation of the model were based on the unconfined groundwater levels at 3 locations (i.e. South Kofu, Chuo and Isawa) and stream water stage at Kamisone. This model was calibrated for the period from February to December 1990, and then the data in 1991 was used to validate the model.

During the initial stages of the calibration, it is necessary to interactively adjust the parameters such as transmissivities, storativities within-field measured ranges so that the results calculated approximate to the measured data as closely as possible.

The root-mean-square error (RMSE) was used to evaluate the goodness of fit between simulated and observed water table. RMSE values estimated at three wells and one stream stage point during calibration and validation period are tabulated in Table 1.

The results of the calibration and validation at the three wells are in a good agreement with the observed groundwater levels (Figure 5). However, Kamisone at Fuefuki River has a large value of RMSE, the reason for this is that the discharge from the Fuefuki River is over estimated from the investigation of water use in the area (Figure 6).

5.4 *Results*

5.4.1 *Seasonal changes of the water exchange between aquifer and Fuefuki River*

Figure 7 illustrates the stream-groundwater exchange process from February 1990 to December 1991.

Table 1. RMSE values for calibration and validation period at three wells and one stream stage point.

Observed location	Calibration period (Feb.–Dec. 1990)	Validation period (Jan.–Dec. 1991)
Chuo	0.13 m	0.23 m
South Kofu	0.59 m	0.67 m
Isawa	0.23 m	0.22 m
Kamisone	1.12 m	0.95 m

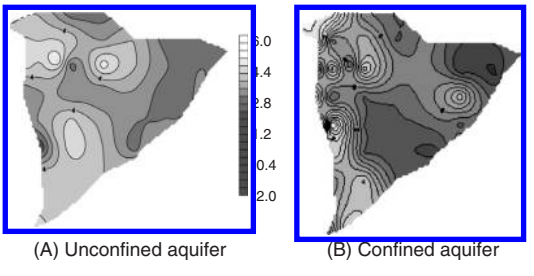


Figure 4. The contours of log k of unconfined and confined aquifers.

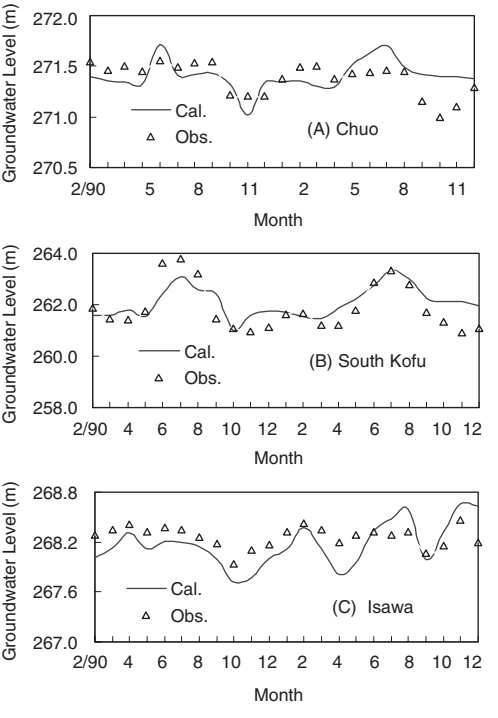


Figure 5. Comparison of calculated and observed unconfined groundwater levels at 3 locations.

Copyright © 2003 Swets & Zeitlinger B.V., Lisse, The Netherlands

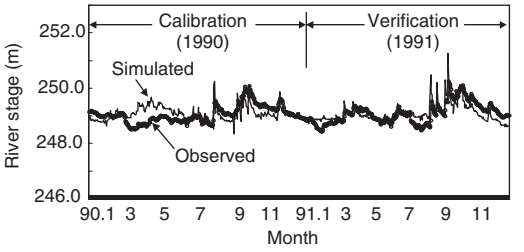


Figure 6. The simulated and observed stream stage at Kamisone (time step = 1hour).

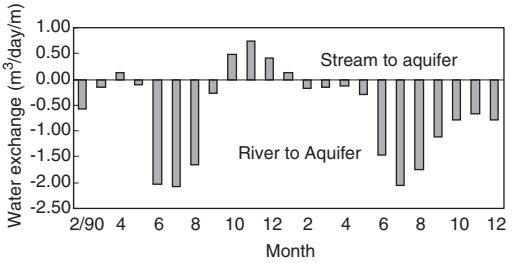


Figure 7. The water exchange between the aquifer of alluvial plain and Fuefuki River.

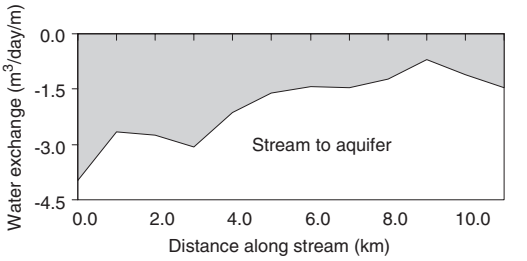


Figure 8. The stream-groundwater exchange along the stream (July, 1991).

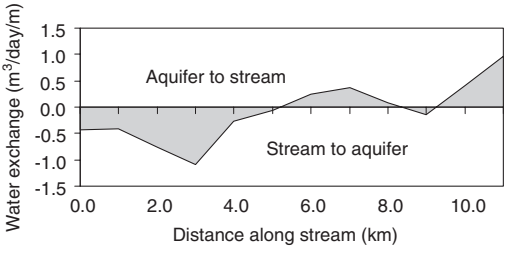


Figure 9. The stream-groundwater exchange along the stream (March, 1991).

In flood season from June to August in 1990, the direction of stream-groundwater exchange was from Fuefuki River to aquifer along the study reach, favorable recharge rate from the river to the groundwater system was 1.94 m^3/day/m. Because low-flow conditions were persisted from the winter months of 1990 to the beginning of 1991, and the groundwater level was higher than the river stage, the direction of stream-groundwater exchange was changed, i.e. the groundwater supply to Fuefuki River with mean discharge rate of 0.38 m^3/day/m.

From January to December 1991, the stream water was directed into the groundwater with mean recharge rate of 0.85 m^3/day/m. During the flood season from June to August, the mean water exchange rate increases from 1.54 m^3/day/m to 2.05 m^3/day/m.

5.4.2 *Spatial variation for the stream-groundwater exchange*

In flood season between June and August, the river stage was higher than the groundwater level at each section, and the groundwater was recharged by the Fuefuki River. For example, in July 1991, the stream-groundwater exchange was directed into the groundwater system, and the recharge rate increased from 0.7 m^3/day/m reach length to 3.7 m^3/day/m reach length along the stream flow direction (Figure 8).

During low-flow conditions, the direction of water exchange between the stream and the aquifer became spatially heterogeneous. For example, in the study reach from the junction of the Ara River and Fuefuki River to HotaruBashi in March 1991, the groundwater was recharged by Fuefuki River with mean recharge rate of 0.51 m^3/day/m. On the Contrary, the groundwater flowed into the river with mean discharge 0.13 m^3/day/m reach length at the upper-stream (Figure 9).

6 CONCLUSIONS

An integrated stream-groundwater interaction model with multi-layer aquifer was developed in this study. The multi-layer groundwater flow model consists of a quasi-3D groundwater model, which was discretized using triangular mesh finite difference. The stream-flow is simulated using the Kinematic wave model, which was solved using the Koren upwind difference with the third-order accuracy.

The model was applied to the Kofu alluvial plain, Japan. The groundwater and stream flow was simulated for two years from 1990 to 1991. On the basis of the results of the simulation, the following conclusions can be reached:

1) The simulated unconfined groundwater level has a relatively good agreement with the field data. Additionally, although the stream stages at Kamisone from February 1990 to December 1991 do not

Copyright © 2003 Swets & Zeitlinger B.V., Lisse, The Netherlands

perfectly match with the observed data, both are quite similar.

2) During the flood season from June to August, the direction of stream-groundwater exchange was from the Fuefuki River to the aquifer, and the water exchange rate is high along the study reach. As the stream stage decreases from November to February of the following year, the exchange water was directed from the river to the aquifer at downstream, whereas the direction of water exchange changed at the upper-stream.

REFERENCES

Cunningham, A.B. & Sinclair, P.J., 1979. Application and Analysis of a Coupled Surface and Groundwater Model. *J. Hydrol*., 43: 129–148.

Holstad, A., 2000. A mathematical and numerical model for reactive fluid flow systems. *Comput. Geosci*., 4: 103–139.

Illangasekare, T.H. & H.J. Morel-Seytoux, 1986. A discrete kernel simulation model for conjunctive management of a stream-aquifer system. *J. Hydrol*., 85: 319–338.

Lal, A.M.W., 1999: Modification of canal flow due to stream-aquifer interaction, *J. Hydrau. Eng.*, 127(7): 567–576.

Nippon Koei CO. LTD. Report on investigation of water resources supply for Yamanashi Prefecture, *Bureau of Yamanashi Prefecture Planing*, 1994.

Perkins, S.P. & Antonis D. Koussis, 1996. Stream-aquifer interaction model with diffusive wave routing. *J. Hydrau. Eng*., 122(4): 210–218.

Pinder, G.F. & Sauer, S.P., 1971. Numerical simulation of flood wave modification due to bank storage effects. *Water Resour. Res*., 7(2): 63–70.

Querner, E.P., 1997. Description and application of the combined surface and groundwater flow model MOGROW. J. Hydro., 192: 158–188.

Sun, Ne-Zheng., 1999. Inverse problems in groundwater modeling, *Kluwer Academic Publishers*, The Netherlands: 161–210.

Sweby, P.K., 1984. High resolution scheme using flux limiters for hyperbolic conservation laws, *SIAM J. Numer. Anal*., 21: 995–1011.

Yan, J.S. & Simith, K.R., 1994. Simulation of Integrated Surface Water and Groundwater Systems-Model Formulation, *Water Resour. Bull*., 30(5): 879–890.

Zhang, X.W., Takeuchi K. & Ishidaira H., 2001. Study on the spurious oscillation and stability in quasi three-dimensional groundwater simulation using FEM and comparison with SFEM and TFDM (in Japanese). *J. Japan Soci. Hydro. Water Resour*., 14(7): 351–363.

Copyright © 2003 Swets & Zeitlinger B.V., Lisse, The Netherlands

Experimental study of permeability of a minute gap

T. Yoden
NEWJEC Inc., Osaka, Japan

T. Deguchi
Foundation of River and Watershed Environment Management, Osaka, Japan

N. Matsui
Kansai Electric Power Company, Osaka, Japan

ABSTRACT: In this study, permeability of a minute gap like the crack layer bedrock is experimentally evaluated as the example of high permeability in the ground. We made the permeability test equipment which is able to make high hydraulic pressure. As a result, it is shown that the larger the hydraulic gradient grows, the smaller the water volume of a minute gap becomes, to less value than calculated by the Darcy's law. And, the relation between permeability and hydraulic gradient is formulated. Moreover, it is shown that there is a constant relation in the open width on a visible side and the width of possible seepage.

1 INTRODUCTION

The permeability defined by Darcy's Law is represented as a proportionality constant under the condition that the velocity of seepage flow is proportional to hydraulic gradient. Generally in the analysis of groundwater flow, permeability in each aquifer is defined as a constant value according to Darcy's Law. In addition, seepage flow in a parallel gap, such as a fracture in rock, is defined by Poiseuille's Law in view of the balance between pressure and viscosity shearing force. If seepage flow assumes laminar flow, permeability is proportional to the size of a gap and inversely proportional to the coefficient of viscosity of fluid, as shown in Equation 1:

$$K = \frac{\delta^2}{12\mu}\rho g \tag{1}$$

where δ = size of a gap; μ = coefficient of viscosity of fluid; and ρ = density. This indicates that permeability in a parallel gap is also treated as a constant value on the condition that the size of the gap remains unchanged.

If seepage flow assumes turbulent flow, however, this definition would be invalid. It is known, for instance, when hydraulic gradient becomes larger than a certain value, a linear relationship between the velocity of flow and the hydraulic gradient fails to be established in the process of a permeability experiment in which coarse sand is used and Equation 1 becomes invalid even in a parallel gap.

Thus, depending on the environment where groundwater exists, when hydraulic gradient becomes large, Darcy's Law may break out.

At the design of underground structures, analytic solving methods or numerical solving methods are used in order to evaluate the magnitude of the hydraulic pressure working on them or the amount of spring water coming out during excavation. Darcy's Law forms the basis for these approaches, where the basic equations of groundwater flow adopted have been developed and expressed numerically. The

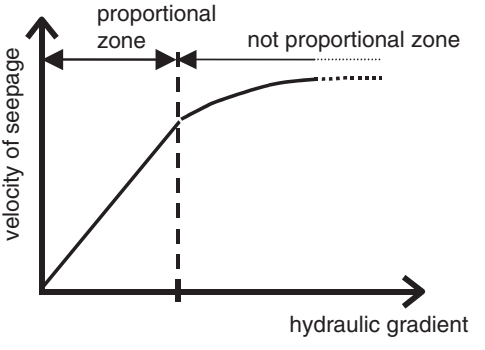


Figure 1. Relationship between velocity of seepage and hydraulic gradient.

Copyright © 2003 Swets & Zeitlinger B.V., Lisse, The Netherlands

permeability of surrounding ground or fractured rock serves as an important parameter which leads to accurate evaluation.

At the underground structures of the power plant, sometimes the structure is just transformed when the condition generated electricity is changed. And then it is act the high pressure from surrounding groundwater in an instant. Therefore, in the analysis of groundwater flow at these zone, it is convenient to think that if hydraulic gradient becomes larger than a certain value, permeability changes corresponding to the function of hydraulic gradient (that is, becomes smaller), as shown in Equation 2:

$$v = K_I \cdot I \tag{2}$$

where v = velocity; I = hydraulic gradient; and if

$$0 < I < x \text{ then } K_I = \text{constant value} \tag{3}$$
$$I > x \text{ then } K_I = K(I)$$

where $K(I)$ = permeability defined as the function of hydraulic gradient.

The author and others paid attention to the existence of a minute gap such as a fracture in rock and experimentally evaluated the differences in permeability associated with changes in the hydraulic gradient. For the purpose of imposing the condition of large hydraulic gradient, we made such experimental apparatus as to be able to apply high hydraulic pressure and provided it with a specimen having an artificially made minute gap. In implementation of a permeability experiment, hydraulic gradient and seepage discharge were measured. Based on the results, the relationship between permeability and hydraulic gradient was gotten regarding a minute gap under the condition of high hydraulic gradient.

2 METHOD OF PERMEABILITY EXPERIMENT

In the permeability experiment, high hydraulic pressure was applied to the artificially made minute gap and then changes in the rate of flow passing through the gap were measured. In view of cost, safety and technical matters, it was difficult to perform a constant pressure permeability test under the condition of high hydraulic pressure. So that a falling-pressure permeability test from a high pressure level to a low pressure level was carried out.

2.1 *Experimental apparatus*

Figure 2 shows the experimental apparatus. It consists of an electro pressure pump, pressure tanks, permeability test equipment, a water tank and a hydrometry tank. Three types of pressure tanks were used; 5 liter, 20 liter and 100 liter. This enabled us to make the volume of tank as large as possible with the aim of preventing a lowering of measurement accuracy due to a rapid pressure drop during the experiment, and on the other hand to shorten the experimental time by reducing the capacity of tank after pressure lowered.

The permeability test equipment was connected with piping from pressure tanks and provided inside with a specimen having a minute gap. Water was completely checked at the upper and lower faces of the specimen with rubber covers so as to be able to pass through the minute gap alone. The rate of the flow passed through the minute gap was calculated in the hydrometry tank by the conversion of a pressure measured by the pressure gauges.

The experiment was performed according to the following procedures:

1) Pressure was applied to the pressure tanks and the permeability test equipment through the electro pressure pump (maximum 200 N/cm^2), with valve #1 closed.
2) After application of pressure, the electro pressure pump was stopped and valve #2 closed.
3) The situation in the above 2) was left for several minutes to confirm that no pressure lowering occurred due to water leakage.
4) Valve #1 was opened and measurement started.

The pressure tanks, piping, permeability test equipment and hydrometry tank were respectively equipped with pressure gauges. With the aid of instrumentation, data from each pressure gauge sensor was measured at intervals of 3 seconds by the use of personal computer. Air and water temperatures were also measured during the experiment.

2.2 *Preparation of a specimen with a minute gap*

Two types of minute gaps were prepared to study permeability. On the assumption of fractures in rock, one type was formed into uneven and unparallel shape (hereafter referred to as crack shape). And the other was formed into parallel shape. In addition, the parallel-shape type had two cases to evaluate differences in the material for the one side of the gap using iron and acrylic resin.

A concrete block of a cylindrical form with a diameter of 15 cm and a height of 30 cm was prepared and divided into two parts. Then, one part was laid over the other part and a gap at the interface was so adjusted to form a minute gap.

In case of crack shape, the block was divided into two parts by a splitting test machine. In case of parallel shape, iron plate and acrylic resin were placed at the time of placing the concrete block. After being solid, the block was divided and one side was glued with an adhesive agent. Since only one minute gap was needed, cut-off rubber sheet was put on the gap of

Copyright © 2003 Swets & Zeitlinger B.V., Lisse, The Netherlands

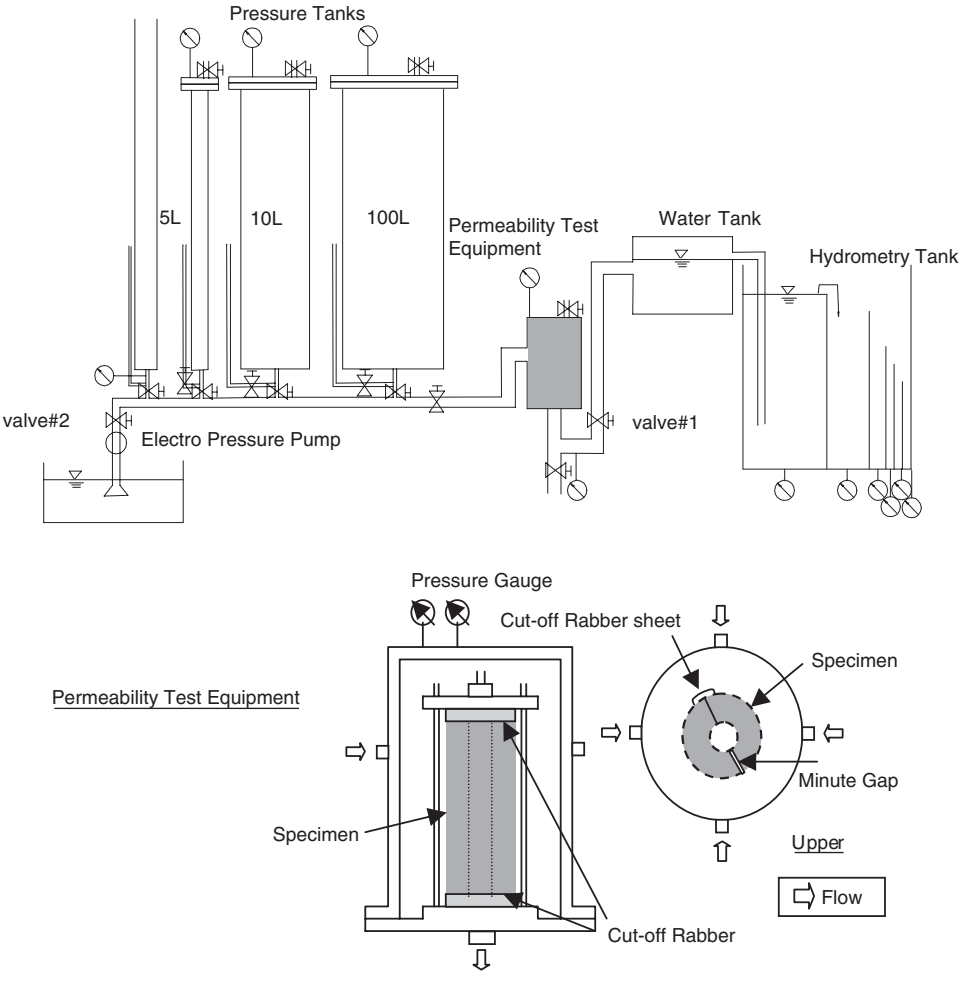


Figure 2. The experimental apparatus.

the other side, which was not used for the permeability experiment, to prevent water from passing through.

The space of the minute gap was adjusted by pushing a conical wedge bolt into the hollow part of the specimen, and also in order to keep the space unchanged when pressure was applied into the permeability test equipment, the specimen was equipped with a binding belt.

2.3 *Experimental cases*

As shown in Table 1, the following cases were implemented in the permeability experiment:

a. Crack shape
b. Iron-concrete gap
c. Acrylic resin-concrete gap

Table 1. Permeability experimental cases.

Form of gaps	Gap width (measured in mm)	Divided method
Crack shape	0.0−1.0	Splitting test machine
Iron-concrete gap	0.0−1.0	Placed the material
Acrylic resin-concrete gap	0.0−1.0	Placed the material

For each form of gaps, five patterns of gap width [D] were set in the range from 0.0 mm to 1.0 mm. Gap width was obtained by measuring the distance between the two points on opposite sides of a gap on the specimen.

Copyright © 2003 Swets & Zeitlinger B.V., Lisse, The Netherlands

3 EXPERIMENTAL RESULTS AND EVALUATION OF PERMEABILITY

By the use of two hydraulic-pressure data obtained after the beginning of experiment from inside the permeability test equipment and the point between the permeability test equipment and the water tank, the hydraulic gradient in the minute gap was calculated. In Figure 3, the relationship between the hydraulic gradient and seepage discharge inside the minute gap is illustrated. The figure indicates that there was no proportional relationship between changes in hydraulic gradient and increments in discharge. This explains, when Equation 2 was applied, that permeability changed corresponding to the function of hydraulic gradient.

The results of experiment, in this stage, were summarized according to not a width of real flow through the minute gap but a width measured on the specimen surface. The fact that an outcome of discharge was obtained even at a measured width of 0.0 mm describes that the measured width did not represent the real-flow width.

While, for the calculation of permeability of a minute gap by the use of Equation 2, a cross-sectional area of flow, or an accurate width of flow, should be adopted. In this experiment, since it was difficult to measure the specimen for an accurate width of flow, 'an effective width of flow [t]' was calculated in each experimental case, on the assumption that when hydraulic gradient is very small and flow is perfectly laminar flow, the permeability of a minute gap may be expressed by Equation 1. The results of calculation are shown in Figure 4. From this figure, it can be seen that although a proportional relationship is observed between measured widths and 'effective widths of

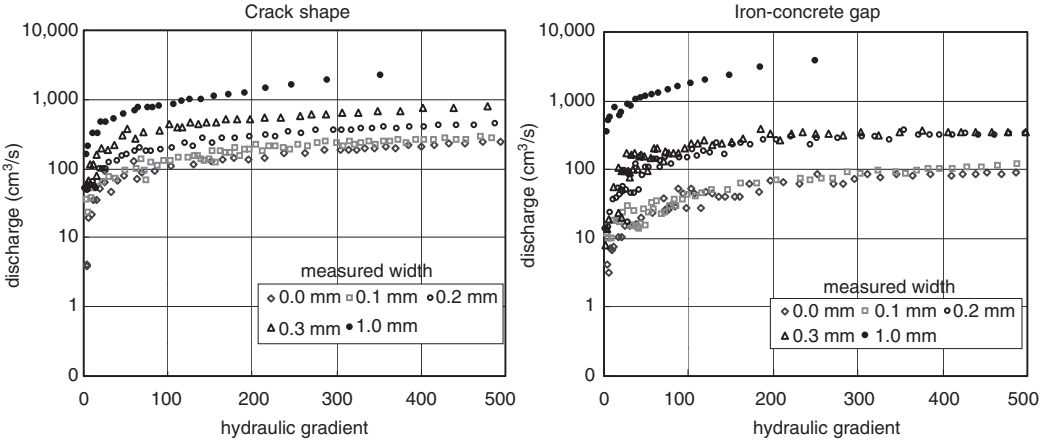


Figure 3. The relationship between the hydraulic gradient and seepage discharge inside the minute gap.

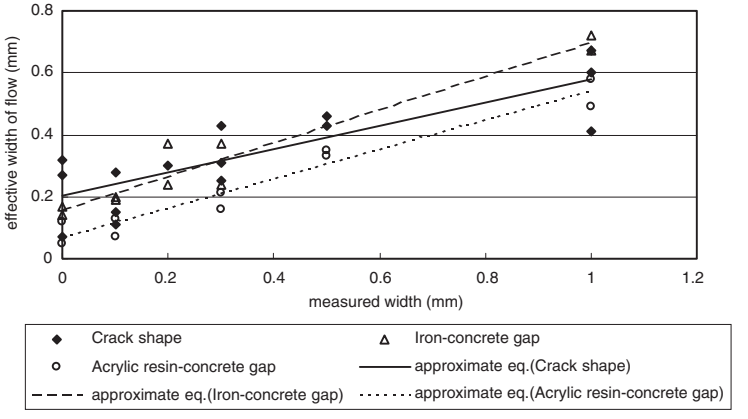


Figure 4. Relationship between measured width and 'effective width of flow' on minute gap.

Copyright © 2003 Swets & Zeitlinger B.V., Lisse, The Netherlands

flow' on minute gaps, the values were underestimated when measured widths were small and overestimated when large. Furthermore, the shape of minute gaps made differences between measured widths and widths of flow and, in case of crack shape, there was only a low correlation between them.

Figure 5 illustrates the relationship between permeability and hydraulic gradient, which was obtained through the calculation using 'effective widths of flow.' Based on this figure, the following were pointed out:

1) Depending on the magnitude of hydraulic gradient, the value of permeability becomes smaller by an order of magnitude and more, in comparison with that when seepage flow is laminar flow.
2) In the vicinity of the value of hydraulic gradient = 50, a point of inflection for the gradient of permeability is observed.
3) Changes in permeability become greater as 'an effective width of flow' becomes larger.

4 FORMULATION OF EXPERIMENTAL RESULTS

In order to make the relationship between hydraulic gradient and permeability obtained from the experiment applicable to seepage analysis and others, it was necessary for it to be formulated. So we made the correlation analysis between these factors. Table 2 shows an equation to calculate the value of permeability of a minute gap. The formulation of this relationship was implemented by the use of an approximation method. As a result, it was made clear that the value of hydraulic gradient: $I = 50$ served as a boundary point across which a different equation needed to be applied for minute gaps even with the same shape. The point to bear in mind is that these equations were verified only when the values of hydraulic gradient were relatively large. In addition, in respect to their application, 'an effective width of flow [t]' should be used; therefore, care needs to be devoted in adopting a measured width of a minute gap.

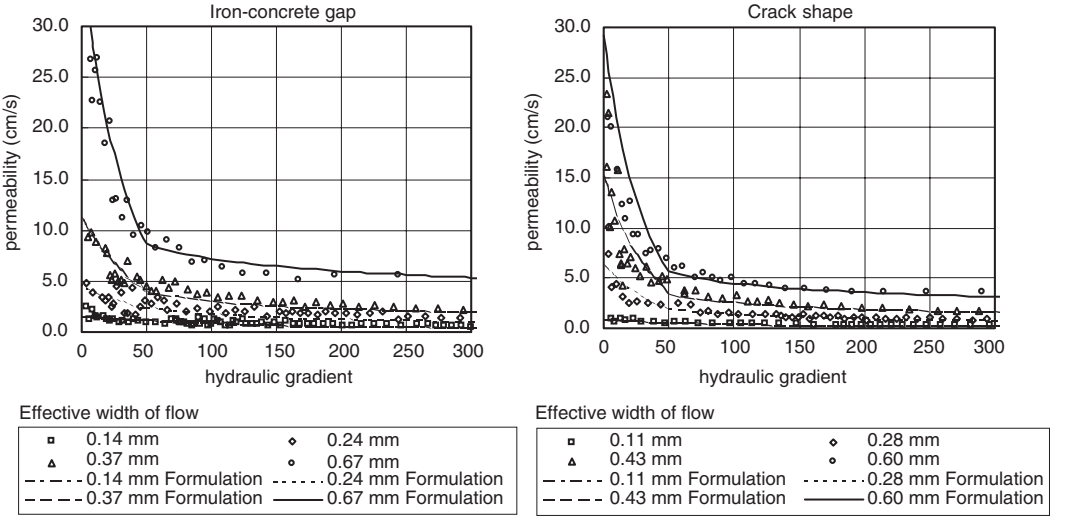


Figure 5. The relationship between permeability and hydraulic gradient.

Table 2. Equation to calculate the value of permeability of a minute gap.

	Equation	X=	A	B	C	D
Crack shape	$I \leqq X \quad K=Ae^{-BI}$	50	$\frac{A}{100} = \frac{\gamma_w \times (t/100)^2}{12\mu}$	B=0.0136Ln(t)+0.071	C=7.96Ln(t)+42.3	D=−5.1t+0.63
Iron-concrete gap	$I \geqq X \quad K=C\,I^{-D}$	50		B=0.015Ln(t)+0.07	C=11Ln(t)+55	D=−4t+0.54
Acrylic Resin concrete gap		50		B=0.0067Ln(t)+0.039	C=1580t−13.1	D=−1.8t+0.64

γ_w=density; μ=coefficient of viscosity of fluid; t=effective width of flow; I=hydraulic gradient; and K=permeability.

Copyright © 2003 Swets & Zeitlinger B.V., Lisse, The Netherlands

Furthermore, for the verification of the applicability of this formula, a large cylindrical model with a known width was built and a permeability experiment was conducted. And the results were compared with the results of the groundwater simulation performed by the use of the analysis codes, in which the relationship between hydraulic gradient and permeability had been built. A full detail regarding the experiment and analysis will be given some other time, but satisfactory consistency has been obtained.

5 CONCLUSION

The author and others have built permeability test equipment, which allows large hydraulic gradient to be involved, and conducted a permeability experiment for a minute gap. The findings are shown as follows:

1) Under the condition of large hydraulic gradient, it was verified experimentally that the increments of hydraulic gradient and discharge were not represented in such a proportional relationship as Darcy's Law defined.
2) It was found that there was difference between a width measured on the specimen surface and 'an effective width of flow'. There are some methods to measure the surface width. But to establish a measurement method for this 'effective width of flow' will be necessary in the future.
3) It was pointed out that when hydraulic gradient became larger than a certain value, permeability of a minute gap became smaller than that in a state of laminar flow by an order of magnitude and more.
4) It was gotten the experimental formula for permeability of a minute gap when hydraulic gradient was relatively large. It is used the hydraulic gradient and 'an effective width of flow' as parameters.

REFERENCES

Ang, A.H-S. & Tang, W.H. 1977. *Permeability Concepts in Engineering Planning and Design*. Tokyo: Maruzen.

Sato, K. & Iwasa, Y. 2002. *Groundwater hydraulics*. Tokyo: Maruzen.

Yoden, Y., Ashida, Y. & Matsui, N. 2001. *The experimental studies about the permeability of the minute gap under the high hydraulic gradient*. The proceeding of the 56th JSCE Annual Meeting: 478–479.

Copyright © 2003 Swets & Zeitlinger B.V., Lisse, The Netherlands

The effect of underground liquefied petroleum gas storage base construction to the surface oil-refinery complex facilities at Kurashiki

J. Oriyama & T. Otake
Japan National Oil Corporation, Tokyo, Japan

K. Taniuchi
Japan LPG Storage Co., Ltd, Kurashiki City, Okayama Pref., Japan

T. Yamaishi
Nikko Exploration and Development Co., Ltd, Tokyo, Japan

ABSTRACT: A national storage base capable of storing 400,000 tons of liquefied propane in underground storage caverns with water-sealing system is being planned at Kurashiki City, Okayama Prefecture. This storage base will be constructed underneath the surface facilities of an oil-refinery. Therefore it will be absolutely necessary to secure the safety of the refinery during construction and operating the base. One of the serious hazards to the surface structures is land subsidence caused by the change of the groundwater level. A 3-dimensional hydrological and hydrogeological simulation model incorporating geologic and metrological data of the area was constructed and groundwater level changes were analyzed by unsteady-state 3-dimensional groundwater flow simulator incorporating the program for construction and operation of the underground storage facility. Land subsidence of the area was examined on the basis of these results. Countermeasures for preventing the lowering of groundwater level and the system for groundwater level monitoring are also discussed.

1 OUTLINE OF NATIONAL PETROLEUM GAS STORAGE PROGRAM

In order to attain stable supply of LP gas, the national stockpiling system was established in 1994 in accordance with the Petroleum Stockpiling Law. The objective is to improve the stockpiling level besides the private legal stockpiling corresponding to the amount imported in 50 days. The project is now being promoted to achieve the national LP gas storage of 1,500,000 tons by fiscal year 2010.

JNOC (Japan National Oil Corporation) selected five sites (the Nanao site, Ishikawa Prefecture, Fukushima site, Nagasaki Prefecture, Namikata site, Ehime Prefecture, Kurashiki site, Okayama Prefecture, and Kamisu site, Ibaraki Prefecture) for this project.

Of the above five sites, the Kurashiki site is located underneath the surface facilities of an oil refinery complex, and thus particular care needs to be taken during the construction of underground storage base. In this paper, the effects of the petroleum gas storage base construction to the surface facilities are reported.

2 TOPOGRAPHY AND GEOLOGY OF THE KURASHIKI SITE

2.1 *Topography of the Kurashiki site*

The Kurashiki site is located at the western foot of the Kojima Peninsula, the southern part of Okayama Prefecture, and it is in a vast reclaimed land (N-S 7 km, E-W 6 km, and elevation about 5 m) toward the Mizushima sea, and is directly under Japan Energy Co. Ltd., Mizushima Oil-refinery (hereafter, “surface facilities”). Figure 1 shows a map of the vicinity of the Kurashiki site.

To the east of reclaimed land beyond the Yobimatsu waterway, mountain range of 200–250 m in elevation extends in the N-S direction in Kojima Peninsula. The seabed topography of Mizushima port surrounding the Kurashiki site is comparatively gentle with depth of about 10–20 m to the sea of Mizushima which lies about 3 km to the south-southwest, and thick sediments are distributed on the seabed. It is inferred that a widespread shoal or tidal flats existed before reclamation.

Copyright © 2003 Swets & Zeitlinger B.V., Lisse, The Netherlands

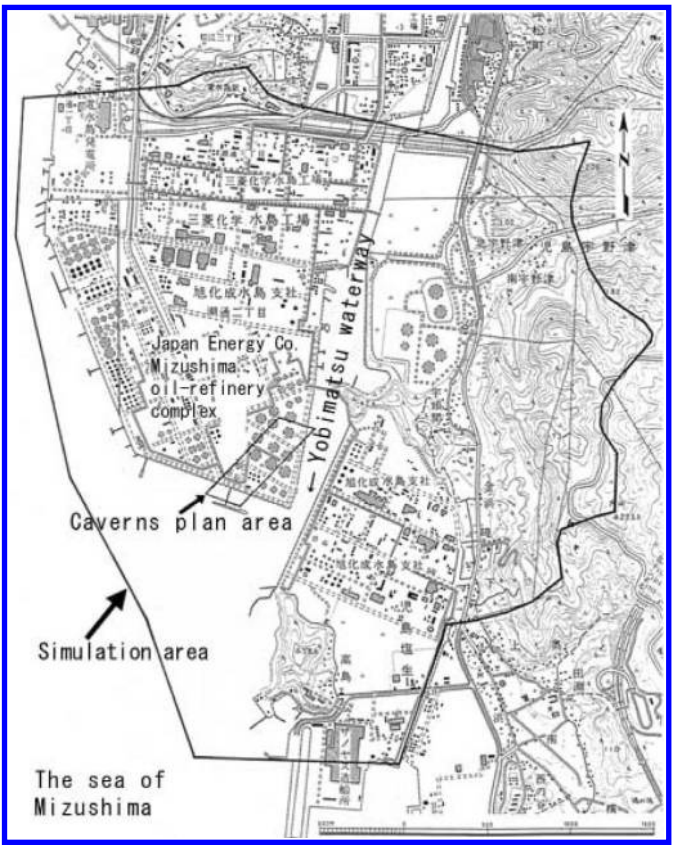


Figure 1. Map around Kurashiki site.

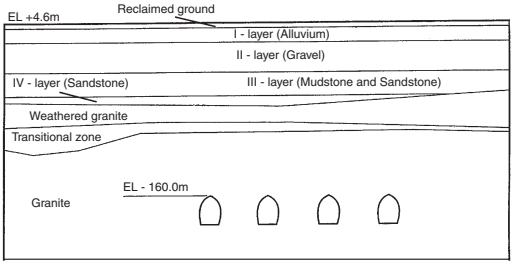


Figure 2. Geological section of the Kurashiki site.

2.2 *Geology of the Kurashiki site*

A typical geological section of the site is shown in Figure 2. Fresh Cretaceous granite occurs in depth zone deeper than 90–110 m. Thick sediment layers are developed overlying granite, and the reclaimed land is distributed over the sediments. The sediment layers are divided from upper into I-layer (alluvium), II-layer (gravel), III-layer (mudstone and sandstone), and IV-layer (sandstone). The weathered part (about 70–90 m deep) and transitional zone (about 90–100 m deep) are generally developed in the upper part of granite.

By detailed investigation, considerable fresh and solid rock was widely recognized in the eastern region where the caverns are planned to be situated.

3 OUTLINE OF THE KURASHIKI BASE

3.1 *Facilities*

The cavern concept is shown in Figure 3 and the cross section of the caverns is shown in Figure 4. The rock caverns will be constructed in granite about 165 m below the surface facilities. The size of each cavern is 18 m wide, 22 m high, and 640 m long.

A total of 400,000 tons of propane will be stored in the four caverns. The water sealing tunnels and the water sealing boreholes will be set up to supply water to the rock. They will stabilize the groundwater pressure in the upper part of caverns.

Copyright © 2003 Swets & Zeitlinger B.V., Lisse, The Netherlands

3.2 *Construction*

Table 1 shows the outline of construction process. The underground excavation at the Kurashiki site will start from construction of access tunnel from the opposite bank beyond the waterway. The access tunnel about 2.1 km in total length will be excavated down to −187 m. Side by side with this excavation, water sealing access tunnels and water sealing tunnels will branch out from the access tunnel, and water sealing holes will be drilled, after that, the rock caverns will be excavated. The NATM (New Austrian Tunneling Method) will be used for the excavation of these tunnels.

Before the excavation of caverns, water will be supplied to the surrounding rock by the water sealing facilities consisting of the water seal tunnels and the water sealing boreholes to reduce the lowering of groundwater level during excavation. When access tunnel, water sealing tunnels, and vertical shafts are filled with water, the basic equipment is completed. After general trial and safety confirmation of facilities, LP gas will be charged into caverns.

It is expected that peripheral groundwater level will lower during excavation of caverns. With the lowering of the water level, the possibility of subsidence due to compaction of sediments might affect the surface facilities.

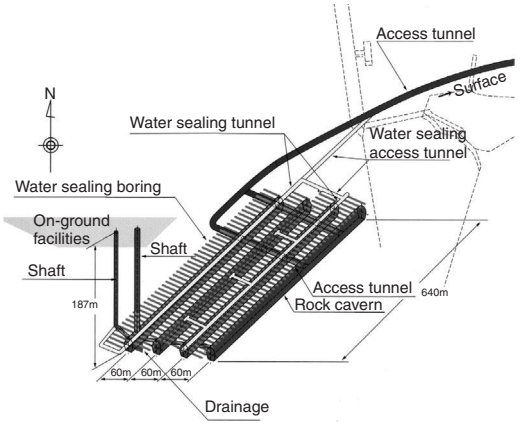


Figure 3. The general concept of caverns.

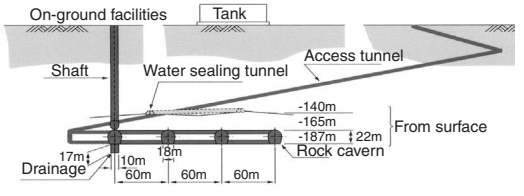


Figure 4. The cross section of caverns.

3.3 *Outline of the surface facilities (Mizushima Oil-refinery)*

Japan Energy, Mizushima Oil-refinery started its operation in 1961, and is now one of the largest domestic oil refineries with a capacity to process 200,000 barrels of crude oil per day. The oil refinery site is about 1,650,000 m^2. Number of facilities is about 30 refining units on-site and 200 tanks or more (total 3,400,000 KL) off-site.

After ground improvement of the on-site area, most of the facilities are supported by pilings to the sand/gravel layer. On the other hand, the tanks are designed to rest directly on the ground in the off-site area. Because soft 12–15 m-thick silt layer exists in the subsurface zone, ground strength was artificially increased to endure tank load by accelerating compaction and subsidence by sand-drain and preloading method.

Since tanks were constructed, subsidence has been measured annually. There is no increase in subsidence now, though some subsidence was observed immediately after the tank construction.

4 EFFECTS TO THE SURFACE FACILITIES

Figure 5 shows a flowchart for investigating the influence of subsidence by compaction due to the lowering of groundwater level.

4.1 *Estimation of the lowering of groundwater level as a result of cavern excavation*

A 3-dimensional analysis model was constructed from geologic, hydrologic, and hydrogeologic data

Table 1. Timetable of main constructions at the Kurashiki site.

Year	2001	2002	2003	2004	2005	2006	2007	2008	2009
Development of reclamation									
Access tunnel									
Propane caverns*									
Surface facilities									
General trial operation									

* Propane caverns include constructions of plumbing shaft, water sealing tunnel, and plumbing

Copyright © 2003 Swets & Zeitlinger B.V., Lisse, The Netherlands

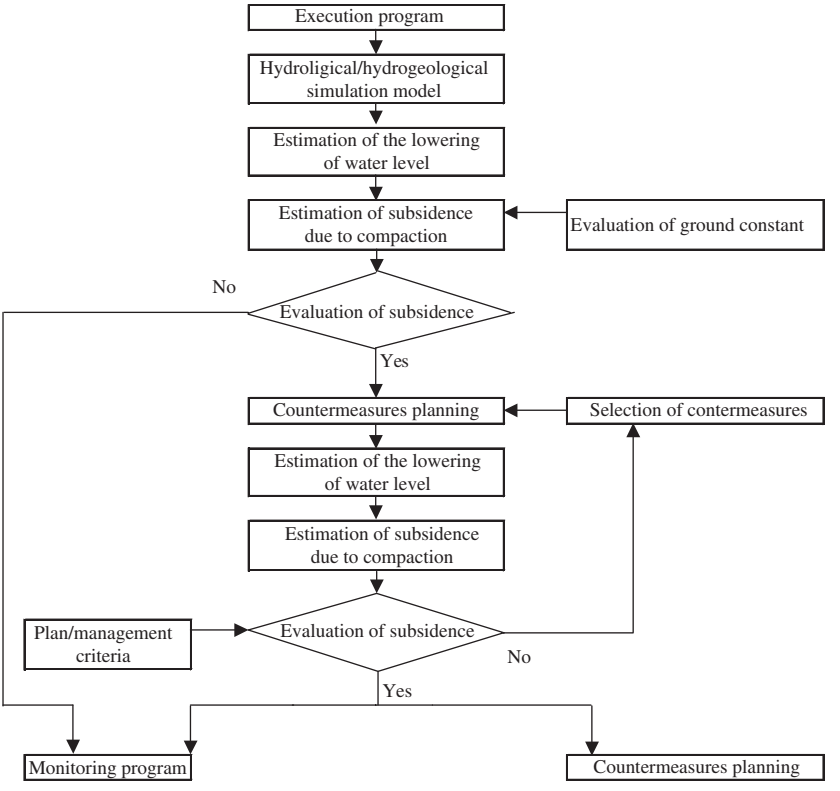


Figure 5. Flowchart showing evaluation and investigation of subsidence due to compaction by the lowering of groundwater level.

acquired and accumulated in the past. Unsteady-state 3-dimensional groundwater flow analysis was carried out incorporating the planned construction and operation process (excavation of caverns and tunnels, supply of sealing water, gas-in etc.), and time-series distribution of water level lowering was estimated.

4.1.1 *Outline of unsteady-state 3-dimensional groundwater flow analysis*

The unsteady-state 3-dimensional groundwater flow analysis was carried out using the surface-subsurface-coupled, 2-component 2-phase, 3-dimension fluid flow simulator, GETFLOWS (developed by Hiroyuki Tosaka, Assistant Professor, Department of Geosystem Engineering, Graduate School of Engineering, The University of Tokyo) (Tosaka et al. 1996).

By this simulator, it is possible to analyze not only the 2-component, 2-phase air-water flows in subsurface zones, but also the behavior of the surface-subsurface-coupled, 2-component, 2-phase fluids (air-water) taking surface/river flow into consideration at the same time. A general groundwater flow analysis (saturation/unsaturation analysis) is a simplified 1-component, pseudo-2-phase, simulation only for the underground zone ignoring the movement of air. On the other hand, by this simulator, various phenomena concerning the flow can be expressed more adequately.

The fundamental equation is the Darcy's law and the law of conservation of mass concerning 2-component, 2-phase compressibility fluid system of water and air. The unknown quantities are air-phase pressure and water saturation ratio.

For surface flow, the 2-phase nonlinear Darcy flow was put into the frame by converting Manning surface flow velocity formula into the same form to Darcy's law.

As a result, the surface/subsurface water circulation process (rainfall, surface flow, and underground infiltration) is consistently modeled, and this process is calculated at the same time in the simulation system.

4.1.2 *Three-dimensional analysis model*

The target area for simulation analysis is 11.1 km^2, N-S 4.2 km, E-W 3.8 km. It is centered on the planned underground cavern site (Figure 1). As the analytical boundaries, the ridge line in eastern/northern side and the sea or the waterway in western/southern side were used.

Copyright © 2003 Swets & Zeitlinger B.V., Lisse, The Netherlands

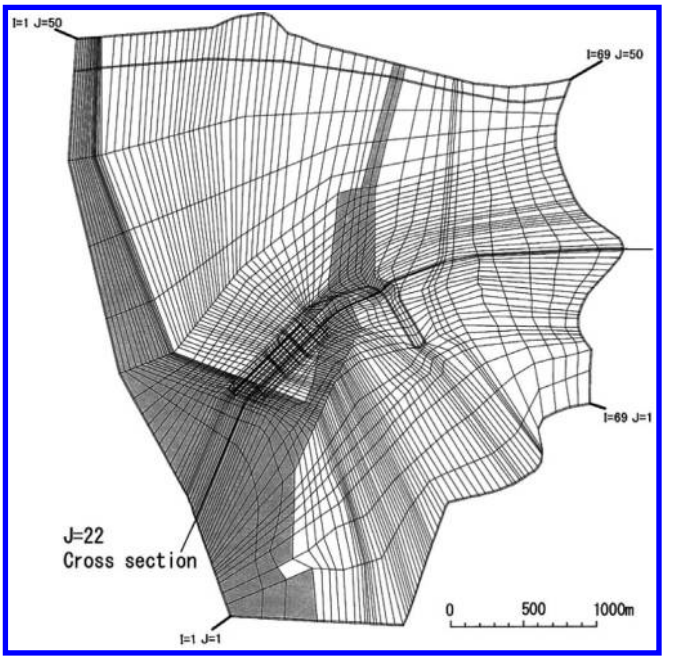


Figure 6. Lateral grids of the simulation model.

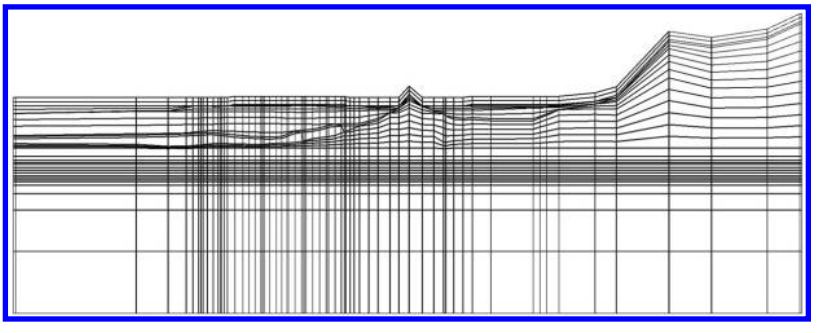


Figure 7. Vertical grids of the simulation model.

The 50 m grid data of the Geographical Survey Institute was used for the altitude of the land part, and 1/10,000 nautical chart of the Japan Coast Guard for the seafloor. The average tide level of Mizushima port, EL+1.9 m, was used for the sea surface.

The area division of the 3-dimensional model was made so that it would precisely express geographical and geological structures, which are assumed to have a large effect on groundwater flow. And caverns and the tunnels were calculated to agree with their real size. A plane area (Figure 6) is divided into 69 grids in the E-W direction and 48 grids in the N-S direction. The number of grids on the plane is 3,450.

The direction of depth (Figure 7) is divided into 31 grids. The area from the lower limit, EL–500 m, to the surface was divided into 29 layers, and two layers further (10 m in the layer thickness) were added on the ground level as an atmospheric layer (area to analyze the surface flow). Sediments layers on granite were divided along the geological boundary. The number of total grids in analysis models is 106,950.

4.1.3 *Layout of geological classification*

A 3-dimensional geological model was made from the results of previous investigation. Geological classification is nine as reclaimed ground, silt layer, gravel, alternation of sandstone and mudstone layer, sandstone layer, weathered granite, granite transitional zone, fresh granite and the sea. The geological classification was allocated for individual grids, and physical property values such as permeability were provided the geological classification.

Copyright © 2003 Swets & Zeitlinger B.V., Lisse, The Netherlands

4.1.4 *Analytical conditions*

Permeability and porosity (Table 2) were acquired from the results of previous permeability tests, laboratory soil tests, and laboratory rock tests. The waterway/seaside boundary corresponds to a concrete sidewall, and permeability of 1.0×10^{-8} cm/s was used for the sidewall on reclaimed ground.

Relationship between water saturation ratio and relative permeability ratio [water – air], and relationship between water saturation ratio and capillary pressure, were given as an unsaturation characteristic (Yamaishi et al. 1998).

Regarding recharge, rainfall minus evaporation was given on the ground level (secondarily layer in an atmospheric layer) as influx. The amount of underground infiltration is automatically calculated in simulating. The amount of drainage from the outlet on reclaimed ground was similarly excluded. The amount of rainfall, evaporation, and drainage were estimated referring to the previous hydrological investigation (Table 3).

As the lateral boundary condition, the sea boundary was assumed an open boundary with hydrostatic pressure of average tide level EL+1.9 m, and the ridge boundary a closed boundary with neither inflow nor outflow of water. The river boundary was set to have only outflow from the surface. In a vertical direction, the first atmospheric layer (K = 1) was fixed to one atmospheric pressure as the boundary condition, and the bottom a boundary without inflow or outflow of water. Hydrostatic pressure from EL+1.9 m was given to the grids corresponding to the sea in the model.

Table 2. List of permeability and porosity.

Geological classification	Permeability (cm/s)	Porosity (%)
Reclaimed ground	1.8×10^{-3}	40
Silt layer	5.3×10^{-6}	59
Gravel layer	3.7×10^{-3}	20
Alternation of sandstone and mudstone		38
Horizontal	8.4×10^{-4}	
Vertical	2.9×10^{-6}	
Sandstone layer	6.0×10^{-4}	29
Weathered granite	2.6×10^{-4}	19
Transitional zone	1.3×10^{-5}	7
Fresh granite	3.5×10^{-5}	2

4.1.5 *Initializing*

To reproduce the natural surface/subsurface flow around caverns, the initializing simulation was done under the following preconditions.

- The groundwater level in the subsurface zone around the planned cavern area is about EL3 m.
- The groundwater level in the observation hole is referred to.
- The coefficient of Manning's roughness is used as a parameter for water level matching.

The initializing simulation was carried out for up to 40,000 days to acquire sufficient equilibrium, the coefficient of Manning's roughness was corrected by trial & error, and the water level was matched. As a result of the analysis, the coefficient of Manning's roughness was finally assumed to 10 $m^{-1/3}$ s on the mountain side, 1 $m^{-1/3}$ s on reclaimed ground.

4.1.6 *Simulation of the construction process*

Table 4 shows construction and operation process incorporated in this simulation. The calculation time indicated in Table 4 is the accumulation days in which the construction start day is 0.

4.1.7 *Estimation of subsidence due to compaction by the decrease of hydraulic head*

The change of hydraulic head in the silt layer and in upper and lower layers (reclaimed ground and gravel layer) is shown in Figure 8 (central part of caverns shown). The silt bed is the layer which will be compacted and cause subsidence, and the other two layers affect these phenomena. The hydraulic head decrease in the order of; reclaimed ground, silt layer, and gravel layer throughout the period. The hydraulic head value of the silt layer is in-between those of the reclaimed ground and gravel layer. The decrease of hydraulic head of the reclaimed ground is less than half of that of gravel. Hydraulic head tends to decrease notably at about the time the access tunnel passes under waterway (About 600 days).

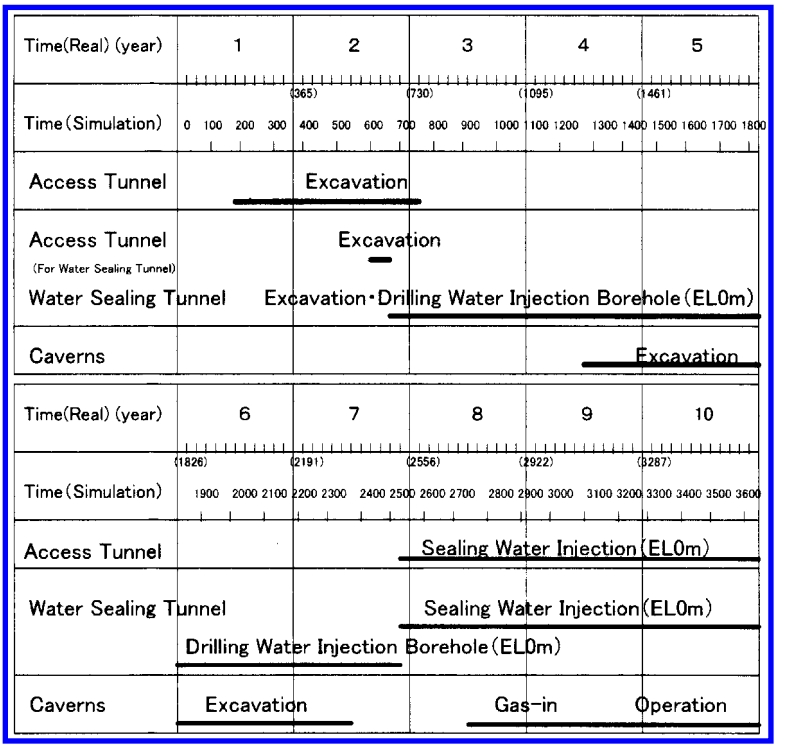
Figure 9(a) shows the transition of the decrease of hydraulic head in the gravel layer (against the initial value). The decrease of water level in the gravel layer

Table 3. List of rainfall and evaporation.

	Rainfall (%) (1,183 mm/year)	Evaporation + draining (%)	Influx into atmosphere layer on surface (%)
Mountain side	100	65 (65 + 0)	35 (1.13 mm/day)
Reclaimed ground	100	90 (65 + 25)	10 (0.32 mm/day)

Copyright © 2003 Swets & Zeitlinger B.V., Lisse, The Netherlands

Table 4. Construction and operation schedule.



progresses concentrically centered at the northern part of caverns. When excavation of the water sealing tunnel is completed (1,277 days), the decrease of the head becomes 1.7 m. It decreases further when excavation of caverns starts and the maximum decrease of hydraulic head is 2.6 m after excavation of caverns is completed (2,540 days). However, the hydraulic head starts to rise when the water sealing tunnel and the access tunnel are filled with water, and it recovers further by pressure increase after gas-in. During operation, the value stabilizes at the conditions after the gas-in is completed (the maximum lowering is 0.6 m in one year after the start of operation).

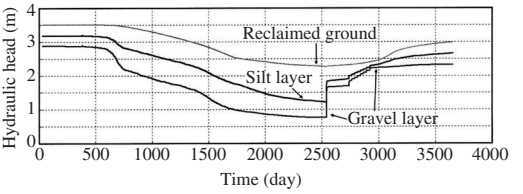


Figure 8. History of hydraulic head.

4.2 *Estimation of subsidence due to compaction by the lowering of groundwater level*

The geological units from surface downward are as follows. The silt is the layer which is compacted by the decrease of hydraulic head and thus causes subsidence.

Reclaimed ground (about 5 m thick)
Silt layer (about 8–16 m thick)
Gravel layer (about 25–30 m thick).

The primary factor for compaction subsidence of the silt layer is the decrease of hydraulic head in the upper and lower layers, the effective stress of silt layer increases by the decrease of water level, and the compaction subsidence is caused.

The amount of compaction subsidence was calculated by 1-dimensional compaction theory of Terzaghi, using distribution of the hydraulic head decrease in the reclaimed ground and silt layer from result of the unsteady-state 3-dimensional groundwater flow analysis and the thickness distribution of the silt layer. The load due to the hydraulic head decrease was arrived at simply by analogy to the gradual increase load such as banking, acquired the elapsed time, and reflected the degree of compaction.

From the calculation of compaction subsidence, it was evaluated that harmful subsidence affecting

Copyright © 2003 Swets & Zeitlinger B.V., Lisse, The Netherlands



Figure 9. Distribution of hydraulic head decrease in gravel layer. (a) No countermeasures constructions. (b) Countermeasures constructions (3 water injection holes).

the surface facilities would not occur when cavern excavation was completed.

5 PREVENTION OF THE LOWERING OF GROUNDWATER LEVEL

The water injection method by vertical boreholes was adopted as a measure to prevent the lowering of groundwater, and unsteady-state 3-dimensional groundwater flow analysis including the water injection method was carried out, and the effect of the method was evaluated.

Specifications of water injection method were assumed to be as follows:

- Specifications of water injection hole: drilled vertically from surface to the lower zone of gravel layer with 30 cm hole diameter, and water injection only to the gravel layer.
- Water injection level: ground level (EL4.5 m).

Copyright © 2003 Swets & Zeitlinger B.V., Lisse, The Netherlands

- Start of water injection: when excavation of access tunnel passes under the Yobimatsu waterway.

Figure 9(b) shows the distribution of hydraulic head decrease in gravel layer after the cavern excavation completion in case of three water injection hole. The maximum hydraulic head decrease was calculated to be 0.8 m, and a total of 660 m^3/day to be injected from the injection hole at this time.

6 OBSERVATION SYSTEM DURING CONSTRUCTION AND OPERATION

Distribution of groundwater level lowering caused by construction of underground base was continuously monitored by the unsteady-state 3-dimensional groundwater flow analysis, and conditions regarding compaction subsidence were also shown. From the results of the above, monitoring program of groundwater level and subsidence during construction and operation (specification and arrangement of observation points) are established.

As a system for management, the management level is provided, and countermeasures are carried out according to the management level. Based on the monitoring and analysis, the management level will be evaluated from current state and estimation of future. The management criteria for determining the management level will be established in accordance with the legislation, surface facilities, etc.

7 CONCLUSIONS

Precise 3-dimensional analysis model was constructed based on geological features, hydrological and hydrogeological data accumulated in the past in order to evaluate the effect of the lowering of groundwater level by construction of LP gas underground rock caverns on the surface facilities. Unsteady-state 3-dimensional groundwater flow analysis incorporating construction and the operation process was carried out, and compaction subsidence was estimated by continuous analysis of hydraulic head decrease distribution. As a result, it was proved that a harmful subsidence would not occur. The effect of prevention countermeasures the groundwater lowering was also estimated by this analysis, and it was concluded that the required effect should be expected. Based on this result, the monitoring program of groundwater level and subsidence will be established, and the management of construction and operation will be managed accordingly.

REFERENCES

Tosaka, H., Kojima, K., Miki, A. & Chino, T. 1996. Numerical simulation of surface-subsurface-coupled, 2-phase, 3-dimensional fluid behavior, Journal of Groundwater Hydrology, 38(4): 253–267.

Yamaishi, T., Kobayashi, H., Tani, T., Okamoto, A., Tosaka, H. & Kojima, K. 1998. Complete numerical modeling and history matching of surface-subsurface-coupled fluid behavior around underground oil storage plant, Journal of Groundwater Hydrology, 40(2): 167–183.

Copyright © 2003 Swets & Zeitlinger B.V., Lisse, The Netherlands

Geochemical approaches to understanding a deep groundwater flow system in the Tono area, Gifu-ken, Japan

R. Metcalfe, K. Hama, K. Amano, T. Iwatsuki, H. Saegusa
Japan Nuclear Cycle Development Institute, Tono Geoscience Center, Toki, Japan

ABSTRACT: During a study of the Cretaceous Toki Granite near Tono, central Japan, generic geochemical approaches for understanding deep (to c. 1000 m) fresh groundwater flow are being evaluated. Methods have been developed to sample groundwaters with little contamination, allowing natural chemical variations to be determined. Waters nearer to recharge areas are relatively Ca-rich and HCO_3-dominated. Shallower waters also have relatively low pH. Waters that are deeper and further from recharge areas are generally more Na- and F-rich and of higher pH. At locations thought to be furthest from recharge, Na-Cl waters with TDS > 1000 mg/l occur. Radiocarbon data from groundwater and fracture-filling calcite suggest that fresh water penetrated to depths of around 1000 m within the last 50,000 years. The study shows that in the Tono area geochemical data of sufficient quality to constrain models for deep fresh groundwater flow can be obtained with present methods.

1 INTRODUCTION

Internationally, many investigations of deep groundwater flow (several hundred metres to >1000 m) aim to model past flow patterns and fluxes over long time-scales (a million years or more if considering deep geological disposal of certain radioactive wastes). These models may then be extended to future flow. However, a flow system's current state may differ from past states and may not be at equilibrium with present driving forces (i.e. be transient). Therefore, it is desirable that numerical flow models are constrained using geochemical information from groundwater and minerals in addition to hydrogeological data such as hydraulic conductivities and groundwater heads. The geochemical data enable interpretations based on hydrogeological data to be checked and allow a flow history to be deduced more confidently than can be done from physical hydrogeological measurements alone. Geochemistry has been used in this way in several countries (Nuclear Energy Agency, 1999). However, these investigations, have generally focused on saline groundwater (Total Dissolved Solids, TDS > 10,000 mg/l) and brine (TDS > 100,000 mg/l). Geochemistry has been less used to understand deep fresh and brackish groundwater flow (TDS $\ll$ 10,000 mg/l). Consequently there remain uncertainties about how best to apply geochemical methods developed mainly for saline groundwaters, to freshwater systems.

Here, we describe generic research being undertaken by the Japan Nuclear Cycle Development Institute (JNC) at Tono, Gifu-ken, central Japan, that is helping to address these uncertainties.

2 STUDY AREA

Miocene to Pleistocene sedimentary rocks lie on the eroded surface of the late Cretaceous Toki Granite (Fig.1). The sedimentary rocks are mostly almost horizontally-bedded sandstones, siltstones, mudstones and conglomerates (Yusa et al. 1993). The Miocene rocks form the Mizunami Group and bottom to top consists of three formations separated by unconformities: the Toki Formation, the Akeyo Formation and the Oidawara Formation. The Toki Formation is mainly a freshwater lacustrine deposit. In contrast, the Akeyo Formation represents brackish to shallow marine sedimentation, while the overlying Oidawara Formation is a deeper water marine deposit. These Miocene rocks are unconformably overlain by the Pliocene to Pleistocene Seto Group which was deposited within a fluviatile environment.

In the 1970's, drilling was done to establish the limits of the Tono uranium deposit, which occurs near the base of the sedimentary rocks. Later an exploratory mine, Tono Mine, was developed. However, the deposit was found to be of sub-economic grade and the mine was not worked commercially. Instead, the mine became a research facility in which generic methods for characterizing deep underground environments are being developed. These investigations have included

Copyright © 2003 Swets & Zeitlinger B.V., Lisse, The Netherlands

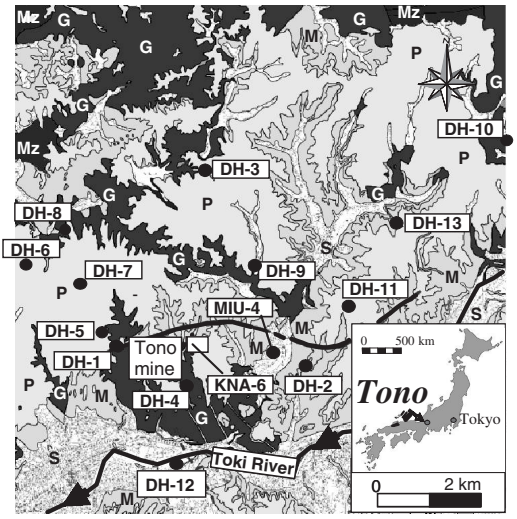


Figure 1. Study area showing selected boreholes. Mz = Mezozoic sedimentary rocks; P = Pliocene to Pleistocene; M = Miocene; G = Toki Granite.

characterization of the geochemical environment in the sedimentary tocks and the upper part of the Toki Granite. From the mid-1990s, a regional hydrogeology programme has investigated an area of 30 km × 30 km with Tono Mine near its centre. Deep (to c. 1000 m) boreholes have been drilled into the Toki Granite. Most recently, other studies have focused on the site of an underground research laboratory, the Mizunami Underground Research Laboratory (MIU) which is to be constructed near to the town of Mizunami.

3 METHODS

Some of the data used here have been reported previously elsewhere. Koide et al. (1996) and Iwatsuki et al. (2000) summarize hydrogeological data while Iwatsuki et al. (1995) and Iwatsuki & Yoshida (1999) describe variations in the major ion chemistry of the groundwaters. Radiocarbon data and stable carbon isotope data are detailed in Mizutani et al. (1992) and Iwatsuki et al. (2000, 2002). Here, these previously published data are reviewed and summarized together with halide and ^{36}Cl data that are reported for the first time.

Some boreholes drilled during the early uranium exploration studies were artesian and waters flowing naturally from these boreholes could be sampled at the surface. In the cases of the deep boreholes drilled more recently, the groundwaters were sampled from either multi-packer systems or from between double packers. The samples with the highest and/or known quality generally came from boreholes drilled during the regional hydrogeological programme and the MIU studies (Fig. 1).

Except in borehole DH-12, samples were obtained from the packed-off intervals, either by pumping to the surface or by using down-hole sampling apparatus. Parameters such as pH, Eh, pS, Electrical Conductivity (EC) and temperature were measured in surface flow-through cells or down-hole using a geochemical probe. In DH-12, the flow was artesian and samples could be produced at the surface without pumping. Unlike the earlier exploration boreholes however, these DH-12 samples came from well-constrained packed-off intervals.

The boreholes were typically drilled with fresh water dosed with a tracer, usually uranine, though Amino-G acid, Na-naphthionate and LiCl have also been used. The basic approach was usually to pump each test interval until the concentration of the tracer in the recovered water was less than 1% of the initial tracer concentration in the drilling fluid. The final sample was then analysed to obtain the composition of the in-situ, uncontaminated groundwater.

Common methods have been employed to analyse major, minor and trace constituents (Inductively Coupled Plasma Spectrometry, Ion Chromatography, colorimetric methods and Mass Spectrometry etc). Radiocarbon data have been obtained for selected samples either by beta counting (Mizutani et al. 1992) or by Accelarator Mass Spectrometry (Iwatsuki et al. 2001). Data for ^{36}Cl were obtained for a small number of groundwater samples by AMS at PRIMElab, University of Indiana, Perdue. The methods are described in Elmore et al. (1993).

Boreholes drilled during the regional hydrogeological investigations and MIU investigations were all cored. Rock core is also available for many of the earlier boreholes. Rock samples were taken from selected sections of core and subjected to a range of petrographical and geochemical investigations (Hama et al. 2002). Carbon and oxygen isotopic measurements were made on mineral separates (Iwatsuki et al. 2002).

4 RESULTS

By June 2001, 298 water compositions were available. Of these, 127 are for samples from boreholes connected with the generic research programme of JNC, or its predecessor, Power Reactor and Nuclear Fuel Development Corporation (PNC). Fifty eight of these compositions come from the most recent deep boreholes (DH-series, MIU-4 borehole; Fig. 1). There are additionally 57 groundwater compositions from the earlier uranium exploration boreholes.

Groundwater sampled to the north of the Toki River is all fresh and gives stable oxygen and hydrogen isotope analyses that plot near the meteoric water

Copyright © 2003 Swets & Zeitlinger B.V., Lisse, The Netherlands

Table 1. Summary of Cl data (mg/l), except Tono mine data.

Water	Minimum	Maximum	Mean	Number
Deep research boreholes, N of Toki River				
Rain	<1	2.06	N/A	18
Soil	0.54	6.14	1.96	30
River	1.00	4.00	1.74	48
Seto	4.00	3.00	3.50	2
Oidawara	1.00	2.99	2.05	5
Akeyo	0.85	3.73	1.66	9
T. Lignite (Upper)	1.11	8.40	3.08	7
T. Lignite (Lower)	0.72	4.57	2.22	12
T. Granite	0.63	19.20	4.01	50
Deep research boreholes, S of Toki River				
DH-12	52.60	175.00	98.32	6
Other waters				
U exploration boreholes	0.65	600.00	58.64	57
Spring	916.00	916.00	916.00	1

Table 2. Summary of F data (mg/l), except Tono Mine data.

Water	Minimum	Maximum	Mean	Number
Deep research boreholes, N of Toki River				
Rain	<0.02	0.04	N/A	18
Soil	0.02	0.37	0.09	30
River	<0.1	0.11	N/A	48
Seto	0.10	0.20	0.15	2
Oidawara	0.10	1.04	0.75	6
Akeyo	0.16	2.53	0.80	9
T. Lignite (Upper)	0.10	4.77	1.98	8
T. Lignite (Lower)	0.85	6.67	3.7	14
T. Granite	0.60	12.93	5.51	50
Deep research boreholes, S of Toki River				
DH-12	9.40	14.80	11.55	6
Other waters				
U exploration boreholes	0.04	20.90	8.64	57
Spring	7.30	7.30	7.30	1

line. Deeper groundwater generally has a higher pH than shallower water, though >200 m below ground level pH varies from c. 8 to c. 10, with no clear trend. Shallower groundwater is generally Ca-Na-HCO_3-dominated while deeper water tends to be more Na-HCO_3-dominated. In contrast, south of the Toki River deeper groundwater is Na-Cl dominated. Most data from this area are from the older uranium exploration boreholes. The artesian flow in many of these older boreholes means that depths from which sampled water originated are uncertain. However, in borehole DH-12, which was drilled in 2000 and in which sampling depths are well constrained, Na-Cl water occurred as shallow as 160 m, in the Toki Lignite Formation. Data for Cl, F and Br are summarized in Tables 1, 2 and 3 respectively. There is no correlation between F and Cl concentrations (Fig. 2), but Cl and Br concentrations are strongly correlated (Fig. 3). Unlike Cl and F, Br was not analyzed routinely in the earlier boreholes. There are only 31 Br concentrations above the detection limit (c. 0.02 to 0.1 mg/l), 27 of which are from the older uranium exploration boreholes.

In borehole DH-7, in the Toki Granite, the F-contents of groundwaters increase with respect to depth, but in other boreholes there is a less clear depth dependency (Fig. 4). Samples from DH-12 and MIU-4 had higher F than suggested by the depth-related trend interpolated among other samples.

The ^{36}Cl data were obtained for 11 samples in 3 localities and show clear differences from place to

Copyright © 2003 Swets & Zeitlinger B.V., Lisse, The Netherlands

Table 3. Summary of Br data (mg/l), except Tono mine data.

Water	Minimum	Maximum	Mean	Number
Deep research boreholes, N of Toki River				
Rain	N/R	N/R	N/A	0
Soil	N/R	N/R	N/A	0
River	N/R	N/R	N/A	0
Seto	N/R	N/R	N/A	0
Oidawara	<0.02	<0.02	<0.02	1
Akeyo	N/R	N/R	N/A	0
T. Lignite (Upper)	<0.02	<0.02	<0.02	1
T. Lignite (Lower)	<0.02	<0.1	N/A	2
T. Granite	<0.02	0.08	N/A	15
Deep research boreholes, S of Toki River				
DH-12	<0.2	0.37	N/A	6
Other waters				
U exploration boreholes	<0.02	1.09	N/A	55
Spring	2.20	N/R	N/A	1

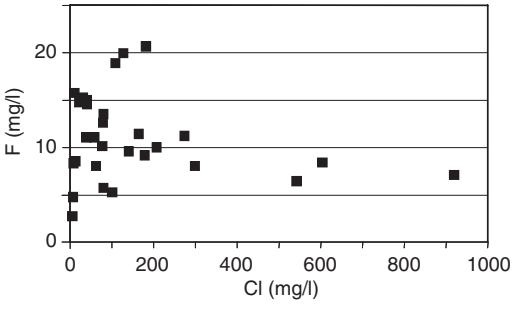


Figure 2. F versus Cl for groundwater from the Toki Granite.

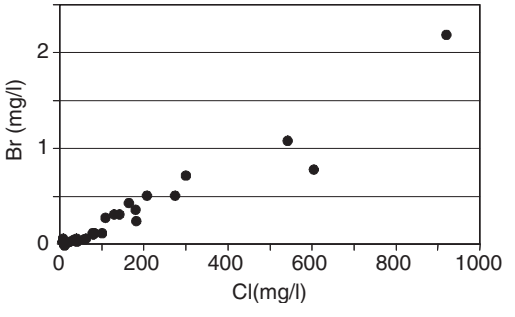


Figure 3. Br versus Cl for groundwater from the Toki Granite.

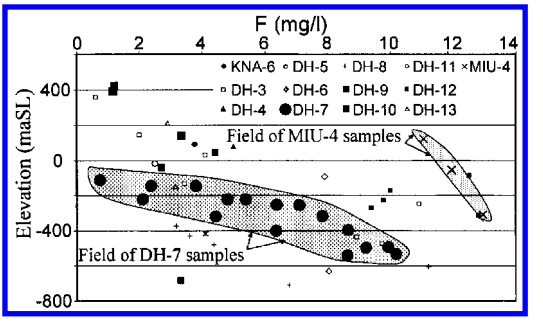


Figure 4. F concentrations versus elevation for groundwaters for the granite.

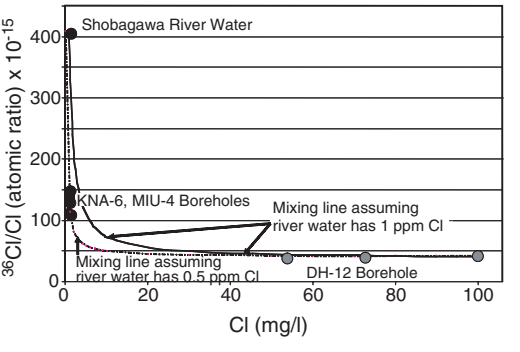


Figure 5. ^{36}Cl/Cl versus Cl concentrations for selected groundwater samples.

place (Fig. 5). River water had the highest ^{36}Cl/Cl (c. 400×10^{-15}). Lower ^{36}Cl/Cl values were obtained from boreholes located nearer to the recharge area (c. 140×10^{-15}) whereas the lowest ^{36}Cl/Cl values were obtained from boreholes nearer to the groundwater discharge area (c. 40×10^{-15}).

Radiocarbon data suggest that groundwater from near the base of the sedimentary rocks around Tono Mine were recharged about 13,000 years ago. Radiocarbon was also detected in fracture-filling calcite

Copyright © 2003 Swets & Zeitlinger B.V., Lisse, The Netherlands

in the Toki Granite suggesting that even as deep as 1000 m, some calcite has been precipitated within the last 50,000 years. Stable carbon and oxygen isotopic data for other fracture-filling calcite samples suggest that some calcite precipitated from seawater. However, these samples were too small to analyse for ^{14}C and their ages could not be constrained.

5 DISCUSSION

5.1 *Hydrogeological setting*

The hydrogeological data are almost all from the north of the Toki River. These data show that flow is topographically-driven, deeper water flowing generally from high ground in the north-east towards the Toki river in the south-west. Shallower flow is more variable, being controlled by local topography. It is likely that to the south of the river, groundwater flow will similarly be driven mainly by topographical gradients, but in this case from high ground in the south, northwards towards the river.

It is uncertain which of these two flow systems dominates in the vicinity of DH-12. However, regardless of whether or not the flow systems are different, DH-12 and the nearby uranium exploration boreholes are probably much further from recharge zones than more northerly boreholes.

5.2 *Br and Cl data*

Marine waters were present in the Tono area in the past, because some of the sedimentary rocks are marine in origin. Stable carbon isotope data from fracture-lining calcite in the granite suggest that this water may have penetrated deep into the granite (Iwatsuki et al. 2002). Therefore, one possibility is that the Na-Cl dominated salinity near the Toki River represents a component of residual marine water. The Br and Cl data can be used test this hypothesis. Ratios of these solutes can distinguish salinity of marine origin (Br/Cl mass ratio $3.5\,c \times 10^{-3}$) from salinity that has other sources (Hanor, 1994).

The strong correlation between Br and Cl concentrations suggests a common origin for these solutes (Fig. 3). Experience elsewhere suggests that a minimum 2σ precision on the Br/Cl ratios at the observed Br levels would be $\pm 10\%$. At this precision all except the most dilute samples would have ratios significantly less than seawater. Support for this conclusion is given by two relatively high-quality samples from borehole DH-12, which gave Br above detection and corresponding Br/Cl mass ratios of 2.0×10^{-3} and 2.3×10^{-3}.

Therefore, it seems likely that the Na-Cl water is not seawater, though its actual origin cannot be determined. Possibly, water/rock interactions have modified the original marine ratios, though this cannot be confirmed from the present data.

5.3 *F data*

The lack of a correlation between Cl and F concentrations suggests that different processes control the abundances of these elements in the groundwaters of the Tono area. One possibility is that mixing between the different groundwaters is a more important control on variations in Cl concentrations than are water/rock interactions, whereas the reverse is true for F. Generally, F reacts much more strongly with non-evaporitic (e.g. non-halite-bearing) rock matrices than do Br and Cl (Worden 1996).

If water/rock interactions control F concentrations in the Tono area, possible candidates for the source of the F are fluorite, apatite and biotite. All of these minerals occur in the Toki Granite, while altered biotite has been found in the sedimentary rocks.

Higher temperatures and/or longer groundwater residence times at greater depths could possibly explain the general increase in F concentrations with respect to depth. The departures from this trend in MIU-4 and DH-12 could possibly be due to local variations in groundwater circulation rates and/or by these boreholes lying relatively large distances from the recharge locations. It is emphasized that this model does not necessarily imply that the groundwaters in DH-12, to the south of the Toki River, are genetically related to the groundwaters in the other boreholes, to the north of the Toki River.

5.4 *^{36}Cl data*

The radioactive isotope ^{36}Cl has a half-life of 3.01×10^5 years (Endt and van der Leun 1973). It is produced in the atmosphere, mainly by the action of cosmic rays on ^{40}Ar, and in the sub-surface below a few tens of metres, mainly by neutron activation of ^{35}Cl. Given long enough the $^{36}Cl/Cl$ ratio of dissolved Cl in deep groundwater should approach an equilibrium value at which rates of radioactive decay and in-situ production of ^{36}Cl balance. In the absence of significant water/rock interactions water would need to reside in a rock for about 1.5 million years for this equilibrium value to be reached.

The relatively high $^{36}Cl/Cl$ ratio of the surface water from the Tono area is expected because ^{36}Cl production rates in the atmosphere and near-surface are generally greater than deep underground, where cosmic rays do not penetrate.

At the time of writing, complete chemical analyses for rocks in DH-12 and MIU-4 are unavailable. However, preliminary estimates of in-situ, equilibrium $^{36}Cl/Cl$ can be made using the equations of Andrews et al. (1986, 1989) and U and Th analyses from other

Copyright © 2003 Swets & Zeitlinger B.V., Lisse, The Netherlands

boreholes. This approach suggests that the mean equilibrium $^{36}Cl/Cl$ in the Toki Granite is c. 45×10^{-15}. This is very close to values reported for the samples from borehole DH-12, but only around 30% of the values from KNA-6 and MIU-4 (Fig. 5).

One possible explanation for these differences is that Cl in the DH-12 waters has resided in the granite for more than c. 1.5 million years. The higher ratios in boreholes further north could possibly reflect mixing between this 'old' Cl and more recently recharged Cl (Fig. 5).

Alternatively, since any Cl derived from the rock should be 'old' and at local equilibrium, progressive water/rock interactions along a flow path, for example between the recharge zone and samples from boreholes MIU-4 or KNA-6, could produce a similar effect to groundwater mixing. This model is plausible for the waters in the north because rain water and HCO_3-dominated groundwater samples have similar Cl contents. However, the relatively high Cl contents of the waters from DH-12 mean that water/rock interactions are less likely to contribute a major proportion of the dissolved Cl in this case.

A third possibility is that the variable $^{36}Cl/Cl$ ratios could be due to the Toki Granite having a variable composition. An implication of this explanation would be that the Toki Granite in the vicinity of DH-12 has lower U and/or Th on average than the granite further north in MIU-4.

A combination of these processes could also explain the variability in the $^{36}Cl/Cl$ ratios across the site. However, coupled with the higher Cl in the DH-12 groundwaters compared to the MIU-4 groundwaters, a general implication is that the Cl in the DH-12 groundwater had a relatively long residence time. This would be consistent with the general understanding of the flow system based on hydraulic data in so far as the DH-12 borehole lies further from a recharge zone than do the more northerly boreholes.

5.5 *Carbon isotopic data*

There is no evidence for residual marine groundwater to the north of the Toki River. Therefore, the marine water component indicated by stable carbon isotopic data from calcite has been flushed, at least to c. 1000 m. The ^{14}C detected in other fracture-filling calcite samples does not indicate the time of this flushing, but indicates that a component of recharge water has reached depths as great as 1000 m within the last c. 50,000 years. However, this ^{14}C will have been diluted by ^{12}C and ^{13}C from older calcite and therefore an absolute time of calcite formation cannot be calculated.

The half-life of ^{14}C (5730 years) is much shorter than that of ^{36}Cl. On the time-scales of groundwater flow indicated by the ^{14}C data from groundwater and calcite samples, there would have been little variation in $^{36}Cl/Cl$ ratios due to radioactive decay. Instead, the variations in this isotope will reflect mainly mixing between Cl from different sources.

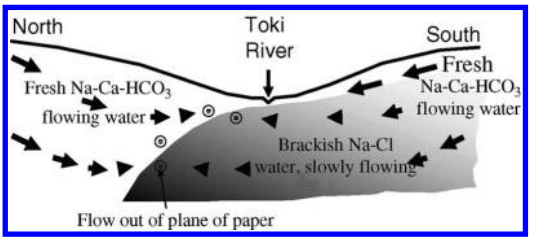


Figure 6. Summary conceptual model.

5.6 *Summary model*

Figure 6 shows a general conceptual model for variations in groundwater chemistry within the Tono area. Several possible alternative variations to this model also fit the observed data. In particular, the location and nature of the transition between the HCO_3-dominated groundwater to the north and the Cl-dominated water to the south of the Toki River is uncertain. The Na-Cl dominated water is interpreted to be relatively old water (recharged a relatively long time ago) although the precise recharge time and origin of the salinity are uncertain.

6 CONCLUSIONS

1. Groundwater sampling techniques developed during the Tono investigations produced samples of sufficiently high quality to distinguish variations in deep, fresh groundwater chemistry.
2. The variations in groundwater chemistry are consistent with patterns of groundwater flow interpreted from hydrogeological data.
3. Br and Cl, and ^{36}Cl isotope data can be used to identify different groundwater types.
4. The Na-Cl water in the southern part of the study area is not marine, although it could be a chemically modified marine water.
5. The Br and Cl in the Na-Cl waters possibly have a common origin and variations in these constituents could potentially be used as an indicator of mixing between the Na-Cl waters and Ca-Na-HCO_3 waters further to the north.
6. Variations in F concentrations are controlled by different processes to those that control Br and Cl concentrations. The abundances of F possibly reflect water/rock interactions and groundwater residence time rather than mixing alone.
7. Radiocarbon data from calcite can identify areas that have been invaded by a component of water recharged within the last 50,000 years.

Copyright © 2003 Swets & Zeitlinger B.V., Lisse, The Netherlands

REFERENCES

Andrews, J. N., Fontes, J. C., Michelot, J. L. & Elmore, D. 1986. In-situ neutron flux, ^{36}Cl production and groundwater evolution in crystalline rocks at Stripa, Sweden. Earth and Planetary Science Letters 77, 49–58.

Andrews, J. N., Davis, S. N., Fabryka-Martin, J., Fontes, J.-C., Lehmann, B. E., Loosli, H. H., Michelot, J.-L., Moser, H., Smith, B. & Wolf, M. 1989. The in-situ production of radioisotopes in rock matrices with particular reference to the Stripa granite. Geochimica et Cosmochimica Acta 53, 1803–1815.

Elmore, D. and 16 others, 1993. The Perdue rare isotope measurement laboratory. Perdue University, Indiana Report.

Endt, P. M. & van der Leun, C. 1973. Energy levels of A = 21–44 nuclei. V. Nuclear Physics A214, 1–625.

Hama, K., Amano, K., Metcalfe, R., Yoshida, H., Iwatsuki, T., Milodowski, A. E. & Gillespie, M. R. 2002. Mineralogical and petrological evidence for the hydrogeological characteristics of the Tsukiyoshi Fault, Japan. Quarterly Journal of Engineering Geology and Hydrogeology, 35, 189–202.

Hanor, J. D. 1994. Origins of saline fluids in sedimentary basins. In Geofluids: origin, migration and evolution of fluids in sedimentary basins, Vol. 78 (ed. J. S. Parnell), pp. 151–174. Geological Society of London.

Iwatsuki, T., Sato, K., Seo, T. & Hama, K. 1995. Hydrogeochemical investigation of groundwater in the Tono area, Japan. Materials Research Society Symposium Proceedings, 353, 1251–1257.

Iwatsuki, T. & Yoshida, H. 1999. Characterising the chemical containment properties of the deep geosphere: water-rock interactions in relation to fracture systems within deep crystalline rock in the Tono area, Japan. In: Metcalfe, R. & Rochelle, C.H. (eds) Chemical Containment of Waste in the Geosphere. Geological Society of London, Special Publications, 157, 71–84.

Iwatsuki, T., Xu, S., Mizutani, Y., Hama, K., Saegusa, H. & Nakano, K. 2001. Carbon-14 study of groundwater in the Tono study site, central Japan. Applied Geochemistry, 16, 849–859.

Iwatsuki, T., Satake, H., Metcalfe, R., Yoshida, H. & Hama, K. 2002. Isotopic and morphological features of fracture calcite from granitic rocks in the Tono area, Japan: a promising palaeohydrogeological tool. Applied Geochemistry. In Press.

Koide, K., Sugihara, K., Yoshida, H., Seo, T. & Yanagizawa 1996. Current state of geoscientific studies in and around the Tono mine in Japan. Proceedings of the International Conference on Deep Geological Disposal of Radioactive Waste, Winnipeg, Manitoba, 7–19 to 7–29.

Mizutani, Y., Seo, T., Ota, K., Nakamura, N. & Murai, Y. 1992. Carbon-14 ages of deep groundwater from the Tono uranium mine, Gifu Prefecture, Japan. Proceedings of the Symposium on Accelerator Mass Spectrometry and Interdisciplinary Application of Carbon Isotopes, Nagoya University, Japan, 28–29 November 1991. Dating and Materials Research Center, Nagoya University, Japan. 159–168.

Nuclear Energy Agency, 1999. Use of hydrogeochemical information in testing groundwater flow models. Proceedings of an international workshop, Borgholm, Sweden, 1–3 September 1997.

Worden R. H. 1996. Controls on halogen concentrations in sedimentary formation waters. Mineralogical Magazine 60, 259–274.

Yusa, Y., Ishimaru, K., Ota, K. & Umeda, K. 1993. Geological and geochemical indicators of palaeohydrogeology in Tono uranium deposits, Japan. Palaeohydrogeological Methods and their Applications, Proceedings of the NEA Workshop, Paris, 117–146.

Copyright © 2003 Swets & Zeitlinger B.V., Lisse, The Netherlands

Hydrogeological modeling and groundwater flow simulation for effective hydrogeological characterization in the Tono area, Gifu, Japan

H. Saegusa, K. Inaba, K. Maeda, K. Nakano & G. McCrank
Japan Nuclear Cycle Development Institute, Tono Geoscience Center, Toki, Japan

A. Sawada
Japan Nuclear Cycle Development Institute, Tokai Works, Tokaimura, Japan

ABSTRACT: It is difficult to obtain complete data-set for hydrogeological modeling and groundwater flow simulations. Because hydrogeological condition in fractured rock such as granite has heterogeneity due to faults and joints and the information that can be obtained from surface and borehole investigations is often limited. Therefore it is important to prioritize each investigation activity according to subject and to establish the most effective procedures for the geological/hydrogeological characterization. Hydrogeological modeling and groundwater flow simulations were applied in order to select geological features considered essential for hydrogeological characterization. Sensitivity analyses focused on these features were performed to assess their influence on the groundwater flow simulations. From the sensitivity analyses, faults or inferred structures considered essential for effective characterization of the hydrogeological condition at the site could be identified and an effective hydrogeological field investigation procedure for characterization of the faults was proposed.

1 INTRODUCTION

The main goal of the Mizunami Underground Research Laboratory (MIU) project and the regional hydrogeological study project, which are broad scientific studies of the deep geological environment in Japan, is to establish comprehensive techniques for investigating and characterizing geological and hydrogeological conditions. The results of these projects are intended to provide a basis for research into practical applications of the knowledge such as the geological disposal of nuclear wastes. In these projects, geological, geophysical, hydrogeological, hydrochemical and rock mechanical surveys on the surface and in the deep boreholes have been carried out in the Tono area.

To demonstrate an understanding of the deep hydrogeological condition at a scale of several kilometers, a study using three dimensional hydrogeological models can be most efficient and useful.

Hydrogeological condition in fractured rock such as granite has heterogeneity due to faults and joints and the information that can be obtained from surface and borehole investigations is often limited. The heterogeneity and limited information are sources of uncertainty in the hydrogeological models. Consequently, it is important to prioritize each investigation activity according to the subject and to establish the most effective procedures for the geological and hydrogeological field investigations, hydrogeological modeling and groundwater flow simulations.

In this study, hydrogeological modeling and groundwater flow simulations were applied in order to select geological features considered essential for hydrogeological characterization. In order to assess their influence on the groundwater flow simulations, sensitivity analyses focused on these features were performed over the several kilometers scale of investigation in the Tono area, including the MIU shoba-sama site.

2 OUTLINE OF STUDY AREA, TOPOGRAPHY AND GEOLOGY

2.1 *Study area*

The area is approximately 4 km by 6 km and centered on the MIU shoba-sama site as shown in Figure 1. The boundaries of the study area were divided in the ridges at the north, east and west sides and the Toki River at the south side. The bottom boundary is set to −3,000 meters above sea level.

2.2 *Topography around the study area*

The overall topographic gradient across the study area is approximately 4% from NNE to SSW. There are

Copyright © 2003 Swets & Zeitlinger B.V., Lisse, The Netherlands

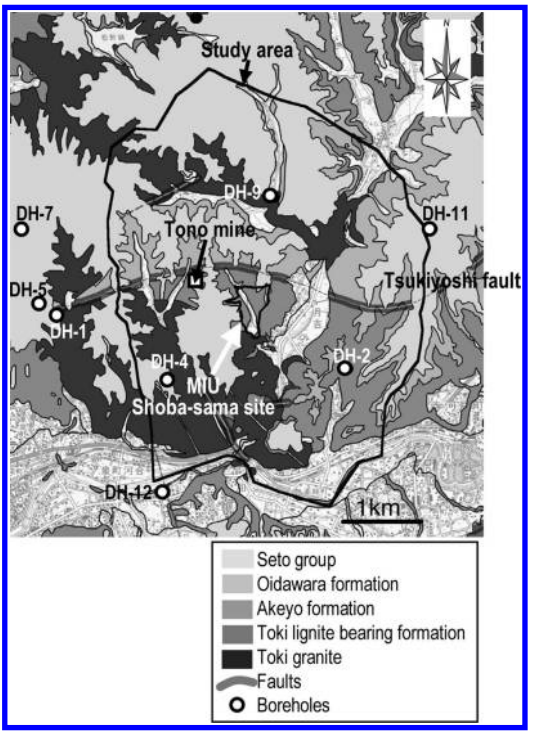


Figure 1. Study area and geological map.

some rivers such as the Toki, Hiyoshi and Garaishi River, and these branches.

2.3 *Geological setting*

Figure 1 also shows the geological map around the study area. In the study area, Tertiary sedimentary rocks widely and uncomformably overlay the Cretaceous Toki Granite (about 60–70 Ma) (Itoigawa, 1980). The Tertiary sedimentary rocks are lithologically divided into two groups, the Mizunami Group (about 15–20 Ma; Toki Lignite-bearing Formation, Akeyo Formation and Oidawara Formation in ascending order) and the Seto Group (0.7–5 Ma). The lower part of the Mizunami Group is composed of mainly tuff, silt/sandstone and conglomerate. Middle and upper parts of the Mizunami Group are composed of mainly mudstone and silt/sandstone alternations with shallow marine facies (Sakamaki, 1985). The Seto Group consists of unconsolidated clay with sand and gravel.

The Toki Granite is typically a felsic granite, subdivided based on variations in biotite content. The granite is also subdivided into structural domains based on variations in fracture development. Below the unconformity with the Miocene sedimentary rocks, the upper part of the Toki Granite has weathered.

The Tsukiyoshi fault extends in the study area with strike of E-W and a dip of 70 to 80S. The Toki Granite and Mizunami Group are displaced by the fault with approximately 30 meters of vertical displacement.

3 GEOLOGICAL MODELING

3.1 *Geological model*

Topographical feature, lithological units and geological structures, all of which are considered to have great effect on groundwater flow and/or groundwater quality, are spatially represented in the geological model. Therefore, the geological model serves as a template for the hydrogeological and the geochemical models.

3.2 *Selection of the lithological units and structures for inclusion in the geological model*

Topographical feature, discontinuities such as faults and variations in rock mass hydraulic properties are considered to strongly influence the groundwater flow at the several kilometers scale.

The following lithological units and structures were selected for the geological modeling.

- Topographical feature
- Faults and damaged zones along the faults
- Seto Group
- Mizunami Group
- Weathered granite
- Hydraulic heterogeneities in granite on the macro scale

3.2.1 *Faults and damaged zones along the faults*

Assessment of major topographic lineaments and their modeling as structural features of significance to groundwater flow is based on these criteria: if the trace length of a lineament is 3 km or over, it is included as an inferred fault in the geological model. The criterion for trace length 3 km or over is after Inoue et al. (1992). According to Inoue, if the trace length of the lineament observed on SPOT imagery is over 3 km, then it can be considered that the lineament corresponds to a fault. The selection was supplemented by comparison of selected features with regional structural deformation patterns and known faults in the region and surface examination.

Based on the process, the following five faults in Figure 2 were selected and modeled as essential features for hydrogeological characterization.

(1) Tsukiyoshi fault

The Tsukiyoshi fault was selected based on the existing geological mapping, correlations between boreholes in the MIU shoba-sama site, the map trace of the fault (Itoigawa, 1980) and information from the Tono mine.

Copyright © 2003 Swets & Zeitlinger B.V., Lisse, The Netherlands

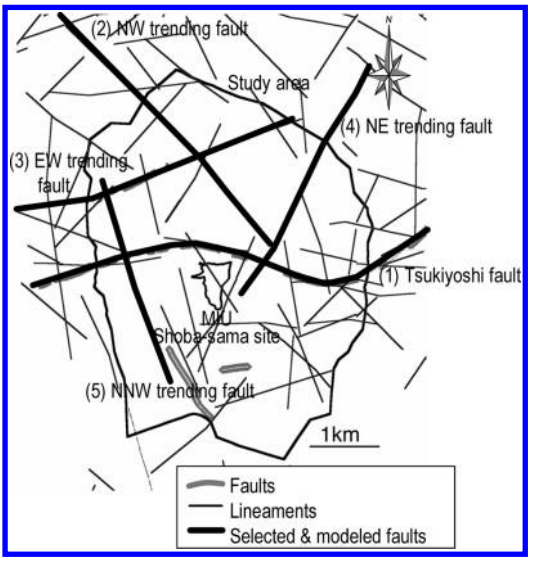


Figure 2. Distribution of lineaments and selected faults.

(2) NW trending fault
A NW trending lineament occurs from the Hiyoshi River to the Matsuno Lake and is about 10 km long. Since the NW trending lineament is straight and long, dip of the fault is assumed to be vertical to sub vertical. A shear zone is observed (strike: NW, dip: SW) in a granite outcrop at the northwestern part of this lineament at the Matsuno Lake. On the other hand, the fault is not intersected by the DH-9 borehole located NE of and near the lineament. Therefore, dip of the fault is assumed to be to the SW.

(3) EW trending fault
An EW trending fault intersected by the DH-7 borehole was interpreted to continue to the east from the information from geological map. The strike and dip are quite similar to the Tsukiyoshi fault, as indicated by BTV data.

(4) NE trending fault
A straight and long, NE trending, lineament coincides with the Hiyoshi River. The length of the lineament is about 5 km. The dip of the inferred fault is unknown and is assumed to be vertical because there were no boreholes drilled in or near the lineament.

(5) NNW trending fault
A NNW trending lineament is visible west of the Tono Mine. The trace length of the lineament is about 3 km. No boreholes intersected the inferred fault.

The width of the damaged zone along the fault is estimated based on the relationship between the lineament trace length and the fault breccia width Ogata (1976).

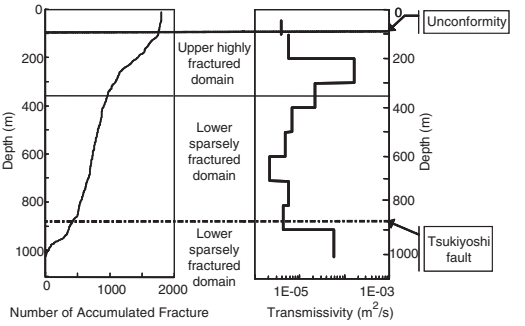


Figure 3. Relationship between number of accumulated fracture and transmissivity.

3.2.2 *Seto and Mizunami Groups*

There is a large contrast in hydraulic conductivity of the Seto and Mizunami Groups. Hydraulic tests indicate relatively higher values in the Seto Group than the Mizunami Group. These two groups are included in the geological model based on their geological map extent and borehole data stratigraphy. The distribution of the basement unconformity between the Mizunami Group and Toki Granite is estimated from the geological map, borehole data and the geophysical data.

3.2.3 *Weathered granite*

Hydraulic tests indicate that the hydraulic conductivities of the weathered granite are higher than the Mizunami Groups and most structural units of the Toki Granite. Therefore, the weathered granite is included in the geological model. The spatial distribution of the weathered granite is estimated from interpolation of the borehole data and represented in the geological model.

3.2.4 *Hydraulic heterogeneity in granite at the macro-scale*

Two structural domains, an upper highly fractured domain and a lower sparsely fractured domain, can be distinguished in the Toki granite based on the data of fracture frequency in the MIU Shoba-sama site. Open fractures are observed in the upper highly fractured domain, and the hydraulic conductivity is higher than the sparsely fractured domain, as shown in Figure 3. These structural domains are taken into account in the hydrogeological model.

3.3 *3-D Geological modeling*

Geometries of the selected lithological units and structures were modeled independently at first. Then, a 3-D geological model was constructed combining the 3-D tectonic structure model (Figure 4) and the geological sequence, as shown in Figure 5.

Copyright © 2003 Swets & Zeitlinger B.V., Lisse, The Netherlands

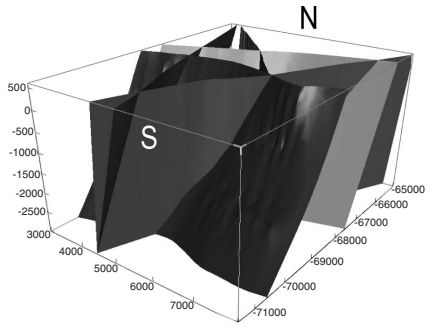


Figure 4. 3-D tectonic structure model.

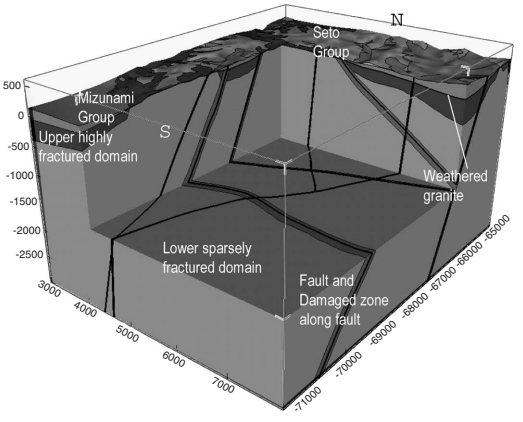


Figure 5. 3-D geological model.

4 HYDROGEOLOGICAL MODELING

4.1 *Hydraulic parameters assignment*

In the geological modeling, the lithological units and structures were classified from a hydrogeological point of view. Hydraulic conductivity in each lithological unit was assumed to be homogeneous and were assigned a geometric mean values from the results of long interval hydraulic testing (JNC, 2000 and JNC, 2001), as shown in Table 1. The weathered granite and upper highly fractured domain are treated as a single unit in the hydrogeological model, because their geometric mean, maximum and minimum values are quite similar.

Since the inferred faults from the lineament have not been investigated by borehole, there is no information on their structural, geometric or hydraulic character at depth. In addition, although the Tsukiyoshi fault has been extensively investigated, hydraulic conductivity across the fault has not been obtained. Therefore, several variations of the hydraulic conductivity for these structures were assigned.

Table 1. Hydraulic parameters.

	Log [k (m/s)]	Porosity
Seto Group	−6.0	0.3
Mizunami Group	−7.1	0.2
Weathered granite + Upper highly fractured domain	−6.6	0.05
Lower sparsely fractured domain	−7.3	0.02
Faults	*	0.02
Damaged zones along the faults	−6.7	0.05

* Hydraulic conductivities of faults are summarized in Table 3.

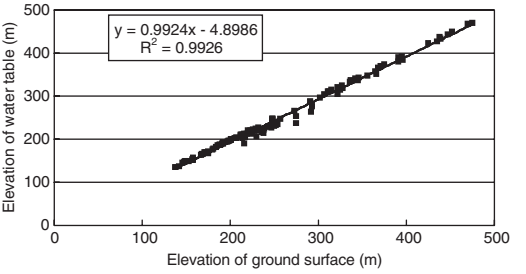


Figure 6. Relationship between elevation of water table and ground surface.

Table 2. Boundary conditions.

Top	Constant head boundary dependent on the elevation of estimated water table
Side	
Ridge	Constant static head boundary dependent on the elevation of estimated water table
Toki River	No flow
Bottom	No flow
Internal	Constant flux at the Tono mine

Porosities were not also obtained from field investigations. The porosities of each lithological unit and the faults are estimated based on literature information.

4.2 *Water table distribution*

In this study, since 3-D steady-state groundwater flow simulations under saturated conditions were performed, the water table distribution was set as the model top boundary. The water table distribution was estimated based on the relationship between the elevation of water table and ground surface at the boreholes for water table measuring, as shown in Figure 6.

4.3 *Boundary conditions*

Boundary conditions were set as shown in Table 2. Regarding the side boundary conditions at the ridges, constant static head are set, because head profiles for

Copyright © 2003 Swets & Zeitlinger B.V., Lisse, The Netherlands

Table 3. Hydraulic conductivities of the faults in sensitivity analyses (Log [k (m/s)]).

	EW		NW		NNW		NE	
Fault case	C	P	C	P	C	P	C	P
Tsuki11	−11	−8	−11	−8	−11	−8	−11	−8
EW11	−11	**−11**	−11	−8	−11	−8	−11	−8
EW13	**−13**	−8	−11	−8	−11	−8	−11	−8
EW6	**−6.7**	**−6.7**	−11	−8	−11	−8	−11	−8
NW11	−11	−8	−11	**−11**	−11	−8	−11	−8
NW13	−11	−8	**−13**	−8	−11	−8	−11	−8
NW6	−11	−8	**−6.7**	**−6.7**	−11	−8	−11	−8
NWW11	−11	−8	−11	−8	−11	**−11**	−11	−8
NWW13	−11	−8	−11	−8	**−13**	−8	−11	−8
NNW6	−11	−8	−11	−8	**−6.7**	**−6.7**	−11	−8
NE11	−11	−8	−11	−8	−11	−8	−11	**−11**
NE13	−11	−8	−11	−8	−11	−8	**−13**	−8
NE6	−11	−8	−11	−8	−11	−8	**−6.7**	**−6.7**

C: normal to fault; P: in-plane of fault.

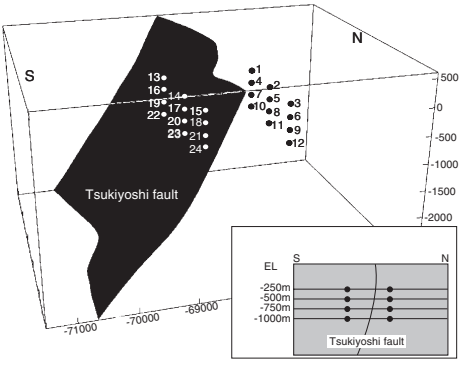


Figure 7. Initial points for particle tracking calculation.

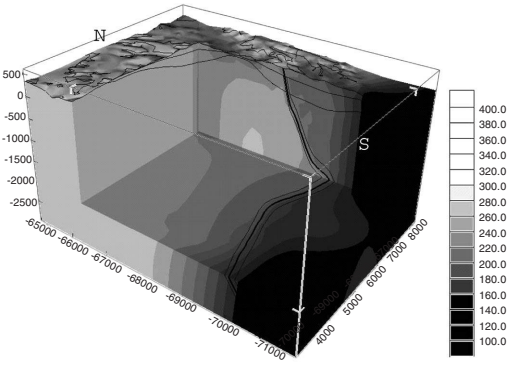


Figure 8. Hydraulic head distribution.

the boreholes in the study area indicate hydro-statistic condition in general except for the boreholes, which are penetrated into the footwall of the Tsukiyoshi fault.

5 SENSITIVITY ANALYSES CASES

In this study, sensitivity analyses were performed focused on hydraulic parameters of the modeled faults. Regarding the Tsukiyoshi fault, hydraulic conductivities across the fault were assigned three different values. These were k = 1E-10, 1E-11 and 1E-12 m/s (Tsuki10, Tsuki11 and Tsuki12).

The case which was taken account of only the Tsukiyoshi fault was also a sensitivity analysis case (Tsuki11B). In this case, the inferred fault was not modeled.

The hydraulic conductivities of the faults were assigned as shown in Table 3. As shown in the table, four cases, having different hydraulic conductivities, were run for the each inferred fault while maintaining hydraulic conductivities constant for the other structures.

Groundwater travel times and path length to model boundaries of twenty-four particles were used for comparison in the sensitivity analyses (Figure 7).

These were calculated using a particle tracking technique.

6 RESULTS OF GROUNDWATER FLOW SIMULATION

3-D steady-state groundwater flow was simulated using Frac-Affinity (Inaba et al., 2002).

6.1 *Groundwater flow direction*

The major groundwater flow direction in the study area is from north to south, consistent with the topographical feature in all the cases (Figure 8).

Copyright © 2003 Swets & Zeitlinger B.V., Lisse, The Netherlands

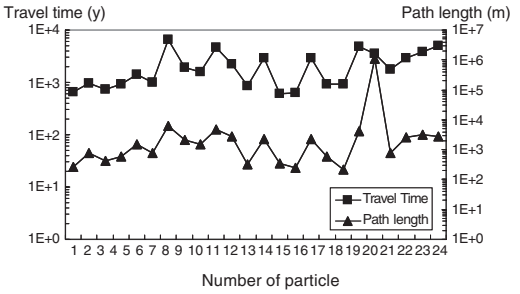


Figure 9. Path length and travel time from the case of "Tsuki11".

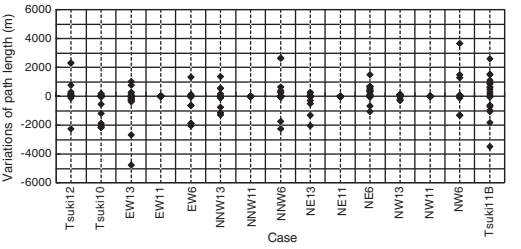


Figure 10. Distribution of variations of the path lengths between the cases of "Tsuki11" and others (24 particles).

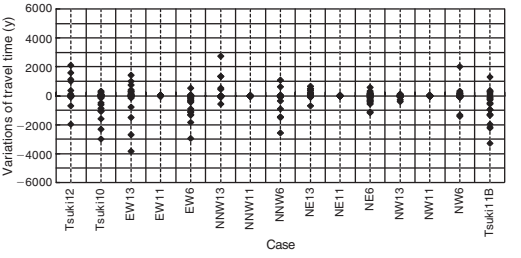


Figure 11. Distribution of variations of the travel times between the cases of "Tsuki11" and others (24 particles).

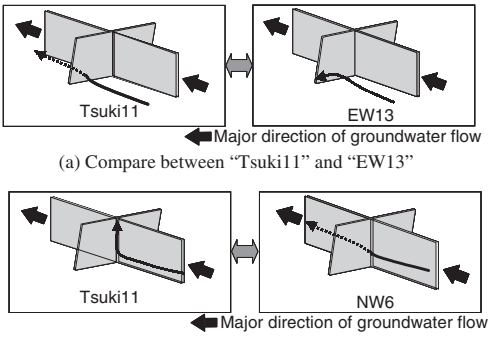


Figure 12. Difference of the path line.

6.2 *Path length and travel times*

Figure 9 shows the path length and travel time from the case of "Tsuki11". Figure 10 shows the distribution of the path length variations between the case of "Tsuki11" and the other sensitivity analysis cases. There are large differences in path length in the case of modeling only the Tsukiyoshi fault (Tsuki11B), the case of the EW trending fault and the Tsukiyoshi fault with low permeability (EW13 and Tsuki12) and the case of the NNW and NW trending fault with relative high permeability (NNW6 and NW6). In the case of "Tsuki11B", there is a particle whose path length is approximately 3,500 meters shorter than the case of "Tsuki11". In the case of "EW13", there is a particle whose path length is approximately 4,800 meters shorter than the case of "Tsuki11". On the other hand, there are particles whose path lengths are approximately 2,500 to 3,700 meters longer than the case of "Tsuki11", for example, in the "NNW6" and "NW6" cases.

Figure 11 shows distribution of travel time variations between "Tsuki11" and the other sensitivity analyses cases. There are also large differences of travel times in the case of "EW13", "NNW6", "NW6", "Tsuki12" and "Tsuki11B" compared with the case of "Tsuki11". Significantly, in the case of "EW13", there are particles with travel times approximately 7,100 years longer and 3,900 years shorter than the case of "Tsuki11".

The reasons for these differences can be considered as follows, with reference to Figure 12;

– The inferred faults influence the groundwater flow path.
– The particles which pass through the fault normal to the major groundwater flow direction and move toward downstream in the case of "Tsuki11" ("Tsuki11" in Figure 12 (a)) do not pass the fault and move toward side of model boundary in the case of the EW trending fault with low permeability such as the "EW13" ("EW13" in Figure 12 (a)).
– The particles which do not pass through the fault normal to the major groundwater flow direction and move upward vertically to the top boundary in the case of "Tsuki11" ("Tsuki11" in Figure 12 (b)) pass through the fault and moves toward downstream horizontally along the relative high permeability fault parallel to the major direction of groundwater flow in the case of the "NNW6" and "NW6" ("NW6" in Figure 12 (b)).

6.3 *Proposal to future investigations*

From a hydrogeological point of view, it is proposed that investigations of the inferred faults in the

Copyright © 2003 Swets & Zeitlinger B.V., Lisse, The Netherlands

directions parallel to and normal to the major groundwater flow direction should be carried out in order to confirm their existence, using combined surface mapping and geophysical investigations. Borehole investigations would also provide information on the hydraulic properties of the faults.

7 CONCLUSION

The sensitivity analyses carried out focused on the geometry and hydraulic characteristics of the modeled fault system. It was clearly shown from the results of this study that the geometry and hydraulic characteristics of the faults parallel to and normal to the major direction of groundwater flow strongly influence the groundwater travel times and path lengths and therefore have a major role in the groundwater flow system.

The accuracy of the structural input to the model is essential to simulation of the actual flow system. The method used in this study to select the essential features is intended to increase confidence in the accuracy of the structures selected.

An effective hydrogeological field investigation procedure for the characterization of the faults was also proposed for further confidence building.

REFERENCES

Inaba, K., Saegusa, H., White, J. M. & Robinson, P. 2002. Outline of the integrated simulation system (GEOMASS system) in order to evaluate groundwater flow and application to groundwater simulation in the Tono area. Journal of Japanese Association of Groundwater Hydrology, 44-2, pp. 105–123.

Inoue, D., Mizuochi, Y. & Sakurada, H. 1992. Geological characteristics of “lineament” and its evaluation on fractures system. Journal of the Japan society of engineering geology, 33-3, pp. 25–34.

Itoigawa, J. 1980. Geology of the Mizunami district, central Japan. Monograph of the Mizunami Fossil Museum No. 1, pp. 1–50.

JNC 2000. Regional Hydrogeological Study Project. Results from 1992–1999 Period. JNC Technical Report, JNC TN7400 2000-014.

JNC 2001. Mizunami Underground Research Laboratory Project. Results from 1996–1999 Period. JNC Technical Report, JNC TN7400 2001–001.

Ogata, S. 1976. Activity evaluation of fault in the basement terrain. Journal of the Japan society of engineering geology, 17–3, pp. 30–33.

Sakamaki, Y. 1985. Geological environments of Ningyo-Toge and Tono uranium deposit, Japan. Geological environments of sandstone type uranium deposits. TECDOC-328 IAEA, Vienna, pp. 135–154.

Copyright © 2003 Swets & Zeitlinger B.V., Lisse, The Netherlands

Fundamental characteristics of transport phenomenon in unsaturated zone

K. Inoue, A. Kobayashi, N. Teramura & S. Aoyama
Graduate School of Agricultural Science, Kyoto University, Kyoto, Japan

ABSTRACT: The objectives of this study are to examine the characteristics of transport phenomenon in porous media, especially in unsaturated zone through laboratory experiments and to investigate the relationship among dispersion coefficient, dispersivity, and flow velocity. Dye tracers were injected into the capillary and saturated zone of the flow system under the steady state flow conditions in two-dimensional tank filled with glass beads. Photographs of tracer movement were taken periodically during the experiments and the dispersion coefficient was estimated using image analysis based on statistical model. It was shown that while the flow velocity became small with the decrease of the mean grain size, the dispersion coefficient and the dispersivity became large. It was observed that the dispersivity in the capillary zone was larger than that in the saturated zone.

1 INTRODUCTION

Several contaminants have been found in groundwater, drinking water and soils. The source of these contaminations includes the leakage from septic tanks, waste disposal system, and excess application of fertilizers and pesticides. Such contaminants have the ability to travel from a pollution source through the unsaturated zone to the groundwater, where they can enter drinking water and infect humans. It is considered in general that the contaminants move in saturated zone in groundwater. However, the transport in unsaturated zone is extremely important in order to examine the degree of flux of contaminants inputs to the saturated zone. In the present study, the basic behavior of solute in the unsaturated zone is focused on.

In order to understand the transport and the behavior of contaminants in the underground environment, the transport parameters such as the longitudinal and transverse dispersivity are some of the key factors that play an important role in spreading the contaminants. However, it is extremely difficult to measure even roughly the transfer parameters of solutes in unsaturated zones. To investigate the mechanisms of solute movement in the unsaturated zone, some theoretical and experimental studies have been carried out. Russo (1993) has shown that solute spreading in unsaturated formations might be predicted by the saturated hydraulic conductivity and a pore size distribution parameter through stochastic analysis. De Smedt and Wierenga (1984) have indicated that longitudinal and transverse solute movement increase when the water saturation in the porous media decreases through laboratory experiments. However, there have been insufficient experimental investigations available for the prediction of solute transport in the unsaturated zone.

Although the tracer experiments are effective procedures that capture the spread of solutes, the spatial and temporal variations of tracer concentrations, in general, are determined either by sampling the soil water or taking soil cores. In recent years, time domain reflectometry (TDR) has been widely used to measure the water content or solute concentrations of tracers such as NaCl in the field or laboratory experiments (e.g. Kachanoski et al. 1992). On the other hand, several attempts have been made to quantify the spatial distributions of dye tracers. A few researchers have adopted digitalized images to visualize the tracer movement in the soil (e.g. Schincariol et al. 1993, Forrer et al. 2000). Image analysis techniques may have excellent ability to characterize the solute phenomena and to evaluate the complicated flow patterns. There is currently no accepted understanding of the influence of water content on solute transport under steady state unsaturated flow conditions for dependency of dispersivity on water content and pore space geometry, especially in unsaturated porous media, whereas numerous studies have focused on the solute transport.

The objective of this study is to investigate the behavior of dye tracers in saturated and unsaturated porous media. Laboratory experiments using dye tracers were carried out in two-dimensional tank packed

Copyright © 2003 Swets & Zeitlinger B.V., Lisse, The Netherlands

with glass beads under different steady state flow conditions. The spatial dye distributions were analyzed to estimate the dispersion coefficient and dispersivity using image analysis. This paper describes the characteristics of the solute movement in porous media.

2 TRANSPORT EXPERIMENTS

2.1 *Materials*

New coccin (Red No. 102), with the concentration of 1.5×10^3 g/m^3 was used as a dye tracer. The specific gravity of dye tracer is the same as water, due to the low concentration of solution. This dye is a completely conservative tracer and an appropriate material for visualizing the transport situations of tracer plume. The flow fields were comprised of porous media consisting of two sizes of glass beads with the mean particle diameters of 0.6 mm and 0.07 mm. Tracer experiments were carried out in the tank filled with three different mixing ratios of two types of glass beads in order to investigate the difference of tracer behavior under the various pore structures, (1) 0.6 mm diameter, (2) a mixture of two types of glass beads of 90 wt.% of 0.6 mm diameter and 10 wt.% of 0.07 mm diameter, and (3) a mixture of two types of glass beads of 80 wt.% of 0.6 mm diameter and 20 wt.% of 0.07 mm diameter. Before the tracer experiments, pF tests were performed in order to obtain the relation between suction and volumetric water content. The results of three types of water retention curves are shown in Figure 1. In this figure, the curves based on van Genuchten's model (van Genuchten 1980) are also depicted. In Table 1, the dry density, hydraulic conductivity at saturation, and porosity for each mixing ratio of glass beads are listed.

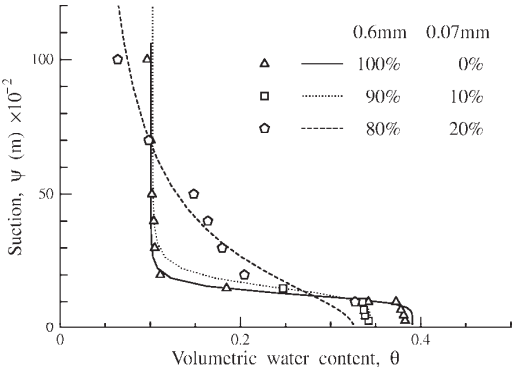


Figure 1. Water retention curves of glass beads used in the experiments.

Table 1. Properties of glass beads for each mixture ratio.

	Mixing ratio (%) (0.6 mm:0.07 mm)		
	(100:0)	(90:10)	(80:20)
Dry density Mg/m^3	2.48	2.48	2.48
Hydraulic conductivity m/s	4.51×10^{-4}	9.32×10^{-5}	4.72×10^{-5}
Porosity	0.39	0.35	0.33

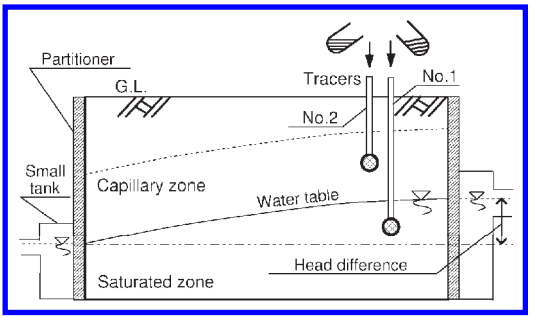


Figure 2. A schematic drawing of experimental setup.

2.2 *Experimental apparatus and procedures*

The tracer experiments were conducted in an acrylic tank (100 cm length, 40 cm height and 10 cm width). Eight manometers were set to measure the water level. Figure 2 shows a schematic drawing of the experimental setup. After the tank was packed uniformly with glass beads, a steady state flow condition with water table was established by adjusting the tanks at upstream and downstream sides. The difference of water level between both sides was set at 4 cm and 6 cm. It was assumed that a steady state flow condition was reached when drainage rates became constant. In this study, six experiments were conducted under three different mixture ratios of glass beads, and two different water levels between upstream and downstream sides.

After steady state conditions were established, 40 cm^3 dye tracers were injected instantaneously using four acrylic pipes to simulate the point sources at both saturated zone and capillary zone which has the suction less than 0.1 m (Fig. 1) and has the moisture content close to saturation. The four pipes were set in the direction of width. The amount of tracer for one pipe is 10 cm^3, which corresponds to the pore volume of 25 cm^3 media. The profiles of tracer distributions were photographed regularly during the experiments and the images were then analyzed by image analysis techniques. Since the symmetry for the vertical and horizontal direction was kept during the experiments, the effect of gravity and sorption could be neglected in this study. The experiments in the same condition were performed twice or three times.

Copyright © 2003 Swets & Zeitlinger B.V., Lisse, The Netherlands

3 PARAMETER ESTIMATION BASED ON STATISTICAL MODEL

A few procedures which stochastically identify the parameters characterizing solute transport in porous media, have been developed. At the molecular scale, diffusion causes mixing and at microscopic scale, mixing is caused by the velocity distribution resulting from porous media characteristics such as the porosity, tortuosity and dead-end pores. At a macroscopic scale, mixing is caused by the velocity distribution resulting from the variability of hydraulic conductivity. A distinction is generally made between Fickian and non-Fickian dispersion. If the transport is considered as Fickian, the longitudinal variance of the plume grows linearly with time. For non-Fickian transport, the longitudinal variance of the plume does not grow linearly with time and is related to the heterogeneous porous media. The relation between the dispersion coefficients and the variance of plume is depicted by the following equation (Bear 1972).

$$D_i = \frac{1}{2}\frac{d\sigma^2}{dt} \tag{1}$$

where σ^2 is the longitudinal variance of the plume, D_i is the dispersion coefficient, and t is time.

In the present study, it is assumed that the dispersion coefficient can be estimated using this relation. As seen in Figure 3, tracer distribution in the porous media at $t = t_1$ alters its shape with movement and its distribution becomes larger at $t = t_2$ than that at $t = t_1$. The mean vector of particles during $\Delta t (= t_2 - t_1)$ can be represented as d through the moving distance from G_1 to G_2, which mean the centroids of tracer distributions. $\bar{x}$ and $\bar{z}$ denote the global coordinates and x and z show the temporal coordinates. θ is the direction between x and $\bar{x}$. In order to estimate the dispersion coefficients, the photographs were processed and analyzed according to the following steps: (1) by image processing, the outlines of tracer distributions at $t = t_1$ and $t = t_2$ were extracted and the centroid G_1 and G_2 of plume were obtained from outlines, (2) the pore water velocity in x direction $|V_x|$ was determined using the time Δt and the distance between G_1 and G_2, (3) the vectors $\bar{\boldsymbol{d}}_n^1(\bar{x}_n^1, \bar{z}_n^1)$ from the centroid to the outlines of tracers were calculated, where superscript denotes time and subscript shows the number of vectors for each angle, (4) the dispersion coefficient tensor related to the movement of tracers during Δt could be computed using the following equation.

$$D_{ij} = \begin{pmatrix} D_{\bar{x}\bar{x}} & D_{\bar{x}\bar{z}} \\ D_{\bar{z}\bar{x}} & D_{\bar{z}\bar{z}} \end{pmatrix} = \begin{pmatrix} \frac{1}{n}\sum_{m=1}^{n}\frac{\bar{x}_m^2}{2\Delta t} & \frac{1}{n}\sum_{m=1}^{n}\frac{\bar{x}_m\bar{z}_m}{2\Delta t} \\ \frac{1}{n}\sum_{m=1}^{n}\frac{\bar{z}_m\bar{x}_m}{2\Delta t} & \frac{1}{n}\sum_{m=1}^{n}\frac{\bar{z}_m^2}{2\Delta t} \end{pmatrix} \tag{2}$$

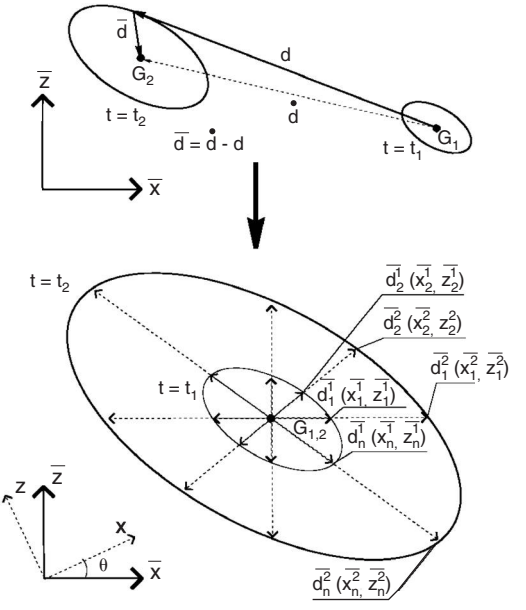


Figure 3. Estimation procedure of the dispersion coefficient tensor based on statistical model.

where D_{ij} is the dispersion coefficient tensor and $\bar{x}_m = \bar{x}_m^2 - \bar{x}_m^1$ and $\bar{z}_m = \bar{z}_m^2 - \bar{z}_m^1 (m = 1, \ldots, n)$ where n is the number of vector for each angle.

$$\begin{pmatrix} D_{xx} & D_{xz} \\ D_{zx} & D_{zz} \end{pmatrix} = R D_{ij} R^T \tag{3}$$

$$R = \begin{pmatrix} \cos\theta & \sin\theta \\ -\sin\theta & \cos\theta \end{pmatrix} \tag{4}$$

where T is the transpose matrix. Although the dispersion coefficient tensor has four components, in this study, the longitudinal dispersion coefficient D_{xx} and transverse dispersion coefficient D_{zz} are focused on.

Neglecting the diffusion and assuming the porosity n to be constant for the entire region, the longitudinal dispersivity α_L and transverse dispersivity α_T of the porous media are given as follows:

$$\alpha_L = \frac{D_{xx}}{|V_x|n} \quad \alpha_T = \frac{D_{zz}}{|V_x|n} \tag{5}$$

4 RESULTS AND DISCUSSIONS

Figure 4 shows the typical images of the tracer experiments. In the figure, the water surface measured by the manometers is depicted. It was observed that the degree of the spread in horizontal direction of the tracers injected into the saturated zone was larger than

Copyright © 2003 Swets & Zeitlinger B.V., Lisse, The Netherlands

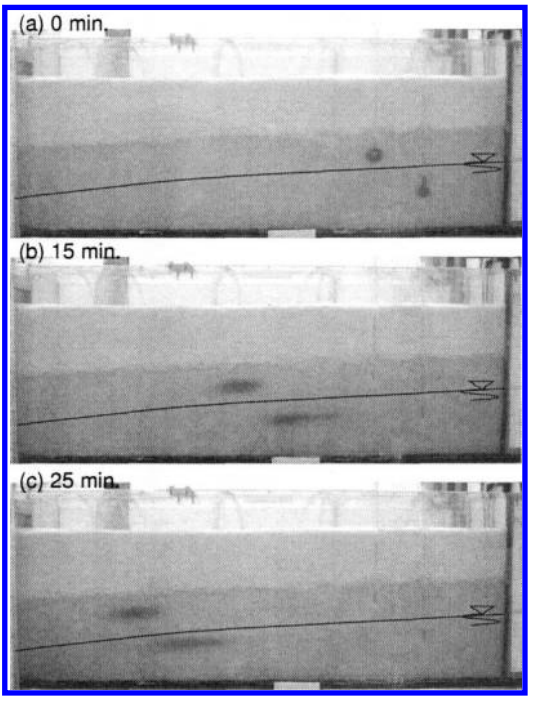


Figure 4. Images of the tracer experiments at various times under the 6 cm head difference in porous media filled with 0.6 mm glass beads: (a) initial state, (b) t = 15 minutes, and (c) t = 25 minutes.

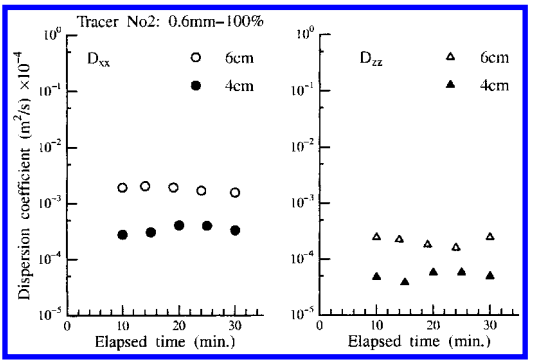


Figure 5. Estimation results of dispersion coefficients in capillary zone.

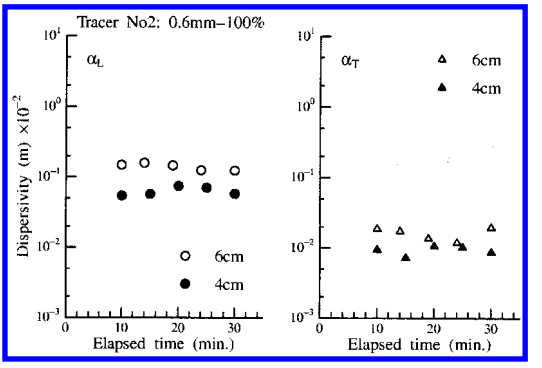


Figure 6. Estimation results of dispersivities in capillary zone.

that in the capillary zone during the experiments. In addition, in all the experimental runs, the tracers injected into the capillary zone horizontally moved and spread only within the capillary zone. It is found that gravity does not have any effect on the flow through the capillary zone. It is also seen from the water retention curves that the air entry value is about 0.1 m, which coincides with the height of the capillary zone.

To examine the effect of flow velocity on the dispersion phenomena, the results of the dispersion coefficients in the capillary zone, as a function of time elapsed since solute injection with 4 cm and 6 cm differences of the water level, are shown in Figure 5. The plotted values are averages for two or three experiments for each water level. The longitudinal dispersion coefficient D_{xx} shows little variation during the transport of tracers and the transverse dispersion coefficient D_{zz} also remain constant during the experiments. It is probable that much less spatial variations of the velocity lead to these results. In fact, it can be seen from the centroid movement that there is no remarkable difference of flow velocities between the upstream and downstream parts in the flow system.

Both values of the dispersion coefficients D_{xx} and D_{zz} for the experiments under the 6 cm head difference are estimated about ten times larger than those for experiments under the 4 cm head difference.

Figure 6 shows the results of the dispersivities α_L and α_T. There are little temporal variations of dispersivities as well as the results of the dispersion coefficients. The dispersivities hardly depend on the flow velocity. In particular, the transverse dispersivity α_T is mostly independent of the flow velocity.

In order to examine the differences of the tracers' behavior between the saturated and capillary zones filled with 0.6 mm particle size glass beads, the dispersion coefficients and the dispersivities are plotted with elapsed time of experiments in Figures 7 and 8, respectively. The variations of the dispersion coefficients D_{xx} and D_{zz} in the saturated zone are in agreement with those in the capillary zone. In the flow field, which is filled with only 0.6 mm glass beads and the 6 cm head difference is maintained, it is inferred that there is no large difference in the flow velocities between the capillary and the saturated zones.

The same tendency of the results of dispersion coefficients can be seen in the results of dispersivities α_L and α_T. The values of α_L range from 0.06 to 0.31 cm and α_T values are about five to ten times smaller than

Copyright © 2003 Swets & Zeitlinger B.V., Lisse, The Netherlands

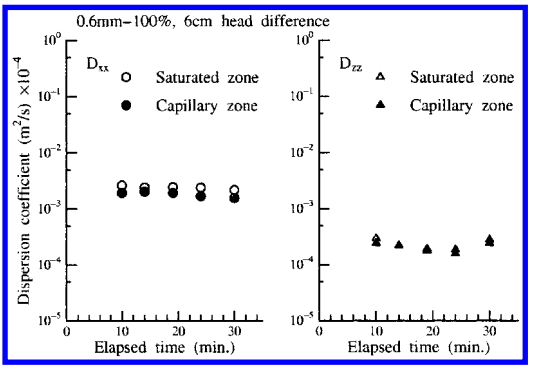


Figure 7. Comparison of dispersion coefficients between saturated and capillary zones.

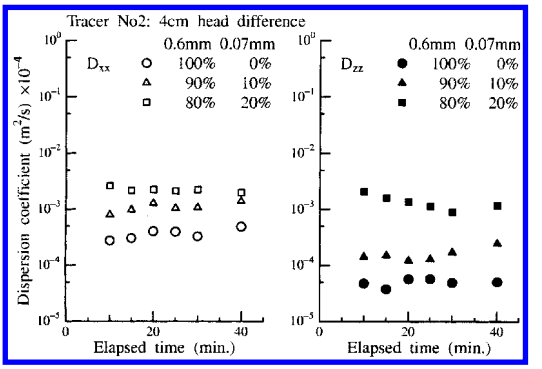


Figure 9. Results of analysis for the dispersion coefficient in unsaturated zone.

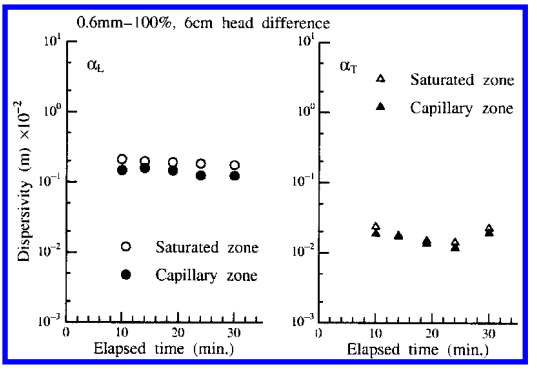


Figure 8. Comparison of dispersivities between saturated and capillary zones.

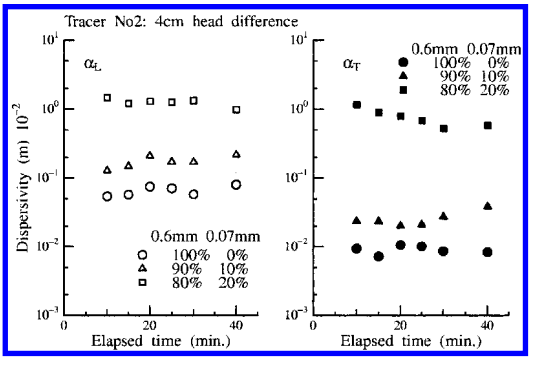


Figure 10. Results of analysis for the dispersivity in capillary zone.

those of α_L. Bear (1972) indicated that the value of the longitudinal dispersivity ranged from 0.1 to 2 cm for packed homogeneous soil columns. In fact, the dispersivity obtained in this study is almost the same as that obtained by Huang et al. (1995) under the saturated conditions in the laboratory. They performed the column experiments under a uniformly packed homogeneous medium sand with 0.33 of porosity. It is, therefore, reasonable to obtain the above values of the longitudinal dispersivity in these experiments.

The obtained results of the dispersion coefficients for each mixing ratio are shown in Figure 9. The dispersion coefficients hardly depended on the traveling time of the tracers and the values are constant for each mixing ratio. The dispersion coefficient becomes large as the mixing ratio of 0.07 mm increases. It can be seen in Figure 9 that the longitudinal dispersion coefficient D_{xx} is similar to the transverse dispersion coefficient D_{zz} in the case where the mixing ratio of 0.07 mm is 20%. On the other hand, the transverse dispersion coefficient D_{zz} is smaller than the longitudinal dispersion coefficient D_{xx} for the other cases. It is likely that a mixture of 0.6 mm and 0.07 mm glass beads affects the dispersion phenomena.

Through image analysis, the average pore water velocities in the flow field were calculated to be as follows: 1.44×10^{-4} m/s for 100% of mixing ratio of 0.6 mm, 1.20×10^{-4} m/s for 90% of mixing ratio of 0.6 mm, and 5.38×10^{-5} m/s for 80% of mixing ratio of 0.6 mm, respectively. The velocity gradually becomes small as the mixing ratio of 0.07 mm glass beads increases, which means that the mean grain size becomes small. Thus, the Peclet number, which is defined by $\upsilon \times d_m/D$ where υ is the flux of water, d_m is the mean grain size, and D is the dispersion coefficient, becomes small with the increase of the mixing ratio of 0.07 mm glass beads. It can be concluded from the experimental results that the dispersion coefficient increases with decrease of Peclet number, in the case of the 4 cm head difference.

The obtained results of the dispersivities are shown in Figure 10. It is seen that the dispersivity becomes large, as the mixing ratio of 0.07 mm glass beads increases. The longitudinal dispersivity α_L is similar to

Copyright © 2003 Swets & Zeitlinger B.V., Lisse, The Netherlands

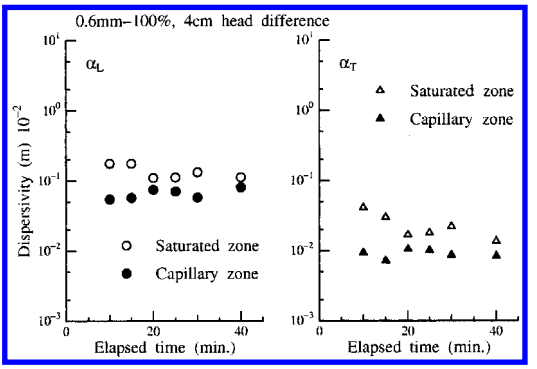


Figure 11. Comparison of the dispersivity between saturated and unsaturated zones.

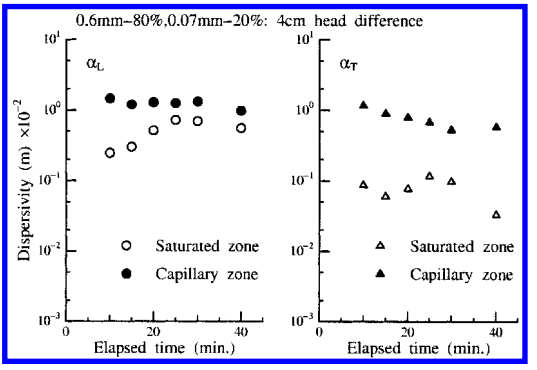


Figure 12. Comparison of the dispersivity between saturated and unsaturated zones.

the transverse dispersivity α_T, as well as the results of the dispersion coefficient, in the case where the mixing ratio of 0.07 mm beads is 20%.

To compare the capillary and saturated results with the 4 cm of head difference, the obtained dispersivities for 100% of mixing ratio of 0.6 mm and for 80% of mixing ratio of 0.6 mm are plotted in Figures 11 and 12, respectively. Both the longitudinal and transverse dispersivities have little variations for the duration of each experiment. The value of the dispersivity becomes approximately ten times larger than that of transverse dispersivity. Whereas the dispersivities in the saturated zone are larger than those in the capillary zone in Figure 11, the opposite results are shown in Figure 12. The experiments of De Smedt and Wierenga (1984) on solute transport through unsaturated porous media showed that the dispersivity under unsaturated conditions was larger than that under saturated conditions. Their experiments was conducted in a 30 cm long column filled with a 50–50% mixture, by volume, of two types of glass beads, whose diameter range 0.088–0.125 mm and 0.074–0.105 mm, with 0.37 porosity. They indicated that for unsaturated columns, the dispersivity was about 20 times larger than for saturated columns. As a comparison with the results of De Smedt and Wierenga (1984), it is concluded that the obtained results of the dispersivities in this study are appropriate.

5 CONCLUSIONS

In the present study, the behavior of solutions in saturated and capillary zone composed of two types of glass beads was examined through tracer experiments in the laboratory and the dispersion coefficient and the dispersivity were estimated using image analysis. The following findings were obtained.

1. In the capillary zone, the injected dye tracers spread according to flow without leaching to the saturated zone. This means that the solute transport in capillary zone should be examined as well as that under groundwater table.
2. In the case where the flow field is composed of 100% of 0.6 mm glass beads, the dispersion coefficient becomes large with the increase of the flow velocity. The dispersivity in the capillary zone is the same as that in the saturated zone.
3. In the case where the flow field is composed of different size of glass beads, although the flow velocity becomes small with the increase of the mixing rate of 0.07 mm glass beads, the dispersion coefficient becomes large with the decrease of the mean grain size.
4. In the case of a 80–20% mixture of 0.6 mm and 0.07 mm glass beads, the longitudinal dispersivity is mostly the same as the transverse dispersivity in capillary zone, while the longitudinal dispersivity is ten times larger than the transverse dispersivity in saturated zone. Moreover, it is observed that the dispersivity in the capillary zone is larger than that in the saturated zone.

Although it is difficult to theoretically explain the results of tracer experiments, it is speculated that there is a close relation between the complexity of distributions of pore space and the increase of the dispersivity. In particular, the presence of air in capillary zone, where the amount of volume of air becomes gradually larger as the increase of mixing ratio of small particles, may influence on the dispersion phenomena.

REFERENCES

Bear, J. 1972. *Dynamics of fluids in porous media*. New York: Elsevier.

De Smedt, F. & P.J. Wierenga 1984. Solute transfer through columns of glass beads. *Water Resources Research*. 20(2): 225–232.

Copyright © 2003 Swets & Zeitlinger B.V., Lisse, The Netherlands

Forrer, I., A. Papritz, R. Kasteel, H. Flühler & D. Luca 2000. Quantifing dye tracers in soil profiles by image processing. *European Journal of Soil Science*. 51: 313–322.

Huang, K., N. Toride & M.Th. van Genuchten 1995. Experimental investigation of solute transport in large, homogeneous, and heterogeneous, saturated soil columns. *Transport in Porous Media*. 18: 283–302.

Kachanoski, R.G., E. Pingle & A. Ward 1992. Field measurement of solute travel times using time domain reflectometry. *Soil Science Society of America Journal*. 56: 47–52.

Russo, D. 1993. Stochastic modeling of macrodispersion for solute transport in a hetegeneous unsaturated porous formations. *Water Resources Research*. 29: 383–397.

Schincariol, R.A., E.E. Herderick & F.W. Schwartz 1993. On the application of image analysis to determine concentration distributions in laboratory experiments. *Journal of Contaminant Hydrology*. 12: 197–215.

van Genuchten, M.Th. 1980. A closed-form equation for predicting the hydraulic conductivity of unsaturated soils. *Soil Science Society of America Journal*. 44: 892–898.

Copyright © 2003 Swets & Zeitlinger B.V., Lisse, The Netherlands

Prediction error of groundwater behavior by inverse modeling with bootstrap re-sampling method

K. Masumoto
Shimane University, Matsue, Japan

ABSTRACT: Reliability of groundwater model parameters obtained by inverse analysis has been evaluated by some researchers, and applying bootstrap re-sampling method to groundwater inverse modeling, one of the reliability estimation method, has already been proposed (Masumoto & Valle 2000). However, for many practical cases, the real purpose of groundwater modeling is not to obtain a model but to predict and to control groundwater behavior. For these reasons, the prediction error is more essential in evaluating groundwater model rather than the error of estimated parameters obtained by inverse analysis. In this paper, in order to estimate the prediction error of groundwater behavior, we used various patterns of hydraulic property distributions obtained by numerical inversion with bootstrap re-sampling method. By numerical experiments, we examined the usefulness of the prediction error obtained by the method. The results show the method is useful for evaluating the inverse modeling method and the measuring method when the real model is not known.

1 INTRODUCTION

In groundwater modeling for the decision making, the main objective of making the model is to evaluate the reliability of the model and that of the prediction calculated by the model. There are various studies on the subject (Sun 1994). Some of these use stochastic method and assume probability functions. But, for practical purposes, the most difficult error to treat is the modeling error. Due to the assumptions of stochastic methods, the mean value and the standard deviation, etc., the modeling error cannot be treated correctly. This is so because the effect of modeling error cannot usually be expressed by a function of random number. Additional assumptions may cause more uncertainties due to the new modeling errors. To avoid such risks, the bootstrap method (Efron 1979) has been developed in the field of statistics. The bootstrap method, by data re-sampling, can evaluate indices numerically without assuming the type of probability distribution of error. Masumoto & Valle (2000) applied it to evaluate the confidence interval of model parameters estimated by inverse analysis for groundwater modeling. In this paper, by extending the bootstrap method, a method to evaluate the prediction error obtained by the model is suggested. Numerical experiments by one dimensional model were carried out. Various measurement patterns and pressure-change rate matching method were considered in order to check the validity of the method.

2 METHODOLOGY

2.1 *Inversion method*

A quasi-Newton method with adjoint state method for minimizing the objective function which includes a term for the pressure-change rate matching (Masumoto et al. 1998) was used to solve inverse problems in groundwater modeling numerically. The form of the objective function J considered here is the sum of J_1 and J_2 expressed as follows.

$$J = J_1 + J_2 \tag{1}$$

where:

$$J_1 = \sum_{n=1}^{Nt} \sum_{m=1}^{Nw} W_1^{m,n} \left(p_{cal}^{m,n} - p_{obs}^{m,n}\right)^2 \tag{2}$$

$$J_2 = \sum_{n=1}^{Nt} \sum_{m=1}^{Nw} W_2^{m,n} \times \left(\frac{p_{cal}^{m,n} - p_{cal}^{m,n-1}}{\Delta t^n} - \frac{p_{obs}^{m,n} - p_{obs}^{m,n-1}}{\Delta t^n} \right)^2 \tag{3}$$

where p_{cal}: calculated pressure, p_{obs}: observed pressure, m: index of observation point, n: index of time step, Δt: time step interval, W: weighting.

p_{cal} is calculated by the flow equations for slightly compressible fluid in a confined aquifer.

Copyright © 2003 Swets & Zeitlinger B.V., Lisse, The Netherlands

2.2 *Bootstrap re-sampling*

The bootstrap re-sampling method developed by Efron (1979) is a type of Monte-Carlo method. It is for numerically calculating statistical indices, such as standard deviation or confidence intervals, from many *bootstrap samples*. A *bootstrap sample* can be made by randomly re-sampling the data for '*N*' times with allowing replacement. Here, *N* is the number of data. Masumoto & Valle (2000) applied it to groundwater inverse problems in order to derive an index for objectively evaluating the confidence interval and the reliability of estimations of hydraulic properties obtained by inversion. They treated the discrete transient pressure data as if they were independent data, and made many weighting patterns like many *bootstrap samples* through multiplying the repetition number of a data by the original weighting. This means a weighting pattern obtained corresponds to a *bootstrap sample*. The following are the merits of the bootstrap method.

1) Probability density function is not required as an assumption.
2) Required number of *bootstrap samples* is only 25–200 (Efron 1993), while the usual Monte-Carlo method needs a few thousands of estimations.
3) Other merits of Monte-Carlo method remain, such as the applicability to complex nonlinear model.
4) Many estimations with some deviation can be derived without using information from the true model.

Even though the method by Masumoto & Valle (2000) differs from the original bootstrap method, it permits estimations with some deviation that can be considered to reflect the sensitivity or accuracy or reliability of the inversion result obtained by using transient pressure data. In this study, we extended the method to evaluate the prediction errors obtained by estimates from numerical inversion.

2.3 *Prediction error estimation*

Figure 1 shows the procedure of prediction error evaluation by the modified bootstrap re-sampling method. Here, we fixed the number of *bootstrap samples* as 100. By bootstrap re-sampling, 100 patterns of weightings can be made. Then, the next step, by 100 inversions, 100 sets of unknown parameters can be obtained for a certain pattern of inversion model and observation method. Using these 100 sets of estimations, we can calculate future behavior of the flow by numerical simulation, and then obtain 100 predictions. By these predictions, we can derive the prediction error. Here, 90% confidence interval of calculated pressure was used to describe the prediction error by bootstrap method. In order to check the validity of the method,

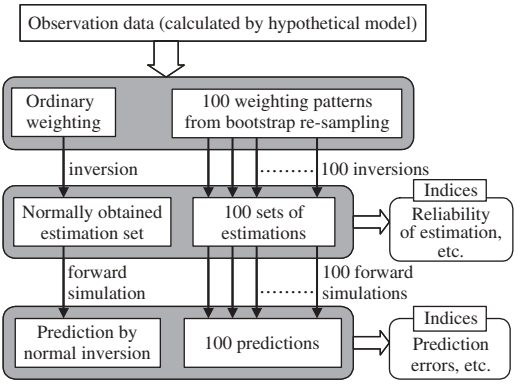


Figure 1. Procedure of prediction error evaluation by bootstrap method.

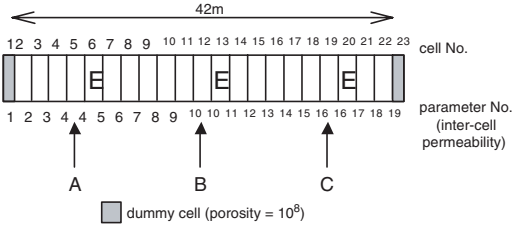


Figure 2. One dimensional numerical model.

we compared it to the standard prediction errors (the difference between the correct model simulation and the prediction simulated using the normal inversion result). Also we calculated the reliability index of the estimated model by the 100 inversion results. In Chapter 4, the modeling error and the prediction error caused by the estimated model will be discussed.

3 NUMERICAL CASE STUDIES

Figure 2 shows the one dimensional hypothetical heterogeneous model with 3 observation points A, B and C. Permeability distribution of the 'true' model is shown in Figure 3. The objective of inversion is to reconstruct the permeability distribution by the transient data obtained from the observation points. In the case studies, the observation data for each case (Table 1) is calculated by changing the measurement method, such as the flow rate or flow pattern or the number of observation points. Predictions and permeability distribution were obtained for each case. The prediction errors and reliability indices of permeability distributions were calculated by the bootstrap method. Figure 4 shows the injected flow rate patterns used in this study. Also, we use 2 types of objective function,

Copyright © 2003 Swets & Zeitlinger B.V., Lisse, The Netherlands

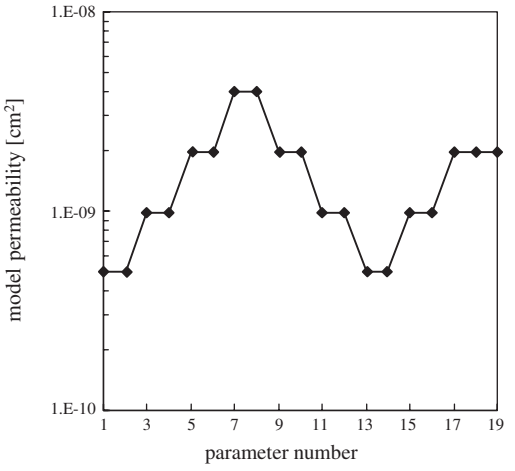


Figure 3. One dimensional hypothetical model permeability distribution.

Table 1. Observation types of each case.

Case name	Injection points	Observation points	Injection type	Injection time
case 1	A, B, C	A, B, C	Pulse	300 [s]
case 2	A, B, C	A, B, C	Pulse	600 [s]
case 3	A, B, C	A, B, C	Continuous	300 [s]
case 4	A, C	A, B, C	Continuous	600 [s]
case 5	A, C	A, B, C	Pulse	300 [s]
case 6	A, C	A, B, C	Pulse	600 [s]
case 7	A, C	A, B, C	Continuous	300 [s]
case 8	A, C	A, B, C	Continuous	600 [s]
case 9	A, C	A, C	Pulse	300 [s]
case 10	A, C	A, C	Pulse	600 [s]
case 11	A, C	A, C	Continuous	300 [s]
case 12	A, C	A, C	Continuous	600 [s]

one is J_1 only and the other is J_1+J_2 for the 12 observation patterns. In total, 24 cases were studied using the bootstrap method. Table 2 shows the fixed conditions for all cases in this study.

4 RESULTS AND DISCUSSIONS

The best inversion estimated set of permeabilities occurs when $J_1 + J_2$ is used in case2 (Fig. 5). Here the reliability index $R^*(= (\Sigma \mathrm{KCI90}^2)^{-1})$, calculated by using the bootstrap method, is used to judge the best result. KCI90 means 90% confidence interval (difference between the 6th largest estimation of permeability logarithm and the 6th smallest one of the 100 estimations). Figure 6 shows the worst inversion estimated set of permeabilities, which occurs when $J_1 + J_2$ is used in case 11. Estimation errors differ very much, depending on the injected flow method and the objective function. To discuss the prediction error, we used simple injection of long term constant flow rate as the prediction model (1.0 [cm^3/s], 30,000 [s]).

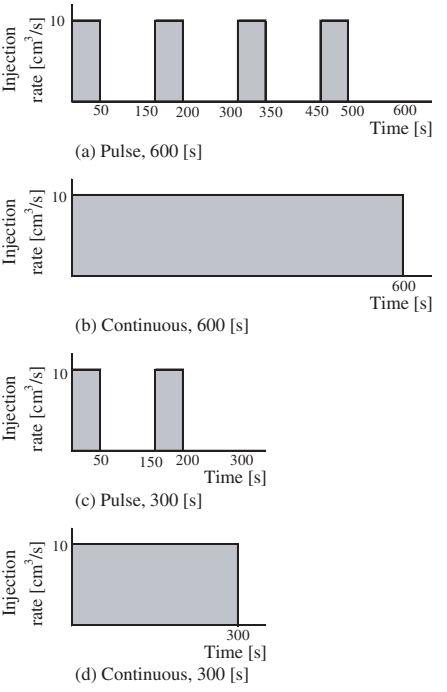


Figure 4. Injection types for case studies.

Table 2. Fixed conditions for numerical case studies.

Injection rate	10 [cm^3/s]
Timestep interval	5 [s]
Number of timesteps	60 (when case number is odd) 120 (when case number is even)
Intial guess for inversion	0.987E-10 [cm^2] for all, except for case 12*
Porosity	0.15 for all cells, except for the two terminal dummy cells
Boundary condition	Constant pressure (porosity of both terminal dummy cells is set as 1.0E+8 to approximate constant pressure)
Initial condition	101325 [Pa] for all grid points
Original weighting in J1 and J2	$W_1 = 1$, $W_2 = 1.0$E-6 (or 0.0)
Number of inversion iterations	100 for all cases
Number of resampling	N = 100

* The initial guess of 1.18E-10 [cm^2] was used only in case 12 when $J = J_1 + J_2$.

Copyright © 2003 Swets & Zeitlinger B.V., Lisse, The Netherlands

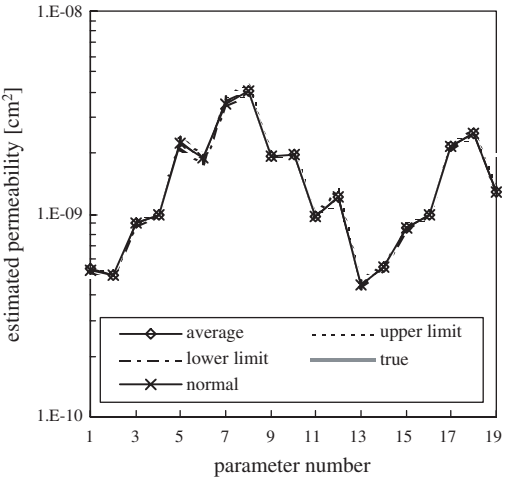


Figure 5. Average and 90% confidence interval of estimated permeabilities by numerical inversions (case 2 when $J = J_1 + J_2$).

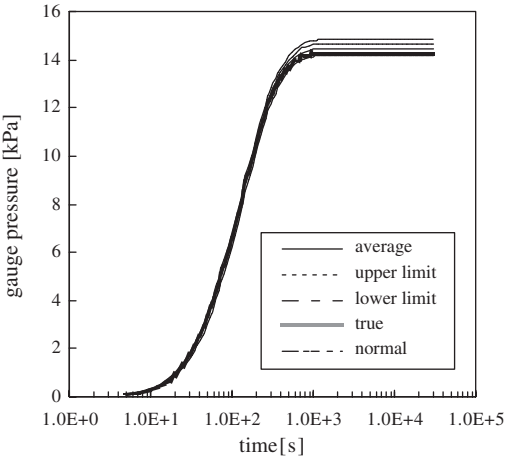


Figure 7. Average and 90% confidence interval of predicted pressure by numerical models (case 11 when $J = J_1 + J_2$, injection in A, Observation in B).)

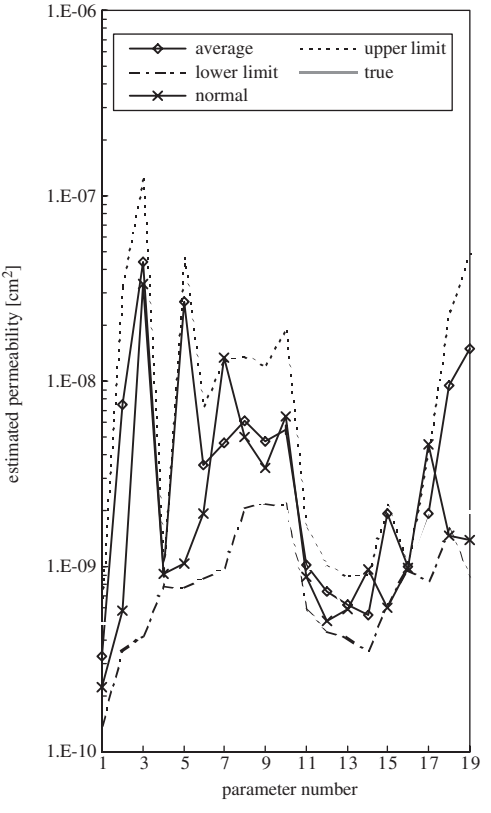


Figure 6. Average and 90% confidence interval of estimated permeabilities by numerical inversions (case 11 when $J = J_1 + J_2$).

Three points are used for the injection and 3 predictions were obtained for each model of estimated permeability distribution. Calculations for the predictions were done for all the 24 cases. A total of 7200 simulations ($= 3 \times 24 \times 100$) were performed for the predictions of the numerical case study. Figure 7 shows an example of predicted pressure behavior observed at B when A is used as the injection point, which has the largest error of the 24 cases. Note that the predicted pressure at B can be calculated even when B is not considered as an observation point during the measurement. Here, the upper pressure limit means the 6th largest one at the timestep in the 100 simulations, and the lower pressure limit is the 6th smallest one. Figure 8 shows the difference between the average, upper and lower pressures and one calculated by using normal inversion results, with normal weighting patterns (all weighting = 1.0). The prediction errors (PCI90) by bootstrap method are evaluated by the difference between the upper and lower pressures. From the results, the pressure prediction error is not so large in comparison to the error of the estimated set of permeabilities.

Figure 9 shows the correlation between the total error of permeabilities estimated by the bootstrap method ($\Sigma\{\ln(K_{est}/K_{true})\}^2$) and the normally evaluated total error of permeabilities ($\Sigma KCI90^2$). The correlation coefficient is calculated as 0.908. It means that the reliability index evaluated by the bootstrap method for permeability estimation can be used for this model. To check the validity of the bootstrap method, $\Sigma PCI90^2$ (sum of squares of confidence interval of predicted pressure) versus normal pressure errors are plotted for each observation point for all cases, as shown in Figure 10. These normal pressure errors

Copyright © 2003 Swets & Zeitlinger B.V., Lisse, The Netherlands

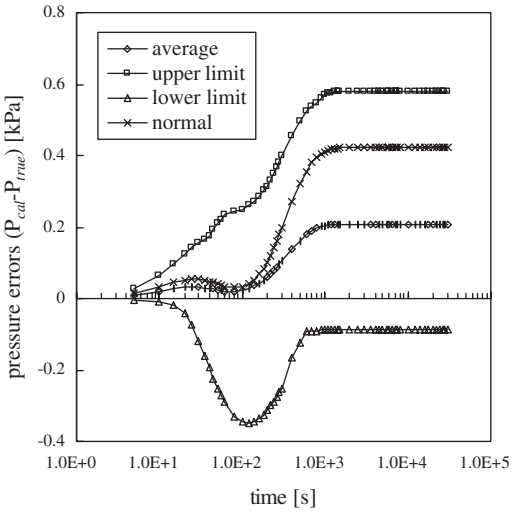


Figure 8. Predicted pressure errors (case 11 when $J = J_1 + J_2$, injection in A, Observation in B).

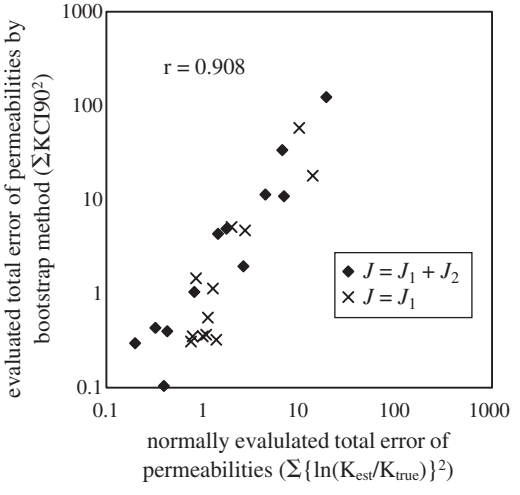


Figure 9. Correlation between Σ KCI90^2 and $\Sigma\{\ln(K_{est}/K_{true})\}^2$.

were calculated using the sum of square differences between the predicted pressure, obtained from the normal inversion results, and pressures calculated by the 'true' model. The correlation coefficient of the prediction error evaluated by bootstrap method (Ep_{bs}) and that of normal inversion (Ep_{normal}) is 0.945 which is larger than the value calculated for permeabilities. This means that the bootstrap method is more effective in evaluating the prediction error for this model. As shown in Figure 9 and Figure 10, the best set of

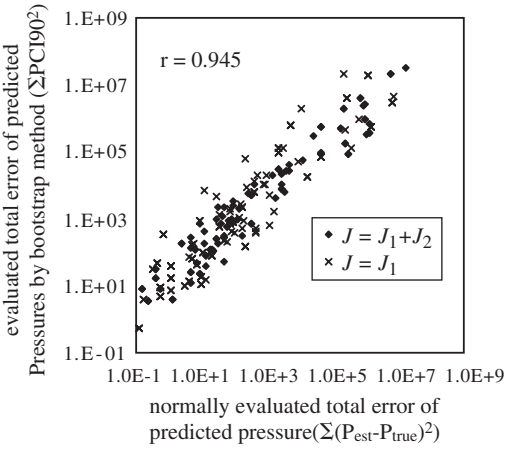


Figure 10. Correlation between Σ PCI90^2 and Σ ($P_{est} - P_{true}$)^2.

permeabilities was obtained with the pressure-change rate matching method ($J = J_1 + J_2$), while the best prediction (the smallest prediction error of pressure) occurs when $J = J_1$. This is because the prediction model uses constant flow rate. The case study for other prediction models might cause different results, and an investigation of this is recommended as a future work. However, we can say that the prediction error and the modeling error are different. It means that it is better to evaluate the prediction error directly when the purpose of modeling is not hydraulic properties but predictions.

5 CONCLUSIONS

Bootstrap re-sampling method was applied to the evaluation of the prediction error of the groundwater model obtained by inversion using one dimensional numerical case studies. We conclude that:

1. The reliability index calculated numerically by using the bootstrap method can be used to express the reliability of permeability distribution estimated by inversion. The method can be used to evaluate the suitability of the observation design.
2. The estimated prediction error obtained from the bootstrap method was positively correlated to the error obtained by normal inversion.
3. For estimating the permeability distribution, the pressure change rate matching is suitable when an appropriate observation pattern is selected. On the other hand, for long term prediction of constant injection rate model, the prediction using the model estimated by inversion without the pressure change rate matching is better.

Copyright © 2003 Swets & Zeitlinger B.V., Lisse, The Netherlands

6 ACKNOWLEDGMENT

The authors thank Mr. Shingo Nishikori for his assistance with case studies, and to Mr. Sergio Torres for his assistance with the edition.

REFERENCES

Efron, B. and Tibshirani, R. 1993. An Introduction to the Bootstrap. Chapman & Hall.

Efron, B. 1979. Bootstrap methods: another look at the jackknife, Ann. Statist., 7: 1–26.

Masumoto, K., Tosaka, H. and Kojima, K. 1998. New Algorithm for Identifying Hydraulic Property Distribution of Rock Mass by Simultaneous Fitting of Pressure and its Change rate at Multi-Points in Multi-Wells, J. Groundwater Hydrology of JAGH, 40(3): 273–287.

Masumoto, K. and Valle, M. 2000. Confidence intervals of hydraulic properties estimated by highly efficient numerical inversion with pressure change rate matching, Proceedings of the International Symposium 2000 on Groundwater, IAHR in Omiya, Japan: 375–380.

Sun, Ne-Zheng 1994. Inverse Problems in Groundwater Modeling, Kluwer Academic Publishers.

Copyright © 2003 Swets & Zeitlinger B.V., Lisse, The Netherlands

Analysis of groundwater flow around a fault zone in fractured rock mass – use of fractured rock aquifer as a reliable groundwater sources for Tangalle area, Sri Lanka

D.G.K.M. Kumari & K. Watanabe
Geosphere Research Institute, Saitama University, Saitama, Japan

Y. Morita
Pakage D Co., Saitama University, Saitama, Japan

ABSTRACT: The behavior of groundwater flow in an idealized model of fracture rock mass in the Tangalle area, southern part of Sri Lanka was studied by numerical simulation. The fractured rock model of the area consisted of water barrier fracture, major fractures and minor fractures. This study shows the sensitivity of groundwater drawdown by pumping from two wells in the area. Variation of drawdown due to the different groundwater extraction rates around a big fault zone in the fractured rock mass were successfully simulated using channel network model named Don-Chan (Donen-Saitama Channeling Flow Model).

1 INTRODUCTION

Groundwater has been pumped mainly from alluvium sediment that is filling in the low lands of the southern part of Sri Lanka for domestic and agricultural use. However, due to the population growth and the severe increase of water demand, groundwater contained in the fractured rock mass is now thought as a possible resource that should be developed to meet future water demand. The total precipitation in the southern part of Sri Lanka is low and the surface water has been highly used for paddy cultivation, thus, the potential of further development of surface water resources is minimal. A development of groundwater resource in deep underground seems to be one of the possible ways of solving the problem of water shortage in the southern part of Sri Lanka.

Although groundwater flow in fractured rock mass has been previously studied by many workers: Schwartz et al., 1983; Long and Witherspoon, 1985; Andersson and Dverstorp, 1987; Rouleau and Gale 1987; Cacas et al., 1990; Panda and Kulatilake 1998a,b, a proper technique for numerically analyzing the flow has not been established. A proper technique should be developed to evaluate the groundwater flow around a network of pumping wells. In this study, Don-Chan model (Donen-Saitama Channeling Flow Model) was applied in order to analyze the groundwater flow in an idealized model of fractured rock mass in Sri Lanka.

The first objective of this study was to illustrate the applicability of this model to the fractured aquifer in the southern part of Sri Lanka. Hydro-geological data of fracture system in rock mass is indispensable for the study of groundwater flow. Geological information obtained before well drilling is in usual limited. The second objective of this study is to clarify the process of properly modeling the actual rock mass on the basis of limited amount of hydro-geological data. The third objective is to analyze the effect of a big fault zone on groundwater flow. A big fault has hydraulically anisotropic feature and the hydraulic conductivity in the direction perpendicular to the fault zone is much smaller than other directions so that the big fault is thought to act as a water barrier in the fractured rock mass. Some big fault zones in this area act as an important factor in groundwater storage.

2 HYDRO-GEOLOGICAL CONDITIONS OF SOUTHERN PART OF SRI LANKA AND TANGALLE AREA

2.1 *Geology of Tangalle area*

Figure 1 shows the location of Tangalle area, which is located in southern part of Sri Lanka. The basement of the study area consists of gneisses rock of Highland Complex and Vijayan Complex (Cooray, 1997). The Bed strike is generally in NWW-SEE direction and the

Copyright © 2003 Swets & Zeitlinger B.V., Lisse, The Netherlands

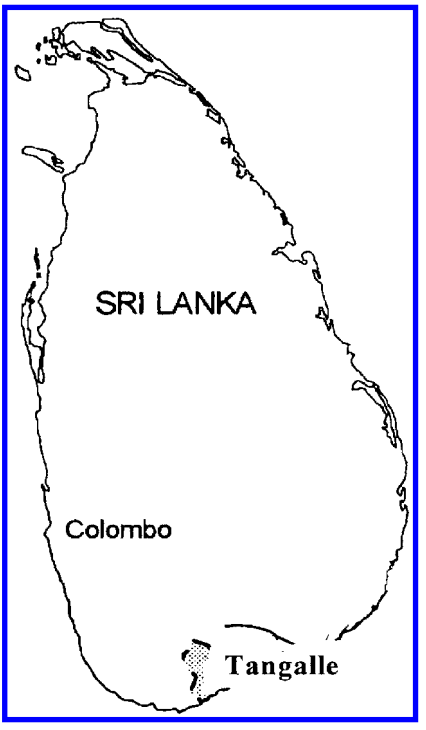


Figure 1. Location of Tangalle area.

dip angle is 50°–60° to the South. These rocks were originally deposited in the Precambrian sea, then, were severely metamorphosed.

Many lineaments are found from air photos and satellite images in the studied area. The general directions of these lineaments are classified into two patterns, NW-SE and NE-SW. It was also found from field observations that there were many horizontal fractures with low dip angle. Hence, three directions of fractures, NW-SE, NE-SW and horizontal, were thought to be dominant in the study area.

2.2 *Geometry of studied area and precipitation*

The geometry of the study area consists of combinations of high land and low land. The height difference between the high land and the low land is about 10–20 m and the ground surface is gently sloped from high land toward low land. The elevation of highland from sea level is about 35 m.

The thickness of the weathered rock and the soil cover in the highland area is about 1–2 m, which causes a low rain water storage in the highland and large amount of rainwater rapidly flows toward the low land area. The river system is well developed in the low land area and which water flows towards sea. The surface water flowing in the low land are stored in retention reservoirs (tanks) and used to meet agricultural and domestic needs.

The climatic condition in the southern part of Sri Lanka is characterized by; the South-West Monsoon and the North-East Monsoon (De Silva et al., 1997). Highest rainfall amounts usually occur during the months of May to September, during the South-West Monsoon, and December to February, during the North-East Monsoon, respectively. The average annual rainfall of the Tangalle area is about 1180 mm. This annual precipitation is not enough for paddy field, even though many retention reservoirs are used for storage.

2.3 *Aquifer*

There are several types of aquifers in the southern part of Sri Lanka. The most common aquifer exists in the alluvium deposit in the low land. The thickness of the alluvium sediment commonly ranges from 2 to 10 meters. Most people meet their domestic demand from dug wells by exploiting groundwater from this aquifer. The depth of dug wells varies from few meters to about 10 m. Some dug wells completely dries up during the dry season and fill up to the ground level during the rain season. Groundwater contained in weathered rock and fractured rock is pumped up in the highland by using hand pumps, which reach depths of 10–30 m. This can be considered as the second type of aquifer. The quality of water extracted by hand pumps are fairly good for drinking in most parts of the area. But, due to the low yielding capacity of this aquifer, it is impossible to meet the future water demand from these wells alone. Therefore it is imperative to evaluate the possibility of extracting groundwater from deeper aquifers in fractured rock mass by using deep wells which reach depths of 100–200 m. However, the third type of aquifers is in deep rock mass, whose groundwater behavior has not been clarified yet.

3 MODELING OF FRACTURED ROCK MASS AND ANALYSIS OF FRACTURE FLOW

3.1 *Don-Chan model*

The channel network model “Don-Chan” (Watanabe et al., 1997) was used in this study for the analysis of groundwater flow in an idealized model of fractured rock mass developing in the Tangalle area.

In this model, fractures are divided into three categories as follows;

(a) Minor fractures (randomly developed).
(b) Major fractures (extend long in the area).
(c) Fault zone.

These fractures are schematically illustrated in Figure 2. Each type of fracture is modeled by the following procedure.

Copyright © 2003 Swets & Zeitlinger B.V., Lisse, The Netherlands

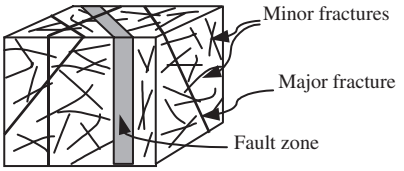


Figure 2. Schematic illustration of fractured rock.

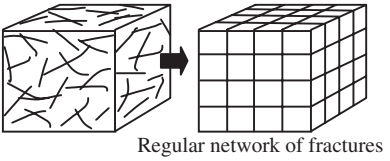


Figure 3. Modeling of minor fractures.

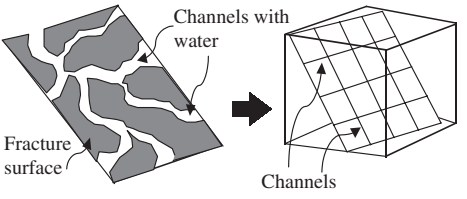


Figure 4. Modeling of channel in fractures.

The minor fractures can be seeing as an equivalent system of fracture properties over the fractured rock. Therefore these minor fractures are modeled as a regular channel network of horizontal and vertical fractures, as shown in Figure 3.

The direction of major fractures can be estimate from small lineaments. In this study only low angle major fractures are considered because this major fractures are dominant by field survey. Water in fracture plane flows in complicated channels on the plane (Figure 4). These channels may intersect in three-dimensional space and form a network of channels for the movement and mixing of flowing water (Neretnieks, 1993). The regular channel network, as illustrated in Figure 4, approximate the flow through the fracture plan. The directions of regular channels can be decided from some features of the fractures, such as the displacement direction of those fractures. Moreno and Neretnieks (1993) represented this network with stochastic conductance values arranged on a rectangle grid and Moreno et al., (1997) conceptually represented the channels as discrete. In this study, two channel sets in the direction of strike and dip are assumed to developed as the first step.

As illustrated in the Figure 5(a), a fault zone is modeled by a combination of high permeable planes and a low permeable plane which act as a water barrier.

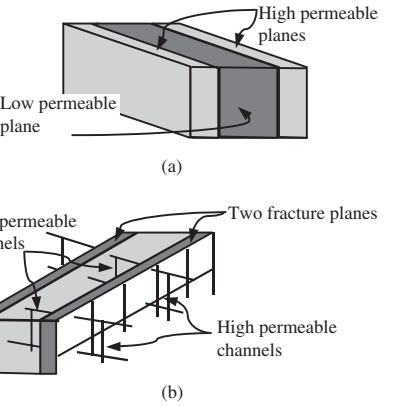


Figure 5. Modeling of a water barrier fractures. (a) Three planes assumed in a water barrier fracture (b) channels defined in the low permeable plane and the high permeable planes.

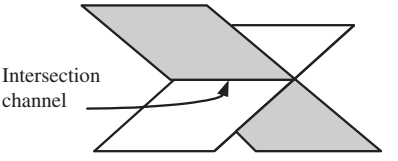


Figure 6. Schematic illustration of two fractures intersection channel.

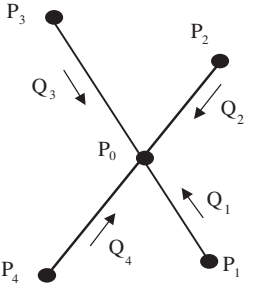


Figure 7. The flow conditions in the channels.

A fault zone is approximated by two fracture planes in the Don-Chan model, as shown in the Figure 5(b). When many channels representing major fractures or minor fractures cross the fault zone, the channels in between the two planes are thought as low permeable channels as shown in the Figure 5(b).

The intersection line among all the fractures mentioned above is also assumed to be a channel, as shown in the Figure 6. A 3D channel network is constructed by combining all of these channels.

The Don-Chan model calculates the groundwater flow in 3-D channel network thus formed. Figure 7

Copyright © 2003 Swets & Zeitlinger B.V., Lisse, The Netherlands

illustrates an example of two channels that intersect at point P_0 and surrounding points P_i ($i = 1, \ldots, 4$). Q_1, Q_2, Q_3 and Q_4 represent the discharge of groundwater flowing into P_0 from the surrounding points. Under steady-state conditions, the sum of Q_1, Q_2, Q_3 and Q_4 must be zero.

$$Q_1 + Q_2 + Q_3 + Q_4 = 0 \quad (1)$$

The discharge from a neighboring point Q_i ($i = 1, \ldots 4$) can be written as

$$Q_i = A_i \times k_i \times (H_i - H_0)/L_i = T_i(H_i - H_0)/L_i \quad (2)$$

Where, A_i is the cross-sectional area of channel, k_i is the hydraulic conductivity of the layer, H_i is the piezometric head of point P_i ($i = 0, \ldots, 4$), L_i is the length of the channel. T_i is a parameter presenting water discharge along each channel. Unit is m^3s^{-1}.

Similar equations can be constructed for every cross point of the network in similar manner. By solving all the equations under the given boundary conditions, the piezometric head can be calculated.

3.2 *Idealized model of fractured rock*

For this study, a surface area of 2 km^2 was selected and the model was built up to a depth of 500 m. The uneven surface of the area was roughly approximated by the combination of 800 triangular planes.

The fracture orientation is not uniformly distributed over a wide area but it is spatially changing. The fractured rock mass was thought to be composed of different rock masses which consist of different fracture systems. In this study, the Don-Chan model was modified to analyze groundwater flow in an area composed of different fracture systems.

Figure 8 illustrates the conceptual model developed for this study. One big fault (water barrier fracture) is running in the study area. The fracture orientation on both sides of the faults is different from each other, as shown in Figure 8. Figure 8 shows only the major fractures and fault zone but minor fractures assumed in the model are not illustrated. On both sides, 2 different major fracture sets are assumed. The directions of those fracture sets are as follows:

Right hand side; strike of fracture is 50° from East to South and the Dip angle of bed is 15° SW direction.

Left hand side; strike of fracture is 30° from East to South and the Dip angle of bed is 35° to SW direction.

The spacing between all the major fracture sets were set as 100 m in this study. The minor fractures were approximated by 54 sets of fractures having vertical and horizontal directions with at intervals of 80 m.

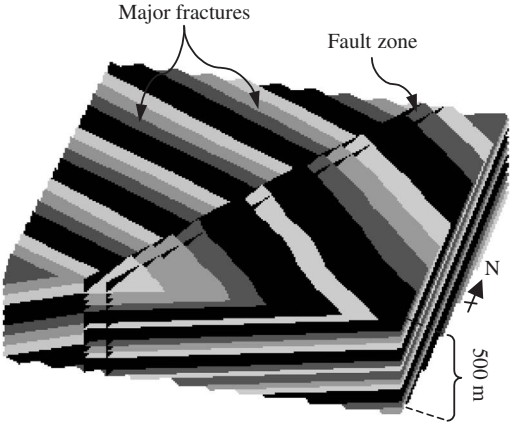


Figure 8. A fault zone and low angle major fractures.

4 SENSITIVITY ANALYSIS

Don-Chan model can analysis the groundwater flow in the channel network system. The proper estimation of transmissivity (T_i in equation 2) of every channel is indispensable for the calculation. One possible way to estimate the channel transmissivity is the back analysis of well tests. From this viewpoint, sensitivity analysis of groundwater pumping from two wells was carried out.

To study the behavior of the piezometric head distribution under the different channel transmissivity values, a sensitivity analysis was carried out by changing the channel transmissivity of the minor fractures. The assumed channel transmissivity values under different cases are summarized in Table 1. Four cases of analysis were performed. The major fracture channel transmissivity of the left hand side and the right hand side of fault zone were changed as in Table 1. The channel transmissivity of the high permeable planes of water barrier fracture defined same as the major fractures. Although the channel transmissivity given in every case seems to be small and only low angle major fractures were treated the general tendency of the piezometric head can be discussed.

It was assumed that the North, South, bottom and surface boundaries were no-flow boundaries, while the East and the West boundaries were considered as constant head boundaries with 480 m and 490 m of piezometric head, respectively. The boundary conditions are summarized in Figure 9.

Two wells, well A and well B with a depth of 180 m and located 100 m away from the water barrier fracture, as illustrated in the Figure 9, were selected. These wells were selected to find the variation of the piezometric head under different pumping rates. Figure 10 shows the piezometric head distribution of Case 2 with a discharge rate of 0.006 m^3s^{-1} on the horizontal plane at a level of 180 m from the top. In this case, water is pumped from wells A and B. Due to the low

Copyright © 2003 Swets & Zeitlinger B.V., Lisse, The Netherlands

Table 1. Channel transmissivity.

Channel transmissivity (m^3s^{-1})					
				Major fractures	
Case	Water barrier fracture low permeable plane	Minor fractures	Fracture intersections	Left hand side	Right hand side
1	6.5×10^{-9}	3.2×10^{-3}	5×10^{-6}	1.2×10^{-7}	2×10^{-6}
2	6.5×10^{-9}	6.4×10^{-4}	5×10^{-6}	1.2×10^{-7}	2×10^{-6}
3	6.5×10^{-9}	3.2×10^{-4}	5×10^{-6}	1.2×10^{-7}	2×10^{-6}
4	6.5×10^{-9}	6.4×10^{-5}	5×10^{-6}	1.2×10^{-7}	2×10^{-6}

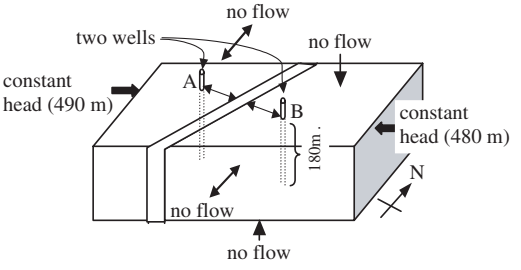


Figure 9. Illustration of boundary conditions given in the model and wells A and B.

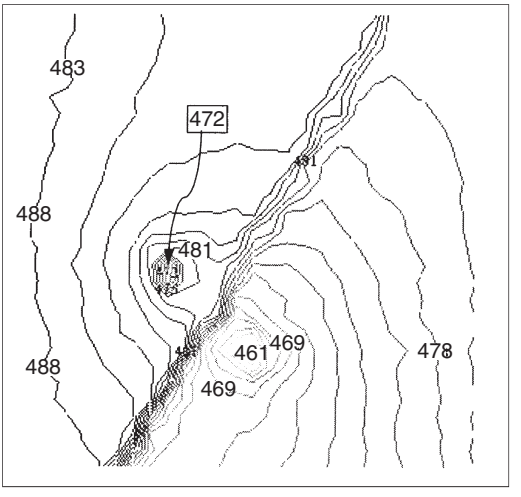


Figure 10. Illustration of piezometric head distribution of Case 2 on the horizontal plane at the 180 m (in case of pumping from well A and B).

channel transmissivity of the water barrier fracture a large piezometric head difference is found between the discharge points. Figure 11 shows the variation of piezometric head at points A and B, due to the change of the pumping rate from well A. Due to the

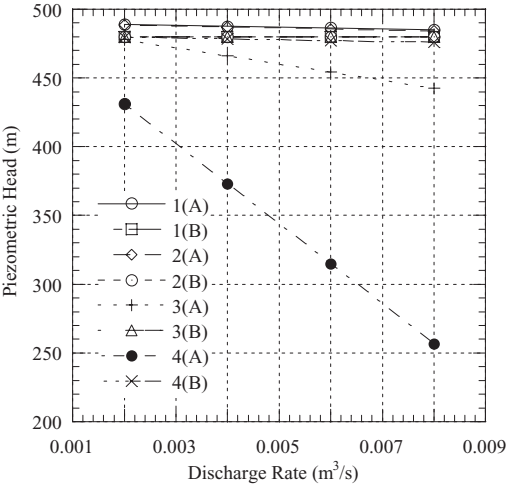


Figure 11. Variation of piezometric head at points A and B under various pumping rate from well A.

water barrier nature of the big fault zone, the effect of pumping was not significant in well B. In well A, the drawdown was not much significant for Cases 1–3. But, for Case 4 the drawdown was very sensitive to varying pumping rates.

The variation of the piezometric head at wells A and B, due to the pumping of water from well B, is shown in Figure 12. The drawdown at well B was negligible when the water was pumped from well B and when the channel transmissivity of the minor fractures were grater than $6.4 \times 10^{-5}\,m^3s^{-1}$. The drawdown of Well B was also sensitive when the channel transmissivity of the minor fractures were equal to $6.4 \times 10^{-5}\,m^3s^{-1}$.

The variation of the piezometric head at wells A and B, due to the pumping of water from wells A and B, is shown in Figure 13. As the surface elevations of the wells were at two different levels and the piezometric head value difference of East and West boundaries was 10 m, the drawdown of well A and B shows a big difference for Case 4. This is shown in Figure 13. This

Copyright © 2003 Swets & Zeitlinger B.V., Lisse, The Netherlands

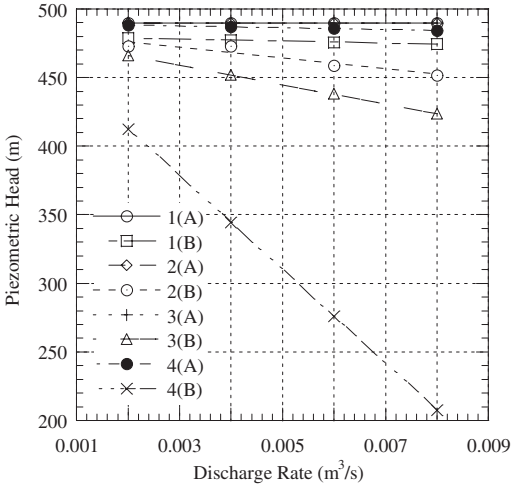


Figure 12. Variation of piezometric head at points A and B under various pumping rate from well B.

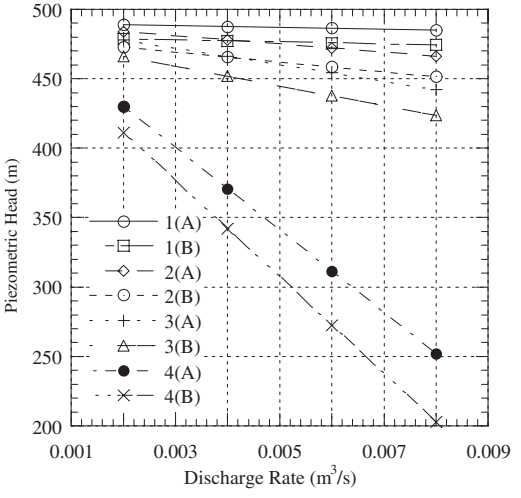


Figure 13. Variation of piezometric head at points A and B under same pumping rate from each well at point A and B.

may be due to the extraction of water by well A as it flows upstream. Therefore, the possibility of reaching the upstream water towards well B was reduced. According to Figure 10, well B received water from the water barrier and the downstream of the water barrier.

5 DISCUSSION AND CONCLUSION

This study shows the application of a technique of groundwater flow calculation: modeling of minor fractures, major fractures and water barrier fracture, which was applied to the Tangalle area, Sri Lanka.

Due to the surface cover, it was difficult to determine fracture patterns through field surveys only. Therefore, the major fractures and water barrier fracture were extracted from the lineament data obtained from remote sensing. The topological map in the Tangalle area was used for constructing the surface geometry. Furthermore, giving the fix boundary condition for the model domain, a technique was constructed to calculate the groundwater flow in fractured rock mass on the basis of geological data.

The drawdown due to pumping from two wells located in a fractured rock mass was studied in order to determine the behavior of the flow pattern. It was found that the effect of pumping from a well located downstream of a water barrier fracture was minimal when the transmissivity of the minor fractures was high. The discharge rate and piezometric head shows a linear relationship in the model developed.

If the correct processes are included in the model, it is expected that the model results will mimic reasonably well the observed dynamics. Therefore, it is recommended that the actual behavior of flow patterns and other physical and environmental conditions of the field be studied in order to calibrate the developed model and then apply to other simulations.

In this study, only the transmissivity of minor fractures were varied in order to study the variation of drawdown. But the variation of transmissivity in the major fractures can also influence the drawdown. This is not examined in this study.

Although the sensitivity of the model was studied, calibration of the model with the observed data is not carried out yet. The proper hydro-geological model of an actual fractured rock mass on the basis of detailed geological investigation is indispensable before the application.

REFERENCES

Andersson, J., Dverstorp, B., 1987. Conditional simulations of fluid flow in three-dimensional networks of discrete fractures. Water Resource Research 3(10): 1876–1886.

Cacas, M.C., Ledoux, E., Marsily, D. De., Tille, B., Barbreau, A., Durand, E., Feuga, B., Peaudecerf, P., 1990. Modelling of fracture flow with the stochastic discrete fracture network: calibration and validation-1, the flow model. Water Resource Research 26(3): 479–489.

Cooray, P.G., 1997. Geology. In: Somasekaram, T., Perera, M.P., de Silva, M.B.G., Godellawatta, H., Arjuna's Atlas of Sri Lanka, pp. 8–11.

Long, J.C.S., Witherspoon, P.A., 1985. The relationship of the degree of interconnection to permeability in fracture networks. J. Geophysics Research 90(B4): 3087–3097.

Moreno, L., Neretnieks, I., 1993. Fluid flow and solute transport in a network of channels. J. Contaminant Hydrology 14(2): 163–192.

Copyright © 2003 Swets & Zeitlinger B.V., Lisse, The Netherlands

Moreno, L., Gylling, B., Neretnieks, I., 1997. Solute transport in fractured media-the important mechanisms for performance assessment. J. Contaminant Hydrology 25: 283–298.

Neretnieks, I., 1993. Solute transport in fractured rock-applications to radionuclide waste repositories. In: Bear, J., Tsang, C.F., de Marsily, G. (Eds.). Flow and Contaminant Transport in Fractured Rock. Academic Press, New York.

Panda, B.B., Kulatilake, P.H.S.W., 1998a. Influence of discontinuity geometry parameters and transmisivity on hydraulic behavior of discontinuous rock. ASCE, J. Engineering Mechanics 125(1): 41–50.

Panda, B.B., Kulatilake, P.H.S.W., 1998b. Relation between fracture tensor parameters and permeability tensor parameters for discontinues rock. ASCE, J. Engineering Mechanics 125(1): 51–59.

Rouleau, A., Gale, J.E., 1987. Stochastic discrete fracture simulation of groundwater flow into an underground excavation in granite. Int. J. Rock Mechanics of Mine Science and Geo-mechanics Abstr. 24(2): 99–112.

Schwartz, F.W., Smith, W.L., Crowe, A.S., 1983. A stochastic analysis of microscopic dispersion in fractured media. Water Resource Research 19(5): 1253–1265.

Silva, M.B.G.De., 1997. Climate. In: Somasekaram, T., Perera, M.P., de Silva, M.B.G., Godellawatta, H., Arjuna's Atlas of Sri Lanka, pp. 16–22.

Watanabe, K., Sugimura, Y., Morita, Y., Tanaka, T., 1997. Channel network modeling of the fractured granite in the Hinachi area, Japan. In: Kanaori, Y. Earthquake Proof Design and Active Faults, pp. 247–262.

Copyright © 2003 Swets & Zeitlinger B.V., Lisse, The Netherlands

Use of DEM to model the contact force between soil particles in moist condition

H. Fujimura & H. Kiyama
Department of Civil Engineering, Tottori University, Tottori, Japan

ABSTRACT: In this study, Distinct Element Method (DEM) is applied to numerically simulate a saturated soil mass and estimate the contact force between particles. A two-dimensional model of soil is prepared considering the soil particles as circular elements, assembled to represent a lump of soil. Gaps between the circular elements in the assembly, representing soil pores, are considered to contain water so that the soil is saturated. The soil mass is separately subjected to a vertical load and a horizontal earthquake load. DEM is then used to estimate the inter-element contact forces. The results are also compared with those under dry soil condition.

1 INTRODUCTION

In soil mechanics, the soil is considered as a three-phase material composed of solid particles, pore water and air. The presence of water in soil pores plays an very important role in the engineering analysis of soil behavior, such as in liquefaction and slope failure problems. The fundamental feature of DEM (Cundall 1971, Kiyama 1983) is that the mass of soil is taken as an assemblage of distinct rigid blocks, the contact between any two adjoining blocks being analogous to a mechanical set up shown in Figure 1. In this research, an additional parameter, namely pore water, has been introduced into the assemblage, while ensuring that all fundamental assumptions of DEM remain valid.

Two separate analyses are performed: one, when the assemblage is saturated with pore water, and another, when it is completely dry. Computing and comparing the contact forces between the elements for the dry and moist situations is the objective of the study.

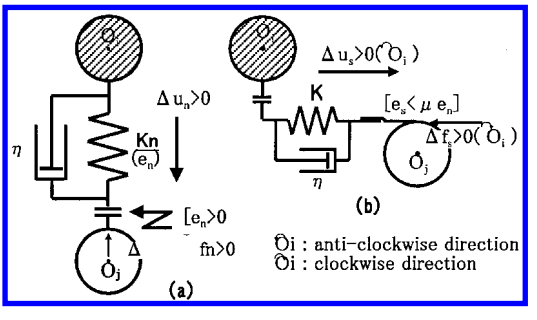


Figure 1. Mechanical model representing two adjacent DEM elements.

2 ANALYTICAL MODEL

The analytical model consists of an assemblage of fifteen circular elements of radius 1 cm each, as illustrated in Figure 2. An impervious layer is assumed to be present at the bottom so that the pore water cannot escape to be outside. The assemblage as a whole is in an undrained state, but the inter-pore flow of water within the assemblage is permitted.

Two types of external forces are applied independently to the model assembly. A uniform vertical force is superimposed on the topmost element, while a variable horizontal acceleration is applied on the bottommost layer to simulate earthquake force.

As an important feature of the model, the compressibility of pore water is not neglected. The impact of

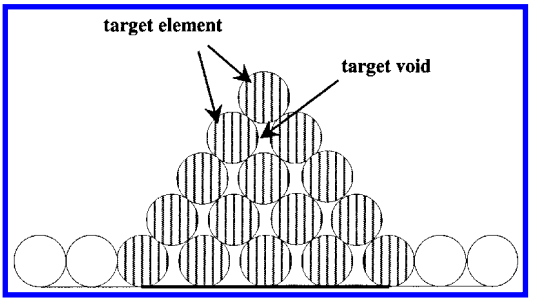


Figure 2. Analytical model.

Copyright © 2003 Swets & Zeitlinger B.V., Lisse, The Netherlands

this assumption on the analysis is that the pore water pressure varies in response to the external force, which in turn results in the variation in contact force between the elements. Such variations in contact force and pore water pressure are evaluated in the study, assuming that the pore water pressure component adds up to the contact pressure.

During the analysis, a state of equilibrium for the assembly is first achieved, and then external forces are applied. While applying the vertical load, the movement of the bottom layer elements is restrained in the vertical direction. Similarly, while applying the horizontal (earthquake) load, the bottom layer elements can move in the horizontal direction, but always maintain the relative spacing (between the elements).

3 CALCULATION OF PORE WATER PRESSURE

Flow of pore water within the model soil mass follows Darcy's law. Figure 3 shows four adjacent soil elements i_1, i_2, i_3 and i_4 that constitute a soil pore l in between, and four outside pores m_1, m_2, m_3 and m_4. All five pores are saturated with water.

At time $t - \Delta t$, the respective volumes of pore water are V_l, $V_{m1} \sim V_{m4}$, and the corresponding excess pore water pressures are u_l, $u_{m1} \sim u_{m4}$. Changes in the volume of pore water after an incremental time Δt are shown in Figure 4. Volume V_l changes to V_l' $(= V_l - \Delta V_l)$. In addition, the volume of pore water changes by an amount $\Delta V_{wl,}$ as a result of the outgoing discharge, Δq_l, and the change in excess pore water pressure, Δu_l.

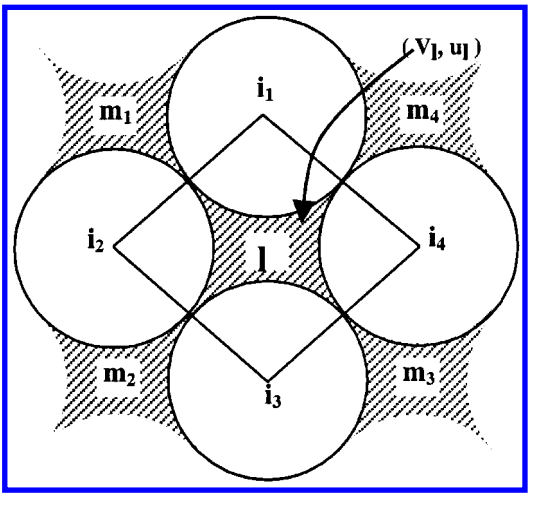


Figure 3. Soil pore formed by four elements.

From Darcy's Law, the change in discharge within the pore l from adjoining pores during time Δt can be expressed as

$$\Delta q_l = -\sum_i \frac{(u_{mi} - u_l)}{L_{lm}\gamma_w} \kappa_e S_{lm} \Delta t \qquad (1)$$

where Σ represents summation for pores $m_1 \sim m_4$; L_{lm} represents the flow length between pores l and m; and S_{lm} represents the cross-section across the flow.

As shown in Figure 5, S_{lm} could be represented by the distance S_{ij} between the centers of two adjacent elements. Similarly, L_{lm} can be represented by

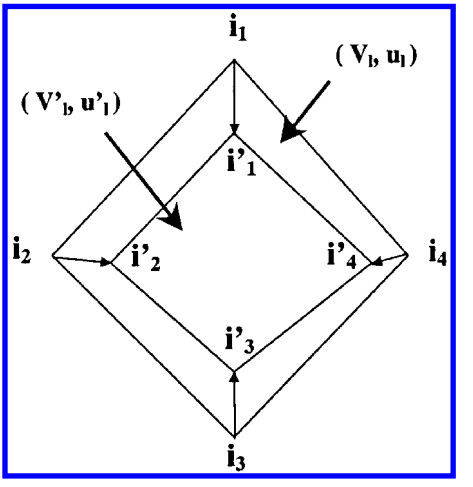


Figure 4. Deformation of soil pore and the skeleton.

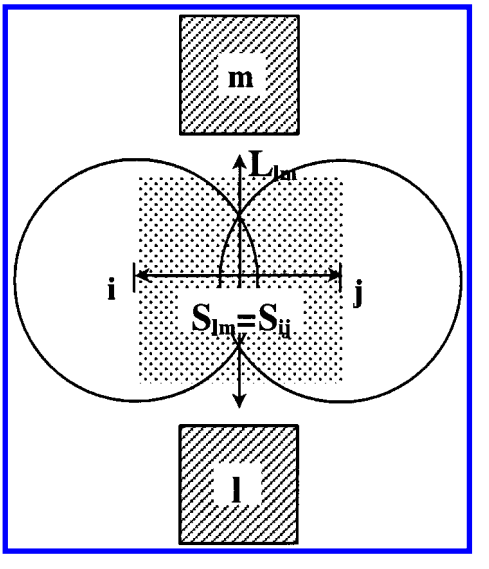


Figure 5. Flow area and flow length.

Copyright © 2003 Swets & Zeitlinger B.V., Lisse, The Netherlands

the diameter of the element. This will result in the equation:

$$L_{lm} = 2r \times \frac{2r}{S_{ij}} \tag{2}$$

Combining the above two equations gives

$$\Delta q_l = -\sum_i \frac{(u_{mi} - u_l)}{\gamma_w} \kappa_e \left(\frac{S_{ij}}{2r}\right)^2 \Delta t \tag{3}$$

The net change in volume of pore l, i.e. ΔV_l, is the summation of the change in discharge Δq_l and the volume change ΔV_{wl} due to the increment in excess pore water pressure, thereby yielding the following relation.

$$\Delta V_{wl} = \Delta V_l - \Delta q_l = V_l - V_l' - \Delta q_l \tag{4}$$

Knowing the volumetric change ΔV_{wl} from the above equation, the increase in excess pore water pressure Δu_l during time Δt can be evaluated from the following relation.

$$\Delta u_l = E_w \frac{\Delta V_{wl}}{V_l} \tag{5}$$

where E_w is the volume elastic modulus.

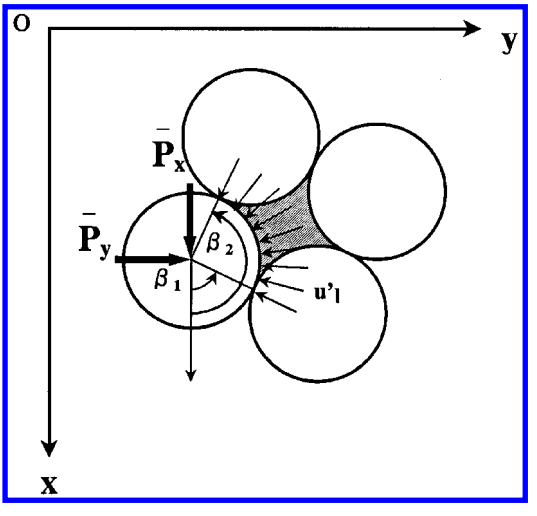


Figure 6. Pore water pressure acting on an element.

Table 1. Physical parameters of pore water.

Density	ρ_w: 1.0 g/cm^3
Volume elastic modulus	E_w: 2.0 × 10^6 kPa
Coefficient of permeability	K_e: 1 × 10^{-4} cm/s

The value of Δu_l obtained from this equation can be added up to u_l to get the excess pore water pressure u_l' corresponding to the volume V_l' at time t.

$$u_l' = u_l + \Delta u_l \tag{6}$$

By combining equations (1) to (6) with the basic DEM equations, it would be possible to work out for each time step the contact force between the elements, displacement of elements, changes in pore water pressure, and flow behavior of pore water.

Referring to Figure 6, the pore water pressure acting on an element along axes x and y can be expressed as the following two equations.

$$\overline{P_x} = \int_{\beta_1}^{\beta_2} -u_l' r \cos\beta \, d\beta = -u_l' r(\sin\beta_2 - \sin\beta_1)$$

$$\overline{P_y} = \int_{\beta_1}^{\beta_2} -u_l' r \sin\beta \, d\beta = u_l' r(\cos\beta_2 - \cos\beta_1)$$

The mechanical properties of pore water assumed in the analysis are summarized in Table 1.

4 RESULTS AND DISCUSSION

When the vertical external load is applied, the results in Figure 7 are observed. This Figure shows the case when the applied load was equal to three times the weight of a single element. It is seen that the contact force between the elements is smaller when the soil mass is saturated. This is thought to be the influence of excess pore water pressure.

Figure 8 shows the temporal variation in contact force between elements 13 and 15. Likewise, Figure 9 shows the temporal variation in pore water pressure in the pore enclosed by elements 11, 13, 14 and 15. A larger contact force in the case of dry soil as compared to wet soil is also evident from Figure 8.

As is seen in Figure 9, the pore water pressure increases with increasing vertical load.

Figures 10 and 11 illustrate the results when the external force is the earthquake force applied as a

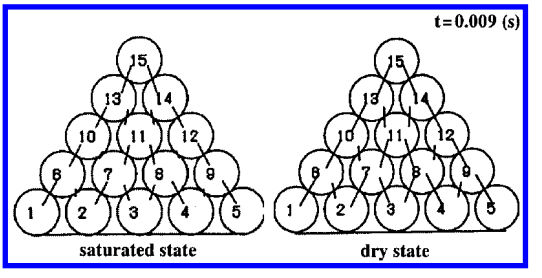


Figure 7. Variation in contact force with a load equal to the weight of three elements.

Copyright © 2003 Swets & Zeitlinger B.V., Lisse, The Netherlands

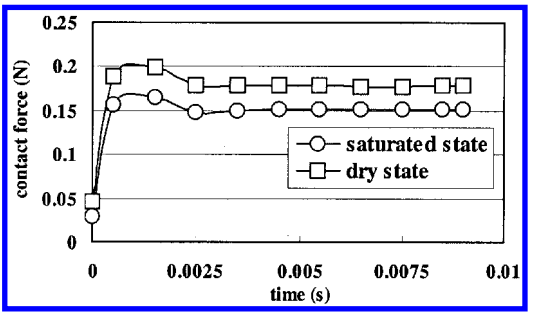


Figure 8. Variation in contact force with load.

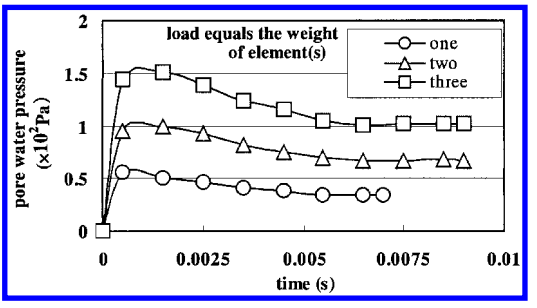


Figure 9. Variation in pore water pressure with load.

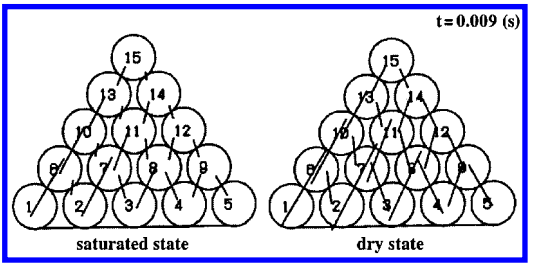


Figure 10. Contact forces due to horizontal acceleration of 150 gal, 5 Hz.

horizontal acceleration. The contact forces for the saturated and dry soil are shown in figure 10, and the pore water pressure values are shown in Figure 11.

In both the dry and wet conditions, the left half of the soil mass experiences higher contact force

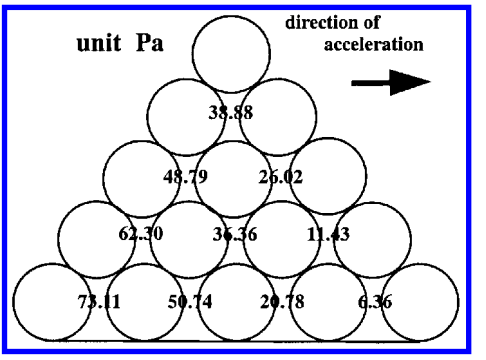


Figure 11. Distribution of pore water pressure when maximum acceleration of 150 gal, 5 Hz was applied.

as compared to the right half. A similar pattern is observed in the calculation of pore water pressure as well.

5 CONCLUSION

It has been possible, through this study, to combine the behavior of pore water with the traditional DEM analysis.

Under external loadings on the soil mass, the contact forces between soil elements differ according to their state of saturation. In particular, the contact force is smaller in a wet soil mass. This is due to the occurrence of excess pore water pressure. The instability of soil mass increases with increasing amount of external force working on the mass.

REFERENCES

Cundall, P.A. 1971. *A Computer Model for Simulating Progressive Large Scale Movements in Blocky Rock Systems. ISRM Proceedings* 2: 129–136.

Kiyama, H. & Fujimura, H. 1983. *Application of Cundall's Discrete Block Method to Gravity Flow Analysis of Rock-like Granular Materials. Proc. of JSCE,* (333): 137–146 (*in Japanese*).

Copyright © 2003 Swets & Zeitlinger B.V., Lisse, The Netherlands

Advection and dispersion analysis in Gaussian and non-Gaussian random field of permeability

S. Nishimura, A. Murakami & T. Nishiyama
Okayama University, Okayama, Japan

H. Fujii
Geoenvironmental and Disaster Prevention Institute, Okayama, Japan

ABSTRACT: The dispersion behavior of a substance in the ground water flow depends on the random field characteristics of the permeability. In this study, we clarify how the Gaussian and the non-Gaussian random fields of permeability affect the dispersion behavior. The finite difference method (FDM), combined with the Monte Carlo method (MCM), is used in the analysis to solve the advection and dispersion equations. The results of the analysis are evaluated by the mean and standard deviation of the concentration. Firstly, a tracer mixed with water is analyzed as a single-phase problem. Then, the migration of the DNAPL pool in the ground water is treated as a two-phase problem.

1 INTRODUCTION

The dispersion behavior of a substance in the ground water flow depends on the random field characteristics of the permeability. The type of dispersion dealt with here is macro-dispersion. It is caused by advection in the random field of permeability. The effect of the differences in random field properties, mean, variance, spatial correlation, and type of statistical distribution on the dispersion characteristics is shown.

The finite difference code, UTCHEM (Brown et al. 1994), is used in this study to solve the dispersion and advection of substances. The code is applied along with the Monte Carlo method (MCM) in order to take the random field properties into account. Considering the spatial variability of the permeability of the ground, a Gaussian distribution is often assumed in a statistical seepage analysis for the logarithm of the parameter. In this study, the Gaussian distribution is firstly considered. Then, the non-Gaussian random distribution is considered for the logarithm of the permeability. The effect of the difference in distribution on the results of the seepage analysis is verified. In this study, a newly proposed non-Gaussian random field generation method (Nishimura 2001) is used.

In geotechnical problems, the shortage of information on the spatial distribution of soil parameters is often serious. In the case of a random field simulation, a multivariate normal joint distribution is assumed. However, it is very difficult to obtain enough data to identify the multivariate joint distribution. Usually, only the marginal distribution or the first and the second order statistical moments are known.

The proposed method is based on a numerical optimization technique, such that the generated random numbers satisfy the known first and second order statistical moments or the marginal distribution of the soil permeability. An optimization method is necessary for minimizing the errors between the statistical moments and the marginal distribution of the target permeability distribution and those from the generated random numbers. The genetic algorithm (GA) (Goldberg 1989) is used for optimization in the proposed method.

Firstly, the tracer is combined with water and analyzed as a single-phase problem. In this problem, the effect of the differences in statistical moments or correlation distances on the dispersion is verified. Secondly, the migration of the DNAPL pool in the ground water is treated as a two-phase problem. In this case, the difference in the results between the Gaussian and the non-Gaussian simulations is discussed.

2 MODEL DESCRIPTION

2.1 *Mathematical formulations*

Mass conservation and pressure equations are necessary mathematical formulations in UTCHEM. The

Copyright © 2003 Swets & Zeitlinger B.V., Lisse, The Netherlands

details of these equations are described in Brown et al. (1994). The mass conservation equation, Equation (1), is given to describe the uniqueness of this study. The total volume of component κ in all phase-per-unit pore volumes (concentration of κ component) is signified as C_κ. The component κ is water or NAPL here. In this study, only macro-dispersion is considered in the analysis; general dispersion and diffusion terms are not taken into account in the equation. For simplicity, the adsorption term is not considered either.

$$\frac{\partial}{\partial t}\left(\phi C_\kappa \rho_\kappa\right) + \nabla \cdot \left[\sum_{l=1}^{n_p} \rho_\kappa C_{\kappa l} \boldsymbol{u}_l\right] = R_\kappa \tag{1}$$

$$C_\kappa = \sum_{l=1}^{n_p} S_l C_{\kappa l} \tag{2}$$

$$\boldsymbol{u}_l = -\frac{k_{rl}\mathbf{K}}{\mu_l} \cdot \left(\nabla P_l - \gamma_l \nabla h\right) \tag{3}$$

where, t is the time, ϕ is the effective porosity, $C_{\kappa l}$ is the volume concentration of κ component in the phase l, ρ_κ; is the density of the component κ, R_κ is the source term of the component κ, S_l is the saturation of the phase l, n_p is the number of phases considered in the analysis. Single- and two-phase problems are addressed in this study. Phase 1 is aqueous and phase 2 is non-aqueous. The vector $\boldsymbol{u}_l$ is the velocity of phase l, k_{rl} and μ_l are the relative permeability and the viscosity, respectively, P_l is the pressure of phase l, h is the vertical coordinate, γ_l is the specific weight of the phase l, $\mathbf{K}$ is the intrinsic permeability tensor.

2.2 *Parametric models*

In this study, a two phase problem is solved. To the relative permeabilities of the two phases, k_{r1} and k_{r2}, the following Corey type equations are employed:

$$k_{r1} = k_{r1}^0 \left(S_{n1}\right)^{n_1} \tag{4}$$

$$k_{r2} = k_{r2}^0 \left(1 - S_{n1}\right)^{n_2} \tag{5}$$

$$S_{n1} = \frac{S_1 - S_{1r}}{1 - S_{1r} - S_{2r}} \tag{6}$$

in which, S_1, S_2, S_{1r} and S_{2r} are the saturations and the residual saturations of phase 1 and phase 2, respectively. The parameters n_1, n_2, k_{r1}^0 and k_{r2}^0, determined from the experiments, are exponents and endpoints of the relative permeability, respectively.

The capillary pressure between water and NAPL, P_{c12} is given in the following equation.

$$\left(P_b / P_{c12}\right)^{\lambda_i} = 1 - S_{n1} \tag{7}$$

in which, P_b is the entry pressure replaced by the Equation (8), λ_i^b and C_i is the experimental constants, σ_{12} is the interfacial tension, and k_a is the spatial mean permeability.

$$P_b = C_i \sigma_{12} \sqrt{\phi / k_a} \tag{8}$$

3 RANDOM FIELD SIMULATION METHOD

3.1 *Statistical properties of permeability*

The lognormal distribution is often assumed for the soil permeability. In this study, the two-dimensional random field is analyzed. The horizontal $x-y$ plane is descretized into $n = n_x \times n_y$ grids. The logarithm of permeability k, $Y = \log_{10} k$ is assigned to each grid, as shown in Figure 1. The logarithmic permeability has the following covariance function.

$$A_C(\Delta x, \Delta y) = \sigma_Y^2 \exp\left[-\sqrt{\left(\Delta x / l_x\right)^2 + \left(\Delta y / l_y\right)^2}\right] \tag{9}$$

In this equation, Δx and Δy are the distances between two points s and t on the x and y axes, respectively. The parameters, l_x and l_y are the correlation distances, respectively, and σ_Y is the standard deviation of $\log_{10} k$.

3.2 *Gaussian random field simulation*

The covariance matrix decomposition method (Rubinstein 1981) is used here. The matrix $\boldsymbol{C}_P = [A_C(\Delta x, \Delta y)]$ is defined as the covariance between two logarithmic permeabilities at points s and t. Matrix $\boldsymbol{C}_P$ is further divided into lower and upper triangular matrices, C and $\boldsymbol{C}^T$.

$$\boldsymbol{C}_P = \boldsymbol{C}\boldsymbol{C}^T \tag{10}$$

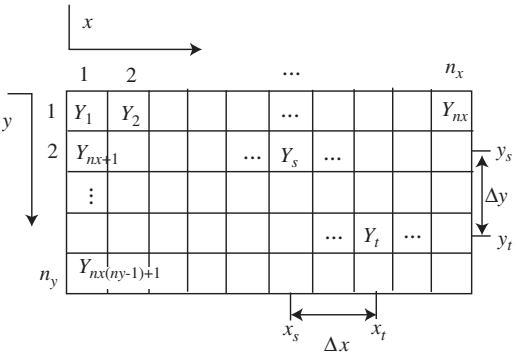


Figure 1. Descretized two-dimensional random field.

Copyright © 2003 Swets & Zeitlinger B.V., Lisse, The Netherlands

Correlated random numbers $\boldsymbol{v} = (v_1, v_2, \ldots, v_n)$ are generated by the following equation.

$$\boldsymbol{v} = \boldsymbol{Ca} \tag{11}$$

The components of vector **a** are independent N (0,1) type normal random variables. The random number v; is transformed into the logarithmic permeability by the relationship, $Y = \mu_Y + \sigma_Y v$ (μ_Y is the mean value).

3.3 *Non-Gaussian random field simulation*

The proposed method generates $n \times m$ random numbers for the logarithmic permeabilities, in which n is the number of grids (see Figure 1) and m is the number of samples. The vector for random numbers is signified as $\boldsymbol{Y} = [Y_i^j]$, $(i = 1, \ldots, n \quad j = 1, \ldots, m)$, which is the probabilistic logarithmic permeability vector. The random numbers are generated to minimize the objective function, $g(\boldsymbol{Y})$, denoted in Equation (12). The genetic algorithm (GA) is used to minimize the function $g(\boldsymbol{Y})$.

$$g(\boldsymbol{Y}) = \sum_{l=1}^{n_c} \eta_l(\boldsymbol{Y}) \tag{12}$$

in which n_c is the number of residual functions, $\eta_l(\boldsymbol{Y})$ is the residual function. The concrete form of the function $\eta_l(\boldsymbol{Y})$ is given below.

The function η_1 is the sum of the squared residuals between the calculated correlation coefficient from the generated random numbers, r_{st} and theoretical one, ρ_{st} based on the Equation (9).

$$\eta_1(\boldsymbol{k}) = \sum_{s=1}^{n}\left[\sum_{t=s}^{n}\left(r_{st} - \rho_{st}\right)^2\right] \tag{13}$$

$$r_{st} = \frac{\frac{1}{m}\sum_{j=1}^{m} Y_s^j Y_t^j - R_1^s R_1^t}{R_2^S R_2^t} \tag{14}$$

$$R_1^s = \frac{1}{m}\sum_{j=1}^{m} Y_s^j, \quad R_1^t = \frac{1}{m}\sum_{j=1}^{m} Y_t^j$$

$$R_2^s = \sqrt{\frac{1}{m}\sum_{j=1}^{m}\left(Y_s^j\right)^2 - \left(R_1^s\right)^2}, \quad R_2^t = \sqrt{\frac{1}{m}\sum_{j=1}^{m}\left(Y_t^j\right)^2 - \left(R_1^t\right)^2}$$

$$\rho_{st} = \frac{1}{\sigma_Y^2} A_c[\Delta x, \Delta y] \tag{15}$$

The function η_2 is the sum of the residuals of the coefficient of correlation considering the ergodicity. The functions, r_u^{xe} and r_u^{ye} are calculated coefficients of correlation for x and y directions considering ergodicity based on the generated random numbers. The arrangement of the random numbers, Y_s is shown in the Figure 1, and the calculations of Equations (17) and (18) follow the arrangement.

$$\eta_2(\boldsymbol{k}) = \sum_{u=1}^{n_x-1}\left(r_u^{xe} - \rho_{1,u+1}\right)^2 + \sum_{u=1}^{n_y-1}\left(r_u^{ye} - \rho_{1,n_x u+1}\right)^2 \tag{16}$$

$$r_u^{xe} = \frac{\frac{1}{m \times n_y\left(n_x - u\right)}\sum_{j=1}^{m}\sum_{t=1}^{n_y}\sum_{s=n_x(t-1)+1}^{n_x t-u} Y_s^j Y_{s+u}^j - \left(S_1^e\right)^2}{\left(S_2^e\right)^2} \tag{17}$$

$$r_u^{ye} = \frac{\frac{1}{n_x\left(n_y - u\right)m}\sum_{j=1}^{m}\sum_{t=1}^{n_x}\sum_{s=1}^{n_y-u} Y^j_{n_x(s-1)+t} Y^j_{n_x(s-1+u)+t} - \left(S_1^e\right)^2}{\left(S_2^e\right)^2} \tag{18}$$

$$S_1^e = \frac{1}{n \times m}\sum_{i=1}^{n}\sum_{j=1}^{m} Y_i^j$$

$$\left(S_2^e\right)^2 = \frac{1}{n \times m}\sum_{i=1}^{n}\sum_{j=1}^{m}\left(Y_i^j\right)^2 - \left(S_1^e\right)^2$$

The function η_3 exists so that the generated random numbers satisfy the known marginal distribution of logarithmic permeability. An example of the discrete probability density function is shown in Figure 2.

$$\eta_3(\boldsymbol{k}) = \sum_{i=1}^{n}\sum_{l=1}^{L}\left(P\left[Y_i^j = v_l\right] - p_l\right)^2 \tag{19}$$

in which $P[Y_i^j = v_l]$ is the probability whereby the value of a random number, Y_i^j, equals the discretized value of probabilistic variable, v_l. The discrete probabilities, p_l $(l = 1, 2, \ldots, L)$ are based on the known marginal distribution and L is the number of the discretization of the probability density function.

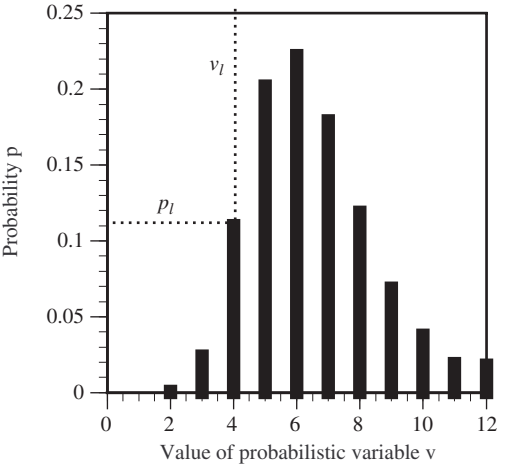


Figure 2. Example of discrete probability density function.

Copyright © 2003 Swets & Zeitlinger B.V., Lisse, The Netherlands

4 ANALYSIS OF TRACER

4.1 *Model description*

The case tracer, injected into the injection well, is considered in this section, as shown in Figure 3. The effect of random field parameters on the dispersion of tracer is clarified. In Figure 3, the water flows due to the pressure difference between the left-hand side (39.2 kPa) and the right-hand side (0 kPa). In this case, the median value of the intrinsic permeability is 14 μm^2, the effective porosity is 0.5. The normal random field is assumed here for the logarithmic permeability. For the standard deviation and correlation distance of logarithmic permeability, the following three cases are analyzed.

Case1: $\sigma_Y = 0.3 \quad l_x = l_y = 1.0\,\mathrm{m}$
Case2: $\sigma_Y = 0.3 \quad l_x = 5.0\,m \quad l_y = 1.0\,\mathrm{m}$
Case3: $\sigma_Y = 0.15 \quad l_x = l_y = 1.0\,\mathrm{m}$

4.2 *Results of analysis*

In Figure 4, a single sample of the permeability field is given for each case. The MCM is repeated 100 times. Thus, one hundred patterns of permeability fields are generated, as shown in Figure 4. In Figures 4(a) and 4(b), the correlation distances are different. Since the correlation distance in the x-direction in Figure 4(b) is five times longer than in Figure 4 (a), the fluctuation frequency of the permeability seems lower than in Figure 4(a). Figure 4(c) shows a case the variability is smaller than in the other two cases.

Figures 5–10 show the results of the MCM. The (a) figures are the results of time 1.1d, while the (b) figures are the results of time 4.6d. Figures 5, 7, and 9 show the mean values of the concentrations of tracer plume, while Figures 6, 8, and 10 represent the standard deviations. According to Figures 5 and 6, the dispersion of the plume grows larger with time. The standard deviation also increases with time. The points at the high mean concentration coincide with the high standard deviation points. The mean concentration has the shape of a two-dimensional normal distribution. This tendency is the same as those in Cases 2 and 3. The longer correlation distance causes the plume to become more dispersed, as can be seen in the comparison between Cases 1 and 2. A greater variability (greater standard deviation) also causes a greater dispersion. This is shown in the comparison between Cases 1 and 3.

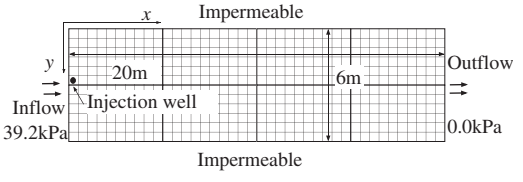


Figure 3. Model of tracer flow problem.

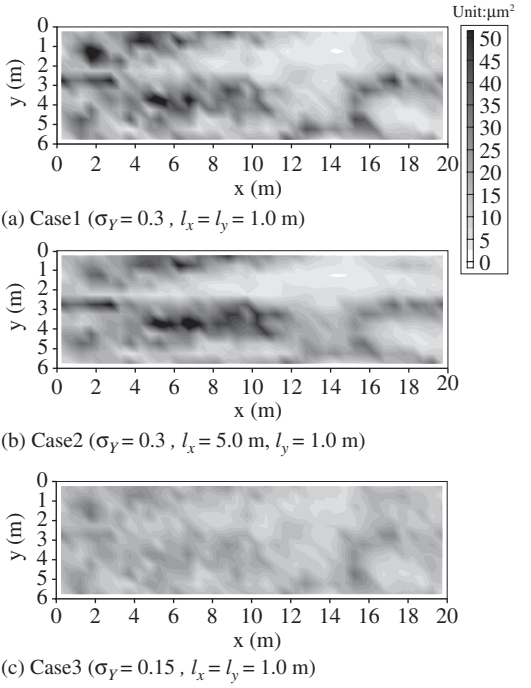


Figure 4. Sample of random field of intrinsic permeability. (Median = 14 μm^2)

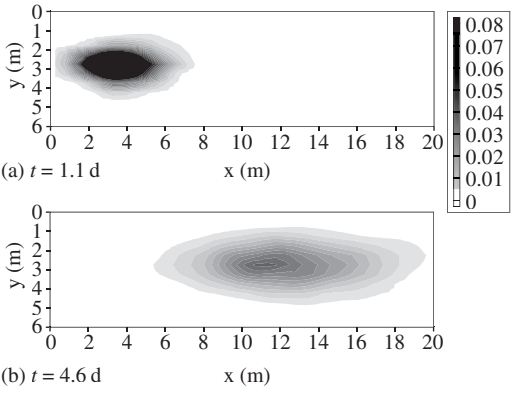


Figure 5. Mean of volume concentration (Case 1).

5 ANALYSIS OF DNAPL

5.1 *Model description*

The horizontal two-dimensional model is shown in Figure 11. The shaded area in the figure shows the

Copyright © 2003 Swets & Zeitlinger B.V., Lisse, The Netherlands

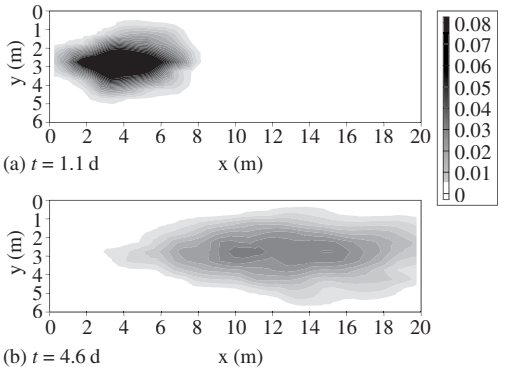


Figure 6. Standard deviation of volume concentration (Case 1).

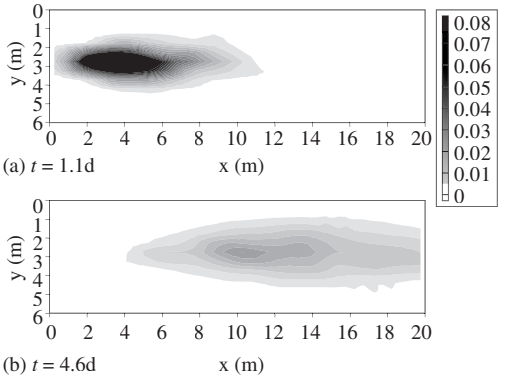


Figure 7. Mean of volume concentration (Case 2).

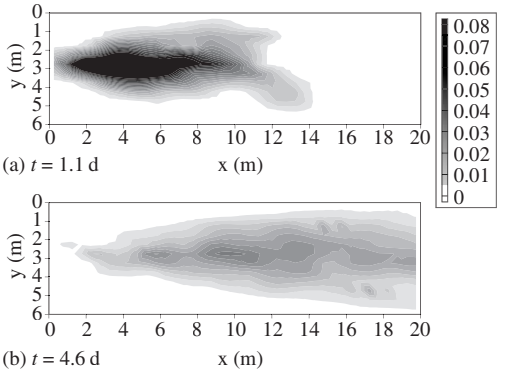


Figure 8. Standard deviation of volume concentration (Case 2).

initial DNAPL pool. The pool disperses with flow of water. The initial saturation of DNAPL is 80%. The water flows due to the difference in water pressure. The water pressure on the left-hand side is 19.6 kPa,

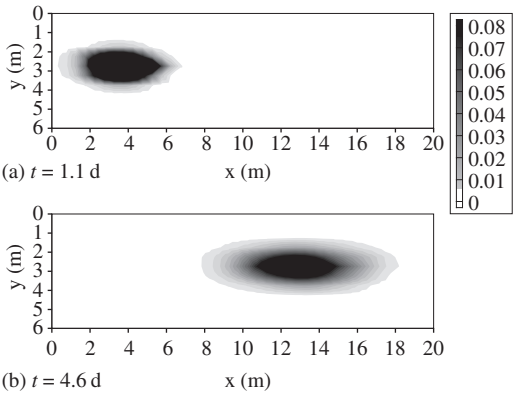


Figure 9. Mean of volume concentration (Case 3).

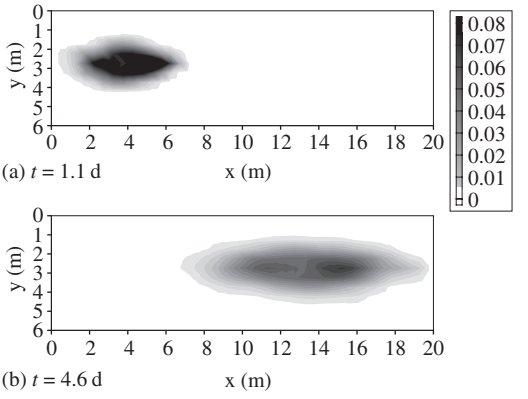


Figure 10. Standard deviation of volume concentration (Case 3).

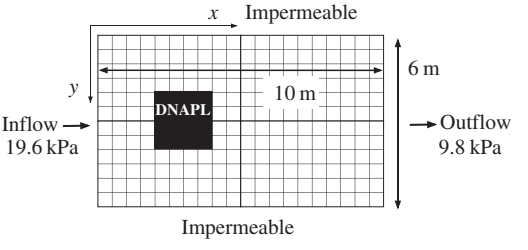


Figure 11. Analytical two-dimensional model of PCE problem.

while the water pressure on the right-hand side is 9.8 kPa. PCE is considered here as the DNAPL, and a profile of the PCE is given in Table 1. The effective porosity is set at 0.35. For the statistical profile of intrinsic permeability, the same Case 3 as that shown in section 4.1 is employed, and the median is 14 μm^2.

Copyright © 2003 Swets & Zeitlinger B.V., Lisse, The Netherlands

Table 1. Profile of PCE.

Density	1 g/cm^3 (water), 1.625 g/cm^3 (PCE)
Viscosity	1 cp (water), 0.89 cp (PCE)
Interfacial tension	PCE/water = 45 dyn/cm
Residual saturation	$S_{1r} = 0.24$(aqueous),
	$S_{2r} = 0.17$ (non-aqueous)
Capillary pressure	$c_i = 0.44$, $\lambda_i = -0.5$
Relative	$k^0_{r1} = 0.49$, $n_1 = 2.0$ (Water),
permeability	$k^0_{r2} = 0.65$, $n_2 = 2.70$ (DNAPL)

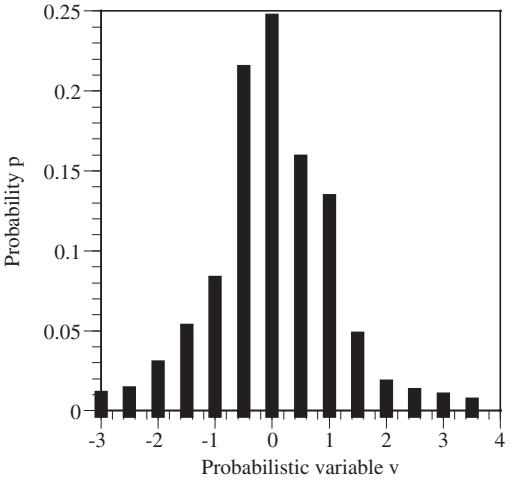


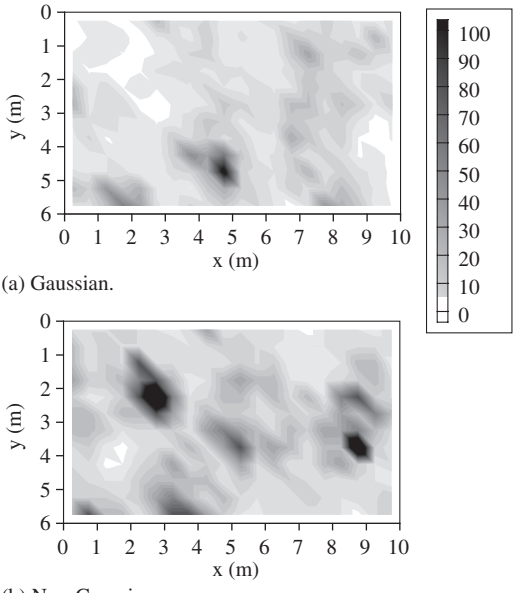
Figure 12. Example of non-Gaussian distribution.

In this section, the cases in which logarithmic permeability Y is Gaussian and non-Gauissian are compared. The non-Gaussian probability density function used here is given in Figure 12. The distribution is similar to the normal distribution. However, the distribution has the upper and lower boundaries, and a discrete type probability density function is employed. Since the distribution shown in the figure is normalized, the actual distribution is transformed to $Y = \mu_Y + \sigma_Y \nu$, (μ_Y is the mean value of Y.)

5.2 *Result of analysis*

Figure 13 shows samples of the Gaussian and non-Gaussian random fields. There is not much of a difference between the amplitude and the frequency of fluctuation for the two cases.

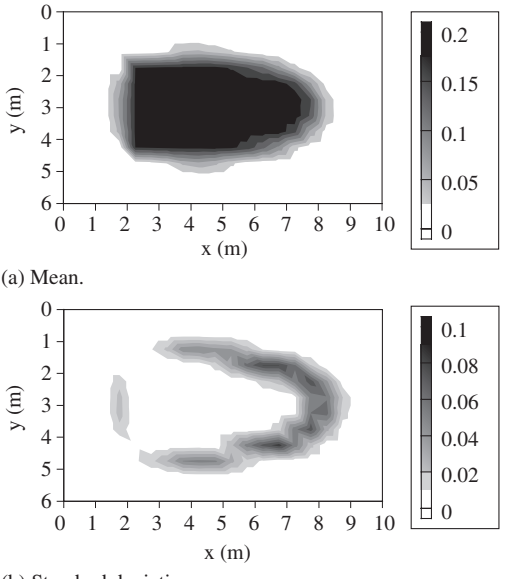
The Figures 14 and 15 show the results of Gaussian and non-Gaussian analyses for time 100d, respectively. Figures 14(a) and 15(a) show the mean values, while Figures 14(b) and 15(b) present the standard deviations, respectively. The plume of DNAPL migrates to the right with the water flow, and the saturation of DNAPL decreases to the 20%. It is characteristic for the variability of DNAPL to be high in front of



(a) Gaussian.

(b) Non-Gaussian.

Figure 13. Sample of random field of intrinsic permeability (Unit: μm^2. Mean = 14 μm^2 $\sigma_Y = 0.15$).



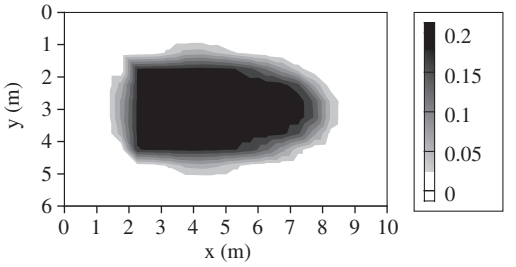
(a) Mean.

(b) Standard deviation.

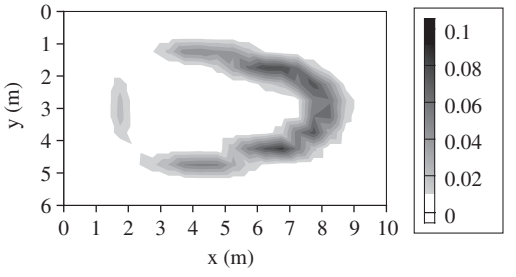
Figure 14. Result of Gaussian random field simulation.

the source and to be relatively low in the center, as shown in Figures 14(b) and 15(b). In comparing the Gaussian (Figure 14) and the non-Gaussian analyses (Figure 15), the analytical results are similar. This is attributed to the fact that the non-Gaussian marginal

Copyright © 2003 Swets & Zeitlinger B.V., Lisse, The Netherlands



(a) Mean.



(b) Standard deviation.

Figure 15. Result of non-Gaussian random field simulation.

distribution employed here has a similar shape with Gaussian distribution.

6 CONCLUSIONS

1. Single-phase (tracer mixed with water) and two-phase (water and DNAPL) problems have been solved in this study. The finite difference code (UTCHEM), combined with the Monte Carlo method (MCM), has been employed as a numerical method. The Gaussian and the non-Gaussian random fields of intrinsic permeability have been analyzed in this study.
2. The newly-proposed non-Gaussian random field simulator has been employed. The method is based on a numerical optimization method, namely, genetic algorithm (GA).
3. The effect of t random field parameters on the advection and dispersion of tracer has been clarified as a single phase problem. It has been shown that the greater variability or longer correlation distances cause the dispersion to increase.
4. The dispersion of DNAPL has been analyzed. In the DNAPL analysis, the mean value of DNAPL concentration is not affected with the random field characteristics of the intrinsic permeability, while the standard deviation is affected greatly.
5. In the DNAPL analysis, the assumption of the multivariate Gaussian distribution for the random field of the intrinsic permeability is accurate enough, if the marginal distribution is similar to the Gaussian distribution, since Gaussian and non-Gaussian results are similar.

REFERENCES

Brown, C. L., Pope, G. A., Abriola, L. M. & Sepehrnoori, K. 1994. Simulation of surfactant-en-hanced aquifer remediation: *Water Resources Research*, 30(11): 2959–2977.

Goldberg, D. E. 1989. *Genetic algorithm in search, optimization and machine learning*. Massachusetts: Addison – Wesley.

Nishimura, S. 2001. Determination of optimum distribution of permeability and non-Gaussian random field simulation: Shüeller & Spanos (eds), *Monte Carlo Simulation*, the Netherlands: A. A. Balkema, 123–128.

Rubinstein, R. Y. 1981. *Simulation and Monte Carlo method*. New York: John Wiley & Sons.

Copyright © 2003 Swets & Zeitlinger B.V., Lisse, The Netherlands

Case studies on designs of multi-well system with matrix scheme

Y. Shinshi, H. Kano & T. Wada
Konoike Construction Co., Ltd., Osaka, Japan

ABSTRACT: A matrix scheme has been introduced as the scheme which calculates discharge rates of wells under a multi-well system with a well interference phenomenon (e.g. Shinshi et al. 1996). Simply speaking, the scheme solves analytically a set of simultaneous equations of drawdowns of wells for discharge rates. The basic concept of the scheme has been originally proposed a long time ago (Muskat 1946) but it is not so popular in a contemporary engineering phase. In the paper, four case studies are summarized in order to explain applicability of the proposed scheme.

1 INTRODUCTION

On working multiple wells, each well suffers interferences from the other wells. The interference is that well discharge rates are different between on conditions of working a single well and multiple wells when the drawdown in each well is independent on the conditions, as shown in Figure 1. Under the interference phenomenon, discharge rates of wells under a multi-well system are less than those of a singly working well. The phenomenon is important in designing a dewatering technique because the number of wells is commonly estimated by dividing the total discharge rate for the site by a discharge rate of a well. Neglecting the phenomenon, the number of wells can be estimated less than the required number. The phenomena can be explained mathematically by using the Muskat's superimposition (1946). Moreover, Muskat (1946) and Leonard (1962), respectively, summarized the interference ratios ($=q_{wm}/q_{ws}$, see in Figure 1) for several cases of discharge well arrangements. Although, of course, they gave us how to estimate the interference ratios and/or the well discharge rates, q_{wm}, under an interference phenomenon, only the results of their case studies have been used in the most practical designing phase, at least in Japan.

The authors review the calculation scheme for determining the discharge rates of wells under the interference phenomenon and report four case studies by using the scheme in this paper.

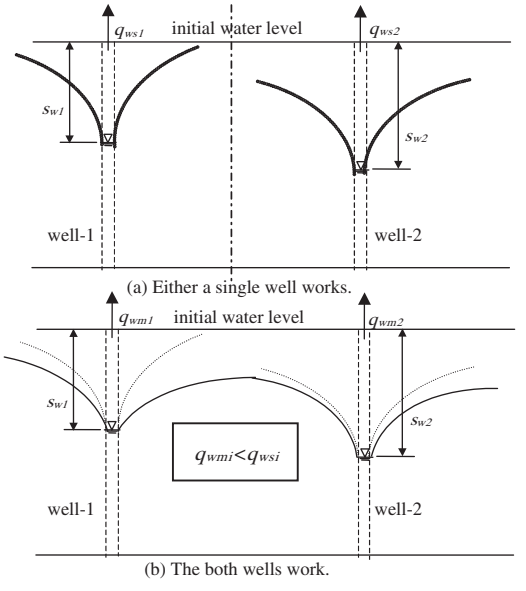


Figure 1. Interference of multi-well system.

2 BASIC COMPUTATION

The equation below expresses the Muskat's superimposition theorem.

$$s_P = \sum_{i}^{N} f_{Pi} \cdot q_i \qquad (1)$$

where s_P: drawdown at location P, q_i: discharge rate of the i-th well, i: index of well, N: the number of wells and f_{Pi}: drawdown function, for example, in steady state as follows.

Copyright © 2003 Swets & Zeitlinger B.V., Lisse, The Netherlands

for confined non-leaky aquifer

$$f_{Pi} = \frac{\ln(R/r_{Pi})}{2\pi T} \tag{2a}$$

for unconfined non-leaky aquifer

$$f_{Pi} = \frac{\ln(R/r_{Pi})}{\pi K} \text{ and } s_P \equiv h_P^2 - h_{wi}^2 \tag{2b}$$

for confined leaky aquifer

$$f_{Pi} = \frac{K_0(r_{Pi}/B)}{2\pi T} \tag{2c}$$

where r_{Pi}: distance between the location P and the i-th well, R: influence radius, T: transmissivity, K: hydraulic conductivity, h_P: head at the location P, h_{Wi}: head in i-th well, K_0: the zero-order modified Bessel function of the second kind, B: leakage factor ($=\sqrt{(Tb'/K')}$) in the Hantush model (1964), K': hydraulic conductivity of leakage layer, b': thickness of leakage layer.

This theorem is available for a linear well function, f, which is not only for steady but also for unsteady state.

Considering a well interference phenomenon, the restriction condition is that the drawdown of each well does not change in spite of the number of working wells; that is, the drawdown is prescribed as a boundary condition. Introducing this condition of wells into the equation (1), the following equation is obtained.

$$s_{wj} = \sum_{i}^{N} f_{ji} \cdot q_i \tag{3}$$

where j: index of well, r_{ij}: distance between the i- and j-th wells, if $i = j$, $r_{ij} = r_{wj}$. The equation (3) is a series for $j = 1$ to N.

Now, in the equation (3), the discharge rate, q_i, of each well is unknown, but the drawdown in each well, s_{wj}, is known. Therefore, the equation (3) should be solved for q. For explaining this work, the equation (3) was rewritten as the matrix form below.

$$\begin{matrix} \{S_w\} = & [F] & \{q\} \end{matrix}$$

$$\begin{Bmatrix} S_{w1} \\ S_{w2} \\ \cdot \\ S_{wN} \end{Bmatrix} = \begin{bmatrix} f_{11} & f_{12} & \cdot & f_{1N} \\ f_{12} & f_{22} & \cdot & f_{2N} \\ \cdot & \cdot & \cdot & \cdot \\ f_{N1} & f_{N2} & \cdot & f_{NN} \end{bmatrix} \begin{Bmatrix} q_1 \\ q_2 \\ \cdot \\ q_N \end{Bmatrix} \tag{4}$$

This solution for $\{q\}$ is the followings.

$$\{q\} = [F]^{-1}\{s_w\} \tag{5}$$

Reviewing the case studies of Muskat (1946) and Leonard (1962), the s_w and r_w of every well in their case studies are the same, respectively. Also, the arrangement of wells is regular. These conditions were introduced in order to solve the equation with the calculation technique available in several decades ago. At present, we can solve equation (5) with a personal computer program without introducing these conditions such as the same s_w and/or r_w. The scheme was named as the matrix scheme in this paper.

The main features of the matrix scheme are the followings:

(a) Wells can be arranged arbitrarily.
(b) The configurations of wells can be different from each other.
(c) The drawdowns of wells can be selected different from each other and be recognized as constant.
(d) A constant condition of discharge rates can be introduced into the equation (5), too.
(e) By using a computational program for solving a matrix equation, the large number of wells can be treated effortlessly.

3 CASE STUDIES AND DISCUSSION

In order to explain the applicability of the matrix scheme, four case studies are discussed as follows. Figure 2 shows the basic configuration of the concerning aquifer for the case studies. For simplicity, it is non-leaky confined.

3.1 *Case of large number of wells: case(1)*

Consider the case of large number of wells such as those in a well-point system. The conditions of wells and discharge are the followings:

$s_w = 6\,\text{m}$, $r_w = 0.05\,\text{m}$, $R = 20\,\text{m}$, $K = 10^{-5}\,\text{m/s}$, $T = 10^{-4}\,\text{m}^2/\text{s}$

the required drawdown area: $20\,\text{m} \times 200\,\text{m}$.

The discharge rate of a well under working a single well, q_{ws}, was calculated as follows:

$$q_{WS} = \frac{2\pi T s_W}{\ln(R/r_W)} = 6.30 \times 10^{-5}\text{m}^3/\text{s} \tag{6}$$

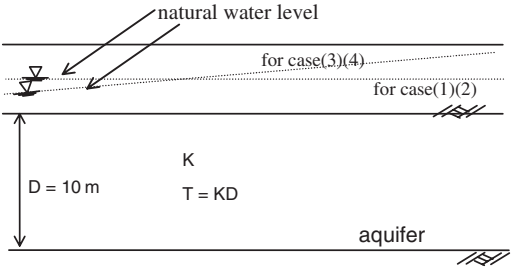


Figure 2. Aquifer model.

Copyright © 2003 Swets & Zeitlinger B.V., Lisse, The Netherlands

The wells were regularly arranged at the same space from its neighboring well; the space was chosen from three values, 5, 7.5 and 10 m. Table 1 shows the case study conditions and their results. The interference ratios, q_{wm}/q_{ws}, depend definitely on the space between wells and the number in a consequence of the number. Although the number of wells exceeds fifty, the computational effort of each case was not much, only a few seconds (well distance 7.5, 10 m) or a few ten seconds (well distance 5 m) by using an ordinary personal computer.

3.2 *Case of discharge and recharge wells: case(2)*

Consider the case of using both of the discharge and recharge wells simultaneously in the same site. The conditions of wells, discharge and recharge are the followings:

$s_w = 6\,\text{m}$ (discharge), $s_w = -1\,\text{m}$ (recharge),
$r_w = 0.5\,\text{m}$, $R = 1000\,\text{m}$, $K = 10^{-3}\,\text{m/s}$,
$T = 10^{-2}\,\text{m}^2/\text{s}$

The discharge and recharge rates of wells under working a single well, q_{ws}, were calculated as follows:

$$q_{ws} = \frac{2\pi Ts_w}{\ln(R/r_w)} = 4.96 \times 10^{-2}\,\text{m}^3/\text{s}: \text{discharging} \tag{7}$$

$$q_{ws} = \frac{2\pi Ts_w}{\ln(R/r_w)} = -8.27 \times 10^{-3}\,\text{m}^3/\text{s}: \text{recharging} \tag{8}$$

In the superimposition theorem, discharge and recharge wells can be distinguished by using different signs of drawdown and discharge rate of a well from each other; the plus is for discharge and the minus is for recharge. Figure 3 shows the interference ratios on discharging and recharging. All of the rates are larger than ones on a working single well.

3.3 *Case of discharging in groundwater flow*

3.3.1 *Creating natural groundwater flow: case(3a)*

A hydraulic gradient of the natural groundwater flow, I, was uniform and $I = 0.01$. In order to create this situation, two constant head boundaries, which were parallel and apart in 1 km, were introduced as shown in Figure 4. The lengths of the boundaries were 4 Km, respectively, and they are long enough that the flow is uniform in the focused area. On the boundaries, there were image wells whose influence radius, R', was 10^{10} m in order to obtain the uniform gradient on the area. The other parameters for this case are summarized in Figure 4.

3.3.2 *Discharge well in the natural groundwater flow: case(3b)*

Consider the drawdown on working a discharge well in the area with the natural groundwater flow. Conditions of wells and discharge are the followings adding to the condition of the case (3a).

$s_w = 6\,\text{m}$ (below initial level for calculation),
$r_w = 0.5\,\text{m}$, $R = 200\,\text{m}$, $K = 10^{-4}\,\text{m/s}$,
$T = 10^{-3}\,\text{m}^2/\text{s}$

The discharge well is located at the coordinate (x, y) = (500 m, 0 m).

The contours of drawdown (below initial level for calculation) is shown in Figure 5.

In such cases, the matrix scheme can handle the problem with a site of natural groundwater flows and

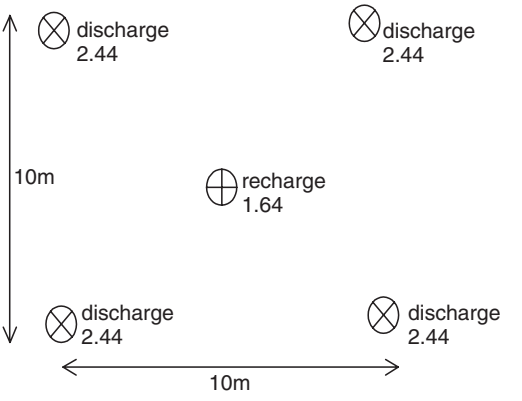


Figure 3. Ratios (q_{wm}/q_{ws}) of discharge and recharge wells.

Table 1. Conditions and results of the analysis.

Number of wells	Well space (m)	q_{wm}/q_{ws} Maximum	Minimum	Average	Minimum drawdown (m)
203	5	0.628	0.131	0.284	4.08
82	7.5	0.662	0.349	0.503	2.07
61	10	0.784	0.536	0.665	2.00

Copyright © 2003 Swets & Zeitlinger B.V., Lisse, The Netherlands

additional actions there by using the constant head boundaries as image wells.

3.4 *Case of collection wells for polluted groundwater in natural groundwater flows*

Consider performance of collection wells for polluted groundwater in naturally flowing. The case of the natural groundwater flow has already illustrated in the above, sec. 3-3. Collection wells were under the following condition.

$s_w = 1\,\text{m}$ (below natural level), $r_w = 0.05\,\text{m}$,
$R = 20\,\text{m}, K = 10^{-4}(\text{m/s}),\ \ T = 10^{-3}(\text{m}^2/\text{s})$

The collection wells were arranged on the line from $y = -60$ to $+60$ and $x = 500\,\text{m}$.

The natural groundwater flow was the same condition as the case (3a).

In this case, the superimposition theorem was used not only for drawdowns but also for traveling velocity vectors of groundwater flow. The velocity vector is calculated by the following procedure. On an arbitrary point $P(x_P, y_P)$, discharging with the i-th well (x_{wi}, y_{wi}) makes the velocity vector below.

$$\text{scalar of vector, } |\overrightarrow{v_{Pi}}| = \frac{q_{wi}}{2\pi r_{Pi} Dn} \tag{9}$$

unit positioning vector,

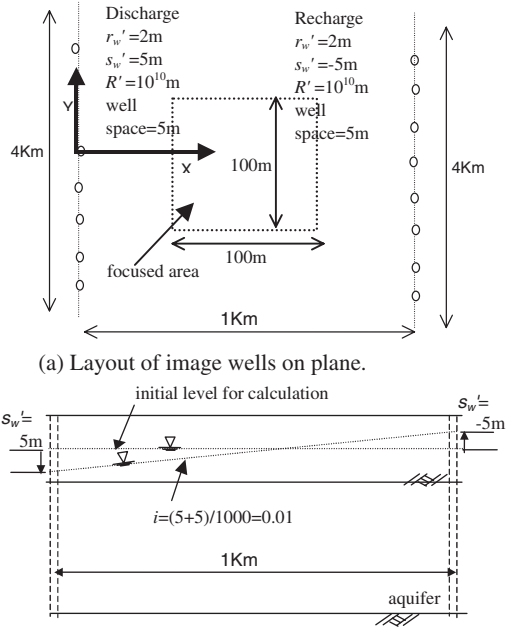
$$\overrightarrow{e_{Pi}} = \frac{(x_{wi} - x_P, y_{wi} - y_P)}{\sqrt{(x_{wi} - x_P)^2 + (y_{wi} - y_P)^2}} \tag{10}$$

Then,

$$\overrightarrow{v_{Pi}} = |\overrightarrow{v_{Pi}}|\,\overrightarrow{e_{Pi}} \tag{11}$$

Thus, the velocity vector at the point P is composed as follows:

$$\overrightarrow{v_P} = \sum_{i=1}^{N} \overrightarrow{v_{Pi}} \tag{12}$$



(a) Layout of image wells on plane.

(b) Layout of image wells on vertical section.

Figure 4. Layout of image wells.

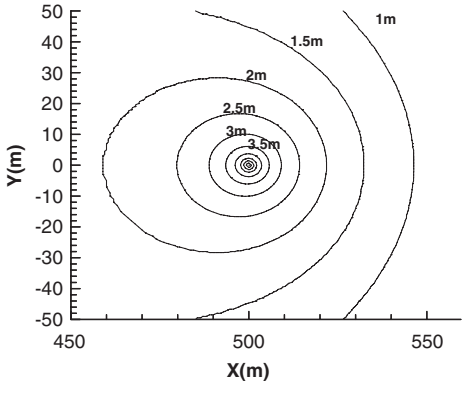


Figure 5. Drawdown (from initial level for calculation) contours in the focused area (X = 450, Y = −50)−(550, 50) (m).

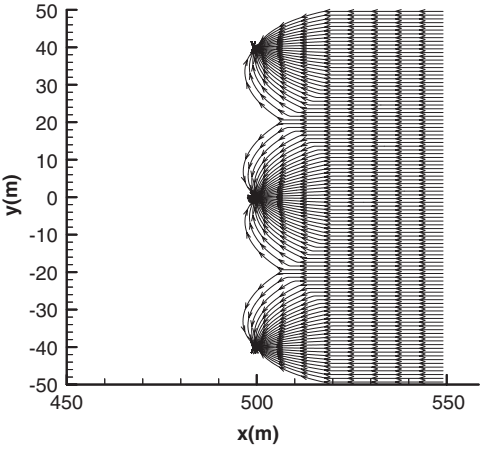


Figure 6. Stream lines around collection wells in polluted groundwater flow.

Copyright © 2003 Swets & Zeitlinger B.V., Lisse, The Netherlands

where n = porosity of aquifer, r_{Pi} = distance between point P and the i-th well.

When the vectors of all interesting points in the area were calculated, stream lines of the area were drawn by using a graphic drawing application. In such a case, an engineer might determine the space between wells and the discharge rate of each well in order not to escape the polluted groundwater flows. The case in the 40 m-space between neighboring wells is shown in Figure 6.

4 CONCLUSION

The performance of a matrix scheme considering the interference in a system of multiple well was introduced. By using the matrix scheme, it has been made clear that the impossible cases with a hand operated calculation could be solved on the base of the conventional superimposition theorem. In spite of the superimposition theorem, the condition of a well can be selected not only the discharge rate condition but also the drawdown condition.

Moreover, the most significant feature is that an effort of the work on searching the optimum arrangement of wells and the optimum management of discharge has been largely reduced.

REFERENCES

Hantush, M.S. 1964. Hydraulics of wells, Advances in Hydroscience, 1, 281–432.

Leonard, G.A. 1962. Foundation Engineering, McGraw-Hill Book Company, Inc., 297–306.

Muskat, M. 1946. The flow of homogeneous fluids through porous media, McGraw-Hill Book Company, Inc., 507–617.

Shinshi, Y. et al. 1996. Determining flow rate of well considering well interference behavior, Proceedings of the 31st JGS annual meeting 2153–2154, (in Japanese).

Copyright © 2003 Swets & Zeitlinger B.V., Lisse, The Netherlands

Numerical modeling of the groundwater flow changes due to the construction of the Äspö Hard Rock Laboratory

T. Hasegawa & Y. Tanaka
Central Research Institute of Electric Power industry, Abiko, Japan

ABSTRACT: Site scale groundwater flow is quite important in the study of contaminant transport. It is uncertain that the numerical model based on in-situ investigations represents the site scale groundwater flow. In this study, a numerical model was examined to represent site scale groundwater flow during the construction of Äspö Hard Rock Laboratory (Äspö HRL). The numerical model took into account for 17 Hydraulic Conductor domains and 1 Hydraulic Rock Mass. The unsteady state groundwater flow was simulated considering the progress of the tunnel construction and the inflow rate change with time. These datasets of time series are quite useful in order to calibrate hydraulic properties because these relationships clarify impacts and responses. The measured drawdowns were roughly represented by the numerical model based on in-situ investigations. The proper modeling of geometric relationship and progress of tunnel construction is important to represent the measured drawdown. This kind of approach is valuable to validate the numerical model representing the site scale groundwater flow.

1 INTRODUCTION

Groundwater flow on site scale is one of the most important factors to predict contaminant transport. In accessing the radioactive waste disposal, the direction and flow rate of groundwater flow will be key issue. It is supposed that these values are predicted by the numerical modeling based on in-situ investigation, e.g. pumping test and hydraulic conductivity test. However, these results are based on local scale investigation, it is uncertain that it could represent groundwater flow on site scale.

Therefore we simulated groundwater flow to focus on the change of groundwater flow due to tunnel construction that induces the significant impact to the groundwater flow on site scale. We simulated the change of groundwater flow during the construction of Äspö Hard Rock Laboratory (Äspö HRL), which is the laboratory of nuclear waste disposal.

2 DESCRIPTION OF MODELING SITE

2.1 *Overview of Äspö HRL*

The Äspö HRL was constructed by the Swedish Nuclear Fuel and Waste Management Co. (SKB) near Oskarshamn, southeastern Sweden, to investigate high-level waste disposal in a deep geological formation. The detailed information of characterization was provided by SKB (Rhen et al., 1997).

It consists of a spiral tunnel and a series of niches. The tunnel starts on the mainland at Simpevarp and two spirals under Äspö island reach a depth of −450 m with a total length of 3600 m. Tunnel construction started in October 1990 and was completed in September 1995. Construction was by two methods; blasting from the entrance to a distance of 3200 m, and TBM for the final 400 m. The elevator and ventilation shaft were also constructed during the tunnel construction. This elevator is connected to the tunnel at −220 m, −340 m and −450 m depths.

2.2 *Geological and hydrogeological models*

Äspö belongs to the Trans-Scandinavian Granite-Porphyry Belt and the main rock types at the site comprise Äspö diorite, Småland granite, greenstones and fine-grained granites. It is estimated by the U-Pb method that these rocks were formed about 1800 Ma ago. With respect to structures, on a regional scale the most dominating features are trending NS, EW and NW, whilst at the scale of the Äspö site a NE-ENE trending structure dominates. These structures are also considered to have been formed about 1800 Ma ago.

Copyright © 2003 Swets & Zeitlinger B.V., Lisse, The Netherlands

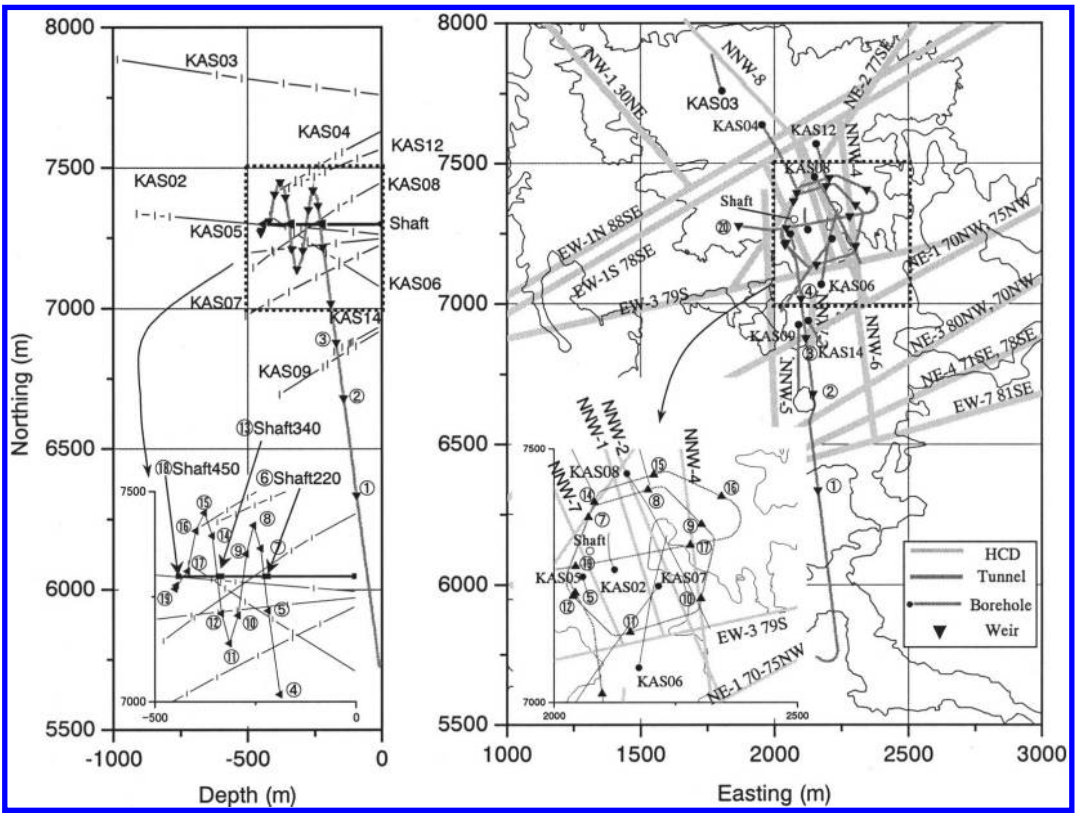


Figure 1. Overview of Äspö HRL. This figure shows borehole, borehole section, tunnel, shaft, weir and Hydraulic Conductor Domain.

The hydraulic properties of rock are categorized into the Hydraulic conductor domain (HCD) and the Hydraulic rock mass domain (HRD). The HCD is of a few tens of meters in width and a few orders higher in conductivity than HRD. There are 17 HCDs defined around Äspö. The mean hydraulic conductivity of HRD is the order of 10^{-9}m/s on logarithm scale. The HRD has some minor fractures excepted for HCD, and the hydraulic conductivity of rock zone without minor fracture is a few orders smaller than that of HRD.

2.3 *Site investigation*

Prior to the tunnel construction, the geological, hydrogeological and hydrochemical investigations using boreholes to depths around 800–900 m were conducted to characterize the groundwater flow and geochemical distribution on site scale. Before the tunnel construction, groundwater monitoring was conducted using packed off section of the borehole.

The inflows to the tunnel section were measured on the weirs placed at 150 m intervals in the tunnel. These locations are shown in Figure 1.

3 DESCRIPTION OF MODELING

3.1 *Outline of modeling*

The change of groundwater flow caused by the tunnel construction was simulated. We have the datasets that are the progress of tunnel, the inflow to the tunnel section, and head measured at the borehole section. Considering these datasets, we decided on the modeling area, hydraulic properties, and boundary conditions. In this modeling the previous work is cited (Hasegawa et al., 2001).

3.2 *Modeling tool*

We use FEGM (Kawanishi et al. 1994) to simulate the drawdown. This code is a finite element code, using Galerkin approach to solve the governing equations of groundwater flow described by the continuum equation and Darcy's law.

The continuum equation of groundwater flow is as follows:

$$S_s \frac{\partial h}{\partial t} + \frac{\partial}{\partial x_i} V_i + Q = 0 \quad (1)$$

Copyright © 2003 Swets & Zeitlinger B.V., Lisse, The Netherlands

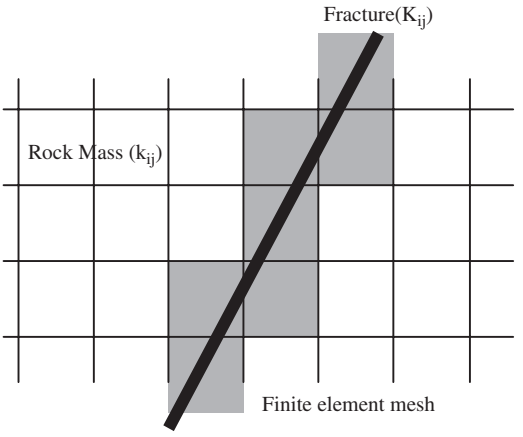


Figure 2. Concept of smeared fracture model. The properties of finite element intersected by fracture are calculated by the volume weighted value of HCD and HRD.

Darcy's law is as follows:

$$V_i = -k_{ij}\left(\frac{\partial h}{\partial x_i} + \frac{\partial z}{\partial x_i}\right) \tag{2}$$

where t: time, x_i: coordinate, S_s: specific storage, V_i: Darcy's velocity, Q: sink/source term, k_{ij}: hydraulic conductivity tensor, h: pressure head, z: vertical coordinate.

In order to treat the fractures in a simple manner, FEGM-B has a smeared fracture model that integrates the property of the fracture into finite elements by the volume-weighted method. When the fracture intersects several finite elements as shown in Figure 2, the parameters of the shadowed finite elements were calculated by the volume weighted average method.

3.3 *Modeling area*

In this study the groundwater flow was simulated around Äspö during tunnel construction. Therefore, the modeling area should include the tunnel and the general Äspö area. To exclude the boundary effect, the modeling area is defined in the range of 1000 to 3000 m easting, 5500 to 8000 m northing and 0 to −1000 m in depth within the Äspö coordinate system.

The modeling area and finite element diagram are shown in Figure 3. The HRD is expressed by hexahedral elements. The tunnel and elevator shaft were modeled by line elements. The HCDs are modeled by the smeared fracture model, and it was not shown in finite element diagrams.

Since the topography around Äspö is relatively flat that is about ten meters at the highest point, the topography is neglected in this modeling.

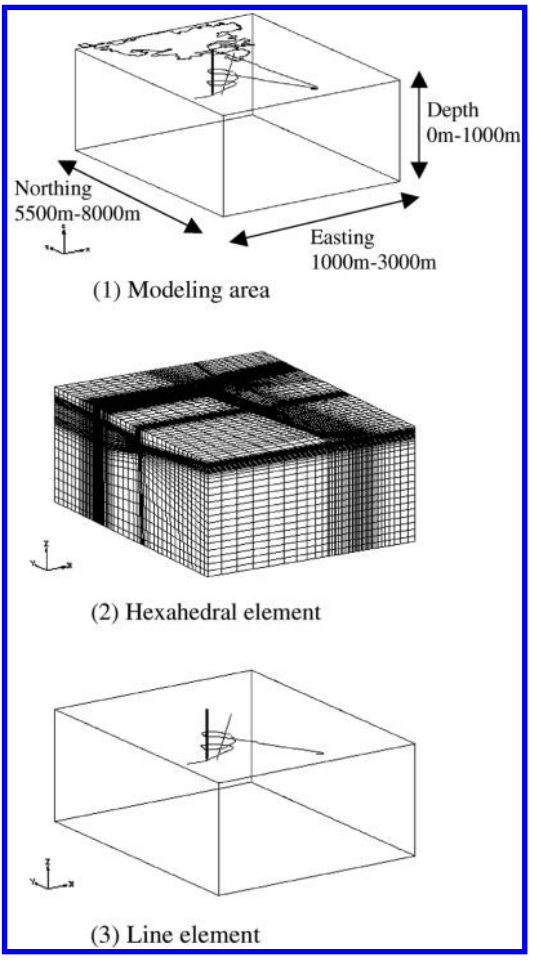


Figure 3. Modeling area and finite element mesh. The modeling area consists of 159,214 hexahedral elements and 349 line elements. Hexahedral and line elements express HCD and tunnel, respectively. HCD is considered by smeared fracture model.

3.4 *Data used*

The hydraulic conductivity of the Äspö bedrock is categorized into HCDs and HRDs. There are 17 HCDs around Äspö as shown in Figure 1; the hydraulic conductivity and thickness of the HCD are listed in Table 1. The geometric mean value of hydraulic conductivity is listed. These HCDs are modeled by the smeared fracture model as mentioned before. Some HCDs were more than 10 m thick. The HCDs are expressed by the series of planes that are parallel and located at every 10 m. For example, a 30 m thickness of a HCD is expressed by three planes and the central plane is located on the geometry of the HCD.

The hydraulic conductivity of the HRD is in the order of 10^{-9} m/s. The results of the hydraulic

Copyright © 2003 Swets & Zeitlinger B.V., Lisse, The Netherlands

Table 1. Hydraulic properties of HCD.

HCD	Width (m)	T initial (m^2/s)	T calibrated (m^2/s)
EW-1N	30	5.20E−07	
EW-1S	30	1.20E−05	
EW-3	15	1.70E−05	8.50E−05
EW-7	10	1.50E−05	
NE-1	30	2.20E−04	1.10E−04
NE-2	5	1.20E−07	
NE-3	50	3.20E−04	
NE-4	40	3.10E−05	
NW-1	10	4.10E−07	
NNW-1	10	8.60E−06	
NNW-2	20	2.40E−05	
NNW-3	20	2.00E−05	
NNW-4	20	6.50E−05	
NNW-5	10	4.00E−06	2.00E−05
NNW-6	20	1.40E−05	
NNW-7	20	7.50E−06	1.50E−05
NNW-8	20	8.40E−06	

conductivity test depend on the test scale. The hydraulic conductivity on the 3 m and 15 m scale are 1.5×10^{-9} and 6.0×10^{-9} m/s, respectively. The applied hydraulic conductivity is the value of 6.0×10^{-9} m/s.

3.5 *Boundary conditions*

The unsteady state of groundwater flow during tunnel construction was simulated by considering the progress of tunnel construction.

The grouting effect is directly related to the drawdowns (Tanaka et al., 1996), but it is difficult to quantify the grouting effect. Excluding the grouting and skin effect, the measured inflows at the weir were assigned to the tunnel sections as the flux boundary. The skin effect is the decreasing of hydraulic conductivity around the tunnel caused by stress redistribution and rock alteration. The inflows have been measured at tunnel sections divided by the weir placed at every 150 m in the tunnel length.

The progress of the tunnel and the flux to the tunnel section are shown in Figures 4 and 5.

The tunnel was modeled as a number of one-dimensional elements. The hydraulic conductivity of the tunnel was used to express whether the tunnel was excavated or not. The excavated tunnel section was expressed as high hydraulic conductivities, which is of 100 m^2/s in transmissivity. The progress of the tunnel reflects the numerical model at each time step.

The tunnel section is modeled by the connection of line element; the weir is modeled as the disconnection of line element. The measured inflow is extracted from the top of the node consisting of the tunnel section. As a result, the measured flux is collected from the tunnel section divided by the weir.

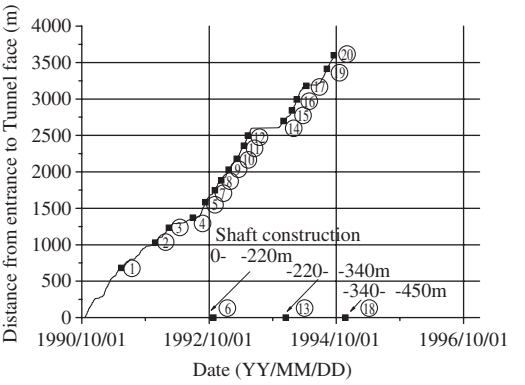


Figure 4. The progress of tunnel excavation. The number shows the wier location in the tunnel and shaft.

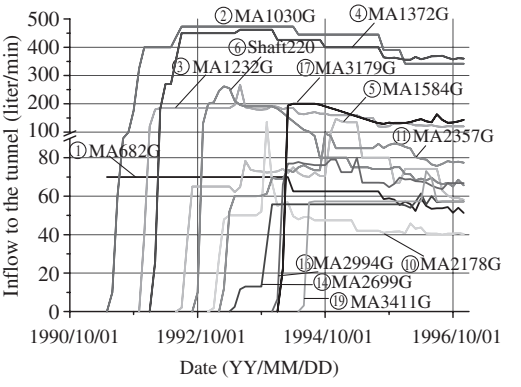


Figure 5. The measured inflow at the weir. The line shows the average inflow of month measured at each weir. The weir name shows the distance from entrance to the position of wier in the tunnel.

The bottom boundary and side boundary conditions were constrained as a no-flux boundary and hydrostatic pressure, respectively.

Boundary conditions on surface are categorized into the areas of sea and islands. The boundary condition of the sea area is a prescribed head equal to the Baltic Sea level.

The nodes on the island area are represented by a constant flux boundary. The infiltration rate applied to the Äspö area is determined by representing the measured pressure distribution under Äspö before tunnel construction. The measured excess hydraulic pressure is around 5 m at the level of −50 m under Äspö. The constant flux corresponding to this excess pressure is around 10 mm/y. It is assumed that the infiltration rate is 10 mm/y and constant during tunnel construction.

Copyright © 2003 Swets & Zeitlinger B.V., Lisse, The Netherlands

4 SIMULATION RESULTS

4.1 *Condition of numerical simulation*

- The unsteady state groundwater flow was simulated by considering tunnel construction and the inflow change with time.
- The simulation time is from 1990/10/1 to 1997/1/1. The time step is 15-days through the simulation.
- The effect of unsaturated zone is neglected because it is difficult to decide the unsaturated properties and to avoid nonlinear calculation.
- The initial condition used is as hydrostatic condition.

4.2 *Groundwater flow during tunnel construction*

At first, the numerical simulation was performed to compile the data as mentioned before. The simulated and measured drawdowns did not agree at first calculation. The transmissivities of HCDs are modified to take into account the geometric relationship and time series of inflow and drawdown as follows:

The significant drawdowns occurred at the shallower sections of KAS02 and KAS05 in October '92 and at the deeper sections of KAS02, KAS05 and KAS06 in August '94. These timing of drawdowns are corresponding to the Shaft construction and the tunnel construction at around 3400 m, respectively. Furthermore, the inflows from ⑥ Shaft220 and ⑲ MA3411G are higher than the other sections. On the basis of the geometrical relationship, the shaft cross NNW-7 and tunnel cross NNW-1, NNW-2 and NNW-7. Therefore these drawdowns could be induced by these crossings. The transmissivities of HCDs were modified on the basis of the inflow and transmissivity of HCD. As mentioned before, the geometrical information and time series information are useful to clarify impacts and responses.

However, since the hydraulic conductivity of HCD is influenced by the many drawdowns, it is difficult to understand the correlation between them. Therefore, the sensitivity analyses were conducted to clarify the influence of transmissivity modification. The transmissivity of each HCD reduced to the value of one tenth of the original value by turns.

The results are shown in Figure 6. This figure shows the change ratio of sum total of simulated drawdowns. NE-1 and NNW-7 are sensitive to the drawdown. The reasons are as follows,

1. NE-1 having high transmissivity and dipping to north supplies the groundwater to the other HCD crossing the tunnel.
2. NNW-7 induced the large inflow to shaft and significant drawdown at shallower sections of KAS02 and KAS05

The other HCDs are not sensitive to drawdowns because the transmissivity modifications of these

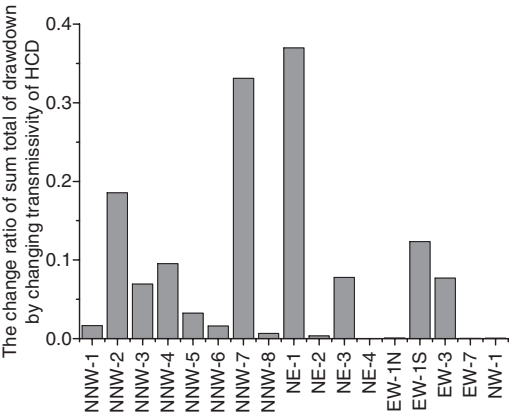


Figure 6. The sensitivity of drawdown by changing transmissivity of HCD.

HCDs are not sensitive to drawdowns. The reasons are as follows,

1. The inflows from these HCDs were not so much, and the inflow did not depend on the transmissivity of HCD because of grouting and skin effect.
2. The significant drawdown did not occur because of low inflow rate and high transmissivity of these HCDs.
3. The positions of monitoring point are not close to these HCDs, and the effect of the transmissivity change are masked by the other HCD.

On the basis of these sensitivities, the transmissivities of HCD were calibrated. The calibrated transmissivities are listed in Table 1. The relationship between measured and simulated drawdowns is shown in Figure 7. This figure shows that the measured drawdowns are roughly repented by the numerical model based on pre-investigation. The simulated and measured drawdowns are shown in Figure 8. The line and dot show the simulated and measured drawdowns, respectively. The drawdowns were measured every day, but the data varied widely and could not be measured in some intervals.

The main difficulties of model calibration are follows:

1. Since the weirs are set around 150 m intervals, the tunnel may cross some HCDs in some tunnel sections. In this case, it is difficult to quantify the inflow rate from each HCD, because the inflow did not depend on the transmissivity of HCD by grouting and skin effect. Thus, it is desirable to identify what HCD induce the inflow to the tunnel for model calibration.
2. The drawdowns are not only depending on one HCD, but on some HCDs. It is difficult to evaluate these interactions and to decide the transmissivity

Copyright © 2003 Swets & Zeitlinger B.V., Lisse, The Netherlands

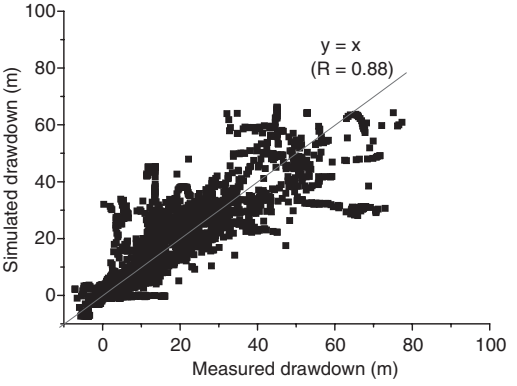


Figure 7. The relationship between measured and simulated drawdowns. The line show the agreement between measured and simulated drawdown. Where R is correlation coefficient.

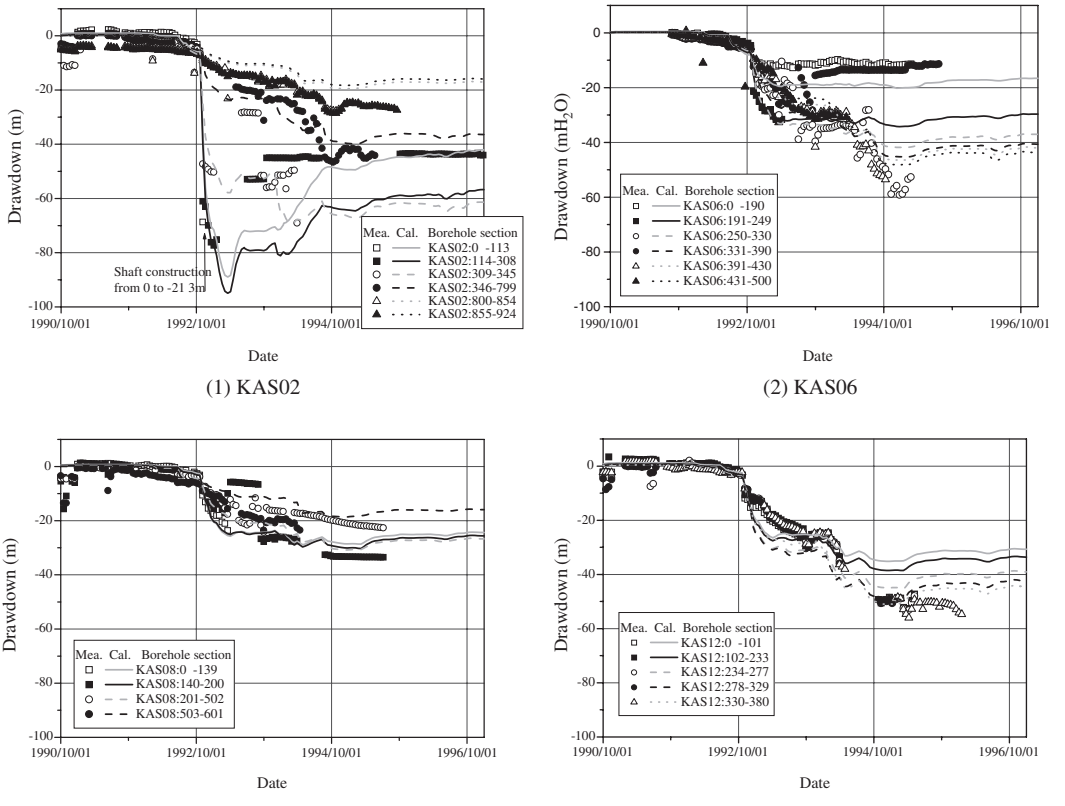
of HCD because there could be many transmissivity combinations of HCD.

Nevertheless, some simulated drawdowns do not agree with the measured drawdowns, and there are still some need to refine the inflow assignment and the location of HCD.

5 MAIN RESULTS

The numerical modeling of groundwater flow was conducted to simulate the drawdowns due to tunnel construction. The main results of this simulation is as follows,

1. Geometrical relationships between tunnel and HCDs are important to evaluate the inflow to the tunnel.
2. The time series datasets are useful to identify the correlation between inflows, HCDs and drawdowns.



(1) KAS02 (2) KAS06

(3) KAS08 (4) KAS12

Figure 8. The measured and simulated drawdown during tunnel construction. The lines and dots show the measured and calculated drawdown, respectively.

Copyright © 2003 Swets & Zeitlinger B.V., Lisse, The Netherlands

3. The effect of grouting and skin effect will be key issue to evaluate groundwater flow considering inflow to the tunnel, therefore the relationship between inflow and HCD should be identified.
4. The drawdown were roughly represented by the numerical model based on pre-investigation. It is expected that the result of pre-investigation could be useful to estimate site scale groundwater flow.

This kind of numerical simulation is useful for model validation on the site scale groundwater flow.

ACKNOWLEDGEMENT

This work is one part of international cooperation project hosted by SKB. We wish to thank Dr. I. Rhen, Dr. J. Smellie and Dr. P. Wickberg for providing datasets and advice to this work. We also wish to thank Mr. T. Ide for supporting the numerical simulation.

REFERENCES

Hasegawa, T., Tanaka, Y., Mahara, Y. & Igarashi, T., 2001. Dynamic changes of groundwater flow and geochemical distribution during tunnel construction Modeling Task 5, Impact of the tunnel construction on the groundwater system at Äspö: A hydrological–hydrochemical model assessment exercise, *SKB ICR* (in printing).

Kawanishi, M., Tanaka & Igarashi, T., 1994. Development of performance assessment method on natural barrier system for geological disposal of HLW (I): Analysis model for groundwater flow in fractured rocks, *CRIEPI Rep.* U93054 (in Japanese).

Rhen, I., Gustafson, G., Stanfors, R. & Wikberg, P., 1997. Äspö HRL – Geoscientific evaluation 1997/5, Models based on site characterization 1986–1995. *SKB TR-97-06.*

Tanaka, Y., Miyakawa, K., Igarashi, T. & Shigeno, Y., 1996. Application of three-dimensional smeared fracture model to the hydraulic impact of Äspö tunnel, *SKB ICR-96-07*.

Copyright © 2003 Swets & Zeitlinger B.V., Lisse, The Netherlands

3D lattice Boltzmann simulation of fluid flow in fractured rock

T. Miyoshi, T. Matsuoka, S. Murata & Y. Ashida
Kyoto University, Kyoto, Japan

ABSTRACT: It is important to estimate fluid flow in reservoir rocks for an enhanced oil recovery and evaluation of the productivities of the fracture reservoir. In this study, the Lattice Boltzmann Method (LBM), which is a new numerical computation method for the fluid flow, was applied to fracture flow. Consequently, we concluded that the flow obeys the cubic law even in the case of a very complex surface when the parallel fracture surfaces are the same shapes. The deviation from the cubic flow, however, is controlled by the standard deviation of the aperture of the fracture. This means that the variance of the topology of the fracture surface is not an important parameter compared with the variance of the aperture width.

1 INTRODUCTION

We have conventionally used Reynolds equation for evaluating fluids flow behavior in single fracture, but we cannot evaluate the exact channel flow. In a simple approach using Reynolds equation, the vertical flow in the fracture cannot be evaluated. To overcome this problem, the Lattice Boltzmann Method (LBM) (Qian et al. 1992, Rothman & Zaleski 1997, Succi 2001, Wolf-Gladrow 2000, Yoshino 2000) has been applied in this study. LBM has an advantage that we can evaluate the 3D flow behavior with the complex boundary conditions. In this study, we developed 2D & 3D LBM programs and applied them to the fracture generated by the fractal algorithm. We have done the following simulation studies. The fluid flow generally becomes less than the theoretical quantity when the fracture aperture is narrower. This phenomenon is shown in this simulation and the deviation from the cubic law is discussed in detail. The two parameters of fracuture topology influence this deviation.

2 BASIC THEORIES FOR LBM

2.1 *Lattice Boltzmann method*

A finite difference method or a finite element method have conventionally been used for the simulation of fluid behavior. These methods are based on Navier-Stokes equation. In contrast to these method, the LBM approximates fluid as particles. The collision and movement of particles and boundary conditions are expressed by density distribution functions. And the fluid velocity, density and pressure (macroscopic parameters) are calculated from the distribution functions (microscopic parameter). The distribution functions must be set as if the collision, movement, and boundary conditions retained the character of continuation of fluid. Various models of different lattice or collision rules are suggested, but we adopted the BGK (Bhatnagar-Gross-Krook) model (Bhatnagar et al. 1954) and set 9 velocity model for 2D and 15 velocity model for 3D.

2.2 *Basic equations*

The concept of the LBM in the 15 velocity model for 3D is as follows. At first the three dimensional space is divided into unit lattices. It is assumed that the particles are on the lattices, and the number of particles corresponding to a particle density are expressed by the distribution functions. Furthermore, the virtual particles on each lattices have 15 velocity, as expressed in Equation 1. Figure 1 shows the velocity of each particle.

$$\mathbf{c} = \begin{pmatrix} 0 & 1 & 0 & 0 & -1 & 0 & 0 & 1 & -1 \\ 0 & 0 & 1 & 0 & 0 & -1 & 0 & 1 & 1 \\ 0 & 0 & 0 & 1 & 0 & 0 & -1 & 1 & 1 \\ 1 & 1 & -1 & 1 & -1 & -1 & & & \\ -1 & 1 & -1 & -1 & 1 & -1 & & & \\ 1 & -1 & -1 & -1 & -1 & 1 & & & \end{pmatrix} \quad (1)$$

In addition, all particles exist on the lattices and there are no particles on the way of between lattices in each calculation time step. The distribution functions according to each 15 velocity are given on all lattices. It is very important for the distribution functions to change with time steps in the LBM.

Copyright © 2003 Swets & Zeitlinger B.V., Lisse, The Netherlands

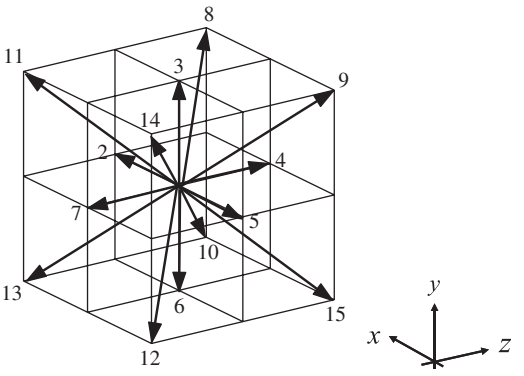


Figure 1. The three dimension lattice is shown. The virtual particles move to each 15 direction.

There are four parts in this method. The first step is the collision part. The evoluation of the distribution function $f_i(\mathbf{x}, t)$ with the velocity $\mathbf{c}_i$ at the point $\mathbf{x}$ and time t is calculated by the following equations

$$f_i(\mathbf{x}+\mathbf{c}_i\Delta t, t+\Delta t) - f_i(\mathbf{x},t) = -\frac{1}{\tau}\{f_i(\mathbf{x},t) - f_i^{\mathrm{eq}}(\mathbf{x},t)\} \quad (2)$$

where Δx is a lattice spacing, Δt is a time step, τ is a single relaxation time and f^{eq} is an equilibrium distribution function that is given from fluid macroscopic velocity $\mathbf{u}$ and density ρ using Equation 3. The equilibrium disutribution function is a particle density distribution that reached equilibrium in the finite space like lattices.

$$f_i^{\mathrm{eq}} = E_i\rho\{1+3(\mathbf{c}_i\cdot\mathbf{u}) + \frac{9}{2}(\mathbf{c}_i\cdot\mathbf{u})^2 - \frac{3}{2}\mathbf{u}^2\} \quad (3)$$

$$E_1 = 2/9$$

$$E_i = 1/9 \quad (i = 2,...,7)$$

$$E_i = 1/72 \quad (i = 8,...,15)$$

The second step is the movement part. The particles on each lattice move in 15 directions according to particle velocity $\mathbf{c}_i$ when a time step advances. The number of particles which move in each direction is defined as the distribution function. The third step is the evaluation of the boundary conditions. We will describe this in detail in the following section. The last step is the macroscopic part. The fluid velocity, density and pressure, which are macroscopic parameters on each lattice, are calculated from the distribution functions (Eq 4 to Eq 6). These distribution functions are given from the movement step. When these four steps are repeated, the evoluation of fluid flow can be calculated.

$$\rho = \sum_i f_i \quad (4)$$

$$\mathbf{u} = \frac{1}{\rho}\sum_i f_i\mathbf{c}_i \quad (5)$$

$$p = \frac{\rho}{3} \quad (6)$$

2.3 *Boundary conditions*

All the distribution functions are not known on the surface of a boundary wall because the particles does not move from outside of the fluid area. So the unknown distribution functions must be determined from the known distribution functions. Several boundary conditions are proposed. We use the Inamuro's method in this study (Inamuro et al. 1995). When a lower half of Figure 1 is a wall, the distribution function f_3, f_8, f_9, f_{11} and f_{14} having speed of $c_y > 0$ are unknown. Then each distribution function is guessed as Equation 7.

$$f_i = E_i\rho'\{1+3(u_0+v_{\mathrm{w}}+w_0) + \frac{9}{2}(u_0+v_{\mathrm{w}}+w_0)^2 - \frac{3}{2}[(u_{\mathrm{w}}+u')^2 + v_{\mathrm{w}}^2 + (w_{\mathrm{w}}+w')^2]\} \quad (i = 3,8,9,11,14) \quad (7)$$

where u_{w}, v_{w} and w_{w} are wall velocity to each direction. The wall velocity is zero in this simulation.

$$u_0 = 0 \qquad w_0 = 0 \qquad (i = 3)$$

$$u_0 = u_{\mathrm{w}} + u' \qquad w_0 = w_{\mathrm{w}} + w' \qquad (i = 8)$$

$$u_0 = -u_{\mathrm{w}} - u' \qquad w_0 = w_{\mathrm{w}} + w' \qquad (i = 9)$$

$$u_0 = u_{\mathrm{w}} + u' \qquad w_0 = -w_{\mathrm{w}} - w' \qquad (i = 11)$$

$$u_0 = -u_{\mathrm{w}} - u' \qquad w_0 = -w_{\mathrm{w}} - w' \qquad (i = 14)$$

In Equation 7 the unknown parameters, ρ', u', and w' are given as follows, since the fluid velocity must be equal to the wall velocity and three equations on velocity are made according to each direction. Moreover, the fluid density on the boundary lattices ρ_{w} is unknown quantity and is calculated by Equation 4. Equations 8–11 are provided as a solution of these equations.

$$\rho_{\mathrm{w}} = \frac{1}{1-v_{\mathrm{w}}}[f_1 + f_2 + f_4 + f_5 + f_7 + 2(f_6 + f_{10} + f_{12} + f_{13} + f_{15})] \quad (8)$$

Copyright © 2003 Swets & Zeitlinger B.V., Lisse, The Netherlands

$$\rho' = 6\frac{\rho_w v_w + (f_6 + f_{10} + f_{12} + f_{13} + f_{15})}{1 + 3v_w + 3v_w^2} \quad (9)$$

$$u' = \frac{1}{1+3v_w}[\frac{6}{\rho'}\{\rho_w u_w - (f_2 - f_5 + f_{10} - f_{12} + f_{13} - f_{15})\} - u_w - 3u_w v_w] \quad (10)$$

$$w' = \frac{1}{1+3v_w}[\frac{6}{\rho'}\{\rho_w w_w - (f_4 - f_7 + f_{10} - f_{12} - f_{13} + f_{15})\} - w_w - 3v_w w_w] \quad (11)$$

Next, for the boundary condition with an intersecting borderline and corner of a wall we assume a virtual boundary surface including boundary node and apply the above boundary condition on the virtual surface.

A periodic boundary condition is adopted at the inlet and outlet surfaces. This boundary condition is set according to the pressure difference between the inlet and outlet. Supposing that the pressure difference is generated to the x axis and the surface $x = 0$ is the inlet and $x = L_x$ is the outlet, the disutribution function f_2, f_8, f_{10}, f_{11} and f_{13} are unknown on the node of the inlet surface and f_5, f_9, f_{12}, f_{14} and f_{15} on the outlet surface. Then as f_2 is known at the outlet surface, this function is introduced into the inlet side. That is, adding the pressure difference K, f_2 at the inlet side is given by Equation 12. In addition, the other unknown distribution functions obey Equation 13. The unknown functions at the outlet side are determined, as well as the inlet side (Eq 14 & 15). The pressure difference K is given by Equation 16.

$$f_2|_{in} = f_2|_{out} + K \quad (12)$$

$$f_i|_{in} = f_i|_{out} + \frac{1}{8}K \quad (i = 8, 10, 11, 13) \quad (13)$$

$$f_5|_{out} = f_5|_{in} - K \quad (14)$$

$$f_i|_{out} = f_i|_{in} - \frac{1}{8}K \quad (i = 9, 12, 14, 15) \quad (15)$$

$$K = \Delta p - \frac{1}{3}(f_1|_{in} - f_1|_{out} + f_3|_{in} - f_3|_{out} + f_4|_{in} - f_4|_{out} + f_6|_{in} - f_6|_{out} + f_7|_{in} - f_7|_{out}) \quad (16)$$

3 THE FLUID FLOW IN THE FRACTURE

3.1 *The deviation from the cubic law of fracture permeability*

It is known that the flux through a single fracture is proportional to the cubic of mean aperture if a model is a parallel flat wall (Brown 1989). But as the aperture narrows, the flux does not obey the cubic law. We examined this result using the LBM. Since the fracture surface is generally fractal, a fracture surface



Figure 2. 2D fracture model. This model is divided into 1000 × 100 lattices.

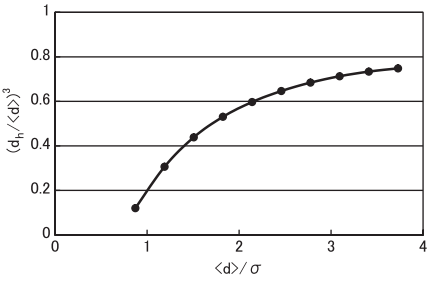


Figure 3. The deviation from the cubic law for the 2D fracture model. The deviation becomes larger according to narrowing the aperture.

model was made by the fractal algorithm, as shown in Figure 2. The two fracture surfaces were parallel each other. The boundary conditions was set as follows. The pressure difference at two boundaries each other was set and the fluid flow in this direction was calculated. Next, the fracture aperture was changed by moving the upper surface upwards or downwards. The mean aperture is defined by Equation 17.

$$< d >= \frac{\iint d(x,y)dxdy}{L_x L_y} \quad (17)$$

where $d(x, y)$ is the distribution of the fracture aperture, L_x and L_y are the length of a fracture to each direction. Now, when the flux Q is calculated by the LBM, the hydraulic aperture that conforms to the cubic law is determined by Equation 18.

$$d_h = \left(\frac{12\mu Q}{L_y \Delta p / L_x}\right)^{\frac{1}{3}} \quad (18)$$

where μ is the viscosity of the fluid and Δp is the pressure difference to the x direction. If the ratio of $d_h/<d>$ is equal to one, this fracture model perfectly conforms to the cubic law. The cubic of this ratio means a deviation from the cubic law of fracture permeability.

Figure 3 shows the result of this simulation. In this Figure, the vertical axis is the cubic of the ratio $(d_h/<d>)^3$ and the horizontal axis is the mean aperture normalized by standard deviation of fracture surface. It can be seen that the $(d_h/<d>)^3$ deviates from the cubic law with the decrease in the aperture. This result is almost the same as Figure 10 in Brown (1989).

Copyright © 2003 Swets & Zeitlinger B.V., Lisse, The Netherlands

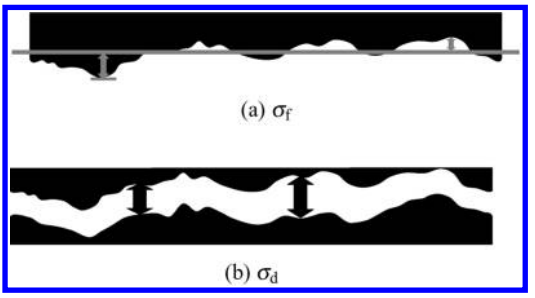


Figure 4. The schematic drawings of σ_f (a) and σ_d (b). σ_f is standard deviation of fracture height and σ_d is that of the aperture.

3.2 *Parameters of the deviation*

It is shown in the subsection 3.1 that the narrower the mean aperture, the larger the deviation from the cubic law. But if the model is a parallel flat wall, the deviation from the cubic law cannot be found theoretically no matter how narrow the aperture is. Then a roughness of fracture is considered as the parameter of the deviation. In this study, the standard deviation of fracture height σ_f and the standard deviation of the aperture σ_d are used for the roughness parameter. Figure 4 shows schematic drawings of σ_f and σ_d. The fracture model made by the fractal theory has almost the same value of σ_f for the upper and lower surface. If the upper and lower wall are the same, σ_d is equal to zero because the aperture is uniform.

3.3 *Analysis of 2D models*

We analyzed the deviation with the following 2D models.

Model 2D-A: the upper and lower surface whose shape is a sine curve have the unifrom aperture (Figure 5(a))

Model 2D-B: the upper surface is a sine curve and the lower is flat (Figure 5(b))

Model 2D-C: the upper and lower surface are the same surface which is made by the fractal theory, and then, the upper wall is moved to the fracture length direction (Figure 5(c))

Several models of different σ_f are made according to the amplitude of a sine curve in model 2D-A. The bigger the amplitude, the larger the standard deviation of the surface σ_f. However, σ_d is equal to zero because the aperture is uniform in each fracture. In Figure 6, the deviation of the models for different σ_f is ploted as a function of the aperture. The legend "σ" are σ_f. The solid line whose legend is "fracture" corresponds to that shown in Figure 3. This figure shows that the deviation from the cubic law as a result of narrowing the aperture cannot be found even if σ_f changes that.

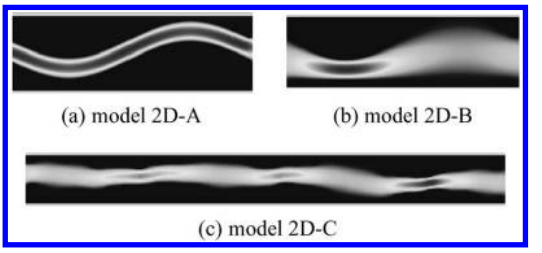


Figure 5. Models for analysis of the parameter contributing the deviation from the cubic law. The size of models is; 333 × 33 lattices (2D-A and 2D-B); 1000 × 100 lattices (2D-C).

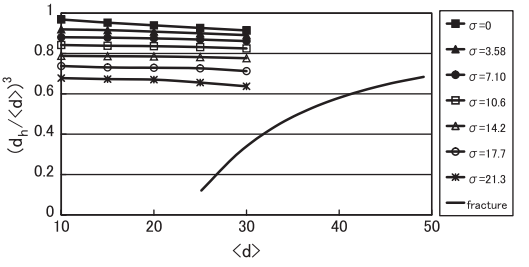


Figure 6. The lines with symbols are the rusult of model 2D-A. The solid line corresponds to Figure 3. The legend "σ" is all σ_f. σ_d is zero. The deviation from the cubic law cannot be seen.

In the model 2D-B, the aperture changes along the profile because the lower wall is flat. Then σ_f is equal to σ_d . The rusult of model 2D-B is the three dashed lines with filled symbols in Figure 7. Due not only to narrowing the aperture but also increasing σ, the deviation from the cubic law is increasing.

In the model 2D-C, at first the upper wall and the lower wall which are made by the fractal theory are the same. Next the upper wall is moved to the fracture length direction. Then σ_f is fixed at 12.6. The roughness of the aperture distribution increases according to the shift length of the upper wall. The result of 2D-C is the three lines with unfilled symbols in Figure 7. The deviation becomes larger with increasing σ_d.

These things show that the standard deviation of the aperture distribution σ_d controls the deviation from the cubic law on the flux in the fracture.

3.4 *Conclusions*

The flux in a fracture is proportional to the cubic of the mean aperture only when the aperture is uniform. That is, as the upper and lower walls are the same, the deviation from the cubic law does not occur even if the surface is too complex, but the deviation becomes larger with σ_d. The separation is strongly controled not by the roughness of the fracture surface but by the

Copyright © 2003 Swets & Zeitlinger B.V., Lisse, The Netherlands

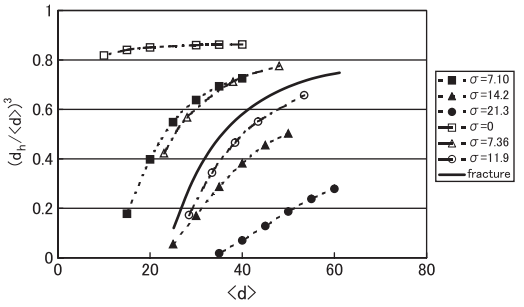


Figure 7. The result of model 2D-B & model 2D-C. The legend "σ" is σ_d. The dashed lines with filled symbols are the result of model 2D-B. The dashdotted lines with unfilled symbols are the result of model 2D-C. The solid line corresponds to Figure 3. The deviation from the cubic law becomes larger with increasing of the σ_d.

roughness of the aperture. As a conclusion, σ_d is a more important parameter to be considered in the deviation from the cubic law, and the deviation is larger with increasing roughness of distribution of aperture.

3.5 *3D fracture model*

We described the 2D models in the previous section but when we compare the results for this simulation to the experimental results, 3D analysis is more valuable. In this section, we analyzed 3D fracture models using the 3D LBM, and compared them to 2D.

In the 2D analysis, the 2D models were made cutting out from the 3D fractured model whereas in the 3D analysis the 3D fracture model is used as it is. We made various models for the same fractal dimension 1.2. And we paid attention to the σ_f and σ_d and examined them as well as in the 2D analysis. Figure 8 is a lower surface which is divided into $256 \times 256 \times 15$ lattices. And in Figure 9, the visualized 3D fluid flow is shown. The Axis value is a lattice number. The solid lines are streamlines and the gray plate is a section of the fracture. The vertical fluid flow which cannot be seen by Reynolds equation can be seen.

3.6 *Analysis of 3D models*

Two kinds of models are used for the 3D analysis. Figure 10 shows the 2D section of the following models.

Model 3D-A: (the tensile type fracture) The roughness of aperture σ_d is 0.65 for all but the roughness of the fracture surface, σ_f, is varied in each model.

Model 3D-B: (the strike-slip type fracture) Using one of the 3D-A models, the upper surface is moved to the horizontal direction. The σ_d increases from 0.65 according to the shift length but σ_f is constant.

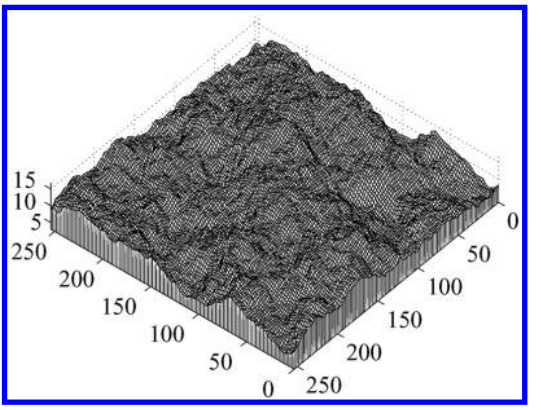


Figure 8. The lower surface of the 3D fracture model made by the fractal algorithm, which is divided into $256 \times 256 \times 15$.

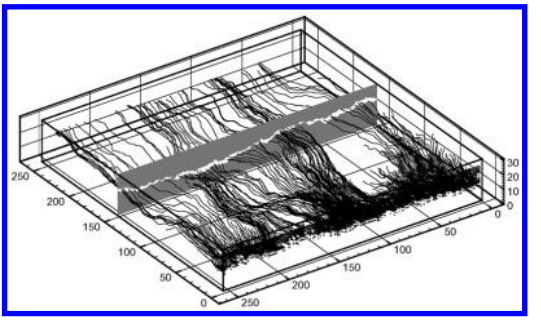


Figure 9. The visualized fluid flow through the 3D fracture. A solid line is a streamline for fluid flow. A gray plate is a section of the fracture.

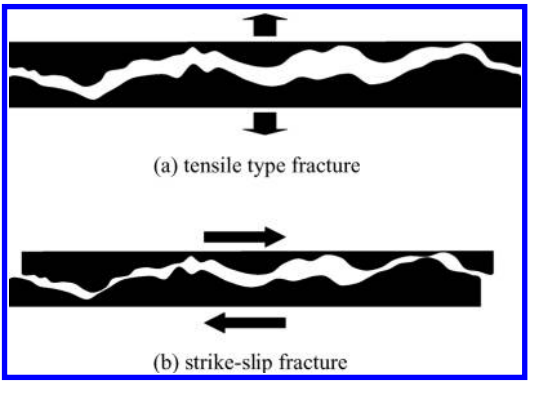


Figure 10. The schematic drawings of the 2D section for two fracture types.

In model 3D-A, we made three models whose σ_f is 2.97, 1.88 and 2.34, respectively. And the standard deviation of aperture σ_d is about 0.65. $(d_h/<d>)^3$ for these three models are calculated using the 3D LBM

Copyright © 2003 Swets & Zeitlinger B.V., Lisse, The Netherlands

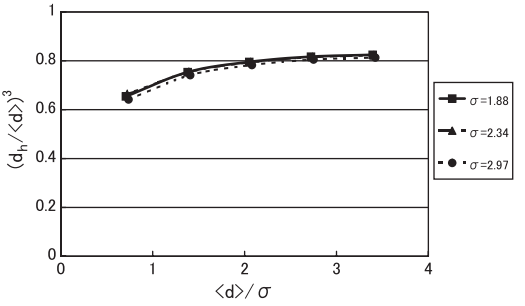


Figure 11. The model 3D-A. The legend "σ" is σ_f. The σ_d is constant. The trend of the deviation is the same in each model.

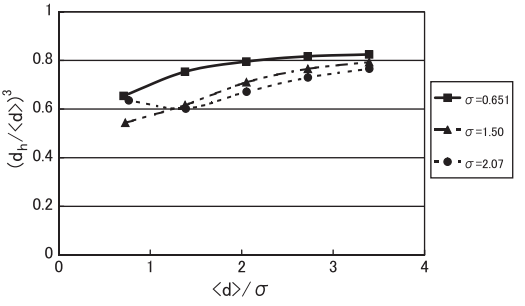


Figure 12. The model 3D-B. The legend "σ" is σ_d. The σ_f is constant. The deviation becomes larger according to the σ_d.

and plotted as a function of the aperture normalized by the standard deviation of the aperture (Figure 11). Even if the roughness of surface (σ_f) is different, the trend of the deviation from the cubic law is almost the same. This result is almost the same as the 2D analysis.

In model 3D-B, the surface which is one of model 3D-A ($\sigma_f = 1.88$) is not changed as the shape, but it is moved in the direction of fluid flow. This model is assumed to be the fracture with strike-slip. First σ_d is 0.65, and it increases according to the shift length. The lower surface is fixed, and the upper surface is moved with X to the x direction. Then the upper wall does not exist at $0 \leq x \leq X$. So using the periodic boundary condition, the empty area is filled by the upper surface data at $L_x - X \leq x \leq L_x$. In this condition, σ_d is maximum as $L_x/2$ shifts because the two surfaces do not fit. In this simulation, the shift length is 4–8% of the fracture length. In the Figure 12, the legend σ is all σ_d , and σ_f is equal to 1.88. As the fracture surface is almost equal, the deviation of the cubic law is larger with the increase in σ_d.

3.7 *Conclusions*

This is the same result as the 2D analysis. The deviation from the cubic law is almost the same when σ_d is fixed and σ_f is changed. When σ_f is fixed and σ_d is changed, the separation becomes larger as σ_d increases.

4 CONCLUSIONS

In this study, we confirm that the lattice Boltzmann metheod is valuable for the simulation of fluid flow through the reservoir rock like the porous media or fracture. Using this method, the fluid flow in a complete 3D space can be calculated more correctly.

From our study, we concluded that when the parallel fracture surfaces are the same topology, fluid flow obeys the cubic law even in the case of a very complex surface. This means that the variance of the topology of the fracture surface is not an important parameter, compared to the variance of the aperture. The deviation from the cubic law is controlled by the standard deviation of the aperture of the fracture. In the tensile type fracture, the permeability will be near to that estimated from the cubic law because the upper surface and lower surface fit each other very well whereas in the strike-slip type fracture, the permeability will become less because the distribution of the aperture is disturbed. Therefore at the tensile type fracture, more amount of fluid can flow than the strike-slip type fracture which has the same mean aperture.

REFERENCES

Bhatnagar, P. L., Gross, E. P. & Krook, M. 1954. A model for collision processes in gases. I. Small amplitude processes in charged and neutral one-component systems. *Phys. Rev.* 94: 511–525.

Brown, S. R. 1989. Transport of fluid and electric current through a single fracture. *J. Geophys. Res.* 94: 9429.

Inamuro, T., Yoshino, M. & Ogino, F. 1995. A non-slip boundary condition for lattice boltzmann simulations. *Phys. Fluids* 7: 2928–2930; Erratum: 8 (1996): 1124.

Qian, Y. H., d'Humieres, D. & Lallemand, P. 1992. Lattice BGK models for Navier-Stokes equation. *Europhys. Lett.* 17: 479.

Rothman, D. H. & Zaleski, S. 1997. *Lattice-gas cellular automata-simple models of complex hydrodynamics.* Cambridge: Cambridge University Press.

Succi, S. 2001. *The Lattice Boltzmann Equation for Fluid Dynamics and Beyond.* New York: Oxford University Press.

Wolf-Gladrow 2000. *Lattice-gas cellular automata and lattice Boltzmann models. LNM 1725* Berlin: Springer.

Yoshino, M. 2000. *Numerical analysis of transport phenomena in porous structure by the lattice Boltzmann method*: Ph.D. thesis. Kyoto University.

Copyright © 2003 Swets & Zeitlinger B.V., Lisse, The Netherlands